# SPRING HIPPOCAMPAL RESEARCH CONFERENCE AND BEYOND

EDITED BY: Jochen C. Meier, Steven James Mennerick, Lisa Topolnik, Mariangela Chisari, Akiva Cohen and James Ainge

PUBLISHED IN: Frontiers in Molecular Neuroscience, Frontiers in Neuroscience, Frontiers in Cellular Neuroscience, Frontiers in Behavioral Neuroscience, Frontiers in Systems Neuroscience and Frontiers in Synaptic Neuroscience

frontiers Research Topics

**Frontiers eBook Copyright Statement**

The copyright in the text of individual articles in this eBook is the property of their respective authors or their respective institutions or funders. The copyright in graphics and images within each article may be subject to copyright of other parties. In both cases this is subject to a license granted to Frontiers.

The compilation of articles constituting this eBook is the property of Frontiers.

Each article within this eBook, and the eBook itself, are published under the most recent version of the Creative Commons CC-BY licence. The version current at the date of publication of this eBook is CC-BY 4.0. If the CC-BY licence is updated, the licence granted by Frontiers is automatically updated to the new version.

When exercising any right under the CC-BY licence, Frontiers must be attributed as the original publisher of the article or eBook, as applicable.

Authors have the responsibility of ensuring that any graphics or other materials which are the property of others may be included in the CC-BY licence, but this should be checked before relying on the CC-BY licence to reproduce those materials. Any copyright notices relating to those materials must be complied with.

Copyright and source acknowledgement notices may not be removed and must be displayed in any copy, derivative work or partial copy which includes the elements in question.

All copyright, and all rights therein, are protected by national and international copyright laws. The above represents a summary only. For further information please read Frontiers' Conditions for Website Use and Copyright Statement, and the applicable CC-BY licence.

ISSN 1664-8714
ISBN 978-2-88971-814-6
DOI 10.3389/978-2-88971-814-6

## About Frontiers

Frontiers is more than just an open-access publisher of scholarly articles: it is a pioneering approach to the world of academia, radically improving the way scholarly research is managed. The grand vision of Frontiers is a world where all people have an equal opportunity to seek, share and generate knowledge. Frontiers provides immediate and permanent online open access to all its publications, but this alone is not enough to realize our grand goals.

## Frontiers Journal Series

The Frontiers Journal Series is a multi-tier and interdisciplinary set of open-access, online journals, promising a paradigm shift from the current review, selection and dissemination processes in academic publishing. All Frontiers journals are driven by researchers for researchers; therefore, they constitute a service to the scholarly community. At the same time, the Frontiers Journal Series operates on a revolutionary invention, the tiered publishing system, initially addressing specific communities of scholars, and gradually climbing up to broader public understanding, thus serving the interests of the lay society, too.

## Dedication to Quality

Each Frontiers article is a landmark of the highest quality, thanks to genuinely collaborative interactions between authors and review editors, who include some of the world's best academicians. Research must be certified by peers before entering a stream of knowledge that may eventually reach the public - and shape society; therefore, Frontiers only applies the most rigorous and unbiased reviews.
Frontiers revolutionizes research publishing by freely delivering the most outstanding research, evaluated with no bias from both the academic and social point of view. By applying the most advanced information technologies, Frontiers is catapulting scholarly publishing into a new generation.

## What are Frontiers Research Topics?

Frontiers Research Topics are very popular trademarks of the Frontiers Journals Series: they are collections of at least ten articles, all centered on a particular subject. With their unique mix of varied contributions from Original Research to Review Articles, Frontiers Research Topics unify the most influential researchers, the latest key findings and historical advances in a hot research area! Find out more on how to host your own Frontiers Research Topic or contribute to one as an author by contacting the Frontiers Editorial Office: frontiersin.org/about/contact

# SPRING HIPPOCAMPAL RESEARCH CONFERENCE AND BEYOND

Topic Editors:
**Jochen C. Meier,** Technische Universitat Braunschweig, Germany
**Steven James Mennerick,** Washington University in St. Louis, United States
**Lisa Topolnik,** Laval University, Canada
**Mariangela Chisari,** University of Catania, Italy
**Akiva Cohen,** University of Pennsylvania, United States
**James Ainge,** University of St Andrews, United Kingdom

**Citation:** Meier, J. C., Mennerick, S. J., Topolnik, L., Chisari, M., Cohen, A., Ainge, J., eds. (2021). Spring Hippocampal Research Conference and Beyond. Lausanne: Frontiers Media SA. doi: 10.3389/978-2-88971-814-6

# Table of Contents

frontiers in Molecular Neuroscience

EDITORIAL
published: 12 October 2021
doi: 10.3389/fnmol.2021.773308

# Editorial: Spring Hippocampal Research Conference and Beyond

*James A. Ainge*[1†], *Mariangela Chisari*[2†], *Akiva Cohen*[3†], *Steven J. Mennerick*[4†], *Lisa Topolnik*[5,6†] *and Jochen C. Meier*[7*†]

[1] School of Psychology and Neuroscience, University of St Andrews, St Andrews, United Kingdom, [2] Section of Pharmacology, Department of Biomedical and Biotechnological Sciences, University of Catania, Catania, Italy, [3] University of Pennsylvania and Children's Hospital of Philadelphia, Philadelphia, PA, United States, [4] Department of Psychiatry, Taylor Family Institute for Innovative Psychiatric Research, Washington University in St. Louis School of Medicine, St. Louis, MO, United States, [5] Department of Biochemistry, Microbiology and Bio-Informatics, Laval University, Québec City, QC, Canada, [6] Neuroscience Axis, CHU de Québec Research Center (CHUL), Québec City, QC, Canada, [7] Division Cell Physiology, Technical University Braunschweig, Zoological Institute, Braunschweig, Germany

**Keywords: hippocampus, memory, mood, neurotransmitters, development**

## Editorial on the Research Topic

## Spring Hippocampal Research Conference and Beyond

The Spring Hippocampal Research Conference is devoted to all aspects of hippocampal structure, connectivity, function, and malfunction. It is an open meeting built around small symposia proposed by the participants. The meeting brings together some of the leading figures in hippocampal research but also provides an opportunity for early career researchers to present to a specialist audience. As such the meeting tackles the latest issues in hippocampal research and provides one of the most important forums in the world for discussing all aspects of the hippocampus. It has been held every other year since 1988, except 2021 due to Covid-19 pandemic. While it does not make up for the meeting we all missed in 2021, this special issue has provided an opportunity for researchers to present recent research in rodents, primates and humans examining the hippocampus from all of these different perspectives.

The special issue contains a number of articles examining the role of the hippocampus in spatial memory and navigation. Bretas et al. examined place and reward signals in the monkey hippocampus using a virtual navigation task. They showed that, as in rodents, place cells in the monkey hippocampus represent overlapping path sections using distinct ensembles which also code for various characteristics of reward. Two imaging studies present findings of how the human hippocampus processes different aspects of spatial memory. Faulmann et al. show that cognitive map retrieval is predominantly associated with posterior parahippocampal rather than hippocampal activation. They went on to show that this activation is significantly greater during direction but not distance estimation. Dahmani et al. examined the relationship between hippocampal volume and performance on both navigation and olfactory identification tasks. They found that right fimbria-fornix volume was correlated with both tasks in participants who used hippocampus-based spatial memory strategies.

The special issue also includes articles examining hippocampal oscillations. Grossberg presents a comprehensive review of spatial representations within the hippocampal-entorhinal network together with a theoretical synthesis that explains many findings regarding theta oscillations within the hippocampus.

Social recognition is fundamental for social decision making and the establishment of long-lasting affiliative behaviors. The study of Cymerblit-Sabba et al. revealed that social recognition and preference rely on activation of the CA2 hippocampal subfield *via* the hypothalamic paraventricular nucleus, which can represent a part of an evolutionary conserved neural circuitry for formation of social memory. Furthermore, encoding of social memory is regulated by oxytocin acting through the oxytocin receptor (Oxtr). Young and Song examined the neuronal expression of

OPEN ACCESS

***Edited and reviewed by:***
*Clive R. Bramham,*
*University of Bergen, Norway*

***Correspondence:**
*Jochen C. Meier*
*jochen.meier@tu-braunschweig.de*

[†]*These authors have contributed equally to this work*

***Specialty section:***
*This article was submitted to Neuroplasticity and Development, a section of the journal Frontiers in Molecular Neuroscience*

***Received:*** *09 September 2021*
***Accepted:*** *20 September 2021*
***Published:*** *12 October 2021*

***Citation:***
*Ainge JA, Chisari M, Cohen A, Mennerick SJ, Topolnik L and Meier JC (2021) Editorial: Spring Hippocampal Research Conference and Beyond. Front. Mol. Neurosci. 14:773308. doi: 10.3389/fnmol.2021.773308*

Oxtr transcripts in the dorsal hippocampus. The study revealed that in addition to CA2 and CA3 principal cells, Oxtr is present in different types of inhibitory interneurons, pointing to a potentially important role of oxytocin in coordination of hippocampal network activity by modulating inhibitory circuits.

The region-specific differences in the modulation of synaptic transmission along the dorso-ventral axis of the hippocampus remain in focus of research. Recently, Dubovyk and Manahan-Vaughan reported a much higher expression of dopamine receptor 2 in the ventral portion of the hippocampus, which can support the region-specific synaptic plasticity and dopamine-dependent behavioral outcomes. Furthermore, Trompoukis and Papatheodoropoulos revealed a different contribution of the GABA-B receptors to heterosynaptic depression between the two hippocampal regions.

There were and still are many studies highlighting a critical role of the hippocampal formation in neuropsychiatric disorders. In this issue, we paid particular attention to Alzheimer disease (AD), epilepsy, aging and cognitive decline, psychosis and schizophrenia, multiple sclerosis, and traumatic brain injury.

In particular, rewiring and synaptic reorganization in the dentate gyrus after brain injury were discussed by Del Turco et al. The authors studied re-innervation of the denervated dentate gyrus in organotypic tissue cultures of the entorhinal cortex and hippocampus. They found that the majority of sprouting associational calretinin-positive axons are mossy cell axons—nearly the entire dentate gyrus entorhinal target zone was re-innervated by sprouting of associational and commissural mossy cell axons.

Along this line, by deleting BDNF receptor TrkB from serotonergic neurons in the adult brain, Sahu et al. investigated the effects of increased brain serotonin levels on energy metabolism and learning and memory. In spite of increased food intake, the transgenic mice were significantly leaner than their wildtype littermates. The results suggest that loss of the TrkB receptor in the 5-HT neurons increases 5-HT levels, thereby regulating neuronal plasticity and behavior. Furthermore, reduction of TrkB in 5-HT neurons increased proliferation, but not long-term survival, of hippocampal cells that was consistent with increase in immature neuronal markers such as doublecortin and calretinin in the transgenic animals.

Bartsch and Behr used N-methyl-D-aspartate receptor (NMDAR) antagonist MK-801 to model first-episode psychosis in rats and studied long-term potentiation (LTP) in subicular regular-firing cells in acute hippocampal slices. The authors provide evidence for a non-canonical postsynaptic NMDAR-independent LTP in ventral subicular but not in CA1 regular-firing pyramidal cells, which was dependent on D1/D5 dopamine receptor activation, postsynaptic $Ca^{2+}$ signaling and activation of protein kinase A. This aberrant form of LTP in ventral subicular regular-firing neurons was suggested to interfere with physiological hippocampal output processing and to contribute to hippocampal dysfunction in psychotic events.

Manzella et al. examined another negative modulator of NMDA receptor function, ketamine, when administered in early life, simulating pediatric anesthetic use. Previous work has shown that anesthetics produce neurotoxicity in brain areas like the subiculum and adverse neurocognitive outcomes. Here, the authors showed that subiculum-related gamma oscillations during non-REM sleep were altered by early ketamine exposure when assayed in adolescence. Synaptic plasticity, measured as LTP, was also disrupted. However, the authors found no overt disruption of sleep macrostructure. The results offer a potential functional substrate for neurocognitive impairments observed with early exposure to anesthetics.

In contrast to the classical role of neurotransmitter dysregulation in disease Shen et al. provided evidence for a novel role of sarcosine (aka N-methylglycine; a glycine transporter 1 GlyT1 inhibitor) as antiepileptic drug. The authors previously demonstrated in rodent epilepsy models that augmentation of glycine suppressed chronic seizures and altered acute seizure thresholds. In this study, they developed a rapid hippocampal kindling model to produce stable epileptogenesis and demonstrated a resultant overexpression of GlyT1 and dysregulated DNA methylation in kindled rats. They further provided experimental evidence that sarcosine can delay kindling epileptogenesis, which was associated with altered DNA methylation. Sarcosine treatment during kindling changed hippocampal 5 mC and 5 hmC levels and modified the expression levels of the demethylase TET1.

Disinhibition can be important for different forms of hippocampal learning, and its structural or functional alterations can be involved in cognitive decline associated with aging. However, how the properties of cells making up the disinhibitory circuits may change during aging remains unknown. Francavilla et al. discover the age-dependent changes in morphological and physiological properties of vasoactive intestinal peptide (VIP)-expressing, type 3 interneuron-specific (IS3) GABAergic neurons that reside in the CA1 hippocampus. The age-dependent changes in the intrinsic properties and the firing of IS3 cells occur in parallel with changes in the inhibitory drive received by their postsynaptic GABAergic targets. These data provide first evidence on the age-dependent remodeling in intrinsic properties of a disinhibitory cell type in the hippocampus and demonstrate an overall increase in inhibition of inhibitory interneurons, with a possible hyperactivity of CA1 pyramidal cells.

Karunakaran researches behavioral methods for determining if an individual will develop Alzheimer's disease at a later stage. A mouse model for Alzheimer's disease, APPswe/PS1dE9 (APP/PS1) displays amyloidosis and is a model for Alzheimer's disease-like symptoms. Previous studies have attempted to study cognitive deficits in these mice, but these previous experiments lack sensitivity and specificity. This study analyzes the results of the Morris Water Maze behavioral test in different ways that allow for increased specificity in behavioral testing. This study found that even if APP/PS1 mice had a similar success rate on the final day of testing, they had more unsuccessful trials during training to get to that result. This study also examined the strategies that the mice used to find the platform. Some of these strategies were spatially based, meaning that they used the hippocampus. Some of these strategies were non-spatial, meaning that they were used independent of the hippocampus. When tested, the wild-type mice and APP/PS1 employed different sequences of learning strategies to find the

platform. Specifically, many of the APP/PS1 mice employed a non-spatial strategy called circling. This study demonstrates that by examining behavioral experiments with more details, it is possible to find minor alterations in behavior that can lead to significant discoveries, which could lead to earlier diagnoses in humans.

The pro-inflammatory cytokines that are released in response to CNS injury are involved in a number of neurodegenerative disorders. However, still little is known regarding the involvement of these factors in normal brain functioning. The study of Chai et al. examined the developmental profile in expression of the pro-inflammatory cytokine macrophage inhibitory factor (MIF) in hippocampus. Interestingly, in addition to glial precursor cells in dentate gyrus, MIF was expressed in parvalbumin- and reelin-expressing interneurons and involved in neurite outgrowth during hippocampal development.

Cinalli et al. examines the different roles that hippocampal CA1 and the Perirhinal cortex (Prh) play in spatial object memory. The authors had mice perform a novel object behavior task where they explored objects for different lengths of time to form "weak" or "strong" memories. For weak memories, the animals explored the objects for 10 s, for strong memories the animals explored the objects for 30 s. The animals were then tested 24 h later by replacing one of the objects. For one group of mice, the researchers bilaterally infused muscimol into either the CA1 or the Prh immediately after the learning session. During the test session, inactivation of CA1 impaired the mice from strong object memory, but not weak object memory. Inactivation of the Prh impaired weak object memory but not strong object memory. The researchers also examined the levels of the protein ARC, a protein that is involved with synaptic plasticity by using immunohistochemistry to examine protein and qPCR to examine the levels of mRNA. The researchers found that there were higher levels of ARC protein in CA1 after strong object memory compared to the Prh and higher levels of ARC protein in the Prh after weak object memory compared to CA1. ARC mRNA was significantly lower in the Prh during the strong object memory task, which may indicate that synaptic plasticity is reduced in the Prh during strong object memory formation. Overall, this paper provides evidence that CA1 is involved in the formation of strong object memories and Prh is involved in the formation of weak object memories. The authors suggest that these two processes are complementary and the two regions may work together in object memory formation.

Smith et al. demonstrates that unilateral and bilateral damage to the vestibular system causes spatial memory impairment and hippocampal place cell dysfunction, few studies have investigated the vestibular system's role in modulating hippocampal LTP and NMDA receptor expression. This review compares and evaluates *in vivo* and *in vitro* rodent studies investigating the nature of LTP in the hippocampus following vestibular lesions. The review cites evidence of decreased neuronal excitability *in vitro* following a unilateral vestibular lesion (UVL), but states *in vivo* studies found no such difference following a bilateral vestibular lesion (BVL). *In vivo* BVL studies were also inconsistent amongst each other, with contradictory findings in the hippocampal dentate gyrus subregion following LTP. Finally, one study found NMDA receptor subunit expression decreased following UVL, whereas another study found no change in NMDA receptor subunit expression after UVL. The review concludes that, using the body of literature available, it is difficult to form a cohesive view of the vestibular system's role in modulating hippocampal LTP due to inconsistent findings and multiple methodological differences between studies.

Although it is known that hippocampal oriens-lacunosum/moleculare (OLM) cells express hyperpolarization-activated cation channels (h-channels), it is unclear whether these h-channels are localized in OLM dendrites. Sekulić et al. constructed three computational multi-compartment models of OLM cells from the hippocampal CA1 region based on biophysical, morphological and h-channel parameters derived from experimental OLM cell recordings. After determining their models could correctly predict OLM cell biophysical properties, the authors combined electrophysiology together with a computational multi-compartmental model of OLM cells to identify h-channels in OLM cells based on their biophysical properties. Results demonstrated that their multi-compartment models of OLM cells needed h-channels present in the dendrites in order to be compatible with experimental data, suggesting h-channels are present in the dendrites of CA1 OLM cells. Overall, this work establishes that it is possible to combine experimental methods with computational modeling to characterize the biophysical properties of neurons.

Experiments performed by Memon et al. explore for the first time the possibility that in protein PTEN-induced kinase 1 (PINK1) KO rats, a model for autosomal recessive familial Parkinson's disease (PD), non-motor symptoms such as cognitive dysfunction might be affected by the lack of this protein. They tested this hypothesis evaluating short- and long-term plasticity along with the synaptic transmission in hippocampal CA3-CA1 pathway. Their results indicate that hippocampal plasticity is not affected by PINK1 loss, at an early age when motor symptoms are starting to appear and the excitatory transmission is already compromised in the striatum.

Glycine represents an important inhibitory influence in the brainstem and spinal cord *via* glycine-activated chloride channels, and GABA-A receptors medicate inhibition throughout the CNS. New modulators of these receptor classes could represent therapeutics. Bukanova et al. examined the effect of novel androstane and andrestene neuroactive steroids on both receptor types and found generally stronger and more potent effects on glycine receptors. Because glycine receptors are found on many brain cells, even those without glycinergic synapses, these compounds could be of widespread utility. Schaefer et al. investigated the role of glycine receptor mutations on anxiety and startle phenotypes. Kaouane et al. discuss the role of corticosterone and glucocorticoid receptor activation in the dorsal hippocampus with regard to post-traumatic stress disorder and fear memory. Meanwhile, Lu et al. re-examined the role of GABA-A receptor subclasses in mediating the impact of pregnane neurosteroids on inhibition. Using knock-in, pharmacoresistant mouse lines, they found, in contrast with some previous results, little evidence for subtype selectivity

of allopregnanolone and allotetrahydrodeoxycorticosterone (THDOC). This could alter understanding of the impact of neurosteroids on behaviors, including mood.

Dawitz et al. investigated the role of GABA and glutamate in the emergence of spontaneous synchronized network activity (SSNA) and their role in the development of neuronal circuits during the 1st postnatal weeks. They confirm that in mouse medial entorhinal cortex during the 2nd postnatal week, SSNA persists and in fact peaks, and is dependent on ionotropic glutamatergic signaling. More specifically, the authors say: SSNA differs from that observed during the 1st postnatal week in two ways: First, the entorhinal cortex does not drive network activity in the hippocampus but only in the neighboring neocortex. Second, GABA does not drive network activity but influences it in a manner that is dependent both on age and receptor type. The authors conclude that while there is a partial mechanistic overlap in SSNA between the 1st and 2nd postnatal weeks, unique mechanistic features do emerge during the 2nd week, suggestive of different or additional functions of medial entorhinal cortex within the hippocampal-entorhinal circuitry with increasing maturation.

Altogether, this article collection addressed the latest hippocampal research and can be inspiring for the next Spring Hippocampal Research Conference in Verona (Italy) in 2023, which we are all looking forward to attending in person.

## AUTHOR CONTRIBUTIONS

All authors listed have made a substantial, direct and intellectual contribution to the work, and approved it for publication.

**Conflict of Interest:** The authors declare that the research was conducted in the absence of any commercial or financial relationships that could be construed as a potential conflict of interest.

**Publisher's Note:** All claims expressed in this article are solely those of the authors and do not necessarily represent those of their affiliated organizations, or those of the publisher, the editors and the reviewers. Any product that may be evaluated in this article, or claim that may be made by its manufacturer, is not guaranteed or endorsed by the publisher.

*Copyright © 2021 Ainge, Chisari, Cohen, Mennerick, Topolnik and Meier. This is an open-access article distributed under the terms of the Creative Commons Attribution License (CC BY). The use, distribution or reproduction in other forums is permitted, provided the original author(s) and the copyright owner(s) are credited and that the original publication in this journal is cited, in accordance with accepted academic practice. No use, distribution or reproduction is permitted which does not comply with these terms.*

frontiers in Systems Neuroscience

ORIGINAL RESEARCH
published: 12 September 2019
doi: 10.3389/fnsys.2019.00048

# Neural Representation of Overlapping Path Segments and Reward Acquisitions in the Monkey Hippocampus

*Rafael Vieira Bretas[1,2], Jumpei Matsumoto[1], Hiroshi Nishimaru[1], Yusaku Takamura[1], Etsuro Hori[1], Taketoshi Ono[1] and Hisao Nishijo[1]**

[1] System Emotional Science, Graduate School of Medicine and Pharmaceutical University, University of Toyama, Toyama, Japan, [2] Symbolic Cognitive Development, Center for Biosystems Dynamics Research, RIKEN, Kobe, Japan

Disambiguation of overlapping events is thought to be the hallmark of episodic memory. Recent rodent studies have reported that when navigating overlapping path segments in the different routes place cell activity in the same overlapping path segments were remapped according to different goal locations in different routes. However, it is unknown how hippocampal neurons disambiguate reward delivery in overlapping path segments in different routes. In the present study, we recorded monkey hippocampal neurons during performance of three virtual navigation (VN) tasks in which a monkey alternately navigated two different routes that included overlapping path segments (common central hallway) and acquired rewards in the same locations in overlapping path segments by manipulating a joystick. The results indicated that out of 106 hippocampal neurons, 57 displayed place-related activity (place-related neurons), and 18 neurons showed route-dependent activity in the overlapping path segments, consistent with a hippocampal role in the disambiguation of overlapping path segments. Moreover, 75 neurons showed neural correlates to reward delivery (reward-related neurons), whereas 56 of these 75 reward-related neurons showed route-dependent reward-related activity in the overlapping path segments. The ensemble activity of reward-related neurons represented reward delivery, locations, and routes in the overlapping path segments. In addition, ensemble activity patterns of hippocampal neurons more distinctly represented overlapping path segments than non-overlapping path segments. The present results provide neurophysiological evidence of disambiguation in the monkey hippocampus, consistent with a hippocampal role in episodic memory, and support a recent computational model of "neural differentiation," in which overlapping items are better represented by repeated retrieval with competitive learning.

**Keywords: hippocampus, place cells, navigation, overlapping, disambiguation, neural differentiation**

OPEN ACCESS

***Edited by:***
*James Ainge, University of St Andrews, United Kingdom*

***Reviewed by:***
*Amy L. Griffin, University of Delaware, United States*
*Sylvia Wirth, Centre National de la Recherche Scientifique (CNRS), France*

***Correspondence:**
*Hisao Nishijo*
*nishijo@med.u-toyama.ac.jp*

***Received:*** *06 June 2019*
***Accepted:*** *29 August 2019*
***Published:*** *12 September 2019*

***Citation:***
*Bretas RV, Matsumoto J, Nishimaru H, Takamura Y, Hori E, Ono T and Nishijo H (2019) Neural Representation of Overlapping Path Segments and Reward Acquisitions in the Monkey Hippocampus. Front. Syst. Neurosci. 13:48. doi: 10.3389/fnsys.2019.00048*

## INTRODUCTION

The hippocampal formation (HF) has been implicated in human episodic memory and spatial navigation (Scoville and Milner, 1957; O'Keefe and Nadel, 1978; Squire and Zola-Morgan, 1991; Tulving and Markowitsch, 1998; Burgess et al., 2002). Consistent with these roles of the HF, neurophysiological studies have also reported that HF place cells code subject's own position in

a specific place of the environment that the rodents navigate (O'Keefe and Dostrovsky, 1971; McNaughton et al., 1983; Muller and Kubie, 1987; Eichenbaum et al., 1990). In monkeys, the activity of place-related neurons in the HF increased when the subjects navigated a particular location in a virtual or real environmental space (Ono et al., 1993; Matsumura et al., 1999; Ludvig et al., 2004; Hori et al., 2005; Furuya et al., 2014; Wirth et al., 2017; Hazama and Tamura, 2019). This has also been demonstrated in the human HF (Ekstrom et al., 2003; Miller et al., 2013). It has been proposed that these place cells play an important role in episodic memory (O'Keefe and Nadel, 1978; Eichenbaum, 2017).

The ability to distinguish overlapping items in time and space is critical to episodic memory. Human fMRI studies have reported that the HF encodes distinctly the same path segments in different routes (Brown et al., 2010; Chanales et al., 2017). In rodent studies, animals navigated different routes that shared a common path segment, and some HF place cells fired differently in this segment depending on the routes (Frank et al., 2000; Wood et al., 2000; Ferbinteanu and Shapiro, 2003; Dayawansa et al., 2006; Ainge et al., 2007, 2012; Grieves et al., 2016). That is, the neurons differentially fired in the same position depending on where the animal had come from or where it was going (route-dependent activity). These results suggested that the HF plays a role in prospective and retrospective coding in episodic memory, in which a sequence of specific behaviors is coded in association with spatial information (Catanese et al., 2014). However, route-dependent neuronal activity in non-human primates remains unknown.

Neuronal responses to rewards are another important factor of episodic memory. A human fMRI study reported that reward values associated with items affected the encoding of those items in the HF (Kuhl et al., 2010). The HF receives reward-related signals from dopaminergic, cholinergic, and amygdalar neurons (Lisman and Grace, 2005; Terada et al., 2013; Teles-Grilo Ruivo et al., 2017). Furthermore, the activity of rodent and monkey HF neurons changed in response to reward delivery or locations associated with reward (Rolls and Xiang, 2005; Ho et al., 2008, 2011; Xia et al., 2017). A recent study using rodents reported that some HF neurons specialized for encoding reward location are active not only in one environment but also across multiple environments (Gauthier and Tank, 2018). However, it is unknown whether reward-related neurons are active in multiple environments in primates. Furthermore, it is also unknown how HF neurons disambiguate reward delivery in overlapping situations in both rodents and primates.

Thus, two types of HF neurons, place cells coding subject's own positions and reward-related neurons (goal-directed cells) coding locations of goals, are supposed to play an important role in episodic memory as well as navigation to a goal in rodent and bat HF (Burgess and O'Keefe, 1996; Poucet and Hok, 2017; Sarel et al., 2017). However, it is unknown how these HF neurons contribute to disambiguation of routes and reward delivery in primates.

We hypothesized that both of these types of HF neurons were involved in disambiguation of routes and reward delivery in monkeys, and that environments surrounding a maze could affect responsiveness of reward-related neurons (i.e., different reward-related neurons would respond in different environments) since a previous study reported that monkey HF neurons were sensitive to the surrounding environment of the maze (Hori et al., 2005). In the present study, the monkeys navigated along a figure 8-shaped track to acquire rewards in a virtual environment, and we analyzed the HF neuronal activity while they passed the overlapping segments and received the reward. We examined whether population activity of place-related and reward-related HF neurons in the overlapping path segments disambiguates overlapping items (navigation and reward delivery in the same path segment but in different routes), and as well as whether reward-related activity across different environmental settings could differentiate multiple environments.

# MATERIALS AND METHODS

## Animals

Two male adult Japanese monkey (Macaca fuscata), weighing 9.0 (monkey A), and 10.5 (monkey B) kg, respectively, were used in the current experiment. The monkeys were housed individually in the home cage and supplied with monkey rations *ad libitum* and daily fruits or vegetables. Environmental enrichment, in the form of toys, was provided daily. Although the animals were deprived of water in the home cage, they were able to receive liquid reward during the experimental session. Supplemental water and vegetables were given after each day's session. To assess the monkey's health, their weight was routinely monitored. The experiment was conducted in strict compliance with the United States Public Health Service Policy on Human Care and Use of Laboratory Animals, the National Institutes of Health Guide for the Care and Use of Laboratory Animals, and the Guidelines for the Care and Use of Laboratory Animals at the University of Toyama. The experimental protocol was approved by the ethical committee for animal experiments in the University of Toyama.

## Experimental Apparatus

During the recording session, the animal was placed on a restraining chair and had its head painlessly fixed with an acrylic U-shaped frame that was surgically implanted into the monkey's skull, which worked as a movement restrainer (Ono et al., 1993; Matsumura et al., 1999; Hori et al., 2005; Furuya et al., 2014). The chair consisted of an acrylic box with wheels, in which the monkey could be transferred from its home cage to the experimental room. Inside this box, the monkey could sit comfortably to perform the task. An infrared charge-coupled device (CCD) camera for eye-movement monitoring was firmly attached to the chair with a steel rod. During recording sessions, the monkey's eye position was monitored with 33 ms time resolution using an eye-monitoring system (Matsuda, 1996). In the experimental room, the chair was positioned 2.6 m away from a wide projector panel, which was 1.5 m high × 1.9 m wide, displaying 3D polarized images projected by an LCD projector located behind and above the monkey (**Figure 1A**). The animal was trained to perform the task by looking at the screen using

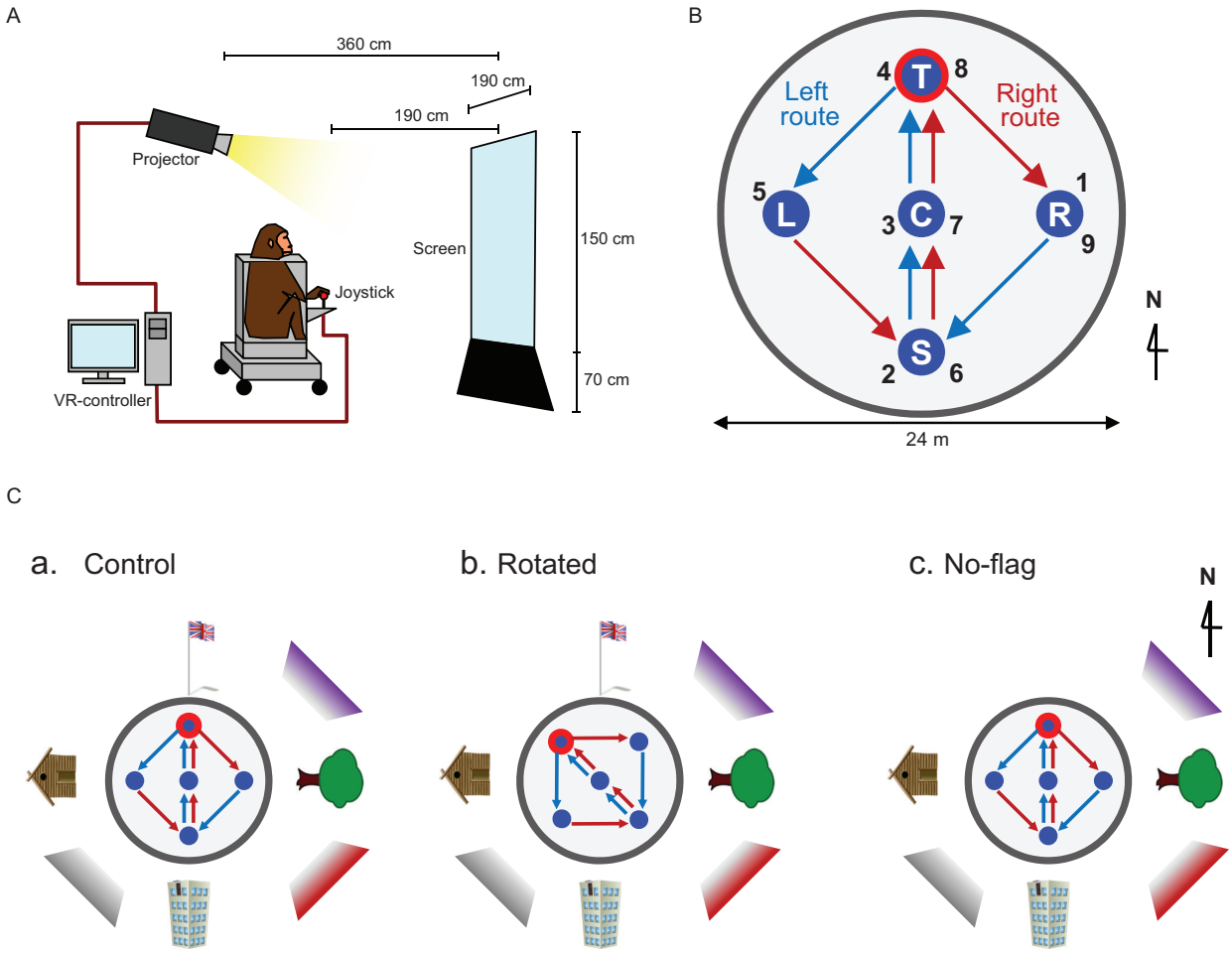


**FIGURE 1 |** Schematic illustration of virtual navigation (VN) in monkeys. **(A)** Experimental set up. **(B)** Movable area. In the task, the subject was required to navigate the movable area in a specific sequence. In the left route (blue arrows), the monkey was required to navigate, and visit the reward areas in the following order: location sequence numbers 1–5. In the right route (red arrows), the monkey was required to navigate, and visit the reward areas in the following order: location sequence numbers 5–9. The common central hallway (location sequence numbers 2–4 and 6–8) was overlapped by the two routes. **(C)** Spatial arrangement of the three VN tasks used in the current study.

polarized lenses, attached to the outer part of the chair, i.e., as if the monkey was wearing 3D polarized glasses. During the task, the room lights were turned off and the animal had no view of the experimenter.

A joystick was attached to the front wall of the chair. The animal could acquire a liquid reward (i.e., sports drink) by manipulating the joystick through a window in the chair. Liquid delivery was controlled using an electromagnetic valve connected to a tube projecting through the rear side of the monkey's chair. The monkey could not reach any object other than the joystick.

## Behavioral Paradigms

The animals were first trained to perform a control virtual navigation (VN) task, where they were required to navigate in a 3D environment by manipulating the joystick (Hori et al., 2005; Furuya et al., 2014). For this task, a large 3D open-field space with a 180-m diameter was created using a 3D software (EON Studio ver. 2.5.2, EON Reality, United States) (**Figure 1B**). However, the monkey could move only inside a limited 24-m diameter space located in the center of the open-field, surrounded by a wall (with a height of 0.5 m). This central part of the virtual space will be henceforth referred to as the mobility area. The open field contained five reward areas (with a diameter of 2.8 m) that were placed in the center and apex of a diamond shape within the mobility area (S, C, T, L, and R in **Figure 1B**). Extra-maze cues (i.e., one tree, one hut, one building, and one flag) were located 2.0 m away from the wall outside the mobility area. Another extra-maze reference points (i.e., three posters) were located on the background, serving as the distal cues.

In this task, the animal was required to track the reward areas in a specific order; (1) R → S → C → T → L (location sequence from No. 1 to 5; left route), and (2) L → S → C → T → R (location sequence from No. 5 to 9; right route) (**Figure 1B**). The animal received a liquid reward immediately after entering each reward area in the correct sequence; the monkey could obtain a total of 8 rewards in each trial. No delay time before reward

delivery was imposed in each reward area. Thus, the left and right routes shared the same path segment (common central hallway). The movements on the common central hallway were associated with right and left turn at T-reward area, respectively. Each HF neuron was tested with at least 7 trials.

One monkey (monkey A) was trained only with a control environment (a control VN task). Spatial arrangement of the distal cues in the control VN task is shown in **Figure 1Ca**. To investigate reward-related activity in multiple environments (see section "Introduction"), another monkey (monkey B) was trained not only in the control VN task but also in two different environments (rotated and no-flag VN tasks). In the rotated VN task, the reward locations in the movable area and two routes were rotated by 45° in the counter-clockwise direction (**Figure 1Cb**). In the no-flag VN task, the spatial arrangement of the distal cues was the same as that in the control VN task except that the flag was eliminated (**Figure 1Cc**). The intra-maze cues and routes were identical in all these different virtual spaces.

## Training

Initially the monkeys were trained on a pointer translocation task in which it learned to operate the joystick (Furuya et al., 2014). First, they had to move a large pointer to two different reward areas with a large size on the screen. Initially, only movements in one dimension were allowed, under a virtual guide path making impossible for the cursor to leave the horizontal or vertical axis. As they became more skillful, the virtual guide was removed, the size of the reward areas was gradually decreased and locations of the reward areas moved apart from each other until the animal developed the ability to control the joystick on every axis. It took 4 months for the monkeys to learn to move the joystick freely in all directions without the cursor movement limitation. When the monkeys could perform the cursor translocation task with a criterion of 99% correct responses, they were moved to the next level and training for the VN tasks began.

For the VN training, the animal had to get used to the VN environment as well. In the first step of training the subject manipulated a monkey avatar on the screen from a top down view. Each day the camera angle and distance from the avatar was decreased. At the end of the training the subject performed from a first-person view in a real-world like perspective. The monkey initially manipulated the joystick under physical limitations, made with a metal plate below the joystick, which allowed three movements simultaneously to the left, right and front only, so the animal could learn that he must be facing the reward area to acquire the reward. By moving the joystick to the front, the monkey could move forward in the virtual space. By moving the joystick to the right and left, the monkey could turn clockwise and anti-clockwise in the virtual space, respectively. Both monkeys were initially trained in the control VN task, and then monkey B was further trained in the rotated and no-flag VN tasks.

## Surgery

After the completion of the training period (approximately 1 year), the animal was implanted with a head movement restrainer (U-shaped acrylic frame) on the skull (Hori et al., 2005; Furuya et al., 2014). The surgical procedure was conducted under aseptic conditions. The animal was anesthetized with a combination of medetomidine hydrochloride (0.5 mg/kg, i.m.) and ketamine hydrochloride (5.0 mg/kg, i.m.). The frame was anchored with dental acrylic to tungsten bolts inserted in the skull. During the surgery, heart, respiratory functions, and rectal temperature were monitored (LifeScope14, Nihon Kohden, Tokyo, Japan). A thermal blanket was used to maintain the body temperature at 36 ± 0.5°C. Antibiotics were administered topically and systemically for 1 week to prevent infection. Two weeks after the surgery, training was resumed with the subject's head fixed to the stereotaxic apparatus. Performance criterion (95% correct ratio) was once again attained within 2 weeks. A brain MRI was acquired and stereotaxic coordinates of the target area were checked against the stereotaxic atlas (Kusama and Mabuchi, 1970). Finally, the subject was again anesthetized with ketamine hydrochloride (0.5 mg/kg, i.m.) and a hole was opened in the animal's skull above the target area, so that the electrode could be inserted in the recording sessions.

## Recording Procedures and Data Acquisition

After the monkey was placed in the monkey chair, a quartz insulated platinum tetrode (Thomas Recording GmbH, Giessen, Germany; $Z$ = 0.6–1.0 MΩ at 1000 Hz) was stereotaxically inserted stepwise with a pulse motor-driven manipulator (SM-21S, Narishige, Tokyo, Japan) into various parts of the HF. In monkey A, neuronal activity was recorded from the left HF while the monkey performed the control VN task. In monkey B, neuronal activity was recorded from the right HF while the monkey performed the three VN tasks. Data on the analog signals of neuronal activities, triggers for the liquid reward, X-Y coordinates of the monkey in the virtual space, joystick positions, and eye position were digitized and stored on a computer via a Multichannel Acquisition Processor system (Plexon Inc., Dallas, TX, United States). The amplified neuronal signals were digitized at a 40-kHz sampling rate; 800-μs waveforms that crossed an experimenter-defined threshold were stored on a computer hard disk for offline spike sorting.

## Unit Identification

The digitized waveforms of the isolated units were superimposed to check for invariability during the recording sessions. The data were then transferred to the analysis software NeuroExplorer (Nex Technologies, Littleton, MA, United States). Recorded waveforms were projected to a principal component subspace using NDManager (Hazan et al., 2006)[1] and semi-automatically sorted into single units using KlustaKwik (Harris et al., 2000)[2] and Kluster (Hazan et al., 2006; see text footnote 1) as outlined by previous studies (e.g., Maingret et al., 2016; Patrono et al., 2017). Each cluster of neuronal spikes was then assessed manually to ensure that the cluster boundaries were well separated and that the waveform shapes were consistent with action potentials. Further, an autocorrelogram

[1] http://neurosuite.sourceforge.net/

[2] http://klustakwik.sourceforge.net/

was constructed for each isolated cluster. An absolute refractory period of at least 1.0 ms was used to exclude suspected multiple units.

## Neural Correlates to Space

For the analysis of place fields, the mobility area in the VN tasks was divided into 30 × 30 pixels grids. The mean firing rate for each pixel was defined as the average number of spikes per second for all visits to that pixel during VN. Then, a whole task mean firing rate (M) for each VN task was calculated by averaging the mean firing rate during the whole task duration. Finally, the firing rate was smoothed using a Gaussian function according to a 3-pixel radius. If the subject did not visit the same pixel for at least 300 ms during the task, those pixel data were not considered for place field analysis.

Place fields in the VN tasks, which were defined as the pixels in which the activities of the HF neurons increased, were identified based on the mean firing rates (Furuya et al., 2014). Only place fields that had at least one pixel with a mean firing rate exceeding twice the mean firing rates and one adjacent pixel with a mean firing rate exceeding 1.5-times the mean firing rates were analyzed separately in each route in each VN task. The place fields could be expanded through any edge shared by two pixels meeting the criterion (>1.5-times the mean firing rates). If one or more neighboring pixels satisfied the criterion, the field was expanded to include those pixel(s). Each added pixel was then tested for the presence of a neighboring pixel that met the criterion. When no neighboring pixel satisfied the criterion, the limit of the field was identified. The minimum size for a place field was set at 9 pixels with a minimum of three visits during the task. Place-related neurons in the VN tasks were defined as neurons that displayed the place field(s), as noted above, in the either left or right route, in at least one of the three VN tasks. The definition of place field in reference to the total mean firing rates was based on previous studies (Muller et al., 1987; Kobayashi et al., 1997; Matsumura et al., 1999; Harvey et al., 2009). The monkey's trajectory was divided into two routes as follows: the left and right routes. To make sure the place field(s) located in the transition between the two routes were detected, there was a 1-s overlap between the left and right routes: the initial 1-s data of the right route included the last 1-s of the left route before entering the left reward area, while the initial 1-s data of the left route included the last 1-s of the right route before entering the right reward area. Place fields were separately analyzed using data in each route. The firing rate maps of either the left or right route in the control VN task were used as the control. The firing rate maps in the other tasks were also constructed separately for the left and right routes.

To analyze effects of different routes on place-related activity in the same path segment, the common central hallway between the two reward locations (C and T) was divided into three zones (i.e., zones 1, 2, and 3). Neural activity in the common central hallway was analyzed using a two-way analysis of variance (ANOVA) with zone and route as factors. Neurons that displayed a significant main effect of route ($p < 0.05$) and/or a significant interaction between zone and route ($p < 0.05$) were defined as route-dependent neurons.

## Neural Correlates to Reward Delivery

Mean firing rates around reward delivery were analyzed using one-way and three-way ANOVAs to examine whether reward influenced the activity of the HF neurons. A one-way ANOVA using peri-event histograms constructed during a period of 4 s (2 s before and 2 s after reward delivery) in successive 1-s bins in each reward area, was used to estimate the neural responses to rewards. Reward-related neurons were defined as such if they showed a significant main effect at least at one of the reward areas in either the left or right route.

To examine the effects of routes on responses to reward delivery in the common central hallway, the firing rates were analyzed using a three-way ANOVA with reward area (T vs. C vs. S), period (two 1-s periods before and after reward delivery), and route (left vs. right route) as factors. The responses to rewards were considered to be modulated by routes (route-dependent reward-related neurons) if a significant main effect of route and/or significant interactions between reward area and route, period and route, or reward area, route, and period were observed ($p < 0.05$). For the neurons with significant interaction(s), simple main effects were used as a *post hoc* test to analyze firing rates ($p < 0.05$) in each specific condition depending on the interaction.

In the present study, the path segment to the T-reward area overlapped in the left and right routes (overlapping path condition), whereas the path segments to L- and R-reward areas did not overlap (non-overlapping path condition). Previous fMRI studies reported that overlapping items were more distinctly represented than non-overlapping items in the human HF (Chanales et al., 2017; Kim et al., 2017). If pre-reward activity carries route information, we hypothesized that representation of the six path segments by ensemble pre-reward activity in the left and right routes across the three VN tasks would be more distinct in the overlapping, rather than the non-overlapping, path condition. To test this hypothesis, the mean correlation among population vectors consisting of ensemble pre-reward neuronal activity in the six path segments in the overlapping path condition was compared to that in the non-overlapping path condition (paired $t$-test, $p < 0.05$). Each pre-reward activity was normalized by mean firing rate in each VN task.

The 54 reward-related neurons were tested with the all three VN tasks, and these neurons responded different reward areas in the different VN tasks (see section "Results"). To analyze how these neurons remapped to different reward areas across the tasks, we analyzed the correlation of reward-related responses between two different tasks. There were 10 reward areas in the two routes in each task. In a given reward-related neuron, firing rates in the four 1-s bins around reward delivery was calculated in each reward area in each task. Then, correlation of reward-related responses across the 10 reward areas between given two tasks was computed in each reward-related neuron.

To analyze the spatial distribution of locations where activity of reward-related and place-related neurons increased, averaged

firing rates maps were separately created in place- and reward-related neurons in the control VN task. First, firing rates in each pixel were normalized by scaling the minimum and maximum values to 0 and 1, respectively, (min-max feature scaling normalization) in each neuron (Munn and Bilkey, 2012; Royer et al., 2012). Then, averaged firing rate maps of place- and reward-related neurons were created separately.

## Bayesian Decoding

We used Bayesian decoding to check whether the population activity of route-dependent neurons in the central common hallway can predict the direction of the turn (i.e., route) (Zhang et al., 1998; Quiroga and Panzeri, 2009). The Bayesian decoding method computes the posterior probability of the turn direction D given spike counts S, p(D| S). The prediction by the decoder for given spike counts S is defined as the D maximizing p(D| S). The input data of Bayesian decoding were derived from the route coding neurons with significant route effects using a two-way ANOVA. We used route-dependent neurons that were tested in more than 10 trials for each route ($n = 7$) in the control VN task.

To test prediction accuracy of the decoder, we used "leave-one-out" validation, which allows to efficiently create the decoder and test with a small number of trials as small as 6 trials (Bower et al., 2005; Quiroga et al., 2007; Quiroga and Panzeri, 2009). To validate the decoder, data used for optimizing the decoder (training data) and evaluating the performance (test data) were separated to prevent an artificially high performance. In the "leave-one-out" validation, all data, except those from one trial, were used for training [i.e., optimizing p (D| S)]; the prediction was tested for the remaining trial. The process was repeated to calculate the prediction of all trials. Further, the percentage of correct predictions was calculated as the prediction accuracy. This process ensured that the largest possible number of trials could be utilized to train and test the decoder.

To test whether prediction accuracy was significantly larger than chance level, a "bootstrap" procedure was used to estimate the chance distribution (Bower et al., 2005). In this procedure, the direction memberships of each population neural activity were randomized, and the prediction accuracy was calculated. The chance distribution of the accuracy was obtained by repeating this process 10,000 times. In addition to route decoding, data matrix of mean firing rates in the three zones between T and C reward areas (zones 1, 2, and 3) were similarly submitted to zone decoding in each route.

We also examined whether responses to reward delivery in the common central hallway would include route information as well as temporal information of reward delivery. To decode this information from reward responses, HF neurons that had significant reward responses ($p < 0.05$, one-way ANOVA), at least at the T and/or C reward areas, in either routes were identified. Mean firing rates of these neurons, which showed not only significant reward responses at the T-reward area ($p < 0.05$, one-way ANOVA) but also significant activity changes during the pre-reward period (i.e., during the 2 s before reward delivery) from the mean firing rates ($p < 0.05$, one sample $t$-test), during the 2-s period before reward delivery at the T reward area in both routes were submitted to route decoding. In the same way, mean firing rates of the neurons, which showed not only significant reward responses at the C-reward area ($p < 0.05$, one-way ANOVA) but also significant activity changes during the post-reward period (i.e., during the 2 s after reward delivery) from the mean firing rates ($p < 0.05$, one sample $t$-test), during the 2-s period after reward delivery at C reward area in both routes were submitted to route decoding. Further, mean firing rates during the 2-s period before and after reward delivery at the T and C reward areas in both routes were separately submitted to temporal decoding of reward delivery in the same way.

## Neural Correlates to Saccades

Instantaneous speeds of eye movements were calculated from the X-Y positions of the eye. The rapid onset of eye movements, which were defined as an eye movement amplitude exceeding the experimenter-defined threshold (i.e., 0.3 mm/s), were identified. The minimum interval between two saccades was set at 100 ms; all eye movements within 100 ms from preceding saccades were ignored. The effect of saccades on HF neuronal activity within place fields were analyzed by creating peri-event histograms around saccade onsets. The significance of the saccade modulation was determined by comparing the neuronal activity between the 125-ms pre- and post-periods using a $t$-test ($p < 0.05$). Of 57 place-related neurons, one neuron displayed significant correlations to saccades inside place fields (**Supplementary Figure 1**).

A previous study reported vicarious trial and error (VTE)-like behaviors around a choice point in rodents (Johnson et al., 2007). To investigate possible VTE-like eye movements, we analyzed number of saccades around zones 3 and 2 before the choice point (T reward area) in each recording session for each task; number of saccades during 1 s just before reward delivery at T reward area (1 s from −1 to 0 s before the reward delivery at T reward area) was compared with that during a control period for 1 s from −2 to −1 s before reward delivery at T reward area ($p < 0.05$, two sample $t$-test). The results indicated that, only in four sessions out of a total of 66 sessions, there were significant differences in number of saccades between the 2 periods ($p < 0.05$). A previous study reported that VTE can be observed during the learning and early exposure to a task (Johnson et al., 2007), and this lack of VTE-like eye movements in the present study might be ascribed to the fact that the tasks were highly familiar to the monkeys since the monkeys were repeatedly trained until the correct response rate exceeded 99% in the present study. Although four neurons were found during these four sessions with significant differences in number of saccades, these four neurons showed no reward-related nor place-related responses before or in the choice point.

## Stereotaxic Localization of the Recording Sites

Before the start of each recording session, a three-dimensional magnetic resonance imaging (3-D MRI) scan of the monkey's head was performed (Hori et al., 2005). The locations of HF neurons were based on the zero coordinates

defined in the stereotaxic atlas of the Macaca fuscata brain (Kusama and Mabuchi, 1970).

# RESULTS

## HF Place-Related Activity

A total of 106 neurons were recorded from the left and right HF. **Figure 2** shows an example of the raw signal of a HF neuron. Typical waveforms, which were simultaneously recorded from the same tetrode (EL 1–4), of two HF neurons (N1 and N2) are shown in **Figure 2A**. **Figure 2B** displays the results of spike sorting using offline cluster cutting of neuronal activities shown in **Figure 2A**. Each dot represents one spike. Two clusters of dots, which are indicated by different colors, were recognized. The autocorrelograms of these neurons indicated that their refractory periods were more than 1 ms, which suggests that these spikes were recorded from single neurons (**Figure 2C**).

Of the 106 neurons recorded, 57 (53.8%) neurons displayed place field(s) in at least one of three VN tasks (place-related neurons) (**Table 1**). **Figure 3** shows an example of a HF place-related neuron. The activity of the neuron increased around reward areas (**Figure 3Aa**). Place field analysis in the separate routes indicated place fields around the R-reward area in the left route (**Figure 3Ab**) and the C- and L-reward areas in the right route (**Figure 3Ac**). Moreover, this neuron demonstrated route-dependent activity. It displayed a place field in zone 1 in the common central hallway in the right route (**Figure 3Ac**), while no place field was recognized in the corresponding area in the left route (**Figure 3Ab**). **Figure 3B** shows mean firing rates in the three zones of the left and right routes. A two-way ANOVA indicated that there was a significant interaction between route and zone in the common straight path segment [$F(2,55) = 6.8263$, $p = 0.0220$]. *Post hoc* comparisons indicated that activity in the zone 1 of the right route was significantly larger than that in the left route (Bonferroni test, $p < 0.05$). Another example of a route-dependent activity is shown in **Figure 4**. A two-way ANOVA indicated that there was a significant effect of route [$F(1,61) = 1.5033$, $p = 0.0029$]. A total of 18 neurons displayed similar route-dependent activity in the common central hallway between the C and T reward areas (**Table 1**).

In the control VN task, there were seven neurons that were tested in more than 10 trials in each route, which showed route-dependent activity in the common central hallway. When the mean firing rates in the three zones (zones 1–3) were used for route decoding, the ensemble activity of these seven neurons significantly predicted route ($p < 0.05$) (**Figure 5Aa**). The ensemble activity of these seven neurons also significantly predicted route when the data were confined to those in zone 3 (**Figure 5Ab**). However, neither the ensemble data in zone 1 ($p > 0.05$) nor those in zone 2 ($p > 0.05$) significantly predicted the route (**Figures 5Ac,d**). Moreover, ensemble activity of these seven neurons significantly predicted zone ($p < 0.05$) when mean firing rates in the three zones of the left route were submitted to zone decoding (**Figure 5Ba**). When the mean firing rates in the three zones of the right route were submitted to zone decoding, the ensemble activity of these seven neurons significantly predicted zone ($p < 0.01$) (**Figure 5Bb**). These results indicated that ensemble activity of the route-dependent neurons in the common central hallway conveyed route and zone information. We also submitted all the neurons which were tested in more than 10 trials, regardless of response types ($n = 57$), to route decoding analyses, but no ensemble data predicted the route (data not shown).

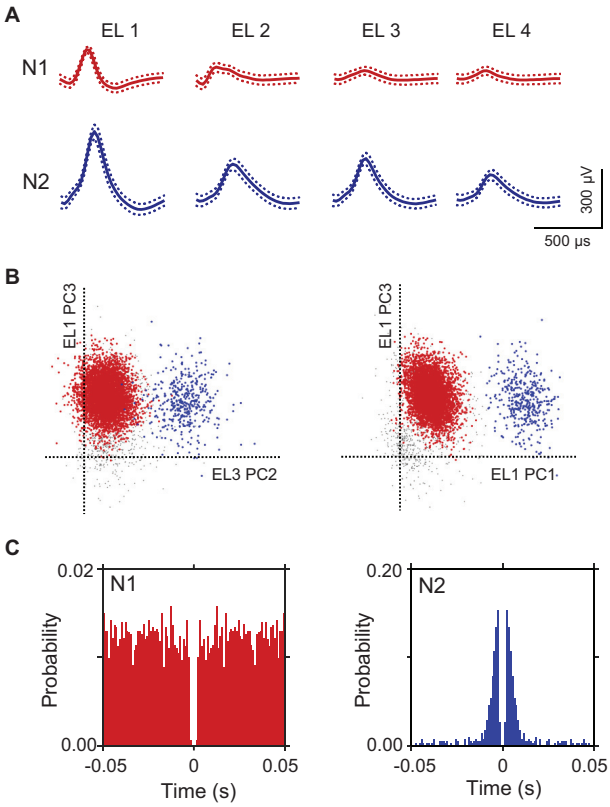


**FIGURE 2 |** An example of an offline spike sorting. **(A)** Waveforms (mean ± standard deviation, indicated by solid and dotted lines, respectively) recorded from four electrodes (tetrode; EL 1–4). The N1 (red) and N2 (blue) waveforms correspond to two individual neurons, identified by offline spike sorting in B. **(B)** Results of offline spike sorting. Each axis represents a principle component (PC1-3). Each dot represents one neuronal spike. Semi-automatic spike sorting resulted in two clusters of neuronal signals (red and blue dots, corresponding to N1 and N2 in A, respectively). Gray dots represent unsorted spikes. **(C)** Autocorrelograms of the neurons. Bin width = 1 ms. Ordinates indicate probability, where bin counts were divided by the number of spikes in the spike train.

**TABLE 1 |** Classification and number of hippocampal (HF) neuronal activity.

| | Total | Control | Rotated | No-flag |
|---|---|---|---|---|
| Tested neurons | 106 | 106 | 57 | 57 |
| Place-related | 57 | 43 | 26 | 25 |
| Route-dependent | 18 | 12 | 5 | 1 |
| Reward-related | 75 | 65 | 35 | 39 |
| Route-dependent reward-related | 56 | 47 | 24 | 24 |

*Control, control virtual navigation (VN) task; Rotated, rotated VN task; No-flag, no-flag VN task.*

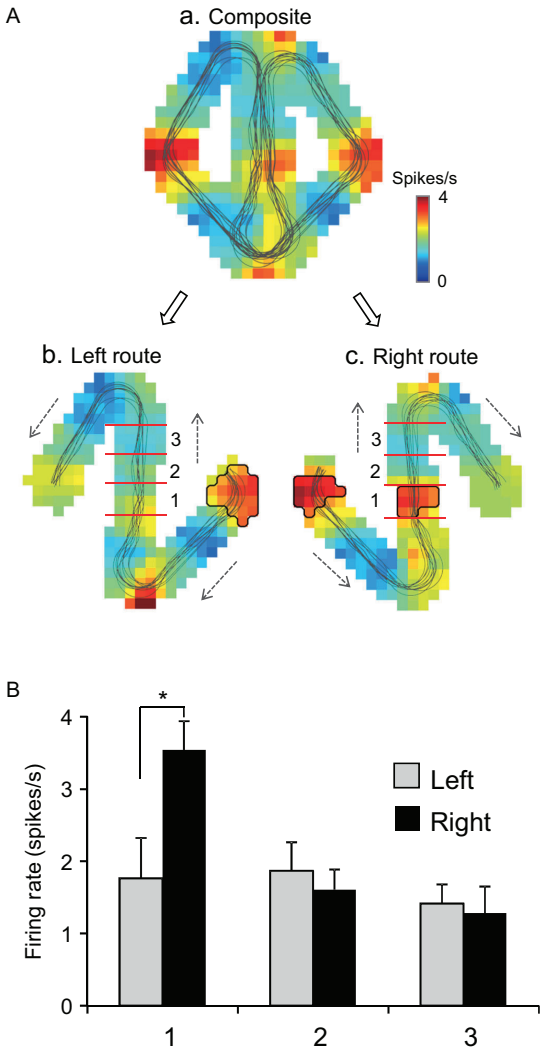


**FIGURE 3 |** An example of a route-dependent place-related neuron in the VN task. **(A)** Firing rate maps. Place fields were identified near the R-reward area in the left route (b), and near the L- and C-reward areas in the right route (c). Trajectories of the monkey are indicated by thin lines on the firing rate maps. The place fields are marked using thick lines. **(B)** Comparison of mean firing rates in the three zones (1–3) in the left and right routes. *$p < 0.05$.

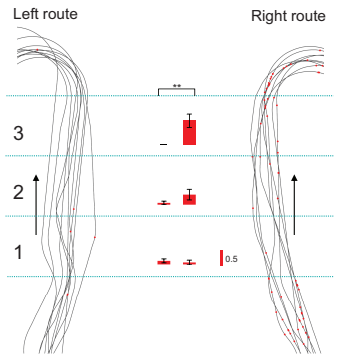


**FIGURE 4 |** Another example of a route-dependent neuron in the VN task. Red dots on trails indicate neuronal spikes. Left and right histograms indicate mean firing rates in the three zones in the common central hallway (1–3) in the left and right routes, respectively. Calibration in the right bar indicates 0.5 spikes/s. **$p < 0.01$.

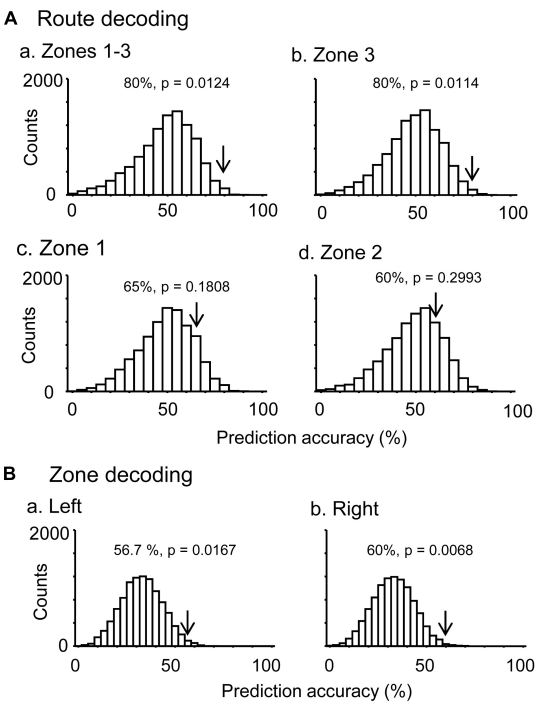


**FIGURE 5 |** Bayesian decoding of overlapping path segments from ensemble place-related activity. **(A)** Route decoding from place-related activity in zones 1–3 (a), zone 3 (b), zone 1 (c), and zone 2 (d). **(B)** Zone decoding from place-related activity in the left (a) and right (b) routes. The arrow in each histogram indicates the actual prediction accuracy, while the histogram indicates the chance level distribution obtained using the "bootstrap" procedure (10,000 repetitions). The *p*-value for each prediction accuracy was calculated as the ratio of the count of the values ≥ the actual prediction accuracy in the chance.

## Neural Correlates to Reward Delivery

The 57 place-related neurons displayed place field(s) in various area(s), some of which overlapped the reward areas in 36 place-related neurons. Regardless of place field(s), however, the activity of 75 neurons were modulated by reward delivery, in at least one of reward areas (reward-related neurons), in at least one of the three VN tasks (**Table 1**). These 75 neurons showed reward responses in some but not in all reward areas. In fact, there were no neuron that showed reward-related responses in every reward areas. Moreover, reward-related activity of 56 neurons in the common central hallway was modulated by route (route-dependent reward-related neurons) (**Table 1**). **Figure 6** shows an example of a route-dependent reward-related HF neuron in the common central hallway. A three-way ANOVA indicated that there was a significant interaction among route, reward area, and period [$F(6,218) = 2.4098$, $p = 0.0283$].

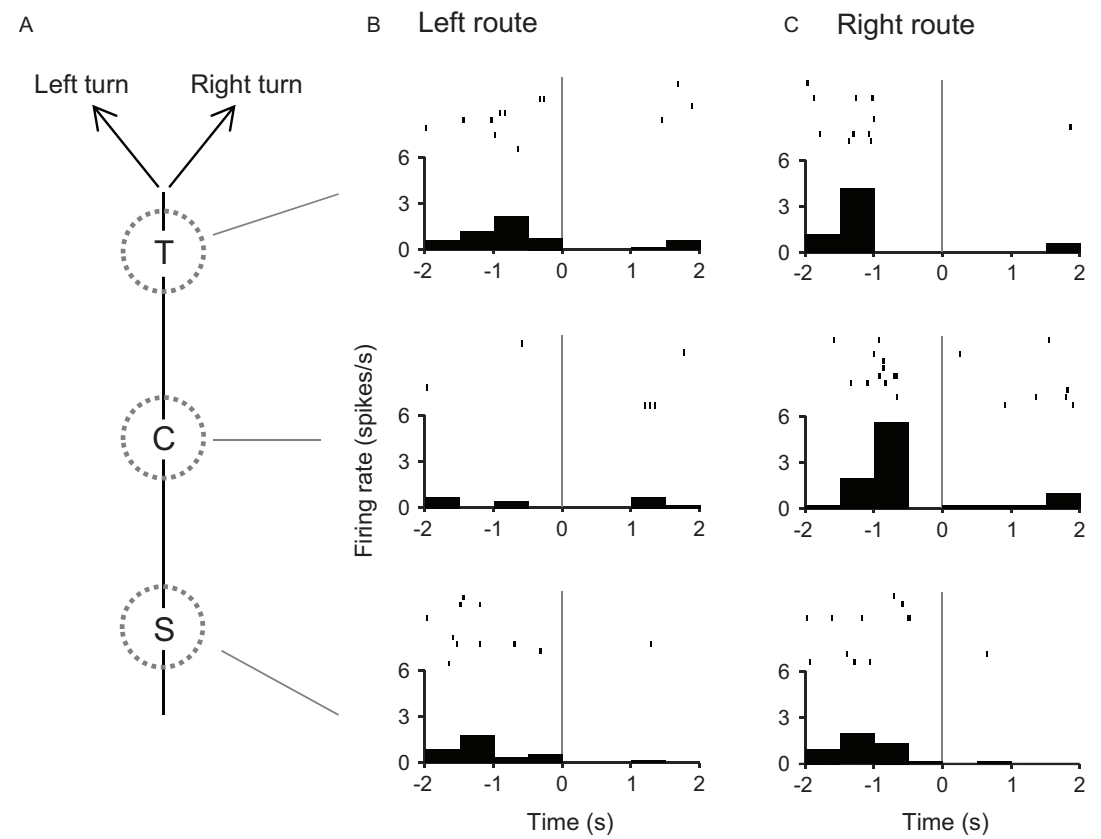


**FIGURE 6 |** An example of a route-dependent reward-related neuron in the VN task. **(A)** Schematic illustration of the left and right routes in the common central hallway. **(B,C)** Three peri-event time histograms and raster plots around reward delivery at the T-, C-, and S-reward areas in the left **(B)** and right **(C)** routes. Gray lines indicate reward delivery.

We hypothesized that responses to reward delivery would include route and temporal information. In the T-reward area in the control VN task, there were eight neurons that showed significant reward modulation ($p < 0.05$, one-way ANOVA) and significant activity changes during the pre-reward period (i.e., during the 2 s before reward delivery) from the mean firing rates ($p < 0.05$, one sample $t$-test). The ensemble activity of these eight neurons in the pre-reward period in the T-reward area was submitted to route decoding (**Figure 7A**). The results indicated that ensemble activity of these eight reward-related neurons with pre-reward responses significantly predicted route before reward delivery ($p < 0.05$). We also analyzed activity of reward-related neurons in the C-reward area in the same way, and there were five reward-related neurons with post-reward responses in the C-reward area in the control VN task. However, ensemble data in the post-reward period in the C-reward area did not significantly predict route ($p > 0.05$) (**Figure 7B**). In the other VN tasks, the ensemble data in the T-reward area tended to predict route in the rotated VN task ($p < 0.1$) and significantly predicted route in the no-flag VN task ($p < 0.01$).

Moreover, ensemble activity of the reward-related neurons predicted reward delivery at the T- and C-reward areas (**Figure 8**). The ensemble activity of 25 neurons, which showed reward-related activity at the T-reward-area in the left route ($p < 0.05$, one-way ANOVA), significantly predicted reward delivery ($p < 0.0001$) when mean firing rates during the 2-s periods before and after reward delivery in the T-reward area of the left route were submitted to temporal decoding in the control VN task (**Figure 8A**). In the same way, the ensemble activity of 14 neurons, which showed reward-related activity at the C-reward-area in the left route ($p < 0.05$, one-way ANOVA), significantly predicted reward delivery at the C-reward area in the left route ($p < 0.0001$) (**Figure 8B**) and T- and C-reward areas in the right route ($p < 0.0001$, 0.01, respectively) (**Figures 8C,D**). In the rotated and no-flag VN tasks, the decoding analyses of temporal relations showed comparative results (data not shown).

Previous fMRI studies have reported that overlapping items were more distinctly represented than non-overlapping items in the human HF (Chanales et al., 2017; Kim et al., 2017). In the present study, the path segment to the T-reward area overlapped in the left and right routes (overlapping path condition), whereas the path segments to L- and R-reward areas did not overlap (non-overlapping path condition) (**Figure 9A**). The above results suggest that pre-reward activity carries route information, which further suggest that the representation of the six path segments by ensemble pre-reward activity in the left and right routes across

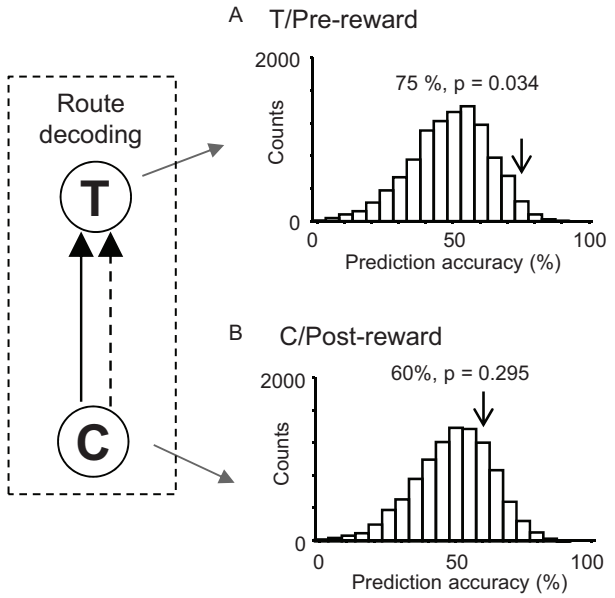


**FIGURE 7 |** Bayesian decoding of overlapping path segments from reward-related activity in the control VN task. **(A)** Route decoding from pre-reward activity before reward delivery at the T-reward area. **(B)** Route decoding from post-reward activity after reward delivery at the C-reward area. The arrow in each histogram indicates the actual prediction accuracy, while the histogram indicates the chance level distribution obtained using the "bootstrap" procedure (10,000 repetitions). The *p*-value for each prediction accuracy was calculated as the ratio of the count of the values ≥ the actual prediction accuracy in the chance.

the three VN tasks would be more distinct in the overlapping path condition than the non-overlapping path condition. A total of 16 neurons showed reward correlates in the T-reward area in one of the three VN tasks at least, whereas 20 neurons showed reward correlates in the L- and/or R-reward areas in one of the three VN tasks at least. The mean correlation among population vectors consisting of these 16 and 20 neuronal activities are shown in **Figure 9B**. The mean correlation was significantly smaller in the overlapping path condition than in the non-overlapping path condition (paired *t*-test, $p < 0.05$).

A recent rodent study has reported that some HF neurons specialized for encoding reward location are active not only in one environment but also across multiple environments (Gauthier and Tank, 2018). In the present study, 54 out of 57 HF neurons tested with the all three VN tasks showed reward-related responses in at least one of the three VN tasks. Of these 54 reward-related neurons, 15 (27.8%) neurons showed reward-related responses only one of the three VN tasks while 39 (72.2%) neurons showed reward-related responses in the multiple VN tasks. Across the different VN tasks, 23 of these 39 reward-related neurons were active in some of the same (but not all) reward areas while the remaining 16 neurons were active in different reward areas. Thus, no reward-related neurons showed identical reward-related responses across the 3 tasks. Consistently, correlation of reward-related responses across 10 reward areas in the two routes between the given two mazes was low: correlation between the control and no-flag VN tasks, 0.061 ± 0.023; correlation between the control and rotated VN tasks, 0.082 ± 0.022; correlation between the no-flag and rotated VN tasks, 0.108 ± 0.018. These findings indicate that the reward-related neurons remapped to different reward areas across the different VN tasks.

## Relationships Between Place-Related and Reward-Related Responses

Out of 57 place-related neurons, 49 showed reward-related responses in certain reward areas. Out of 75 reward-related neurons, 49 showed place-related responses in certain areas. **Figure 10** shows averaged firing rate maps of place-related and reward-related neurons in the control VN task. When the data of the all place-related ($n = 43$) and reward-related ($n = 65$) neurons were analyzed (**Figure 10A**), activity of the neurons was increased around the T and S reward areas in both place-related and reward-related neurons. The firing rate maps of these two types of HF neurons were highly correlated ($r = 0.872$). There were 12 place-related neurons without reward-related responses and 34 reward-related neurons without place-related responses in the control VN task. When the data analyses were confined to these specific types of the HF neurons (**Figure 10B**), the averaged firing rate maps showed similar trends in the place-related neurons without reward-related neurons (**Figure 10Ba**) and reward-related neurons without place-related neurons (**Figure 10Bb**). The firing rate maps of these two types of HF neurons still showed high spatial correlation ($r = 0.659$).

## Recording Sites

**Figure 11** shows the recording sites in the HF indicated by red dots. A total of 125 penetrations were performed in both sides of HF, and 49 neurons were recorded in the left HF (monkey A) while 57 neurons, in the right HF (monkey B) (indicated by red dots). In both sides of the HF, comparative numbers of place-related neurons (left HF, $n = 16$; right HF, $n = 25$) and reward-related neurons (left HF, $n = 26$; right HF, $n = 31$) were found in the control VN task. Statistical analyses indicated that there were no significant differences in ratios of place-related and reward-related neurons between the left and right HF ($p > 0.05$ for both place-related and reward-related neurons, Fisher's exact test). Based on the stereotaxic atlas of the monkey brain (Kusama and Mabuchi, 1970), these recording sites correspond to CA1 and CA3 subfields, and dentate gyrus in both right and left HF. These results indicated that the data were comparable between the left and right sides of the HF.

# DISCUSSION

## Place-Related Activity in the HF

In the present study, consistent with previous studies in human and non-human primates (Ono et al., 1993; Nishijo et al., 1997; Matsumura et al., 1999; Ekstrom et al., 2003; Hori et al., 2005; Miller et al., 2013; Furuya et al., 2014), place-related activity was observed in the monkey HF. Further, a total of 18 HF neurons displayed activity in the common central

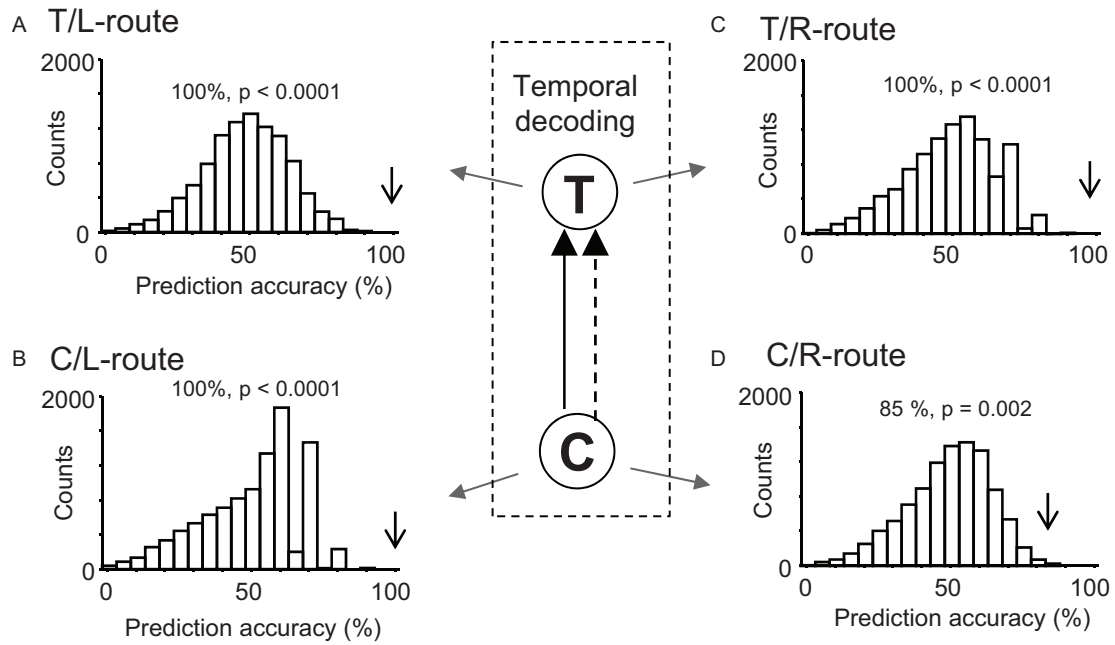


**FIGURE 8 |** Bayesian decoding of reward delivery from reward-related activity in the control VN task. **(A,B)** Temporal decoding from reward-related activity around the T- (A) and C- (B) reward area in the left route. **(C,D)** Temporal decoding from reward-related activity around the T- (C) and C- (D) reward area in the right route. The arrow in each histogram indicates the actual prediction accuracy, while the histogram indicates the chance level distribution obtained using the "bootstrap" procedure (10,000 repetitions). The *p*-value for each prediction accuracy was calculated as the ratio of the count of the values ≥ the actual prediction accuracy in the chance.

hallway, which was modulated by route. The decoding results suggest that the ensemble activity of these neurons carries information of route and monkey's location in the three zones. During navigation in the common central hallway before turning (path segment between T- and C-reward areas), the monkey always faced the same visual cues, suggesting that this route-dependent activity was not ascribed to view differences of the monkey but to the routes. Consistent with previous rodent studies in which animals navigated the same path segment in specific direction(s) in different routes (Frank et al., 2000; Wood et al., 2000; Ferbinteanu and Shapiro, 2003; Dayawansa et al., 2006), the current study provided evidence that the activity of primate HF neurons is also route-dependent. A previous study on monkeys reported that place fields of place-related neurons were dependent on the size of virtual spaces (Furuya et al., 2014), consistent with a rodent study (O'Keefe and Burgess, 1996). Furthermore, a recent neurophysiological study in monkeys reported a similar type of HF neurons that responded differently when the subject rotated to the same direction in the same position but in different action contexts (Wirth et al., 2017), indicating the context-dependency in this HF neuronal responses. These findings extend previous findings in rodents by demonstrating the disambiguation of overlapping path segments in non-human primates.

In a previous study in rats, 10 (43.4%) of 23 route-dependent place-differential neurons still showed route-dependent place responses while animals were passively dislocated without locomotion, while the rest of these neurons were sensitive to locomotion (Dayawansa et al., 2006). Since the activity of the 18 neurons was dependent on the routes in the VN without locomotion in this study, it is suggested that such neurons in primates and rodents might code visual information (e.g., optic flow and landmarks) to form route-dependent activity.

Human fMRI studies reported that the HF is important and active when subjects navigate overlapping path segments in a virtual space (Brown et al., 2010; Chanales et al., 2017). The present decoding results indicated that route coding was more evident in zone 3 near the bifurcation point than in zones 1 and 2. This suggests that ensemble HF neuronal activity in zone 3 carries important information to reach reward goals (L- and R-reward areas). Rodent studies reported that ensemble activity near choice points carried prospective information to reach goals (Johnson and Redish, 2007; Catanese et al., 2014), but such activity was less observable in the same location when discrimination of route was not required (Griffin et al., 2012). Consistent with the results of the present study and previous rodent studies, a computational study also suggested that episodic memory regarding routes is used to navigate by cueing retrieval at the choice point (Zilli and Hasselmo, 2008). These findings suggest that route-dependent activity in zone 3 might be involved in future behavioral decision, and that disambiguation of the same path segment in the same environment is a hallmark of the HF in episodic memory (Griffin and Hallock, 2013; Eichenbaum, 2017).

## Reward-Related Activities

In the present study, 75 neurons showed neural correlates to reward delivery (reward-related neurons in **Table 1**), which

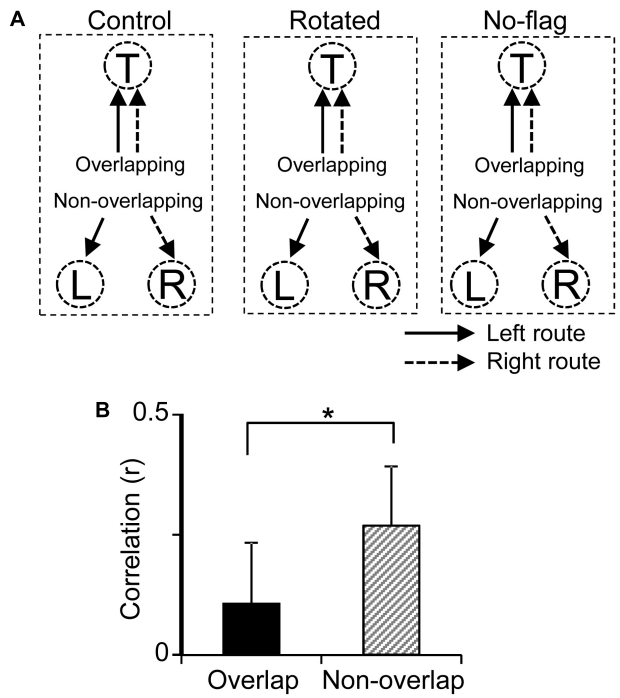


**FIGURE 9 |** Representation of the overlapping and non-overlapping path segments by pre-reward activity of the reward-related neurons across the VN tasks. **(A)** Schematic illustration of overlapping and non-overlapping path conditions in the three VN tasks. **(B)** Comparison of mean correlation coefficients across the six path segments between the overlapping and non-overlapping path conditions. *$p < 0.05$.

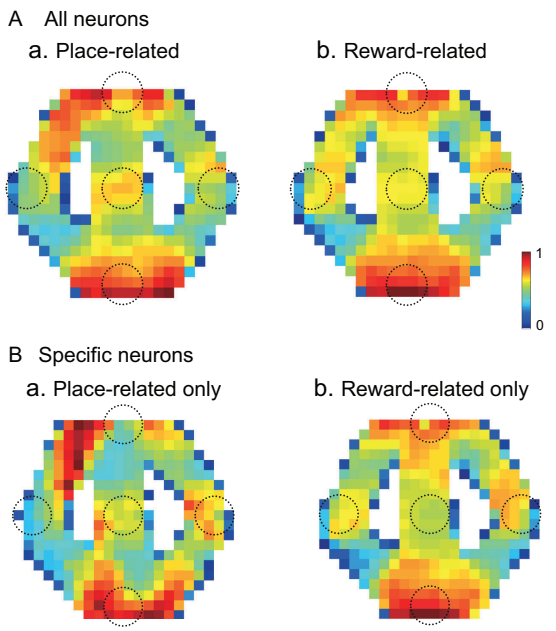


**FIGURE 10 |** Averaged firing rate maps of the place- and reward-related neurons in the control VN task. **(A)** Averaged firing rate maps of the place-related ($n$ = 43) (a) and reward-related ($n$ = 65) (b) neurons when the all neurons in each category were analyzed. **(B)** Averaged firing rate maps of the place-related neurons without reward-related responses ($n$ = 12) (a) and reward-related neurons without place-related responses ($n$ = 34) (b).

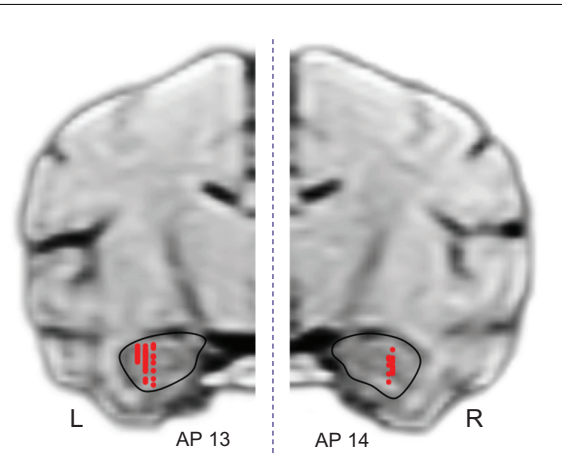


**FIGURE 11 |** Recording sites in the hippocampal formation (HF). A total of 125 penetrations were performed in the HF. Red dots indicate recording sites of HF neurons. R, right hemisphere; L, left hemisphere.

was consistent with previous studies suggesting that reward is one of the important determinants of the neuronal activities in the monkey HF (Ono et al., 1993; Rolls and Xiang, 2005). Furthermore, the averaged firing rate maps indicated that place-related neurons without reward-related responses showed activity increases around reward areas similar to those in the reward-related neurons. Such accumulation of place fields around the goal (reward) areas has been reported in rodents as well (Hollup et al., 2001; Kobayashi et al., 2003; Hok et al., 2007). A similar phenomenon was observed in the current study; about 30% (36/106) of the HF neurons displayed their place fields overlapping with the reward (goal) areas, which was comparative to previous studies (Hollup et al., 2001; Kobayashi et al., 2003; Hok et al., 2007). The HF is implicated in reward-related functions, including place-reward association, conditioned place preference, and reinforcement learning (Hampton et al., 2004; Rolls and Xiang, 2005; Ito et al., 2008; Ho et al., 2011; Davidow et al., 2016), which might be a neural basis of drug addiction (Trouche et al., 2016; Xia et al., 2017). Neurons in the HF with goal (reward)-directed activity project to the nucleus accumbens, which plays a role in motivation and reward processing (Ciocchi et al., 2015), and reward-induced synchronization of neuronal activity between the HF and nucleus accumbens (Tabuchi et al., 2000). This HF-accumbal connection has also been implicated in reward memory in humans (Davidow et al., 2016).

The current study also indicated that HF neural correlates to reward delivery was route-dependent in the common central hallway. During the VN tasks, all reward (goal) areas provided the animals with a reward if the animals visited them in the correct order. This suggests that the association between reward (or reward expectation) and specific places in space

could be the cause of the observed goal responses (Hölscher et al., 2003; Hok et al., 2005). Therefore, we postulated that HF neuronal activity around reward delivery would carry spatial information required for the navigation in the overlapping path segment in the same environment. Consistent with our hypothesis, route information was decoded from ensemble neuronal activity before reward delivery at the T-reward area. Further, the decoding analysis suggests that ensemble activity in each route carries temporal information of reward delivery. Reward delivery (i.e., reward outcome) is one of the important factors in episodic memory (Mason et al., 2017); it modulates HF neuronal activity (Lee et al., 2012; Tryon et al., 2017; Boccara et al., 2019). These findings suggest that the HF plays an important role in disambiguation of overlapping action (navigation)-reward outcome association. Furthermore, about 30% of reward-related neurons showed reward-related responses in only one of the three VN tasks while about 70% of reward-related neurons showed reward-related responses in the multiple tasks. The former type of the reward-related neurons might code task (context)-specific information of reward areas, while the latter type might simply code reward events (Gauthier and Tank, 2018). In spite of the remap to new reward areas across the different VN tasks in reward-related neurons, activity of these neurons predicted routes and reward delivery. Taken together, these results suggest that HF neuronal activity carries multiple information, including route, outcome (reward delivery), and context information. The present results extend the role of the HF to disambiguation of reward outcome, consistent with the role the HF in episodic memory.

Consistent with the present decoding findings suggesting that route-dependent reward-related neurons contribute to navigation, activity of reward-related neurons was reported to be correlated to spatial memory performance in rodents (Dupret et al., 2010). This may suggest that the relatively small number of route-dependent neurons compared with reward-related neurons in the present study might be ascribed to the task design. This may also explain the insignificant results in the decoding analysis using whole sample neurons. In many previous studies in rodents, the reward was provided at the end of a trajectory, while in this study, the entire path could be segmented by each reward areas along the route. Thus, the route-dependent reward-related neurons could provide sufficient information for navigation to a next reward area in the present study, and consequently information from route-dependent (reward non-related) neurons might not be fully required for navigation in such a path segment. The present results are consistent with a previous study (Bower et al., 2005), in which rats were trained to trace reward areas in sequence and route-dependent activity was not evident compared with the other rodent studies (see section "Introduction"). However, route-dependent (reward non-related) place cells might be required to correctly navigate an overlapping path segment that is not segmented by reward areas (e.g., Wood et al., 2000). In such cases, combination of route-dependent place cells and a set of goal cells might code a specific route to that final destination (Burgess and O'Keefe, 1996). Monkey HF neurons were sensitive to multiple variables (Wirth et al., 2017), with neurons encoding egocentric and allocentric references in relation to the surrounding environment. The present findings add reward as another encoded factor when it has relevance for spatial navigation (as a waypoint). Consistently, the place-related neurons without reward-related responses also showed similar activity increases around the reward areas as did the reward-related neurons.

In addition, representation of the six path segments by ensemble pre-reward activity were more distinct in the overlapping path condition (pre-reward activity in the common path segments from the C to T reward areas) than in the non-overlapping path condition (pre-reward activity in path segments from the T to L or R reward areas) (**Figure 9**). These results also corroborate with a previous human fMRI study, in which overlapping path segments or objects were more distinctly represented than non-overlapping path segments or objects (Hulbert and Norman, 2015; Chanales et al., 2017). In a computational model, known as "neural differentiation," neuronal ensembles representing overlapping events (or items) become differentiated (separate neural ensembles) by competition due to repeated retrieval (Hulbert and Norman, 2015). The present results provide novel neurophysiological evidence supporting neural differentiation.

## CONCLUSION

The HF is implicated in disambiguation of overlapping spaces in rodents (Frank et al., 2000; Wood et al., 2000; Ferbinteanu and Shapiro, 2003; Dayawansa et al., 2006; Ainge et al., 2007; Grieves et al., 2016). Here we demonstrated this role in monkeys, by recording HF neuronal activity, while animals navigated **Figure 8** pathways, including an overlapping common central hallway in a virtual space to acquire rewards. Route-dependent neural activity was observed in 18 neurons, with decoding data suggesting that the ensemble activity of these neurons carries information about route and the monkey's location in the three zones of the common central hallway. Moreover, this role in disambiguation was observed to extend to reward acquisition, with 56 neurons showing route-dependent reward-related activity. Decoding data suggest that the ensemble activity of these neurons also carries information on route and reward delivery (outcome). Understanding the relations between memory, navigation, and reward may bring new insights into the role of the HF in addiction (Trouche et al., 2016; Xia et al., 2017) and motivation (Kennedy and Shapiro, 2009; Lebreton et al., 2013). Moreover, overlapping reward areas were more distinctly represented than the non-overlapping ones. These findings suggest an impact of reward on HF coding of overlapping items. Consistent with the present idea, overlapping stimuli associated with high rewards were less susceptible to interference, being associated with increased HF activity (Kuhl et al., 2010). Taken together, the present results may provide neural evidence that disambiguation

of overlapping items is organized based on neural differentiation (Hulbert and Norman, 2015) in the non-human primate HF.

## DATA AVAILABILITY

The datasets generated for this study are available on request to the corresponding author.

## ETHICS STATEMENT

The animal study was reviewed and approved by the ethical committee for animal experiments in the University of Toyama.

## AUTHOR CONTRIBUTIONS

HisN conceived the study and designed the experiments. RB performed the experiments. RB and JM analyzed the data and wrote the manuscript. HisN, HirN, JM, YT, EH, and TO revised the manuscript. All authors discussed the results and commented on the manuscript, and read and approved the final manuscript.

## FUNDING

This research was supported partly by a research grant from the University of Toyama.

## ACKNOWLEDGMENTS

This study was performed as a doctoral thesis in University of Toyama, and a part of the results is available in abstract form from the university website (Bretas, 2018).

## SUPPLEMENTARY MATERIAL

The Supplementary Material for this article can be found online at: https://www.frontiersin.org/articles/10.3389/fnsys.2019.00048/full#supplementary-material

## REFERENCES

Ainge, J. A., Meer, M. A. A., van der Langston, R. F., and Wood, E. R. (2007). Exploring the role of context-dependent hippocampal activity in spatial alternation behavior. *Hippocampus* 17, 988–1002. doi: 10.1002/hipo.20301

Ainge, J. A., Tamosiunaite, M., Wörgötter, F., and Dudchenko, P. A. (2012). Hippocampal place cells encode intended destination, and not a discriminative stimulus, in a conditional T-maze task. *Hippocampus* 22, 534–543. doi: 10.1002/hipo.20919

Boccara, C. N., Nardin, M., Stella, F., O'Neill, J., and Csicsvari, J. (2019). The entorhinal cognitive map is attracted to goals. *Science* 363, 1443–1447. doi: 10.1126/science.aav4837

Bower, M. R., Euston, D. R., and McNaughton, B. L. (2005). Sequential-context-dependent hippocampal activity is not necessary to learn sequences with repeated elements. *J. Neurosci.* 25, 1313–1323. doi: 10.1523/JNEUROSCI.2901-04.2005

Bretas, V. R. (2018). *Neural Representation of Overlapping Trajectories and Reward Acquisitions in the Monkey Hippocampus*. Available at: https://toyama.repo.nii.ac.jp/?action=pages_view_main&active_action=repository_view_main_item_detail&item_id=16103&item_no=1&page_id=32&block_id=36 (accessed April 1, 2018).

Brown, T. I., Ross, R. S., Keller, J. B., Hasselmo, M. E., and Stern, C. E. (2010). Which way was I going? Contextual retrieval supports the disambiguation of well learned overlapping navigational routes. *J. Neurosci.* 30, 7414–7422. doi: 10.1523/JNEUROSCI.6021-09.2010

Burgess, N., Maguire, E. A., and O'Keefe, J. (2002). The human hippocampus and spatial and episodic memory. *Neuron* 35, 625–641. doi: 10.1016/S0896-6273(02)00830-9

Burgess, N., and O'Keefe, J. (1996). Neuronal computations underlying the firing of place cells and their role in navigation. *Hippocampus* 6, 749–762. doi: 10.1002/(sici)1098-1063(1996)6:6<749::aid-hipo16>3.0.co;2-0

Catanese, J., Viggiano, A., Cerasti, E., Zugaro, M. B., and Wiener, S. I. (2014). Retrospectively and prospectively modulated hippocampal place responses are differentially distributed along a common path in a continuous T-maze. *J. Neurosci.* 34, 13163–13169. doi: 10.1523/JNEUROSCI.0819-14.2014

Chanales, A. J. H., Oza, A., Favila, S. E., and Kuhl, B. A. (2017). Overlap among spatial memories triggers repulsion of hippocampal representations. *Curr. Biol.* 27, 2307.e5–2317.e5. doi: 10.1016/j.cub.2017.06.057

Ciocchi, S., Passecker, J., Malagon-Vina, H., Mikus, N., and Klausberger, T. (2015). Selective information routing by ventral hippocampal CA1 projection neurons. *Science* 348, 560–563. doi: 10.1126/science.aaa3245

Davidow, J. Y., Foerde, K., Galván, A., and Shohamy, D. (2016). An upside to reward sensitivity: the hippocampus supports enhanced reinforcement learning in adolescence. *Neuron* 92, 93–99. doi: 10.1016/j.neuron.2016.08.031

Dayawansa, S., Kobayashi, T., Hori, E., Umeno, K., Tazumi, T., Ono, T., et al. (2006). Conjunctive effects of reward and behavioral episodes on hippocampal place-differential neurons of rats on a mobile treadmill. *Hippocampus* 16, 586–595. doi: 10.1002/hipo.20186

Dupret, D., O'neill, J., Pleydell-Bouverie, B., and Csicsvari, J. (2010). The reorganization and reactivation of hippocampal maps predict spatial memory performance. *Nat. Neurosci.* 13, 995–1002. doi: 10.1038/nn.2599

Eichenbaum, H. (2017). The role of the hippocampus in navigation is memory. *J. Neurophysiol.* 117, 1785–1796. doi: 10.1152/jn.00005.2017

Eichenbaum, H., Stewart, C., and Morris, R. G. (1990). Hippocampal representation in place learning. *J. Neurosci.* 10, 3531–3542. doi: 10.1523/JNEUROSCI.10-11-03531.1990

Ekstrom, A. D., Kahana, M. J., Caplan, J. B., Fields, T. A., Isham, E. A., Newman, E. L., et al. (2003). Cellular networks underlying human spatial navigation. *Nature* 425, 184–188. doi: 10.1038/nature01964

Ferbinteanu, J., and Shapiro, M. L. (2003). Prospective and retrospective memory coding in the hippocampus. *Neuron* 40, 1227–1239. doi: 10.1016/S0896-6273(03)00752-9

Frank, L. M., Brown, E. N., and Wilson, M. (2000). Trajectory encoding in the hippocampus and entorhinal cortex. *Neuron* 27, 169–178. doi: 10.1016/S0896-6273(00)00018-0

Furuya, Y., Matsumoto, J., Hori, E., Boas, C. V., Tran, A. H., Shimada, Y., et al. (2014). Place-related neuronal activity in the monkey parahippocampal gyrus and hippocampal formation during virtual navigation. *Hippocampus* 24, 113–130. doi: 10.1002/hipo.22209

Gauthier, J. L., and Tank, D. W. (2018). A dedicated population for reward coding in the hippocampus. *Neuron* 99, 179–193. doi: 10.1016/j.neuron.2018.06.008

Grieves, R. M., Wood, E. R., and Dudchenko, P. A. (2016). Place cells on a maze encode routes rather than destinations. *eLife* 5:e15986. doi: 10.7554/eLife.15986

Griffin, A. L., and Hallock, H. L. (2013). Hippocampal signatures of episodic memory: evidence from single-unit recording studies. *Front. Behav. Neurosci.* 7:54. doi: 10.3389/fnbeh.2013.00054

Griffin, A. L., Owens, C. B., Peters, G. J., Adelman, P. C., and Cline, K. M. (2012). Spatial representations in dorsal hippocampal neurons during a tactile-visual

conditional discrimination task. *Hippocampus* 22, 299–308. doi: 10.1002/hipo.20898

Hampton, R. R., Hampstead, B. M., and Murray, E. A. (2004). Selective hippocampal damage in rhesus monkeys impairs spatial memory in an open-field test. *Hippocampus* 14, 808–818. doi: 10.1002/hipo.10217

Harris, K. D., Henze, D. A., Csicsvari, J., Hirase, H., and Buzsáki, G. (2000). Accuracy of tetrode spike separation as determined by simultaneous intracellular and extracellular measurements. *J. Neurophysiol.* 84, 401–414. doi: 10.1152/jn.2000.84.1.401

Harvey, C. D., Collman, F., Dombeck, D. A., and Tank, D. W. (2009). Intracellular dynamics of hippocampal place cells during virtual navigation. *Nature* 461, 941–946. doi: 10.1038/nature08499

Hazama, Y., and Tamura, R. (2019). Effects of self-locomotion on the activity of place cells in the hippocampus of a freely behaving monkey. *Neurosci. Lett.* 701, 32–37. doi: 10.1016/j.neulet.2019.02.009

Hazan, L., Zugaro, M., and Buzsáki, G. (2006). Klusters, NeuroScope, NDManager: a free software suite for neurophysiological data processing and visualization. *J. Neurosci. Methods* 155, 207–216. doi: 10.1016/j.jneumeth.2006.01.017

Ho, A. S., Hori, E., Nguyen, P. H. T., Urakawa, S., Kondoh, T., Torii, K., et al. (2011). Hippocampal neuronal responses during signaled licking of gustatory stimuli in different contexts. *Hippocampus* 21, 502–519. doi: 10.1002/hipo.20766

Ho, S. A., Hori, E., Kobayashi, T., Umeno, K., Tran, A. H., Ono, T., et al. (2008). Hippocampal place cell activity during chasing of a moving object associated with reward in rats. *Neuroscience* 157, 254–270. doi: 10.1016/j.neuroscience.2008.09.004

Hok, V., Lenck-Santini, P.-P., Roux, S., Save, E., Muller, R. U., and Poucet, B. (2007). Goal-related activity in hippocampal place cells. *J. Neurosci.* 27, 472–482. doi: 10.1523/JNEUROSCI.2864-06.2007

Hok, V., Save, E., Lenck-Santini, P. P., and Poucet, B. (2005). Coding for spatial goals in the prelimbic/infralimbic area of the rat frontal cortex. *Proc. Natl. Acad. Sci. U.S.A.* 102, 4602–4607. doi: 10.1073/pnas.0407332102

Hollup, S. A., Molden, S., Donnett, J. G., Moser, M.-B., and Moser, E. I. (2001). Accumulation of hippocampal place fields at the goal location in an annular watermaze task. *J. Neurosci.* 21, 1635–1644. doi: 10.1523/JNEUROSCI.21-05-01635.2001

Hölscher, C., Jacob, W., and Mallot, H. A. (2003). Reward modulates neuronal activity in the hippocampus of the rat. *Behav. Brain Res.* 142, 181–191. doi: 10.1016/S0166-4328(02)00422-9

Hori, E., Nishio, Y., Kazui, K., Umeno, K., Tabuchi, E., Sasaki, K., et al. (2005). Place-related neural responses in the monkey hippocampal formation in a virtual space. *Hippocampus* 15, 991–996. doi: 10.1002/hipo.20108

Hulbert, J. C., and Norman, K. A. (2015). Neural differentiation tracks improved recall of competing memories following interleaved study and retrieval practice. *Cereb. Cortex* 25, 3994–4008. doi: 10.1093/cercor/bhu284

Ito, R., Robbins, T. W., Pennartz, C. M., and Everitt, B. J. (2008). Functional interaction between the hippocampus and nucleus accumbens shell is necessary for the acquisition of appetitive spatial context conditioning. *J. Neurosci.* 28, 6950–6959. doi: 10.1523/JNEUROSCI.1615-08.2008

Johnson, A., and Redish, A. D. (2007). Neural ensembles in ca3 transiently encode paths forward of the animal at a decision point. *J. Neurosci.* 27, 12176–12189. doi: 10.1523/JNEUROSCI.3761-07.2007

Johnson, A., van der Meer, M. A., and Redish, A. D. (2007). Integrating hippocampus and striatum in decision-making. *Curr. Opin. Neurobiol.* 17, 692–697. doi: 10.1016/j.conb.2008.01.003

Kennedy, P. J., and Shapiro, M. L. (2009). Motivational states activate distinct hippocampal representations to guide goal-directed behaviors. *PNAS* 106, 10805–10810. doi: 10.1073/pnas.0903259106

Kim, G., Norman, K. A., and Turk-Browne, N. B. (2017). Neural differentiation of incorrectly predicted memories. *J. Neurosci.* 32, 2022–2031. doi: 10.1523/JNEUROSCI.3272-16.2017

Kobayashi, T., Nishijo, H., Fukuda, M., Bures, J., and Ono, T. (1997). Task-dependent representations in rat hippocampal place neurons. *J. Neurophysiol.* 78, 597–613. doi: 10.1152/jn.1997.78.2.597

Kobayashi, T., Tran, A. H., Nishijo, H., Ono, T., and Matsumoto, G. (2003). Contribution of hippocampal place cell activity to learning and formation of goal-directed navigation in rats. *Neuroscience* 117, 1025–1035. doi: 10.1016/S0306-4522(02)00700-5

Kuhl, B. A., Shah, A. T., DuBrow, S., and Wagner, A. D. (2010). Resistance to forgetting associated with hippocampus-mediated reactivation during new learning. *Nat. Neurosci.* 13, 501–506. doi: 10.1038/nn.2498

Kusama, T., and Mabuchi, M. (1970). *Stereotaxic Atlas of the Brain of Macaca fuscata: by Toshio Kusama and Masako Mabuchi*. Baltimore: University of Tokyo Press.

Lebreton, M., Bertoux, M., Boutet, C., Lehericy, S., Dubois, B., Fossati, P., et al. (2013). A critical role for the hippocampus in the valuation of imagined outcomes. *PLoS Biol.* 11:e1001684. doi: 10.1371/journal.pbio.1001684

Lee, H., Ghim, J.-W., Kim, H., Lee, D., and Jung, M. (2012). Hippocampal neural correlates for values of experienced events. *J. Neurosci.* 32, 15053–15065. doi: 10.1523/JNEUROSCI.2806-12.2012

Lisman, J. E., and Grace, A. A. (2005). The hippocampal-VTA loop: controlling the entry of information into long-term memory. *Neuron* 46, 703–713. doi: 10.1016/j.neuron.2005.05.002

Ludvig, N., Tang, H. M., Gohil, B. C., and Botero, J. M. (2004). Detecting location-specific neuronal firing rate increases in the hippocampus of freely-moving monkeys. *Brain Res.* 1014, 97–109. doi: 10.1016/j.brainres.2004.03.071

Maingret, N., Girardeau, G., Todorova, R., Goutierre, M., and Zugaro, M. (2016). Hippocampo-cortical coupling mediates memory consolidation during sleep. *Nat. Neurosci.* 19, 959–964. doi: 10.1038/nn.4304

Mason, A., Farrell, S., Howard-Jones, P., and Ludwig, C. J. H. (2017). The role of reward and reward uncertainty in episodic memory. *J. Mem. Lang.* 96, 62–77. doi: 10.1016/j.jml.2017.05.003

Matsuda, K. (1996). Measurement system of the eye positions by using oval fitting of a pupil. *Neurosci. Res.* 25, S270–S270.

Matsumura, N., Nishijo, H., Tamura, R., Eifuku, S., Endo, S., and Ono, T. (1999). Spatial- and task-dependent neuronal responses during real and virtual translocation in the monkey hippocampal formation. *J. Neurosci.* 19, 2381–2393. doi: 10.1523/JNEUROSCI.19-06-02381.1999

McNaughton, B. L., Barnes, C. A., and O'Keefe, J. (1983). The contributions of position, direction, and velocity to single unit activity in the hippocampus of freely-moving rats. *Exp. Brain Res.* 52, 41–49. doi: 10.1007/BF00237147

Miller, J. F., Neufang, M., Solway, A., Brandt, A., Trippel, M., Mader, I., et al. (2013). Neural activity in human hippocampal formation reveals the spatial context of retrieved memories. *Science* 342, 1111–1114. doi: 10.1126/science.1244056

Muller, R. U., and Kubie, J. L. (1987). The effects of changes in the environment on the spatial firing of hippocampal complex-spike cells. *J. Neurosci.* 7, 1951–1968. doi: 10.1523/JNEUROSCI.07-07-01951.1987

Muller, R. U., Kubie, J. L., and Ranck, J. B. (1987). Spatial firing patterns of hippocampal complex-spike cells in a fixed environment. *J. Neurosci.* 7, 1935–1950. doi: 10.1523/JNEUROSCI.07-07-01935.1987

Munn, R. G., and Bilkey, D. K. (2012). The firing rate of hippocampal CA1 place cells is modulated with a circadian period. *Hippocampus* 22, 1325–1337. doi: 10.1002/hipo.20969

Nishijo, H., Ono, T., Eifuku, S., and Tamura, R. (1997). The relationship between monkey hippocampus place-related neural activity and action in space. *Neurosci. Lett.* 226, 57–60. doi: 10.1016/S0304-3940(97)00255-3

O'Keefe, J., and Burgess, N. (1996). Geometric determinants of the place fields of hippocampal neurons. *Nature* 381, 425–428. doi: 10.1038/381425a0

O'Keefe, J., and Dostrovsky, J. (1971). The hippocampus as a spatial map: preliminary evidence from unit activity in the freely-moving rat. *Brain Res.* 34, 171–175. doi: 10.1016/0006-8993(71)90358-1

O'Keefe, J., and Nadel, L. (1978). *The Hippocampus as a Cognitive Map*. Oxford: Clarendon Press.

Ono, T., Nakamura, K., Nishijo, H., and Eifuku, S. (1993). Monkey hippocampal neurons related to spatial and nonspatial functions. *J. Neurophysiol.* 70, 1516–1529. doi: 10.1152/jn.1993.70.4.1516

Patrono, E., Matsumoto, J., Nishimaru, H., Takamura, Y., Chinzorig, I. C., Ono, T., et al. (2017). Rewarding effects of operant dry-licking behavior on neuronal firing in the nucleus accumbens core. *Front. Pharmacol.* 8:536. doi: 10.3389/fphar.2017.00536

Poucet, B., and Hok, V. (2017). Remembering goal locations. *Curr. Opin. Behav. Sci.* 17, 51–56. doi: 10.1016/j.cobeha.2017.06.003

Quiroga, R. Q., and Panzeri, S. (2009). Extracting information from neuronal populations: information theory and decoding approaches. *Nat. Rev. Neurosci.* 10, 173–185. doi: 10.1038/nrn2578

Quiroga, R. Q., Reddy, L., Koch, C., and Fried, I. (2007). Decoding visual inputs from multiple neurons in the human temporal lobe. *J. Neurophysiol.* 98, 1997–2007. doi: 10.1152/jn.00125.2007

Rolls, E. T., and Xiang, J.-Z. (2005). Reward-spatial view representations and learning in the primate hippocampus. *J. Neurosci.* 25, 6167–6174. doi: 10.1523/JNEUROSCI.1481-05.2005

Royer, S., Zemelman, B. V., Losonczy, A., Kim, J., Chance, F., Magee, J. C., et al. (2012). Control of timing, rate and bursts of hippocampal place cells by dendritic and somatic inhibition. *Nat. Neurosci.* 15, 769–775. doi: 10.1038/nn.3077

Sarel, A., Finkelstein, A., Las, L., and Ulanovsky, N. (2017). Vectorial representation of spatial goals in the hippocampus of bats. *Science* 355, 176–180. doi: 10.1126/science.aak9589

Scoville, W. B., and Milner, B. (1957). Loss of recent memory after bilateral hippocampal lesions. *J. Neurol. Neurosurg. Psychiatry* 20, 11–21. doi: 10.1136/jnnp.20.1.11

Squire, L. R., and Zola-Morgan, S. (1991). The medial temporal lobe memory system. *Science* 253, 1380–1386. doi: 10.1126/science.1896849

Tabuchi, E. T., Mulder, A. B., and Wiener, S. I. (2000). Position and behavioral modulation of synchronization of hippocampal and accumbens neuronal discharges in freely moving rats. *Hippocampus* 10, 717–728. doi: 10.1002/1098-1063200010:6<717::AID-HIPO1009<3.0.CO;2-3

Teles-Grilo Ruivo, L. M., Baker, K. L., Conway, M. W., Kinsley, P. J., Gilmour, G., Phillips, K. G., et al. (2017). Coordinated acetylcholine release in prefrontal cortex and hippocampus is associated with arousal and reward on distinct timescales. *Cell Rep.* 18, 905–917. doi: 10.1016/j.celrep.2016.12.085

Terada, S., Takahashi, S., and Sakurai, Y. (2013). Oscillatory interaction between amygdala and hippocampus coordinates behavioral modulation based on reward expectation. *Front. Behav. Neurosci.* 7:177. doi: 10.3389/fnbeh.2013.00177

Trouche, S., Perestenko, P. V., Ven, G. M., van de Bratley, C. T., McNamara, C. G., Campo-Urriza, N., et al. (2016). Recoding a cocaine-place memory engram to a neutral engram in the hippocampus. *Nat. Neurosci.* 19, 564–567. doi: 10.1038/nn.4250

Tryon, V. L., Penner, M. R., Heide, S. W., King, H. O., Larkin, J., and Mizumori, S. J. Y. (2017). Hippocampal neural activity reflects the economy of choices during goal-directed navigation. *Hippocampus* 27, 743–758. doi: 10.1002/hipo.22720

Tulving, E., and Markowitsch, H. J. (1998). Episodic and declarative memory: role of the hippocampus. *Hippocampus* 8, 198–204. doi: 10.1002/(SICI)1098-106319988:3<198::AID-HIPO2<3.0.CO;2-G

Wirth, S., Baraduc, P., Planté, A., Pinède, S., and Duhamel, J. R. (2017). Gaze-informed, task-situated representation of space in primate hippocampus during virtual navigation. *PLoS Biol.* 15:e2001045. doi: 10.1371/journal.pbio.2001045

Wood, E. R., Dudchenko, P. A., Robitsek, R. J., and Eichenbaum, H. (2000). Hippocampal neurons encode information about different types of memory episodes occurring in the same location. *Neuron* 27, 623–633. doi: 10.1016/S0896-6273(00)00071-4

Xia, L., Nygard, S. K., Sobczak, G. G., Hourguettes, N. J., and Bruchas, M. R. (2017). Dorsal-CA1 hippocampal neuronal ensembles encode nicotine-reward contextual associations. *Cell Rep.* 19, 2143–2156. doi: 10.1016/j.celrep.2017.05.047

Zhang, K., Ginzburg, I., McNaughton, B. L., and Sejnowski, T. J. (1998). Interpreting neuronal population activity by reconstruction: unified framework with application to hippocampal place cells. *J. Neurophysiol.* 79, 1017–1044. doi: 10.1152/jn.1998.79.2.1017

Zilli, E. A., and Hasselmo, M. E. (2008). Modeling the role of working memory and episodic memory in behavioral tasks. *Hippocampus* 18, 193–209. doi: 10.1002/hipo.20382 doi: 10.1002/hipo.20382

**Conflict of Interest Statement:** The authors declare that the research was conducted in the absence of any commercial or financial relationships that could be construed as a potential conflict of interest.

*Copyright © 2019 Bretas, Matsumoto, Nishimaru, Takamura, Hori, Ono and Nishijo. This is an open-access article distributed under the terms of the Creative Commons Attribution License (CC BY). The use, distribution or reproduction in other forums is permitted, provided the original author(s) and the copyright owner(s) are credited and that the original publication in this journal is cited, in accordance with accepted academic practice. No use, distribution or reproduction is permitted which does not comply with these terms.*

frontiers in Molecular Neuroscience

ORIGINAL RESEARCH
published: 12 November 2019
doi: 10.3389/fnmol.2019.00270

# Re-innervation of the Denervated Dentate Gyrus by Sprouting Associational and Commissural Mossy Cell Axons in Organotypic Tissue Cultures of Entorhinal Cortex and Hippocampus

*Domenico Del Turco, Mandy H. Paul, Viktor J. Beeg Moreno, Lars Hildebrandt-Einfeldt and Thomas Deller**

*Institute of Clinical Neuroanatomy, Dr. Senckenberg Anatomy, Neuroscience Center, Goethe University Frankfurt, Frankfurt, Germany*

Collateral sprouting of surviving axons contributes to the synaptic reorganization after brain injury. To study this clinically relevant phenomenon, we used complex organotypic tissue cultures of mouse entorhinal cortex (EC) and hippocampus (H). Single EC-H cultures were generated to analyze associational sprouting, and double EC-H cultures were used to evaluate commissural sprouting of mossy cells in the dentate gyrus (DG) following entorhinal denervation. Entorhinal denervation (transection of the perforant path) was performed at 14 days *in vitro* (DIV) and associational/commissural sprouting was assessed at 28 DIV. First, associational sprouting was studied in genetically hybrid EC-H cultures of beta-actin-GFPtg and wild-type mice. Using calretinin as a marker, associational axons were found to re-innervate almost the entire entorhinal target zone. Denervation experiments performed with EC-H cultures of Thy1-YFPtg mice, in which mossy cells are YFP-positive, confirmed that the overwhelming majority of sprouting associational calretinin-positive axons are mossy cell axons. Second, we analyzed associational/commissural sprouting by combining wild-type EC-H cultures with calretinin-deficient EC-H cultures. In these cultures, only wild-type mossy cells contain calretinin, and associational and commissural mossy cell collaterals can be distinguished using calretinin as a marker. Nearly the entire DG entorhinal target zone was re-innervated by sprouting of associational and commissural mossy cell axons. Finally, viral labeling of newly formed associational/commissural axons revealed a rapid post-lesional sprouting response. These findings demonstrate extensive and rapid re-innervation of the denervated DG outer molecular layer by associational and commissural mossy cell axons, similar to what has been reported to occur in juvenile rodent DG *in vivo*.

**Keywords: calretinin, calretinin-knock out, collateral sprouting, entorhinal cortex lesion, perforant path transection, plasticity, regeneration**

OPEN ACCESS

***Edited by:***
*Jochen C. Meier, Technische Universitat Braunschweig, Germany*

***Reviewed by:***
*Robert S. Sloviter, Morehouse School of Medicine, United States*
*Carola A. Haas, University of Freiburg, Germany*

***Correspondence:**
*Thomas Deller*
*t.deller@em.uni-frankfurt.de*

***Received:*** *26 August 2019*
***Accepted:*** *22 October 2019*
***Published:*** *12 November 2019*

***Citation:***
*Del Turco D, Paul MH, Beeg Moreno VJ, Hildebrandt-Einfeldt L and Deller T (2019) Re-innervation of the Denervated Dentate Gyrus by Sprouting Associational and Commissural Mossy Cell Axons in Organotypic Tissue Cultures of Entorhinal Cortex and Hippocampus. Front. Mol. Neurosci. 12:270. doi: 10.3389/fnmol.2019.00270*

## INTRODUCTION

Regardless of the underlying cause, central nervous system (CNS) injuries result in primary damage at the lesion site and secondary denervation damage in connected brain areas. Thus, even spatially circumscribed CNS lesions cannot be considered local injuries since every lesion challenges the neuronal network. In line with this view of CNS damage, the CNS reacts to lesions with a profound rewiring of its connections. This lesion-induced plastic response may homeostatically restabilize or destabilize the perturbed network, causing changes in the throughput of information in denervated areas (Steward, 1994; Vlachos et al., 2012a,b, 2013). In some cases, the reorganization of surviving pathways may even be functionally restorative, resulting in the recovery of some of the functions that have been lost (Fawcett, 2009; Garcia-Alias et al., 2009; Maier et al., 2009; Filli and Schwab, 2015).

One of the mechanisms contributing to the reorganization of connections in denervated areas of the CNS is collateral sprouting of surviving axons. Although collateral sprouting was described several decades ago, and considerable efforts have gone into understanding the rules of sprouting (Steward, 1994; Deller and Frotscher, 1997; Deller et al., 2007; Perederiy and Westbrook, 2013), we do not fully understand the dynamics, specificity, or the regulatory mechanisms underlying axon sprouting, needed to exploit its potential in therapy. Although rehabilitation of patients with CNS injuries aims at training and enhancing the function of surviving pathways and, thus, the rewiring mechanisms, there are no standardized pharmacological treatments that target sprouting in a clinical setting (Filli and Schwab, 2015). Thus, a reinvestigation of the mechanisms underlying denervation-induced collateral sprouting may be useful in the search for novel targets.

A useful strategy for addressing the above questions related to sprouting is the use of an *in vitro* denervation model in which sprouting conditions can be controlled. Accordingly, we transferred the classic *in vivo* entorhinal denervation model (Steward et al., 1974; Lynch et al., 1976; Cotman and Nadler, 1978; Steward, 1994; Deller and Frotscher, 1997) to organotypic tissue cultures, and demonstrated robust collateral sprouting of associational axons following entorhinal denervation *in vitro* (Prang et al., 2003; Del Turco and Deller, 2007). Using this same model, we analyzed dendritic changes of granule cells in response to entorhinal denervation and identified sphingosin-1-phosphate (S1P) as a regulatory molecule and potential therapeutic target (Willems et al., 2016). Furthermore, we demonstrated the role of homeostatic plasticity mechanisms in the context of brain reorganization (Vlachos et al., 2012a,b, 2013). In all of these studies, single entorhinal cortex (EC) and hippocampus (H) cultures (EC-H) were used in which associational mossy cell axons sprout and re-innervate the entorhinal zone (Prang et al., 2003). Under *in vivo* conditions, however, mossy cells have commissural collaterals, which contribute to the re-innervation of the contralateral dentate gyrus *in vivo* (Del Turco et al., 2003). Whether these collaterals would also sprout *in vitro* has remained unclear. To study associational and commissural mossy cell sprouting systematically, and to extend the model for sprouting analysis, we have built complex tissue culture systems using double cultures of EC and H. In these complex cultures, we revisited associational sprouting and studied, for the first time, commissural sprouting *in vitro*. Our data indicate that both collaterals of the mossy cells sprout and contribute to the re-innervation of the denervated entorhinal target zone in the dentate outer molecular layer. Mossy cell sprouting *in vitro* is extensive and similar to what has been reported previously in juvenile rodents (Gall and Lynch, 1978, 1980; Gall et al., 1980; McWilliams and Lynch, 1983).

## MATERIALS AND METHODS

### Animals

Thy1-YFPtg (Feng et al., 2000) and beta-actin-GFPtg (Okabe et al., 1997) reporter mice, as well as calretinin-deficient (Schurmans et al., 1997) and wild-type mice (C57Bl6/J), were used in this study. Mice were maintained in a 12 h light/dark cycle with food and water available *ad libitum*. Every effort was made to minimize distress of animals. Animal care and experimental procedures were performed in agreement with the German law on the use of laboratory animals (animal welfare act; TierSchG). Animal welfare was supervised and approved by the Institutional Animal Welfare Officer of Goethe-University Frankfurt, Faculty of Medicine.

### Organotypic Tissue Cultures

Entorhino-hippocampal tissue cultures were prepared from mouse brain at postnatal days 4–5 according to previously published protocols (Prang et al., 2003; Del Turco and Deller, 2007). To prepare complex cultures of wild-type hippocampus with GFP-positive entorhinal cortex, animals were decapitated and wild-type hippocampi without attached entorhinal cortex and entorhinal cortex (EC) of beta-actin–GFPtg hippocampi were dissected. For Thy1-YFPtg cultures, animals were decapitated and hippocampi with attached entorhinal cortex (entorhino-hippocampal culture, EC-H) were dissected. To prepare complex cultures of two entorhino-hippocampal cultures, animals were decapitated and EC-H of wild-type and calretinin-deficient animals were dissected. For brain dissection, ice-cold preparation medium (Minimal essential medium (MEM, Gibco) containing 2 mM Glutamax (Gibco), pH 7.3) was used. Slices (300–350 μm) were cut using a Leica vibratome (VT1200S, Leica). Organotypic tissue cultures were maintained on porous-membrane filter insets (Millicell-CM, Millipore) and incubated in a humidified atmosphere with 5% $CO_2$ at 37°C. Medium for cultivation contained 42% MEM, 25% basal medium eagle (Gibco), 25% heat-inactivated normal horse serum (Gibco), 2.5% HEPES buffer solution (Invitrogen), 0.15% bicarbonate (Invitrogen), 0.675% glucose (Sigma-Aldrich), 0.1 mg/ml streptomycin (Sigma-Aldrich), 100 U/ml penicillin (Sigma-Aldrich) and 2 mM Glutamax. The pH was adjusted to 7.3 and the medium was replaced every 2–3 days. Organotypic tissue cultures were incubated for up to 28 days *in vitro* (DIV).

## Perforant Path Lesion *in vitro*

Entorhino-hippocampal cultures were allowed to mature until 14 DIV. Using a sterile scalpel blade, entorhino-hippocampal cultures were completely transected as described (Del Turco and Deller, 2007). After the lesion, the cultures were placed back into the incubator and kept until 14 days post lesion.

## Adeno-Associated Virus Production

HEK293T cells were transfected with pDP1rs (Plasmid Factory), pDG (Plasmid Factory), and GFP-vector plasmid (12:8:5) by calcium phosphate seeding and precipitation adapted from Grimm (2002). Cells were collected 48 h after transfection, washed twice with Phosphate Buffered Saline (PBS), centrifuged at 800 rpm for 4 min and re-suspended in PBS. Viral particles within the cells were released by 4 freeze- and thaw cycles and supernatant was centrifuged at 10,000 rpm for 10 min to remove cell debris. The final supernatant was collected, aliquoted, and stored at −80 °C.

## Viral Labeling

To label hilar mossy cells, tissue cultures were transduced with an adeno-associated virus serotype 2 (AAV2) containing GFP under the human Synapsin 1 promoter (AAV2-hSyn1-GFP). Injections were performed using an injection pipette pulled from thin-walled borosilicate capillaries (Harvard Apparatus, 30-0066). Pipettes were held by a head stage with a HL-U holder (Axon Instruments) and positioned using a micro-manipulator (Luigs and Neumann). Approximately 0.05–0.1 µl of AAV2-hSyn1-GFP was injected directly into the hilar region of the dentate gyrus using a syringe. Tissue cultures were visualized with an upright microscope (Nikon FN1) using a 10× water immersion objective lens (Nikon Plan Fluor, NA 0.30). All injections were performed 3–4 days after the tissue cultures were prepared.

## Time-Lapse Imaging of Organotypic Tissue Cultures

Live imaging of tissue cultures was performed as previously described (Muller et al., 2010). The membrane insert with the cultures was placed into a 30 mm petri dish that contained imaging medium (37 °C) which consisted of NaCl 129 mM, KCl 4 mM, $MgCl_2$ 1 mM, $CaCl_2$ 2 mM, glucose 4.2 mM, HEPES 10 mM, Trolox 0.1 mM, streptomycin 0.1 mg/ml, penicillin 100 U/ml; pH 7.4. The osmolarity of the imaging medium was adjusted with sucrose to the osmolarity of the incubation medium. Imaging was done with an upright confocal microscope (Zeiss, Pascal; 488 nm excitation laser) equipped with a temperature-regulated stage (37 °C), using a 10× water immersion objective lens (0.3 NA; Zeiss) to visualize tissue cultures and to identify AAV-labeled mossy cells in the hilus of the DG. Image stacks (approximately 20 images per stack; *z*-axis interval between consecutive frames: 5 µm) of DG regions were obtained at a resolution of 1024 × 1024 pixels. Tissue cultures were imaged on 14, 17, 20, 24, and 28 days *in vitro* for less than 10 min per culture in order to keep exposure time and phototoxic damage minimal. GFP-intensity levels of AAV-injected cultures were equalized at DIV 14 using Adobe Photoshop CS6 (Version 13.0.1 × 64) to account for differences in GFP expression between cultures.

## Immunofluorescence

Tissue cultures were fixed in 4% paraformaldehyde (PFA) in 0.1 M PBS (pH 7.4) for 4 h. After several washes with 50 mM Tris–buffered saline (TBS; pH 7.4), cultures were re-sliced into 30 µm sections on a vibratome (VT 1000S, Leica). For cutting on a cryostat cultures were fixed in 4% PFA in 0.1 M PBS (pH 7.4) and 4% sucrose for 1 h at room temperature (RT), followed by 2% PFA and 30% sucrose in PBS overnight at 4°C. After several washes with 50 mM TBS (pH 7.4), cultures were re-sliced into 30 µm sections on a cryostat (CM3050 S, Leica). Free-floating sections were washed several times in 50 mM TBS containing 0.1% Triton X-100, incubated in a blocking buffer (0.5% Triton X-100, 5% bovine serum albumin (BSA) in 50 mM TBS) for 30 min at RT and subsequently incubated with the appropriate primary antibody (diluted in 0.1% Triton X-100, 1% BSA in 0.05 M TBS) for 2 days at RT. Rabbit anti-calretinin (1:1000, Swant) and mouse anti-NeuN (1:1000, Chemicon) were used as primary antibodies. After several washing steps, sections were incubated with the appropriate secondary Alexa-conjugated antibodies (1:2000, Invitrogen) for 4 h at RT, counterstained with DRAQ5 (1:10,000, Thermo Fisher Scientific) or Hoechst (1:50,000, Sigma-Aldrich) to visualize nuclei, and mounted in Fluorescence Mounting Medium (Dako, Agilent Technologies).

## Quantification of the Sprouting Response Following Denervation

To quantify the expansion of the associational or commissural fiber plexus from the inner into the denervated outer molecular layer, confocal image stacks (EZ-C1, Nikon) of middle sections from re-sliced tissue cultures were captured (10× objective; pinhole size: 30 µm). Using the counterstains to visualize the cytoarchitecture of the DG, the width of the total molecular layer was determined from the outer border of the granule cell layer to the hippocampal fissure using ImageJ (Schneider et al., 2012). This was done at three locations ($0^\circ$, $-60^\circ$, $+60^\circ$), with $0^\circ$ being defined as a line from the middle of the hilus through the crest of the DG to the hippocampal fissure. In a second step, the width of the calretinin-positive or the YFP-positive fiber plexus was measured from the outer border of the granule cell layer to the outer border of the main plexus. The percentage of the molecular layer covered by the calretinin-positive or the YFP-positive fiber plexus was calculated for the three locations in control and denervated cultures and subsequently averaged per culture. This algorithm ensured defined sampling of the supra- and infrapyramidal blades of the DG as well as the crest region and, thus, yielded an overall parameter of the extent of sprouting.

## Statistics

Statistical analysis was done using GraphPad Prism 6 Software. Mann–Whitney test or Kruskal–Wallis test was used. Significance

level was set at: $^{*}p < 0.05$. Individual tests and test parameters are indicated in figure captions.

## RESULTS

### Laminar Termination of Calretinin-Positive Associational and Entorhinal Axons in the Dentate Gyrus of Re-sliced Entorhino-Hippocampal Hybrid Cultures

To determine whether the laminar termination pattern of the two major projection systems to the dentate gyrus, i.e., the calretinin-positive associational projection arising from hilar mossy cells and the entorhinal projection arising from layer II neurons of the entorhinal cortex (EC), were maintained in organotypic tissue cultures, genetically hybrid cultures were generated at postnatal day 4–5. Entorhinal cortex derived from a beta-actin-GFPtg reporter mouse was co-cultured with hippocampus obtained from wild-type mice, and maintained *in vitro* until DIV 28. After fixation, re-slicing and immunolabeling for calretinin, essentially all calretinin-positive mossy cell axons and all GFP-positive entorhinal axons present within the culture could be visualized using confocal imaging (**Figure 1**). Although a segregated termination of calretinin-positive associational and entorhinal axons could be seen at all levels of the re-sliced DG (**Figure 1**), the most defined termination pattern of the two projections was found in middle sections (**Figures 1b,c**).

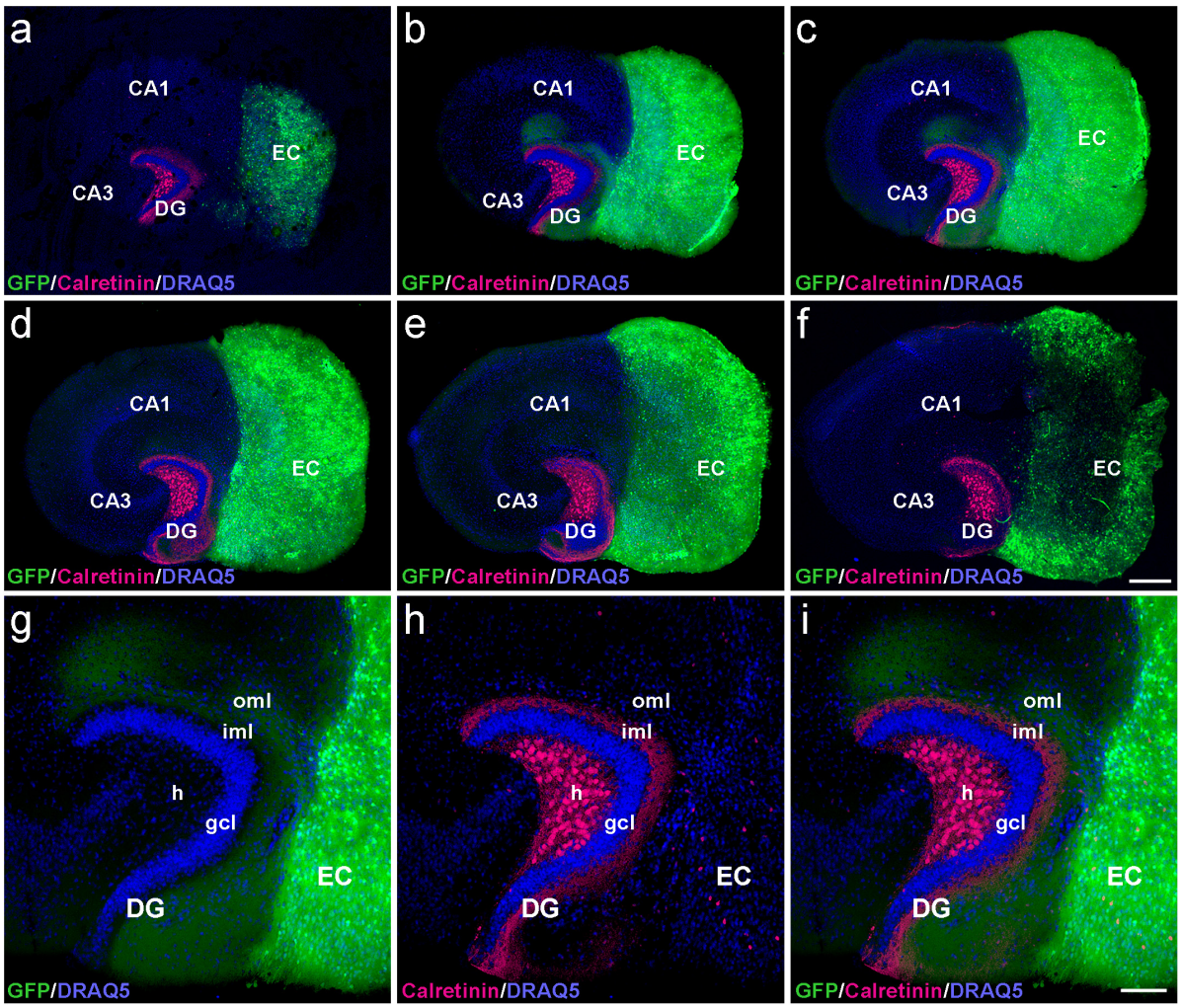


**FIGURE 1 |** Serial confocal sections of re-sliced entorhino-hippocampal culture. **(a–f)** Serial sections (30 μm) of a control entorhino-hippocampal tissue culture (DIV 28) composed of wild-type mouse hippocampus and beta-actin-GFPtg mouse entorhinal cortex (EC). Note the laminar termination pattern of calretinin-positive axons (magenta) in the inner molecular layer (iml) and of entorhinal axons (GFP; green) in the outer molecular layer (oml) of the dentate gyrus (DG). Although fiber lamination is maintained throughout all levels of the re-sliced DG **(a–f)**, the best-defined and most organotypic termination pattern of the two projections is seen in middle sections **(b,c)**. Accordingly, such sections were used for the quantification of denervation-induced axonal sprouting. **(g–i)** Higher magnification of the middle section illustrated in **(c)**, exhibiting a well-organized DG with an organotypic cyto- and fiber-architecture. DRAQ5 (blue) was employed to visualize nuclei. h, hilus; gcl, granule cell layer; CA1, cornu ammonis subfield 1; CA3, cornu ammonis subfield 3. Scale bars: 250 μm **(a–f)**; 100 μm **(g–i)**.

At this culture level, the shape of the granule cell layer as well as the laminar termination pattern of calretinin-positive fibers in the inner molecular layer and entorhinal axons in the outer molecular layer appeared closest to the *in vivo* situation, i.e., most organotypic (**Figures 1g–i**).

In the part of our study in which we analyzed and quantified denervation-induced sprouting, we focused on the middle sections of re-sliced cultures. We consider this methodological approach important, since it takes the three-dimensional organization of the tissue cultures into account and clear tissue borders are needed for reliable quantification of the sprouting response. In addition, the shape of the granule cell layer varied toward more superficial levels, possibly because proliferation and differentiation of granule cells continues *in vitro* for days after preparation of the culture (Radic et al., 2017).

## Associational Sprouting of Mossy Cell Axons Following Lesion

After assessing the 3D-organization, we used the hybrid EC-H tissue cultures described above for the analysis of associational sprouting following entorhinal denervation (**Figure 2**). At DIV 14 the entorhino-hippocampal projection was transected using a sterile scalpel and at DIV 28 associational sprouting was analyzed in middle sections of re-sliced cultures labeled for calretinin (**Figures 2b,d**). Non-lesioned cultures (DIV 28) served as controls (**Figures 2a,c**). Because GFP-positive entorhinal axons could be identified using direct fluorescence, completeness of the lesion could be verified by the absence of EC axons in the dentate gyrus prior to re-slicing of the culture.

In controls (**Figures 2a,c,e,f**) the calretinin-positive fiber plexus in the inner molecular layer was well-defined, easy to identify, and it covered ∼30% of the width of the molecular layer (**Figure 2i**). Of note, in addition to the calretinin-positive mossy cells, some hippocampal interneurons also contain calretinin (Blasco-Ibanez and Freund, 1997). The axons of these interneurons are present throughout the culture, including the molecular layer of the dentate gyrus. However, compared to the dense calretinin-positive plexus in the inner molecular layer formed by hilar mossy cells, calretinin-positive axons of presumed interneurons are scarce. The border between the calretinin-positive mossy cell axons and the "entorhinal zone" of the molecular layer is, thus, well-defined and amenable to quantification (**Figures 2a,c,e**).

Following entorhinal denervation (**Figures 2b,d,g,h**) GFP-positive EC axons were lost. In contrast, virtually the entire molecular layer was filled with calretinin-positive axons. These axons reached up to the hippocampal fissure and covered ∼95% of the width of the molecular layer (**Figure 2i**). This result was highly reproducible, robust and massive, since the density of calretinin-positive fibers in the denervated zone was close to the density of calretinin-positive fibers in the inner molecular layer in some cases (e.g., **Figures 2d,g**).

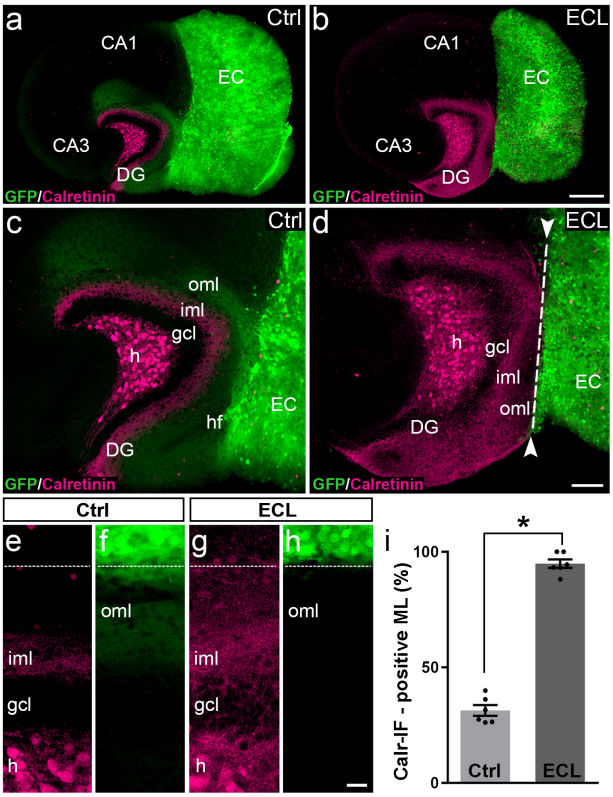


**FIGURE 2 |** Associational sprouting of calretinin-positive axons following lesion at DIV 14. **(a)** Control (Ctrl) entorhino-hippocampal culture (re-sliced; middle section) composed of wild-type mouse hippocampus and beta-actin-GFPtg mouse entorhinal cortex (EC) at DIV 28. Mossy cell axons (calretinin-immunolabeling; magenta) and entorhinal axons (green) terminate in their respective layers of the dentate gyrus (DG). **(b)** Following transection of the entorhinal projection at DIV 14, EC axons are lost and an extensive sprouting of calretinin-positive mossy cells axons into the "entorhinal zone" of the DG is observed 14 days post lesion (DIV 28). **(c–h)** Higher magnifications of the cultures shown in **(a)** and **(b)**. In the non-lesioned culture **(c,e,f)** calretinin-positive fibers occupy the inner molecular layer (iml). In the lesioned culture **(d,g,h)** calretinin-positive fibers cover the iml and the outer molecular layer (oml) up to the hippocampal fissure (hf; dashed line). **(i)** Quantitative analysis of the sprouting response of calretinin-positive axons. The width of the main calretinin plexus in the molecular layer (ML) was measured in control (31.32 ± 2.33%, Ctrl) and EC-lesioned cultures (94.82 ± 1.87%, ECL). Mann–Whitney test; mean ± SEM; $*p < 0.05$; $N = 6$ cultures per group; h, hilus; gcl, granule cell layer; CA1, cornu ammonis subfield 1; CA3, cornu ammonis subfield 3. Scale bars: 250 μm **(a,b)**; 100 μm **(c,d)**; 20 μm **(e–f)**.

We conclude from our observations *in vitro* that sprouting calretinin-positive axons extensively re-innervate the entire "entorhinal zone" of the slice-cultured dentate gyrus.

## Changes in Calretinin-Immunofluorescence Observed After Entorhinal Denervation Reflect Sprouting of Hilar Mossy Cell Axons

The re-innervation of the outer dentate molecular layer by calretinin-immunopositive axons strongly suggests that mossy cell axons leave their classical "associational" termination zone

in the inner molecular layer and invade the "entorhinal zone" of the dentate gyrus. However, since calretinin is also present in the axons of some GABAergic interneurons (Blasco-Ibanez and Freund, 1997), which may also sprout following entorhinal denervation (Nadler et al., 1974; Nadler, 1981; Goldowitz et al., 1982; Deller et al., 1995a; Houser, 2014), we wanted to corroborate and validate our findings using a second approach. To accomplish, we generated EC-H cultures of Thy1-YFP-transgenic animals (Feng et al., 2000). In the dentate gyrus of these cultures, variable numbers of granule cells and mossy cells express the YFP-transgene (**Figure 3**). In some cultures, mossy cells predominate, and a well-defined YFP-positive mossy cell axon plexus was observed in the inner molecular layer (**Figures 3b,d**). Both, mossy cell somata and mossy cell axons targeting the inner molecular layer were strongly calretinin-positive (**Figures 3a,b,d–f**) in these YFPtg culture preparations.

Next, we performed an entorhinal denervation experiment and denervated EC-H cultures prepared from Thy1-YFPtg mouse brains at DIV 14. At DIV 28, the cultures were fixed, re-sliced, and immunolabeled for calretinin. Similar to what we have shown above for calretinin immunolabeling (**Figure 2**), calretinin-immunopositive axons were abundant throughout the denervated "entorhinal target zone" (**Figures 3h,i**). This pattern of sprouting was mirrored by YFP-positive fibers arising from hilar mossy cells (**Figures 3g,i**). Following denervation, calretinin and YFP-positive fibers covered 96% and 100% of the width of the molecular layer, respectively (**Figures 3j,k**). The overlay of both markers indicates that the overwhelming majority of axons re-innervating the denervated outer molecular layer of the dentate gyrus are double-labeled, i.e., are mossy cell axons.

We conclude from these experiments that associational mossy cell axons are primarily responsible for the re-innervation of the denervated dentate gyrus in EC-H single cultures (denervation occurring at DIV 14).

## Associational and Commissural Sprouting Following Bilateral Entorhinal Denervation of Wild-Type and Calretinin-Deficient Double Cultures

In the intact brain, axons of hilar mossy cells form both the ipsilateral inner molecular layer (the associational projection)

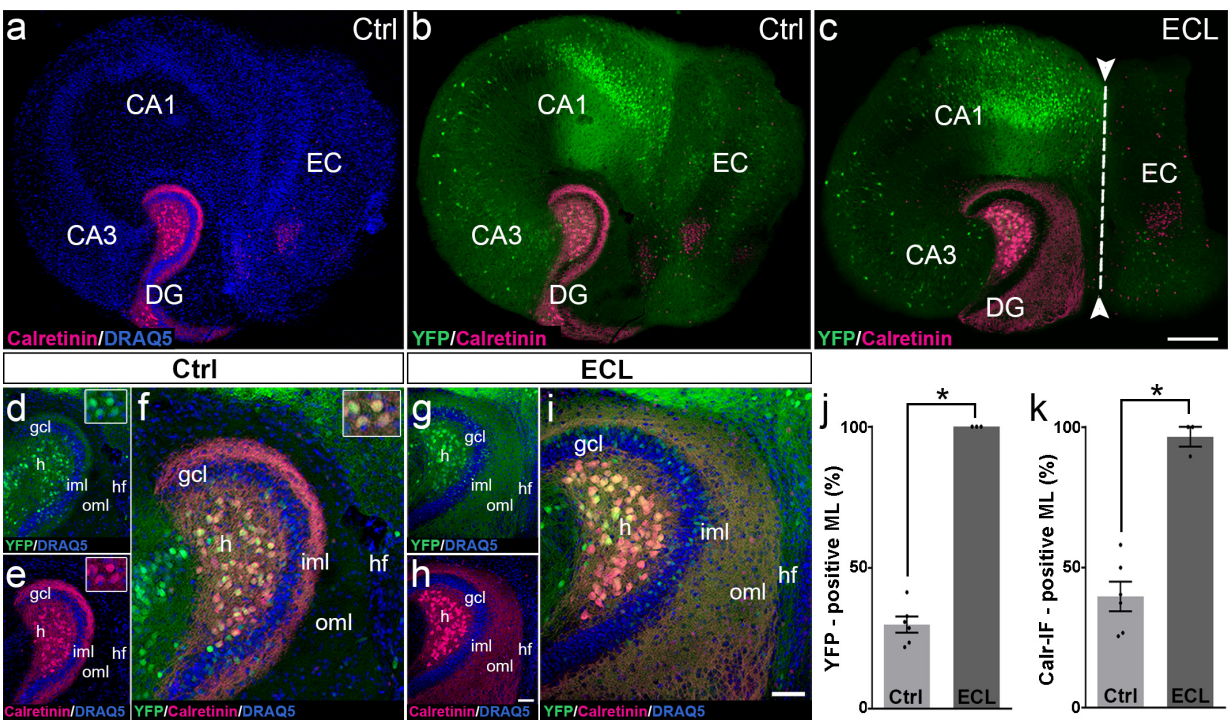


**FIGURE 3 |** Changes in calretinin-immunofluorescence observed after entorhinal denervation reflect sprouting of hilar mossy cell axons. **(a–i)** Entorhino-hippocampal tissue cultures (DIV 28) generated from Thy1-YFPtg mouse hippocampus immunolabeled for calretinin (magenta) and counterstained with DRAQ5 (blue). Overviews **(a,b)** and higher magnifications **(d–f)** of the dentate gyrus (DG) of a non-denervated control culture reveal YFP- (green) and calretinin- (magenta) positive axons in the inner molecular layer (iml) of the DG. Note the almost complete overlap of the two markers **(f)**. Insets show YFP- and calretinin-positive mossy cell somata in the hilus (h). Overview **(c)** and higher magnification **(g–i)** of the DG of a culture with an entorhinal cortex lesion (ECL; dashed line in c indicates knife cut) performed at DIV 14. YFP-positive mossy cell axons **(g)** as well as calretinin-positive axons **(h)** are abundant in the denervated outer molecular layer (oml) and reach up to the hippocampal fissure (hf). Note almost complete overlap of the two markers. **(j,k)** Quantitative analysis of the axonal sprouting response into the molecular layer (ML). Comparable results are obtained for YFP (29.81 ± 2.87%, Ctrl; 100 ± 0%, ECL) and calretinin (Calr; 39.65 ± 5.22%, Ctrl; 96.53 ± 3.47%, ECL). Mann–Whitney test; mean ± SEM; $^*p < 0.05$; $N$ = 3–6 cultures per group; gcl, granule cell layer; CA1, cornu ammonis subfield 1; CA3, cornu ammonis subfield 3. Scale bars: 200 μm **(a–c)**; 50 μm **(d–i)**.

and the same region of the contralateral dentate gyrus (the commissural projection). Therefore, we determined whether the commissural axon collateral of mossy cells *in vitro* forms the same reorganization as it does *in vivo*.

One way to address this question is to study the response of both axon collaterals to entorhinal denervation *in vitro*. Since calretinin is a robust marker for mossy cells and their axons, we used calretinin to study sprouting of both mossy cell axon collaterals. To distinguish between ipsi- and contralateral mossy cell axons, we co-cultured an EC-H culture generated from the brain of a wild-type mouse (mossy cells are calretinin-positive), with an EC-H culture generated from the brain of a calretinin-deficient mouse in which the mossy cells are calretinin-negative. Immunostaining of these cultures for calretinin only reveals the calretinin-positive wild-type axons whereas the calretinin-negative mossy cell axons arising from the calretinin-deficient EC-H culture are unlabeled (**Figure 4**).

Indeed, in calretinin-immunolabeled control double cultures, calretinin-positive mossy cell somata were seen only in the hilus of the wild-type culture (**Figure 4**). In line with this, the associational and commissural calretinin-positive axon plexuses were present in the ipsi- and contralateral dentate gyrus (**Figures 4a,b,d**), covering 38 and 36% of the molecular layer, respectively (**Figure 4f**). We then performed an entorhinal cortex lesion at DIV 14 and quantified the expansion of both calretinin-positive fiber plexus at DIV 28. At this time point, calretinin-positive fibers covered nearly the entire molecular layer in both dentate gyri (**Figures 4c,e,f**). Calretinin-positive axons covered 93 and 91% of the width of the molecular layers associationally and commissurally, respectively (**Figure 4f**).

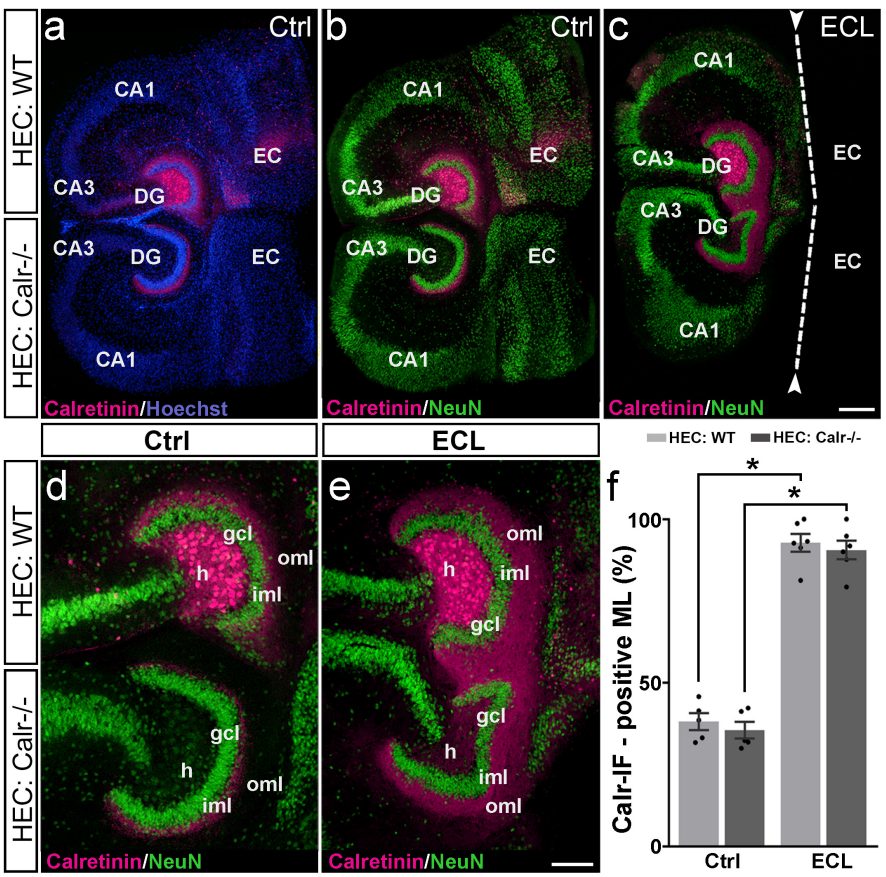


**FIGURE 4 |** Associational and commissural sprouting following bilateral entorhinal denervation of wild-type and calretinin-deficient double cultures. **(a–c)** Hybrid double cultures of wild-type (WT) and calretinin-deficient (Calr−/−) mouse hippocampus (DIV 28) immunolabeled for calretinin (magenta) and counterstained with Hoechst (blue) or NeuN (green). Overview **(a,b)** and higher magnification **(d)** of a non-denervated double culture. Calretinin-positive mossy cells found only in the hilus (h) of the wild-type culture form associational (wild-type culture) and commissural (Calr−/− culture) collaterals to the inner molecular layer (iml). Overview **(c)** and higher magnification **(e)** of a double culture in which the entorhinal projection has been removed at DIV 14 (entorhinal cortex lesion, ECL; dashed line in **(c)** indicates knife cut). At DIV 28 calretinin-positive axons are abundant in the outer molecular layer (oml) of the dentate gyrus (DG) on both the ipsi- (wild-type; associational) and contralateral (Calr−/−; commissural) side. **(f)** Quantitative analysis of the axonal sprouting response into the molecular layer (ML). On the wild-type side (associational sprouting; light gray bars) a significant expansion of the calretinin-plexus occurs (38.16 ± 2.59%, Ctrl; 92.84 ± 2.72%, ECL). On the Calr−/− side (commissural sprouting; dark gray bars) a similar expansion of the calretinin-plexus is detected (35.56 ± 2.57%, Ctrl; 90.61 ± 2.86%, ECL). Kruskal-Wallis with Dunn's multiple comparison *post hoc* test; mean ± SEM; $^*p < 0.05$; $N = 5–6$ cultures per group; gcl, granule cell layer; CA1, cornu ammonis subfield 1, CA3, cornu ammonis subfield 3; EC, entorhinal cortex. Scale bars: 200 μm **(a–c)**; 100 μm **(d–e)**.

We conclude from our findings that entorhinal denervation can induce associational as well as commissural mossy cell sprouting.

## Associational and Commissural Sprouting Begins Within Days After Entorhinal Denervation of Wild-Type Double Cultures

Next, we assessed the dynamics of sprouting after *in vitro* entorhinal cortex lesion. To address this question, wild-type EC-H double cultures were prepared and AAV2-hSyn1-GFP was injected into one hilus. At 14 DIV, one group of cultures was lesioned (**Figures 5f–j**), whereas the other group served as non-lesioned controls (**Figures 5a–e**). Otherwise, both groups were treated identically and repetitively imaged as whole mounts (**Figure 5**). At the end of the imaging period some cultures were fixed, re-sliced, and immunostained for calretinin (**Figure 6**; see next paragraph).

In both groups, the AAV successfully transduced granule cells and hilar neurons with hSyn1-GFP. In general, injections were limited to the DG. Within the injected dentate gyrus, the site and size of the injection, as well as the number of transduced cells varied between cultures. Expression of GFP was detected ∼8–10 days following injection of the virus and GFP expression levels increased throughout the entire observation period (**Figure 5**). Because of this change in GFP expression we used only differences in the distribution pattern (and not in signal strength) of GFP-labeled axons between time-matched control and lesioned cultures for the evaluation of sprouting.

Control cultures injected with AAV showed in the molecular layer ipsilateral to the injection ("associational side") a dense GFP-labeled axon plexus in the inner molecular layer and numerous GFP-labeled axons in the outer molecular layer. In those injections in which some granule cells had also been transduced, GFP-labeled granule cell dendrites were present in parts of the molecular layer. Of note, the border of the GFP-axon plexus in the inner molecular layer, which arises from mossy cell axons, could be well-delineated. Although the intensity of the GFP-signal increased with time, the termination pattern of these inner molecular layer fibers remained apparently unchanged in controls. Likewise, in the molecular layer of the dentate gyrus contralateral to the injection ("commissural side") a dense GFP-labeled axon plexus was seen in the inner molecular layer. A much smaller number of GFP-labeled commissural axons were also found in the outer molecular layer, as seen

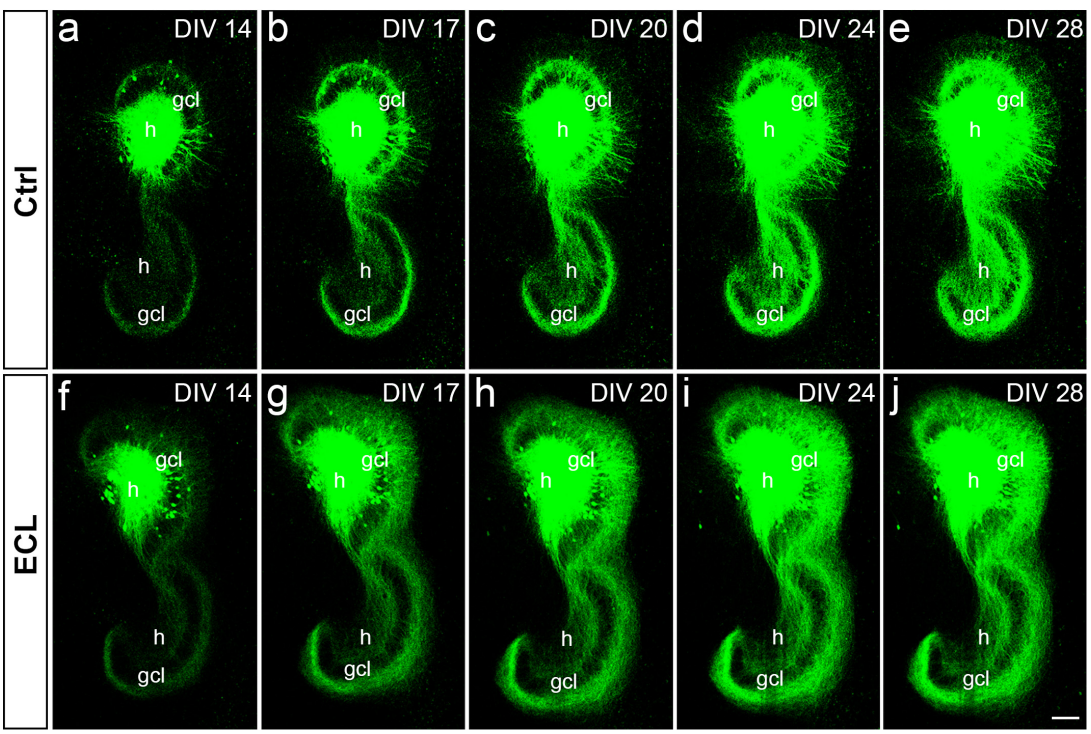


**FIGURE 5 |** Associational and commissural sprouting in wild-type double cultures after entorhinal denervation visualized by hilar injection of AAV2-hSyn1-GFP. **(a–j)** Time-lapse imaging of wild-type entorhino-hippocampal double cultures without **(a–e)** and with entorhinal cortex lesion [ECL; **(f–j)**]. At DIV 4 all cultures received an injection of AAV2-hSyn1-GFP into one hilus (h). On DIV 14 one group of cultures received bilateral ECL **(f–j)**, whereas the other group served as non-lesioned control **(a–e)**. Both groups were treated identically and imaged (whole mount cultures) with the same imaging parameters at the time points indicated until DIV 28. Although the expression level of GFP (green) increased in both groups with observation time, the termination pattern of GFP-positive associational and commissural fibers showed major differences: Whereas GFP-positive associational and commissural fibers were most abundant in the inner molecular layer (iml) of the non-lesioned culture, GFP-associational and commissural fibers also invaded the outer molecular layer (oml) of the ECL culture. Sprouting into the oml occurred as already as 3 days post lesion [**(g)**; DIV 17] and seemed to be complete around 10 days post lesion [**(i)**; DIV 24]. gcl, granule cell layer; Scale bar: 100 μm.

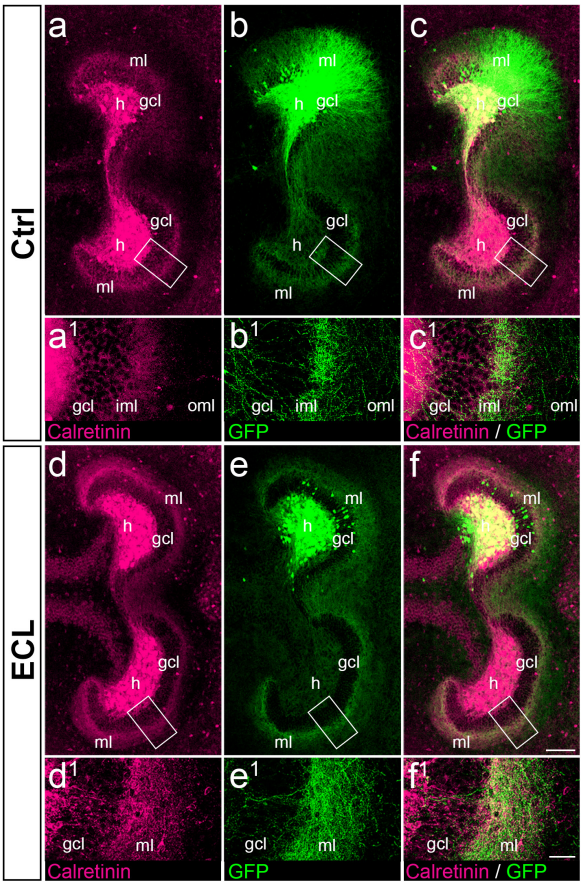


**FIGURE 6 |** Associational and commissural sprouting after entorhinal denervation of AAV2-hSyn1-GFP injected wild-type double cultures corresponds to the sprouting of calretinin-positive fibers. **(a–c)** Entorhino-hippocampal double culture (DIV 28; control (Ctrl) culture; fixed and re-sliced) immunolabeled for calretinin (magenta) and injected with AAV2-hSyn1-GFP (green; injection at DIV 4). Overlay of **(a)** and **(b)** shown in **(c)**. Boxed areas are illustrated at higher magnification **($a^1$–$c^1$)**. Note the preference of associational/commissural calretinin-positive and of commissural GFP-positive axons for the inner molecular layer (iml). **(d–f)** Entorhino-hippocampal double culture with entorhinal cortex lesion (ECL; 14 days post lesion; DIV 28; fixed and re-sliced). Overlay of **(d)** and **(e)** shown in **(f)**. Boxed areas are illustrated at higher magnification **($d^1$–$f^1$)**. Calretinin-positive associational/commissural axons as well as GFP-positive commissural axons are found throughout the entire molecular layer and show extensive overlap. Scale bars: 100 μm **(a–f)**; 20 μm **($a^1$–$f^1$)**.

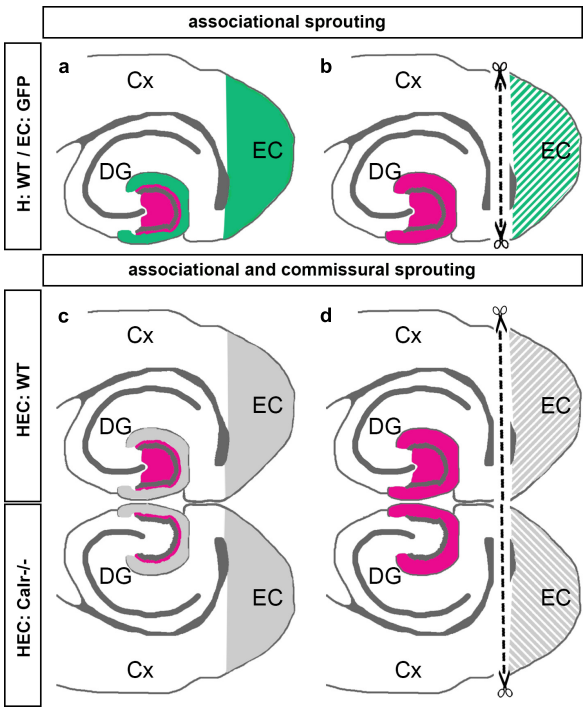


**FIGURE 7 |** Schematic summary diagram of associational and commissural sprouting following entorhinal denervation in organotypic tissue cultures of mouse hippocampus. **(a,b)** Associational sprouting following entorhinal denervation at DIV 14 in single entorhino-hippocampal tissue cultures (c.f. **Figures 1**–**3**). **(a)** In non-denervated control cultures hilar mossy cells (magenta) terminate in the inner molecular layer of the dentate gyrus (DG). Entorhinal axons (green) terminate in the outer molecular layer. **(b)** Following transection and loss of entorhino-hippocampal axons (dashed line) associational mossy cell axons sprout and cover the "entorhinal zone" of the DG. **(c,d)** Associational and commissural sprouting following denervation at DIV 14 in double entorhino-hippocampal tissue cultures generated from wild-type (HEC: WT) and calretinin-deficient (HEC: Calr−/−) mouse hippocampus (c.f. **Figure 4**). **(c)** In non-denervated double cultures calretinin-positive mossy cells are only found in the HEC: WT culture. Axons of these neurons (magenta) innervate the ipsilateral (associational) and the contralateral (commissural) inner molecular layer of the DG. Using this hybrid approach associational and commissural axons of mossy cells can be identified using calretinin-immunofluorescence. Entorhinal fibers are shown in gray. **(d)** Following entorhinal cortex lesion (dashed line) associational and commissural calretinin-positive mossy cell axons sprout into the outer molecular layer, i.e., the "entorhinal zone" of the DG, on both sides; Cx, cortex; EC, entorhinal cortex.

*in vivo* (Deller et al., 1995b, 1996). Similar to the associational side, the outer border of the commissural GFP-plexus in the inner molecular layer could be readily defined. In controls, the termination pattern of these commissural fibers remained apparently unchanged.

In denervated cultures injected with the AAV, the situation was similar to controls at DIV 14. However, as early as DIV 17, GFP-positive fibers from the inner molecular layer were observed to enter the denervated "entorhinal target zone" of the dentate gyrus. This sprouting response continued and appeared to be relatively complete by DIV 24, i.e., 10 days post lesion. We conclude from these data that associational/commissural sprouting starts rapidly, i.e., within only a few days following entorhinal denervation *in vitro* at DIV 14.

## Associational and Commissural Sprouting Seen in AAV2-hSyn1-GFP-Injected Wild-Type Double Cultures Mirrors Sprouting of Calretinin-Positive Fibers

Since AAV injections transduce all types of neurons, we wanted to confirm that the majority of GFP-positive axons seen in the inner molecular layer of controls and in the entire molecular

layer of denervated cultures were calretinin-positive. As shown *in vivo* (Blasco-Ibanez and Freund, 1997), and in this *in vitro* study (**Figure 3**), calretinin primarily labels mossy cell axons and is a marker for mossy cell axon sprouting. Accordingly, we fixed, re-sliced, and immunostained the AAV-injected wild-type double cultures for calretinin (**Figure 6**).

In control as well as in denervated cultures an extensive overlap between GFP-positive and calretinin-positive axons was seen (**Figure 6**), in particular in the inner molecular layer of controls (**Figures 6a–c**) and in the entire molecular layer following denervation (**Figures 6d–f**). As expected, overlap of the two markers was not as complete as that seen in the case of the YFPtg cultures (c.f. **Figure 3**), since some GFP-positive axons do not arise from mossy cells.

## DISCUSSION

In the absence of any specific treatment for CNS damage, e.g., stem cells to replace neurons, or drugs that might induce axonal regeneration to restore anatomical connectivity, lesion-induced reorganization in the CNS might be an effective strategy. Since collateral sprouting is one of the mechanisms in this rewiring process, it appears to be timely to reinvestigate its rules and mechanisms using *in vitro* systems, such as the entorhinal denervation model *in vitro* (Prang et al., 2003; Del Turco and Deller, 2007; Vlachos et al., 2012a, 2013).

The present study was performed to better understand the sprouting of mossy cell axons following entorhinal denervation *in vitro*. Our findings can be summarized as follows: (1) Using EC-H co-cultures of beta-actin-GFPtg and wild-type mice, we could show that calretinin-positive associational axons re-innervate the denervated "entorhinal" zone of the DG (**Figures 7a,b**). (2) Using EC-H cultures of Thy1-YFPtg mice, we demonstrated that calretinin-immunolabeling can be used to visualize mossy cell sprouting. (3) In double cultures of EC-H, a hippocampal commissural system forms. By co-culturing EC-H of wild-type and EC-H of calretinin-deficient mice, the associational and commissural collaterals of the wild-type mossy cell population could be distinguished. Following entorhinal lesions of these double cultures, re-innervation of the entorhinal zone by associational axons was seen in the wild-type DG and re-innervation by commissural axons was observed on the calretinin-deficient side (**Figures 7c,d**). (4) Using AAV injected wild-type double-cultures, we found that associational/commissural sprouting of mossy cell axons occurs rapidly post-lesion. Taken together, we conclude that the associational and the commissural collaterals of mossy cells respond rapidly to entorhinal denervation *in vitro*. The speed and extent of the *in vitro* sprouting response was similar to that reported in juvenile rodents *in vivo*.

### Calretinin as a Marker for the Analysis of Sprouting Mossy Cell Axons

In previous work (Prang et al., 2003), we provided the first evidence for the sprouting of associational calretinin-positive axons after entorhinal denervation *in vitro*. In our present study, we revisited this phenomenon using genetically hybrid and re-sliced EC-H co-cultures. The data show that sprouting of associational calretinin-positive axons is robust, with sprouting calretinin-positive axons re-innervating the molecular layer all the way to the hippocampal fissure.

The use of calretinin as a marker for mossy cell axons is possible in mouse tissue, because mossy cells in mice, in contrast to rat mossy cells, express this calcium-binding protein constitutively (Blasco-Ibanez and Freund, 1997). However, calretinin is not only present in mossy cells, but also in a subpopulation of interneurons in the DG and hippocampus (Blasco-Ibanez and Freund, 1997). Since interneurons have been shown to contribute to the re-innervation of the denervated DG (Nadler et al., 1974; Nadler, 1981; Goldowitz et al., 1982; Deller et al., 1995a), we could not exclude that a substantial fraction of sprouting calretinin-positive fibers arises from such calretinin-positive interneurons. Therefore, we decided to use a second approach and employed EC-H cultures generated from Thy1-YFPtg mouse brain. In these cultures, mossy cells and granule cells but not calretinin-positive interneurons express YFP and, thus, sprouting YFP-positive axons in the molecular layer following entorhinal denervation are sprouting mossy cell axons. Using these cultures, we were able to directly compare mossy cell axon sprouting to the sprouting response seen with calretinin immunolabeling, which reflects sprouting of calretinin-positive mossy cells and, potentially, sprouting of calretinin-positive interneurons. This approach also allowed us to detect and estimate the fraction of sprouting axons arising from calretinin-positive interneurons. Of note, almost all YFP-positive axons found in the denervated outer molecular layer were also calretinin-positive (and vice versa), demonstrating that the overwhelming majority of calretinin-positive axons re-innervating the molecular layer after entorhinal denervation originate from mossy cell axons. Compared to the number of sprouting mossy cell axons, sprouting of axons of calretinin-positive interneurons appears to be, in fact, negligible. We also conclude, that calretinin is an excellent and highly robust marker that can be used to visualize sprouting mossy cell axons in mouse tissue cultures.

However, if Thy1-YFPtg tissue cultures are more specific for mossy cell axons, why did we continue to use calretinin-immunolabeling to visualize the sprouting response instead of switching to Thy1-YFPtg cultures? Several methodological reasons explain this choice: In our hands the use of calretinin-immunofluorescence is technically simple, results are highly robust and the extent of sprouting can readily be quantified. Also, the standardized use of calretinin as a marker for sprouting mossy cell axons makes it possible to compare the extent of sprouting across all conditions. In contrast, preparations from Thy1-YFPtg mice contain variable numbers of YFP-positive mossy and granule cells, considerably increasing the number of cultures needed for experimentation. Only a minority of cultures show a useful YFP-expression pattern. This is an even greater constraint in the case of YFP-positive double-cultures. Thus, although Thy1-YFPtg cultures were of the essence to demonstrate the overlap of calretinin and mossy cells, they do not appear to

be the ideal choice for the routine analysis of sprouting, e.g., in high-throughput assays.

## Calretinin-Deficient Mice as a Tool to Dissect Associational and Commissural Mossy Cell Sprouting

After validating calretinin as an excellent marker for sprouting mossy cell axons, we considered analyzing mossy cell sprouting in double cultures of wild-type EC-H. In such double cultures organotypic commissural projections exist and mossy cells project axon collaterals into the ipsi- as well as the contralateral DG. However, within the inner molecular layer of the DG, calretinin-positive associational collaterals from one side mix with calretinin-positive commissural collaterals from the other side. Since calretinin-immunolabeling will visualize both collaterals, this does not allow for a separate analysis of the two mossy cell axon collaterals. To solve this problem, we co-cultured a wild-type EC-H with an EC-H generated from calretinin-deficient mice. In these preparations only the mossy cell axons originating from the wild-type mouse contain calretinin and, thus, calretinin could be employed to visualize and quantify sprouting of associational and the commissural mossy cell axon collaterals, respectively.

Since we used tissue from calretinin-deficient mutant mice as a tool, we wondered whether removing calretinin from mossy cells could affect the sprouting response of the wild-type axons we were monitoring. Our observations do not provide any evidence for such an influence on wild-type sprouting axons since (i) sprouting in the wild-type-calretinin-deficient double cultures was similar to sprouting observed in the wild-type condition (associational sprouting), (ii) sprouting was not altered in the environment of the calretinin-deficient DG, and, (iii) sprouting was similar in virally traced wild-type and calretinin-deficient preparations. We conclude that although absence of calretinin from adult neurons may have some specific effects (Schurmans et al., 1997; Gurden et al., 1998), it does not seem to grossly affect the sprouting response of calretinin-positive wild-type axons in the hybrid EC-H double cultures.

## Associational and Commissural Axon Collaterals of Mossy Cells React Rapidly, Simultaneously and Massively to Entorhinal Denervation

Mossy cells are remarkable relay cells that connect large parts of both hippocampi (Scharfman and Schwartzkroin, 1988; Sloviter, 1994; Deller et al., 1995b; Zappone and Sloviter, 2001; Scharfman and Myers, 2012; Scharfman, 2016; Bui et al., 2018). Loss of hilar mossy cells is commonly seen in human temporal lobe epilepsy (Sloviter, 1996) and it can be reproducibly induced in temporal-lobe epilepsy mouse models (Kienzler et al., 2006, 2009; Volz et al., 2011; Kienzler-Norwood et al., 2017). Accordingly, mossy cells have received much attention in recent years and their role in physiology and pathology has been intensely investigated (see Scharfman, 2016 for review). In comparison, much less is known about their restorative abilities, e.g., their ability to reshape their axonal arbors using collateral sprouting. In particular in disease contexts, e.g., temporal lobe epilepsy, knowledge about their ability to contribute to brain repair could be helpful.

In the present study, we have seen that mossy cells react to denervation rapidly and very strongly, i.e., they start re-innervating the denervated DG within the first days after the lesion and they cover the entire denervated zone. Of note, both axon collaterals showed this massive growth response, suggesting that a given mossy cell can react with its entire axonal arbor to denervation. Furthermore, the sprouting response on one side did not appear to be limited by the fact that sprouting occurred on the other side. This massive growth propensity of the mossy cells is remarkable, since axonal sprouting – other than axonal regeneration following axotomy – does not require reprograming of the reacting neuron (Steward, 1995; Caroni, 1997). The ability of neurons to undergo this reprograming and to regenerate their axons is age-dependent and ends in mouse EC-H cultures after the first week *in vitro* (Prang et al., 2001, 2003; Del Turco and Deller, 2007). Mossy cells are, thus, using their structural plasticity programs to extensively re-innervate the dentate gyrus between DIV 14 and DIV 28.

Of note, the reactive response of mossy cell axons to entorhinal denervation is limited to the molecular layer of the dentate gyrus. Although entorhinal cortex lesion also denervates the neighboring stratum lacunosum-moleculare of CA3 and CA1, mossy cell axons stay within the DG and do not leave their home region. Since axonal guidance occurs at the growth cone of a growing axon (Campbell and Holt, 2001), a number of attractive or repulsive factors, for example matrix molecules (Smith et al., 2015), neurotransmitters and soluble neurotrophic factors (Zheng et al., 1994; Zhang and Poo, 2002) derived from neurons or glial cells, could play a role in this region-specific response (Goldberg, 2003; Stoeckli, 2018).

## Sprouting of Mossy Cell Axons *in vitro* Is Similar to Sprouting of Mossy Cell Axons in Juvenile Rodents *in vivo*

The sprouting response of mossy cell axons in our culture preparations was extensive and covered the entire denervated zone. This is much more extensive than what we have seen following entorhinal denervation in adult mice *in vivo* using a combination of anterograde tracing and calretinin-labeling (Del Turco et al., 2003). In adult brains calretinin-positive mossy cell axons grow only for short distances into the "entorhinal zone". Nevertheless, the mossy cell sprouting response observed in adult mice was still more extensive than the one observed in rats, where mossy cell axons remain primarily within their home territory (Frotscher et al., 1997).

What could explain these differences in the sprouting propensity of mossy axons? With regard to the difference between the *in vitro* situation studied here and the sprouting observed in adult mice (Del Turco et al., 2003), we propose that the age of the cultures plays an important role. Although relevant maturation

and differentiation steps have occurred (Prang et al., 2001, 2003), organotypic tissue cultures are still "juvenile" and, thus, highly plastic. More specifically, cultures are generated between postnatal days 4–5 and lesions are performed at DIV 14, corresponding to juvenile animals lesioned *in vivo* between 2–3 weeks postnatally. Such animals have been investigated previously and a much stronger sprouting response of juveniles has been reported compared to adults (Gall and Lynch, 1980, 1981; Gall et al., 1980): Mossy cell axons of juveniles leave their home layer in large numbers and re-innervate the entire denervated "entorhinal zone" of the dentate, similar to what we have seen *in vitro*. This effect is also much faster than in adults (Gall and Lynch, 1978; McWilliams and Lynch, 1983). Of note, strength as well as speed of re-innervation diminish with age (Gall and Lynch, 1981; Hoff et al., 1982a,b; McWilliams and Lynch, 1983), suggesting that the growth propensity or plasticity of mossy cells decreases with maturation (Caroni, 1997; Goldberg, 2003) or other molecules are expressed that restrict and pattern the sprouting response (Deller et al., 2000). The same considerations hold true for the differences observed between mouse and rat (Deller et al., 2007): Intrinsic factors regulating the strength of the growth response or extrinsic factors guiding and/or limiting the sprouting response of mossy cell axons could be different, which could explain the differences in mossy axon sprouting seen between the species.

## DATA AVAILABILITY STATEMENT

Datasets generated for this study may be made available on request to the corresponding author.

## AUTHOR CONTRIBUTIONS

DD, MP, VB, and LH-E acquired and analyzed the data. DD and TD conceived and supervised the study, and wrote the manuscript. All authors were involved in data interpretation, critically revising the manuscript, read, and approved the final manuscript.

## FUNDING

This work was supported by BMBF (OGEAM 031L0109B) and Deutsche Forschungsgemeinschaft (CRC1080).

## ACKNOWLEDGMENTS

The authors thank Serge N. Schiffmann, Bruxelles, for the calretinin-deficient animals and Heike Korff, Ute Fertig, David Danehl, and Charlotte Nolte-Uhl for expert technical assistance.

## REFERENCES

Blasco-Ibanez, J. M., and Freund, T. F. (1997). Distribution, ultrastructure and connectivity of calretinin-immunoreactive mossy cells of the mouse dentate gyrus. *Hippocampus* 7, 307–320. doi: 10.1002/(sici)1098-1063(1997)7:3<307::aid-hipo6>3.0.co;2-h

Bui, A. D., Nguyen, T. M., Limouse, C., Kim, H. K., Szabo, G. G., Felong, S., et al. (2018). Dentate gyrus mossy cells control spontaneous convulsive seizures and spatial memory. *Science* 359, 787–790. doi: 10.1126/science.aan4074

Campbell, D. S., and Holt, C. E. (2001). Chemotropic responses of retinal growth cones mediated by rapid local protein synthesis and degradation. *Neuron* 32, 1013–1026. doi: 10.1016/s0896-6273(01)00551-7

Caroni, P. (1997). Intrinsic neuronal determinants that promote axonal sprouting and elongation. *Bio Essays* 19, 767–775. doi: 10.1002/bies.950190906

Cotman, C. W., and Nadler, J. V. (1978). "Reactive synaptogenesis in the hippocampus," in *Neuronal Plasticity*, ed. C. W. Cotman, (New York, NY: Raven Press), 227–271.

Del Turco, D., and Deller, T. (2007). Organotypic entorhino-hippocampal slice cultures–a tool to study the molecular and cellular regulation of axonal regeneration and collateral sprouting in vitro. *Methods Mol. Biol.* 399, 55–66. doi: 10.1007/978-1-59745-504-6_5

Del Turco, D., Woods, A. G., Gebhardt, C., Phinney, A. L., Jucker, M., Frotscher, M., et al. (2003). Comparison of commissural sprouting in the mouse and rat fascia dentata after entorhinal cortex lesion. *Hippocampus* 13, 685–699. doi: 10.1002/hipo.10118

Deller, T., Del Turco, D., Rappert, A., and Bechmann, I. (2007). Structural reorganization of the dentate gyrus following entorhinal denervation: species differences between rat and mouse. *Prog. Brain Res.* 163, 501–528. doi: 10.1016/s0079-6123(07)63027-1

Deller, T., and Frotscher, M. (1997). Lesion-induced plasticity of central neurons: sprouting of single fibers in the rat hippocampus after unilateral entorhinal lesion. *Prog. Neurobiol.* 53, 687–727. doi: 10.1016/s0301-0082(97)00044-0

Deller, T., Frotscher, M., and Nitsch, R. (1995a). Morphological evidence for the sprouting of inhibitory commissural fibers in response to the lesion of the excitatory entorhinal input to the rat dentate gyrus. *J. Neurosci.* 15, 6868–6878. doi: 10.1523/jneurosci.15-10-06868.1995

Deller, T., Nitsch, R., and Frotscher, M. (1995b). *Phaseolus vulgaris*-leucoagglutinin (PHAL) tracing of commissural fibers to the rat dentate gyrus: evidence for a previously unknown commissural projection to the outer molecular layer. *J. Comp. Neurol.* 352, 55–68. doi: 10.1002/cne.903520105

Deller, T., Haas, C. A., and Frotscher, M. (2000). Reorganization of the rat fascia dentata after a unilateral entorhinal cortex lesion: role of the extracellular matrix. *Ann. N.Y. Acad. Sci.* 911, 207–220. doi: 10.1111/j.1749-6632.2000.tb06728.x

Deller, T., Nitsch, R., and Frotscher, M. (1996). Heterogeneity of the commissural projection to the rat dentate gyrus: a *Phaseolus vulgaris*-leucoagglutinin tracing study. *Neuroscience* 75, 111–121. doi: 10.1016/0306-4522(96)00255-2

Fawcett, J. W. (2009). Recovery from spinal cord injury: regeneration, plasticity and rehabilitation. *Brain* 132(Pt 6), 1417–1418. doi: 10.1093/brain/awp121

Feng, G., Mellor, R. H., Bernstein, M., Keller-Peck, C., Nguyen, Q. T., Wallace, M., et al. (2000). Imaging neuronal subsets in transgenic mice expressing multiple spectral variants of GFP. *Neuron* 28, 41–51. doi: 10.1016/s0896-6273(00)00084-2

Filli, L., and Schwab, M. E. (2015). Structural and functional reorganization of propriospinal connections promotes functional recovery after spinal cord injury. *Neural Regen. Res.* 10, 509–513. doi: 10.4103/1673-5374.155425

Frotscher, M., Heimrich, B., and Deller, T. (1997). Sprouting in the hippocampus is layer-specific. *Trends Neurosci.* 20, 218–223. doi: 10.1016/s0166-2236(96)01018-1

Gall, C., and Lynch, G. (1978). Rapid axon sprouting in the neonatal rat hippocampus. *Brain Res.* 153, 357–362. doi: 10.1016/0006-8993(78)90415-8

Gall, C., and Lynch, G. (1981). Fiber architecture of the dentate gyrus following ablation of the entorhinal cortex in rats of different ages: evidence for two forms of axon sprouting in the immature brain. *Neuroscience* 6, 903–910. doi: 10.1016/0306-4522(81)90171-8

Gall, C., and Lynch, G. S. (1980). The regulation of fiber growth and synaptogenesis in the developing hippocampus. *Curr. Top. Dev. Biol.* 1, 159–180. doi: 10.1016/s0070-2153(08)60119-2

Gall, C., McWilliams, R., and Lynch, G. (1980). Accelerated rates of synaptogenesis by " sprouting " afferents in the immature. hippocampal formation. *J. Neurol.* 193, 1047–1061. doi: 10.1002/cne.901930416

Garcia-Alias, G., Barkhuysen, S., Buckle, M., and Fawcett, J. W. (2009). Chondroitinase ABC treatment opens a window of opportunity for task-specific rehabilitation. *Nat. Neurosci.* 12, 1145–1151. doi: 10.1038/nn.2377

Goldberg, J. L. (2003). How does an axon grow? *Genes Dev.* 17, 941–958. doi: 10.1101/gad.1062303

Goldowitz, D., Vincent, S. R., Wu, J. Y., and Hökfelt, T. (1982). Immunohistochemical demonstration of plasticity in GABA neurons of the adult rat dentate gyrus. *Brain Res.* 238, 413–420. doi: 10.1016/0006-8993(82)90116-0

Grimm, D. (2002). Production methods for gene transfer vectors based on adeno-associated virus serotypes. *Methods* 28, 146–157. doi: 10.1016/s1046-2023(02)00219-0

Gurden, H., Schiffmann, S. N., Lemaire, M., Böhme, G. A., Parmentier, M., and Schurmans, S. (1998). Calretinin expression as a critical component in the control of dentate gyrus long-term potentiation induction in mice. *Eur. J. Neurosci.* 10, 3029–3033. doi: 10.1111/j.1460-9568.1998.00373.x

Hoff, S. F., Scheff, S. W., Bernado, L. S., and Cotman, C. W. (1982a). Lesion-induced synaptogenesis in the dentate gyrus of aged rats. *J. Comp. Neurol.* 205, 246–252. doi: 10.1002/cne.902050304

Hoff, S. F., Scheff, S. W., and Cotman, C. W. (1982b). Lesion-induced synaptogenesis in the dentate gyrus of aged rats.II. demonstration of an impaired degeneration clearing response. *J. Comp. Neurol.* 205, 253–259. doi: 10.1002/cne.902050305

Houser, C. R. (2014). Do structural changes in GABA neurons give rise to the epileptic state? *Adv. Exp. Med. Biol.* 813, 151–160. doi: 10.1007/978-94-017-8914-1_12

Kienzler, F., Jedlicka, P., Vuksic, M., Deller, T., and Schwarzacher, S. W. (2006). Excitotoxic hippocampal neuron loss following sustained electrical stimulation of the perforant pathway in the mouse. *Brain Res.* 1085, 195–198. doi: 10.1016/j.brainres.2006.02.055

Kienzler, F., Norwood, B. A., and Sloviter, R. S. (2009). Hippocampal injury, atrophy, synaptic reorganization, and epileptogenesis after perforant pathway stimulation-induced status epilepticus in the mouse. *J. Comp. Neurol.* 515, 181–196. doi: 10.1002/cne.22059

Kienzler-Norwood, F., Costard, L., Sadangi, C., Muller, P., Neubert, V., Bauer, S., et al. (2017). A novel animal model of acquired human temporal lobe epilepsy based on the simultaneous administration of kainic acid and lorazepam. *Epilepsia* 58, 222–230. doi: 10.1111/epi.13579

Lynch, G., Gall, C., Rose, G., and Cotman, C. W. (1976). Changes in the distribution of the dentate gyrus associational system following unilateral or bilateral entorhinal lesion in the adult rat. *Brain Res.* 110, 57–71. doi: 10.1016/0006-8993(76)90208-0

Maier, I. C., Ichiyama, R. M., Courtine, G., Schnell, L., Lavrov, I., Edgerton, V. R., et al. (2009). Differential effects of anti-Nogo-A antibody treatment and treadmill training in rats with incomplete spinal cord injury. *Brain* 132(Pt 6), 1426–1440. doi: 10.1093/brain/awp085

McWilliams, J. R., and Lynch, G. (1983). Rate of synaptic replacement in denervated rat hippocampus declines precipitously from the juvenile period to adulthood. *Science* 221, 572–574. doi: 10.1126/science.6867730

Muller, C. M., Vlachos, A., and Deller, T. (2010). Calcium homeostasis of acutely denervated and lesioned dentate gyrus in organotypic entorhino-hippocampal co-cultures. *Cell Calcium* 47, 242–252. doi: 10.1016/j.ceca.2009.12.006

Nadler, J. V. (1981). Desensitization-like changes in GABA-receptor binding of rat fascia dentata after entorhinal lesion. *Neurosci. Lett.* 26, 275–281. doi: 10.1016/0304-3940(81)90145-2

Nadler, J. V., Cotman, C. W., and Lynch, G. (1974). Biochemical plasticity of short-axon interneurons: increased glutamate decarboxylase activity in the denervated area of the rat dentate gyrus following entorhinal lesion. *Brain Res.* 45, 403–413. doi: 10.1016/0014-4886(74)90128-9

Okabe, M., Ikawa, M., Kominami, K., Nakanishi, T., and Nishimune, Y. (1997). 'Green mice' as a source of ubiquitous green cells. *FEBS Lett.* 407, 313–319. doi: 10.1016/s0014-5793(97)00313-x

Perederiy, J. V., and Westbrook, G. L. (2013). Structural plasticity in the dentate gyrus- revisiting a classic injury model. *Front. Neural Circuits* 7:17. doi: 10.3389/fncir.2013.00017

Prang, P., Del Turco, D., and Deller, T. (2003). Associational sprouting in the mouse fascia dentata after entorhinal lesion *in vitro*. *Brain Res.* 978, 205–212. doi: 10.1016/s0006-8993(03)02836-1

Prang, P., Del Turco, D., and Kapfhammer, J. P. (2001). Regeneration of entorhinal fibers in mouse slice cultures is age dependent and can be stimulated by NT-4, GDNF, and modulators of G-proteins and protein kinase C. *Exp. Neurol.* 169, 135–147. doi: 10.1006/exnr.2001.7648

Radic, T., Jungenitz, T., Singer, M., Beining, M., Cuntz, H., Vlachos, A., et al. (2017). Time-lapse imaging reveals highly dynamic structural maturation of postnatally born dentate granule cells in organotypic entorhino-hippocampal slice cultures. *Sci. Rep.* 7:43724. doi: 10.1038/srep43724

Scharfman, H. E. (2016). The enigmatic mossy cell of the dentate gyrus. *Nat. Rev. Neurosci.* 17, 562–575. doi: 10.1038/nrn.2016.87

Scharfman, H. E., and Myers, C. E. (2012). Hilar mossy cells of the dentate gyrus: a historical perspective. *Front. Neural Circ.* 6:106. doi: 10.3389/fncir.2012.00106

Scharfman, H. E., and Schwartzkroin, P. A. (1988). Electrophysiology of morphologically identified mossy cells of the dentate hilus recorded in guinea pig hippocampal slices. *J. Neurosci.* 8, 3812–3821. doi: 10.1523/jneurosci.08-10-03812.1988

Schneider, C. A., Rasband, W. S., and Eliceiri, K. W. (2012). NIH Image to ImageJ: 25 years of image analysis. *Nat. Methods* 9, 671–675. doi: 10.1038/nmeth.2089

Schurmans, S., Schiffmann, S. N., Gurden, H., Lemaire, M., Lipp, H. P., Schwam, V., et al. (1997). Impaired long-term potentiation induction in dentate gyrus of calretinin-deficient mice. *Proc. Natl. Acad. Sci. U.S.A.* 94, 10415–10420. doi: 10.1073/pnas.94.19.10415

Sloviter, R. S. (1994). The functional organization of the hippocampal dentate gyrus and its relevance to the pathogenesis of temporal lobe epilepsy. *Ann. Neurol.* 35, 640–654. doi: 10.1002/ana.410350604

Sloviter, R. S. (1996). Hippocampal pathology and pathophysiology in temporal lobe epilepsy. *Neurologia* 11(Suppl. 4), 29–32.

Smith, P. D., Coulson-Thomas, V. J., Foscarin, S., Kwok, J. C., and Fawcett, J. W. (2015). GAG-ing with the neuron: the role of glycosaminoglycan patterning in the central nervous system. *Exp. Neurol.* 274(Pt B), 100–114. doi: 10.1016/j.expneurol.2015.08.004

Steward, O. (1994). "Reorganization of neuronal circuitry following central nervous system trauma: naturally occurring processes and opportunities for therapeutic intervention," in *The Neurobiology of Central Nervous System Trauma*, eds S. K. Salzman, and A. I. Faden, (New York, NY: Oxford University Press), 266–287.

Steward, O. (1995). The process of reinnervation in the dentate gyrus of adult rats: gene expression by neurons during the period of lesion-induced growth. *J. Comp. Neurol.* 359, 391–411. doi: 10.1002/cne.903590304

Steward, O., Cotman, C. W., and Lynch, G. (1974). Growth of a new fiber projection in the brain of adult rats: reinnervation of the dentate gyrus by the contralateral entorhinal cortex following ipsilateral entorhinal lesion. *Exp. Brain Res.* 20, 45–66.

Stoeckli, E. T. (2018). Understanding axon guidance: are we nearly there yet? *Development* 145:dev151415. doi: 10.1242/dev.151415

Vlachos, A., Bas Orth, C., Schneider, G., and Deller, T. (2012a). Time-lapse imaging of granule cells in mouse entorhino-hippocampal slice cultures reveals changes in spine stability after entorhinal denervation. *J. Comp. Neurol.* 520, 1891–1902. doi: 10.1002/cne.23017

Vlachos, A., Becker, D., Jedlicka, P., Winkels, R., Roeper, J., and Deller, T. (2012b). Entorhinal denervation induces homeostatic synaptic scaling of excitatory postsynapses of dentate granule cells in mouse organotypic slice cultures. *PLoS One* 7:e32883. doi: 10.1371/journal.pone.0032883

Vlachos, A., Helias, M., Becker, D., Diesmann, M., and Deller, T. (2013). NMDA-receptor inhibition increases spine stability of denervated mouse dentate

granule cells and accelerates spine density recovery following entorhinal denervation in vitro. *Neurobiol. Dis.* 59, 267–276. doi: 10.1016/j.nbd.2013.07.018

Volz, F., Bock, H. H., Gierthmuehlen, M., Zentner, J., Haas, C. A., and Freiman, T. M. (2011). Stereologic estimation of hippocampal GluR2/3- and calretinin-immunoreactive hilar neurons (presumptive mossy cells) in two mouse models of temporal lobe epilepsy. *Epilepsia* 52, 1579–1589. doi: 10.1111/j.1528-1167.2011.03086.x

Willems, L. M., Zahn, N., Ferreiros, N., Scholich, K., Maggio, N., Deller, T., et al. (2016). Sphingosine-1-phosphate receptor inhibition prevents denervation-induced dendritic atrophy. *Acta Neuropathol. Commun.* 4:28. doi: 10.1186/s40478-016-0303-x

Zappone, C. A., and Sloviter, R. S. (2001). Commissurally projecting inhibitory interneurons of the rat hippocampal dentate gyrus: a colocalization study of neuronal markers and the retrograde tracer fluoro-gold. *J. Comp. Neurol.* 441, 324–344.

Zhang, X., and Poo, M. M. (2002). Localized synaptic potentiation by BDNF requires local protein synthesis in the developing axon. *Neuron* 36, 675–688.

Zheng, J. Q., Felder, M., Connor, J. A., and Poo, M. M. (1994). Turning of nerve growth cones induced by neurotransmitters. *Nature* 368, 140–144.

**Conflict of Interest:** The authors declare that the research was conducted in the absence of any commercial or financial relationships that could be construed as a potential conflict of interest.

*Copyright © 2019 Del Turco, Paul, Beeg Moreno, Hildebrandt-Einfeldt and Deller. This is an open-access article distributed under the terms of the Creative Commons Attribution License (CC BY). The use, distribution or reproduction in other forums is permitted, provided the original author(s) and the copyright owner(s) are credited and that the original publication in this journal is cited, in accordance with accepted academic practice. No use, distribution or reproduction is permitted which does not comply with these terms.*

frontiers in Systems Neuroscience

ORIGINAL RESEARCH
published: 14 January 2020
doi: 10.3389/fnsys.2019.00087

# Fimbria-Fornix Volume Is Associated With Spatial Memory and Olfactory Identification in Humans

*Louisa Dahmani[1], Blandine Courcot[2], Jamie Near[2], Raihaan Patel[2], Robert S. C. Amaral[2], M. Mallar Chakravarty[2] and Véronique D. Bohbot[3]**

[1]Integrated Program in Neuroscience, McGill University, Montreal, QC, Canada, [2]Douglas Brain Imaging Center, Department of Psychiatry, McGill University, Montreal, QC, Canada, [3]Douglas Mental Health University Institute, Department of Psychiatry, McGill University, Montreal, QC, Canada

White matter pathways that surround the hippocampus comprise its afferent and efferent connections, and are therefore crucial in mediating the function of the hippocampus. We recently demonstrated a role for the hippocampus in both spatial memory and olfactory identification in humans. In the current study, we focused our attention on the fimbria-fornix white matter bundle and investigated its relationship with spatial memory and olfactory identification. We administered a virtual navigation task and an olfactory identification task to 55 young healthy adults and measured the volume of the fimbria-fornix. We found that the volume of the right fimbria-fornix and its subdivisions is correlated with both navigational learning and olfactory identification in those who use hippocampus-based spatial memory strategies, and not in those who use caudate nucleus-based navigation strategies. These results are consistent with our recent finding that spatial memory and olfaction rely on similar neural networks and structures.

**Keywords: spatial memory, navigation, hippocampus, fimbria-fornix, white matter, olfaction**

OPEN ACCESS

***Edited by:***
*James Ainge, University of St Andrews, United Kingdom*

***Reviewed by:***
*Benjamin J. Clark, University of New Mexico, United States*
*Ehren Lee Newman, Indiana University Bloomington, United States*

****Correspondence:***
*Véronique D. Bohbot*
*veronique.bohbot@mcgill.ca*

***Received:*** *17 October 2019*
***Accepted:*** *23 December 2019*
***Published:*** *14 January 2020*

***Citation:***
*Dahmani L, Courcot B, Near J, Patel R, Amaral RSC, Chakravarty MM and Bohbot VD (2020) Fimbria-Fornix Volume Is Associated With Spatial Memory and Olfactory Identification in Humans. Front. Syst. Neurosci. 13:87. doi: 10.3389/fnsys.2019.00087*

## INTRODUCTION

Many people have experienced instances where a smell spontaneously brought back a vivid memory. Therefore, it would not come as a surprise that olfaction could be closely associated with hippocampal-dependent memory, characterized by its vividness and richness in detail (Moscovitch et al., 2005). Olfaction is a vital navigation tool for many species. Many animals use olfactory cues and gradients to locate prey or pups, identify territory, or to go back to previously visited places. Although not crucial for survival, humans are also capable of finding a target location using olfactory cues (Jacobs et al., 2015).

Over the years, numerous studies have investigated spatial memory and its neural correlates. Animal and human studies have found the hippocampus to play a critical role in both spatial memory (O'Keefe and Nadel, 1978; Packard et al., 1989; McDonald and White, 1993; Pigott and Milner, 1993; Maguire et al., 1998; Bohbot et al., 2002, 2004; Hartley et al., 2003; Iaria et al., 2003; Head and Isom, 2010) and olfaction (see Suzuki et al., 2001; Lundström et al., 2011 for reviews; Kjelvik et al., 2012; Wu et al., 2012).

Up until recently, the relationship between spatial memory and olfaction had not been directly investigated. In 2018, we demonstrated the existence of an intrinsic relationship between the two processes (Dahmani et al., 2018). However, this relationship is specific to certain types of navigation but not others. There are two distinct memory systems that can be used for navigation.

One of these is the hippocampal memory system, which is critical for the spatial memory strategy. This strategy involves learning precise spatial relationships between landmarks in the environment, so as to form a cognitive map, or mental representation, of one's environment (O'Keefe and Nadel, 1978). The other memory system involves the caudate nucleus, which is critical for the stimulus-response strategy. This strategy involves learning a set of stimulus-response associations, e.g., a series of motor actions in response to a stimulus (Packard et al., 1989; McDonald and White, 1993). An example of this is route learning, where one must learn to turn left or right in response to various stimuli (e.g., turn left at the gas station). The stimulus-response strategy mainly relies on the caudate nucleus/dorsal striatum (Packard et al., 1989; McDonald and White, 1993; White and McDonald, 2002; Hartley et al., 2003; Iaria et al., 2003; Bohbot et al., 2007; Head and Isom, 2010; Konishi et al., 2013). Importantly, studies from our laboratory showed that gray matter in the hippocampus and caudate nucleus correlates with the respective use of spatial memory and stimulus-response strategies in dual-solution tasks (Iaria et al., 2003; Bohbot and Corkin, 2007; Etchamendy et al., 2012; Konishi and Bohbot, 2013; Konishi et al., 2013; Dahmani and Bohbot, 2015; Dahmani et al., 2018). Using these paradigms to identify individuals' spontaneous navigation strategies, we showed in a recent report that olfactory identification is associated with faster learning in participants who spontaneously used a spatial memory strategy (spatial learners), but not in those who used a stimulus-response strategy (response learners; Dahmani et al., 2018). This finding was consistent with our hypothesis that olfactory identification would be related to hippocampal-dependent navigation only. In the same study, we measured hippocampal gray matter volume and found it to be positively associated with both olfactory identification and spatial learning, but not with stimulus-response learning.

In the current artice, we turn our attention to white matter. In rodents, many lesion studies have found the fimbria-fornix to be of crucial importance in spatial memory (Olton and Samuelson, 1976; Olton and Papas, 1979; Packard et al., 1989; McDonald and White, 1993, 1995; de Bruin et al., 2001), as it connects the hippocampus to most of its output regions. In contrast, fimbria-fornix lesions do not impair stimulus-response learning (Packard et al., 1989; McDonald and White, 1993; de Bruin et al., 2001). In humans, Iaria et al. (2008) found that hippocampal fractional anisotropy, which is thought to be a measure of structural white matter integrity, was positively associated with spatial learning and memory. However, whether the fimbria-fornix has a dissociable role in human spatial learning and stimulus-response learning is still unknown. Additionally, diffusion magnetic resonance imaging (MRI) measures, including fractional anisotropy, are still under debate, as their association with underlying white matter structure is not clear (Jones et al., 2013; Scholz et al., 2014). In the current study, we investigate the volume of the fimbria-fornix and use a dual-solution virtual navigation task to examine its association with spatial memory and stimulus-response learning. Similar to our previous study (Dahmani et al., 2018), we hypothesized that greater volume of the fimbria-fornix fiber system would be positively associated with navigation and olfactory identification in spatial learners, but not response learners.

# MATERIALS AND METHODS

## Participants

We tested 60 healthy young adults between the ages of 18 and 35 (mean age = 22.9 ± 3.5; 29 women, 31 men). This represents the same dataset as reported in Dahmani et al. (2018). Participants were excluded if they were not right-handed, if they had a history of neurological or psychiatric disorders, a history of alcohol or drug abuse, or if they suffered a head trauma followed by a loss of consciousness. Three participants did not complete the navigation task (4-on-8 Virtual Maze, described below) and two participants did not undergo MRI scanning. We, therefore, had 55 participants for the navigation and olfaction analyses. The protocol was approved by the local ethics committee of the Douglas Mental Health University Institute. All subjects gave written informed consent in accordance with the Declaration of Helsinki.

## Olfactory Identification

To assess olfactory identification, we administered the Monell Extended Sniffin' Sticks Identification Test (MONEX-40; Freiherr et al., 2012). This test consists of 40 felt-tip pens, each infused with an odor. The experimenter places each pen under the participant' nose for one to 2 s and the participant inhales the odor. For each pen, participants are asked to identify the odor from four written choices shown on a screen. The pens were developed to yield at least 35% accuracy across participants (Lundström, personal communication). Thus, in the current study, pens that yielded an overall accuracy that was lower than 35% were excluded from the analysis. Two pens were excluded (warm milk and honey) and the olfactory identification score was based on 38 items. Possible reasons for poor accuracy are degradation of the odor over time, unfamiliarity due to cultural differences, or variability in performance in specific cohorts.

## 4-on-8 Virtual Maze (4/8 VM)

The 4/8 VM (**Figure 1**) was developed using Unreal Tournament 2003 (Epic Games, Raleigh, NC, USA). The task was adapted from a maze task originally used in rodents (Olton and Samuelson, 1976; Packard et al., 1989) and consists in a radial maze surrounded by a rich landscape with proximal and distal landmarks. The maze is made of a central platform with eight paths branching out around it. There are two parts to each learning trial:

- Part 1: Out of the eight paths, four are blocked and four are accessible. Participants are instructed to visit the accessible paths, to retrieve objects at the end of the paths (which are not visible from the central platform), and to memorize their location. When ready, participants are taken to Part 2.
- Part 2: Here, we remove the barriers to make all the paths accessible. Participants are asked to avoid the paths they just visited in order to retrieve the remaining objects. Participants can use either a spatial memory strategy, by learning the spatial relationships between landmarks in the environment and the

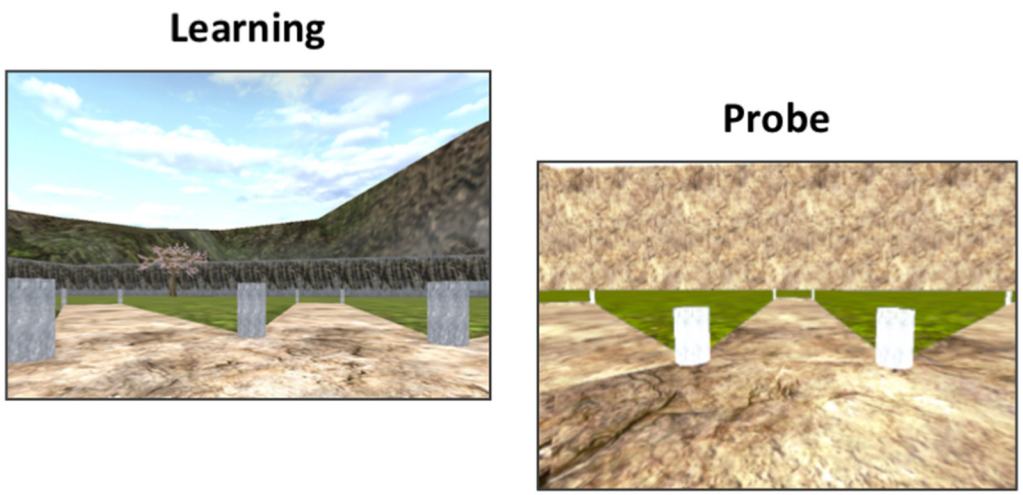


**FIGURE 1 |** The 4-on-8 Virtual Maze. The 4-on-8 Virtual Maze (4/8 VM) consists in an 8-arm radial maze surrounded by landmarks. In Part 1, four of the paths are blocked and four are open. Participants have to retrieve objects at the end of the open paths. In Part 2, the barriers are removed. Participants have to avoid the paths they visited in Part 1 to retrieve the remaining objects. They can learn the object locations using a spatial memory strategy (e.g., "the path is to the left of the boulder") or a stimulus-response strategy ("From the starting position, I have to take the path straight ahead and then skip a path on the right"). Once participants learn the task to criterion, they are taken to a probe stage, where a wall is raised around the maze that hides the landmarks. People who used a spatial memory strategy during learning make more errors than people who used stimulus-response strategies, as they can no longer use landmarks to find the target paths. At the end of the task, participants have to draw a map of the maze and are administered a verbal report, which serves to determine the strategy they used as well as the number of landmarks they used (e.g., "I used the rock and the tree to find the objects") and noticed (e.g., "I saw a mountain but I did not use it").

target paths (e.g., "there is an object to the left of the tree and one to the right of the boulder"), or they can use a stimulus-response strategy, by learning a series of motor actions in response to a stimulus (e.g., "from the starting position, I have to go straight ahead and then skip the path on the right").

A minimum of three and a maximum of eight learning trials are administered. The location of the objects does not change throughout the task except in the second trial. Participants are required to find the objects in Part 2 without making errors in at least one of the trials in order to reach the learning criterion. Once this is achieved, we administer a probe trial. Part 1 of the probe trial is the same as above. In Part 2, a wall is erected around the radial maze, blocking the landmarks from the participants' view. Participants who used a spatial memory strategy ("spatial learners") to memorize the object locations make more errors than participants who used a stimulus-response strategy ("response learners"), as they can no longer rely on the landmarks to find the paths containing the objects (Iaria et al., 2003). The probe trial is followed by a normal trial. Once the task is done, we conduct a verbal report, where we ask participants to describe how they solved the task. We used the verbal report to categorize participants into spatial or response learners. If participants mentioned learning the location of the pathways relative to several landmarks, they were categorized as spatial learners. If they mentioned using a counting strategy or a sequence starting from the start position of a single position demarked by one landmark, they were categorized as response learners. We previously showed that spontaneous strategies, i.e., strategies used in the very first trial, are associated with increased functional magnetic resonance imaging (fMRI) blood oxygenation-level-dependent (BOLD) activity and gray matter in our regions of interest (Iaria et al., 2003; Bohbot et al., 2007). The verbal report is also used to determine how many landmarks participants noticed in the environment and how many landmarks they used on average throughout the learning trials.

The dependent variables are number of trials to criterion, the average number of errors on Part 2 of the learning trials (these provide two slightly different measures of navigational learning), spontaneous navigation strategy, number of landmarks noticed the average number of landmarks used during the learning phase of the task, and probe errors.

## Neuropsychological Assessment

To assess potential differences between spatial and response learners in neuropsychological status, we administered the following neuropsychological tests: the Rey Auditory Verbal Learning Task (Rey, 1941) to evaluate verbal memory, the Rey-Osterrieth Complex Figure (Meyers and Meyers, 1995) to assess visuospatial memory, and the Test of Non-verbal Intelligence-3 (Brown et al., 1997) to assess non-verbal intelligence. Spatial and response learners did not differ on these tests (all Bootstrap BCa 95% CI crossed 0).

## MRI Data Acquisition

We acquired anatomical MRI data at the Douglas Cerebral Imaging Centre, using a 3 Tesla Siemens Magnetom Trio scanner equipped with 12-channel array coil. We immobilized participants' heads using support cushions. A localizer scan was first acquired, followed by a T1-weighted 3D MPRAGE anatomical scan with 192 contiguous 1 mm slices in the sagittal

plane (TR = 2,300 ms; TE = 2.98 ms; flip angle = 9; the field of view = 256 $mm^2$), resulting in an acquisition time of 9:14 min.

## MRI Data Analysis

The Multiple Automatically Generated Templates (MAGeT) Brain tool was used to automatically segment extra-hippocampal white matter fiber bundles (Amaral et al., 2018; **Figure 2A**). This tool was developed to use a small set of high-quality atlases that were manually segmented as input. Participants' structural scans were processed with N4 intensity correction (Tustison et al., 2010). We then applied a head mask to ameliorate registration before running MAGeT-Brain. The Winterburn Atlas (Winterburn et al., 2013) was adapted to include the extra-hippocampal white matter bundles and is comprised of five manually-segmented brains (Amaral et al., 2018). In MAGeT-Brain, a library of 21 templates (Pipitone et al., 2014) is used to bootstrap each individual's segmentation. The templates were chosen by first segmenting all of the samples using the five manually segmented brains and then selecting the ones presenting the best registrations in order to increase registration quality for the full sample analysis. We used non-linear atlas-to-template registration to segment and label each template, which resulted in a unique delineation of the subfields for each individual template. The bootstrapping yields 105 candidate labels for each individual (5 atlases × 21 templates), which are subsequently fused through a voxel-wise majority vote to output one final segmentation (**Figure 2B**). We used the Automatic Normalization Tools (ANTS) registration technique for non-linear registration[1]. The extra-hippocampal white matter bundles that we inspected included the fimbria, fornix, and alveus of the hippocampus. Together, these form the fimbria-fornix white matter bundle. We visually inspected each output segmentation for quality control, which all segmentations passed.

## Analysis

We used SPSS Statistics 20 (IBM) for data analysis. We performed partial correlations between our olfaction and 4/8 VM variables and white matter volumes. Sex was used as a covariate because men have on average a larger brain than women. We used bootstrapped bias-corrected and accelerated 95% confidence intervals (Bootstrap BCa 95% CI; Field, 2009) to determine significance. Bootstrapping is a resampling method that uses a sample dataset and simulates 1,000 datasets from this set by resampling with replacement. This method is useful in that it inherently corrects for multiple comparisons (Westfall and Young, 1993; Field et al., 2012). Confidence intervals are an estimation of the population's true value, which makes them both more accurate and more robust than *p*-values (Rothman, 1978; Poole, 2001; Greenland et al., 2016), especially when bootstrapping methods are used (Westfall and Young, 1993). Resampling methods also offer the advantage of estimating Type I and Type II error rates more precisely than standard *p*-value adjustment methods (Field et al., 2012). It is, therefore, unnecessary to further correct for multiple comparisons. Another advantage of bootstrapping methods is that they are non-parametric, and thus do not require to transform the data when it is not normally distributed (Haukoos and Lewis, 2005; Field et al., 2012). We used one-tailed confidence intervals when analyses were hypothesis-driven. We first investigated the overall right and left fimbria-fornix white matter volumes. These were determined by calculating the sum of the fimbria, fornix, and alveus of the hippocampus, for each hemisphere. If no significant correlation was found between overall fimbria-fornix volumes and our measures of interest, then we investigated the sub-regions (fimbria, fornix, and alveus of the hippocampus) separately to see if any effect existed at a smaller scale.

[1]https://github.com/vfonov/mincANTS

# RESULTS

Using participants' 4/8 VM verbal report, we categorized 23 participants as spatial learners and 32 participants as response learners. We performed two sets of analyses: we looked at the associations between: (1) navigation and white matter volumes; and (2) olfaction and white matter volumes. We hypothesized that, as with our previous behavioral and structural neuroimaging results (Dahmani et al., 2018), only spatial learners would show an association between fimbria-fornix volume, olfaction, and navigation. **Table 1** shows the correlation coefficients and bootstrap BCa 95% CI of the correlations between white matter volumes and navigation and olfaction variables for spatial and response learners, with sex as a covariate.

## Navigation

In spatial learners, we found that faster learning correlates with fimbria-fornix white matter volume: there was a significant negative correlation between right fimbria-fornix volume and average navigational learning errors [$r = -0.40$, Bootstrap BCa 95% CI ($-0.66$, $-0.15$; **Figure 3**, left)], and between right fimbria volume and number of trials to criterion [$r = -0.35$, Bootstrap BCa 95% CI ($-0.57$, $-0.15$)]. Additionally, there was a marginally significant negative correlation between left fimbria volume and average navigational learning errors [$r = -0.31$, Bootstrap BCa 95% CI ($-0.60$, 0.004)]. Average navigational learning errors did not significantly correlate with the left fimbria-fornix volume, although the correlation was in the hypothesized direction [$r = -0.19$, Bootstrap BCa 95% CI ($-0.52$, 0.10)]. Thus, faster learning in spatial learners is predominantly associated with the right fimbria-fornix.

Response learners showed no significant associations between fimbria-fornix volumes and navigational learning [all Bootstrap BCa 95% CIs crossed 0; e.g., average navigational learning errors and right fimbria-fornix volume, $r = 0.10$, Bootstrap BCa 95% CI ($-0.26$, 0.37; **Figure 3**, right)]. There were also no significant associations with sub-regions of the left or right fimbria-fornix (all Bootstrap BCa 95% CIs crossed 0).

Spatial and response learners did not show any correlations between fimbria-fornix volumes and either number of landmarks noticed/used or probe errors (all Bootstrap BCa 95% CIs crossed 0).

**TABLE 1** | Partial correlations between variables of interest and white matter bundle volumes for spatial and response learners.

| | Spatial learners *r* (CI) | Response learners *r* (CI) |
|---|---|---|
| **Average navigational learning errors** | | |
| R fimbria-fornix | −0.40 (−0.66, −0.15)* | 0.10 (−0.26, 0.37) |
| R fimbria | – | −0.09 (−0.42, 0.24) |
| R fornix | – | 0.05 (−0.34, 0.41) |
| R alveus | – | 0.23 (−0.16, 0.48) |
| L fimbria-fornix | −0.19 (−0.52, 0.10) | 0.04 (−0.27, 0.29) |
| L fimbria | −0.31 (−0.60, 0.004)† | 0.08 (−0.23, 0.32) |
| L fornix | −0.21 (−0.52, 0.08) | 0.02 (−0.25, 0.25) |
| L alveus | 0.003 (−0.40, 0.33) | 0.04 (−0.32, 0.33) |
| **Number of trials to criterion** | | |
| R fimbria-fornix | −0.09 (−0.42, 0.25) | 0.08 (−0.19, 0.31) |
| R fimbria | −0.35 (−0.57, −0.15)* | −0.13 (−0.40, 0.14) |
| R fornix | −0.18 (−0.48, 0.14) | 0.06 (−0.27, 0.31) |
| R alveus | 0.17 (−0.15, 0.45) | 0.20 (−0.16, 0.63) |
| L fimbria-fornix | 0.05 (−0.26, 0.35) | 0.01 (−0.28, 0.34) |
| L fimbria | −0.17 (−0.49, 0.13) | 0.06 (−0.20, 0.39) |
| L fornix | 0.06 (−0.25, 0.36) | −0.05 (−0.40, 0.31) |
| L alveus | 0.09 (−0.16, 0.34) | 0.09 (−0.19, 0.32) |
| **Olfactory identification** | | |
| R fimbria-fornix | 0.24 (−0.10, 0.55) | −0.12 (−0.37, 0.20) |
| R fimbria | 0.41 (0.08, 0.68)* | 0.18 (−0.13, 0.47) |
| R fornix | 0.07 (−0.28, 0.41) | −0.24 (−0.50, 0.14) |
| R alveus | 0.26 (−0.05, 0.69) | 0.02 (−0.28, 0.31) |
| L fimbria-fornix | 0.14 (−0.16, 0.43) | −0.03 (−0.35, 0.25) |
| L fimbria | 0.01 (−0.37, 0.39) | 0.03 (−0.28, 0.34) |
| L fornix | 0.20 (−0.18, 0.52) | 0.06 (−0.31, 0.35) |
| L alveus | 0.01 (−0.33, 0.42) | −0.19 (−0.41, 0.05) |

*Correlation coefficients (r) are shown with bootstrap bias-corrected and accelerated 95% confidence intervals in brackets. All correlations were covaried with sex. R: Right; L: Left. *Indicates correlations that are significant (bootstrap bias-corrected and accelerated 95% confidence intervals do not cross 0). †Denotes marginally significant correlations (confidence intervals barely cross 0).*

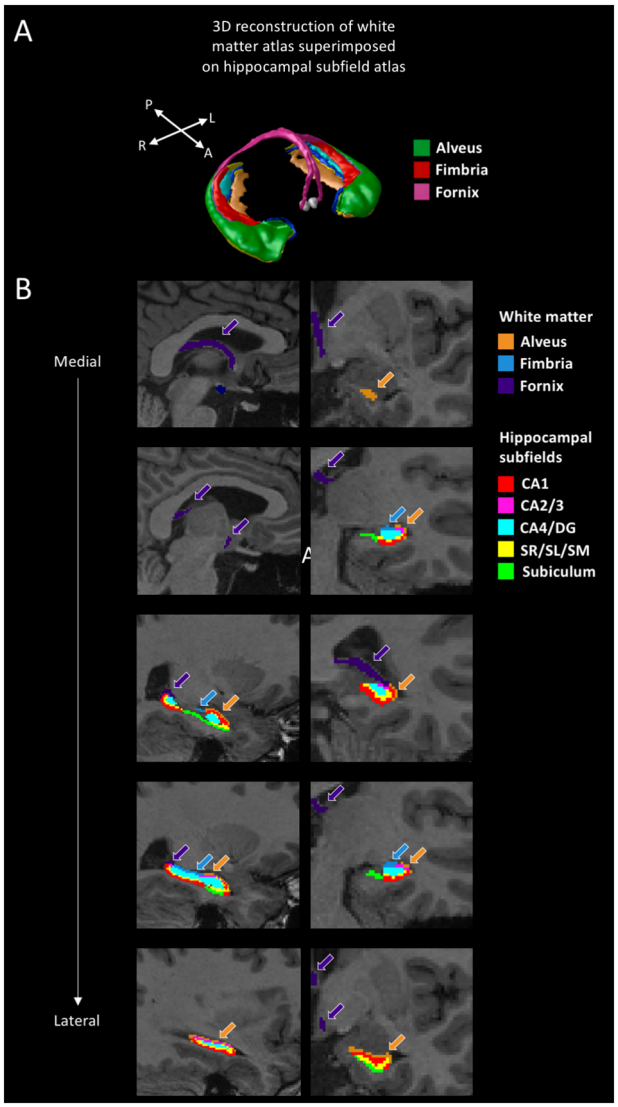


**FIGURE 2** | White matter segmentation. **(A)** 3D reconstruction of the white matter atlas (Amaral et al., 2018), showing the alveus, fimbria, and fornix, superimposed on the hippocampal subfield atlas (Pipitone et al., 2014). **(B)** Segmentations of the alveus (in orange), fimbria (in blue), and fornix (in purple) are shown for a representative participant. The other colors represent the various hippocampal subfields (not discussed in this article but see Dahmani et al., 2018). Sagittal views are shown on the left, coronal views are shown on the right. A: anterior; P: posterior; R: right; L: left; CA: cornu ammonis; DG: dentate gyrus; SR/SL/SM: stratum radiatum, lacunosum, and moleculare.

## Olfactory Identification

Spatial learners showed a significant positive correlation between olfactory identification and volume of the right fimbria [$r = 0.41$, Bootstrap BCa 95% CI (0.08, 0.68; **Figure 4**, left)]. They did not show a significant correlation between olfactory identification and right [$r = 0.24$, Bootstrap BCa 95% CI (−0.10, 0.55)] or left [$r = 0.14$, Bootstrap BCa 95% CI (−0.16, 0.43)] fimbria-fornix volumes, or with any sub-regions of the left fimbria-fornix (all Bootstrap BCa 95% CIs crossed 0).

In response learners, there were no associations between olfactory identification and right [$r = -0.12$, Bootstrap BCa 95% CI (−0.37, 0.20)] or left [$r = -0.03$, Bootstrap BCa 95% CI (−0.35, 0.25)] fimbria-fornix volumes. There were also no correlations with any of the fimbria-fornix sub-region volumes (all Bootstrap BCa 95% CIs crossed 0; e.g., right fimbria: **Figure 4**, right).

# DISCUSSION

In the current study, we examined whether the fimbria-fornix has a dissociable role in spatial learning and stimulus-response learning in humans. We found fimbria-fornix volume to be positively associated with spatial memory. As hypothesized, there is no association between fimbria-fornix volume and stimulus-response learning, further strengthening the idea that these two forms of navigation rely on separate neural networks (O'Keefe and Nadel, 1978; Packard et al., 1989; McDonald and White, 1993). Similarly, within spatial learners, olfactory identification shows positive correlations with the fimbria-fornix, which is not the case within response learners.

These findings are consistent with our previous study (Dahmani et al., 2018), where we found both spatial learning and olfactory identification to be associated with hippocampal

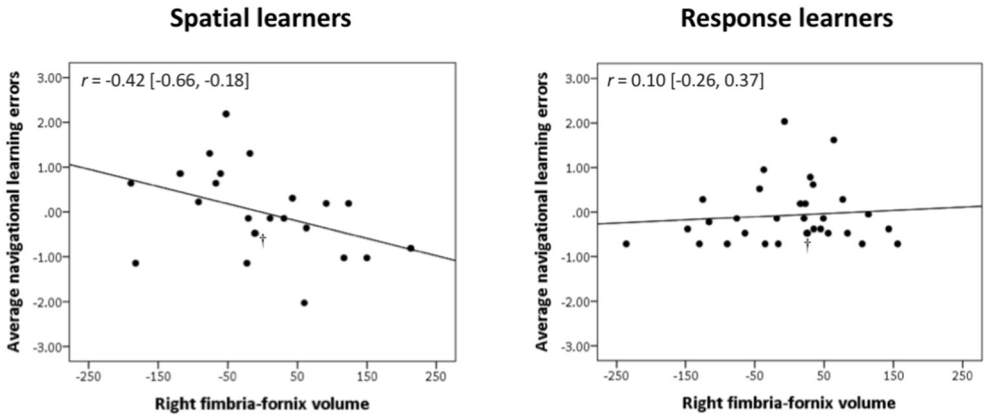


**FIGURE 3 |** Right fimbria-fornix volume is associated with fewer errors during navigational learning in spatial learners, but not response learners. Within spatial learners, average navigational learning errors correlate negatively with right fimbria-fornix volume (shown on the left), $r = -0.42$ [Bootstrap BCa 95% CI (−0.66, −0.18)], but not with left fimbria-fornix volume (Bootstrap BCa 95% CI cross 0). Within the left fimbria-fornix sub-regions, average navigational learning errors show a marginally significant negative correlation with the left fimbria, $r = -0.31$ [Bootstrap BCa 95% CI (−0.60, 0.004)], but not with the other sub-regions (Bootstrap BCa 95% CI cross 0). Within response learners, average navigational learning errors do not correlate with left or right fimbria-fornix volume (shown on the right is the right fimbria-fornix volume correlation for comparison, $r = 0.10$ [Bootstrap BCa 95% CI (−0.26, 0.37)], or any of their sub-regions (Bootstrap BCa 95% CI cross 0). These results indicate that more efficient spatial learning is mainly associated with a greater volume of the right fimbria-fornix fiber system. Stimulus-response learning does not show any correlations with the left or right fimbria-fornix system. †Indicates two overlapping data points.

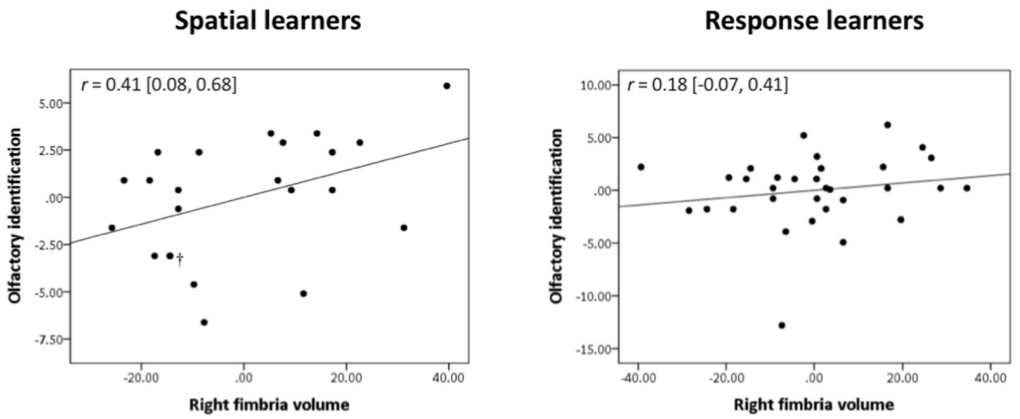


**FIGURE 4 |** Olfactory identification correlates positively with right fimbria volume within spatial learners only. Within spatial learners, olfactory identification correlates positively with right fimbria volume (shown on the left), $r = 0.41$, Bootstrap BCa 95% CI (0.08, 0.68), but not with the left fimbria-fornix or any of its sub-regions (Bootstrap BCa 95% CI cross 0). Within response learners, olfactory identification does not correlate positively with either left or right fimbria-fornix volume or any of their sub-regions {shown on the right is the association with right fimbria volume for comparison, $r = 0.18$ [Bootstrap BCa 95% CI (−0.07, 0.41)]; all other Bootstrap BCa 95% CI cross 0}. These results indicate that olfactory identification correlates positively with a sub-region of the right fimbria-fornix fiber system in those who use hippocampal-dependent navigation strategies only. †Indicates two overlapping datapoints.

gray matter volume, while there were no associations between stimulus-response learning and hippocampal volume.

In terms of lateralization, in our previous report we found an association between spatial memory, olfactory identification, and right hippocampal volume (Dahmani et al., 2018). Our white matter findings are concordant, as the effects we found predominantly involved the right fimbria-fornix fiber system. This is also consistent with a right-sided hippocampal lateralization for spatial memory and olfactory identification often reported in the literature (Habib and Sirigu, 1987; Zatorre and Jones-Gotman, 1990; Zatorre et al., 1992; Jones-Gotman and Zatorre, 1993; Barrash, 1998; Bohbot et al., 1998; Savic et al., 2000; Burgess, 2002; Frasnelli et al., 2010; Kjelvik et al., 2012; Smitka et al., 2012).

The positive association between olfactory identification and the right fimbria-fornix bundle was observed in spatial learners, but not response learners, a pattern of results that reflects that of our previous study (Dahmani et al., 2018). These findings indicate that the fimbria-fornix is involved in olfactory identification in individuals who spontaneously use the hippocampal memory system. The hippocampus itself is reported to be involved in olfactory identification in

approximately half of the studies in the literature, while the other half does not report such involvement (Suzuki et al., 2001; Kjelvik et al., 2012, 2014; Seubert et al., 2013; Smitka et al., 2012; Segura et al., 2013). This inconsistency may be a product of inter-individual variability in hippocampal involvement. The fact that we found a correlation between olfactory identification and fimbria-fornix white matter among spatial learners but not response learners indicates that it may be useful to identify individuals' spontaneous navigation strategies in order to capture this inter-individual variability. We speculated in Dahmani et al. (2018) that response learners may more heavily rely on other nodes of the olfactory network, or that they may use a different neural network for olfactory processing. There is a lot of evidence that olfaction is influenced by top-down processing (Zatorre et al., 2000; Finkel et al., 2001; Gottfried and Dolan, 2003; de Araujo et al., 2005; Grabenhorst and Rolls, 2010; Ferdenzi et al., 2017) and cognitive strategies may influence the neural networks underlying it (Karunanayaka et al., 2014). Future studies should seek to elucidate the neural networks involved in olfactory identification using functional connectivity methods and to determine whether spatial and response learners differ in the way they process olfactory information.

Our findings may have implications for aging research. Both olfaction and spatial memory are impaired early on in cognitive aging and Alzheimer's disease (Henderson et al., 1989; Pai and Jacobs, 2004; Tu and Pai, 2006; Wilson et al., 2007, 2009; Devanand et al., 2008, 2015; Head and Isom, 2010; Stanciu et al., 2014; Allison et al., 2016; Lafaille-Magnan et al., 2017). Atrophy of the olfactory bulb, olfactory tract, entorhinal cortex, and hippocampus is also observed early in the disease (Pearson et al., 1985; Ferreyra-Moyano and Barragan, 1989; Talamo et al., 1989; Fox et al., 1996; Kaye et al., 1997; den Heijer et al., 2006). Our results suggest that dissociating individuals based on navigation strategies (spatial vs. response) combined with measuring errors during navigational learning and olfactory identification may be more sensitive to variations in hippocampal volume and hippocampal network white matter integrity, compared to looking at navigational learning errors or olfactory identification alone. It would be of interest to pursue this question in a future line of research.

In summary, our finding that fimbria-fornix volume is associated with spatial learning and olfactory identification is in line with our previous results (Dahmani et al., 2018). Not only are these two processes behaviorally linked, but they also share many neuroanatomical substrates (Dahmani et al., 2018). In a comprehensive review, Jacobs et al. (2015) describes that the size of the olfactory bulb, a primary olfactory area, covaries with hippocampal size in many mammals (Reep et al., 2007) and with navigational demand, according to factors such as home range size (Gittleman, 1991) and predatory strategy (Reep et al., 2007). Taken together, these pieces of evidence are consistent with our findings that spatial memory and olfaction are closely linked.

## DATA AVAILABILITY STATEMENT

The raw data supporting the conclusions of this article will be made available by the authors, without undue reservation, to any qualified researcher.

## ETHICS STATEMENT

The studies involving human participants were reviewed and approved by the Institutional Review Board of the Douglas Mental Health University Institute. The patients/participants provided their written informed consent to participate in this study.

## AUTHOR CONTRIBUTIONS

LD and VB designed the study. JN, LD, and VB devised the MRI scanning protocol. LD performed the study, analyzed the data, and wrote the manuscript. BC, JN, and RP assisted with neuroimaging data preprocessing. RP, RA, and MC assisted with the MAGeT-Brain pipeline. VB supervised the study. All authors edited the manuscript.

## FUNDING

This research was supported by Natural Sciences and Engineering Research Council of Canada (NSERC) grant no. 239896-2013 and a Canadian Institutes of Health Research (CIHR) Frederick Banting and Charles Best Doctoral Training Award.

## ACKNOWLEDGMENTS

We would like to thank Erica Chan, Meagan Bristowe, and Melissa Berman for their help with data collection.

## REFERENCES

Allison, S. L., Fagan, A. M., Morris, J. C., and Head, D. (2016). Spatial navigation in preclinical Alzheimer's disease. *J. Alzheimers Dis.* 52, 77–90. doi: 10.3233/JAD-150855

Amaral, R. S., Park, M. T. M., Devenyi, G. A., Lynn, V., Pipitone, J., Winterburn, J., et al. (2018). Manual segmentation of the fornix, fimbria, and alveus on high-resolution 3T MRI: application *via* fully-automated mapping of the human memory circuit white and grey matter in healthy and pathological aging. *Neuroimage* 170, 132–150. doi: 10.1016/j.neuroimage.2016.10.027

Barrash, J. (1998). A historical review of topographical disorientation and its neuroanatomical correlates. *J. Clin. Exp. Neuropsychol.* 20, 807–827. doi: 10.1076/jcen.20.6.807.1114

Bohbot, V. D., and Corkin, S. (2007). Posterior parahippocampal place learning in HM. *Hippocampus* 17, 863–872. doi: 10.1002/hipo.20313

Bohbot, V. D., Iaria, G., and Petrides, M. (2004). Hippocampal function and spatial memory: evidence from functional neuroimaging in healthy participants and performance of patients with medial temporal lobe resections. *Neuropsychology* 18, 418–425. doi: 10.1037/0894-4105.18.3.418

Bohbot, V. D., Jech, R., Ruzicka, E., Nadel, L., Kalina, M., Stepánková, K., et al. (2002). Rat spatial memory tasks adapted for humans: characterization in subjects with intact brain and subjects with selective medial temporal lobe thermal lesions. *Physiol. Res.* 51, S49–S65.

Bohbot, V. D., Kalina, M., Stepankova, K., Spackova, N., Petrides, M., and Nadel, L. (1998). Spatial memory deficits in patients with lesions to the right

hippocampus and to the right parahippocampal cortex. *Neuropsychologia* 36, 1217–1238. doi: 10.1016/s0028-3932(97)00161-9

Bohbot, V. D., Lerch, J., Thorndycraft, B., Iaria, G., and Zijdenbos, A. P. (2007). Gray matter differences correlate with spontaneous strategies in a human virtual navigation task. *J. Neurosci.* 27, 10078–10083. doi: 10.1523/JNEUROSCI.1763-07.2007

Brown, L., Sherbenou, R. J., and Johnsen, S. K. (1997). *Test of Nonverbal Intelligence*. 3rd Edn. Austin, TX: Pro-Ed.

Burgess, N. (2002). The hippocampus, space, and viewpoints in episodic memory. *Q. J. Exp. Psychol. A* 55, 1057–1080. doi: 10.1080/02724980244000224

Dahmani, L., and Bohbot, V. D. (2015). Dissociable contributions of the prefrontal cortex to hippocampus-and caudate nucleus-dependent virtual navigation strategies. *Neurobiol. Learn. Mem.* 117, 42–50. doi: 10.1016/j.nlm.2014.07.002

Dahmani, L., Patel, R. M., Yang, Y., Chakravarty, M. M., Fellows, L. K., and Bohbot, V. D. (2018). An intrinsic association between olfactory identification and spatial memory in humans. *Nat. Commun.* 9:4162. doi: 10.1038/s41467-018-06569-4

de Araujo, I. E., Rolls, E. T., Velazco, M. I., Margot, C., and Cayeux, I. (2005). Cognitive modulation of olfactory processing. *Neuron* 46, 671–679. doi: 10.1016/j.neuron.2005.04.021

de Bruin, J. P. C., Moita, M. P., de Brabander, H. M., and Joosten, R. N. (2001). Place and response learning of rats in a Morris water maze: differential effects of fimbria fornix and medial prefrontal cortex lesions. *Neurobiol. Learn. Mem.* 75, 164–178. doi: 10.1006/nlme.2000.3962

den Heijer, T., Geerlings, M. I., Hoebeek, F. E., Hofman, A., Koudstaal, P. J., and Breteler, M. M. (2006). Use of hippocampal and amygdalar volumes on magnetic resonance imaging to predict dementia in cognitively intact elderly people. *Arch. Gen. Psychiatry* 63, 57–62. doi: 10.1001/archpsyc.63.1.57

Devanand, D. P., Lee, S., Manly, J., Andrews, H., Schupf, N., Doty, R. L., et al. (2015). Olfactory deficits predict cognitive decline and Alzheimer dementia in an urban community. *Neurology* 84, 182–189. doi: 10.1212/wnl.0000000000001132

Devanand, D. P., Liu, X., Tabert, M. H., Pradhaban, G., Cuasay, K., Bell, K., et al. (2008). Combining early markers strongly predicts conversion from mild cognitive impairment to Alzheimer's disease. *Biol. Psychiatry* 64, 871–879. doi: 10.1016/j.biopsych.2008.06.020

Etchamendy, N., Konishi, K., Pike, G. B., Marighetto, A., and Bohbot, V. D. (2012). Evidence for a virtual human analog of a rodent relational memory task: a study of aging and fMRI in young adults. *Hippocampus* 22, 869–880. doi: 10.1002/hipo.20948

Ferdenzi, C., Joussain, P., Digard, B., Luneau, L., Djordjevic, J., and Bensafi, M. (2017). Individual differences in verbal and non-verbal affective responses to smells: influence of odor label across cultures. *Chem. Senses* 42, 37–46. doi: 10.1093/chemse/bjw098

Ferreyra-Moyano, H., and Barragan, E. (1989). The olfactory system and Alzheimer's disease. *Int. J. Neurosci.* 49, 157–197. doi: 10.3109/00207458909084824

Field, A. (2009). *Discovering Statistics Using SPSS*. London: Sage Publications.

Field, A., Miles, J., and Field, Z. (2012). *Discovering Statistics Using R*. Thousand Oaks: Sage Publications.

Finkel, D., Pedersen, N. L., and Larsson, M. (2001). Olfactory functioning and cognitive abilities: a twin study. *J. Gerontol. B Psychol. Sci. Soc. Sci.* 56, P226–P233. doi: 10.1093/geronb/56.4.p226

Fox, N., Warrington, E., Freeborough, P., Hartikainen, P., Kennedy, A., Stevens, J., et al. (1996). Presymptomatic hippocampal atrophy in Alzheimer's disease: a longitudinal MRI study. *Brain* 119, 2001–2007. doi: 10.1093/brain/119.6.2001

Frasnelli, J., Lundstrom, J. N., Boyle, J. A., Djordjevic, J., Zatorre, R. J., and Jones-Gotman, M. (2010). Neuroanatomical correlates of olfactory performance. *Exp. Brain Res.* 201, 1–11. doi: 10.1007/s00221-009-1999-7

Freiherr, J., Gordon, A. R., Alden, E. C., Ponting, A. L., Hernandez, M. F., Boesveldt, S., et al. (2012). The 40-item monell extended sniffin' sticks identification test (MONEX-40). *J. Neurosci. Methods* 205, 10–16. doi: 10.1016/j.jneumeth.2011.12.004

Gittleman, J. L. (1991). Carnivore olfactory bulb size: allometry, phylogeny and ecology. *J. Zool.* 225, 253–272. doi: 10.1111/j.1469-7998.1991.tb03815.x

Gottfried, J. A., and Dolan, R. J. (2003). The nose smells what the eye sees: crossmodal visual facilitation of human olfactory perception. *Neuron* 39, 375–386. doi: 10.1016/s0896-6273(03)00392-1

Grabenhorst, F., and Rolls, E. T. (2010). Attentional modulation of affective versus sensory processing: functional connectivity and a top-down biased activation theory of selective attention. *J. Neurophysiol.* 104, 1649–1660. doi: 10.1152/jn.00352.2010

Greenland, S., Senn, S. J., Rothman, K. J., Carlin, J. B., Poole, C., Goodman, S. N., et al. (2016). Statistical tests, P values, confidence intervals and power: a guide to misinterpretations. *Eur. J. Epidemiol.* 31, 337–350. doi: 10.1007/s10654-016-0149-3

Habib, M., and Sirigu, A. (1987). Pure topographical disorientation: a definition and anatomical basis. *Cortex* 23, 73–85. doi: 10.1016/s0010-9452(87)80020-5

Hartley, T., Maguire, E. A., Spiers, H. J., and Burgess, N. (2003). The well-worn route and the path less traveled: distinct neural bases of route following and wayfinding in humans. *Neuron* 37, 877–888. doi: 10.1016/s0896-6273(03)00095-3

Haukoos, J. S., and Lewis, R. J. (2005). Advanced statistics: bootstrapping confidence intervals for statistics with "difficult" distributions. *Acad. Emerg. Med.* 12, 360–365. doi: 10.1197/j.aem.2004.11.018

Head, D., and Isom, M. (2010). Age effects on wayfinding and route learning skills. *Behav. Brain Res.* 209, 49–58. doi: 10.1016/j.bbr.2010.01.012

Henderson, V. W., Mack, W., and Williams, B. W. (1989). Spatial disorientation in Alzheimer's disease. *Arch. Neurol.* 46, 391–394. doi: 10.1001/archneur.1989.00520400045018

Iaria, G., Lanyon, L. J., Fox, C. J., Giaschi, D., and Barton, J. J. (2008). Navigational skills correlate with hippocampal fractional anisotropy in humans. *Hippocampus* 18, 335–339. doi: 10.1002/hipo.20400

Iaria, G., Petrides, M., Dagher, A., Pike, B., and Bohbot, V. D. (2003). Cognitive strategies dependent on the hippocampus and caudate nucleus in human navigation: variability and change with practice. *J. Neurosci.* 23, 5945–5952. doi: 10.1523/JNEUROSCI.23-13-05945.2003

Jacobs, L. F., Arter, J., Cook, A., and Sulloway, F. J. (2015). Olfactory orientation and navigation in humans. *PLoS One* 10:e0129387. doi: 10.1371/journal.pone.0129387

Jones, D. K., Knösche, T. R., and Turner, R. (2013). White matter integrity, fiber count, and other fallacies: the do's and don'ts of diffusion MRI. *Neuroimage* 73, 239–254. doi: 10.1016/j.neuroimage.2012.06.081

Jones-Gotman, M., and Zatorre, R. J. (1993). Odor recognition memory in humans: role of right temporal and orbitofrontal regions. *Brain Cogn.* 22, 182–198. doi: 10.1006/brcg.1993.1033

Karunanayaka, P., Eslinger, P. J., Wang, J. L., Weitekamp, C. W., Molitoris, S., Gates, K. M., et al. (2014). Networks involved in olfaction and their dynamics using independent component analysis and unified structural equation modeling. *Hum. Brain Mapp.* 35, 2055–2072. doi: 10.1002/hbm.22312

Kaye, J. A., Swihart, T., Howieson, D., Dame, A., Moore, M., Karnos, T., et al. (1997). Volume loss of the hippocampus and temporal lobe in healthy elderly persons destined to develop dementia. *Neurology* 48, 1297–1304. doi: 10.1212/wnl.48.5.1297

Kjelvik, G., Evensmoen, H. R., Brezova, V., and Håberg, A. K. (2012). The human brain representation of odor identification. *J. Neurophysiol.* 108, 645–657. doi: 10.1152/jn.01036.2010

Kjelvik, G., Saltvedt, I., White, L. R., Stenumgård, P., Sletvold, O., Engedal, K., et al. (2014). The brain structural and cognitive basis of odor identification deficits in mild cognitive impairment and Alzheimer's disease. *BMC Neurol.* 14:168. doi: 10.1186/s12883-014-0168-1

Konishi, K., and Bohbot, V. D. (2013). Spatial navigational strategies correlate with gray matter in the hippocampus of healthy older adults tested in a virtual maze. *Front. Aging Neurosci.* 5:1. doi: 10.3389/fnagi.2013.00001

Konishi, K., Etchamendy, N., Roy, S., Marighetto, A., Rajah, N., and Bohbot, V. D. (2013). Decreased fMRI activity in the hippocampus in favor of the caudate nucleus in older adults tested in a virtual navigation task. *Hippocampus* 23, 1005–1014. doi: 10.1002/hipo.22181

Lafaille-Magnan, M.-E., Poirier, J., Etienne, P., Tremblay-Mercier, J., Frenette, J., Rosa-Neto, P., et al. (2017). Odor identification as a biomarker of preclinical AD in older adults at risk. *Neurology* 89, 327–335. doi: 10.1212/WNL.0000000000004159

Lundström, J. N., Boesveldt, S., and Albrecht, J. (2011). Central processing of the chemical senses: an overview. *ACS Chem. Neurosci.* 2, 5–16. doi: 10.1021/cn1000843

Maguire, E. A., Burgess, N., Donnett, J. G., Frackowiak, R. S., Frith, C. D., and O'Keefe, J. (1998). Knowing where and getting there: a human navigation network. *Science* 280, 921–924. doi: 10.1126/science.280.5365.921

McDonald, R. J., and White, N. M. (1993). A triple dissociation of memory systems: hippocampus, amygdala, and dorsal striatum. *Behav. Neurosci.* 107, 3–22. doi: 10.1037//0735-7044.107.1.3

McDonald, R. J., and White, N. M. (1995). Hippocampal and nonhippocampal contributions to place learning in rats. *Behav. Neurosci.* 109, 579–593. doi: 10.1037/0735-7044.109.4.579

Meyers, J. E., and Meyers, K. R. (1995). *Rey Complex Figure Test and Recognition Trial: Professional Manual.* Odessa, FL: Psychological Assessment Resources.

Moscovitch, M., Rosenbaum, R. S., Gilboa, A., Addis, D. R., Westmacott, R., Grady, C., et al. (2005). Functional neuroanatomy of remote episodic, semantic and spatial memory: a unified account based on multiple trace theory. *J. Anat.* 207, 35–66. doi: 10.1111/j.1469-7580.2005.00421.x

O'Keefe, J., and Nadel, L. (1978). *The Hippocampus as a Cognitive Map*. Oxford: Clarendon.

Olton, D. S., and Papas, B. C. (1979). Spatial memory and hippocampal function. *Neuropsychologia* 17, 669–682. doi: 10.1016/0028-3932(79)90042-3

Olton, D. S., and Samuelson, R. J. (1976). Remembrance of places passed: spatial memory in rats. *J. Exp. Psychol. Anim. Behav. Process.* 2, 97–116. doi: 10.1037/0097-7403.2.2.97

Packard, M. G., Hirsh, R., and White, N. M. (1989). Differential effects of fornix and caudate nucleus lesions on two radial maze tasks: evidence for multiple memory systems. *J. Neurosci.* 9, 1465–1472. doi: 10.1523/jneurosci.09-05-01465.1989

Pai, M. C., and Jacobs, W. J. (2004). Topographical disorientation in community-residing patients with Alzheimer's disease. *Int. J. Geriatr. Psychiatry* 19, 250–255. doi: 10.1002/gps.1081

Pearson, R., Esiri, M., Hiorns, R., Wilcock, G., and Powell, T. (1985). Anatomical correlates of the distribution of the pathological changes in the neocortex in Alzheimer disease. *Proc. Natl. Acad. Sci. U S A* 82, 4531–4534. doi: 10.1073/pnas.82.13.4531

Pigott, S., and Milner, B. (1993). Memory for different aspects of complex visual scenes after unilateral temporal-or frontal-lobe resection. *Neuropsychologia* 31, 1–15. doi: 10.1016/0028-3932(93)90076-c

Pipitone, J., Park, M. T. M., Winterburn, J., Lett, T. A., Lerch, J. P., Pruessner, J. C., et al. (2014). Multi-atlas segmentation of the whole hippocampus and subfields using multiple automatically generated templates. *Neuroimage* 101, 494–512. doi: 10.1016/j.neuroimage.2014.04.054

Poole, C. (2001). Low P-values or narrow confidence intervals: which are more durable? *Epidemiology* 12, 291–294. doi: 10.1097/00001648-200105000-00005

Reep, R., Finlay, B., and Darlington, R. (2007). The limbic system in mammalian brain evolution. *Brain Behav. Evol.* 70, 57–70. doi: 10.1159/000101491

Rey, A. (1941). L'examen psychologique dans les cas d'encéphalopathie traumatique. *Arch. Psychol.* 28, 215–285.

Rothman, K. J. (1978). A show of confidence. *N. Engl. J. Med.* 299, 1362–1363. doi: 10.1056/NEJM197812142992410

Savic, I., Gulyas, B., Larsson, M., and Roland, P. (2000). Olfactory functions are mediated by parallel and hierarchical processing. *Neuron* 26, 735–745. doi: 10.1016/s0896-6273(00)81209-x

Scholz, J., Tomassini, V., and Johansen-Berg, H. (2014). "Individual differences in white matter microstructure in the healthy brain," in *Diffusion MRI*, eds H. Johansen-Berg and T. E. J. Behrens (Cambridge, MA: Elsevier), 301–316.

Segura, B., Baggio, H. C., Solana, E., Palacios, E. M., Vendrell, P., Bargalló, N., et al. (2013). Neuroanatomical correlates of olfactory loss in normal aged subjects. *Behav. Brain Res.* 246, 148–153. doi: 10.1016/j.bbr.2013.02.025

Seubert, J., Freiherr, J., Frasnelli, J., Hummel, T., and Lundström, J. N. (2013). Orbitofrontal cortex and olfactory bulb volume predict distinct aspects of olfactory performance in healthy subjects. *Cereb. Cortex* 23, 2448–2456. doi: 10.1093/cercor/bhs230

Smitka, M., Puschmann, S., Buschhueter, D., Gerber, J. C., Witt, M., Honeycutt, N., et al. (2012). Is there a correlation between hippocampus and amygdala volume and olfactory function in healthy subjects? *Neuroimage* 59, 1052–1057. doi: 10.1016/j.neuroimage.2011.09.024

Stanciu, I., Larsson, M., Nordin, S., Adolfsson, R., Nilsson, L.-G., and Olofsson, J. K. (2014). Olfactory impairment and subjective olfactory complaints independently predict conversion to dementia: a longitudinal, population-based study. *J. Int. Neuropsychol. Soc.* 20, 209–217. doi: 10.1017/s1355617713001409

Suzuki, Y., Critchley, H. D., Suckling, J., Fukuda, R., Williams, S. C., Andrew, C., et al. (2001). Functional magnetic resonance imaging of odor identification: the effect of aging. *J. Gerontol. A Biol. Sci. Med. Sci.* 56, M756–M760. doi: 10.1093/gerona/56.12.m756

Talamo, B. R., Rudel, R., Kosik, K. S., Lee, V. M.-Y., Neff, S., Adelman, L., et al. (1989). Pathological changes in olfactory neurons in patients with Alzheimer's disease. *Nature* 337, 736–739. doi: 10.1038/337736a0

Tu, M.-C., and Pai, M.-C. (2006). Getting lost for the first time in patients with Alzheimer's disease. *Int. Psychogeriatr.* 18, 567–570. doi: 10.1017/s1041610206224025

Tustison, N. J., Avants, B. B., Cook, P. A., Zheng, Y., Egan, A., Yushkevich, P. A., et al. (2010). N4ITK: improved N3 bias correction. *IEEE Trans. Med. Imaging* 29, 1310–1320. doi: 10.1109/TMI.2010.2046908

Westfall, P. H., and Young, S. S. (1993). *Resampling-Based Multiple Testing: Examples and Methods for p-value adjustment.* New York, NY: John Wiley and Sons.

White, N. M., and McDonald, R. J. (2002). Multiple parallel memory systems in the brain of the rat. *Neurobiol. Learn. Mem.* 77, 125–184. doi: 10.1006/nlme.2001.4008

Wilson, R. S., Arnold, S. E., Schneider, J. A., Boyle, P. A., Buchman, A. S., and Bennett, D. A. (2009). Olfactory impairment in presymptomatic Alzheimer's disease. *Ann. N Y Acad. Sci.* 1170, 730–735. doi: 10.1111/j.1749-6632.2009.04013.x

Wilson, R. S., Arnold, S. E., Schneider, J. A., Tang, Y., and Bennett, D. A. (2007). The relationship between cerebral Alzheimer's disease pathology and odour identification in old age. *J. Neurol. Neurosurg. Psychiatry* 78, 30–35. doi: 10.1136/jnnp.2006.099721

Winterburn, J. L., Pruessner, J. C., Chavez, S., Schira, M. M., Lobaugh, N. J., Voineskos, A. N., et al. (2013). A novel *in vivo* atlas of human hippocampal subfields using high-resolution 3T magnetic resonance imaging. *Neuroimage* 74, 254–265. doi: 10.1016/j.neuroimage.2013.02.003

Wu, K. N., Tan, B. K., Howard, J. D., Conley, D. B., and Gottfried, J. A. (2012). Olfactory input is critical for sustaining odor quality codes in human orbitofrontal cortex. *Nat. Neurosci.* 15, 1313–1319. doi: 10.1038/nn.3186

Zatorre, R. J., and Jones-Gotman, M. (1990). Right-nostril advantage for discrimination of odors. *Percept. Psychophys.* 47, 526–531. doi: 10.3758/bf03203105

Zatorre, R. J., Jones-Gotman, M., Evans, A. C., and Meyer, E. (1992). Functional localization and lateralization of human olfactory cortex. *Nature* 360, 339–340. doi: 10.1038/360339a0

Zatorre, R. J., Jones-Gotman, M., and Rouby, C. (2000). Neural mechanisms involved in odor pleasantness and intensity judgments. *Neuroreport* 11, 2711–2716. doi: 10.1097/00001756-200008210-00021

**Conflict of Interest**: The authors declare that the research was conducted in the absence of any commercial or financial relationships that could be construed as a potential conflict of interest.

*Copyright © 2020 Dahmani, Courcot, Near, Patel, Amaral, Chakravarty and Bohbot. This is an open-access article distributed under the terms of the Creative Commons Attribution License (CC BY). The use, distribution or reproduction in other forums is permitted, provided the original author(s) and the copyright owner(s) are credited and that the original publication in this journal is cited, in accordance with accepted academic practice. No use, distribution or reproduction is permitted which does not comply with these terms.*

frontiers in Molecular Neuroscience

ORIGINAL RESEARCH
published: 23 January 2020
doi: 10.3389/fnmol.2020.00006

# Lack of Neurosteroid Selectivity at δ vs. γ2-Containing $GABA_A$ Receptors in Dentate Granule Neurons

*Xinguo Lu[1], Charles F. Zorumski[1,2,3] and Steven Mennerick[1,2,3]**

[1] Department of Psychiatry, Washington University School of Medicine, St. Louis, MO, United States, [2] Department of Neuroscience, Washington University School of Medicine, St. Louis, MO, United States, [3] Taylor Family Institute for Innovative Psychiatric Research, Washington University School of Medicine, St. Louis, MO, United States

$GABA_A$ receptors mediate a large fraction of inhibitory neurotransmission in the central nervous system. Two major classes of $GABA_A$ receptors are γ2-containing receptors and δ-containing receptors, which are largely located synaptically and extrasynaptically, respectively. Neuroactive steroids such as allopregnanolone (3α5αP) and allotetrahydrodeoxycorticosterone (THDOC) are hypothesized to selectively affect δ-containing receptors over γ2-containing receptors. However, the selectivity of neurosteroids on $GABA_A$ receptor classes is controversial. In this study, we re-examined this issue using mice with picrotoxin resistance associated with either the δ or γ2 subunit. Our results show that 3α5αP potentiated phasic inhibition of $GABA_A$ receptors, and this is mainly through γ2-containing receptors. 3α5αP, with or without exogenous GABA, potentiated tonic inhibition through $GABA_A$ receptors. Surprisingly, potentiation arose from both γ2- and δ-containing receptors, even when a δ selective agonist THIP was used to activate current. Although ethanol has been proposed to act through neurosteroids and to act selectively at δ receptors, we found no evidence for ethanol potentiation of $GABA_A$ receptor function at 50 mM under our experimental conditions. Finally, we found that the actions of pentobarbital exhibited very similar effects on tonic current as 3α5αP, emphasizing the broad spectrum nature of neurosteroid potentiation. Overall, using chemogenetic analysis, our evidence suggests that in a cell population enriched for δ-containing receptors, neurosteroids act through both δ-containing and non-δ-containing receptors.

**Keywords: hippocampus, $GABA_A$ receptor, neurosteroid, allopregnanolone (3α5αP), phasic inhibition, tonic inhibition**

OPEN ACCESS

***Edited by:***
*Bernhard Lüscher, The Pennsylvania State University (PSU), United States*

***Reviewed by:***
*Beverley Anne Orser, University of Toronto, Canada*
*Trevor G. Smart, University College London, United Kingdom*

****Correspondence:***
*Steven Mennerick*
*menneris@wustl.edu*

***Received:*** *01 October 2019*
***Accepted:*** *09 January 2020*
***Published:*** *23 January 2020*

***Citation:***
*Lu X, Zorumski CF and Mennerick S (2020) Lack of Neurosteroid Selectivity at δ vs. γ 2-Containing $GABA_A$ Receptors in Dentate Granule Neurons. Front. Mol. Neurosci. 13:6. doi: 10.3389/fnmol.2020.00006*

## INTRODUCTION

$GABA_A$ receptors are ligand-gated, chloride-permeable ion channels mediating inhibitory neuronal transmission. They play essential roles in regulating neuronal activity and behavior (Sigel and Steinmann, 2012; Lee and Maguire, 2014). As heteromeric pentamers (Pirker et al., 2000), they are sometimes divided into two major classes: synaptically located γ2-containing receptors (γ2 receptors) and extrasynaptically located δ-containing receptors (δ receptors) (Wei et al., 2003). Developing subunit-selective drugs is a major goal of the pharmaceutical industry (Möhler, 2006, 2011); specifically δ selective drugs may have important applications in neuropsychiatry

(Orser, 2006). For instance, neurosteroids have recently generated enthusiasm as antidepressants (Kanes et al., 2017; Gunduz-Bruce et al., 2019). Their psychoactive profile could result from selective effects on δ $GABA_A$ receptors (Spigelman et al., 2003; Stell et al., 2003; Carver and Reddy, 2016), but some studies suggest limited selectivity (Shu et al., 2012). Here we reinvestigate neurosteroid subunit selectivity in native receptors with new tools in a well-studied class of δ-subunit expressing neurons.

Neurosteroids are one example of a wide variety of clinically important positive allosteric modulators of $GABA_A$ receptors. Other positive modulators include benzodiazepines, barbiturates, and ethanol (Olsen et al., 2007; Olsen, 2018; Reddy, 2018; Masiulis et al., 2019). Ethanol and neurosteroids are proposed to share δ selectivity (Wallner et al., 2003; Wei et al., 2004; Olsen et al., 2007). In fact, ethanol's positive effects on δ $GABA_A$ receptor function may be mediated by altered endogenous neurosteroid production and/or release (Sanna et al., 2004; Tokuda et al., 2011; Izumi et al., 2015). Benzodiazepines are dependent on both the specific α subunit and γ subunit composition of receptors (Pritchett et al., 1989), and barbiturates are broad spectrum modulators (Olsen, 2018).

Neurosteroids prolong the $GABA_A$ receptor response to synaptic GABA (IPSCs) and increase tonic GABA current (Stell et al., 2003). A prevalent view is that γ2 receptors are responsible for phasic inhibition, and δ receptors (in neurons that express the δ subunit) are responsible for tonic current, sometimes along with α5/γ2 receptors (Stell et al., 2003; Glykys et al., 2008; Brickley and Mody, 2012; Whissell et al., 2015). Previous studies are equivocal on whether the effects of neurosteroids on IPSCs are through γ2 or through δ receptors (Spigelman et al., 2003; Stell et al., 2003). Our own previous work suggests that slow, δ driven IPSCs are prominent in dentate granule cells (Sun et al., 2018) and so might explain neurosteroid effects. Tonic current is thought to arise largely (though not exclusively) from high-affinity δ receptors in cells that express δ subunits (Stell et al., 2003; Glykys et al., 2008; Brickley and Mody, 2012; Whissell et al., 2015), so δ-mediated tonic current also offers a potentially important substrate for δ-selective neurosteroid actions.

Previous studies employed genetic deletion to test neurosteroid selectivity (Stell et al., 2003; Glykys et al., 2008; Carver and Reddy, 2016), in part because of the lack of pharmacological tools to separate δ receptors from γ2 receptors. Although genetic deletion is typically considered more definitive than pharmacology, knockouts and knockdowns have caveats of compensation or other secondary changes that might affect outcomes (Gunther et al., 1995; Korpi et al., 2002; Peng et al., 2002). Further, sensitivity is sacrificed without the ability to measure pharmacological actions on different receptor populations in the same cell.

We recently revisited the role of δ receptors in phasic and tonic transmission using a knock-in/chemogenetic approach. We generated mice with picrotoxin (PTX) resistance associated with either the γ2 subunit (γ2* KI) or δ subunit (δ* KI)

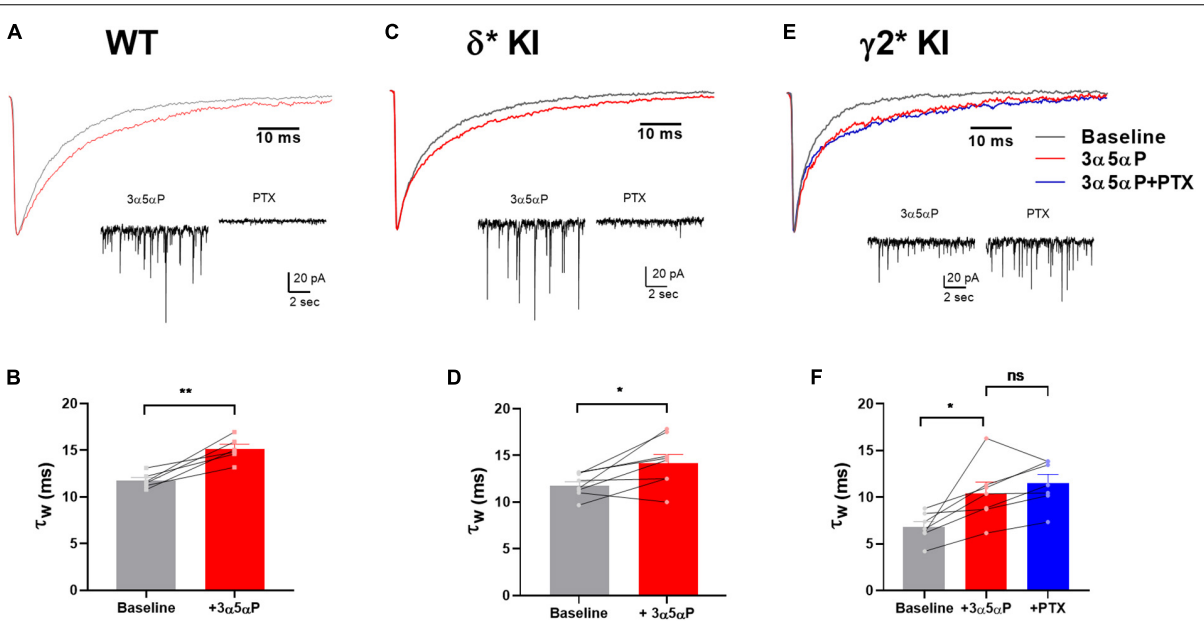


**FIGURE 1 |** Prolongation of sIPSC decay by 3α5αP in hippocampal DGCs. **(A)** Representative WT average sIPSC waveforms obtained before (black) and in the presence (red) of 100 nM 3α5αP. **(B)** WT DGC $\tau_w$ of sIPSC decay under baseline (11.7 ± 0.3 ms) and 3α5αP (15.1 ± 0.5 ms). **(C)** δ* KI average sIPSC waveforms obtained before, in the presence of 100 nM 3α5αP. **(D)** δ* KI DGC $\tau_w$ of sIPSC decay under baseline (11.9 ± 0.4 ms) and 3α5αP (14.3 ± 0.9 ms). **(E)** γ2* KI average sIPSC waveforms obtained before, in the presence of 100 nM 3α5αP, and with addition of 50 μM PTX. **(F)** γ2* KI DGC $\tau_w$ of sIPSC decay under baseline (6.8 ± 0.6 ms) and 3α5αP (10.4 ± 1.2 ms), and 3α5αP/PTX (11.5 ± 0.9 ms). Paired *t* test showed that 100 nM 3α5αP significantly increased $\tau_w$ of sIPSC decay in WT ($n = 6$, $p = 3 \times 10^{-3}$) and δ* KI ($n = 8$, $p = 0.02$). In γ2* KI ($n = 7$) one-way ANOVA on $\tau_w$ of sIPSC decay showed a drug effect ($F(1.3,7.7) = 15.3$, $p = 4 \times 10^{-3}$), with a significant difference between baseline and 3α5αP (Holm-Sidak, $p = 0.04$), and no change between 3α5αP and PTX (Holm-Sidak, $p = 0.2$). The $\tau_w$ of sIPSC decay after PTX was not included in panels **(B,D)** due to the elimination of most sIPSCs by PTX.

(Gurley et al., 1995; Sedelnikova et al., 2006). This strategy confers picrotoxin resistance onto receptors containing only a single mutated subunit (Gurley et al., 1995; Sun et al., 2018). Here we employed the new mouse lines to reinvestigate the selectivity of neurosteroids for the two main classes of $GABA_A$ receptors in DGCs.

Our results showed that 3α5αP potentiated phasic inhibition by prolonging the decay of sIPSCs through an effect on γ2 receptors. 3α5αP also potentiated $GABA_A$ tonic inhibition in slices from WT and the two knock-in genotypes. Based on complementary PTX sensitivity in the two mutants, the tonic current was mediated approximately equally by δ receptors and γ2 receptors. Furthermore, the potentiation of tonic current by neurosteroids persisted under conditions of no added agonist, when co-applied with exogenous GABA, and when co-applied with the δ-selective exogenous agonist THIP. We conclude that neurosteroids are not selective for δ receptors and that selectivity is unlikely to underlie unique psychoactive effects.

# MATERIALS AND METHODS

## Slice Preparation

Mice from postnatal (P)25 to P32 $GABA_A$ receptor δ* KI, γ2* KI, or WT littermates of both sexes were used (Sun et al., 2018). Mice were anesthetized with isoflurane and decapitated according to protocols approved by the Washington University IACUC. After attaching to a Leica VT1200 specimen holder with cyanoacrylate, coronal brain slices, 300-μM-thick, were cut in ice-cold, modified artificial CSF (aCSF; used for slicing in mM: 87 NaCl, 75 sucrose, 25 glucose, 25 $NaHCO_3$, 2.5 KCl, 1.25 $NaH_2PO_4$, equilibrated with 95% oxygen-5% $CO_2$ plus 0.5 $CaCl_2$, 3 $MgCl_2$; 320 mOsm). Slices recovered in choline-based ACSF (in mM: 92 choline chloride, 25 glucose, 30 $NaHCO_3$, 2.5 KCl, 1.2 $NaH_2PO_4$, 20 HEPES, 2 thiourea, 5 Na ascorbate, 3 Na pyruvate, 2 $CaCl_2$, and 1 $MgCl_2$, equilibrated with 95% oxygen-5% $CO_2$; 300 mOsm) at 32°C for 30 min. After recovery, slices were stored in regular aCSF (in mM: 125 NaCl, 25 glucose, 25 $NaHCO_3$, 2.5 KCl, 1.25 $NaH_2PO_4$, equilibrated with 95% oxygen-5% $CO_2$ plus 2.6 $CaCl_2$, 1.2 $MgCl_2$; 310 mOsm) for at least 1 h at 25°C before experimental recording. Drugs were obtained from Thermo Fisher Scientific except where noted.

## Whole-Cell Recording

Slices were transferred to a recording chamber with continuous perfusion (2 ml/min, 32°C) of oxygenated, regular aCSF. To measure phasic and tonic inhibition of $GABA_A$ receptors, 10 μM NBQX (Tocris Bioscience) and 50 μM D-APV (Tocris Bioscience) were added in the regular aCSF to inhibit ionotropic glutamate receptors. To isolate current generated by the respective δ or γ2 subpopulation of $GABA_A$ receptors, we applied 50 μM PTX (Tocris Bioscience) in the appropriate subunit knock-in tissue.

During somatic, whole-cell recording, hippocampal DGCs were visualized and identified by IR-DIC microscopy (Nikon FN1 microscope and Photometrics Prime camera). Borosilicate glass pipettes (World Precision Instruments, Inc.) with open tip resistance of 3–7 MΩ were used for whole-cell recording. Pipettes were filled with internal solution containing the following (in mM): 130 CsCl, 10 HEPES, 5 EGTA, 2 MgATP, 0.5 NAGTP, and 4 QX-314; pH adjusted to 7.3 with CsOH; 290 mOsm). A 5-min stabilization period was given after the whole-cell configuration was established, and then cells were recorded with a MultiClamp 700B amplifier (Molecular Devices), Digidata 1550 16-bit A/D converter, and pClamp 10.4 software (Molecular Devices).

## Measurement of Phasic and Tonic $GABA_A$ Receptor Current

Cells were voltage-clamped at −70 mV during whole-cell recordings. Spontaneous phasic $GABA_A$ receptor currents were measured before/after the application of 3α5αP (100 nM). Tonic $GABA_A$ receptor currents were activated by GABA (5 μM), THIP (1 μM), and/or 3α5αP (100 nM). In some experiments, DS2 (Tocris Bioscience) and allotetrahydrodeoxycorticosterone (THDOC) were used as comparators. PTX was added at the end to isolate δ* KI or γ2* KI-mediated $GABA_A$ receptor currents. A 5-min perfusion of each drug was used to ensure maximal effect. All recordings were acquired in gap-free mode at 5 kHz, filtered at 2 kHz using an 8-pole Bessel filter.

## Analysis and Statistics

Both phasic and tonic $GABA_A$ currents were measured after cells reached steady state for each condition. sIPSCs and tonic currents were measured as described previously (Sun et al., 2018). At least

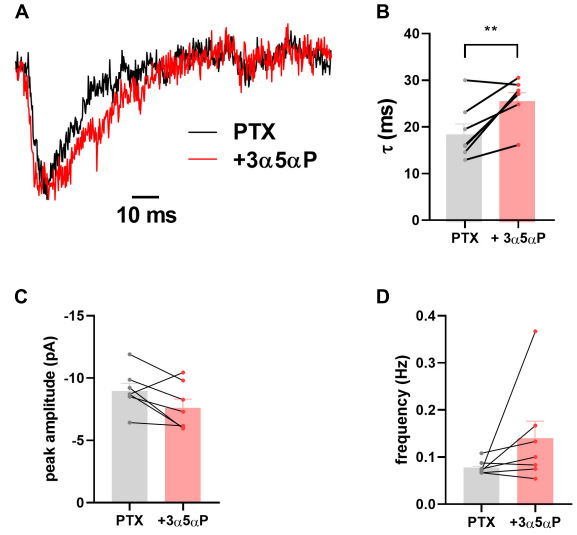


**FIGURE 2 |** Prolongation of δ sIPSC decay. In the presence of 50 μM PTX δ sIPSCs were isolated as described (Sun et al., 2018). **(A)** Scaled sIPSC waveforms from baseline and in the presence of 100 nM 3α5αP from 15 and 17 events, respectively. **(B–D)** In δ* KI DGCs ($n$ = 7) decays were prolonged by 100 nM 3α5αP from 18.9 ± 2.3 ms to 26.1 ± 1.8 ms (paired $t$ test, $p$ = 0.01). Neither sIPSC amplitude (−9.1 ± 0.6 pA vs. −7.7 ± 0.7 pA) nor frequency (0.08 ± 0.006 Hz vs. 0.14 ± 0.04 Hz) was reliably altered (paired $t$ test, $p$ = 0.08, 0.2, respectively).

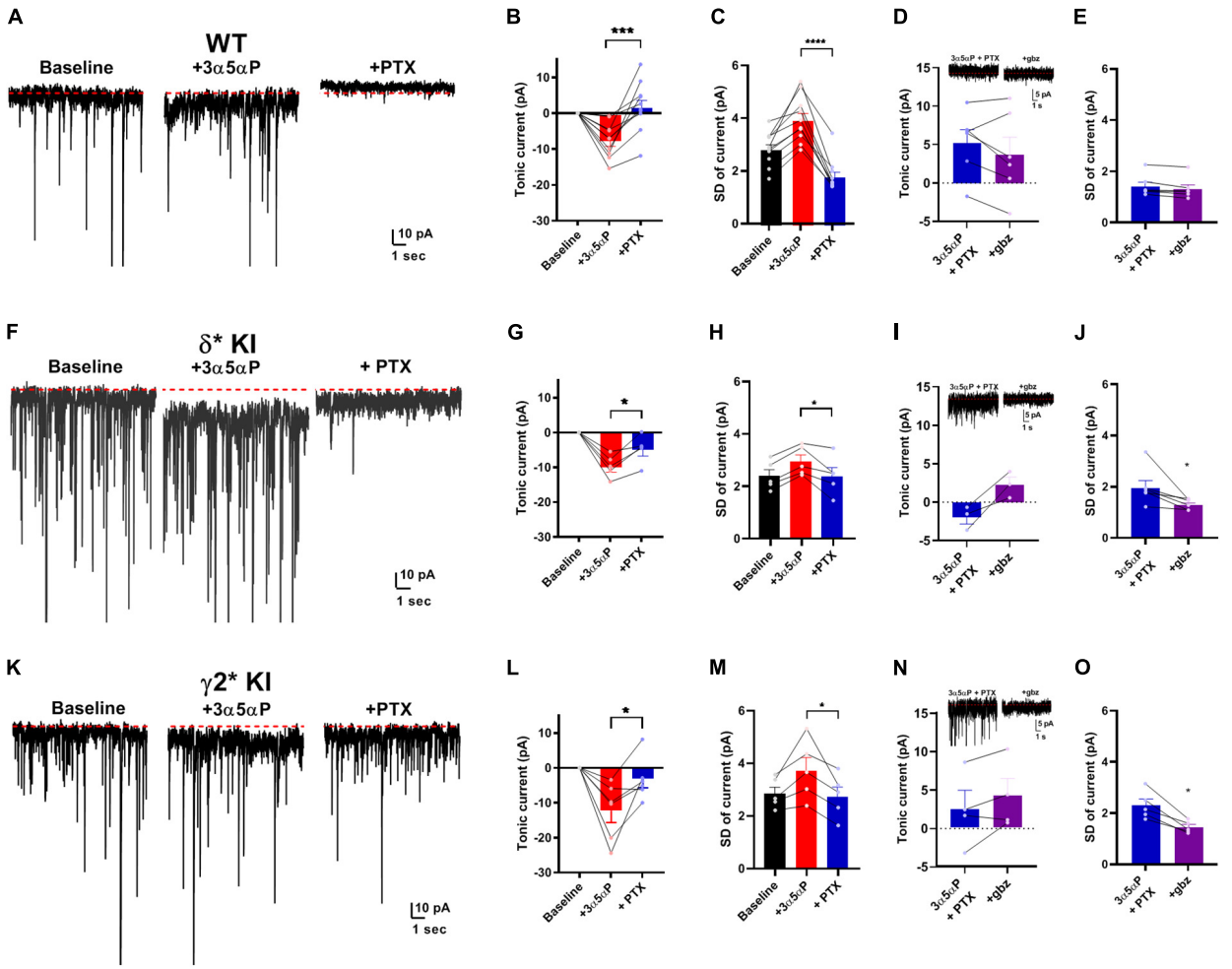


**FIGURE 3 |** Potentiation of tonic current by 3α5αP alone. **(A)** Effect of 100 nM 3α5αP in a representative DGC from a WT slice. 3α5αP resulted in a tonic current that was blocked by 50 μM PTX. Note that the sIPSCs were also largely inhibited by PTX, as also shown in **Figure 1**. **(B)** Summary of changes in mean current relative to baseline. 3α5αP increased tonic current to −7.4 ± 1.5 pA, and PTX decreased it to 2.0 ± 2.2 pA. **(C)** Summary of the standard deviation of current (baseline: 2.9 ± 0.2 pA, 3α5αP: 4.0 ± 0.3 pA, and 3α5αP+PTX: 1.8 ± 0.2 pA). **(D)** In a subset of neurons, 50 μM gabazine (gbz) was tested and produced no clear further impact on tonic current beyond the effect of PTX. Inset shows representative current samples. **(E)** Gbz also produced minimal change in the standard deviation of the current, indicating that PTX fully inhibited tonic current. **(F–J)** The same experiment from δ* KI DGCs. 3α5αP increased tonic current from baseline to −9.6 ± 1.5 pA, and PTX decreased it to −4.6 ± 1.8 pA. Standard deviation of current for baseline, 3α5αP, and 3α5αP+PTX was 2.4 ± 0.3 pA, 3.0 ± 0.3 pA, and 2.4 ± 0.3 pA, respectively. **(K–O)** Results from γ2* KI animals. 3α5αP increased tonic current from baseline to -12.3 ± 3.4 pA, and PTX decreased it to −3.3 ± 2.5 pA. Standard deviation of current for baseline, 3α5αP, and 3α5αP+PTX was 2.9 ± 0.3 pA, 3.8 ± 0.5 pA, and 2.8 ± 0.4 pA, respectively. Paired *t* test showed significant difference of tonic currents between 3α5αP and PTX in WT ($n$ = 10, $p = 9 \times 10^{-4}$), δ* KI ($n$ = 5, $p$ = 0.01), and γ2* KI ($n$ = 6, $p$ = 0.03). To compare genotype effects, we examined differences in the SD values prior to and during gabazaine (not directly shown; statistics performed on difference between connected SD values). An ANOVA between 3α5αP+PTX and 3α5αP+PTX+gabazine showed a genotype effect ($F(2.0,14.0) = 4.2$, $p$ = 0.03), with both δ* (0.7 ± 0.3 pA, $n$ = 6) and γ2* (0.9 ± 0.2 pA, $n$ = 5) exhibiting a difference from WT (0.1 ± 0.03 pA, $n$ = 6) (Holm-Sidak, $p$ = 0.05, 0.03, respectively). For panels sample current traces in this and subsequent figures, some of the largest sIPSCs have been truncated for clarity of depiction of tonic current.

40 events contributed to average sIPSC waveforms. sIPSC decays were fit to the sum of two exponential functions, extrapolated to the peak IPSC. Decay time course is reported as a weighted time constant ($\tau_w$) (Sun et al., 2018). Tonic $GABA_A$ currents were obtained by subtracting baseline holding currents. A paired *t* test or one-way repeated-measures ANOVA was performed using GraphPad Prism 8 to detect the effects within cells. Specific analyses are described in the Results. Significance is presented at the level of $^*p \leq 0.05$, **0.01, ***0.001, and ****0.0001. Summary data are presented as mean ± SEM.

# RESULTS

## Potentiation of Phasic Inhibition by 3α5αP

Neurosteroids like 3α5αP and THDOC potentiate phasic inhibition by prolonging the decay of sIPSCs in hippocampal DGCs (Stell et al., 2003). Although this effect has previously been associated with γ2 receptors, neurosteroids at sufficiently modest concentrations may have selective effects on δ

receptors (Stell et al., 2003; Carver and Reddy, 2016), which may participate more prominently in phasic transmission in DGCs than typically appreciated (Spigelman et al., 2003; Sun et al., 2018). In WT cells, 100 nM 3α5αP prolonged the weighted time constant ($\tau_w$) of sIPSC decay (**Figures 1A,B**). In δ* KI DGCs, 3α5αP showed a similar prolongation of sIPSC decay (**Figures 1C,D**). PTX eliminated most sIPSCs in both WT and δ* KI DGCs (**Figures 1A,C**). In γ2* KI DGCs, 100 nM 3α5αP also prolonged the $\tau_w$ of sIPSC decay (**Figures 1E,F**). However, baseline γ2* sIPSC decay was faster than the other genotypes, as previously reported (Sun et al., 2018). After PTX addition, the prolongation of sIPSC decay persisted in γ2* cells (**Figures 1E,F**). Taken together, these results indicate that 3α5αP prolongs the decay of sIPSCs in DGCs, and this potentiation is mainly through γ2 receptors. These results also confirm observations of others (Stell et al., 2003) but are in contrast with results suggesting a large impact of neuroactive steroids on a δ component of sIPSCs (Spigelman et al., 2003).

Although the major effect of neurosteroids is on IPSC time course, we also examined sIPSC frequency and amplitude. There was a trend toward decreased frequency with 3α5αP addition in each of the three genotypes: [WT, $n$ = 6: 2.1 ± 0.5 Hz vs. 1.5 ± 0.2 Hz; δ*, $n$ = 8: 3.8 ± 0.7 Hz vs. 2.8 ± 0.5 Hz; γ2*, $n$ = 7: 2.7 ± 0.8 Hz vs. 2.2 ± 0.4 Hz; ($F$(1.0,18.0) = 6.7, $p$ = 0.02); 2-way ANOVA, with repeated measures for frequency]. This likely reflects a general suppression of network activity by the pro-inhibitory neurosteroid. By contrast, there was no consistent effect of 3α5αP on amplitude of sIPSCs [WT: −38.9 ± 1.4 pA vs. −32.5 ± 2.0 pA; δ*: −37.7 ± 2.5 pA vs. −39.9 ± 1.8 pA; γ2*: −54.8 ± 11.9 pA vs. −50.1 ± 6.0 pA; ($F$(1.0,18.0) = 0.8, $p$ = 0.4)].

We have previously shown that sIPSCs mediated by δ receptors are detectable in DGCs, albeit at a low frequency

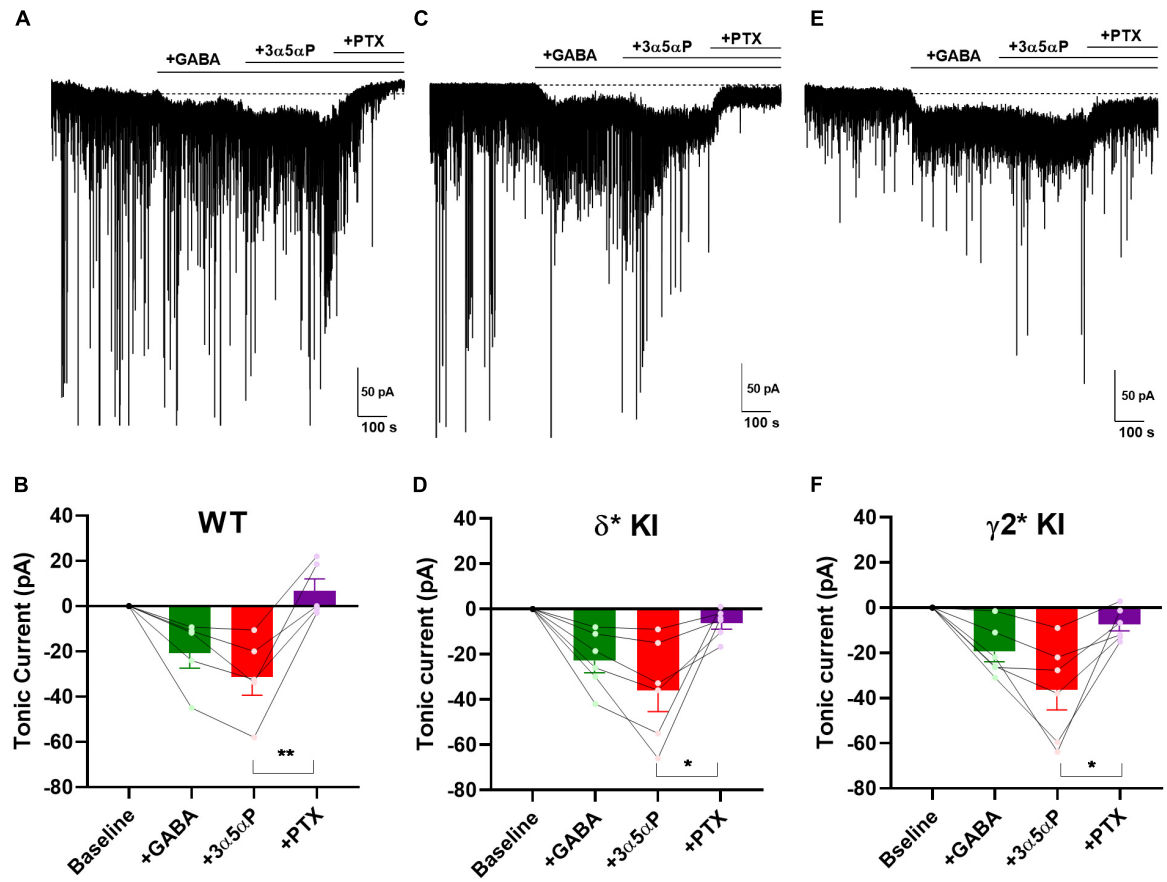


**FIGURE 4 |** 3α5αP potentiation of tonic inhibition with exogenous GABA is non-selective. **(A)** Effects of exogenous GABA (5 μM) in a representative DGC from a WT slice. GABA generated a current superimposed on ongoing spontaneous phasic sIPSCs. 3α5αP (100 nM) potentiated the GABA response, and 50 μM PTX abolished both the phasic and tonic currents. **(B)** Summary of the GABA/3α5αP current in the indicated conditions from cells of WT animals ($n$ = 5). GABA produced a tonic current of −20.2 ± 6.7 pA, and 3α5αP increased it to −31.0 ± 7.8 pA, while PTX decreased the tonic current to 7.3 ± 5.4 pA. **(C,D)** The same experiment from δ* KI DGCs ($n$ = 6). Similar as WT, GABA generated a tonic current of −22.6 ± 5.2 pA. Note that the GABA/3α5αP tonic current was partially blocked by PTX (from −35.6 ± 9.0 pA to −6.2 ± 2.6 pA), and phasic currents were strongly reduced. **(E,F)** Same experiment from γ2* KI DGCs ($n$ = 6). Comparable to δ* KI slices, GABA activated a tonic current of -19.6 ± 4.6 pA. The GABA/3α5αP current was also partially blocked by PTX (from −36.6 ± 8.8 pA to −7.5 ± 2.9 pA), but the phasic currents were left mostly intact. Dotted line in panels **(A,C,E)** shows mean initial holding current, which was subtracted for pooled results in panels **(B,D,F)**. One-way ANOVA on tonic current showed a drug effect in WT ($F$(1.9,7.4) = 17.0, $p = 2 \times 10^{-3}$), δ* KI ($F$(1.3,6.4) = 11.3, $p$ = 0.01), and γ2* KI ($F$(1.4,6.9) = 13.5, $p$ = 0.02). PTX significantly decreased GABA/3α5αP current in WT (Holm-Sidak, $p = 5 \times 10^{-3}$), δ* KI (Holm-Sidak, $p$ = 0.03), and γ2* KI (Holm-Sidak, $p$ = 0.02).

compared with γ2-dominated sIPSCs (Sun et al., 2018). In δ* slices incubated in 50 μM PTX, we found that 3α5αP similarly prolonged δ sIPSCs (**Figure 2**). Because of the small number of baseline δ sIPSCs detected, the overall impact on phasic transmission mediated by δ receptors was modest.

## Potentiation of Tonic Inhibition by 3α5αP Alone

Given that neurosteroid effects on IPSCs do not appear to involve strong δ selectivity, we turned to tonic currents, where evidence more strongly supports selective δ receptor effects of neurosteroids. A prevalent view is that δ receptors mediate a strong tonic component in DGCs. The selectivity hypothesis predicts that potentiation of tonic inhibition by neurosteroids is mainly through δ receptors (Stell et al., 2003; Glykys et al., 2008; Carver and Reddy, 2016). Under similar conditions to **Figure 1**, we examined the effect of 3α5αP on tonic current. 3α5αP similarly potentiated a tonic current in all three genotypes [one-way ANOVA, ($F(2.0,18.0) = 1.4$, $p = 0.3$)]. In WT slices, both 3α5αP tonic current and phasic current were completely blocked by PTX (**Figures 3A,B**). In both δ* KI and γ2* KI DGCs, PTX partially inhibited the 3α5αP tonic current (**Figures 3F,G,K,L**).

Because the currents observed were very small, and because holding current may be affected by technical factors over time, we examined an alternate measure of GABA channel activity. Channel-mediated currents are characterized by fluctuations (noise) that result from the stochastic nature of channel opening and closing (Anderson and Stevens, 1973). At low probabilities of channel opening, current fluctuations should correlate with the tonic current (Farrant and Nusser, 2005; Lingle, 2006) As a simple measure of these current fluctuations, we calculated the root mean squared noise level (standard deviation after subtracting the mean current) in each experimental condition. **Figures 3C,H,M** show that the results of this analysis parallel results from measures of the mean current and are arguably more sensitive than changes in current amplitudes. In a subset of cells, we also tested the impact of gabazine co-applied following PTX addition. Results showed trends toward further reduction in the two mutant phenotypes with no change in WT (**Figures 3D,I,N**).

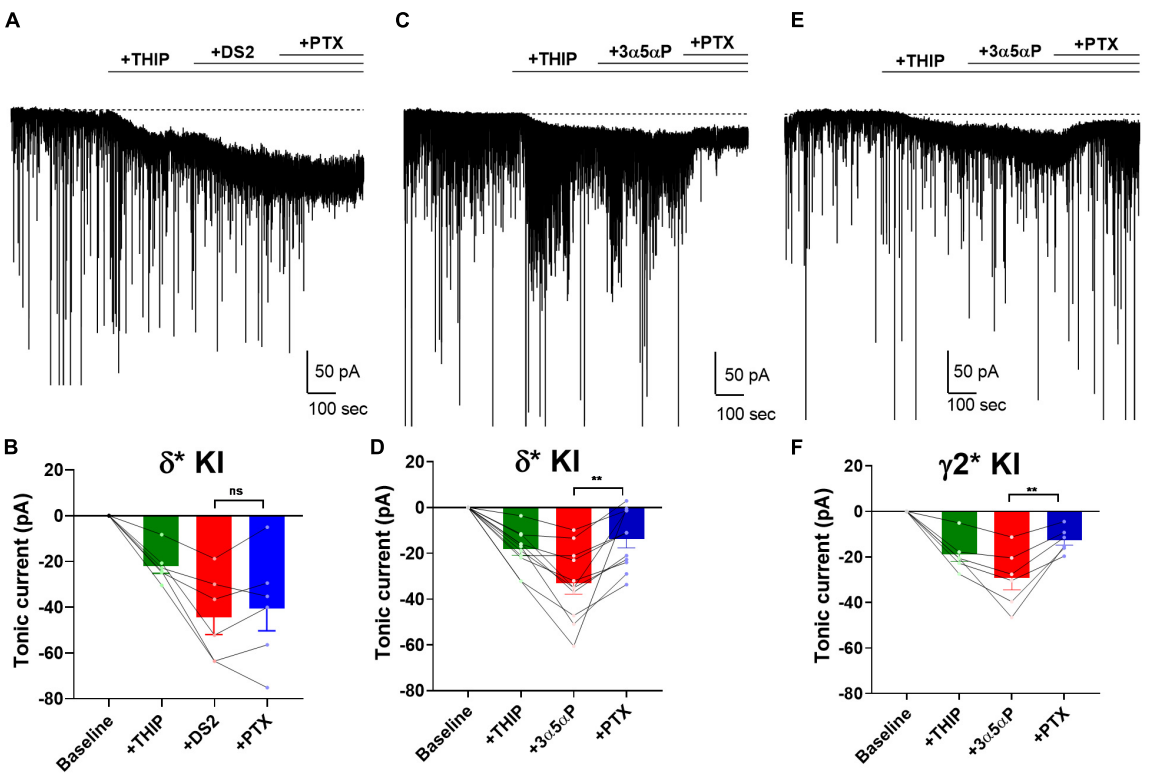


**FIGURE 5 |** 3α5αP potentiates THIP-generated current. **(A)** Effects of 1 μM THIP plus 10 μM DS2 in a representative DGC from a δ* KI slice. DS2 potentiated the THIP-evoked current, and this current was resistant to 50 μM PTX. **(B)** Summary of the current in the indicated conditions from cells of δ* KI animals ($n = 6$). Tonic current under THIP, THIP+DS2, and THIP+DS2+PTX was −21.9 ± 3.0 pA, −44.1 ± 7.6 pA, and −40.2 ± 9.8 pA, respectively. **(C)** Effects of THIP/100 nM 3α5αP in a representative DGC from a δ* KI slice. 3α5αP potentiated the THIP-generated current, but this current was partially blocked by PTX. **(D)** Summary of the THIP/3α5αP current in δ* KI DGCs ($n = 11$). Tonic current under THIP, THIP+3α5αP, and THIP+3α5αP+PTX was -18.4 ± 2.6 pA, −33.2 ± 4.8 pA, and -13.9 ± 3.9 pA, respectively. **(E,F)** Same experiment from γ2* KI DGCs ($n = 6$). Tonic current under THIP, THIP+3α5αP, and THIP+3α5αP+PTX was -19.1 ± 3.1 pA, −29.3 ± 5.2 pA, and -12.7 ± 2.2 pA, respectively. Note that the GABA/3α5αP current was also partially blocked by PTX, while the phasic currents were mostly left intact. One-way ANOVA on tonic current showed a drug effect in δ* KI THIP/DS2 ($F(1.3,6.4) = 18.5$, $p = 3 \times 10^{-3}$), δ* KI THIP/3α5αP ($F(2.3,22.7) = 25.1$, $p < 1 \times 10^{-4}$), and γ2* KI THIP/3α5αP ($F(1.5,7.4) = 25.7$, $p = 7 \times 10^{-4}$). PTX did not change the THIP/DS2 tonic current in δ* KI (Holm-Sidak, $p = 0.4$), however PTX significantly decreased THIP/3α5αP generated tonic current in both δ* KI (Holm-Sidak, $p = 2 \times 10^{-3}$), and γ2* KI (Holm-Sidak, $p = 7 \times 10^{-3}$).

Measures of SD were clearer and showed minimal effect of gabazine on fluctuations following PTX addition (**Figure 3E**) but reduced fluctuations in both δ* and γ2* backgrounds (**Figures 3J,O**). Taken together, the results demonstrate that in the absence of added agonist, both γ2 and δ receptors contribute to the effect of 3α5αP on tonic GABA currents.

## Potentiation of Tonic Inhibition by 3α5αP With Exogenous GABA

Perhaps the near absence of ambient GABA, suggested by the small effect of PTX in WT slices and gabazine in mutant slices (**Figure 3**), is not physiological and therefore does not invoke selectivity that might otherwise be generated by neurosteroids. To ensure that neurosteroids have the opportunity to interact with agonist-bound receptors, we applied 5 μM GABA to produce a tonic current of about 30 pA (**Figure 4**) (Lee and Maguire, 2014). Note that the actual GABA concentration reaching cells is likely much lower, as a result of avid GABA transport by neurons and glia (Nusser and Mody, 2002; Jensen et al., 2003; Zhan and Nadler, 2009). 100 nM 3α5αP increased the tonic current, and PTX fully blocked this current (**Figures 4A,B**). In δ* KI DGCs, GABA/3α5αP produced a current of similar amplitude to WT that was partially sensitive to PTX (**Figures 4C,D**). This suggests that the 3α5αP-potentiated tonic current is only partially mediated by δ receptors in DGCs and a substantial fraction is mediated by γ2 receptors. Also, in γ2* KI DGCs, GABA/3α5αP generated a similar amount of tonic current as WT and δ* KI. A one-way ANOVA showed no difference among genotypes ($F(2.0,14.0) = 0.1$, $p = 0.9$). sIPSCs persisted in PTX, again consistent with γ2 receptors as the main drivers of phasic inhibition. Interestingly, PTX did not fully block the tonic current in γ2* slices (**Figures 4E,F**). The complementary results from δ* and γ2* KI DGCs suggests that 3α5αP potentiates tonic current arising from both γ2 and δ receptors.

## Potentiation of Tonic Inhibition by 3α5αP and THDOC With Subunit-Selective Agonist

Surprisingly, our results showed that 3α5αP potentiated both δ and γ2 receptors to produce/potentiate tonic inhibition. To determine whether selectivity can be increased by activating receptors with a low concentration of δ-preferring agonist, we employed THIP as agonist. Previously, we showed that 1 μM THIP plus 10 μM DS2 potentiated tonic inhibition in DGCs, and this drug combination yielded a current mainly through δ receptors in DGCs (Sun et al., 2018). To evaluate the selectivity of 3α5αP on $GABA_A$ receptors when a δ-selective agonist is used, we co-applied THIP and 3α5αP to KI slices. As a positive control, we repeated our previous experiment using DS2, a positive allosteric modulator selective for δ receptors (Jensen et al., 2013). As expected, in δ* KI slices, the tonic current generated by THIP plus DS2 was resistant to PTX (**Figures 5A,B**). Although THIP/3α5αP resulted in a tonic current in δ* KI slices comparable in amplitude to the THIP plus DS2 current, this current was only partially inhibited by PTX, indicating a contribution from non-δ receptors (**Figures 5C,D**). THIP/3α5αP resulted in a similar tonic current in γ2* KI slices. Complementary to the result in δ* KI slices, this current was also partially blocked by PTX (**Figures 5E,F**).

To probe neurosteroid selectivity further, we employed another commonly used neurosteroid, THDOC. In WT slices, THDOC potentiated the THIP-generated tonic current, and this current was fully blocked by PTX (**Figures 6A,B**). Similar to THIP/3α5αP results, in δ* KI slices the THIP/THDOC tonic current was again only partially inhibited by PTX (**Figures 6C,D**), indicating the partial contribution of δ receptors to the tonic inhibition. Taken together, our results show that in contrast to DS2, either 3α5αP or THDOC co-applied with THIP acts on both δ and γ2 receptors to potentiate tonic currents.

## Lack of Potentiation of Tonic Inhibition by Ethanol

Ethanol has been shown to potentiate $GABA_A$ receptors by enhancing a tonic current through δ receptors (Wallner et al., 2003; Wei et al., 2004; Olsen et al., 2007). However, other studies suggest that ethanol has no effect on $GABA_A$ currents, or that potentiation may simply depend on ambient GABA concentration (Borghese et al., 2006; Yamashita et al., 2006;

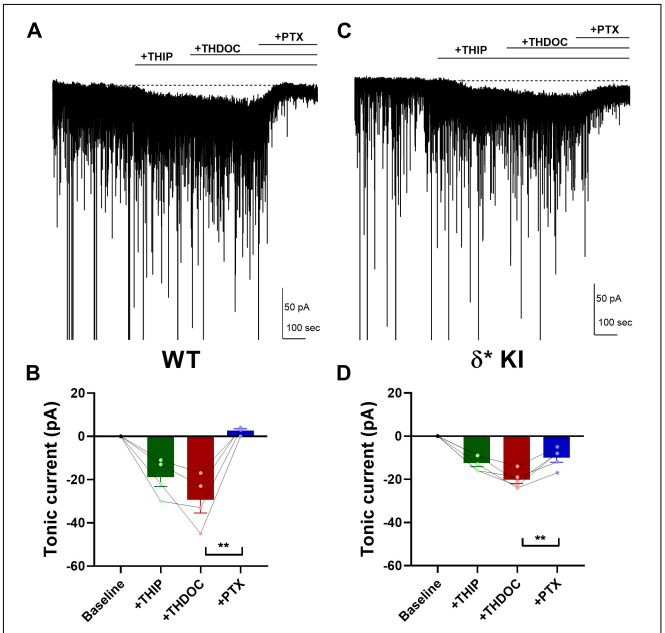


**FIGURE 6 |** THDOC potentiates THIP-produced current. **(A)** Effect of 100 nM THDOC in a representative DGC from a WT slice. THDOC potentiated the THIP (1 μM) generated current, which was blocked by 50 μM PTX. **(B)** Summary of the current in the indicated conditions from WT DGCs ($n = 4$). Tonic current under THIP, THIP+THDOC, and THIP+THDOC+PTX was -19.0 ± 4.4 pA, −29.5 ± 6.1 pA, and 2.5 ± 0.9 pA, respectively. **(C,D)** Same experiment from δ* KI DGCs ($n = 5$). Note that the THIP/THDOC current was partially blocked by PTX. Tonic current under THIP, THIP+THDOC, and THIP+THDOC+PTX was -12.6 ± 1.6 pA, −20.2 ± 1.8 pA, and -10.0 ± 2.1 pA, respectively. One-way ANOVA on tonic current showed a drug effect in WT ($F(1.6,4.8) = 22.9$, $p = 4 \times 10^{-3}$), and δ* KI ($F(2.7,10.6) = 42.9$, $p < 1 \times 10^{-4}$). PTX significantly decreased THIP/THDOC tonic current in WT (Holm-Sidak, $p = 0.01$) and δ* KI (Holm-Sidak, $p = 3 \times 10^{-3}$).

Fleming et al., 2011). Thus, it remains unclear and controversial whether ethanol directly targets $GABA_A$ receptors. To investigate the effects of ethanol on $GABA_A$ receptors, we applied 50 mM ethanol with 5 μM GABA to hippocampal DGCs. Despite robust GABA-generated currents (**Figures 7A–F**), ethanol failed to potentiate the current in any of the three genotypes (**Figures 7B,D,F**). Our results show that in contrast to 3α5αP, ethanol does not target $GABA_A$ receptors responsible for GABA-generated tonic current in DGGs under these conditions.

## Potentiation of Tonic Inhibition by Pentobarbital With Exogenous GABA

We previously found that δ receptors do not contribute much to the overall current generated by a saturating GABA concentration and maximum δ receptor current was only 10–15% that of total current in DGCs (Sun et al., 2018). This difference in maximum contribution could mask δ receptor selectivity of neurosteroids. To address this possibility, we tested the PTX sensitivity of pentobarbital (Pbt), a broad-spectrum positive allosteric modulator, at a concentration chosen to mimic 100 nM 3α5αP on tonic current in the three genotypes. We found that 10 μM Pbt produced quantitatively similar sIPSC prolongation and increased tonic current to a similar degree as 100 nM 3α5αP (**Figures 8A,B**). In WT slices, 10 μM Pbt produced near 30 pA tonic current with exogenous GABA (**Figure 8C**), which is comparable to the GABA/3α5αP tonic current (**Figures 4A,B**). The GABA/Pbt tonic current was fully inhibited by PTX (**Figure 8C**), indicating that the entirety of the Pbt effect is mediated by $GABA_A$ receptors. Importantly, in δ* KI slices, the GABA/Pbt generated tonic current was only partially blocked by PTX (**Figure 8D**), to a very similar degree as 3α5αP potentiated current (**Figures 4C,D**). Thus, we conclude that 3α5αP exhibits no more selectivity than the broad spectrum positive modulator, Pbt at an equivalent concentration.

# DISCUSSION

In this study, we used subunits engineered to resist PTX antagonism to revisit the selectivity of neurosteroids on δ $GABA_A$ receptors in mouse hippocampal DGCs. Our approach allowed us to measure pharmacological actions on different receptor populations in the same cell. First, we verified that 3α5αP potentiated phasic inhibition of $GABA_A$ receptors mainly through γ2 receptors, although we recently showed a δ receptor component to IPSCs (Sun et al., 2018). Second, we showed that 3α5αP augmented tonic inhibition with or without exogenous GABA through both δ and γ2 $GABA_A$ receptors. Third, our results showed that even with the subunit-selective agonist THIP, both 3α5αP and THDOC acted non-selectively at δ and γ2 receptor populations. Finally, the quantitatively similar effect of Pbt on PTX-resistant receptors mediating tonic

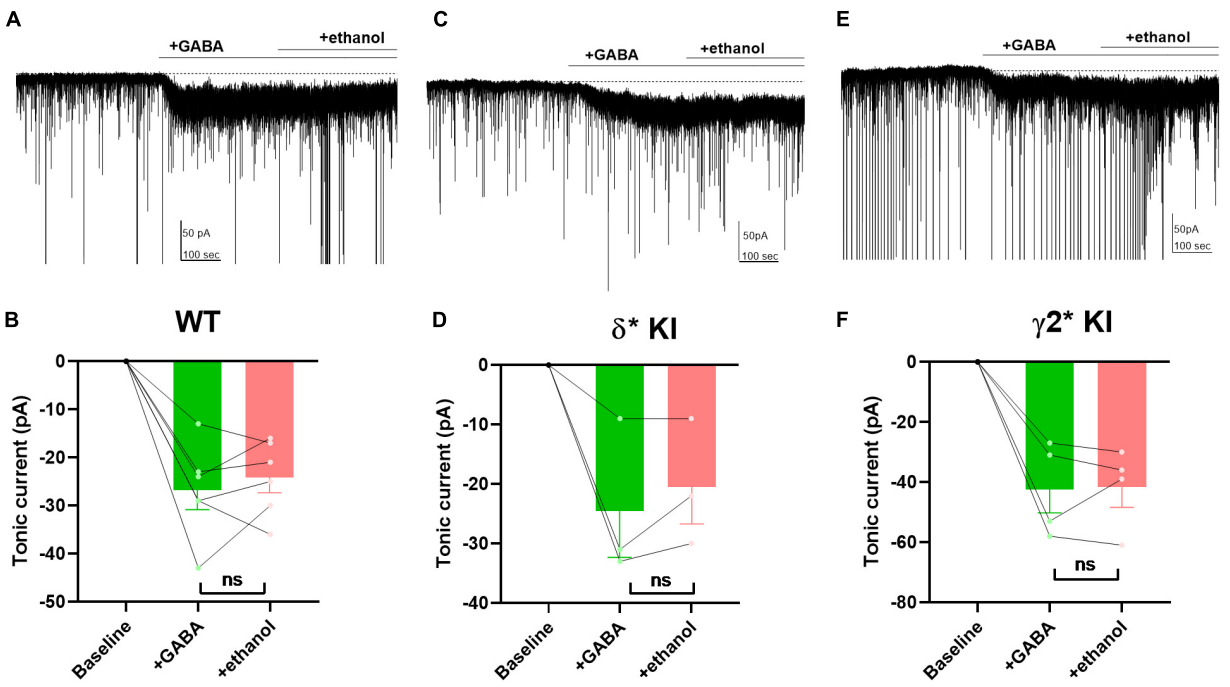


**FIGURE 7 |** Lack of potentiation of tonic current by ethanol. **(A)** Effects of 50 mM ethanol after 5 μM GABA in a representative DGC from a WT slice. GABA activated a current superimposed on ongoing spontaneous phasic sIPSCs. Ethanol did not potentiate the tonic current. **(B)** Summary of the GABA/ethanol current in the indicated conditions from cells of WT animals. Tonic current activated by GABA and GABA+ethanol was −26.8 ± 4.0 pA and −24.2 ± 3.2, respectively. **(C,D)** Same experiment from δ* KI animals. Tonic current generated by GABA and GABA+ethanol was −24.3 ± 7.7 pA and −20.3 ± 6.1 pA, respectively. **(E,F)** Same experiment from γ2* KI animals. Tonic current produced by GABA and GABA+ethanol was −42.3 ± 7.8 pA and −41.5 ± 6.8 pA, respectively. Paired *t* test showed no difference of the tonic currents between GABA and ethanol in WT ($n = 6$, $p = 0.4$), δ* KI ($n = 3$, $p = 0.3$), and γ2* ($n = 4$, $p = 0.9$).

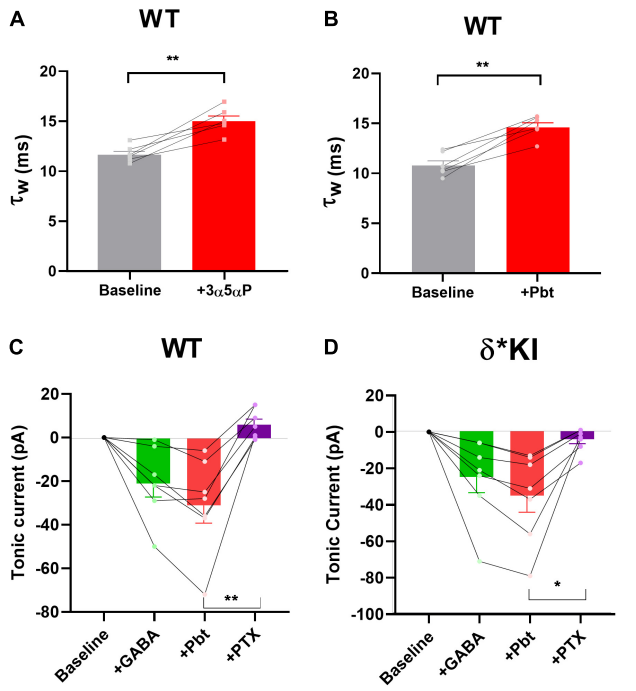


**FIGURE 8 |** Pbt potentiates tonic current with exogenous GABA. **(A)** Replot of the effect of 100 nM 3α5αP on $\tau_w$ of sIPSCs (from **Figure 1B**) for comparison with Pbt effects. **(B)** 10 μM Pbt increased the $\tau_w$ of sIPSC decay in WT DGCs from 10.0 ± 0.5 ms to 14.7 ± 0.5 ms ($n$ = 7). **(C)** Summary of GABA/Pbt generated current in indicated conditions in WT DGCs ($n$ = 7). Tonic current under GABA, GABA+Pbt, and GABA+Pbt+50 μM PTX was −20.7 ± 6.2 pA, −30.7 ± 8.3 pA, and 6.3 ± 2.6 pA, respectively. **(D)** Summary of GABA/Pbt generated tonic current in indicated conditions in δ* KI DGCs ($n$ = 7). Tonic current under GABA, GABA+Pbt, and GABA+Pbt+PTX was −25.3 ± 8.6 pA, −35.4 ± 9.3 pA, and −4.4 ± 2.4 pA, respectively. Pbt prolonged the decay of sIPSC (paired $t$ test, $p = 1 \times 10^{-3}$). One-way ANOVA on tonic current showed a drug effect in WT ($F(1.6,4.8) = 22.9$, $p = 4 \times 10^{-3}$), and δ* KI ($F(2.7,10.6) = 42.9$, $p < 1 \times 10^{-4}$). PTX significantly decreased GABA/Pbt current in WT (Holm-Sidak, $p = 2 \times 10^{-3}$) and δ* KI (Holm-Sidak, $p = 0.01$).

current emphasizes the broad spectrum nature of neurosteroid potentiation. Overall, using a sensitive methodology, our results revise a prevalent view of neurosteroid selectivity on δ $GABA_A$ receptors and reveal the broad spectrum nature of neurosteroid-augmented tonic inhibition. Our results indicate that the psychotropic actions of neurosteroids are unlikely to arise from selectivity at δ $GABA_A$ receptors, although we do not exclude psychotherapeutic effects via extrasynaptic receptors.

In this study, we used mice with PTX resistance in either δ or γ2 $GABA_A$ receptors. Mice were generated with a knock-in/chemogenetic approach described in our earlier work (Sun et al., 2018). The advantage of our approach is that we are able to investigate the selectivity of neurosteroids within the same cell, and there is less opportunity than with genetic deletions for compensation or other secondary effects to influence results. A caveat is that the γ2 mutation leads to faster IPSCs (Sun et al., 2018) (**Figures 1E,F**). Nevertheless, the complementary results obtained from the two mutant lines help mitigate the possibility that changes secondary to the T6'Y mutation account for results. Both mutant mouse lines showed similar response as WT to GABA and neurosteroid application throughout our experiments (**Figures 3–8**). Thus it is unlikely that the non-selectivity of neurosteroids results from different pharmacological profiles caused by the mutations. We cannot entirely exclude the possibility that PTX sensitivity is different in the presence of neurosteroid compared with agonist alone, and that this sensitivity changes with the induced mutations. However, previous results have shown that positive allosteric modulators gate currents entirely sensitive to PTX (Thompson et al., 1996).

Because the focus of our study was pharmacological actions of neurosteroids, we did not revisit the receptor source of endogenous tonic current in the absence of neurosteroid. In fact, in our hands the DGC standing current is very small (present study) or undetectable (Sun et al., 2018). In principle, the modest contribution of δ receptors to 3α5αP potentiation of tonic current could reflect recruitment of γ2 receptors that are silent in the presence of ambient GABA alone. Alternatively, the lack of selectivity could represent amplification of both receptor types already activated by ambient GABA. Past evidence favors the idea that γ2 receptors, perhaps those coupled with α5, may mediate some tonic current in DGCs and other cell types (Glykys et al., 2008; Kasugai et al., 2010; Patel et al., 2016).

Neurosteroids potentiate the actions of ambient GABA at low modulator concentration but directly gate the channel at somewhat higher concentration (Callachan et al., 1987; Cottrell et al., 1987; Puia et al., 1990; Shu et al., 2004). Because some cells showed no evidence of measurable ambient GABA current (**Figure 3**), we cannot exclude the possibility that direct gating in the absence of GABA explains current generated by γ2 receptors in some cells (Shu et al., 2004). As noted above, however, it may be more likely that 3α5αP increased the effectiveness of very low concentrations of GABA present, which are ineffective at baseline. Despite the presence of a non-saturating δ-preferring THIP concentration in **Figure 5**, the effect on γ2 appears to dominate. This seems surprising, as 3α5αP will increase agonist potency at both receptor classes. The balance of effects may be explained by the comparatively large number of γ2 receptors. Nevertheless, the discrepancy between the lack of neurosteroid selectivity and the high degree of DS2 selectivity is striking (**Figure 5**).

Our motivation was mainly to understand recent therapeutic, pharmacological effects of neurosteroid administration (Gunduz-Bruce et al., 2019). 3α5αP is also an endogenous neurosteroid that may contribute to ongoing inhibitory tone. Estimates of endogenous concentrations vary, but non-pregnancy neurosteroid levels likely reach 30–70 nM in humans (Bixo et al., 1997). We cannot exclude the possibility that these concentrations of neurosteroid contributed to the "baseline" IPSC and tonic-current profiles in our studies.

Our data indicate that the steroid-generated current was mediated approximately equally by δ receptors and γ2 receptors. Our previous results suggest that at saturating GABA concentrations, δ receptor current in DGCs is only 10–15% of total current (Sun et al., 2018). Thus, 50% contribution to neurosteroid-generated tonic current could reflect preference for δ receptors. However, because Pbt quantitatively mimicked

the effect of steroids, we propose that the outsized effect of neurosteroid on δ receptors is likely the result of the higher GABA affinity of δ receptors compared with γ2 receptors rather than true selectivity of δ receptors for neurosteroid or Pbt (Brown et al., 2002; Wohlfarth et al., 2002). The low ambient GABA concentration will preferentially recruit δ receptors, and active receptors are more strongly affected by the positive allosteric effects of the steroid (Brown et al., 2002; Wohlfarth et al., 2002).

Although we found that 100 nM 3α5αP was necessary to reliably potentiate both phasic and tonic inhibition (**Figures 1–3**), a previous study showed that as little as 10 nM THDOC generated selective δ receptor effects, with higher concentrations exhibiting less selectivity (Stell et al., 2003). However, another study showed δ selectivity of 3α5αP up to 1 μM (Carver and Reddy, 2016), and still another found increased selectivity of δ receptor effects up to 10 μM of the synthetic neurosteroid alphaxalone (Spigelman et al., 2003). Thus, selectivity has been observed over a wide range of concentrations. Behavioral results have suggested that anesthetic and anxiolytic effects of neurosteroids are reduced in δ-deficient animals (Mihalek et al., 1999). By contrast with these studies, our results, using a different approach, support the idea that at moderate concentrations, neurosteroids do not preferentially target δ receptors.

Neurosteroids and ethanol share a proposed direct link, which was the motivation for us to examine ethanol as a $GABA_A$ receptor modulator. $GABA_A$ δ receptors may act as a sensor of low concentrations of ethanol (Wallner et al., 2003; Wei et al., 2004; Olsen et al., 2007), and at least some of ethanol's effects on $GABA_A$ receptors are proposed to occur through altered neurosteroid synthesis (Sanna et al., 2004; Tokuda et al., 2011), offering an explanation for δ selectivity. Although some results have disputed the δ selectivity of ethanol (Borghese et al., 2006; Yamashita et al., 2006; Fleming et al., 2011), we hypothesized that δ* and γ2* mice would provide new tools to revisit this issue. Our results failed to reveal significant potentiation of $GABA_A$ mediated tonic current in DGCs, so at least in this cell type under our conditions, the results do not allow us to comment on the selectivity of ethanol or on ethanol-induced steroidogenesis for δ receptors.

In summary, we have used genetic, pharmacological, and electrophysiological approaches to investigate the selectivity of neurosteroids on $GABA_A$ receptors. The sensitivity of our approach supports a broad spectrum action of neurosteroids. Recently, 3α5αP and another neuroactive steroid, SGE-217, have been shown to have antidepressant effects (Kanes et al., 2017; Gunduz-Bruce et al., 2019) and 3α5αP (brexanolone) was approved for treatment of postpartum depression by the Food and Drug Administration. Our work here suggests that δ selectivity is unlikely to underlie the benefit. Other targets for neurosteroids likely remain to be discovered that differ from other $GABA_A$ receptor modulators, such as barbiturates and benzodiazepines, to account for antidepressant benefit.

## DATA AVAILABILITY STATEMENT

The datasets generated for this study are available on request to the corresponding author.

## ETHICS STATEMENT

The animal study was reviewed and approved by the Washington University IACUC (Institutional Animal Care and Use Committee) Committee.

## AUTHOR CONTRIBUTIONS

XL, SM, and CZ contributed to the conception and design of the experiments, revised the manuscript critically for intellectual content, and approved it for submission. XL performed experiments and wrote the first draft of the manuscript.

## FUNDING

This work was supported by MH111461, MH114866, and AA026753.

## REFERENCES

Anderson, C. R., and Stevens, C. F. (1973). Voltage clamp analysis of acetylcholine produced end-plate current fluctuations at frog neuromuscular junction. *J. Physiol.* 235, 655–691. doi: 10.1113/jphysiol.1973.sp010410

Bixo, M., Andersson, A., Winblad, B., Purdy, R. H., and Bäckström, T. (1997). Progesterone, 5α-pregnane-3,20-dione and 3α-hydroxy-5α-pregnane-20-one in specific regions of the human female brain in different endocrine states. *Brain Res.* 764, 173–178. doi: 10.1016/S0006-8993(97)00455-451

Borghese, C. M., Stórustovu, S. Í, Ebert, B., Herd, M. B., Belelli, D., Lambert, J. J., et al. (2006). The δ subunit of γ-Aminobutyric acid type a receptors does not confer sensitivity to low concentrations of ethanol. *J. Pharmacol. Exp. Ther.* 316, 1360–1368. doi: 10.1124/jpet.105.092452

Brickley, S. G., and Mody, I. (2012). Extrasynaptic GABAA receptors: their function in the CNS and implications for disease. *Neuron* 73, 23–34. doi: 10.1016/j.neuron.2011.12.012

Brown, N., Kerby, J., Bonnert, T. P., Whiting, P. J., and Wafford, K. A. (2002). Pharmacological characterization of a novel cell line expressing human α4β3δ GABAA receptors. *Br. J. Pharmacol.* 136, 965–974. doi: 10.1038/sj.bjp.0704795

Callachan, H., Cottrell, G. A., Hather, N. Y., Lambert, J. J., Nooney, J. M., and Peters, J. A. (1987). Modulation of the GABA(A) receptor by progesterone metabolites. *Proc. R. Soc. Lond. Biol. Sci.* 231, 359–369. doi: 10.1098/rspb.1987.0049

Carver, C. M., and Reddy, D. S. (2016). Neurosteroid structure-activity relationships for functional activation of extrasynaptic GABAA receptors. *J. Pharmacol. Exp. Ther.* 357, 188–204. doi: 10.1124/jpet.115.229302

Cottrell, G. A., Lambert, J. J., and Peters, J. A. (1987). Modulation of GABAA receptor activity by alphaxalone. *Br. J. Pharmacol.* 90, 491–500. doi: 10.1111/j.1476-5381.1987.tb11198.x

Farrant, M., and Nusser, Z. (2005). Variations on an inhibitory theme: phasic and tonic activation of GABAA receptors. *Nat. Rev. Neurosci.* 6, 215–229. doi: 10.1038/nrn1625

Fleming, R. L., Acheson, S. K., Moore, S. D., Wilson, W. A., and Swartzwelder, H. S. (2011). GABA Transport modulates the ethanol sensitivity of

tonic inhibition in the rat dentate gyrus. *Alcoholism* 45, 577–583. doi: 10.1016/j.alcohol.2011.03.003

Glykys, J., Mann, E. O., and Mody, I. (2008). Which GABAA receptor subunits are necessary for tonic inhibition in the hippocampus? *J. Neurosci.* 28, 1421–1426. doi: 10.1523/JNEUROSCI.4751-07.2008

Gunduz-Bruce, H., Silber, C., Kaul, I., Rothschild, A. J., Riesenberg, R., Sankoh, A. J., et al. (2019). Trial of SAGE-217 in patients with major depressive disorder. *N. Engl. J. Med.* 381, 903–911. doi: 10.1056/nejmoa1815981

Gunther, U., Benson, J., Benke, D., Fritschy, J. M., Reyes, G., Knoflach, F., et al. (1995). Benzodiazepine-insensitive mice generated by targeted disruption of the γ2 subunit gene of γ-aminobutyric acid type a receptors. *Proc. Natl. Acad. Sci. U.S.A.* 92, 7749–7753. doi: 10.1073/pnas.92.17.7749

Gurley, D., Amin, J., Ross, P. C., Weiss, D. S., and White, G. (1995). Point mutations in the M2 region of the α, β, or γ subunit of the GABA(A) channel that abolish block by picrotoxin. *Recept. Channels* 3, 13–20.

Izumi, Y., O'Dell, K. A., and Zorumski, C. F. (2015). Corticosterone enhances the potency of ethanol against hippocampal long-term potentiation via local neurosteroid synthesis. *Front. Cell. Neurosci.* 9:254. doi: 10.3389/fncel.2015.00254

Jensen, K., Chiu, C. S., Sokolova, I., Lester, H. A., and Mody, I. (2003). GABA transporter-1 (GAT1)-deficient mice: differential tonic activation of GABAA versus GABAB receptors in the hippocampus. *J. Neurophysiol.* 90, 2690–2701. doi: 10.1152/jn.00240.2003

Jensen, M. L., Wafford, K. A., Brown, A. R., Belelli, D., Lambert, J. J., and Mirza, N. R. (2013). A study of subunit selectivity, mechanism and site of action of the delta selective compound 2 (DS2) at human recombinant and rodent native GABAA receptors. *Br. J. Pharmacol.* 168, 1118–1132. doi: 10.1111/bph.12001

Kanes, S., Colquhoun, H., Gunduz-Bruce, H., Raines, S., Arnold, R., Schacterle, A., et al. (2017). Brexanolone (SAGE-547 injection) in post-partum depression: a randomised controlled trial. *Lancet* 390, 480–489. doi: 10.1016/S0140-6736(17)31264-31263

Kasugai, Y., Swinny, J. D., Roberts, J. D. B., Dalezios, Y., Fukazawa, Y., Sieghart, W., et al. (2010). Quantitative localisation of synaptic and extrasynaptic GABAA receptor subunits on hippocampal pyramidal cells by freeze-fracture replica immunolabelling. *Eur. J. Neurosci.* 32, 1868–1888. doi: 10.1111/j.1460-9568.2010.07473.x

Korpi, E. R., Mihalek, R. M., Sinkkonen, S. T., Hauer, B., Hevers, W., Homanics, G. E., et al. (2002). Altered receptor subtypes in the forebrain of GABA(A) receptor delta subunit-deficient mice: recruitment of gamma 2 subunits. *Neuroscience* 109, 733–743. doi: 10.1016/s0306-4522(01)00527-529

Lee, V., and Maguire, J. (2014). The impact of tonic GABAA receptor-mediated inhibition on neuronal excitability varies across brain region and cell type. *Front. Neural. Circuits* 8:3. doi: 10.3389/fncir.2014.00003

Lingle, C. J. (2006). Empirical considerations regarding the use of ensemble-variance analysis of macroscopic currents. *J. Neurosci. Methods* 158, 121–132. doi: 10.1016/j.jneumeth.2006.05.027

Masiulis, S., Desai, R., Uchański, T., Serna Martin, I., Laverty, D., Karia, D., et al. (2019). GABAA receptor signalling mechanisms revealed by structural pharmacology. *Nature* 565, 454–459. doi: 10.1038/s41586-018-0832-835

Mihalek, R. M., Banerjee, P. K., Korpi, E. R., Quinlan, J. J., Firestone, L. L., Mi, Z. P., et al. (1999). Attenuated sensitivity to neuroactive steroids in γ-aminobutyrate type a receptor delta subunit knockout mice. *Proc. Natl. Acad. Sci. U.S.A.* 96, 12905–12910. doi: 10.1073/pnas.96.22.12905

Möhler, H. (2006). GABAA receptor diversity and pharmacology. *Cell Tissue Res.* 326, 505–516. doi: 10.1007/s00441-006-0284-283

Möhler, H. (2011). The rise of a new GABA pharmacology. *Neuropharmacology* 60, 1042–1049. doi: 10.1016/j.neuropharm.2010.10.020

Nusser, Z., and Mody, I. (2002). Selective modulation of tonic and phasic inhibitions in dentate gyrus granule cells. *J. Neurophysiol.* 87, 2624–2628. doi: 10.1152/jn.2002.87.5.2624

Olsen, R. W. (2018). GABAA receptor: positive and negative allosteric modulators. *Neuropharmacology* 136, 10–22. doi: 10.1016/j.neuropharm.2018.01.036

Olsen, R. W., Hanchar, H. J., Meera, P., and Wallner, M. (2007). GABAA receptor subtypes: the "one glass of wine". *Receptors. Alcohol.* 41, 201–209. doi: 10.1016/J.ALCOHOL.2007.04.006

Orser, B. A. (2006). Extrasynaptic GABAA receptors are critical targets for sedative-hypnotic drugs. *J. Clin. Sleep Med.* 2, S12–S18.

Patel, B., Bright, D. P., Mortensen, M., Frølund, B., and Smart, T. G. (2016). Context-dependent modulation of GABAAR-mediated tonic currents. *J. Neurosci.* 36, 607–621. doi: 10.1523/JNEUROSCI.2047-15.2016

Peng, Z., Hauer, B., Mihalek, R. M., Homanics, G. E., Sieghart, W., Olsen, R. W., et al. (2002). GABA(A) receptor changes in delta subunit-deficient mice: altered expression of Alpha4 and Gamma2 subunits in the forebrain. *J. Comp. Neurol.* 446, 179–197. doi: 10.1002/cne.10210

Pirker, S., Schwarzer, C., Wieselthaler, A., Sieghart, W., and Sperk, G. (2000). GABA(A) receptors: immunocytochemical distribution of 13 subunits in the adult rat brain. *Neuroscience* 101, 815–850. doi: 10.1016/S0306-4522(00)00442-445

Pritchett, D. B., Sontheimer, H., Shivers, B. D., Ymer, S., Kettenmann, H., Schofield, P. R., et al. (1989). Importance of a novel GABAA receptor subunit for benzodiazepine pharmacology. *Nature* 338, 582–585. doi: 10.1038/338582a0

Puia, G., Santi, M. R., Vicini, S., Pritchett, D. B., Purdy, R. H., Paul, S. M., et al. (1990). Neurosteroids act on recombinant human GABAA receptors. *Neuron* 4, 759–765. doi: 10.1016/0896-6273(90)90202-Q

Reddy, D. S. (2018). Gabaa receptors mediate tonic inhibition and neurosteroid sensitivity in the brain. *Vitam. Horm.* 107, 177–191. doi: 10.1016/bs.vh.2017.12.001

Sanna, E., Talani, G., Busonero, F., Pisu, M. G., Purdy, R. H., Serra, M., et al. (2004). Brain steroidogenesis mediates ethanol modulation of GABAA receptor activity in rat hippocampus. *J. Neurosci.* 24, 6521–6530. doi: 10.1523/JNEUROSCI.0075-04.2004

Sedelnikova, A., Erkkila, B. E., Harris, H., Zakharkin, S. O., and Weiss, D. S. (2006). Stoichiometry of a pore mutation that abolishes picrotoxin-mediated antagonism of the GABAA receptor. *J. Physiol.* 577, 569–577. doi: 10.1113/jphysiol.2006.120287

Shu, H. J., Bracamontes, J., Taylor, A., Wu, K., Eaton, M. M., Akk, G., et al. (2012). Characteristics of concatemeric GABAA receptors containing α4/δ subunits expressed in xenopus oocytes. *Br. J. Pharmacol.* 165, 2228–2243. doi: 10.1111/j.1476-5381.2011.01690.x

Shu, H.-J., Eisenman, L. N., Jinadasa, D., Covey, D. F., Zorumski, C. F., and Mennerick, S. (2004). Slow actions of neuroactive steroids at GABAA receptors. *J. Neurosci.* 24, 6667–6675. doi: 10.1523/JNEUROSCI.1399-04.2004

Sigel, E., and Steinmann, M. E. (2012). Structure, function, and modulation of GABAA Receptors. *J. Biol. Chem.* 287, 40224–40231. doi: 10.1074/jbc.R112.386664

Spigelman, I., Li, Z., Liang, J., Cagetti, E., Samzadeh, S., Mihalek, R. M., et al. (2003). Reduced inhibition and sensitivity to neurosteroids in hippocampus of mice lacking the GABAA receptor δ subunit. *J. Neurophysiol.* 90, 903–910. doi: 10.1152/jn.01022.2002

Stell, B. M., Brickley, S. G., Tang, C. Y., Farrant, M., and Mody, I. (2003). Neuroactive steroids reduce neuronal excitability by selectively enhancing tonic inhibition mediated by subunit-containing GABAA receptors. *Proc. Natl. Acad. Sci. U.S.A.* 100, 14439–14444. doi: 10.1073/pnas.2435457100

Sun, M. Y., Shu, H. J., Benz, A., Bracamontes, J., Akk, G., Zorumski, C. F., et al. (2018). Chemogenetic isolation reveals synaptic contribution of δ GABAA receptors in mouse dentate granule neurons. *J. Neurosci.* 38, 8128–8145. doi: 10.1523/JNEUROSCI.0799-18.2018

Thompson, S. A., Whiting, P. J., and Wafford, K. A. (1996). Barbiturate interactions at the human GABAA receptor: dependence on receptor subunit combination. *Br. J. Pharmacol.* 117, 521–527. doi: 10.1111/j.1476-5381.1996.tb15221.x

Tokuda, K., Izumi, Y., and Zorumski, C. F. (2011). Ethanol enhances neurosteroidogenesis in hippocampal pyramidal neurons by paradoxical NMDA receptor activation. *J. Neurosci.* 31, 9905–9909. doi: 10.1523/JNEUROSCI.1660-11.2011

Wallner, M., Hanchar, H. J., and Olsen, R. W. (2003). Ethanol enhances α4β3δ and α6β3δ γ-aminobutyric acid type a receptors at low concentrations known to affect humans. *Proc. Natl. Acad. Sci. U. S. A.* 100, 15218–15223. doi: 10.1073/pnas.2435171100

Wei, W., Faria, L. C., and Mody, I. (2004). Low ethanol concentrations selectively augment the tonic inhibition mediated by δ subunit-containing GABAA receptors in hippocampal neurons. *J. Neurosci.* 24, 8379–8382. doi: 10.1523/JNEUROSCI.2040-04.2004

Wei, W., Zhang, N., Peng, Z., Houser, C. R., and Mody, I. (2003). Perisynaptic localization of delta subunit-containing GABA(A) receptors and their activation by GABA spillover in the mouse dentate gyrus. *J. Neurosci.* 23, 10650–10661. doi: 10.1523/JNEUROSCI.23-33-10650.2003

Whissell, P. D., Lecker, I., Wang, D. S., Yu, J., and Orser, B. A. (2015). Altered expression of δGABAA receptors in health and disease. *Neuropharmacology* 88, 24–35. doi: 10.1016/j.neuropharm.2014.08.003

Wohlfarth, K. M., Bianchi, M. T., and Macdonald, R. L. (2002). Enhanced neurosteroid potentiation of ternary GABAA receptors containing the δ subunit. *J. Neurosci.* 22, 1541–1549. doi: 10.1523/JNEUROSCI.22-05-01541.2002

Yamashita, M., Marszalec, W., Yeh, J. Z., and Narahashi, T. (2006). Effects of ethanol on tonic GABA currents in cerebellar granule cells and mammalian cells recombinantly expressing GABAA receptors. *J. Pharmacol. Exp. Ther.* 319, 431–438. doi: 10.1124/jpet.106.106260

Zhan, R. Z., and Nadler, J. V. (2009). Enhanced tonic GABA current in normotopic and hilar ectopic dentate granule cells after pilocarpine-induced status epilepticus. *J. Neurophysiol.* 102, 670–681. doi: 10.1152/jn.00147.2009

**Conflict of Interest:** CZ is a member of the Scientific Advisory Board of Sage Therapeutics. Sage Therapeutics had no role in the design of execution of these studies.

The remaining authors declare that the research was conducted in the absence of any commercial or financial relationships that could be construed as a potential conflict of interest.

*Copyright © 2020 Lu, Zorumski and Mennerick. This is an open-access article distributed under the terms of the Creative Commons Attribution License (CC BY). The use, distribution or reproduction in other forums is permitted, provided the original author(s) and the copyright owner(s) are credited and that the original publication in this journal is cited, in accordance with accepted academic practice. No use, distribution or reproduction is permitted which does not comply with these terms.*

frontiers in Molecular Neuroscience

ORIGINAL RESEARCH
published: 18 March 2020
doi: 10.3389/fnmol.2020.00040

# Characterization of Oxytocin Receptor Expression Within Various Neuronal Populations of the Mouse Dorsal Hippocampus

*W. Scott Young* and June Song*

*Section on Neural Gene Expression, National Institute of Mental Health, National Institutes of Health, Bethesda, MD, United States*

Oxytocin, acting through the oxytocin receptor (Oxtr) in the periphery, is best known for its roles in regulating parturition and lactation. However, it is also now known to possess a number of important social functions within the central nervous system, including social preference, memory and aggression, that vary to different degrees in different species. The Oxtr is found in both excitatory and inhibitory neurons within the brain and research is focusing on how, for example, activation of the receptor in interneurons can enhance the signal-to-noise of neuronal transmission. It is important to understand which neurons in the mouse dorsal hippocampus might be activated during memory formation. Therefore, we examined the colocalization of transcripts in over 5,000 neurons for Oxtr with those for nine different markers often found in interneurons using hairpin chain reaction *in situ* hybridization on hippocampal sections. Most pyramidal cell neurons of CA2 and many in the CA3 express Oxtr. Outside of those excitatory neurons, over 90% of Oxtr-expressing neurons co-express glutamic acid decarboxylase-1 (Gad-1) with progressively decreasing numbers of co-expressing cholecystokinin, somatostatin, parvalbumin, neuronal nitric oxide synthase, the serotonin 3a receptor, the vesicular glutamate transporter 3, calbindin 2 (calretinin), and vasoactive intestinal polypeptide neurons. Distributions were analyzed within hippocampal layers and regions as well. These findings indicate that Oxtr activation will modulate the activity of ∼30% of the Gad-1 interneurons and the majority of the diverse population of those, mostly, interneuron types specifically examined in the mouse hippocampus.

**Keywords: cornu ammonis 2, hairpin chain reaction, glutamic acid decarboxylase, somatostatin, parvalbumin, calbindin, nitric oxide synthase, cholecystokinin**

OPEN ACCESS

***Edited by:***
*Lisa Topolnik, Laval University, Canada*

***Reviewed by:***
*Ludovic Tricoire, Université Pierre et Marie Curie, France*
*José Miguel Blasco Ibáñez, University of Valencia, Spain*

****Correspondence:***
*W. Scott Young*
*wsy@mail.nih.gov*

***Received:*** *17 December 2019*
***Accepted:*** *28 February 2020*
***Published:*** *18 March 2020*

***Citation:***
*Young WS and Song J (2020) Characterization of Oxytocin Receptor Expression Within Various Neuronal Populations of the Mouse Dorsal Hippocampus. Front. Mol. Neurosci. 13:40. doi: 10.3389/fnmol.2020.00040*

## INTRODUCTION

Oxytocin (Oxt) was originally found to regulate parturition (Dale, 1906) and lactation (Ott and Scott, 1910; Schafer and Mackenzie, 1911), acting through a single oxytocin receptor (Oxtr) in the uterus and breasts, respectively (Kimura et al., 1992). Beginning in the mid-1980's, it was discovered that the Oxtr is distributed heterogeneously in the central nervous system, including in the hippocampus (de Kloet et al., 1985; van Leeuwen et al., 1985). Shortly thereafter, intracerebroventricular administration of an Oxt antagonist was shown to inhibit social recognition

(Engelmann et al., 1998) that was confirmed by knockouts of the Oxt (Ferguson et al., 2000) and Oxtr (Takayanagi et al., 2005) genes. The role of Oxt in regulating social behaviors has been well-documented (Lee et al., 2009).

Conditional removal of the Oxtr from forebrain excitatory neurons, including pyramidal cells of the hippocampus, indicated that those receptors are necessary for intrastrain social recognition (Macbeth et al., 2009) and for reduction in freezing behavior during acquisition, as well as during context and cue retention (Pagani et al., 2011). More recently, more precisely targeted inactivation of the Oxtr in the hippocampus has been possible through the use of this floxed Oxtr line (Lee et al., 2008). For example, virally targeted expression of Cre recombinase to the hilar region of the dentate gyrus to eliminate the Oxtr there leads to reduced social discrimination as did elimination of Oxtr in the dorsal CA2 and immediately adjacent CA3 (Raam et al., 2017). Another study targeting those latter same neurons showed reduced long-term social memory (Lin et al., 2018). These results in the CA2 region are consistent with its role in social behavior (Wersinger et al., 2002; Young et al., 2006; Hitti and Siegelbaum, 2014; Pagani et al., 2014; Stevenson and Caldwell, 2014; Smith et al., 2016). A recent review delves into these and similar studies in further detail (Cilz et al., 2019).

Some of the Oxtr inactivation studies involved excitatory as well inhibitory neurons in the hippocampus [e.g., (Raam et al., 2017)]. Abnormalities in inhibitory neurons of the hippocampus have been seen in neuropsychiatric illnesses such as schizophrenia and bipolar depression (Benes et al., 1991, 1998; Benes and Berretta, 2001; Zhang et al., 2002) and Alzheimer's disease (Brady and Mufson, 1997). Therefore, the increasing interest in the roles of Oxt in modulating inhibitory interneuronal activity is especially warranted. And while the literature on the roles of interneurons in the hippocampus is extensive, there are a number of insights worth mentioning. Hippocampal interneurons are involved in generating various rhythms within the hippocampus (Gloveli et al., 2005; Korotkova et al., 2010; Stark et al., 2014). Interneurons also play a role in improving signal-to-noise and other fine-tuning of pyramidal neurons (Basu et al., 2013; Owen et al., 2013; Piskorowski and Chevaleyre, 2013). Activation of Oxtr augments GABAergic transmission throughout the different subfields of the hippocampus including the DG (Harden and Frazier, 2016), CA2 (Tirko et al., 2018), and CA1 (Zaninetti and Raggenbass, 2000; Owen et al., 2013; Maniezzi et al., 2019) regions. Specificity in Oxtr expression across interneuron subtypes is suggested by, for example, Oxtr depolarizing fast-spiking hippocampal CA1 interneurons in the pyramidal cell layer and statum oriens, but not regular-spiking interneurons there, to fine-tune feedforward inhibition (Owen et al., 2013). Further reviews are available [e.g., (Pelkey et al., 2017; Booker and Vida, 2018; Cilz et al., 2019)]. They discuss the extremely numerous types of interneurons in the hippocampus based on projections, intrahippocampal locations and gene expression patterns and their roles in hippocampal functions. To gain some appreciation of how and where Oxt is acting within the hippocampus, we chose nine markers found in various inhibitory neurons and studied their expression in relation to Oxtr expression.

# MATERIALS AND METHODS

## Animals

This study was conducted according to United States National Institutes of Health guidelines for animal research and housing and approved by the National Institute of Mental Health Animal Care and Use Committee. Two adult C57BL/6J mice (Jackson Laboratory, Bar Harbor, ME, USA), a female and a male, were used for colocalization of Oxtr with markers often expressed in interneurons (here abbreviated as INM). An additional male was used to examine INM expression within glutamic acid decarboxylase 1 (Gad-1) neurons and for the

**TABLE 1 |** Probe information.

| Name | Symbol* | Amplifier† | Accession no. | Probe pairs | Lot no. |
|---|---|---|---|---|---|
| Oxytocin receptor | Oxtr | B4 | NM_001081147.1 | 30 | PRA262 |
| Glutamic acid decarboxylase 1 | Gad-1 | B2 | NM_008077 | 20 | PRD099 |
| Parvalbumin | Parv | B3 | NM_001330686 | 16 | PRA211 |
| Somatostatin | Sst | B5 | NM_009215 | 11 | PRA354 |
| Cholecystokinin | Cck | B1 | NM_031161.4 | 11 | PRA355 |
| Vasoactive intestinal polypeptide | Vip | B3 | NM_001313969, NM_011702 | 20 | PRA356 |
| Vesicular glutamate transporter-3 (Slc17a8) | Vglut3 | B5 | AF510321.1 | 20 | PRA357 |
| Calbindin 2 (calretinin) | Calb2 | B1 | NM_007586.1 | 20 | PRA358 |
| 5-hydroxytryptamine receptor 3A | 5Htr3a | B5 | NM_013561.2 | 30 | PRA359 |
| Neuronal nitric oxide synthase (Nos1) | nNos | B5 | NM_008712.3 | 30 | PRA360 |
| Bcl2-related ovarian killer protein | Bok | B3 | NM_016778 | 20 | 2492/B231 |
| Transient receptor potential cation channel, subfamily C, member 4 | Trpc4 | B2 | NM_016984 | 20 | 2492/B239 |
| Adhesion molecule with Ig like domain 2 | Amigo2 | B5 | NM_178114.4 | 20 | PRD098 |

*Symbol used in this article.
† is the linker type on the probe to which the matched amplifiers anneal.

hippocampal CA-specific markers (Mori et al., 1998; Lein et al., 2005; Laeremans et al., 2013) transient receptor potential cation channel, subfamily C, member 4 (Trpc4, for CA1), adhesion molecule with Ig like domain 2 (Amigo2, for CA2) and Bcl2-related ovarian killer protein (Bok, for CA3) (**Table 1**).

## *In situ* Hybridization Using the Hairpin Chain Reaction Method

We used the Hairpin Chain Reaction (HCR) approach (Choi et al., 2018), with some modifications, in our mapping study to locate transcripts. This technique uses sets of probe pairs targeting a specific mRNA. The probe pair enables improved signal-to-noise as both members of the pair need to hybridize next to each other to initiate signal production by hairpin chain amplification (Choi et al., 2018). All pairs in each proprietary probe set are tagged with only one of the five specifically engineered amplifier recognition sites, B1–B5, enabling multiplex *in situ* hybridization histochemistry. The slide-mounted, fresh-frozen sections were fixed in 4% formaldehyde/PBS at room temperature (RT) for 5 min. Following fixation, sections were briefly washed in PBS at RT twice for 1 min each. Then the sections were incubated in a solution of acetic anhydride in triethanolamine, pH 8, for 10 min. The sections were first processed through a series of ethanol steps (70%, 1 min; 80%, 1 min; 95%, 2 min; 100%, 1 min) followed by CHCl3 for 5 min and then back through ethanol (100%, 1 min; 95%, 1 min). Then the sections were air-dried. Next, probes (at a working concentration of 4.0 nM) were added to a nucleic acid mix (100 μg/ml salmon sperm DNA, 250 μg/ml yeast total RNA, 250 μg/ml yeast tRNA; all Sigma-Aldrich), heated to 65°C for 5 min, and then cooled on ice for 5 min. This mixture was added to the hybridization buffer [50% formamide/600 mM NaCl/80 mM Tris-HCl, pH 7.5/4 mM EDTA/0.1% sodium

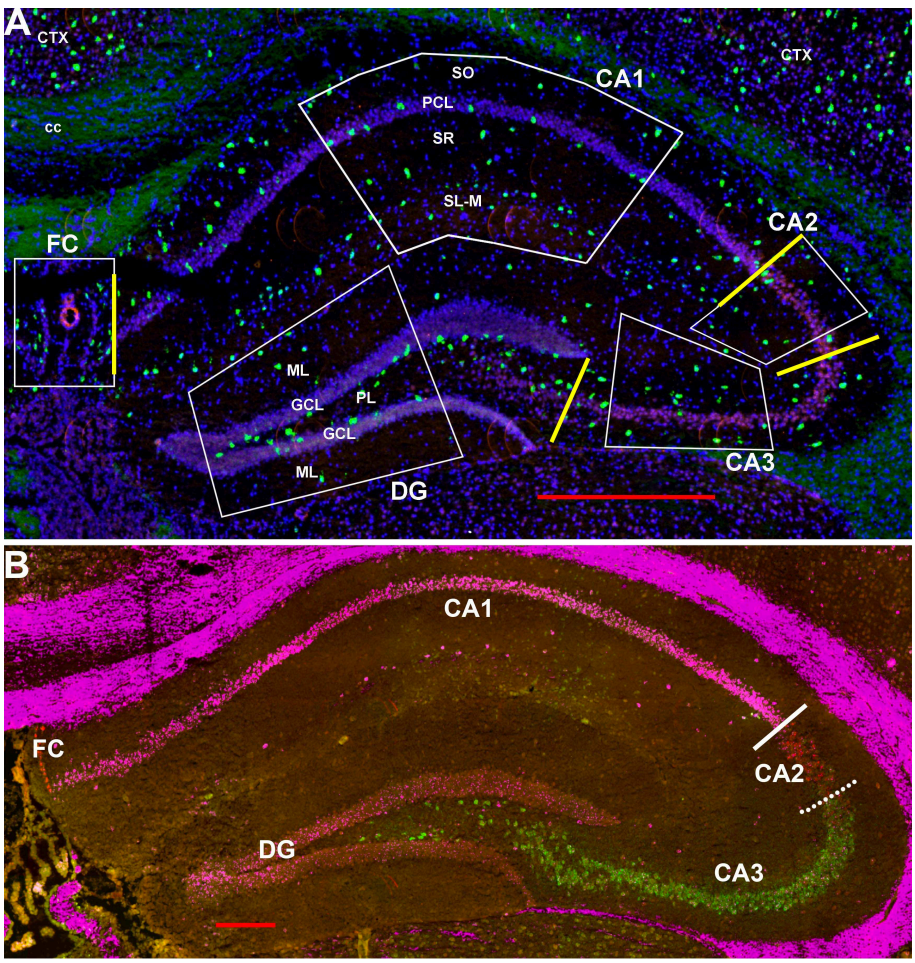


**FIGURE 1 | (A)** Representative areas in which interneurons were counted at 1.8 mm behind the bregma showing Gad-1 cells. CA1-4, cornu ammonis 1–4 regions; cc, corpus callosum; Ctx, neocortex; DF, dentate gyrus; FC, fasciola cinereum; GCL, granule cell layer; PCL, pyramidal cell layer; PL, polymorphic layer (hilus); SL-M, stratum lacunosum-moleculaire; SO, stratum oriens; SR, stratum radiatum. Yellow bars indicate the boundaries used between FC, CA1, CA2, CA3, and DG to calculate region lengths for **Figure 9**. Bar is 500 μm. **(B)** Similar section probed for Trpc4 in CA1 (magenta), Amigo2 in CA2 (red), and Bok in CA3 (green) to show the CA1-CA2 and CA2-CA3 boundaries. Whereas, the former boundary is fairly strict, there is considerable mixing of CA2 and CA3 cell types at that "border." Bar is 200 μm.

pyrophosphate/0.2% SDS/0.2 mg/ml sodium heparin/2% sodium polyacrylate]. The probe cocktail was added to the sections and then incubated in a humid chamber for 24 h at 37°C. The next day, sections were washed in 1xSSPE (150 mM NaCl, 10 mM $NaH_2PO_4$, and 1 mM EDTA, pH 7.4) four times for 30 min each at 37°C with gentle rotation. The sections were

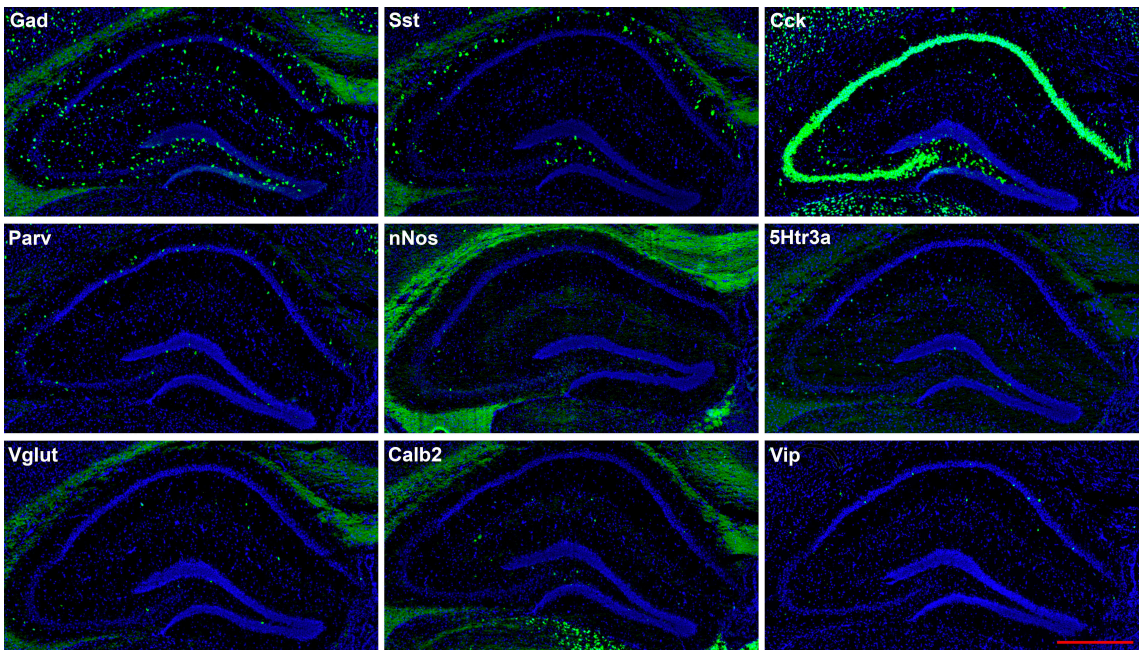


**FIGURE 2 |** Representative low-magnification photomicrographs showing expression of nine interneuron types in sections 1.8 mm behind the bregma. This is the level at which the interneurons were counted. See **Figure 1** for hippocampal layer and region delineations. White matter tracts show some autofluorescence (green) in some panels. In this and subsequent figures, Gad and Vglut stand for Gad-1 and Vglut3, respectively. The bar equals 500 μm for all panels.

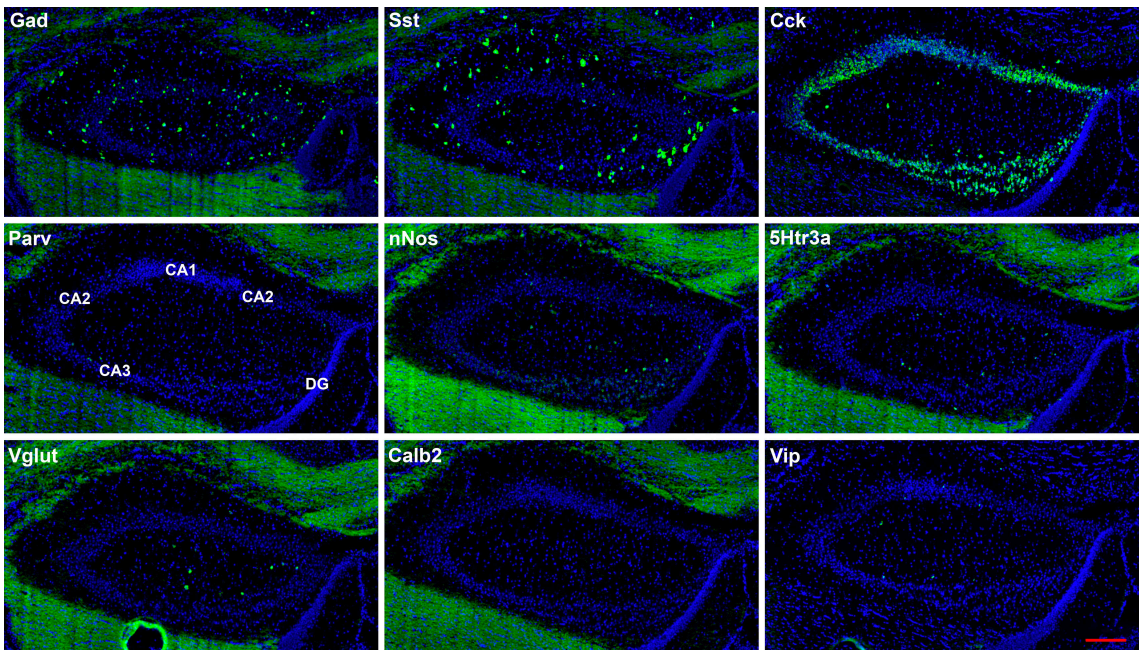


**FIGURE 3 |** Representative low-magnification photomicrographs of very anterior dorsal hippocampus at 1.1 mm behind the bregma showing expression of nine interneuron types. White matter tracts show some autofluorescence (green) in some panels. The bar equals 200 μm for all panels.

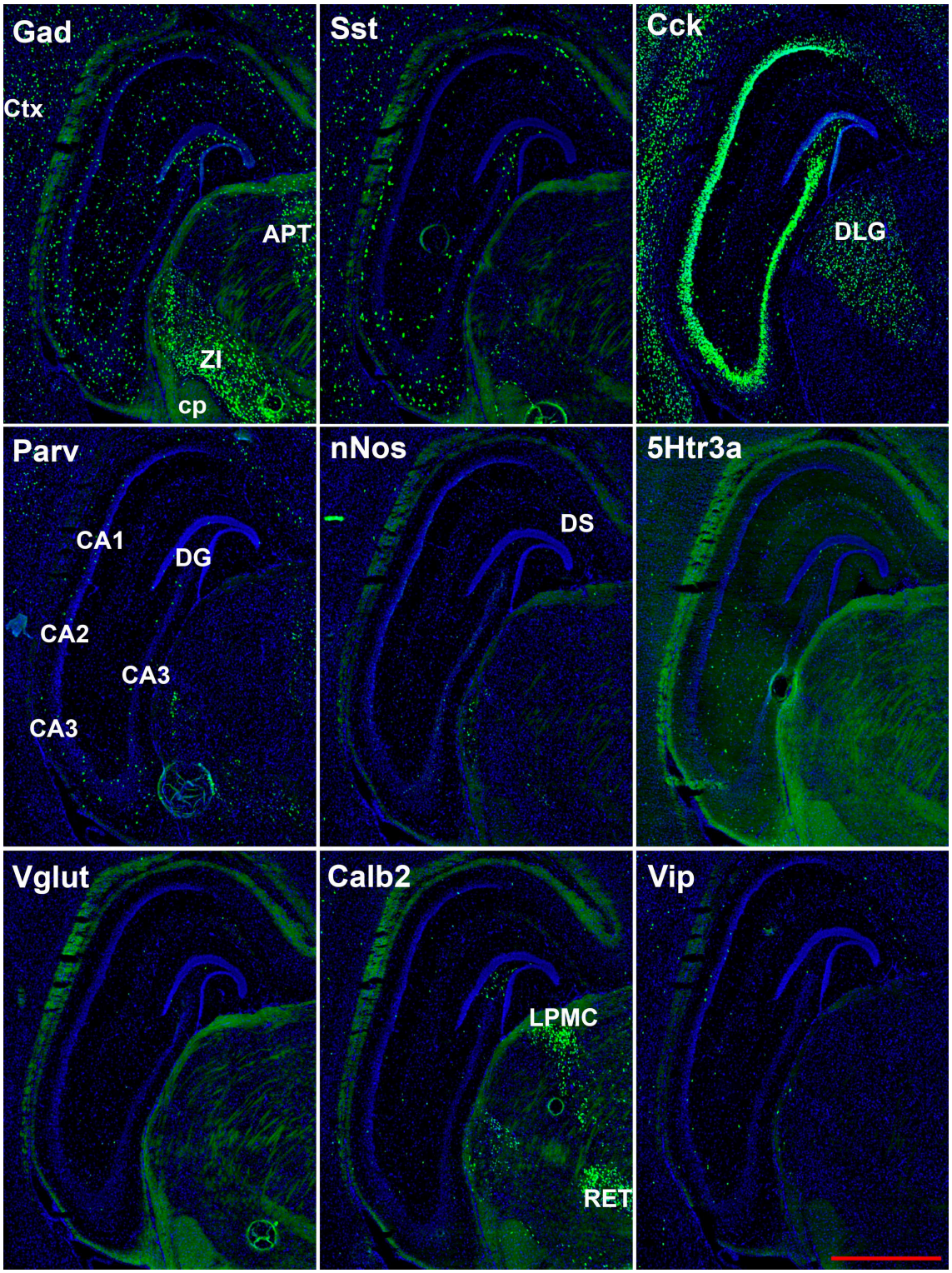


**FIGURE 4 |** Representative low-magnification photomicrographs showing expression of nine interneuron types 2.6 mm behind the bregma. White matter tracts show some autofluorescence (green) in some panels. Bar equals 1 mm for all panels. APT, anterior pretectal n. caudal; cp, cerebral peduncle; Ctx, neocortex; DLG, dorsal lateral geniculate; DS, dorsal subiculum; LPMC, lateral posterior nucleus mediocaudal; RET, retroethmoid nucleus; ZI, zona incerta. The bar equals 1 mm for all panels.

then washed in 1x SSPE for 5 min at RT and then in 5xSSPE for 5 min. The hairpin amplification took place with minimal light exposure, including dimming lights when possible. At a working concentration of 60 nM, each hairpin, specifically tagged to label probe pairs of a probe set through the matching B1–B5 binding site, was heated separately at 95°C for 1.5 min and then cooled to RT for 30 min. The sections were then hybridized at RT for 24 h. The next day, sections were washed at RT in 5xSSPE with 0.1% Tween-20 four times for 30 min each with gentle rotation. The sections were briefly rinsed in 5xSSPE and then counterstained with DAPI in 5xSSPE for 1 min. In order to minimize any autofluorescence, sections were then incubated in 1x TrueBlack in 70% ethanol for 2 min. Finally, the sections were washed at RT in PBS 3 times for 5 min each, followed by a quick dip in 70% EtOH before air-drying.

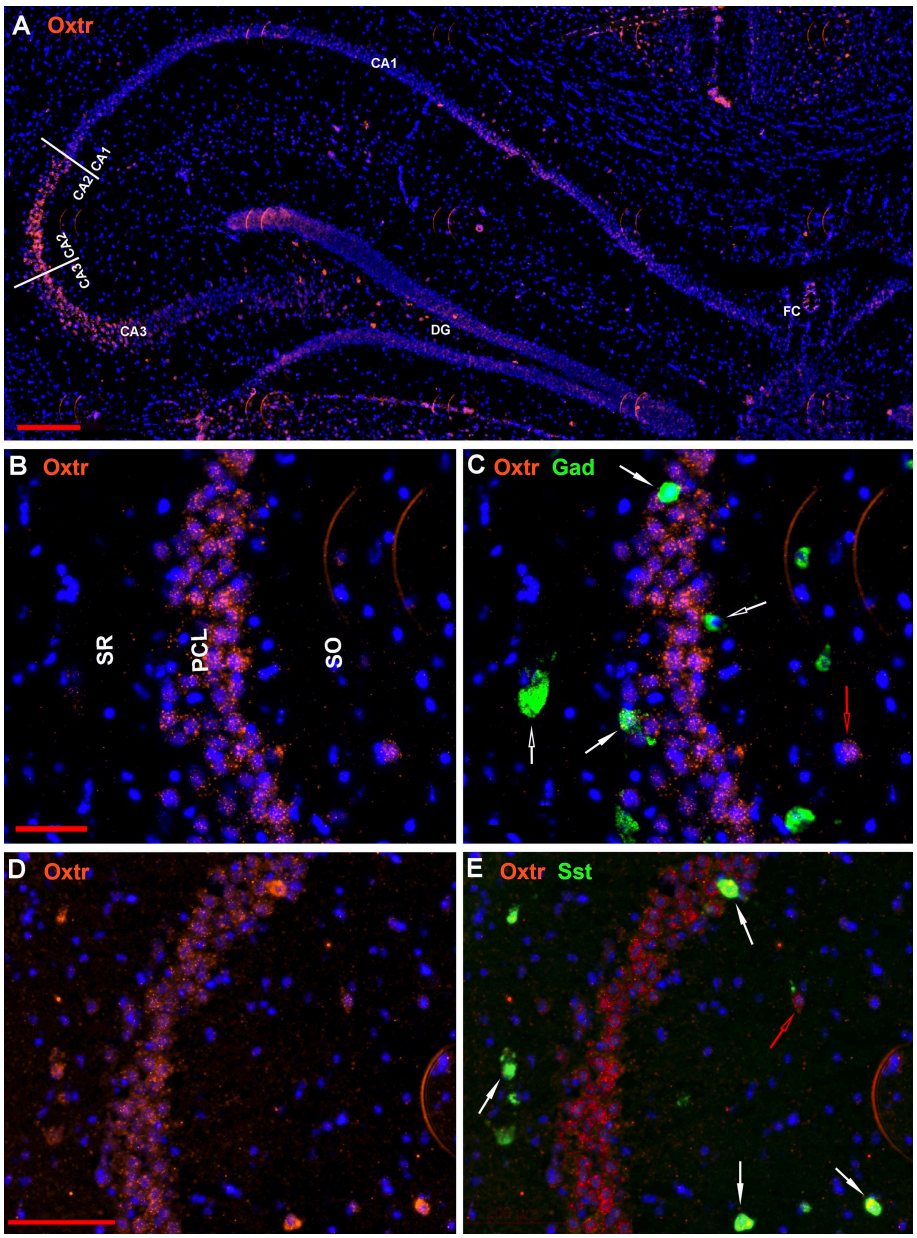


**FIGURE 5 |** Examples of the distribution of Oxtr neurons within the hippocampus. **(A)** shows the distribution in a low magnification view (scale bar equals 200 μm). **(B)** shows higher magnification within the CA2 region and **(C)** shows the Oxtr colocalization with Gad-1 [scale bar of 50 μm for **(B,C)**]. **(D)** shows higher magnification within the CA2 region and **(E)** shows the Oxtr colocalization with Sst [scale bar equals 100 μm for **(D,E)**]. Solid white arrows indicate colocalization of Oxtr transcripts with the INM transcripts. Open white arrows indicate only expression of the INM. Open red arrows indicate only expression of Oxtr.

## Probes

The proprietary probe pairs and hairpin amplifiers were ordered from Molecular Instruments, Inc. (Los Angeles, CA), and details about the probes are presented in **Table 1**. We targeted the following genes: oxytocin receptor, Oxtr; glutamic acid decarboxylase 1, Gad-1 (also known as Gad-67); parvalbumin, Parv; somatostatin, Sst; cholecystokinin, Cck; vasoactive intestinal polypeptide, Vip; vesicular glutamate transporter-3, Vglut3; calbindin 2, Calb2 (also known as calretinin); 5-hydroxytryptamine receptor 3A, 5Htr3a; and neuronal nitric oxide synthase, nNos. For the Oxtr/INM colocalization studies, the Oxtr mRNA probe was decorated with Alexa 546-labeled hairpins via the B4 amplifier link and the other INM mRNA probes with Alexa 647 through the B1, B2, B3, or B5 amplifier links (Choi et al., 2018). For the Gad-1/non-Oxtr INM colocalization studies, the Gad-1 mRNA probe was labeled with Alexa 647 via the B2 amplifier link and the non-Oxtr mRNA probes with Alexa 546 via the B3 or B5 links (see **Table 1**). The Trpc4, Amigo2, and Bok probes were labeled with Alexas 647 (B2), 546 (B5), and 488 (B3), respectively.

## Imaging and Analysis

Scans were obtained using a Zeiss Axio ScanZ1 (20x objective) and ZENlite software (Thornwood, NY, USA). Each layer within each region in the hippocampus (regions CA1-3, fasciola cinereum, and dentate gyrus) was examined bilaterally in two coronal sections (four samples) from ∼1.8 mm behind the bregma (see **Figures 1A**, **2**). Boundaries between CA1 and CA2 and between CA2 and CA2 are indicated in **Figure 1B** using the hippocampal CA-specific markers Trpc4 (CA1), Amigo2 (CA2), and Bok (CA3). As the "border" zone between CA2 and CA3 is rather fuzzy due to intermingling of cell types, the CA2 region proximal to CA1 and away from this zone was counted. Cells were counted within the stratum oriens (SO), pyramidal cell layer (PCL), stratum radiatum (SR), and stratum lacunosum-moleculaire (SL-M) of the CA regions. The SR to SL-M border was taken as when the cell density increased (**Figure 1A**). Cells within the stratum lucidum in CA3 (and any there in CA2) were counted with stratum radiatum. Neurons in the fasciola cinereum (FC) were only counted as within the pyramidal cell layer (PCL) or not. Neurons in the dentate gyrus (DG) were counted in the molecular layer (ML), granule cell layer (GCL), and plexiform layer (PL). Neurons were counted manually from the scan images. We counted, in the two-dimensional scans, cells in relationship to the pyramidal and granule cell layers for 292, 1,009, 255, 443, and 679 μm along the FC, CA1, CA2, CA3, and DG, respectively. We then simply converted to counts per 100 μm or per region (for the latter based on total region

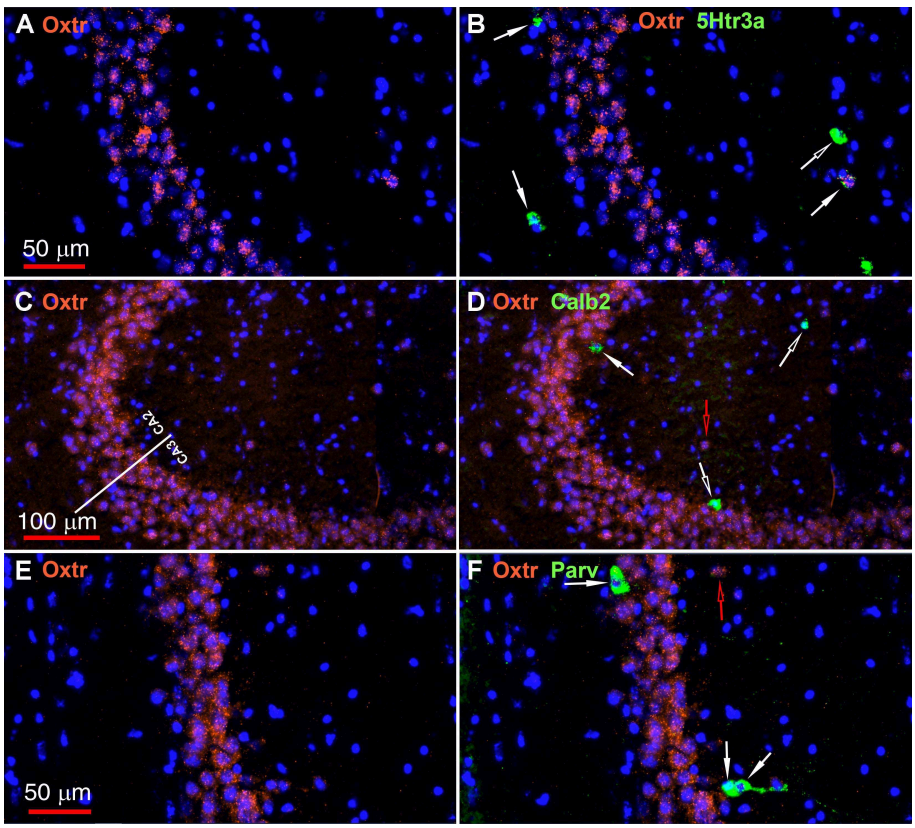


**FIGURE 6 |** Examples of the distribution of Oxtr within the CA2 hippocampal region. **(A)** shows Oxtr expression in the CA2 and **(B)** shows its colocalization with 5Htr3a transcripts. **(C)** shows Oxtr expression in the CA2 and **(D)** shows expression with Calb2 transcripts. **(E)** shows Oxtr expression in the CA2 and panel F shows its colocalization with Parv transcripts. Scale bars in **(A)** 50 μm, **(C)** 100 μm, and **(E)** 50 μm are also for **(B,D,F)**, respectively. Solid white arrows indicate colocalization of Oxtr transcripts with the INM transcripts. Open white arrows indicate only expression of the INM. Open red arrows indicate only expression of Oxtr.

lengths of 292, 2,083, 255, 787, and 856 μm, respectively). As there were no obvious differences detected between the male and female hippocampal counts in the different regions and layers (**Supplemental Image 1**), the counts were combined for data presentation. Although the color channels were set the same, some sections show an autofluoresence in the white matter tracts for unknown reasons. This was not an issue for counting for two reasons: the background did not appear as dots under high power as is the case for the interneurons (unless at higher densities of expression) and white matter tracts were not in the counted areas.

## RESULTS

The hairpin chain reaction technique enabled us to examine the distribution of the genes expressed within interneuronal populations. Representative low-magnification views are displayed in **Figures 1**–**4**. Interneurons were counted in sections about 1.8 mm behind the bregma (**Figures 1**, **2**). **Figures 3**, **4** show representative sections from more rostral and caudal sections, respectively. With few exceptions (see below), all 10 genes are expressed in all hippocampal regions and layers within.

The oxytocin receptor is expressed prominently in the pyramidal neurons of the CA2 and adjacent CA3 (**Figure 5A**) but also in neurons there that express Gad-1 (**Figures 5B,C**), Sst (**Figures 5D,E**), 5Htr3a (**Figures 6A,B**), Calb2 (**Figures 6C,D**), Parv (**Figures 6E,F**), Cck (**Figures 7A,B**), nNos (**Figures 7C,D**), Vglut3 (**Figures 7E,F**), and Vip (**Figures 7G,H**). Oxtr and Cck are also colocalized in CA2 and CA3 pyramidal neurons (compare **Figure 3**-Cck and **Figure 5A**; **Figures 7A,B**). Note that Cck expression in pyramidal neurons, although still

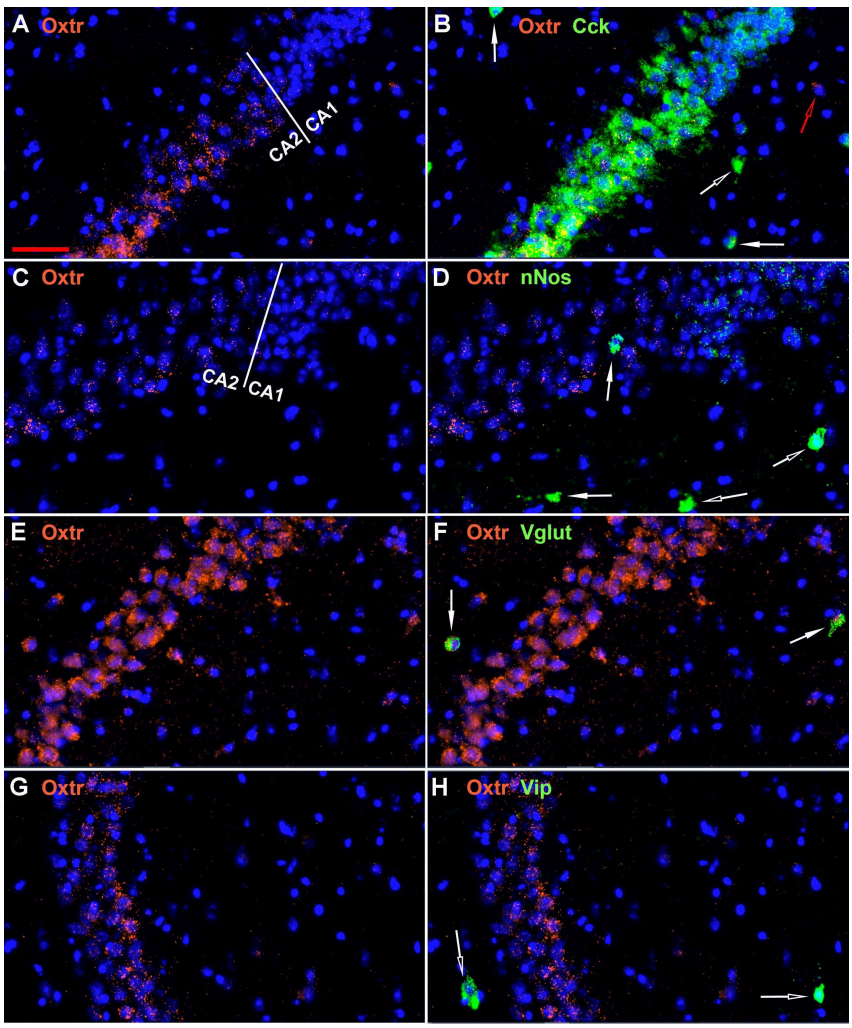


**FIGURE 7 |** Examples of the distribution of Oxtr within the CA2 hippocampal region. **(A)** shows Oxtr expression in the CA2 and **(B)** shows its colocalization with Cck transcripts. Cck expression also occurs in pyramidal neurons but less in the CA1 neurons. **(C)** shows Oxtr expression in the CA2 and **(D)** shows co-expression with nNos transcripts. In contrast to Cck, nNos expression is not apparent in the CA2 but is present in the CA1 pyramidal neurons. **(E)** shows Oxtr expression in the CA2 and **(F)** shows its colocalization with Vglut3 (Vglut) transcripts. **(G)** shows Oxtr expression in the CA2 and **(H)** shows its expression with Vip transcripts. Bar in **(A)** is 50 μm and applies to all panels. Solid white arrows indicate colocalization of Oxtr transcripts with the INM transcripts. Open white arrows indicate only expression of the INM. Open red arrow indicates only expression of Oxtr.

present, falls off considerably from CA2 to CA1 (**Figure 7B**). In contrast, nNos expression abruptly picks up in CA1 at the CA2/CA1 boundary where Oxtr expression stops (**Figures 7C,D**). The Cck+/Oxtr+ PCL neurons in FC, CA2, or CA3 were not included in our counts. Nor were the PCL Oxtr+/INM- (Oxtr only) neurons in those regions. CCK only neurons were not counted in the FC, CA2, or CA3 PCL neurons.

A few other regional examples are presented in **Figure 8**. All 9 non-Oxtr genes are expressed in the dentate gyrus, and especially Gad-1, Sst, and Cck in the polymorphic layer, often colocalized with Oxtr (**Figures 1–4**, **8A–D**). All of the 9 non-Oxtr genes are expressed within CA1 as well, again often colocalized with Oxtr (**Figures 1–4**, **8E,F**). The fasciola cinereum has a similar gene expression pattern as CA2 with Oxtr expressed in the pyramidal cells and occasional co-expression with the other 9 genes (**Figures 8G,H** with Vip).

As noted above, we manually counted over 5,000 neurons to examine the distribution of the nine non-Oxtr markers as well as their co-expression with Oxtr. We examined both a male and a female mouse brain and saw no obvious sex differences for any of the distributions (**Supplemental Image 1**). Therefore, the

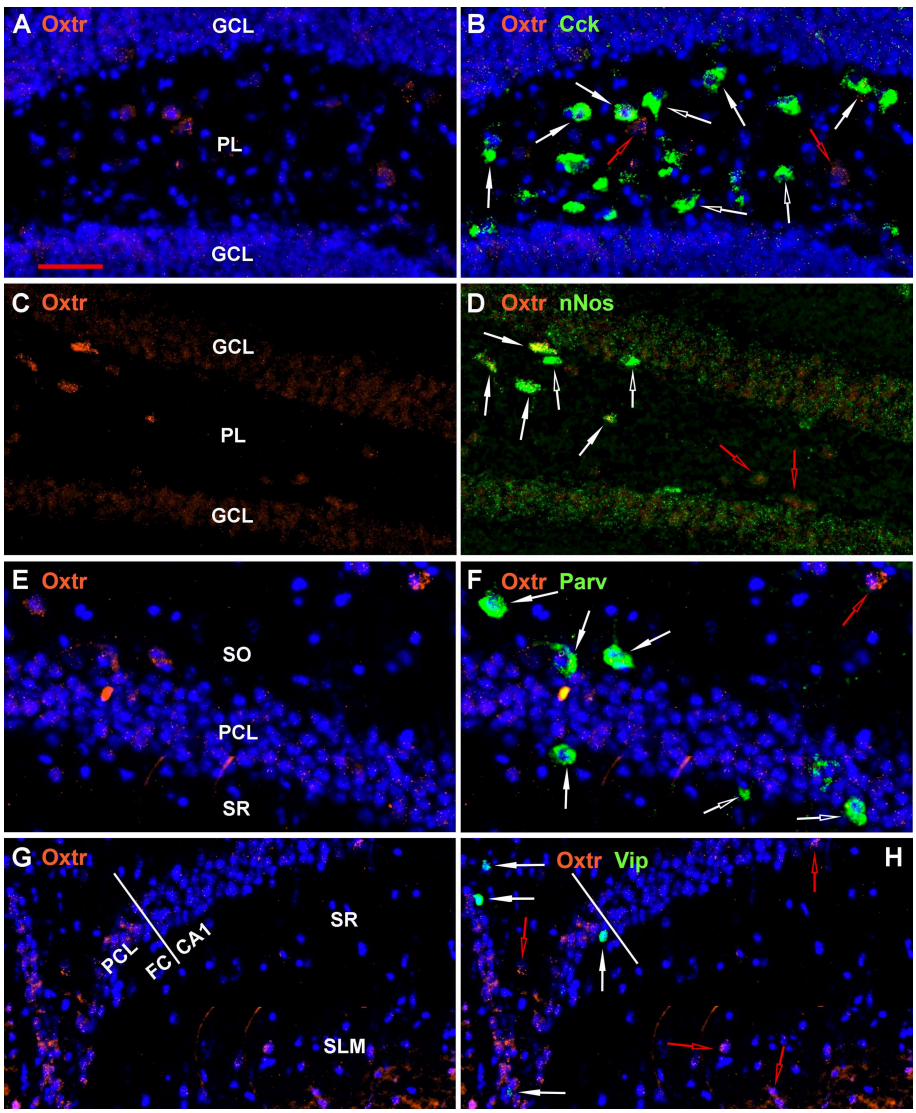


**FIGURE 8 |** Examples of the distribution of Oxtr within some hippocampal regions. **(A)** shows Oxtr expression in the DG and **(B)** shows its colocalization with Cck transcripts. **(C)** shows Oxtr expression in the DG and **(D)** shows its co-expression with nNos transcripts. In contrast to Cck, nNos expression is not apparent in the CA2 but is present in the CA1 pyramidal neurons. **(E)** shows Oxtr expression in the CA1 and **(F)** shows its colocalization with Parv transcripts. **(G)** shows Oxtr expression in the FC and CA1 regions and **(H)** shows its colocalization with Vip transcripts. FC pyramidal cells express Oxtr similarly to the CA2. Bar in **(A)** is 50 μm and applies to all panels. Solid white arrows indicate colocalization of Oxtr transcripts with the INM transcripts. Open white arrows indicate only expression of the INM. Open red arrows indicate only expression of Oxtr.

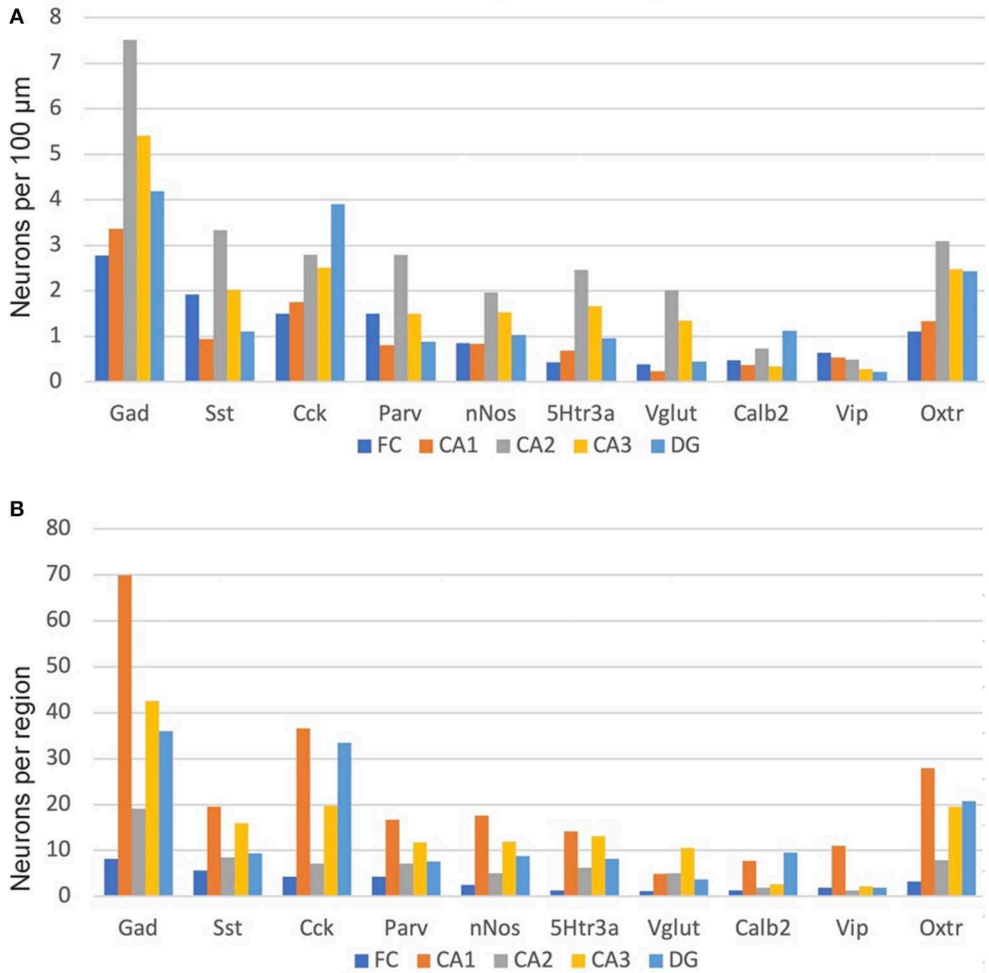


**FIGURE 9 |** Interneuron types per length in the hippocampal regions **(A)** and, as well, as per total hippocampal region area **(B)**. See the Methods and Methods for the measured lengths and calculations. Cck and Oxtr neurons in the PCL of FC, CA2, and CA3 were counted if they co-expressed Gad-1.

graphs we present show the combined counts. As both Cck and Oxtr are expressed in excitatory pyramidal neurons of CA2-CA3 as well as FC, those neurons were only counted if co-expressed with Gad-1. This could miss Cck and Oxtr interneurons that did not co-express Gad-1 but did express Gad-2, of course. We did count infrequent Cck+Oxtr neurons in the PCL of the CA1 so we may have counted some pyramidal neurons there. As shown in **Figure 9**, Gad-1 expressing interneurons are the most abundant, approximately twice as abundant as the next most abundant, Cck. This holds true whether considered per length in a region or per region. The distributions per length are relatively even for all of the regions with a slight preponderance in CA2. Per region area, the CA1 in total generally has the most of any region, followed by CA3. Specifically, this holds true for Gad-1, Sst, Parv, nNos, 5Htr3a, and Vip. CA1 and DG have the most neurons for Cck, Calb2 and Oxtr. The specific co-expression of the INMs with Oxtr in different regions and layers is available in the **Supplemental Data 1**.

The sublayer distributions of the nine non-Oxtr interneurons in each region are quite varied (**Figure 10**). **Figure 11** presents the sublayer distributions of the nine non-Oxtr interneurons in CA1-CA3 again, but grouped by gene. In general, the sublayer distributions were similar across the three CA regions, with some exceptions such as Vglut3 and Sst in CA1 and Calb2 and Vip in CA3.

**Figure 12** presents the data on Oxtr colocalization, either as a percentage of the INM-labeled neuron (**Figure 12A**) or INM colocalization as a percentage of Oxtr-labeled neurons (**Figure 12B**). For the latter, the neurons are presented in descending order of Oxtr-positive neurons expressing the INM, from over 90% with Gad-1 to <10% with Vip. This, of course, also reflects the abundance of the various INM-expressing neurons (numbers shown under INM group). Three thousand seven hundred Oxtr-expressing non-PCL neurons (except CA1) neurons were counted across all regions and layers for all INMs. This averages to about 411 Oxtr neurons per INM sample. Other

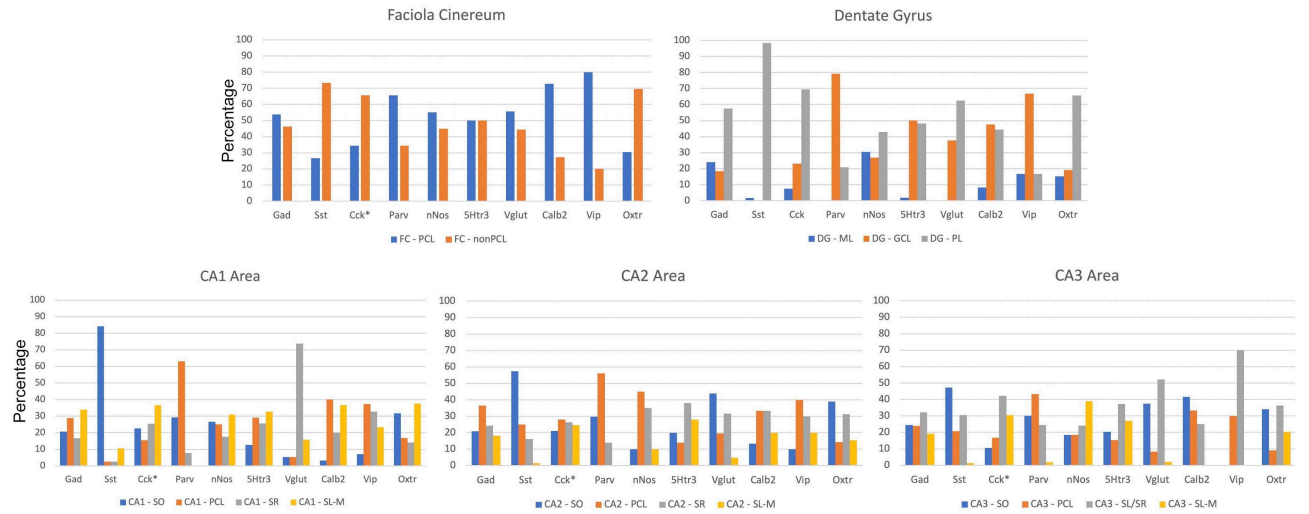


**FIGURE 10 |** Distribution of interneurons in sublayers of the hippocampus by region by percentage. *Cck and Oxtr neurons in the PCL of FC, CA2, and CA3 were counted if they co-expressed Gad-1. GCL, granule cell layer; ML, molecular layer; PCL, pyramidal cell layer; SL/SR, stratum lucidum/radiatum; SL-M, stratum lacunosum-moleculare; SO, stratum oriens; SR, stratum radiatum.

than Gad-1 and nNos neurons, at least two-thirds of the neurons co-express Oxtr (**Figure 12A**).

Finally, we looked at the colocalization of Gad-1 expression with the other 8 non-Oxtr genes. Although we did not quantitate these observations, essentially all Vip, Sst, Parv, nNos, and Vglut3 neurons express Gad-1. Calb2 and Cck neurons frequently did not co-express Gad-1 in the DG polymorphic layer, and a smaller percentage of 5Htr3a did not express Gad-1 in non-PCL neurons (**Figure 13**). A side note to consider is that not all GABAergic neurons confine their processes to the hippocampus and would not, strictly speaking, be interneurons (Jinno and Kosaka, 2002a).

## DISCUSSION

Our results present an overview of the distribution of the expression of 10 interneuronal markers in the dorsal hippocampus of the mouse. Of course, split into whether or not they co-express Oxtr leads to at 18 different types, although there is certainly overlap with the various interneuronal markers. In our study, 59% of the 3,700 Oxtr neurons counted did not show co-expression with one of the INMs even though about 95% did co-express Gad-1, consistent with overlap (and no more than 5% inclusion of excitatory pyramidal cell neurons). An excellent recent review (Booker and Vida, 2018) discussed 29 types of interneurons in the CA1 area of the hippocampus alone based on projections, intrahippocampal locations and gene expression patterns. We have not attempted to match up our findings with that neuroanatomical data. However, our results suggest that there are interneurons that did not make it into that review further demonstrating the complexity of the distributions. For example, there are CA1 neurons in the stratum radiatum that express Sst or Vglut3 and in the stratum oriens that express nNos or Vip. A study of the spatiotemporal origins of mouse hippocampal neurons in CA1 (Tricoire et al., 2011) expressing Parv, Sst, nNos, Cck, and Vip found quite similar patterns to ours. Examples of reports of similar distributions of the INM-expressing neurons include: Gad-1 (Jinno et al., 1998), Sst and Parv (Uchida et al., 2014), Cck and Vip (and Sst) (Jinno and Kosaka, 2003), nNos (Jinno et al., 1999), 5Htr3a (Koyama et al., 2017), Vglut3 (Schafer et al., 2002), and Calb2 (Jinno et al., 2001). In addition, comparisons with the maps provided at the Allen Brain Atlas mouse brain site are essentially identical (https://mouse.brain-map.org) (Lein et al., 2004).

The quantitative results by Jinno et al. provide an opportunity to compare our numbers for seven INM-expressing neurons within the same C57BL/6J strain of mice (Jinno et al., 1999; Jinno and Kosaka, 2000, 2002b, 2003). The image maps seem similar for the most part. We compared the percentage distributions in all regional sublayers for each INM (**Supplemental Data 2**). This yielded an average R-squared of 0.536 (0.934 for Parv, 0.822 for Sst, 0.7 for Vip, 0.586 for nNos, 0.376 for Calb2, 0.332 for Gad-1, and 0.004 for Cck) after removing 4 of 77 points observed as outliers (average R-squared of 0.431 with points included). Cck showed no correlation perhaps due to the presence of pyramidal cells that we excluded, missing some interneurons that might be Oxtr- and Gad-1-positive, and including some displaced pyramidal neurons that are Oxtr- and Gad-1 positive. Also, we are comparing the results from two different techniques: immunohistochemistry and *in situ* hybridization. One approach may be more sensitive than the other for a particular gene product depending on the abundance and antibody sensitivity relative to the transcript detection.

Another issue arises with regard to the numbers of neurons shown in **Figure 9**. Only about 30% of the Gad-1 neurons express Oxtr. However, 80% of the total of the rest of the neurons expressing a non-Gad-1 INM express Oxtr. This is, likely, largely explained by the interneurons expressing several of the INMs in

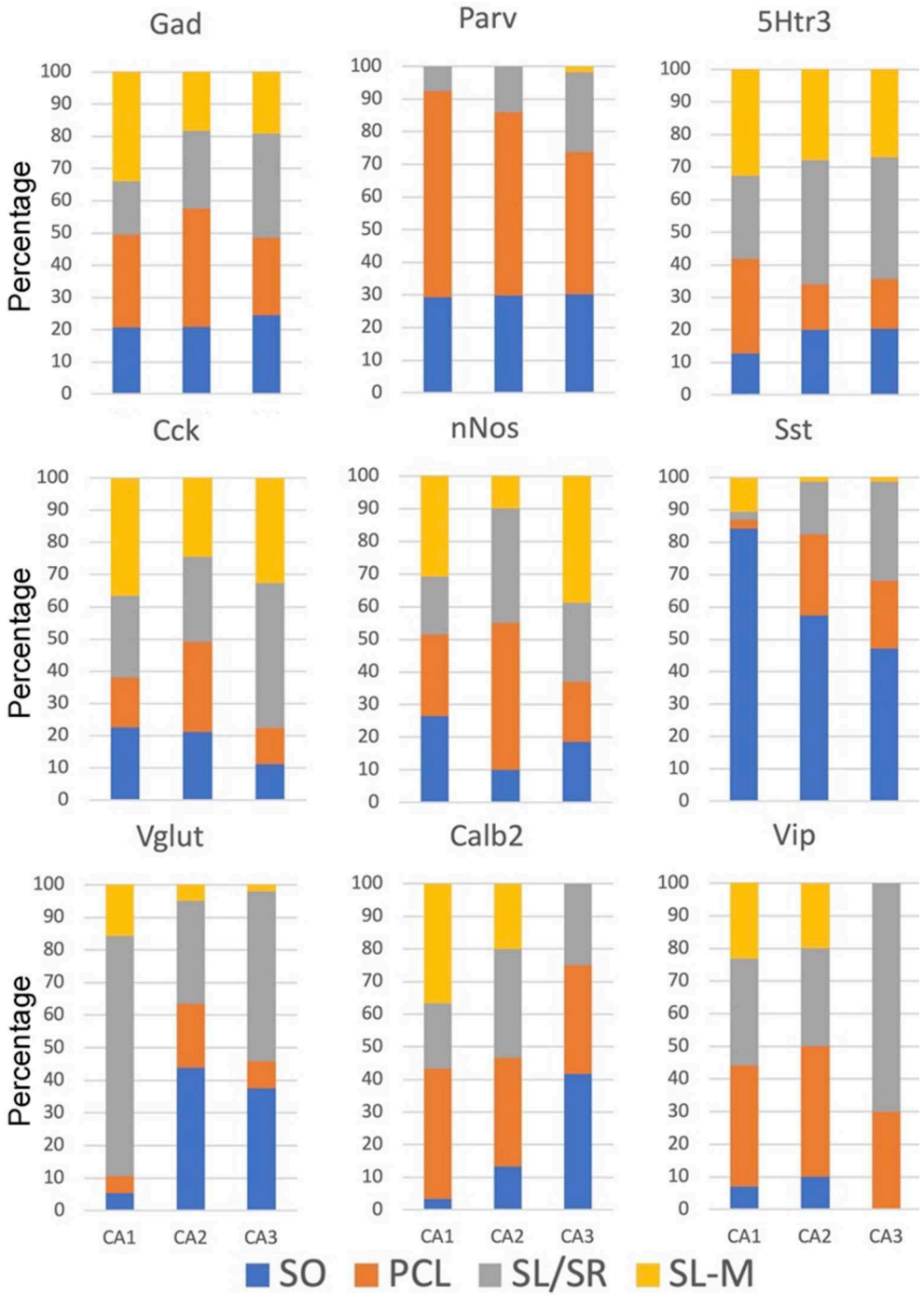


**FIGURE 11 |** Percentages of different interneurons in sublayers of the CA regions by marker. Cck neurons in the PCL of FC, CA2, and CA3 were counted if they co-expressed Gad-1. GCL, granule cell layer; ML, molecular layer; PCL, pyramidal cell layer; SL/SR, stratum lucidum/radiatum; SL-M, stratum lacunosum-moleculare; SO, stratum oriens; SR, stratum radiatum.

various overlapping combinations. In addition, it is also likely that some of the Oxtr-expressing neurons express the other glutamic acid decarboxylase, Gad-2 (Gad-65) (Wieronska et al., 2010; Wang et al., 2014). Additionally, Cck and Sst, and nNos to a lesser apparent extent, are present in pyramidal neurons. For this reason, although we excluded those neurons that have INM expression from our counts and we believe that the large majority of our Oxtr-expressing cells that we counted also express one of the other INMs, it is likely we counted displaced neurons from those layers.

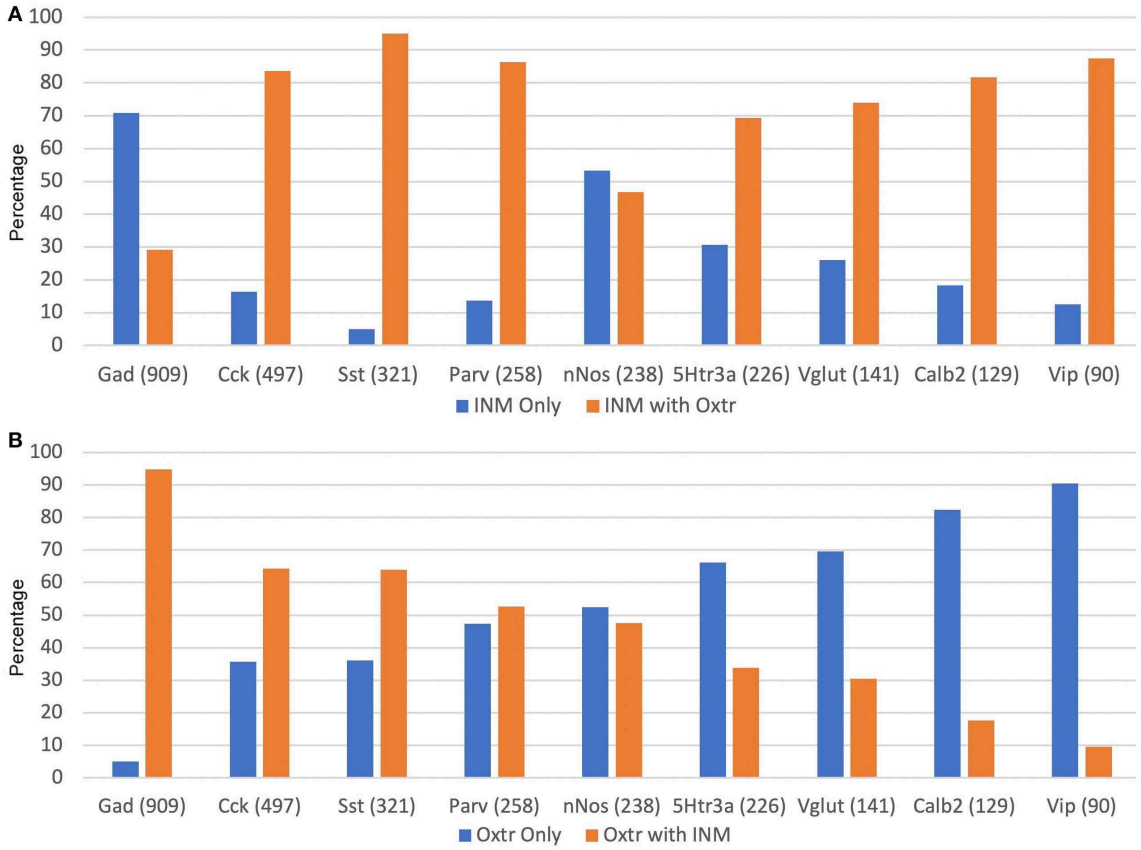


**FIGURE 12 |** Percentages of INM-expressing neurons containing Oxtr **(A)** or Oxtr-expressing neurons containing an interneuron marker **(B)**. The total numbers of each type of INM-expressing neuron are indicated within parentheses. Three thousand seven hundred total Oxtr interneurons were counted.

Further, we may have simply counted other non-GABAergic neurons expressing INMs. For example, as **Figure 13** shows, a sizable proportion of the DG Calb2 (calretinin) neurons, especially in the inner part of the granule cell layer, do not express GABA, as noted by others (Liu et al., 1996; Jinno, 2011; Anstotz and Maccaferri, 2020). These were included in our analyses and one should be more cautious about the DG numbers with regard to Calb2 as interneurons. For these reasons, we are confident in the location of the Oxtr-expressing neurons with respect to the INMs, but less so with regard to their interneuron status, except for the Gad-1/Oxtr co-expressors.

Raam et al. (2017) also examined the co-expression of Oxtr with some markers in the mouse hippocampus permitting some comparison of the overlapping genes examined: Gad-1, Parv, and Sst. For example, about 86, 24, and 37% of DG Oxtr cells express Gad-1, Parv and Sst, respectively, in their study, compared to our similar values of 73, 41, and 42%. In the CA2, however, they found that only 9.5% of the Oxtr neurons express Gad-1, whereas we found that 92% of interneurons do. The discrepancy is due our exclusion of CA2 Oxtr-expressing pyramidal excitatory neurons from the evaluation. They found that about 47 and 26% of Parv and Sst neurons, respectively, express Oxtr, compared to our 85 and 93%. As we used the same strain, the reason for differences in these areas in unknown.

We are particularly interested in the CA2 region as noted in the Introduction because of its role in social behaviors, especially with regard to Oxtr and the vasopressin 1b receptor. An earlier study examined 8 INMs in the rat hippocampus with focus on the CA2 region (Botcher et al., 2014). Our findings for the five INMs that we both studied were similar. For example, they found in the rat that Parv interneurons are more abundant in the PCL of the CA2 than of CA1 or CA3 when consider per length. And more abundant in the PCL than other layers in all 3 CA regions. Our findings in the mouse mirror this (**Figures 9**, **10**; **Supplemental Data 1**). The ability to discern Oxtr and Cck interneurons in the PCL of the CA2 (as well as CA3 and FC) using *in situ* hybridization was limited by their expression in PCL pyramidal neurons there. We were able to count those that co-expressed with Gad-1, however. The data in this study suggests that between 30 and 50% of those interneurons express Cck or Oxtr.

The CA2 area and the structures of its neurons were exquisitely analyzed and defined by Golgi impregnations in

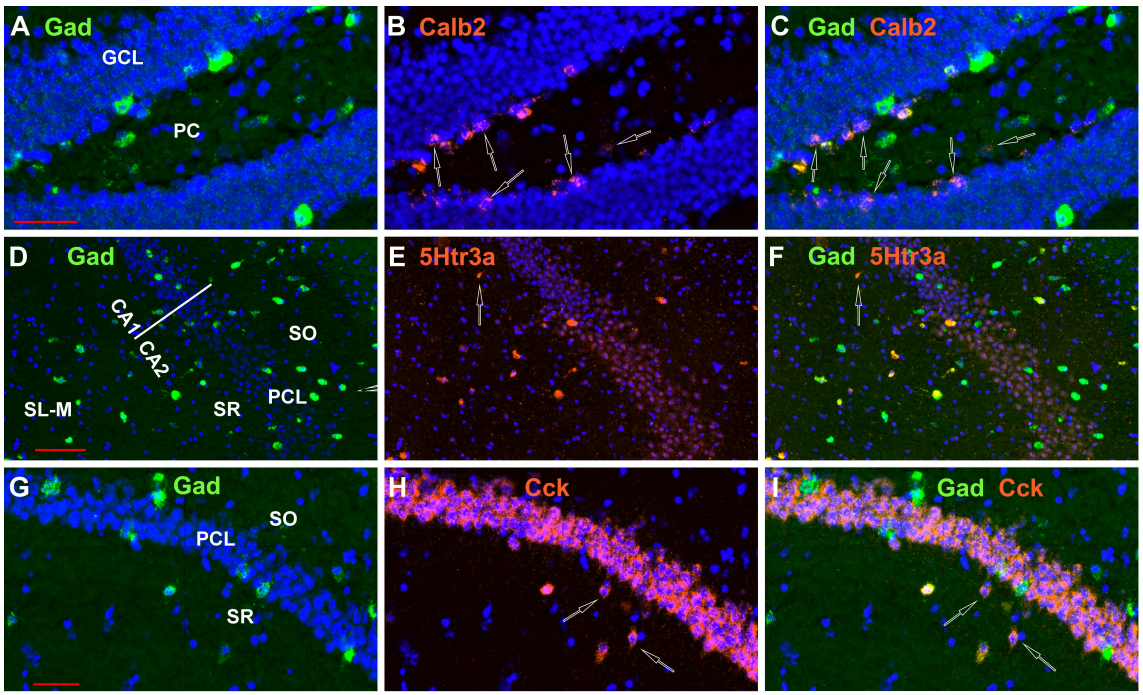


**FIGURE 13 |** Not all neurons examined expressing INMs in the hippocampus express Gad-1, although the great majority do. Examples of Calb2 neurons in the DG, a 5Htr3a neuron in CA1, and two Cck neurons in CA1 that do not express Gad-1 are indicated by the open arrows in **(A–C,D–F,G–I)**, respectively. Scale bars for **(A–C,D–F,G–I)**, are 50, 100, and 50 μm, respectively.

1934 (de No Lorente, 1934). Molecular biological techniques such as *in situ* hybridization further confirmed the distinctness of this region (Lein et al., 2005). Interestingly, the even more sparsely studied fasciola cinereum is much more similar in gene expression to the CA2 than any other hippocampal (or brain) region (Lein et al., 2005), and appears not to be an extension of the fascia dentata of the dentate gyrus (Hjorth-Simonsen and Zimmer, 1975). Therefore, we were also interested in how the patterns of interneuron distributions in the FC compares with those in the CA2 and other hippocampal areas. In this regard, although the correlation between numbers of FC and CA2 interneurons per 100 μm length (9 points, excluding Cck numbers) was slightly higher than the next best fit (R-squared for FC/CA2 = 0.77 vs. FC/CA3 = 0.68), the conclusion to be drawn is that the gene expression similarity between FC and CA2 is not reflected in interneuron distributions, at least for the nine analyzed here.

The Oxtr interneurons are present rather evenly throughout the regions per length and sublayers. Also, other than Gad-1 and nNos neurons, at least two-thirds of each neuronal population we studied co-express Oxtr. This indicates that Oxtr is situated to potentially exert an overarching regulation of hippocampal neuronal activity. However, as our data show, 70% of the Gad-1 interneurons do not express Oxtr so they would not be directly impacted by oxytocin innervation. We do not know which other interneurons fall into that large non-Oxtr expressing group. We also do not know the extent of overlap of INM gene expression beyond that with Oxtr, and only generally with Gad-1, amongst the populations we studied here with respect to their neuroanatomical distributions. These would be areas for future study.

## DATA AVAILABILITY STATEMENT

All datasets generated for this study are included in the article/**Supplementary Material**.

## ETHICS STATEMENT

The animal study was reviewed and approved by National Institute of Mental Health Animal Care and Use Committee.

## AUTHOR CONTRIBUTIONS

WY and JS designed, performed, and analyzed the experiments and prepared the manuscript.

## FUNDING

This research was supported by the Intramural Research Program of the NIMH (ZIAMH002498).

## ACKNOWLEDGMENTS

The authors acknowledge the helpful comments by members of the Section on Neural Gene Regulation as well as conversations with Drs. Chris McBain and Charles Gerfen.

## SUPPLEMENTARY MATERIAL

The Supplementary Material for this article can be found online at: https://www.frontiersin.org/articles/10.3389/fnmol.2020.00040/full#supplementary-material

## REFERENCES

Anstotz, M., and Maccaferri, G. (2020). A toolbox of criteria for distinguishing cajal-retzius cells from other neuronal types in the postnatal mouse hippocampus. *eNeuro* 7:ENEURO.0516-19.2019. doi: 10.1523/ENEURO.0516-19.2019

Basu, J., Srinivas, K. V., Cheung, S. K., Taniguchi, H., Huang, Z. J., and Siegelbaum, S. A. (2013). A cortico-hippocampal learning rule shapes inhibitory microcircuit activity to enhance hippocampal information flow. *Neuron* 79, 1208–1221. doi: 10.1016/j.neuron.2013.07.001

Benes, F. M., and Berretta, S. (2001). GABAergic interneurons: implications for understanding schizophrenia and bipolar disorder. *Neuropsychopharmacology* 25, 1–27. doi: 10.1016/S0893-133X(01)00225-1

Benes, F. M., Kwok, E. W., Vincent, S. L., and Todtenkopf, M. S. (1998). A reduction of non-pyramidal cells in sector CA2 of schizophrenics and manic depressives. *Biol. Psychiatry* 44, 88–97. doi: 10.1016/S0006-3223(98)00138-3

Benes, F. M., Sorensen, I., and Bird, E. D. (1991). Reduced neuronal size in posterior hippocampus of schizophrenic patients. *Schizophr. Bull.* 17, 597–608. doi: 10.1093/schbul/17.4.597

Booker, S. A., and Vida, I. (2018). Morphological diversity and connectivity of hippocampal interneurons. *Cell Tissue Res.* 373, 619–41. doi: 10.1007/s00441-018-2882-2

Botcher, N. A., Falck, J. E., Thomson, A. M., and Mercer, A. (2014). Distribution of interneurons in the CA2 region of the rat hippocampus. *Front. Neuroanat.* 8:104. doi: 10.3389/fnana.2014.00104

Brady, D. R., and Mufson, E. J. (1997). Parvalbumin-immunoreactive neurons in the hippocampal formation of Alzheimer's diseased brain. *Neuroscience* 80, 1113–25. doi: 10.1016/S0306-4522(97)00068-7

Choi, H. M. T., Schwarzkopf, M., Fornace, M. E., Acharya, A., Artavanis, G., Stegmaier, J., et al. (2018). Third-generation in situ hybridization chain reaction: multiplexed, quantitative, sensitive, versatile, robust. *Development* 145:dev165753. doi: 10.1101/285213

Cilz, N. I., Cymerblit-Sabba, A., and Young, W. S. (2019). Oxytocin and vasopressin in the rodent hippocampus. *Genes Brain Behav.* 18:e12535. doi: 10.1111/gbb.12535

Dale, H. H. (1906). On some physiological actions of ergot. *J. Physiol.* 34, 163–206. doi: 10.1113/jphysiol.1906.sp001148

de Kloet, E. R., Rotteveel, F., Voorhuis, T. A., and Terlou, M. (1985). Topography of binding sites for neurohypophyseal hormones in rat brain. *Eur. J. Pharmacol.* 110, 113–9. doi: 10.1016/0014-2999(85)90036-6

de No Lorente, R. (1934). Studies on the structure of the cerebral cortex. II. Continuation of the study of ammonic system. *J. Psychol. Neurol.* 46, 113–77.

Engelmann, M., Ebner, K., Wotjak, C. T., and Landgraf, R. (1998). Endogenous oxytocin is involved in short-term olfactory memory in female rats. *Behav. Brain Res.* 90, 89–94. doi: 10.1016/S0166-4328(97)00084-3

Ferguson, J. N., Young, L. J., Hearn, E. F., Matzuk, M. M., Insel, T. R., and Winslow, J. T. (2000). Social amnesia in mice lacking the oxytocin gene. *Nat. Genet.* 25, 284–8. doi: 10.1038/77040

Gloveli, T., Dugladze, T., Rotstein, H. G., Traub, R. D., Monyer, H., Heinemann, U., et al. (2005). Orthogonal arrangement of rhythm-generating microcircuits in the hippocampus. *Proc. Natl. Acad. Sci. U. S. A.* 102, 13295–300. doi: 10.1073/pnas.0506259102

Harden, S. W., and Frazier, C. J. (2016). Oxytocin depolarizes fast-spiking hilar interneurons and induces GABA release onto mossy cells of the rat dentate gyrus. *Hippocampus* 26, 1124–39. doi: 10.1002/hipo.22595

Hitti, F. L., and Siegelbaum, S. A. (2014). The hippocampal CA2 region is essential for social memory. *Nature* 508, 88–92. doi: 10.1038/nature13028

Hjorth-Simonsen, A., and Zimmer, J. (1975). Crossed pathways from the entorhinal area to the fascia dentata. I. Normal in rabbits. *J. Comp. Neurol.* 161, 57–70. doi: 10.1002/cne.901610106

Jinno, S. (2011). Topographic differences in adult neurogenesis in the mouse hippocampus: a stereology-based study using endogenous markers. *Hippocampus* 21, 467–80. doi: 10.1002/hipo.20762

Jinno, S., Aika, Y., Fukuda, T., and Kosaka, T. (1998). Quantitative analysis of GABAergic neurons in the mouse hippocampus, with optical disector using confocal laser scanning microscope. *Brain Res.* 814, 55–70. doi: 10.1016/S0006-8993(98)01075-0

Jinno, S., Aika, Y., Fukuda, T., and Kosaka, T. (1999). Quantitative analysis of neuronal nitric oxide synthase-immunoreactive neurons in the mouse hippocampus with optical disector. *J. Comp. Neurol.* 410, 398–412.

Jinno, S., Kinukawa, N., and Kosaka, T. (2001). Morphometric multivariate analysis of GABAergic neurons containing calretinin and neuronal nitric oxide synthase in the mouse hippocampus. *Brain Res.* 900, 195–204. doi: 10.1016/S0006-8993(01)02292-2

Jinno, S., and Kosaka, T. (2000). Colocalization of parvalbumin and somatostatin-like immunoreactivity in the mouse hippocampus: quantitative analysis with optical dissector. *J. Comp. Neurol.* 428, 377–88.

Jinno, S., and Kosaka, T. (2002a). Immunocytochemical characterization of hippocamposeptal projecting GABAergic nonprincipal neurons in the mouse brain: a retrograde labeling study. *Brain Res.* 945, 219–31. doi: 10.1016/S0006-8993(02)02804-4

Jinno, S., and Kosaka, T. (2002b). Patterns of expression of calcium binding proteins and neuronal nitric oxide synthase in different populations of hippocampal GABAergic neurons in mice. *J. Comp. Neurol.* 449, 1–25. doi: 10.1002/cne.10251

Jinno, S., and Kosaka, T. (2003). Patterns of expression of neuropeptides in GABAergic nonprincipal neurons in the mouse hippocampus: quantitative analysis with optical disector. *J. Comp. Neurol.* 461, 333–49. doi: 10.1002/cne.10700

Kimura, T., Tanizawa, O., Mori, K., Brownstein, M. J., and Okayama, H. (1992). Structure and expression of a human oxytocin receptor. *Nature* 356, 526–9. doi: 10.1038/356526a0

Korotkova, T., Fuchs, E. C., Ponomarenko, A., von Engelhardt, J., and Monyer, H. (2010). NMDA receptor ablation on parvalbumin-positive interneurons impairs hippocampal synchrony, spatial representations, and working memory. *Neuron* 68, 557–69. doi: 10.1016/j.neuron.2010.09.017

Koyama, Y., Kondo, M., and Shimada, S. (2017). Building a 5-HT3A receptor expression map in the mouse brain. *Sci. Rep.* 7:42884. doi: 10.1038/srep42884

Laeremans, A., Nys, J., Luyten, W., D'Hooge, R., Paulussen, M., and Arckens, L. (2013). AMIGO2 mRNA expression in hippocampal CA2 and CA3a. *Brain Struct. Funct.* 218, 123–30. doi: 10.1007/s00429-012-0387-4

Lee, H. J., Caldwell, H. K., Macbeth, A. H., Tolu, S. G., and Young, W. S., 3rd. (2008). A conditional knockout mouse line of the oxytocin receptor. *Endocrinology* 149, 3256–63. doi: 10.1210/en.2007-1710

Lee, H. J., Macbeth, A. H., Pagani, J. H., and Young, W. S., 3rd. (2009). Oxytocin: the great facilitator of life. *Progr. Neurobiol.* 88, 127–51. doi: 10.1016/j.pneurobio.2009.04.001

Lein, E. S., Callaway, E. M., Albright, T. D., and Gage, F. H. (2005). Redefining the boundaries of the hippocampal CA2 subfield in the mouse using gene expression and 3-dimensional reconstruction. *J. Comp. Neurol.* 485, 1–10. doi: 10.1002/cne.20426

Lein, E. S., Zhao, X., and Gage, F. H. (2004). Defining a molecular atlas of the hippocampus using DNA microarrays and high-throughput in situ hybridization. *J. Neurosci.* 24, 3879–89. doi: 10.1523/JNEUROSCI.4710-03.2004

Lin, Y. T., Hsieh, T. Y., Tsai, T. C., Chen, C. C., Huang, C. C., and Hsu, K. S. (2018). Conditional deletion of hippocampal CA2/CA3a oxytocin receptors impairs the persistence of long-term social recognition memory in mice. *J. Neurosci.* 38, 1218–31. doi: 10.1523/JNEUROSCI.1896-17.2017

Liu, Y., Fujise, N., and Kosaka, T. (1996). Distribution of calretinin immunoreactivity in the mouse dentate gyrus. I. General description. *Exp. Brain Res.* 108, 389–403. doi: 10.1007/BF00227262

Macbeth, A. H., Lee, H. J., Edds, J., and Young, W. S., 3rd. (2009). Oxytocin and the oxytocin receptor underlie intrastrain, but not interstrain, social recognition. *Genes Brain Behav.* 8, 558–67. doi: 10.1111/j.1601-183X.2009.00506.x

Maniezzi, C., Talpo, F., Spaiardi, P., Toselli, M., and Biella, G. (2019). oxytocin increases phasic and tonic GABAergic transmission in CA1 region of mouse hippocampus. *Front. Cell Neurosci.* 13:178. doi: 10.3389/fncel.2019.00178

Mori, Y., Takada, N., Okada, T., Wakamori, M., Imoto, K., Wanifuchi, H. et al. (1998). Differential distribution of TRP Ca2+ channel isoforms in mouse brain. *Neuroreport* 9, 507–15.

Ott, I., and Scott, J. C. (1910). The action of infundibulum upon mammary secretion. *Proc. Soc. Exp. Biol.* 8, 48–49. doi: 10.3181/00379727-8-27

Owen, S. F., Tuncdemir, S. N., Bader, P. L., Tirko, N. N., Fishell, G., and Tsien, R. W. (2013). Oxytocin enhances hippocampal spike transmission by modulating fast-spiking interneurons. *Nature* 500, 458–62. doi: 10.1038/nature12330

Pagani, J. H., Lee, H. J., and Young, W. S., 3rd. (2011). Postweaning, forebrain-specific perturbation of the oxytocin system impairs fear conditioning. *Genes Brain Behav.* 10, 710–9. doi: 10.1111/j.1601-183X.2011.00709.x

Pagani, J. H., Zhao, M., Cui, Z., Williams Avram, S. K., Caruana, D. A., Dudek, S. M., et al. (2014). Role of the vasopressin 1b receptor in rodent aggressive behavior and synaptic plasticity in hippocampal area CA2. *Mol. Psychiatry.* 20, 490–499. doi: 10.1038/mp.2014.47

Pelkey, K. A., Chittajallu, R., Craig, M. T., Tricoire, L., Wester, J. C., and McBain, C. J. (2017). Hippocampal GABAergic inhibitory interneurons. *Physiol. Rev.* 97, 1619–747. doi: 10.1152/physrev.00007.2017

Piskorowski, R. A., and Chevaleyre, V. (2013). Delta-opioid receptors mediate unique plasticity onto parvalbumin-expressing interneurons in area CA2 of the hippocampus. *J. Neurosci.* 33, 14567–78. doi: 10.1523/JNEUROSCI.0649-13.2013

Raam, T., McAvoy, K. M., Besnard, A., Veenema, A. H., and Sahay, A. (2017). Hippocampal oxytocin receptors are necessary for discrimination of social stimuli. *Nat. Commun.* 8:2001. doi: 10.1038/s41467-017-02173-0

Schafer, E. A., and Mackenzie, K. (1911). The action of animal extracts on milk secretion. *Proc. Royal Soc. Lond. Ser. B* 84, 16–22. doi: 10.1098/rspb.1911.0042

Schafer, M. K., Varoqui, H., Defamie, N., Weihe, E., and Erickson, J. D. (2002). Molecular cloning and functional identification of mouse vesicular glutamate transporter 3 and its expression in subsets of novel excitatory neurons. *J. Biol. Chem.* 277, 50734–48. doi: 10.1074/jbc.M206738200

Smith, A. S., Williams Avram, S. K., Cymerblit-Sabba, A., Song, J., and Young, W. S. (2016). Targeted activation of the hippocampal CA2 area strongly enhances social memory. *Mol. Psychiatry* 21, 1137–1144. doi: 10.1038/mp.2015.189

Stark, E., Roux, L., Eichler, R., Senzai, Y., Royer, S., and Buzsaki, G. (2014). Pyramidal cell-interneuron interactions underlie hippocampal ripple oscillations. *Neuron* 83, 467–80. doi: 10.1016/j.neuron.2014.06.023

Stevenson, E. L., and Caldwell, H. K. (2014). Lesions to the CA2 region of the hippocampus impair social memory in mice. *Eur. J. Neurosci.* 40, 3294–301. doi: 10.1111/ejn.12689

Takayanagi, Y., Yoshida, M., Bielsky, I. F., Ross, H. E., Kawamata, M., Onaka, T., et al. (2005). Pervasive social deficits, but normal parturition, in oxytocin receptor-deficient mice. *Proc. Natl. Acad. Sci. U. S. A.* 102, 16096–101. doi: 10.1073/pnas.0505312102

Tirko, N. N., Eyring, K. W., Carcea, I., Mitre, M., Chao, M. V., Froemke, R. C., et al. (2018). Oxytocin transforms firing mode of ca2 hippocampal neurons. *Neuron* 100, 593–608 e3. doi: 10.1016/j.neuron.2018.09.008

Tricoire, L., Pelkey, K. A., Erkkila, B. E., Jeffries, B. W., Yuan, X., and McBain, C. J. (2011). A blueprint for the spatiotemporal origins of mouse hippocampal interneuron diversity. *J. Neurosci.* 31, 10948–70. doi: 10.1523/JNEUROSCI.0323-11.2011

Uchida, K., Taguchi, Y., Sato, C., Miyazaki, H., Kobayashi, K., Kobayashi, T., et al. (2014). Amelioration of improper differentiation of somatostatin-positive interneurons by triiodothyronine in a growth-retarded hypothyroid mouse strain. *Neurosci. Lett.* 559, 111–6. doi: 10.1016/j.neulet.2013.11.052

van Leeuwen, F. W., van Heerikhuize, J., van der Meulen, G., and Wolters, P. (1985). Light microscopic autoradiographic localization of [3H]oxytocin binding sites in the rat brain, pituitary and mammary gland. *Brain Res.* 359, 320–325. doi: 10.1016/0006-8993(85)91443-X

Wang, X., Gao, F., Zhu, J., Guo, E., Song, X., Wang, S., and Zhan, R. Z. (2014). Immunofluorescently labeling glutamic acid decarboxylase 65 coupled with confocal imaging for identifying GABAergic somata in the rat dentate gyrus-A comparison with labeling glutamic acid decarboxylase 67. *J. Chem. Neuroanat.* 61–62, 51–63. doi: 10.1016/j.jchemneu.2014.07.002

Wersinger, S. R., Ginns, E. I., O'Carroll, A. M., Lolait, S. J., and Young, W. S., 3rd. (2002). Vasopressin V1b receptor knockout reduces aggressive behavior in male mice. *Mol. Psychiatry* 7, 975–84. doi: 10.1038/sj.mp.4001195

Wieronska, J. M., Branski, P., Siwek, A., Dybala, M., Nowak, G., and Pilc, A. (2010). GABAergic dysfunction in mGlu7 receptor-deficient mice as reflected by decreased levels of glutamic acid decarboxylase 65 and 67kDa and increased reelin proteins in the hippocampus. *Brain Res.* 1334, 12–24. doi: 10.1016/j.brainres.2010.03.078

Young, W. S., Li, J., Wersinger, S. R., and Palkovits, M. (2006). The vasopressin 1b receptor is prominent in the hippocampal area CA2 where it is unaffected by restraint stress or adrenalectomy. *Neuroscience* 143, 1031–1039. doi: 10.1016/j.neuroscience.2006.08.040

Zaninetti, M., and Raggenbass, M. (2000). Oxytocin receptor agonists enhance inhibitory synaptic transmission in the rat hippocampus by activating interneurons in stratum pyramidale. *Eur. J. Neurosci.* 12, 3975–84. doi: 10.1046/j.1460-9568.2000.00290.x

Zhang, Z., Sun, J., and Reynolds, G. P. (2002). A selective reduction in the relative density of parvalbumin-immunoreactive neurons in the hippocampus in schizophrenia patients. *Chin. Med. J.* 115, 819–23.

**Conflict of Interest:** The authors declare that the research was conducted in the absence of any commercial or financial relationships that could be construed as a potential conflict of interest.

*Copyright © 2020 Young and Song. This is an open-access article distributed under the terms of the Creative Commons Attribution License (CC BY). The use, distribution or reproduction in other forums is permitted, provided the original author(s) and the copyright owner(s) are credited and that the original publication in this journal is cited, in accordance with accepted academic practice. No use, distribution or reproduction is permitted which does not comply with these terms.*

frontiers in Molecular Neuroscience

ORIGINAL RESEARCH
published: 20 March 2020
doi: 10.3389/fnmol.2020.00044

# Neurosteroids as Selective Inhibitors of Glycine Receptor Activity: Structure-Activity Relationship Study on Endogenous Androstanes and Androstenes

*Julia V. Bukanova[1], Elena I. Solntseva[1]* and Eva Kudova[2]**

[1] Research Center of Neurology, Moscow, Russia, [2] Institute of Organic Chemistry and Biochemistry, Czech Academy of Sciences, Prague, Czechia

The ability of androstane and androstene neurosteroids with modifications at C-17, C-5, and C-3 (compounds **1**-**9**) to influence the functional activity of inhibitory glycine and γ-aminobutyric acid (GABA) receptors was estimated. The glycine- and GABA-induced chloride current ($I_{Gly}$ and $I_{GABA}$) were measured in isolated pyramidal neurons of the rat hippocampus and isolated rat cerebellar Purkinje cells, correspondingly, using the patch-clamp technique. Our results demonstrate that all the nine neurosteroids display similar biological activity, namely, they strongly inhibited $I_{Gly}$ and weakly inhibited $I_{GABA}$. The threshold concentration of neurosteroids inducing effects on $I_{Gly}$ was 0.1 μM, and for effects on $I_{GABA}$ was 10–50 μM. Moreover, our compounds accelerated desensitization of the $I_{Gly}$ with the $IC_{50}$ values varying from 0.12 to 0.49 μM and decreased the peak amplitude with $IC_{50}$ values varying from 16 to 22 μM. Interestingly, our study revealed that only compounds **4** (epiandrosterone) and **8** (dehydroepiandrosterone) were able to cause a significant change in $I_{GABA}$ in 10 μM concentration. Moreover, compounds **3** (testosterone), **5** (epitestosterone), **6** (dihydroandrostenedione), and **9** (etiocholanedione) did not modulate $I_{GABA}$ up to the concentration of 50 μM. Thus, we conclude that compounds **3**, **5**, **6**, and **9** may be identified as selective modulators of $I_{Gly}$. Our results offer new avenues of investigation in the field of drug-like selective modulators of $I_{Gly}$.

**Keywords: neurosteroid, GABA receptor, glycine receptor, androstane, androstene, structure-activity relationship**

OPEN ACCESS

***Edited by:***
*Steven James Mennerick, Washington University in St. Louis, United States*

***Reviewed by:***
*Joseph Henry Steinbach, Washington University in St. Louis, United States*
*Enrico Sanna, University of Cagliari, Italy*

****Correspondence:***
*Elena I. Solntseva*
*synaptology@mail.ru*
*Eva Kudova*
*kudova@uochb.cas.cz*

***Received:*** *09 December 2019*
***Accepted:*** *04 March 2020*
***Published:*** *20 March 2020*

***Citation:***
*Bukanova JV, Solntseva EI and Kudova E (2020) Neurosteroids as Selective Inhibitors of Glycine Receptor Activity: Structure-Activity Relationship Study on Endogenous Androstanes and Androstenes. Front. Mol. Neurosci. 13:44. doi: 10.3389/fnmol.2020.00044*

## INTRODUCTION

γ-Aminobutyric acid receptors type A and glycine receptor ($GABA_AR$ and GlyR) channels are the major inhibitory ligand-gated ion channels of the central nervous system which mediate both fast synaptic and tonic extrasynaptic inhibition (Lynch, 2009; Ziegler et al., 2009; Yevenes and Zeilhofer, 2011). Disturbance of functional activity of GlyRs and $GABA_ARs$ underlies many neurological disorders. Dysfunction of $GABA_ARs$ leads to channelopathies associated with epilepsy, insomnia, anxiety, and chronic pain (Möhler, 2006). Malfunctions of GlyR have been linked to a range of neurological disorders caused by mutations in genes which encode GlyR subunits, including hyperekplexia (mutations in the GlyR α1-subunit gene) (Lynch, 2004) or autism (mutations in the human GlyR α2-subunit gene) (Dougherty et al., 2013; Zhang et al., 2017). Finally, the α3 GlyRs

have emerged as a promising therapeutic target for chronic pain, as the selective enhancement of the magnitude of the α3 GlyR current has been shown to exhibit analgesic effects in animal models of inflammatory pain (Lynch et al., 2017). In summary, diminished glycinergic inhibition (e.g., hyperekplexia, autism) would benefit most from facilitated glycinergic inhibition, through positive allosteric GlyR modulators. Interestingly, GlyRs modulation also plays a crucial role in synaptogenesis (Ganser and Dallman, 2009), neurite outgrowth (Tapia et al., 2000), or produces neuroprotection against metabolic stress such as oxygen/glucose deprivation (Tanabe et al., 2010). Given these considerations, GlyR-modulating compounds offer great potential for research on novel drug-like compounds.

The function of GlyRs can be modulated by various ligands, including neurosteroids (NS). Neurosteroids are compounds that accumulate in the nervous system independently of the steroidogenic endocrine glands and which can be synthesized *de novo* in the nervous system from cholesterol or other steroidal precursors imported from peripheral sources (Baulieu, 1998). The steroid numbering, ring letters, stereochemistry and nomenclature is summarized in **Figure 1**. The biosynthetic pathway (Do Rego et al., 2009) of NS (**Figure 2**) is triggered by the conversion of cholesterol to pregnenolone (PREG). Then, PREG is converted to progesterone (PROG) and dehydroepiandrosterone (DHEA). Subsequently, PROG is metabolized to 5α- or 5β-dihydroprogesterone, followed by their reduction to 3α-hydroxy-5α-pregnan-20-one (allopregnanolone) or 3α-hydroxy-5β-pregnan-20-one (pregnanolone).

These compounds and their synthetic analogs are mainly known as potent modulators of $GABA_A$Rs (Chen et al., 2019) and *N*-methyl-*D*-aspartate receptors (NMDARs) (Burnell et al., 2019), respectively. Neurosteroids and their synthetic analogs (neuroactive steroids, NAS) have been extensively studied during last three decades as they modify neuronal activity and thus brain function via a fast, non-genomic action (Rebas et al., 2017), by acting as allosteric modulators of various ligand-gated ion channels, including $GABA_A$R and GlyR. In brief, NS and NAS are effective modulators of $GABA_A$R-induced chloride current ($I_{GABA}$) and their modulatory action is dependent on their structure and subtype (for a review, see: Majewska et al., 1988; Wu et al., 1990; Belelli and Lambert, 2005; Korinek et al., 2011; King, 2013; Zorumski et al., 2013). Those that potentiate GABA activity are termed as "potentiating NS" and these include, e.g., allopregnanolone (3α-hydroxy-5α-pregnan-20-one) or pregnanolone (3α-hydroxy-5β-pregnan-20-one) (Park-Chung et al., 1999). The α-configuration at C-3 is extremely important for potentiating steroids, contrasting with a relatively vague requirement for a 3α/3β-configuration for "inhibitory NS" that are referred to as those that antagonize $I_{GABA}$ (Park-Chung et al., 1999). The inhibitory NS incorporate mainly a subclass known as the C-3 sulfated steroids (e.g., pregnenolone sulfate and DHEA sulfate) (Gibbs et al., 2006) or the C-3 hemiester steroids (e.g., pregnanolone hemisuccinate) (Seljeset et al., 2015), although C-3 negative charge is not obligatory for the inhibition (e.g., DHEA). The relevance of configuration or double bond at C-5 for the potentiation/inhibitory action is driven by its combination with α/β-configuration at C-3 (Park-Chung et al., 1999) that define a planar or "bent-shape" of the molecule (**Figure 1E**). Interestingly, the nature of the group at C-17, concerning inhibition, is less stringent given that 17-acetyl, 17-acetoxy, and 17-keto groups substituted onto a 3β-hydroxy-androst-5-ene retain similar inhibitory activities. On the other hand, 17-acetyl, 17-acetoxy, 17-hydroxyl or 17-keto groups substituted onto a 3α-hydroxy-5α-androstane exhibit markedly various enhancement of $I_{GABA}$ varying up to 9-folds (Park-Chung et al., 1999). For example, the reduction of the C-20 ketone of 3α-hydroxy-5α-pregnane-20-one to its 20α-hydroxy analog greatly decreases the efficacy of potentiation 166% vs. 1373%.

The GlyR-induced chloride current ($I_{Gly}$) has been also shown to be modulated by NS, but the data on potencies are rather limited to compounds with a pregnane skeleton (**Figure 1F**). Allopregnanolone (**Figure 2**) enhanced the glycine-induced current of native or recombinant receptors (Weir et al., 2004; Jiang et al., 2006), while Fodor et al. (2006) showed that micromolar concentrations of allopregnanolone blocked GlyRs of native cells. These variances may be ascribed to the difference between neuronal and recombinant GlyRs (Kung et al., 2001). Next, pregnanolone (**Figure 2**) proved to be an inhibitor of both α1 GlyRs and native cells (Weir et al., 2004; Fodor et al., 2006; Jiang et al., 2006). Finally, 3β-hydroxy-5α-pregnan-20-one and 3β-hydroxy-5β-pregnan-20-one were demonstrated as inactive on both neurons and recombinant α1 receptors (Wu et al., 1990; Weir et al., 2004). Interestingly, PROG exhibited incomplete and non-competitive inhibition of GlyR currents in contrast to the full and competitive inhibition by its sulfated analog (PREG-S) of chick spinal cord (Wu et al., 1997) and selectively inhibited embryonic α2 GlyRs, with no effect on α1 and α1β GlyRs (Maksay et al., 2001). To date, only three androstane compounds were tested – DHEA sulfate and 3β-hydroxy-5α-androstan-17-one, and 3α-hydroxy-5α-androstan-17-one inhibited $I_{Gly}$ currents in micromolar range on recombinant α1 receptors (Maksay et al., 2001). As such, the biological potential of androstane and androstene skeletons (**Figure 1F**) concerning their effect on GlyR remains unknown.

In our previous work, a series of pregnanolone derivatives (modulators of NMDA receptors) displayed the effects on the $I_{GABA}$ and $I_{Gly}$ in rat pyramidal hippocampal neurons (Bukanova et al., 2018). Interestingly, we demonstrated that the nature of the substituent at C-3 defines the positive or negative character of $I_{GABA}$. Indeed, pregnanolone glutamate was found to potentiate $I_{GABA}$, while pregnanolone hemisuccinate and pregnanolone hemipimelate inhibited $I_{GABA}$, and all three steroids inhibited $I_{Gly}$. The conversion of the 5β-pregnanolone skeleton into an 5β-androstane skeleton, an analog that lacks the C-17 acetyl moiety, eliminated the effects on both $GABA_A$Rs and GlyRs.

As mentioned previously, the modulatory effect of NS on $GABA_A$Rs or GlyRs is a relevant avenue of investigation in neuropharmacology. To understand the structure-activity relationship of NS on $I_{GABA}$ and $I_{Gly}$, further structure-activity relationship studies (SAR) are required. In the present study, we examine the effects of a series of endogenous NS on the GABA- and Gly-induced current in voltage-clamped rat cerebellar Purkinje cells and rat hippocampal neurons, respectively. This series contained 9 natural NS with an androstane and androstene

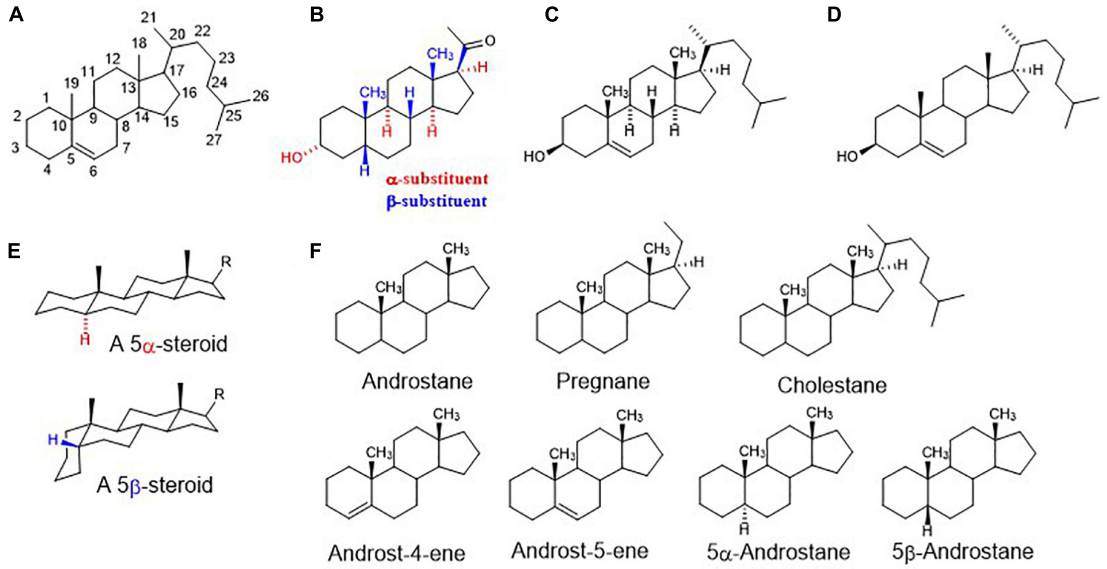


**FIGURE 1 | (A)** Steroid numbering and ring letters; **(B)** schematic orientation of substituents. When the rings of a steroid are denoted as projections onto the plane of the paper, the α-substituent (hashed bond) lies below and the β-substituent (bold bond) lies above the plane of the paper; **(C)** explicitly written configuration for all sterocenters of cholesterol; **(D)** unless implied or stated to the contrary in figures and schemes, the stereochemistry of steroid molecule is simplified. Depicted structure implies that atoms or groups attached at the bridgehead positions 8, 9, 14, and 17 are oriented as shown in formula C (8β,9α,14α). Angular methyles ($CH_3$) at positions 10, 13 are omitted and shown only as bold bonds; **(E)** a perspective representation of planar 5α-steroid and a bent molecule of 5β-steroid; **(F)** fundamental names of steroid skeletons relevant to this paper.

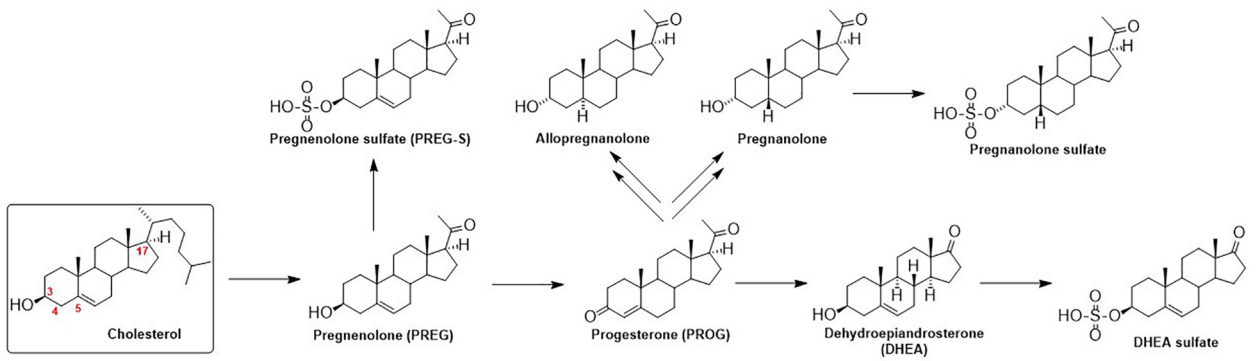


**FIGURE 2 |** Schematic illustration of neurosteroid biosynthesis.

skeleton with variable substituents at C-3, C-5, and C-17 positions (**Table 1**).

## MATERIALS AND METHODS

### Cell Preparation

All experiments were conducted per the requirements of the Ministry of Public Health of the Russian Federation and were consistent with the EU directive for Use of Experimental Animals of the European Community. The study was approved by the Ethics Committee of the Scientific Center of Neurology, Protocol No. 2-5/19 of 02.20.19. The cells were isolated from transverse hippocampal slices as described in detail elsewhere (Vorobjev, 1991). Briefly, the slices (200–500 μm) of Wistar rats (11–14 days of age) hippocampus or cerebellum were incubated at room temperature for at least 2 h in a solution containing the following components (in mM): 124 NaCl, 3 KCl, 2 $CaCl_2$, 2 $MgSO_4$, 25 $NaHCO_3$, 1.3 $NaH_2PO_4$, 10 D-glucose, pH 7.4. The saline was continuously stirred and bubbled with carbogen (95% $0_2$ + 5% $CO_2$). Single pyramidal neurons from the hippocampal CA3 area or Purkinje cells from sagittal slices of the cerebellum were isolated by a vibrating fused glass pipette with a spherical tip.

### Current Recordings

Isolated neurons were patch clamped and then lifted into the outflow of the control bath solution. Bath solution flowed

**TABLE 1 |** Structure-activity relationship study overview for compounds **1**-**9**: their chemical names, structures, $\tau_{des}$ ($I_{Gly}$ vs. $I_{GABA}$) values.

| Cmpd. | Chemical name | Common name | Structure | [a]$\tau_{des}$ | |
|---|---|---|---|---|---|
| | | | | $I_{Gly}$ | $I_{GABA}$ |
| 1 | 17β-Hydroxyandrost-4-en-3-one | Testosterone | 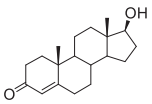 | −67% | [b]No effect |
| 2 | Androst-4-en-3,17-dione | Androstenedione | 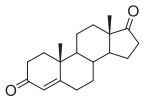 | −84% | [b]No effect |
| 3 | 17β-Hydroxy-5α-androstan-3-one | 5α- Dihydrotestosterone | 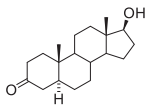 | −82% | [c]No effect |
| 4 | 3β-Hydroxy-5α-androstan-17-one | Epiandrosterone | 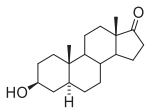 | −64% | −20% |
| 5 | 17α-Hydroxyandrost-4-en-3-one | Epitestosterone | 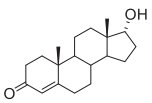 | −72% | [c]No effect |
| 6 | 5α-Androstane-3,17-dione | Dihydroandrostenedione | 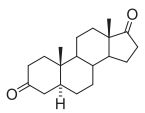 | −72% | [c]No effect |
| 7 | 3β,17β-Androst-5-ene-3,17-diol | Androstenediol | 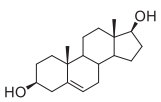 | −70% | [b]No effect |
| 8 | 3β-Hydroxy-androst-5-en-17-one | Dehydroepiandrosterone (DHEA) | 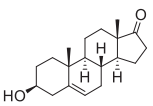 | −79% | −12% |
| 9 | 5β-Androstane-3,17-dione | Etiocholanedione | 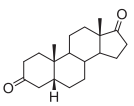 | −68% | [c]No effect |

*The first column gives number of compound, second gives the chemical name, the third column indicates a common name accepted for this compound, and the fourth column shows its structure. The effect of compounds **1**-**9** at 10 μM concentration on the value of time constant of desensitization ($\tau_{des}$) of the $I_{Gly}$ and $I_{GABA}$ is expressed in the fifth column. [a]The effect of compounds **1**-**9** on the value of time constant of desensitization ($\tau_{des}$) of the $I_{Gly}$ and $I_{GABA}$. [b]Compounds did not modulate $I_{GABA}$ up to the concentration of 10 μM. [c]Compounds did not modulate $I_{GABA}$ up to the concentration of 50 μM.*

through a tube with a diameter of 1.5 mm at a speed of 0.6 ml/min. The substances were applied through glass capillary, 0.1 mm in diameter, which could be rapidly displaced laterally (Vorobjev et al., 1996). A fast perfusion technique allows a complete exchange of external solution surrounding a neuron within 20 ms. Glycine-activated currents ($I_{Gly}$) and GABA-activated currents ($I_{GABA}$) in isolated neurons were induced by a step application of agonist for 600–1000 ms with 30–40 s intervals. Transmembrane currents were recorded using a conventional patch-clamp technique in the whole-cell configuration. Patch-clamp electrodes had a tip resistance of ∼2 MΩ. The solution in the recording pipette contained the following (in mM): 40 CsF, 100 CsCl, 0.5 $CaCl_2$, 5 EGTA, 3 $MgCl_2$, 4 NaATP, 5 HEPES, pH 7.3. The composition of the extracellular solution was as follows (in mM): 140 NaCl, 3 KCl, 3 $CaCl_2$, 3 $MgCl_2$, 10 D-glucose, 10 HEPES hemisodium, and pH 7.4. Recording of the currents was performed using EPC7 patch-clamp amplifier (HEKA Electronik, Germany). The holding potential was maintained at −70 mV. Transmembrane currents were filtered at 3 kHz, stored and analyzed with IBM-PC computer, using homemade software.

## Reagents

All the drugs used for intracellular and extracellular solutions were purchased from Sigma-Aldrich (United States). Compounds **1**-**9** are available from Sigma-Aldrich or Carbosynth under the following CAS and catalog numbers: compound **1** (Sigma, CAS 58-22-0, Cat. No. T1500), compound **2** (Sigma, CAS 63-05-8, Cat. No. 46033), compound **3** (Sigma, CAS 521-18-6, Cat. No. A8380), compound **4** (Sigma, CAS 481-29-8, Cat. No.

E3375), compound **5** (Sigma, CAS 481-30-1, Cat. No. 1646031), compound **8** (CAS 53-43-0, Cat No. D4000). Compound **7** (CAS 521-17-5) was prepared by sodium borohydride reduction from compound **8** according to the literature (Liu et al., 2012). Compound **6** (CAS 846-46-8) and compound **9** (CAS 1229-12-5) were prepared by Jones oxidation from compound **5** and 3α-hydroxy-5β-androstan-17-one (Sigma, CAS 53-42-9, Cat. No. E5126), respectively, according to the literature (Katona et al., 2008). The purity of all used steroids was >95%. The tested substances were dissolved in 100% DMSO to make 10 mM stock solution, which was aliquoted and stored at −20°C. Then, drugs were dissolved in external saline to the final concentrations immediately before the experiments. The maximal percentage of solvent in the tested drug solutions was 1%. The $I_{Gly}$ and $I_{GABA}$ were measured in the presence of 1% DMSO ($n$ = 6), and any current changes was not found under these conditions.

## Data Analysis

Statistical analysis was performed with the help of *Prism Graphpad* software. All comparisons were made with ANOVA-test using Dunnett's multiple comparison test and Student's unpaired $t$-test at a significance level of $p$ = 0.05. $N$ = 5–8 cells from 3 to 4 animals for every concentration. In results descriptions, mean and standard error of the mean (SEM) are specified. The meanings of asterisks (probability levels) in figures is the following: $^{*}P < 0.05$, $^{**}P < 0.01$. The $IC_{50}$ values for steroids inhibition of the $I_{Gly}$ and $I_{GABA}$ were determined using the equation: $Y = 1 - [\max/(1 + (IC_{50}/C)^{n})]$, where *max* is the maximum inhibition attainable, $C$ is the concentration of steroid, $IC_{50}$ is the half-maximal inhibitory concentration and $n$ is the slope factor (Hill coefficient).

# RESULTS

## Effect of Neurosteroids 1-9 on the $I_{Gly}$ and $I_{GABA}$

The effects of compounds **1**-**9** (**Table 1**) were studied at a concentration range of 0.01–100 μM on isolated rat hippocampal neurons and rat cerebellar Purkinje cells. First, the ability of steroids to affect the holding current at voltage-clamp regime was tested. We have found that compounds **1**-**9** by themselves did not cause any currents through the cell membrane (data not shown). Next, the influence of compounds **1**-**9** on glycine-activated chloride current ($I_{Gly}$) and GABA-activated chloride current ($I_{GABA}$) were evaluated. The experiments with $I_{Gly}$ were conducted on rat hippocampal neurons, and experiments with $I_{GABA}$ were conducted on rat cerebellar Purkinje cells. The $I_{Gly}$ is larger in amplitude and more stable on hippocampal cells, and, conversely, the $I_{GABA}$ is more convenient to study on Purkinje cells, since GABA receptors on Purkinje cells are more homogeneous (Kelley et al., 2013). Glycine (100 μM) and GABA (5 μM) were applied to the neurons through an application pipette during 600–1000 ms and compounds **1**-**9** were added to the same pipette in different concentrations (0.01–100 μM). Our experiments demonstrate that neuronal GlyRs are highly sensitive, whilst neuronal $GABA_A$Rs are weakly sensitive to tested compounds **1**-**9**.

## Effects of Compounds 1-9 on the $I_{Gly}$

Short (600–1000 ms) application of 100 μM glycine on pyramidal neurons of rat hippocampus evoked $I_{Gly}$ which amplitude and kinetics were dependent on glycine concentration with an $EC_{50}$ value of 90 ± 7 μM. An average value of the reversal potential of $I_{Gly}$ −9.6 ± 0.8 mV matched well the chloride reversal potential calculated for the chloride concentrations used (−9.5 mV, not shown). We used agonist concentration of 100 μM that was near $EC_{50}$, because it allow to achieve stable current with well visible and measurable either suppressive or augmenting effect. All 9 compounds caused a similar effect on the $I_{Gly}$, which consisted of two components: acceleration of desensitization and decrease in peak amplitude. The effects were reversible upon washout during 1–2 min. The effect of desensitization acceleration developed at significantly lower concentrations of NS than the effect of peak amplitude suppression. Noteworthy, the threshold concentration of NS for initiating the effect of desensitization acceleration was 0.1 μM, while the threshold concentration of the same compounds for developing the effect of the peak amplitude reduction was 10 μM. A representative effect of NS on $I_{Gly}$ of one cell is shown in **Figure 3A**. Compound **1** in low concentrations of 0.1 and 1 μM accelerated desensitization without effect on the peak amplitude, while at a concentration of 10 and 100 μM it causes two effects: acceleration of desensitization and a decrease in peak amplitude. The effects of the remaining eight NS on the $I_{Gly}$ did not differ significantly from the testosterone effect (for details, see **Figures 3B,C** and **Table 2**). When co-applied with glycine, NS at concentration 0.1 μM barely affected the $I_{Gly}$ peak amplitude but decreased the time constant of $I_{Gly}$ desensitization ($\tau_{des}$) by 27–35% ($P < 0.01$ or $P < 0.05$). On the contrary, when applied at a concentration of 10 μM, NS accelerated desensitization by 67–82% ($P < 0.01$) and reduced the peak current amplitude by 18–25% ($P < 0.01$ or $P < 0.05$). **Figure 4** shows the concentration dependence of the NS effect on the normalized peak amplitude (**Figure 4A**) and normalized $\tau_{des}$ of the $I_{Gly}$ (**Figure 4C**). An increase in the concentration of NS up to 100 μM caused a decrease in the peak amplitude of the $I_{Gly}$ by 45–70% with the $IC_{50}$ values of 16–22 μM (**Figure 4B** and **Table 3**). Maximal decrease (70–90%) of the $\tau_{des}$ can be observed in the presence of 10 μM of NS. The $IC_{50}$ values for the effect on the $\tau_{des}$ are in the range of 0.12–0.49 μM (**Figures 4C,D** and **Table 3**), which are two orders of magnitude lower than the $IC_{50}$ values for the effect on peak amplitude.

## Effects of Compounds 1-9 on the $I_{GABA}$

The brief application of GABA for 600–1000 ms on isolated Purkinje cells evoked a chloride current ($I_{GABA}$) with an amplitude-dependent on GABA concentration with an $EC_{50}$ value of 7.5 ± 2.9 μM. The specific antagonist of $GABA_A$ receptors bicuculline (3 μM) reversibly blocked the current (data not shown), which allows us to classify the receptors as $GABA_A$ type. We studied $I_{GABA}$ evoked by 5 μM of GABA. **Figure 5** shows the effects of NS on $I_{GABA}$. Our experiments demonstrate that $GABA_A$Rs are much less sensitive to the studied NS than

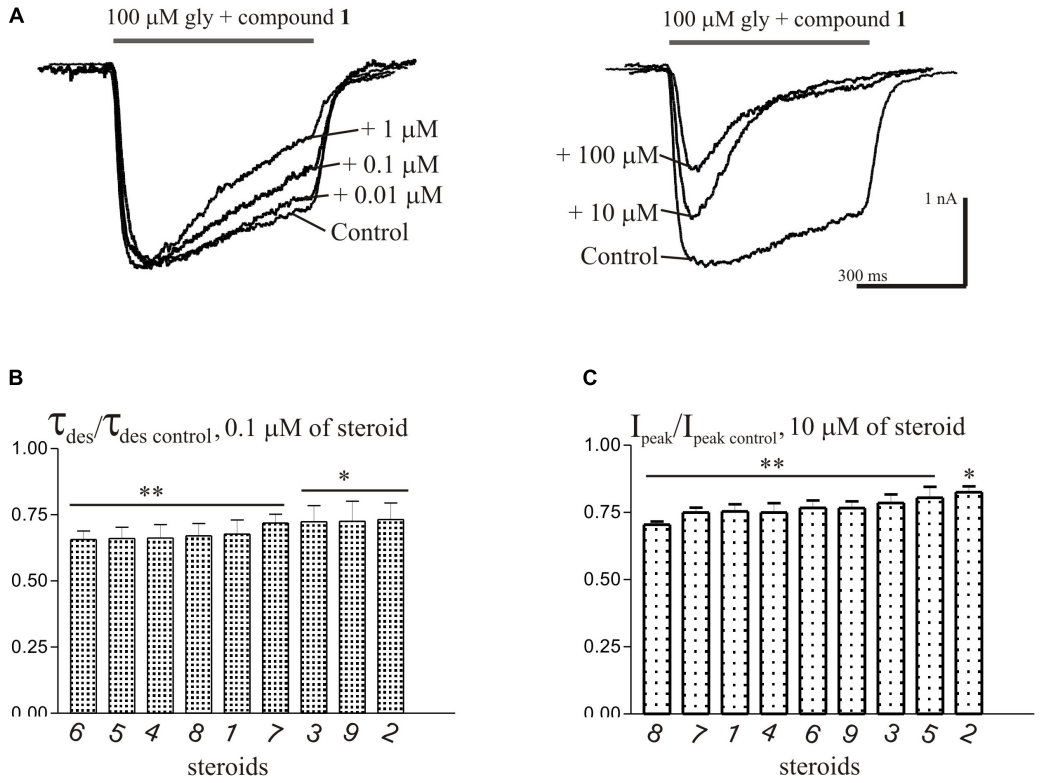


**FIGURE 3 |** The effects of compounds **1**-**9** on $I_{Gly}$ of hippocampal neurons. **(A)** Representative traces of $I_{Gly}$ induced by 600 ms application of 100 μM glycine, obtained in control and the presence of 0.01, 0.1, and 1 μM (left), or 10 and 100 μM (right) of testosterone (compound **1**). **(B)** Mean ± SEM of the normalized values of the time constant of desensitization ($\tau_{des}$) of $I_{Gly}$ in the presence of 0.1 μM of compounds **1**-**9**. **(C)** Mean ± SEM of the normalized values of the peak amplitude of $I_{Gly}$ in the presence of 10 μM of compounds **1**-**9**. Results show greater action of NS on desensitization than on peak amplitude of $I_{Gly}$. Probability levels were estimated with ANOVA-test using Dunnett's multiple comparison test.

GlyRs. The addition of compounds **1**, **2**, **3**, **5**, **7**, **9** to the applicator pipette at a concentration of 0.1–10 μM did not change either the peak amplitude or the rate of decay of $I_{GABA}$. Only two out of nine compounds – compounds **4** and **8** – in 10 μM concentration were able to cause a significant change in $I_{GABA}$, which consisted of the acceleration of decay (**Figures 5A,B** and **Table 4**). When the concentration of the tested compound was increased up to 50 μM, compounds **3**, **5**, **6**, and **9** remained inactive. In contrast, compounds **1**, **2**, **4**, **7**, and **8** at 50 μM concentration showed an inhibitory effect with a decrease in the peak amplitude of the current by 14–25% ($P < 0.01$ or $P < 0.05$) and the acceleration of its decay by 23–45% ($P < 0.01$) (**Figure 5** and **Table 4**). **Figure 6** shows a comparison of the effects of compounds **1**-**9** on the $I_{Gly}$ and the $I_{GABA}$. Our results demonstrate that tested NS in the concentration of 10 μM cause strong action on $I_{Gly}$ and weak action on $I_{GABA}$.

**TABLE 2 |** The inhibitory effect of the tested neurosteroids on the time constant of desensitization ($\tau_{des}$) and peak amplitude ($I_{peak}$) of the $I_{Gly}$. Mean ± SEM of the normalized values of the $\tau_{des}$ and $I_{peak}$ of the $I_{Gly}$ are shown.

| Cmpd. | $\tau_{des}/\tau_{des\ control}$, 0.1 μM of steroid | *P*-value | n | $I_{peak}/I_{peak\ control}$ 10 μM of steroid | *P*-value | n |
|---|---|---|---|---|---|---|
| 1 | 0.68 ± 0.05 | 0.0055 | 5 | 0.75 ± 0.03 | 0.0006 | 7 |
| 2 | 0.73 ± 0.06 | 0.0199 | 5 | 0.82 ± 0.02 | 0.0199 | 7 |
| 3 | 0.72 ± 0.06 | 0.0186 | 5 | 0.78 ± 0.03 | 0.0037 | 8 |
| 4 | 0.66 ± 0.05 | 0.0033 | 5 | 0.75 ± 0.03 | 0.0023 | 7 |
| 5 | 0.66 ± 0.04 | 0.0014 | 7 | 0.80 ± 0.04 | 0.0181 | 7 |
| 6 | 0.65 ± 0.03 | 0.0002 | 8 | 0.76 ± 0.03 | 0.0011 | 8 |
| 7 | 0.72 ± 0.03 | 0.0013 | 8 | 0.75 ± 0.02 | 0.0004 | 7 |
| 8 | 0.67 ± 0.05 | 0.0027 | 5 | 0.70 ± 0.01 | 0.0003 | 7 |
| 9 | 0.72 ± 0.07 | 0.0358 | 5 | 0.77 ± 0.03 | 0.0006 | 7 |

*All comparisons with control value were made with unpaired Student's t-test. Significance level of P = 0.05. n- the number of cells used.*

## DISCUSSION

In the present study, we examined the effects of a series of endogenous NS on the GABA- and Gly-induced current in rat central neurons. It is known that NS modulate $GABA_A$Rs and GlyRs functions in subunit-specific manner (Maksay et al., 2001; Belelli and Lambert, 2005) and this has implications for native receptors that may differentiate throughout development. We used in our experiments Wistar rats at 11–14 days of age where GlyRs and $GABA_A$Rs were studied in pyramidal hippocampal neurons and cerebellar Purkinje cells, accordingly. Literature

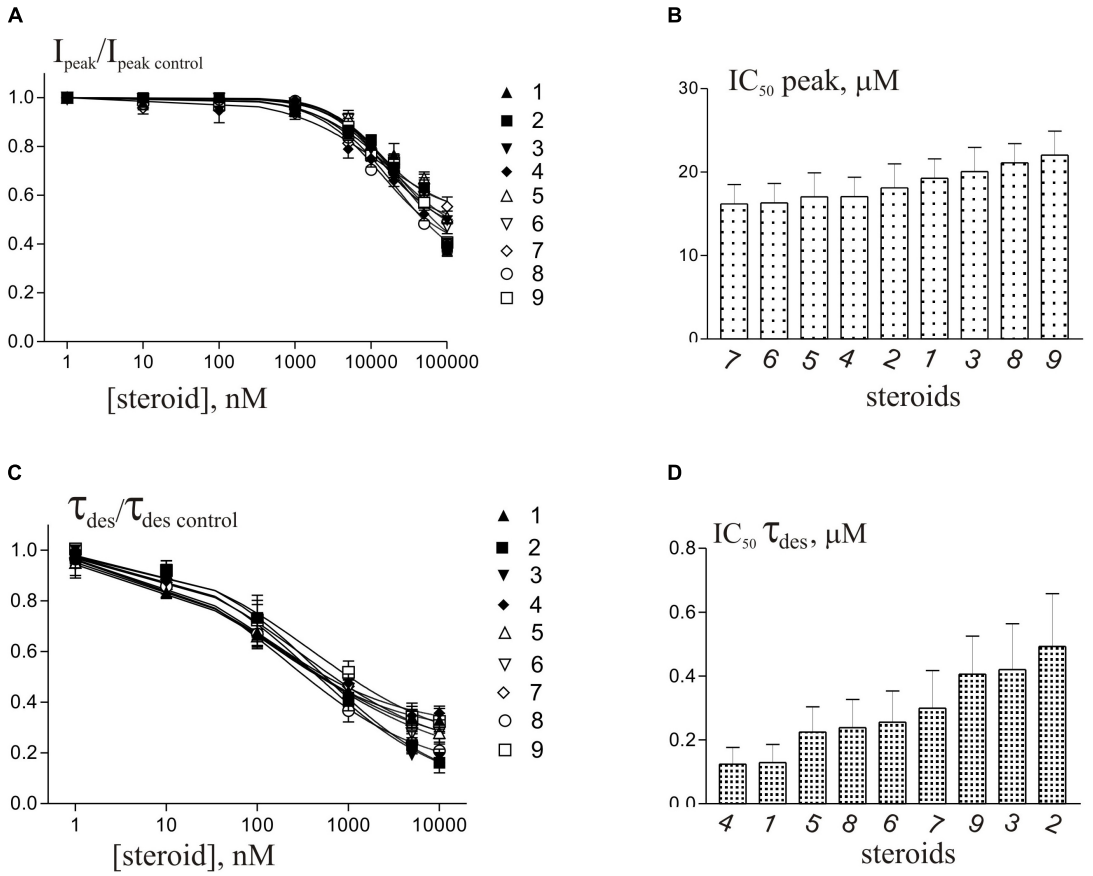


**FIGURE 4 |** Concentration dependence of NS effects on the $I_{Gly}$ of hippocampal neurons. **(A)** Concentration dependence of compounds **1**-**9** effect on the normalized peak amplitude of $I_{Gly}$. Data were fitted with the Hill equation (see section Materials and Methods). **(B)** Mean ± SEM of the $IC_{50}$ values calculated for the effect of inhibition by NS of the peak amplitude of $I_{Gly}$. **(C)** Concentration dependence of compounds **1**-**9** effect on the normalized $\tau_{des}$ of $I_{Gly}$. Data were fitted with the Hill equation. **(D)** Mean ± SEM of the $IC_{50}$ values calculated for the effect of accelerating desensitization (decrease in the $\tau_{des}$) of $I_{Gly}$ by NS.

**TABLE 3 |** The values of the maximum inhibition attainable (*max*), the half-maximal inhibitory concentration ($IC_{50}$) and the slope factor (Hill coefficient) for the effects of tested steroids on the peak amplitude ($I_{peak}$) and $\tau_{des}$ of the $I_{Gly}$.

| Cmpd. | $I_{peak}$ | | | $\tau_{des}$ | | |
|---|---|---|---|---|---|---|
| | ***max*** | **$IC_{50}$ (μM)** | **Hill coefficient** | ***max*** | **$IC_{50}$ (μM)** | **Hill coefficient** |
| 1 | 0.58 ± 0.10 | 19.3 ± 2.3 | 1.1 ± 0.32 | 0.72 ± 0.08 | 0.13 ± 0.06 | 0.58 ± 0.20 |
| 2 | 0.55 ± 0.09 | 18.1 ± 2.9 | 1.1 ± 0.36 | 0.97 ± 0.10 | 0.49 ± 0.16 | 0.60 ± 0.11 |
| 3 | 0.61 ± 0.08 | 20.1 ± 2.8 | 0.86 ± 0.15 | 0.97 ± 0.11 | 0.42 ± 0.14 | 0.58 ± 0.13 |
| 4 | 0.64 ± 0.08 | 17.1 ± 2.3 | 0.97 ± 0.21 | 0.70 ± 0.07 | 0.12 ± 0.05 | 0.59 ± 0.16 |
| 5 | 0.46 ± 0.09 | 17.0 ± 2.9 | 1.2 ± 0.34 | 0.81 ± 0.11 | 0.22 ± 0.08 | 0.51 ± 0.15 |
| 6 | 0.51 ± 0.05 | 16.3 ± 2.4 | 1.2 ± 0.35 | 0.86 ± 0.10 | 0.26 ± 0.09 | 0.48 ± 0.10 |
| 7 | 0.52 ± 0.09 | 16.2 ± 2.3 | 0.71 ± 0.16 | 0.81 ± 0.09 | 0.29 ± 0.12 | 0.56 ± 0.13 |
| 8 | 0.73 ± 0.08 | 21.3 ± 2.2 | 0.92 ± 0.14 | 0.88 ± 0.09 | 0.24 ± 0.09 | 0.57 ± 0.14 |
| 9 | 0.68 ± 0.09 | 22.0 ± 2.8 | 1.0 ± 0.19 | 0.79 ± 0.11 | 0.40 ± 0.12 | 0.56 ± 0.14 |

*The fits were made to the averaged data with the fitting program.*

data indicate that starting from the second postnatal week, the subunit composition of GlyR in the hippocampal neurons (Aroeira et al., 2011) and $GABA_AR$ in the Purkinje cells of the cerebellum (Laurie et al., 1992) is close to that in the brain of adult animals. Extrasynaptic GlyRs with different subunit composition are described in pyramidal hippocampal neurons. There may be either heteromeric receptors with α (1, 2, or 3) and β subunits, or homomeric ones with multiple α subunits (for review, see Keck and White, 2009; Xu and Gong, 2010). The major adult isoform of $GABA_ARs$ in Purkinje cells was shown to be composed of $\alpha_1\beta_2\gamma_2$

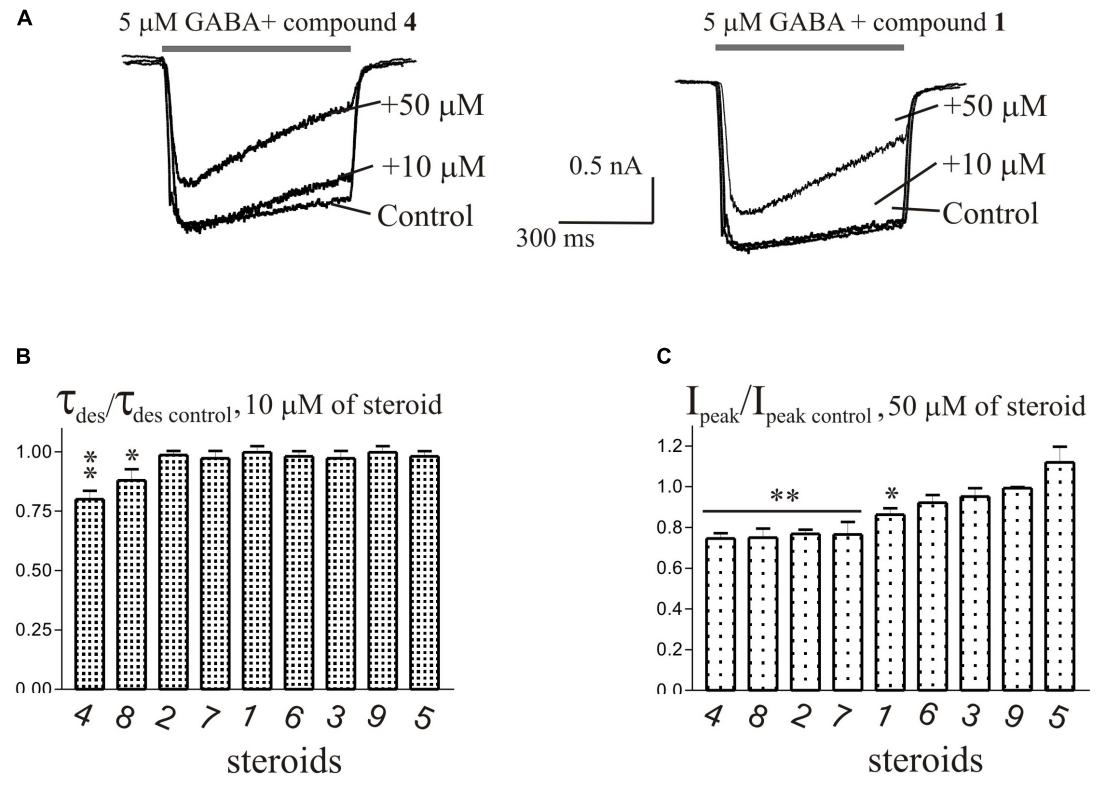


**FIGURE 5 |** The effects of compounds **1**-**9** on $I_{GABA}$ of cerebellar Purkinje cells. **(A)** Representative traces of $I_{GABA}$ induced by 600 ms application of 5 μM GABA, obtained in control and the presence of 10 and 50 μM of compound **4** (epiandrosterone) (left), or compound **1** (testosterone) (right). **(B)** Mean ± SEM of the normalized values of the time constant of desensitization ($\tau_{des}$) of $I_{GABA}$ in the presence of 10 μM of compounds **1**-**9**. **(C)** Mean ± SEM of the normalized values of the peak amplitude of $I_{GABA}$ in the presence of 50 μM of compounds **1**-**9**. Probability levels were estimated with ANOVA-test using Dunnett's multiple comparison test.

subunits and with a subunit stoichiometry of 2:2:1 (Pirker et al., 2000; Sieghart and Savić, 2018).

The series of steroids we studied included endogenous androstane and androstene NS (compounds **1**-**9**) with variable substituents at positions C-3, C-5, and C-17 (**Table 1**). In brief, compounds **1**, **3**, **7,** and **5** bear 17β- and 17α-hydroxyl groups, respectively. Compounds **2**, **4**, **6**, **8,** and **9** have a carbonyl group at C-17. Compounds **1**, **2**, **5**, **7**, and **8** have a double bond in their skeleton and as such belong to a family of androstene steroids. Oppositely, compounds **3**, **4**, **6** (5α-H), and **9** (5β-H) are fully saturated androstanes. The results of our study show that biological activity is similar for all compounds. In summary, compounds **1**-**9** at a concentration up to 10 μM strongly affected $I_{Gly}$ and had weak action on $I_{GABA}$. The effect of NS on $I_{Gly}$ contained two components: a decrease in peak amplitude and an acceleration of decay. The effect of NS on $I_{Gly}$ decay and the associated decrease in time constant of desensitization ($\tau_{des}$) was 2–3 times stronger than on the peak of $I_{Gly}$. Such a different regulation of these two $I_{Gly}$ parameters by NS suggests the existence of two independent mechanisms of their action on GlyRs, one of which regulates the peak amplitude, and the second – the desensitization process. This assumption is supported by our previous research (Bukanova et al., 2018), where it was shown that these two effects of NS afford different outcome with increasing glycine concentration. Namely, the effect on the peak amplitude of $I_{Gly}$ disappeared and the acceleration of desensitization remained. The fact that peak inhibition is reduced at higher agonist concentration suggest that inhibiting drugs act as competitive inhibitors of agonist

**TABLE 4 |** The inhibitory effect of the tested neurosteroids on the peak amplitude ($I_{peak}$) and time constant of desensitization ($\tau_{des}$) of the $I_{GABA}$.

| Cmpd. | $\tau_{des}/\tau_{des\ control}$ 10 μM of steroid | *P*-value | *n* | $I_{peak}/I_{peak\ control}$ 50 μM of steroid | *P*-value | *n* |
|---|---|---|---|---|---|---|
| 1 | 0.99 ± 0.02 | 0.8273 | 5 | 0.86 ± 0.03 | 0.0040 | 8 |
| 2 | 0.98 ± 0.02 | 0.4625 | 6 | 0.77 ± 0.02 | 0.0001 | 7 |
| 3 | 0.98 ± 0.02 | 0.5264 | 6 | 0.95 ± 0.03 | 0.2608 | 6 |
| 4 | 0.80 ± 0.03 | 0.0014 | 6 | 0.75 ± 0.03 | 0.0001 | 7 |
| 5 | 0.97 ± 0.03 | 0.4228 | 6 | 1.12 ± 0.08 | 0.2069 | 8 |
| 6 | 0.99 ± 0.02 | 0.8273 | 5 | 0.92 ± 0.04 | 0.0926 | 7 |
| 7 | 0.98 ± 0.02 | 0.4626 | 5 | 0.77 ± 0.06 | 0.0055 | 7 |
| 8 | 0.88 ± 0.05 | 0.0265 | 6 | 0.75 ± 0.04 | 0.0005 | 8 |
| 9 | 0.97 ± 0.03 | 0.4228 | 5 | 0.99 ± 0.01 | 0.5690 | 8 |

*Mean ± SEM of the normalized values of the $\tau_{des}$ and $I_{peak}$ of the $I_{GABA}$ are shown. All comparisons with control value were made with unpaired Student's t-test. Significance level of P = 0.05. n- the number of cells used.*

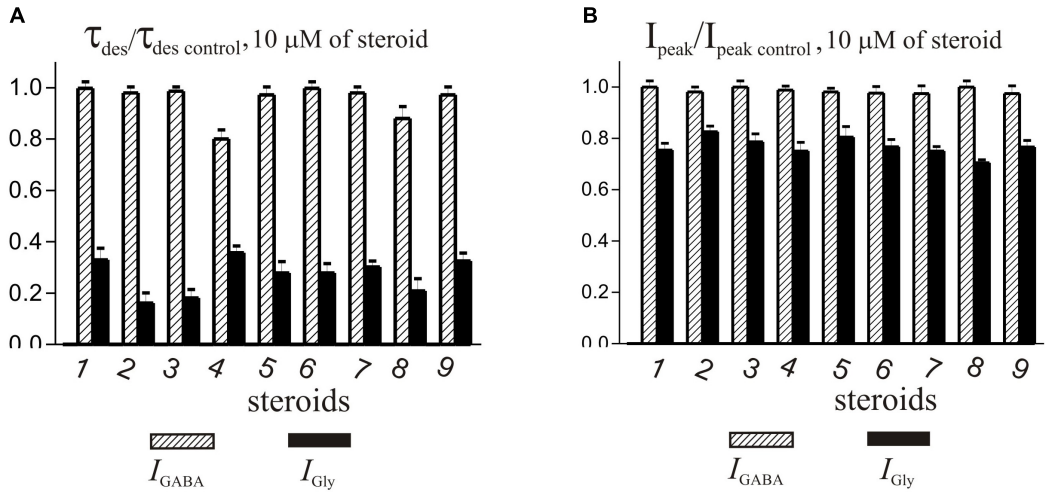


**FIGURE 6 |** Comparison of the effects of NS on $I_{Gly}$ and the $I_{GABA}$. **(A)** Mean ± SEM of the normalized values of the time constant of desensitization ($\tau_{des}$) of $I_{GABA}$ (shaded columns) and $I_{Gly}$ (black columns) in the presence of 10 μM of compounds **1**-**9**. **(B)** Mean ± SEM of the normalized values of the peak amplitude of $I_{GABA}$ (shaded columns) and $I_{Gly}$ (black columns) in the presence of 10 μM of compounds **1**-**9**. Results show greater action of all nine compounds on the $I_{Gly}$ than on the $I_{GABA}$.

binding or that the inhibitors preferentially bind to resting states of the receptor (Li et al., 2007). However, the effect of NS on desensitization is insensitive to agonist concentration and therefore requires other explanations. In our opinion, the acceleration of the $I_{Gly}$ decay can be explained by the slow block of the open channel or/and the acceleration of the desensitization gate (Gielen et al., 2015). Other authors (Borovska et al., 2012; Vyklicky et al., 2016) described the acceleration of the decay of NMDA current under the influence of NS and explain this effect by slow NS diffusion to the site of action at the extracellular vestibule of the NMDAR. At present, we cannot give preference to any of these assumptions regarding the mechanisms for accelerating the desensitization of $I_{Gly}$ under the influence of NS. This remains to be elucidated.

Interestingly, in the literature, we have not found any indications of the ability of NS to accelerate the desensitization of $I_{Gly}$. The published studies of the action of steroids on $I_{Gly}$ were performed on recombinant GlyRs expressed in frog oocytes (Maksay et al., 2001), a chicken spinal neuron culture (Wu et al., 1990), and a rat hippocampal and spinal neuron culture (Jiang et al., 2009). In all of the described models available in the literature, the authors describe a decrease in the $I_{Gly}$ peak amplitude under the influence of NS. The reason for this contradiction may be due to the features of the methodological approach. We use short (600–1000 ms) co-application of glycine and NS, while other authors used 10–30 s pre-application of the NS followed by 10–15 s application of glycine along with the NS. It is possible that the prolonged exposure of NS to the nerve cell leads to a change in properties of the structures responsible for the desensitization of the GlyRs. However, this issue requires special research. The $IC_{50}$ values for the effect of compounds **1**-**9** on the $\tau_{des}$ of $I_{Gly}$ were in the range of 0.12–0.49 μM, and on the peak amplitude – in the range of 16-22 μM. Our results are consistent with data from other authors who studied the effects of androsta(e)ne steroids with substitutions at C-17 on GlyRs. Maksay et al. (2001) showed that DHEA sulfate inhibits the recombinant GlyRs expressed in frog oocytes with an $IC_{50}$ value of 2.5–6.3 μM.

As mentioned previously, GlyR-modulating compounds offer great potential for research on novel drug-like compounds. However, their parallel effect on $GABA_AR$ might be a disadvantage from the pharmacological perspective. Therefore, the discovery of a selective steroidal modulator of GlyR is a challenging task that has not been, according to our knowledge, described previously in the literature. Here, we demonstrate that the addition of compounds **3**, **5**, **6**, and **9** at a concentration of 0.1–50 μM did not change either the peak amplitude or the rate of desensitization of $I_{GABA}$ in isolated Purkinje cells. In contrast, compounds **1**, **2**, **4**, **7**, and **8** at 50 μM concentration showed an inhibitory effect with a decrease in the peak amplitude of the current by 14–25% ($P < 0.01$ or $P < 0.05$) and the acceleration of its desensitization by 23–45% ($P < 0.01$). We conclude that compounds **3**, **5**, **6**, and **9** are selective modulators of $I_{Gly}$. Their structures, however, do bear similar structural features to those that were able to affect $I_{GABA}$. Therefore, establishing a pharmacophore from these results would be highly speculative. The data from the literature clearly indicate that a combination of C-3 and C-5 stereochemistry or the presence of double bond (4-ene/5-ene) of a steroid skeleton direct the effect on GlyRs and $GABA_ARs$ activity (Park-Chung et al., 1999; Maksay et al., 2001; Fodor et al., 2006). Unfortunately, a simple additive approach cannot define pharmacophore for the desired combination of activity on one or both receptors. It is important to highlight that saturated 5α-H and unsaturated (4-ene/5-ene) steroidal skeletons possess a planar shape of the molecule, while the 5β-H skeleton is a "bent" structure. The global shape of the molecule is then significantly affected by the stereochemistry of the C-3 substituent. Note, that the

3α-hydroxy group of the planar 5α-H skeleton is axial, whereas the 3α-hydroxy group of the bent 5β-H skeleton is equatorial. Next, in case the substituent at C-3 is a carbonyl group, its location is in between axial and equatorial configuration. Finally, the nature of the modulatory effect seems to be defined by the substituent at position C-17. Taken together with the previously mentioned facts, we believe that we cannot define a pharmacophore for NS that would afford its modulatory action. Rather, a delicate balance of structural features at positions C-3, C-5, and C-17 could manage this extremely challenging task. The results of our unique study confirm this hypothesis. Our discovery of steroidal selective modulators of $I_{Gly}$ provides a great potential for further structure-activity relationship studies affording novel compounds. Moreover, such research could lead to the identification of structural requirements of giving active compounds.

## DATA AVAILABILITY STATEMENT

All datasets generated for this study are included in the article/supplementary material.

## ETHICS STATEMENT

The study was approved by the Ethics Committee of the Scientific Center of Neurology, Protocol No. 2-5/19 of 02.20.19.

## AUTHOR CONTRIBUTIONS

JB conducted experiments to study the effects of neurosteroids on GABA- and glycine-activated current in rat neurons. ES wrote a physiological part of the manuscript. EK prepared compounds **6**-**9** as described in Materials and Methods section and wrote a chemical part of the manuscript.

## FUNDING

This work was supported by Technology Agency of the Czech Republic: Czech National Centres of Competence, project "PerMed" Personalized Medicine – Diagnostics and Therapy TN01000013, and ERDF/ESF Project "PharmaBrain," Grant CZ.02.1.01/0.0/0.0/16_025/0007444 and by Academy of Sciences of the Czech Republic (AS CR) – grant RVO 61388963.

## REFERENCES

Aroeira, R. I., Ribeiro, J. A., Sebastião, A. M., and Valente, C. A. (2011). Age-related changes of glycine receptor at the rat hippocampus: from the embryo to the adult. *J. Neurochem.* 118, 339–353. doi: 10.1111/j.1471-4159.2011.07197.x

Baulieu, E. E. (1998). Neurosteroids: a novel function of the brain. *Psychoneuroendocrinology* 23, 963–987. doi: 10.1016/s0306-4530(98)00071-7

Belelli, D., and Lambert, J. J. (2005). Neurosteroids: endogenous regulators of the GABA(A) receptor. *Nat. Rev. Neurosci.* 6, 565–575. doi: 10.1038/nrn1703

Borovska, J., Vyklicky, V., Stastna, E., Kapras, V., Slavikova, B., Horak, M., et al. (2012). Access of inhibitory neurosteroids to the NMDA receptor. *Br. J. Pharmacol.* 166, 1069–1083. doi: 10.1111/j.1476-5381.2011.01816.x

Bukanova, J. V., Solntseva, E. I., Kolbaev, S. N., and Kudova, E. (2018). Modulation of GABA and glycine receptors in rat pyramidal hippocampal neurons by 3α5β-pregnanolone derivates. *Neurochem. Int.* 118, 145–151. doi: 10.1016/j.neuint.2018.06.002

Burnell, E. S., Irwin, M., Fang, G., Sapkota, K., Jane, D. E., and Monaghan, D. T. (2019). Positive and negative allosteric modulators of N-methyl-D-aspartate (n.d.) receptors: structure-activity relationships and mechanisms of action. *J. Med. Chem.* 62, 3–23. doi: 10.1021/acs.jmedchem.7b01640

Chen, Z. W., Bracamontes, J. R., Budelier, M. M., Germann, A. L., Shin, D. J., Kathiresan, K., et al. (2019). Multiple functional neurosteroid binding sites on GABAA receptors. *PLoS Biol.* 17:e3000157. doi: 10.1371/journal.pbio.3000157

Do Rego, J. L., Seong, J. Y., Burel, D., Leprince, J., Luu-The, V., Tsutsui, K., et al. (2009). Neurosteroid biosynthesis: enzymatic pathways and neuroendocrine regulation by neurotransmitters and neuropeptides. *Front. Neuroendocrinol.* 30:259–301. doi: 10.1016/j.yfrne.2009.05.006

Dougherty, J. D., Maloney, S. E., Wozniak, D. F., Rieger, M. A., Sonnenblick, L., Coppola, G., et al. (2013). The disruption of Celf6, a gene identified by translational profiling of serotonergic neurons, results in autism-related behaviors. *J. Neurosci.* 33, 2732–2753. doi: 10.1523/JNEUROSCI.4762-12.2013

Fodor, L., Boros, A., Dezso, P., and Maksay, G. (2006). Expression of heteromeric glycine receptor-channels in rat spinal cultures and inhibition by neuroactive steroids. *Neurochem. Int.* 49, 577–583. doi: 10.1016/j.neuint.2006.04.013

Ganser, L. R., and Dallman, J. E. (2009). Glycinergic synapse development, plasticity, and homeostasis in zebrafish. *Front. Mol. Neurosci.* 2:30. doi: 10.3389/neuro.02.030.2009

Gibbs, T. T., Russek, S. J., and Farb, D. H. (2006). Sulfated steroids as endogenous neuromodulators. *Pharmacol. Biochem. Behav.* 84, 555–567. doi: 10.1016/j.pbb.2006.07.031

Gielen, M., Thomas, P., and Smart, T. G. (2015). The desensitization gate of inhibitory Cys-loop receptors. *Nat. Commun.* 6:6829. doi: 10.1038/ncomms7829

Jiang, P., Kong, Y., Zhang, X. B., Wang, W., Liu, C. F., and Xu, T. L. (2009). Glycine receptor in rat hippocampal and spinal cord neurons as a molecular target for rapid actions of 17-beta-estradiol. *Mol. Pain* 5:2. doi: 10.1186/1744-8069-5-2

Jiang, P., Yang, C. X., Wang, Y. T., and Xu, T. L. (2006). Mechanisms of modulation of pregnanolone on glycinergic response in cultured spinal dorsal horn neurons of rat. *Neuroscience* 141, 2041–2050. doi: 10.1016/j.neuroscience.2006.05.009

Katona, B. W., Krishnan, K., Cai, Z. Y., Manion, B. D., Benz, A., Taylor, A., et al. (2008). Neurosteroid analogues. 12. Potent enhancement of GABA-mediated chloride currents at GABAA receptors by ent-androgens. *Eur. J. Med. Chem.* 43, 107–113. doi: 10.1016/j.ejmech.2007.02.017

Keck, T., and White, J. A. (2009). Glycinergic inhibition in the hippocampus. *Rev. Neurosci.* 20, 13–22. doi: 10.1515/revneuro.2009.20.1.13

Kelley, M. H., Ortiz, J., Shimizu, K., Grewal, H., Quillinan, N., and Herson, P. S. (2013). Alterations in Purkinje cell GABAA receptor pharmacology following oxygen and glucose deprivation and cerebral ischemia reveal novel contribution of β1-subunit-containing receptors. *Eur. J. Neurosci.* 37, 555–563. doi: 10.1111/ejn.12064

King, S. R. (2013). *Neurosteroids and the Nervous System*. New York, NY: Springer-Verlag, 125. doi: 10.1007/978-1-4614-5559-2

Korinek, M., Kapras, V., Vyklicky, V., Adamusova, E., Borovska, J., Vales, K., et al. (2011). Neurosteroid modulation of N-methyl-D-aspartate receptors: molecular mechanism and behavioral effects. *Steroids* 76, 1409–1418. doi: 10.1016/j.steroids.2011.09.002

Kung, A. Y., Rick, C., O'Shea, S., Harrison, N. L., and McGehee, D. S. (2001). Expression of glycine receptors in rat sensory neurons vs. HEK293 cells yields different functional properties. *Neurosci. Lett.* 309, 202–206. doi: 10.1016/s0304-3940(01)02066-3

Laurie, D. J., Wisden, W., and Seeburg, P. H. (1992). The distribution of thirteen GABAA receptor subunit mRNAs in the rat brain. III. Embryonic and postnatal development. *J. Neurosci.* 12, 4151–4572.

Li, W., Jin, X., Covey, D. F., and Steinbach, J. H. (2007). Neuroactive steroids and human recombinant rho1 GABAC receptors. *J. Pharmacol. Exp. Ther.* 323, 236–247. doi: 10.1124/jpet.107.127365

Liu, X. K., Ye, B. J., Wu, Y., Nan, J. X., Lin, Z. H., and Piao, H. R. (2012). Synthesis and antitumor activity of dehydroepiandrosterone derivatives on Es-2, A549, and HepG2 cells in vitro. *Chem. Biol. Drug Des.* 79, 523–529. doi: 10.1111/j.1747-0285.2011.01311.x

Lynch, J. W. (2004). Molecular structure and function of the glycine receptor chloride channel. *Physiol. Rev.* 84, 1051–1095. doi: 10.1152/physrev.00042.2003

Lynch, J. W. (2009). Native glycine receptor subtypes and their physiological roles. *Neuropharmacology* 56, 303–309. doi: 10.1016/j.neuropharm.2008.07.034

Lynch, J. W., Zhang, Y., Talwar, S., and Estrada-Mondragon, A. (2017). Glycine receptor drug discovery. *Adv. Pharmacol.* 79, 225–253. doi: 10.1016/bs.apha.2017.01.003

Majewska, M. D., Mienville, J. M., and Vicini, S. (1988). Neurosteroid pregnenolone sulfate antagonizes electrophysiological responses to GABA in neurons. *Neurosci. Lett.* 90, 279–284. doi: 10.1016/0304-3940(88)90202-9

Maksay, G., Laube, B., and Betz, H. (2001). Subunit-specific modulation of glycine receptors by neurosteroids. *Neuropharmacology* 41, 369–376. doi: 10.1016/s0028-3908(01)00071-5

Möhler, H. (2006). GABAA receptors in central nervous system disease: anxiety, epilepsy, and insomnia. *J. Recept. Signal Transduct. Res.* 26, 731–740. doi: 10.1080/10799890600920035

Park-Chung, M., Malayev, A., Purdy, R. H., Gibbs, T. T., and Farb, D. H. (1999). Sulfated and unsulfated steroids modulate γ-aminobutyric acidA receptor function through distinct sites. *Brain Res.* 830, 72–87. doi: 10.1016/s0006-8993(99)01381-5

Pirker, S., Schwarzer, C., Wieselthaler, A., Sieghart, W., and Sperk, G. (2000). GABAA receptors: immunocytochemical distribution of 13 subunits in the adult rat brain. *Neuroscience* 101, 815–850. doi: 10.1016/s0306-4522(00)00442-5

Rebas, E., Radzik, T., Boczek, T., and Zylinska, L. (2017). Calcium-engaged mechanisms of nongenomic action of neurosteroids. *Curr. Neuropharmacol.* 15, 1174–1191. doi: 10.2174/1570159X15666170329091935

Seljeset, S., Laverty, D., and Smart, T. G. (2015). Inhibitory neurosteroids and the GABAA receptor. *Adv. Pharmacol.* 72, 165–187. doi: 10.1016/bs.apha.2014.10.006

Sieghart, W., and Savić, M. M. (2018). International union of basic and clinical pharmacology. CVI: GABAA receptor subtype- and function-selective ligands: key issues in translation to humans. *Pharmacol. Rev.* 70, 836–878. doi: 10.1124/pr.117.014449

Tanabe, M., Nitta, A., and Ono, H. (2010). Neuroprotection via strychnine-sensitive glycine receptors during post-ischemic recovery of excitatory synaptic transmission in the hippocampus. *J. Pharmacol. Sci.* 113, 378–386. doi: 10.1254/jphs.10150fp

Tapia, J. C., Cárdenas, A. M., Nualart, F., Mentis, G. Z., Navarrete, R., and Aguayo, L. G. (2000). Neurite outgrowth in developing mouse spinal cord neurons is modulated by glycine receptors. *Neuroreport* 11, 3007–3010. doi: 10.1097/00001756-200009110-00036

Vorobjev, V. S. (1991). Vibrodissociation of sliced mammalian nervous tissue. *J. Neurosci. Methods* 38, 145–150. doi: 10.1016/0165-0270(91)90164-u

Vorobjev, V. S., Sharonova, I. N., and Haas, H. L. (1996). A simple perfusion system for patch-clamp studies. *J. Neurosci. Methods* 68, 303–307. doi: 10.1016/0165-0270(96)00097-0

Vyklicky, V., Smejkalova, T., Krausova, B., Balik, A., Korinek, M., Borovska, J., et al. (2016). Preferential inhibition of tonically over phasically activated NMDA receptors by pregnane derivatives. *J. Neurosci.* 36, 2161–2175. doi: 10.1523/JNEUROSCI.3181-15.2016

Weir, C. J., Ling, A. T., Belelli, D., Wildsmith, J. A., Peters, J. A., and Lambert, J. J. (2004). The interaction of anaesthetic steroids with recombinant glycine and GABAA receptors. *Br. J. Anaesth.* 92, 704–711. doi: 10.1093/bja/aeh125

Wu, F. S., Chen, S. C., and Tsai, J. J. (1997). Competitive inhibition of the glycine-induced current by pregnenolone sulfate in cultured chick spinal cord neurons. *Brain Res.* 750, 318–320. doi: 10.1016/s0006-8993(97)00053-x

Wu, F. S., Gibbs, T. T., and Farb, D. H. (1990). Inverse modulation of gamma-aminobutyric acid- and glycine-induced currents by progesterone. *Mol. Pharmacol.* 37, 597–602.

Xu, T. L., and Gong, N. (2010). Glycine and glycine receptor signaling in hippocampal neurons: diversity, function and regulation. *Prog. Neurobiol.* 91, 349–361. doi: 10.1016/j.pneurobio.2010.04.008

Yevenes, G. E., and Zeilhofer, H. U. (2011). Allosteric modulation of glycine receptors. *Br. J. Pharmacol.* 164, 224–236. doi: 10.1111/j.1476-5381.2011.01471.x

Zhang, Y., Ho, T. N. T., Harvey, R. J., Lynch, J. W., and Keramidas, A. (2017). Structure-function analysis of the GlyR α2 subunit autism mutation p.R323L reveals a gain-of-function. *Front. Mol. Neurosci.* 10:158. doi: 10.3389/fnmol.2017.00158

Ziegler, E., Bodusch, M., Song, Y., Jahn, K., Wolfes, H., Steinlechner, S., et al. (2009). Interaction of androsterone and progesterone with inhibitory ligand-gated ion channels: a patch clamp study. *Naunyn Schmiedebergs Arch. Pharmacol.* 380, 277–291. doi: 10.1007/s00210-009-0440-x

Zorumski, C. F., Paul, S. M., Izumi, Y., Covey, D. F., and Mennerick, S. (2013). Neurosteroids, stress and depression: potential therapeutic opportunities. *Neurosci. Biobehav. Rev.* 37, 109–122. doi: 10.1016/j.neubiorev.2012.10.005

**Conflict of Interest:** The authors declare that the research was conducted in the absence of any commercial or financial relationships that could be construed as a potential conflict of interest.

*Copyright © 2020 Bukanova, Solntseva and Kudova. This is an open-access article distributed under the terms of the Creative Commons Attribution License (CC BY). The use, distribution or reproduction in other forums is permitted, provided the original author(s) and the copyright owner(s) are credited and that the original publication in this journal is cited, in accordance with accepted academic practice. No use, distribution or reproduction is permitted which does not comply with these terms.*

frontiers in Molecular Neuroscience

ORIGINAL RESEARCH
published: 03 April 2020
doi: 10.3389/fnmol.2020.00055

# Noncanonical, Dopamine-Dependent Long-Term Potentiation at Hippocampal Output Synapses in a Rodent Model of First-Episode Psychosis

*Julia C. Bartsch*[1†] *and Joachim Behr*[1,2*]

[1]*Department of Psychiatry and Psychotherapy, Charité-Universitätsmedizin Berlin, Berlin, Germany,* [2]*Department of Psychiatry, Psychotherapy and Psychosomatic Medicine, Brandenburg Medical School, Neuruppin, Germany*

OPEN ACCESS

**Edited by:**
*Jochen C. Meier, Technische Universitat Braunschweig, Germany*

**Reviewed by:**
*Eric Hosy, UMR5297 Institut Interdisciplinaire de Neurosciences (IINS), France*
*Nicola Maggio, Sheba Medical Center, Israel*

***Correspondence:**
*Joachim Behr*
*joachim.behr@charite.de*

**[†]Present address:**
*Julia C. Bartsch, Institute of Physiology I, Westfälische Wilhelms-Universität Münster, Münster, Germany*

**Received:** *16 January 2020*
**Accepted:** *17 March 2020*
**Published:** *03 April 2020*

**Citation:**
*Bartsch JC and Behr J (2020) Noncanonical, Dopamine-Dependent Long-Term Potentiation at Hippocampal Output Synapses in a Rodent Model of First-Episode Psychosis. Front. Mol. Neurosci. 13:55. doi: 10.3389/fnmol.2020.00055*

Cognitive deficits and positive symptoms in schizophrenia have both been linked to hippocampal dysfunction. Recently, subregion-specific aberrant and maladaptive hippocampal synaptic plasticity has been suggested as one of the mechanistic underpinnings. The subiculum is the final output hub of the hippocampus and orchestrates hippocampal information transfer to other brain regions. While most CA1 pyramidal neurons show regular-spiking behavior, subicular output neurons comprise bursting and regular-firing pyramidal cells. These two cell types target different brain regions and express unique forms of synaptic plasticity. Here, we used a single systemic application of the noncompetitive glutamatergic N-methyl-D-aspartate receptor (NMDAR) antagonist MK-801 to model first-episode psychosis in rats and studied long-term potentiation (LTP) in subicular regular-firing cells in acute hippocampal slices. Previously, we have reported a facilitation of a presynaptic, late-onset LTP in subicular bursting pyramidal cells after systemic NMDAR antagonism. Here, we show that single systemic NMDAR antagonist application also facilitates the induction of a noncanonical, but postsynaptic NMDAR-independent LTP in ventral subicular but not in CA1 regular-firing pyramidal cells. This form of LTP was dependent on D1/D5 dopamine receptor activation. Activation of D1/D5 dopamine receptors by a specific agonist mimicked and occluded LTP induced by electrical high-frequency stimulation (HFS). Furthermore, our results indicate that this form of LTP relies on postsynaptic $Ca^{2+}$ signaling and requires the activation of protein kinase A. Considering the pivotal role of the subiculum as information gatekeeper between the hippocampus and other brain regions, this aberrant LTP in ventral subicular regular-firing neurons is expected to interfere with physiological hippocampal output processing and might thereby contribute to hippocampal dysfunction in psychotic events.

**Keywords: hippocampus, schizophrenia, synaptic plasticity, subiculum, psychosis, long-term potentiation, MK-801, dopamine**

## INTRODUCTION

Roughly one percent of the global population is affected by schizophrenia. This multifaceted, heterogeneous psychiatric disorder is characterized by positive symptoms, i.e., delusions or hallucinations, negative symptoms, e.g., anhedonia, and cognitive symptoms including aberrant hippocampus-dependent memory encoding and retrieval as well as novelty detection (Heckers et al., 1998; Zierhut et al., 2010; Tamminga et al., 2012b; Pirnia et al., 2015; Ragland et al., 2015; Schott et al., 2015). In light of the accumulating evidence from large-scale genetic studies (Hall et al., 2015), contemporary pathophysiological concepts of schizophrenia suggest aberrations of synaptic plasticity are core to schizophrenia (McGlashan, 2006; Averbeck and Chafee, 2016). Synaptic plasticity in neuronal networks is regarded as one of the underpinning mechanisms for learning and memory enabling the individual to cope with a changing environment. Long-term potentiation (LTP) is one form of synaptic plasticity, defined by a lasting increase in synaptic efficacy following prior activity (Bliss and Lomo, 1973). Hippocampal dysfunction has been linked to both cognitive deficits and positive symptoms in schizophrenia (Bogerts, 1997) and hippocampal dysfunction in rodent model psychosis comprises subregion-specific maladaptive synaptic plasticity (Tamminga et al., 2012a). While no single animal model can completely match all aspects of an inherently human psychiatric disorder like schizophrenia, animal models are key to investigate the neurobiological mechanisms of schizophrenia at the cellular level (Averbeck and Chafee, 2016). Certain cognitive facets of schizophrenia can satisfactorily be modeled and studied in rodents by administering antagonists of the glutamatergic N-methyl-D-aspartate receptor (NMDAR, Neill et al., 2010). This rodent psychosis model originates from the NMDAR hypofunction concept which builds on the observation that acutely given NMDAR antagonists can induce psychosis in healthy humans similar to positive, negative and cognitive symptoms of schizophrenia (Luby et al., 1959). The hippocampal formation consists of the cornu ammonis (CA1–CA3 in rodents, hippocampus proper), the dentate gyrus and the subiculum. The dorsal hippocampus is mainly associated with spatial learning, while the ventral hippocampus is involved in emotion- and motivation-related processes (Fanselow, 2000; Bannerman et al., 2004; reviewed in Jarrard, 1995; Moser and Moser, 1998; Maren, 1999; Sharp, 1999; Fanselow and Dong, 2010; Segal et al., 2010; reviewed in Strange et al., 2014). The subiculum is the final output hub of the hippocampus and orchestrates hippocampal information transfer to other brain regions (O'Mara et al., 2000; Aggleton and Christiansen, 2015). Subicular pyramidal neurons can be distinguished in regular-spiking and burst-spiking neurons (Stewart and Wong, 1993; Taube, 1993; Behr et al., 1996; Mattia et al., 1997; Staff et al., 2000; Harris and Stewart, 2001; Wellmer et al., 2002), both show cell type-specific LTP (Wozny et al., 2008a,b) and target different brain regions. Previously, we have reported a facilitation of a presynaptic, late-onset LTP in subicular bursting pyramidal cells after systemic NMDAR antagonism (Bartsch et al., 2015). Here, we used a single systemic application of the noncompetitive NMDAR antagonist MK-801 to model psychosis in rats and studied LTP specifically in ventral subicular regular-firing cells in acute hippocampal slices.

## MATERIALS AND METHODS

### Animals

All experiments were carried out under the directive 2010/63/EU of the European Parliament and of the council of 22 September 2010. Ethical approval for all rats used in this study was obtained from the Landesamt für Gesundheit und Soziales Berlin (LAGeSo Berlin, Germany). Rats were kept on a 12 h light-dark cycle and had access to food and water *ad libitum*. Wistar rats of both sexes (4–6 weeks old) received a single intraperitoneal injection with either MK-801 [(5S,10R)-(+)-5-methyl-10,11-dihydro-5H-dibenzo(a,d)cyclohepten-5,10-imine maleate, 5 mg/kg body weight], or 0.9% saline (10 ml/kg body weight).

### Slice Preparation

Twenty-four hours after i.p. injection, rats were decapitated under deep anesthesia (isoflurane, 1-chloro-2,2,2-trifluoroethyl-difluoromethylether; 2.5% in $O_2$) and the brains were quickly removed. Horizontal slices (350–400 μm) containing the hippocampal formation and the entorhinal cortex were obtained with a Leica VT1200S vibratome (Leica Microsystems CMS, Mannheim, Germany). Slices were collected from the ventral sector of the hippocampus (∼2 mm of the temporal pole), avoiding the extreme 350 μm end (Maggio and Segal, 2007a). Tissue for sharp microelectrode recordings was prepared in ice-cold, oxygenated (95% $O_2$, 5% $CO_2$) artificial cerebrospinal fluid (ACSF) and the slices were transferred for storage to an interface recording chamber continuously perfused (1.5–2 ml/min) with oxygenated and prewarmed (34°C) ACSF. The composition of the ACSF was as follows (in mM): NaCl 129, $Na_2PO_4$ 1.25, $NaHCO_3$ 26, KCl 3, $CaCl_2$ 1.6, $MgSO_4$ 1.8, glucose 10 at a pH of 7.4. Slices for patch-clamp recordings were prepared in ice-cold, saccharose-based ACSF (in mM): NaCl 87, $Na_2PO_4$ 1.25, $NaHCO_3$ 26, KCl 2.5, $CaCl_2$ 0.5, $MgCl_2$ 7, saccharose 75, glucose 25 at a pH of 7.4. After preparation, slices were kept under submerged conditions at 35°C for approximately 30 min and were then transferred to physiological ACSF solution at room temperature for further storage.

### Electrophysiology

Single-cell recordings in ventral CA1 pyramidal cells and regular-firing pyramidal cells of the subiculum were performed with sharp microelectrodes (40–100 MΩ) filled with 2.5 M potassium acetate in current-clamp bridge mode at resting membrane potential. Patch-clamp recordings were performed under submerged conditions at room temperature in voltage-clamp mode at a holding potential of −70 mV. Patch-clamp electrodes (4–6 MΩ) were filled with (in mM): K-gluconate 135, KCl 20, HEPES 10, phosphocreatine 7, Mg-ATP 2, Na-GTP 0.3, EGTA 0.2 and adjusted with KOH to a pH of 7.2. Access resistance was monitored throughout the experiments and recordings with fluctuating access resistance were discarded. No

series resistance compensation was used. Signals were low-pass filtered at 3 kHz, sampled at 10 kHz by an ITC-16 interface (Instrutech Corp., Great Neck, NY, USA) and processed by TIDA software (HEKA GmbH, Lambrecht, Germany).

To study synaptic plasticity at glutamatergic synapses, all experiments were performed in the presence of bicuculline (5 μM) to block $GABA_A$ receptor-mediated responses. To prevent polysynaptic responses, concentrations of $MgSO_4$ and $CaCl_2$ were elevated to 4 mM each (Nicholls and Purves, 1970; Berry and Pentreath, 1976; Wigström and Gustafsson, 1983; Miles and Wong, 1987; Wozny et al., 2008a). Excitatory postsynaptic potentials or currents (EPSP/EPSC) were evoked at 0.1 Hz by stimulation (100 μs) of Schaffer collaterals or CA1 efferents with an ACSF-filled patch pipette or a bipolar stimulating electrode. Baseline responses were recorded for at least 10 min and the stimulus intensity was set to evoke amplitudes of 30–50% of the maximum response. Depending on the rationale of the experiment, different high-frequency stimulation (HFS) protocols were used for the induction of LTP. Two-hundred pulses at 50 Hz, 25 pulses at 50 Hz, or 10 pulses at 40 Hz. Changes in synaptic strength were measured for 30 min after induction. Amplitudes of evoked EPSP or EPSC were normalized to baseline values. LTP was calculated by averaging the responses collected during the last 5 min of each experiment. Paired-pulse index (PPI) was investigated by analyzing the ratio of the second to the first synaptic response (EPSP2/EPSP1) at an inter-stimulus interval of 60 ms (Zucker and Regehr, 2002).

## Data Analysis/Statistics

Electrophysiological data were analyzed offline with Clampfit software (Molecular Devices Corporation, Sunnyvale, CA, USA), TIDA software (HEKA GmbH, Lambrecht, Germany) and GraphPad Prism (GraphPad Software, La Jolla, CA, USA). All datasets were tested for significant outliers using the Grubbs' test (significance level, $p < 0.05$). Data are presented as mean ± standard error of the mean (SEM) or box and whisker plots (box: 25th to 75th percentiles, whiskers 5th and 95th percentiles). In figures illustrating the experimental time course of normalized amplitudes, data points were binned from six consecutive responses. Representative traces are shown as averages of six responses with clipped stimulation artifacts. The significance level was set to $p < 0.05$. Comparisons within groups were analyzed by paired Student's *t*-tests. Multigroup comparisons were analyzed with the Kruskal–Wallis test followed by Dunn's *post hoc* test against the control group (**Figures 2F**, **3E**). Numbers given in the text (x/y) refer to numbers of neurons (x) recorded in different animals (y).

## Drugs

The following drugs were used: (+)-MK-801 maleate [(5S,10R)-(+)-5-methyl-10,11-dihydro-5H-dibenzo(a,d)cyclohepten-5,10-imine maleate], (-)-bicuculline methiodide ((R-(R*,S*))-5-(6,8-dihydro-8-oxofuro(3,4-e)-1,3-benzodioxol-6-yl)-5,6,7,8-tetrahydro-6,6-dimethyl-1,3-dioxolo(4,5-g)isoquinolinium iodide), 5 μM; SCH23390 hydrochloride ((R)-(+)-7-chloro-8-hydroxy-3-methyl-1-phenyl-2,3,4,5-tetrahydro-1H-3-benzazepine hydrochloride), 10 μM; SKF38393 hydrobromide ((±)-1-phenyl-2,3,4,5-tetrahydro-(1H)-3-benzazepine-7,8-diol hydrobromide), 100 μM; D-AP5 (D-(-)-2-amino-5-phosphonopentanoic acid), 100 μM; (RS)-MCPG ((RS)-α-methyl-4-carboxyphenylglycine), 500 μM; BAPTA (1,2-bis(2-aminophenoxy)ethane-N,N,N′,N′-tetraacetic acid), 30 mM in the intracellular solution; Rp-8-CPT-cAMPS (8-(4-chlorophenylthio)adenosine-3′,5′-cyclic monophosphorothioate), 100 μM. Drugs were purchased from Biolog, Germany; Sigma–Aldrich, Germany; Ascent Scientific, UK and Tocris, UK. Most drugs were bath-applied for at least 10 min before starting the experiment. In experiments using the PKA inhibitor Rp-8-CPT-cAMPS, slices were incubated for at least 1 h before commencement of recordings. Loading recorded neurons with the calcium chelator BAPTA did not alter the discharge behavior of subicular pyramidal cells. Stable baseline responses could be obtained in most of the recordings with BAPTA. Cells that showed a rundown of responses (∼15%, Lapointe et al., 2004) were not included.

# RESULTS

## Facilitated LTP in Ventral Subicular but Not in CA1 Pyramidal Neurons Following Systemic NMDAR Antagonism

As systemic NMDAR antagonism has been reported to facilitate a noncanonical late-onset LTP at CA1-subiculum synapses to bursting pyramidal cells (Bartsch et al., 2015), we first studied whether this holds also true for ventral CA1-subiculum synapses to regular-firing pyramidal cells. Recordings were performed in regular-firing pyramidal cells in the middle portion of the subiculum concerning the proximodistal axis using sharp microelectrodes to leave the intracellular environment physiological (**Figures 1A,B**). We applied a brief HFS protocol (10 pulses, 40 Hz), which was insufficient to induce LTP at CA1–subiculum synapses to regular-firing pyramidal cells under control conditions ($0.99 \pm 0.08$, $n = 7/6$, $p = 0.78$; **Figures 1C–E**). In MK-801-treated rats, however, the subthreshold HFS induced stable LTP appearing as a lasting late-onset increase in EPSP amplitudes in subicular regular-firing pyramidal cells ($2.12 \pm 0.28$, $n = 7/5$, $p < 0.01$; **Figures 1C–E**). Previously, we have shown that this brief HFS does not induce LTP at CA3–CA1 synapses in MK-801-treated rats (Bartsch et al., 2015). Here, we also tested an adapted, slightly stronger brief HFS protocol (25 pulses, 50 Hz) set subthreshold for LTP induction in control rats in CA1 pyramidal cells. In line with our previous results, this adapted brief HFS also failed to induce LTP (control: $0.98 \pm 0.11$, $n = 6/5$, $p = 0.78$; MK-801: $1.20 \pm 0.10$, $n = 5/4$, $p = 0.15$; **Figures 1F–H**). Hence, we conclude that this form of LTP is exclusive to subicular regular-firing pyramidal neurons.

## Facilitated LTP in Regular-Firing Subicular Neurons of MK-801-Treated Rats Is Expressed Postsynaptically and Is Dependent on Postsynaptic $Ca^{2+}$

To investigate the expression site of this facilitated LTP in regular-firing subicular neurons of MK-801-treated rats, we

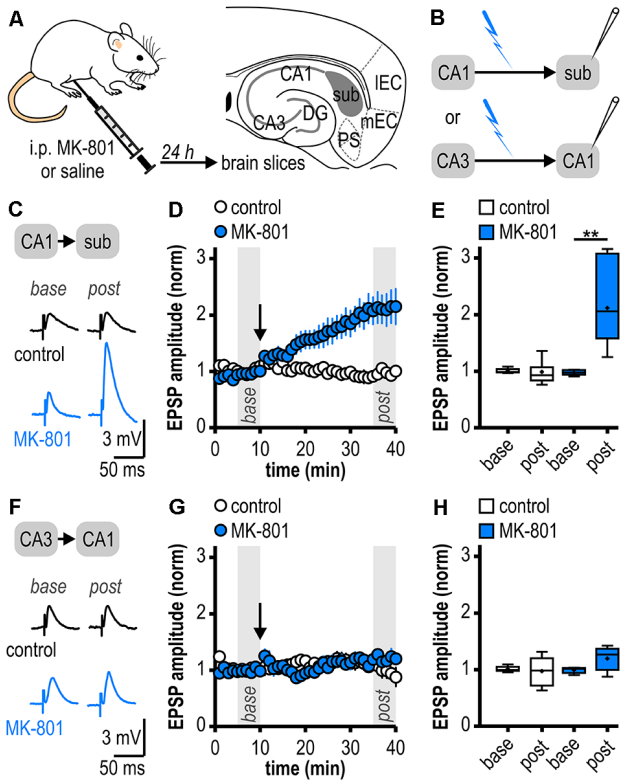


**FIGURE 1 |** Facilitated long-term potentiation (LTP) in ventral subicular regular-firing neurons but not in CA1 pyramidal neurons following systemic N-methyl-D-aspartate receptor (NMDAR) antagonism. **(A)** Study design. Schematic drawing of a horizontal section through the ventral rat hippocampal formation with distinct subregions: medial and lateral entorhinal cortex (mEC, lEC); dentate gyrus (DG); cornu ammonis 1 and 3 (CA3, CA1); subiculum (sub); pre- and parasubiculum (PS). **(B)** Scheme of the experimental approach to study LTP induction at ventral hippocampal output synapses using intracellular recordings with sharp microelectrodes. **(C)** Representative traces of excitatory postsynaptic potentials (EPSPs) recorded in subicular regular-firing neurons before (*base*, min 6–10) and after (*post*, min 36–40) application of brief high-frequency stimulation (HFS; 10 pulses at 40 Hz). **(D)** Time course of mean normalized EPSP amplitudes at CA1–subiculum synapses to regular-firing pyramidal neurons (control: $n$ = 7/6, MK-801: $n$ = 7/5). HFS (arrow) induces robust LTP only in MK-801-treated rats. **(E)** Quantification of mean normalized EPSP amplitudes (control: $n$ = 7/6, paired Student's $t$-test $p$ = 0.78; MK-801: $n$ = 7/5, paired Student's $t$-test $^{**}p < 0.01$). **(F)** Representative traces of EPSPs recorded in CA1 pyramidal neurons before (*base*, min 6–10) and after (*post*, min 36–40) application of brief HFS (25 pulses at 50 Hz). **(G)** Time course of mean normalized EPSP amplitudes at Schaffer collateral input to CA1 pyramidal cells. HFS (arrow) fails to induce LTP in both animal groups. **(H)** Quantification of mean normalized EPSP amplitudes (control: $n$ = 6/5, paired Student's $t$-test $p$ = 0.78; MK-801: $n$ = 5/4, paired Student's $t$-test $p$ = 0.15).

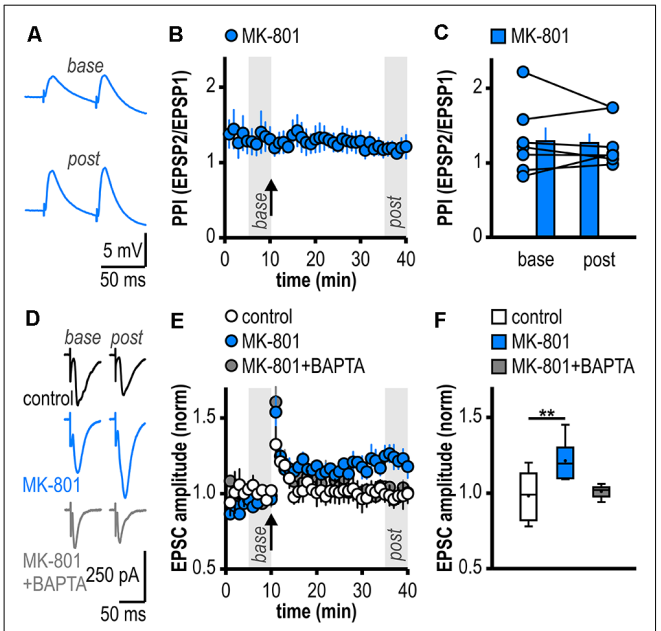


**FIGURE 2 |** Facilitated LTP in regular-firing subicular neurons of MK-801-treated rats is expressed postsynaptically and is dependent on postsynaptic $Ca^{2+}$. **(A)** Representative traces of paired EPSPs (60 ms inter-stimulus interval) recorded in subicular regular-firing neurons of MK-801-treated rats before (*base*, min 6–10) and after (*post*, min 36–40) application of HFS. **(B)** Experimental time course of paired-pulse index (PPI). PPI does not change after the induction of LTP in MK-801-treated rats. **(C)** Quantification of PPI. Filled circles depict the mean value of single neurons before (*base*) and after (*post*) LTP induction, columns represent mean ± SEM of all recorded neurons ($n$ = 7/5, paired Student's $t$-test $p$ = 0.79). **(D)** Representative traces of excitatory postsynaptic currents (EPSCs) recorded in subicular regular-firing neurons before (*base*, min 6–10) and after (*post*, min 36–40) application of brief HFS (200 pulses at 50 Hz) using the whole-cell patch-clamp technique. **(E)** Postsynaptic dialysis with the $Ca^{2+}$ buffer BAPTA prevents the expression of LTP in MK-801-treated rats (control: $n$ = 7/5, MK-801: $n$ = 6/6, MK-801+BAPTA: $n$ = 6/4). **(F)** Quantification of mean normalized EPSC amplitudes (Kruskal–Wallis test: $H_{(2)}$ = 11.01, $p$ = 0.0041, $^{**}p < 0.01$ by *post hoc* Dunn).

analyzed the PPI before and after LTP induction (Zucker and Regehr, 2002). The facilitated LTP in regular-firing neurons of MK-801-treated rats was not associated with significant changes in the PPI (base: 1.30 ± 0.18, LTP: 1.28 ± 0.12, $n$ = 7/5, $p$ = 0.79; **Figures 2A–C**), arguing for a postsynaptic expression site. In the next step, we determined if postsynaptic $Ca^{2+}$ signaling is required for this facilitated LTP in regular-firing neurons of MK-801-treated rats. To this end, we performed whole-cell patch-clamp recordings to guarantee good dialysis of cells with a $Ca^{2+}$ buffer. To replicate the LTP in MK-801-treated animals under patch-clamp conditions, we adjusted the HFS to 200 pulses at 50 Hz applied in current-clamp mode. This stimulation protocol induced LTP in MK-801-treated rats (1.21 ± 0.05, $n$ = 6/6, $p < 0.01$; **Figures 2D–F**), but led to only brief post-tetanic potentiation and no LTP in control animals (1.01 ± 0.02, $n$ = 7/5, $p$ = 0.68; **Figures 2D–F**). As previously reported (Wozny et al., 2008b; Bartsch et al., 2015), in whole-cell patch-clamp recordings under submerged conditions LTP was smaller than in sharp microelectrode recordings under interface condition. Of note, LTP in patch-clamp recordings under submerged conditions exhibited a different time course lacking the late-onset component. A reasonable explanation for this observation might be a difference in oxygen supply under both recording conditions (Hájos et al., 2009). Postsynaptic dialysis of individual regular-firing neurons with the fast $Ca^{2+}$ buffer BAPTA prevented the induction of LTP in MK-801-treated rats (1.01 ± 0.02, $n$ = 6/4, $p$ = 0.56; **Figures 2D–F**),

suggesting that this facilitated LTP in subicular regular-firing neurons after systemic NMDAR antagonism is dependent on postsynaptic $Ca^{2+}$ signaling.

## Noncanonical LTP in MK-801-Treated Rats Depends on the Activation of D1/D5R and the Adenylate Cyclase-cAMP-PKA Signaling Cascade but Is Independent of NMDAR and mGluRI/II

At various synapses in the central nervous system, LTP depends on NMDAR activation (Nicoll and Malenka, 1999; Morris, 2013; Volianskis et al., 2015). Also, subicular regular-firing neurons express NMDAR-dependent LTP (Wozny et al., 2008b). However, the application of the NMDAR antagonist AP5 failed to prevent the aberrant LTP in MK-801-treated rats ($2.70 \pm 0.49$, $n = 6/5$; **Figures 3A,E**). This suggests that this late-onset LTP after systemic MK-801 treatment is NMDAR-independent. To test the involvement of metabotropic glutamate receptors (mGluR) in this NMDAR-independent LTP (O'Leary and O'Connor, 1999), we bath-applied the mGluRI/II antagonist MCGP. Again, this could not prevent LTP induction in regular-firing neurons from MK-801-treated rats ($2.32 \pm 0.40$, $n = 5/5$; **Figures 3B,E**). This argues against a major involvement of mGluR in this aberrant form of LTP.

Previously, we have reported a facilitation of a presynaptic, late-onset LTP in subicular bursting pyramidal cells after systemic NMDAR antagonism that is induced by D1/D5 dopamine receptor (D1/D5R) activation (Bartsch et al., 2015). Thus, we tested if the facilitated LTP in subicular regular-firing neurons is also mediated by D1/D5R. Indeed, in the presence of the specific D1/D5R antagonist SCH23390, LTP-induction was blocked ($1.06 \pm 0.15$, $n = 6/4$; **Figures 3C,E**). D1/D5R are G protein-coupled receptors that stimulate the adenylate cyclase-cAMP-protein kinase A (PKA) signaling cascade (Missale et al., 1998). Consequently, we investigated whether blocking this pathway prevents the induction of LTP in MK-801-treated animals. To this end, hippocampal brain slices were incubated with the PKA inhibitor Rp-8-CPT-cAMPS for at least 1 h before recording. Indeed, this treatment blocked the induction of LTP in MK-801-treated animals ($1.10 \pm 0.11$, $n = 5/3$; **Figures 3D,E**), indicating that this form of LTP needs the activation of PKA. A summary of changes in synaptic strength in the reported experiments is shown in **Figure 3E**.

## D1/D5R Activation Mimics and Occludes Noncanonical HFS-Induced LTP in MK-801-Treated Rats

If D1/D5R activation is crucial for the aberrant LTP in MK-801-treated rats, activating these receptors by a specific agonist should also result in LTP. Accordingly, bath application of the specific D1/D5R agonist SKF38393 resulted in an enhancement of synaptic transmission in subicular regular-firing neurons of MK-801 treated rats ($1.76 \pm 0.12$, $n = 5/4$, $p < 0.01$; **Figures 4A–C**) which mimicked and finally occluded tetanus-induced LTP ($1.10 \pm 0.06$, $n = 5/4$, $p = 0.52$; **Figures 4D–F**). This shows that chemically and electrically induced LTP share common mechanisms.

# DISCUSSION

The present findings confirm and extend previous studies on aberrant hippocampal LTP in a rodent model of acute psychosis. We show that single systemic NMDAR antagonism in young adult Wistar rats facilitates LTP induction at ventral CA1-subiculum synapses to regular-firing pyramidal cells tested *ex vivo* 1 day later. This noncanonical, late-onset LTP in MK-801-treated rats is postsynaptic, NMDAR-independent and relies on the activation of D1/D5R, PKA, and postsynaptic $Ca^{2+}$ signaling.

## Subregion-Specific Changes in Hippocampal LTP in the MK-801 Rodent Model of First-Episode Psychosis

Previous e*x vivo* studies using acute brain slices have shown that a single systemic application of MK-801 can impair LTP at the Schaffer collateral input to CA1 (Wöhrl et al., 2007; Bartsch et al., 2015). Likewise, LTP at the direct cortical input to CA1 was reduced for prolonged periods (Wöhrl et al., 2007). Accordingly, we here also found no facilitation of LTP at the Schaffer collateral input to CA1. The facilitated LTP was exclusive to regular-firing subicular neurons. In line with our results, *ex vivo* field potential recordings at CA1-subiculum synapses indicated facilitated LTP 24 h after a single systemic application of MK-801 (Buck et al., 2006). Therefore, our and previous results argue for subregion-specific patterns of psychosis-induced changes in hippocampal LTP. Notably, the facilitation of LTP seems to be restricted to subicular hippocampal output synapses. The distinct propensity of subicular pyramidal cells to successfully express LTP might depend on various presynaptic and postsynaptic factors as the total number of synaptic contacts, presynaptic and postsynaptic $Ca^{2+}$ influx, the number of release-competent vesicles or the desensitization state of postsynaptic receptors (Schneggenburger et al., 2002) and has to be delineated in more detail in future studies.

## Cell Type-Specific Aberrant LTP at Hippocampal Output Synapses in the MK-801 Rodent Model of First-Episode Psychosis

Adding up to the complexity, while most CA1 pyramidal neurons show regular-spiking behavior, subicular output neurons comprise bursting and regular-firing pyramidal cells (Stewart and Wong, 1993; Taube, 1993; Behr et al., 1996; Mattia et al., 1997; Staff et al., 2000; Harris and Stewart, 2001; Wellmer et al., 2002). These two cell types target different brain regions. Bursting pyramidal cells project to the presubiculum, the medial entorhinal cortex, the hypothalamus, and the retrosplenial cortex while regular-firing pyramidal cells target the lateral entorhinal cortex, the nucleus accumbens and the amygdala (Köhler, 1985; Stewart, 1997; Kim and Spruston, 2012). Interestingly, CA1 efferents to subicular

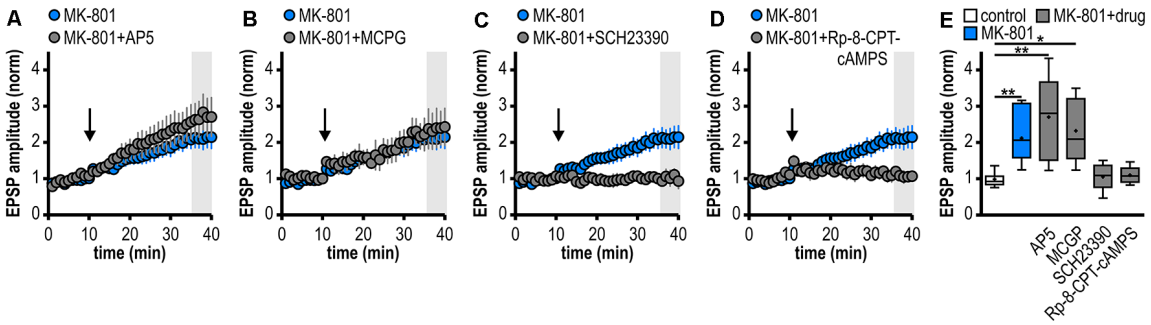


**FIGURE 3 |** Noncanonical LTP in MK-801-treated rats depends on the activation of D1/D5R and the adenylate cyclase-cAMP-PKA signaling cascade but is independent from NMDAR and mGluRI/II. **(A–D)** Time course of mean normalized EPSP amplitudes at CA1–subiculum synapses to regular-firing pyramidal neurons under the bath-application of denoted drugs. MK-801 data taken from **Figure 1D** is replotted for comparison. **(A)** The NMDAR antagonist AP5 failed to prevent LTP in MK-801-treated rats ($n$ = 6/5, paired Student's $t$-test $p < 0.05$). **(B)** The mGluRI/II antagonist MCGP could not block LTP induction ($n$ = 5/5, paired Student's $t$-test $p < 0.05$). **(C)** The specific D1/D5R antagonist SCH23390 blocked LTP-induction ($n$ = 6/4, paired Student's $t$-test $p = 0.64$). **(D)** Preincubation of slices with the PKA inhibitor Rp-8-CPT-cAMPS prevented the induction of LTP ($n$ = 5/3, paired Student's $t$-test $p = 0.68$). **(E)** Summary of changes in synaptic strength following brief HFS for the different experimental groups shown in **(A–D)**. Control and MK-801 data taken from **Figure 1E** is replotted for comparison. Quantification of mean normalized EPSP amplitudes (Kruskal–Wallis test: $H_{(5)} = 23.18$, $p = 0.0003$, $^*p < 0.05$, $^{**}p < 0.01$ by *post hoc* Dunn).

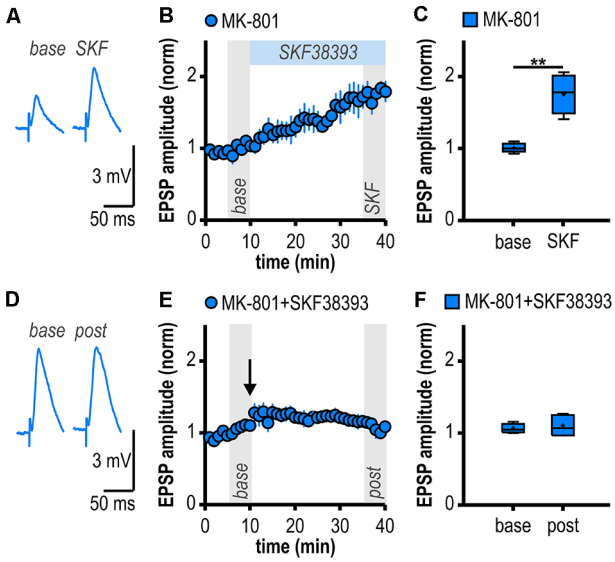


**FIGURE 4 |** D1/D5R activation mimics and occludes noncanonical HFS-induced LTP in MK-801-treated rats. **(A)** Representative traces of EPSPs recorded in subicular regular-firing neurons before (*base*, min 6–10) and after (*SKF*, min 36–40) application of the D1/D5R agonist SKF38393. **(B)** Time course of mean normalized EPSP amplitudes at CA1–subiculum synapses to regular-firing pyramidal neurons. D1/D5R activation enhanced EPSPs in subicular regular-firing pyramidal neurons in MK-801-treated rats. **(C)** Quantification of mean normalized EPSP amplitudes ($n$ = 5/4, paired Student's $t$-test, $^{**}p < 0.01$). **(D)** Representative traces of EPSPs recorded in subicular regular-firing neurons before (*base*, min 6–10) and after (*post*, min 36–40) application of brief HFS following D1/D5R activation. **(E)** SKF38393-induced enhancement of EPSPs prevented HFS-induced LTP (continued recordings of the same cells shown in **B**). **(F)** Quantification of mean normalized EPSP amplitudes (paired Student's $t$-test, $p = 0.52$).

pyramidal cells innately express cell type-specific forms of synaptic plasticity (Fidzinski et al., 2008; Wozny et al., 2008a,b; Aoto et al., 2013). In the MK-801 rodent model of first-episode psychosis, we have previously reported a facilitated late-onset LTP restricted to glutamatergic synapses between CA1 and subicular bursting pyramidal cells (Bartsch et al., 2015). This form of subicular LTP is expressed presynaptically. Here, we show that single systemic MK-801 application also facilitates the induction of a noncanonical, but postsynaptic LTP at glutamatergic CA1-subiculum synapses to regular-firing neurons in the ventral hippocampus: buffering postsynaptic $Ca^{2+}$ signals prevented LTP induction in regular-firing subicular neurons and, in contrast to LTP at CA1 inputs to bursting subicular neurons, LTP in regular-firing neurons was not accompanied by changes in the PPI. Apparently, cell type-specific forms of synaptic plasticity at CA1 inputs to subicular neurons appear in the MK-801 rodent model of first-episode psychosis as well. Two subsets of CA1 terminals with different susceptibility to express a presynaptic form of LTP seem to exist and determine the target-specificity of CA1 inputs to subicular neurons (Fidzinski et al., 2008; Wozny et al., 2008a; Wójtowicz et al., 2010). Cell type-specific forms of subicular LTP might be of important functional relevance. Theoretical and evidence-based theories imply that postsynaptic forms of LTP lead to an unconditional gain of synaptic transmission (Selig et al., 1999) whereas presynaptic forms of LTP redistribute existing synaptic efficacy and thereby alter the dynamics of synaptic transmission (Markram and Tsodyks, 1996). The specific role of both types of subicular neurons during behavior has yet to be determined.

## Dopamine-Dependent Long-Term Potentiation at Hippocampal Output Synapses in a Rodent Model of First-Episode Psychosis

Several lines of evidence support a D1/D5R-dependent induction mechanism of the facilitated LTP in subicular

regular-firing neurons in the MK-801 rodent model of first-episode psychosis. First, blocking D1/D5R with a specific antagonist prevented LTP induction, second, activating D1/D5R with a specific agonist mimicked LTP in MK-801-treated rats and, finally, occluded HFS-induced LTP. This mechanism is consistent with the D1/D5R-dependent facilitated LTP in bursting subicular neurons in MK-801-treated rats (Bartsch et al., 2015) yet differs from it in terms of expression site. In MK-801-treated rats, LTP in regular-firing neurons is dependent on postsynaptic $Ca^{2+}$ signaling while LTP in bursting neurons is not. Previous studies have already shown that D1/D5R activation facilitates either pre- or postsynaptic LTP depending on the subicular cell type (Roggenhofer et al., 2010, 2013). However, facilitated subicular LTP in the MK-801 rodent model of first-episode psychosis is noncanonical in that it is NMDAR-independent and exhibits a differential time course (late-onset) compared with canonical subicular LTP (initial strong post-tetanic potentiation decaying to a stable plateau).

Several origins of hippocampus-projecting dopaminergic fibers and a differential innervation along the hippocampal longitudinal axis have been described. Especially dopaminergic fibers arising from the ventral tegmental area and the substantia nigra pars compacta have been suggested to target the ventral hippocampal sector (reviewed in Edelmann and Lessmann, 2018). Notably, systemic NMDAR application can boost dopamine release in many brain regions (Deutch et al., 1987; Whitton et al., 1992; Breier et al., 1998). Relating to our findings, electrical HFS of the subiculum or regional NMDA application in the subiculum can initiate dopamine release from ventral tegmental area terminals projecting to the hippocampus (Blaha et al., 1997; Taepavarapruk et al., 2000; Floresco et al., 2001, 2003) that most prominently innervate CA1 and the subiculum (Verney et al., 1985). Hence, an increased hippocampal output after systemic MK-801 application represented by the aberrant noncanonical LTP in ventral subicular regular-firing neurons in this study may initiate a positive feedback in the hippocampus-ventral tegmental area loop and in turn, trigger an overdrive of the dopaminergic system. This scenario would be well in agreement with models proposing a hyperactive ventral hippocampus driving mesolimbic dopaminergic hyperfunction and resulting in aberrant dopaminergic signaling (Lodge and Grace, 2007). The distinct susceptibility of ventral subicular pyramidal cells to endogenously released dopamine could result from a region-specific distribution of dopamine receptor subtypes. However, D1R and D5R are expressed in pyramidal cells of the hippocampus proper and prominently in the ventral subiculum in rats (Fremeau et al., 1991). Immunohistochemical staining suggests that D5R mostly reside on cell bodies than on dendrites (Ciliax et al., 2000; Khan et al., 2000). Thus, the number of activated D1/D5R may determine differences in dopamine-dependent LTP facilitation in CA1 and the subiculum.

Considering the postsynaptic expression of LTP reported in this study, the most plausible mechanistic flow, therefore, seems to be the following: after systemic NMDAR antagonism, brief HFS can activate D1/D5R presumably *via* endogenous dopamine release. Activation of D1/D5R, in turn, elevates postsynaptic cAMP concentrations and initiates the cAMP-PKA cascade by a Gs-adenylate cyclase pathway in subicular regular-firing neurons (Missale et al., 1998). This increases postsynaptic $Ca^{2+}$ signaling *via* NMDAR-independent mechanisms (Cepeda et al., 1993, 1998; Surmeier et al., 1995; Hernández-López et al., 1997) which could modulate the membrane potential, favor EPSP summation and thereby lower the induction threshold for LTP resulting in a facilitated LTP.

## Possible Functional Impact of the Aberrant Noncanonical LTP in Ventral Subicular Regular-Firing Neurons

A functional segregation along the longitudinal axis of the hippocampus has been suggested (Moser and Moser, 1998). The dorsal (septal) sector of the hippocampus, corresponding to the human posterior hippocampus, is mostly involved in spatial memory function while the ventral (temporal) pole of the hippocampus, corresponding to the human anterior hippocampus, modulates emotional, motivational and affective processes (reviewed in Fanselow and Dong, 2010; reviewed in Strange et al., 2014). Schizophrenia is associated with anterior hippocampal pathology (Titone et al., 2004; Öngür et al., 2006; Small et al., 2011; Lieberman et al., 2018). The ability to express LTP also varies along the septotemporal axis of the hippocampus: ventral CA1 expresses lower LTP compared with dorsal CA1 but this can change under pathophysiological conditions (Maggio and Segal, 2007a,b, 2011). Bearing in mind the pivotal role of the subiculum as information gatekeeper between the hippocampus and other brain regions, this aberrant LTP in ventral subicular regular-firing neurons is expected to interfere with physiological hippocampal output processing. Thereby, our results add to the notion from previous rodent studies suggesting that subregion-specific reduced synaptic plasticity or aberrant hyperplasticity contributes to hippocampal dysfunction in first-episode psychosis (Tamminga et al., 2012a; Bartsch et al., 2019). Moreover, our observation of a cell type-specific facilitation of subicular LTP after systemic NMDAR antagonism can be considered as a form of metaplasticity. Metaplasticity is defined as a lasting modification in the neuronal state following activation which can hence regulate the duration, magnitude or direction of future synaptic plasticity (Abraham and Bear, 1996; Hulme et al., 2013). Related to first-episode psychosis, this metaplasticity might be maladaptive and could subsequently lead to hyperplasticity in key brain circuits associated with psychosis and schizophrenia (hippocampus-ventral tegmental area; hippocampus-medial prefrontal cortex) resulting in network dysregulation. Such network dysregulation is expected to contribute to the pathophysiology and perpetuation of acute psychotic symptoms and schizophrenia.

## DATA AVAILABILITY STATEMENT

The datasets generated and analyzed during the current study are available from the corresponding author on reasonable request.

## ETHICS STATEMENT

The animal study was reviewed and approved by Landesamt für Gesundheit und Soziales Berlin (LAGeSo Berlin, Germany).

## AUTHOR CONTRIBUTIONS

JCB and JB were responsible for conception of the study, design of the experiments and interpretation of the data and approved the final version and therefore agree to be accountable for all aspects of the work. JCB acquired and analyzed the data and wrote the manuscript with inputs from JB.

## FUNDING

This work was supported by the German Research Foundation (DFG) grants to JB (BE 2011/6-1), and JCB (medical scholar of the GRK 1123).

## ACKNOWLEDGMENTS

We thank Pawel Fidzinski and Christian Wozny for helpful discussion, and Olaf Maassen for excellent technical assistance. We acknowledge support from the German Research Foundation (DFG) and the Open Access Publication Fund of Charité—Universitätsmedizin Berlin.

## REFERENCES

Abraham, W. C., and Bear, M. F. (1996). Metaplasticity: the plasticity of synaptic plasticity. *Trends Neurosci.* 19, 126–130. doi: 10.1016/s0166-2236(96)80018-x

Aggleton, J. P., and Christiansen, K. (2015). The subiculum: the heart of the extended hippocampal system. *Prog. Brain Res.* 219, 65–82. doi: 10.1016/bs.pbr.2015.03.003

Aoto, J., Martinelli, D. C., Malenka, R. C., Tabuchi, K., and Südhof, T. C. (2013). Presynaptic neurexin-3 alternative splicing trans-synaptically controls postsynaptic AMPA receptor trafficking. *Cell* 154, 75–88. doi: 10.1016/j.cell.2013.05.060

Averbeck, B. B., and Chafee, M. V. (2016). Using model systems to understand errant plasticity mechanisms in psychiatric disorders. *Nat. Neurosci.* 19, 1418–1425. doi: 10.1038/nn.4413

Bannerman, D. M., Rawlins, J. N. P., McHugh, S. B., Deacon, R. M. J., Yee, B. K., Bast, T., et al. (2004). Regional dissociations within the hippocampus—memory and anxiety. *Neurosci. Biobehav. Rev.* 28, 273–283. doi: 10.1016/j.neubiorev.2004.03.004

Bartsch, J. C., Fidzinski, P., Huck, J. H., Hörtnagl, H., Kovács, R., Liotta, A., et al. (2015). Enhanced dopamine-dependent hippocampal plasticity after single MK-801 application. *Neuropsychopharmacology* 40, 987–995. doi: 10.1038/npp.2014.276

Bartsch, J. C., Schott, B. H., and Behr, J. (2019). Hippocampal dysfunction in schizophrenia and aberrant hippocampal synaptic plasticity in rodent model psychosis: a selective review. *Pharmacopsychiatry* doi: 10.1055/a-0960-9846 [Epub ahead of print].

Behr, J., Empson, R. M., Schmitz, D., Gloveli, T., and Heinemann, U. (1996). Electrophysiological properties of rat subicular neurons *in vitro*. *Neurosci. Lett.* 220, 41–44. doi: 10.1016/s0304-3940(96)13242-0

Berry, M. S., and Pentreath, V. W. (1976). Criteria for distinguishing between monosynaptic and polysynaptic transmission. *Brain Res.* 105, 1–20. doi: 10.1016/0006-8993(76)90919-7

Blaha, C. D., Yang, C. R., Floresco, S. B., Barr, A. M., and Phillips, A. G. (1997). Stimulation of the ventral subiculum of the hippocampus evokes glutamate receptor-mediated changes in dopamine efflux in the rat nucleus accumbense. *Eur. J. Neurosci.* 9, 902–911. doi: 10.1111/j.1460-9568.1997.tb01441.x

Bliss, T. V., and Lomo, T. (1973). Long-lasting potentiation of synaptic transmission in the dentate area of the anaesthetized rabbit following stimulation of the perforant path. *J. Physiol.* 232, 331–356. doi: 10.1113/jphysiol.1973.sp010273

Bogerts, B. (1997). The temporolimbic system theory of positive schizophrenic symptoms. *Schizophr. Bull.* 23, 423–435. doi: 10.1093/schbul/23.3.423

Breier, A., Adler, C. M., Weisenfeld, N., Su, T. P., Elman, I., Picken, L., et al. (1998). Effects of NMDA antagonism on striatal dopamine release in healthy subjects: application of a novel PET approach. *Synapse* 29, 142–147. doi: 10.1002/(sici)1098-2396(199806)29:2<142::aid-syn5>3.0.co;2-7

Buck, N., Cali, S., and Behr, J. (2006). Enhancement of long-term potentiation at CA1-subiculum synapses in MK-801-treated rats. *Neurosci. Lett.* 392, 5–9. doi: 10.1016/j.neulet.2005.08.054

Cepeda, C., Buchwald, N. A., and Levine, M. S. (1993). Neuromodulatory actions of dopamine in the neostriatum are dependent upon the excitatory amino acid receptor subtypes activated. *Proc. Natl. Acad. Sci. U S A* 90, 9576–9580. doi: 10.1073/pnas.90.20.9576

Cepeda, C., Colwell, C. S., Itri, J. N., Chandler, S. H., and Levine, M. S. (1998). Dopaminergic modulation of NMDA-induced whole cell currents in neostriatal neurons in slices: contribution of calcium conductances. *J. Neurophysiol.* 79, 82–94. doi: 10.1152/jn.1998.79.1.82

Ciliax, B. J., Nash, N., Heilman, C., Sunahara, R., Hartney, A., Tiberi, M., et al. (2000). Dopamine D5 receptor immunolocalization in rat and monkey brain. *Synapse* 37, 125–145. doi: 10.1002/1098-2396(200008)37:2<125::aid-syn7>3.0.co;2-7

Deutch, A. Y., Tam, S. Y., Freeman, A. S., Bowers, M. B., and Roth, R. H. (1987). Mesolimbic and mesocortical dopamine activation induced by phencyclidine: contrasting pattern to striatal response. *Eur. J. Pharmacol.* 134, 257–264. doi: 10.1016/0014-2999(87)90356-6

Edelmann, E., and Lessmann, V. (2018). Dopaminergic innervation and modulation of hippocampal networks. *Cell Tissue Res.* 373, 711–727. doi: 10.1007/s00441-018-2800-7

Fanselow, M. S. (2000). Contextual fear, gestalt memories, and the hippocampus. *Behav. Brain Res.* 110, 73–81. doi: 10.1016/s0166-4328(99)00186-2

Fanselow, M. S., and Dong, H. W. (2010). Are the dorsal and ventral hippocampus functionally distinct structures? *Neuron* 65, 7–19. doi: 10.1016/j.neuron.2009.11.031

Fidzinski, P., Shor, O., and Behr, J. (2008). Target-cell-specific bidirectional synaptic plasticity at hippocampal output synapses. *Eur. J. Neurosci.* 27, 1111–1118. doi: 10.1111/j.1460-9568.2008.06089.x

Floresco, S. B., Todd, C. L., and Grace, A. A. (2001). Glutamatergic afferents from the hippocampus to the nucleus accumbens regulate activity of ventral tegmental area dopamine neurons. *J. Neurosci.* 21, 4915–4922. doi: 10.1523/JNEUROSCI.21-13-04915.2001

Floresco, S. B., West, A. R., Ash, B., Moorel, H., and Grace, A. A. (2003). Afferent modulation of dopamine neuron firing differentially regulates tonic and phasic dopamine transmission. *Nat. Neurosci.* 6, 968–973. doi: 10.1038/nn1103

Fremeau, R. T. Jr., Duncan, G. E., Fornaretto, M. G., Dearry, A., Gingrich, J. A., Breese, G. R., et al. (1991). Localization of D1 dopamine receptor mRNA in brain supports a role in cognitive, affective and neuroendocrine aspects of dopaminergic neurotransmission. *Proc. Natl. Acad. Sci. U S A* 88, 3772–3776. doi: 10.1073/pnas.88.9.3772

Hájos, N., Ellender, T. J., Zemankovics, R., Mann, E. O., Exley, R., Cragg, S. J., et al. (2009). Maintaining network activity in submerged hippocampal slices: importance of oxygen supply. *Eur. J. Neurosci.* 29, 319–327. doi: 10.1111/j.1460-9568.2008.06577.x

Hall, J., Trent, S., Thomas, K. L., O'Donovan, M. C., and Owen, M. J. (2015). Genetic risk for schizophrenia: convergence on synaptic pathways involved in plasticity. *Biol. Psychiatry* 77, 52–58. doi: 10.1016/j.biopsych.2014.07.011

Harris, E., and Stewart, M. (2001). Intrinsic connectivity of the rat subiculum: II. Properties of synchronous spontaneous activity and a demonstration of multiple generator regions. *J. Comp. Neurol.* 435, 506–518. doi: 10.1002/cne.1047

Heckers, S., Rauch, S., Goff, D., Savage, C., Schacter, D., Fischman, A., et al. (1998). Impaired recruitment of the hippocampus during conscious recollection in schizophrenia. *Nat. Neurosci.* 1, 318–323. doi: 10.1038/1137

Hernández-López, S., Bargas, J., Surmeier, D. J., Reyes, A., and Galarraga, E. (1997). Receptor activation enhances evoked discharge in neostriatal medium spiny neurons by modulating an L-type $Ca^{2+}$ conductance. *J. Neurosci.* 17, 3334–3342. doi: 10.1523/JNEUROSCI.17-09-03334.1997

Hulme, S. R., Jones, O. D., and Abraham, W. C. (2013). Emerging roles of metaplasticity in behaviour and disease. *Trends Neurosci.* 36, 353–362. doi: 10.1016/j.tins.2013.03.007

Jarrard, L. E. (1995). What does the hippocampus really do? *Behav. Brain Res.* 71, 1–10. doi: 10.1016/0166-4328(95)00034-8

Khan, Z. U., Gutiérrez, A., Martín, R., Peñafiel, A., Rivera, A., and de la Calle, A. (2000). Dopamine D5 receptors of rat and human brain. *Neuroscience* 100, 689–699. doi: 10.1016/s0306-4522(00)00274-8

Kim, Y., and Spruston, N. (2012). Target-specific output patterns are predicted by the distribution of regular-spiking and bursting pyramidal neurons in the subiculum. *Hippocampus* 22, 693–706. doi: 10.1002/hipo.20931

Köhler, C. (1985). Intrinsic projections of the retrohippocampal region in the rat brain. I. The subicular complex. *J. Comp. Neurol.* 236, 504–522. doi: 10.1002/cne.902360407

Lapointe, V., Morin, F., Ratté, S., Croce, A., Conquet, F., and Lacaille, J. C. (2004). Synapse-specific mGluR1-dependent long-term potentiation in interneurones regulates mouse hippocampal inhibition. *J. Physiol.* 555, 125–135. doi: 10.1113/jphysiol.2003.053603

Lieberman, J. A., Girgis, R. R., Brucato, G., Moore, H., Provenzano, F., Kegeles, L., et al. (2018). Hippocampal dysfunction in the pathophysiology of schizophrenia: a selective review and hypothesis for early detection and intervention. *Mol. Psychiatry* 23, 1764–1772. doi: 10.1038/mp.2017.249

Lodge, D. J., and Grace, A. A. (2007). Aberrant hippocampal activity underlies the dopamine dysregulation in an animal model of schizophrenia. *J. Neurosci.* 27, 11424–11430. doi: 10.1523/JNEUROSCI.2847-07.2007

Luby, E. D., Cohen, B. D., Rosenbaum, G., Gottlieb, J. S., and Kelley, R. (1959). Study of a new schizophrenomimetic drug—sernyl. *Arch. Neurol. Psychiatry* 81, 363–369. doi: 10.1001/archneurpsyc.1959.02340150095011

Maggio, N., and Segal, M. (2007a). Striking variations in corticosteroid modulation of long-term potentiation along the septotemporal axis of the hippocampus. *J. Neurosci.* 27, 5757–5765. doi: 10.1523/JNEUROSCI.0155-07.2007

Maggio, N., and Segal, M. (2007b). Unique regulation of long term potentiation in the rat ventral hippocampus. *Hippocampus* 17, 10–25. doi: 10.1002/hipo.20237

Maggio, N., and Segal, M. (2011). Persistent changes in ability to express long-term potentiation/depression in the rat hippocampus after juvenile/adult stress. *Biol. Psychiatry* 69, 748–753. doi: 10.1016/j.biopsych.2010.11.026

Maren, S. (1999). Neurotoxic or electrolytic lesions of the ventral subiculum produce deficits in the acquisition and expression of Pavlovian fear conditioning in rats. *Behav. Neurosci.* 113, 283–290. doi: 10.1037/0735-7044.113.2.283

Markram, H., and Tsodyks, M. (1996). Redistribution of synaptic efficacy between neocortical pyramidal neurons. *Nature* 382, 807–810. doi: 10.1038/382807a0

Mattia, D., Kawasaki, H., and Avoli, M. (1997). *In vitro* electrophysiology of rat subicular bursting neurons. *Hippocampus* 7, 48–57. doi: 10.1002/(sici)1098-1063(1997)7:1<48::aid-hipo5>3.0.co;2-3

McGlashan, T. H. (2006). Schizophrenia in translation: is active psychosis neurotoxic? *Schizophr. Bull.* 32, 609–613. doi: 10.1093/schbul/sbl032

Miles, R., and Wong, R. K. (1987). Inhibitory control of local excitatory circuits in the guinea-pig hippocampus. *J. Physiol.* 388, 611–629. doi: 10.1113/jphysiol.1987.sp016634

Missale, C., Nash, S. R., Robinson, S. W., Jaber, M., and Caron, M. G. (1998). Dopamine receptors: from structure to function. *Physiol. Rev.* 78, 189–225. doi: 10.1152/physrev.1998.78.1.189

Morris, R. G. M. (2013). NMDA receptors and memory encoding. *Neuropharmacology* 74, 32–40. doi: 10.1016/j.neuropharm.2013.04.014

Moser, M. B., and Moser, E. I. (1998). Functional differentiation in the hippocampus. *Hippocampus* 8, 608–619. doi: 10.1002/(sici)1098-1063(1998)8:6<608::aid-hipo3>3.0.co;2-7

Neill, J. C., Barnes, S., Cook, S., Grayson, B., Idris, N. F., McLean, S. L., et al. (2010). Animal models of cognitive dysfunction and negative symptoms of schizophrenia: focus on NMDA receptor antagonism. *Pharmacol. Ther.* 128, 419–432. doi: 10.1016/j.pharmthera.2010.07.004

Nicholls, J. G., and Purves, D. (1970). Monosynaptic chemical and electrical connexions between sensory and motor cells in the central nervous system of the leech. *J. Physiol.* 209, 647–667. doi: 10.1113/jphysiol.1970.sp009184

Nicoll, R. A., and Malenka, R. C. (1999). Expression mechanisms underlying NMDA receptor-dependent long- term potentiation. *Ann. N Y Acad. Sci.* 868, 515–525. doi: 10.1111/j.1749-6632.1999.tb11320.x

O'Leary, D. M., and O'Connor, J. J. (1999). Potentiation of synaptic transmission by (S)-3,5-dihydroxy phenylglycine in the rat dentate gyrus *in vitro*: a role for voltage dependant calcium channels and protein kinase C. *Prog. Neuropsychopharmacol. Biol. Psychiatry* 23, 133–147. doi: 10.1016/s0278-5846(98)00095-5

O'Mara, S. M., Commins, S., and Anderson, M. (2000). Synaptic plasticity in the hippocampal area CA1-subiculum projection: implications for theories of memory. *Hippocampus* 10, 447–456. doi: 10.1002/1098-1063(2000)10:4<447::aid-hipo11>3.0.co;2-2

Öngür, D., Cullen, T. J., Wolf, D. H., Rohan, M., Barreira, P., Zalesak, M., et al. (2006). The neural basis of relational memory deficits in schizophrenia. *Arch. Gen. Psychiatry* 63, 356–365. doi: 10.1001/archpsyc.63.4.356

Pirnia, T., Woods, R. P., Hamilton, L. S., Lyden, H., Joshi, S. H., Asarnow, R. F., et al. (2015). Hippocampal dysfunction during declarative memory encoding in schizophrenia and effects of genetic liability. *Schizophr. Res.* 161, 357–366. doi: 10.1016/j.schres.2014.11.030

Ragland, J. D., Ranganath, C., Harms, M. P., Barch, D. M., Gold, J. M., Layher, E., et al. (2015). Functional and neuroanatomic specificity of episodic memory dysfunction in schizophrenia. *JAMA Psychiatry* 72, 909–916. doi: 10.1001/jamapsychiatry.2015.0276

Roggenhofer, E., Fidzinski, P., Bartsch, J., Kurz, F., Shor, O., and Behr, J. (2010). Activation of dopamine D1/D5 receptors facilitates the induction of presynaptic long-term potentiation at hippocampal output synapses. *Eur. J. Neurosci.* 32, 598–605. doi: 10.1111/j.1460-9568.2010.07312.x

Roggenhofer, E., Fidzinski, P., Shor, O., and Behr, J. (2013). Reduced threshold for induction of LTP by activation of dopamine D1/D5 receptors at hippocampal CA1-subiculum synapses. *PLoS One* 8:e62520. doi: 10.1371/journal.pone.0062520

Schneggenburger, R., Sakaba, T., and Neher, E. (2002). Vesicle pools and short-term synaptic depression: lessons from a large synapse. *Trends Neurosci.* 25, 206–212. doi: 10.1016/s0166-2236(02)02139-2

Schott, B. H., Voss, M., Wagner, B., Wüstenberg, T., Düzel, E., and Behr, J. (2015). Fronto-limbic novelty processing in acute psychosis: disrupted relationship with memory performance and potential implications for delusions. *Front. Behav. Neurosci.* 9:144. doi: 10.3389/fnbeh.2015.00144

Segal, M., Richter-Levin, G., and Maggio, N. (2010). Stress-induced dynamic routing of hippocampal connectivity: a hypothesis. *Hippocampus* 20, 1332–1338. doi: 10.1002/hipo.20751

Selig, D. K., Nicoll, R. A., and Malenka, R. C. (1999). Hippocampal long-term potentiation preserves the fidelity of postsynaptic responses to presynaptic bursts. *J. Neurosci.* 19, 1236–1246. doi: 10.1523/JNEUROSCI.19-04-01236.1999

Sharp, P. E. (1999). Complimentary roles for hippocampal versus subicular/entorhinal place cells in coding place, context, and events. *Hippocampus* 9, 432–443. doi: 10.1002/(sici)1098-1063(1999)9:4<432::aid-hipo9>3.0.co;2-p

Small, S. A., Schobel, S. A., Buxton, R. B., Witter, M. P., and Barnes, C. A. (2011). A pathophysiological framework of hippocampal dysfunction in ageing and disease. *Nat. Rev. Neurosci.* 12, 585–601. doi: 10.1038/nrn3085

Staff, N. P., Jung, H. Y., Thiagarajan, T., Yao, M., and Spruston, N. (2000). Resting and active properties of pyramidal neurons in subiculum and CA1 of rat hippocampus. *J. Neurophysiol.* 84, 2398–2408. doi: 10.1152/jn.2000.84.5.2398

Stewart, M. (1997). Antidromic and orthodromic responses by subicular neurons in rat brain slices. *Brain Res.* 769, 71–85. doi: 10.1016/s0006-8993(97)00690-2

Stewart, M., and Wong, R. K. S. (1993). Intrinsic properties and evoked responses of guinea pig subicular neurons *in vitro*. *J. Neurophysiol.* 70, 232–245. doi: 10.1152/jn.1993.70.1.232

Strange, B. A., Witter, M. P., Lein, E. S., and Moser, E. I. (2014). Functional organization of the hippocampal longitudinal axis. *Nat. Rev. Neurosci.* 15, 655–669. doi: 10.1038/nrn3785

Surmeier, D. J., Bargas, J., Hemmings, H. C. Jr., Nairn, A. C., and Greengard, P. (1995). Modulation of calcium currents by a D1 dopaminergic protein kinase/phosphatase cascade in rat neostriatal neurons. *Neuron* 14, 385–397. doi: 10.1016/0896-6273(95)90294-5

Taepavarapruk, P., Floresco, S. B., and Phillips, A. G. (2000). Hyperlocomotion and increased dopamine efflux in the rat nucleus accumbens evoked by electrical stimulation of the ventral subiculum: role of ionotropic glutamate and dopamine D1 receptors. *Psychopharmacology* 151, 242–251. doi: 10.1007/s002130000376

Tamminga, C. A., Southcott, S., Sacco, C., Wagner, A. D., and Ghose, S. (2012a). Glutamate dysfunction in hippocampus: relevance of dentate gyrus and CA3 signaling. *Schizophr. Bull.* 38, 927–935. doi: 10.1093/schbul/sbs062

Tamminga, C. A., Thomas, B. P., Chin, R., Mihalakos, P., Youens, K., Wagner, A. D., et al. (2012b). Hippocampal novelty activations in schizophrenia: disease and medication effects. *Schizophr. Res.* 138, 157–163. doi: 10.1016/j.schres.2012.03.019

Taube, J. S. (1993). Electrophysiological properties of neurons in the rat subiculum *in vitro*. *Exp. Brain Res.* 96, 304–318. doi: 10.1007/bf00227110

Titone, D., Ditman, T., Holzman, P. S., Eichenbaum, H., and Levy, D. L. (2004). Transitive inference in schizophrenia: impairments in relational memory organization. *Schizophr. Res.* 68, 235–247. doi: 10.1016/s0920-9964(03)00152-x

Verney, C., Baulac, M., Berger, B., Alvarez, C., Vigny, A., and Helle, K. B. (1985). Morphological evidence for a dopaminergic terminal field in the hippocampal formation of young and adult rat. *Neuroscience* 14, 1039–1052. doi: 10.1016/0306-4522(85)90275-1

Volianskis, A., France, G., Jensen, M. S., Bortolotto, Z. A., Jane, D. E., and Collingridge, G. L. (2015). Long-term potentiation and the role of N-methyl-d-aspartate receptors. *Brain Res.* 1621, 5–16. doi: 10.1016/j.brainres.2015.01.016

Wellmer, J., Su, H., Beck, H., and Yaari, Y. (2002). Long-lasting modification of intrinsic discharge properties in subicular neurons following status epilepticus. *Eur. J. Neurosci.* 16, 259–266. doi: 10.1046/j.1460-9568.2002.02086.x

Whitton, P. S., Biggs, C. S., Pearce, B. R., and Fowler, L. J. (1992). Regional effects of MK-801 on dopamine and its metabolites studied by *in vivo* microdialysis. *Neurosci. Lett.* 142, 5–8. doi: 10.1016/0304-3940(92)90607-9

Wigström, H., and Gustafsson, B. (1983). Facilitated induction of hippocampal long-lasting potentiation during blockade of inhibition. *Nature* 301, 603–604. doi: 10.1038/301603a0

Wöhrl, R., Eisenach, S., Manahan-Vaughan, D., Heinemann, U., and von Haebler, D. (2007). Acute and long-term effects of MK-801 on direct cortical input evoked homosynaptic and heterosynaptic plasticity in the CA1 region of the female rat. *Eur. J. Neurosci.* 26, 2873–2883. doi: 10.1111/j.1460-9568.2007.05899.x

Wójtowicz, A. M., Fidzinski, P., Heinemann, U., and Behr, J. (2010). Beta-adrenergic receptor activation induces long-lasting potentiation in burst-spiking but not regular-spiking cells at CA1-subiculum synapses. *Neuroscience* 171, 367–372. doi: 10.1016/j.neuroscience.2010.09.028

Wozny, C., Maier, N., Fidzinski, P., Breustedt, J., Behr, J., and Schmitz, D. (2008a). Differential cAMP signaling at hippocampal output synapses. *J. Neurosci.* 28, 14358–14362. doi: 10.1523/JNEUROSCI.4973-08.2008

Wozny, C., Maier, N., Schmitz, D., and Behr, J. (2008b). Two different forms of long-term potentiation at CA1-subiculum synapses. *J. Physiol.* 586, 2725–2734. doi: 10.1113/jphysiol.2007.149203

Zierhut, K., Bogerts, B., Schott, B., Fenker, D., Walter, M., Albrecht, D., et al. (2010). The role of hippocampus dysfunction in deficient memory encoding and positive symptoms in schizophrenia. *Psychiatry Res. Neuroimaging* 183, 187–194. doi: 10.1016/j.pscychresns.2010.03.007

Zucker, R. S., and Regehr, W. G. (2002). Short-term synaptic plasticity. *Annu. Rev. Physiol.* 64, 355–405. doi: 10.1146/annurev.physiol.64.092501.114547

**Conflict of Interest**: The authors declare that the research was conducted in the absence of any commercial or financial relationships that could be construed as a potential conflict of interest.

*Copyright © 2020 Bartsch and Behr. This is an open-access article distributed under the terms of the Creative Commons Attribution License (CC BY). The use, distribution or reproduction in other forums is permitted, provided the original author(s) and the copyright owner(s) are credited and that the original publication in this journal is cited, in accordance with accepted academic practice. No use, distribution or reproduction is permitted which does not comply with these terms.*

frontiers in Cellular Neuroscience

ORIGINAL RESEARCH
published: 21 April 2020
doi: 10.3389/fncel.2020.00091

# Distinct Synchronous Network Activity During the Second Postnatal Week of Medial Entorhinal Cortex Development

*Julia Dawitz*†, Tim Kroon†, J. J. Johannes Hjorth, Huib D. Mansvelder and Rhiannon M. Meredith*

*Integrative Neurophysiology, Center for Neurogenomics and Cognitive Research, Vrije Universiteit Amsterdam, Amsterdam, Netherlands*

The medial entorhinal cortex (MEC) contains specialized cell types whose firing is tuned to aspects of an animal's position and orientation in the environment, reflecting a neuronal representation of space. The spatially tuned firing properties of these cells quickly emerge during the third postnatal week of development in rodents. Spontaneous synchronized network activity (SSNA) has been shown to play a crucial role in the development of neuronal circuits prior to week 3. SSNA in MEC is well described in rodents during the first postnatal week, but there are little data about its development immediately prior to eye opening and spatial exploration. Furthermore, existing data lack single-cell resolution and are not integrated across layers. In this study, we addressed the question of whether the characteristics and underlying mechanisms of SSNA during the second postnatal week resemble that of the first week or whether distinct features emerge during this period. Using a combined calcium imaging and electrophysiology approach *in vitro*, we confirm that in mouse MEC during the second postnatal week, SSNA persists and in fact peaks, and is dependent on ionotropic glutamatergic signaling. However, SSNA differs from that observed during the first postnatal week in two ways: First, EC does not drive network activity in the hippocampus but only in neighboring neocortex (NeoC). Second, GABA does not drive network activity but influences it in a manner that is dependent both on age and receptor type. Therefore, we conclude that while there is a partial mechanistic overlap in SSNA between the first and second postnatal weeks, unique mechanistic features do emerge during the second week, suggestive of different or additional functions of MEC within the hippocampal-entorhinal circuitry with increasing maturation.

**Keywords: development, medial entorhinal cortex, giant depolarizing potentials, early network oscillations, GABA, synchronization**

OPEN ACCESS

***Edited by:***
*Jochen C. Meier, Technische Universität Braunschweig, Germany*

***Reviewed by:***
*Saikat Ray, Weizmann Institute of Science, Israel*
*Guzel Sitdikova, Kazan Federal University, Russia*

****Correspondence:***
*Julia Dawitz*
*j.dawitz@gmail.com*

*† These authors have contributed equally to this work*

***Specialty section:***
*This article was submitted to Cellular Neurophysiology, a section of the journal Frontiers in Cellular Neuroscience*

***Received:*** *17 January 2020*
***Accepted:*** *26 March 2020*
***Published:*** *21 April 2020*

***Citation:***
*Dawitz J, Kroon T, Hjorth JJJ, Mansvelder HD and Meredith RM (2020) Distinct Synchronous Network Activity During the Second Postnatal Week of Medial Entorhinal Cortex Development. Front. Cell. Neurosci. 14:91. doi: 10.3389/fncel.2020.00091*

## INTRODUCTION

The medial entorhinal cortex (MEC) contains specialized cell types whose firing is tuned to aspects of an animal's position and orientation in the environment, reflecting a neuronal representation of space (Moser and Moser, 2008). The spatially tuned firing properties of these cells quickly emerge during the third postnatal week of development in rodents (Langston et al., 2010;

Wills and Cacucci, 2014). Firing patterns of grid cells, the most abundant spatially tuned cell-type in superficial MEC (sMEC) (Sargolini et al., 2006), depend on local inhibitory connectivity according to attractor network models (McNaughton et al., 2006; Couey et al., 2013; Pastoll et al., 2013). Recurrent inhibition in sMEC layers starts to develop during the third postnatal week (Couey et al., 2013; Pastoll et al., 2013). Additionally, it has recently been shown that proper maturation of the hippocampal circuits depends on layer II MEC stellate cells, starting from postnatal day (P)14 onward (Donato et al., 2017). Thus, during the third postnatal week, there is a rapid maturation of MEC circuits that drives the development of the hippocampal formation. However, MEC network maturation starts well before the third postnatal week.

In many brain regions, spontaneous synchronized network activity (SSNA) has been shown to be essential for several developmental processes underlying early network maturation (see Spitzer, 2006; Blankenship and Feller, 2009 for reviews). Such SSNA has also been observed in the MEC during the first two postnatal weeks (Jones and Heinemann, 1989; Sheroziya et al., 2009; Namiki et al., 2013). During the first postnatal week, SSNA is initialized in layer III of the lateral entorhinal cortex (LEC), and then travels to MEC, hippocampus, and neocortex (NeoC; Namiki et al., 2013). Thus, SSNA of EC is synchronized with neocortical, CA1, and CA3 activity and has therefore been proposed as a cortical "pacemaker" whose intrinsic activity drives neighboring neocortical regions during early postnatal development (Garaschuk et al., 2000; Namiki et al., 2013). Indeed, it has been shown *in vivo* that during the first postnatal week MEC drives hippocampal sharp-waves (Valeeva et al., 2019). SSNA in EC depends on ionotropic glutamate receptors (iGluRs) (Jones and Heinemann, 1989; Sheroziya et al., 2009; Namiki et al., 2013) and it is suggested that the disappearance of SSNA in hippocampus and NeoC is mediated by the maturation of GABA-A receptor activity (Garaschuk et al., 2000; Allène et al., 2008; for review: Blankenship and Feller, 2009). Although SSNA is most extensively studied during the first postnatal week, field potential recordings have shown that in layer III of the MEC, SSNA peaks around P9/10 (Sheroziya et al., 2009). However, these data lack single cell resolution. Additionally, very little is known about the effects of GABAergic signaling on SSNA in MEC during the second postnatal week. In summary, while SSNA in MEC during the first postnatal week is well described, there are little data about the second postnatal week, while existing data lack single-cell resolution.

Therefore, the question arises whether SSNA of MEC during the second postnatal week is an extension of the activity observed during the first week or whether it has its own characteristics and mechanisms and therefore a potentially distinct function at cellular and computational levels. We hypothesize that MEC activity during the second postnatal week is in a transitional phase with some similarities to those reported during the first postnatal week but distinct emerging characteristics and mechanisms that could potentially prepare the layer II stellate cells for their determining role in hippocampal development from the third week onward.

To address this, we used calcium imaging and electrophysiology to dissect characteristics and mechanisms of MEC neuron activity during the second postnatal week. Upon mapping the SSNA during the second postnatal week, we determined the correlation of activation within MEC and between MEC and NeoC, CA1, and CA3. Finally, we probed the involvement of iGluRs, as well as GABA-A and GABA-B receptors during these developmental activity patterns. We find that while there is a partial mechanistic overlap in SSNA between the first and second postnatal weeks, unique mechanistic features do emerge during the second week, suggestive of different or additional functions of MEC within the hippocampal-entorhinal circuitry with increasing maturation.

# MATERIALS AND METHODS

## Animal Usage

All procedures involving animals were conducted in accordance to Dutch regulations and were approved by the animal ethics committee (DEC) of the Vrije Universiteit Amsterdam. C57BL/6 mouse pups of both sexes aged from postnatal day 7 (P7) to P15 were used for slice experiments.

## Reagents

If not indicated otherwise, all reagents were purchased from Sigma–Aldrich. For pharmacology, the following concentrations of blockers were added to the standard artificial cerebral spinal fluid (ACSF): DL-2-amino-5-phosphonopentanoic acid (DL-APV, Abcam): 100 μM, 6-cyano-7-nitroquinoxaline-2,3-dione (CNQX, Abcam): 2 μM, Gabazine (Tocris): 10 μM (blockade of phasic and tonic), CGP 55845 (CGP, Tocris): 4 μM.

## Preparation of Horizontal Brain Slices

Horizontal entorhinal cortex slices were prepared as described previously (Dawitz et al., 2011). Briefly, animals were rapidly decapitated, and their brains dissected out in ice cold cutting solution containing (in mM): 110 Choline chloride, 26 $NaHCO_3$, 10 D-glucose, 11.6 sodium ascorbate, 7 $MgCl_2$, 3.1 sodium pyruvate, 2.5 KCl, 1.25 $NaH_2PO_4$ (Merck), and 0.5 $CaCl_2$. 300 μm thick slices were obtained using a HR2 slicer (Slicer HR-2; Sigmann Elektronik, Hueffenhardt, Germany; vibration frequency: 36 Hz, vibration amplitude: 0.7 mm, propagation speed: 0.05 mm/s). After a minimum recovery period of 1 h, slices were transferred into a holding chamber containing ACSF with slightly elevated magnesium levels at room temperature composed of (mM): 125 NaCl, 26 $NaHCO_3$, 10 D-glucose, 3 KCl, 2.5 $MgCl_2$, 1.6 $CaCl_2$, and 1.25 $NaH_2PO_4$ (Merck) and continuously bubbled with carbogen gas (95% $O_2$, 5% $CO_2$).

## Fura2-AM Bulk Loading and Two-Photon Data Acquisition

After recovery slices were transferred into an interface-chamber filled with 1 ml elevated magnesium ACSF heated to approximately 34°C. 50 μg Fura2-AM (Invitrogen) diluted in 9 μl DMSO and 1 μl Pluronic® F-127 (20% solution

in DMSO; Invitrogen) was pipetted directly on top of the entorhinal cortex and incubated from 20 min—for slices of P7/8 animals, to 40 min—for slices of P14/15. Slices from animals older than P12 were pre-incubated for three minutes in 3 ml ACSF with 8 μl 0.5% cremophor (Fluka) diluted in DMSO, to facilitate Fura2-AM uptake. After incubation slices were briefly transferred back into the holding chamber and any residual surface dye was washed off. To improve stability of recordings a poly(ethyleneimine)-solution [1 ml poly(ethyleneimine) in 250 ml boric buffer containing 40 mM boric acid and 10 mM sodium tetraborate decahydrate] was used to attach slices onto the recording chambers. After coating of the recording chambers for 1 h, slices were mounted in elevated magnesium ACSF. The attached slices were placed into a humidified interface container, perfused with carbogen and left for at least 1 h to (a) achieve a stable attachment and (b) to allow for esterase activity to take place within the neurons to trap and activate Fura2-AM. Full methodology, details of slice preparation and imaging are published previously (Dawitz et al., 2011).

Functional multiphoton calcium dye network imaging data were acquired on a Trimscope (LaVision Biotec) connected to an Olympus microscope using a Ti-sapphire (Coherent) laser tuned to 820 nm wavelength. All recordings of sMEC were acquired using a 20x lens (NA 0.95) and a 350 × 350 μm field of view. Parallel recordings of deep MEC (dMEC) and sMEC were obtained with a 10x objective (NA 0.3) and a 700 × 700 μm field of view. During data acquisition, slices were continuously perfused with oxygenated standard ACSF (recipe as above but with 1.5 mM $MgCl_2$) heated to approximately 27°C. Superficial layers of the MEC were visually identified using light microscopy. Using a Hamamatsu C9100 EM-CCD camera as a detector, two time-lapse movies (2000 frames each) in sMEC or sMEC and dMEC were acquired with a sampling frequency of approximately 10 Hz. For neuron detection, at the end of each recording condition a z-stack ± 20 μm around the central plane with 1 μm optical slice thickness was acquired.

For simultaneous network imaging and cell-attached stellate cell recording (for solutions used, see section "Field Recordings and Analysis"), data were acquired on a Leica RS2 two-photon laser-scanning microscope tuned to 820 nm wavelength with a 20x lens and 400 × 400 μm field of view. Time-lapse data were acquired on a PMT at a rate of 565 ms/frame (425 frames each) in sMEC with simultaneous cell-attached recording. Spike rates were acquired using Clampex 10.2 (MDS Analytical Technologies) at an acquisition rate of 10 kHz. Cells in layer II were filled with Alexa-594 (80 μM, Invitrogen) for putative anatomical identification based on their morphology (Canto and Witter, 2012). Neuronal morphology was reconstructed using NeuroMantic software (Myatt et al., 2012).

Drugs were washed in for minimally 10 min prior to recording. Hippocampal and NeoC lesions were prepared under a low magnification microscope (4x) using a surgical knife. After lesioning, two time-lapse movies and a z-stack were recorded as described above.

## Analysis of Imaging Data

Custom-built Matlab® (Mathworks) software was used to analyze calcium data (Hjorth et al., 2016). Neurons were detected within the z-stack recorded at the end of each condition. After localizing putative neuronal centers using local intensity peaks, deformed spheres were placed around these centers within the 3D stack to fit the putative neurons. A neuron was added to the contour mask if the spheres had the volume corresponding to a radius of 2–20 μm and the intersection of the sphere and the imaging plane had a minimum area of 25 $\mu m^2$. By marking the pia, the distance for individual neurons in the slice to it could be calculated. The pia was indicated on the final mask to determine the distance to pia of individual neurons in the slice. For each detected neuron, the corresponding fluorescent raw trace was extracted from the two consecutive frames in time-lapse recordings and the relative fluorescence trace was calculated ($\Delta F/F$). The baseline was estimated using the running median of the relative trace. Frames with a drop in intensity of at least 10% in the relative trace were considered as a putative event. Additionally, the event had to be at least 1 standard deviation (SD) below the baseline, and the trace had to remain significantly below this baseline for a minimum of five frames (tested with a one-sided *t*-test). To confirm onset times and to increase sensitivity of onset detection, we repeated this procedure three times excluding the detected putative events from the running median and using a two-sided *t*-test comparing the putative event frames against the filtered baseline for significance in the consecutive iterations. The result was manually inspected and corrected where necessary.

Groups of synchronized neurons were detected as follows: Onset times of detected events from all neurons were summed together on a frame-by-frame basis and the resulting activity vector was smoothed using a Gaussian with a full width at half-maximum of five frames (500 ms). All local peaks exceeding the threshold were defined as network events. The threshold was five times the SD of 500 activity vectors derived from the same traces but with randomly shuffled inter-event intervals. A neuron was assigned to the synchronized group if it participated in at least 40% of network events. during the trace.

Thus, from this analysis, three categories of neurons were derived: silent neurons that do not show any activity, active neurons that show activity, and synchronized neurons that are active and whose activity is synchronized to other neurons in the network (**Figure 1A**). The frequency of each group and the network event frequency were calculated. Finally, another Matlab® (Mathworks) script was used to align masks of different experimental conditions to extract repeated measurements of parameters for testing based on individual neurons. All frequency values in the text and figures are derived from these within neuron comparisons. Synchronized activity is referred to as network events to clarify activity measures taken from calcium imaging data. Similar rhythmic activity measured with field and patch-clamp recordings from individual cells are referred to as network bursts throughout the manuscript.

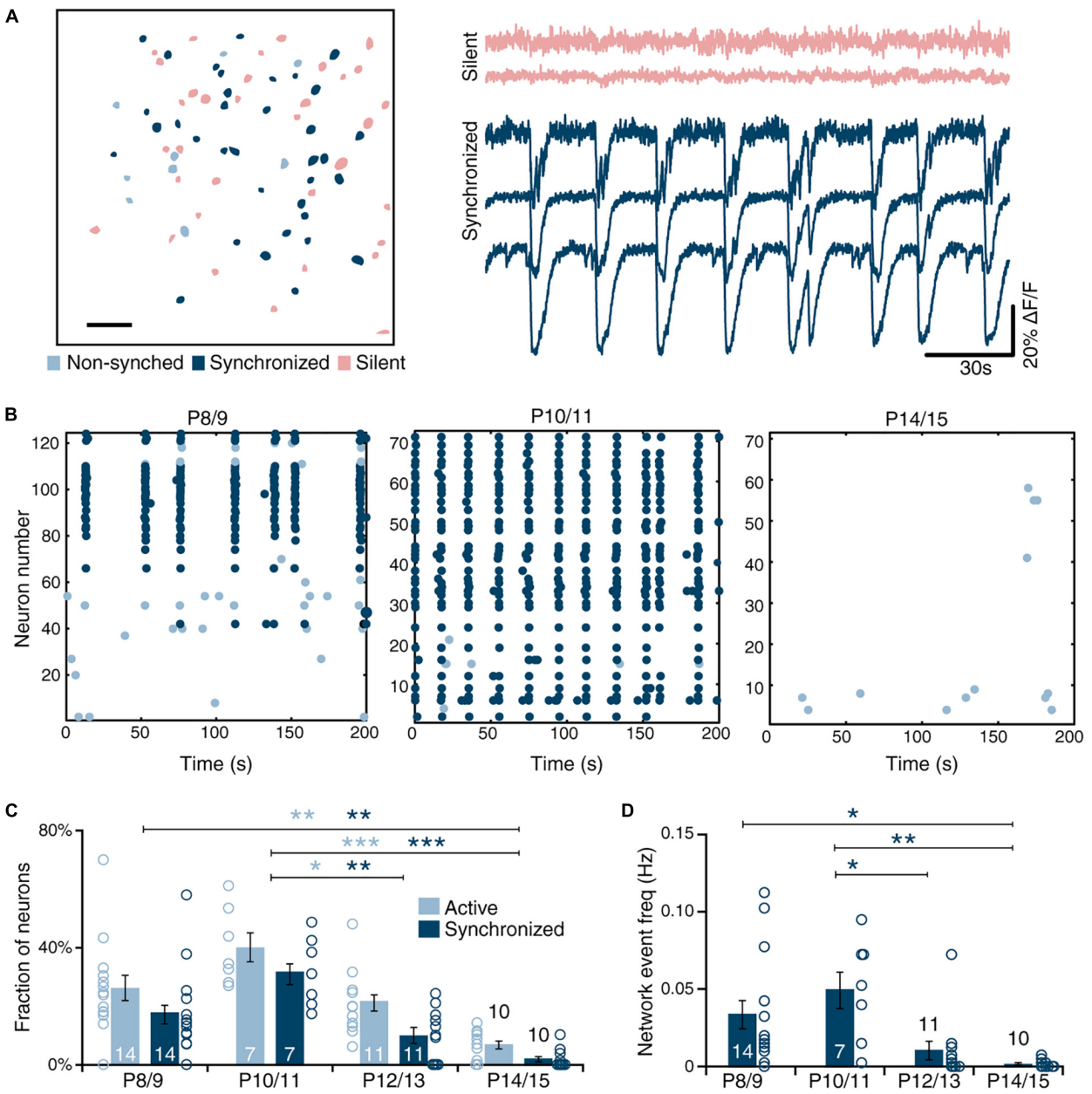


**FIGURE 1 |** Developmental dynamics of spontaneous sMEC activity. **(A)** Left: Contour map of Fura2-AM ester bulk-loaded cells in superficial medial entorhinal cortex networks imaged at P10/11. Active neurons (light blue), silent neurons (red), and synchronized neurons (dark blue) indicated. Scale bar 50 μm. Right: Example traces of silent and synchronously active neurons. **(B)** Representative raster plots of superficial MEC (sMEC) network activity at P8/9, P10/11, and P14/15, color-coded as in **(A)**. **(C)** Quantification of the fraction of active and synchronized neurons during postnatal development showed a significant age-dependent peak at P10/11 in fraction of cells that are active [one-way ANOVA, $F(3,41) = 10.1$, $p < 0.001$; Bonferroni corrected, P8/9 vs. P14/15, $p = 0.004$; P10/11 vs. P12/13, $p = 0.028$; P10/11 vs. P14/15, $p < 0.001$], as well as the fraction of cells that are synchronized [one-way ANOVA, $F(3,41) = 11.1$, $p < 0.001$; Bonferroni corrected, P8/9 vs. P14/15, $p = 0.008$; P10/11 vs. P12/13 $p = 0.001$; P10/11 vs. P14/15, $p < 0.001$]. **(D)** Frequency of network events (see section "Materials and Methods" for definition) is highest at P10/11 and virtually absent by P14/15 [one-way ANOVA, $F(3,41) = 5.8$, $p = 0.002$; Bonferroni corrected: P8/9 vs. P14/15, $p = 0.043$; P10/11 vs. P12/13, $p = 0.032$; P10/11 vs. P14/15, $p = 0.006$]. Bar graphs represent the mean ± standard error of the mean (SEM). *N* shown in bars as the number of slices. Number of animals used, P8/9: 4, P10/11: 2, P12/13: 3. P14/15: 2. $^*p < 0.05$; $^{**}p < 0.01$; $^{***}p < 0.001$.

## Field Recordings and Analysis

dMEC, sMEC, NeoC (perirhinal cortex), and the different hippocampal areas were visually identified with an Olympus microscope (4x lens) using oblique contrast. Field electrodes (chloride-coated silver electrodes inserted into 2–3 MΩ borosilicate glass pipettes filled with ACSF) were lowered into the regions of interest using micromanipulators (Luigs-Neuman, Ratingen), and placed at regions with good signal-to-noise

readings. Field potentials were acquired with Multiclamp 400B amplifiers (Molecular Devices) using Clampex 10.2 (MDS Analytical Technologies) at an acquisition rate of 10 kHz.

Analysis was carried out using custom-made Matlab® (Mathworks) software. First, signals were high-pass filtered at 1 Hz to eliminate any slow frequency drift of the signal. Then, a threshold of 5.5 times SD was applied to detect field potentials. For the dMEC-sMEC recordings customized thresholds (between 4.5 and 12 times SD) were used to achieve the optimal detection rates. Spikes were grouped as one burst if they were preceded by another spike within 3 s. The first spike of a burst was defined as the burst onset and used to calculate event frequency. Given the long duration of network bursts, a synchronous event between different regions and sMEC was defined as the occurrence of a burst in the region of interest within a time-window of 2.5 s preceding or following an sMEC event. The proportion of synchrony between different regions relative to sMEC was then calculated.

## Patch-Clamp Recordings

For patch-clamp recordings, the same recording apparatus was used as for field recordings (see above), but the microscope was equipped with a 60x lens. Borosilicate pipettes with a resistance of ∼10 MΩ were filled with intracellular solution containing (in mM): 148 Kgluconate, 1 KCl, 10 Hepes, 4 Mg-ATP, 4 $K_2$-phosphocreatine, 0.4 GTP, and 0.2% biocytin, adjusted with KOH to pH 7.3. For cell-attached recordings in **Figure 2** (2–10 min), active cells of interest were selected in dMEC and sMEC and recorded simultaneously in GΩ-resistance seal configurations. After up to 10 min of continuous voltage-clamp recordings, whole-cell access was made if possible and step protocols were acquired in whole-cell current-clamp mode to electrophysiologically identify neuron type and to fill neurons with biocytin for *post hoc* anatomical confirmation. Stellate cells were electrophysiologically identified based on their characteristic sag and prominent rebound amplitudes often evoking a rebound action potential that pyramidal cells do not have (Canto and Witter, 2012). To measure synaptic inputs of identified neurons in some cases up to 10 min voltage-Clamp, whole-cell recordings were acquired. After recordings, slices were fixed in 4% paraformaldehyde (PFA) for at least 1 week before staining.

Cell-attached data were analyzed using Matlab® (Mathworks) scripts adapted from the field recording analysis. Due to stable baselines, no filtering was applied. Customized thresholds for action-potential (AP) detection ranged from 2 to 40 times SD. APs were grouped to be part of one network burst if they were preceded by another spike within a time-window of 1.5 s. As a measure of synchrony, the proportion of bursts in sMEC that are followed or preceded within 1 s from time of burst onset in the dMEC was calculated. For anatomical identification, slices were stained for biocytin using a modified avidin-biotin-peroxidase method. Note that staining of the entire dendritic tree was limited caused by the high input resistance due to the 10 MΩ pipettes.

## DiI Tracing

To trace the entorhinal innervation of hippocampus *ex vivo*, horizontal slices were prepared as described above. Slices were allowed to recover in ACSF for one hour and fixed in 4% PFA in phosphate buffered saline for 1 h at room temperature. 1,1′-Dioctadecyl-3,3,3′3′-tetramethylindocarbocyanine perchlorate (Vybrant DiI, Invitrogen) was pressure-injected into the entorhinal cortex. After incubation at 37°C in PBS containing 0.2% ethylenediaminetetraacetic acid (EDTA) and 1% PFA for 1 week, slices were rinsed in PBS. Staining with PBS containing 4′,6-diamidino-2-phenylindole (DAPI, Thermo Fisher Scientific) for 5 min was used to visualize cell bodies and slices were then mounted in Fluoromount. Image stacks were obtained with a Leica TCS-SP8 confocal using a 20x air objective (NA 0.5) with a resolution of 1.51 μm by 1.51 μm by 2 μm (*xyz*) per voxel.

## Statistics

Statistical tests used are indicated in the figure legends for individual experiments. In general, to compare two conditions within the same experiment, a paired *t*-test was used unless data were not normally distributed and then a Wilcoxon Signed Rank test was used. To compare means from different experiments independent *t*-tests were performed, or Mann–Whitney *U*-tests when data were not normally distributed. Multiple means were compared using one-way ANOVAs. *Post hoc* analysis was carried out using Bonferroni-corrected *t*-tests. Reported is the abbreviation of test statistic with the degrees of freedom in brackets equaling the value of the test statistic. Differences were defined as significant if *p*-values were smaller than 0.05. In figures, * indicates significance ($p < 0.05$), # indicates a trend ($p < 0.1$). All statistics were performed on slice level except the % frequency change in **Figures 4**, **5**, and the activity frequencies in **Figure 5**. Data regarding glutamate and GABA receptor blockers are shown in figures as percentages of baseline values or percentage changes relative to baseline values, in order to make effect sizes more readily comparable. However, all statistical tests on these data are performed on the raw values (see **Table 1**).

# RESULTS

## Entorhinal Cortex Shows Robust SSNA During the Second Postnatal Week

To unravel the mechanisms underlying SSNA, we utilized an *in vitro* slice live-imaging approach. Using multiphoton calcium imaging with single cell resolution, we found that networks in the sMEC consisted of silent and active cells, of which the majority of the latter were synchronously active (**Figure 1A**). To establish the developmental time-course of SSNA, we mapped spontaneous network events during the second postnatal week, which precedes the onset of spatially tuned neuronal firing in MEC (Langston et al., 2010; Wills and Cacucci, 2014). In each neuron, somatic calcium events reflecting suprathreshold activity were binarized and their synchronization across the network was calculated (**Figures 1B–D**, see section "Materials and Methods"). SSNA peaked at P10/11, exhibiting the highest proportion of

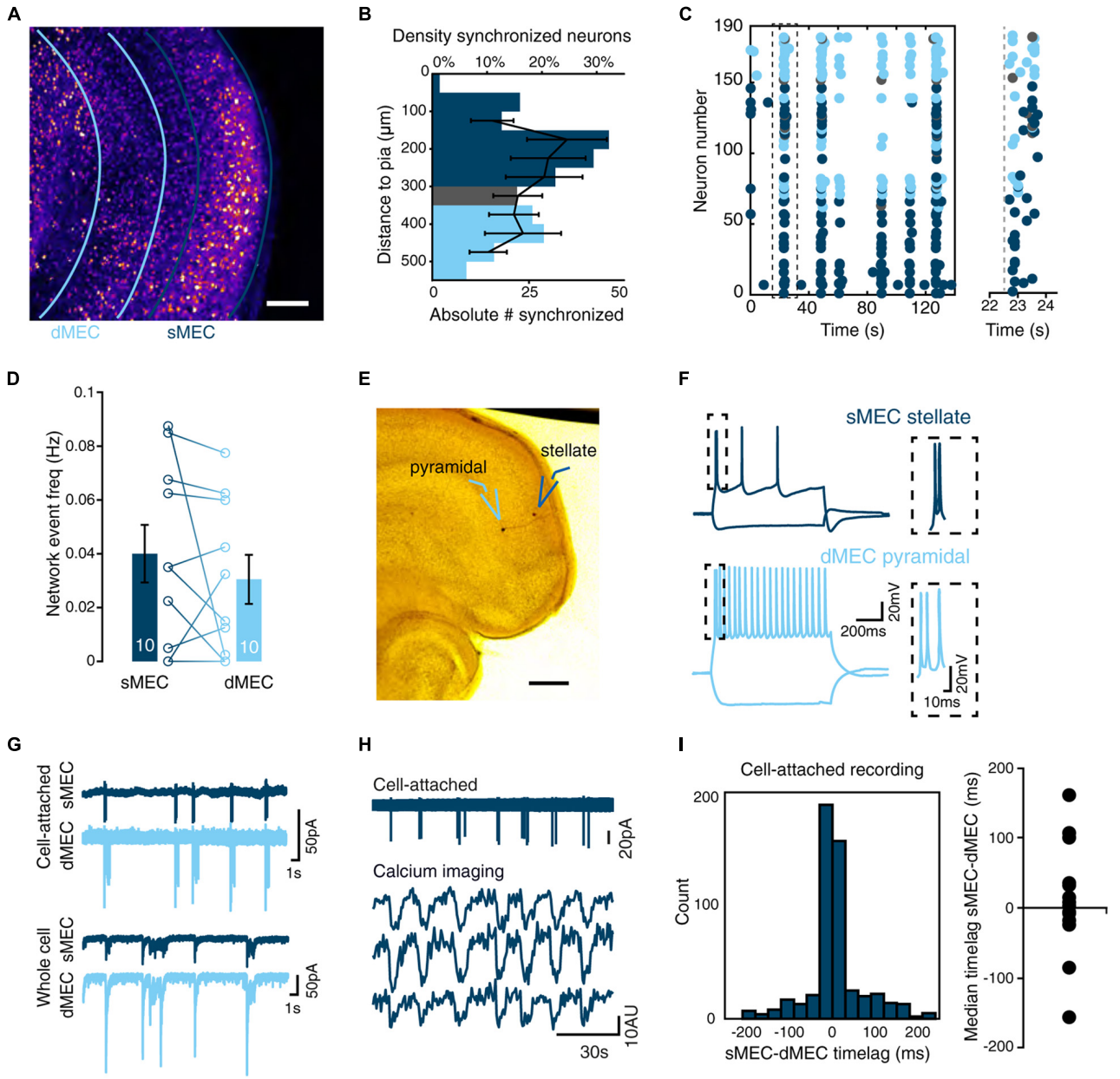


**FIGURE 2 |** Synchrony between deep and superficial layer networks in immature MEC. **(A)** Two-photon image of entire intact MEC loaded with Fura2-AM calcium dye. Scale bar 100 µm. **(B)** Density of synchronized neurons (black lines, mean ± SEM) is not significantly different between deep (light-blue) and superficial layers (dark-blue) and intermediate (gray) layers [one-way ANOVA, $F(7,69) = 0.76$, $p = 0.622$]. Absolute number of synchronized neurons per distance bin indicated as bars. *N* is 8 slices. **(C)** Left: Representative raster plot of deep, superficial and intermediate layer MEC activity showing correlated synchrony across layers. Right: magnified view of the first network event indicated on the left by the dashed black box. Gray dashed line indicates onset of activity. **(D)** Quantification reveals no significant difference in frequency of synchronized network activity between deep and superficial networks [paired $t(9) = 0.98$, $p = 0.353$]. *N* shown in bars. **(E)** Representative biocytin-filled spiny stellate and deep layer pyramidal neuron taken from paired recordings in deep MEC (dMEC) and sMEC (scale bar 250 µm). **(F)** Spike-profile of layer II stellate cell (top) and deep pyramidal neuron. **(G)** Example of cell-attached ($n = 14$ pairs) and whole-cell recordings ($n = 6$ pairs) showing synchrony of spike rates and synaptic inputs. **(H)** Example trace of a cell-attached recording in sMEC and simultaneously recorded calcium imaging traces from three neighboring neurons. **(I)** Histogram of the observed time lag for event onset using high temporal resolution cell-attached recordings ($n = 14$ pairs) show correlated synchrony between deep and superficial layers (left) but no directionality (right, Wilcoxon signed rank test $W = 64$, $p = 0.52$) in immature MEC. Bar graphs represent the mean ± SEM. *N* shown in bars as the number of slices.

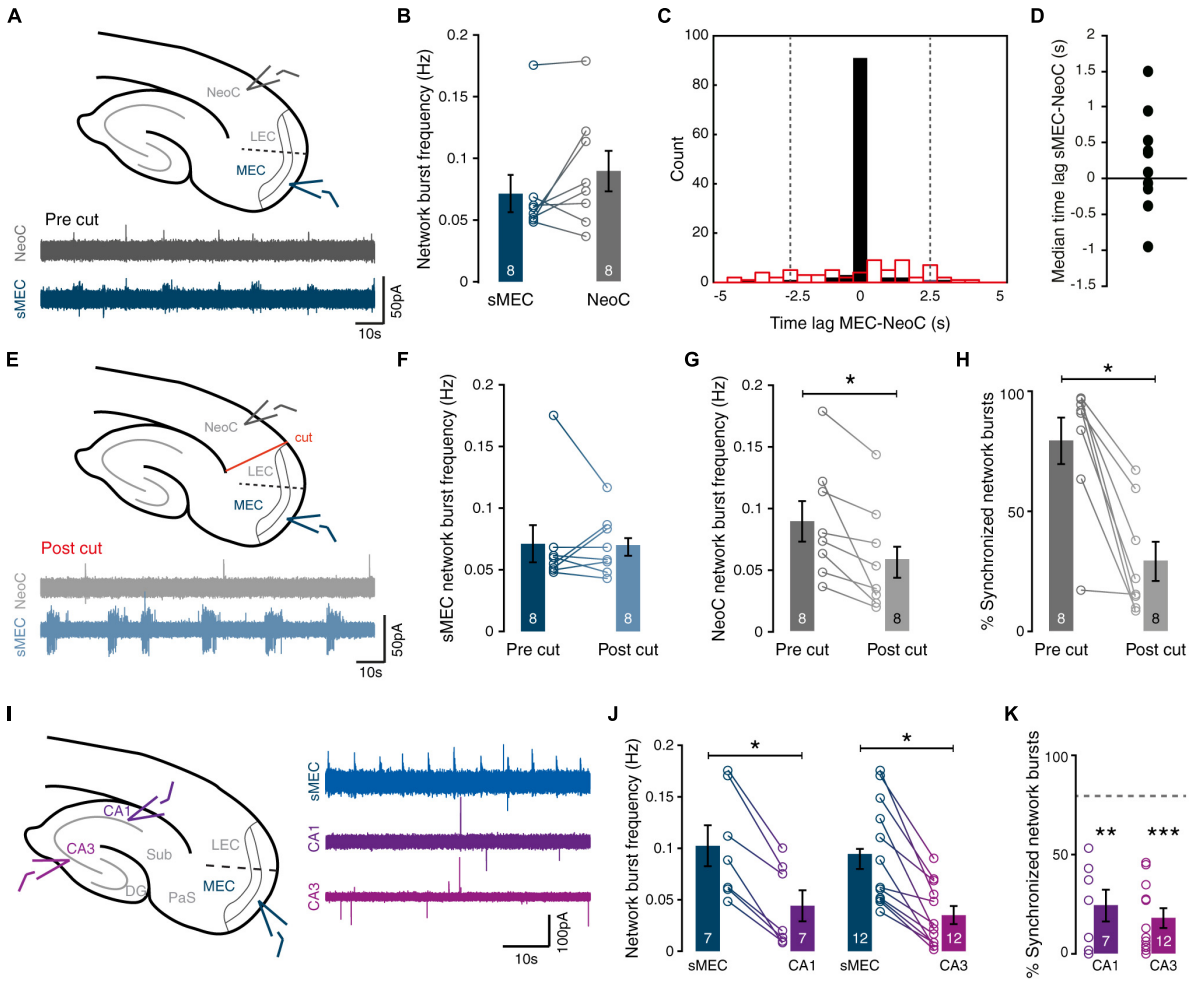


**FIGURE 3 |** Spontaneous network activity in immature MEC synchronizes network activity in neocortex. **(A)** Top: Schematic view of field recordings. Bottom: Example traces of simultaneous recordings from sMEC (blue) and superficial neocortex (NeoC, gray). **(B)** Network burst frequency is similar between sMEC and NeoC [paired $t(7) = 1.58$, $p = 0.157$]. **(C)** Representative time-lag histogram for onset times of network bursts between sMEC and NeoC pre- (black bars) and post-lesion (red open bars, see **E**). All bursts with a time lag within ± 2.5 s (between gray dotted lines) are considered synchronized. **(D)** No reliable time-lag [one-sample $t(9) = 1.06$, $p = 0.317$] indicating no directionality of activity between sMEC and NeoC. **(E)** Top: Schematic view of field recordings and lesion site. Bottom: Example traces of simultaneous recordings from sMEC (blue) and superficial neocortex (NeoC, gray) after lesion ("post cut"). **(F)** No change in the frequency of sMEC network bursts following lesion [paired $t(7) = 0.10$, $p = 0.923$]. **(G)** Lesion decreased the frequency of NeoC network bursts [paired $t(7) = 3.19$, $p = 0.015$]. **(H)** Decrease in synchronized bursts between sMEC and NeoC after lesion [paired $t(7) = 5.10$, $p = 0.001$]. **(I)** Left: field recording sites (CA1, CA3, sMEC). Right: example traces of simultaneous recordings. **(J)** Network burst frequencies are lower in CA1 and CA3 than in sMEC [CA1: paired $t(6) = 6.95$, $p < 0.001$. CA3: paired $t(11) = 6.12$, $p < 0.001$]. **(K)** Levels of synchrony between CA1-sMEC and CA3-sMEC are significantly weaker than sMEC-NeoC (gray dashed line) [CA1-sMEC vs. NeoC-sMEC: $t(15) = 3.87$, $p = 0.002$; CA3-sMEC vs. NeoC-sMEC: $t(20) = 5.72$, $p < 0.001$]. Bar graphs represent the mean ± SEM. *N* shown in bars as the number of slices. $^*p < 0.05$; $^{**}p < 0.01$; $^{***}p < 0.001$.

active neurons (**Figure 1C**, light-blue bars, 40.1 ± 4.9% cells), and significantly decreased toward P14/15 (7 ± 2% cells, **Figure 1C**, light-blue bars). Within the active network, the fraction of active neurons that were synchronized followed a similar profile, peaking at P10/11 (**Figure 1C**, dark-blue bars, 31 ± 4% cells) and decreasing by P14/15 (**Figure 1C**, dark-blue bars, 2 ± 1% cells). Frequency of synchronized events across the network ("network events"—see section "Materials and Methods" for definition), also peaked at P10/11 (**Figure 1D**, 0.050 ± 0.013 Hz) and virtually disappeared by P14/15 (**Figure 1D**, 0.002 ± 0.001 Hz). In summary, SSNA in MEC peaks at P10/11. Unless otherwise stated, all data in the following paragraphs are reported from peak activity ages P8-11 *in vitro*.

## Time-Locked Network Synchrony Across Layers of MEC

Spontaneous synchronized network activity in entorhinal cortex during the first postnatal week is led by activity in layer III (Namiki et al., 2013). We used low-magnification calcium imaging of entorhinal cortex in P10/11 slices to determine whether this holds true during the second postnatal week. Deep (dMEC, light-blue) and superficial (sMEC, dark-blue) MEC

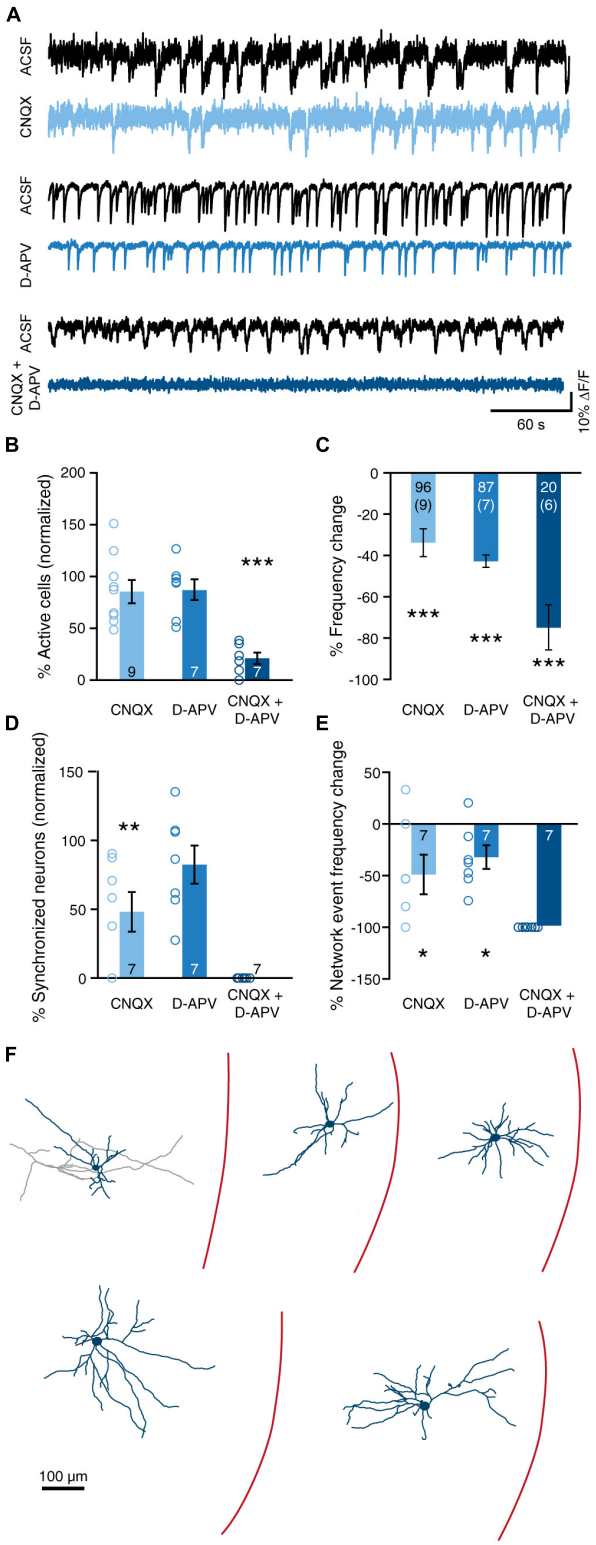


**FIGURE 4 |** Ionotropic glutamatergic signaling drives spontaneous synchronized network activity in immature sMEC. **(A)** Example traces of individual neurons before (ACSF, black) and after inhibition of AMPA (CNQX, top) receptors, NMDA (D-APV, middle) receptors, and both simultaneously (CNQX + D APV, bottom). **(B)** Blockade of AMPA or NMDA receptors does not significantly affect the proportion of active cells [CNQX: paired $t(8) = 1.88$, $p = 0.096$; D-APV: paired $t(6) = 1.20$, $p = 0.277$]. Simultaneous inhibition of both receptors decreases the proportion of active cells [CNQX + D-APV: paired $t(6) = 8.70$, $p < 0.001$]. **(C)** Blockade of AMPA and/or NMDA receptors decreased overall frequency of activity in permanently active cells [CNQX: paired $t(95) = 5.11$, $p < 0.001$; D-APV: paired $t(86) = 14.53$, $p < 0.001$; CNQX + D-APV: paired $t(19) = 6.93$, $p < 0.001$]. *N* shown in bars, number of slices shown in brackets. Note that one slice in the CNQX + D-APV group did not contain any cells that were active in both the ACSF and drug condition. **(D)** Inhibition of AMPA, but not NMDA, receptors decreased the proportion of clustered cells [CNQX: paired $t(6) = 4.39$, $p = 0.005$; D-APV: paired $t(6) = 1.22$, $p = 0.268$]. Data shown as percentage of cells that were clustered in the ACSF condition. Note that in two slices in the CNQX group, no network events were present in the ACSF condition, and that these slices were excluded from the network activity analysis. Simultaneous inhibition of both AMPA and NMDA receptors abolished all network activity. **(E)** Blockade of either AMPA or NMDA receptors caused a reduction in the frequency of network events [CNQX: paired $t(6) = 2.48$, $p = 0.0481$; D-APV: paired $t(6) = 3.26$, $p = 0.017$]. As CNQX + D-APV abolished all network events, the reduction in frequency was 100% in all slices. **(F)** Reconstructions of Alexa-594-stained intrinsically active neurons. Bar graphs represent the mean ± SEM. *N* shown in bars as either number of slices or "cells (slices)." $^*p < 0.05$; $^{**}p < 0.01$; $^{***}p < 0.001$.

was defined prior to event analysis based on cytoarchitecture (**Figure 2A**). Synchronized neurons were found in both dMEC and sMEC, with no difference in density between layers or relative to pial distance (**Figure 2B**). Network events in dMEC and sMEC were synchronized across individual neurons (**Figure 2C**), with a similar frequency (**Figure 2D**, 0.04 ± 0.01 Hz vs. 0.03 ± 0.01 Hz).

To investigate the temporal relationship between dMEC and sMEC with millisecond resolution, we used paired cell-attached recordings of sMEC stellate cells and dMEC pyramidal neurons (**Figure 2E**). We measured infrequent periods of activity during which several spikes occurred, which we termed "network bursts" (**Figure 2G**). Simultaneous cell-attached recording and calcium imaging showed that these network bursts coincided with network events (**Figure 2H**). At the end of each experiment, we switched to whole-cell configuration for subsequent electrophysiological cell-type identification (**Figures 2E–H**). As with network events recorded by calcium imaging, network bursts were highly synchronized (**Figure 2G**; cell-attached recordings: 76 ± 6%, $n = 14$, data not shown). There was no significant time-lag between cell pairs or layers, providing no evidence that superficial layers were driving spontaneous superficial network activity (**Figure 2I**, cell-attached median time lag: 6 ms IQR: -0.14 to + 0.36 ms). Finally, paired whole-cell voltage-clamp recordings from electrophysiologically identified stellate cells in sMEC and dMEC pyramidal neurons showed strikingly similar spontaneous input patterns during network bursts (**Figure 2G**, lower traces). In conclusion, we did not observe superficial neurons to be the initiators of network events during the second postnatal week.

## Entorhinal Cortex Drives Synchronous Network Activity in Neocortex

Immature entorhinal cortex has been proposed as a cortical "pacemaker" whose intrinsic activity drives neighboring

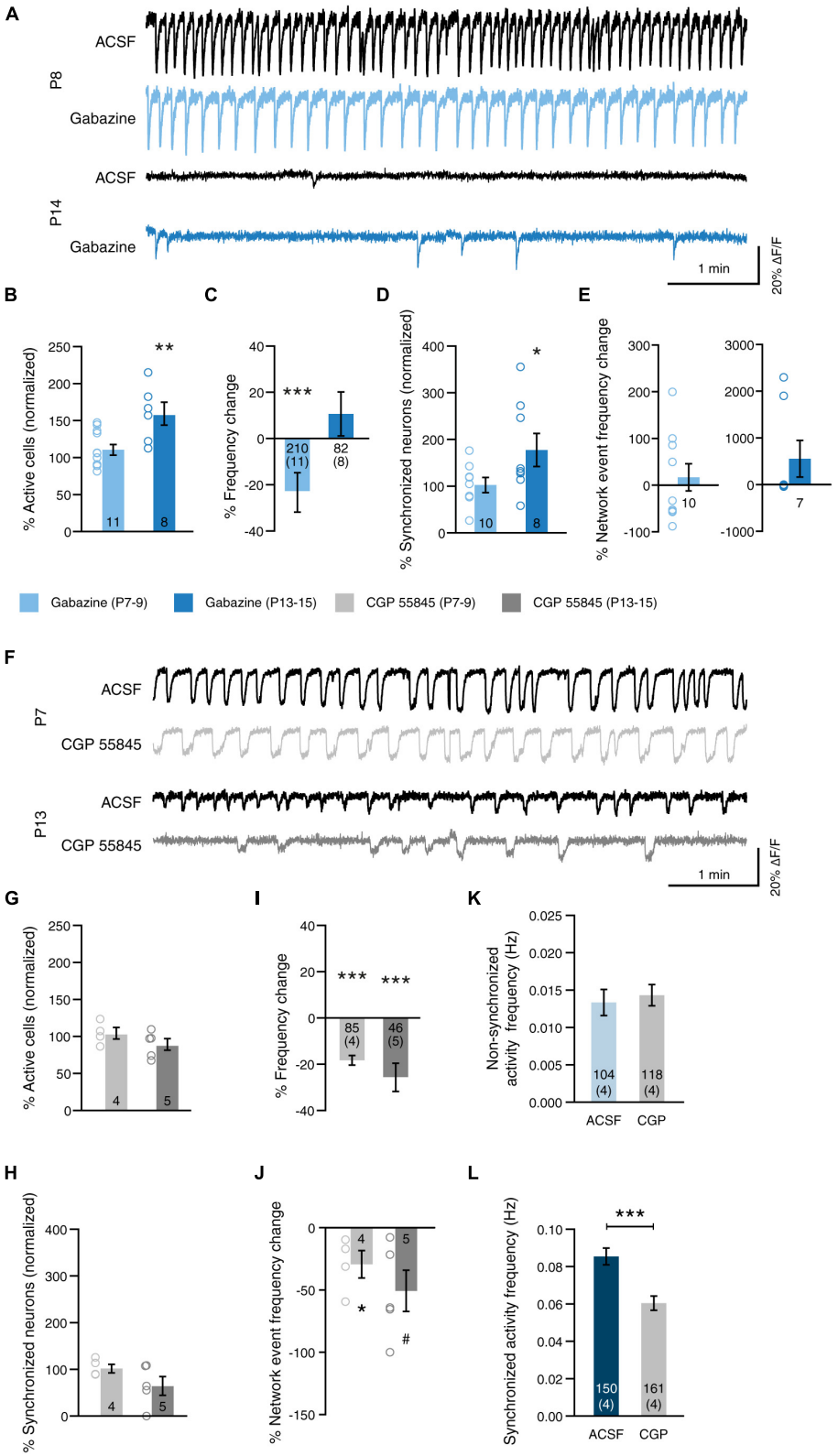


**FIGURE 5 |** GABA modulates network activity in a receptor-type-dependent manner. **(A)** Example traces before (ACSF, black) and after blockade of GABA-A receptors (Gabazine, blue) at P8 and at P14. **(B)** Blockade of GABA-A receptors at 2 weeks (P13–15) increased the proportion of active cells [gabazine 2 weeks:

*(Continued)*

**FIGURE 5 |** Continued
paired $t(7) = 4.39$, $p = 0.003$]. Blocking GABA-A receptors at 1 week (P7–9), had no significant effect [gabazine 1 week: paired $t(10) = 1.08$, $p = 0.307$]. **(C)** Blockade of GABA-A signaling reduced the frequency of permanently active cells at 1 week, but not at 2 weeks [gabazine 1 week: paired $t(210) = 2.74$, $p = 0.007$; gabazine 2 weeks: paired $t(82) = 1.17$, $p = 0.244$]. **(D)** Blockade of GABA-A receptors at 2 weeks increased the proportion of cells that participate in network events [gabazine 1 week: paired $t(9) = 1.85$, $p = 0.097$; gabazine 2 weeks: paired $t(7) = 2.44$, $p = 0.045$]. Data shown as percentage of cells that were clustered in the ACSF condition. Note that in one slice of the gabazine 1 week group, no network events were present in the ACSF condition, and that this slice was excluded from the network activity analysis. *N* shown in bars. **(E)** The frequency of network events was not affected by inhibition of GABA-A receptors [gabazine 1 week: paired $t(9) = 1.46$, $p = 0.178$; gabazine 2 weeks: Wilcoxon signed rank $W = 0$, $p = 1.0$]. *N* as in **(D)**. **(F)** Example traces before (ACSF, black) and after blockade of GABA-B receptors (CGP 55845, gray) at P8 and at P14. **(G)** Blockade of GABA-B receptors at either age had no significant effect on the proportion of active cells [CGP 55845 1 week: paired $t(3) = 0.21$, $p = 0.847$; CGP 55845 2 weeks: paired $t(4) = 1.67$, $p = 0.170$]. **(H)** Blockade of GABA-B receptors did not the proportion of cells that participate in network events [CGP 55845 1 week: paired $t(3) = 0.35$, $p = 0.751$; CGP 55845 2 weeks: paired $t(4) = 1.42$, $p = 0.228$]. Data shown as percentage of cells that were clustered in the ACSF condition. **(I)** Blockade of GABA-B signaling reduced the frequency of permanently active cells at both ages [CGP 55845 1 week: paired $t(85) = 9.05$, $p < 0.001$; CGP 55845 2 weeks: paired $t(46) = 4.26$, $p < 0.001$]. **(J)** The frequency of network events was reduced by inhibition of GABA-B receptors at 1 week [CGP 55845 1 week: paired $t(3) = 3.41$, $p = 0.042$; CGP 55845 2 weeks: paired $t(4) = 2.40$, $p = 0.074$]. **(K)** The frequency of activity that is not part of network events is unchanged by blocking GABA-B receptors at 1 week (Mann–Whitney $U = 5996$, $p = 0.769$). **(L)** The frequency of activity that is part of network events is reduced by GABA-B receptor blockade (Mann–Whitney $U = 5644$, $p < 0.001$). Bar graphs represent the mean ± SEM. *N* shown in bars as either number of slices or "cells (slices)."

neocortical regions during early postnatal development (Garaschuk et al., 2000; Namiki et al., 2013). Therefore, we next sought to determine whether network events in the entorhinal cortex were synchronized with activity or driving in different brain regions.

To first confirm that sMEC can self-generate its own SSNA during the second postnatal week, we utilized calcium imaging in isolated MEC mini-slice preparations (**Supplementary Figure S1A**). Frequency of network events dropped upon isolation (**Supplementary Figure S1C**, right, 0.12 ± 0.02 vs. 0.06 ± 0.01 Hz). However, we observed no significant changes in fractions of active (**Supplementary Figure S1B**, left, 47 ± 3 vs. 47 ± 5%), synchronized neurons (**Supplementary Figure S1B**, right, 31 ± 4 vs. 29 ± 6%) or activity levels (**Supplementary Figure S1C**, left, 0.04 ± 0.009 vs. 0.02 ± 0.006 Hz) indicating that intrinsic synchrony persists, similar to the intact slice preparation.

To test whether EC bursts drive neocortical activity, we used simultaneous field recordings in both sMEC (blue traces) and NeoC (gray traces) to measure spontaneous network bursts (**Figure 3A**). Neocortical network bursts were highly synchronized with sMEC bursts, with no significant difference in frequency (**Figure 3B**, sMEC: 0.79 ± 0.2 Hz, NeoC: 0.089 ± 0.2 Hz). We saw no significant time-lag between sMEC and NeoC to indicate a consistent origin of activity and propagation [**Figure 3C** (black bins), **Figure 3D**; average median time lag sMEC-NeoC: 0.230 ± 0.218 s].

To directly test if EC paces NeoC activity, we lesioned all interregional connections (**Figure 3E**). Both sMEC and NeoC displayed rhythmic network bursts following lesioning (**Figure 3E**, bottom traces), indicating that neocortical activity must be partly generated by a source other than EC. However, neocortical network burst frequency significantly dropped following separation from EC (**Figure 3G**), with no change in sMEC network burst frequency (**Figure 3F**). Importantly, sMEC-NeoC synchrony was strongly decreased post-lesion (**Figure 3H**, pre: 79 ± 10%, post: 29 ± 8%, **Figure 3C**, red bins), suggesting that neocortical bursts are driven by EC activity.

To test whether SSNA in sMEC could be driven by the immature hippocampus, we made simultaneous field recordings in CA1-sMEC, CA3-sMEC, and CA1-CA3-sMEC (**Figure 3I**). Frequency of spontaneous activity was significantly higher in sMEC compared to CA1 (**Figure 3J**, left, 0.1 ± 0.02 vs. 0.04 ± 0.015 Hz), and CA3 (**Figure 3J**, right, 0.09 ± 0.015 vs. 0.04 ± 0.008 Hz). Furthermore, the proportion of network bursts that were synchronized with sMEC (**Figure 3K**) was significantly lower for both CA1 (24 ± 8%) and CA3 (18 ± 5%) compared to synchrony observed between sMEC and NeoC (**Figure 3K**, dotted line). To show that the lack of clear synchrony between MEC and hippocampus is not caused by disturbed connectivity caused by the slicing procedure, we performed DiI tracing of perforant pathway fibers. Although DiI injections were relatively superficial and therefore prone to be affected by slicing, we observed significant innervation of CA1 and dentate gyrus by fibers originating from entorhinal cortex (**Supplementary Figure S2**). This indicates that entorhinal-hippocampal connectivity in our slice preparations is not affected more than entorhinal-NeoC connectivity, in line with previous results (Xiong et al., 2017).

In summary, network activity during week 2 is highly synchronized between MEC and NeoC and MEC influences the frequency of activity in NeoC. In contrast, there is little synchrony between MEC and hippocampal regions CA1 and CA3.

## Ionotropic Glutamatergic Activity Underlies Immature MEC Synchrony

Spontaneous synchronized network activity has previously been shown to be dependent on glutamatergic transmission (Garaschuk et al., 2000; Allène et al., 2008; Namiki et al., 2013). We sought to gain a better understanding of how glutamatergic transmission through AMPA and NMDA receptors affects activity of individual neurons, and how they are enlisted into network events. AMPA and NMDA receptors were selectively blocked by bath application of 2 μM CNQX and 100 μM D-APV, respectively (**Figure 4A** and **Table 1**). Blockade of either receptor did not decrease the percentage of neurons that showed activity, whereas application of both blockers simultaneously caused a large reduction in the number of active neurons (**Figure 4B**). We then analyzed the frequency of neurons that were active

**TABLE 1 |** Non-normalized values for all data shown in **Figures 4**, **5**.

| Measurement | Pre (mean ± SEM) | Post (mean ± SEM) |
|---|---|---|
| **CNQX** | | |
| Fraction active cells | 0.58 ± 0.08 | 0.48 ± 0.07 |
| Fraction synchronized cells | 0.41 ± 0.1 | 0.26 ± 0.11 |
| Overall event frequency | 0.07 ± 0.01 | 0.04 ± 0.01 |
| Network event frequency | 0.03 ± 0.01 | 0.01 ± 0.01 |
| **D-APV** | | |
| Fraction active cells | 0.54 ± 0.05 | 0.47 ± 0.06 |
| Fraction synchronized cells | 0.46 ± 0.04 | 0.38 ± 0.07 |
| Overall event frequency | 0.12 ± 0 | 0.07 ± 0 |
| Network event frequency | 0.12 ± 0.01 | 0.08 ± 0.01 |
| **CNQX + D-APV** | | |
| Fraction active cells | 0.54 ± 0.05 | 0.13 ± 0.03 |
| Fraction synchronized cells | 0.46 ± 0.04 | 0 ± 0 |
| Overall event frequency | 0.13 ± 0.01 | 0.03 ± 0.01 |
| Network event frequency | 0.12 ± 0.01 | 0 ± 0 |
| **GABAzine (P7-9)** | | |
| Fraction active cells | 0.56 ± 0.07 | 0.6 ± 0.05 |
| Fraction synchronized cells | 0.25 ± 0.04 | 0.39 ± 0.07 |
| Overall event frequency | 0.03 ± 0.003 | 0.02 ± 0.002 |
| Network event frequency | 0.04 ± 0.01 | 0.02 ± 0.004 |
| **GABAzine (P13-15)** | | |
| Fraction active cells | 0.26 ± 0.06 | 0.47 ± 0.09 |
| Fraction synchronized cells | 0.33 ± 0.05 | 0.49 ± 0.06 |
| Overall event frequency | 0.06 ± 0.01 | 0.07 ± 0.01 |
| Network event frequency | 0.06 ± 0.02 | 0.06 ± 0.01 |
| **CGP 55845 (7-9)** | | |
| Fraction active cells | 0.61 ± 0.11 | 0.62 ± 0.08 |
| Fraction synchronized cells | 0.5 ± 0.12 | 0.51 ± 0.11 |
| Overall event frequency | 0.1 ± 0.01 | 0.08 ± 0.005 |
| Network event frequency | 0.1 ± 0.03 | 0.07 ± 0.03 |
| **CGP 55845 (P13-15)** | | |
| Fraction active cells | 0.43 ± 0.09 | 0.38 ± 0.08 |
| Fraction synchronized cells | 0.34 ± 0.08 | 0.28 ± 0.1 |
| Overall event frequency | 0.09 ± 0.01 | 0.07 ± 0.01 |
| Network event frequency | 0.07 ± 0.02 | 0.04 ± 0.02 |

*Note that the CNQX + D-APV experiment was performed in the same slices as the D-APV experiment, and therefore baseline values are the identical.*

both in the ACSF condition and after drug application. CNQX and D-APV individually caused a reduction in event frequency 34.2 ± 6.7 and 43.2 ± 3.0%, respectively (**Figure 4C**). Application of CQNX and D-APV simultaneously reduced event frequency by 75.0 ± 10.8% (**Figure 4C**).

Application of CNQX, but not D-APV, significantly reduced the fraction of synchronized neurons (**Figure 4D**). Either compound caused a small reduction in the frequency of network events (**Figure 4E**). In line with previous studies (Sheroziya et al., 2009; Namiki et al., 2013), the combination of CNQX and D-APV completely blocked the occurrence of network events (**Figures 4D,E**). Thus, SSNAs during the second postnatal week are driven by glutamatergic synaptic transmission, with AMPA receptors in particular playing a large role in attracting cells into network events.

Note that even when blocking both AMPA and NMDA receptors, on average approximately 13% of neurons within a slice continued to show activity. We performed cell-attached recordings of these neurons and filled them with Alexa-594. Reconstructions of these Alexa-594-stained neurons revealed mixed multipolar morphologies among which stellate-like cells (**Figure 4F**).

## GABAergic Signaling Modulates Network Activity

Spontaneous synchronized network activity in sMEC becomes asynchronous and sparse at the end of the second postnatal week (**Figure 2**, see also Golshani et al., 2009 for data in NeoC). We hypothesized that increased GABAergic tone and maturation of the GABAergic system could mediate the abolition of SSNA like in NeoC and hippocampus (Garaschuk et al., 2000; Allène et al., 2008; for review: Blankenship and Feller, 2009). Thus, to determine the role of GABA, we tested the blockade of both GABA-A and GABA-B receptors during synchronous activity at the start of the second postnatal week (P7–9), and during asynchronous sparse activity at P13–15 (**Figures 5A,F** and **Table 1**).

Blockade of GABA-A receptors by bath application of 10 μM gabazine increased the number of active neurons at the end of the second postnatal week, but not the end of week 1 (**Figures 5A,B**, week 1: 112.3 ± 7.1% of baseline, week 2: 159.3 ± 15.6% of baseline). Interestingly, when looking at neurons that are active both in the baseline condition and after wash-in of the drug, blockade of GABA-ARs reduced the frequency of those neurons after 1 week, but not after 2 weeks (**Figure 5C**, week 1: -23.3 ± 8.5% compared to ACSF, week 2: 11.22 ± 9.6% compared to ACSF). At 1 week, blockade of GABA-ARs did not significantly affect either, the fraction of synchronized neurons participating in network events, or network event frequency (**Figures 5D,E**, light-blue, synchronized neurons: 5.6 ± 16.1% compared to ACSF, network event frequency: 119.9 ± 29.1% of baseline). At 2 weeks, on the other hand, GABA-A receptor blockade significantly increased the number of synchronized cells that participate in network events (**Figure 5D**, dark-blue, 80.4 ± 35.3% compared to ACSF).

In juvenile MEC (third postnatal week), metabotropic GABA-B receptors play a role in terminating persistent network activity of layer III pyramidal neurons (Mann et al., 2009). In contrast to GABA-A receptor blockade, GABA-B receptor blockade by 4 μM CGP 55845 did not significantly increase the number of active nor synchronously active neurons (**Figures 5F–H**, active neurons: week 1, 104.4 ± 7.8%, week 2, 89.3 ± 7.9% of baseline; synchronized neurons: week 1, + 4.7 ± 9.1%, week 2, -32.8 ± 20.0% compared to ACSF). However, inhibition of GABA-B receptors decreased the frequency of activity in general (**Figure 5I**, week 1: -18.9 ± 2.1%; week 2: -26.2 ± 6.2% compared to ACSF), and the frequency of synchronous network events (**Figure 5J**, week 1: 70.8 ± 11.0%; week 2: 48.2 ± 16.6% of baseline). Because we have found that most neuronal activity in our slice preparations is part of network events (see **Figure 1**), we hypothesized that GABA-B primarily affects event frequency,

which in turn affects the readout of frequency in general. To test this, we separated individual calcium events at 1 week into those that were part of a network event ("synchronized activity") and those that were not part of a network event ("non-synchronized activity"). We found that the frequency of non-synchronized activity was not significantly altered by GABA-B receptor blockade (**Figure 5K**, ACSF: median 0.010 Hz, IQR 0.005–0.018 Hz; CGP 55845: median 0.010 Hz, IQR 0.004–0.023 Hz). In contrast, the frequency of synchronized activity was reduced by blocking GABA-B receptors (**Figure 5L**, ACSF: median 0.078 Hz, IQR 0.059–0.080 Hz; CGP 55845: median 0.050 Hz, IQR 0.045–0.055 Hz). We therefore conclude that GABA-B receptors primarily affect synchronous network activity, rather than activity in general, in MEC at this stage of development.

Thus, GABA-A and GABA-B have opposing effects on activity and synchrony in developing MEC. Importantly, GABA-A and GABA-B receptors do not drive SSNA but significantly modulate network activity levels overall by P13-15 and regulate activity in comparable patterns to those reported from the third postnatal week onward.

# DISCUSSION

In this study, we asked whether the characteristics and underlying mechanisms of SSNA during the second postnatal week resemble the activity during the first week or whether there are distinct features during this period. We found some characteristics and underlying mechanisms that are similar to week 1. In particular, we confirm that MEC drives synchrony in NeoC and that SSNA in MEC is dependent on iGluRs. In contrast, we show that SSNA in week 2 displays distinct characteristics; specifically, we find a lack of correlation with hippocampal activity and differential effects of GABA-A and GABA-B receptor activity on the network. These results suggest different or additional functions of MEC network activity within the hippocampal-entorhinal circuitry with increasing maturation.

Using a calcium imaging approach with single cell resolution across layers, we find that SSNA in sMEC peaks at P10–11, in line with previous studies that reported similar activity using field potential recordings in specific layers (Jones and Heinemann, 1989; Sheroziya et al., 2009). In contrast, Garaschuk et al. (2000) report that network bursts vanish in entorhinal cortex after P6. The peak frequency we measure (0.06 Hz at P10/11) is similar to the burst frequencies reported in earlier studies (Jones and Heinemann, 1989; Sheroziya et al., 2009). However, entorhinal network activity during the first postnatal week reported by Garaschuk et al. (2000) was markedly slower (median frequency 0.004 Hz) and only increased to similar frequencies right before activity stopped (numbers not reported). Thus, our results on SSNA during the second postnatal week in MEC are in line with most previous studies.

## Synchrony of Network Activity Within MEC and Across Brain Regions

Our data show that SSNA in MEC during the second postnatal week is highly temporally correlated between superficial and deep layers of MEC. This is in contrast to lateral EC during the first postnatal week, where cells in layer III reliably precede those in deeper layers (Namiki et al., 2013). One possibility to explain this difference is that SSNA becomes more synchronous across layers as it spreads from the initiation site. Thus, while neurons in layer III precede those in deeper layers in LEC near the initiation site, this asynchrony is no longer present when the network burst reaches the MEC. Alternatively, assemblies of neurons that are synchronously active may grow in size with age, so that by the second postnatal week network events span multiple layers. A similar pattern has been observed for assemblies of GABAergic neurons in barrel cortex, which increased in size over the course of several days (Mòdol et al., 2020). In line with this, P10–11 is also the age range at which the largest proportion of neurons participates in network event, after which activity becomes more sparsely distributed.

Interestingly, this coincides with the decorrelation of activity in the barrel cortex, a process that is unaffected by deprivation of whisker input (Golshani et al., 2009). We find that, similar to the first postnatal week (Namiki et al., 2013), SSNA in the EC during the second postnatal week sets the pace for network activity in the NeoC. Thus, our results further substantiate the role of the MEC as a developmental hub (Garaschuk et al., 2000; Mòdol et al., 2017). Therefore, we hypothesize that sparsification of activity in the EC toward the end of the second postnatal week could act as a signal for desynchronization of activity in the NeoC.

In contrast to the highly synchronized activity between NeoC and MEC, we do not observe a high degree of synchronized activity between the MEC and the hippocampus during the second postnatal week. This is contrary to what is observed during the first postnatal week *in vivo* (Valeeva et al., 2019) and *in vitro* (Namiki et al., 2013). SSNA in hippocampus drops off earlier during development than that in EC, around P8-10 (Ben-Ari et al., 1989; Garaschuk et al., 1998). This might well be because hippocampal network activity relies on depolarizing actions of GABA (Ben-Ari et al., 2007), and GABA becomes inhibitory in the hippocampus around that time (Ben-Ari et al., 2007; Murata and Colonnese, 2019). Indeed, network burst frequency as measured by field potential recordings was consistently lower in hippocampus than in EC. Thus, while EC drives hippocampal network activity during the first postnatal week, synchrony between these brain regions disappears as activity in the hippocampus is desynchronized during the second postnatal week.

## Synaptic Mechanisms of Network Activity

We confirm that iGluR activation is the synaptic mechanism that underlies immature MEC SSNA also in week 2 (Jones and Heinemann, 1989; Garaschuk et al., 2000; Sheroziya et al., 2009; Namiki et al., 2013). Interestingly, there are some cells that remain active after iGluR blockade, similar to what (Namiki et al., 2013) report during week 1. At least some of those cells resemble stellate cell morphologies. It is possible that these cells generate spontaneous activity that initiates network events in MEC. Interestingly, from the third postnatal week on,

stellate cells in MEC drive the maturation of other cell types in both EC and hippocampus (Donato et al., 2017). We thus hypothesize that stellate cells may be involved in generating MEC network activity during the second postnatal week, in addition to their role in maturation of the hippocampal-EC circuit during later development.

Where GABAergic signaling drives SSNA in hippocampus (Garaschuk et al., 1998) and is suggested to terminate SSNA in other brain regions (for review: Blankenship and Feller, 2009), it plays a more subtle role in network activity in the entorhinal cortex. At the end of the first postnatal week, GABAergic neurons in MEC may be hub neurons that can single-handedly influence network activity (Mòdol et al., 2017). In our data, GABA-A signaling does not influence the frequency of network events or the participation of individual cells in those events. This could be explained by individual (hub) neurons that can increase or decrease network event frequency (Luccioli et al., 2018). Thus, blocking all GABA-A signaling may cancel out effects that individual (hub) neurons have on the network.

Additionally, we find that the effect of GABAergic transmission on network event frequency can be mediated by GABA-B receptors, as blocking GABA-B receptors decreases the frequency of network events. This seems counterintuitive, as the main function of GABA-B receptors is to inhibit neurotransmitter release through inhibition of N-type and P/Q-type calcium channels and activation of inwardly rectifying potassium channels (Pinard et al., 2010). Indeed, activation of GABA-B receptors during the third postnatal week decreases the excitability of stellate cells in the EC (Deng et al., 2009).

Notably, the distribution and action of GABA-B receptors may not be homogenous throughout the network. Research in the prefrontal cortex has shown that presynaptic GABA-B activation causes short-term depression of inhibitory inputs, and that inputs from somatostatin (SST)-expressing interneurons (SST-INs) are more strongly affected than those of parvalbumin (PV)-expressing interneurons (Liu et al., 2017). Hub cells that strongly influence SSNA tend to be SST-INs (Mòdol et al., 2017). Therefore, the effect we find of GABA-B signaling on network activity might be mediated through inputs from this cell type. However, the exact mechanism through which GABA-B activation influences SSNA, and whether this process involves SST-INs remains to be determined.

The effect of GABAergic signaling on activity in the network changes with age. We find that blockade of GABA-A receptors decreases the activity of neurons at the end of the first postnatal week, indicating a depolarizing effect of GABA at this age (Ben-Ari et al., 2007). However, we did not observe GABA-driven cortical giant depolarizing potentials (cGDPs, Allène et al., 2008), indicating that these are restricted to the NeoC at this age. In contrast, blocking GABA-A receptors at the end of the second postnatal week increases both the number of active cells in the slice and the proportion of cells participating in the network. Thus, there seems to be a proportion of neurons that is integrated in the network but fails to participate in network events due to their being silenced by GABAergic inhibition. Hence, increased inhibitory GABAergic drive toward the end of the second postnatal week contributes to sparsification of the network, similar to what was shown in NeoC before (Garaschuk et al., 2000). However, in contrast to what has been reported before in NeoC (Garaschuk et al., 2000), blockade of GABA-A receptors does not reinitialize SSNA at the end of the second postnatal week. We can therefore conclude that while GABA-A dependent inhibition contributes to sparsification of SSNA, it is not the mechanism through which network activity terminates during development. This may instead be due to more cell-intrinsic mechanisms, such as a developmental decrease in input resistance and therefore excitability (Burton et al., 2008). Thus, while we have made strides to elucidate the synaptic mechanisms underlying SSNA, we have yet to determine the precise origin of this characteristic activity and the cause for its termination during development.

## DATA AVAILABILITY STATEMENT

The datasets generated for this study are available on request to the corresponding author.

## ETHICS STATEMENT

The animal study was reviewed and approved by the Animal Ethics Committee (Dierexperimentele Commissie DEC) of the Vrije Universiteit Amsterdam.

## AUTHOR CONTRIBUTIONS

JD and TK performed and analyzed the experiments. TK, JD, and RM wrote the manuscript. JH wrote the scripts for the calcium data analysis. JD wrote the scripts for the analysis of electrophysiological experiments. RM and HM supervised the project.

## FUNDING

This work was supported by the Nederlandse Organisatie voor Wetenschappelijke-Onderzoek (NWO-ZonMW, Grant No. 917.10.372 to RM), by the European Commission Seventh Framework Program grant agreement (Grant No. FP7-People-ITN-2008- 238055 "BrainTrain").

## ACKNOWLEDGMENTS

We thank Ioannis Kramvis for his detailed comments on earlier versions of this manuscript. Data and text in this article have been reposited in BioRxiv http://dx.doi.org/10.1101/121459 (Dawitz et al., 2017).

## SUPPLEMENTARY MATERIAL

The Supplementary Material for this article can be found online at: https://www.frontiersin.org/articles/10.3389/fncel.2020.00091/full#supplementary-material

## REFERENCES


Allène, C., Cattani, A., Ackman, J. B., Bonifazi, P., Aniksztejn, L., Ben-Ari, Y., et al. (2008). Sequential generation of two distinct synapse-driven network patterns in developing neocortex. *J. Neurosci.* 28, 12851–12863. doi: 10.1523/JNEUROSCI.3733-08.2008

Ben-Ari, Y., Cherubini, E., Corradetti, R., and Gaiarsa, J. L. (1989). Giant synaptic potentials in immature rat CA3 hippocampal neurones. *J. Physiol.* 416, 303–325. doi: 10.1113/jphysiol.1989.sp017762

Ben-Ari, Y., Gaiarsa, J. L., Tyzio, R., and Khazipov, R. (2007). GABA: a pioneer transmitter that excites immature neurons and generates primitive oscillations. *Physiol. Rev.* 87, 1215–1284. doi: 10.1152/physrev.00017.2006

Blankenship, A. G., and Feller, M. B. (2009). Mechanisms underlying spontaneous patterned activity in developing neural circuits. *Nat. Rev. Neurosci.* 11, 18–29. doi: 10.1038/nrn2759

Burton, B. G., Economo, M. N., Lee, G. J., and White, J. A. (2008). Development of theta rhythmicity in entorhinal stellate cells of the juvenile rat. *J. Neurophysiol.* 100, 3144–3157. doi: 10.1152/jn.90424.2008

Canto, C. B., and Witter, M. P. (2012). Cellular properties of principal neurons in the rat entorhinal cortex. II. The medial entorhinal cortex. *Hippocampus* 22, 1277–1299. doi: 10.1002/hipo.20993

Couey, J. J., Witoelar, A., Zhang, S. J., Zheng, K., Ye, J., Dunn, B., et al. (2013). Recurrent inhibitory circuitry as a mechanism for grid formation. *Nat. Neurosci.* 16, 318–324. doi: 10.1038/nn.3310

Dawitz, J., Hjorth, J. J. J., Kroon, T., Ruiperez-Alonso, M., Chandrasekhar, N., Hartung, H., et al. (2017). Transient network synchrony of the developing medial entorhinal cortex. *bioRxiv* [Preprint]. doi: 10.1101/121459

Dawitz, J., Kroon, T., Johannes Hjorth, J. J., and Meredith, R. M. (2011). Functional calcium imaging in developing cortical networks. *J. Vis. Exp.* 56:e3550. doi: 10.3791/3550

Deng, P. Y., Xiao, Z., Yang, C., Rojanathammanee, L., Grisanti, L., Watt, J., et al. (2009). GABAB receptor activation inhibits neuronal excitability and spatial learning in the entorhinal cortex by activating TREK-2 K+ channels. *Neuron* 63, 230–243. doi: 10.1016/j.neuron.2009.06.022

Donato, F., Jacobsen, R. I., Moser, M. B., and Moser, E. I. (2017). Stellate cells drive maturation of the entorhinal-hippocampal circuit. *Science* 355:eaai8178. doi: 10.1126/science.aai8178

Garaschuk, O., Hanse, E., and Konnerth, A. (1998). Developmental profile and synaptic origin of early network oscillations in the CA1 region of rat neonatal hippocampus. *J. Physiol.* 507, 219–236. doi: 10.1111/j.1469-7793.1998.219bu.x

Garaschuk, O., Linn, J., Eilers, J., and Konnerth, A. (2000). Large-scale oscillatory calcium waves in the immature cortex. *Nat. Neurosci.* 3, 452–459. doi: 10.1038/74823

Golshani, P., Gonçalves, J. T., Khoshkhoo, S., Mostany, R., Smirnakis, S., and Portera-Cailliau, C. (2009). Internally mediated developmental desynchronization of neocortical network activity. *J. Neurosci.* 29, 10890–10899. doi: 10.1523/JNEUROSCI.2012-09.2009

Hjorth, J. J. J., Dawitz, J., Kroon, T., Pires, J., Dassen, V. J., Berkhout, J. A., et al. (2016). Detection of silent cells, synchronization and modulatory activity in developing cellular networks. *Dev. Neurobiol.* 76, 357–374. doi: 10.1002/dneu.22319

Jones, R. S. G., and Heinemann, U. (1989). Spontaneous activity mediated by NMDA receptors in immature rat entorhinal cortex in vitro. *Neurosci. Lett.* 104, 93–98. doi: 10.1016/0304-3940(89)90335-2

Langston, R. F., Ainge, J. A., Couey, J. J., Canto, C. B., Bjerknes, T. L., Witter, M. P., et al. (2010). Development of the spatial representation system in the rat. *Science* 328, 1576–1580. doi: 10.1126/science.1188210

Liu, L., Ito, W., and Morozov, A. (2017). GABAb receptor mediates opposing adaptations of GABA release from two types of prefrontal interneurons after observational fear. *Neuropsychopharmacology* 42, 1272–1283. doi: 10.1038/npp.2016.273

Luccioli, S., Angulo-Garcia, D., Cossart, R., Malvache, A., Módol, L., Sousa, V. H., et al. (2018). Modeling driver cells in developing neuronal networks. *PLoS Comput. Biol.* 14:e1006551. doi: 10.1371/journal.pcbi.1006551

Mann, E. O., Kohl, M. M., and Paulsen, O. (2009). Distinct roles of GABAA and GABAB receptors in balancing and terminating persistent cortical activity. *J. Neurosci.* 29, 7513–7518. doi: 10.1523/JNEUROSCI.6162-08.2009

McNaughton, B. L., Battaglia, F. P., Jensen, O., Moser, E. I., and Moser, M. B. (2006). Path integration and the neural basis of the "cognitive map. *Nat. Rev. Neurosci.* 7, 663–678. doi: 10.1038/nrn1932

Mòdol, L., Bollmann, Y., Tressard, T., Baude, A., De Marco García, N. V., and Cossart, R. (2020). Assemblies of perisomatic GABAergic neurons in the developing barrel cortex. *Neuron* 105, 93–105. doi: 10.1016/j.neuron.2019.10.007

Mòdol, L., Sousa, V. H., Malvache, A., Tressard, T., Baude, A., and Cossart, R. (2017). Spatial embryonic origin delineates GABAergic hub neurons driving network dynamics in the developing entorhinal cortex. *Cereb. Cortex* 27, 4649–4661. doi: 10.1093/cercor/bhx198

Moser, E. I., and Moser, M.-B. (2008). A metric for space. *Hippocampus* 18, 1142–1156. doi: 10.1002/hipo.20483

Murata, Y., and Colonnese, M. T. (2019). Regional heterogeneity of early GABAergic interneuron excitation in vivo. *bioRxiv* [Preprint]. doi: 10.1101/701862

Myatt, D. R., Hadlington, T., Ascoli, G. A., and Nasuto, S. J. (2012). Neuromantic – from Semi-manual to semi-automatic reconstruction of neuron morphology. *Front. Neuroinform.* 6:4. doi: 10.3389/fninf.2012.00004

Namiki, S., Norimoto, H., Kobayashi, C., Nakatani, K., Matsuki, N., and Ikegaya, Y. (2013). Layer III neurons control synchronized waves in the immature cerebral cortex. *J. Neurosci.* 33, 987–1001. doi: 10.1523/JNEUROSCI.2522-12.2013

Pastoll, H., Solanka, L., van Rossum, M. C. W., and Nolan, M. F. (2013). Feedback inhibition enables theta-nested gamma oscillations and grid firing fields. *Neuron* 77, 141–154. doi: 10.1016/j.neuron.2012.11.032

Pinard, A., Seddik, R., and Bettler, B. (2010). "GABAb receptors. physiological functions and mechanisms of diversity," in *Advances in Pharmacology*, ed T. P. Blackburn (Cambridge, MA: Academic Press Inc), 231–255. doi: 10.1016/S1054-3589(10)58010-4

Sargolini, F., Fyhn, M., Hafting, T., McNaughton, B. L., Witter, M. P., Moser, M. B., et al. (2006). Conjunctive representation of position, direction, and velocity in entorhinal cortex. *Science* 312, 758–762. doi: 10.1126/science.1125572

Sheroziya, M. G., Von Bohlen, U. H. O., Unsicker, K., and Egorov, A. V. (2009). Spontaneous bursting activity in the developing entorhinal cortex. *J. Neurosci.* 29, 12131–12144. doi: 10.1523/JNEUROSCI.1333-09.2009

Spitzer, N. C. (2006). Electrical activity in early neuronal development. *Nature* 444, 707–712. doi: 10.1038/nature05300

Valeeva, G., Janackova, S., Nasretdinov, A., Rychkova, V., Makarov, R., Holmes, G. L., et al. (2019). Emergence of coordinated activity in the developing entorhinal–hippocampal network. *Cereb. Cortex* 29, 906–920. doi: 10.1093/cercor/bhy309

Wills, T. J., and Cacucci, F. (2014). The development of the hippocampal neural representation of space. *Curr. Opin. Neurobiol.* 24, 111–119. doi: 10.1016/j.conb.2013.09.006

Xiong, G., Metheny, H., Johnson, B. N., and Cohen, A. S. (2017). A comparison of different slicing planes in preservation of major hippocampal pathway fibers in the mouse. *Front. Neuroanat.* 11:107. doi: 10.3389/fnana.2017.00107


**Conflict of Interest:** The authors declare that the research was conducted in the absence of any commercial or financial relationships that could be construed as a potential conflict of interest.

*Copyright © 2020 Dawitz, Kroon, Hjorth, Mansvelder and Meredith. This is an open-access article distributed under the terms of the Creative Commons Attribution License (CC BY). The use, distribution or reproduction in other forums is permitted, provided the original author(s) and the copyright owner(s) are credited and that the original publication in this journal is cited, in accordance with accepted academic practice. No use, distribution or reproduction is permitted which does not comply with these terms.*

frontiers in Molecular Neuroscience

ORIGINAL RESEARCH
published: 23 April 2020
doi: 10.3389/fnmol.2020.00061

# Inducing Partner Preference in Mice by Chemogenetic Stimulation of CA2 Hippocampal Subfield

*Adi Cymerblit-Sabba*[1]*, *Adam S. Smith*[1,2]*, *Sarah K. Williams Avram*[1,3], *Michelle Stackmann*[1,4], *Austin C. Korgan*[1,5], *Maria C. Tickerhoof*[2] *and W. Scott Young*[1]

[1]Section on Neural Gene Expression, National Institute of Mental Health (NIMH), National Institute of Health, Bethesda, MD, United States, [2]Neuroscience Program, Department of Pharmacology and Toxicology, School of Pharmacy, University Kansas, Lawrence, KS, United States, [3]Systems Neuroscience Imaging Resource, National Institute of Mental Health (NIMH), National Institute of Health, Bethesda, MD, United States, [4]Neurobiology and Behavior Program, Columbia University, New York, NY, United States, [5]Center for Alzheimer and Dementia Research, The Jackson Laboratory, Bar Harbor, ME, United States

Social recognition is fundamental for social decision making and the establishment of long-lasting affiliative behaviors in behaviorally complex social groups. It is a critical step in establishing a selective preference for a social partner or group member. C57BL/6J lab mice do not form monogamous relationships, and typically do not show prolonged social preferences for familiar mice. The CA2 hippocampal subfield plays a crucial role in social memory and optogenetic stimulation of inputs to the dorsal CA2 field during a short memory acquisition period can enhance and extend social memories in mice. Here, we show that partner preference in mice can be induced by chemogenetic selective stimulation of the monosynaptic projections from the hypothalamic paraventricular nucleus (PVN) to the CA2 during the cohabitation period. Specifically, male mice spend more time in social contact, grooming and huddling with the partner compared to a novel female. Preference was not induced by prolonging the cohabitation period and allowing more time for social interactions and males to sire pups with the familiar female. These results suggest that PVN-to-CA2 projections are part of an evolutionarily conserved neural circuitry underlying the formation of social preference and may promote behavioral changes with appropriate stimulation.

**Keywords: partner preference, PVN, dCA2, mice, chemogenetic**

OPEN ACCESS

***Edited by:***
*Lisa Topolnik, Laval University, Canada*

***Reviewed by:***
*Genaro Alfonso Coria-Avila, University of Veracruz, Mexico*
*Wendy Saltzman, University of California, Riverside, United States*

***Correspondence:**
*Adi Cymerblit-Sabba*
*adi.cymerblit-sabba@nih.gov*
*Adam S. Smith*
*a437s784@ku.edu*

***Received:*** *10 January 2020*
***Accepted:*** *31 March 2020*
***Published:*** *23 April 2020*

***Citation:***
*Cymerblit-Sabba A, Smith AS, Williams Avram SK, Stackmann M, Korgan AC, Tickerhoof MC and Young WS (2020) Inducing Partner Preference in Mice by Chemogenetic Stimulation of CA2 Hippocampal Subfield. Front. Mol. Neurosci. 13:61. doi: 10.3389/fnmol.2020.00061*

## INTRODUCTION

The evolution of social behaviors and mating strategies is naturally affected by the environment in which a species has to survive. Specifically, pair bonding is a long-lasting preferential association between two sexually mature adults, often described in the monogamous prairie vole, that includes the formation of partner preference, selective aggression toward unfamiliar conspecifics and bi-parental care of the offspring. Thus, selective affiliation toward a familiar conspecific is an inherent aspect of opposite-sex pair bonding and a critical step in the formation of enduring relationships (Young et al., 2011). While mating styles may differ, prosocial behaviors such as selective affiliation toward a familiar peer are observed across monogamous and even promiscuous voles (Lee et al., 2019). This social selectivity has been suggested to underly the establishment of vole social structure.

In the monogamous prairie voles, partner preference formation is indicated by a selective display of pro-social behaviors such as side-by-side contact ("huddling") and grooming toward a partner rather than other conspecifics. Male partner preference is often assessed in an established test (PPT; Williams et al., 1992) that includes a long term (3 h) presentation of both the familiar and a novel female to the tested male, following 24 h of cohabitation with the familiar female.

Since laboratory mice (typically *Mus musculus*) generally do not display a monogamous mating style or behavioral characteristics of pair bonding, they are not used to model this behavior. Still, mice can recognize potential genetically attractive (dissimilar at the major histocompatibility complex) mate through odor cues (Penn and Potts, 1999), they are highly prosocial animals demonstrating high-order social interactions (Shemesh et al., 2013) and exhibit a rich repertoire of social behaviors. Moreover, they demonstrate helping-like behavior toward a familiar littermate as well as a novel conspecific (Ueno et al., 2019). This is a behavior that could arise from a desire for social interaction (Silberberg et al., 2014). Typically, however, in short, behavioral tests, they prefer to investigate social novelty. Moreover, in a comparative study, mice tested in the common 3-h PPT failed to show preference toward the familiar conspecific unlike the tested prairie voles (Beery et al., 2018). In contrast, it was also reported that no species difference was found in the short (10 min) social preference test, commonly used to test mice (Beery et al., 2018). Given the many conserved features at the anatomical, cellular, and molecular levels within the microtine rodents, it is possible that the neural substrate of partner preference behavior exists and is suppressed, perhaps epigenetically.

Social recognition enables animals to identify and discriminate between conspecifics and to interact based on experience. It is frequently used in varied social behaviors, such as mate choice (Mateo, 2004; Zala et al., 2004), and is required for species living in complex social systems (Ferguson et al., 2002). Social recognition also has been described as an inherent process in the formation of partner preference in prairie voles, governed by a neuronal mechanism that is suggested to be highly conserved across species (Young et al., 2005, 2011; Choleris et al., 2009) and is context dependent. Specifically, pair-bonded male prairie voles show social recognition for females, whereas single males do not (Zheng et al., 2013; Blocker and Ophir, 2015). These results suggest an interaction between mating status and social context when encoding social identity. Furthermore, multiple brain regions such as the lateral septum and medial amygdala were found to be involved in both social recognition and pair-bonding behaviors through the actions of the neurohormone vasopressin (Avp; Young et al., 2011).

We previously established the critical role of the vasopressinergic projections from the paraventricular nucleus of the hypothalamus (PVN) to dorsal hippocampal CA2 area (dCA2) through its vasopressin 1b receptor (Avpr1b) in the formation of social memories (Wersinger et al., 2002; Smith et al., 2016). Furthermore, we were able to dramatically enhance social memories in mice while stimulating this direct neuronal pathway. Taken together with previous data from Avpr1b knock-out mice showing decreased social motivation (Wersinger et al., 2004) and accumulated evidence supporting vasopressin involvement in affiliative behavior across species (Caldwell et al., 2008; Williams Avram and Cymerblit-Sabba, 2017), we aimed to investigate the effect of stimulating the PVN-to-dCA2 projection on opposite-sex partner preference. We hypothesized that stimulation of the pathway underlying social memory while the mouse is experiencing social reinforcement—specifically, cohabitating and assumed mating with a female conspecific—would result in partner preference.

We used a chemogenetic approach, with the delivery of an excitatory coupled synthetic designer receptor exclusively activated by designer drugs (Gq-DREADDs) *via* a herpes simplex virus (HSV) vector into the dCA2 followed by micro delivery of the designer drug clozapine-N-oxide (CNO, an agonist of the DREADD) through a cannula directly into the PVN before the cohabitation. This allowed a transient activation of the neuronal projections from the PVN to dCA2 at the time of cohabitation. For comparison, since studies in prairie voles suggest that the quality and quantity of the social interactions between a pair contribute to the possibility of partner preference formation (Young, 2003), we also examined the effect of a longer, 6-week period of cohabitation of paired mice (without CNO) followed by co-parenting of the offspring, on partner preference. The DREADD activation resulted in the appearance of partner preference whereas the 6-week cohabitation did not. Our results suggest mice could be used to model and study the complex social behavior of partner preference and may provide an important addition to current approaches.

# MATERIALS AND METHODS

## Mouse Housing Conditions

All housing and procedures were approved by the Animal Care and Use Committee of the National Institute of Mental Health. Male and female C57Bl/6J mice (6–8 weeks old) were purchased from Jackson Laboratory (Bar Harbor, ME, USA). They were housed in an AAALAC-accredited, specific pathogen-free, vivarium at a constant temperature (∼21°C) and humidity (50%) in plastic micro-isolator cages (12″ × 6.5″ × 5.5″) containing wood chip bedding and cotton nestlets. They were maintained on a 12-h light cycle (lights off at 15:00 h) with *ad libitum* access to food and water. Cages were changed on a bi-weekly basis primarily by the same animal caretaker. All animals used in behavioral experiments were adults that were group-housed with littermates until they were cohabitated (see below).

## Surgical Procedures

### Viral Delivery and Cannulation

Male mice (7–9 weeks old) were anesthetized with an intraperitoneal injection of tribromoethanol (Avertin®, 20 mg/ml solution in sterile normal saline; 0.2 ml per 10 g of mouse weight) and placed into a stereotaxic apparatus. After leveling the head position using bregma and lambda as reference points, the skull was exposed *via* a small incision and holes were drilled bilaterally to target the hippocampal

dCA2 subfield (2.18 mm posterior to Bregma, ±2.56 mm lateral to the midline, 1.96 mm below the brain surface). An HSV vector was used to deliver either the excitatory DREADD, hM3D(Gq) fused to a fluorescent marker (mCherry), or the fluorescent marker alone into dCA2. Ten mice in the experimental group were injected with 1 μl of hsv-hEF1a-hM3D(Gq)-mCherry ($PVN^{Gq}$; $5 \times 10^9$ units/ml, MIT viral core, Cambridge, MA, USA). Similarly, ten control mice were injected with 1 μl of or hsv-hEF1a-mCherry ($PVN^{mCherry}$; $5 \times 10^9$ units/ml, MIT viral core).

Viruses were delivered *via* a 5 μl syringe (26 g, Hamilton, Reno, NV, USA) at a rate of 200 nl/min with a 33 g small gauge RN needle attachment and a Micro4 microsyringe pump (World Precision Instruments, Sarasota, FL, USA). Following the injection, the needle was left for an additional 5 min before slowly retracting it from the brain. The skin was then closed with a wound clip. Following 2 weeks of recovery, cannulae (0315GA-SPC, 5 mm cut; Plastics One, Roanoke, VA, USA) were implanted bilaterally into the PVN (0.82 mm posterior to Bregma, ±0.29 mm lateral to the midline, 4.3 mm below the brain surface). Dummy implants (c3151dc-SPC; 5.5 mm; PlasticsOne) were inserted and covered with dust caps (3030DCF; PlasticsOne). Following a week of recovery, each mouse was paired for 24 h with an ovariectomized and estrogen-primed female. Behavioral testing began when the animals were 10–12 weeks old. Only male mice observed with well-targeted viral expression were included in behavioral data analysis.

### Ovariectomy

Female mice (6–8 weeks old) were ovariectomized. Briefly, a small dorsal midline incision was made, the muscle wall spread using forceps, and the ovaries were removed. Following 4 weeks of recovery, females were either paired with a cannulated male mouse ($PVN^{Gq}$ or $PVN^{mCherry}$) for 24 h cohabitation or used as an unfamiliar stimulus in the partner preference test described below.

### Estrogen Priming

Ovariectomized females were each administered 1 μg of estrogen benzoate in 100 μl sesame oil subcutaneously for three consecutive days between the hours of 10:00 and 12:00 PM before the day of pairing with a male.

### Clozapine-N-Oxide Administration

The designer drug and DREADD agonist, CNO, was manufactured under contract for the National Institutes of Health as part of the Rapid Access to Investigative Drug Program funded by the National Institute of Neurological Disease and Stroke for DREADD studies and is pharmaceutical grade. CNO was diluted in DMSO, and then in sterile saline and stored in the dark at 4°C between uses. CNO solution was used up to 72 h after dilution. All male mice, previously injected with the virus, were administered 18 ng CNO directly into the PVN in a 60 nl volume at 100 nl/min rate, 30 min before the partner pairing (cohabitation; stimulated: $PVN^{Gq+CNO}$ or control: $PVN^{mCherry+CNO}$).

## Behavioral Paradigms

### Twenty-four Hour Partner Pairing—Cohabitation

Experimental and control groups (10 mice each initially; eight and nine, respectively, after discarding three for inaccurate injections sites), $PVN^{Gq+CNO}$ and $PVN^{mCherry+CNO}$, respectively, were brought to the testing room 30 min before the beginning of the dark cycle and, administered CNO, and placed in a fresh mouse cage. After this 30 min interval, an ovariectomized estrogen-primed female was added to the cage. The video was collected for 4 h to allow the monitoring of interactions. The following morning the female and the cage were searched for sperm plugs.

### Six-Weeks Partner-Pairing Cohabitation

Six female mice were weighed and each paired with a male mouse for 6 weeks with routine cage changes. Females were weighed weekly to determine likely gestational day (GD). When females had gained at least 30% of their original body weight, they were declared pregnant. Estimations of GD were made from weight gain. Females were monitored daily for the appearance of pups. On the day of birth, or postpartum day (PPD) 0, litters were weighed, counted, and sexed. The number of pups ranged from 4 to 10, and females and sires were allowed to keep their entire litter. Males remained in the cage with females and pups even after pup weaning at ∼21 days. The father was tested in the PPT with it mate and a stranger female 2–5 days after weaning.

### Partner Preference Test

The PPT chamber consisted of three modified transparent mouse cages (12″ × 6.5″ × 5.5″) separated by 10″ of Plexiglas tubing (radius: 4″; **Figure 2A**). Each mouse cage was filled with fresh bedding for each test session. Metal grid lids were affixed to the tops of the three chambers to prevent experimental mice from leaving the PPT test. Each stimulus mouse was tethered to a corner of one of the outer chambers allowing for full access by the test animal (adapted from Winslow, 2003). Stimulus mice were habituated to the tethering collars for 15–30 min before being placed in the chamber. The location of the partner was counterbalanced between outer cages. The tested mouse was placed in the center cage and allowed free interaction for the 3-h session. Videos of behavioral tests were recorded from above and coded by an observer blind to the identity of the mice using JWatcher Software[1] (Blumstein et al., 2010). Behavioral analysis consisted of duration in the chamber, sniffing, allogrooming, and side-by-side contact (huddling). Sniffing behavior was defined as the mouse's nose touching the body anywhere from the anogenital region, including the base of the tail, to the head, including the nose, mouth, and ears. Twenty-four hours after testing, the tested mice were euthanized for histology.

## Histology and Imaging

Animals were anesthetized with isoflurane and transcardially perfused with 4% paraformaldehyde. Brains were removed and post-fixed for 24 h. Following an overnight rinse in 1 M

[1] http://www.jwatcher.ucla.edu/

phosphate-buffered saline (PBS), brains were transferred to a 30% sucrose solution for another 24 h after which they were quickly frozen with powdered dry ice. Brains were sliced at 16 um on a cryostat (Leica3050 Biosystems, Buffalo Grove, IL, USA), the sections were mounted onto charged slides, and immunohistochemistry for mCherry amplification was performed. Briefly, sections were incubated at 4° overnight in a rabbit anti-RFP antibody (catalog number 600-401-379, Rockland Antibodies and Assays, Limerick, PA, USA) solution: 10 μl anti-RFP, 800 μl goat serum, 1 ml 20% Triton X-100, and 20 ml PBS. The next day, the sections were rinsed 3 × 10 min in PBS followed by incubation at room temperature for 1 h in the secondary antibody (anti-rabbit, Alexa Fluor 555, Catalog number A27039, Thermo Fisher Scientific, Waltham, MA, USA) solution: 100 μl anti-rabbit, 400 μl goat serum, 1 ml 20% Triton X-100, and 20 ml PBS. The sections were then rinsed in PBS. Sections were imaged using the Zeiss AxioScan Z1 slide scanner and online stitching and shading correction using a 20 × 0.8 NA objective. Images of the hippocampus were collected on a Nikon C2 point-scanning confocal microscope using a 20×, 0.8 NA objective. Z-stacks were collected using a resolution of 1,024 × 1,024 pixels/field and 2× averaging. A maximum projection image is presented.

## Statistical Analyses

Data are presented as mean ± SEM. Behavioral data for CNO treated mice were analyzed by repeated-measures two-way ANOVA with Sidak's multiple comparisons. The stimulated group $PVN^{Gq+CNO}$ included eight mice and the control group $PVN^{mCherry+CNO}$ included nine mice. For the six mice tested following the 6-week cohabitation, we used Wilcoxon matched-pairs signed-rank test. All statistical tests were carried out using Prism 8 (Graphpad Software Inc.). The level of significance was set to $P < 0.05$.

# RESULTS

## Histology

hM3D(Gq) receptor (tagged with m-Cherry) or m-Cherry were delivered by HSV bilaterally into the dCA2 to allow retrograde transport to projecting neurons, including the PVN, and onset of neuronal expression. We followed viral delivery with cannula implantation to allow selective delivery of the designer drug, CNO, directly to the PVN neurons (**Figure 1A**). Immunoreactive fibers for mCherry were observed at the site of injection in hippocampal dCA2 (**Figure 1B**) confirming retrograde transport of the virus to projecting neurons. Although the labeling within the PVN in the 16 μm sections collected was sparse (**Figure 1C**), labeled cells were observed in multiple sections examined from each mouse.

## Chemogenetic Stimulation of PVN Projections to dCA2 Induces Partner Preference

Following 24 h of cohabitation and verification of sexual contact, mice were tested in a 3-chamber apparatus for partner preference (**Figure 2A**). Chemogenetic activation of PVN neuronal projections to dCA2 during cohabitation led stimulated mice ($PVN^{Gq+CNO}$) to spend extensively more time in physical contact with their cohabiting partner (mean 21.78 ± 3.6 min) than with the stranger (mean 12.49 ± 2.4 min; **Figure 2B**). Repeated measures two-way ANOVA of time in contact showed a main effect of stimulus (partner/stranger: $F_{(1,15)} = 7.778$, $P = 0.0138$) and no interaction (group × stimulus: $F_{(1,15)}$ $P = 0.084$). *Post hoc* within-group analysis using Sidak's multiple comparison test showed a significant effect of stimulus (partner/stranger) of $P < 0.013$ in the stimulated group ($PVN^{Gq+CNO}$) and not in the control ($PVN^{mCherry+CNO}$) group ($P < 0.76$).

Stimulated mice ($PVN^{Gq+CNO}$) also spent more time allogrooming their partner (mean 174 ± 44.3 s than the stranger female (mean 4.1 ± 2.8 s; **Figure 2C**). Repeated measures two-way ANOVA of time spent allogrooming showed a main effect of stimulus (partner/stranger: $F_{(1,15)} = 12.80$, $P = 0.0028$) as well as interaction (group × stimulus: $F_{(1,15)} = 8.3$, $P = 0.00113$) with no main effect of group. *Post hoc* within-group analysis using Sidak's multiple comparison test showed a significant effect of stimulus (partner/stranger) of $P < 0.0009$ only in the stimulated group ($PVN^{Gq+CNO}$) and not in the control ($PVN^{mCherry+CNO}$) group ($P < 0.9$).

For side-by-side contact, $PVN^{Gq+CNO}$ mice again demonstrated longer sedentary contact with their partner (mean 157.2 ± 37.25 s) than with the stranger (mean 6.2 ± 15.3 s; **Figure 2D**). Repeated measures two-way ANOVA of side-by-side duration showed a main effect of stimulus (partner/stranger: $F_{(1,15)} = 19.03$, $P = 0.0006$) with no effect of group or interaction (group × stimulus: $F_{(1,15)} = 1.444$, $P = 0.248$). *Post hoc* within-group analysis using Sidak's multiple comparison test showed a significant effect of stimulus (partner/stranger: $P < 0.003$) only in the $PVN^{Gq+CNO}$ mice but not in the control ($PVN^{mCherry+CNO}$) mice ($P < 0.07$).

There was no difference between groups for sniffing (**Figure 3A**). Both control and stimulated mice spent similar times sniffing both the partner and the stranger (group × stimulus: $F_{(1,15)} = 0.5489$, $P = 0.4702$). Moreover, stimulated and control mice spent similar amounts of time in the cage of the partner (means of 47.3 ± 6.1 min and 46.9 ± 5.5 min, respectively) as in the cage of the stranger (means of 50.6 ± 6.0 min and 50.41 ± 7.4 min, respectively; **Figure 3B**). Still, when comparing the time spent in all three cages, including the empty center one, repeated measures two-way ANOVA showed a main effect of a cage ($F_{(1.567,23.51)} = 3.798$, $P = 0.0465$). While the *post hoc* analysis could not identify a significant difference, it seems that both stimulated and control mice spent extensive time in the center empty cage (means of 67.7 ± 10.7 min and 73.6 ± 9.4 min, respectively).

Finally, extending the cohabitation period to 6 weeks, in a second experimental group of non-injected mice, as well as allowing the male mice to sire pups to allow a prolonged interaction time, did not affect partner preference in measures of sniffing (Wilcoxon test partner/stranger: $P = 0.87$), proximity (Wilcoxon test partner/stranger: $P > 0.999$) or side-by-side contact (Wilcoxon test partner/stranger: $P = 0.843$; **Figure 4**).

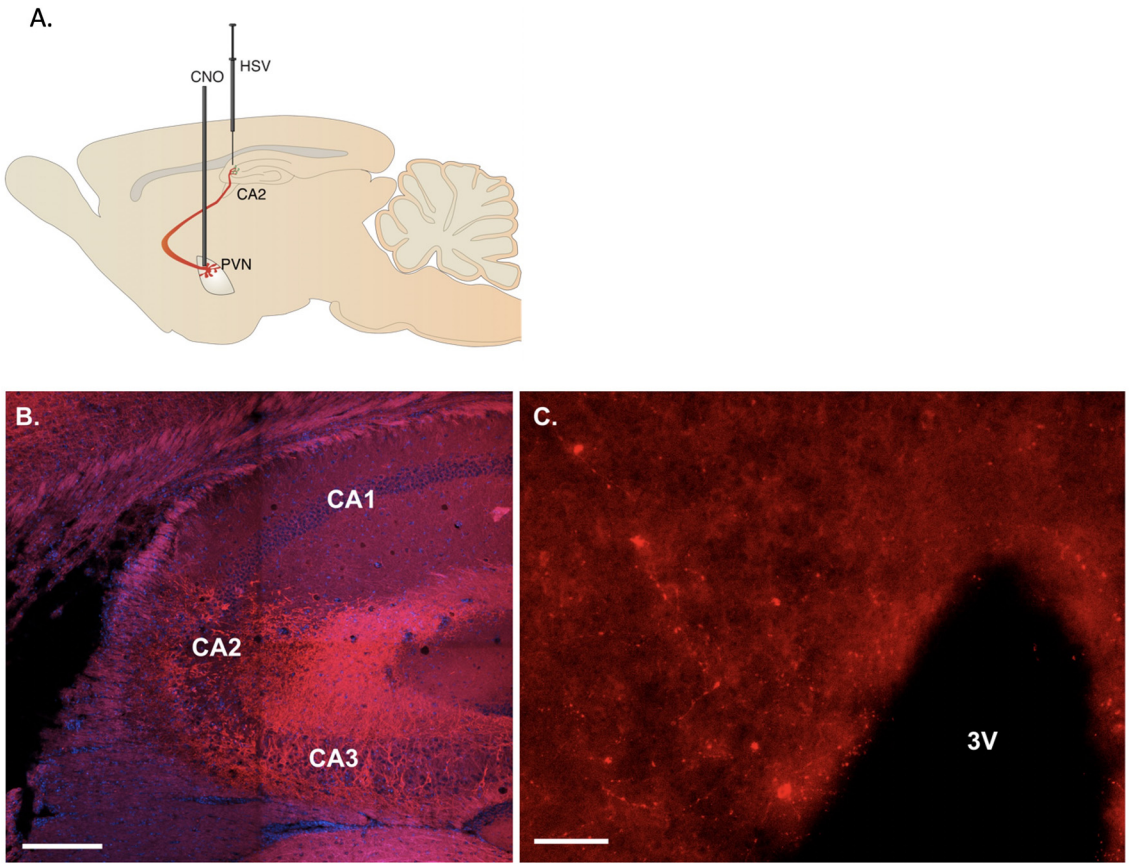


**FIGURE 1 |** Representative viral labeling. **(A)** Diagram illustrating the viral delivery to dorsal CA2 and subsequent expression in CA2 fibers and paraventricular hypothalamic nucleus (PVN) cells and then their fibers with cannulation for CNO delivery into PVN. **(B)** Coronal section showing the expression of immunoreactive fibers in the hippocampus projecting to dorsal CA2 (scale bar 200 μm). **(C)** Sixteen micrometer coronal section showing sparse cell labeling in the PVN (scale bar 20 μm).

## DISCUSSION

Studies of neuronal mechanisms underlying partner-directed affiliative behaviors come mostly from prairie voles. Accumulated data suggest these mechanisms involve the integration of social input coming from the conspecific together with reinforcement of the reward system as a result of the interaction. Thus, an interplay between the neuromodulators vasopressin, oxytocin and dopamine is involved. While the neurocircuitry has been intensely investigated, the precise neural mechanisms underlying selective affiliation requires further research (Walum and Young, 2018). All of the behavioral components of pair bonding—selective affiliation toward the partner, biparental care of offspring, and selective aggression defending territory and the partner—require social recognition.

While lab mice do not fully express the complex traits of social monogamy, they are highly prosocial animals demonstrating high-order social interactions (Shemesh et al., 2013) and a rich repertoire of social behaviors. Moreover, although evolutionary processes may lead to different neurochemical profiles in different brain regions (O'Connell and Hofmann, 2012) and epigenetic modifications may occur that are not attributable to changes in DNA sequence (Robinson et al., 2008), the social neural network's major nodes (McGraw and Young, 2010; Ko, 2017) are similar across the different species. Significant longitudinal changes following social bonding were described in the dorsal hippocampus of prairie voles (López-Gutiérrez et al., 2019). Also, within the social network, the CA2 subfield of the hippocampus is a key player in the modulation of social behaviors (Ko, 2017). Together with evidence of its receptor repertoire that includes Avpr1b, Oxtr (Pagani et al., 2015; Williams Avram and Cymerblit-Sabba, 2017; Piskorowski and Chevaleyre, 2018) and dopamine receptors (Gangarossa et al., 2012), the CA2 is a potential candidate to be part of the neural circuitry underlying partner preference.

Surprisingly, while neuronal labeling appeared to be sparse in the PVN, mice expressing the excitatory Gq and treated with CNO, delivered directly into the PVN during cohabitation, demonstrated increased time in contact as well as allogrooming and side-by-side sedentary contact with their partner, unlike their littermates expressing the mCherry tag alone. These are the cardinal measures of partner preference used in this behavioral

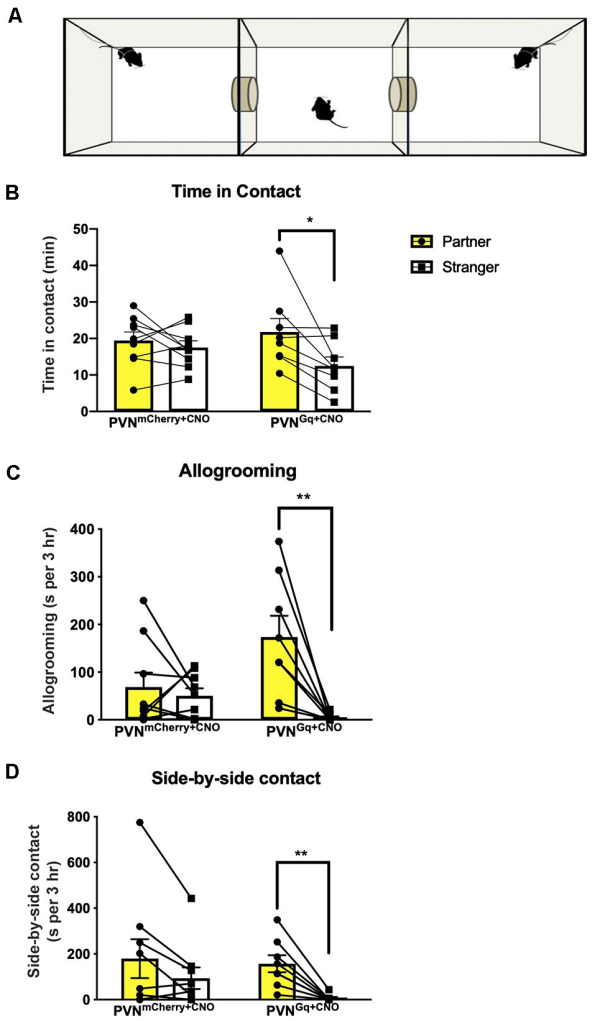


**FIGURE 2 |** Partner preference induced by CNO treatment. **(A)** Schematic illustration of partner preference test. Tested mice freely explored the chambers while stimulus females were tethered ($PVN^{Gq+CNO}$ mice = 8, $PVN^{mCherry+CNO}$ mice = 9). **(B)** $PVN^{mCherry+CNO}$ mice spent equal time in contact with their partner or the stranger, while $PVN^{Gq+CNO}$ mice demonstrated a significantly longer time in contact with their partner ($^{*}P < 0.02$). **(C)** $PVN^{Gq+CNO}$ mice spent significantly longer time allogrooming their partners, while the $PVN^{mCherry+CNO}$ group did not ($^{**}P < 0.0045$). **(D)** $PVN^{Gq+CNO}$ mice spent significantly longer in side-by-side contact ("huddling") with their partners, while the $PVN^{mCherry+CNO}$ did not ($^{**}P < 0.002$).

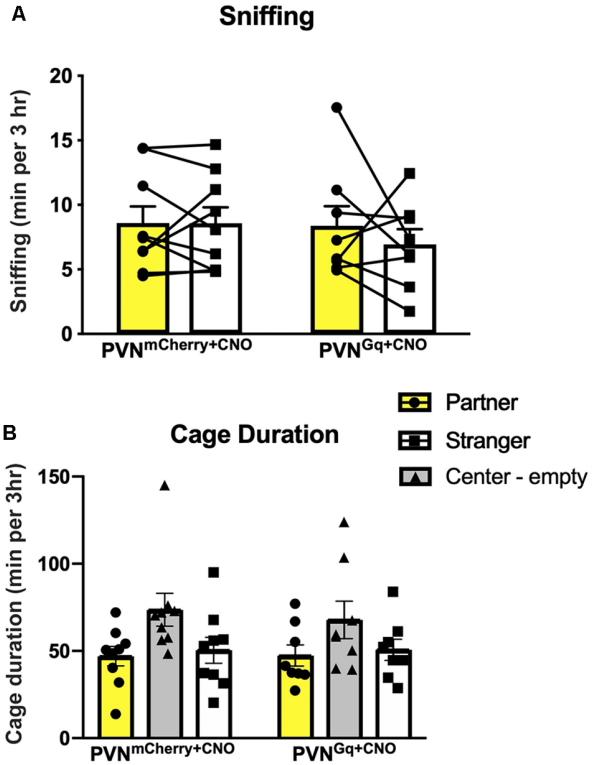


**FIGURE 3 |** Social behaviors are unchanged by CNO treatment. **(A)** Sniffing duration of either the partner or stranger were similar within and across the tested groups. **(B)** Mice spent similar times in the chambers of the partner or the stranger conspecific in both groups as well as extensive time in the empty center chamber.

paradigm when performed in voles. The enhanced partner preference behavior in the stimulated mice ($PVN^{Gq+CNO}$), appears to be dependent on the coupling of excitatory inputs from the PVN to dCA2 with the 24 h cohabitation with the female. The connections of CA2 with multiple brain regions involved in social and non-social behaviors, such as dentate gyrus, CA1, CA3, septum and median raphe (Cui et al., 2013; Benoy et al., 2018) place it in a position of a network hub. The mechanism by which CA2 interfaces with the different brain systems to facilitate several socially related behaviors requires more research, including how it may be involved in partner preference as our study suggests. Studies to see if the dCA2 is necessary for pair-bonding in prairie voles, for example, would be worthwhile as well.

The lack of partner preference in our 6-week cohabitating and mated mice allows us to conclude that social context manipulation alone is not sufficient to change the typical behavior in the lab mice, emphasizing the need for a direct stimulation of a specific neuronal pathway to produce the partner preference. The lack of monogamy seen in mice is likely a result of evolutionary changes leading to different biological valence of the social context. Phylogenetic studies suggest polygamy in mice maximizes evolutionary fitness by allowing for higher paternity success and stimulating selection competition that results in higher-quality offspring (Emlen and Oring, 1977; Firman and Simmons, 2012). Moreover, they agree with a previous study, comparing partner preference between mice and voles (Beery et al., 2018).

We previously reported that optogenetic stimulation of vasopressinergic fibers in the dCA2 resulted in enhanced social memory, as measured by a difference in sniffing durations. The lack of difference in the sniffing behavior may arise from the limitation of the particular behavioral paradigm. In mice, social memory or approach is typically tested in brief (5–10 min) encounters with the conspecific stimuli, in which

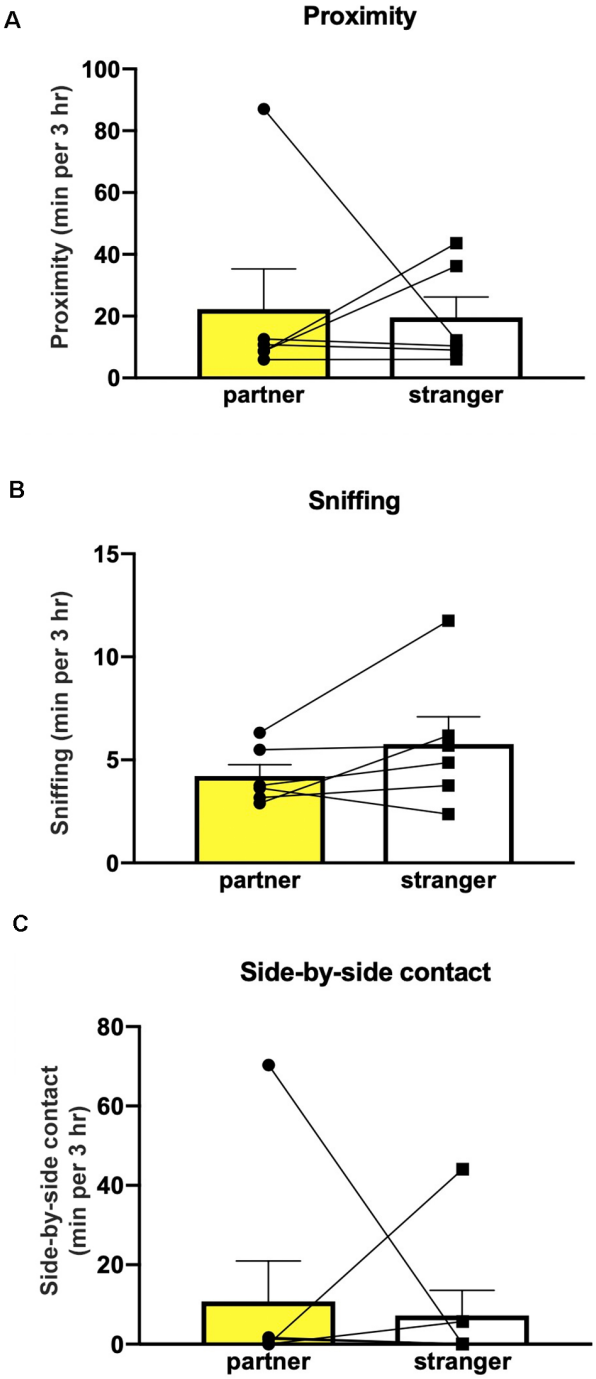


**FIGURE 4 |** The extended cohabitation period did not induce partner preference. Mice ($n$ = 6) did not show preference in sniffing **(A)**, proximity **(B)** or side-by-side contact **(C)**.

mice demonstrate recognition of a familiar conspecific by sniffing it less than the novel conspecific. These differences in duration are typically less than 60 s. In the current study, mice were presented with a familiar partner and a novel female for a prolonged period (3 h). This large increase in the testing time could conceal changes in sniffing. Also, while individual recognition is required behavior for the development of selective affiliation and pair-bonding in voles (Young et al., 2011) when they are tested for social recognition in a social preference test with a short 10-min encounter, voles spend similar times investigating either the familiar or the novel stimulus (Beery et al., 2018). Thus, while the partner preference test allowed us to investigate relevant affiliative behaviors, it may limit the ability to compare recognition memory to the commonly used mouse paradigms. Moreover, the lack of difference in the time spent in each chamber could arise from the mouse's exploratory behavior. Beery et al. (2018) showed that the mice were more active than the voles in the partner preference test and often crossed into the center chamber. We also observe that the mice tend to spend a greater percentage of time in the center chamber rather than in either of the outer chambers.

## CONCLUSION

Our results demonstrate that the underlying neurocircuit of partner preference exists in non-monogamous lab mice, and appropriate stimulation may induce this species-atypical behavior. As has been suggested by previous studies, although the social neural network is distributed across multiple brain regions, social interaction can be modulated by manipulating a single key element (Lim et al., 2004; Chen and Hong, 2018). Thus, our study promotes the needed evolutionary and comparative investigations of affiliative behaviors and their underlying mechanisms across and within species exhibiting different social organizations and behaviors.

## DATA AVAILABILITY STATEMENT

The datasets generated for this study are available on request to the corresponding author.

## ETHICS STATEMENT

The animal study was reviewed and approved by Animal Care and Use Committee, Division of Intramural Research, National Institute of Mental Health.

## AUTHOR CONTRIBUTIONS

AC-S: experimental design, surgeries for viral delivery, data analysis, manuscript preparation. AS: experimental design, surgeries for cannula placement, behavioral data collection and analysis. SW: experimental design, behavioral data collection and analysis, image data collection. MS, AK and MT: behavioral data collection and analysis. MT: behavioral data collection and analysis. WY: experimental design and manuscript preparation.

## FUNDING

This research was supported by the intramural research program of the National Institute of Mental Health (NIMH; ZIAMH002498).

## REFERENCES


Beery, A. K., Christensen, J. D., Lee, N. S., and Blandino, K. L. (2018). Specificity in sociality: mice and prairie voles exhibit different patterns of peer affiliation. *Front. Behav. Neurosci.* 12:50. doi: 10.3389/fnbeh.2018.00050

Benoy, A., Dasgupta, A., and Sajikumar, S. (2018). Hippocampal area CA2: an emerging modulatory gateway in the hippocampal circuit. *Exp. Brain Res.* 236, 919–931. doi: 10.1007/s00221-018-5187-5

Blocker, T. D., and Ophir, A. G. (2015). Social recognition in paired but not single male prairie voles. *Anim. Behav.* 108, 1–8. doi: 10.1016/j.anbehav.2015.07.003

Blumstein, D., Daniel, J., and Evans, C. (2010). *JWatcher Software*. Available online at: http://www.jwatcher.ucla.edu. Accessed October 5, 2012.

Caldwell, H. K., Lee, H. J., Macbeth, A. H., and Young, W. S. III. (2008). Vasopressin: behavioral roles of an "original" neuropeptide. *Prog. Neurobiol.* 84, 1–24. doi: 10.1016/j.pneurobio.2007.10.007

Chen, P., and Hong, W. (2018). Neural circuit mechanisms of social behavior. *Neuron* 98, 16–30. doi: 10.1016/j.neuron.2018.02.026

Choleris, E., Clipperton-Allen, A. E., Phan, A., and Kavaliers, M. (2009). Neuroendocrinology of social information processing in rats and mice. *Front. Neuroendocrinol.* 30, 442–459. doi: 10.1016/j.yfrne.2009.05.003

Cui, Z., Gerfen, C. R., and Young, W. S. III. (2013). Hypothalamic and other connections with dorsal CA2 area of the mouse hippocampus. *J. Comp. Neurol.* 521, 1844–1866. doi: 10.1002/cne.23263

Emlen, S. T., and Oring, L. W. (1977). Ecology, sexual selection and the evolution of mating systems. *Science* 197, 215–223. doi: 10.1126/science.327542

Ferguson, J. N., Young, L. J., and Insel, T. R. (2002). The neuroendocrine basis of social recognition. *Front. Neuroendocrinol.* 23, 200–224. doi: 10.1006/frne.2002.0229

Firman, R. C., and Simmons, L. W. (2012). Male house mice evolving with post-copulatory sexual selection sire embryos with increased viability. *Ecol. Lett.* 15, 42–46. doi: 10.1111/j.1461-0248.2011.01706.x

Gangarossa, G., Longueville, S., De Bundel, D., Perroy, J., Herve, D., Girault, J. A., et al. (2012). Characterization of dopamine D1 and D2 receptor-expressing neurons in the mouse hippocampus. *Hippocampus* 22, 2199–2207. doi: 10.1002/hipo.22044

Ko, J. (2017). Neuroanatomical substrates of rodent social behavior: the medial prefrontal cortex and its projection patterns. *Front. Neural Circuits* 11:41. doi: 10.3389/fncir.2017.00041

Lee, N. S., Goodwin, N. L., Freitas, K. E., and Beery, A. K. (2019). Affiliation, aggression, and selectivity of peer relationships in meadow and prairie voles. *Front. Behav. Neurosci.* 13:52. doi: 10.3389/fnbeh.2019.00052

Lim, M. M., Wang, Z., Olazabal, D. E., Ren, X., Terwilliger, E. F., and Young, L. J. (2004). Enhanced partner preference in a promiscuous species by manipulating the expression of a single gene. *Nature* 429, 754–757. doi: 10.1038/nature02539

López-Gutiérrez, M. F., Ortiz, J. J., Camacho, F. J., Young, L. J., Paredes, R. G., Diaz, N. F., et al. (2019). Social bonding induces changes in brain functional connectivity in male and female monogamous voles: a longitudinal fMRI study. *bioRxiv 752345*. doi: 10.1101/752345

Mateo, J. M. (2004). Recognition systems and biological organization: the perception component of social recognition. *Ann. Zool. Fenn.* 41, 729–745.

McGraw, L. A., and Young, L. J. (2010). The prairie vole: an emerging model organism for understanding the social brain. *Trends Neurosci.* 33, 103–109. doi: 10.1016/j.tins.2009.11.006

O'Connell, L. A., and Hofmann, H. A. (2012). Evolution of a vertebrate social decision-making network. *Science* 336, 1154–1157. doi: 10.1126/science.1218889

Pagani, J. H., Zhao, M., Cui, Z., Avram, S. K., Caruana, D. A., Dudek, S. M., et al. (2015). Role of the vasopressin 1b receptor in rodent aggressive behavior and synaptic plasticity in hippocampal area CA2. *Mol. Psychiatry* 20, 490–499. doi: 10.1038/mp.2014.47

Penn, D. J., and Potts, W. K. (1999). The evolution of mating preferences and major histocompatibility complex genes. *Am. Nat.* 153, 145–164. doi: 10.1086/303166

Piskorowski, R. A., and Chevaleyre, V. (2018). Memory circuits: CA2. *Curr. Opin. Neurobiol.* 52, 54–59. doi: 10.1016/j.conb.2018.04.015

Robinson, G. E., Fernald, R. D., and Clayton, D. F. (2008). Genes and social behavior. *Science* 322, 896–900. doi: 10.1126/science.1159277

Shemesh, Y., Sztainberg, Y., Forkosh, O., Shlapobersky, T., Chen, A., and Schneidman, E. (2013). High-order social interactions in groups of mice. *Elife* 2:e00759. doi: 10.7554/eLife.00759

Silberberg, A., Allouch, C., Sandfort, S., Kearns, D., Karpel, H., and Slotnick, B. (2014). Desire for social contact, not empathy, may explain "rescue" behavior in rats. *Anim. Cogn.* 17, 609–618. doi: 10.1007/s10071-013-0692-1

Smith, A. S., Williams Avram, S. K., Cymerblit-Sabba, A., Song, J., and Young, W. S. (2016). Targeted activation of the hippocampal CA2 area strongly enhances social memory. *Mol. Psychiatry* 21, 1137–1144. doi: 10.1038/mp.2015.189

Ueno, H., Suemitsu, S., Murakami, S., Kitamura, N., Wani, K., Matsumoto, Y., et al. (2019). Helping-like behaviour in mice towards conspecifics constrained inside tubes. *Sci. Rep.* 9:5817. doi: 10.1038/s41598-019-42290-y

Walum, H., and Young, L. J. (2018). The neural mechanisms and circuitry of the pair bond. *Nat. Rev. Neurosci.* 19, 643–654. doi: 10.1038/s41583-018-0072-6

Wersinger, S. R., Ginns, E. I., O'Carroll, A. M., Lolait, S. J., and Young, W. S. III. (2002). Vasopressin V1b receptor knockout reduces aggressive behavior in male mice. *Mol. Psychiatry* 7, 975–984. doi: 10.1038/sj.mp.4001195

Wersinger, S. R., Kelliher, K. R., Zufall, F., Lolait, S. J., O'Carroll, A. M., and Young, W. S. III. (2004). Social motivation is reduced in vasopressin 1b receptor null mice despite normal performance in an olfactory discrimination task. *Horm. Behav.* 46, 638–645. doi: 10.1016/j.yhbeh.2004.07.004

Williams Avram, S. K., and Cymerblit-Sabba, A. (2017). "Vasopressin: roles in modulating social behavior," in *Hormones, Brain, and Behavior*, ed. D. W. P. A. M. Joels. (Oxford: Elsevier), 279–304.

Williams, J. R., Catania, K. C., and Carter, C. S. (1992). Development of partner preferences in female prairie voles (Microtus ochrogaster): the role of social and sexual experience. *Horm. Behav.* 26, 339–349. doi: 10.1016/0018-506x(92)90004-f

Winslow, J. T. (2003). Mouse social recognition and preference. *Curr. Protoc. Neurosci.* 22:8.16.11. doi: 10.1002/0471142301.ns0816s22

Young, L. J. (2003). "The neural basis of pair bonding in a monogamous species: a model for understanding the biological basis of human behavior," in *National Research Council (US) Panel for the Workshop on the Biodemography of Fertility and Family Behavior*, eds R. A. Bulatao and K. W. Wachter (Washington, DC: National Academies Press (US): Offspring: Human Fertility Behavior in Biodemographic Perspective).

Young, K. A., Gobrogge, K. L., Liu, Y., and Wang, Z. (2011). The neurobiology of pair bonding: insights from a socially monogamous rodent. *Front. Neuroendocrinol.* 32, 53–69. doi: 10.1016/j.yfrne.2010.07.006

Young, L. J., Murphy Young, A. Z., and Hammock, E. A. (2005). Anatomy and neurochemistry of the pair bond. *J. Comp. Neurol.* 493, 51–57. doi: 10.1002/cne.20771

Zala, S. M., Potts, W. K., and Penn, D. J. (2004). Scent-marking displays provide honest signals of health and infection. *Behav. Ecol.* 15, 338–344. doi: 10.1093/beheco/arh022

Zheng, D. J., Foley, L., Rehman, A., and Ophir, A. G. (2013). Social recognition is context dependent in single male prairie voles. *Anim. Behav.* 86, 1085–1095. doi: 10.1016/j.anbehav.2013.09.015


**Conflict of Interest**: The authors declare that the research was conducted in the absence of any commercial or financial relationships that could be construed as a potential conflict of interest.

*Copyright © 2020 At least a portion of this work is authored by Adi Cymerblit-Sabba, Adam S. Smith, Sarah K. Williams Avram, Michelle Stackmann, Austin C. Korgan, and W. Scott Young on behalf of the U.S. Government and, as regards Dr. Cymerblit-Sabba, Dr. Smith, Dr. Williams Avram, Dr. Stackmann, Dr. Korgan, Dr. Scott Young and the U.S. Government, is not subject to copyright protection in the United States. Foreign and other copyrights may apply. This is an open-access article distributed under the terms of the Creative Commons Attribution License (CC BY). The use, distribution or reproduction in other forums is permitted, provided the original author(s) and the copyright owner(s) are credited and that the original publication in this journal is cited, in accordance with accepted academic practice. No use, distribution or reproduction is permitted which does not comply with these terms.*

frontiers in Systems Neuroscience

ORIGINAL RESEARCH
published: 26 May 2020
doi: 10.3389/fnsys.2020.00026

# Neonatal Ketamine Alters High-Frequency Oscillations and Synaptic Plasticity in the Subiculum But Does not Affect Sleep Macrostructure in Adolescent Rats

*Francesca M. Manzella[1,2†], Srdjan M. Joksimovic[1†], James E. Orfila[1], Brier R. Fine[1], Robert M. Dietz[3], Dayalan Sampath[4], Hanna K. Fiedler[1], Vesna Tesic[5], Navya Atluri[6], Yogendra H. Raol[7], Vesna Jevtovic-Todorovic[1], Paco S. Herson[1,2] and Slobodan M. Todorovic[1,2]**

[1]Department of Anesthesiology, University of Colorado Anschutz Medical Campus, Aurora, CO, United States, [2]Neuroscience Graduate Program, University of Colorado Anschutz Medical Campus, Aurora, CO, United States, [3]Department of Pediatrics, University of Colorado Anschutz Medical Campus, Aurora, CO, United States, [4]Department of Neuroscience and Experimental Therapeutics, University of Texas A&M, College Station, TX, United States, [5]Department of Pathology, University of Colorado Anschutz Medical Campus, Aurora, CO, United States, [6]Department of Anesthesiology, University of Virginia, Charlottesville, VA, United States, [7]Department of Pediatrics, Division of Neurology, University of Colorado Anschutz Medical Campus, Aurora, CO, United States

OPEN ACCESS

**Edited by:**
Steven James Mennerick, Washington University in St. Louis, United States

**Reviewed by:**
Ben Julian Agustin Palanca, Washington University in St. Louis, United States
Therese M. Jay, Institut National de la Santé et de la Recherche Médicale (INSERM), France

***Correspondence:**
Slobodan M. Todorovic
slobodan.todorovic@cuanschutz.edu

†These authors have contributed equally to this work

**Received:** 17 January 2020
**Accepted:** 21 April 2020
**Published:** 26 May 2020

**Citation:**
Manzella FM, Joksimovic SM, Orfila JE, Fine BR, Dietz RM, Sampath D, Fiedler HK, Tesic V, Atluri N, Raol YH, Jevtovic-Todorovic V, Herson PS and Todorovic SM (2020) Neonatal Ketamine Alters High-Frequency Oscillations and Synaptic Plasticity in the Subiculum But Does not Affect Sleep Macrostructure in Adolescent Rats. Front. Syst. Neurosci. 14:26. doi: 10.3389/fnsys.2020.00026

Exposure to sedative/hypnotic and anesthetic drugs, such as ketamine, during the critical period of synaptogenesis, causes profound neurotoxicity in the developing rodent and primate brains and is associated with poor cognitive outcomes later in life. The subiculum is especially vulnerable to acute neurotoxicity after neonatal exposure to sedative/hypnotic and anesthetic drugs. The subiculum acts as a relay center between the hippocampal complex and various cortical and subcortical brain regions and is also an independent generator of gamma oscillations. Gamma oscillations are vital in neuronal synchronization and play a role in learning and memory during wake and sleep. However, there has been little research examining long-term changes in subicular neurophysiology after neonatal exposure to ketamine. Here we explore the lasting effects of neonatal ketamine exposure on sleep macrostructure as well as subicular neuronal oscillations and synaptic plasticity in rats. During the peak of rodent synaptogenesis at postnatal day 7, rat pups were exposed to either 40 mg/kg of ketamine over 12 h or to volume matched saline vehicle. At weaning age, a subset of rats were implanted with a cortical and subicular electroencephalogram electrode, and at postnatal day 31, we performed *in vivo* experiments that included sleep macrostructure (divided into the wake, non-rapid eye movement, and rapid eye movement sleep) and electroencephalogram power spectra in cortex and subiculum. In a second subset of ketamine exposed animals, we conducted *ex vivo* studies of long-term potentiation (LTP) experiments in adolescent rats. Overall, we found that neonatal exposure to ketamine increased subicular gamma oscillations during non-rapid eye movement sleep but it did not alter sleep macrostructure. Also, we observed a significant decrease in subicular LTP. Gamma

oscillations during non-rapid eye movement sleep are implicated in memory formation and consolidation, while LTP serves as a surrogate for learning and memory. Together these results suggest that lasting functional changes in subiculum circuitry may underlie neurocognitive impairments associated with neonatal exposure to anesthetic agents.

**Keywords: ketamine, sedation, brain development, EEG, long-term potentiation**

## INTRODUCTION

Each year, millions of infants and young children are exposed to sedative/hypnotic and anesthetic agents (McGowan and Davis, 2008). These agents are traditionally γ-aminobutyric acid subtype A ($GABA_A$) receptor agonists, such as sevoflurane and propofol, and N-methyl-D-aspartate (NMDA) receptor antagonists, such as ketamine. However, exposure to sedative/hypnotic and anesthetic drugs during the neonatal period is associated with profound neurotoxicity and cognitive impairments in rodent and non-human primate models (Jevtovic-Todorovic et al., 2003; Paule et al., 2011; Brambrink et al., 2012; Atluri et al., 2018; Talpos et al., 2019). Currently, there is conflicting evidence on the effect of sedative-hypnotic and anesthetic drugs in infants and young children. Similar to studies conducted in non-human primates, some research suggests that a single, brief exposure may not result in neurodevelopmental delay (Wilder et al., 2009; Pick et al., 2011; McCann et al., 2019). However, there is also some evidence to suggest that repeated exposure to anesthetics during infancy can lead to cognitive impairments in humans (Wilder et al., 2009; Ing et al., 2014). There is also consensus between these studies indicating the need for more research in assessing the risk of future neurocognitive impairment with repeated or prolonged neonatal anesthesia exposures. Because prolonged exposures are less common, they are vastly underrepresented in clinical research (Bartels et al., 2018).

One of the most widely used anesthetics in infants is ketamine, specifically for its effectiveness, availability, and low cost (Bhutta, 2007). It is well established that neonatal exposure to ketamine is associated with developmental neurotoxicity and long-term neurocognitive impairment in rodents and non-human primates, yet there has been little research studying its long-term effects on neuronal physiology, such as its effects on neuronal oscillations when given during infancy (Paule et al., 2011; Brambrink et al., 2012; Atluri et al., 2018; Talpos et al., 2019). Although there is little research on short- or long-term physiological outcomes of neonatal ketamine exposure, its acute effects in adults point to changes in neuronal oscillations, specifically in the high-frequency bands during wake and sleep (Ahnaou et al., 2017; Ye et al., 2018).

Ketamine exposure in different species can create aberrant short-term increases in gamma during wake and sleep periods; although, it is unknown if these effects have a lasting impact (Ahnaou et al., 2017; Richardson et al., 2017; Mahdavi et al., 2019). We speculate that possibly children who receive ketamine either as a one-time anesthetic or as a sedative/hypnotic during long-term hospital stays may also develop these short-term aberrant increases in gamma oscillations. Hence, we propose that changes in high-frequency gamma oscillations during sleep may be an underlying mechanism by which neonatal anesthetics contribute to potentially worrisome cognitive outcomes. However, until recently there has been little research on how exposure to neonatal sedative/hypnotics and anesthetics affect long-term sleep macrostructure, corresponding neuronal oscillations, and synaptic plasticity.

The main purpose of this study is to examine the long-term effects of neonatal ketamine on sleep oscillations and synaptic plasticity in the rat subiculum. The subiculum is especially vulnerable to neurotoxic insult from neonatal anesthesia (Atluri et al., 2018; Joksimovic et al., 2020). It is also a key relay center between hippocampal complex and various cortical and subcortical structures and can independently generate gamma oscillations needed for memory consolidation (O'Mara et al., 2009; Jackson et al., 2011). Thus, neurotoxic damage to the subiculum may contribute to physiological dysfunction contributing to learning impairments. We hypothesized that exposure to ketamine during the peak of synaptogenesis in a rat model at postnatal day 7 may disrupt long-term sleep macrostructure and neuronal oscillations in the subiculum. We also hypothesized subicular dysfunction would manifest as a disruption of synaptic plasticity. We used *in vivo* cortical and subicular electroencephalogram (EEG) and local field potential (LFP) recordings for characterizing sleep macrostructure and neuronal oscillations during sleep, and we used *ex vivo* electrophysiology to measure changes in long-term potentiation (LTP) as a surrogate for memory formation in the subiculum. Together these studies will help expand on understanding the underlying mechanisms by which exposure to neonatal sedative/hypnotics and anesthetics contribute to poor neurocognitive outcomes.

## MATERIALS AND METHODS

### Animals

All experiments were approved by the Institutional Animal Care and Use Committee at the University of Colorado Anschutz Medical Campus and adhered to the NIH Guide for the Care and Use of Laboratory animals. Ketamine exposure experiments were conducted in Sprague-Dawley (Envigo, US) rat pups of both sexes. Pups were housed with their mothers until initiation of experiment. Animals were maintained on a 14:10 light-dark cycle and had access to food and water *ad libitum*.

### Drugs and Chemicals

Ketamine (Par Pharmaceutical, Woodcliff Lake, NJ, USA) was diluted with saline at a concentration of 20 mg/ml and delivered

to rat pups *via* intraperitoneal injection (IP) at a volume of 2 μl per gram body weight for a total dose of 40 mg/kg.

## Ketamine Exposure

At postnatal day (P) 7, rat pups were removed from their home cages and randomly assigned to receive exposure to either the ketamine condition or the saline sham condition. This time period corresponds to the peak of synaptogenesis when animals are most vulnerable to the effects of anesthesia (Jevtovic-Todorovic et al., 2003). Those in the ketamine condition were injected with ketamine 40 mg/kg every 2 h for 12 h (six doses total, Ketamine group). Previous work from our group has found that the sub-anesthetic dose of 40 mg/kg of ketamine given at this regimen is sufficient for inducing hypnosis and apoptosis in a rodent model (Atluri et al., 2018). Pups in the saline condition were only administered saline vehicle at equal volume (Saline group). A heating blanket adjusted to 35°C was used to keep the pups warm during exposure period. Pups appeared pink and healthy and did not show physical signs of hypoxia, such as graying or pallid skin tone. Following the 12-h exposure, Ketamine and Saline pups were allowed to recover and returned to their mothers (**Figure 1A**, P7 time point).

The dose of 40 mg/kg was a sedative/hypnotic dose in the rat pups. Although all rat pups were not showing visible signs of spontaneous movement and righting reflex, we observed that they still retained the subanesthetic withdrawal reflex upon pinching their leg with a forceps (data not shown). Thus our data show detriments at sub-anesthetic doses. During surgical interventions, children may receive higher doses to induce full anesthetic effect or sedative/hypnotic dose for prolonged sedation, usually in the intensive care unit setting. Hence, our experimental paradigm is more relevant to the later scenario although any relevance of our study to humans would need to be scrutinized in carefully designed clinical studies.

## Electrode Implantation and EEG Acquisition

To study the effects of neonatal hypnosis/anesthesia on sleep, a subset of Ketamine and Saline animals underwent stereotaxic surgeries between P21 and P23 (**Figure 1A**, P21 time point). Anesthesia was induced at 3% isoflurane *via* inhalation and maintained between 0.5–2%. Lidocaine (1%) was applied at the incision site as a local anesthetic. Because both groups were past the critical period for anesthesia induced neurotoxicity, there was no concern in exposing the Saline group briefly to isoflurane for surgery. A screw electrode was implanted with stereotaxic coordinates in the range of barrel cortex: AP −2.8, ML 3.0. For studying LFPs in the subiculum, animals were also implanted with a depth electrode (AP −4.8, ML 2.4, DV 2.5). Two screw electrodes were implanted just caudal to lambda: one left of the midline, which served as the ground electrode and one right of the midline, which served as the reference electrode. An insulated silver wire hook was inserted in the nuchal muscle to measure electromyography (EMG). Dental acrylic was used to fix the electrodes to the skull, forming the EEG headpiece. Animals were treated post-operatively with Banamine (2.5 mg/ml subcutaneously) for analgesia every 24 h for 48 h.

Animals were housed individually and given at least a week to recover from surgery and to adjust to the headpiece. EEG recording and acquisition took place between P30–33 (**Figure 1A**, P30 time point). EEG signals were recorded using the Pinnacle system (Pinnacle Technology, Inc., Lawrence, KS, USA) alongside synchronized, time-locked video. We acquired the EEG signals using a 1–500 Hz bandpass filter, which were digitized at 2,000 Hz and stored on a hard disk for offline analysis.

## Sleep Macrostructure and Analysis

EEG and EMG for sleep analysis was taken from day three of recording at P32 so that animals had substantial time to acclimate to the recording device. We separated the recordings into the light and dark cycles (14:10 cycle), and the data were sampled over three continuous hours of the light cycle and three continuous hours of the dark cycle. These were analyzed first separately and then together.

Sleep stages were divided into Wake, non-rapid eye movement sleep (NREM), and rapid-eye movement sleep (REM). Because NREM encompasses a wide range of neuronal oscillations, we further subdivided it into NREM 1 (N1) and NREM 2 (N2). In addition, NREM and REM stages were combined to study effects on overall sleep vs. wake behavior (Sleep). Sleep stages were manually scored in 10 s epochs using Sirenia Sleep Pro (Pinnacle Technology, Inc., Lawrence, KS, USA). Manual sleep scoring was aided by visualization of epoch by epoch spectral plots. Wake stages were characterized by high frequency, mixed amplitude cortical EEG and high frequency EMG when animal was moving (**Figure 1B**). N1 stages were characterized by low frequency, high amplitude EEG and minimal signal in the EMG (**Figure 1C**). N2 was differentiated from N1 in that it contained a larger proportion of lower frequency oscillations (1–4 Hz) in at least 50% or more of the epoch (Neckelmann and Ursin, 1993; Wei et al., 2019; **Figure 1C**). We confirmed the presence of low frequency oscillations by dominance of slow and delta power in the epoch's power spectral plot. Finally, REM stages were characterized by high frequency, low amplitude EEG resembling awake periods but with flat line signal in the EMG (**Figure 1D**). REM stages also corresponded to increase in theta power spectra. Time locked videos were used to confirm behavior. All sleep scoring was conducted with experimenter blinded to the treatment condition.

Sleep macrostructure was analyzed using various sleep behavioral outcomes. First, we measured the average sum time spent in each sleep stage. Switching between different sleep stages was measured as the number of transitions between stages. Although, groups may not show changes in overall time spent in each sleep stage, this may be masked by sleep fragmentation. For example, one group may have fewer, but longer sleep episodes while the other group has more, but shorter sleep episodes. To assess changes in sleep fragmentation, we measured the number of episodes animals spent in each sleep stage, as well as the mean duration of each episode (Jang et al., 2010; Leemburg et al., 2010; Lunardi et al., 2019). A sleep episode was defined as a continuous period of time spent in one stage before transitioning into another different stage. Mean episode length was evaluated

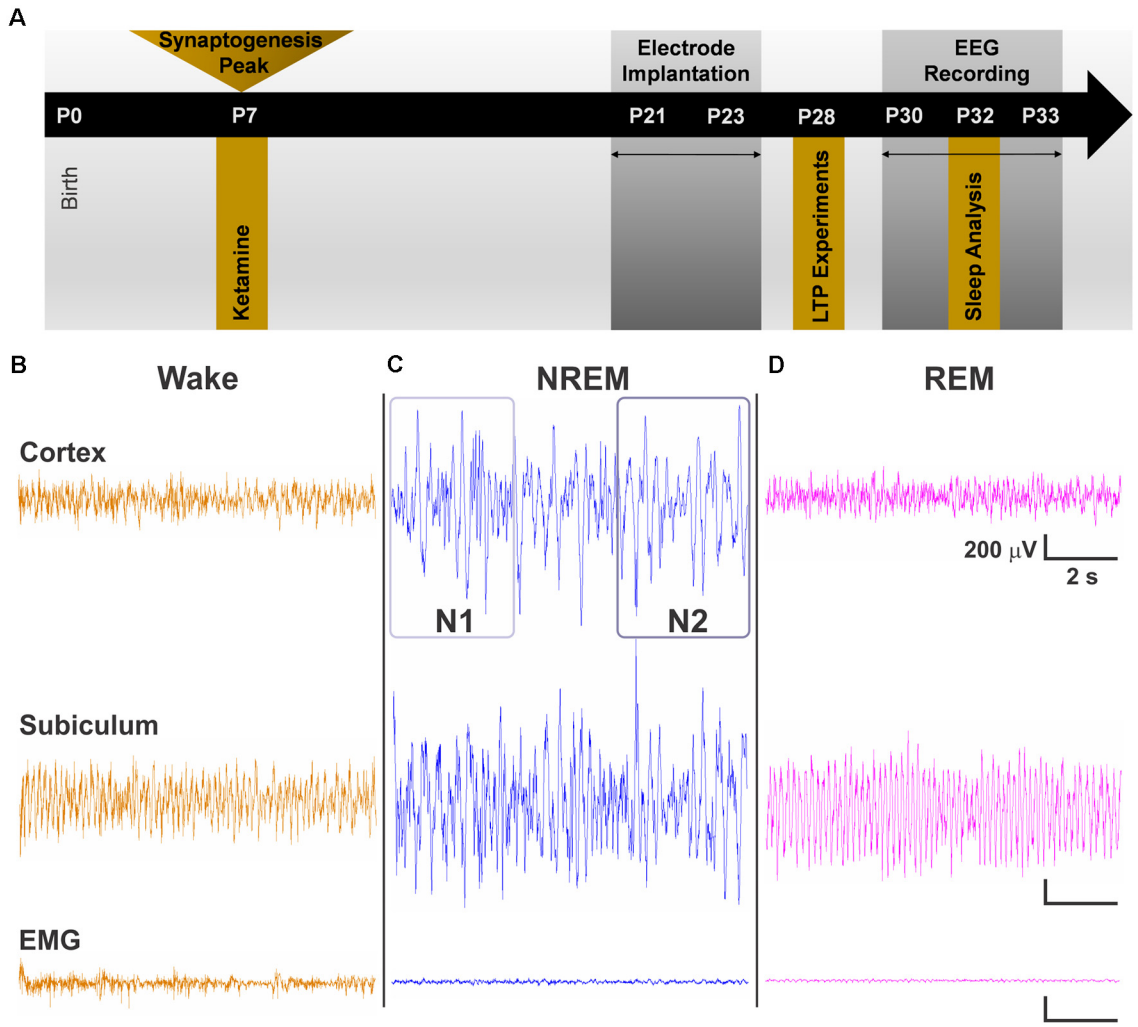


**FIGURE 1 | (A)** Schematic representation of the timeline of events for the experiment. Exposure to a 12-h regimen of ketamine 40 mg/kg occurred at P7 during peak synaptogenesis. A subset of animals was used for long-term potentiation (LTP) experiments at P28. The other subset were weaned from their mothers between P21 and P23. Electroencephalogram (EEG) recordings began at P30 after rats recovered from surgery, and data were obtained from day 3 of recordings at P32. **(B–D)** Representative traces of cortical EEG, subicular local field potential (LFP), and of electromyography (EMG) signals used alongside time-locked videos to score sleep. **(B)** Traces during wake represent an animal that was freely and actively moving as noted by its high-frequency EMG. **(C)** Representative traces during non-rapid eye movement sleep (NREM) show low frequency cortical oscillations and minimal movement in EMG. N1 and N2 were distinguished by differences in the predominance of delta oscillations, with delta comprising >50% epoch in N2. **(D)** Cortical oscillations during REM are similar to those of the Wake stage but with a nearly flat line in the EMG.

by summing the total time spent in each episode and dividing that value by the number of episodes.

## Power Analysis

EEG waveform data from cortex and LFP waveform data from subiculum underwent fast Fourier transform using Sirenia Sleep Pro to obtain power spectra values. Data were divided into six frequency bands: delta (1–4 Hz), theta (4–8 Hz), alpha (8–12 Hz), sigma (9–15 Hz), beta (12–30 Hz), low gamma (30–59 Hz), and high gamma (61–100 Hz). Absolute power values were summed for each sleep stage and divided by the number of episodes for that particular stage. Statistical outliers were determined using the Graphpad outlier calculator and were crosschecked to the original EEG to determine if figures were due to normal physiological variation or to EEG artifact. Only outliers that reached statistical significance of $P < 0.01$ and also contained artifacts were removed from analysis.

## Long-Term Potentiation (LTP)

Hippocampal slices were prepared from rats at P28 after neonatal exposure to ketamine (40 mg/kg) or saline treatment. Rats were anesthetized with 3% isoflurane in an $O_2$-enriched chamber. Rats were transcardially perfused with ice-cold (2–5°C) oxygenated (95% $O_2$/5% $CO_2$) artificial cerebral spinal fluid (ACSF) for 2 min prior to decapitation. The composition of ACSF was the following (in mmol/L): 126 NaCl, 2.5 KCl, 25 $NaHCO_3$,

1.3 $NaH_2PO_4$, 2.5 $CaCl_2$, 1.2 $MgCl_2$ and 12 glucose. Horizontal hippocampal slices (300 μm thick) were cut with a Vibratome 1200S (Leica) and transferred to a holding chamber containing ACSF for at least 1 h before recording.

Synaptically evoked field potentials were recorded from hippocampal slices that were placed on a temperature controlled (31 ± 0.5°C) interface chamber perfused with ACSF at a rate of 1.5 ml/min. For subiculum extracellular recordings, a bipolar electrode was placed in stratum oriens at the very end of the CA1 region. Excitatory post-synaptic potentials (fEPSP) were produced by recording in the stratum-radiatum of the distal dendrites of subicular neurons. The fEPSPs were adjusted to 50% of the maximum slope and test pulses were evoked every 20 s. A 20-min stable baseline was established before delivering a theta burst stimulation (TBS) train of four pulses delivered at 100 Hz in 30 ms bursts repeated 10 times with 200 ms interburst intervals. Following TBS, the fEPSP was recorded for 60 min. The averaged 10-min slope from 50 to 60 min after TBS was divided by the average of the 10-min baseline (set to 100%) prior to TBS to determine the amount of potentiation. Analog fEPSPs were amplified (1,000×) and filtered through a pre-amplifier (Model LP511 AC, Grass Instruments) at 1.0 kHz, digitized at 10 kHz and stored on computer for later off-line analysis (Clampfit 10.4, Axon Instruments). The derivative (dV/dT) of the initial fEPSP slope was measured. For time course graphs, normalized fEPSP slope values were averaged and plotted as the percent change from baseline. Two electrophysiologists (RD and JO) independently verified all LTP results in this report.

## Data and Statistical Analysis

Graphpad Prism 8.0 (GraphPad Software Inc., San Diego, CA, USA) was used for all analyses. Two-tailed independent samples *t*-tests were used to compare groups when equal variances were assumed. Unpaired *t*-tests with Welch's correction were used for groups for which equal variances were not assumed (F test for equal variances, $P < 0.05$). Cohen's *d* was calculated to measure effect size. Effect size allows for measurement of the strength of the relationship between the means (Sullivan and Feinn, 2012; Lakens, 2013). Data were considered significant at $P < 0.05$ and are presented in text as mean and standard deviation and graphically as mean and standard error of mean.

# RESULTS

We first measured the effects of neonatal ketamine on different sleep macrostructure parameters in ketamine treated ($N = 11$, six females and five males) and saline treated ($N = 8$, five females and three males) rats. We found that neonatal exposure to ketamine did not result in any significant changes in sleep macrostructure across all of the sleep stages. There were no changes in the number of episodes spent in each stage or the length of each episode (**Figures 2A,B**). There were also no differences in the total length of each stage (**Figure 2C**). These results were consistent across the light and the dark cycle; thus, data are presented as combined across cycles. Finally, there were no differences in the number of transitions between stages during the light cycle, dark cycle, or across both combined (**Figure 2D**).

Although there were no changes in sleep macrostructure, we found that exposure to neonatal ketamine significantly impacted LFP power spectra in the subiculum. During the light cycle, animals exposed to ketamine showed a significant increase in power in the low gamma frequency band during N1 (4,048 ± 2,820 $\mu V^2$, $t_{(13.83)} = 2.158$, $P = 0.049$, Cohen's $d = 0.94$) and N2 (3,570 ± 2,443 $\mu V^2$, $t_{(13.72)} = 2.370$, $P = 0.030$, Cohen's $d = 1.04$) compared to saline treated animals (2,025 ± 1,113 $\mu V^2$ and 1,652 ± 947.4 $\mu V^2$ for N1 and N2, respectively, **Figure 3A**). There were no changes in low gamma oscillations during N1 of the dark cycle. However, the increase in low gamma persisted during N2 of the dark cycle ($t_{(12.81)} = 2.283$, $P = 0.040$, Cohen's $d = 0.99$). Rats exposed to ketamine (4,214 ± 3,226 $\mu V^2$) had higher low gamma during N2 of the dark cycle than saline controls (1,833 ± 1,065 $\mu V^2$, **Figure 3B**). When both light and dark cycles were combined, changes were observed again during N1 ($t_{(13.27)} = 2.170$, $P = 0.049$, Cohen's $d = 0.95$) with ketamine exposed animals (4,360 ± 3,195 $\mu V^2$) having higher low gamma power than saline controls (2,091 ± 1,149 $\mu V^2$, **Figure 3C**). As with the separated cycles, when data were combined, there were persistent changes in low gamma during N2 ($t_{(13.26)} = 2.373$, $P = 0.033$, Cohen's $d = 1.03$), ketamine exposed rats (3,919 ± 2,791 $\mu V^2$) had higher low gamma power than saline controls (1,753 ± 1,002 $\mu V^2$, **Figure 3C**).

Similar to what we observed with low gamma during the light cycle, we also saw an increase in high gamma during both N1 (1,319 ± 972.4 $\mu V^2$, $t_{(12.92)} = 2.241$, $P = 0.043$, Cohen's $d = 0.97$) and N2 (1,187 ± 901.3 $\mu V^2$, $t_{(12.71)} = 2.282$, $P = 0.040$, Cohen's $d = 0.99$) for ketamine exposed animals compared to saline controls (612.2 ± 327.7 $\mu V^2$ and 523.7 ± 291.9 $\mu V^2$ for N1 and N2, respectively, **Figure 4A**). However, unlike changes seen with low gamma, statistical changes in high gamma power did not persist into the dark cycle and were not observed when cycles were combined (**Figures 4B,C**). While there was a significant increase in low and high gamma oscillations in the subiculum, we did not observe changes in gamma oscillations in the simultaneous EEG recordings from the cortex (data not shown).

In addition to analyzing gamma oscillations, we also independently analyzed changes in delta, theta, alpha, sigma, and beta oscillations in the subiculum. However, we did not note any statistical differences between ketamine treated rats and saline treated rats across those frequency bands (data not shown).

Finally, to determine the effect of ketamine on hippocampal function in developing brain, extracellular field recordings of subicular neurons were analyzed from P28 rats following neonatal ketamine exposure. Following a stable 20 min baseline, a brief TBS (40 pulse TBS) was applied. The results showed a significant ($P = 0.032$, Cohen's $d = 1.47$) LTP impairment in ketamine exposed rats (122.80 ± 9.52%, $n = 5$) when compared to saline treated rats [187.60 ± 61.78%, ($n = 7$), **Figure 5A**]. **Figure 5B** shows a bar graph summary of these results.

# DISCUSSION

It is well established that treatment with ketamine during the neonatal period of synaptogenesis causes severe apoptosis in rodent and non-human primate models as well as lasting

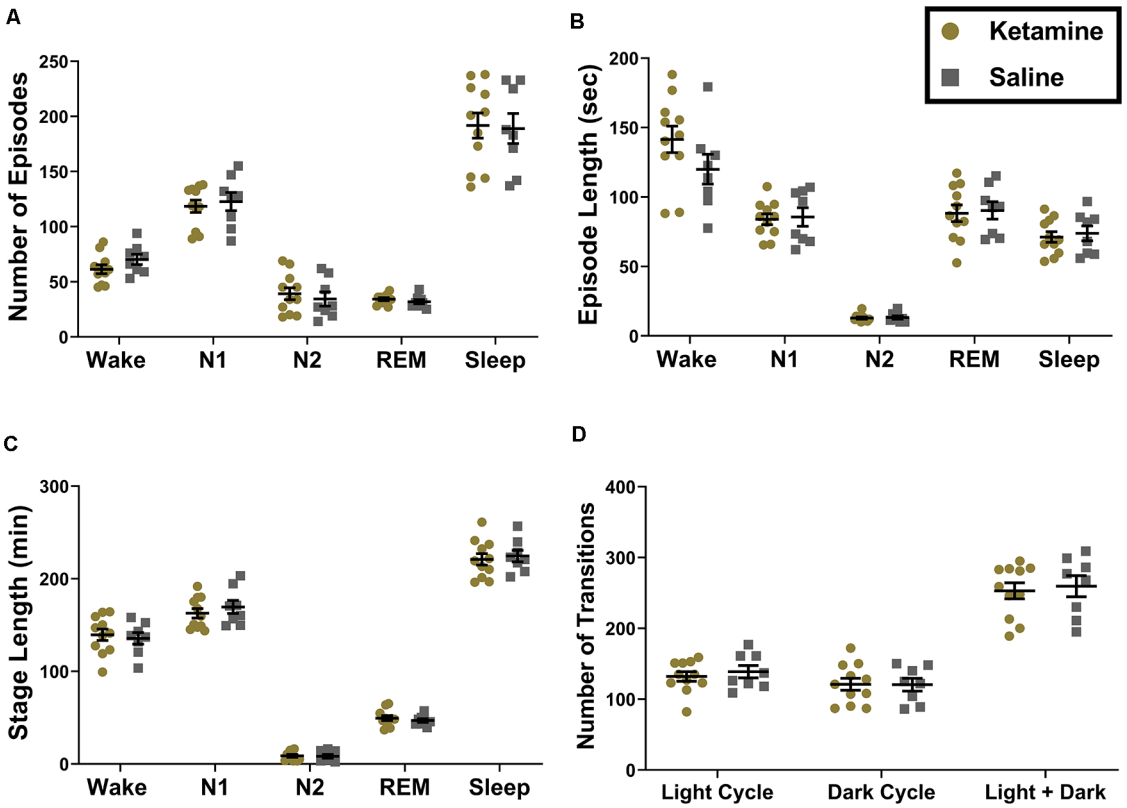


**FIGURE 2 |** Ketamine exposure during the neonatal period does not result in changes in sleep macrostructure measured across light and dark cycles combined. **(A)** We did not note any changes in the number of episodes in the Wake ($P = 0.165$), N1 ($P = 0.663$), N2 ($P = 0.581$), REM ($P = 0.322$) and total Sleep stages ($P = 0.880$). **(B)** Moreover, the average length of each episode did not differ between groups for Wake ($P = 0.154$), N1 ($P = 0.823$), N2 ($P = 0.772$), REM ($P = 0.824$), and total Sleep ($P = 0.687$). **(C)** The total amount of time spent in each sleep stage also did not change as a result neonatal ketamine exposure across Wake ($P = 0.685$), N1 ($P = 0.439$), N2 ($P = 0.836$), REM ($P = 0.824$), or total Sleep ($P = 0.691$). **(D)** Finally, we measured how often rats transitioned from one sleep stage to another and found no changes in this parameter across the light cycle ($P = 0.533$), dark cycle ($P = 0.969$), and when cycles were combined ($P = 0.733$) in response to neonatal ketamine exposure.

neurocognitive impairments (Ikonomidou et al., 1999; Brambrink et al., 2012; Talpos et al., 2019). We show that in addition to acute neurotoxicity, neonatal ketamine produces significant changes in subicular gamma oscillations during NREM sleep without affecting sleep macrostructure. Moreover, ketamine exposure negatively impacted synaptic plasticity in the subiculum.

During the period of synaptogenesis around postnatal day 7, rodents do not yet exhibit fully developed sleep patterns, as noted by lack of synchronization in the EEG (Gramsbergen, 1976; Khazipov and Luhmann, 2006). An interplay of $GABA_A$ and NMDA receptor activation contributes in generating and localizing the spindle burst activity necessary for maturing sleep centers, particularly the thalamo-cortical circuit (Seelke and Blumberg, 2008; Minlebaev et al., 2011). An interplay between GABAergic inputs from the nucleus reticularis thalami and glutamatergic inputs from the ventrobasal thalamus and cortex contribute to the circuit wide burst firing pattern which underlies natural sleep and anesthesia (Steriade, 2006). However, exposure to anesthetic drugs during this period also causes profound apoptosis in both thalamus and cortex (Jevtovic-Todorovic et al., 2003). Despite acute insult to key sleep centers during this critical period, we did not find any effects of neonatal ketamine exposure across any of the sleep macrostructure parameters. These results are in line with results from our group also showing that a 6-h neonatal exposure to 1.5% isoflurane does not result in changes in sleep macrostructure in adolescent rats (unpublished results). However, our results differ from the findings of Lunardi et al. (2019), which found that exposure to a cocktail of midazolam, isoflurane, and nitrous oxide during the neonatal period resulted in increases in REM sleep in adolescent rats (Lunardi et al., 2019). This discrepancy may be due to choice of anesthetic regimen. Because an interplay of $GABA_A$ and NMDA activation are required for development of sleep circuitry and subsequent oscillations, treatment with ketamine alone may not be sufficient to elicit a change in sleep macrostructure.

Although we did not note any changes in sleep macrostructure with anesthetic treatment, we did observe changes in neuronal oscillations in the subiculum during NREM sleep. The subiculum receives unidirectional outgoing information from CA1 area, and is thus in a privileged

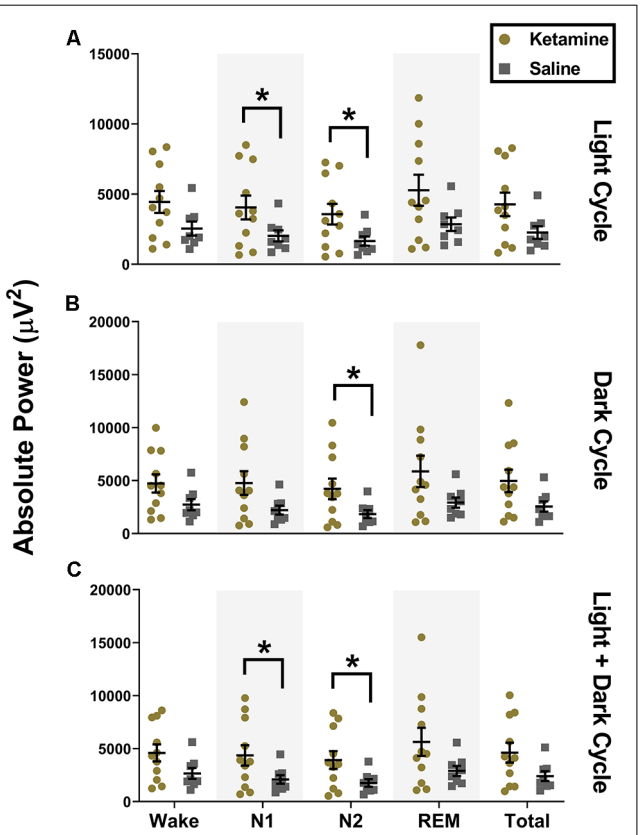


**FIGURE 3 |** Neonatal ketamine exposure increases subicular low gamma power during N1 and N2. **(A)** Neonatal ketamine exposure resulted in a significant increase in power spectra in the low gamma frequency ranges during N1 and N2 of the light cycle ($P = 0.049$ and $P = 0.033$ for N1 and N2, respectively). However, also during the light cycle, there were no changes in low gamma oscillations during Wake ($P = 0.078$), REM ($P = 0.065$), or across total recording period ($P = 0.052$). **(B)** During the dark cycle, there was an increase in low gamma power during N2 ($P = 0.040$), but not during N1 ($P = 0.053$), Wake ($P = 0.096$), REM ($P = 0.083$), or across total recording period ($P = 0.057$). **(C)** When both cycles were combined, we saw an increase in low gamma during N1 ($P = 0.049$) and N2 ($P = 0.033$). Consistent with results in the light and dark cycle separately, we did not note any changes in low gamma oscillations during Wake ($P = 0.083$), REM ($P = 0.075$), and across the total recording period when both cycles were combined ($P = 0.052$; $^*P < 0.05$).

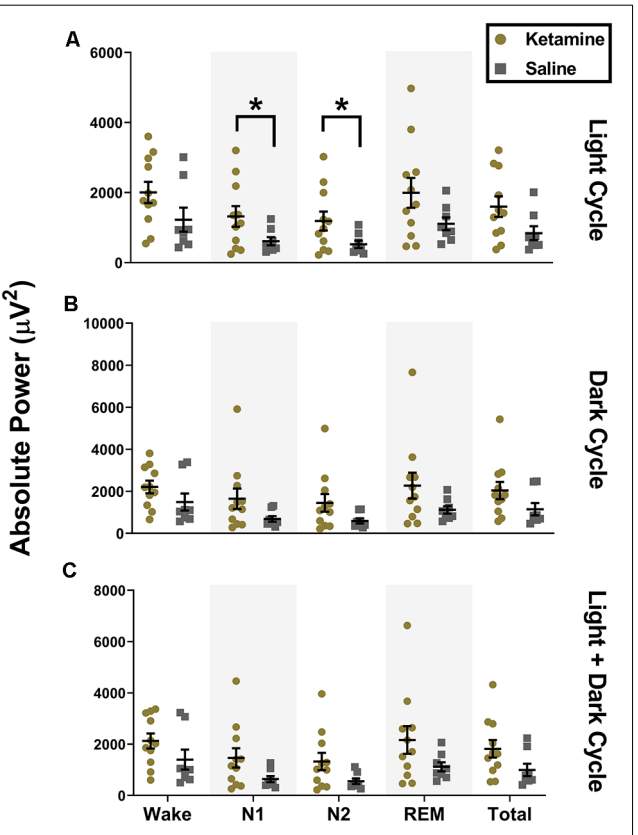


**FIGURE 4 |** Neonatal ketamine exposure increases subicular high gamma power during N1 and N2 of the light cycle. **(A)** Neonatal ketamine exposure resulted in a significant increase in power spectra in the high gamma frequency range during N1 and N2 of the light cycle ($P = 0.043$ and $P = 0.040$ for N1 and N2, respectively). However, also during the light cycle, there were no changes in high gamma oscillations during Wake ($P = 0.109$), REM ($P = 0.078$), or across total recording period ($P = 0.066$). **(B)** During the dark cycle, there were no changes in high gamma power during N1 ($P = 0.083$) or N2 ($P = 0.073$). There were also no differences in high gamma oscillations during Wake ($P = 0.163$), REM ($P = 0.099$), or across total recording period ($P = 0.117$). **(C)** When light and dark cycles were combined, changes in high gamma during N1 ($P = 0.083$) and N2 ($P = 0.051$) were not statistically significant. Consistent with results in the light and dark cycle separately, we did not note any changes in high gamma oscillations during Wake ($P = 0.144$), REM ($P = 0.090$), and across the total recording period when both cycles were combined ($P = 0.087$; $^*P < 0.05$).

position to serve as a relay center between the hippocampal complex and numerous cortical and subcortical structures (O'Mara et al., 2009). It can also generate low and high gamma oscillations independent of other hippocampal regions, such as CA3 (Jackson et al., 2011). Low and high gamma oscillations generated from various regions of the hippocampal complex are prominent during wake, especially when animals are involved in a cognitive task reviewed in Colgin (2015). They are also present, to a lesser extent, during NREM sleep, where they couple to low frequency oscillations in the 0.1–4 Hz range (Isomura et al., 2006; Le Van Quyen et al., 2010; Valderrama et al., 2012). This coupling is associated with synchronization of neuronal activity and is related to memory formation and consolidation during sleep (Takeuchi et al., 2015). While coupling of gamma oscillations to slow oscillations is necessary for proper cognitive processing, increases in gamma during NREM may not necessarily be beneficial.

Normally, rodents display changes in oscillatory behavior characterized by overall decreases in gamma oscillations while transitioning from wake into NREM sleep in favor of slower range delta oscillations (Corsi-Cabrera et al., 2001). Indeed, we observed these characteristics in our control animals. Instead, an increase in gamma after neonatal ketamine exposure may represent long-term abnormal changes in subicular oscillatory behavior, which may affect accurate transformation of information during sleep resulting in maladaptive plasticity.

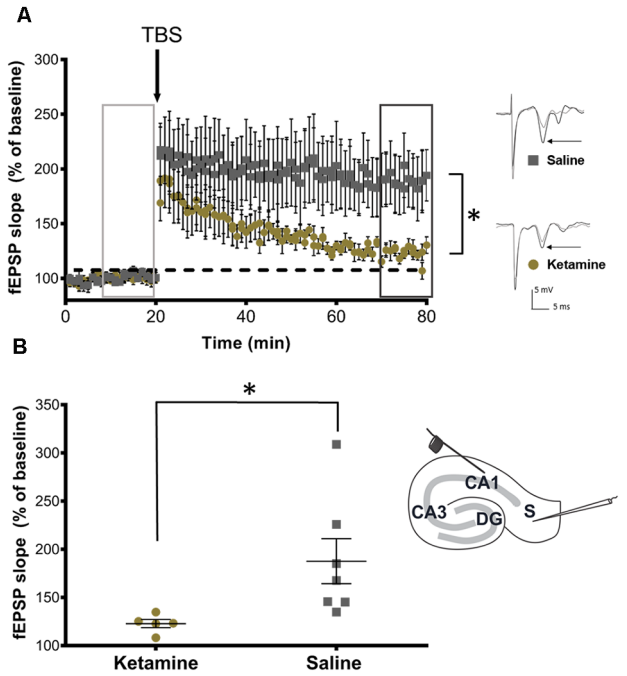


**FIGURE 5 |** Neonatal ketamine exposure impairs synaptic plasticity in adolescent rats. **(A)** Time plots of fEPSP slope from CA1 to Subiculum pathway in P28 rats exposed to neonatal saline and ketamine. Theta burst stimulation (TBS) arrow indicates the timing of theta-burst stimulation (40 pulses, 100 Hz). Insets indicate sample traces of fEPSPs before (light gray trace) and after (dark gray trace) TBS stimulation in saline and ketamine treated groups. Inset arrows indicate representative trace components used in analyses. **(B)** Quantification of change in fEPSP slope after 60 min following TBS (dark gray box) normalized to baseline (light gray box) in ipsilateral slices and contralateral slices, set at 100%. Rats exposed to neonatal ketamine showed significant impairment in LTP ($P = 0.032$). Each point represents a hippocampal slice (experiment) that was recorded with no more than two experiments per animal used. Inset depicting stimulating electrode placement in stratum oriens at the edge of the CA1 and recording electrode in stratum-radiatum subicular neurons, $^*P < 0.05$.

During sedation with ketamine in non-human primates, Richardson et al. (2017) found increases in low gamma (around 40 Hz) oscillations and that low gamma amplitude coupled with the phase of slow oscillations under 1 Hz. However, the patterns of gamma coupling to slow oscillations was different in naturally sleeping monkeys, which exhibited high gamma (around 70 Hz coupling to slow oscillations; Richardson et al., 2017). While the authors attribute the differences in coupling to a distinction between natural sleep and sedation, this may also be an abnormal result from ketamine exposure. Indeed, our results support that ketamine has lasting direct effects on hippocampal gamma oscillations during sleep, specifically those generated in the subiculum. Ketamine exposed animals had an increase in gamma power, not seen in saline controls. We observed increases in low gamma oscillations during both N1, which is characterized by sleep spindles and K-complexes, and N2, which is characterized by predominance of slow and delta waves. Moreover, increases in gamma oscillations were more consistent during N2, occurring during both the light and the dark cycle. This indicates a possible relationship between gamma and slower N2 oscillations, which may underlie proper memory consolidation and future cognitive function.

Further evidence of ketamine affecting sleep oscillatory behavior can be observed when mimicking NREM sleep with pentobarbital. Using this paradigm Mahdavi et al. (2019) found that ketamine produced a decrease in cortical and thalamic delta oscillations while transiently increasing gamma, indicating that ketamine alone can increase gamma oscillations independent of sedation (Mahdavi et al., 2019). Although our own results were limited to increases in subicular, and not cortical gamma, it is clear that exposure to ketamine may lead to dysregulation of various gamma generating circuitry and that the subiculum may be particularly vulnerable during development.

In addition to changes occurring directly during sedation and sleep, ketamine can transiently modulate high and low frequency oscillations during wake states. Acute sub-anesthetic doses of ketamine produce an increase in hippocampal low gamma (35–55 Hz) and high frequency gamma oscillations between 120–160 Hz. Acute ketamine exposure also caused increases in broadband gamma EEG between 40 and 140 Hz, which the authors speculated prevented segmenting and coupling of distinct high frequency oscillations to other lower frequency oscillations, such as theta and delta, potentially resulting in behavioral impairments (Ye et al., 2018). Similar to increases in gamma oscillations in the hippocampus, acute ketamine administration also increases gamma power across the cortex and increases cross-frequency coupling between gamma oscillations and lower frequency oscillations in the theta and delta range (Ahnaou et al., 2017). Thus, it is evident that ketamine treatment can increase high frequency oscillations across various brain regions, but especially the hippocampal complex. Although we did not note broadband in the LFPs, an increase in both low and high gamma oscillation may be indicative of lack of segmentation required for proper low frequency coupling during NREM sleep. Moreover, these published effects of ketamine are not long-term and do not persist after a week. Our results indicate long-term changes in neuronal circuitry in animals exposed to neonatal sedative/hypnotics and anesthetics. This may be due to the greater plasticity of the brain during synaptogenesis, in which circuitry is more vulnerable to permanent changes. Specifically, ketamine induced NMDA hypofunction during development may directly play a role on lasting functional and behavioral changes after neonatal exposure.

NMDA hypofunction is closely associated with abnormal elevated gamma band oscillations in patients with schizophrenia. Elevated gamma band oscillations are the result of NMDA hypofunction at the level of parvalbumin GABAergic interneurons, resulting in downstream disinhibition of pyramidal neurons (McNally and McCarley, 2016). Indeed, we found that early exposure to anesthesia leads to lasting hyperexcitability of pyramidal neurons in the rat subiculum, possibly contributing to elevated gamma oscillations (Joksimovic et al., 2020). Furthermore, functional changes associated with schizophrenia can be recapitulated in rodent ketamine models of the disorder, which also display increased gamma oscillations. Increases in gamma oscillations in these models are thought to

be associated with underlying sensory and cognitive symptoms of schizophrenia (Ehrlichman et al., 2009; Jadi et al., 2016). Similarly, long-term cognitive impairment is a known outcome of neonatal treatment with anesthetic agents. Neonatal exposure to ketamine results in lasting memory deficits in rodents and non-human primates (Paule et al., 2011; Brambrink et al., 2012; Atluri et al., 2018; Talpos et al., 2019). We propose that long-term changes in gamma oscillations in the subiculum may also play a role in overall learning and memory in animals exposed to ketamine as neonates. As stated earlier, gamma oscillations coupled to low frequency oscillations during NREM sleep play a role synchronizing neuronal activity and facilitating memory formation (Takeuchi et al., 2015).

LTP represents a long-lasting activity-dependent increase in synaptic efficacy and is considered to be the best available model of a cellular mechanism underlying memory formation (Bliss and Collingridge, 1993). This form of synaptic plasticity is most extensively studied in the hippocampal formation, CA3→CA1 (Schaffer collateral) pathway in particular. Much less is known about LTP in CA1→subiculum pathway; however, it appears that synaptic plasticity at this synapse heavily depends on glutamatergic neurotransmission *via* NMDA and AMPA receptors (reviewed in Behr et al., 2009), which may explain its susceptibility to ketamine exposure. It is possible that ketamine-induced NMDA hypofunction during synaptogenesis alters circuitry in the subiculum leading to dysregulation of gamma generation and further decreases in synaptic plasticity, all of which may be detrimental to learning and memory. Our recent data supports this notion since we found that ketamine treated rat pups exhibited decreased learning/memory in adolescence using the radial arm test (Atluri et al., 2018).

Synaptic plasticity and neuronal oscillations are not separate phenomena; on the contrary, the power and relationship of theta and gamma oscillations dictate synaptic plasticity in the hippocampal formation (Dragoi and Buzsáki, 2006). Along these lines, the TBS protocol used in our study was developed to mimic theta-modulated gamma rhythms that occur during animal behavior (Larson and Munkácsy, 2015). Therefore, it could be expected that the overall increase in the power of gamma oscillations may lead to changes in synaptic plasticity in the subiculum, and consequently, affect certain aspects of learning and memory. We found that the LTP induction at the CA1→subiculum synapse was suppressed even in the condition of artificially inducing TBS, which implies that early exposure to ketamine permanently perturbed this particular circuitry.

While we were able to generate an informative understanding of long-term sleep macrostructure after neonatal ketamine exposure, this study was limited in that we did not study changes in sleep microstructure: presence of K-complexes and sleep spindles during N1 and N2. Because spindles are dominant in the sigma frequency band between 9 and 16 Hz, we included sigma in our power analysis (Benington et al., 1994; Seibt et al., 2017; Uygun et al., 2019). However, we did not note any changes between the experimental and control groups (data not shown). Furthermore, we found consistent increases in gamma oscillations consistently during N2, when slow and delta waves are most prominent, but we were unable to assess cross frequency coupling between gamma and delta. Future experiments will benefit from the addition of this assessment, which may further cement that exposure to neonatal ketamine impacts subicular physiology.

In conclusion, our results suggest that neonatal exposure to ketamine produces long-term aberrant increases in gamma during NREM sleep of adolescent rats without affecting sleep macrostructure. These animals also experience a decrease in synaptic plasticity in the subiculum, postulating possible lasting changes in subicular circuitry, which could be contributing to poor neurocognitive outcomes.

## DATA AVAILABILITY STATEMENT

The datasets generated for this study are available on request to the corresponding author.

## ETHICS STATEMENT

The animal study was reviewed and approved by Institutional Animal Care and Use Committee at University of Colorado Anschutz Medical Campus.

## AUTHOR CONTRIBUTIONS

FM, SJ, JO, BF, RD, DS, HF, VT, NA, and YR performed experiments and analyzed the data. FM, SJ, VJ-T, PH, and ST designed the studies, supervised the overall project, and performed final manuscript preparation.

## FUNDING

This work was supported by the National Institutes of Health 2R01 GM102525 awarded to ST; by the National Institutes of Health 1R01HD097990 and 5R01GM118197-13 awarded to VJ-T; and by funding from the University of Colorado Anschutz Medical Campus.

## ACKNOWLEDGMENTS

We thank the *in vivo* Neurophysiology Core, which is part of the NeuroTechnology Center of University of Colorado Anschutz Medical Campus, for providing facilities to acquire video-EEG data.

## REFERENCES

Ahnaou, A., Huysmans, H., Biermans, R., Manyakov, N. V., and Drinkenburg, W. H. I. M. (2017). Ketamine: differential neurophysiological dynamics in functional networks in the rat brain. *Transl. Psychiatry* 7:e1237. doi: 10.1038/tp.2017.198

Atluri, N., Joksimovic, S. M., Oklopcic, A., Milanovic, D., Klawitter, J., Eggan, P., et al. (2018). A neurosteroid analogue with T-type calcium channel blocking

properties is an effective hypnotic, but is not harmful to neonatal rat brain. *Br. J. Anaesth.* 120, 768–778. doi: 10.1016/j.bja.2017.12.039

Bartels, D. D., McCann, M. E., Davidson, A. J., Polaner, D. M., Whitlock, E. L., and Bateman, B. T. (2018). Estimating pediatric general anesthesia exposure: quantifying duration and risk DR. *Paediatr* 28, 520–527. doi: 10.1111/pan.13391

Behr, J., Wozny, C., Fidzinski, P., and Schmitz, D. (2009). Synaptic plasticity in the subiculum. *Prog. Neurobiol.* 89, 334–342. doi: 10.1016/j.pneurobio.2009.09.002

Benington, J. H., Kodali, S. K., and Heller, H. C. (1994). Scoring transitions to REM sleep in rats based on the EEG phenomena of pre-REM sleep: an improved analysis of sleep structure. *Sleep* 17, 28–36. doi: 10.1093/sleep/17.1.28

Bhutta, A. T. (2007). Ketamine: a controversial drug for neonates. *Semin. Perinatol.* 31, 303–308. doi: 10.1053/j.semperi.2007.07.005

Bliss, T. V. P., and Collingridge, G. L. (1993). A synaptic model of memory: LTP in the hippocampus. *Nature* 361, 31–39. doi: 10.1038/361031a0

Brambrink, A. M., Evers, A. S., Avidan, M. S., Farber, N. B., Smith, D. J., Martin, L. D., et al. (2012). Ketamine-induced neuroapoptosis in the fetal and neonatal rhesus macaque brain. *Anesthesiology* 116, 372–384. doi: 10.1097/ALN.0b013e318242b2cd

Colgin, L. L. (2015). Do slow and fast γ rhythms correspond to distinct functional states in the hippocampal network? *Brain Res.* 1621, 309–315. doi: 10.1016/j.brainres.2015.01.005

Corsi-Cabrera, M., Pérez-Garci, E., Del Río-Portilla, Y., Ugalde, E., and Guevara, M. A. (2001). EEG bands during wakefulness, slow-wave, and paradoxical sleep as a result of principal component analysis in the rat. *Sleep* 24, 374–380. doi: 10.1093/sleep/24.4.374

Dragoi, G., and Buzsáki, G. (2006). Temporal encoding of place sequences by hippocampal cell assemblies. *Neuron* 50, 145–157. doi: 10.1016/j.neuron.2006.02.023

Ehrlichman, R. S., Gandal, M. J., Maxwell, C. R., Lazarewicz, M. T., Finkel, L. H., Contreras, D., et al. (2009). N-methyl-d-aspartic acid receptor antagonist-induced frequency oscillations in mice recreate pattern of electrophysiological deficits in schizophrenia. *Neuroscience* 158, 705–712. doi: 10.1016/j.neuroscience.2008.10.031

Gramsbergen, A. (1976). The development of the rat EEG. *Dev. Psychobiol.* 9, 501–515. doi: 10.1002/dev.420090604

Ikonomidou, C., Bosch, F., Miksa, M., Bittigau, P., Vöckler, J., Dikranian, K., et al. (1999). Blockade of NMDA receptors and apoptotic neurodegeneration in the developing brain. *Science* 283, 70–74. doi: 10.1126/science.283.5398.70

Ing, C. H., DiMaggio, C. J., Malacova, E., Whitehouse, A. J., Hegarty, M. K., Feng, T., et al. (2014). Comparative analysis of outcome measures used in examining neurodevelopmental effects of early childhood anesthesia exposure. *Anesthesiology* 120, 1319–1332. doi: 10.1097/aln.0000000000000248

Isomura, Y., Sirota, A., Özen, S., Montgomery, S., Mizuseki, K., Henze, D. A., et al. (2006). Integration and segregation of activity in entorhinal-hippocampal subregions by neocortical slow oscillations. *Neuron* 52, 871–882. doi: 10.1016/j.neuron.2006.10.023

Jackson, J., Goutagny, R., and Williams, S. (2011). Fast and slow γ rhythms are intrinsically and independently generated in the subiculum. *J. Neurosci.* 31, 12104–12117. doi: 10.1523/JNEUROSCI.1370-11.2011

Jadi, M. P., Behrens, M. M., and Sejnowski, T. J. (2016). Abnormal γ oscillations in N-Methyl-D-aspartate receptor hypofunction models of schizophrenia. *Biol. Psychiatry* 79, 716–726. doi: 10.1016/j.biopsych.2015.07.005

Jang, H. S., Jung, J. Y., Jang, K. H., and Lee, M. G. (2010). Effects of isoflurane anesthesia on post-anesthetic sleep-wake architectures in rats. *Korean J. Physiol. Pharmacol.* 14, 291–297. doi: 10.4196/kjpp.2010.14.5.291

Jevtovic-Todorovic, V., Hartman, R. E., Izumi, Y., Benshoff, N. D., Dikranian, K., Zorumski, C. F., et al. (2003). Early exposure to common anesthetic agents causes widespread neurodegeneration in the developing rat brain and persistent learning deficits. *J. Neurosci.* 23, 876–882. doi: 10.1523/JNEUROSCI.23-03-00876.2003

Joksimovic, S. M., DiGruccio, M. R., Boscolo, A., Jevtovic-Todorovic, V., and Todorovic, S. M. (2020). The role of free oxygen radicals in lasting hyperexcitability of rat subicular neurons after exposure to general anesthesia during brain development. *Mol. Neurobiol.* 57, 208–216. doi: 10.1007/s12035-019-01770-y

Khazipov, R., and Luhmann, H. J. (2006). Early patterns of electrical activity in the developing cerebral cortex of humans and rodents. *Trends Neurosci.* 29, 414–418. doi: 10.1016/j.tins.2006.05.007

Lakens, D. (2013). Calculating and reporting effect sizes to facilitate cumulative science: a practical primer for t-tests and ANOVAs. *Front. Psychol.* 4:863. doi: 10.3389/fpsyg.2013.00863

Larson, J., and Munkácsy, E. (2015). Theta-burst LTP. *Brain Res.* 1621, 38–50. doi: 10.1016/j.brainres.2014.10.034

Leemburg, S., Vyazovskiy, V. V., Olcese, U., Bassetti, C. L., Tononi, G., and Cirelli, C. (2010). Sleep homeostasis in the rat is preserved during chronic sleep restriction. *Proc. Natl. Acad. Sci. U S A* 107, 15939–15944. doi: 10.1073/pnas.1002570107

Le Van Quyen, M., Staba, R., Bragin, A., Dickson, C., Valderrama, M., Fried, I., et al. (2010). Large-scale microelectrode recordings of high-frequency γ oscillations in human cortex during sleep. *J. Neurosci.* 30, 7770–7782. doi: 10.1523/JNEUROSCI.5049-09.2010

Lunardi, N., Sica, R., Atluri, N., Salvati, K. A., Keller, C., Beenhakker, M. P., et al. (2019). Disruption of rapid eye movement sleep homeostasis in adolescent rats after neonatal anesthesia. *Anesthesiology* 130, 981–994. doi: 10.1097/ALN.0000000000002660

Mahdavi, A., Qin, Y., Aubry, A.-S., Cornec, D., Kulikova, S., and Pinault, D. (2019). Sleep-related thalamocortical spindles and delta oscillations are reduced during a ketamine-induced psychosis-relevant transition state. *bioRxiv* [Preprint]. doi: 10.1101/833459

McCann, M. E., de Graaff, J. C., Dorris, L., Disma, N., Withington, D., Bell, G., et al. (2019). Neurodevelopmental outcome at 5 years of age after general anaesthesia or awake-regional anaesthesia in infancy (GAS): an international, multicentre, randomised, controlled equivalence trial. *Lancet* 393, 664–677. doi: 10.1016/S0140-6736(18)32485-1

McGowan, F. X. Jr., and Davis, P. J. (2008). Anesthetic-related neurotoxicity in the developing infant: of mice, rats, monkeys and, possibly, humans. *Anesth. Analg.* 106, 1599–1602. doi: 10.1213/ane.0b013e31817330cf

McNally, J. M., and McCarley, R. W. (2016). γ band oscillations: a key to understanding schizophrenia symptoms and neural circuit abnormalities. *Curr. Opin. Psychiatry* 29, 202–210. doi: 10.1097/yco.0000000000000244

Minlebaev, M., Colonnese, M., Tsintsadze, T., Sirota, A., and Khazipov, R. (2011). Early γ oscillations synchronize developing thalamus and cortex. *Science* 334, 226–229. doi: 10.1126/science.1210574

Neckelmann, D., and Ursin, R. (1993). Sleep stages and EEG power spectrum in relation to acoustical stimulus arousal threshold in the rat. *Sleep* 16, 467–477. doi: 10.1093/sleep/16.5.467

O'Mara, S. M., Sanchez-Vives, M. V., Brotons-Mas, J. R., and O'Hare, E. (2009). Roles for the subiculum in spatial information processing, memory, motivation and the temporal control of behaviour. *Prog. Neuropsychopharmacol. Biol. Psychiatry* 33, 782–790. doi: 10.1016/j.pnpbp.2009.03.040

Paule, M. G., Li, M., Allen, R. R., Liu, F., Zou, X., Hotchkiss, C., et al. (2011). Ketamine anesthesia during the first week of life can cause long-lasting cognitive deficits in rhesus monkeys. *Neurotoxicol. Teratol.* 33, 220–230. doi: 10.1016/j.ntt.2011.01.001

Pick, J., Chen, Y., Moore, J. T., Sun, Y., Wyner, A. J., Friedman, E. B., et al. (2011). Rapid eye movement sleep debt accrues in mice exposed to volatile anesthetics. *Anesthesiology* 115, 702–712. doi: 10.1097/aln.0b013e31822ddd72

Richardson, A. G., Liu, X., Weigand, P. K., Hudgins, E. D., Stein, J. M., Das, S. R., et al. (2017). Hippocampal γ-slow oscillation coupling in macaques during sedation and sleep. *Hippocampus* 27, 1125–1139. doi: 10.1002/hipo.22757

Seelke, A. M. H., and Blumberg, M. S. (2008). The microstructure of active and quiet sleep as cortical delta activity emerges in infant rats. *Sleep* 31, 691–699. doi: 10.1093/sleep/31.5.691

Seibt, J., Richard, C. J., Sigl-Glöckner, J., Takahashi, N., Kaplan, D. I., Doron, G., et al. (2017). Cortical dendritic activity correlates with spindle-rich oscillations during sleep in rodents. *Nat. Commun.* 8:684. doi: 10.1038/s41467-017-00735-w

Steriade, M. (2006). Grouping of brain rhythms in corticothalamic systems. *Neuroscience* 137, 1087–1106. doi: 10.1016/j.neuroscience.2005.10.029

Sullivan, G. M., and Feinn, R. (2012). Using effect size—or why the P value is not enough. *J. Grad. Med. Educ.* 4, 279–282. doi: 10.4300/JGME-D-12-00156.1

Takeuchi, S., Mima, T., Murai, R., Shimazu, H., Isomura, Y., and Tsujimoto, T. (2015). γ oscillations and their cross-frequency coupling in the primate hippocampus during sleep. *Sleep* 38, 1085–1091. doi: 10.5665/sleep.4818

Talpos, J. C., Chelonis, J. J., Li, M., Hanig, J. P., and Paule, M. G. (2019). Early life exposure to extended general anesthesia with isoflurane and nitrous oxide reduces responsivity on a cognitive test battery in the nonhuman primate. *Neurotoxicology* 70, 80–90. doi: 10.1016/j.neuro.2018.11.005

Uygun, D. S., Katsuki, F., Bolortuya, Y., Aguilar, D. D., McKenna, J. T., Thankachan, S., et al. (2019). Validation of an automated sleep spindle detection method for mouse electroencephalography. *Sleep* 42:zsy218. doi: 10.1093/sleep/zsy218

Valderrama, M., Crépon, B., Botella-Soler, V., Martinerie, J., Hasboun, D., Alvarado-Rojas, C., et al. (2012). Human γ oscillations during slow wave sleep. *PLoS One* 7:e33477. doi: 10.1371/journal.pone.0033477

Wei, T. Y., Young, C. P., Liu, Y. T., Xu, J. H., Liang, S. F., Shaw, F. Z., et al. (2019). Development of a rule-based automatic five-sleep-stage scoring method for rats. *Biomed. Eng. Online* 18:92. doi: 10.1186/s12938-019-0712-8

Wilder, R. T., Flick, R. P., Sprung, J., Katusic, S. K., Barbaresi, W. J., Mickelson, C., et al. (2009). Early exposure to anesthesia and learning disabilities in a population-based birth cohort. *Anesthesiology* 110, 796–804. doi: 10.1097/01.anes.0000344728.34332.5d

Ye, T., Bartlett, M. J., Schmit, M. B., Sherman, S. J., Falk, T., and Cowen, S. L. (2018). Ten-hour exposure to low-dose ketamine enhances corticostriatal cross-frequency coupling and hippocampal broad-band γ oscillations. *Front. Neural Circuits* 12:61. doi: 10.3389/fncir.2018.00061

**Conflict of Interest**: The authors declare that the research was conducted in the absence of any commercial or financial relationships that could be construed as a potential conflict of interest.

*Copyright © 2020 Manzella, Joksimovic, Orfila, Fine, Dietz, Sampath, Fiedler, Tesic, Atluri, Raol, Jevtovic-Todorovic, Herson and Todorovic. This is an open-access article distributed under the terms of the Creative Commons Attribution License (CC BY). The use, distribution or reproduction in other forums is permitted, provided the original author(s) and the copyright owner(s) are credited and that the original publication in this journal is cited, in accordance with accepted academic practice. No use, distribution or reproduction is permitted which does not comply with these terms.*

frontiers in Molecular Neuroscience

ORIGINAL RESEARCH
published: 05 June 2020
doi: 10.3389/fnmol.2020.00097

# Sarcosine Suppresses Epileptogenesis in Rats With Effects on Hippocampal DNA Methylation

*Hai-Ying Shen*, Landen Weltha, John M. Cook, Raey Gesese, Wakaba Omi, Sadie B. Baer, Rizelle Mae Rose, Jesica Reemmer and Detlev Boison†*

*RS Dow Neurobiology Laboratories, Department of Translational Neuroscience, Legacy Research Institute, Portland, OR, United States*

Epileptogenesis is a common consequence of brain insults, however, the prevention or delay of the epileptogenic process remains an important unmet medical challenge. Overexpression of glycine transporter 1 (GlyT1) is proposed as a pathological hallmark in the hippocampus of patients with temporal lobe epilepsy (TLE), and we previously demonstrated in rodent epilepsy models that augmentation of glycine suppressed chronic seizures and altered acute seizure thresholds. In the present study we evaluated the effect of the GlyT1 inhibitor, sarcosine (aka N-methylglycine), on epileptogenesis and also investigated possible mechanisms. We developed a modified rapid kindling model of epileptogenesis in rats combined with seizure score monitoring to evaluate the antiepileptogenic effect of sarcosine. We used immunohistochemistry and Western blot analysis for the evaluation of GlyT1 expression and epigenetic changes of 5-methylcytosine (5mC) and 5-hydroxymethylcytosine (5hmC) in the epileptogenic hippocampi of rats, and further evaluated expression changes in enzymes involved in the regulation of DNA methylation, ten-eleven translocation methylcytosine dioxygenase 1 (TET1), DNA-methyltransferase 1 (DNMT1), and DNMT3a. Our results demonstrated: (i) experimental evidence that sarcosine (3 g/kg, i.p. daily) suppressed kindling epileptogenesis in rats; (ii) the sarcosine-induced antiepileptogenic effect was accompanied by a suppressed hippocampal GlyT1 expression as well as a reduction of hippocampal 5mC levels and a corresponding increase in 5hmC; and (iii) sarcosine treatment caused differential expression changes of TET1 and DNMTs. Together, these findings suggest that sarcosine has unprecedented disease-modifying properties in a kindling model of epileptogenesis in rats, which was associated with altered hippocampal DNA methylation. Thus, manipulation of the glycine system is a potential therapeutic approach to attenuate the development of epilepsy.

**Keywords: epileptogenesis, sarcosine, DNA methylation, dentate gyrus, GlyT1 inhibition, TET1, DNMT**

OPEN ACCESS

***Edited by:***
*Jochen C. Meier, Technische Universitat Braunschweig, Germany*

***Reviewed by:***
*Gary Patrick Brennan, University College Dublin, Ireland*
*Dinesh Upadhya, Manipal Academy of Higher Education, India*

****Correspondence:***
*Hai-Ying Shen*
*hshen@downeurobiology.org*

***†Present address:***
*Detlev Boison, Department of Neurosurgery, Rutgers Robert Wood Johnson Medical School, Rutgers University, Piscataway, NJ, United States*

***Received:*** *06 March 2020*
***Accepted:*** *06 May 2020*
***Published:*** *05 June 2020*

***Citation:***
*Shen H-Y, Weltha L, Cook JM, Gesese R, Omi W, Baer SB, Rose RM, Reemmer J and Boison D (2020) Sarcosine Suppresses Epileptogenesis in Rats With Effects on Hippocampal DNA Methylation. Front. Mol. Neurosci. 13:97. doi: 10.3389/fnmol.2020.00097*

## INTRODUCTION

Prevention of epileptogenesis remains an unmet medical challenge because underlying mechanisms involved in this process remain unclear (Pitkanen and Lukasiuk, 2011; Terrone et al., 2016). No effective treatment is currently available to prevent or delay the epileptogenic process while various therapeutic strategies were explored recently (Rowles and Olsen, 2012; Kaminski et al., 2014;

Tchekalarova et al., 2014; Guo et al., 2015; Rensing et al., 2015; Siniscalchi and Mintzer, 2015; Castro et al., 2017; Long et al., 2017; Namvar et al., 2017; Talos et al., 2018; Upadhya et al., 2018, 2019). Epigenetic modification may play an important role in epileptogenesis (Hsieh and Gage, 2005; Kobow and Blumcke, 2012) and in particular global hypermethylation was identified in the epileptic hippocampus (Zhu et al., 2012). Such epigenetic changes can modify pathophysiological events in epileptogenesis and is also linked to the resistance to antiepileptic drugs (AEDs) (Kobow et al., 2013). These works support a role for methylation in the development and maintenance of epilepsy.

The dentate gyrus (DG) is a crucial brain region involved in the initiation or propagation of seizures (Dudek and Sutula, 2007; Sloviter et al., 2012) in temporal lobe epilepsy (TLE) due to its gating role from its densely packed, hyperpolarized granule cells (Toader et al., 2013). Our previous work demonstrated robust overexpression of glycine transporter 1 (GlyT1) in the hippocampus of human TLE samples and the DG region of epileptic rodents (Shen et al., 2015). Exogenous glycine administration can suppress neuronal excitation in the DG (Chattipakorn and McMahon, 2003) and reduce action potential firing in hippocampal neurons (Song et al., 2006). Augmentation of glycine has antiictogenic effects to suppress chronic seizures and alter the acute seizure threshold in rodents (Shen et al., 2015). Sarcosine (aka N-methylglycine), is a glycine transporter 1 (GlyT1) inhibitor that can increase extracellular glycine (Lopez-Corcuera et al., 1998; Herdon et al., 2001) via blockade of GlyT1-mediated glycine uptake or through a hetero-exchange of sarcosine for glycine (Herdon et al., 2001). Sarcosine agonizes the glycine receptor (GlyR) via binding to its strychnine-sensitive site (Salceda and Aguirre-Ramirez, 2005; Zhang et al., 2009). In addition, sarcosine acts as a co-agonist of N-methyl-D-aspartate receptor (NMDAR) (Ryley Parrish et al., 2013). Dysfunctional NMDAR signaling may contribute to the development of seizures and epilepsy (Barker-Haliski and White, 2015; Parrish et al., 2018). Finally, as an essential intermediate in one-carbon metabolism, sarcosine is involved in methyl balance and transmethylation fluxes (Ueland et al., 2007) and contributes to the dynamic homeostasis of transmethylation (Mudd et al., 2007; Moore et al., 2013). However, whether sarcosine's actions through transmethylation have any relationship to seizure outcomes and epileptogenesis has not been previously evaluated.

Because status epilepticus can result in a hypermethylation status in the epileptogenic hippocampus (Miller-Delaney et al., 2013, 2015) and sarcosine is tightly linked to transmethylation pathways in the brain beyond its GlyT1 inhibition, thus sarcosine application may provide a novel strategy to ameliorate several aspects of epileptogenesis. We therefore hypothesized that manipulation of the glycine pathway via sarcosine may alter the progress of epileptogenesis via the transmethylation process and glycine-mediated inhibitory actions in the hippocampus. In the present study, we developed a rapid model of epileptogenesis for the purpose of establishment of a fast, stable, and reliable model to efficiently test the antiepileptic effects of pharmacological interventions. We then evaluated the potential antiepileptogenic role of sarcosine and explored epigenetic changes in the DG neurons for possible contributing mechanisms.

# MATERIALS AND METHODS

## Animals

All animal procedures were conducted in a facility accredited by the Association for the Assessment and Accreditation of Laboratory Animal Care in accordance with protocols approved by the Institutional Animal Care and Use Committee of the Legacy Research Institute and the principles outlined by the National Institutes of Health (NIH). Male Sprague Dawley rats (280–300 g) were purchased from Jackson Labs (Sacramento, CA, United States). All rats were acclimatized for 1 week before being used in the experiments and the animals were housed in a temperature- and humidity-controlled room with a 12 h light/dark cycle (lights on at 7:00 a.m.) throughout the experimental period.

## Rat Kindling Model of Epileptogenesis

The rat rapid electrical hippocampal kindling model of epileptogenesis was developed with modification from published kindling protocols (McNamara, 1986; Morimoto et al., 2004; De Smedt et al., 2007; Morales et al., 2014) to test drug effects on the process of epileptogenesis (paradigm see **Figure 1A**). Adult male Sprague Dawley rats were implanted with bipolar, coated stainless steel electrodes (0.20 mm in diameter; Plastics One, Roanoke, VA, United States) into the left hippocampus using the following stereotactic coordinates ($AP = -5$ mm, ML = +5 mm, DV = −7.5 mm, to bregma) and fixed with a headset of dental acrylate. All surgical procedures were performed under anesthesia induced with 3% isoflurane, 67% $N_2$, 30% $O_2$ and maintained with 1.5% isoflurane, 68.5% $N_2$, 30% $O_2$, while rats were placed in a Kopf stereotactic frame (David Kopf Instruments, CA, United States).

After recovery for 10 days, the rats were kindled based on a rapid kindling paradigm that consisted of three periods: 5-day kindling period, 5-day stimulus-free incubation period, and 5-day testing period. Briefly, using a Grass S-88 stimulator (Grass Telefa, United States), rats received six stimulations daily (1-ms square wave biphasic pulses of 200 μA, 50 Hz frequency, and 10 s duration at an interval of 30 min between stimulations) for 5 consecutive days. Behavioral seizures were scored according to the scale of Racine (1978), and electrical brain activity was amplified (Grass Technologies) and digitized (PowerLab; AD Instruments) for periods spanning one min prior- and five min post-application of each stimulating pulse. Following a 5-day stimulus-free incubation period, rats received six stimulations (as described above) daily for another 5 consecutive days (testing period) to evaluate the progression of epileptogenesis evidenced by their Racine scores post-stimulation.

For pharmacological experiments, rats were kindled as described above while being treated with sarcosine (SRC, 3 g/kg; #131776, Aldrich, CA, United States), valproic acid (VPA, 200 mg/kg; P4543, Sigma, CA, United States), 5-Aza-2′-deoxycytidine (5-AZA, 1.2 mg/kg; A3656, Sigma, CA, United States), or 0.9% saline (as vehicle control). Drugs were administered intraperitoneally (i.p.) 30 min prior to the first kindling session of each day for 5 consecutive days. After

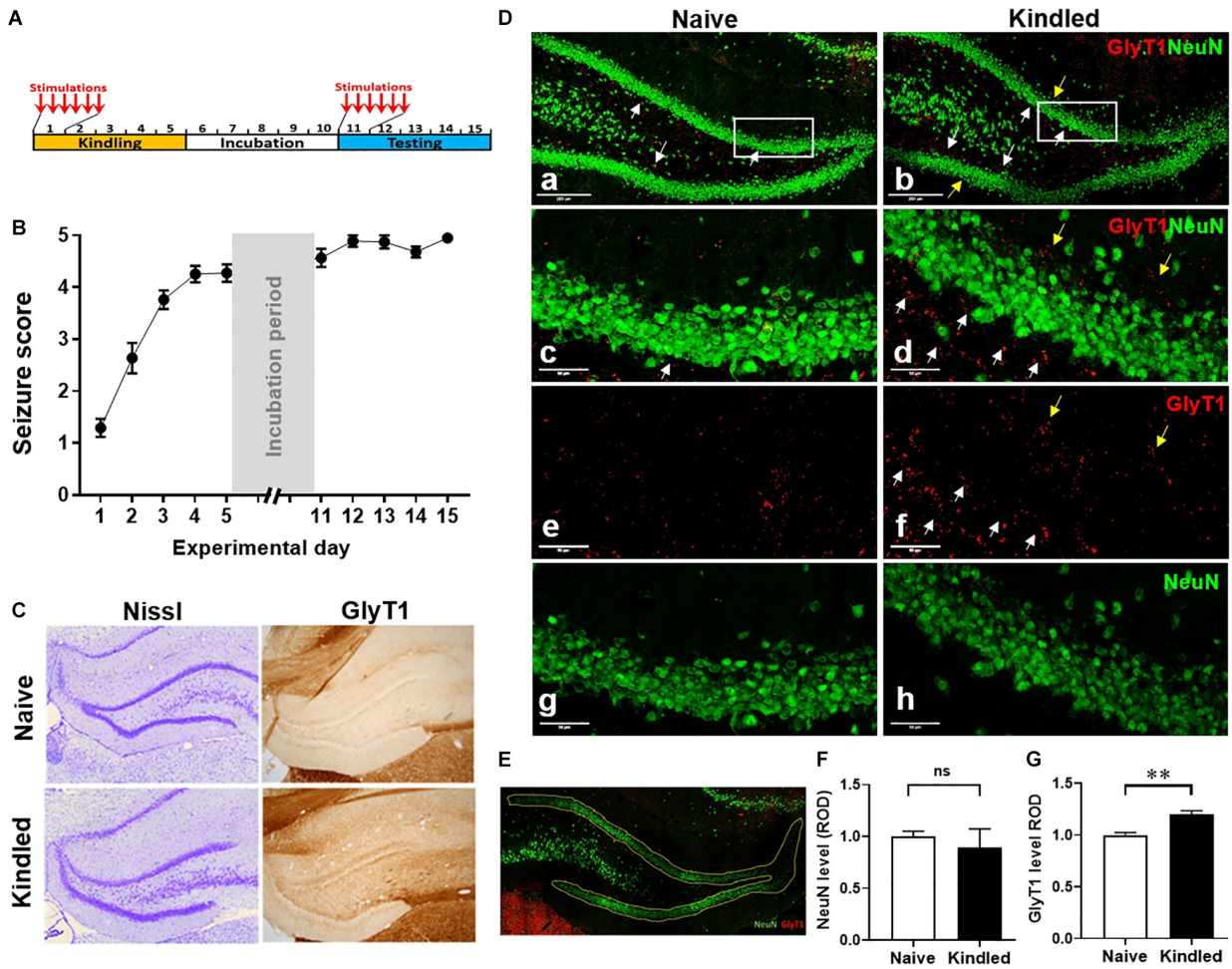


**FIGURE 1 |** Hippocampal kindling induces overexpression of GlyT1. **(A)** Rat kindling paradigm that consists of a 5-day kindling period (days 1 –5), 5-day stimulation free incubation period (days 6–10), and a 5-day (re-kindling) testing period (days 11–15). **(B)** Averaged Racine stages of rats during their kindling and testing days. Data are mean ± SEM from six stimulations of each day. **(C)** Representative images of Nissl and GlyT1 immunochemistry DAB staining of fully kindled rats vs. non-kindled naïve controls. **(D)** Representative images of IF staining for GlyT1 and NeuN in the DG of fully kindled rats vs. non-kindled controls. **(E)** A representative selection of the DG area for the quantitative analysis of target positive staining. **(F)** Quantitative analysis of the DG expression levels of NeuN, or **(G)** GlyT1 in kindled rats (Kindled) vs. non-kindled controls (Naïve). White arrows pointing to dentate inner molecular layer, yellow arrows pointing to the dentate outer molecular layer. Data are mean ± SEM. $^{**}p < 0.01$ vs. non-kindled controls, ns, no significance. Scale bar = 250 μm (a,b) or 50 μm (c–h).

each stimulation, animals were scored for Racine stages to demonstrate and compare the seizure response in the presence of each experimental drug. Following a drug- and stimulus-free 5-day incubation period, rats received kindling stimuli and again were scored for Racine stages to evaluate the drugs' antiepileptogenic potential. Rats were sacrificed at defined experimental time points (6, 11, or 16 days after initiation of kindling), with non-kindled rats as controls. Brains were either perfused for immunohistochemistry evaluation or fresh dissected for Western blot assessment.

## Immunohistochemistry Evaluation

Under anesthesia (with 68.5% $N_2$, 30% $O_2$, and 1.5% isoflurane), rats were transcardially perfused with ice-cold PBS followed by 4% formaldehyde. Brains were subsequently removed and post-fixed in 4% formaldehyde and then washed in PBS, infiltrated with a 30% sucrose PBS solution for cryoprotection. 30 μm coronal sections were sectioned using a cryostat (VT 1000S, Leica, Bannockburn, IL, United States). Sections were incubated for 1 h in 2% donkey blocking buffer (DBB, made of PBS containing 2% NDS, 1% BSA, and 0.02% Triton X-100), then incubated for 24 h at 4°C in blocking buffer containing primary antibodies, GlyT1, 5-methylcytosine (5mC), 5-hydroxy methylcytosine (5hmC), neuronal nuclei (NeuN), and glial fibrillary acidic protein (GFAP), as listed in **Table 1**. Then, for 3,3'-diaminobenzidine tetrahydrochloride (DAB) staining of GlyT1 (Shen et al., 2015), biotinylated goat anti-rabbit IgG (1:200, GE Healthcare, Diegem, Belgium) was used as the secondary antibody and the ABC mix (Vectastain ABC kit, Peroxidase Standard pk-4000, Vector Laboratories, Burlingame, CA, United States) coupled with 50 mg DAB peroxidase (HRP) substrate (SK-4105, Vector

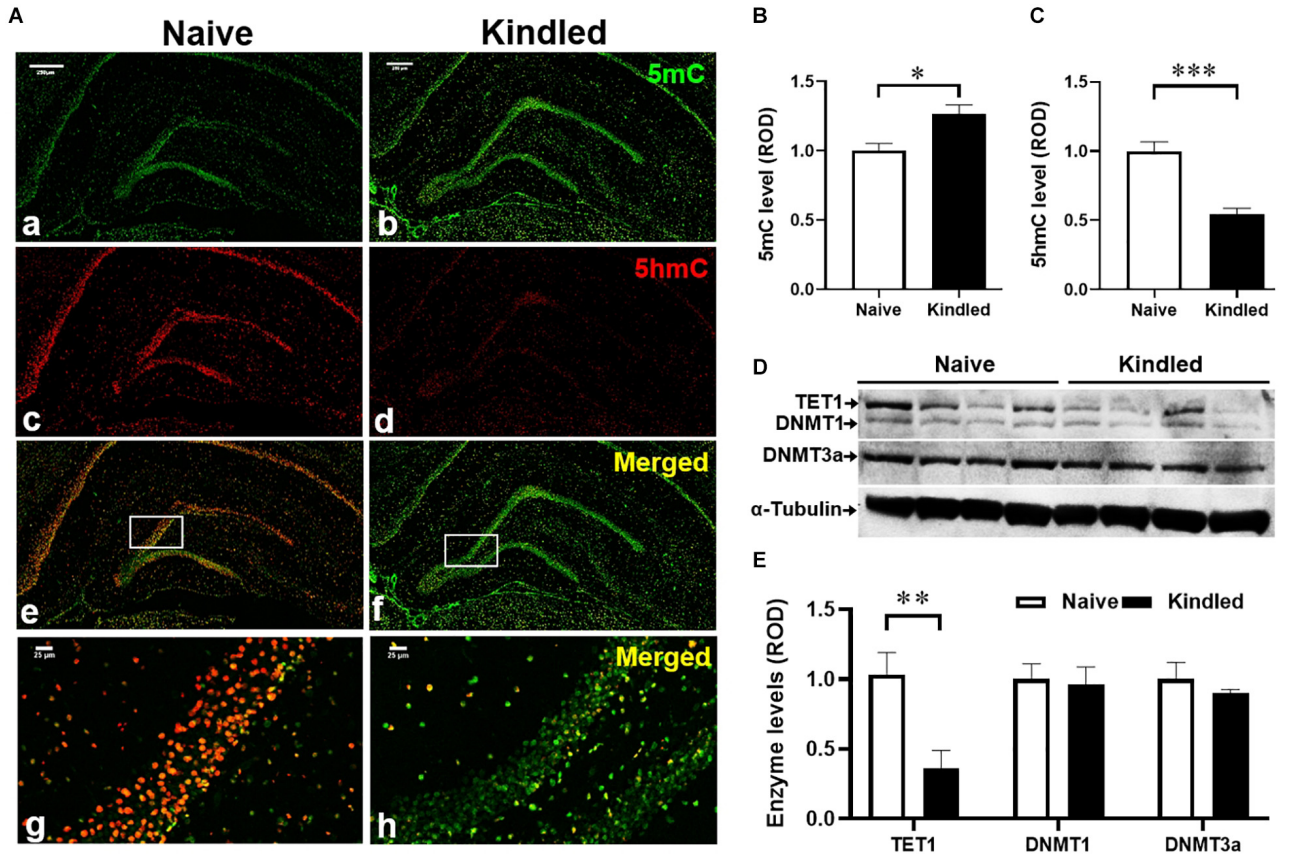


**FIGURE 2 |** Changes of DNA methylation in kindling epileptogenesis. **(A)** Immunofluorescence staining for 5mC and 5hmC n the hippocampus of fully kindled rats vs. non-kindled naïve controls. Scale bar = 250 μm (a–f) and 25 μm (g,h). Quantitative analysis of the DG levels of **(B)** 5mC and **(C)** 5hmC in non-kindled naïve controls and fully kindled rats. **(D)** Representative Western blot imaging of TET1, DNMT1, and DNMT3a. **(E)** Quantification of hippocampal levels of TET1, DNMT1, and DNMT3a in fully kindled rats vs. non-kindled naïve controls. Data are mean ± SEM. $^{*}p < 0.05$, $^{**}p < 0.01$, $^{****}p < 0.0001$ vs. non-kindled naïve controls.

Labs) was used for detection. For immunofluorescence staining (Chouliaras et al., 2013), after several washes in PBS, sections were incubated with a blocking buffer containing corresponding fluorochrome-conjugated secondary antibodies in **Table 1** for detection. The sections were then washed and mounted using the mounting medium with DAPI for fluorescence microscopy observation on a Leica TCS SPE confocal laser-scanning microscope (LAS X 3.1.2.16221). All sections were processed in parallel using identical solutions and identical incubation times, while slices without either primary or secondary antibody were used for controls.

## Image Quantification of Densitometry

High-resolution digital images were acquired under identical conditions, and all image processing was applied identically across experimental groups. The images of immunofluorescence staining were acquired using the LasX software system (Leica, Buffalo Grove, IL, United States). Fluorescence intensity analysis was performed using Leica Application Suite Analysis software (Leica, Buffalo Grove, IL, United States). The dentate gyrus was selected using binary processing of the LasX software system (Leica, Buffalo Grove, IL, United States) as shown in **Figure 1E**, and immunoreactive material was measured in the same designated area of the DG for each sample and expressed as relative optical density (ROD) by area. Three levels were measured for each rat, and data analysis is expressed as the mean ± SEM of ROD. The average levels in treatment groups were normalized according to that in the control group (as baseline).

## Western Blot Assay

Hippocampi were freshly dissected after animals were sacrificed at designed experimental time points, brain tissue was processed for the extraction of aqueous membrane proteins and a 30 μg sample of protein from each specimen was loaded and electrophoresed on a 10% Bis-Tris gel. After the transfer of the proteins onto nitrocellulose membranes, the blots were blocked for 1 h in TBSTM (10 mM Tris/HCl, pH 8, 0.15 M NaCl, 0.05 % Tween 20, containing 5% nonfat milk) at room temperature, followed by incubation with primary antibodies (**Table 1**): anti-ten-eleven translocation methylcytosine dioxygenase 1 (TET1), anti-DNA methyltransferase1 (DNMT1), or anti-DNMT3a, overnight at 4°C in TBSTM, 4 × 10 min washes with TBST and incubation with corresponding secondary antibodies

**TABLE 1 |** Antibodies used for immunohistochemistry and Western blot evaluation.

| Antibody | Catalog # | Manufacturers | Dilution |
|---|---|---|---|
| GlyT1 | n/a | In house (Shen HY, 2015)* | 1:250 (IHC) |
| 5mC | A-1014 | Epigentek, Farmingdale, NY | 1:2000 (IHC) |
| 5hmC | 39769 | Active Motif, Carlsbad, CA | 1:3000 (IHC) |
| NeuN | MAB-377 | Millipore Sigma, Burlington, MA | 1:500 (IHC) |
| GFAP | NB100-53809 | Novus Biologicals, Centennial, CO | 1:1000 (IHC) |
| TET1 | PA5-72805 | Thermo Fisher Scientific, Waltham, MA | 1:1000 (WB) |
| DNMT1 | D63A6 | Cell signaling, Beverly, MA | 1:1000 (WB) |
| DNMT3a | 3598S | Cell signaling, Beverly, MA | 1:1000 (WB) |
| α-tubulin | sc-8035 | Santa Cruz Biotechnology, CA, USA | 1:5000 (WB) |
| Alexa Fluor 488 donkey anti-mouse IgG | A21202 | Life Technologies, Carlsbad, CA | 1:500 (IHC) |
| Alexa Fluor 555 donkey anti-rabbit IgG | A31572 | Life Technologies, Carlsbad, CA | 1:350 (IHC) |
| Alexa Fluor 633 donkey anti-goat IgG | A21082 | Life Technologies, Carlsbad, CA | 1:1000 (IHC) |
| Alexa Fluor 488 goat anti-mouse IgG | A1101 | Life Technologies, Carlsbad, CA | 1:400 (IHC) |
| Alexa Fluor 555 goat anti-rabbit IgG | A21428 | Life Technologies, Carlsbad, CA | 1:400 (IHC) |

*GlyT1, glycine transporter 1; 5mC, 5-methylcytosine; 5hmC, 5-hydroxy methylcytosine; NeuN, neuronal nuclei; GFAP, glial fibrillary acidic protein; TET1, ten-eleven translocation methylcytosine dioxygenase 1; DNMT1 and DNMT3a, DNA methyltransferase 1 and 3a; GAPDH, Glyceraldehyde 3-phosphate dehydrogenase; IHC, immunohistochemistry; WB, Western blot. *Reference: Shen et al. (2015).*

(#7074, 1:8,000, Cell Signaling, Boston, MA, United States) at RT for 1 h. After 4 × 10 min washing with TBST, immunoreactivity was detected by chemiluminescence (#34087, Pierce, IL, United States); the immunoblots were quantified using a ChemiDoc Touch Imaging System (#17001401, Bio-Rad, Hercules, CA, United States). To normalize protein loading, a mouse monoclonal anti-α-tubulin antibody (sc-8035, Santa Cruz Biotechnology, CA, United States) was used to re-probe the same blot and the OD ratio of ADK to α-tubulin was calculated.

## Statistics

Quantitative data were analyzed using GraphPad Prism 8 software. All data are presented as mean ± SEM, and data were analyzed using one-way, two-way ANOVA, or *t*-tests assuming the non-Gaussian distribution of the data as appropriate. A $p < 0.05$ was considered significant.

# RESULTS

## Hippocampal Kindling Induced Epileptogenesis and GlyT1 Overexpression in the Dentate Gyrus

We developed a rapid kindling model of epileptogenesis in rats (**Figure 1A**) to evaluate phenotypical and molecular changes in epileptogenesis. More than 90% of rats (11 out of 12) were fully kindled after 5-days of kindling, as defined by scoring a Racine seizure stage of 4–5 after the first test stimulus on each day of testing (**Figure 1B**). The histological evaluation of Nissl staining at experimental day 16 showed a similar morphology of neuronal cells in DG between fully kindled rats and non-kindled controls. In contrast, GlyT1-DAB staining demonstrated an overt increase of GlyT1-positive staining in the epileptogenic hippocampus (**Figure 1C**). Of note, the overexpressed GlyT1 was predominantly located at the dentate inner molecular layer, whereas a lesser increase was seen in the dentate outer molecular layer (**Figure 1D**). Quantitative analysis from DG-focused IF staining (**Figure 1E**) demonstrated that NeuN-positive staining in the DG was not significantly different between fully kindled rats and the non-kindled naive controls ($p = 0.6476$, unpaired *t*-test, $n = 3$–4 per group) (**Figure 1F**); this is in line with Nissl observations and strongly indicates that neuronal cell death is not a contributing pathophysiological feature of our rapid kindling model of epileptogenesis. Importantly, quantitative analysis from IF staining of GlyT1 demonstrated a significant (20.2%) increase of GlyT1 in the DG of fully kindled rats vs. non-kindled controls ($p = 0.0066$, unpaired *t*-test, $n = 3$–4 per group) (**Figure 1G**). These results, which are in line with our previous findings, demonstrate pathological increases in GlyT1 in the rapid rat hippocampal kindling model of epileptogenesis.

## Dysregulated DNA Methylation in the Epileptogenic DG of Kindled Rats

To explore potential epigenetic mechanisms underlying epileptogenesis in kindled rats, we evaluated the methylation changes in the DG of kindled vs. non-kindled rats. The IF staining showed that the expression levels of 5mC, a biomarker of DNA methylation, were significantly increased in the granule cell layer of the DG in kindled rats on experimental day 16 compared to non-kindled controls ($p = 0.017$, unpaired *t*-test, $n = 4$–5 per group) (**Figures 2A,B**). In contrast, the expression levels of 5hmC, a demethylation biomarker, were significantly decreased in the granule cell layer of the DG in kindled rats vs. non-kindled controls ($p < 0.0001$, unpaired *t*-test, $n = 4$–5 per group) (**Figures 2A,C**). These findings suggest an altered methylation status of 5mC and 5hmC in the epileptogenic brain. To validate and further probe mechanisms contributing to those findings, we assessed related changes of the expression levels of DNA methyltransferases DNMT1 and DNMT3a, and the demethylase

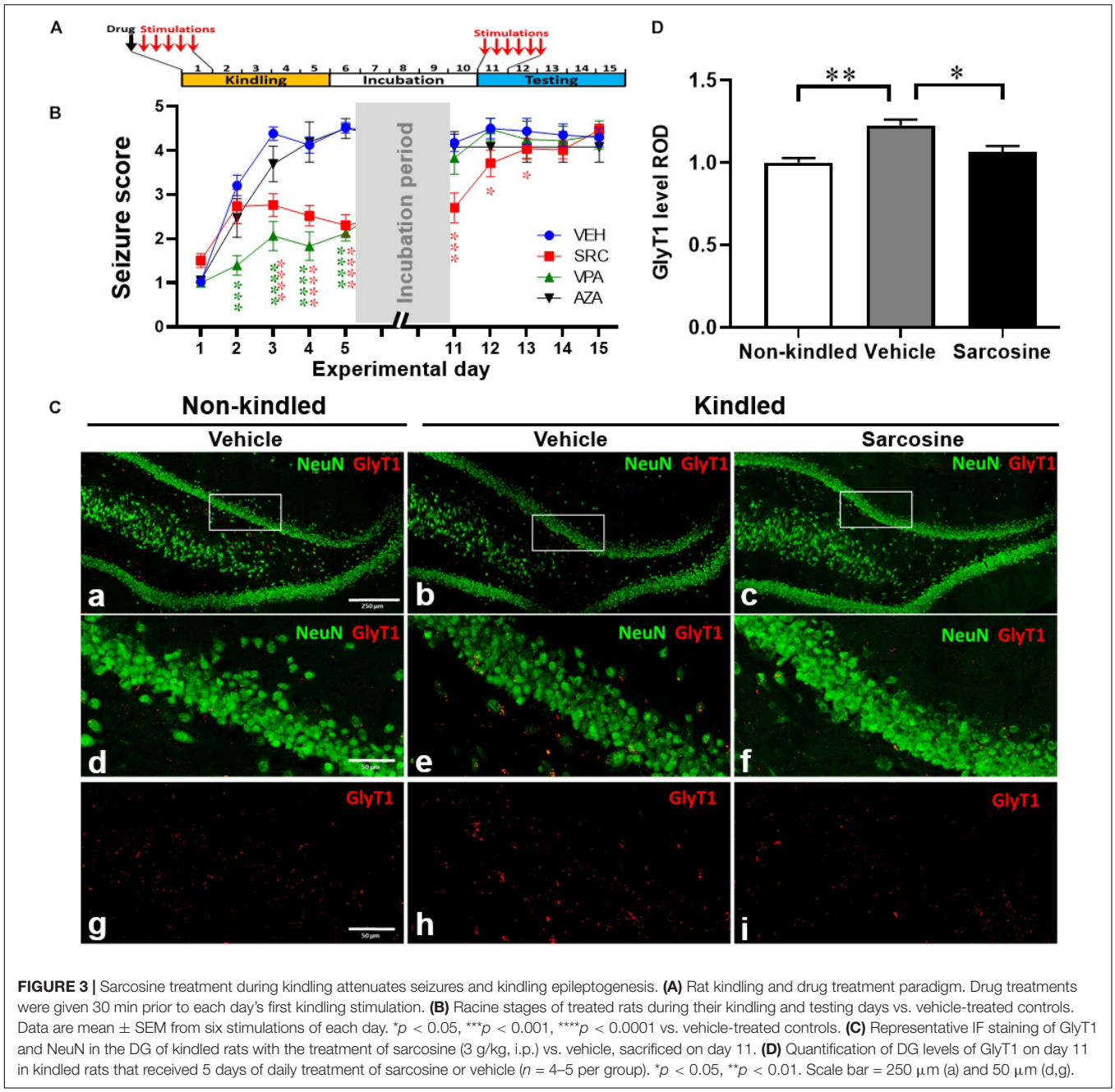


**FIGURE 3 |** Sarcosine treatment during kindling attenuates seizures and kindling epileptogenesis. **(A)** Rat kindling and drug treatment paradigm. Drug treatments were given 30 min prior to each day's first kindling stimulation. **(B)** Racine stages of treated rats during their kindling and testing days vs. vehicle-treated controls. Data are mean ± SEM from six stimulations of each day. $^{*}p < 0.05$, $^{***}p < 0.001$, $^{****}p < 0.0001$ vs. vehicle-treated controls. **(C)** Representative IF staining of GlyT1 and NeuN in the DG of kindled rats with the treatment of sarcosine (3 g/kg, i.p.) vs. vehicle, sacrificed on day 11. **(D)** Quantification of DG levels of GlyT1 on day 11 in kindled rats that received 5 days of daily treatment of sarcosine or vehicle ($n$ = 4–5 per group). $^{*}p < 0.05$, $^{**}p < 0.01$. Scale bar = 250 μm (a) and 50 μm (d,g).

TET1. Our Western blot data demonstrate that kindling-induced epileptogenesis resulted in differential response on expression between methylase DNMT1, DNMT3a, and demethylase TET1 [$p$ = 0.0325, $F_{(1,9)}$ = 6.374, kindling effect; $p$ = 0.0463, $F_{(2,\ 9)}$ = 4.408, enzyme effect; two-way ANOVA]. Specifically, the hippocampal expression of TET1 was significantly lower in fully kindled rats vs. controls ($p$ = 0.0081, unpaired $t$-test, $n$ = 4 per group) (**Figures 2D,E**), whereas expression levels of DNMT1 and DNMT3a were not significantly different between kindled and non-kindled rats ($p$ = 0.4138 and $p$ = 0.2237, correspondingly, unpaired $t$-test, $n$ = 4 per group). The above findings suggest that DNA methylation is dysregulated in kindled rats.

## Sarcosine Effectively Suppresses Kindling Epileptogenesis

Having identified a disease state of hypermethylation and dysregulated GlyT1 expression in epileptogenesis of rats, we used a separate cohort of rats to evaluate the potential antiepileptogenic actions of sarcosine and its effects on transmethylation. During the kindling period rats were given a single daily i.p. injection of the GlyT1 inhibitor sarcosine (SRC,

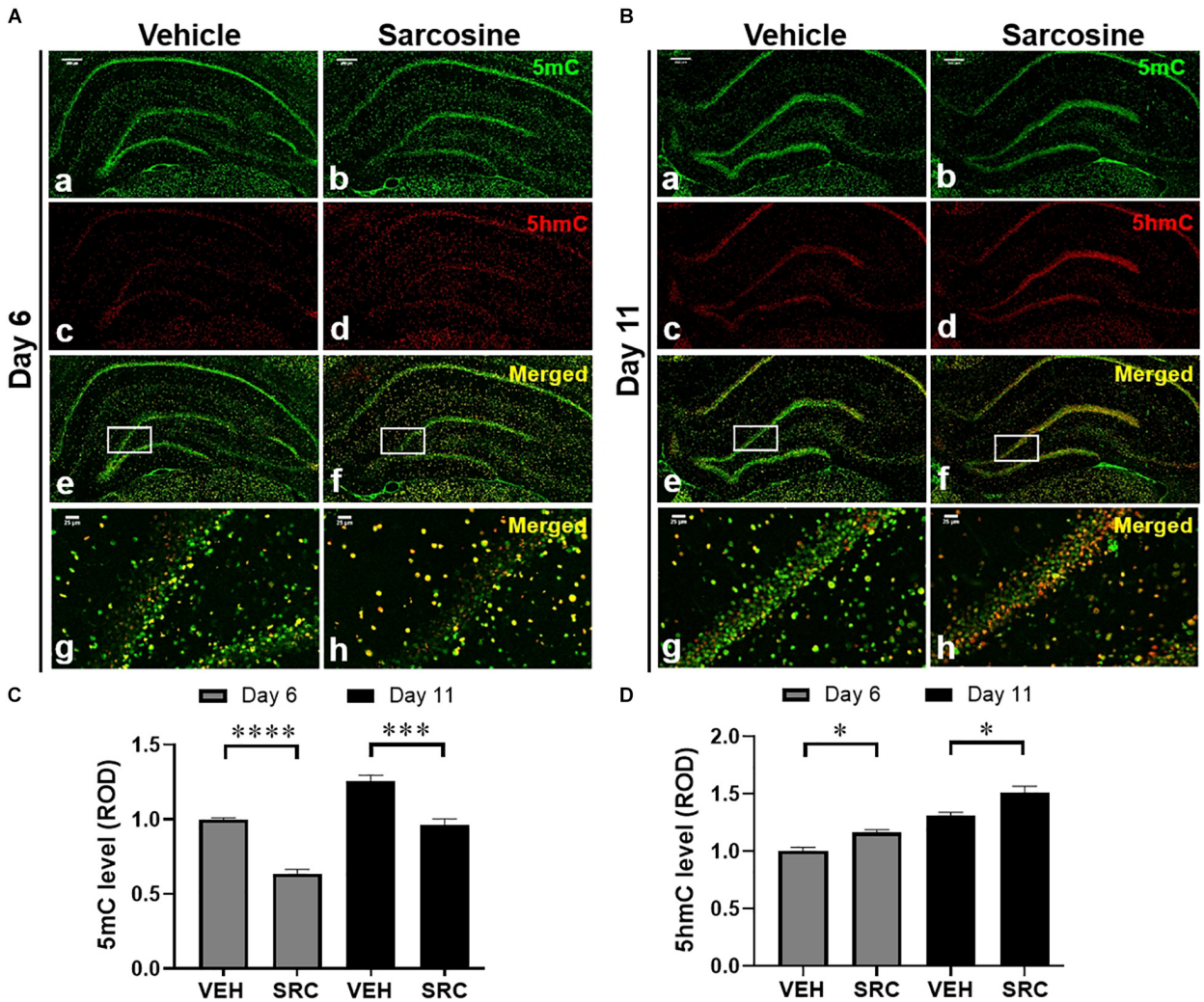


**FIGURE 4 |** Sarcosine affects DNA methylation in kindling epileptogenesis. Immunofluorescence staining of 5mC and 5hmC in the hippocampus of kindled rats on day 6 **(A)** or day 11 **(B)**, which received sarcosine or vehicle treatment. Scale bar = 250 μm (a–f) and 50 μm (g,h). Quantitative analysis of the DG levels of 5mC **(C)** and 5hmC **(D)** in rats with sarcosine vs. vehicle treatment. *$p < 0.05$, ***$p < 0.001$, and ****$p < 0.0001$ vs. vehicle-treated controls.

3 g/kg), a conventional AED, valproic acid (VPA, 200 mg/kg), the demethylating agent 5-azacytidine (5-AZA, 1.2 mg/kg), or 0.9% saline (as vehicle control) for 5 days, 30 min prior to each day's first kindling stimulation (**Figure 3A**). Vehicle-treated rats (**Figure 3B**) ($n$ = 15) rapidly reached an average Racine score of at least 4 at the end of the kindling period, and maintained high seizure responses during the testing period, confirming our established rapid-epileptogenic kindling model (as shown in **Figure 1**). SRC treatment significantly suppressed kindling-induced epileptogenesis [$p < 0.0001$, $F_{(3,46)} = 17.31$, treatment effect, $p < 0.0001$, $F_{(9,389)} = 92.77$, time effect; and $p < 0.0001$, $F_{(27,\ 389)} = 6.085$, treatment × time effects; two-way ANOVA] with reduced seizure scores during kindling period, day 3, 4, and 5 ($p < 0.0001$, $t$-test, $n$ = 30), and a lasting suppression of seizure responses during the testing period, day 11, 12, and 13 ($p < 0.001$, $p = 0.0145$, $p = 0.0254$, correspondingly, $t$-test, $n$ = 17), which indicates SRC-induced anti-ictogenic and anti-epileptogenic effects. Treatment with the conventional AED drug VPA (200 mg/kg, $n$ = 8) suppressed seizure responses during the kindling period but had no lasting effects during the testing period. Interestingly, treatment with the demethylating agent, 5-AZA, at a dose of 1.2 mg/kg showed neither an anti-ictogenic nor an anti-epileptogenic effect ($n$ = 6) (**Figure 3B**). The above findings support a novel antiepileptogenic effect of sarcosine.

## Sarcosine Treatment Normalizes GlyT1 Expression in the Kindled Rats

To investigate whether sarcosine treatment during kindling affects GlyT1 expression, we evaluated the expression levels of GlyT1 in the DG of rats that received sarcosine treatment during the first 5 days of kindling (**Figure 3C**). The quantitative analysis from IF staining showed a significant treatment effect

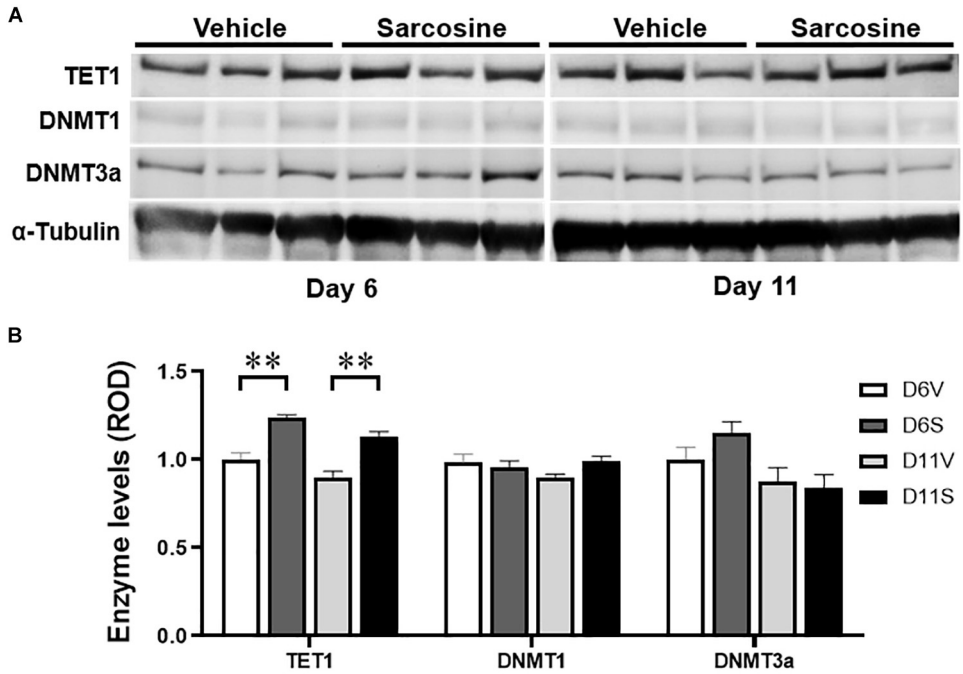


**FIGURE 5 |** Sarcosine affects DNA methylase and demethylase. **(A)** Representative Western blot imaging of TET1, DNMT1, and DNMT3a of the hippocampus of rats exposed to sarcosine during kindling and dissected on experimental days 6 and 11. **(B)** Quantification of hippocampal levels of TET1, DNMT1, and DNMT3a in sarcosine-treated rats vs. vehicle-treated controls. Data are mean ± SEM. $^{**}p < 0.01$ vs. controls.

of sarcosine on the DG GlyT1 levels of kindled rats [$n = 4$–5 per group, $p = 0.0021$, $F_{(2,\ 10)} = 12.13$, one-way ANOVA]. While GlyT1 levels in the DG of vehicle-treated kindled rats were significantly higher than in non-kindled controls ($p = 0.0021$, unpaired $t$-test), the sarcosine (3 g/kg, i.p.) treatment significantly suppressed the overexpression of DG GlyT1 (by 21.5%) compared to vehicle-treated kindled rats on day 11 ($p = 0.0165$, unpaired $t$-test) (**Figure 3D**). Thus, sarcosine treatment normalized GlyT1 expression levels in kindled rats, to levels similar to those found in non-kindled rats ($p = 0.4601$, unpaired $t$-test).

## Sarcosine Treatment Affects DNA Methylation in Kindled Rats

To explore the effects of sarcosine administration during kindling on DNA methylation, we evaluated 5mC and 5hmC expression levels in the DG and assessed hippocampal expression levels of methylase and demethylase. Tissue samples were taken on day 6 (24 h after the last sarcosine treatment) (**Figure 4A**) and day 11 (after 5 days of drug washout and the stimulus-free period) (**Figure 4B**). The IF staining data showed that sarcosine treatment significantly reduced the 5mC levels in the DG vs. vehicle-treated controls ($n = 4$–5 per group) [$p < 0.0001$, $F_{(1,\ 46)} = 52.91$, treatment effect; $F_{(1,\ 46)} = 33.84$, time effect, two-way ANOVA] on both day 6 and day 11 ($p < 0.0001$ and $p = 0.0003$, correspondingly, unpaired $t$-test) (**Figure 4C**). In contrast, the sarcosine treatment increased the DG 5hmC levels in rats treated with sarcosine vs. vehicle [$n = 4$–5 per group, $p = 0.0005$, $F_{(1,\ 46)} = 14.07$, treatment effect; $p = 0.0005$, $F_{(1,\ 46)} = 27.93$, time effect, two-way ANOVA] on day 6 and day 11 ($p = 0.0477$ and $p = 0.0127$, correspondingly, unpaired $t$-test) (**Figure 4D**).

In addition, our Western blot assay showed that sarcosine treatment increased hippocampal TET1 expression levels vs. vehicle-treated kindled rats [$p = 0.0004$, $F_{(1,10)} = 27.54$, treatment effect; $p = 0.2687$, $F_{(2,\ 10)} = 1.371$, time effect; two-way ANOVA; $n = 6$ per group] on both day 6 and day 11 ($p = 0.0080$ and $p = 0.0081$, correspondingly, unpaired $t$-test) (**Figures 5A,B**, left panel), which correlated to increased DG 5hmC levels on day 6 and day 11. However, the hippocampal expression levels of DNMT3a were not significantly different between sarcosine- and vehicle-treated rats on either day 6 or day 11 [$p = 0.6537$, $F_{(1,\ 10)} = 0.2138$, treatment effect; $p = 0.6962$, $F_{(2,\ 10)} = 0.6962$, time effect; two-way ANOVA; $n = 6$ per group] (**Figures 5A,B**, middle panels). Similarly, the hippocampal levels of DNMT3a of the sarcosine-treated rats were not different from vehicle-treated rats on either day 6 or day 11 (**Figures 5A,B**, right panel) The above data showed that sarcosine altered DNA methylation in the DG of kindled rats, by decreasing 5mC and increasing 5hmC and TET1.

# DISCUSSION

There exists an urgent and unmet clinical need to prevent or delay the development of epilepsy (Pitkanen and Lukasiuk, 2011; Di Maio, 2014; Younus and Reddy, 2017). Despite extensive studies exploring possible mechanisms of epileptogenesis (Rakhade and

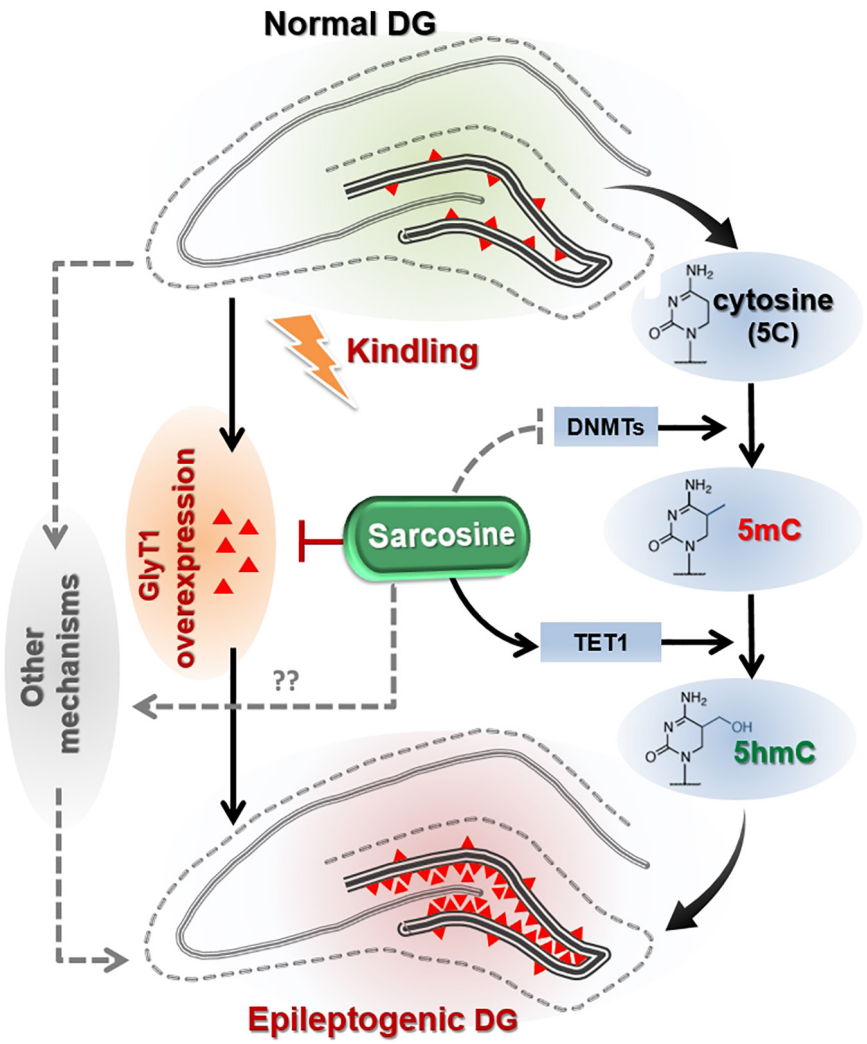


**FIGURE 6 |** Hypothetical pathways linking sarcosine with antiepileptogenic activity. Kindling of the hippocampus in rats results in GlyT1 overexpression and DNA hypermethylation in the hippocampal dentate gyrus (DG), two putative mechanisms thought to promote epileptogenesis. Sarcosine can suppress the overexpression of GlyT1 in the epileptogenic DG and reduce the hypermethylation status via enhancement of TET1 expression and its demethylation process of converting 5mC into 5hmC.

Jensen, 2009; Goldberg and Coulter, 2013; Engel and Pitkanen, 2019) and therapeutic strategies for reducing the impact of epileptogenesis (Rowles and Olsen, 2012; Kaminski et al., 2014; Tchekalarova et al., 2014; Guo et al., 2015; Rensing et al., 2015; Siniscalchi and Mintzer, 2015; Castro et al., 2017; Long et al., 2017; Namvar et al., 2017; Talos et al., 2018; Upadhya et al., 2018, 2019), no pharmacological interventions are currently available to reduce or delay the progression of epileptogenesis. In the present study, we developed a rapid hippocampal kindling model to produce stable epileptogenesis (**Figure 1A**) and demonstrated a resultant overexpression of GlyT1 and dysregulated DNA methylation in kindled rats. We further provided experimental evidence that sarcosine can delay kindling epileptogenesis, which was associated with altered DNA methylation changes and normalized GlyT1 expression levels. Sarcosine treatment during kindling changed hippocampal 5mC and 5hmC levels and modified the expression levels of the demethylase TET1. To better understand the role of sarcosine in epileptogenesis and its therapeutic potential, the following aspects of sarcosine warrant further discussion.

## Role of GlyT1 in the Dentate Gyrus During Kindling

The DG, as a primary source of seizure activity, has long been a focal point to study possible molecular, cellular, and network mechanisms responsible for epileptogenesis in TLE (Dudek and Sutula, 2007; Toader et al., 2013; Wei et al., 2015). While multiple mechanisms can contribute to epileptogenesis in acquired TLE, neuroprotection provided immediately after epileptogenic insults were proposed to be the most effective strategy against epileptogenesis (Sloviter et al., 2012). Recently we demonstrated

pathological overexpression of GlyT1 in the epileptogenic DG of kindled rats. Thus, inhibition of GlyT1, by its inhibitor sarcosine was used as a rationale to both block GlyT1 directly and also act as a source of glycine, thereby increasing the availability of an inhibitory neuromodulator during epileptogenesis. Noteworthy, we observed that overexpressed GlyT1 in the epileptogenic DG was specifically located at the dentate inner molecular layer, which is innervated by *excitatory* hilar mossy cells, but not at the dentate outer molecular layer, which is innervated by *inhibitory* interneurons (**Figure 1D**). Overexpression of GlyT1 at the dentate inner molecular layer could lead to reduced availability of extracellular glycine and weakened activation of glycine receptor-mediated inhibition, which in turn, may exacerbate excitation of mossy cells, which may contribute to epileptogenesis. Indeed, sarcosine treatment during kindling reduced the expression of GlyT1 in the DG. However, full validation of the underlying mechanisms requires future work including electrophysiological studies for granule cell excitability in a subset of cell populations, and also hippocampal pyramidal cells.

## Sarcosine Affects DNA Methylation During Kindling

Recent studies have indicated that DNA methylation is tightly linked to seizure development and epileptogenesis (Kobow et al., 2013; Wang et al., 2017). Overall, a general hippocampal DNA hypermethylation status appears to be associated with chronic epilepsy (Wang et al., 2016; Boison and Rho, 2019). At the same time, hypomethylation in specific genes was observed in (myoclonic) epilepsy, such as in genes encoding the Na-K-2Cl cotransporter isoform 1 (*NKCC1*) and the K-Cl cotransporter isoform 2 (*KCC2*), which affect accumulating and extruding chloride ion (Cl-) flows (Genc et al., 2019). The purpose of this study was not to perform a gene ontology analysis of those genes displaying differential methylation in the TLE model; rather, our study assessed global DNA methylation changes as possible epigenetic mechanisms linked to sarcosine, which might be mobilized for the suppression of epileptogenesis. First, we demonstrated an increase of 5mC in the epileptogenic dentate gyrus of kindled rats, whereas we failed to observe correlate changes in the hippocampal expression of the DNA methylases DNMT1 or DNMT3a. Importantly, a significant decrease in 5hmC was identified in the epileptic DG indicating a dysregulation in the demethylation process. Conversely, treatment with sarcosine during kindling increased the level of 5hmC in the DG and this effect was associated with a delay in the progression of epileptogenesis. Namely, sarcosine treatment resulted in a reduced global DNA methylation status likely linked to enhanced demethylation. The increase of TET1 expression in the DG of kindled rats treated with sarcosine may contribute to facilitated demethylation of DNA via the formation of increased 5hmC (**Figure 6**). It is worth noting that the lack of changes in hippocampal DNMT1 and/or DNMT3a levels could be due to Western blot evaluation, which lacks spatial resolution to reflect local changes in the DG. Taken together, our findings support our hypothesis that manipulation of the glycine pathway via sarcosine can modify epileptogenesis and epigenetic processes in the hippocampus. However, sarcosine-mediated DNA methylation changes seem to be unique, because our study showed that the conventional demethylating agent, 5-AZA, neither delayed epileptogenesis in kindled rats nor suppressed seizures during kindling. Differences between the effects of sarcosine and 5-AZA can best be explained by our findings suggesting an involvement of sarcosine in active DNA demethylation, whereas 5-AZA interferes with DNA methylation: e.g., the different targets between sarcosine (enhanced TET1) and 5-AZA (suppressed global methylation). It is therefore likely that any anti-epileptogenic effects of sarcosine which might be mediated via methylation status are likely nuanced and site-specific. In addition, in contrast to 5-AZA, sarcosine exerts multiple activities, such as GlyT1 inhibition and action on the glutamatergic signaling pathway as a co-agonist of NMDARs, which may synergistically or independently contribute to the antiepileptogenesis (**Figure 6**). Additional GlyT1 inhibitors, and/or epileptogenesis models are warranted to further the unique features of sarcosine. Indeed, in a pilot study, lower doses of sarcosine (1 and 2 g/kg) were unable to delay kindling epileptogenesis or suppress seizures during kindling (data not shown).

# CHALLENGES AND REMARKS

As prevention of epileptogenesis is an unmet medical challenge, there have been many studies attempting to repurpose current AEDs to explore their antiepileptogenic potential (Pitkanen, 2010; Pitkanen et al., 2013; Loscher and Friedman, 2020). However, most attempts have had less than satisfactory outcomes to delay or slow down the progression of epilepsy (Lukawski et al., 2018). As shown in this study, a conventional AED, valproic acid, only acutely suppressed the kindling ictogenic seizures, but did not affect epileptogenesis. In contrast, sarcosine effectively suppressed ictogenic seizures and suppressed kindling epileptogenesis, indicating a unique feature of GlyT1 inhibition in the treatment of epilepsy. However, several limitations can be addressed in future studies: for instance, the behavioral aspects of spontaneous status epilepticus were not monitored in the present study; rather, the response seizure score to kindling was used as the major index to study epileptogenesis. Also, the electrophysiological evaluation of spontaneous activity within the granule cell layer should be included in future studies, which will extend our understanding of sarcosine and other GlyT1 inhibitors on epileptogenesis. Finally, the epigenetic studies need to be expanded to assess specific DNA methylation changes at individual target genes. In conclusion, our findings suggest that manipulation of the glycine system represents a novel and promising approach to preventing or minimizing epileptogenesis.

# DATA AVAILABILITY STATEMENT

The datasets generated for this study are available on request to the corresponding author.

## ETHICS STATEMENT

The animal study was reviewed and approved by Legacy Research Institute.

## AUTHOR CONTRIBUTIONS

H-YS and DB: conception and experimental design. LW, JC, RG, WO, SB, and HY-S: acquisition of data or material support. JC, RG, H-YS, JR, and RR: analysis and interpretation of data. H-YS: manuscript writing.

## FUNDING

This work was supported by grants from the Good Samaritan Research Foundation (H-YS) and the NIH (R01 NS084920, H-YS and DB).

## ACKNOWLEDGMENTS

The authors wish to thank Drs. Danielle Osborne and Joseph Frascella for their discussion and intellectual contribution.

## REFERENCES

Barker-Haliski, M., and White, H. S. (2015). Glutamatergic mechanisms associated with seizures and epilepsy. *Cold Spring Harb. Perspect. Med.* 5:a022863. doi: 10.1101/cshperspect.a022863

Boison, D., and Rho, J. M. (2019). Epigenetics and epilepsy prevention: the therapeutic potential of adenosine and metabolic therapies. *Neuropharmacology* 167:107741. doi: 10.1016/j.neuropharm.2019.107741

Castro, D., Upadhya, M., Kodali, R., and Shetty, A. K. (2017). Resveratrol for easing status epilepticus induced brain injury, inflammation, epileptogenesis, and cognitive and memory dysfunction-are we there yet? *Front. Neurol.* 8:603. doi: 10.3389/fneur.2017.00603

Chattipakorn, S. C., and McMahon, L. L. (2003). Strychnine-sensitive glycine receptors depress hyperexcitability in rat dentate gyrus. *J. Neurophysiol.* 89, 1339–1342. doi: 10.1152/jn.00908.2002

Chouliaras, D., Mastroeni, E., Delvaux, A., Grover, G., Kenis, P. R., Hof, H. W., et al. (2013). Consistent decrease in global DNA methylation and hydroxymethylation in the hippocampus of Alzheimer's disease patients. *Neurobiol. Aging* 34, 2091–2099. doi: 10.1016/j.neurobiolaging.2013.02.021

De Smedt, S., De Rouck, R., Raedt, T., Wyckhuys, L., Waterschoot, V., De Herdt, A., et al. (2007). Serial day rapid kindling is an effective tool in screening the anti-epileptic properties of topiramate. *Seizure* 16, 620–626. doi: 10.1016/j.seizure.2007.04.013

Di Maio, R. (2014). Neuronal mechanisms of epileptogenesis. *Front. Cell Neurosci.* 8:29.

Dudek, F. E., and Sutula, T. P. (2007). Epileptogenesis in the dentate gyrus: a critical perspective. *Prog. Brain Res.* 163, 755–773. doi: 10.1016/S0079-6123(07)63041-6

Engel, J., and Pitkanen, A. (2019). Biomarkers for epileptogenesis and its treatment. *Neuropharmacology* 167:107735.

Genc, M., Kara, Y., Unal, E., Uygur Kucukseymen, Y., Bicer Gomceli, T., Kaynar, K., et al. (2019). Methylation of cation-chloride cotransporters NKCC1 and KCC2 in patients with juvenile myoclonic epilepsy. *Neurol Sci.* 40, 1007–1013. doi: 10.1007/s10072-019-03743-4

Goldberg, E. M., and Coulter, D. A. (2013). Mechanisms of epileptogenesis: a convergence on neural circuit dysfunction. *Nat. Rev. Neurosci.* 14, 337–349. doi: 10.1038/nrn3482

Guo, J., Guo, J., Li, M., Zhou, F., Qin, S., Zhang, B., et al. (2015). Statin treatment reduces the risk of poststroke seizures. *Neurology* 85, 701–707. doi: 10.1212/WNL.0000000000001814

Herdon, F. M., Godfrey, A. M., Brown, S., Coulton, J. R., Evans, P., and Cairns, W. J. (2001). Pharmacological assessment of the role of the glycine transporter GlyT-1 in mediating high-affinity glycine uptake by rat cerebral cortex and cerebellum synaptosomes. *Neuropharmacology* 41, 88–96. doi: 10.1016/s0028-3908(01)00043-0

Hsieh, J., and Gage, F. H. (2005). Chromatin remodeling in neural development and plasticity. *Curr. Opin. Cell Biol.* 17, 664–671. doi: 10.1016/j.ceb.2005.09.002

Kaminski, M. A., Rogawski, M., and Klitgaard, H. (2014). The potential of antiseizure drugs and agents that act on novel molecular targets as antiepileptogenic treatments. *Neurotherapeutics* 11, 385–400. doi: 10.1007/s13311-014-0266-1

Kobow, K., and Blumcke, I. (2012). The emerging role of DNA methylation in epileptogenesis. *Epilepsia* 53(Suppl. 9), 11–20. doi: 10.1111/epi.12031

Kobow, K., El-Osta, A., and Blumcke, I. (2013). The methylation hypothesis of pharmacoresistance in epilepsy. *Epilepsia* 54(Suppl. 2), 41–47. doi: 10.1111/epi.12183

Long, D., Upadhya, B., Hattiangady, D. K., Kim, S. Y., An, B., Shuai, D. J., et al. (2017). Intranasal MSC-derived A1-exosomes ease inflammation, and prevent abnormal neurogenesis and memory dysfunction after status epilepticus. *Proc. Natl. Acad. Sci. U.S.A.* 114, E3536–E3545. doi: 10.1073/pnas.1703920114

Lopez-Corcuera, R., Martinez-Maza, E., Nunez, M., Roux, S., Supplisson, S., and Aragon, C. (1998). Differential properties of two stably expressed brain-specific glycine transporters. *J. Neurochem.* 71, 2211–2219. doi: 10.1046/j.1471-4159.1998.71052211.x

Loscher, W., and Friedman, A. (2020). Structural, molecular, and functional alterations of the blood-brain barrier during epileptogenesis and epilepsy: a cause, consequence, or both? *Int. J. Mol. Sci.* 21:591. doi: 10.3390/ijms21020591

Lukawski, M., Andres-Mach, M., Czuczwar, J. J., Luszczki, K., Kruszynski, K., and Czuczwar, J. (2018). Mechanisms of epileptogenesis and preclinical approach to antiepileptogenic therapies. *Pharmacol. Rep.* 70, 284–293. doi: 10.1016/j.pharep.2017.07.012

McNamara, J. O. (1986). Kindling model of epilepsy. *Adv. Neurol.* 44, 303–318.

Miller-Delaney, K., Bryan, S., Das, R. C., McKiernan, I. M., Bray, J. P., Reynolds, R., et al. (2015). Differential DNA methylation profiles of coding and non-coding genes define hippocampal sclerosis in human temporal lobe epilepsy. *Brain* 138, 616–631. doi: 10.1093/brain/awu373

Miller-Delaney, S. F., Das, S., Stallings, R. L., and Henshall, D. C. (2013). Investigating gene promoter methylation in a mouse model of status epilepticus. *Methods Mol. Biol.* 1067, 87–101. doi: 10.1007/978-1-62703-607-8_7

Moore, L. D., Le, T., and Fan, G. (2013). DNA methylation and its basic function. *Neuropsychopharmacology* 38, 23–38.

Morales, C., Alvarez-Ferradas, M., Roncagliolo, M., Fuenzalida, M., Wellmann, F. J., and Nualart, R. (2014). A new rapid kindling variant for induction of cortical epileptogenesis in freely moving rats. *Front. Cell Neurosci.* 8:200. doi: 10.3389/fncel.2014.00200

Morimoto, M., Fahnestock, K., and Racine, R. J. (2004). Kindling and status epilepticus models of epilepsy: rewiring the brain. *Prog. Neurobiol.* 73, 1–60. doi: 10.1016/j.pneurobio.2004.03.009

Mudd, J. T., Brosnan, M. E., Brosnan, R. L., Jacobs, S. P., Stabler, R. H., Allen, D. E., et al. (2007). Methyl balance and transmethylation fluxes in humans. *Am. J. Clin. Nutr.* 85, 19–25. doi: 10.1093/ajcn/85.1.19

Namvar, Y., Fathollahi, M., Javan, M., Zeraati, M., Mohammad-Zadeh, A., and Shojaei, R. (2017). The antiepileptogenic effect of low-frequency stimulation on perforant path kindling involves changes in regulators of G-protein signaling in rat. *J. Neurol. Sci.* 375, 450–459. doi: 10.1016/j.jns.2017.02.047

Parrish, N. K., Codadu, C., Racca, C., and Trevelyan, A. J. (2018). Pyramidal cell activity levels affect the polarity of activity-induced gene transcription changes in interneurons. *J. Neurophysiol.* 120, 2358–2367. doi: 10.1152/jn.00287.2018

Pitkanen, A. (2010). Therapeutic approaches to epileptogenesis–hope on the horizon. *Epilepsia* 51(Suppl. 3), 2–17. doi: 10.1111/j.1528-1167.2010.02602.x

Pitkanen, A., and Lukasiuk, K. (2011). Mechanisms of epileptogenesis and potential treatment targets. *Lancet Neurol.* 10, 173–186. doi: 10.1016/S1474-4422(10)70310-0

Pitkanen, A., Nehlig, A. R., Brooks-Kayal, F. E., Dudek, D., Friedman, A. S., Galanopoulou, F. E., et al. (2013). Issues related to development of antiepileptogenic therapies. *Epilepsia* 54(Suppl. 4), 35–43. doi: 10.1111/epi.12297

Racine, R. (1978). Kindling: the first decade. *Neurosurgery* 3, 234–252.

Rakhade, S. N., and Jensen, F. E. (2009). Epileptogenesis in the immature brain: emerging mechanisms. *Nat. Rev. Neurol.* 5, 380–391. doi: 10.1038/nrneurol.2009.80

Rensing, L., Han, N., and Wong, M. (2015). Intermittent dosing of rapamycin maintains antiepileptogenic effects in a mouse model of tuberous sclerosis complex. *Epilepsia* 56, 1088–1097. doi: 10.1111/epi.13031

Rowles, J., and Olsen, M. (2012). Perspectives on the development of antioxidant antiepileptogenic agents. *Mini. Rev. Med. Chem.* 12, 1015–1027. doi: 10.2174/138955712802762266

Ryley Parrish, A. J., Albertson, S. C., Buckingham, J. J., Hablitz, K. L., Mascia, W., and Davis, W. (2013). Status epilepticus triggers early and late alterations in brain-derived neurotrophic factor and NMDA glutamate receptor Grin2b DNA methylation levels in the hippocampus. *Neuroscience* 248C, 602–619. doi: 10.1016/j.neuroscience.2013.06.029

Salceda, R., and Aguirre-Ramirez, M. (2005). Characterization of strychnine-sensitive glycine receptor in the intact frog retina: modulation by protein kinases. *Neurochem. Res.* 30, 411–416. doi: 10.1007/s11064-005-2616-1

Shen, E. A., van Vliet, K. A., Bright, M., Hanthorn, N. K., Lytle, J., Gorter, E., et al. (2015). Glycine transporter 1 is a target for the treatment of epilepsy. *Neuropharmacology* 99, 554–565. doi: 10.1016/j.neuropharm.2015.08.031

Siniscalchi, A., and Mintzer, S. (2015). Statins for poststroke seizures: the first antiepileptogenic agent? *Neurology* 85, 661–662. doi: 10.1212/WNL.0000000000001878

Sloviter, A. V., Bumanglag, R., Schwarcz, R., and Frotscher, M. (2012). "Abnormal dentate gyrus network circuitry in temporal lobe epilepsy," in *Jasper's Basic Mechanisms of the Epilepsies*, eds J. L. Noebels, M. Avoli, M. A. Rogawski, R. W. Olsen, and A. V. Delgado-Escueta (Bethesda, MD: National Center for Biotechnology Information).

Song, S. C., Chattipakorn, W., and McMahon, L. L. (2006). Glycine-gated chloride channels depress synaptic transmission in rat hippocampus. *J. Neurophysiol.* 95, 2366–2379. doi: 10.1152/jn.00386.2005

Talos, L. M., Jacobs, S., Gourmaud, C. A., Coto, H., Sun, K. C., Lim, T. H., et al. (2018). Mechanistic target of rapamycin complex 1 and 2 in human temporal lobe epilepsy. *Ann. Neurol.* 83, 311–327. doi: 10.1002/ana.25149

Tchekalarova, N. M., Ivanova, D. M., Pechlivanova, D., Atanasova, N., Lazarov, L., Kortenska, R., et al. (2014). Antiepileptogenic and neuroprotective effects of losartan in kainate model of temporal lobe epilepsy. *Pharmacol. Biochem. Behav.* 127, 27–36. doi: 10.1016/j.pbb.2014.10.005

Terrone, R., Pauletti, R., Pascente, A., and Vezzani, A. (2016). Preventing epileptogenesis: A realistic goal? *Pharmacol. Res.* 110, 96–100. doi: 10.1016/j.phrs.2016.05.009

Toader, N., Forte, M., Orlando, E., Ferrea, A., Raimondi, P., Baldelli, F., et al. (2013). Dentate gyrus network dysfunctions precede the symptomatic phase in a genetic mouse model of seizures. *Front. Cell Neurosci.* 7:138. doi: 10.3389/fncel.2014.00138

Ueland, O., Midttun, A., Windelberg, A., Svardal, R., Skalevik, R., and Hustad, S. (2007). Quantitative profiling of folate and one-carbon metabolism in large-scale epidemiological studies by mass spectrometry. *Clin. Chem. Lab. Med.* 45, 1737–1745. doi: 10.1515/CCLM.2007.339

Upadhya, B., Hattiangady, O. W., Castro, B., Shuai, M., Kodali, S., Attaluri, A., et al. (2019). Human induced pluripotent stem cell-derived MGE cell grafting after status epilepticus attenuates chronic epilepsy and comorbidities via synaptic integration. *Proc. Natl. Acad. Sci. U.S.A.* 116, 287–296. doi: 10.1073/pnas.1814185115

Upadhya, O. W., Castro, R., Upadhya, R., and Shetty, A. K. (2018). Prospects of cannabidiol for easing status epilepticus-induced epileptogenesis and related comorbidities. *Mol. Neurobiol.* 55, 6956–6964. doi: 10.1007/s12035-018-0898-y

Wang, X., Fu, X., Peng, Z., Xiao, Z., Li, G., and Chen, G. (2016). DNA methylation profiling reveals correlation of differential methylation patterns with gene expression in human epilepsy. *J. Mol. Neurosci.* 59, 68–77. doi: 10.1007/s12031-016-0735-6

Wang, Y., Zhang, J., Fang, F., Yu, D., Heng, Y., Fan, J., et al. (2017). Decreased methylation level of H3K27me3 increases seizure susceptibility. *Mol. Neurobiol.* 54, 7343–7352. doi: 10.1007/s12035-016-0197-4

Wei, F., Yang, Y., Wang, F., Yang, C., Wu, S. X., and Wu, D. (2015). Degeneration and regeneration of GABAergic interneurons in the dentate gyrus of adult mice in experimental models of epilepsy. *CNS Neurosci. Ther.* 21, 52–60. doi: 10.1111/cns.12330

Younus, I., and Reddy, D. S. (2017). Epigenetic interventions for epileptogenesis: a new frontier for curing epilepsy. *Pharmacol. Ther.* 177, 108–122. doi: 10.1016/j.pharmthera.2017.03.002

Zhang, A., Lyons-Warren, A., and Thio, L. L. (2009). The glycine transport inhibitor sarcosine is an inhibitory glycine receptor agonist. *Neuropharmacology* 57, 551–555. doi: 10.1016/j.neuropharm.2009.07.019

Zhu, L., Wang, Y., Zhang, F. H., Zhao, J., Luo, Z., Xiao, G. J., et al. (2012). Increased expression of DNA methyltransferase 1 and 3a in human temporal lobe epilepsy. *J. Mol. Neurosci.* 46, 420–426. doi: 10.1007/s12031-011-9602-7

**Conflict of Interest:** The authors declare that the research was conducted in the absence of any commercial or financial relationships that could be construed as a potential conflict of interest.

*Copyright © 2020 Shen, Weltha, Cook, Gesese, Omi, Baer, Rose, Reemmer and Boison. This is an open-access article distributed under the terms of the Creative Commons Attribution License (CC BY). The use, distribution or reproduction in other forums is permitted, provided the original author(s) and the copyright owner(s) are credited and that the original publication in this journal is cited, in accordance with accepted academic practice. No use, distribution or reproduction is permitted which does not comply with these terms.*

frontiers in Synaptic Neuroscience

ORIGINAL RESEARCH
published: 18 June 2020
doi: 10.3389/fnsyn.2020.00024

# Dorsal-Ventral Differences in Modulation of Synaptic Transmission in the Hippocampus

*George Trompoukis and Costas Papatheodoropoulos**

*Laboratory of Physiology, Department of Medicine, University of Patras, Patras, Greece*

Functional diversification along the longitudinal axis of the hippocampus is a rapidly growing concept. Modulation of synaptic transmission by neurotransmitter receptors may importantly contribute to specialization of local intrinsic network function along the hippocampus. In the present study, using transverse slices from the dorsal and the ventral hippocampus of adult rats and recordings of evoked field postsynaptic excitatory potentials (fEPSPs) from the CA1 stratum radiatum, we aimed to compare modulation of synaptic transmission between the dorsal and the ventral hippocampus. We found that transient heterosynaptic depression (tHSD, <2 s), a physiologically relevant phenomenon of regulation of excitatory synaptic transmission induced by paired stimulation of two independent inputs to stratum radiatum of CA1 field, has an increased magnitude and duration in the ventral hippocampus, presumably contributing to increased input segregation in this segment of the hippocampus. $GABA_B$ receptors, $GABA_A$ receptors, adenosine A1 receptors and L-type voltage-gated calcium channels appear to contribute differently to tHSD in the two hippocampal segments; $GABA_B$Rs play a predominant role in the ventral hippocampus while both $GABA_B$Rs and A1Rs play important roles in the dorsal hippocampus. Activation of $GABA_B$ receptors by an exogenous agonist, baclofen, robustly and reversibly modulated both the initial fast and the late slow components of excitatory synaptic transmission, expressed by the fEPSPslope and fEPSP decay time constant ($fEPSP_\tau$), respectively. Specifically, baclofen suppressed fEPSP slope more in the ventral than in the dorsal hippocampus and enhanced $fEPSP_\tau$ more in the dorsal than in the ventral hippocampus. Also, baclofen enhanced paired-pulse facilitation in the two hippocampal segments similarly. Blockade of $GABA_B$ receptors did not affect basal paired-pulse facilitation in either hippocampal segment. We propose that the revealed dorsal-ventral differences in modulation of synaptic transmission may provide a means for specialization of information processing in the local neuronal circuits, thereby significantly contributing to diversifying neuronal network functioning along the dorsal-ventral axis of hippocampus.

**Keywords: hippocampus, dorsal-ventral, synaptic transmission, heterosynaptic modulation, $GABA_B$ receptor, A1 adenosine receptor, $GABA_A$ receptor, ion channel**

OPEN ACCESS

***Edited by:***
*Lisa Topolnik,*
*Laval University, Canada*

***Reviewed by:***
*Imre Vida,*
*Charité – Universitätsmedizin Berlin, Germany*
*Rostislav Turecek,*
*Academy of Sciences of the Czech Republic (ASCR), Czechia*

***Correspondence:**
*Costas Papatheodoropoulos*
*cepapath@upatras.gr*

***Received:*** *17 January 2020*
***Accepted:*** *14 May 2020*
***Published:*** *18 June 2020*

***Citation:***
*Trompoukis G and Papatheodoropoulos C (2020) Dorsal-Ventral Differences in Modulation of Synaptic Transmission in the Hippocampus. Front. Synaptic Neurosci. 12:24. doi: 10.3389/fnsyn.2020.00024*

## INTRODUCTION

Hippocampus is an elongated prototypical brain structure thought to be composed of the repetition of a basic neural circuit of excitatory synaptic connections transversely positioned to the longitudinal axis of the structure, which in rodents is extended from a septal location, dorsally, to the temporal lobe, ventrally. Hippocampus has been found to be implicated in several

brain functions which, however, are heterogeneously distributed along the longitudinal axis of the structure (Small et al., 2011; Strange et al., 2014). According to a current consensus, the role played by the most dorsally located hippocampal segment is on cognitive operations like spatial navigation, while internally monitoring functions related to emotionality are taken on by the ventral segment of the hippocampus (Bannerman et al., 2014; Strange et al., 2014). Though this functional segregation along the dorsal-ventral hippocampal axis might be considerably supported by a differentiated pattern of extrahippocampal connections of consecutive hippocampal segments, it nevertheless poses an important issue about the role that the endogenous neuronal circuitry may play in this uneven distribution of functions. Indeed, a growing body of recently acquired experimental evidence indicates that the endogenous network of the hippocampus is diversified along the long axis of the structure according to several aspects of organization, including gene expression patterns, intrinsic properties of principal cells and properties of synaptic plasticity (Papatheodoropoulos and Kostopoulos, 2000a; Maruki et al., 2001; Dong et al., 2009; Dougherty et al., 2012; Honigsperger et al., 2015; Cembrowski et al., 2016; Kouvaros and Papatheodoropoulos, 2016b; Malik et al., 2016; Milior et al., 2016; Schreurs et al., 2017; Floriou-Servou et al., 2018; Manahan-Vaughan, 2019); recently reviewed (Papatheodoropoulos, 2018). These data suggest that specializations in the endogenous hippocampal circuitry may fundamentally support functional segregation which is observed at a higher level of organization. Accordingly, the revealing of mechanisms of intrinsic network diversification along the dorsal-ventral hippocampal axis is a major challenge in the field of hippocampus research.

Among the most fundamental mechanisms that can functionally diversify local neuronal networks is the modulation of synaptic transmission (Giocomo and Hasselmo, 2007; Dayan, 2012; Marder, 2012; McCormick and Nusbaum, 2014). In the hippocampus, particularly interesting forms of regulation of excitatory synaptic transmission with important physiological implication are those phenomena of short-lasting heterosynaptic plasticity, lasting from seconds to minutes, collectively called heterosynaptic depression (Isaacson et al., 1993; Vogt and Nicoll, 1999; Molyneaux and Hasselmo, 2002; Serrano et al., 2006; Andersson et al., 2007; Covelo and Araque, 2016). Experimentally, heterosynaptic depression is manifested as a suppression of glutamatergic excitatory synaptic transmission in inactive synapses induced by strong stimulation of a different synaptic input into the same neuronal population (Covelo and Araque, 2016). Heterosynaptic depression is a complex phenomenon encompassing different forms of suppression of excitatory transmission, distinguished between each other based on time-course and underlying mechanisms. Short-lasting heterosynaptic depression lasting from milliseconds to a few seconds can be induced by short bursts of high-frequency stimulation (Isaacson et al., 1993; Zhang et al., 2003; Andersson et al., 2007), while induction of heterosynaptic depression that lasts up to several minutes requires long trains of high-frequency stimulation (Grover and Teyler, 1993a; Manzoni et al., 1994; Serrano et al., 2006). Given the physiologically important role that heterosynaptic depression can play (Dunwiddie and Lynch, 1978; Frerking and Ohliger-Frerking, 2006) it is especially interesting to examine this phenomenon comparatively between the dorsal and the ventral hippocampus.

In principle, the mechanisms that control the release of transmitter via activation of receptors sited at presynaptic terminals (Wu and Saggau, 1997; Miller, 1998; Frerking and Wondolowski, 2008) play pivotal roles in regulating synaptic transmission and the balance between excitation and inhibition, thereby crucially modulating local neuronal circuit function (Giocomo and Hasselmo, 2007; Dayan, 2012). In the hippocampus several neurotransmitter receptors regulate the synaptic release of transmitters (Thompson et al., 1993; Wu and Saggau, 1997; Miller, 1998). Among these receptors $GABA_B$ receptor ($GABA_BR$) is a key regulator of excitatory and inhibitory transmitter release in the hippocampus (Vizi and Kiss, 1998; Ulrich and Bettler, 2007). $GABA_BRs$ have a broad distribution in the hippocampus (Bowery et al., 1987) and recent immunohistochemical data show that $GABA_BRs$ in the apical dendrites of CA1 pyramidal cells are more abundant in the ventral than in the dorsal hippocampus (Dubovyk and Manahan-Vaughan, 2018). However, the role of $GABA_BRs$ in controlling excitatory synaptic transmission in the dorsal and the ventral hippocampus has never examined before.

In the present study, we aimed to compare forms of regulation of synaptic transmission between the dorsal and the ventral CA1 hippocampal field, using two experimental approaches. We studied transient heterosynaptic depression (tHSD) comparatively in the two hippocampal segments and we found a stronger heterosynaptic effect in the ventral compared with the dorsal hippocampus. Several mechanisms appeared to contribute to tHSD, including $GABA_BRs$, $GABA_A$ receptors, adenosine A1 receptors, and L-type voltage-gated calcium channels (L-VGCCs). Furthermore, these mechanisms contribute differently to t-HSD in the dorsal and the ventral hippocampus. We also examined the effects of $GABA_BR$ activation by an exogenous agonist, baclofen, and we found that baclofen suppressed the initial fast component of excitatory synaptic transmission more in the ventral than in the dorsal hippocampus and enhanced the late slow component of excitatory transmission more in the dorsal than in the ventral hippocampus. Finally, exogenous activation of $GABA_BRs$ produced a similar enhancement of paired-pulse facilitation in the two segments of the hippocampus. Possible implications of these dorsal-ventral differences are discussed.

# MATERIALS AND METHODS

## Animals and Slice Preparation

One hundred and eighteen adult male Wistar rats (RRID: RGD_10028) were used in this study. Animals were maintained at the Laboratory of Experimental Animals of the Department of Medicine, University of Patras (license No: EL-13-BIOexp-04), under controlled conditions of light-dark cycle (12/12 h) and temperature (20−22°C), and they had free access to food and water. All animal treatment and experimental procedures

were conducted in accordance with the European Communities Council Directive Guidelines for the care and use of Laboratory animals (2010/63/EU − European Commission) and they have been approved by the "Protocol Evaluation Committee" of the Department of Medicine of the University of Patras and the Directorate of Veterinary Services of the Achaia Prefecture of Western Greece Region (reg. number: 187531/626, 26/06/2018). Thin slices from the dorsal and the ventral hippocampus were prepared as previously described (Papatheodoropoulos and Kostopoulos, 2000a; Kouvaros and Papatheodoropoulos, 2016b). Specifically, rats were sacrificed by decapitation under deep anaesthesia with diethyl-ether, then the brain was removed from the cranium and placed in ice-cold (2−4°C) standard artificial cerebrospinal fluid (ACSF) containing, in mM: 124 NaCl, 4 KCl, 2 $CaCl_2$, 2 $MgSO_4$, 26 $NaHCO_3$, 1.25 $NaH_2PO_4$ and 10 glucose. ACSF was equilibrated with 95% $O_2$ and 5% $CO_2$ gas mixture at a pH = 7.4. The hippocampus was excised free from the brain and transverse 500 μm-thick slices were prepared from the dorsal and ventral hippocampus extending between 0.5 and 4.0 mm from each end of the longitudinal structure of hippocampus using a McIlwain tissue chopper. Immediately after their preparation slices were transferred to an interface type recording chamber where they were continuously perfused with fresh ACSF of the same composition as above described at a rate of ∼1.5 ml/min. Slices were humidified with a mixed gas consisting of 95% $O_2$ and 5% $CO_2$ at a constant temperature of $30.0 \pm 0.5^{o}$C.

## Stimulation and Recordings

Electrophysiological recordings started at 1.5−2.0 h after the placement of slices in the recording chamber. Recordings of evoked field potentials consisting of fiber volley (Fv) and field excitatory postsynaptic potentials (fEPSP) in CA1 region were made from the middle of stratum radiatum following electrical stimulation of Schaffer collaterals. We positioned stimulation and recording electrodes in the middle of the stratum radiatum both in the transverse and the radial axis, and, more particularly, 250 and 300−350 μm from the pyramidal cell layer in dorsal and ventral slices, respectively. Considering that the length of stratum radiatum in the middle hippocampus, which is assumed to have similar histological characteristics with the dorsal hippocampus is about 500 μm (Ishizuka et al., 1995), and the length of a CA1 pyramidal cell is about 25−30% higher in the ventral than in the dorsal hippocampus (Dougherty et al., 2012), we assumed that the length of stratum radiatum in dorsal and ventral hippocampal slices is roughly 500 and 600−650 μm, respectively. For recordings we used carbon fiber electrodes (diameter 7 μm, Kation Scientific, Minneapolis, MN, United States), and for stimulation we used a bipolar platinum/iridium electrode (25 μm diameter, at an inter-wire distance of 100 μm, World Precision Instruments, United States). The distance between stimulating and recording electrodes was about 350 μm. Stimulation consisted of electrical current pulses with amplitude of 10−300 μA and a fixed duration of 100 μs. We delivered baseline stimulation every 30 s. Input-output curves between intensity of stimulation current and synaptic response were systematically made in every slice (**Figure 1A**). Only slices which displayed stable Fv and fEPSP for at least 10 min under fixed stimulation intensity were selected for further experimentation.

We studied transient heterosynaptic depression (tHSD) by applying a brief high-frequency burst (the conditioning stimulation, CS) to a set of afferent hippocampal fibers and observed the depression which is produced in a test (conditioned) response evoked by a single-pulse stimulation of a naive set of adjacent excitatory afferent inputs (Isaacson et al., 1993; Molyneaux and Hasselmo, 2002; Chandler et al., 2003; Zhang et al., 2003; Serrano et al., 2006; Andersson et al., 2007). This pattern of CS resembles physiological neuronal activity in the hippocampus (Lisman, 1997; Buhl and Buzsaki, 2005). More specifically, we placed stimulating electrodes in stratum radiatum of CA1 field, on opposite site of a recording electrode to stimulate two overlapping but independent sets of fibers. We randomly alternated the sides of conditioning and test stimulations between slices, so in some experiments the conditioning stimulus was given at the side of subiculum and in other experiments was applied to the site toward CA3 field. In order to avoid contamination of heterosynaptic depression with homosynaptic effects, we examined the effect of paired-pulse stimulation (PPS). Specifically, we paired single shock stimulation of one pathway with single shock stimulation of the other pathway, using an inter-pulse interval (IPI) of 50 ms. We studied tHSD by applying a burst of five pulses at 50 Hz on one pathway and a single pulse of electrical current to the other pathway (**Figure 1B**). We adjusted the current intensity of the conditioned stimulus to evoke a subthreshold fEPSP (see Results). We examined the duration of tHSD by varying the interval between the conditioning and test stimulus between 50 and 1700 ms. We repeated the heterosynaptic stimulation protocol three times using three different current intensities of the conditioning stimulus producing an fEPSP with an amplitude of 1 mV (weak conditioning stimulus), 2 mV (moderate conditioning stimulus) and maximum amplitude (strong CS), respectively. Also, we constructed input-output curves between conditioning and test responses by using a moderate CS intensity and a varying amplitude of test stimulation. We also studied the time-course of paired-pulse facilitation (PPF) under control and pharmacological conditions, using a varying IPI (IPIs), from 20 to 1000 ms. We should note here that although fEPSPs that we used to study excitatory synaptic transmission represent mostly postsynaptic depolarizations, however, they are compound synaptic potentials involving monosynaptic excitation as well as monosynaptic and disynaptic (feed-forward) inhibition; furthermore, fEPSPs evoked by relatively high stimulus intensities may also contain polysynaptic components due to anterograde activation of CA1 pyramidal cells and consequent activation of feed-back inhibition, as well as reverberation of CA3 cell excitation, which could then result in CA1 synaptic activation.

## Data Processing and Analysis

Field potentials were amplified 500 times and band-pass filtered at 0.5 Hz − 2 kHz using a Neurolog amplifier

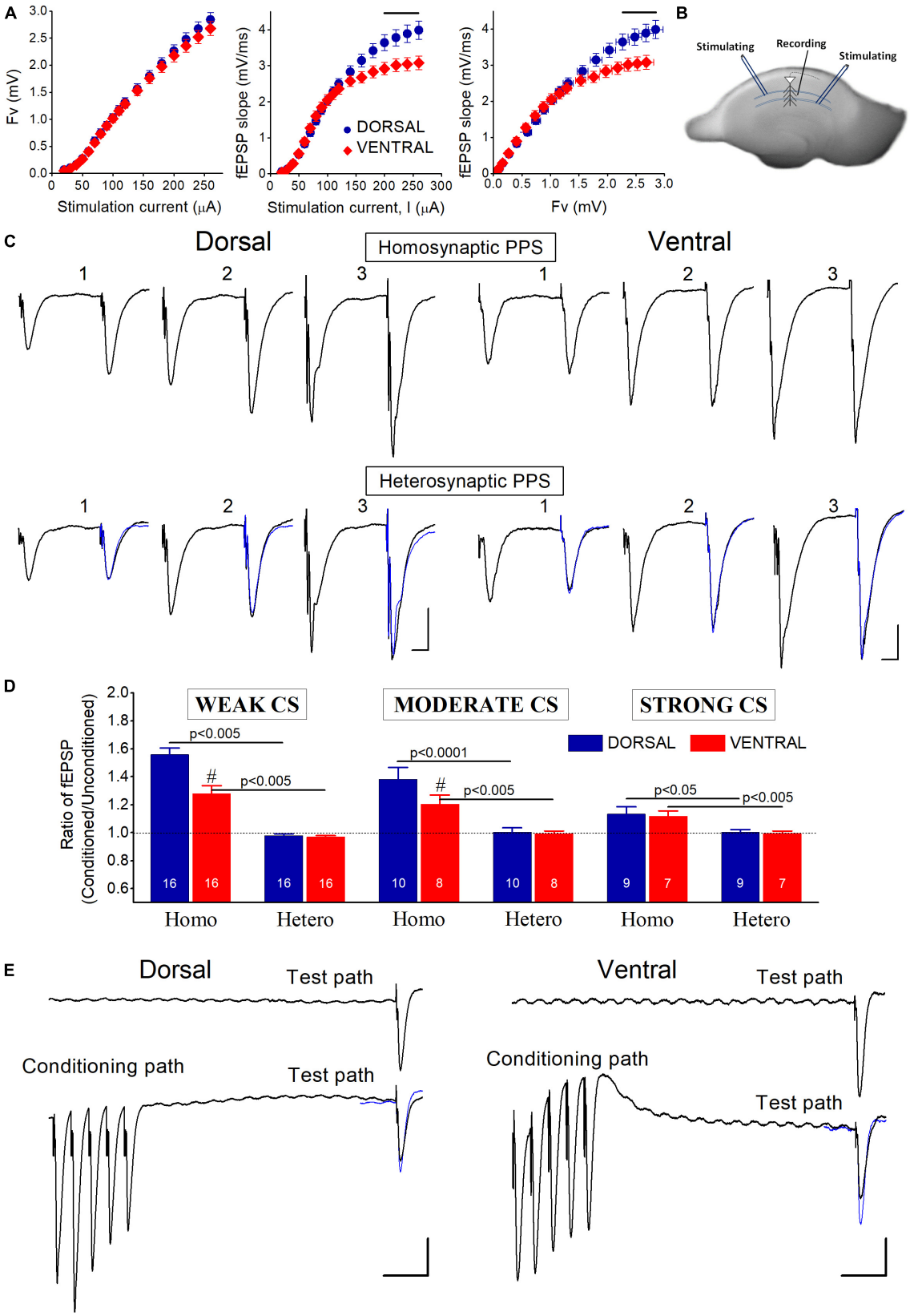


**FIGURE 1 |** Continued

**FIGURE 1 | (A)** Baseline input-output curves of evoked field potentials in the dorsal and the ventral hippocampus. fEPSPs evoked by relatively strong stimulation (≥200 μA), corresponding to large fiber volleys (>2 mV), were significantly larger in the dorsal than in the ventral hippocampus (horizontal lines above data, $p < 0.05$). Data were collected from 83 dorsal and 61 ventral slices obtained from 40 rats. **(B)** Photograph of a transverse hippocampal slice in which is depicted the method of electrical stimulation and recording used to study transient heterosynaptic depression (tHSD) in the CA1 hippocampal field. Two stimulation electrodes were positioned at stratum radiatum on either side of a recording electrode in a way to excite two different sets of presynaptic fibers converging to CA1 pyramidal neurons. One of the inputs was used to condition the response of a test input. The sites of conditioning and test pathways relative to recording electrode randomly alternated between slices. **(C)** Example traces of fEPSPs evoked by paired-pulse stimulation (PPS) of either the same pathway (upper panel, Homosynaptic PPS) or two different pathways (lower panel, Heterosynaptic PPS), in a dorsal and a ventral hippocampal slice. Responses of conditioning and conditioned (test) pathways were evoked by stimulation current of weak (1), moderate (2), and strong (3) intensity. In heterosynaptic PPS panel, superimposed to the conditioned responses are the (unconditioned) responses evoked by the first stimulus in homosynaptic PPS (traces in blue) for comparison sake. The interval between the two pulses in either stimulation configuration (i.e., homosynaptic or heterosynaptic) was 50 ms. Calibration bars: 0.5 mV and 10 ms. The independence of the two pathways was confirmed by the absence of interaction (i.e., facilitation or depression) between conditioning and conditioned responses in the heterosynaptic PPS configuration. On the contrary, homosynaptic PPS produced facilitation of conditioned responses. **(D)** Collective data of the ratio Conditioned fEPSP/Unconditioned fEPSP in homosynaptic (Homo) and heterosynaptic (Hetero) PPS, applied with weak, moderate, and strong conditioning stimulation (CS) current intensity. The number of slices used in each condition is indicated at the bottom of columns. Diesis (#) on top of columns indicate statistically significant difference between the dorsal and the ventral hippocampus (independent *t*-test, $p < 0.005$). Homosynaptic PPS produced synaptic facilitation. On the contrary, heterosynaptic PPS did not significantly affect test responses. **(E)** Examples of tHSD of a test input (Test path) produced by a high-frequency burst (50 Hz) delivered to a distinct set of adjacent fibers (Conditioning path). Upper traces represent responses of the test input before the application of the conditioning burst stimulation, while traces on the bottom represent responses to heterosynaptic stimulation at 300 ms. Calibration bars: 0.5 mV and 50 ms. In the heterosynaptic condition, unconditioned responses of the test pathway (traces in blue) are superimposed to the conditioned responses for comparison. Note that the conditioning burst stimulation produces suppression of fEPSP evoked by stimulation of the test pathway. All artifacts in trace recordings are truncated for clarity.

(Digitimer Limited, United Kingdom). Signal was digitized at 10 kHz and stored in a computer disk using the CED 1401-plus interface and the Signal6 software (Cambridge Electronic Design, Cambridge, United Kingdom) for off-line analysis. We quantified tHSD as the ratio or the percent change between the conditioned and unconditioned response, i.e., conditioned fEPSP/unconditioned fEPSP or ((conditioned fEPSP − unconditioned fEPSP)/ unconditioned fEPSP)*100. Similarly, we quantified PPF as the ratio between the second and the first response induced by PPS, i.e., fEPSP2/fEPSP1 or ((fEPSP2- fEPSP1)/fEPSP1)*100. Also, changes in tHSD or PPF between different experimental/pharmacological conditions may be expressed by the percent change in the ratio between conditioned (or fEPSP2) and unconditioned response (or fEPSP1) (it is specified in the corresponding text). The fast rising and the slower falling phase of fEPSP were distinctly quantified by the slope and the decay constant "τ," respectively. In particular, the slope of initial rising phase of fEPSP ($fEPSP_{slope}$) was measured at a time window about 1 ms-wide, after the occurrence of the presynaptic fiber volley; the time constant of fEPSP decay ($fEPSP_{\tau}$) was measured by the time required for fEPSP to decrease by 63% from its maximum amplitude. The size of $fEPSP_{slope}$ is an accurate indication of the strength of synaptic activation, while $fEPSP_{\tau}$ closely reflects changes in the slow decaying phase of fEPSP. Fv was quantified by its amplitude measured by the difference between the baseline and the peak negative voltage.

## Drugs

The following drugs were used: the selective antagonists of $GABA_BR$ 3-[[(3,4-Dichlorophenyl)methyl]amino]propyl] diethoxymethyl)phosphinic acid (CGP 52432, 10 μM) and 3-aminopropyl)(cyclohexylmethyl)phosphinic acid (CGP 46381, 50 μM); the selective agonist of $GABA_BRs$ baclofen; the competitive selective antagonist of NMDA receptor 3-((R)-2-Carboxypiperazin-4-yl)-propyl-1-phosphonic acid (CPP, 10 μM); the selective antagonist of adenosine $A_1R$ 8-Cyclopentyl-1,3-dipropylxanthine (DPCPX, 150 nM), the blocker of $GABA_AR$ picrotoxin (PTX, 5 μM) and the blocker of L-VGCCs nimodipine (20 μM). DPCPX, CGP46381, CGP52432, baclofen, CPP and nimodipine were purchased from Tocris Cookson Ltd., United Kingdom; PTX was obtained from Sigma-Aldrich, Germany. Drugs were first prepared as stock solutions and then dissolved in standard medium and bath applied to the tissue. Stock solutions of baclofen, CGP52432 and CPP were prepared in distilled water, whereas stock solutions of PTX, DPCPX and nimodipine were prepared in dimethyl-sulfoxide (DMSO) at a concentration that when diluted for bath application the final volume of DMSO was lower than 0.005%.

## Statistical Analysis

The following tests were used for statistical comparisons: paired and independent *t*-tests, multivariate general linear model (MANOVA), one-way analysis of variance (ANOVA), non-linear regression analysis and bivariate correlation analysis. The IBM SPSS and GraphPad Prism 8 software packages were used for statistical analyses. The values in the text and figures express mean ± SEM. Values are expressed as mean ± S.E.M and "n" throughout the text indicates the number of slices used in the analysis.

# RESULTS

## tHSD Is Stronger in the Ventral Compared With the Dorsal Hippocampus

In this study we made field recordings from 194 dorsal and 168 ventral hippocampal slices prepared from 118 adult rats. Input-output curves showed that presynaptic fiber volley (Fv) was similar in dorsal and ventral slices along the entire range of stimulation current intensities used (50−260 μA) (**Figure 1A**). However, fEPSPs evoked by strong presynaptic activation corresponding to stimulation

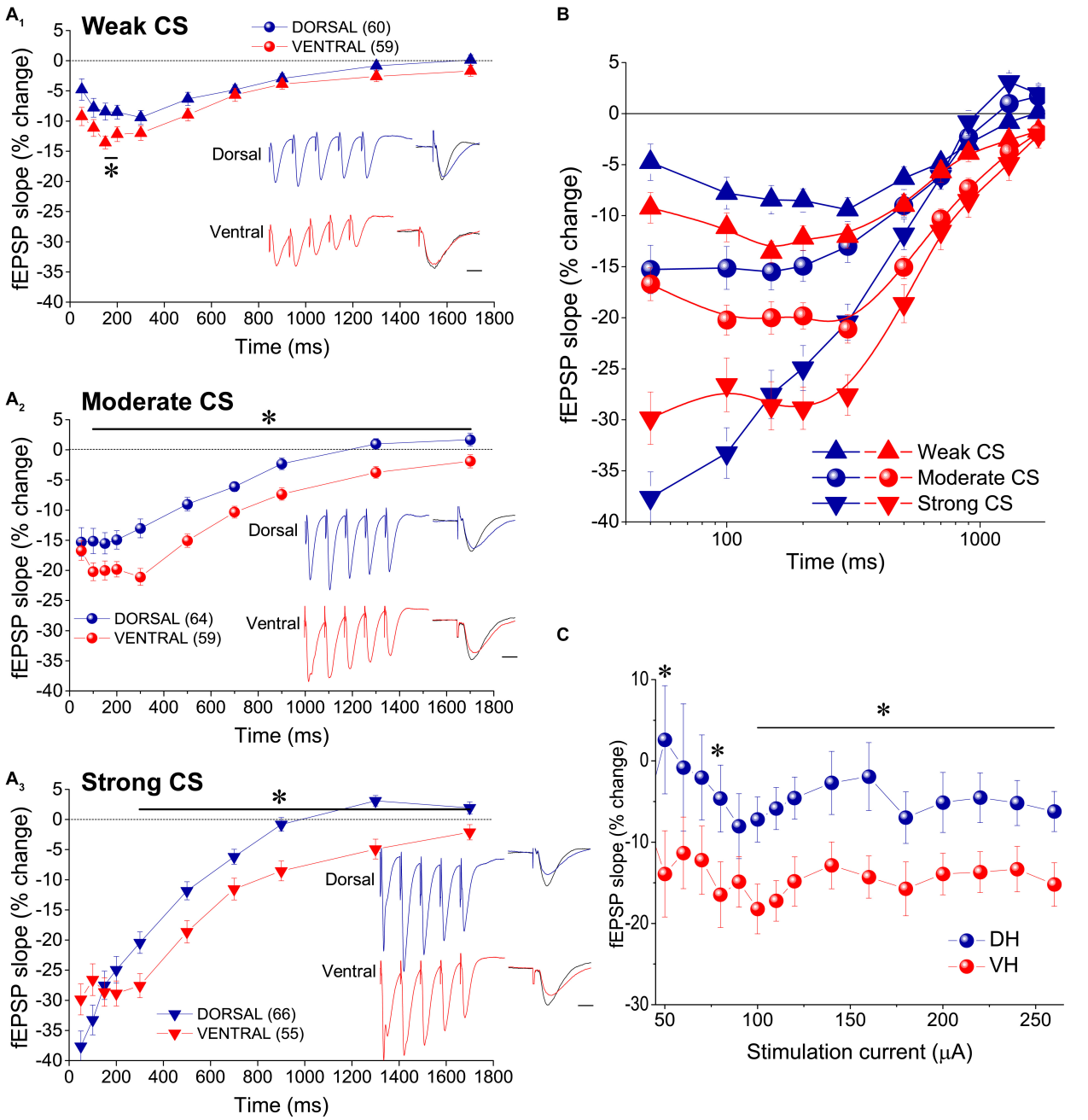


**FIGURE 2 |** tHSD is stronger and longer in the ventral compared with the dorsal hippocampus. **(A)** Diagrams presenting the time course of tHSD induced in the dorsal and the ventral hippocampus by weak **($A_1$)**, moderate **($A_2$)**, or strong **($A_3$)** intensity of CS. Horizontal bars with an asterisk indicate the interval of statistically significant differences in tHSD between the dorsal and the ventral hippocampus, at $p < 0.05$ (paired *t*-test). Insert graphs represent example fEPSP trace recordings; a 150 ms-long interval between conditioning and test response is omitted for clarity. Traces in black denote control responses at the conditioned path. Calibration bars: 1 mV, 10 ms. Artifacts are truncated. **(B)** Time courses of tHSD induced by the three intensities of CS are shown for the dorsal and the ventral hippocampus for comparison. **(C)** Dorsal-ventral difference in tHSD produced by a CS of moderate intensity on a test response evoked by a stimulation intensity of variable size. The inter-stimulation interval was set at 300 ms.

current ≥200 μA and Fv > 2 mV, were significantly larger in the dorsal than in the ventral hippocampus (independent *t*-test, $p < 0.05$).

Considering that at CA3-CA1 synapses both time-course and mechanisms involved in heterosynaptic depression depend on the intensity of afferent fiber activation (Isaacson et al., 1993; Manzoni et al., 1994; Scanziani et al., 1996; Zhang et al., 2003; Serrano et al., 2006; Andersson et al., 2007), we studied the effects of heterosynaptic stimulation using three different levels of CS intensity: weak, moderate, and

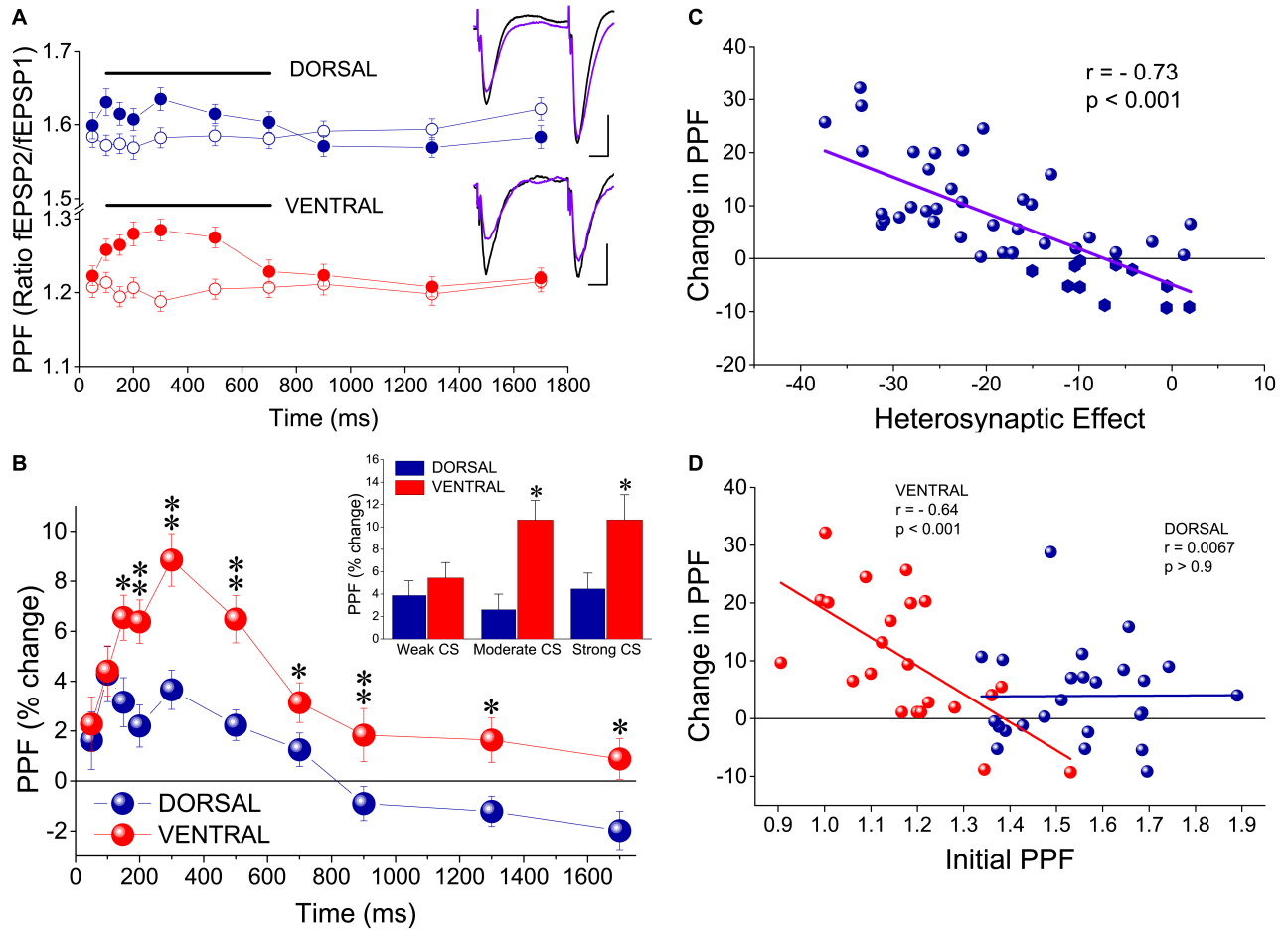


**FIGURE 3 |** tHSD is associated with a greater increase in paired-pulse facilitation (PPF) in the ventral compared with the dorsal hippocampus. **(A)** PPF before (open symbols) and during tHSD (filled symbols) in dorsal and ventral hippocampal slices. PPF is shown as the ratio between the second and the first fEPSP evoked by PPS of the test pathway at an IPI of 50 ms. Examples of recordings illustrating PPF at the test pathway before (traces in black) and after burst stimulation at the conditioning path are also shown. Calibration bars: 0.5 mV, 10 ms. Artifacts are truncated. Data were obtained from all three intensities of CS. Horizontal bars indicate statistically significant differences (paired *t*-test). The level of significance for the dorsal hippocampus is $p < 0.05$ (200 ms, 700 ms) and $p < 0.005$ (100–150 ms, 300–500 ms), and for the ventral hippocampus $p < 0.001$ (100–500 ms) and $p < 0.01$ (700 ms). **(B)** Comparison of PPF increase between the dorsal and the ventral hippocampus. Asterisks indicate statistically significant differences between the two hippocampal segments at $^{*}p < 0.05$, $^{**}p < 0.005$. Data were obtained from all three intensities of CS. Insert: Comparison of PPF increase produced by heterosynaptic CS at 300 ms between the dorsal and the ventral hippocampus. Data are shown separately for the three intensities of CS. Asterisk denote statistically significant difference between the two hippocampal segments at $p < 0.05$. **(C)** Diagram of PPF changes induced by heterosynaptic CS plotted against corresponding scores of tHSD. Changes in PPF significantly correlated with the amount of tHSD (bivariate correlation analysis). **(D)** Diagram of change in PPF plotted against initial PPF. Data are shown separately for the dorsal and the ventral hippocampus. Changes in PPF inversely correlated with (relatively low) initial amount of PPF in the ventral but not the dorsal hippocampus (bivariate correlation analysis). Symbols represent mean value of individual slices calculated by pooling all three intensities of CS for an IPI of 300 ms.

strong CS, that evoked an $fEPSP_{slope}$ of 0.48 ± 0.02 mV/ms, 1.1 ± 0.04 mV/ms, and 2.0 ± 0.1 mV/ms, respectively. We adjusted the stimulation current intensity to evoke a test $fEPSP_{slope}$ of 0.57 ± 0.03 mV/ms in dorsal ($n$ = 67) and 0.55 ± 0.02 mV/ms in ventral slices ($n$ = 59). Independence of the two stimulated pathways was ascertain by applying a PPS paradigm in which two fast succeeding stimuli were delivered to either the same stimulating electrode or the two different stimulating electrodes, at an IPI of 50 ms (Sastry et al., 1986; Grover and Teyler, 1993a; Zhang et al., 2003; Andersson et al., 2007). We proceeded to study tHSD when heterosynaptic PPS produced no change on conditioned synaptic responses, as opposed to facilitation produced by PPS delivered to an individual pathway. We examined independence of conditioning and test pathways using weak, moderate, and strong stimulation intensities. Homosynaptic PPS produced significant facilitation of $fEPSP_{slope}$ in both dorsal and ventral hippocampal slices, at all stimulation current intensities (paired *t*-test in each hippocampal segment and stimulation current intensity, $p < 0.05$) (**Figures 1C,D**). Furthermore, homosynaptic PPF was significantly greater in dorsal than in ventral hippocampal synapses when produced by weak and moderate, but not strong, stimulation intensity (independent *t*-test, $p < 0.05$), as previously described (Papatheodoropoulos and

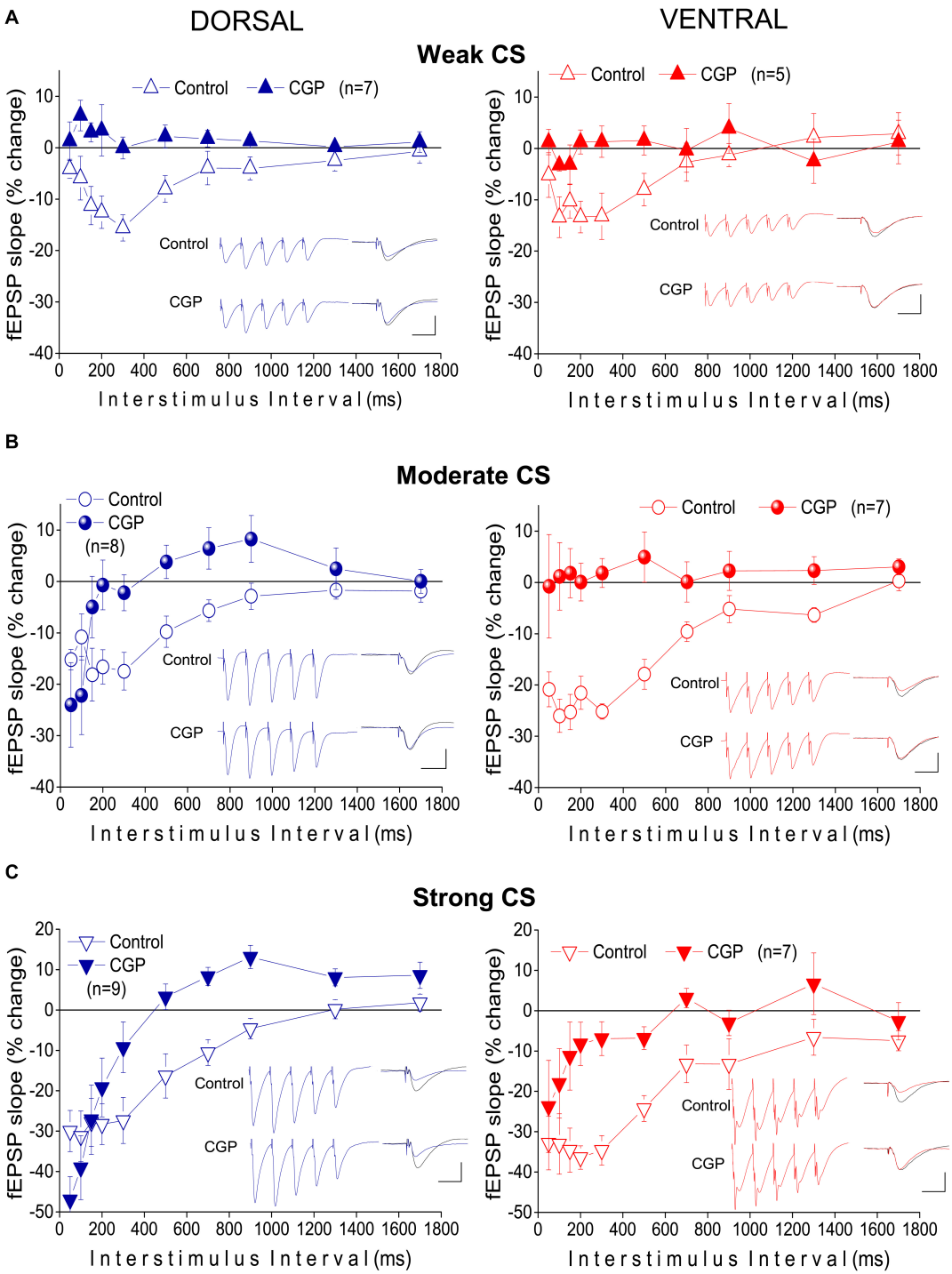


**FIGURE 4 |** Heterosynaptic depression depends on $GABA_BRs$ in both the dorsal and the ventral hippocampus. Time courses of tHSD induced under normal conditions (open symbols) or blockade of $GABA_BRs$ by their selective antagonists CGP 52432 (10 μM) or CGP 46381 (50 μM) (filled symbols), in the dorsal and the ventral hippocampus. Three intensities of CS, weak **(A)**, moderate **(B)**, or strong **(C)** were used to induce tHSD. Numbers into parenthesis indicate the number of slices used. Insets are examples of fEPSP recordings for an inter-stimulus interval of 200 ms; a 150 ms-long interval between conditioning and test response is omitted for clarity reasons. Traces in black denote control responses of the conditioned path. Calibration bars: 1 mV, 10 ms. Artifacts are truncated. Note that blockade of $GABA_BRs$ by CGP eliminates tHSD induced by weak CS, in both hippocampal segments, and tHSD induced by moderate CS in the ventral hippocampus. However, significant tHSD induced by moderate CS under blockade of $GABA_BRs$ remained in the dorsal hippocampus, at 50–100 ms. Also, significant tHSD induced by strong CS under blockade of $GABA_BRs$ remained in the dorsal (50–200 ms) and the ventral hippocampus (50–100 ms).

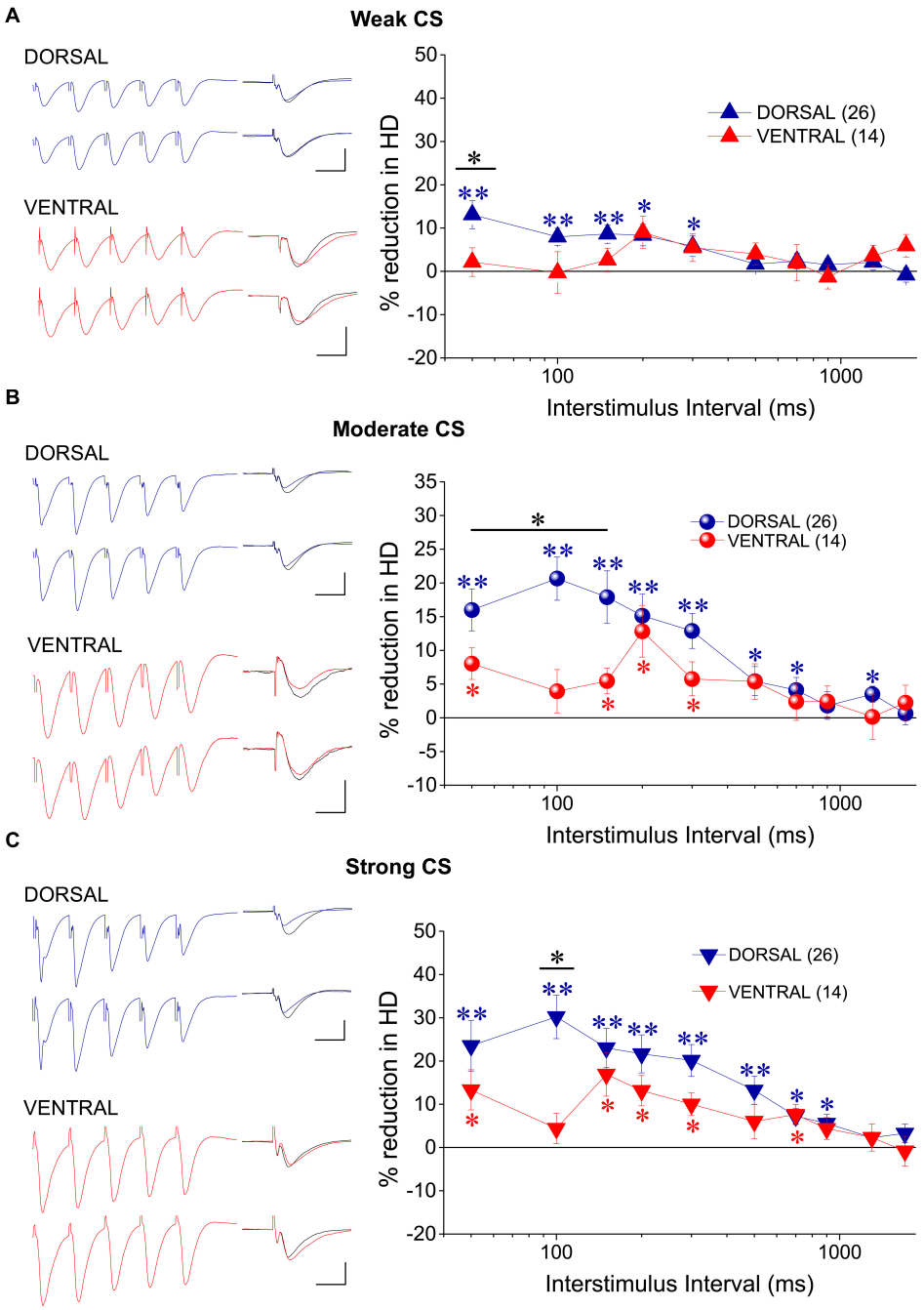


**FIGURE 5 |** tHSD involves activation of adenosine $A_1$Rs more in dorsal than in ventral hippocampus. Examples of fEPSP recordings (at an inter-stimulus interval of 200 ms) and collective results are shown in the left and the right panel, respectively. The reducing effects of the antagonist of $A_1$Rs DPCPX (150 nM) on tHSD are presented as a percent change of tHSD between normal and drug conditions. The drug effects are shown for weak **(A)**, moderate **(B)**, and strong intensity of CS **(C)**. In example traces, a 150 ms-long interval between conditioning and test response is omitted for clarity reasons. Traces in black denote control responses at the conditioned path. Calibration bars: 1 mV, 10 ms. Artifacts are truncated. Numbers into parenthesis indicate the number of slices used. Asterisks above (dorsal hippocampus) or below symbols (ventral hippocampus) denote statistically significant differences between normal and drug conditions, at $*p < 0.05$ and $**p < 0.001$ (paired *t*-test). Horizontal bars denote statistically significant differences between the dorsal and the ventral hippocampus, at $*p < 0.05$ and $**p < 0.001$ (independent *t*-test). For additional statistical tests (ANOVA, MANOVA) see main text.

Kostopoulos, 2000b; Maruki et al., 2001; Papatheodoropoulos, 2015b; Milior et al., 2016; Babiec et al., 2017). Heterosynaptic PPS, however, produced no significant change in $fEPSP_{slope}$ at any intensity of CS, in either kind of hippocampal slices (**Figures 1C,D**), verifying the independence of the two pathways.

In order to study tHSD in CA1 field we applied a conditioning brief tetanus consisting of a five pulse-burst at 50 Hz to a set of Schaffer collaterals (conditioning path) and we observed the depression induced in a different test response evoked by stimulation of a naive set of excitatory afferent inputs (test path). We examined the time course of tHSD by varying the interval between conditioning and test stimulus, from 50 to 1700 ms. We found that burst stimulation of the conditioning pathway reliably induced a transient reduction of $fEPSP_{slope}$ in the test pathway in either kind of hippocampal slices. Furthermore, the magnitude of tHSD depended on the intensity of CS; tHSD was stronger at IPIs of 50−300 ms and fainted at longer intervals, of 1300−1700 ms (**Figure 2**). Importantly, tHSD was stronger and lasted longer in ventral compared with dorsal hippocampal slices. More specifically, the weak CS produced a significant reduction in the test $fEPSP_{slope}$ at IPIs of 50−900 ms in dorsal slices and 50−700 in ventral slices (paired *t*-test between control and test $fEPSP_{slope}$ in each interval and hippocampal segment, $p < 0.05$) (**Figures 2A$_1$,B**). CS of moderate strength significantly reduced $fEPSP_{slope}$ at 50−900 ms in dorsal and 50−1700 ms in ventral slices (paired *t*-test, between control and test $fEPSP_{slope}$, $p < 0.05$) (**Figures 2A$_2$,B**). The depression of the test $fEPSP_{slope}$ was significantly greater in ventral than in dorsal slices for IPIs 150−200 ms when induced by weak intensity of CS, and for IPIs 100−1700 ms when induced by moderate intensity of CS (independent *t*-test between dorsal and ventral slices, for each intensity of CS and IPIs, $p < 0.05$) (**Figure 2A$_2$**). Strong CS induced tHSD at 50−700 ms in dorsal slices and 50−1300 ms in ventral slices (paired *t*-test between control and test $fEPSP_{slope}$ in each interval and hippocampal segment, $p < 0.05$) (**Figures 2A$_3$,B**). tHSD induced by strong CS was significantly stronger in the ventral than in the dorsal hippocampus at IPIs of 300−1300 ms (independent *t*-test, $p < 0.05$). The dorsal-ventral difference in tHSD was also evident when comparing the effect of a conditioning stimulus of moderate strength on test response of variable size, at an IPI of 300 ms (**Figure 2C**). These results showed that tHSD is stronger and longer in the ventral than in the dorsal hippocampus.

## PPF Increases During tHSD

It has been previously proposed that tHSD results principally from a reduction in glutamate release, thereby tHSD is associated with an increase in synaptic facilitation as revealed by a PPS paradigm (Molyneaux and Hasselmo, 2002). Accordingly, we examined whether tHSD is accompanied by a change in PPF by applying two stimuli of equal intensity to the test input and observed the effect of heterosynaptic CS. We found that PPF of the test input was significantly increased when preceded by a burst delivered to the conditioning input. Specifically, PPF significantly increased in both the dorsal and the ventral hippocampus at intervals of 100−700 ms (paired *t*-test of test responses before and after CS, $p < 0.05$ in the dorsal, and $p < 0.01$ in the ventral hippocampus) (**Figure 3A**). Furthermore, the increase in PPF was higher in the ventral than in the dorsal hippocampus at a range of IPIs from 150 to 500 ms (independent *t*-test; level of significance from $p < 0.05$ to $p < 0.001$; see the legend of **Figure 3** for more statistics) (**Figure 3B**). Additionally, we found a significant dorsal-ventral difference for moderate and strong, but not weak, CS (insert in **Figure 3B**). The change in PPF induced by heterosynaptic stimulation was positively correlated with tHSD, i.e., higher scores of tHSD associated with higher changes in PPF (**Figure 3C**). Interestingly, the changes in PPF induced by heterosynaptic stimulation inversely correlated with the initial amount of PPF in the ventral but not the dorsal hippocampus (**Figure 3D**). These data suggested that presynaptic mechanisms contribute to tHSD.

## tHSD Depends on $GABA_BR$ in Both Hippocampal Segments

The previous results showed that under the specified experimental conditions short-lasting tHSD in CA1 field is stronger and last longer in the ventral compared with the dorsal hippocampus. In the CA1 hippocampal field, all forms of heterosynaptic depression including fast or tHSD has been proposed to depend on heterosynaptic $GABA_BRs$ (Isaacson et al., 1993; Serrano et al., 2006; Andersson et al., 2007). According to a proposed mechanism, the GABA released by the conditioning high-frequency burst stimulation spill over into neighboring excitatory synapses and depress glutamate release by activating presynaptic $GABA_B$ heteroreceptors (Isaacson et al., 1993; Covelo and Araque, 2016). To determine whether tHSD involved activation of $GABA_BRs$, we applied the selective $GABA_BR$ antagonists CGP 52432 (10 μM) or CGP 46381 (50 μM) to dorsal and ventral slices. We found that blockade of $GABA_BRs$ completely abolished tHSD induced by weak CS in both the dorsal and the ventral hippocampus (paired *t*-test between control and drug conditions, in each hippocampal segment, $p < 0.05$) (**Figure 4A**). Also, blockade of $GABA_BRs$ eliminated tHSD induced by moderate CS at IPIs $\geq$ 150 ms in the dorsal, and IPIs $\geq$ 50 ms in the ventral hippocampus (paired *t*-test in each hippocampal segment, $p < 0.05$). Thus, in the dorsal but not the ventral hippocampus, CS of moderate intensity continued to induce significant depression of the test response at 50−100 ms under blockade of $GABA_BRs$ (**Figure 4B**). Furthermore, blockade of $GABA_BRs$ abolished depression induced by strong CS at $\geq$ 300 ms in the dorsal and $\geq$ 150 ms in the ventral hippocampus (paired *t*-test, $p < 0.05$) (**Figure 4C**). The depression of $fEPSP_{slope}$ produced by strong CS in the dorsal hippocampus remained significant at 50−200 ms (paired *t*-test, $p < 0.05$). Therefore, in the dorsal hippocampus, pharmacological blockade of $GABA_BRs$ failed to reduce tHSD that was induced at relatively short IPIs by moderate or strong CS. Furthermore, under blockade of $GABA_BRs$, the test $fEPSP_{slope}$ in the dorsal hippocampus significantly increased by strong CS at IPIs $\geq$ 700 ms (paired *t*-test, $p < 0.05$). Blockade of $GABA_BRs$ significantly increased baseline $fEPSP_{slope}$ in dorsal (by 10.1 ± 2.3%, $n = 22$, $p < 0.01$) but not ventral hippocampal slices (5.9 ± 2.5%, $n = 15$, $p > 0.05$). $fEPSP_{slope}$ was adjusted to pre-drug levels before performing heterosynaptic stimulation. These results suggested that $GABA_BRs$ are involved in tHSD in both hippocampal segments, with an increased role in the ventral hippocampus, especially at higher intensities of CS.

## $A_1$Rs, $GABA_A$Rs, and L-VGCCs Differently Contribute to tHSD in the Dorsal and the Ventral Hippocampus

It has been previously shown that the mechanism through which $GABA_B$Rs induce tHSD may involve activity of adenosine $A_1$ receptors ($A_1$Rs) located on glutamatergic terminals that inhibit glutamate release (Zhang et al., 2003; Serrano et al., 2006). Therefore, we investigated whether $A_1$Rs participate to tHSD by applying heterosynaptic stimulation in the presence of DPCPX (150 μM), in 26 dorsal and 14 ventral hippocampal slices. We found that blockade of $A_1$Rs consistently reduced tHSD more in dorsal than in ventral hippocampal slices (**Figure 5**). In the dorsal hippocampus, DPCPX significantly reduced tHSD induced by CS of weak (ANOVA, $F = 4.23$, $p < 0.001$), moderate (ANOVA, $F = 7.95$, $p < 0.001$), and strong intensity (ANOVA, $F = 6.8$, $p < 0.001$) (for more statistical details, see legend of **Figure 5**). Regarding the duration of tHSD produced by weak, moderate, and strong CS in the dorsal hippocampus, we observed statistically significant drug-induced changes at 50−300, 50−700, and 50−1300 ms, respectively (paired $t$-test, $p < 0.001 - p < 0.05$; the exact level of significance in given in **Figure 5**). In the ventral hippocampus, DPCPX reduced tHSD induced by moderate and strong CS, but not weak CS, at a limited range of IPIs (50, 150−300 ms, paired $t$-test, $p < 0.05$; see **Figure 5**). The effects of DPCPX were significantly greater in the dorsal than in the ventral hippocampus for moderate (MANOVA, $F = 14.52$, $p < 0.001$), and strong CS (MANOVA, $F = 15.22$, $p < 0.001$). DPCPX significantly increased baseline $fEPSP_{slope}$ in both dorsal (30.21 ± 5.13%, $n = 23$, $p < 0.001$) and ventral hippocampal slices (23.35 ± 9.32%, $n = 15$, $p < 0.05$) similarly (independent $t$-test, $p > 0.5$), as also previously observed (Reis et al., 2019). $fEPSP_{slope}$ was adjusted to pre-drug levels before performing heterosynaptic stimulation.

Considering that in addition of presynaptic $GABA_B$ heteroreceptors, postsynaptic $GABA_A$ receptors may be involved in reducing conditioned responses (Davies and Collingridge, 1996), we examined the effects of PTX on tHSD in five dorsal and four ventral hippocampal slices. We used a low concentration of PTX (5 μM) to avoid possible confounding effects of PTX through actions on serotonergic or nicotinic receptors (Liu et al., 1994; Erkkila et al., 2004; Das and Dillon, 2005; Thompson, 2013). We found that PTX significantly reduced tHSD induced by strong CS in the dorsal hippocampus (ANOVA, $F = 7.4$, $p < 0.001$). This effect was seen at relatively short IPIs (50−200 ms) (**Figure 6A**). We observed no significant effects of PTX on tHSD induced in the ventral hippocampus at any intensity of CS or IPI (**Figure 6A**). PTX increased baseline $fEPSP_{slope}$ in both dorsal (by 13.7 ± 2.5%, paired $t$-test, $p < 0.01$) and ventral hippocampal slices (by 11.3 ± 1.1%, paired $t$-test, $p < 0.01$). Thus, we adjusted $fEPSP_{slope}$ to pre-drug levels before performing heterosynaptic stimulation.

Postsynaptic depolarization induced by conditioning burst-stimulation may recruit L-VGCCs in the dendrites of CA1 pyramidal cells (Andreasen and Lambert, 1995; Geier et al., 2011), Activation of L-VGCCs by conditioning input may then reduce conditioned fEPSPs, located near conditioning input, by shunting excitatory synaptic currents (Häusser et al., 2001). Following application of the blocker of L-VGCCs nimodipine we observed a significant reduction in tHSD induced by weak, moderate, and strong CS, in both hippocampal segments (**Figure 6B**). Specifically, nimodipine applied in the dorsal hippocampus produced reduction in tHSD induced by weak ($F = 3.6$, $p < 0.005$), moderate ($F = 4.6$, $p < 0.001$), and strong intensity of CS ($F = 3.7$, $p < 0.005$) (ANOVA). Similarly, application of nimodipine in the ventral hippocampus reduced tHSD induced by weak ($F = 3.2$, $p < 0.05$), moderate ($F = 2.0$, $p < 0.05$), and strong intensity of CS ($F = 2.1$, $p < 0.05$) (ANOVA). Drug-reduced reductions in tHSD were higher at shorter IPIs (see results from paired $t$-test in **Figure 6B**). Also, nimodipine significantly increased the baseline $fEPSP_{slope}$ in the dorsal (10.6 ± 2.5%, $n = 11$, paired $t$-test, $p < 0.005$) but not the ventral hippocampus (2.0 ± 3.2%, $n = 6$, paired $t$-test, $p > 0.5$). We adjusted $fEPSP_{slope}$ to pre-drug levels before performing heterosynaptic stimulation in the presence of nimodipine.

## $GABA_B$R Suppresses $fEPSP_{Slope}$ and Enhances $fEPSP_{\tau}$ Differently in the Two Hippocampal Segments

To investigate the effects of $GABA_B$Rs' activation by the endogenous GABA on excitatory synaptic transmission, comparatively in the dorsal and the ventral hippocampus, we applied the agonist of $GABA_B$R baclofen in dorsal and ventral hippocampal slices and we measured drug effects on fast and slow components of fEPSP. Specifically, we measured $fEPSP_{slope}$ that represents the fast component of excitatory synaptic transmission, and the decay time constant "τ" of fEPSP ($fEPSP_{\tau}$) that represents the time required for a fEPSP to fall to 37% of its maximum amplitude and quantifies the slow component of synaptic transmission. We applied baclofen at a wide range of concentrations that covered extracellular GABA levels in the hippocampus (Wilson et al., 1996; Çavuş et al., 2016) and saturating drug concentrations (Pfrieger et al., 1994; Labouèbe et al., 2007). Also, in an effort to reduce a possible effect of $GABA_B$R desensitization (Froestl, 2010; Turecek et al., 2014), we applied only one drug concentration in individual slices. We adjusted stimulation current intensity to evoke a half-maximum $fEPSP_{slope}$, in dorsal (1.41 ± 0.06 mV/ms, $n = 61$) and ventral (1.36 ± 0.09, $n = 50$) hippocampal slices. We found that baclofen produced robust and concentration-dependent changes in $fEPSP_{slope}$ in both the dorsal (ANOVA, $F = 40.1$, $p < 0.0001$) and the ventral hippocampus ($F = 65.1$, $p < 0.0001$). Furthermore, the suppressive effect of baclofen significantly differed between the two hippocampal segments, as demonstrated by comparing the concentration-response curves (**Figure 7C**). Specifically, following fitting Boltzmann function to data we found a significantly higher suppression of $fEPSP_{slope}$ in the ventral than in the dorsal hippocampus; non-linear regression analysis, $F$(DFn, DFd) = 9.023 (3, 122), $p < 0.0001$. $EC_{50}$ values were 2.87 μM for the dorsal and 6.92 μM for the ventral hippocampus. These results suggested

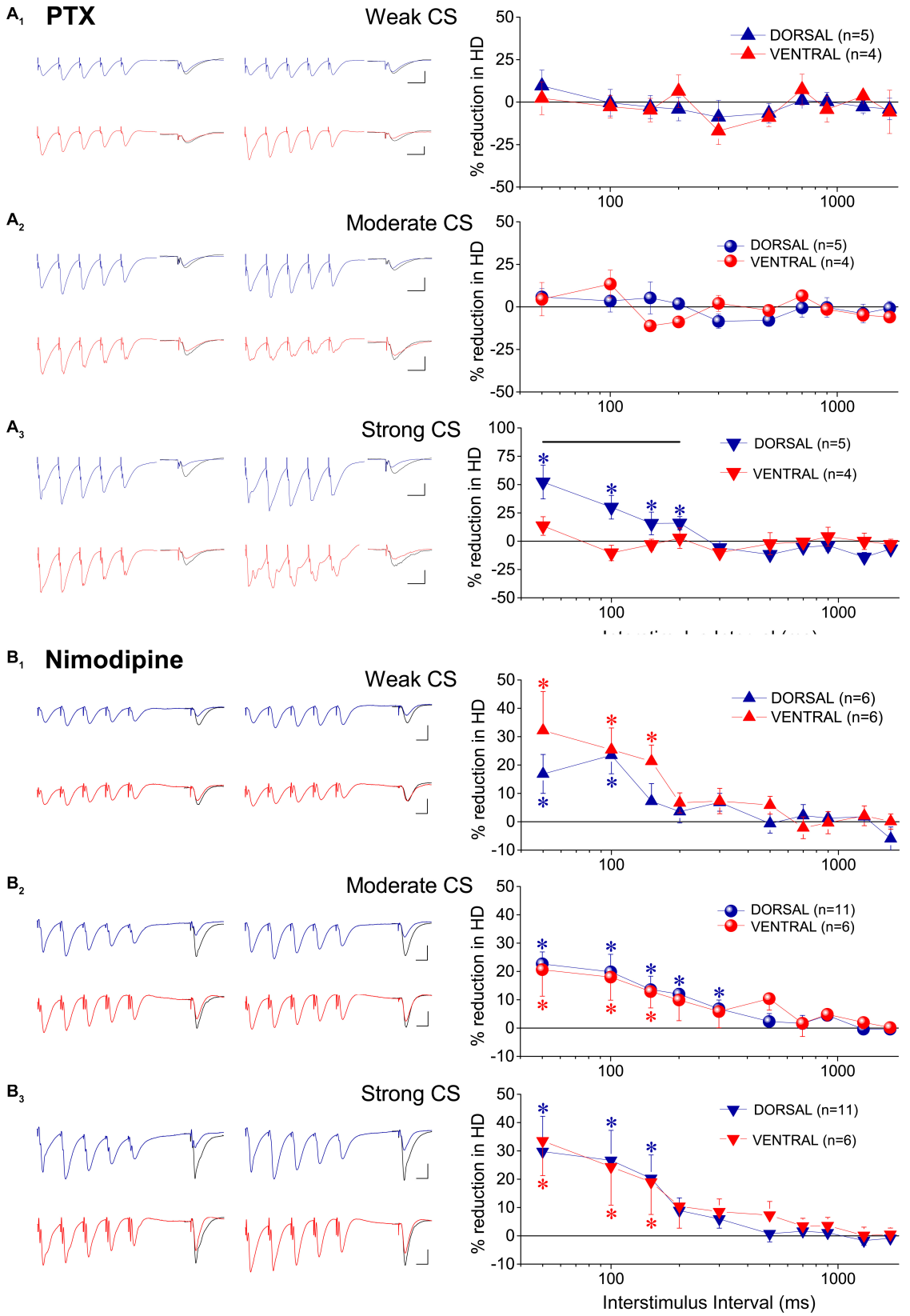


**FIGURE 6 |** Continued

**FIGURE 6 |** $GABA_A$Rs and L-VGCCs are differently involved in tHSD in the dorsal and the ventral hippocampus. The effects of blockade of $GABA_A$Rs by 5 μM PTX, and the effects of blockade of L-VGCCs by nimodipine are shown in **(A,B)**, respectively. Examples of fEPSP recordings (at an inter-stimulus interval of 100 ms and 50 ms for PTX and nimodipine, respectively) and collective results (percent change of tHSD between normal and drug conditions) are shown in the left and the right panel, respectively. In example traces for PTX, a 60 ms-long interval between conditioning and test response is omitted for clarity. Traces in black denote control responses at the conditioned path. Calibration bars: 1 mV, 10 ms. All artifacts are truncated. Numbers into parenthesis indicate the number of slices used. Asterisks above or below symbols denote statistically significant differences between normal and drug conditions, at $^*p < 0.05$ (paired *t*-test). Horizontal bar denotes statistically significant differences between the dorsal and the ventral hippocampus, at $p < 0.05$ (independent *t*-test). For additional statistical tests see main text. Note that blockade of $GABA_A$Rs significantly reduced tHSD induced by strong CS at short intervals, only in the dorsal hippocampus. Blockade of L-VGCCs reduced tHSD induced by all intensities of CS, in both hippocampal segments.

that the potency of baclofen to suppress excitatory synaptic transmission is higher in the ventral compared with the dorsal hippocampus.

Baclofen, in addition to suppress $fEPSP_{slope}$, produced a significant increase in $fEPSP_\tau$ in both hippocampal segments (**Figures 7A,B**). Furthermore, the enhancement of $fEPSP_\tau$ was depended on the drug concentration in the dorsal hippocampus (ANOVA, $F = 7.2$, $p < 0.0001$) but not the ventral hippocampus (ANOVA, $F = 1.6$, $p > 0.1$). In dorsal slices this effect was remarkably fast, and at large drug concentrations the prolongation of fEPSP (i.e., the increase in $fEPSP_\tau$) preceded the reduction in $fEPSP_{slope}$, as it is evident in the time courses of drug effects (see **Figure 7A**). Strikingly, $fEPSP_\tau$ increased despite a robust reduction in $fEPSP_{slope}$, and baclofen concentrations (0.5−1 μM) that did not significantly affect $fEPSP_{slope}$ produced a considerable increase in $fEPSP_\tau$ (15.8 ± 6.3% and 22.3 ± 3.9% at 0.5 and 1 μM, respectively, paired *t*-test, $p < 0.05$). In the ventral hippocampus the maximum baclofen-induced increase in $fEPSP_\tau$ (47.4 ± 12.9%) was about half of the maximum drug effect observed in the dorsal hippocampus (105.2 ± 17.8%) and the effects of baclofen on $fEPSP_\tau$ across all baclofen concentrations significantly differed between the dorsal and the ventral hippocampus [non-linear regression analysis, $F$(DFn, DFd) = 15.25 (3, 100), $p < 0.0001$] (**Figure 7D**). The dorsal-ventral difference in baclofen effects was also observed after pooling all drug concentrations together, for $fEPSP_{slope}$ (-43 ± 4.2% vs. -55.7 ± 3.7% in the dorsal and ventral hippocampus, respectively; independent *t*-test, $p < 0.05$) and $fEPSP_\tau$ (67.7 ± 7.2% vs. 35.0 ± 5.8% in the dorsal and ventral hippocampus, respectively, independent *t*-test, $p < 0.001$) (**Figure 7E**). The effects of baclofen on $fEPSP_{slope}$ and $fEPSP_\tau$ were fully reversed following application of the specific antagonist of $GABA_B$ receptors CGP52432 (10 μM), in both dorsal and ventral hippocampal slices (**Figure 7F**).

The effects of baclofen on $fEPSP_{slope}$, but not $fEPSP_\tau$, most probably result from the activation of $GABA_B$ heteroreceptors located on glutamatergic terminals. The baclofen effects on $fEPSP_\tau$, however, appeared to be consistent with an activation of $GABA_B$ autoreceptors. $GABA_B$ autoreceptors suppress GABA release and reduce postsynaptic inhibition (Thompson and Gahwiler, 1992; Bowery, 1993), thereby allowing generation of an EPSP with increased duration (Nathan and Lambert, 1991; Davies and Collingridge, 1996). Interestingly, suppression of fast postsynaptic inhibition facilitates the activation of NMDA receptors (Dingledine et al., 1986), and NMDA receptors may significantly contribute to the decay phase of fEPSP in CA1 hippocampal field (Andreasen et al., 1989; Papatheodoropoulos, 2015b). Therefore, we hypothesized that NMDA receptors may contribute to the baclofen-induced increase in $fEPSP_\tau$. In order to test this hypothesis, we applied CPP in seven dorsal and seven ventral hippocampal slices before the application of 50 μM baclofen. We found that blockade of NMDA receptors by CPP did not prevent the enhancing effect of baclofen on $fEPSP_\tau$ (**Figure 8**). Also, CPP did not significantly change basal $fEPSP_\tau$ and $fEPSP_{slope}$ and did not significantly affect the suppressive effect of baclofen on $fEPSP_{slope}$. These results suggested that baclofen increased $fEPSP_\tau$ by indirectly enhancing the activation of non-NMDA glutamatergic receptors.

## $GABA_B$R Increases Synaptic Facilitation in the Ventral and Dorsal Hippocampus Similarly

Presynaptic receptors that control transmitter release can also modulate short-term synaptic plasticity, which is typically represented by PPF. PPF is inversely correlated with changes in transmitter release and manipulations that reduce transmitter release enhance PPF (Manabe et al., 1993). Therefore, given the higher baclofen-induced suppression of excitatory synaptic transmission in the ventral compared with the dorsal hippocampus, we asked whether baclofen could affect PPF differently in the two hippocampal segments. We examined the effects of varying concentrations of baclofen on PPF (measured as the percentage of fEPSP2/fEPSP1 ratio) at an IPI of 50 ms in both kinds of hippocampal slices. We found that baclofen significantly increased PPF in a concentration-dependent manner in both hippocampal segments, similarly (**Figure 9A**). These effects reversed upon application of 10 μM CGP 52432 (**Figure 9B**). We also characterized the effect of 10 μM baclofen on the time course of PPF at a wide range of IPIs, from 20 to 1000 ms. We found that baclofen significantly increased PPF in both the dorsal and the ventral hippocampus. Specifically, baclofen significantly increased PPF in the dorsal hippocampus for IPIs up to 200 ms (paired *t*-test, $p < 0.05$) and in the ventral hippocampus for IPIs up to 333 ms (paired *t*-test, $p < 0.05$) (**Figure 9C**). It is known that PPF depends on the size of the conditioning fEPSP (i.e., fEPSP1) (Manabe et al., 1993; Papatheodoropoulos, 2015b), which is shown here that is robustly reduced by baclofen. Therefore, in the condition of baclofen, we examined PPF also after adjusting the $fEPSP_{slope}$ to the control levels to exclude the case that the baclofen-induced increase in PPF was secondary to the reduction of fEPSP1. We found that PPF

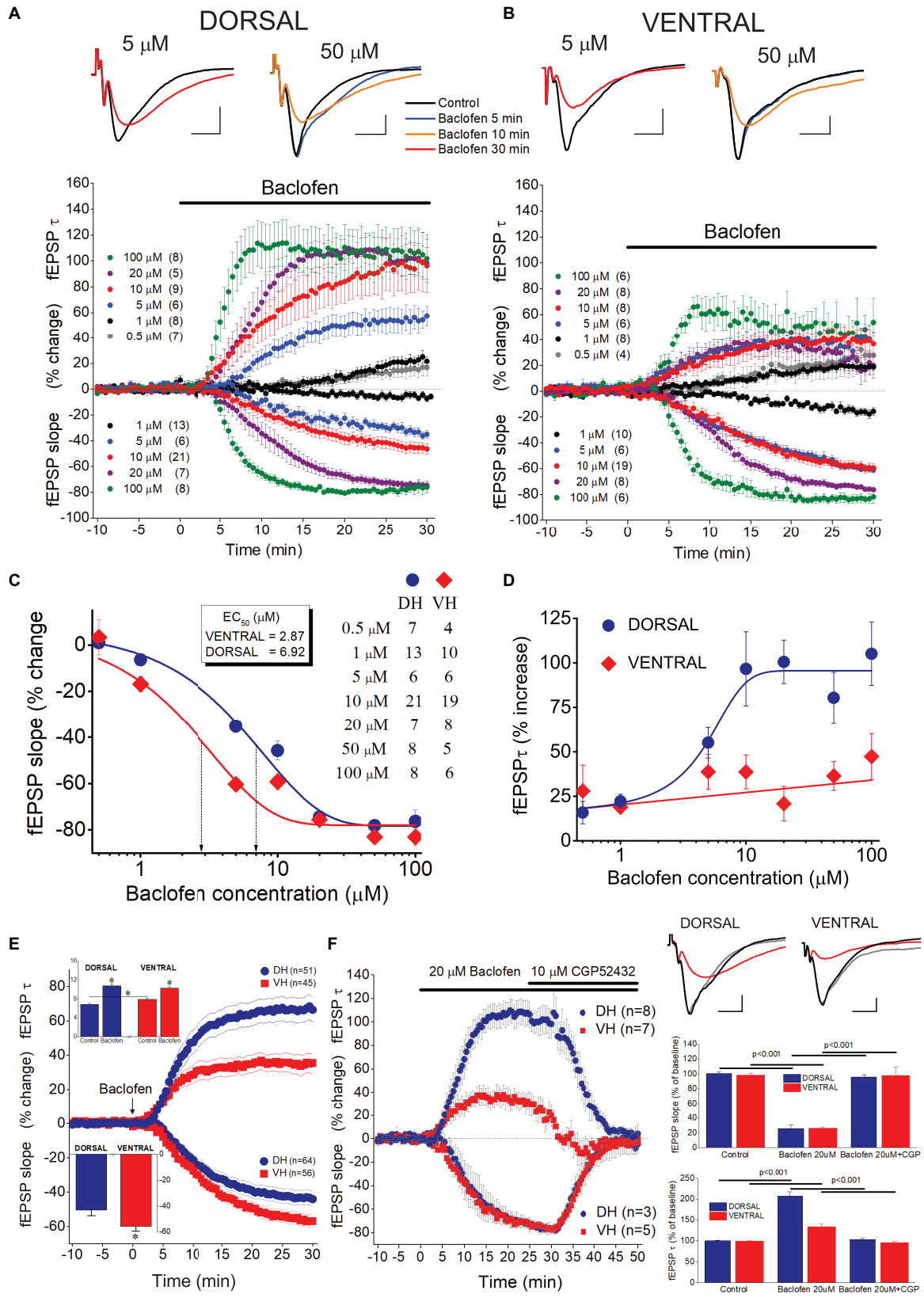


**FIGURE 7 |** Continued

**FIGURE 7 |** Activation of $GABA_BRs$ by baclofen suppresses $fEPSP_{slope}$ more in the ventral than in the dorsal hippocampus and prolongs $fEPSP_{\tau}$ more in the dorsal than in the ventral hippocampus. Collective time courses of percent change of $fEPSP_{slope}$ and $fEPSP_{\tau}$ illustrating the action of baclofen in the dorsal hippocampus and the ventral hippocampus are shown in panels **(A,B)**, respectively. In collective diagrams, values shown below and above zero correspond to changes in $fEPSP_{slope}$ and $fEPSP_{\tau}$, respectively. The number of slices studied is shown into parenthesis in collective graph legends. Data for 0.5 μM ($fEPSP_{slope}$) and 50 μM ($fEPSP_{slope}$ and $fEPSP_{\tau}$) are not shown in collective graphs for clarity reasons. Representative examples of fEPSP traces, shown on the top of graphs, were collected under control conditions and under 5 or 50 μM baclofen. Calibration bars: 0.5 mV, 5 ms. Note that 5 μM baclofen suppresses $fEPSP_{slope}$ more in the ventral than in the dorsal hippocampus and at the same time prolongs the decay phase of fEPSP in the dorsal but not the ventral hippocampus. Also note that a 5 min application of 50 μM baclofen induces an increase in fEPSP decay phase in the dorsal but not the ventral hippocampus, i.e., before any change in $fEPSP_{slope}$ occurs (blue trace, baclofen 5 min). **(C)** Concentration-effect curves for baclofen actions on $fEPSP_{slope}$. Curves were constructed using the Boltzmann function. The number of slices used is indicated in the legend. Dotted arrowed lines indicate $EC_{50}$ values for the ventral (VH, 2.57 μM) and the dorsal hippocampus (DH, 5.98 μM). The two curves differ significantly (non-linear regression analysis, $p < 0.0001$). **(D)** Concentration-effect relationship of baclofen actions on $fEPSP_{\tau}$. The number of slices used for all baclofen concentrations, but 50 μM, is shown in panel **(B)**; the effects of 50 μM baclofen were studied in eight dorsal and five ventral hippocampal slices. **(E)** Graph of cumulative time courses of baclofen-induced changes in $fEPSP_{slope}$ and $fEPSP_{\tau}$ (suppression and enhancement, respectively) in the dorsal and the ventral hippocampus, constructed by pooling data from all baclofen concentrations. Lines on both sides of symbols indicate SEM. The number of slices studied in given into parenthesis. Arrow depicts the start of baclofen application (time = 0), which continues for the next 30 min. The inset graph on the top-left of panel shows the mean values of $fEPSP_{\tau}$ under control and drug conditions. Asterisks indicate statistically significant differences at $p < 0.05$ (paired *t*-test and independent *t*-test were used for comparisons inside and between hippocampal segments, respectively). Note that under control conditions the value of $fEPSP_{\tau}$ is higher in the ventral than in dorsal hippocampus; following baclofen application the value of $fEPSP_{\tau}$ becomes similar in the two hippocampal segments. The inset graph on the bottom-left of the panel shows that baclofen-induced suppression of $fEPSP_{slope}$ was significantly higher in the ventral than in dorsal hippocampus (asterisk, independent *t*-test, $p < 0.05$). **(F)** Are shown time course diagrams (graph on the left), example traces of fEPSP recordings (upper-right panel) and aggregate data under control and drug conditions (lower-right graphs) illustrating that 10 μM CGP52432 fully reversed the effects of 20 μM baclofen on $fEPSP_{slope}$ and $fEPSP_{\tau}$ in the dorsal and the ventral hippocampus. Horizontal lines indicate statistically significant differences; the level of significance is also given. Calibration bars: 0.5 mV, 5 ms.

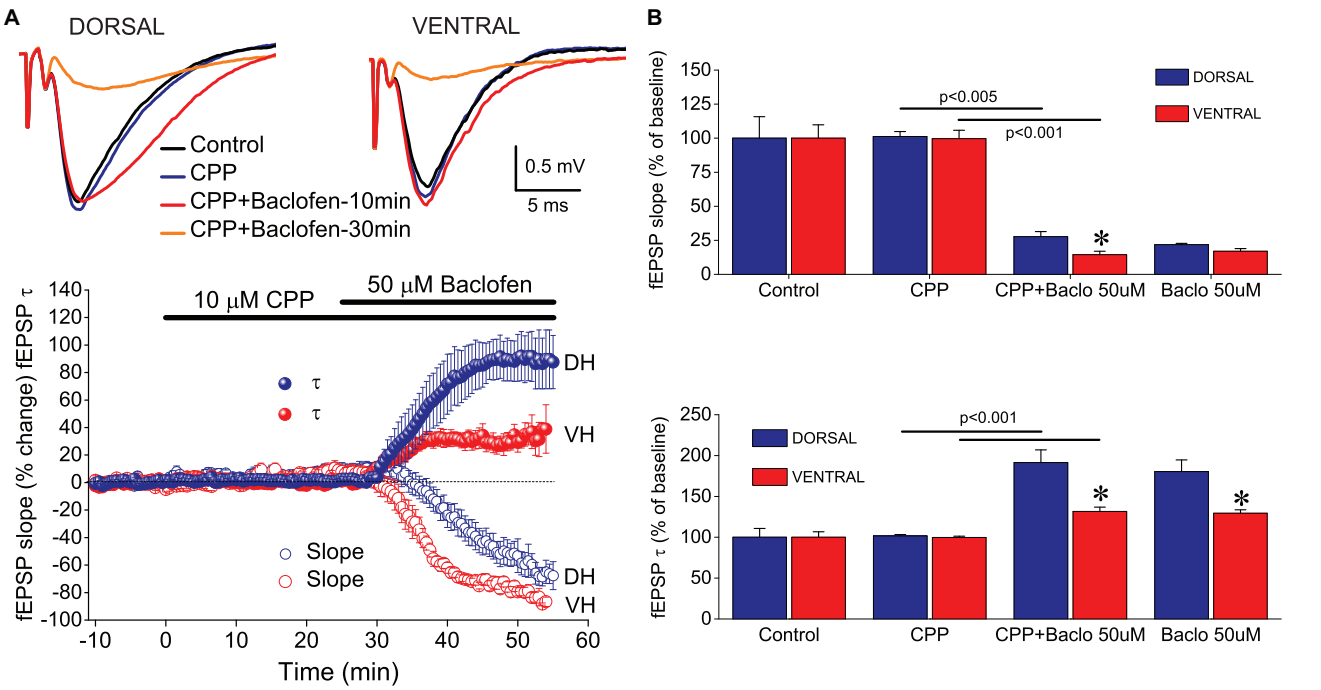


**FIGURE 8 |** NMDA receptors are not involved in baclofen-induced effects on fEPSP. **(A)** Example traces of fEPSP recordings (upper panel) and time-courses (graph on the bottom) of percent changes in $fEPSP_{slope}$ and $fEPSP_{\tau}$ induced by 50 μM baclofen under blockade of NMDA receptors by CPP. **(B)** Cumulative data obtained during application of CPP (25 min) and CPP + baclofen (30 min) are shown for $fEPSP_{\tau}$ and $fEPSP_{slope}$ (upper and lower graph, respectively). Statistically significant differences between experimental conditions are shown by horizontal lines and the level of significance is given above lines. Asterisks indicate statistically significant differences between the dorsal and the ventral hippocampus, at $p < 0.05$. CPP did not prevent the effects of baclofen on $fEPSP_{\tau}$ or $fEPSP_{slope}$ in either hippocampal segment.

after $fEPSP_{slope}$ correction was similar with that measured before correction (**Figure 9C**, Baclofen 10 μM, correction). Furthermore, blockade of $GABA_BR$ under basal conditions did not significantly affect PPF in either hippocampal segment (**Figure 9C**, CGP).

## DISCUSSION

The main findings of this study are the following: (a) tHSD induced by paired stimulation of two independent inputs to stratum radiatum of CA1 field is stronger in the ventral compared

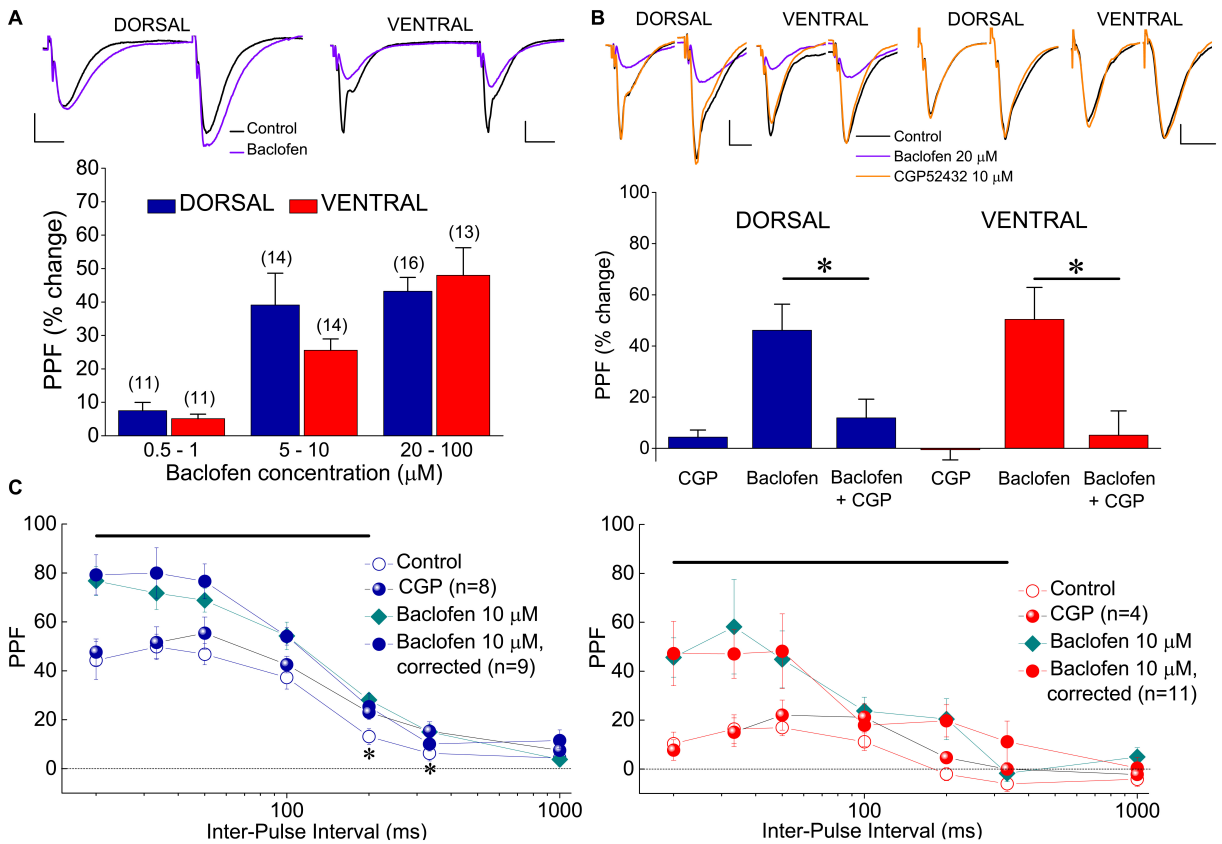


**FIGURE 9 |** Baclofen enhances PPF of $fEPSP_{slope}$. **(A)** Cumulative data of the effects of various baclofen concentrations on PPF are shown for the dorsal and the ventral hippocampus; example traces obtained before (traces in black) and during application of 10 μM baclofen (traces in violet) in a dorsal and a ventral slice are shown on the top of the graph. In the example of the dorsal hippocampus, similar unconditioned $fEPSP_{slope}$ under control and drug conditions were selected for comparison reasons. Drug concentrations are segregated into three groups: 0.5–1, 5–10, and 20–100 μM. PPF is expressed as the percent change of the ratio fEPSP2/fEPSP1 observed under baclofen with respect to control conditions. The number of slices used in each condition is indicated into parenthesis on the top of each bar. Baclofen significantly increased PPF in both hippocampal segments (ANOVA, $F = 4.8$, $p < 0.005$ in dorsal and $F = 5.6$, $p < 0.001$ in ventral hippocampus). **(B)** The antagonist of $GABA_BR$ CGP52432 (10 μM) reversed the increase of PPF induced by 20 μM baclofen in four dorsal and four ventral slices (asterisks indicate statistically significant difference with respect to control values, at $p < 0.05$, paired $t$-test). Blockade of $GABA_BRs$ under basal conditions did not significantly affect PPF in either dorsal ($n = 8$) or ventral ($n = 4$) hippocampal slices. In all cases PPF was induced at 50 ms. Respective examples are shown on the top of the graph. **(C)** PPF plotted as a function of IPI in dorsal (left) and ventral (right) under control conditions, application of CGP52432, and application of baclofen with or without adjustment of $fEPSP_{slope}$ to control levels. Horizontal bars denote statistically significant differences between control and baclofen-corrected conditions (paired $t$-test, $p < 0.05$). Also, asterisks in the left graph indicate that application CGP52432 significantly increased PPF in dorsal slices.

with the dorsal hippocampus; (b) Induction of tHSD depends on several mechanisms, with a predominant participation of $GABA_BRs$ and A1Rs in the dorsal hippocampus and $GABA_BRs$ in the ventral hippocampus; (c) Exogenous activation of $GABA_BRs$ by baclofen, suppresses the initial fast component of excitatory synaptic transmission more efficiently in the ventral than in the dorsal hippocampus, and enhances the late slow component of excitatory transmission more efficiently in the dorsal than in the ventral hippocampus; (d) Exogenous, but not endogenous tonic, activation of $GABA_BRs$ enhances PPF in the dorsal and the ventral hippocampus similarly.

## Dorsal-Ventral Differences in Heterosynaptic Interactions

In keeping with previous studies (Gustafsson et al., 1989; Isaacson et al., 1993; Molyneaux and Hasselmo, 2002; Chandler et al., 2003; Zhang et al., 2003; Andersson et al., 2007; Guetg et al., 2009) we found that short burst of high-frequency stimulation induces tHSD that lasts less than 2 s. Furthermore, we show for the first time that tHSD has a greater magnitude and lasts longer in the ventral than in the dorsal hippocampus. Several mechanisms, have been implicated in heterosynaptic depression in hippocampus (Covelo and Araque, 2016). A commonly accepted general mechanism that is proposed for the induction of tHSD includes the release of GABA from interneurons and activation of inhibitory presynaptic $GABA_B$ heteroreceptors on glutamate terminals, resulting thus in suppression of glutamate release and reduction of excitatory synaptic transmission (Isaacson et al., 1993; Molyneaux and Hasselmo, 2002; Chandler et al., 2003; Serrano et al., 2006; Andersson et al., 2007; Guetg et al., 2009). Furthermore, adenosine released during high-frequency

CS may also participate to tHSD via activation of presynaptic $A_1$Rs on glutamate terminals, thereby contributing to reduction of excitatory glutamate transmission (Grover and Teyler, 1993b; Zhang et al., 2003). In keeping with these proposed mechanisms, we found that tHSD induced in both the dorsal and the ventral hippocampus involves activation of $GABA_B$Rs and A1Rs. However, in this study we found that $GABA_B$Rs and A1Rs do not contribute, similarly, to the dorsal and the ventral hippocampus (see **Supplementary Table 1** for a schematically illustrated contribution of various mechanisms to tHSD in the two hippocampal segments). $GABA_B$Rs and A1Rs appear to have an overall similar participation in the induction of tHSD in the dorsal hippocampus, although the participation of $GABA_B$Rs increases toward weak stimulation intensities and the relative contribution of A1Rs increases toward strong intensities (**Supplementary Table 1**). In the ventral hippocampus, $GABA_B$Rs appear to play a more prominent role than A1Rs, which participate at relatively strong, and not weak, CS intensities. Seemingly, A1Rs are involved more in the dorsal than in the ventral hippocampus, presumably reflecting the increased expression of these receptors in the dorsal CA1 hippocampal field (Lee et al., 1983; Reis et al., 2019). The putative action of presynaptic mechanisms in tHSD is corroborated by the fact that tHSD is associate with an enhancement in PPF since reduction in presynaptic transmitter release can produce an increase in the magnitude of PPF (Manabe et al., 1993; Dumas and Foster, 1998b). However, additional, presumably postsynaptic, $GABA_B$R-dependent mechanisms may participate in tHSD, contributing to dorsal-ventral diversification. For instance, strong CS delivered in the dorsal and not the ventral hippocampus under blockade of $GABA_B$Rs uncovered a facilitation of the test response at IPIs $\geq$ 700 ms (**Figure 5C**), suggesting that under control conditions postsynaptic $GABA_B$Rs may participate in suppressing conditioned responses in the dorsal hippocampus, thereby contributing to dorsal-ventral difference in tHSD induced by strong CS. Interestingly, previous observations have suggested that postsynaptic $GABA_B$R-mediated hyperpolarizations are greater in the dorsal than in the ventral hippocampal pyramidal cells (Papatheodoropoulos et al., 2002) and $GABA_B$Rs appear to control postsynaptic depolarizations in CA1 pyramidal cells more efficiently in the dorsal than in the ventral hippocampus (Papatheodoropoulos, 2015a).

In addition, here we provide the first evidence for the involvement of $GABA_A$Rs and L-VGCCs in tHSD, and we show that $GABA_A$Rs have an increased contribution to tHSD in the dorsal hippocampus, while L-VGCCs have a similar participation in the two hippocampal segments. The increased contribution of $GABA_A$Rs to tHSD in the dorsal hippocampus is consistent with the increased $GABA_A$R-dependent inhibition in this hippocampus segment (Petrides et al., 2007). The reduction of tHSD by nimodipine may involve blockade of L-VGCCs (Moyer and Disterhoft, 1994), and reduction of the slow afterhyperpolarization (Power et al., 2002; Kaczorowski, 2011), which can be enhanced by activation of L-VGCCs (Thibault and Landfield, 1996). Voltage-dependent potassium channels, activation of which can inhibit postsynaptic depolarizations, may also contribute to the effects of nimodipine on tHSD since nimodipine can block these channels in some preparations (Caro et al., 2011). Overall, the present evidence suggests that tHSD in the CA1 hippocampal field presents different properties between the dorsal and the ventral hippocampus. Furthermore, a multitude of presynaptic and postsynaptic mechanisms contribute in shaping tHSD, and a distinct pattern of these mechanism participation occurs between the two segments of the hippocampus.

Presynaptic inhibition, in addition to simply restrict transmitter release, may play important functional roles in brain networks. For example, heterosynaptic depression may increase contrast between activated and non-activated synapses (Dunwiddie and Lynch, 1978), or between background activity and responses to specific external stimuli in brain networks (Frerking and Ohliger-Frerking, 2006), and may also enhance the importance of a relatively strong input in a field (Frerking and Ohliger-Frerking, 2006). Also, heterosynaptic depression may increase and restrict synaptic saturation (Lynch et al., 1977). Accordingly, we hypothesize that the observed dorsal-ventral differences in tHSD may reflect an important facet of diversified organization along hippocampus, concerning input segregation and input selectivity. $GABA_B$Rs appear to play a prominent role in tHSD. Given that $GABA_B$Rs require pooling of synaptically released GABA to be activated (Scanziani, 2000; Kulik et al., 2003, 2006), $GABA_B$Rs may contribute to tHSD during transients in extracellular GABA that can occur under conditions of enhanced and/or synchronous activity of GABAergic neurons, and they may serve to detect this activity in local networks (Osten et al., 2007). Interestingly, sharp wave and ripples, an endogenous network activity of the hippocampus that importantly assist in the process of memory consolidation (Buzsaki, 2015), reflects synchronized GABAergic cell activity in CA1 local network (Wu et al., 2002; Papatheodoropoulos, 2008), and displays an increased generation in the ventral hippocampus (Kouvaros and Papatheodoropoulos, 2017). Furthermore, during sharp wave-ripples there is a very selective activation of hippocampal CA1 principal cells (Chrobak and Buzsaki, 1996; Papatheodoropoulos, 2008). Hence, we speculate that an increased tHSD in the ventral hippocampus may facilitate sharpening of input segregation and assist the property of input-output selectivity in the functioning of local CA1 circuit on the context of sharp wave-ripples, according to their role as carries of bits of mnemonic information.

## $GABA_B$R-Dependent Control of $fEPSP_{Slope}$ and $fEPSP_{\tau}$

$GABA_B$ receptor is a heterodimeric metabotropic G protein-coupled receptor for GABA with both presynaptic and postsynaptic actions (Jones et al., 1998; Bowery et al., 2002; Bettler et al., 2004). Heterosynaptic $GABA_B$Rs on glutamatergic terminals is a powerful mechanism that controls excitatory synaptic transmission in the hippocampus, among other

brain regions (Ault and Nadler, 1982; Dutar and Nicoll, 1988a; Thompson and Gahwiler, 1992; Bowery, 1993; Chalifoux and Carter, 2011). Furthermore, the suppressive effects of baclofen on excitatory transmission at CA3-CA1 synapses is well known (Ault and Nadler, 1982; Dutar and Nicoll, 1988b; Thompson and Gahwiler, 1992). However, this study investigated for the first time the effects of $GABA_BRs$' activation by an exogenous agonist on excitatory synaptic transmission, comparatively between the dorsal and the ventral hippocampus. The present results suggest that $GABA_BRs$ control the fast component of glutamatergic transmission more efficiently in the ventral than in the dorsal hippocampus; furthermore, somewhat surprisingly, we found that baclofen robustly increased the slow decaying phase of fEPSP, more in the dorsal than in the ventral hippocampus. Thus, it appears that activation of $GABA_BR$ has a dual effect on the excitatory synaptic transmission in the CA1 hippocampal field, restricting the fast component and promoting the slow component of glutamatergic transmission. Furthermore, the efficiency of this dual effect is reverse in the two segments of the hippocampus.

The dual effects of baclofen on $fEPSP_{slope}$ and $fEPSP_{\tau}$, may have different mechanistic interpretations. On the one side, the baclofen-induced suppression of $fEPSP_{slope}$ could safely be explained in terms of action of $GABA_B$ heteroreceptor on glutamate terminals, as previously established (Ault and Nadler, 1982; Dutar and Nicoll, 1988b; Thompson and Gahwiler, 1992; Bowery, 1993; Vizi and Kiss, 1998; Ulrich and Bettler, 2007; Chalifoux and Carter, 2011). The enhancing effect of baclofen on $fEPSP_{\tau}$, on the other side, may result from an interaction between presynaptic and postsynaptic mechanisms. Specifically, the slow decaying phase of fEPSP, represented by $fEPSP_{\tau}$, temporally coincides with the period of fast postsynaptic $GABA_AR$-mediated inhibition (Andersen et al., 1964; Alger and Nicoll, 1982), which can very effectively control the duration of postsynaptic depolarizations (Nathan and Lambert, 1991; Davies and Collingridge, 1996). It is then obvious that the waveform of fEPSP reflects a compound synaptic potential shaped not only by monosynaptically produced depolarizations, but also by mononynaptic and disynaptic (feed-forward/feed-back) inhibition. At high stimulus intensities may also contribute polysynaptic components resulted from reverberation of CA3 cell excitation that can result in CA1 synaptic activation. Accordingly, a reduction in $GABA_AR$-mediated postsynaptic inhibition may contribute to the enhancement of $fEPSP_{\tau}$. Indeed, activation of $GABA_B$ autoreceptors on GABAergic terminals leads to a reduction in GABA release followed by suppression in postsynaptic inhibition (Davies et al., 1990, 1991; Nathan and Lambert, 1991; Thompson and Gahwiler, 1992; Bowery, 1993; Davies and Collingridge, 1996). Therefore, we hypothesize that the baclofen-induced increase in $fEPSP_{\tau}$ could result from an increased activity of $GABA_B$ autoreceptors and a consequent reduction in postsynaptic fast inhibition. The differences we observed in the effects of baclofen between the dorsal and the ventral hippocampus could not easily be interpreted by the recently reported increased expression of $GABA_BRs$ in the CA1 stratum radiatum of the ventral hippocampus (Dubovyk and Manahan-Vaughan, 2018), since although we found a lower $EC_{50}$ value for baclofen in the ventral than in the dorsal hippocampus, the maximum drug action did not differ between the two hippocampal segments, as could be suggested by the increased quantitative $GABA_BR$ expression in the ventral hippocampus. In addition, expression profiles found in the above-cited study could refer either to $GABA_B$ heteroreceptors or to $GABA_B$ autoreceptors, as well as to postsynaptic $GABA_BRs$. Alternatively, the dorsal-ventral difference in baclofen-induced effects on fEPSP could be related to the wide molecular and functional heterogeneity of $GABA_BRs$ (Ulrich and Bettler, 2007; Schwenk et al., 2010).

Presynaptic mechanisms that control the release of neurotransmitter play a crucial role in regulating the balance between excitation and inhibition in local neuronal circuits and thus determining the dynamic state of excitability required for normal activity in brain networks (Haider et al., 2006). Several lines of evidence suggest that an increased excitability characterizes the intrinsic neuronal network of the ventral hippocampus, presumably representing a constitutive property of this segment of hippocampus that can reliably assist to its normal functions (Papatheodoropoulos, 2018). For instance, pyramidal cells in the ventral hippocampus have an increased intrinsic excitability (Dougherty et al., 2012; Honigsperger et al., 2015; Malik et al., 2016; Milior et al., 2016), reduced $GABA_A$ receptor-mediated synaptic inhibition (Papatheodoropoulos et al., 2002; Petrides et al., 2007; Maggio and Segal, 2009), and increased NMDA receptor-dependent activity (Papatheodoropoulos et al., 2005). Nevertheless, under some conditions the ventral hippocampus displays an increased tendency to fall into a hyperexcitability state that results in pathologic activity, as shown both *in vivo* (Spencer et al., 1984; Quigg et al., 1997) and *in vitro* (Bragdon et al., 1986; Borck and Jefferys, 1999; Mikroulis and Psarropoulou, 2012; Papatheodoropoulos, 2015a). However, the requirements for long-term stability and normal function, suggest that some mechanisms intrinsic to the local network may function to counterbalance the tendency of the ventral hippocampus for increased excitability. For instance, ventral pyramidal cells display decreased network-driven spontaneous activity (Kouvaros and Papatheodoropoulos, 2017), and increased level of calcium-activated potassium channels of SK-type (Babiec et al., 2017). Most $GABA_BRs$, including presynaptic ones, are located distant from sites of GABA release and presumably require increased level of GABA to be activated (Davies and Collingridge, 1996; Scanziani, 2000; Lopez-Bendito et al., 2004; Kulik et al., 2006). Increased levels of GABA can be achieved under conditions of increased network activity that may endow the risk of runaway excitation (Kulik et al., 2003). Interestingly, in the present study we observed a greater suppressive effect of baclofen on fast excitatory transmission in the ventral compared with the dorsal hippocampus, at low micromolar baclofen concentrations, similar with those of GABA that occur under conditions of intense network activity (Roth and Draguhn, 2012). Furthermore, the enhancing effects of baclofen on the slow decaying phase of fEPSP were limited in the ventral

compared with the dorsal hippocampus. Thus, activation of $GABA_BRs$ under conditions of increased network activity may represent a homeostatic mechanism that contributes to keep network activity in the ventral hippocampus within a physiological range.

## Effects of $GABA_BRs$ on Short-Term Plasticity

Because changes in the probability that a transmitter is released by a presynaptic terminal affect the amount of transmitter released by subsequent afferent activity, one of the functional roles that presynaptic inhibition of transmitter release can play is the modulation of short-term synaptic plasticity (Hennig, 2013; Mukunda and Narayanan, 2017; Cheng et al., 2018). Short-term synaptic plasticity crucially influences the dynamics of local neuronal network activity and can play important roles in information processing performed by brain networks, including information filtering and input diversification (Silver, 2010; Jackman and Regehr, 2017). Decreased ability for short-term synaptic plasticity can directly influence the ability of a synapse to sustain bursts of presynaptic activity and to forward neural information in local brain networks (Lisman, 1997; Koutsoumpa and Papatheodoropoulos, 2019). In addition, a reduced short-term synaptic plasticity may crucially hamper the ability for induction of long-term plasticity, especially under conditions of long bouts of afferent activity (Kouvaros and Papatheodoropoulos, 2016b; Papaleonidopoulos et al., 2018). Among other mechanisms, short-term synaptic plasticity critically depends on the properties of transmitter release, including transmitter release probability; for instance, PPF is inversely related to the probability of transmitter release at a given synapse (Dobrunz and Stevens, 1997; Fioravante and Regehr, 2011; Regehr, 2012).

In keeping with previous results (Papatheodoropoulos and Kostopoulos, 2000b; Maruki et al., 2001; Papatheodoropoulos, 2015b; Kouvaros and Papatheodoropoulos, 2016a; Moschovos and Papatheodoropoulos, 2016; Babiec et al., 2017; Dubovyk and Manahan-Vaughan, 2018), we found that PPF in CA hippocampal fields is higher in dorsal than in ventral hippocampal synapses, an observation that represents one of the most remarkable and established intrinsic differences between the dorsal and the ventral hippocampus. Considering the inverse relationship between PPF and probability of transmitter release, it has been proposed that ventral hippocampal synapses possess an increased transmitter release probability (Papatheodoropoulos and Kostopoulos, 2000b; Papatheodoropoulos, 2015b). It has been shown that experimental manipulations that inhibit transmitter release will impact on synapse with higher than lower probability of transmitter release (Manabe et al., 1993). Indeed, activation of $GABA_BRs$ by baclofen increase PPF in hippocampus (Manabe et al., 1993; Dumas and Foster, 1998a; Margrie et al., 2000; Lei and McBain, 2003). Here, we tested the hypothesis of increased transmitter release probability in the ventral hippocampal synapses by asking whether activation of $GABA_BRs$ by baclofen will produce a higher enhancement of PPF in the ventral than in the dorsal hippocampus. Contrary to the hypothetical prediction, we found that baclofen produced a similar increment in PPF in dorsal and ventral hippocampus, suggesting that dorsoventral differences in PPF involve complex mechanisms of regulation of transmitter release that may not entirely reside in properties like the probability of transmitter release (Babiec et al., 2017). However, during heterosynaptic stimulation, that represents a more physiologically relevant condition compared with application of an exogenous $GABA_BR$ agonist, PPF increases significantly more in the ventral than in the dorsal hippocampus (see **Figure 3**) and the change in PPF induced by heterosynaptic stimulation inversely correlated with initial PPF scores only in the ventral hippocampus, suggesting that basal probability of transmitter release in CA1 excitatory synapses differs between the two hippocampal segments. Importantly, however, PPF did not change in either the dorsal or the ventral hippocampus following blockade of $GABA_BRs$ suggesting that $GABA_BRs$ do not tonically regulate basal probability of glutamate release in either hippocampal segments which, therefore, may have similar probabilities of transmitter release. Predictively, a more precise determination of the glutamate release probability at the CA3-CA1 synapses in the dorsal and the ventral hippocampus should await future research, engaging several approaches that by necessity include detailed quantal analysis of transmitter release.

# CONCLUSON

Concluding, we argue that the present data show that the excitatory synaptic transmission is differently modulated between the dorsal and the ventral CA1 hippocampal field. tHSD of the excitatory transmission has an increased magnitude and duration in the ventral hippocampus, and depends on multiple mechanisms, which have, however, a different participation in the two segments of the hippocampus. $GABA_BRs$ predominate in the ventral hippocampus and both $GABA_BRs$ and A1Rs play important roles in the dorsal hippocampus. Activation of $GABA_BRs$ by an exogenous agonist controls the initial fast component of excitatory synaptic transmission more in the ventral than in the dorsal hippocampus and enhances the late slow component of excitatory transmission mainly in the dorsal hippocampus. We propose that under conditions of increased neuronal activity (experimentally mimicked by relatively intense heterosynaptic stimulation or baclofen application), input segregation is increased in the ventral hippocampus, while at the same time, the reduction in excitatory transmission may contribute in dampening the, endogenously increased, neuronal excitability of the ventral hippocampus network. Furthermore, the increased $GABA_BR$-dependent control of the slow component of glutamatergic transmission in the dorsal hippocampus may serve to gate excitatory input more efficiently in this segment of the hippocampus. The shown differences may provide a means for specialization of information processing in the local neuronal circuits, thereby significantly contributing to functional segregation along hippocampus.

## DATA AVAILABILITY STATEMENT

The raw data supporting the conclusions of this article will be made available by the authors, without undue reservation, to any qualified researcher.

## ETHICS STATEMENT

The animal study was reviewed and approved by the Protocol Evaluation Committee of the Department of Medicine of the University of Patras and the Directorate of Veterinary Services of the Achaia Prefecture of Western Greece Region, Papadiamanti 14 and Aretha, 26443, Patras.

## AUTHOR CONTRIBUTIONS

GT performed the experiments and analyzed the data. CP designed the study, analyzed the data, and wrote and prepared the manuscript.

## FUNDING

This research was co-financed by the Greece and the European Union (European Social Fund-ESF) through the Operational Program «Human Resources Development, Education and Lifelong Learning 2014–2020» in the context of the project "Rat Hippocampal Longitudinal Axis: Modulation of Synaptic Transmission – Plasticity & Rhythmogenesis in Physiology and Autism" (MIS 5047171).

## ACKNOWLEDGMENTS

We wish to thank Nikoleta Spiropoulou for animal care.

## SUPPLEMENTARY MATERIAL

The Supplementary Material for this article can be found online at: https://www.frontiersin.org/articles/10.3389/fnsyn.2020.00024/full#supplementary-material

## REFERENCES

Alger, B. E., and Nicoll, R. A. (1982). Feed-forward dendritic inhibition in rat hippocampal pyramidal cells studied *in vitro*. *J. Physiol.* 328, 105–123. doi: 10.1113/jphysiol.1982.sp014255

Andersen, P., Eccles, J. C., and Loyning, Y. (1964). Pathway of postsynaptic inhibition in the hippocampus. *J. Neurophysiol.* 27, 608–619. doi: 10.1152/jn.1964.27.4.608

Andersson, M., Blomstrand, F., and Hanse, E. (2007). Astrocytes play a critical role in transient heterosynaptic depression in the rat hippocampal CA1 region. *J. Physiol.* 585(Pt 3), 843–852. doi: 10.1113/jphysiol.2007.142737

Andreasen, M., and Lambert, J. D. (1995). Regenerative properties of pyramidal cell dendrites in area CA1 of the rat hippocampus. *J. Physiol.* 483(Pt 2), 421–441. doi: 10.1113/jphysiol.1995.sp020595

Andreasen, M., Lambert, J. D., and Jensen, M. S. (1989). Effects of new non-N-methyl-D-aspartate antagonists on synaptic transmission in the *in vitro* rat hippocampus. *J. Physiol.* 414, 317–336. doi: 10.1113/jphysiol.1989.sp017690

Ault, B., and Nadler, J. V. (1982). Baclofen selectively inhibits transmission at synapses made by axons of CA3 pyramidal cells in the hippocampal slice. *J. Pharmacol. Exp. Ther.* 223, 291–297.

Babiec, W. E., Jami, S. A., Guglietta, R., Chen, P. B., and O'Dell, T. J. (2017). Differential regulation of NMDA receptor-mediated transmission by SK channels underlies dorsal-ventral differences in dynamics of schaffer collateral synaptic function. *J. Neurosci.* 37, 1950–1964. doi: 10.1523/JNEUROSCI.3196-16.2017

Bannerman, D. M., Sprengel, R., Sanderson, D. J., McHugh, S. B., Rawlins, J. N., Monyer, H., et al. (2014). Hippocampal synaptic plasticity, spatial memory and anxiety. *Nat. Rev. Neurosci.* 15, 181–192. doi: 10.1038/nrn3677

Bettler, B., Kaupmann, K., Mosbacher, J., and Gassmann, M. (2004). Molecular structure and physiological functions of GABA(B) receptors. *Physiol. Rev.* 84, 835–867. doi: 10.1152/physrev.00036.2003

Borck, C., and Jefferys, J. G. (1999). Seizure-like events in disinhibited ventral slices of adult rat hippocampus. *J. Neurophysiol.* 82, 2130–2142. doi: 10.1152/jn.1999.82.5.2130

Bowery, N. G. (1993). GABAB receptor pharmacology. *Annu. Rev. Pharmacol. Toxicol.* 33, 109–147. doi: 10.1146/annurev.pa.33.040193.000545

Bowery, N. G., Bettler, B., Froestl, W., Gallagher, J. P., Marshall, F., Raiteri, M., et al. (2002). International Union of Pharmacology. XXXIII. Mammalian gamma-aminobutyric acid(B) receptors: structure and function. *Pharmacol. Rev.* 54, 247–264. doi: 10.1124/pr.54.2.247

Bowery, N. G., Hudson, A. L., and Price, G. W. (1987). GABAA and GABAB receptor site distribution in the rat central nervous system. *Neuroscience* 20, 365–383. doi: 10.1016/0306-4522(87)90098-4

Bragdon, A. C., Taylor, D. M., and Wilson, W. A. (1986). Potassium-induced epileptiform activity in area CA3 varies markedly along the septotemporal axis of the rat hippocampus. *Brain Res.* 378, 169–173. doi: 10.1016/0006-8993(86)90300-8

Buhl, D. L., and Buzsaki, G. (2005). Developmental emergence of hippocampal fast-field "ripple" oscillations in the behaving rat pups. *Neuroscience* 134, 1423–1430. doi: 10.1016/j.neuroscience.2005.05.030

Buzsaki, G. (2015). Hippocampal sharp wave-ripple: a cognitive biomarker for episodic memory and planning. *Hippocampus* 25, 1073–1188. doi: 10.1002/hipo.22488

Caro, A., Tarabova, B., Rojo-Ruiz, J., and Lacinova, L. (2011). Nimodipine inhibits AP firing in cultured hippocampal neurons predominantly due to block of voltage-dependent potassium channels. *Gen. Physiol. Biophys.* 30, S44–S53. doi: 10.4149/gpb_2011_SI1_44

Çavuş, I., Romanyshyn, J. C., Kennard, J. T., Farooque, P., Williamson, A., Eid, T., et al. (2016). Elevated basal glutamate and unchanged glutamine and GABA in refractory epilepsy: microdialysis study of 79 patients at the yale epilepsy surgery program. *Ann. Neurol.* 80, 35–45. doi: 10.1002/ana.24673

Cembrowski, M. S., Bachman, J. L., Wang, L., Sugino, K., Shields, B. C., and Spruston, N. (2016). Spatial gene-expression gradients underlie prominent heterogeneity of CA1 pyramidal neurons. *Neuron* 89, 351–368. doi: 10.1016/j.neuron.2015.12.013

Chalifoux, J. R., and Carter, A. G. (2011). GABAB receptor modulation of synaptic function. *Curr. Opin. Neurobiol.* 21, 339–344. doi: 10.1016/j.conb.2011.02.004

Chandler, K. E., Princivalle, A. P., Fabian-Fine, R., Bowery, N. G., Kullmann, D. M., and Walker, M. C. (2003). Plasticity of GABA(B) receptor-mediated heterosynaptic interactions at mossy fibers after status epilepticus. *J. Neurosci.* 23, 11382–11391. doi: 10.1523/jneurosci.23-36-11382.2003

Cheng, Q., Song, S. H., and Augustine, G. J. (2018). Molecular mechanisms of short-term plasticity: role of synapsin phosphorylation in augmentation and potentiation of spontaneous glutamate release. *Front. Synaptic Neurosci.* 10:33. doi: 10.3389/fnsyn.2018.00033

Chrobak, J. J., and Buzsaki, G. (1996). High-frequency oscillations in the output networks of the hippocampal-entorhinal axis of the freely behaving rat. *J. Neurosci.* 16, 3056–3066. doi: 10.1523/jneurosci.16-09-03056.1996

Covelo, A., and Araque, A. (2016). Lateral regulation of synaptic transmission by astrocytes. *Neuroscience* 323, 62–66. doi: 10.1016/j.neuroscience.2015.02.036

Das, P., and Dillon, G. H. (2005). Molecular determinants of picrotoxin inhibition of 5-hydroxytryptamine type 3 receptors. *J. Pharmacol. Exp. Ther.* 314, 320–328. doi: 10.1124/jpet.104.080325

Davies, C. H., and Collingridge, G. L. (1996). Regulation of EPSPs by the synaptic activation of GABAB autoreceptors in rat hippocampus. *J. Physiol.* 496(Pt 2), 451–470. doi: 10.1113/jphysiol.1996.sp021698

Davies, C. H., Davies, S. N., and Collingridge, G. L. (1990). Paired-pulse depression of monosynaptic GABA-mediated inhibitory postsynaptic responses in rat hippocampus. *J. Physiol.* 424, 513–531. doi: 10.1113/jphysiol.1990.sp018080

Davies, C. H., Starkey, S. J., Pozza, M. F., and Collingridge, G. L. (1991). GABA autoreceptors regulate the induction of LTP. *Nature* 349, 609–611. doi: 10.1038/349609a0

Dayan, P. (2012). Twenty-five lessons from computational neuromodulation. *Neuron* 76, 240–256. doi: 10.1016/j.neuron.2012.09.027

Dingledine, R., Hynes, M. A., and King, G. L. (1986). Involvement of N-methyl-D-aspartate receptors in epileptiform bursting in the rat hippocampal slice. *J. Physiol.* 380, 175–189. doi: 10.1113/jphysiol.1986.sp016279

Dobrunz, L. E., and Stevens, C. F. (1997). Heterogeneity of release probability, facilitation, and depletion at central synapses. *Neuron* 18, 995–1008. doi: 10.1016/s0896-6273(00)80338-4

Dong, H. W., Swanson, L. W., Chen, L., Fanselow, M. S., and Toga, A. W. (2009). Genomic-anatomic evidence for distinct functional domains in hippocampal field CA1. *Proc. Natl. Acad. Sci. U.S.A.* 106, 11794–11799. doi: 10.1073/pnas.0812608106

Dougherty, K. A., Islam, T., and Johnston, D. (2012). Intrinsic excitability of CA1 pyramidal neurones from the rat dorsal and ventral hippocampus. *J. Physiol.* 590(Pt 22), 5707–5722. doi: 10.1113/jphysiol.2012.242693

Dubovyk, V., and Manahan-Vaughan, D. (2018). Less means more: the magnitude of synaptic plasticity along the hippocampal dorso-ventral axis is inversely related to the expression levels of plasticity-related neurotransmitter receptors. *Hippocampus* 28, 136–150. doi: 10.1002/hipo.22816

Dumas, T. C., and Foster, T. C. (1998a). GABA(b) receptors differentially regulate hippocampal CA1 excitatory synaptic transmission across postnatal development in the rat. *Neurosci. Lett.* 248, 138–140. doi: 10.1016/s0304-3940(98)00344-9

Dumas, T. C., and Foster, T. C. (1998b). Late developmental changes in the ability of adenosine A1 receptors to regulate synaptic transmission in the hippocampus. *Brain Res. Dev. Brain Res.* 105, 137–139. doi: 10.1016/s0165-3806(97)00152-1

Dunwiddie, T., and Lynch, G. (1978). Long-term potentiation and depression of synaptic responses in the rat hippocampus: localization and frequency dependency. *J. Physiol.* 276, 353–367. doi: 10.1113/jphysiol.1978.sp012239

Dutar, P., and Nicoll, R. A. (1988a). Classification of muscarinic responses in hippocampus in terms of receptor subtypes and second-messenger systems: electrophysiological studies *in vitro*. *J. Neurosci.* 8, 4214–4224. doi: 10.1523/jneurosci.08-11-04214.1988

Dutar, P., and Nicoll, R. A. (1988b). Pre- and postsynaptic GABAB receptors in the hippocampus have different pharmacological properties. *Neuron* 1, 585–591. doi: 10.1016/0896-6273(88)90108-0

Erkkila, B. E., Weiss, D. S., and Wotring, V. E. (2004). Picrotoxin-mediated antagonism of alpha3beta4 and alpha7 acetylcholine receptors. *Neuroreport* 15, 1969–1973. doi: 10.1097/00001756-200408260-00027

Fioravante, D., and Regehr, W. G. (2011). Short-term forms of presynaptic plasticity. *Curr. Opin. Neurobiol.* 21, 269–274. doi: 10.1016/j.conb.2011.02.003

Floriou-Servou, A., von Ziegler, L., Stalder, L., Sturman, O., Privitera, M., Rassi, A., et al. (2018). Distinct proteomic, transcriptomic, and epigenetic stress responses in dorsal and ventral hippocampus. *Biol. Psychiatry* 84, 531–541. doi: 10.1016/j.biopsych.2018.02.003

Frerking, M., and Ohliger-Frerking, P. (2006). Functional consequences of presynaptic inhibition during behaviorally relevant activity. *J. Neurophysiol.* 96, 2139–2143. doi: 10.1152/jn.00243.2006

Frerking, M., and Wondolowski, J. (2008). "Regulation of neurotransmitter release by presynaptic receptors," in *Molecular Mechanisms of Neurotransmitter Release*, ed. Z.-W. Wang (Totowa, NJ: Humana Press), 297–314. doi: 10.1007/978-1-59745-481-0_14

Froestl, W. (2010). Chemistry and pharmacology of GABAB Receptor Ligands. *Adv. Pharmacol.* 58, 19–62. doi: 10.1016/s1054-3589(10)58002-5

Geier, P., Lagler, M., Boehm, S., and Kubista, H. (2011). Dynamic interplay of excitatory and inhibitory coupling modes of neuronal L-type calcium channels. *Am J. Physiol. Cell Physiol.* 300, C937–C949. doi: 10.1152/ajpcell.00219.2010

Giocomo, L. M., and Hasselmo, M. E. (2007). Neuromodulation by glutamate and acetylcholine can change circuit dynamics by regulating the relative influence of afferent input and excitatory feedback. *Mol. Neurobiol.* 36, 184–200. doi: 10.1007/s12035-007-0032-z

Grover, L. M., and Teyler, T. J. (1993a). Presynaptic mechanism for heterosynaptic, posttetanic depression in area CA1 of rat hippocampus. *Synapse* 15, 149–157. doi: 10.1002/syn.890150207

Grover, L. M., and Teyler, T. J. (1993b). Role of adenosine in heterosynaptic, posttetanic depression in area CA1 of hippocampus. *Neurosci. Lett.* 154, 39–42. doi: 10.1016/0304-3940(93)90166-i

Guetg, N., Seddik, R., Vigot, R., Turecek, R., Gassmann, M., Vogt, K. E., et al. (2009). The GABAB1a isoform mediates heterosynaptic depression at hippocampal mossy fiber synapses. *J. Neurosci.* 29, 1414–1423. doi: 10.1523/JNEUROSCI.3697-08.2009

Gustafsson, B., Asztely, F., Hanse, E., and Wigstrom, H. (1989). Onset characteristics of long-term potentiation in the guinea-pig hippocampal CA1 region *in vitro*. *Eur. J. Neurosci.* 1, 382–394. doi: 10.1111/j.1460-9568.1989.tb00803.x

Haider, B., Duque, A., Hasenstaub, A. R., and McCormick, D. A. (2006). Neocortical network activity in vivo is generated through a dynamic balance of excitation and inhibition. *J. Neurosci.* 26, 4535–4545. doi: 10.1523/jneurosci.5297-05.2006

Häusser, M., Major, G., and Stuart, G. J. J. S. (2001). Differential shunting of EPSPs by action potentials. *Science* 291, 138–141. doi: 10.1126/science.291.5501.138

Hennig, M. H. (2013). Theoretical models of synaptic short term plasticity. *Front. Comput. Neurosci.* 7:45. doi: 10.3389/fncom.2013.00045

Honigsperger, C., Marosi, M., Murphy, R., and Storm, J. F. (2015). Dorsoventral differences in Kv7/M-current and its impact on resonance, temporal summation and excitability in rat hippocampal pyramidal cells. *J. Physiol.* 593, 1551–1580. doi: 10.1113/jphysiol.2014.280826

Isaacson, J. S., Solis, J. M., and Nicoll, R. A. (1993). Local and diffuse synaptic actions of GABA in the hippocampus. *Neuron* 10, 165–175. doi: 10.1016/0896-6273(93)90308-e

Ishizuka, N., Cowan, W. M., and Amaral, D. G. (1995). A quantitative analysis of the dendritic organization of pyramidal cells in the rat hippocampus. *J. Comp. Neurol.* 362, 17–45. doi: 10.1002/cne.903620103

Jackman, S. L., and Regehr, W. G. (2017). The mechanisms and functions of synaptic facilitation. *Neuron* 94, 447–464. doi: 10.1016/j.neuron.2017.02.047

Jones, K. A., Borowsky, B., Tamm, J. A., Craig, D. A., Durkin, M. M., Dai, M., et al. (1998). GABA(B) receptors function as a heteromeric assembly of the subunits GABA(B)R1 and GABA(B)R2. *Nature* 396, 674–679. doi: 10.1038/25348

Kaczorowski, C. C. (2011). Bidirectional pattern-specific plasticity of the slow afterhyperpolarization in rats: role for high-voltage activated $Ca^{2+}$ channels and I h. *Eur. J. Neurosci.* 34, 1756–1765. doi: 10.1111/j.1460-9568.2011.07899.x

Koutsoumpa, A., and Papatheodoropoulos, C. (2019). Short-term dynamics of input and output of CA1 network greatly differ between the dorsal and ventral rat hippocampus. *BMC Neurosci.* 20:35. doi: 10.1186/s12868-019-0517-5

Kouvaros, S., and Papatheodoropoulos, C. (2016a). Major dorsoventral differences in the modulation of the local CA1 hippocampal network by NMDA, mGlu5, adenosine A2A and cannabinoid CB1 receptors. *Neuroscience* 317, 47–64. doi: 10.1016/j.neuroscience.2015.12.059

Kouvaros, S., and Papatheodoropoulos, C. (2016b). Theta burst stimulation-induced LTP: differences and similarities between the dorsal and ventral CA1 hippocampal synapses. *Hippocampus* 26, 1542–1559. doi: 10.1002/hipo.22655

Kouvaros, S., and Papatheodoropoulos, C. (2017). Prominent differences in sharp waves, ripples and complex spike bursts between the dorsal and the ventral rat hippocampus. *Neuroscience* 352, 131–143. doi: 10.1016/j.neuroscience.2017.03.050

Kulik, A., Vida, I., Fukazawa, Y., Guetg, N., Kasugai, Y., Marker, C. L., et al. (2006). Compartment-dependent colocalization of Kir3.2-containing K+ channels and GABAB receptors in hippocampal pyramidal cells. *J. Neurosci.* 26, 4289–4297. doi: 10.1523/JNEUROSCI.4178-05.2006

Kulik, A., Vida, I., Lujan, R., Haas, C. A., Lopez-Bendito, G., Shigemoto, R., et al. (2003). Subcellular localization of metabotropic GABA(B) receptor subunits

GABA(B1a/b) and GABA(B2) in the rat hippocampus. *J. Neurosci.* 23, 11026–11035.

Labouèbe, G., Lomazzi, M., Cruz, H. G., Creton, C., Luján, R., Li, M., et al. (2007). RGS2 modulates coupling between GABAB receptors and GIRK channels in dopamine neurons of the ventral tegmental area. *Nat. Neurosci.* 10, 1559–1568. doi: 10.1038/nn2006

Lee, K. S., Reddington, M., Schubert, P., and Kreutzberg, G. (1983). Regulation of the strength of adenosine modulation in the hippocampus by a differential distribution of the density of A1 receptors. *Brain Res.* 260, 156–159. doi: 10.1016/0006-8993(83)90779-5

Lei, S., and McBain, C. J. (2003). GABA B receptor modulation of excitatory and inhibitory synaptic transmission onto rat CA3 hippocampal interneurons. *J. Physiol.* 546(Pt 2), 439–453. doi: 10.1113/jphysiol.2002.034017

Lisman, J. E. (1997). Bursts as a unit of neural information: making unreliable synapses reliable. *Trends Neurosci.* 20, 38–43. doi: 10.1016/S0166-2236(96)10070-9

Liu, Q. Y., Dunlap, V., and Barker, J. L. (1994). gamma-Aminobutyric acid type A receptor antagonists picrotoxin and bicuculline alter acetylcholine channel kinetics in cultured embryonic rat skeletal muscle. *Mol. Pharmacol.* 46, 1197–1203.

Lopez-Bendito, G., Shigemoto, R., Kulik, A., Vida, I., Fairen, A., and Lujan, R. (2004). Distribution of metabotropic GABA receptor subunits GABAB1a/b and GABAB2 in the rat hippocampus during prenatal and postnatal development. *Hippocampus* 14, 836–848. doi: 10.1002/hipo.10221

Lynch, G. S., Dunwiddie, T., and Gribkoff, V. (1977). Heterosynaptic depression: a postsynaptic correlate of long-term potentiation. *Nature* 266, 737–739. doi: 10.1038/266737a0

Maggio, N., and Segal, M. (2009). Differential corticosteroid modulation of inhibitory synaptic currents in the dorsal and ventral hippocampus. *J. Neurosci.* 29, 2857–2866. doi: 10.1523/JNEUROSCI.4399-08.2009

Malik, R., Dougherty, K. A., Parikh, K., Byrne, C., and Johnston, D. (2016). Mapping the electrophysiological and morphological properties of CA1 pyramidal neurons along the longitudinal hippocampal axis. *Hippocampus* 26, 341–361. doi: 10.1002/hipo.22526

Manabe, T., Wyllie, D. J., Perkel, D. J., and Nicoll, R. A. (1993). Modulation of synaptic transmission and long-term potentiation: effects on paired pulse facilitation and EPSC variance in the CA1 region of the hippocampus. *J. Neurophysiol.* 70, 1451–1459. doi: 10.1152/jn.1993.70.4.1451

Manahan-Vaughan, D. (2019). *Recording Field Potentials and Synaptic Plasticity from Freely Behaving Rodents. Handbook of Behavioral Neuroscience*, Vol. 28. (New York, NY: Elsevier), 1–42.

Manzoni, O. J., Manabe, T., and Nicoll, R. A. (1994). Release of adenosine by activation of NMDA receptors in the hippocampus. *Science* 265, 2098–2101. doi: 10.1126/science.7916485

Marder, E. (2012). Neuromodulation of neuronal circuits: back to the future. *Neuron* 76, 1–11. doi: 10.1016/j.neuron.2012.09.010

Margrie, T. W., Rostas, J. A., and Sah, P. (2000). Inhibition of transmitter release and long-term depression in the avian hippocampus. *Neurosci. Lett.* 284, 17–20. doi: 10.1016/s0304-3940(00)00992-7

Maruki, K., Izaki, Y., Nomura, M., and Yamauchi, T. (2001). Differences in paired-pulse facilitation and long-term potentiation between dorsal and ventral CA1 regions in anesthetized rats. *Hippocampus* 11, 655–661. doi: 10.1002/hipo.1080

McCormick, D. A., and Nusbaum, M. P. (2014). Editorial overview: neuromodulation: tuning the properties of neurons, networks and behavior. *Curr. Opin. Neurobiol.* 29, iv–vii. doi: 10.1016/j.conb.2014.10.010

Mikroulis, A. V., and Psarropoulou, C. (2012). Endogenous ACh effects on NMDA-induced interictal-like discharges along the septotemporal hippocampal axis of adult rats and their modulation by an early life generalized seizure. *Epilepsia* 53, 879–887. doi: 10.1111/j.1528-1167.2012.03440.x

Milior, G., Castro, M. A., Sciarria, L. P., Garofalo, S., Branchi, I., Ragozzino, D., et al. (2016). Electrophysiological properties of CA1 pyramidal neurons along the longitudinal axis of the mouse hippocampus. *Sci. Rep.* 6:38242. doi: 10.1038/srep38242

Miller, R. J. (1998). Presynaptic receptors. *Annu. Rev. Pharmacol. Toxicol.* 38, 201–227. doi: 10.1146/annurev.pharmtox.38.1.201

Molyneaux, B. J., and Hasselmo, M. E. (2002). GABA(B) presynaptic inhibition has an in vivo time constant sufficiently rapid to allow modulation at theta frequency. *J. Neurophysiol.* 87, 1196–1205. doi: 10.1152/jn.00077.2001

Moschovos, C., and Papatheodoropoulos, C. (2016). The L-type voltage-dependent calcium channel long-term potentiation is higher in the dorsal compared with the ventral associational/commissural CA3 hippocampal synapses. *Neurosci. Res.* 106, 62–65. doi: 10.1016/j.neures.2015.10.008

Moyer, J. R. Jr., and Disterhoft, J. F. (1994). Nimodipine decreases calcium action potentials in rabbit hippocampal CA1 neurons in an age-dependent and concentration-dependent manner. *Hippocampus* 4, 11–17. doi: 10.1002/hipo.450040104

Mukunda, C. L., and Narayanan, R. (2017). Degeneracy in the regulation of short-term plasticity and synaptic filtering by presynaptic mechanisms. *J. Physiol.* 595, 2611–2637. doi: 10.1113/jp273482

Nathan, T., and Lambert, J. D. (1991). Depression of the fast IPSP underlies paired-pulse facilitation in area CA1 of the rat hippocampus. *J. Neurophysiol.* 66, 1704–1715. doi: 10.1152/jn.1991.66.5.1704

Osten, P., Wisden, W., and Sprengel, R. (2007). "Molecular mechanisms of synaptic function in the hippocampus: neurotransmitter Exocystosis and Glutamatergic, GABAergic, and Cholinergic Transmission," in *The Hippocampus Book*, eds P. Andersen, R. Morris, D. Amaral, T. Bliss, and J. O'Keefe (Oxford: Oxford University Press), 243–295.

Papaleonidopoulos, V., Kouvaros, S., and Papatheodoropoulos, C. (2018). Effects of endogenous and exogenous D1/D5 dopamine receptor activation on LTP in ventral and dorsal CA1 hippocampal synapses. *Synapse* 72:e22033. doi: 10.1002/syn.22033

Papatheodoropoulos, C. (2008). A possible role of ectopic action potentials in the *in vitro* hippocampal sharp wave-ripple complexes. *Neuroscience* 157, 495–501. doi: 10.1016/j.neuroscience.2008.09.040

Papatheodoropoulos, C. (2015a). Higher intrinsic network excitability in ventral compared with the dorsal hippocampus is controlled less effectively by GABAB receptors. *BMC Neurosci.* 16:75. doi: 10.1186/s12868-015-0213-z

Papatheodoropoulos, C. (2015b). Striking differences in synaptic facilitation along the dorsoventral axis of the hippocampus. *Neuroscience* 301, 454–470. doi: 10.1016/j.neuroscience.2015.06.029

Papatheodoropoulos, C. (2018). Electrophysiological evidence for long-axis intrinsic diversification of the hippocampus. *Front. Biosci.* 23, 109–145. doi: 10.2741/4584

Papatheodoropoulos, C., Asprodini, E., Nikita, I., Koutsona, C., and Kostopoulos, G. (2002). Weaker synaptic inhibition in CA1 region of ventral compared to dorsal rat hippocampal slices. *Brain Res.* 948, 117–121. doi: 10.1016/s0006-8993(02)02958-x

Papatheodoropoulos, C., and Kostopoulos, G. (2000a). Decreased ability of rat temporal hippocampal CA1 region to produce long-term potentiation. *Neurosci. Lett.* 279, 177–180. doi: 10.1016/s0304-3940(99)01002-2

Papatheodoropoulos, C., and Kostopoulos, G. (2000b). Dorsal-ventral differentiation of short-term synaptic plasticity in rat CA1 hippocampal region. *Neurosci. Lett.* 286, 57–60. doi: 10.1016/s0304-3940(00)01084-3

Papatheodoropoulos, C., Moschovos, C., and Kostopoulos, G. (2005). Greater contribution of N-methyl-D-aspartic acid receptors in ventral compared to dorsal hippocampal slices in the expression and long-term maintenance of epileptiform activity. *Neuroscience* 135, 765–779. doi: 10.1016/j.neuroscience.2005.06.024

Petrides, T., Georgopoulos, P., Kostopoulos, G., and Papatheodoropoulos, C. (2007). The GABAA receptor-mediated recurrent inhibition in ventral compared with dorsal CA1 hippocampal region is weaker, decays faster and lasts less. *Exp. Brain Res.* 177, 370–383. doi: 10.1007/s00221-006-0681-6

Pfrieger, F. W., Gottmann, K., and Lux, H. D. (1994). Kinetics of GABAB receptor-mediated inhibition of calcium currents and excitatory synaptic transmission in hippocampal neurons *in vitro*. *Neuron* 12, 97–107. doi: 10.1016/0896-6273(94)90155-4

Power, J. M., Wu, W. W., Sametsky, E., Oh, M. M., and Disterhoft, J. F. (2002). Age-related enhancement of the slow outward calcium-activated potassium current in hippocampal CA1 pyramidal neurons *in vitro*. *J. Neurosci.* 22, 7234–7243. doi: 10.1523/jneurosci.22-16-07234.2002

Quigg, M., Bertram, E. H., and Jackson, T. (1997). Longitudinal distribution of hippocampal atrophy in mesial temporal lobe epilepsy. *Epilepsy Res.* 27, 101–110. doi: 10.1016/s0920-1211(97)01026-7

Regehr, W. G. (2012). Short-term presynaptic plasticity. *Cold Spring Harb. Perspect. Biol.* 4:a005702. doi: 10.1101/cshperspect.a005702

Reis, S. L., Silva, H. B., Almeida, M., Cunha, R. A., Simoes, A. P., and Canas, P. M. (2019). Adenosine A1 and A2A receptors differently control synaptic plasticity in the mouse dorsal and ventral hippocampus. *J. Neurochem.* 151, 227–237. doi: 10.1111/jnc.14816

Roth, F. C., and Draguhn, A. (2012). GABA metabolism and transport: effects on synaptic efficacy. *Neural Plast.* 2012:805830. doi: 10.1155/2012/805830

Sastry, B. R., Goh, J. W., and Auyeung, A. (1986). Associative induction of posttetanic and long-term potentiation in CA1 neurons of rat hippocampus. *Science* 232, 988–990. doi: 10.1126/science.3010459

Scanziani, M. (2000). GABA spillover activates postsynaptic GABA(B) receptors to control rhythmic hippocampal activity. *Neuron* 25, 673–681. doi: 10.1016/s0896-6273(00)81069-7

Scanziani, M., Malenka, R. C., and Nicoll, R. A. (1996). Role of intercellular interactions in heterosynaptic long-term depression. *Nature* 380, 446–450. doi: 10.1038/380446a0

Schreurs, A., Sabanov, V., and Balschun, D. (2017). Distinct properties of long-term potentiation in the dentate Gyrus along the dorsoventral axis: influence of age and inhibition. *Sci. Rep.* 7:5157. doi: 10.1038/s41598-017-05358-1

Schwenk, J., Metz, M., Zolles, G., Turecek, R., Fritzius, T., Bildl, W., et al. (2010). Native GABA(B) receptors are heteromultimers with a family of auxiliary subunits. *Nature* 465, 231–235. doi: 10.1038/nature08964

Serrano, A., Haddjeri, N., Lacaille, J. C., and Robitaille, R. (2006). GABAergic network activation of glial cells underlies hippocampal heterosynaptic depression. *J. Neurosci.* 26, 5370–5382. doi: 10.1523/jneurosci.5255-05.2006

Silver, R. A. (2010). Neuronal arithmetic. *Nat. Rev. Neurosci.* 11, 474–489. doi: 10.1038/nrn2864

Small, S. A., Schobel, S. A., Buxton, R. B., Witter, M. P., and Barnes, C. A. (2011). A pathophysiological framework of hippocampal dysfunction in ageing and disease. *Nat. Rev. Neurosci.* 12, 585–601. doi: 10.1038/nrn3085

Spencer, D. D., Spencer, S. S., Mattson, R. H., Williamson, P. D., and Novelly, R. A. (1984). Access to the posterior medial temporal lobe structures in the surgical treatment of temporal lobe epilepsy. *Neurosurgery* 15, 667–671. doi: 10.1227/00006123-198411000-00005

Strange, B. A., Witter, M. P., Lein, E. S., and Moser, E. I. (2014). Functional organization of the hippocampal longitudinal axis. *Nat. Rev. Neurosci.* 15, 655–669. doi: 10.1038/nrn3785

Thibault, O., and Landfield, P. W. (1996). Increase in single L-type calcium channels in hippocampal neurons during aging. *Science* 272, 1017–1020. doi: 10.1126/science.272.5264.1017

Thompson, A. J. (2013). Recent developments in 5-HT3 receptor pharmacology. *Trends Pharmacol. Sci.* 34, 100–109. doi: 10.1016/j.tips.2012.12.002

Thompson, S. M., Capogna, M., and Scanziani, M. (1993). Presynaptic inhibition in the hippocampus. *Trends Neurosci.* 16, 222–227. doi: 10.1016/0166-2236(93)90160-n

Thompson, S. M., and Gahwiler, B. H. (1992). Comparison of the actions of baclofen at pre- and postsynaptic receptors in the rat hippocampus *in vitro*. *J. Physiol.* 451, 329–345. doi: 10.1113/jphysiol.1992.sp019167

Turecek, R., Schwenk, J., Fritzius, T., Ivankova, K., Zolles, G., Adelfinger, L., et al. (2014). Auxiliary GABAB receptor subunits uncouple G protein βγ subunits from effector channels to induce desensitization. *Neuron* 82, 1032–1044. doi: 10.1016/j.neuron.2014.04.015

Ulrich, D., and Bettler, B. (2007). GABA(B) receptors: synaptic functions and mechanisms of diversity. *Curr. Opin. Neurobiol.* 17, 298–303. doi: 10.1016/j.conb.2007.04.001

Vizi, E. S., and Kiss, J. P. (1998). Neurochemistry and pharmacology of the major hippocampal transmitter systems: synaptic and nonsynaptic interactions. *Hippocampus* 8, 566–607. doi: 10.1002/(sici)1098-1063(1998)8:6<566::aid-hipo2>3.0.co;2-w

Vogt, K. E., and Nicoll, R. A. (1999). Glutamate and gamma-aminobutyric acid mediate a heterosynaptic depression at mossy fiber synapses in the hippocampus. *Proc. Natl. Acad. Sci. U.S.A.* 96, 1118–1122. doi: 10.1073/pnas.96.3.1118

Wilson, C. L., Maidment, N. T., Shomer, M. H., Behnke, E. J., Ackerson, L., Fried, I., et al. (1996). Comparison of seizure related amino acid release in human epileptic hippocampus versus a chronic, kainate rat model of hippocampal epilepsy. *Epilepsy Res.* 26, 245–254. doi: 10.1016/s0920-1211(96)00057-5

Wu, C., Shen, H., Luk, W. P., and Zhang, L. (2002). A fundamental oscillatory state of isolated rodent hippocampus. *J. Physiol.* 540(Pt 2), 509–527. doi: 10.1113/jphysiol.2001.013441

Wu, L. G., and Saggau, P. (1997). Presynaptic inhibition of elicited neurotransmitter release. *Trends Neurosci.* 20, 204–212. doi: 10.1016/s0166-2236(96)01015-6

Zhang, J. M., Wang, H. K., Ye, C. Q., Ge, W., Chen, Y., Jiang, Z. L., et al. (2003). ATP released by astrocytes mediates glutamatergic activity-dependent heterosynaptic suppression. *Neuron* 40, 971–982. doi: 10.1016/s0896-6273(03)00717-7

**Conflict of Interest:** The authors declare that the research was conducted in the absence of any commercial or financial relationships that could be construed as a potential conflict of interest.

*Copyright © 2020 Trompoukis and Papatheodoropoulos. This is an open-access article distributed under the terms of the Creative Commons Attribution License (CC BY). The use, distribution or reproduction in other forums is permitted, provided the original author(s) and the copyright owner(s) are credited and that the original publication in this journal is cited, in accordance with accepted academic practice. No use, distribution or reproduction is permitted which does not comply with these terms.*

frontiers in Molecular Neuroscience

ORIGINAL RESEARCH
published: 11 August 2020
doi: 10.3389/fnmol.2020.00152

# Anxiety and Startle Phenotypes in *Glrb Spastic* and *Glra1 Spasmodic* Mouse Mutants

*Natascha Schaefer[1], Jérémy Signoret-Genest[1,2], Cora R. von Collenberg[1], Britta Wachter[1], Jürgen Deckert[2], Philip Tovote[1], Robert Blum[1] and Carmen Villmann[1]**

[1] *Institute of Clinical Neurobiology, University Hospital, Julius Maximilians University of Würzburg, Würzburg, Germany,*
[2] *Department of Psychiatry, Psychosomatics and Psychotherapy, Center for Mental Health, University Hospital Würzburg, Würzburg, Germany*

A GWAS study recently demonstrated single nucleotide polymorphisms (SNPs) in the human *GLRB* gene of individuals with a prevalence for agoraphobia. *GLRB* encodes the glycine receptor (GlyRs) β subunit. The identified SNPs are localized within the gene flanking regions (3′ and 5′ UTRs) and intronic regions. It was suggested that these nucleotide polymorphisms modify GlyRs expression and phenotypic behavior in humans contributing to an anxiety phenotype as a mild form of hyperekplexia. Hyperekplexia is a human neuromotor disorder with massive startle phenotypes due to mutations in genes encoding GlyRs subunits. *GLRA1* mutations have been more commonly observed than *GLRB* mutations. If an anxiety phenotype contributes to the hyperekplexia disease pattern has not been investigated yet. Here, we compared two mouse models harboring either a mutation in the murine *Glra1* or *Glrb* gene with regard to anxiety and startle phenotypes. Homozygous *spasmodic* animals carrying a *Glra1* point mutation (alanine 52 to serine) displayed abnormally enhanced startle responses. Moreover, *spasmodic* mice exhibited significant changes in fear-related behaviors (freezing, rearing and time spent on back) analyzed during the startle paradigm, even in a neutral context. *Spastic* mice exhibit reduced expression levels of the full-length GlyRs β subunit due to aberrant splicing of the *Glrb* gene. Heterozygous animals appear normal without an obvious behavioral phenotype and thus might reflect the human situation analyzed in the GWAS study on agoraphobia and startle. In contrast to *spasmodic* mice, heterozygous *spastic* animals revealed no startle phenotype in a neutral as well as a conditioning context. Other mechanisms such as a modulatory function of the GlyRs β subunit within glycinergic circuits in neuronal networks important for fear and fear-related behavior may exist. Possibly, in human additional changes in fear and fear-related circuits either due to gene-gene interactions e.g., with *GLRA1* genes or epigenetic factors are necessary to create the agoraphobia and in particular the startle phenotype.

**Keywords: glycine receptor, spastic, fear, anxiety, startle reaction**

OPEN ACCESS

***Edited by:***
*Mary Chebib,*
*The University of Sydney, Australia*

***Reviewed by:***
*Nathan Absalom,*
*The University of Sydney, Australia*
*Deniz Yilmazer-Hanke,*
*University of Ulm, Germany*

****Correspondence:***
*Carmen Villmann*
*Villmann_C@ukw.de*

***Received:*** *02 May 2020*
***Accepted:*** *22 July 2020*
***Published:*** *11 August 2020*

***Citation:***
*Schaefer N, Signoret-Genest J, von Collenberg CR, Wachter B, Deckert J, Tovote P, Blum R and Villmann C (2020) Anxiety and Startle Phenotypes in Glrb Spastic and Glra1 Spasmodic Mouse Mutants. Front. Mol. Neurosci. 13:152. doi: 10.3389/fnmol.2020.00152*

## INTRODUCTION

Disturbances of glycinergic inhibition in the central nervous system have been associated with neuromotor disorders, changes in pain sensation and autism (Harvey et al., 2004; Chung et al., 2010; Pilorge et al., 2016).

Glycine receptors (GlyRs) enable fast synaptic inhibition in the adult spinal cord and brain stem. They are important for motor coordination and respiratory rhythm (Manzke et al., 2010). Together with the $GABA_{A/C}$ receptor, the $5HT_3$ receptors, and nicotinic acetylcholine receptors (nAChRs), GlyRs are members of the superfamily of Cys-loop receptors (CLRs) (Miller and Smart, 2010). Four possible isoforms of GlyR α-subunits are described (α1 to α4), but only one isoform of the β-subunit. The adult synaptic receptor complex in brainstem and spinal cord is composed of 3α:2β subunits (either α1β or α3β) (Durisic et al., 2012; Patrizio et al., 2017). GlyR β has been also detected outside the brainstem and spinal cord e.g., within the cortex, the habenular nucleus of the hypothalamus and the interposed and medial nuclei of the cerebellum suggesting that the β subunit may have other so far unknown functions (Kingsmore et al., 1994; Weltzien et al., 2012).

Numerous studies investigating disturbances in glycinergic inhibition rely on mutations within the receptor genes *GLRA1* and *GLRB* which have been associated with startle disease (hyperekplexia) derogating the nerve-muscle circuit (Schaefer et al., 2012; Chung et al., 2013). Human hyperekplexia patients suffer from exaggerated startle responses, enhanced muscle tone, and stiffness in infancy.

Glycinergic mouse models have been used to study pathomechanisms of startle disease. *Oscillator*, *spasmodic*, and *shaky* mice harbor *Glra1* mutations. The currently only available mouse model carrying a *Glrb* mutation is the *spastic* mouse. *Oscillator* represents a functional *Glra1* NULL mutation due to a microdeletion. *Shaky* and *spasmodic* carry missense mutations in the N-terminus of the GlyR α1 subunit (Schaefer et al., 2012). *Spasmodic* mice harbor a point mutation (A52S) within the GlyR α1 subunit. The A52S mutation reduces the affinity of the neurotransmitter glycine to the GlyRs and at the functional level alters the efficacy of receptor activation (Saul et al., 1994; Plested et al., 2007). *Spasmodic* mice are known to display changes in startle behavior (Plappert et al., 2001). Homozygous *spastic* mice also develop massive startle reactions typical for startle disease (Kingsmore et al., 1994; Becker et al., 2012). The underlying mutation is an insertion of a LINE-1 element into intron 6 of the *Glrb* gene resulting in aberrant splicing and therefore lower expression levels (<25%) of the full-length GlyRs β subunit in homozygous $Glrb^{spa/spa}$ mice (Kingsmore et al., 1994). Heterozygous $Glrb^{+/spa}$ mice, however, do not show any deficits in motor behavior along with preservation of 70–80% of α1/β receptors (Becker et al., 1986; Hartenstein et al., 1996). At functional level, heterozygous *spastic* mice have been investigated electrophysiologically in superficial dorsal horn (SFDH) neurons. The analysis of mIPSCs revealed no changes in rise time, decay time and frequency compared to wild type mice. In contrast, a dramatic change in channel characteristics leading to decreased glycinergic inhibition in SFDH neurons was described for homozygous *spastic* mice (Graham et al., 2003). Current knowledge on heterozygous *spastic* mice indicates reduced GlyR β protein levels as the major consequence of the *Glrb* mutation.

In the human situation, it has been reported that affected patients with startle disease are anxious to fall due to unexpected noise or tactile stimuli (Andermann et al., 1980). Recently, a link of GlyRs to agoraphobia (Deckert et al., 2017) has been suggested. Agoraphobia is a DSM-V or ICD-10 diagnosis assigned to subjects who suffer from disproportionate fear of public places, often perceiving such environments as too open, crowded or dangerous (Wittchen et al., 2010). A recent GWAS study used an Agoraphobic Cognition Questionnaire (ACQ) and identified several allelic variations within the human *GLRB* gene (intronic region and flanking regions 3′ and 5′ UTRs) suggesting *GLRB* as a candidate gene for agoraphobia (Deckert et al., 2017). Family/twin studies have shown familial aggregation in agoraphobia with an estimated heritability of 48% percent for agoraphobia arguing for an inherited component (Mosing et al., 2009). In a family with hyperekplexia, Kirstein and Silfverskiold provided the first evidence that seizures or startle attacks can be "emotionally elicited, i.e., evoked by surprise, fear, or stress" (Kirstein and Silfverskiold, 1958).

Here we comprehensively characterized anxiety-like and startle behavior in male heterozygous *spastic* as well as homozygous *spasmodic* mice. Homozygous *spasmodic* mice displayed significantly decreased grooming and rearing but increased freezing and startle-induced seizure-like motor episodes whereas *spastic* mice were inconspicuous in diverse paradigms measuring startle behavior.

## MATERIALS AND METHODS

### Animals

Adult $Glra1^{spd}$ mice (*spasmodic*, JAX stock #001278) and $Glrb^{spa}$ mice (*spastic*, JAX stock #000241) both from Jackson Laboratories, Bar Harbor, ME, United States were used (Kingsmore et al., 1994; Ryan et al., 1994). Mice of both lines were kindly provided by Cord-Michael Becker (FAU Erlangen-Nürnberg, Germany) and transferred into the animal facility of the Institute of Clinical Neurobiology (Würzburg, Germany). Here, *spastic* mice were backcrossed to C57BL/6J background for at least 15 generations. *Spasmodic* mice have a C3H background and were backcrossed for more than 15 generations. All experiments were in accordance with European Union guidelines and approved by our local veterinary authority (Veterinäramt der Stadt Würzburg) and Committee on the Ethics of Animal Experiments (Regierung von Unterfranken, Würzburg). The experiments were authorized under reference numbers 55.2-2531.01-09/14; 55.2.2-2532.2-536.

For behavioral investigation, male mice (wild type animals $Glra1^{+/+}$ and homozygous mutants $Glra1^{spd/spd}$ and $Glrb^{+/+}$ and $Glrb^{+/spa}$ animals always from same litters) were transferred to the behavioral unit at an age of 10–11 weeks where they were kept for 1 week prior to experiments until the end of the study. Male mice were housed individually with access to water and food

*ad libitum* at a 12 h light/dark rhythm with lights on at 6.30 a.m. Behavioral studies were performed between 7 a.m. and 6 p.m. during the light cycle. Bodyweight was checked 1 day prior to each behavioral experiment.

## Mouse Genotyping

Genotyping of mice was performed from an ear punch at the age of 3 weeks. Genotypes of *spastic* mice were defined via PCR before and after experimental procedure: $Glrb^{+/spa}$ produce a 250 and 200 bp product with primer pairs AIN/SIN and AIN/SPA (AIN: AACACAGAGCAATTATATTTTAGAAG; SIN: AAGAAGACAGAGCTTTCCATTGT; SPA: AATTTCCTA AGTTCCGGT) in a standard PCR protocol. Wild type mice from the same litter gave rise to only 250 bp product combining AIN with SIN.

Genotypes of *spasmodic* mice were defined via PCR before and after experimental procedure. $Glra1^{+/spd}$ produce a 194 and 187 bp product with primer pairs N/rev and M/rev (N: TACTCACCTATGGTTGTCTCAGC; M: TACTCACCTATGGT TGTCTCAGA; rev: TAGTCTGGCAGAGATGCTAAATG) in a standard PCR protocol. In wild type control mice of the same litter, the PCR gave rise to a 194 bp product, in homozygous $Glra1^{spd/spd}$ only a 187 bp fragment was obtained.

## Rotarod

Motor coordination of mice was tested using a rotarod (accelerating rotarod, Ugo Basile). The latency until mice fell off the rod or started clinging to the rod was recorded. Nine wild type $Glrb^{+/+}$ animals and 10 $Glrb^{+/spa}$ were tested at 1 day in three trials with a 2 h break in between. Each trial consisted of two runs. Starting speed was 5 rpm and accelerated every 30 s until 50 rpm. Total duration was 4.5 min.

## Open Field

Wild type mice $Glra1^{+/+}$ and homozygous $Glra1^{spd/spd}$ mice were placed in a 48 × 48 cm square box, illuminated with ∼40 lux. Animals were monitored for 5 min each and tracked with the Video Mot Software (TSE Systems, Bad Homburg, Germany). For analysis, the box was divided into fields of interest: center of the arena (24 × 24 cm) versus the periphery. Entries into the center, time spent in the center and traveled distances were recorded using a one-point body tracking.

## Elevated Plus Maze

The elevated plus maze (EPM) made of white frosted plastic was used to assess anxiety-like behavior by analyzing the activity in open versus closed arms (Walf and Frye, 2007). The EPM (TSE Systems, Bad Homburg, Germany; length of arm: 30 cm, width: 5 cm, height of closed arm: 15 cm, height above ground: 48 cm) consisted of two closed and two open arms. Luminosity was adjusted to ∼ 60 lux. Mice were video tracked for 10 min using the Video Mot Software (TSE Systems, Bad Homburg, Germany, camera: Logitech). The following parameters were analyzed and compared between open and closed arms: distance traveled and time spent in open and closed arms for the first 5 min.

## Dark/Light Test

Mice were subjected to a dark/light transition test to determine the innate aversion of rodents to brightly illuminated areas and their spontaneous exploratory behavior. The dark-light transition test was performed in the open field (OF) arena. A red acrylic glass box of 47 × 16 × 25 cm was positioned in the box. The dark compartment box carried a small entrance and covered one third of the box. The rest of the box was brightly illuminated. Mouse movements were tracked for 10 min using the Video Mot Software (TSE Germany, camera: Logitech). The following parameters were recorded and analyzed: distance traveled in the light compartment and time spent in each compartment.

## Hot Plate

The hot plate setup (custom made) consisted of a viewing jar, a hollow acrylic glass cylinder (18.7 cm high and 14.2 cm wide) placed on a hot plate (IKA, RCT basic, Staufen, Germany). The temperature was regulated and monitored with a thermometer (IKA, ETS-D5, Staufen, Germany) connected to the metal block. Mice were placed in the viewing jar with the metal block heated up to 54°C (±1°C). The time until the mice licked their hind paws was measured, and the mice were immediately removed from the plate. If the mice started jumping or vocalizing, they were immediately removed from the plate. If none of these criteria were applicable mice were taken off the hot plate after 30 s to prevent tissue damage or other injuries.

## Startle Behavior

A motion sensitive platform with three piezoelectric sensors that transduced the animal's motion into a voltage signal was enclosed by a polycarbonate mouse cage separated into two non-contacting sections held by an aluminum frame. The motion-sensitive platform was custom-made as described in Daldrup et al. (2015). The lower section of the mouse cage (length: 25 cm, width: 19 cm, height: 10.5 cm) was suspended ∼0.5 cm above the motion sensitive platform, and the upper section (25 × 19 × 11.5 cm) had an LED port attached to the outer part in order to signal the triggering of the white noise. The startle apparatus was located inside a sound attenuated box (100 × 80 × 116 cm) and dimly lit from above by a circular LED lamp. The piezoelectric voltage signal was continuously recorded at a 5 kHz sampling rate. The startle stimuli consisted of wide band white noise bursts (20 ms duration) generated by an RZ6 multi-processor and delivered via a multi-field magnetic speaker (MF1) located 20 cm above the motion sensitive platform. The triggering of the startle stimuli was controlled by a Real-time Processor Visual Design Studio software (RPvdsEx; RZ6, MF1 and RPvdsEx are from Tucker-Davis Technologies, Alachua, FL, United States).

A camera located on the side of the cage controlled by video tracking software (CinePlex Studio; Plexon Inc., Dallas, TX, United States) was used to record the animal's behavior during the startle experiments. Mice were acclimated to the context for 300 s, during which no sound was presented. This was immediately followed by 20 startle-eliciting white noise bursts, presented with a randomized inter-stimulus interval

of 30–50 s. The 20 bursts were presented in five series, each containing four different intensities (70, 80, 90, and 100 dB) in a pseudorandomized order. Total duration of startle paradigm was 1110 s.

The startle amplitude was defined as the maximum amplitude in the voltage signal occurring within a 100 ms time window after the onset of each white noise burst, whose threshold was above the mean ± 2 standard deviations of a 500 ms pre-stimulus voltage baseline.

## Fear Conditioning

Mice were subjected to auditory fear conditioning in a brightly illuminated square context (27 cm × 27 cm) with a metal grid floor. A train of 20 tone beeps (7.5 kHz, 75 dB sound pressure level, 500 ms duration, 500 ms inter-beep-interval) was used as the conditioned stimulus (CS) and an electrical foot-shock (0.7 mA dc = direct current, 1 s duration) was used as the unconditioned stimulus (US). During the conditioning session, the mice were exposed to three back-to-back CS–US pairings with a baseline period of 180 s and a minimal inter-stimulus interval of 80 s. On the day after conditioning, mice were exposed to four CS-only presentations in a dimly illuminated context different from the conditioning context after a baseline period of 180 s. While the conditioning context was cleaned with 70% ethanol, the retrieval context was wiped down with 1% acetic acid.

Sounds and shocks presentations were controlled by the same system as for the startle experiments, and movies were recorded from top with the Plexon Cineplex software. The animal's motion was computed from the video recordings by determining the pixel change across frames with custom written MATLAB (MathWorks) code. Freezing episodes were defined as periods when the motion was below an absolute threshold value (the same was used for all the animals). Only events longer than 2 s were defined as freezing episodes, and events closer than 200 ms were merged.

## Statistical Analysis

Data are represented as mean ± S.E.M. (standard error of the mean) and were analyzed using Graph Pad Prism or Origin 9 Software. Differences between genotypes were tested using unpaired *t*-test except for analysis of the startle data where a repetitive ANOVA (two-way ANOVA) with Bonferroni *post hoc* test was performed. The 0-hypothesis was rejected at a level of $p < 0.05$.

# RESULTS

## Heterozygous *Glrb*$^{+/spa}$ Mice Exhibit Normal Motor Behavior and No Change in Pain Sensation Compared to Wild Type Control Animals

Previous studies linked the GlyR β subunit to fear and anxiety-like behavior (Deckert et al., 2017; Lueken et al., 2017). Deckert et al. (2017) demonstrated in humans with *GLRB* polymorphisms an increase in startle responses. Likewise, heterozygous *spastic* mice spent less time in the center than in the periphery of an open field compared to wild type control animals.

In the present study, heterozygous *spastic* mice were investigated to further elucidate the impact of the mutant GlyR β subunit gene on anxiety-like behavior. *Spastic* mice harbor a LINE-1 insertion within intron 6 of the *Glrb* gene (**Figure 1A**) leading to aberrant splice variants of the GlyR β subunit

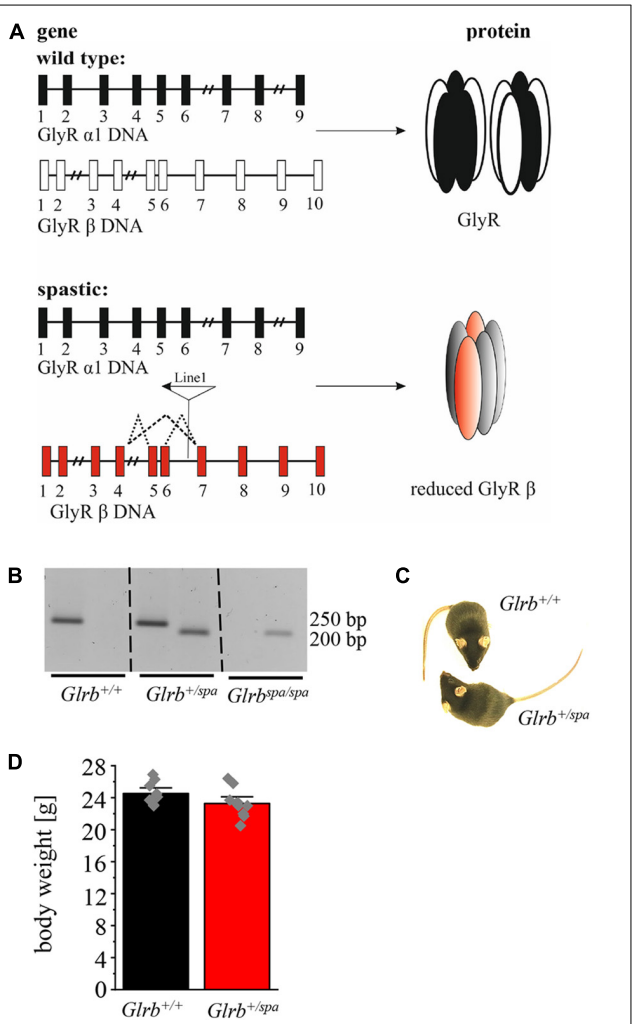


**FIGURE 1 |** A LINE-1 insertion into the *Glrb* gene underlies the mouse mutant *spastic*. **(A)** Schematic overview of *Glra1* (9 exons) and *Glrb* (10 exons) genes and protein level. Upper part shows the wild type situation (black and white), lower part depicts the situation in *spastic* mice (black and red). Left column depicts changes at DNA levels, see insertion of LINE-1 element in *Glrb* generating *spastic* mice (red exons) leading to different splice variants indicated by dotted lines. Right column: protein level of GlyRs. Note that the amount of the full length GlyR β is reduced in *spastic* mice. **(B)** Representative image of genotyped mice (*Glrb*$^{+/+}$, *Glrb*$^{+/spa}$, and *Glrb*$^{spa/spa}$ mice). Wild type (wt) animals show a single 250 bp band, heterozygous animals show two bands (250 and 200 bp), homozygous *spastic* mice display a band of 200 bp. **(C)** Images of wt *Glrb*$^{+/+}$ and heterozygous *spastic* *Glrb*$^{+/spa}$ animals with no obvious changes in size, and appearance of the coat. **(D)** Comparison of the body weight of *Glrb*$^{+/spa}$ mice ($n = 10$, red bar) and *Glrb*$^{+/+}$ mice ($n = 9$, black bar) investigated in this study. Body weight data show mean values ± standard error of the mean (S.E.M). Single data points are shown as gray color squares.

resulting in reduced full-length protein (Becker et al., 2012). Following genotyping of *spastic* mice (**Figure 1B**), the phenotypic appearance of $Glrb^{+/spa}$ mice compared to $Glrb^{+/+}$ wild type (wt) littermates was investigated. No differences in the outer appearance like quality of fur (color or thickness) was observed (**Figure 1C**). In addition, no differences in body weight were detected ($Glrb^{+/spa}$ $n$ = 10, 23.3 ± 0.6 g; $Glrb^{+/+}$ $n$ = 9, 24.5 ± 0.5 g; $p$ = 0.11, $t$ = 1.697, df = 17, $F$-value = 1.608) (**Figure 1D**).

As impaired motor behavior interferes with the readout of anxiety tests, we further analyzed motor coordination in wild type animals versus heterozygous *spastic* littermates. Performing accelerating rotarod test (**Figure 2A**), heterozygous *spastic* mice did not show differences in time spent on the rod ($n$ = 10, 205.1 ± 6.6 s) in comparison to wild type littermates ($n$ = 9, 201.4 ± 9.7 s; $p$ = 0.75, $t$ = 0.32, df = 17, $F$-value = 1.945). In the EPM paradigm, no significant changes were observed in the distance traveled ($Glrb^{+/spa}$ $n$ = 10, 11 ± 2.2 m; $Glrb^{+/+}$ $n$ = 9, 10 ± 1.0 m; $p$ = 0.45, $t$ = 0.76, df = 17, $F$-value = 1.983) (**Figure 2** B). The hot plate test investigates the thermal nociception of rodents (Allen and Yaksh, 2004). The test was used to exclude changes in perception of heterozygous *spastic* mice due to changed *Glrb* levels. Wild type and heterozygous *spastic* mice stayed 12 s on the hot plate ($Glrb^{+/spa}$ $n$ = 10, 12.2 ± 0.5 s; $Glrb^{+/+}$ $n$ = 10, 12.1 ± 1.4 s; $p$ = 0.96, $t$ = 0.05, df = 18, $F$-value = 1.7) (**Figure 2C**). We conclude that $Glrb^{+/spa}$ animals fulfill the prerequisites such as unchanged motor tasks to further study fear-related behavior.

## Heterozygous *Spastic* Mice Reveal Only Slight Preferences for the Dark Compartment

To investigate the impact of *Glrb* levels on fear-related behavior, heterozygous $Glrb^{+/spa}$ mice were monitored in the EPM and in the dark/light test and compared to wild type control littermates.

No differences in the time spent in open and closed arms were detected between heterozygous *spastic* mice and control animals (closed arms: $Glrb^{+/spa}$ $n$ = 10, 2.9 ± 0.2 min; $Glrb^{+/+}$ $n$ = 9, 3.1 ± 0.2 min; $p$ = 0.42, $t$ = 0.817, df = 17, $F$-value = 1.0; open arms: $Glrb^{+/spa}$ $n$ = 10, 2.1 ± 0.2 min; $Glrb^{+/+}$ $n$ = 9, 1.8 ± 0.2 min; $p$ = 0.42, $t$ = 0.817, df = 17, $F$-value = 1.0). Both, wild type and heterozygous *spastic* animals preferred the closed arms compared to the open arms (**Figure 3A**). In line with the total distance traveled (**Figure 2B**), the distances walked in the open and the closed arms were unaltered between heterozygous *spastic* mice and wild type littermates (closed arms: $Glrb^{+/spa}$ $n$ = 10, 7.0 ± 0.5 m; $Glrb^{+/+}$ $n$ = 9, 6.9 ± 0.8 m; $p$ = 0.91, $t$ = 0.102, df = 17, $F$-value = 1.783; open arms: $Glrb^{+/spa}$ $n$ = 10, 2.1 ± 0.2 m; $Glrb^{+/+}$ $n$ = 9, 1.9 ± 0.2 m; $p$ = 0.21, $t$ = 1.299, df = 17, $F$-value = 1.275, **Figure 3B**). To further examine anxiety-related behavior, the dark /light test was performed. Heterozygous $Glrb^{+/spa}$ mice were investigated for the time spent in the light compartment or the dark compartment of the arena. Wild type littermates were expected to explore the light compartment, spending more time in the light than in the dark area. Indeed, $Glrb^{+/+}$ mice spent significantly more time in the light than in the dark compartment (light compartment: $Glrb^{+/+}$ $n$ = 10, 2.9 ± 0.3 min; dark compartment: $Glrb^{+/+}$ $n$ = 10, 2.1 ± 0.3 min; $p$ = 0.046, $t$ = 2.139, df = 18, $F$-value = 1.0) whereas heterozygous $Glrb^{+/spa}$ spent the same amount of time within dark and light compartments (dark compartment: $Glrb^{+/spa}$ $n$ = 10, 2.5 ± 0.3 min; $Glrb^{+/+}$ $n$ = 10, 2.1 ± 0.3 min; $p$ = 0.37, $t$ = 0.9132, df = 18, $F$-value = 1.526; light compartment: $Glrb^{+/spa}$ $n$ = 10, 2.5 ± 0.3 min; $Glrb^{+/+}$ $n$ = 10, 2.9 ± 0.3 min; $p$ = 0.37, $t$ = 0.9132, df = 18, $F$-value = 1.526). The slightly increased time spent in the dark arena did not, however, reach significance (**Figure 3C**). Mice were also monitored for the distance traveled within the light compartment. The determination of the distance traveled in the dark compartment was impossible due to experimental setup. As the distance depends on the time spent within the light compartment, the traveled distance divided by time was analyzed. Again, no obvious differences in distance traveled were observed between both genotypes ($Glrb^{+/spa}$ $n$ = 10, 2.5 ± 0.3 m/min; $Glrb^{+/+}$ $n$ = 9, 2.9 ± 0.3 m/min; $p$ = 0.33, $t$ = 0.99, df = 18, $F$-value = 1.035) (**Figure 3D**).

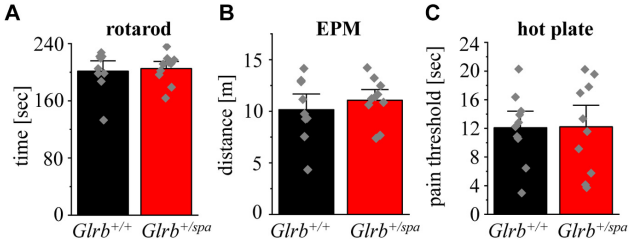


**FIGURE 2 |** Motor behavior and pain sensation are unaffected in heterozygous *spastic* animals. **(A)** Rotarod performance of $Glrb^{+/spa}$ mice ($n$ = 10, red bar) and $Glrb^{+/+}$ mice ($n$ = 9, black bar) with accelerating speed. Time until mice fall off the rod is shown as mean. **(B)** Traveled distance of $Glrb^{+/spa}$ mice ($n$ = 10, red bar) and $Glrb^{+/+}$ mice ($n$ = 9, black bar) within open and closed arms in the elevated plus maze (EPM) test is depicted. **(C)** $Glrb^{+/spa}$ mice ($n$ = 10, red bar) and $Glrb^{+/+}$ mice ($n$ = 10, black bar) were placed on a hot plate. Threshold until mice licking their hind paws was detected. Error bars refer to S.E.M. values. Data points are shown as gray color squares.

## *Glra1* Mutant Mice Are Not Anxious to Cross Open Spaces

To study if the *Glra1* gene has an impact on anxiety-related behavior, we used homozygous *spasmodic* mice. *Spasmodic* is a mouse line carrying a spontaneous mutation A52S in the *Glra1* gene resulting in hyperekplexia (**Figure 4A**) due to lower affinity to the agonist glycine (Saul et al., 1994). It has been reported from humans carrying a *GLRA1* mutation and thus suffering from hyperekplexia that the affected patients are anxious to fall upon exposure to unexpected noise or tactile stimuli (Andermann et al., 1980).

Following genotyping (**Figure 4B**), homozygous *spasmodic* mice were investigated for changes in their outer appearance e.g., quality of fur (color and thickness). Except provoking a startle reaction, homozygous *spasmodic* mice cannot be distinguished from wild type littermates (**Figure 4C**). In addition, no differences in body weight were detectable. Homozygous

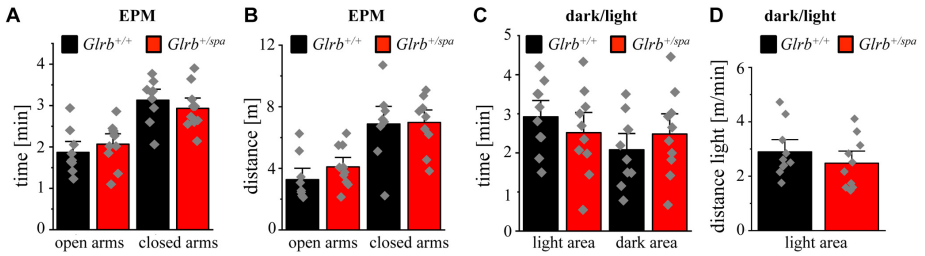


**FIGURE 3 |** Heterozygous *spastic* mice prefer protected areas. **(A)** Time spent and **(B)** distance traveled in closed or open arms in the EPM for $Glrb^{+/spa}$ mice ($n$ = 10, red bars) and $Glrb^{+/+}$ mice ($n$ = 9, black bars). **(C)** Times spent within the dark or light compartments are detected for $Glrb^{+/spa}$ mice ($n$ = 10, red bars) and $Glrb^{+/+}$ mice ($n$ = 10, black bars). **(D)** Distance traveled for $Glrb^{+/spa}$ mice ($n$ = 10, red bar) and $Glrb^{+/+}$ mice ($n$ = 10, black bar) within the light compartment divided by time spent within the light compartment is depicted as bar diagram. Data are presented as mean values ± S.E.M. Data points are shown as gray color squares.

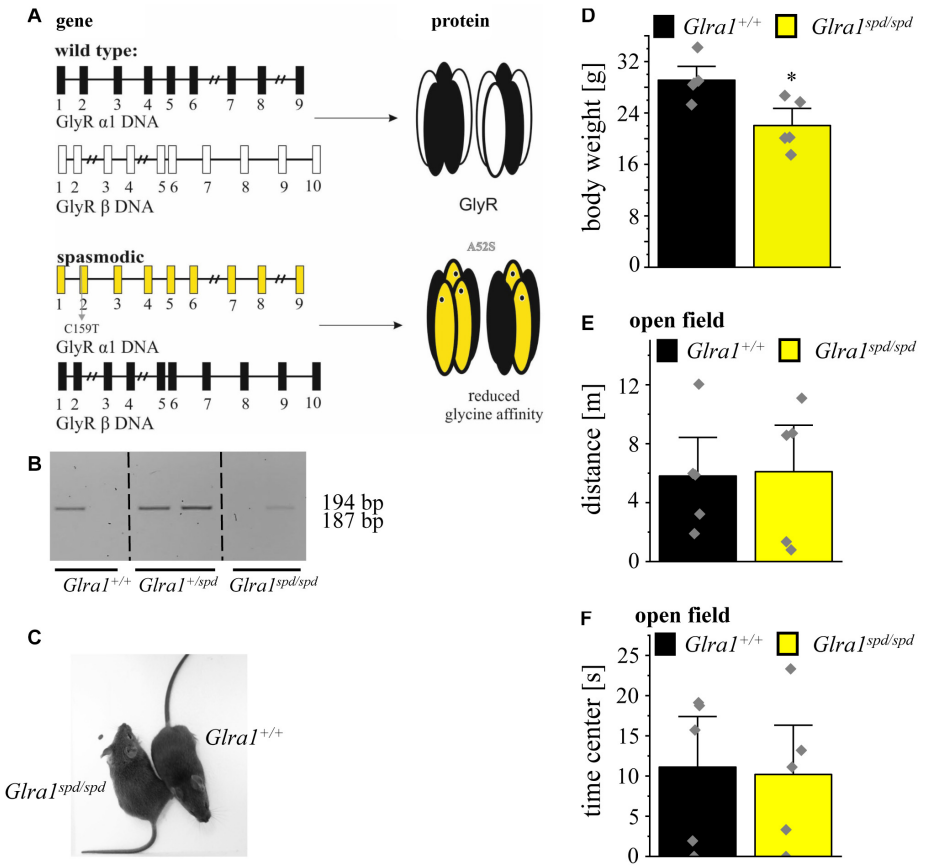


**FIGURE 4 |** Homozygous *spasmodic* mice show no anxiety-like behavior. **(A)** Schematic overview of *Glra1* (9 exons) and *Glrb* (10 exons) genes in *spasmodic* mice. Upper part shows the wild type situation (black and white), lower part depicts the situation in *spasmodic* mice (yellow and black). Left column depicts changes at DNA level, note the base pair exchange C159T in exon 2 of *Glra1* (yellow) which leads to a missense mutation A52S at the protein level. Right column: Protein level of GlyR with $\alpha1^{A52S}$ marked by a black dot within the GlyR α1 subunit (yellow). **(B)** Genotyping of $Glra1^{+/+}$, $Glra1^{+/spd}$, and $Glra1^{spd/spd}$ mice. Wild type animals show a single 194 bp band, heterozygous animals show two amplimers (194 and 187 bp), homozygous *spasmodic* mice display a band at 187 bp. **(C)** Images of $Glra1^{+/+}$ and $Glra1^{spd/spd}$ animals are shown. **(D)** Body weight of $Glra1^{spd/spd}$ mice ($n$ = 5, yellow bar) and $Glra1^{+/+}$ mice ($n$ = 5, black bar). Level of significance refers to $^*p < 0.05$. **(E)** Traveled distance within an open field arena of $Glra1^{spd/spd}$ mice ($n$ = 5, yellow bar) and $Glra1^{+/+}$ mice ($n$ = 5, black bar). **(F)** Time spent in the center of the open field documented for $Glra1^{spd/spd}$ mice ($n$ = 5, yellow bar) and $Glra1^{+/+}$ mice ($n$ = 5, black bar). Data points are shown as gray color squares.

*spasmodic* mice exhibited less body weight but had no obvious constraints in motor behavior ($Glra1^{+/+}$ $n$ = 5, 29.1 ± 1.4 g; $Glra1^{spd/spd}$ $n$ = 5, 22.4 ± 1.8 g; $p$ = 0.0148, $t$ = 3.095, df = 8, $F$-value = 1.526) (**Figure 4D**).

To exhibit if a mutation in the *Glra1* gene interferes with anxiety-related behavior, homozygous *spasmodic* mice were tested in the open field paradigm. Neither the distance traveled ($Glra1^{spd/spd}$ $n$ = 5, 6.1 ± 2.1 m; $Glra1^{+/+}$ $n$ = 5, 5.8 ± 1.8 m;

$p = 0.92$, $t = 0.1088$, df = 8, $F$-value = 1.455) (**Figure 4E**) within the open field arena nor the time spent within the center (*Glra1*$^{spd/spd}$ $n = 5$, *Glra1*$^{+/+}$ $n = 5$, 11.1 ± 4.2 s; 10.2 ± 4.1 s; $p = 0.87$, $t = 0.15$, df = 8, $F$-value = 1.054) (**Figure 4F**) of the open field differed between wild type and homozygous *Glra1*$^{spd/spd}$ littermates. Thus, a mutation in the *Glra1* gene had no impact on anxiety-related behavior at least not in the open field test investigated here.

## *Spasmodic* Mice Show Extensive Startle Reactions With Fear-Related Behavior During Startle

We further focused on the startle reaction paradigm in mice, a typical symptom in hyperekplexia in humans and in rodents. Moreover, it was previously shown that probands with polymorphisms within the *GLRB* gene show an increased startle behavior (Deckert et al., 2017).

A schematic overview about the test paradigms to evoke a startle response by increased intensities of acoustic noises is shown in **Figure 5A**. During the test, mice were exposed to increasing sound pressure levels of 70–100 dB in five blocks with pseudo-randomized order and the startle reaction was analyzed with the help of a piezo sensitive platform to measure the startle amplitude. An increase in startle response was visible for homozygous *spasmodic* mice exhibiting a sound induced startle attack, leading to falls on their backs with prolonged righting time (**Figure 5B**). In contrast, wild type mice did not fall on their backs and displayed only minor startle reactions. Analyzing the startle amplitude of homozygous *Glra1*$^{spd/spd}$ mice, a significant increase in the startle responses was detected with increasing stimulus intensities (repetitive ANOVA (genotype × stimulus intensity) $F(3,27) = 1.728$; $p = 0.1850$; *Glra1*$^{spd/spd}$ $n = 5$, 70 dB: 568 ± 125; 80 dB: 924 ± 176; 90 dB: 1013 ± 105; 100 dB: 1127 ± 206; *Glra1*$^{+/+}$ $n = 5$, 70 dB: 52 ± 8; 80 dB: 126 ± 14; 90 dB: 283 ± 34; 100 dB: 450 ± 69; 70 dB: $p = 0.002$, $t = 3.824$; 80 dB: $p < 0.0001$,

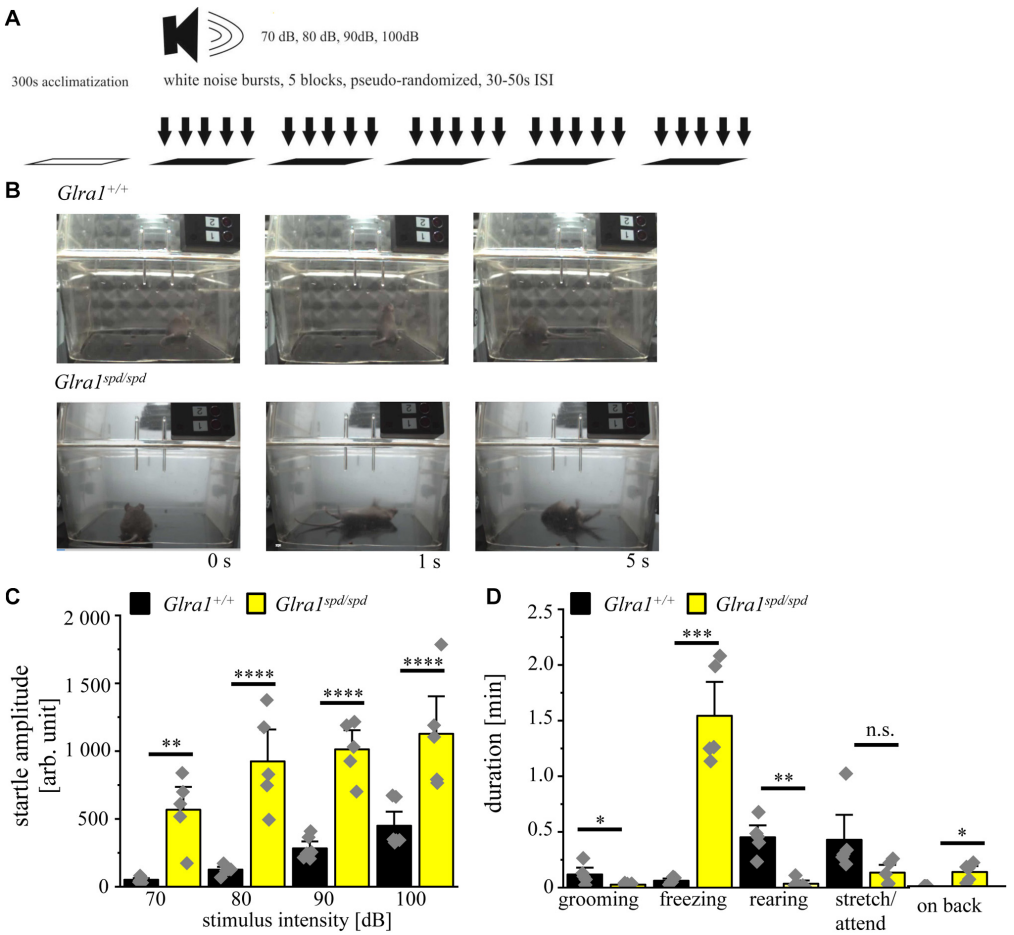


**FIGURE 5 |** Homozygous *spasmodic* mice show extensive startle reactions. **(A)** Schematic overview of the conducted startle test. After 300 s of acclimatization, five blocks with white noise bursts of 70–100 dB in pseudo-randomized order were applied with 30–50 s pause between blocks. **(B)** Representative images of *Glra1*$^{+/+}$ and *Glra1*$^{spd/spd}$ animals during startle test. Note that *Glra1*$^{spd/spd}$ fall on their back immediately after the tone due to evoked startle responses. **(C)** Startle amplitude of *Glra1*$^{spd/spd}$ ($n = 5$, yellow bars) and *Glra1*$^{+/+}$ ($n = 6$, black bars) animals during behavioral startle test are depicted with increasing stimulus intensities (70–100 dB). **(D)** Times spent grooming, freezing, rearing, stretch/attend, and laying on back of *Glra1*$^{spd/spd}$ ($n = 5$, yellow bars) and *Glra1*$^{+/+}$ ($n = 6$, black bars) animals were tracked during the startle test (1110 s). Level of significance refer to $^{*}p < 0.05$, $^{**}p < 0.01$, $^{***}p < 0.001$, $^{****}p < 0.0001$. Gray squares refer to single data points.

$t = 5.91$; 90 dB: $p < 0.0001$, $t = 5.407$; 100 dB: $p < 0.0001$, $t = 5.019$; Bonferroni *post hoc* test) (**Figure 5C**).

We further investigated fear-related behavior during the startle test. The time spent grooming, freezing, rearing, stretch/attend and time spent on back were analyzed. Homozygous *spasmodic* mice spent less time grooming and rearing, but spent much more time freezing and on their backs ($Glra1^{spd/spd}$ $n = 5$, grooming: 0.03 ± 0.01 min $p = 0.056$, $t = 2.23$, df = 8, $F$-value = 30.83, freezing: 1.5 ± 0.2 min, $p < 0.0001$, $t = 7.3$, df = 8, $F$-value = 242, rearing: 0.03 ± 0.02 min, $p = 0.0005$, $t = 5.636$, df = 8, $F$-value = 14, stretch/attend: 0.13 ± 0.05 min, $p = 0.09$, $t = 1.874$, df = 8, $F$-value = 10.46, on back: 0.13 ± 0.04 min, $p = 0.0066$, $t = 3.640$, df = 8, $F$-value = invinity; $Glra1^{+/+}$ $n = 5$, grooming: 0.12 ± 0.04 min, freezing: 0.06 ± 0.01 min, rearing: 0.45 ± 0.07 min, stretch/attend: 0.43 ± 0.15 min, on back: 0 ± 0 min) (**Figure 5D**). In summary, homozygous *spasmodic* mice showed an enhanced startle reaction with multiple significant alterations in fear-related behavior during the startle test.

## Heterozygous *Spastic* Mice Lack Enhanced Startle Responses

The established startle paradigm was used to study the startle responses in heterozygous *spastic* mice. Here, no visible changes in the startle response were apparent in heterozygous *spastic* mice compared to controls. Note that heterozygous *spastic* mice did not fall on their backs as homozygous *spasmodic* mice (**Figure 6A**).

The startle amplitudes estimated in *spastic* mice were unaltered between heterozygous *spastic* animals and control wild type littermates [repetitive ANOVA (genotype × stimulus intensity) $F(3,39) = 0.1642$; $p = 0.9198$; $Glrb^{+/spa}$ $n = 8$, 70 dB: 78 ± 15; 80 dB: 121 ± 19, $p = 0.1$; 90 dB: 198 ± 39; 100 dB: 115 ± 41; $Glrb^{+/+}$ $n = 7$, 70 dB: 67 ± 8.6, 80 dB: 90 ± 10,

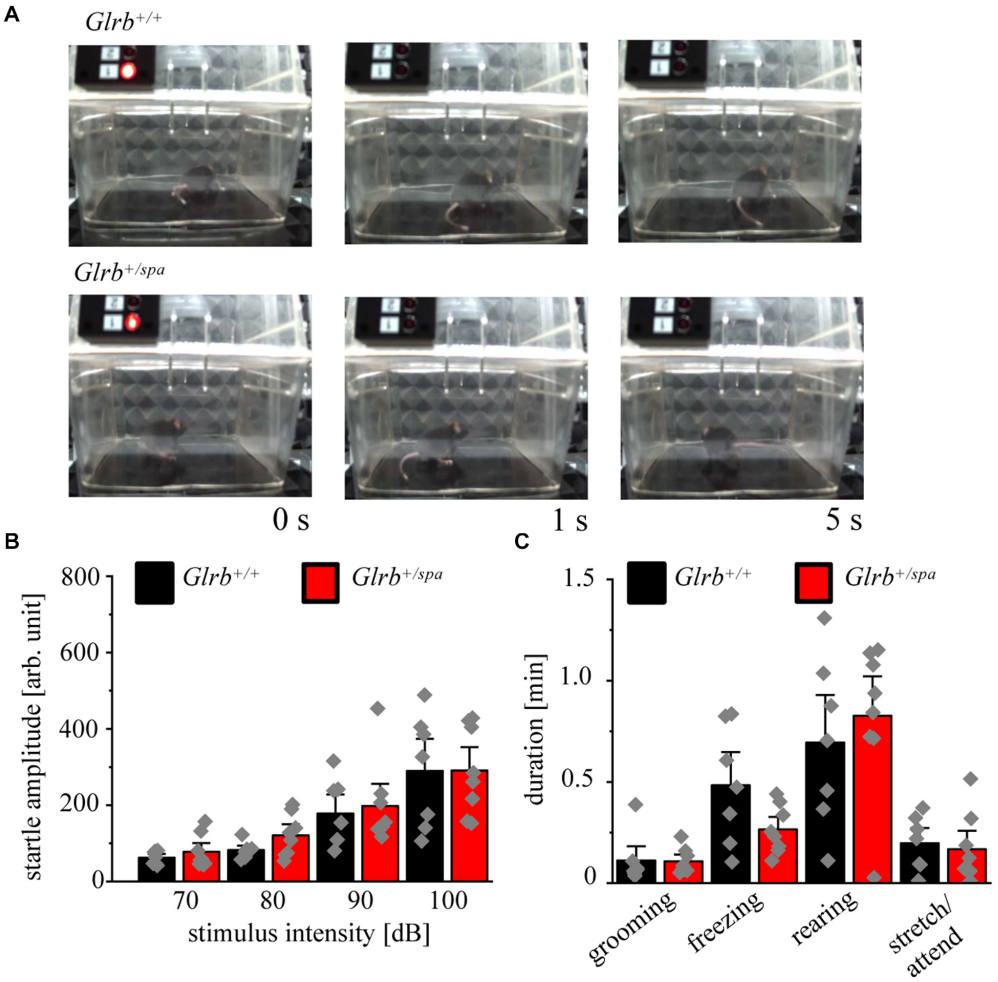


**FIGURE 6 |** Heterozygous *spastic* mice lack enhanced startle responses. **(A)** Representative images of $Glrb^{+/spa}$ ($n = 8$, red bars) and $Glrb^{+/+}$ ($n = 7$, black bars) animals during behavioral startle test. **(B)** Startle amplitudes of $Glrb^{+/spa}$ and $Glrb^{+/+}$ animals during behavioral startle test using increased stimulus intensities (70–100 dB). **(C)** Times spent grooming, freezing, rearing, and stretch/attend of $Glrb^{+/spa}$ ($n = 8$, red bars) and $Glrb^{+/+}$ ($n = 7$, black bars) animals during the startle test (time 1110 s). Data points are shown as gray color squares.

90 dB: 199 ± 41, 100 dB: 1499 ± 230; $p > 0.9999$ for all conditions 70, 80, 90, and 100 dB with $t = 0.3448$ (70 dB); $t = 0.8568$ (80 dB); $t = 0.4319$ (90 dB), $t = 0.02958$ (100 dB); Bonferroni *post hoc* test] (**Figure 6B**). We also documented changes in fear-related behaviors, such as grooming, freezing, rearing and stretch/attend. No significant changes between both genotypes were detectable ($Glrb^{+/spa}$ $n = 8$, grooming: 0.11 ± 0.02 min, $p = 0.9$, $t = 0.08$, df = 13, $F$-value = 3.940; freezing: 0.27 ± 0.04 min, $p = 0.07$, $t = 1.972$, df = 13, $F$-value = 6.0; rearing: 0.83 ± 0.13 min, $p = 0.52$, $t = 0.65$, df = 13, $F$-value = 1.281; stretch/attend: 0.17 ± 0.06 min, $p = 0.72$, $t = 0.36$, df = 13, $F$-value = 1.631; $Glrb^{+/+}$ $n = 7$, grooming: 0.11 ± 0.05 min, freezing: 0.48 ± 0.12 min, rearing: 0.69 ± 0.16 min, stretch/attend: 0.2 ± 0.05 min) (**Figure 6C**). Thus, heterozygous *spastic* mice do not show an increase in fear-related behaviors in comparison to wild type littermates.

## Pavlovian Fear Conditioning Behavior of $Glrb^{+/+}$ and $Glrb^{+/spa}$ Animals

To further investigate the startle behavior of heterozygous *spastic* mice, a Pavlovian fear conditioning test was performed (**Figure 7A**). Pavlovian fear conditioning in mice is a typical paradigm to test for associative learning and memory processing (Johansen et al., 2011; LeDoux, 2014; Tovote et al., 2015). Plasticity defects in amygdala and brain stem circuits are known to interfere with the conditioning of defensive behavior to an auditory cue (tone) (Tovote et al., 2015). In this test, the freezing duration was unchanged in heterozygous *spastic* compared to control animals ($Glrb^{+/spa}$ $n = 8$, freezing 45 ± 9.4%; $Glrb^{+/+}$ $n = 7$, freezing: 59 ± 9.5%; $p = 0.3$, $t = 1.077$, df = 13, $F$-value = 1.445) (**Figure 7B**). In summary, our data demonstrated that heterozygous *spastic* mice do not differ in auditory fear from wild type controls.

# DISCUSSION

Previous studies linked the *GLRB* gene to anxiety disorders, like panic disorder and agoraphobia. Panic disorders are characterized by a rapid rise in anxiety, accompanied by accelerated heart rate, shortness of breath, and losing control upon fear. Emotions and behavioral responses in panic disorders are encoded by a complex, not fully understood, interplay of different neural circuits in the brain (Godemann et al., 2005; Hamm et al., 2016). In humans carrying single non-coding nucleotide *GLRB* variants, increased startle reflexes combined with an avoidance of open spaces were the main behavioral characteristics (Deckert et al., 2017; Lueken et al., 2017).

The present study investigated *spastic* mice carrying a *Glrb* mutation and *spasmodic* mice with a *Glra1* mutation to study anxiety- and fear-related behavior in rodents. Although both mutant mouse lines have different genetic backgrounds (*spastic* C57/BL6; *spasmodic* C3H), C57/BL6 and C3H wild type mice show similar responses to acoustic stimuli. Moreover, the C57/BL6 strain is often used to study fear and anxiety and displays less anxiety-related behavior relative to e.g., 129 substrains (Crawley et al., 1997; Rodgers et al., 2002).

*Spastic* mice display various GlyR β transcripts generated by aberrant splicing as a consequence of a LINE-1 element insertion into intron 6 of the *Glrb* gene. We have observed no alterations in body weight, traveled distances, and pain sensitization in heterozygous *spastic* animals (display around 70–80% full-length GlyR β compared to wild type control animals as a prerequisite to study anxiety-related behavior.

In contrast to the rodent model with reduced GlyR β levels, the rs7688285 variant of the human *GLRB* gene increased *GLRB* transcript expression especially in the midbrain, while expression levels in the forebrain and amygdala were unaffected (Deckert et al., 2017). From genetic *GLRA1* and *GLRB* variants

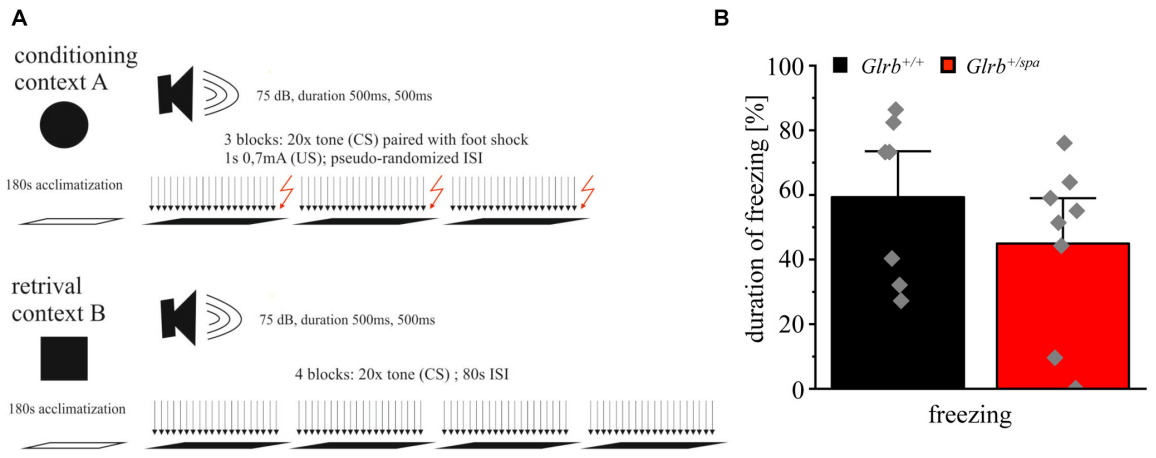


**FIGURE 7 |** Wild type and *spastic* mice show similar contextual fear behavior. **(A)** Schematic overview of the conducted fear conditioning test: Context A shows 180 s of acclimatization followed by three blocks of 20 tones (CS) followed by a foot shock (US) of 1 s and 0.7 mA. Inter-stimulus-intervals (ISIs) are pseudo-randomized. Context B shows the same paradigm without applying foot shocks (US) after each block (four blocks). **(B)** Duration of freezing behavior of $Glrb^{+/spa}$ ($n = 8$; red bar) and $Glrb^{+/+}$ ($n = 7$; black bar) animals shown as the percentage of total time spent freezing with respect to total duration of the fear conditioning paradigm is presented as mean ± S.E.M. Gray squares refer to single data points obtained for one animal.

leading to motor deficits, increased GlyR β expression has not yet been reported. Reduced GlyR expression level or loss of function mutations, however, generate impaired glycinergic signaling, which accounts for muscle stiffness, and increased startle reactions upon sudden tactile or acoustic stimuli. This can even lead to episodes of apnea, when breathing is affected (Manzke et al., 2010). Existing genetic gain of function variants demonstrated increased intracellular chloride level resulting in reduced GlyR cluster numbers and sizes in mature spinal cord neurons (Schwale et al., 2016; Zhang et al., 2016). Increased GlyR β expression as present in *GLRB* risk allele carriers might underlie similar processes resulting in excitation/inhibition imbalances finally explaining the observed general higher defensive reactivity. Therefore, the differences in GlyR β levels in heterozygous *spastic* animals investigated here and in human *GLRB* risk allele carriers might lead to differences in glycinergic signaling.

GlyRs of the α1β or α3β subtypes are mainly expressed in the adult brainstem and spinal cord mediating controlled motor coordination by recurrent inhibition of motoneurons (Malosio et al., 1991; Harvey et al., 2004; Schaefer et al., 2012; Liu and Wong-Riley, 2013). However, GlyR α2 and β transcripts forming homomeric α2 and heteromeric α2β receptors were also identified in the midbrain, cortex, thalamus, lateral amygdala, hippocampus, and cerebellum (Malosio et al., 1991; Waldvogel et al., 2007). GlyR α2 also regulates cortical neurogenesis in the forebrain and promotes interneuron migration (Avila et al., 2013; Morelli et al., 2017). In the adult, α2β receptors are the major subtype in the prefrontal cortex, striatum, and hippocampus regulating neuronal excitability (Jonsson et al., 2012; McCracken et al., 2017). The high abundance of GlyR β in these brain regions might hint to further so far unknown functions of the GlyR β subunit.

Human *GLRB* carriers showed strong activation of the defensive system of the brain specifically in the thalamus and insula. In the early phase of fear conditioning also inverse effects have been observed indicating impaired fear inhibitory learning (Deckert et al., 2017; Lueken et al., 2017). The heterozygous *spastic* mice investigated in this study displayed no significant differences in the EPM or in the light-dark test. This contrasts previous findings, which revealed an avoidance of open spaces in heterozygous *spastic* mice similar to findings from human *GLRB* risk alleles (Deckert et al., 2017). As adult GlyRs are always composed of α and β subunits, we analyzed *spasmodic* mice carrying a *Glra1* mutation in the open field test. Homozygous *spasmodic* mice were, however, indistinguishable from wild type control animals. This result was not unexpected as the GlyR α1 subunit is almost absent from brain regions involved in fear-related behavior, e.g., forebrain, amygdala, thalamus, and hippocampus (Malosio et al., 1991). While human *GLRB* risk allele carriers show anxiety symptoms, they do not suffer from pathological anxiety (Lueken et al., 2017).

A modulation of the startle reflex was identified in human *GLRB* single non-coding nucleotide polymorphism carriers (Deckert et al., 2017; Lueken et al., 2017). Early case reports of human genetic GlyR variants suffering from hyperekplexia mentioned startle attacks evoked by surprise, stress and fear (Kirstein and Silfverskiold, 1958). The acoustic startle response (ASR) to sudden intense stimuli involves neural circuits in the lower brainstem with the caudal pontine reticular nucleus (PnC) as a key element besides the cochlear root neuron and the motoneurons (Koch, 1999; Lang et al., 2000). Genetic mouse models for hyperekplexia show extreme startle responses upon unexpected noise or touch. *Spasmodic* mice displayed significant increases in the startle amplitudes concomitant to enhanced noise intensity. Hence, the *Glra1* defect in *spasmodic* mice cannot be compensated by other α subunits or the β subunit expressed in brainstem. In contrast, heterozygous *spastic* mice do not show enhanced startle responses arguing that the presence of around 70% of full-length GlyR β does not impair the signaling cascade from the cochlear neurons via PnC neurons toward the output motoneurons in the brainstem. Our data are in line with observations from heterozygous *spasmodic* mice and recessive hyperekplexia mutations in humans indicating that one mutated allele (50% GlyR α or β expression) does not disturb glycinergic inhibition with a typical startle phenotype thereof (Plappert et al., 2001; Chung et al., 2010; Schaefer et al., 2015).

The startle reflex is also used to study fear and anxiety states (Davis et al., 2010). Fear states driven by external threat or internal association are defined by defense system activation and its reflexive autonomic (heart beats) and somatic (startle reflex) output (Lang et al., 2000). The defense system, which involves the same brain structures in humans and rodents, includes a subcortical circuit with the central amygdala and outputs to the periaqueductal gray (PAG) and PnC organizing the mode of defense (Fanselow, 1994; Fendt and Fanselow, 1999). Hence, the circuit of the defensive system converges at the level of the PnC with the ASR signaling pathway. Brain nuclei involved in both pathways express GlyR β (Malosio et al., 1991). The defensive phenotype is also characterized by a freezing paradigm. Freezing is described first as crouching, meaning complete absence of movement except for that associated with respiration and tense body posture. Tense body posture includes increased muscle tone (is a third characteristic) (Hagenaars et al., 2014). Interestingly, extreme freezing during the startle paradigm was observed for *spasmodic* mice. Moreover, *spasmodic* mice spent less time grooming and rearing but increased time on their back, in sum showed multiple significant alterations in fear-related behavior. Hence, the glycinergic system might be able to modulate fear conditions.

Learned fear induced by Pavlovian fear conditioning contributes to an enhancement of the ASR. Fear (threat) conditioning combines a conditioned stimulus (CS, such as a tone) with an aversive stimulus (US, like a foot shock). Relay neurons between the amygdala and the PnC such as the PAG contribute to ASR sensitization (Hagenaars et al., 2014). Using classical fear conditioning, the freezing duration was unchanged in heterozygous *spastic* mice compared to wild type controls. As has been pointed out before, the small reduction of the full-length GlyR β protein as present in *spastic* mice does not lead to impaired glycinergic signal transduction. The presence of GlyR β in neural circuits involved in fear-related behavior from the amygdala to the PnC and finally to the output motoneurons suggests that GlyR signaling and

most probably the neurotransmitter glycine might display a modulatory function in these circuits. So far, GABA has been demonstrated to inhibit defensive behavior in the amygdala and the PAG (Tovote et al., 2015, 2016). However, mixed GABAergic/glycinergic synapses that have been described in the brainstem and spinal cord might also exist in other brain regions.

## CONCLUSION

In conclusion, our data showed only subtle differences in fear and anxiety-like phenotypes in *spastic* compared to wild type littermates. While functional alteration of the GlyR α1 in homozygous *spasmodic* mice led to enhanced anxiety-like behavior during the acoustic startle test and to increased startle reactivity, the reduction of GlyR β level in heterozygous *spastic* mice had no effect on anxiety-related behavior.

## DATA AVAILABILITY STATEMENT

The datasets generated for this study are available on request to the corresponding author.

## ETHICS STATEMENT

The animal study was reviewed and approved by the local veterinary authority (Veterinäramt der Stadt Würzburg) and Committee on the Ethics of Animal Experiments, i.e., Regierung von Unterfranken, Würzburg (License numbers 55.2-2531.01-09/14 and 55.2.2-2532.2-536-28).

## AUTHOR CONTRIBUTIONS

CV, JD, RB, NS, BW, and PT participated in research design. CV, NS, JS-G, and CC conducted the experiments. CV, NS, JS-G, CC, and PT performed the data analysis. CV and NS wrote the manuscript. All authors contributed to the article and approved the submitted version.

## FUNDING

This work was funded by the Deutsche Forschungsgemeinschaft (DFG) VI586 to CV, and TRR58 project A10 to RB. NS was supported by funds of the Bavarian State Ministry of Science and the Arts and the University of Würzburg to the Graduate School of Life Sciences (GSLS), University of Würzburg.

## ACKNOWLEDGMENTS

We would like to thank Nadine Vornberger and Dana Wegmann for excellent technical assistance.

## REFERENCES

Allen, J. W., and Yaksh, T. L. (2004). Assessment of acute thermal nociception in laboratory animals. *Methods Mol. Med.* 99, 11–23. doi: 10.1385/1-59259-770-x:139

Andermann, F., Keene, D. L., Andermann, E., and Quesney, L. F. (1980). Startle disease or hyperekplexia: further delineation of the syndrome. *Brain* 103, 985–997. doi: 10.1093/brain/103.4.985

Avila, A., Nguyen, L., and Rigo, J. M. (2013). Glycine receptors and brain development. *Front. Cell Neurosci.* 7:184. doi: 10.3389/fncel.2013.00184

Becker, C. M., Hermans-Borgmeyer, I., Schmitt, B., and Betz, H. (1986). The glycine receptor deficiency of the mutant mouse spastic: evidence for normal glycine receptor structure and localization. *J. Neurosci.* 6, 1358–1364. doi: 10.1523/JNEUROSCI.06-05-01358.1986

Becker, K., Braune, M., Benderska, N., Buratti, E., Baralle, F., Villmann, C., et al. (2012). A retroelement modifies pre-mRNA splicing: the murine Glrb(spa) allele is a splicing signal polymorphism amplified by long interspersed nuclear element insertion. *J. Biol. Chem.* 287, 31185–31194. doi: 10.1074/jbc.M112.375691

Chung, S. K., Bode, A., Cushion, T. D., Thomas, R. H., Hunt, C., Wood, S. E., et al. (2013). GLRB is the third major gene of effect in hyperekplexia. *Hum. Mol. Genet.* 22, 927–940. doi: 10.1093/hmg/dds498

Chung, S. K., Vanbellinghen, J. F., Mullins, J. G., Robinson, A., Hantke, J., Hammond, C. L., et al. (2010). Pathophysiological mechanisms of dominant and recessive GLRA1 mutations in hyperekplexia. *J. Neurosci.* 30, 9612–9620. doi: 10.1523/JNEUROSCI.1763-10.2010

Crawley, J. N., Belknap, J. K., Collins, A., Crabbe, J. C., Frankel, W., Henderson, N., et al. (1997). Behavioral phenotypes of inbred mouse strains: implications and recommendations for molecular studies. *Psychopharmacology* 132, 107–124. doi: 10.1007/s002130050327

Daldrup, T., Remmes, J., Lesting, J., Gaburro, S., Fendt, M., Meuth, P., et al. (2015). Expression of freezing and fear-potentiated startle during sustained fear in mice. *Genes Brain Behav.* 14, 281–291. doi: 10.1111/gbb.12211

Davis, M., Walker, D. L., Miles, L., and Grillon, C. (2010). Phasic vs sustained fear in rats and humans: role of the extended amygdala in fear vs anxiety. *Neuropsychopharmacology* 35, 105–135. doi: 10.1038/npp.2009.109

Deckert, J., Weber, H., Villmann, C., Lonsdorf, T. B., Richter, J., Andreatta, M., et al. (2017). GLRB allelic variation associated with agoraphobic cognitions, increased startle response and fear network activation: a potential neurogenetic pathway to panic disorder. *Mol. Psychiatry* 22, 1431–1439. doi: 10.1038/mp.2017.2

Durisic, N., Godin, A. G., Wever, C. M., Heyes, C. D., Lakadamyali, M., and Dent, J. A. (2012). Stoichiometry of the human glycine receptor revealed by direct subunit counting. *J. Neurosci.* 32, 12915–12920. doi: 10.1523/JNEUROSCI.2050-12.2012

Fanselow, M. S. (1994). Neural organization of the defensive behavior system responsible for fear. *Psychon. Bull. Rev.* 1, 429–438. doi: 10.3758/BF03210947

Fendt, M., and Fanselow, M. S. (1999). The neuroanatomical and neurochemical basis of conditioned fear. *Neurosci. Biobehav. Rev.* 23, 743–760. doi: 10.1016/s0149-7634(99)00016-0

Godemann, F., Siefert, K., Hantschke-Bruggemann, M., Neu, P., Seidl, R., and Strohle, A. (2005). What accounts for vertigo one year after neuritis vestibularis - anxiety or a dysfunctional vestibular organ? *J. Psychiatr. Res.* 39, 529–534. doi: 10.1016/j.jpsychires.2004.12.006

Graham, B. A., Schofield, P. R., Sah, P., and Callister, R. J. (2003). Altered inhibitory synaptic transmission in superficial dorsal horn neurones in spastic and oscillator mice. *J. Physiol.* 551, 905–916. doi: 10.1113/jphysiol.2003.049064

Hagenaars, M. A., Roelofs, K., and Stins, J. F. (2014). Human freezing in response to affective films. *Anxiety Stress Coping* 27, 27–37. doi: 10.1016/j.neubiorev.2014.07.021

Hamm, A. O., Richter, J., Pane-Farre, C., Westphal, D., Wittchen, H. U., Vossbeck-Elsebusch, A. N., et al. (2016). Panic disorder with agoraphobia from a behavioral neuroscience perspective: applying the research principles formulated by the research domain criteria (RDoC) initiative. *Psychophysiology* 53, 312–322. doi: 10.1111/psyp.12553

Hartenstein, B., Schenkel, J., Kuhse, J., Besenbeck, B., Kling, C., Becker, C. M., et al. (1996). Low level expression of glycine receptor beta subunit transgene is sufficient for phenotype correction in spastic mice. *EMBO J.* 15, 1275–1282. doi: 10.1038/sj.emboj.7600828

Harvey, R. J., Depner, U. B., Wassle, H., Ahmadi, S., Heindl, C., Reinold, H., et al. (2004). GlyR α3: an essential target for spinal PGE2-mediated inflammatory pain sensitization. *Science* 304, 884–887. doi: 10.1126/science.1094925

Johansen, J. P., Cain, C. K., Ostroff, L. E., and Ledoux, J. E. (2011). Molecular mechanisms of fear learning and memory. *Cell* 147, 509–524. doi: 10.1016/j.cell.2011.10.009

Jonsson, S., Morud, J., Pickering, C., Adermark, L., Ericson, M., and Soderpalm, B. (2012). Changes in glycine receptor subunit expression in forebrain regions of the Wistar rat over development. *Brain Res.* 1446, 12–21. doi: 10.1016/j.brainres.2012.01.050

Kingsmore, S. F., Giros, B., Suh, D., Bieniarz, M., Caron, M. G., and Seldin, M. F. (1994). Glycine receptor β-subunit gene mutation in spastic mouse associated with LINE-1 element insertion. *Nat. Genet.* 7, 136–141. doi: 10.1038/ng0694-136

Kirstein, L., and Silfverskiold, B. P. (1958). A family with emotionally precipitated drop seizures. *Acta Psychiatr. Neurol. Scand.* 33, 471–476. doi: 10.1111/j.1600-0447.1958.tb03533.x

Koch, M. (1999). The neurobiology of startle. *Prog. Neurobiol.* 59, 107–128. doi: 10.1016/s0301-0082(98)00098-7

Lang, P. J., Davis, M., and Ohman, A. (2000). Fear and anxiety: animal models and human cognitive psychophysiology. *J. Affect. Disord.* 61, 137–159. doi: 10.1016/s0165-0327(00)00343-8

LeDoux, J. E. (2014). Coming to terms with fear. *Proc. Natl. Acad. Sci. U.S.A.* 111, 2871–2878. doi: 10.1073/pnas.1400335111

Liu, Q., and Wong-Riley, M. T. (2013). Postnatal development of glycine receptor subunits α1, α2, α3, and β immunoreactivity in multiple brain stem respiratory-related nuclear groups of the rat. *Brain Res.* 1538, 1–16. doi: 10.1016/j.brainres.2013.09.028

Lueken, U., Kuhn, M., Yang, Y., Straube, B., Kircher, T., Wittchen, H. U., et al. (2017). Modulation of defensive reactivity by GLRB allelic variation: converging evidence from an intermediate phenotype approach. *Transl. Psychiatry* 7:e1227. doi: 10.1038/tp.2017.186

Malosio, M. L., Marqueze-Pouey, B., Kuhse, J., and Betz, H. (1991). Widespread expression of glycine receptor subunit mRNAs in the adult and developing rat brain. *EMBO J.* 10, 2401–2409. doi: 10.1002/j.1460-2075.1991.tb07779.x

Manzke, T., Niebert, M., Koch, U. R., Caley, A., Vogelgesang, S., Hulsmann, S., et al. (2010). Serotonin receptor 1A-modulated phosphorylation of glycine receptor α3 controls breathing in mice. *J. Clin. Invest.* 120, 4118–4128. doi: 10.1172/JCI43029

McCracken, L. M., Lowes, D. C., Salling, M. C., Carreau-Vollmer, C., Odean, N. N., Blednov, Y. A., et al. (2017). Glycine receptor α3 and α2 subunits mediate tonic and exogenous agonist-induced currents in forebrain. *Proc. Natl. Acad. Sci. U.S.A.* 114, E7179–E7186. doi: 10.1073/pnas.1703839114

Miller, P. S., and Smart, T. G. (2010). Binding, activation and modulation of Cys-loop receptors. *Trends Pharmacol. Sci.* 31, 161–174. doi: 10.1016/j.tips.2009.12.005

Morelli, G., Avila, A., Ravanidis, S., Aourz, N., Neve, R. L., Smolders, I., et al. (2017). Cerebral cortical circuitry formation requires functional glycine receptors. *Cereb. Cortex* 27, 1863–1877. doi: 10.1093/cercor/bhw025

Mosing, M. A., Gordon, S. D., Medland, S. E., Statham, D. J., Nelson, E. C., Heath, A. C., et al. (2009). Genetic and environmental influences on the co-morbidity between depression, panic disorder, agoraphobia, and social phobia: a twin study. *Depress. Anxiety* 26, 1004–1011. doi: 10.1002/da.20611

Patrizio, A., Renner, M., Pizzarelli, R., Triller, A., and Specht, C. G. (2017). Alpha subunit-dependent glycine receptor clustering and regulation of synaptic receptor numbers. *Sci. Rep.* 7:10899. doi: 10.1038/s41598-017-11264-3

Pilorge, M., Fassier, C., Le Corronc, H., Potey, A., Bai, J., De Gois, S., et al. (2016). Genetic and functional analyses demonstrate a role for abnormal glycinergic signaling in autism. *Mol. Psychiatry* 21, 936–945. doi: 10.1038/mp.2015.139

Plappert, C. F., Pilz, P. K., Becker, K., Becker, C. M., and Schnitzler, H. U. (2001). Increased sensitization of acoustic startle response in spasmodic mice with a mutation of the glycine receptor α1-subunit gene. *Behav. Brain Res.* 121, 57–67. doi: 10.1016/s0166-4328(00)00385-5

Plested, A. J., Groot-Kormelink, P. J., Colquhoun, D., and Sivilotti, L. G. (2007). Single-channel study of the spasmodic mutation alpha1A52S in recombinant rat glycine receptors. *J. Physiol.* 581, 51–73. doi: 10.1113/jphysiol.2006.126920

Rodgers, R. J., Boullier, E., Chatzimichalaki, P., Cooper, G. D., and Shorten, A. (2002). Contrasting phenotypes of C57BL/6JOlaHsd, 129S2/SvHsd and 129/SvEv mice in two exploration-based tests of anxiety-related behaviour. *Physiol. Behav.* 77, 301–310. doi: 10.1016/s0031-9384(02)00856-9

Ryan, S. G., Buckwalter, M. S., Lynch, J. W., Handford, C. A., Segura, L., Shiang, R., et al. (1994). A missense mutation in the gene encoding the alpha 1 subunit of the inhibitory glycine receptor in the spasmodic mouse. *Nat. Genet.* 7, 131–135. doi: 10.1038/ng0694-131

Saul, B., Schmieden, V., Kling, C., Mulhardt, C., Gass, P., Kuhse, J., et al. (1994). Point mutation of glycine receptor α1 subunit in the spasmodic mouse affects agonist responses. *FEBS Lett.* 350, 71–76. doi: 10.1016/0014-5793(94)00736-5

Schaefer, N., Kluck, C. J., Price, K. L., Meiselbach, H., Vornberger, N., Schwarzinger, S., et al. (2015). Disturbed neuronal ER-Golgi sorting of unassembled glycine receptors suggests altered subcellular processing is a cause of human hyperekplexia. *J. Neurosci.* 35, 422–437. doi: 10.1523/JNEUROSCI.1509-14.2015

Schaefer, N., Vogel, N., and Villmann, C. (2012). Glycine receptor mutants of the mouse: what are possible routes of inhibitory compensation? *Front. Mol. Neurosci.* 5:98. doi: 10.3389/fnmol.2012.00098

Schwale, C., Schumacher, S., Bruehl, C., Titz, S., Schlicksupp, A., Kokocinska, M., et al. (2016). KCC2 knockdown impairs glycinergic synapse maturation in cultured spinal cord neurons. *Histochem. Cell Biol.* 145, 637–646. doi: 10.1007/s00418-015-1397-0

Tovote, P., Esposito, M. S., Botta, P., Chaudun, F., Fadok, J. P., Markovic, M., et al. (2016). Midbrain circuits for defensive behaviour. *Nature* 534, 206–212. doi: 10.1038/nature17996

Tovote, P., Fadok, J. P., and Luthi, A. (2015). Neuronal circuits for fear and anxiety. *Nat. Rev. Neurosci.* 16, 317–331. doi: 10.1038/nrn3945

Waldvogel, H. J., Baer, K., Allen, K. L., Rees, M. I., and Faull, R. L. (2007). Glycine receptors in the striatum, globus pallidus, and substantia nigra of the human brain: an immunohistochemical study. *J. Comp. Neurol.* 502, 1012–1029. doi: 10.1002/cne.21349

Walf, A. A., and Frye, C. A. (2007). The use of the elevated plus maze as an assay of anxiety-related behavior in rodents. *Nat. Protoc.* 2, 322–328. doi: 10.1038/nprot.2007.44

Weltzien, F., Puller, C., O'sullivan, G. A., Paarmann, I., and Betz, H. (2012). Distribution of the glycine receptor β-subunit in the mouse CNS as revealed by a novel monoclonal antibody. *J. Comp. Neurol.* 520, 3962–3981. doi: 10.1002/cne.23139

Wittchen, H. U., Gloster, A. T., Beesdo-Baum, K., Fava, G. A., and Craske, M. G. (2010). Agoraphobia: a review of the diagnostic classificatory position and criteria. *Depress. Anxiety* 27, 113–133. doi: 10.1002/da.20646

Zhang, Y., Bode, A., Nguyen, B., Keramidas, A., and Lynch, J. W. (2016). Investigating the mechanism by which gain-of-function mutations to the α1 glycine receptor cause hyperekplexia. *J. Biol. Chem.* 291, 15332–15341. doi: 10.1074/jbc.M116.728592

**Conflict of Interest:** The authors declare that the research was conducted in the absence of any commercial or financial relationships that could be construed as a potential conflict of interest.

*Copyright © 2020 Schaefer, Signoret-Genest, von Collenberg, Wachter, Deckert, Tovote, Blum and Villmann. This is an open-access article distributed under the terms of the Creative Commons Attribution License (CC BY). The use, distribution or reproduction in other forums is permitted, provided the original author(s) and the copyright owner(s) are credited and that the original publication in this journal is cited, in accordance with accepted academic practice. No use, distribution or reproduction is permitted which does not comply with these terms.*

frontiers in Molecular Neuroscience

REVIEW
published: 11 August 2020
doi: 10.3389/fnmol.2020.00140

# Vestibular Modulation of Long-Term Potentiation and NMDA Receptor Expression in the Hippocampus

*Paul F. Smith*[1,2]*, *Bruno Truchet*[3], *Franck A. Chaillan*[3], *Yiwen Zheng*[1,2] and *Stephane Besnard*[4]

[1]Department of Pharmacology and Toxicology, School of Biomedical Sciences, Brain Health Research Centre, University of Otago, Dunedin, New Zealand, [2]Brain Research New Zealand, The Eisdell Moore Centre for Hearing and Balance Research, University of Auckland, Auckland, New Zealand, [3]Aix Marseille University, CNRS, LNC UMR 7291, FR 3C FR 3512, Marseille, France, [4]Université de Normandie, INSERM U 1075 COMETE, Caen, France

Loss of vestibular function is known to cause spatial memory deficits and hippocampal dysfunction, in terms of impaired place cell firing and abnormal theta rhythm. Based on these results, it has been of interest to determine whether vestibular loss also affects the development and maintenance of long-term potentiation (LTP) in the hippocampus. This article summarizes and critically reviews the studies of hippocampal LTP following a vestibular loss and its relationship to NMDA receptor expression, that have been published to date. Although the available *in vitro* studies indicate that unilateral vestibular loss (UVL) results in reduced hippocampal field potentials in CA1 and the dentate gyrus (DG), the *in vivo* studies involving bilateral vestibular loss (BVL) do not. This may be due to the differences between UVL and BVL or it could be a result of *in vitro/in vivo* differences. One *in vitro* study reported a decrease in LTP in hippocampal slices following UVL; however, the two available *in vivo* studies have reported different results: either no effect or an increase in EPSP/Population Spike (ES) potentiation. This discrepancy may be due to the different high-frequency stimulation (HFS) paradigms used to induce LTP. The increased ES potentiation following BVL may be related to an increase in synaptic NMDA receptors, possibly increasing the flow of vestibular input coming into CA1, with a loss of selectivity. This might cause increased excitability and synaptic noise, which might lead to a degradation of spatial learning and memory.

**Keywords: hippocampal long-term potentiation, NMDA receptors, bilateral vestibular loss, dentate gyrus, CA1, E-S potentiation**

OPEN ACCESS

***Edited by:***
*Akiva Cohen,*
*University of Pennsylvania,*
*United States*

***Reviewed by:***
*Daniel John Whitcomb,*
*University of Bristol, United Kingdom*
*Bin Pan,*
*Medical College of Wisconsin,*
*United States*

***Correspondence:**
*Paul F. Smith*
*paul.smith@otago.ac.nz*

***Received:*** *24 April 2020*
***Accepted:*** *09 July 2020*
***Published:*** *11 August 2020*

***Citation:***
*Smith PF, Truchet B, Chaillan FA, Zheng Y and Besnard S (2020) Vestibular Modulation of Long-Term Potentiation and NMDA Receptor Expression in the Hippocampus. Front. Mol. Neurosci. 13:140. doi: 10.3389/fnmol.2020.00140*

## INTRODUCTION

Numerous studies over the last two decades have shown that damage to the peripheral vestibular system, especially bilateral lesions, results in spatial memory impairment in both animals and humans (for reviews see Besnard et al., 2016; Smith, 2017; Agrawal et al., 2020). This memory impairment has been attributed to the effects of vestibular loss on the hippocampus, although many other areas of the medial temporal lobe and cortex are likely to be involved as well. Many different studies have provided evidence that vestibular information reaches the hippocampus *via* multiple pathways that include the thalamus, theta rhythm-related structures and probably the cerebellum

(Cuthbert et al., 2000; Rancz et al., 2015; Leong et al., 2019; for a review see Hitier et al., 2014). In the early 2000s it was reported that bilateral vestibular loss (BVL) in rats resulted in a substantial dysfunction of hippocampal place cells (Stackman et al., 2002; Russell et al., 2003) as well as theta rhythm (Russell et al., 2006; Neo et al., 2012; Tai et al., 2012). Theta rhythm has been reported to be abnormal in the entorhinal cortex, suggesting the possibility that grid cells are also dysfunctional following BVL (Jacob et al., 2014). Head direction cells in the thalamus also function abnormally following vestibular loss (for a review see Cullen and Taube, 2017). A number of studies in humans have shown that vestibular disorders are associated with various forms of hippocampal atrophy, depending on the specific condition (for a review see Smith, 2017). Therefore, there is ample reason to think that the loss of vestibular function impairs normal hippocampal function and its role in spatial memory.

In addition to the effects of BVL on hippocampal place cells and theta rhythm, an obvious question is whether it has any effect on long-term potentiation (LTP), given the accepted role of LTP in spatial memory (for reviews see Bliss and Collingridge, 1993; Lynch, 2004; Nicoll, 2017). Despite the demonstrations that BVL causes place cell dysfunction, published in 2002 and 2003 (Stackman et al., 2002; Russell et al., 2003), only three studies have addressed this question directly over the last two decades, and their results are inconsistent. The objective of this review is to summarize, compare and critically evaluate these three studies, and other related evidence, to develop a more cohesive view of the role of the vestibular system in the modulation of hippocampal LTP.

## EARLY STUDIES OF THE EFFECTS OF VESTIBULAR LESIONS ON HIPPOCAMPAL FIELD POTENTIALS

Zheng et al. (2003) published a study in which they had performed unilateral surgical vestibular lesions (UVLs) in rats and then removed hippocampal slices at 4–6 weeks or 5–6 months following the lesion. The rationale of the study was to investigate the acute and longer-term effects of UVL on neuronal excitability in the hippocampus *in vitro*. They recorded field potentials in CA1 in response to electrical stimulation of the Schaffer collaterals and analyzed both the field excitatory postsynaptic potentials (fEPSPs) and the population spikes (PSs), the former reflecting the efficacy of the dendritic synaptic inputs and the somal field EPSP (sfEPSP) and the latter, the somal effects of the stimulation.

The input/output (I/O) curves from slices taken from UVL rats exhibited a significant reduction in the PS spike amplitude compared to naïve animals and those that had undergone sham surgery. This was the case for both time points and by 5–6 months, it occurred on the side contralateral to the lesion as well as ipsilaterally. The results were similar for the sfEPSP slopes at 5–6 months.

Ipsilaterally, there was a significant increase in paired-pulse inhibition in the 5–6 month UVL group at the shortest inter-stimulus interval (ISI); however, at longer ISIs there were significant increases in paired-pulse facilitation compared to age-matched controls and the 4–6 week group. On the contralateral side, there was increased paired-pulse inhibition for the shortest ISIs in the 5–6 month group, as well as increased paired-pulse facilitation for all ISIs.

This was the first study to report dramatic changes in electrical excitability in the hippocampus, following UVL, in hippocampal slices *in vitro*. The fact that the decrease in PS amplitude and fEPSP and sfEPSP slopes was bilateral was surprising and suggested that both sides of the hippocampus, or at least CA1, were affected by a UVL and that therefore it receives input from each vestibular labyrinth *via* the vestibular nucleus and/or cerebellum. Furthermore, the effects appeared to become greater at the longer time point. This study included both sham surgery controls and also naïve controls, and therefore involved a robust design. The paired-pulse analysis reflects recurrent and feedforward inhibition as well as changes in glutamate release underlying facilitation. The paired-pulse results obtained in this study suggested that UVL may cause changes in presynaptic neurotransmitter release. Because the study was correlational, it is difficult to determine whether any of these changes represented simply the effects of UVL or some form of compensation for it.

## EFFECTS OF VESTIBULAR STIMULATION ON HIPPOCAMPAL LTP

Based on an earlier study by Horii et al. (1994), which showed that electrical stimulation of the round window in rats could evoke acetylcholine (ACh) release in the hippocampus, Tai and Leung (2012) investigated whether natural vestibular stimulation, in the form of whole-body rotation, could modulate LTP in CA1. The rationale underlying the study was to investigate the role of cholinergic input in hippocampal LTP and whether activation of ACh receptors would increase its magnitude. LTP induction was performed in freely behaving rats who received vestibular stimulation and the results were compared to alert rats who were immobile. They observed that the LTP induced during natural vestibular stimulation was greater than that induced in immobile animals and that pretreatment with atropine, a muscarinic acetylcholine (mACh) receptor antagonist, eliminated this effect, as did selective lesions of the cholinergic neurons in the medial septum. These results suggested that the enhancement of LTP caused by natural vestibular stimulation was mediated by cholinergic input to the hippocampus from the medial septum. So far, this is the only study to investigate the effects of vestibular stimulation on hippocampal LTP.

## EFFECTS OF VESTIBULAR LESIONS ON HIPPOCAMPAL LTP

In the first systematic study of the effects of complete vestibular loss (BVL) on hippocampal LTP, Zheng et al. (2010) used both anesthetized and alert rats and investigated LTP in both CA1 and the dentate gyrus (DG). The rationale for this study was to

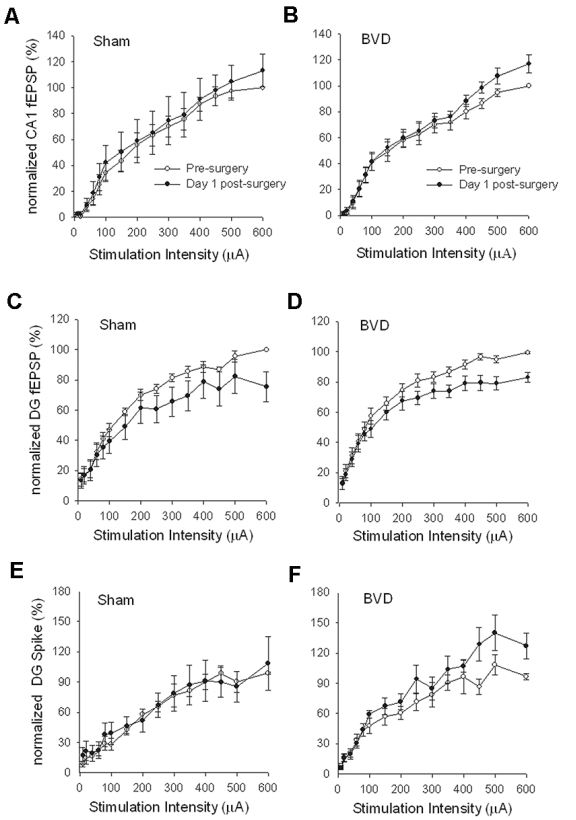


**FIGURE 1 |** Input/output (I/O) curves for sham **(A,C,E)** and bilateral vestibular deafferentation (BVD; **B,D,F**) animals before (open circles) and 1 day after (filled circles) BVD or sham surgery. I/O curves collected in freely moving animals are presented for fEPSP recordings in CA1 **(A,B)** and dentate gyrus (DG; **C,D**) and population spike recordings in the DG **(E,F)**. Each response has been normalized to the response obtained at the highest stimulus intensity (600 μA) in the presurgery I/O curve. ANOVA revealed no effects of BVD surgery on any of these measures. Data represent mean ± SEM, for this and all subsequent figures. $n$ = 5–6 for sham group and $n$ = 5–9 for BVD group. From Zheng et al. (2010) with permission.

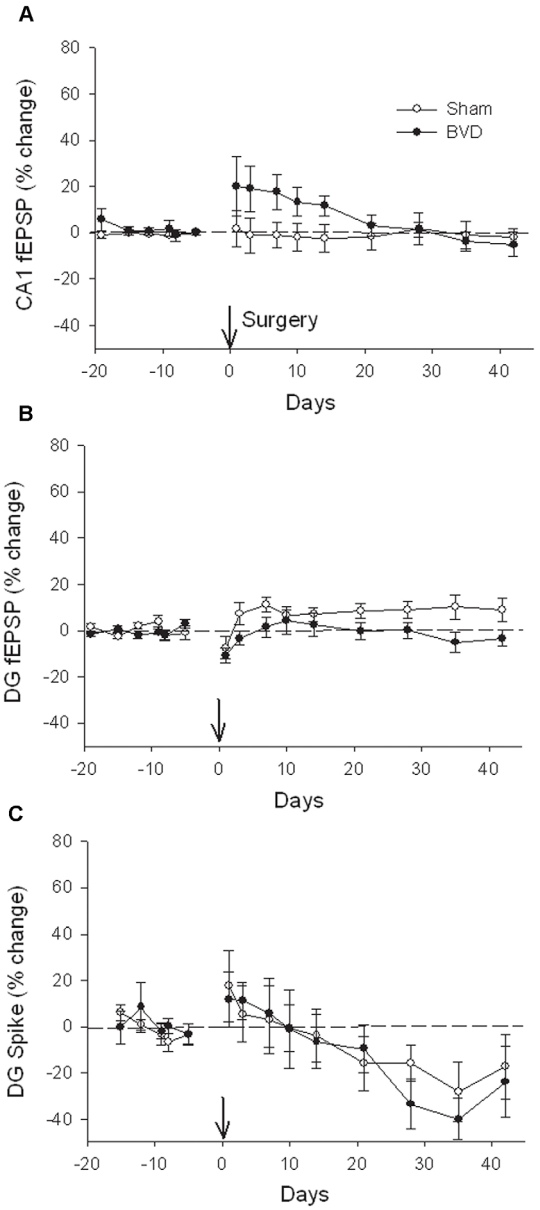


**FIGURE 2 |** Postsurgical stability of field potential recordings in freely moving animals. Field EPSPs (CA1 and DG, **A** and **B**, respectively) and population spikes (DG, **C**) were recorded in sham (open circles) and bilateral vestibular deafferentation (BVD; filled circles) animals for 40 days following surgery (arrow). ANOVA revealed no significant differences between groups across time for any measure. In both groups, the population spikes gradually declined on average over this period. $n$ = 5–6 for sham group and $n$ = 5–8 for BVD group. From Zheng et al. (2010) with permission.

investigate whether complete loss of peripheral vestibular input would impact negatively on LTP. They studied LTP in freely moving rats up to 43 days post-BVL and anesthetized rats at 7 months post-BVL. It is important to note that the BVL involved surgical lesions (see below).

In terms of the I/O curves for the chronic, alert animals, there were no significant differences for the normal fEPSP slopes or PS amplitudes in either CA1 or the DG following BVL, across the 43 day recording period (**Figures 1**, **2**). When LTP was induced in the DG using 20 trains of high-frequency stimulation (HFS) in the perforant path (400 Hz, 25 ms, pulse duration 250 μs), there was no significant difference in either the size or the decay of the LTP (**Figure 3**).

At 7 months post-BVL in acute, anesthetized animals, there was again no significant difference in the fEPSP slope or the PS amplitude in the DG or CA1 between BVL and sham animals (**Figure 4**). Following the induction of LTP, although the slope of the fEPSP in CA1 and the amplitude of the PS in the DG appeared smaller than for sham animals, the differences were not statistically significant (**Figure 5**).

These results were somewhat surprising, especially in light of the earlier study by Zheng et al. (2003), where clear decreases in the normal fEPSP slope and PS amplitude were observed in hippocampal slices from UVL rats. However, UVL and BVL are quite different forms of vestibular lesions. In the

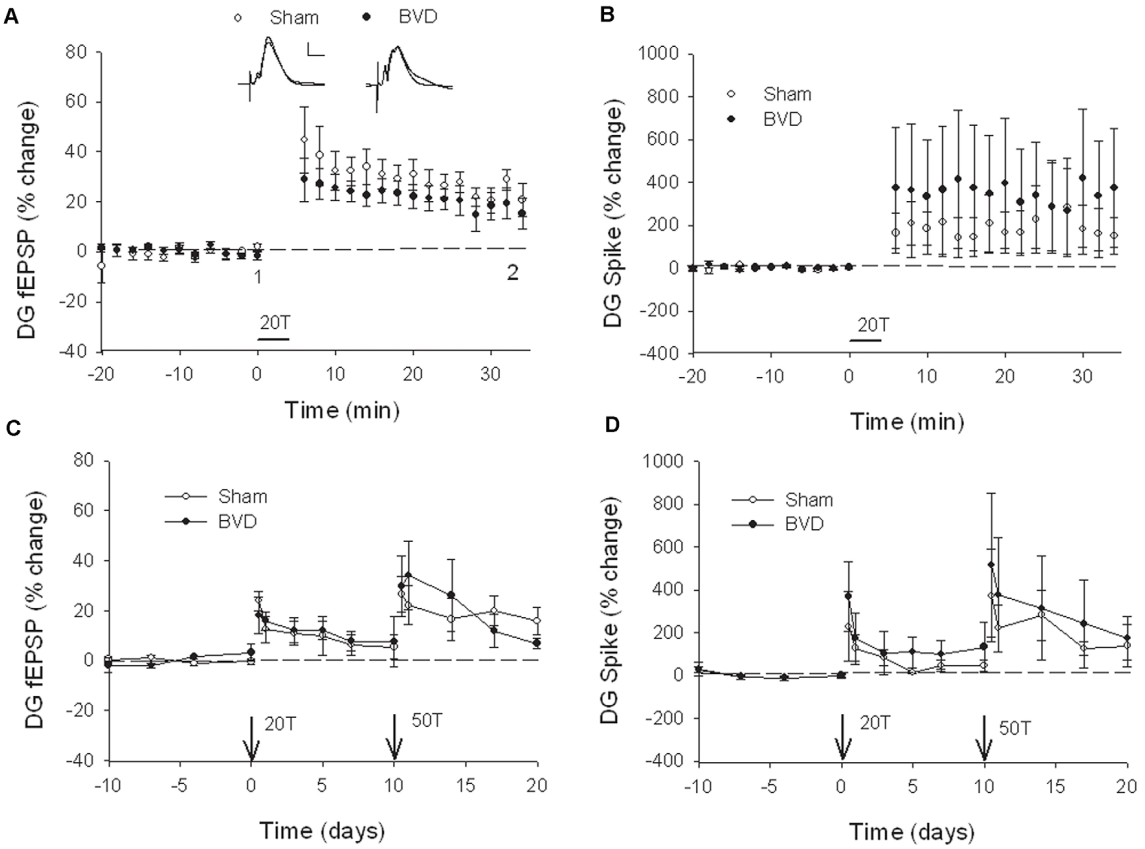


**FIGURE 3 |** Induction and persistence of perforant path long-term potentiation (LTP) in freely moving animals. Tetanisation with 20 trains of high-frequency stimulation (HFS; 20T) produced equivalent initial potentiation across groups for both the field excitatory postsynaptic potential (fEPSP; **A**) and population spike measure **(B)**. There was also no difference between groups in the decay of the LTP over 10 days **(C,D)**. Subsequent tetanisation with a stronger protocol (50T) produced greater LTP, but this was again of equivalent induction and persistence across groups **(C,D)**. Inset representative waveforms are averages of 15 sweeps taken from individual animals in each group, either just before (1) or 30 min (2) after HFS. Calibration bars: 5 μs, 5 mV. $n$ = 5 for sham group and $n$ = 5–6 for BVD group. From Zheng et al. (2010) with permission.

case of UVL, one peripheral vestibular system is eliminated, creating a dramatic imbalance in activity between the vestibular nuclei (VN) on the ipsilateral and contralateral sides. This generates a behavioral syndrome that includes spontaneous ocular nystagmus and a postural asymmetry directed toward the lesioned side. Amongst other effects, the experience of this syndrome is stressful. Following BVL, although vestibular reflexes such as the vestibulo-ocular reflexes (VORs) are abolished, there is no asymmetry in neuronal activity between the bilateral VNs. Thus, the impact of UVL and BVL on the hippocampus could be quite different. A second difference of course is that the study involving UVL was *in vitro*, whereas the BVL study was *in vivo*. *In vitro* studies of the hippocampus necessarily mean that all remaining vestibular input, as well as that from all other cranial nerves, is removed, so that if the vestibular lesion was a UVL, then the vestibular input from the other ear is removed as well.

Lee et al. (2017) conducted an *in vitro* study of the effects of surgical UVL in rats on LTP in CA1 in hippocampal slices. The rationale for this study was to investigate whether unilateral loss of vestibular input would affect LTP induced in the hippocampus, *in vitro*. They used three time-points: 1 day, 1 week, and 1 month following UVL and a microelectrode array was used to record field potentials. Using I/O curves, they found that bilateral slices from animals at 1 day and 1-week post-UVL exhibited reductions in the fEPSP amplitudes compared to sham controls, although the decreases were more obvious on the ipsilateral side at 1-day post-UVL. Theta-burst stimuli (TBS) were used to induce LTP. These consisted of three pulse trains at 20-s intervals with 10 bursts applied at 5 Hz per train and four pulses applied at 100 Hz per burst. In slices from UVL animals, the induction rate of LTP was only 56.9 ± 8.6%, compared to 85.3–88.8% in slices from sham animals. The reduction in the rate of LTP induction occurred at 1-week post-UVL and was present bilaterally.

The pre-LTP field potential I/O results from this study are consistent with those obtained *in vitro* by Zheng et al. (2003). In both cases, a UVL was performed and then hippocampal slices removed. However, the LTP results of Lee et al. (2017) appear inconsistent with those obtained by Zheng et al. (2010)

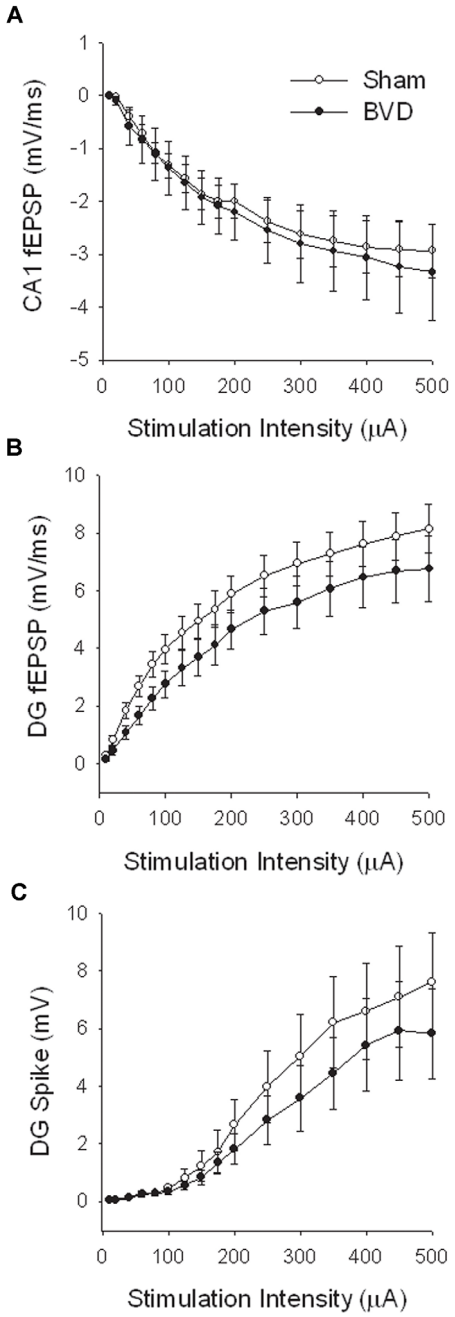


**FIGURE 4 |** Input-output analysis in anesthetized animals, 7 months after surgery. There were no significant differences in fEPSP slope for either CA1 **(A)** or DG **(B)**, or in DG population spike height **(C)**, between the sham (open circles) and BVD (filled circles) groups. *n* = 5–7 for sham and BVD groups, respectively. From Zheng et al. (2010) with permission.

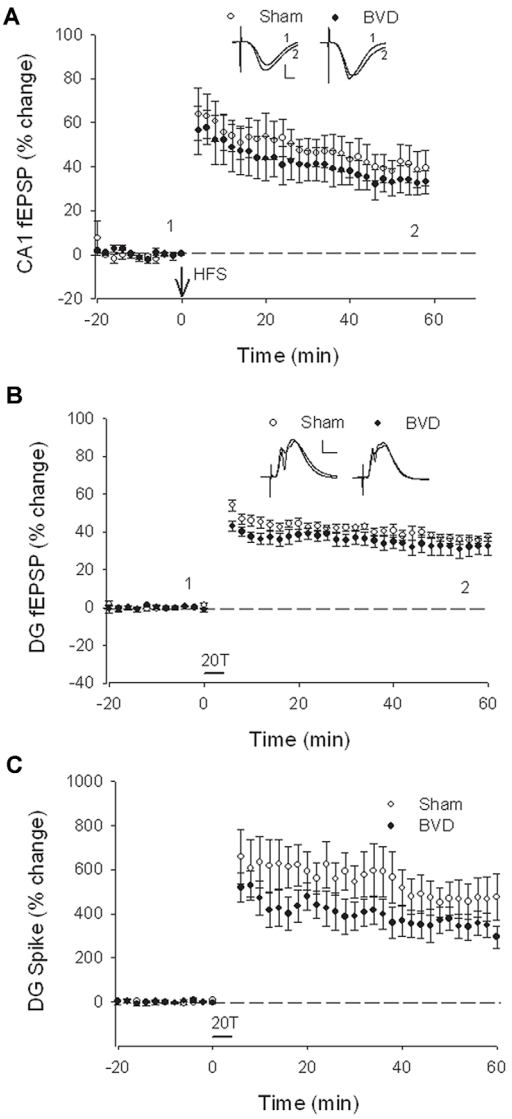


**FIGURE 5 |** Induction of LTP in anesthetized animals, 7 months after surgery. HFS (100 Hz) in neither the Schaffer collaterals **(A)** nor the perforant path (20T, **B,C**) produced differential LTP between sham (open circles) and BVD (closed circles) animals. Inset representative waveforms are averages of 15 sweeps taken from single animals in each group, either just before (1) or 60 min (2) after HFS. Calibration bars: CA1, 4 μs, 4 mV; DG, 5 μs, 5 mV. *n* = 5–7 for sham and BVD groups, respectively. From Zheng et al. (2010) with permission.

*in vivo*. It is difficult to compare the two studies given the difference in the vestibular lesions used (i.e., UVL vs. BVL, see "Discussion" above), the *in vitro/in vivo* difference (see "Discussion" above), but also the nature of the stimuli used for LTP induction was completely different. Zheng et al. (2010) used HFS stimulation (400 Hz, 25 ms, pulse duration 250 μs) of either the perforant path or the Schaffer collaterals, whereas Lee et al. (2017) used TBS consisting of three pulse trains at 20-s intervals with 10 bursts applied at 5 Hz per train and four pulses applied at 100 Hz per burst, in the Schaffer collaterals only. The methods of recording were quite different. Although Zheng et al. (2003) used a conventional recording electrode and Lee et al. (2017) employed a multi-electrode array (a MED64 microelectrode array, 8 × 8), the electrodes had the same features (50 μm diameter Teflon-coated); hence this parameter could not alter the recorded signals. However, biphasic pulses

were not delivered at the same frequency (0.17 Hz, Zheng et al., 2003; 0.05 Hz, Lee et al., 2017). A short interval between two pulses can affect the evoked potential (as during a paired-pulse procedure, range 0–1,000 ms) but not with the range used (6 s or 20 s). Nevertheless, three points could partially explain the discrepancies. First, recordings were performed with a 21–23°C ACSF by Zheng et al. (2003) and 30°C by Lee et al. (2017), which can affect the membrane properties of the neurons and thus the evoked potential (Deisz, 1999; Volgushev et al., 2000; Liebregts et al., 2002). Second, the time points were different, with Zheng et al. (2003) using 4–6 weeks or 5–6 months following the lesion and Lee et al. (2017) using 1 day, 1 week, and 1 month (equivalent to 4–6 weeks) post-lesion. At such time-points, differences in post-lesion edema and/or gliosis processes could develop (Steward et al., 1986; Brace et al., 1997; Tourdias et al., 2011). Finally, the rat strains were different (Wistar vs. Sprague–Dawley), which could have led to electrophysiological discrepancies (Guitart et al., 1993; Potier et al., 1993; Fuzik et al., 2013; Bruzos-Cidón et al., 2014). Despite the methodological differences, the two studies showed similar changes in excitability in the hippocampus, albeit that LTP induction was not specifically measured in Zheng et al. (2003).

In the most recent study, Truchet et al. (2019) investigated the effects of BVL on LTP in anesthetized rats at 30 days following BVL. The rationale for this study was to investigate the effects of complete loss of vestibular function on LTP *in vivo*, at a time when some degree of vestibular compensation had developed. They employed a chemical lesion procedure in which sodium arsanilate is injected through the tympanic membrane. They measured the fEPSP slopes and PS amplitudes in the DG before and after LTP induction. A critical difference from the study by Zheng et al. (2010) was that they used a "moderate" HFS protocol for LTP induction. This consisted of two main trains at a 1 min intertrain interval, each main train consisting of five subtrains at a 1 Hz inter-subtrain interval. Each subtrain contained a burst of 10 biphasic (+250 μs/−250 μs) pulses at 400 Hz. The logical consequence was a lower level of LTP (around 20% vs. 40% fEPSP increase, around 120% vs. 600% PS amplitude increase). This was designed to avoid "LTP saturation" so that increases and decreases in LTP could be detected if they were produced. LTP was measured throughout 3 h post-induction, with the first 5 min excluded due to the possibility of post-tetanic potentiation (PTP; McNaughton, 1982). They observed no significant differences between the BVL and sham groups for any of the stimulation intensities used for the I/O curves in the DG, either before or following the induction of LTP. This was the case for both the fEPSP slope and the PS amplitude (see **Figure 6**). There were few differences in the paired-pulse ratios between the BVL and sham rats. Following LTP, the mean fEPSP slope was increased over the 3 h of recording but this was equally so for both BVL and sham animals (**Figure 7**). By contrast, the level of PS potentiation was higher for the BVL group, and this became more prominent with time (**Figure 7**). EPSP-Spike (ES) Potentiation is a phenomenon in which the ratio of the PS amplitude to the fEPSP slope, increases. After the induction of LTP, there was a tendency for a higher E-S potentiation in the BVL group compared to the sham group, which was more prominent during the final hour of recording (**Figure 7**).

## THE POSSIBLE ROLE OF N-METHYL-D-ASPARTATE (NMDA) RECEPTORS IN HIPPOCAMPAL LTP CHANGES FOLLOWING UVL OR BVL

An early western blotting study demonstrated that the expression of the GluN 1 and GluN 2A subunits of the N-methyl-D-aspartate (NMDA) subtype of glutamate receptor, decreased in the ipsilateral CA2/3 region at 2 weeks following surgical UVL, while the expression of the GluN 2A subunit was also reduced in the contralateral CA2/3 region (Liu et al., 2003). On the other hand, the expression of the GluN 2A subunit was increased in the CA1 region at 10 h following UVL (Liu et al., 2003). The rationale for these early studies was to explore potential changes in hippocampal NMDA receptors following a UVL, given that these receptors were already known to be important in LTP.

With a similar rationale in mind, Besnard et al. (2012) measured NMDA receptor density and affinity using receptor autoradiography at 2 months following BVL. They employed a sequential chemical UVL procedure, involving intratympanic sodium arsanilate injections (i.e., one ear, followed several weeks later by the other ear), and following the second UVL, resulting in a BVL, they observed a significant increase in the NMDA receptor $B_{max}$ and a decrease in $K_d$ in the hippocampus. In a study using simultaneous surgical BVL, Zheng et al. (2013) used western blotting and could find no significant differences in the expression of the GluN 1, GluN 2A, GluN 2B, GluA 2, GluA 3 or GluA 4 subunits in the CA1, CA2/3 or DG subregions of the hippocampus at 24 h, 72 h, 1 week, 1 month or 6 months following BVL.

In the most recent study by Truchet et al. (2019), NMDA receptor expression was investigated in the hippocampus at 7 and 30 days following BVL, using receptor autoradiography as well as flow cytometry. The rationale for these experiments was to determine whether NMDA receptor expression might change differentially at short and longer-term time points and also to correlate NMDA receptor expression with the LTP observed at 30 days post-BVL. These experiments were done as part of the same study that measured changes in LTP following BVL (Truchet et al., 2019); however, separate animals were used for the LTP experiments. The NMDA receptor $B_{max}$ was significantly increased in the dorsal hippocampus at $D_7$ and $D_{30}$ but was higher in the left than the right dorsal hippocampus at $D_7$ and $D_{30}$ compared to controls (**Figure 8**). This increase was also seen when the whole right and left hippocampi were analyzed separately, except that the NMDA receptor upregulation did not reach statistical significance in the left hippocampus at $D_7$ or in the right one at $D_{30}$. This might have been due to the relative lack of change in the ventral hippocampus. A significant increase in NMDA receptor density was observed in CA1 at $D_7$ and $D_{30}$ and also in the DG; however, it remained unchanged in the

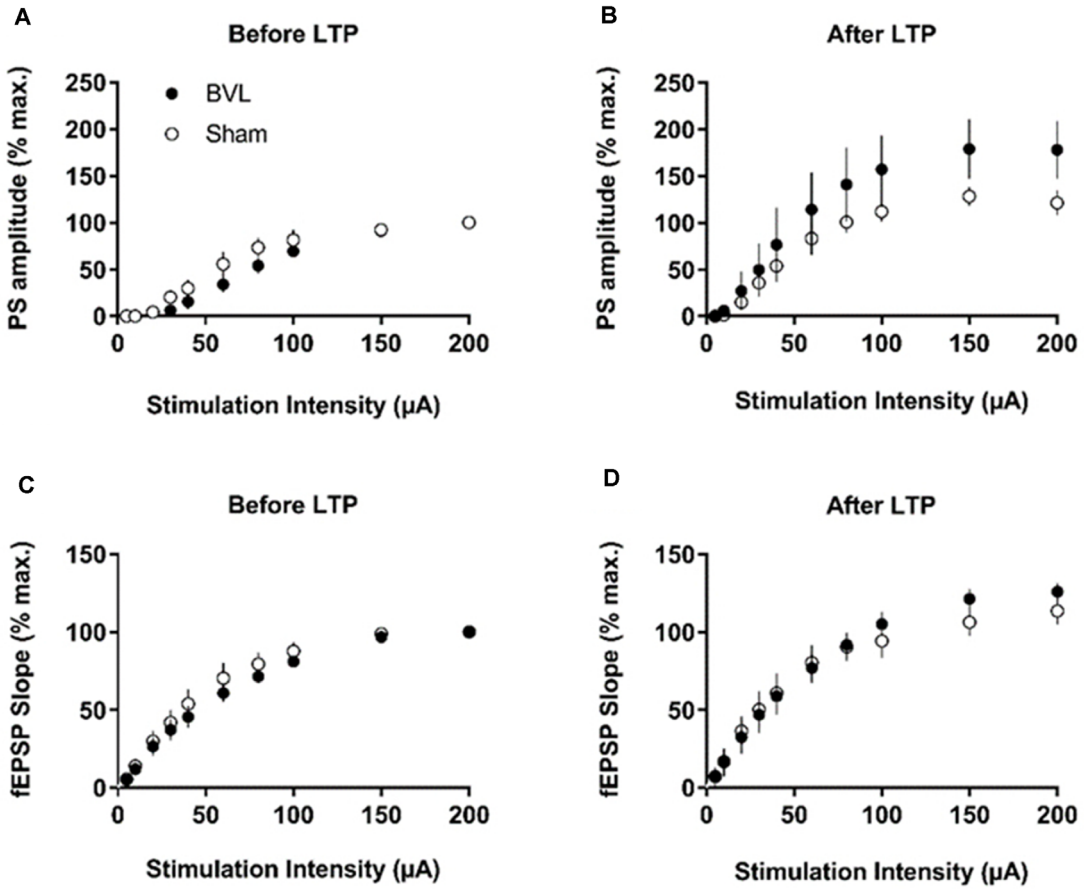


**FIGURE 6 |** IO curves for the population spike (PS) amplitude **(A,B)** and fEPSP slope **(C,D)**, before and after the entire LTP procedure. The IO obtained by a single pulse across an intensity range of 5–200 μA. Measures were repeated four times, every 15 s, normalized for each rat concerning the maximum value (obtained for a 200 μA stimulation intensity), and averaged for each stimulation intensity. Data are expressed as mean ± SEM (BVL: *n* = 7; Sham, *n* = 7). From Truchet et al. (2019) with permission.

CA2/CA3 at $D_7$ and $D_{30}$. From the flow cytometry studies, the number of neurons expressing NMDA receptors was selectively increased in the hippocampus at $D_7$ and $D_{30}$ (see **Figure 9**). Similar results were reported by Benoit et al. (2018a).

None of these studies was directly related to measurements of hippocampal LTP. Therefore, it is difficult to interpret their functional significance. Truchet et al. (2019) suggested that the increase in NMDA receptors may underlie the ES potentiation observed in the hippocampus. If NMDA receptors were up-regulated synaptically, then there would be increased excitation of DG neurons that might lead to a greater PS for a given amount of excitation reflected in the perforant path fEPSP, i.e., the size of the PS would not specifically reflect the stimulated input, which would generate increased synaptic noise.

Once again, the differences between UVL and BVL used in the different studies are important, and the sequential UVLs used by Besnard et al. (2012) are difficult to compare to the simultaneous BVL used by Zheng et al. (2013). There are also substantial differences between surgical and chemical lesions of the peripheral vestibular system (see below).

It is worth noting that BVL has also been demonstrated to result in the down-regulation of $M_1$ mACh receptors across all subregions of the hippocampus (Aitken et al., 2016). This is consistent with the results of Tai and Leung (2012), who reported that a mACh antagonist blocked the enhancement of LTP induced by natural vestibular stimulation and that lesions that eliminated the cholinergic input from the medial septum, also had this effect. Aitken et al. (2017) also reported that although there was no significant change in ACh release into the hippocampus following BVL, there was a surprising increase in the number of cholinergic neurons in the pedunculopontine tegmental nucleus, an important part of the cholinergic pathway that generates theta activity. The functional significance of this finding is unknown.

## DISCUSSION

The investigation of the nature of LTP in the hippocampus following UVL or BVL was motivated by studies showing spatial memory deficits (for reviews see Besnard et al., 2016; Smith, 2017; Agrawal et al., 2020) and hippocampal place cell

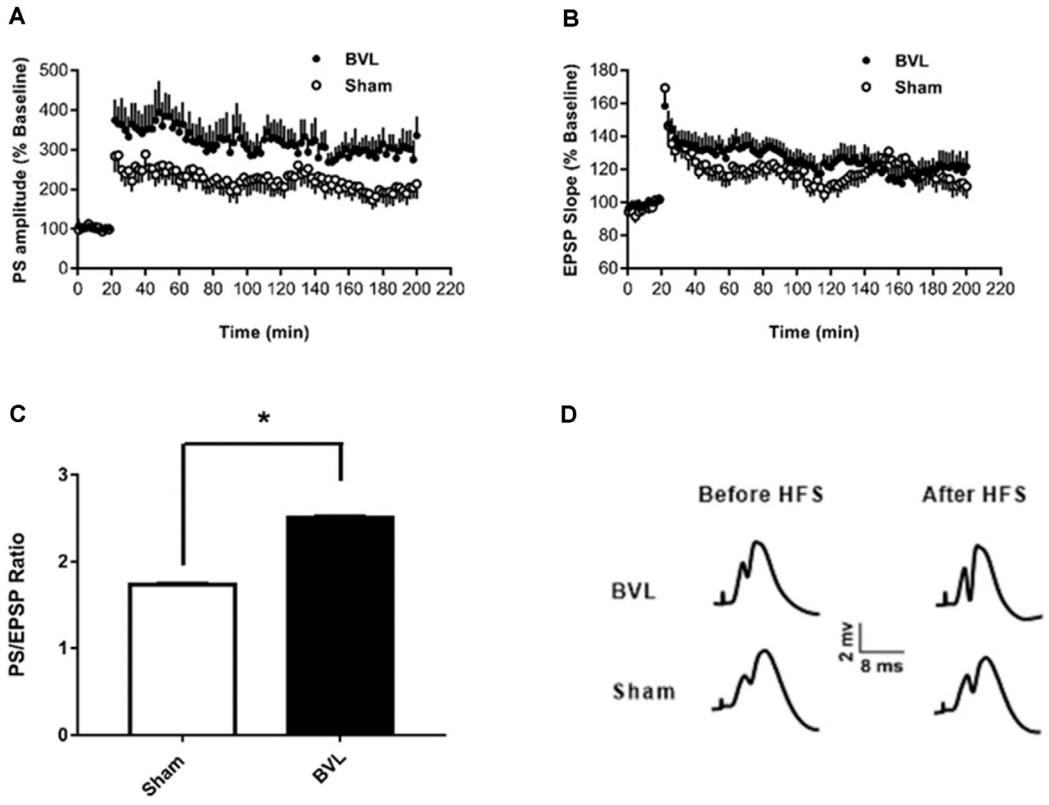


**FIGURE 7 |** LTP. **(A,B)** DG recording obtained before (10 min baseline) and after (3 h) weak tetanus (arrow) of the medial performant path (MPP). Data are expressed as mean ± SEM (BVL: *n* = 7; Sham, *n* = 7). For clarity, each point represents the mean of four plotted measures. Data were normalized concerning the baseline level. **(A)** Percentage changes of the population spike (PS) amplitude. **(B)** Percentage changes of the fEPSP slope. **(C)** E-S potentiation. The (Population spike amplitude)/(EPSP Slope) ratio was calculated using normalized values, expressed in percentage of the baseline for each animal, for each stimulation. Bar graph of the mean ES ratio obtained from the last (third) hour of post-HFS recording (BVL: *n* = 7; Sham, *n* = 7). Error bars represent SEM (**P* = 0.013). **(D)** Representative traces of potential evoked in the DG by stimulation of the MPP, before (baseline) and after HFS (LTP induction), in both groups. From Truchet et al. (2019) with permission.

dysfunction (Stackman et al., 2002; Russell et al., 2003) in animals with vestibular loss. It made sense intuitively that if spatial memory processing in the hippocampus was disrupted, then the mechanisms underlying LTP might be disrupted as well. To date, the few studies conducted have yielded far more complex results. The studies are difficult to compare directly because of the different uses of UVL vs. BVL, *in vitro* vs. *in vivo* models of hippocampal function, different time points post-lesion, and different methods of inducing vestibular dysfunction (chemical vs. surgical labyrinthectomy). Therefore, the available studies can only be compared to those other studies using similar methods, if not the same.

## *In vitro* Studies

In terms of the two *in vitro* studies, what they have in common is that they removed hippocampal slices from rats that had received a UVL, at similar time points, and they recorded field potentials in the slices at various times post-lesion. Both Zheng et al. (2003) and Lee et al. (2017) reported that the fEPSP slope was reduced following UVL, suggesting a decrease in excitability, *in vitro*, as a result of the lost vestibular input. In both cases, the effect was bilateral, which supports the evidence that vestibular information from one vestibular labyrinth is transmitted to both hippocampi (Cuthbert et al., 2000; Rancz et al., 2015). It is noteworthy that there are several differences between the two studies. The methods of recording were quite different, with Zheng et al. (2003) using a conventional recording electrode and Lee et al. (2017) employing an 8 × 8 multi-electrode array, which was positioned under the hippocampal slice. The latter arrangement would probably have resulted in greater variation in recording sites across CA1. The time points were different, with Zheng et al. (2003) using 4–6 weeks or 5–6 months following the lesion and Lee et al. (2017) using 1 day, 1 week, and 1-month post-lesion. Despite the methodological differences, the two studies showed similar changes in excitability in the hippocampus, albeit that LTP induction was not specifically measured in Zheng et al. (2003).

## *In vivo* Studies

Unlike the *in vitro* studies, the *in vivo* studies have mainly concerned LTP in the hippocampus following BVL rather than UVL (Zheng et al., 2010; Truchet et al., 2019). Notably, neither of the *in vivo* studies found the decrease in fEPSP

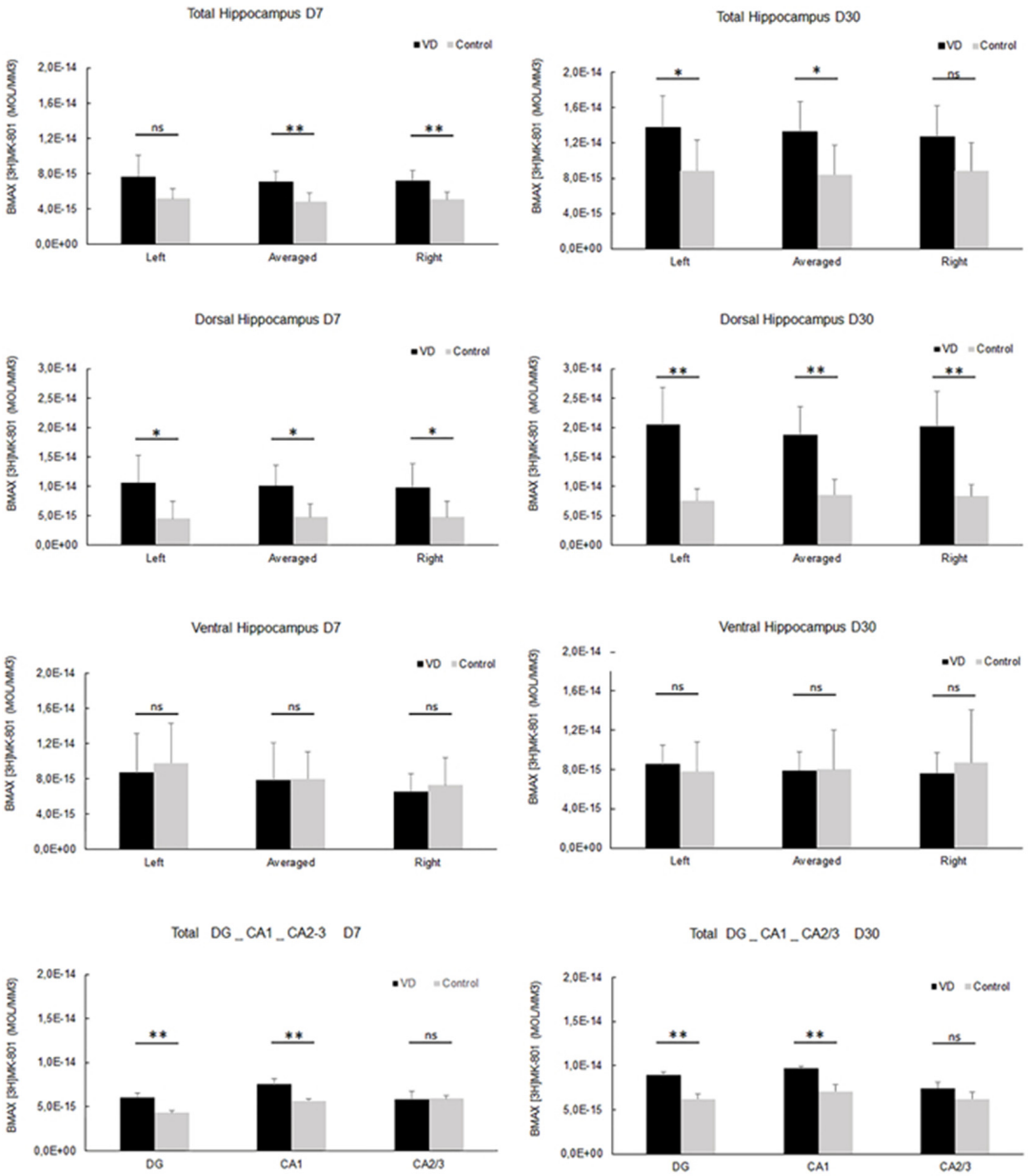


**FIGURE 8 |** NMDA receptor quantitative autoradiography. Time course of hippocampal NMDA receptor density expressed in mol/mm$^3$ at 7 days (left panel) and 30 days (right panel) following trans-tympanic bilateral injection of arsanilate (vestibular deficiency/VD in black $n = 8$) or of saline solution (control in grey, $n = 7$). NMDA receptor density was calculated from the total hippocampus, the left, and right side separately, and the dorsal and ventral parts, the DG, the CA1 and CA2/3 sublayers (combining the right and left parts of the sublayers, due to the lower surface of beta-emission). Statistical abbreviations: ns, non-significant, $^*p < 0.5$, $^{**}p < 0.02$. Error bars represent SD. From Truchet et al. (2019) with permission.

slope or PS amplitude without LTP, that was reported in the *in vitro* studies (Zheng et al., 2003; Lee et al., 2017), which is very interesting. This suggests that UVL and BVL may have completely different effects on the intrinsic excitability of the neurons in the hippocampus, perhaps due to the asymmetrical effects of UVL on the CNS.

The results of the two *in vivo* studies of LTP following BVL are also inconsistent with each other. Zheng et al. (2010) observed no effect of a complete BVL on LTP in the DG or CA1, whereas Truchet et al. (2019) observed an increased PS relative to the fEPSP following LTP in the DG. However, there is a multitude of methodological differences between these two studies. First, while Zheng et al. (2010) employed a surgical BVL, Truchet et al. (2019) used a chemical BVL. A major difference between the surgical and chemical BVLs used in these two studies is the timing between the lesions to the two sides of the vestibule.

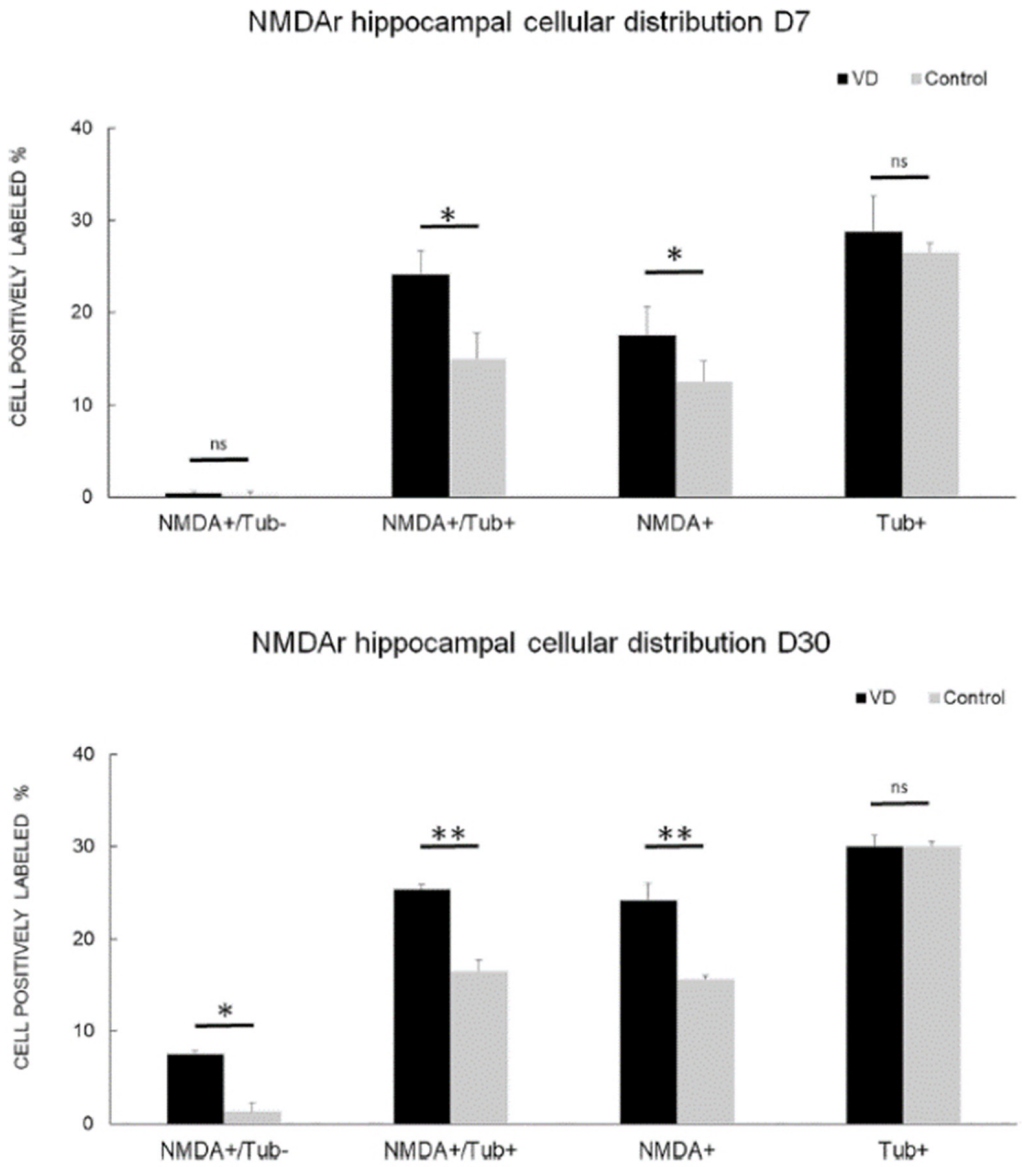


**FIGURE 9 |** NMDA receptor neuronal distribution by flow cytometry. Time course of the distribution of NMDA receptors (NMDA+) on neurons (Tub+) and non-neuronal cells (Tub-) at 7 days (top panel) and 30 days (bottom panel) following trans-tympanic bilateral injection of arsanilate (vestibular deficiency/VD in black = 8) or of saline solution (control in gray, $n = 7$). Results are expressed in percentage of cell samples for each group (VD and control) and labeled for NMDA+/Tub− (non-neuronal cells expressing NMDA receptors), NMDA+/Tub+ (neurons expressing NMDA receptors), NMDA+ (% of cells expressing NMDA receptors irrespective of the type of cells), Tub+ (% of neurons among the cells' samples analyzed). Tub+ = cells positive for beta-Tubulin, a neurofilament marker specific the neurons. Statistical abbreviations: ns, non-significant, $^{*}p < 0.5$, $^{**}p < 0.02$. Error bars represent SD. From Truchet et al. (2019) with permission.

The surgical BVL lesioned both sides during one surgery with one inner ear lesioned about 30 min before the other, while the chemical BVL was performed on one side before the second side was lesioned several weeks later. Therefore, the animals would experience UVL on one side first and undergo vestibular compensation before experiencing a 2nd UVL and vestibular compensation on the other side. Given the fact that the two UVL studies (Zheng et al., 2003; Lee et al., 2017) both reported changes in neuronal excitability in the hippocampus, while the BVL studies did not (Zheng et al., 2010; Truchet et al., 2019), it is perhaps not surprising that there might be a difference in LTP induction between surgical and chemical BVL animals. Also, surgical BVL involves the surgical destruction of the vestibular system, while trying to avoid damage to the cochlea, whereas the injection of sodium arsanilate or any other ototoxin through the tympanic membrane is less well controlled and incurs unknown damage to the cochlea. Second, Zheng et al. (2010) measured LTP for 30–60 mins at multiple time points post-UVL, including up

to 43 days in alert, freely moving animals and then at 7 months in anesthetized animals, whereas Truchet et al. (2019) measured LTP for 3 hs at 1 time-point (3 months) in anesthetized animals following BVL. Third, whereas Zheng et al. (2010) quantified LTP in both CA1 and the DG, Truchet et al. (2019) quantified it only in the DG. Fourth, the two studies used different LTP induction protocols. While the inter- and intra-train frequencies and the pulse durations were the same in both studies, Zheng et al. (2010) used twice as many HFS trains compared to Truchet et al. (2019); 20 vs. 10, for a respective total of 200 and 100 pulses. Therefore, it can be argued that Zheng et al. (2010) used a high-frequency protocol intended to generate a strong LTP, reflected in the higher level of LTP obtained for both the fEPSP and PS in their study. By contrast, Truchet et al. (2019) attempted to induce a "weak" or "moderate" LTP in order to avoid a possible ceiling effect. The fact that Truchet et al. (2019) observed an enhanced LTP of the PS suggests that such an effect might be missed by a ceiling effect in the Zheng et al. (2010) study due to the stronger LTP induction paradigm used.

Tai and Leung (2012) found that natural vestibular stimulation could enhance LTP in the hippocampus *in vivo*. This effect appeared to be mediated by cholinergic input from the medial septum, since an ACh receptor antagonist blocked the effect, as did selective lesions of the septum. How this result might relate to those of Zheng et al. (2010) and Truchet et al. (2019) is unclear. If the results obtained by Truchet et al. (2019) are interpreted as dysfunctional LTP due to reduced input selectivity and increased synaptic noise, then the Tai and Leung (2012) finding that vestibular stimulation increases LTP, could be interpreted as the opposite effect. However, the data obtained from these two studies and those of Zheng et al. (2010) are not necessarily incompatible: when it comes to LTP and memory, the relevant question is not only whether there is more or less LTP, but rather which synapses express LTP. Indeed, a general increase in synaptic efficacy (reflected by a global increase in LTP), due to NMDA receptor upregulation following BVL, can lead to an increase in synaptic noise and therefore learning and memory deficits. On the contrary, natural vestibular stimulation could generate plasticity more similar to that which develops during natural vestibular-hippocampal interactions, specific to synapses involved in learning and memory processes. One must also remember that LTP is generated from an artificial stimulation protocol and that minor variations could result in different effects on LTP.

## NMDA RECEPTORS IN THE HIPPOCAMPUS FOLLOWING BVL

Like the studies of LTP, there are only a few studies of hippocampal NMDA receptors following a vestibular loss. These can only be considered correlational concerning LTP since they were conducted in animals not subjected to LTP-inducing stimuli.

Although some early studies examined NMDA receptor subunit density in the hippocampus at time points up to 2 weeks post-UVL (Liu et al., 2003), the major studies have used BVL. The latter studies have focussed on longer time points due to the interest in long-term spatial memory deficits caused by vestibular loss (for reviews see Besnard et al., 2016; Smith, 2017; Agrawal et al., 2020), and these studies will be emphasized here. Besnard et al. (2012), using receptor autoradiography, observed an increase in the $B_{max}$ for NMDA receptors in the hippocampus at 2 months following BVL, which involved two sequential UVLs. Benoit et al. (2018a) and Truchet et al. (2019) recently reported similar results, using either flow cytometry or receptor autoradiography, or both, at 7 and 30 days following BVL. By contrast, Zheng et al. (2013) could find no difference in any NMDA receptor subunit in any subregion of the hippocampus at 24 h, 72 h, 1 week, 1 month, or 6 months following BVL. Although the different studies involve methodological differences such as chemical (Besnard et al., 2012; Benoit et al., 2018a; Truchet et al., 2019) vs. surgical lesions (Zheng et al., 2013) of the vestibular system as well as different time points post-BVL, the most important difference is probably the use of receptor autoradiography (Besnard et al., 2012; Truchet et al., 2019) and flow cytometry (Benoit et al., 2018a,b; Truchet et al., 2019) vs. western blotting (Zheng et al., 2013). While western blotting permits the use of antibodies to target specific NMDA receptor subunits (as does flow cytometry), it involves quantification of the total amount of protein in the homogenate, including that which is not specific to synapses. By contrast, receptor autoradiography targets receptors that are more likely to be synaptic and therefore may be more representative of NMDA receptors involved in LTP, although this is not certain. On the other hand, only western blotting and flow cytometry can provide information about NMDA receptor subunits. In the end, none of these studies can be related to LTP directly, since they were conducted in animals in which electrophysiological recording was not performed.

## CONCLUSIONS

It is difficult to draw firm conclusions from the few studies of hippocampal LTP following UVL or BVL, conducted so far. Although UVL appears to cause a decrease in hippocampal field potentials following UVL in *in vitro* hippocampal slices (Zheng et al., 2003; Lee et al., 2017), this has not been demonstrated following BVL *in vivo* (Zheng et al., 2010; Truchet et al., 2019) and no UVL *in vivo* investigation has been conducted. The study by Zheng et al. (2010) involved both CA1 and the DG, so the discrepancy is unlikely to be due to the subregion of the hippocampus studied. More likely, the difference may be due to the use of UVL vs. BVL. As mentioned earlier, UVL causes a massive asymmetry between the two VN in the brainstem, which is then transmitted to higher brain regions, whereas BVL removes all vestibular input simultaneously but does not cause such an asymmetry.

Despite the plethora of methodological differences among the LTP studies, the major discrepancy between the two *in vivo* studies is most likely the different lesioning methods and HFS protocols used to induce LTP. It may be that differences in LTP can be detected, depending on the stimulation protocol used. If an increase in ES potentiation does occur following LTP, at least using a "moderate" HFS protocol, then it may be related

to a decrease in feed-forward inhibition mediated by GABAergic interneurons acting on $GABA_A$ receptors on principal cells (Tomasulo et al., 1991; Lu et al., 2000; Ross and Soltesz, 2001). This could happen if BVL caused a reduction in these $GABA_A$ receptors. Previous studies of the CA1 following BVL have shown a significant increase in the spontaneous resting activity of interneurons (Russell et al., 2003), which also suggests that interneuron regulation of principal neurons may change. DG and CA1 hippocampal subfield circuitries display feedforward and feedback inhibition (GABAergic interneurons) of their main cell types, respectively granule and pyramidal cells. Perforant path axons directly connect with inhibitory interneurons underlying the feedforward inhibition. These interneurons fire with very short latencies and their action could control the granule cell activity. Moreover, blocking $GABA_A$ receptors in the DG *in vivo* prevents the leftward shift of the ES curves during LTP induction (Tomasulo et al., 1991). The authors proposed "*. . .that the LTP-associated left shift of the ES curve reflects a real decrease of synaptic efficacy in the inhibitory pathway*" (Tomasulo et al., 1991). Lu et al. (2000) showed that calcineurin activated by NMDA receptors induced long-term depression (LTD) of the $GABA_A$ receptor-dependent inhibitory post-synaptic potential (IPSP) during NMDA receptor-dependent LTP in CA1, and stated that "*. . .this LTD is both necessary and sufficient for the long-lasting increase in enhanced excitability manifest in the E-S coupling*" (Lu et al., 2000).

The results of the studies of NMDA receptor expression in the hippocampus are inconsistent. If there is an increase in synaptic NMDA receptors following BVL, this may cause an increase in synaptic noise that would lead to spatial memory deficits. Future studies should further investigate the effects of UVL and BVL, on LTP, especially *in vivo*, in the different hippocampal subregions and changes in feed-forward GABAergic inhibition. It would be particularly interesting to investigate the effects of restoring GABAergic inhibition in the hippocampus following UVL or BVL, using selective agonists or optogenetics, on E-S potentiation and synaptic noise (Truchet et al., 2019).

## AUTHOR CONTRIBUTIONS

PS conceived and wrote the first draft of the article. BT, FC, YZ, and SB contributed to the writing and editing of the manuscript.

## REFERENCES


Agrawal, Y., Smith, P. F., and Rosenberg, P. B. (2020). Vestibular impairment, cognitive decline and Alzheimer's disease: balancing the evidence. *Aging Ment. Health* 24, 705–708. doi: 10.1080/13607863.2019.1566813

Aitken, P., Benoit, A., Zheng, Y., Philoxene, B., Le Gall, A., Denise, P., et al. (2016). Hippocampal and striatal $M_1$-muscarinic acetylcholine receptors are down-regulated following bilateral vestibular loss in rats. *Hippocampus* 26, 1509–1514. doi: 10.1002/hipo.22651

Aitken, P., Zheng, Y., and Smith, P. F. (2017). Effects of bilateral vestibular deafferentation in rat on hippocampal theta response to somatosensory stimulation, acetylcholine release, and cholinergic neurons in the pedunculopontine tegmental nucleus. *Brain Struct. Funct.* 222, 3319–3332. doi: 10.1007/s00429-017-1407-1

Benoit, A., Besnard, S., Guillamin, M., Philoxene, B., Sola, B., Le Gall, A., et al. (2018a). Differential regulation of NMDA receptor-expressing neurons in the rat hippocampus and striatum following bilateral vestibular loss demonstrated using flow cytometry. *Neurosci. Lett.* 683, 43–47. doi: 10.1016/j.neulet.2018.06.035

Benoit, A., Guillamin, M., Aitken, P., Smith, P. F., Philoxene, B., Sola, B., et al. (2018b). Flow cytometry for receptor analysis from *ex-vivo* brain tissue in adult rat. *J. Neurosci. Methods* 304, 11–23. doi: 10.1016/j.jneumeth.2018.04.005

Besnard, S., Machado, M. L., Vignaux, G., Boulouard, M., Coquerel, A., Bouet, V., et al. (2012). Influence of vestibular input on spatial and nonspatial memory and on hippocampal NMDA receptors. *Hippocampus* 22, 814–826. doi: 10.1002/hipo.20942

Besnard, S., Lopez, C., Brandt, T., Denise, P., and Smith, P. F. (eds) (2016). "The vestibular system in cognitive and memory processes in mammals," in *Frontiers in Integrative Neuroscience* (Lausanne: Frontiers Media), 1–246.

Bliss, T., and Collingridge, G. (1993). A synaptic model of memory: long-term potentiation in the hippocampus. *Nature* 361, 31–39. doi: 10.1038/361031a0

Brace, H., Latimer, M., and Winn, P. (1997). Neurotoxicity, blood-brain barrier breakdown, demyelination and remyelination associated with NMDA-induced lesions of the rat hypothalamus. *Brain Res. Bull.* 43, 447–455. doi: 10.1016/s0361-9230(97)00064-6

Bruzos-Cidón, C., Migulez, C., Rodríguez, J. J., Gutiérrez-Lanza, R., Ugedo, L., and Torrecilla, M. (2014). Altered neuronal activity and differential sensitivity to acute antidepressants of locus coeruleus and dorsal raphe nucleus in Wistar Kyoto rats: a comparative study with Sprague-Dawley and Wistar rats. *Eur. Neuropharmacol.* 24, 1112–1122. doi: 10.1016/j.euroneuro.2014.02.007

Cullen, K. E., and Taube, J. S. (2017). Our sense of direction: progress, controversies and challenges. *Nat. Neurosci.* 20, 1465–1473. doi: 10.1038/nn.4658

Cuthbert, P. C., Gilchrist, D. P., Hicks, S. L., MacDougall, H. G., and Curthoys, I. S. (2000). Electrophysiological evidence for vestibular activation of the guinea pig hippocampus. *Neuroreport* 11, 1443–1447. doi: 10.1097/00001756-200005150-00018

Deisz, R. A. (1999). GABAB receptor-mediated effects in human and rat neocortical neurons *in vitro*. *Neuropharmacology* 38, 1755–1766. doi: 10.1016/s0028-3908(99)00136-7

Fuzik, J., Gellért, L., Olàh, G., Herédi, J., Kocsis, K., Knapp, L., et al. (2013). Fundamental interstrain differences in cortical activity between Wistar and Sprague-Dawley rats during global ischemia. *Neuroscience* 228, 371–381. doi: 10.1016/j.neuroscience.2012.10.042

Guitart, X., Kogan, J. H., Berhow, M., Terwilliger, R. Z., Aghajanian, G. K., and Nestler, E. J. (1993). Lewis and Fischer rat strains display differences in biochemical, electrophysiological and behavioral parameters: studies in the nucleus accumbens and locus coeruleus of drug naïve and morphine-treated animals. *Brain Res.* 611, 7–17. doi: 10.1016/0006-8993(93)91770-s

Hitier, M., Besnard, S., and Smith, P. F. (2014). Vestibular pathways involved in cognition. *Front. Integrat. Neurosci.* 8:59. doi: 10.3389/fnint.2014.00059

Horii, A., Takeda, N., Mochizuki, T., Okakura-Mochizuki, K., Yamamoto, Y., and Yamatodani, A. (1994). Effects of vestibular stimulation on acetylcholine release from rat hippocampus: an *in vivo* microdialysis study. *J. Neurophysiol.* 72, 605–611. doi: 10.1152/jn.1994.72.2.605

Jacob, P.-Y., Poucet, B., Liberge, M., Save, E., and Sargolini, F. (2014). Vestibular control of entorhinal cortex activity in spatial navigation. *Front. Integrat. Neurosci.* 8:38. doi: 10.3389/fnint.2014.00038

Lee, G. W., Kim, J. H., and Kim, M. S. (2017). Reduction of long-term potentiation at Schaffer collateral-CA1 synapses in the rat hippocampus at the acute stage of vestibular compensation. *Korean J. Physiol. Pharmacol.* 21, 423–428. doi: 10.4196/kjpp.2017.21.4.423

Leong, A. T. L., Gu, Y., Chan, Y. S., Zheng, H., Dong, C. M., Chan, R. W., et al. (2019). Optogenetic fMRI interrogation of brain-wide central vestibular pathways. *Proc. Natl. Acad. Sci. U S A* 116, 10122–10129. doi: 10.1073/pnas.1812453116

Liebregts, M. T., McLachlan, R. S., and Leung, L. S. (2002). Hyperthermia induces age-dependent changes in rat hippocampal excitability. *Ann. Neurol.* 52, 318–326. doi: 10.1002/ana.10285

Liu, P., Zheng, Y., King, J., Darlington, C. L., and Smith, P. F. (2003). Long-term changes in hippocampal N-methyl-D-aspartate receptor subunits following unilateral vestibular damage in rat. *Neuroscience* 117, 965–970. doi: 10.1016/s0306-4522(02)00878-3

Lu, Y. M., Mansuy, I. M., Kandel, E. R., and Roder, J. (2000). Calcineurin-mediated LTD of GABAergic inhibition underlies the increased excitability of CA1 neurons associated with LTP. *Neuron* 26, 197–205. doi: 10.1016/s0896-6273(00)81150-2

Lynch, M. A. (2004). Long-term potentiation and memory. *Physiol. Rev.* 84, 87–136. doi: 10.1152/physrev.00014.2003

McNaughton, B. L. (1982). Long-term synaptic enhancement and short-term potentiation in rat fascia dentata act through different mechanisms. *J. Physiol.* 324, 249–262. doi: 10.1113/jphysiol.1982.sp014110

Neo, P., Carter, D., Zheng, Y., Smith, P. F., Darlington, C. L., and McNaughton, N. (2012). Septal elicitation of hippocampal theta rhythm did not repair the cognitive and emotional deficits resulting from vestibular lesions. *Hippocampus* 22, 1176–1187. doi: 10.1002/hipo.20963

Nicoll, R. A. (2017). A brief history of long-term potentiation. *Neuron* 93, 281–290. doi: 10.1016/j.neuron.2016.12.015

Potier, B., Lamour, Y., and Dutar, P. (1993). Age-related alterations in the properties of hippocampal pyramidal neurons among rat strains. *Neurobiol. Aging* 14, 17–25. doi: 10.1016/0197-4580(93)90016-5

Rancz, E. A., Moya, J., Drawitsch, F., Brichta, A. M., Canals, S., and Margrie, T. W. (2015). Widespread vestibular activation of the rodent cortex. *J. Neurosci.* 35, 5926–5934. doi: 10.1523/JNEUROSCI.1869-14.2015

Ross, S. T., and Soltesz, I. (2001). Long-term plasticity in interneurons of the dentate gyrus. *Proc. Natl. Acad. Sci. U S A* 98, 8874–8879. doi: 10.1073/pnas.141042398

Russell, N. A., Horii, A., Smith, P. F., Darlington, C. L., and Bilkey, D. K. (2003). Long-term effects of permanent vestibular lesions on hippocampal spatial firing. *J. Neurosci.* 23, 6490–6498. doi: 10.1523/JNEUROSCI.23-16-06490.2003

Russell, N. A., Horii, A., Smith, P. F., Darlington, C. L., and Bilkey, D. (2006). Lesions of the vestibular system disrupt hippocampal theta rhythm in the rat. *J. Neurophysiol.* 96, 4–14. doi: 10.1152/jn.00953.2005

Smith, P. F. (2017). The vestibular system and cognition. *Curr. Opin. Neurol.* 30, 84–89. doi: 10.1097/WCO.0000000000000403

Stackman, R. W., Clark, A. S., and Taube, J. S. (2002). Hippocampal spatial representations require vestibular input. *Hippocampus* 12, 291–303. doi: 10.1002/hipo.1112

Steward, G. R., Price, M., Olney, J. W., Hartman, B. K., and Cazzari, C. (1986). N-methylaspartate: an effective tool for lesioning basal forebrain cholinergic neurons of the rat. *Brain Res.* 369, 377–382. doi: 10.1016/0006-8993(86)90555-x

Tai, S. K., and Leung, L. S. (2012). Vestibular stimulation enhances hippocampal long-term potentiation via activation of cholinergic hippocampal cells. *Behav. Brain Res.* 232, 174–182. doi: 10.1016/j.bbr.2012.04.013

Tai, S. K., Ma, J., Ossenkopp, K. P., and Leung, L. S. (2012). Activation of immobility-related hippocampal theta by cholinergic septohippocampal neurons during vestibular stimulation. *Hippocampus* 22, 914–925. doi: 10.1002/hipo.20955

Tomasulo, R. A., Levy, W. B., and Steward, O. (1991). LTP-associated EPSP/spike dissociation in the dentate gyrus: GABAergic and non-GABAergic components. *Brain Res.* 561, 27–34. doi: 10.1016/0006-8993(91)90745-h

Tourdias, T., Mori, N., Dragonu, I., Cassagno, N., Boiziau, C., Aussudre, J., et al. (2011). Differential aquaporin 4 expression during edema build-up and resolution phases of brain inflammation. *J. Neuroinflamm.* 8:143. doi: 10.1186/1742-2094-8-143

Truchet, B., Benoit, A., Chaillan, F., Smith, P. F., Philoxene, B., Guillamin, M., et al. (2019). Hippocampal LTP modulation and glutamatergic receptors following vestibular loss. *Brain Struct. Funct.* 224, 699–711. doi: 10.1007/s00429-018-1792-0

Volgushev, M., Vidyasagar, T. R., Chistiakova, M., and Eysel, U. T. (2000). Synaptic transmission in the neocortex during reversible cooling. *Neuroscience* 98, 9–22. doi: 10.1016/s0306-4522(00)00109-3

Zheng, Y., Kerr, D. S., Darlington, C. L., and Smith, P. F. (2003). Peripheral vestibular damage causes a lasting decrease in the electrical excitability of CA1 in hippocampal slices *in vitro*. *Hippocampus* 13, 873–878. doi: 10.1002/hipo.10174

Zheng, Y., Mason-Parker, S. E., Logan, B., Darlington, C. L., Smith, P. F., and Abraham, W. C. (2010). Hippocampal synaptic transmission and LTP *in vivo* are intact following bilateral vestibular deafferentation in the rat. *Hippocampus* 20, 461–468. doi: 10.1002/hipo.20645

Zheng, Y., Wilson, G., Stiles, L., and Smith, P. F. (2013). Glutamate receptor subunit and calmodulin kinase II expression, with and without T maze training, in the rat hippocampus following bilateral vestibular deafferentation. *PLoS One* 8:e54527. doi: 10.1371/journal.pone.0054527

**Conflict of Interest**: The authors declare that the research was conducted in the absence of any commercial or financial relationships that could be construed as a potential conflict of interest.

*Copyright © 2020 Smith, Truchet, Chaillan, Zheng and Besnard. This is an open-access article distributed under the terms of the Creative Commons Attribution License (CC BY). The use, distribution or reproduction in other forums is permitted, provided the original author(s) and the copyright owner(s) are credited and that the original publication in this journal is cited, in accordance with accepted academic practice. No use, distribution or reproduction is permitted which does not comply with these terms.*

frontiers in Molecular Neuroscience

ORIGINAL RESEARCH
published: 12 August 2020
doi: 10.3389/fnmol.2020.00147

# Profile of MIF in Developing Hippocampus: Association With Cell Proliferation and Neurite Outgrowth

*Xuejun Chai[1]*†, Wei Zhang[2†], Lingling Li[2], Yongji Wu[2], Xiaoyan Zhu[2] and Shanting Zhao[2]**

[1] College of Basic Medicine, Xi'an Medical University, Xi'an, China, [2] College of Veterinary Medicine, Northwest A&F University, Yangling, China

Proinflammatory cytokine macrophage migration inhibitory factor (MIF) is a multifunctional cytokine and has been found involved in many neurological diseases such as Alzheimer disease (AD), epilepsy, and multiple sclerosis. Previous studies have shown that MIF is expressed in neocortex, hippocampus, hypothalamus, cerebellum, and spinal cord in adult mice. It is expressed by astrocytes and activates microglias in neuroinflammation. Further studies have shown that MIF is detected in moss fibers of dentate granule cells and in apical dendrites of pyramidal neurons in adult hippocampus. Only NeuroD-positive immature granule neurons but not NeuN-positive mature neurons express MIF. These findings led us eager to know the exact role of MIF in the development of hippocampus. Therefore, we systematically checked the spatial and temporal expression pattern of MIF and characterized MIF-positive cells in hippocampus from mice aged from postnatal day 0 (P0) to 3 months. Our results showed that the lowest level of MIF protein occurred at P7 and *mif* mRNA increased from P0, reached a peak at P7, and stably expressed until P30 before declining dramatically at 3 months. MIF was localized in fibers of GFAP- and BLBP-positive radial glial precursor cells in dentate gyrus (DG). DCX-expressing newly generated neurons were MIF-negative. Inhibition of MIF by MIF antagonist S, R-3-(4-hydroxyphenyl)-4, 5-dihydro-5-isoxazole acetic acid methyl ester (ISO-1) reduced BrdU-positive cells. Interestingly, MIF was expressed by NeuN-positive GABAergic interneurons including parvalbumin- and Reelin-expressing cells in the DG. Neither NeuN-positive granule cells nor NeuN-positive pyramidal neurons expressed MIF. In transgenic mice, POMC-EGFP–positive immature dentate granule cells and Thy1-EGFP–positive mature granule cells were MIF-negative. Treatment of neuronal cultures with ISO-1 inhibited neurite outgrowth. Therefore, we conclude that MIF might be important for feature maintenance of neural stem cells and neurite outgrowth during hippocampal development.

**Keywords: MIF, hippocampal development, interneurons, neurite outgrowth, cell proliferation**

OPEN ACCESS

***Edited by:***
*Lisa Topolnik, Laval University, Canada*

***Reviewed by:***
*Muddanna Sakkattu Rao, Kuwait University, Kuwait*
*Hector J. Caruncho, University of Victoria, Canada*

***Correspondence:**
*Xuejun Chai*
*junchai0708@126.com*
*Shanting Zhao*
*zhaoshanting@nwsuaf.edu.cn*

*† These authors have contributed equally to this work*

***Received:*** *03 March 2020*
***Accepted:*** *15 July 2020*
***Published:*** *12 August 2020*

***Citation:***
*Chai X, Zhang W, Li L, Wu Y, Zhu X and Zhao S (2020) Profile of MIF in Developing Hippocampus: Association With Cell Proliferation and Neurite Outgrowth. Front. Mol. Neurosci. 13:147. doi: 10.3389/fnmol.2020.00147*

## INTRODUCTION

Macrophage migration inhibitory factor (MIF) is a proinflammatory cytokine with molecular weight of 12 kDa and is released into the circulation by the anterior pituitary gland as a consequence of central nervous system (CNS) injury or as toxic response to endotoxemia (Bernhagen et al., 1993). It accumulates in neoplastic astrocytes and promotes microglial activation in neuroinflammation (Bacher et al., 2002; Cox et al., 2013).

MIF has been found to be expressed in neocortex, hippocampus, hypothalamus, cerebellum, choroid plexus, and spinal cord (Nishibori et al., 1997; Bacher et al., 1998; Ogata et al., 1998; Vedder et al., 2000; Li et al., 2008; Danış et al., 2011; Zhang et al., 2019) and involved in Parkinson disease, Alzheimer disease (AD), autism spectrum disorders, multiple sclerosis, schizophrenia, and gliomas (Grigorenko et al., 2008; Mittelbronn et al., 2011; Nicoletti et al., 2011; Cox et al., 2013; Zeiner et al., 2015; Kassaar et al., 2017; Okazaki et al., 2018; Cheng et al., 2020). In AD patients, the concentration of MIF remarkably increased in the cerebrospinal fluid (Bacher et al., 2010; Zhang et al., 2019). Studies have demonstrated that dysfunction of MIF in AD is due to glycation and oxidation of MIF, which inhibit MIF activity to stimulate glial cells leading to deficiency of clearance of amyloid β (Aβ) protein (Kassaar et al., 2017). The binding assay revealed that MIF expression largely associates with Aβ deposits in AD brain (Zhang et al., 2019). In human gliomas, MIF is strongly expressed by tumor cells and its receptors CD74 is only restricted to microglial cells (Zeiner et al., 2015).

In addition to the role in neuropathological diseases, MIF has been reported to be involved in neurogenesis of hippocampus in normal conditions. MIF colocalizes with vimentin and GFAP in hippocampal precursor cells and astrocytes. Loss of MIF leads to reduced expression of PSA-NCAM and DCX in hippocampus (Conboy et al., 2011; Djordjevic et al., 2017).

Previous studies have indicated that MIF is expressed by astrocytes and locates in mossy fibers of dentate granule cells in adult hippocampus (Bacher et al., 1998; Ogata et al., 1998; Bacher et al., 2002; Cox et al., 2013). Few studies have successfully detected MIF immunostaining in neuronal somata, although *in situ* hybridization shows a strong labeling of *mif* mRNA in cytoplasm of granule cells and pyramidal neurons of hippocampus (Bacher et al., 1998). Until 2011, Conboy and his colleagues demonstrated that MIF is expressed by NeuroD-positive immature granule neurons in hippocampus, but not by NeuN-positive mature neurons (Conboy et al., 2011). However, it is still elusive on MIF expression and characteristics, as well as potential functions, especially in the stage of hippocampal development. To address this issue, we systematically examined the spatial and temporal expression pattern of MIF protein and *mif* mRNA by Western blotting and real-time polymerase chain reaction (PCR) and characterized MIF-positive cells in hippocampus of mice aged from postnatal day 0 (P0) to 3 months by immunostaining. Using antagonist of MIF, we blocked MIF function and observed impairment of cell proliferation and neurite outgrowth in hippocampus. Our results suggest that MIF might maintain the feature of neural stem cells and promote outgrowing of neuronal processes in developing hippocampus.

# MATERIALS AND METHODS

## Animals

P7 POMC-EGFP and 3-month Thy1-EGFP transgenic mice were obtained from the animal facility of Hamburg University, UKE, Germany. Animals were housed under standard laboratory conditions in the animal facility at the Center for Molecular Neurobiology Hamburg. All experiments were performed in accordance with the institutional guide for animal care (license number ORG 850). Genotyping was performed by PCR analysis of genomic DNA, as described previously (Overstreet et al., 2004; Vuksic et al., 2008). P0, P3, P7, P14, P30, and 3-month Kunming mice were obtained from the Experimental Animal Center of Xi'an Jiaotong University. All procedures were performed in accordance with the protocol approved by the Institutional Animal Care of Northwest A&F University and Xi'an Medical University.

## Antibodies and Inhibitor

The following primary antibodies were used for immunofluorescence studies and Western blot analyses: rabbit polyclonal anti-MIF (1:500, ABclonal, United States), mouse monoclonal anti-Reelin G10 (dilution 1:1,000, Millipore, United States), mouse monoclonal anti-Parvalbumin (1:500, Abcam, United States), mouse polyclonal anti-GFAP (1:500, DAKO, United States), mouse monoclonal anti-NeuN (1:500, Millipore, United States), mouse monoclonal anti–neurofilament 200 (1:1,000, Millipore, United States), mouse monoclonal anti–β-tubulin (1:500; Sigma-Aldrich, United States), goat polyclonal anti-DCX (1:1,000; Santa Cruz, United States), mouse monoclonal anti-BLBP (1:300, Raybiotech, Inc., United States), and rat polyclonal anti-BrdU (1:500, Bio-Rad Laboratories Inc., United States). The secondary antibodies used for Western blotting were horseradish peroxidase (HRP)–conjugated goat anti–rabbit IgG and goat anti–mouse IgG (1:2,000; Cell Signaling Technology, United States). The secondary antibodies for immunostaining were as follows: Alexa Fluor 488-conjugated goat anti–mouse, Alexa Fluor 568–conjugated goat anti–mouse, Alexa Fluor 488-conjugated goat anti–rabbit IgG, Alexa Fluor 568–conjugated goat anti–rabbit IgG, Alexa Fluor 488-conjugated donkey anti–goat, Alexa Fluor 488–conjugated goat anti-rat. Dyes used were DAPI (1:10,000; Invitrogen, United States) and TRITC-labeled phalloidin (1:4,000; Sigma, United States).

S, R-3-(4- hydroxyphenyl)-4, 5-dihydro-5-isoxazole acetic acid methyl ester (ISO-1), an antagonist of MIF, was purchased from Calbiochem, Germany. BrdU was purchased from Sigma-Aldrich, United States.

## Plasmids Construction

The procedures of pCAG-EGFP and pCAG-MIF-MYC construction were identical as previously described (Zhang et al., 2014). In brief, the MYC tag was inserted into the vector pCAG-MCS (Biowit Technologies, China) by using In-Fusion® HD Cloning Kit (Clontech, United States) according to the manufacturer's protocol, and then the full-length MIF was cloned into pCAG-MCS-MYC by the traditional cloning method. pCAG-EGFP was obtained by the insertion of EGFP fragment into linearized pCAG-MCS using the traditional cloning method.

## HEK293T Cell Culture and Transfection

HEK293T cells were grown in DMEM (Dulbecco modified eagle medium, low glucose; Invitrogen) with 10% fetal calf serum (FCS; Invitrogen) and 1% penicillin-streptomycin

(P/S, 10,000 U/mL; Invitrogen) at 37℃ in a humidified atmosphere of 5% $CO_2$. When reaching 60–70% confluence in 60 mm culture dishes, HEK293T cells were transfected with pCAG-MIF-MYC using Lipofectamine 2000 Kit (Thermo Fisher Scientific, United States). Forty-eight hours after transfection, the cells were collected, frozen in liquid nitrogen, and stored at -80℃ for Western blotting.

## *In utero* Electroporation and Overexpression of MIF in Migrating Neurons

*In utero* electroporation was performed according to the procedure described as previously (Chai et al., 2015, 2016). Timed-pregnant females were deeply anesthetized by intraperitoneal injection of chloral hydrate (4.3 mg per 10 g of body weight). Then, the uterine horns of the pregnant mice were carefully exposed via a midline abdominal incision by pinching gaps between embryos with ring-forceps. Approximately 1–1.5 μL of pCAG-MIF-MYC and pCAG-EGFP (1 mg/mL for each) plasmid solution was injected into the lateral ventricle of mouse embryos on embryonic day 15.5 (E15.5) using a mouth-controlled pipette system and a pulled-glass micropipette. Fast green solution (0.1%) was added to the plasmid solution in a ratio of 1:10 to monitor the injection. The heads of injected embryos in the uterus were placed between the tweezers-type electrodes. Electronic pulses (30–50 V; 50 ms) were charged five times at intervals of 900 ms with an electroporator (Gene Pulser Xcell Electroporation System, United States). The uterine horns were placed back into the abdominal cavity to allow the embryos to continue normal development until sacrificed at P0. Brains ($n$ = 9) were collected and fixed with 4% paraformaldehyde (PFA) at 4℃ overnight. After rinsing in 0.1 M PB, brains were embedded in 5% agar and cut into 40-μm-thick slices on a Leica VT 1000S vibratome (Leica Microsystems, Germany). The sections were placed in a 24-well plate containing 0.1 M PB for immunostaining.

## Preparation of Protein Extracts

P0 and P3 Kunming mice were sacrificed under frozen anesthesia. P7, P14, P30, and 3-month Kunming mice were anesthetized with an overdose of Narkodorm (500 μL/kg) first with 0.9% NaCl and decapitated ($n$ = 4 for each). Hippocampi were prepared and frozen with liquid nitrogen for immediate protein extraction or stored at -80℃. Tissue pellets and cell cultures were taken out from -80℃ and incubated in ice-cold hypertonic lysis buffer [pH 7.6, 50 mM Tris-HCl, 150 mM NaCl, 5 mM EDTA-$Na_2$, 1% (vol/vol) Non-idet P-40, 1% Triton X-100, 0.5% (wt/vol) sodium dodecyl sulfate (SDS), 0.25% (wt/vol) sodium deoxycholate] with 1% protease inhibitor (Sigma, United States), and phosphatase inhibitor cocktails (Sigma). The tissue pellets and cells were lysed by repeated freezing in liquid nitrogen and thawing at 37℃ (five times). After the tissue was triturated with a pipette tip to homogenize larger pieces of tissue and sonicated for 5 min, the suspension was centrifuged at 20,000 × $g$ at 4℃ for 30 min. The resulting crude supernatants were taken, and protein concentration was measured by using BCA Protein Assay Kit (Pierce, United States). Aliquots of the supernatants were immediately used for Western blotting or were stored at -80℃ until use.

## Western Blot Analysis

Five to 10 μg of each sample was diluted in ultrapure water containing 1 × NuPAGE sample buffer (Invitrogen) and 1 × NuPAGE reducing agent (Invitrogen) to final volumes of 24 μL, boiled at 95℃ for 5 min, and then immediately placed on ice. The samples were separated by NuPAGE bis-tris, pH 7.0, 4–12% PAGE (Invitrogen) with 1 × NuPAGE MES-SDS running buffer (Invitrogen), and transferred electrophoretically to polyvinylidene fluoride membranes with 1 × NuPAGE transfer buffer (Invitrogen). For blotting, membranes were blocked with 5% (wt/vol) non-fat milk or 5% bovine serum albumin (BSA) in tris-buffered saline at room temperature (RT) for 1 h and finally incubated with primary antibodies in blocking solution at 4℃ overnight. After three washes, the blots were subsequently incubated with a HRP-conjugated goat anti–rabbit or mouse IgG secondary antibody (1:2,000; Cell Signaling, United States) for 2 h at RT. The immunoreaction was visualized by enhanced chemiluminescence and scanned with a chemiluminescent and fluorescent imaging system (BioRad, United States). Bands were normalized to β-tubulin level to provide a control for equal loading. At least three Western blots were analyzed for each experiment. Blots were quantified by densitometry using ImageJ (NIH, United States). Significance was determined by one-way analysis of variance across all samples followed by Tukey test ($^*P < 0.05$, $^{**}P < 0.01$, $^{***}P < 0.001$) (GraphPad Prism 5, United States).

## Quantitative Real-Time PCR

Quantitative real-time PCR was performed according to the procedure described as previously (Zhang et al., 2014). In brief, P0, P3, P7, P14, P30, and 3-month Kunming mice ($n$ = 4 for each) were anesthetized, and decapitated; hippocampi were prepared and frozen with liquid nitrogen for immediate total RNA extraction or stored at -80℃. Total RNA was extracted using Trizol reagent (Invitrogen, United States). The integrity of RNA was verified by 1% agarose gel, and cDNA was synthesized from 1 μg of total RNA primed with oligo (dT) using RevertAid First Strand cDNA Synthesis Kit (Thermo Scientific, United States). Quantitative PCR was performed using the Bio-Rad CFX96 (Bio-Rad, CA, United States) with Actb as an internal control. All PCR products span an intron in the genomic DNA. The cDNA was amplified with SYBR Premix Ex TaqTM (Takara, Japan). Relative quantification of mRNA levels was performed using the comparative Ct method.

## Neuronal Cultures

Dissociated cultures of hippocampus were prepared as described previously (Chai et al., 2009). For primary cell cultures, newborn (P0) Kunming mice ($n$ = 9) were used. The hippocampi were dissected and put into ice-cold Hanks balanced salt solution (HBSS). After removal of the meninges, the hippocampi of both hemispheres were collected and maintained in 15 mL Falcon tubes (BD Biosciences, United States) containing 3 mL of 0.5%

Trypsin and 0.53 mM EDTAx4Na (Invitrogen, United States) and incubated at 37°C for 10 min. The hippocampi were then washed twice in ice-cold HBSS and manually triturated with a polished glass Pasteur pipette for several times. Then, the cells were centrifuged at low speed (800 × *g*) for 3 min to discard dead cells. The sediment was collected in fresh Falcon tubes and centrifuged again. The supernatant was discarded, and cell pellets were resuspended in 1 mL of neurobasal-A medium (Invitrogen, United States), supplemented with 2% B27 (Invitrogen, United States), 1 mM Glutamax (Invitrogen, United States), 100 U/mL penicillin, and 100 μg/mL streptomycin (Invitrogen, United States). Hippocampal cells were counted using a hemocytometer and suspended at a density of $5 \times 10^5$ cells in 0.5 mL aliquots on glass coverslips inserted in 24-well plates. The coverslips had been coated overnight with a solution of 20 μg/mL poly-L-ornithine (Sigma, United States) prepared in borate buffer, pH 8.1. After 2 h of incubation in a humidified incubator at 37°C and 5% $CO_2$ to allow for cell attachment, the medium was changed to remove dead cells. After 12 h of incubation, cultures were divided into three groups ($n = 12$ wells for each group): one group was allowed to grow about 5 days. The second group was used for ISO-1 treatment for 48 h. The third group was used for control treatment for 48 h. Then the cultures were fixed with 4% PFA in 0.1 M PB, pH 7.4, for 15 min at RT and rinsed in 0.1 M PB for 1 h followed by incubation in blocking solution for immunostaining.

## ISO-1 Treatment *in vitro*

ISO-1 (Calbiochem, Germany) was freshly dissolved in dimethyl sulfoxide (DMSO). Twelve hours after seeding of neurons in 24-well dishes, medium was replaced by serum-free medium containing 10 or 100 μM ISO-1, and neurons were incubated for 48 h before fixing with 4% PFA in 0.1 M PB for immunostaining.

## ISO-1 Treatment *in vivo*, BrdU Injection, and Labeling

P5, P14, P30, and 3-month Kunming mice ($n$ = 4 for each) were injected with BrdU [intraperitoneal (i.p.), 50 mg/kg; Sigma-Aldrich, United States] dissolved in physiological saline 2 h (evidence proliferating cells only, Conboy et al., 2011) before being anesthetized with an overdose of Narkodorm (500 μL/kg) with 0.9% NaCl and then transcardially perfused with 4% PFA in 0.1 M PB (pH 7.4). For MIF inhibition experiment, P6 Kunming mice ($n$ = 8) were injected with ISO-1 (i.p., 7 mg/kg; Calbiochem, Germany) or vehicle (DMSO, i.p.) daily for 9 consecutive days. On P15, mice were injected with BrdU 4 h (to evidence proliferating cells only, due to the blocking effect of MIF by ISO-1, the incubation time was elongated) before being anesthetized and perfused with 4% PFA. Brains were postfixed with 4% PFA in 0.1 M PB overnight at RT, washed 24 h, and cut into 50 μm thick sections on a Leica VT 1000S vibratome (Leica Microsystems, Germany).

BrdU-labeled sections were denatured by incubation with 2 M HCl for 30 min at 37℃ and washed with 0.1 M borate buffer (pH 8.0) for several times. After rinsing with 0.1M PB three times, sections were placed in a 24-well plate for immunohistochemistry.

## Immunohistochemistry

P0 mice were decapitated under hypothermic anesthesia; brains were removed and immersion fixed in 4% PFA. P7, P14, P30, and 3-month mice (including POMC-EGFP and Thy1-EGFP transgenic mice) were anesthetized with an overdose of Narkodorm (500 μL/kg) first with 0.9% NaCl and then transcardially perfused with 4% PFA in 0.1 M PB (pH 7.4). Brains were removed and postfixed in 0.1 M PB (PH7.4) containing 4% PFA overnight at RT. After washing in 0.1 M PB overnight, fixed brains were embedded in 5% agar and cut coronally into 40-μm-thick slices to contain the entire hippocampus on a Leica VT 1000S vibratome (Leica Microsystems, Germany). After washing for 2 h at RT in 0.1 M PB, sections were placed in a 24-well plate containing 0.1 M PB for immunostaining. Sections together with sections from *in utero* electroporation, BrdU experiment, and neuronal cultures treated with ISO-1 and control medium were preincubated with blocking solution (5% normal goat serum and 1% BSA in 0.1 M PB containing 0.2% Triton X-100) at RT for 1 h and then incubated with the primary antibodies diluted in blocking solution overnight at 4°C. After washing in 0.1 M PB for 15 min three times, sections or cultured cells were incubated in secondary antibodies diluted in 0.1 M PB for 2 h at RT. After washing in 0.1 M PB for 15 min three times, sections or cultured cells were counterstained with DAPI (1:10,000; Invitrogen). Some cell cultures were stained for F-actin with TRITC-labeled phalloidin (1:4,000; Sigma). After rinsing in 0.1 M PB 15 min three times, sections and cells were mounted with fluorescent mounting medium (Dako North America, Inc., United States) and photographed by a structured-illumination microscope (Zeiss observer Z1) or using a confocal laser scanning microscope (Olympus FV1000).

## Quantitative Assessments

Quantifications of double-labeled cells with MIF and NeuN, MIF and GFAP, MIF and parvalbumin (Pv), and MIF and Reelin were performed using ImageJ software.

Morphometric measurements of cultured hippocampal neurons treated with vehicle, 10 μM ISO-1, and 100 μM ISO-1 were performed by ZEN 2011 software. Data were from three independent neuronal cultures. At least three fields were randomly photographed in each condition of every experiment; 2.5 DIV neurons have differentiated with a longest neurite, which later will develop into axons. Neurites were traced along the processes. The longest neurite, number of terminal tips, and total length of neurites were analyzed by GraphPad Prism 5. One-way analysis of variance with Tukey post test and Kruskal–Wallis test with Dunn post test were performed for parametric and non-parametric data, respectively. Graphs were represented as the mean ± SEM. Differences were considered significant when $P < 0.05$, and represented as $^*P < 0.05$, $^{**}P < 0.01$, $^{***}P < 0.001$.

Quantification of newly generated cells was calculated by counting BrdU-positive cells in 1,000 μm sectional length in the SGZ and granular cell layer (GCL) of the hippocampus from P6 mice injected with either DMSO or ISO-1 for consecutive 9 days.

Totally, 12 coronal sections for each group were photographed at 20× magnification with a Zeiss microscope. Values were analyzed for significance using the Student two-tailed *t*-test (GraphPad Prism 5).

# RESULTS

## MIF Antibody Is Verified to Be Sufficiently Detectable *in vivo*

In order to identify the effectiveness of MIF antibody purchased commercially, plasmid pCAG-MIF-MYC expressing MIF and MYC tag and plasmid pCAG-EGFP expressing EGFP were constructed and electroporated into embryonic cortical neurons. After birth of mice, brains were collected and cut into sections for MIF immunostaining. We found that neurons transfected with EGFP and MIF plasmids on E15.5 have reached their final destinations in the superficial layer of the cortex. They were perfectly recognized by MIF immunostaining (**Figure 1A**). Plasmid pCAG-MIF-MYC was also transfected into cultured HEK293T cells. Cells were harvested, and MIF protein expression was analyzed by Western blotting. As shown in **Figure 1B**, MIF antibody detected not only endogenous MIF-MYC, but also exogenous MIF (**Figure 1B**). Our observations indicate that MIF antibody purchased commercially is specific and sufficient to examine MIF expression by immunostaining.

## MIF Is Expressed at All Postnatal Ages but With Lowest Expression at P7 During Hippocampal Development

To investigate the expression profile of MIF during development of hippocampus, we first checked *mif* mRNA by using quantitative real-time PCR at different developmental time points: P0, P3, P7, P14, P30, and 3 months. The results showed that expression level of *mif* mRNA gradually increased from P0 to P7, reached the peak at P7, and stably expressed until P30, and then declined dramatically to adulthood (**Figure 2A**). Compared with that at P0, *mif* mRNA increased by 0.6-fold at P7 and decreased by 0.4-fold at adult (**Figure 2A**). Western blotting result demonstrated that MIF was expressed at all postnatal ages (**Figure 2B**). Densitometric analysis from three independent experiments showed that the expression profile of MIF protein during hippocampal development is like an inverted bell with the lowest level at P7 and higher level before or after (**Figure 2C**). Compared to that at P7, the MIF expression was increased by 2.8-fold at P3 and 0.9-fold at P14 (**Figure 2C**). Statistical analysis revealed significant differences between P7 and other time points during development of hippocampus (**Figure 2C**).

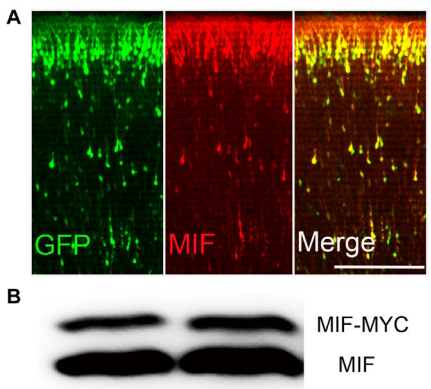


**FIGURE 1 |** MIF antibody verification. **(A)** Embryonic cortical neurons were cotransfected with pCAG-MIF-MYC and pCAG-EGFP using *in utero* electroporation at E15.5 and fixed at P0. Sections were then immunostained with antibody against MIF (red). Strong labeling of MIF was found in cytoplasm and neurites of GFP-labeled neurons. **(B)** Western blotting showed that MIF antibody recognized endogenous MIF (lower band) and exogenous MIF (MIF-MYC, upper band) expressed by transfected-293 tumor cells. Scale bar in **(A)**: 200 μm.

## MIF Is Highly Expressed in Hippocampal Mossy Fibers of P14 Mice

Immunostaining of MIF in P0, P7, P14, and P30 hippocampus further proved that MIF expression at P7 was the lowest compared to those at P0, P14, and P30 ages (**Figure 3A**). In addition, we noticed strong MIF expression in stratum lucidum of CA3 from P14 (**Figure 3A**). To make sure that MIF was located in mossy fiber projections, the axons of granule cells, we performed double-immunolabeling of MIF and tubulin in sections of P14 hippocampus, and results revealed that MIF was perfectly overlapped with tubulin in mossy fibers (**Figures 3B,C**).

## MIF Interacts With Cytoskeletal Structures

In order to explore the relationship between MIF and the nerve fiber structure, immunostaining of MIF and cytoskeletal molecules was performed in cultured neurons. Phalloidin recognizes F-actin (filamentous actin), which forms actin cytoskeleton, and tubulin recognizes microtubule cytoskeleton. Our results clearly showed that MIF colocalized with phalloidin in F-actin and tubulin in microtubules, indicating that MIF interacted with cytoskeletal structures (**Figures 4A,B**).

## MIF Is Expressed in Both NeuN-Positive and NeuN-Negative Cells in Developing Hippocampus

To examine whether the cells expressing MIF are neurons during development of hippocampus, we first performed double-immunostaining for MIF and NeuN in hippocampal sections from 3-month mice. NeuN is a specific marker for mature neurons. Our results showed that many MIF-positive cells were scattered throughout the whole hippocampus, and a group of MIF-positive cells was accumulated in subgranular zone (SGZ) of dentate gyrus (DG) and formed a densely packed cell layer with long processes extending into GCL (**Figure 5A**). Those MIF-expressing cells scattered in hilus of DG (**Figure 5A**) and in stratum oriens (so), stratum radiatum (sr), and stratum lacunosum molecular (slm) of hippocampus proper were found NeuN-positive (**Figures 5B,C**). However, neither NeuN-positive granule cells in the granule layer (GCL) nor NeuN-positive

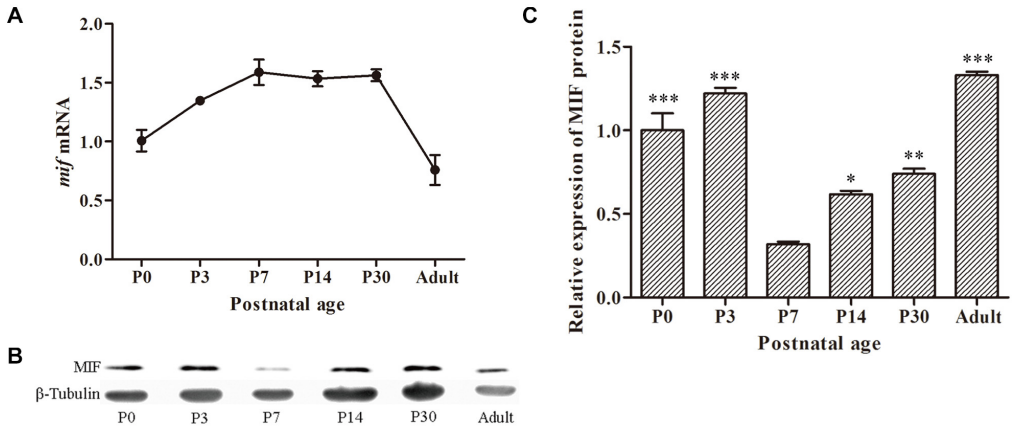


**FIGURE 2 |** MIF expression in developing hippocampus. **(A)** Relative quantitative real-time PCR for *mif* mRNA extracted from P0, P3, P7, P14, P30, and 3-month hippocampi. Expression level of *mif* mRNA started to rise from P0, reached the peak at P7, and stably expressed until P30 and then declined dramatically to adulthood (3 months). **(B)** Immunoblotting analysis for MIF protein from P0 to 3-month hippocampi. The lowest level of MIF expression was found at P7. β-tubulin was used as a loading control. **(C)** Densitometric analysis from three independent experiments showed that the expression profile of MIF protein during hippocampal development is like an inverted bell with the lowest level at P7 and higher level before or after. Statistical analysis indicated that the expression of MIF at P0, P3, P14, and P30 was significantly increased compared to that at P7 (Tukey multiple-comparisons test). All data were presented as mean ± SEM from three different experiments. ***$P < 0.001$, **$P < 0.01$, *$P < 0.05$.

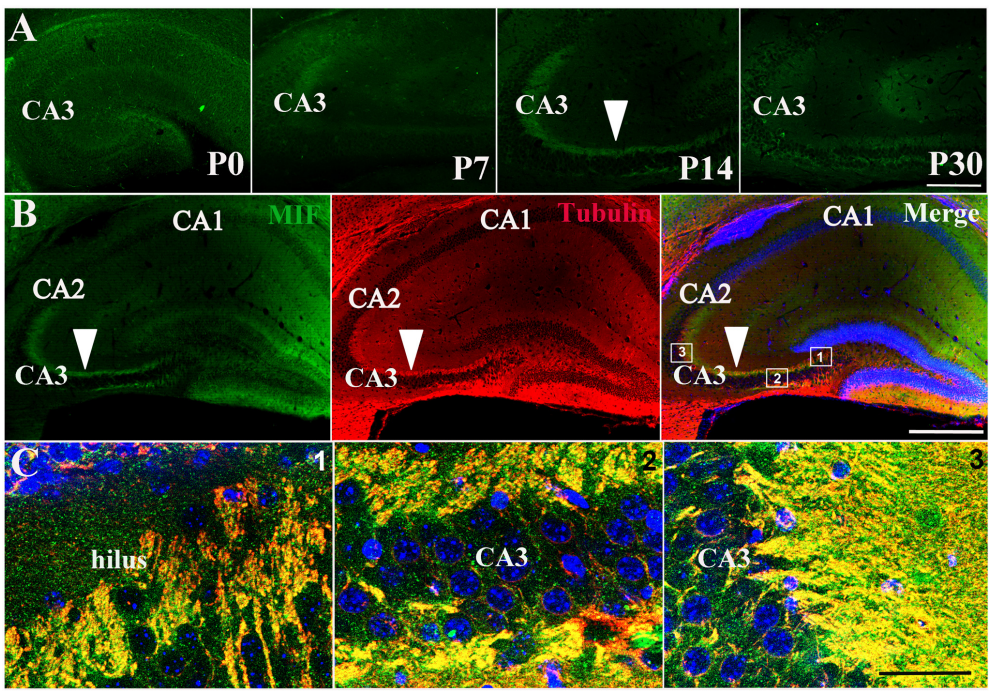


**FIGURE 3 |** MIF is highly expressed in hippocampal mossy fibers of P14 mice. **(A)** Immunofluorescent detection of MIF (green) in hippocampus at P0, P7, P14, and P30. MIF expression at P7 was the lowest compared to that at P0, P14, and P30 (white arrowhead). **(B)** At P14, there was a strong MIF (green) expression in stratum lucidum of CA3 along pyramidal cell layer. Double-labeling of MIF and tubulin (red) revealed that MIF was perfectly overlapped with tubulin in mossy fibers (white arrowheads). **(C)** High magnifications of merged images from regions indicated in the rectangular boxes in B. Nuclei were counterstained with DAPI (blue). Scale bars in **(A)**: 100 μm, **(B)**: 400 μm, **(C)**: 40 μm.

pyramidal neurons in the pyramidal cell layer (PCL) were seen MIF-positive (**Figures 5A–C**). Notably, the densely packed cell layer with MIF expression in SGZ showed NeuN-negative (**Figure 5A**). These results indicated that MIF was expressed in both NeuN-positive and NeuN-negative cells (**Figures 5A–C**). Here again a strong expression of MIF was observed in mossy fibers in sl attached to the pyramidal neurons in CA3 region (**Figure 5C**). We took an area of 0.1 $mm^2$ in

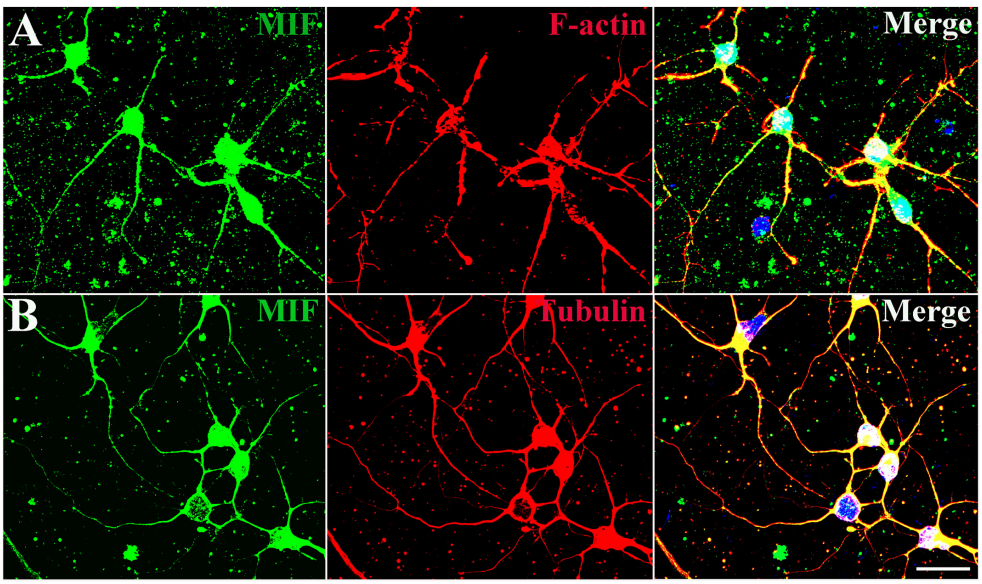


**FIGURE 4 |** MIF interacts with cytoskeletal molecules in cultured neurons. Hippocampal primary neurons were isolated from P0 and cultured for 5 days *in vitro*. **(A)** MIF (green) was overlapped with F-actin (red). **(B)** MIF (green) was merged with tubulin (red). Nuclei were counterstained with DAPI (blue). Scale bars in **(A,B)**: 20 μm.

the DG, CA1, and CA3 areas of each hippocampal slice; counted 10 MIF-positive cells; and calculated the percentage of MIF and NeuN double-labeled cells in MIF-positive cells. Five hippocampal slices in total were used. As shown, the percentages of MIF and NeuN double-labeled cells in MIF-positive cells in CA1,CA3 and DG (h + m) were much higher than that of MIF and NeuN double-positive cells in MIF-positive cells in SGZ (**Figure 5D**).

## MIF Is Expressed by NeuN-Positive GABAergic Interneurons in Developing Hippocampus

As the most of MIF and NeuN double-labeled cells in hippocampus were scattered throughout the whole hippocampus, not in the GCL and PCL, and morphologically very similar to interneurons (**Figure 5**), we speculated that these MIF and NeuN double-positive cells were interneurons. To confirm our supposition, we carried out double-immunolabeling of MIF with parvalbumin (Pv) and Reelin antibodies, respectively, in 3-month-old hippocampus. The results revealed that the majority of MIF-positive cells in hippocampus except the cells in SGZ were colabeled with parvalbumin (**Figures 6A–C**) or Reelin (**Figure 6D**). Given that parvalbumin and Reelin are markers for GABAergic interneurons, these results indicated that the scattered MIF-positive cells in hippocampus were GABAergic interneurons. Finally, we counted MIF-positive cells and parvalbumin-positive cells in 0.03 $mm^2$ area of CA1 and CA3 region, MIF-positive cells, and Reelin-positive cells in 0.03 $mm^2$ area of hippocampal fissure (HF) region. In **Figure 6E**, the rectangular boxes indicate the regions as shown in **Figures 6A–D**. Six hippocampal slices in total were used. We found that parvalbumin- or Reelin-positive cells were all MIF-positive, but not all MIF-positive cells were parvalbumin- or Reelin- positive. The percentage of parvalbumin and MIF double-labeled cells in MIF-positive cells was higher than that of Reelin and MIF double-labeled cells in MIF-positive cells (**Figure 6F**).

## MIF Is Expressed by Neither Immature nor Mature Granule Cells in Developing Hippocampus

As MIF was strongly expressed in mossy fibers (**Figures 3B,C**) and previous study has suggested that NeuroD-positive immature granule cells express MIF (Conboy et al., 2011), wherefore, to find out whether the granule cells express MIF, we used P7 POMC-EGFP and 3-month-old Thy1-EGFP transgenic mice, in which most immature and mature granule cells are labeled by EGFP, respectively. In the transgenic mice, POMC promoter-driven EGFP expression in hippocampal granule cells remains only 1 week after generation. One week after, granule cells began to express EGFP under Thy1 promoter. Therefore, they can represent immature granule cells and mature granule cells. MIF immunostaining showed that neither POMC-EGFP–labeled immature granule cells nor Thy1-EGFP–positive mature granule cells express MIF (**Figure 7**). POMC-EGFP–positive immature granule cells in GCL were not overlapped with any MIF-positive cells distributed in DG (**Figure 7A**). Thy1-EGFP–positive mature granule cells in GCL were also MIF-negative (**Figures 7B,C**). Moreover, MIF-positive cells scattered in SGZ and hilus of DG (DH) displayed giant morphology prompting them as interneurons (**Figures 7B,C**). In

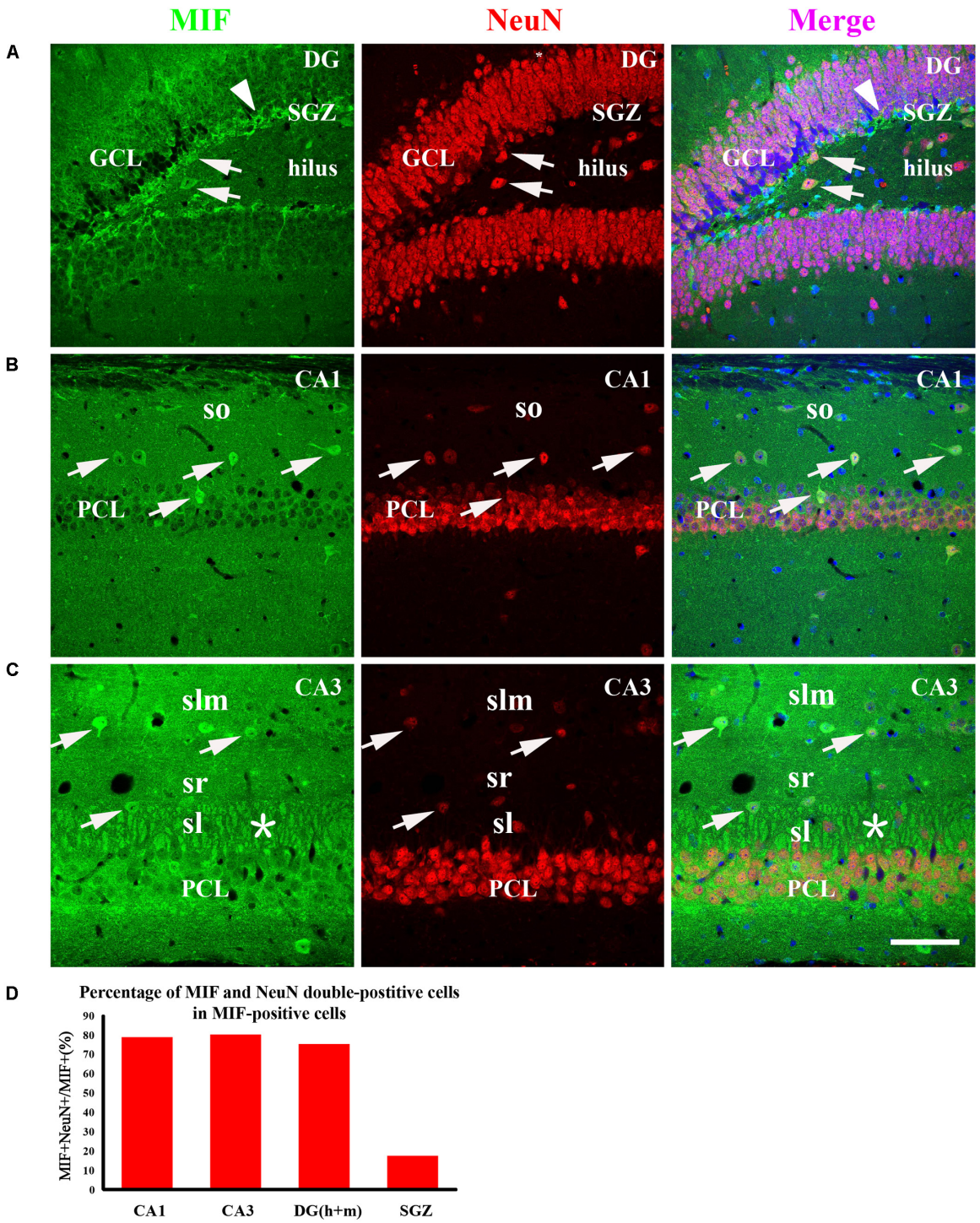


**FIGURE 5 |** MIF is expressed in both NeuN-positive and NeuN-negative cells in whole hippocampus of 3-month-old mice. MIF-positive cells (green) were scattered in the DG, CA1, and CA3 **(A–C)**. They were neither expressed by NeuN-positive granule cells (red) in the granular cell layer (GCL) in the DG (A) nor by NeuN-positive pyramidal neurons (red) in the pyramidal cell layer (PCL) in CA1 **(B)** and CA3 **(C)**. But they were NeuN-positive cells (**A–C**, white arrows). In DG, except some MIF and NeuN double-labeled neurons scattered in hilus, a densely packed MIF-positive cells (green) with their processes extending into GCL in subgranular zone (SGZ) was observed. However, these cells were NeuN-negative (A, white arrowhead). In CA1 and CA3, MIF and NeuN double-labeled neurons were found sporadically distributed in the stratum oriens (so), stratum lacunosum moleculare (slm), stratum lucidum (sl) (**B,C**, white arrows). In CA3, mossy fibers were positive for MIF in sl, marked by an asterisk **(C)**. Quantitative analysis showed that the percentages of MIF and NeuN double-labeled cells in MIF-positive cells in CA1, CA3, and DG (h + m) were significantly increased compared to that in SGZ **(D)**. Means ± SEM, two-tailed Student's *t*-test, $^{***}P < 0.001$, $n = 5$. DG, dentate gyrus. Scale bars in **(A–C)**: 80 μm.

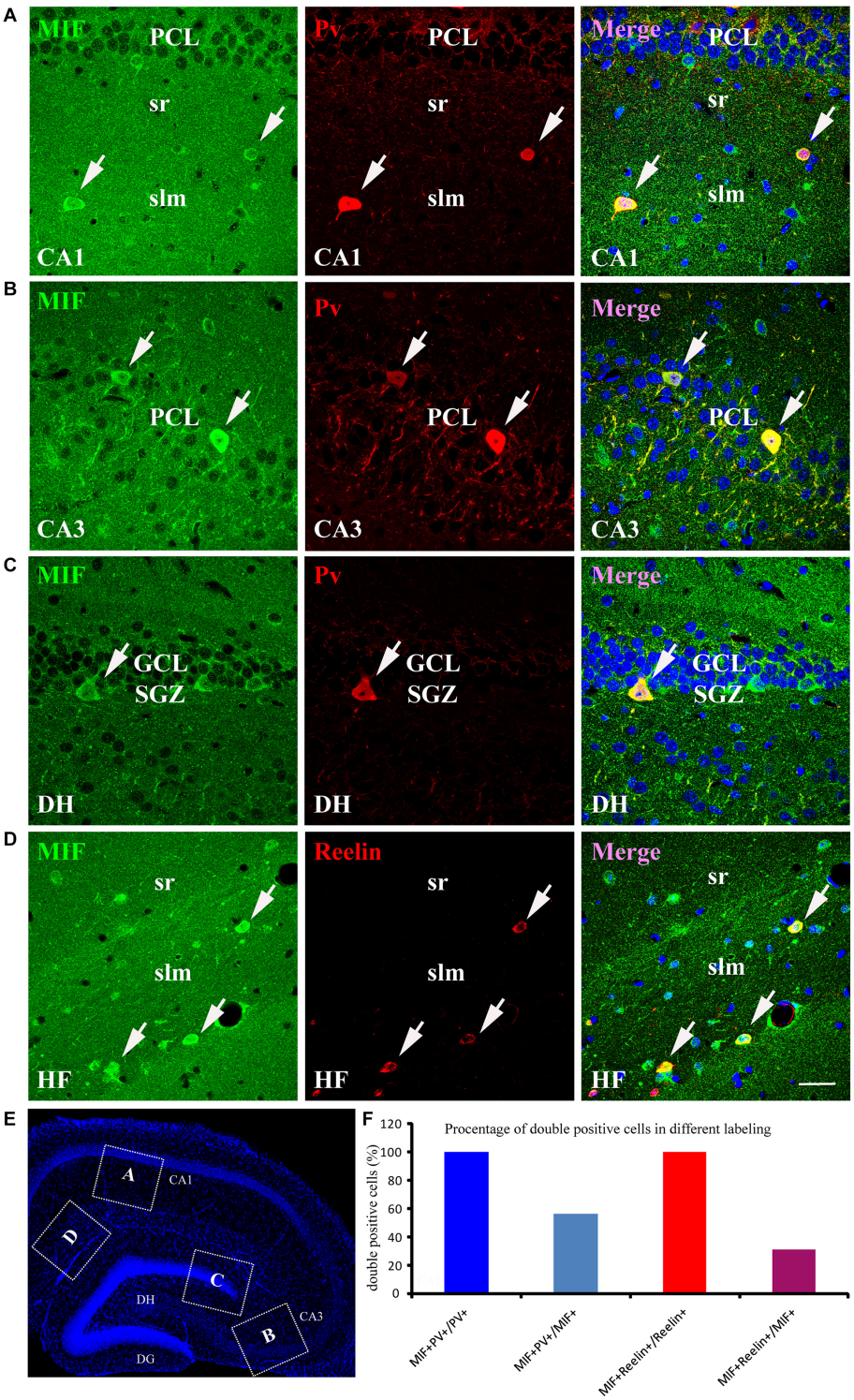


**FIGURE 6 |** MIF is expressed by NeuN-positive GABAergic interneurons in adult hippocampus. **(A–C)** Double-labeling of MIF and parvalbumin (Pv) in CA1, CA3, and DG of the hippocampus. MIF staining (green) was colocalized with parvalbumin-positive interneurons (red) in stratum radiatum (sr), stratum lacunosum moleculare (slm) of CA1 **(A)**, CA3 pyramidal cell layer (PCL) **(B)**, and DG subgranular zone (SGZ) **(C)**. **(D)** Around the hippocampal fissure (HF), MIF was found located in the Reelin-expressing interneurons (red). These cells were smaller than parvalbumin-positive cells. All double-labeled cells were pointed with white arrows. **(E)** The boxed regions indicated the location of **(A–D)** in the hippocampal slice. Nuclei were counterstained with DAPI (blue). **(F)** Quantification results showed that all parvalbumin or Reelin-positive cells were MIF-positive ($MIF^+Pv^+/Pv^+$ or $MIF^+Reelin^+/Reelin^+$), but not all MIF-positive cells were parvalbumin- or Reelin-positive ($MIF^+Pv^+/MIF^+$ or $MIF^+Reelin^+/MIF^+$). DG, dentate gyrus; DH, dentate hilus. Scale bars in **(A–D)**: 30 μm.

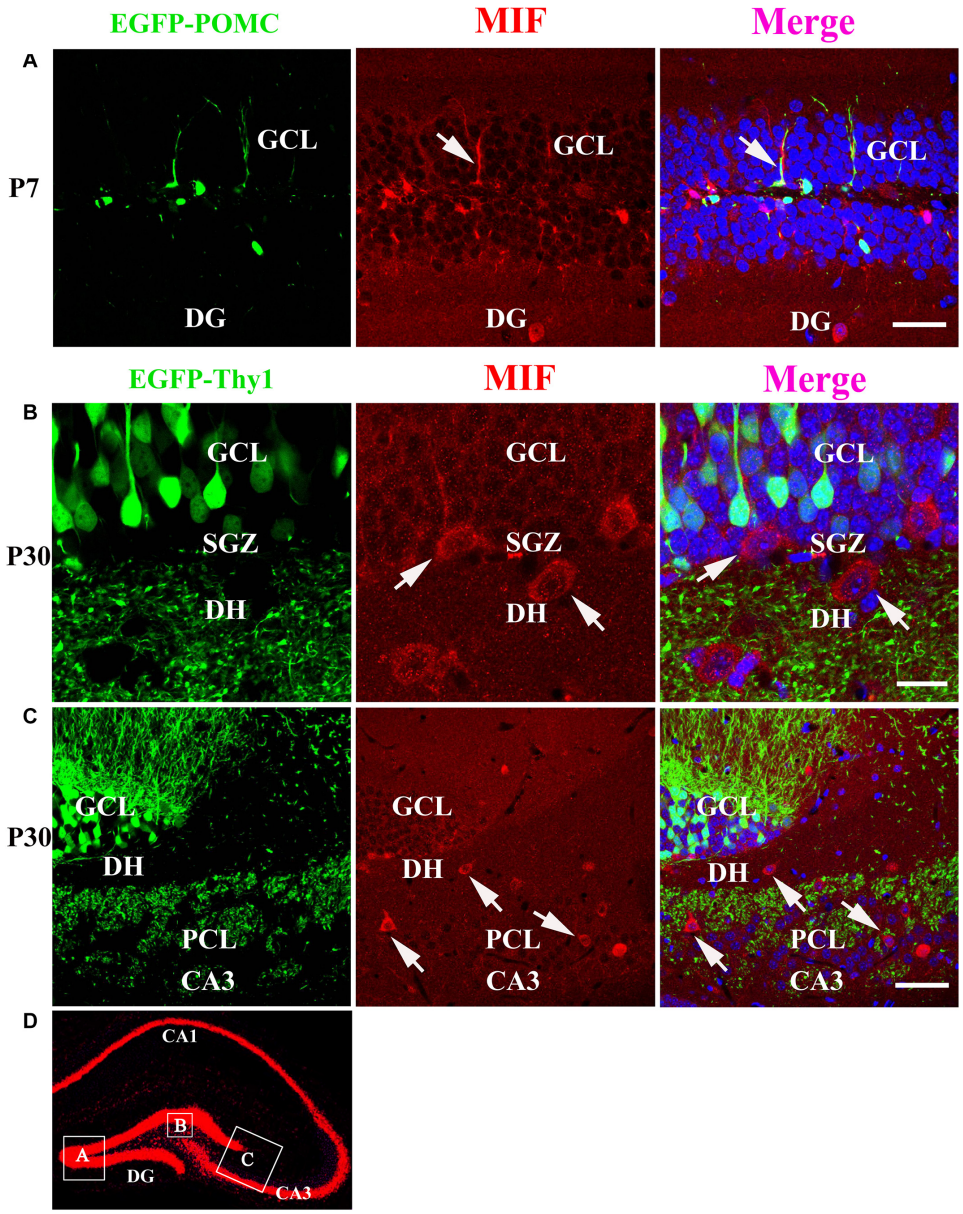


**FIGURE 7 |** MIF is neither expressed by immature granule cells (P7) nor by mature granule cells (P30) in developing hippocampus. **(A)** P7 POMC-EGFP–positive immature granule cells (green) in GCL were not overlapped with MIF-positive cells (red) distributed in the DG. **(B)** Three-month Thy1-EGFP–positive mature granule cells (green) in 3-month-old mice were not colocalized with MIF-expressing cells (red) scattered in subgranular zone (SGZ) and dentate hilus (DH). MIF-positive cells in SGZ and DH displayed giant morphology prompting them as interneurons. **(C)** In CA3 of 3-month Thy1-EGFP hippocampus, many MIF-positive cells (red) were distributed in stratum lucidum (sl) and pyramidal cell layer (PCL). No overlapping of EGFP (green) and MIF (red) was observed. Some of MIF-positive cells were indicated with white arrows in **(A–C)**. **(D)** The rectangular boxes in hippocampus overview represent the regions shown in **(A–C)**. DG, dentate gyrus. Scale bars in **(A)**: 50 μm; **(B)**: 20 μm: **(C)**: 50 μm.

**Figure 7D**, the rectangular boxes indicate the regions shown in **Figures 7A–C**.

## GFAP- and BLBP-Positive Neural Precursor Cells in SGZ Express MIF

We have mentioned above that many MIF-positive cells accumulated in SGZ of DG and formed an MIF-positive cell layer. Interestingly, in contrast to MIF-positive cells in other regions, the MIF-positive cells in SGZ were NeuN-negative and gave rise to MIF-positive processes pointing to molecular layer of DG (**Figure 5A**). It is well known that SGZ is the place where the neural stem cells and newly generated neurons are located, and neurogenesis occurs for whole life (Zhao et al., 2007). Thus, we wondered whether the neural stem cells or newly generated neurons express MIF. To test these possibilities, we

performed double-labeling of MIF with GFAP, BLBP, and DCX, respectively, in 3-month-old hippocampus. Our results showed that most of MIF-positive cells in SGZ were colabeled by GFAP (**Figure 8A**) and BLBP (**Figure 8B**), markers for neural stem cells. We also found some MIF-positive astrocytes around the small blood vessels in the hippocampus proper (data not shown). In contrast, no MIF-positive cells in SGZ were found to be colabeled with DCX (**Figure 8C**), a marker for newly generated immature neurons. It is well known that GFAP is expressed by radial glial cells (neural stem cells), which are located in SGZ of the DG

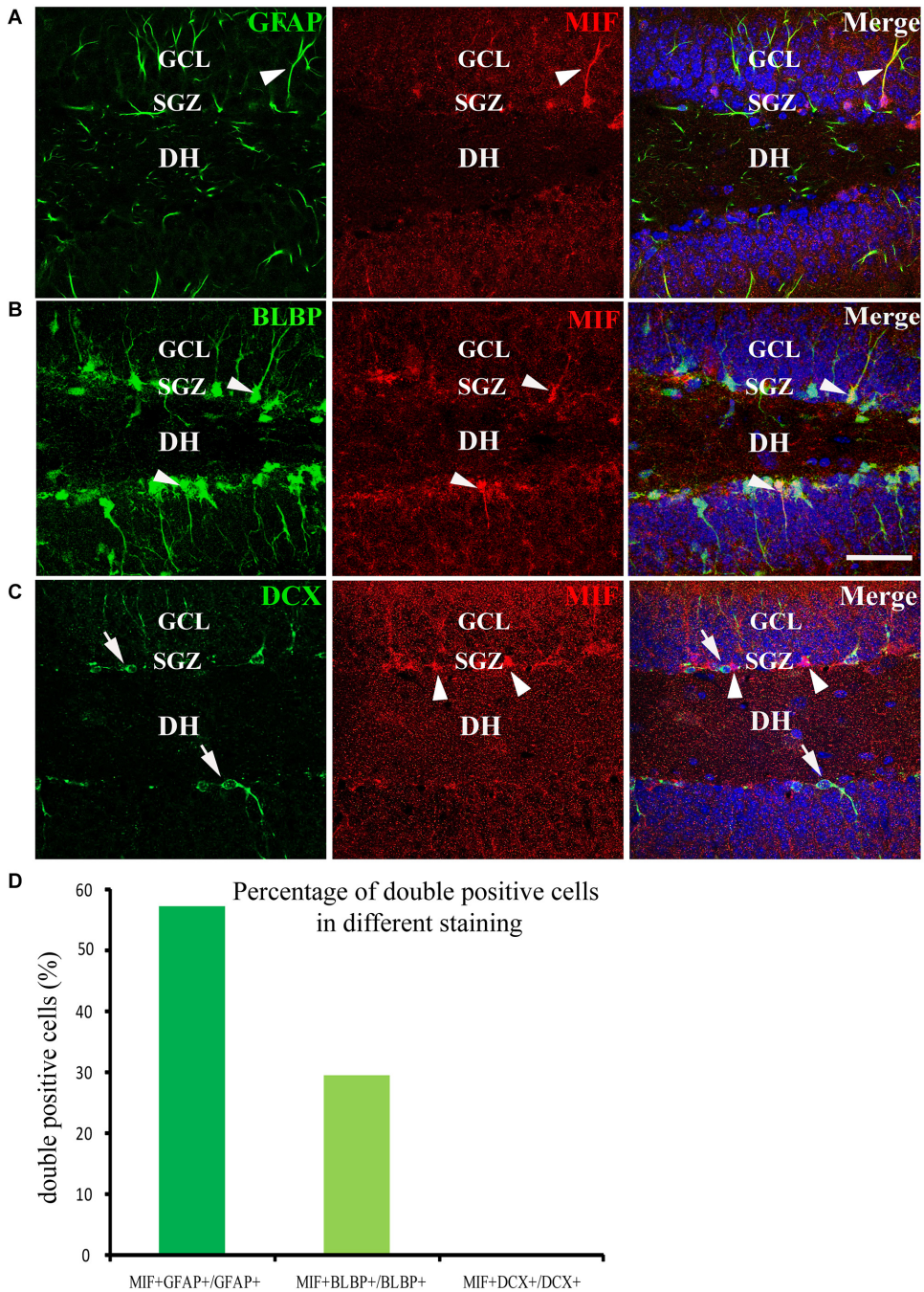


**FIGURE 8 |** MIF is maintained in neural precursor cells. **(A–C)** Double-labeling of MIF with GFAP, BLBP, and DCX, respectively, indicated that MIF (red) was maintained in fibers (green) of GFAP- positive radial glial cells **(A)** and BLBP-positive neural precursor cells (green) located in the subgranular zone (SGZ) of the DG (**B**, white arrowheads). MIF (red, white arrowheads) was not observed in DCX-positive newly generated neurons (green, white arrows) situated in SGZ of the DG **(C)**. **(D)** Quantification results showed the percentage of GFAP and MIF double-labeled cells in GFAP-positive cells, BLBP and MIF double-positive cells in BLBP-expressing cells, and DCX and MIF double-labeled cells in DCX-positive cells. DH, dentate hilus. Scale bars in **(A–C)**: 40 μm.

and act as neural precursor cells in developing hippocampus. In adulthood, most radial glial cells are transformed into astrocytes, whereas GFAP is retained by astrocytes. However, there are still some GFAP-positive radial glial cells in the SGZ acting as neural precursor cells (Zhao et al., 2004; Brunne et al., 2010). BLBP is another marker of neural precursor cells, which recognizes late differentiated radial glial cells (Hartfuss et al., 2003; Brunne et al., 2010). DCX is a microtubule-associated protein and expressed by newly generated neurons in SGZ of DG (Zhao et al., 2007). Our findings suggested that MIF is involved in maintenance of the feature of neural stem cells and cell proliferation. To quantify our results, we counted the number of GFAP-positive cells, BLBP-positive cells, and DCX-positive cells in 0.03 $mm^2$ area in DG respectively. Six hippocampal slices were counted. We found that the percentage of GFAP and MIF double-labeled cells in GFAP-positive cells was higher than that of BLBP and MIF double-positive cells in BLBP-expressing cells; no double-labeled cells with DCX and MIF were found in DG (**Figure 8D**). These results further indicated that MIF is maintained in GFAP- or BLBP-positive neural stem cells during hippocampal development.

## MIF Antagonist Suppresses Cell Proliferation in the Developing Hippocampus

Our data suggested that MIF is involved in cell proliferation. Conboy et al. (2011) have also shown that lack of MIF causes impairment of cell proliferation of adult hippocampus. So we were wondering whether MIF controls cell proliferation of neural stem cells in SGZ of DG during hippocampal development. Then we injected BrdU into P5, P14, P30, and 3-month-old adult mice 2 h before the animals were sacrificed and conducted double-labeling of MIF and BrdU in hippocampus. As revealed in **Figure 9**, BrdU emerged in MIF staining partially in SGZ of DG at all stages. By injection of ISO-1, an antagonist of MIF, into P5 mice for 9 consecutive days, we found a remarkable reduction of BrdU-positive cells in SGZ of DG in treated mice compared to that in control mice (**Figure 10A**). Statistical analysis was shown in **Figure 10B**. Our results indicate that inhibition of MIF impairs hippocampal cell proliferation at an early stage.

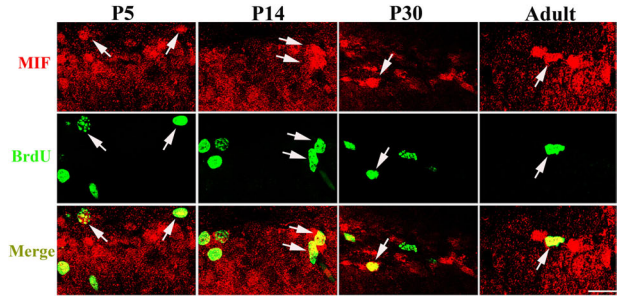


**FIGURE 9 |** MIF is involved in cell proliferation in developing hippocampus. Injection of BrdU into P5, P14, P30, and 3-month-old mice revealed that MIF (red) appeared in some BrdU-positive (green) newborn cells in subgranular zone of the DG (white arrows). Scale bar: 20 μm.

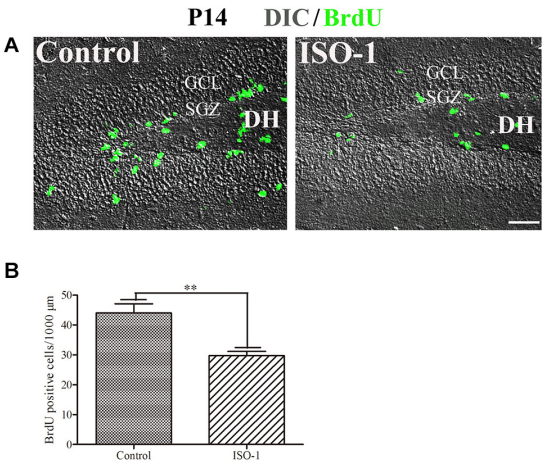


**FIGURE 10 |** Blocking of MIF impaired cell proliferation in P14 hippocampus. **(A)** Differential interference contrast microscope imaging with BrdU fluorescent imaging showed that MIF antagonist ISO-1 reduced BrdU-positive cells (green) in SGZ of the DG from P14 mice compared to that in control mice. **(B)** Statistical analysis exhibited significant difference of BrdU-positive cells in ISO-1–treated and control hippocampus. Data were presented in bar graphs showing means ± SEM, $^{**}P < 0.01$, $n = 12$. DH, dentate hilus. Scale bar in **(A)**: 50 μm.

## MIF Antagonist Hinders Neurite Outgrowth *in vitro*

During hippocampal development, MIF was expressed in mossy fibers projected from granule cells to pyramidal neurons in CA3 region suggesting that MIF might participate in the regulation of axonal outgrowth (**Figure 3**). To test this possibility, we treated primary neuronal cultures with ISO-1 using different concentrations (10 and 100 μM) for 2 days. After fixation with 4%PFA in 0.1 M PB, cultures were visualized with neuronal marker neurofilament 200 and photographed. Three independent fields on a coverslip were imaged. At least three coverslips for each experiment were analyzed. Compared with control condition, treatment at both concentrations of ISO-1 seemed to affect neurite outgrowth (**Figure 11A**). To verify the extent of the effect, we measured the length of processes. The statistical analysis and cumulative probability results showed that 10 and 100 μM ISO-1 strongly decreased the length of the longest neurites of cultured neurons (**Figures 11B,C**). To identify the number of total neurites, we counted the terminal tips of neurites. The result revealed that 10 μM ISO-1 treatment led to a reduction in number of neurites, with significant difference compared with that in control and 100 μM ISO-1–treated neurons (**Figure 11D**). These data implied that appropriate concentration of ISO-1 is critical to block MIF function. In addition, the percentage of neurons with different number of neurites in control and ISO-1–treated cultures was evaluated, and the total length of processes except the longest neurite was measured (**Figure 11E**). No significant difference between control and ISO-1–treated neurons was observed (**Figure 11F**). It is well known that the longest protrusion from a neuron is axon, and the other protrusions differentiate to dendrites. Therefore, our results indicate that

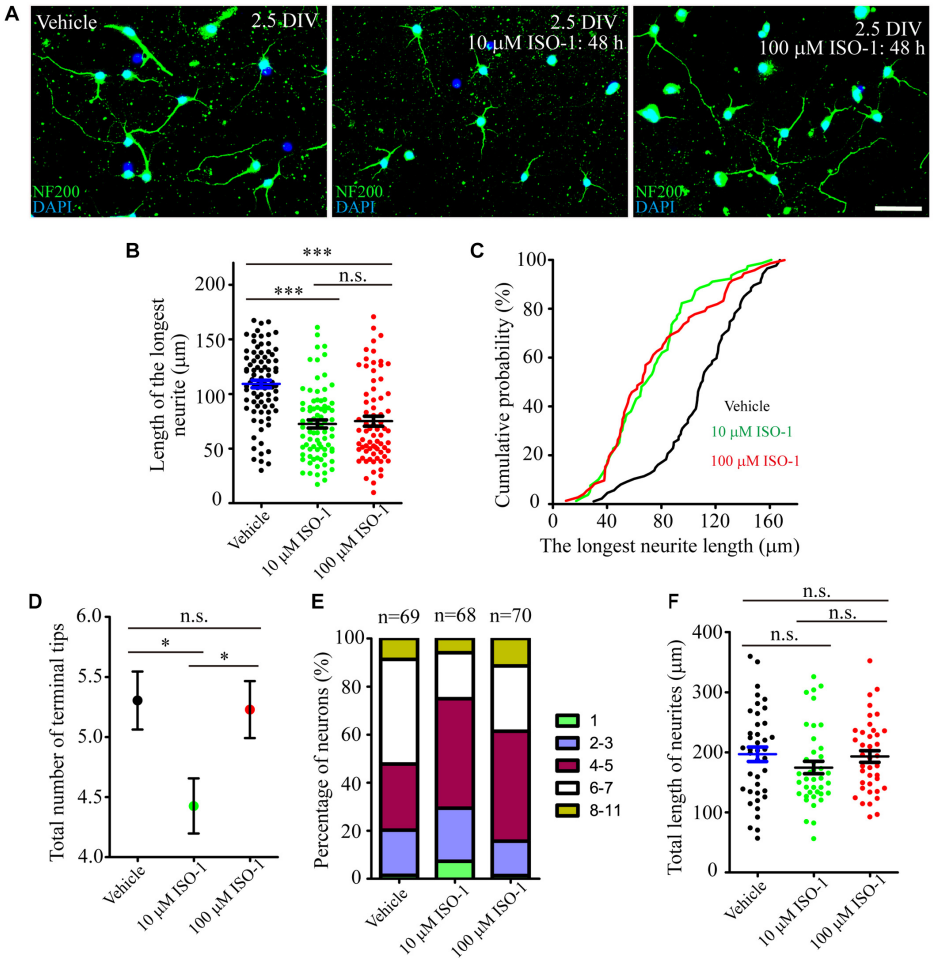


**FIGURE 11 |** MIF antagonist hinders neurite outgrowth *in vitro*. **(A)** Fluorescent microscopic imaging of cultured neurons labeled with neurofilament 200 revealing that 10 μM ISO-1 affected neurite outgrowth. **(B,C)** Statistical analysis and cumulative probability results demonstrated that both 10 and 100 μM ISO-1 strongly decreased the length of the longest neurites of cultured neurons, and the difference was significant. **(D)** 10 μM ISO-1 treatment significantly reduced the number of terminal tips of neurites. **(E)** The percentage of neurons with different number of neurites in control and ISO-1–treated cultures was evaluated. **(F)** No significant difference of total length of neurites between control and ISO-1–treated neurons. Statistical analysis was performed by Kruskal–Wallis with Dunn post test in **(B)** (n.s., no significance; ***$P < 0.001$); one-way analysis of variance with Tukey post test in **(D)** (n.s., no significance; *$P < 0.05$) and **(F)** (n.s., no significance). Scale bar in **(A)**: 50 μm.

MIF might participate in the regulation of mossy fiber projection and dendritic bifurcation. Blocking of MIF with ISO-1 inhibited axonal elongation and dendritic formation.

## DISCUSSION

MIF has been found to be expressed in the neocortex, hippocampus, hypothalamus, cerebellum, choroid plexus, and spinal cord in the CNS (Nishibori et al., 1997; Bacher et al., 1998; Ogata et al., 1998; Vedder et al., 2000; Zhang et al., 2019) and up-regulated in AD and Parkinson disease (Nicoletti et al., 2011; Zhang et al., 2019). Hippocampus is responsible for learning and memory and involved in lots of neurological diseases. However, the spatiotemporal expression pattern of MIF in developing hippocampus has remained unknown. Herein, we examined the expression levels of MIF during hippocampus development both in mRNA and protein quantitatively. We found that MIF is expressed throughout the development of the hippocampus during the postnatal period. Among the selected time points, the lowest level of MIF protein was detected at P7, whereas the higher level of MIF was found both at earlier and later stages. However, our quantitative real-time PCR revealed that the peak of *mif* mRNA was between P7 and P30. These results suggest that there was a mismatch between the levels of MIF protein and *mif* transcript in hippocampus, which was similar with the expression pattern of MIF in the neocortex (Zhang et al., 2014). We speculate that during development, neuronal migration requires a lot of MIF. One week after birth, newly generated neurons finish their migration, and the MIF requirement is reduced. After the neurons grow dendrites and axons and form synaptic connections with their target cells, the

outgrowth of neurites results in increased requirement of MIF. For the stably expressed *mif* mRNA during P7 until P30, our explanation is that from P7 on a vast amount of MIF is used for synaptogenesis, and *mif* mRNA is ready for producing MIF proteins in case needed. It has reported that MIF promotes cancer cell migration in human lung adenocarcinoma and esophageal squamous cell carcinoma (Rendon et al., 2007; Liu et al., 2018). Therefore, it is necessary for the future study to investigate the role of MIF on cytoskeletal dynamics in migrating neurons.

GFAP is a marker for radial glial cells located in the ventricular zone of the cerebral cortex and in the SGZ of the DG during development. They extend their radial fibers as scaffold for the migrating neurons. After the migration, the majority of radial glial cells transform into astrocytes (Zhao et al., 2004; Brunne et al., 2010). In our present study, MIF was found in GFAP-positive and BLBP-positive radial glial cells, which act as neural precursor cells located in SGZ of DG, but not in DCX-positive newly generated neurons in SGZ, suggesting that MIF plays a role in maintenance of neural stem cells and might be involved in cell proliferation. Colocalization of MIF and GFAP in astrocytes has been proved by other researchers (Ogata et al., 1998; Conboy et al., 2011; Li et al., 2015). BrdU has long been used as a sign of cell division and a marker to investigate the neurogenesis and gliogenesis in adult hippocampus (Zhao et al., 2007; Conboy et al., 2011). We found that 2 h after injection BrdU has already been detected in some MIF-positive cells in hippocampus prepared from P5 to 3-month-old mice, and blocking of MIF function in P14 mice reduced the number of BrdU-expressing cells in hippocampus. This result further confirmed the involvement of MIF in cell proliferation during development (Conboy et al., 2011). As MIF was found in GFAP-positive and BLBP-positive neural stem cells and astrocytes around brain blood vessels, not in DCX-positive newly generated neurons, we speculated that MIF maintains the feature of neural stem cells and participates in cell proliferation of neural stem cells during hippocampal development.

To find out whether MIF is expressed in the somata of granular cells in hippocampus during development, we used POMC-EGFP and Thy1-EGFP transgenic mice. Our results revealed that neither POMC-EGFP–labeled immature granule cells nor Thy1-EGFP–labeled mature granule cells in DG express MIF. These results are controversial with the previous study showing that only NeuroD-positive immature cells are MIF-positive in DG (Conboy et al., 2011). We conjectured that either we missed the earlier moment at which NeuroD and MIF proteins are expressed equally in cytoplasm by granule cells in DG, or MIF protein is quickly transported to the terminal of the mossy fiber after production, resulting in a very weak signal of MIF in the cytoplasm of MIF, making it difficult to detect (Nishibori et al., 1996; Ogata et al., 1998). It is worth noting that, in our experiments, MIF immunoreactive labeling in mossy fibers was very strong. In addition, the dual-labeling of MIF and NeuN (markers of mature neurons) further proved that MIF is unable to be detected in somata of granule cells and pyramidal neurons of the hippocampus during development. However, we did find that some NeuN-positive cells scattered in whole hippocampus and strongly expressed MIF in their somata. The morphological features of these cells and the immunolabeling for parvalbumin and Reelin evidenced that they were GABAergic interneurons. And it has been reported that MIF is also expressed by GABAergic interneurons in the cerebral cortex (Inácio et al., 2011; Zhang et al., 2014). GABAergic interneurons play a profound role in regulating cell excitability and interact with glutamatergic pyramidal cell inputs in a domain-specific manner and support synaptic temporal dynamics (Bennett and Zukin, 2004; Klausberger and Somogyi, 2008). This makes us more believe that MIF expressed at mossy fibers buttons may regulate the synapse dynamics of pyramidal neurons in CA3. Interestingly, our previous study has shown that granule cell dispersion in temporal lobe epilepsy patients is due to reduced Reelin expression by GABAergic interneurons (Chai et al., 2014). Studies from other laboratories have demonstrated that parvalbumin-positive interneurons prevent stress-induced synapse loss, and MIF is decreased when parvalbumin is increased by enriched environment in the brain following experimental stroke (Inácio et al., 2011; Chen et al., 2018). Taken together, it is likely that Reelin and parvalbumin stabilize synaptic structure, whereas MIF promotes cytoskeletal dynamics (Chai et al., 2009, 2014, 2016). Considering that the expression intensity of MIF in principal neurons and interneurons is different, we speculate that GABAergic interneurons may express more MIF than principal neurons, or they have different ways of secreting MIF and different mechanisms of action of MIF on target cells.

Mossy fibers are axons of dentate granule cells projecting to the CA3 region. In the present study, we confirmed that MIF was expressed in the mossy fibers at early postnatal stages. Thus, it raises the question whether MIF affects axonal outgrowth. To verify this possibility, cultured neurons were treated with MIF antagonist ISO-1. Results showed that suppression of MIF with 10 μM ISO-1 hindered extension and arborization of neurites. We conclude that a suitable ISO-1 concentration is essential for the function of MIF. Coincidentally, treatment with MIF antibody delays nerve regeneration after sciatic nerve injury (Nishio et al., 2002). It is interesting enough that MIF has been reported to direct initial neurite outgrowth from the statoacoustic ganglion to the developing inner ear, and recombinant MIF promotes directional neurite outgrowth of chick and mouse statoacoustic ganglion (Bank et al., 2012). This discovery strengthens our future exploration of the role and mechanism of MIF in regulating nerve fiber dynamics.

## DATA AVAILABILITY STATEMENT

The raw data supporting the conclusions of this article will be made available by the authors, without undue reservation, to any qualified researcher.

## ETHICS STATEMENT

The animal study was reviewed and approved by the Institutional Animal Care of Hamburg University and Northwest A&F University.

## AUTHOR CONTRIBUTIONS

WZ, XC, and SZ developed the concept of the study and wrote the manuscript. XC, WZ, and SZ wrote the manuscript. All authors contributed to the article and approved the submitted version.

## FUNDING

This work was supported by the National Key Research and Development Program of China (No. 2018YFE0127000 to SZ), Foundation for top talent recruitment of Xi'an Medical College (No. 2018RCYJ04 to XC), General project of basic research of Shaanxi Province (No. 2020JM-603 to XC), Key Research & Development projects of Shaanxi Province (No. 2018ZDXM2 to SZ), and Frontier and cross scientific research projects of Northwest A&F University (No. 2452019200 to SZ).

## ACKNOWLEDGMENTS

We are most grateful to Ms. Runchuan Yan for mRNA test. We would also like to thank Mr. Xuetao Xu for morphometric measurements of neurons.

## REFERENCES

Bacher, M., Deuster, O., Aljabari, B., Egensperger, R., Neff, F., Jessen, F., et al. (2010). The role of macrophage migration inhibitory factor in Alzheimer's disease. *Mol. Med.* 16, 116–121.

Bacher, M., Meinhardt, A., Lan, H. Y., Dhabhar, F. S., Mu, W., Metz, C. N., et al. (1998). MIF expression in the rat brain: implications for neuronal function. *Mol. Med.* 4, 217–230. doi: 10.1007/bf03401919

Bacher, M., Weihe, E., Dietzschold, B., Meinhardt, A., Vedder, H., Gemsa, D., et al. (2002). Borna disease virus-induced accumulation of macrophage migration inhibitory factor in rat brain astrocytes is associated with inhibition of macrophage infiltration. *Glia* 37, 291–306. doi: 10.1002/glia.10013

Bank, L. M., Bianchi, L. M., Ebisu, F., Lerman-Sinkoff, D., Smiley, E. C., Shen, Y. C., et al. (2012). Macrophage migration inhibitory factor acts as a neurotrophin in the developing inner ear. *Development* 139, 4666–4674.

Bennett, M. V., and Zukin, R. S. (2004). Electrical coupling and neuronal synchronization in the Mammalian brain. *Neuron* 41, 495–511. doi: 10.1016/s0896-6273(04)00043-1

Bernhagen, J., Calandra, T., Mitchell, R. A., Martin, S. B., Tracey, K. J., Voelter, W., et al. (1993). MIF is a pituitary-derived cytokine that potentiates lethal endotoxaemia. *Nature* 365, 756–759. doi: 10.1038/365756a0

Brunne, B., Zhao, S., Derouiche, A., Herz, J., May, P., Frotscher, M., et al. (2010). Origin, maturation, and astroglial transformation of secondary radial glial cells in the developing dentate gyrus. *Glia* 58, 1553–1569. doi: 10.1002/glia.21029

Chai, X., Fan, L., Shao, H., Lu, X., Zhang, W., Li, J., et al. (2015). Reelin induces branching of neurons and radial glial cells during corticogenesis. *Cereb. Cortex* 25, 3640–3653. doi: 10.1093/cercor/bhu216

Chai, X., Förster, E., Zhao, S., Bock, H. H., and Frotscher, M. (2009). Reelin stabilizes the actin cytoskeleton of neuronal processes by inducing n-cofilin phosphorylation at serine3. *J. Neurosci.* 29, 288–299. doi: 10.1523/jneurosci.2934-08.2009

Chai, X., Münzner, G., Zhao, S., Tinnes, S., Kowalski, J., Häussler, U., et al. (2014). Epilepsy-induced motility of differentiated neurons. *Cereb. Cortex* 24, 2130–2140. doi: 10.1093/cercor/bht067

Chai, X., Zhao, S., Fan, L., Zhang, W., Lu, X., Shao, H., et al. (2016). Reelin and cofilin cooperate during the migration of cortical neurons: a quantitative morphological analysis. *Development* 143, 1029–1040. doi: 10.1242/dev.134163

Chen, C. C., Lu, J., Yang, R., Ding, J. B., and Zuo, Y. (2018). Selective activation of parvalbumin interneurons prevents stress-induced synapse loss and perceptual defects. *Mol. Psychiatry* 23, 1614–1625. doi: 10.1038/mp.2017.159

Cheng, J., Liao, Y., Dong, Y., Hu, H., Yang, N., Kong, X., et al. (2020). Microglial autophagy defect causes parkinson disease-like symptoms by accelerating inflammasome activation in mice. *Autophagy* 31, 1–13. doi: 10.1080/15548627.2020.1719723

Conboy, L., Varea, E., Castro, J. E., Sakouhi-Ouertatani, H., Calandra, T., Lashuel, H. A., et al. (2011). Macrophage migration inhibitory factor is critically involved in basal and fluoxetine-stimulated adult hippocampal cell proliferation and in anxiety, depression, and memory-related behaviors. *Mol. Psychiatry* 16, 533–547. doi: 10.1038/mp.2010.15

Cox, G. M., Kithcart, A. P., Pitt, D., Guan, Z., Alexander, J., Williams, J. L., et al. (2013). Macrophage migration inhibitory factor potentiates autoimmune-mediated neuroinflammation. *J. Immunol.* 191, 1043–1054. doi: 10.4049/jimmunol.1200485

Danış, O., Demir, S., Günel, A., Aker, R. G., Gülçebi, M., Onat, F., et al. (2011). Changes in intracellular protein expression in cortex, thalamus and hippocampus in a genetic rat model of absence epilepsy. *Brain Res. Bull.* 84, 381–388. doi: 10.1016/j.brainresbull.2011.02.002

Djordjevic, A., Bursaæ, B., Velièkoviæ, N., Gligorovska, L., Ignjatoviæ, D., Tomiæ, M., et al. (2017). Disturbances of systemic and hippocampal insulin sensitivity in macrophage migration inhibitory factor (MIF) knockout male mice lead to behavioral changes associated with decreased PSA-NCAM levels. *Horm. Behav.* 96, 95–103. doi: 10.1016/j.yhbeh.2017.09.008

Grigorenko, E. L., Han, S. S., Yrigollen, C. M., Leng, L., Mizue, Y., Anderson, G. M., et al. (2008). Macrophage migration inhibitory factor and autism spectrum disorders. *Pediatrics* 122, e438–e445.

Hartfuss, E., Förster, E., Bock, H. H., Hack, M. A., Leprince, P., Luque, J. M., et al. (2003). Reelin signaling directly affects radial glia morphology and biochemical maturation. *Development* 130, 4597–4609. doi: 10.1242/dev.00654

Inácio, A. R., Ruscher, K., and Wieloch, T. (2011). Enriched environment downregulates macrophage migration inhibitory factor and increases parvalbumin in the brain following experimental stroke. *Neurobiol. Dis.* 41, 270–278. doi: 10.1016/j.nbd.2010.09.015

Kassaar, O., Pereira Morais, M., Xu, S., Adam, E. L., Chamberlain, R. C., Jenkins, B., et al. (2017). Macrophage migration inhibitory factor is subjected to glucose modification and oxidation in Alzheimer's disease. *Sci. Rep.* 7:42874.

Klausberger, T., and Somogyi, P. (2008). Neuronal diversity and temporal dynamics: the unity of hippocampal circuit operations. *Science* 321, 53–57. doi: 10.1126/science.1149381

Li, H., Gao, Y., Qi, Y., Katovich, M. J., Jiang, N., Braseth, L. N., et al. (2008). Macrophage migration inhibitory factor in hypothalamic paraventricular nucleus neurons decreases blood pressure in spontaneously hypertensive rats. *FASEB J.* 22, 3175–3185. doi: 10.1096/fj.08-108662

Li, S. Q., Yu, Y., Han, J. Z., Wang, D., Liu, J., Qian, F., et al. (2015). Deficiency of macrophage migration inhibitory factor attenuates tau hyperphosphorylation in mouse models of Alzheimer's disease. *J. Neuroinflammation* 12:177.

Liu, R. M., Sun, D. N., Jiao, Y. L., Wang, P., Zhang, J., Wang, M., et al. (2018). Macrophage migration inhibitory factor promotes tumor aggressiveness of esophageal squamous cell carcinoma via activation of Akt and inactivation of GSK3β. *Cancer Lett.* 412, 289–296. doi: 10.1016/j.canlet.2017.10.018

Mittelbronn, M., Platten, M., Zeiner, P., Dombrowski, Y., Frank, B., Zachskorn, C., et al. (2011). Macrophage migration inhibitory factor (MIF) expression in human malignant gliomas contributes to immune escape and tumour progression. *Acta Neuropathol.* 122, 353–365. doi: 10.1007/s00401-011-0858-3

Nicoletti, A., Fagone, P., Donzuso, G., Mangano, K., Dibilio, V., Caponnetto, S., et al. (2011). Parkinson's disease is associated with increased serum levels of macrophage migration inhibitory factor. *Cytokine* 55, 165–167. doi: 10.1016/j.cyto.2011.03.027

Nishibori, M., Nakaya, N., Mori, S., and Saeki, K. (1997). Immunohistochemical localization of macrophage migration inhibitory factor (MIF) in tanycytes,

subcommissural organ and choroid plexus in the rat brain. *Brain Res.* 758, 259–262. doi: 10.1016/s0006-8993(97)00342-9

Nishibori, M., Nakaya, N., Tahara, A., Kawabata, M., Mori, S., and Saeki, K. (1996). Presence of macrophage migration inhibitory factor (MIF) in ependyma, astrocytes and neurons in the bovine brain. *Neurosci. Lett.* 213, 193–196. doi: 10.1016/0304-3940(96)12864-0

Nishio, Y., Nishihira, J., Ishibashi, T., Kato, H., and Minami, A. (2002). Role of macrophage migration inhibitory factor (MIF) in peripheral nerve regeneration: anti-MIF antibody induces delay of nerve regeneration and the apoptosis of Schwann cells. *Mol. Med.* 8, 509–520. doi: 10.1007/bf03402160

Ogata, A., Nishihira, J., Suzuki, T., Nagashima, K., and Tashiro, K. (1998). Identification of macrophage migration inhibitory factor mRNA expression in neural cells of the rat brain by in situ hybridization. *Neurosci. Lett.* 246, 173–177. doi: 10.1016/s0304-3940(98)00203-1

Okazaki, S., Hishimoto, A., Otsuka, I., Watanabe, Y., Numata, S., Boku, S., et al. (2018). Increased serum levels and promoter polymorphisms of macrophage migration inhibitory factor in schizophrenia. *Prog. Neuropsychopharmacol. Biol. Psychiatry* 83, 33–41. doi: 10.1016/j.pnpbp.2018.01.001

Overstreet, L. S., Hentges, S. T., Bumaschny, V. F., de Souza, F. S., Smart, J. L., Santangelo, A. M., et al. (2004). Transgenic marker for newly born granule cells in dentate gyrus. *J. Neurosci.* 24, 3251–3259. doi: 10.1523/jneurosci.5173-03.2004

Rendon, B. E., Roger, T., Teneng, I., Zhao, M., Al-Abed, Y., Calandra, T., et al. (2007). Regulation of human lung adenocarcinoma cell migration and invasion by macrophage migration inhibitory factor. *J. Biol. Chem.* 282, 29910–29918. doi: 10.1074/jbc.m704898200

Vedder, H., Krieg, J. C., Gerlach, B., Gemsa, D., and Bacher, M. (2000). Expression and glucocorticoid regulation of macrophage migration inhibitory factor (MIF) in hippocampal and neocortical rat brain cells in culture. *Brain Res.* 869, 25–30. doi: 10.1016/s0006-8993(00)02336-2

Vuksic, M., Del Turco, D., Bas Orth, C., Burbach, G. J., Feng, G., Müller, C. M., et al. (2008). 3D-reconstruction and functional properties of GFP-positive and GFP-negative granule cells in the fascia dentata of the Thy1-GFP mouse. *Hippocampus* 18, 364–375. doi: 10.1002/hipo.20398

Zeiner, P. S., Preusse, C., Blank, A. E., Zachskorn, C., Baumgarten, P., Caspary, L., et al. (2015). MIF receptor CD74 is restricted to microglia/macrophages, associated with a M1-polarized immune milieu and prolonged patient survival in gliomas. *Brain Pathol.* 25, 491–504. doi: 10.1111/bpa.12194

Zhang, S., Zhao, J., Zhang, Y., Zhang, Y., Cai, F., Wang, L., et al. (2019). Upregulation of MIF as a defense mechanism and a biomarker of Alzheimer's disease. *Alzheimers Res. Ther.* 11:54.

Zhang, W., Li, L., Wang, J., An, L., Hu, X., Xie, J., et al. (2014). Expression of macrophage migration inhibitory factor in the mouse neocortex and posterior piriform cortices during postnatal development. *Cell. Mol. Neurobiol.* 34, 1183–1197. doi: 10.1007/s10571-014-0094-1

Zhao, S., Chai, X., Foerster, E., and Frotscher, M. (2004). Reelin is a positional signal for the lamination of dentate granule cells. *Development* 131, 5117–5125. doi: 10.1242/dev.01387

Zhao, S., Chai, X., and Frotscher, M. (2007). Balance between neurogenesis and gliogenesis in the adult hippocampus: role for reelin. *Dev. Neurosci.* 29, 84–90. doi: 10.1159/000096213

**Conflict of Interest:** The authors declare that the research was conducted in the absence of any commercial or financial relationships that could be construed as a potential conflict of interest.

*Copyright © 2020 Chai, Zhang, Li, Wu, Zhu and Zhao. This is an open-access article distributed under the terms of the Creative Commons Attribution License (CC BY). The use, distribution or reproduction in other forums is permitted, provided the original author(s) and the copyright owner(s) are credited and that the original publication in this journal is cited, in accordance with accepted academic practice. No use, distribution or reproduction is permitted which does not comply with these terms.*

frontiers in Behavioral Neuroscience

ORIGINAL RESEARCH
published: 24 August 2020
doi: 10.3389/fnbeh.2020.00130

# Neuroanatomic Correlates of Distance and Direction Processing During Cognitive Map Retrieval

*Igor Faulmann*[1,2,3]*, *Virginie Descloux*[2,4], *Arnaud Saj*[2,5,6] and *Roland Maurer*[2]

[1]Frontiers Media SA, Lausanne, Switzerland, [2]Faculty of Psychology and Educational Sciences, University of Geneva, Geneva, Switzerland, [3]Ecole Doctorale en Neurosciences Lémaniques, Université de Lausanne, Geneva, Switzerland, [4]Fribourg Cantonal Hospital, Fribourg, Switzerland, [5]Département de Psychologie, Faculté des Arts et des Sciences, Université de Montréal, Montreal, QC, Canada, [6]CRIR/Institut Nazareth et Louis-Braille du CISSS de la Montérégie-Centre, Longueuil, QC, Canada

Navigating toward a goal and mentally comparing distances and directions to landmarks are processes requiring reading information off the memorized representation of the environment, that is, the cognitive map. Brain structures in the medial temporal lobe, in particular, are known to be involved in the learning, storage, and retrieval of cognitive map information, which is generally assumed to be in allocentric form, whereby pure spatial relations (i.e., distance and direction) connect locations with each other. The authors recorded functional magnetic resonance imaging activity, while participants were submitted to a variant of a neuropsychological test (the Cognitive Map Reading Test; CMRT) originally developed to evaluate the performance of brain-lesioned patients and in which participants have to compare distances and directions in their mental map of their hometown. Our main results indicated posterior parahippocampal, but not hippocampal, activity, consistent with a task involving spatial memory of places learned a long time ago; left parietal and left frontal activity, consistent with the distributed processing of navigational representations; and, unexpectedly, cerebellar activity, possibly related to the role of the cerebellum in the processing of (here, imaginary) self-motion cues. In addition, direction, but not distance, comparisons elicited significant activation in the posterior parahippocampal gyrus.

**Keywords: cognitive map, evaluation of distance, evaluation of direction, cognitive map reading test, fMRI, hippocampus**

OPEN ACCESS

***Edited by:***
*James Ainge,*
*University of St. Andrews,*
*United Kingdom*

***Reviewed by:***
*Yasuyuki Ishikawa,*
*Maebashi Institute of Technology,*
*Japan*
*Benjamin J. Clark,*
*University of New Mexico,*
*United States*

***Correspondence:**
*Igor Faulmann*
*igor.faulmann@frontiersin.org*

***Specialty section:***
*This article was submitted to Learning and Memory, a section of the journal Frontiers in Behavioral Neuroscience*

***Received:*** *28 April 2020*
***Accepted:*** *01 July 2020*
***Published:*** *24 August 2020*

***Citation:***
*Faulmann I, Descloux V, Saj A and Maurer R (2020) Neuroanatomic Correlates of Distance and Direction Processing During Cognitive Map Retrieval. Front. Behav. Neurosci. 14:130. doi: 10.3389/fnbeh.2020.00130*

## INTRODUCTION

Spatial cognition consists in a plethora of high-level cognitive abilities; among them, the ability to learn and to navigate in large-scale environments is probably one of the most complex skills. Navigation is here defined as a moving behavior specifically oriented toward a known location, as opposed to the exploration of unknown areas of one's environment.

In the framework defined by O'Keefe and Nadel (1978), the so-called *cognitive map* is thought to be an *allocentric*—that is, viewpoint independent—representation of our environment, built progressively during exploration. The hippocampal *place cells* (O'Keefe and Nadel, 1978; Ekstrom et al., 2003) are potentially the actual neural substrate of the *cognitive map*, together with neurons in neighboring structures, in particular grid cells in the entorhinal cortex (for a review, see Barry and Burgess, 2014).

Many recent studies point to a predominant hippocampal and parahippocampal role in spatial cognition, as well as in the more specific cluster of navigational skills, be it for exploration or navigation *per se* (e.g., Wolbers and Büchel, 2005; for a review, see Burgess, 2008). More recently, hippocampal size has even been shown to predict at which pace a *cognitive map* was learned (Schinazi et al., 2013). Similarly, Nedelska et al. (2012) found in humans a significant correlation between hippocampal size and spatial navigation performance in humans, in both a real-space and a virtual Morris water maze (although this correlation was significant only in amnesic patients diagnosed with mild cognitive impairment and mild and moderate Alzheimer disease, and not on cognitively intact older controls).

Furthermore, a double dissociation between the anterior and the posterior hippocampus has been observed (Iaria et al., 2007; Schinazi et al., 2013): activity in the former is specifically related to the *learning phase*, whereas activity in the latter is more related to the *reading phase*, that is, the moment when information is recalled from the cognitive map.

Epstein (2008) concluded in his review article that the parahippocampal cortex plays a mandatory role in active navigation (e.g., Rosenbaum et al., 2004; Rauchs et al., 2008). In the same line, the results obtained by Park et al. (2007), and more recently by Bastin et al. (2013), also show a parahippocampal role in navigational skills. This may be actually linked to the second cell type thought to play a great role in navigation: the *grid cells*. In the human brain, they seem to be located—among other regions—in the parahippocampal cortex, entorhinal cortex, and in the subicular region (Hafting et al., 2005; Doeller et al., 2010).

Moreover, the hippocampus and the parahippocampal structures (i.e., parahippocampal cortex, subicular, and entorhinal regions), as well as the retrosplenial (Burgess, 2008; Epstein, 2008) and prefrontal cortices (Silk et al., 2010), seem necessary for spatial cognition. To what extent it is so for the storage, recovery, and usage of these representations remains more debated (Ekstrom et al., 2014).

Indeed, some results tend to show a greater implication of these structures for the construction of a cognitive map, compared to a lesser role for the storage, usage, and recovery phases (Rosenbaum et al., 2004; Shrager et al., 2007, 2008). This idea is actually consistent with findings of Schinazi et al. (2013), who found that hippocampal size predicted the pace of the cognitive map learning phase, which again is consistent with a more prominent role in the learning phase than in the usage or recovery phase (although this double dissociation has neither been specifically studied nor observed by the authors).

Recently, Ekstrom et al. (2014) argued in their review that the hippocampus seems not to be the only necessary structure for allocentric processes underlying navigation. They rather proposed in their nonaggregate network model a network-based computation of interacting brain structures, namely, the hippocampus and the parahippocampal, retrosplenial, prefrontal, and parietal cortices.

In another review, Wolbers and Wiener (2014) argue that the strict dissociation, made by many, between, on one side, the parietal/striatal circuits involved in egocentric computing vs., on the other hand, the entorhinal/hippocampal circuits involved in allocentric computing, is actually not compatible with a growing number of experimental data. These authors distinguish between the vista space, which can be globally visualized from a single location or with little exploration only (e.g., single room or a city square), and environmental spaces, such as neighborhoods or towns, which cannot be apprehended from a single point of view, but require extended exploration. They point out the facts that: (1) a determinant role is played by the scale of space (vista space vs. environmental space) used in a given study on the cognitive process recruited, something that, of course, can impact which brain structure is used; and that (2) the variation between studies concerning the (egocentric vs. allocentric) frames involved in the tasks complicates the interpretation of neurophysiological data.

Although it is compatible with the aforementioned theories, Spiers and Maguire (2007) framework does not explicitly make use of concepts like cognitive map or egocentric vs. allocentric representations. They suggested the existence of a large scale (i.e., when the goal location is not visible) navigational guidance system, with goal distance and goal direction coded separately and specifically in the brain. According to these authors, spatial information from hippocampal place cells is needed to guide behavior toward a location, but is not sufficient in and of itself for large-scale navigation. This spatial information is rather integrated with goal-related information, downstream from the hippocampus. Spiers and Maguire (2007) used a virtual simulation of London in a functional magnetic resonance imaging (fMRI) study, where subjects (licensed taxi drivers) had to navigate to goal destinations. They indeed observed a dichotomy between distance and direction, in structures downstream of the hippocampus. They found that medial prefrontal cortex activity correlated positively with goal proximity, whereas subicular/entorhinal activity correlated negatively with it (i.e., the closer the participants get to the goal, the more their medial prefrontal cortex is active, and the less their subicular and entorhinal regions are). For goal direction, a positive correlation was found between bilateral posterior parietal cortex activity and the egocentric direction to the goal (i.e., the smaller the angle between the current egocentric direction and the direction to the goal, the less the posterior parietal cortex is active). Interestingly, they did not find any active voxels at the hippocampal level, which is in accordance with the aforementioned hypothesis (i.e., the hippocampus is not *per se* responsible for navigation).

In an attempt to assess cognitive processes underlying specifically the two primitives of large-scale navigational process (i.e., goal distance and direction), we used a recently designed ecological task called the Cognitive Map Recall Test (CMRT). This task, now validated as part of a three-test set (Descloux et al., 2015; Descloux and Maurer, 2018), was originally developed to assess behavioral differences between healthy subjects and patients with possible topographical disorientation (Aguirre and D'Esposito, 1999), with an emphasis on its ecological properties and its ability to evaluate navigational skills in well-known, large-scale environments. More specifically, this task requires participants to make judgments about distances and directions in their familiar environment (see "*Methods*" section for details).

Descloux (2013) observed no differences in accuracy between judgment about distances and judgment about directions in healthy subjects, while there were significant differences in patients. More specifically, while patients with right posterior lesions were impaired in both categories of questions relative to healthy subjects, they were more impaired in evaluating directions than distances.

By using VLSM [voxel-based lesion-symptom mapping, a technique assessing statistical relationships between specific damaged brain regions and subsequent behavioral deficits (Bates et al., 2003)], Descloux (2013) also inferred the differential neuroanatomic substrates underlying the various response patterns. More precisely, focal lesions in the right anterior parahippocampal gyrus and right insula cause difficulties specifically for the evaluation of distances, whereas larger temporal and parietal lesions cause specific difficulties with directions.

Our main goal with this study is to investigate the neuroanatomic correlates of the processes involved in distance and direction computations while retrieving cognitive map information, during the execution of the CMRT. An ancillary goal is to determine whether this task, which implies a form of mental navigation, taps into the same resources as real navigation. If it indeed does, we expect hippocampal, parahippocampal, and parietal activation, reflecting structures activated during real navigation; we also expect higher activation in the right hemisphere (Javadi et al., 2017).

# METHODS

This research has been approved by the Faculty Ethical Committee of the Psychology and Educational Sciences Faculty, Geneva University. All subjects gave their written consent for participation and use of their data, provided they would be rendered anonymous and averaged, for educational and publication purposes.

## Subjects

Twenty-three subjects participated in the experiment (11 women, 12 men); they were recruited among the experimenter's acquaintances; they were aged between 21 and 61 (mean = 29.04, *SD* = 8.94), and only one was left-handed. Everyone had lived in Geneva for at least 2 years.

## Scanning Protocol and Apparatus

Magnetic resonance imaging data were acquired in the Brain and Behavior Laboratory at University Medical Center, using a 3-T whole-body Siemens MAGNETOM TrioTim syngo MR B17 system with the standard head-coil configuration. A four-button response box, laid on the subject's chest, was used to record responses.

For each participant, a high-resolution anatomical image was acquired before the functional scans, using a T1-weighted sequence [field of view (FOV) = 256 mm, repetition time (TR)/echo time (TE)/flip angle = 1,900 ms/2.27 ms/9°, slice thickness = 1 mm]. This anatomical image was used for coregistration with functional images and subsequent normalization procedure.

Functional T2*-weighted images were obtained using echoplanar imaging (EPI) with axial slices (*FOV* = 205 mm, TR/TE/flip angle = 2,100 ms/30 ms/80°, slice thickness = 3.2 mm). Each functional volume comprised 36 contiguous slices, parallel to the inferior surface of occipital and temporal lobes, with a final voxel size of 3.2 × 3.2 × 3.2 mm.

All fMRI data were processed and analyzed using the general linear model for event-related designs in SPM8 (Wellcome Department of Imaging Neuroscience, London, UK[1]). Functional images were realigned, corrected for slice timing, normalized to an EPI template, and spatially smoothed (5-mm full-width at half-maximum). Statistical analyses were performed on a voxelwise basis across the whole brain.

Parameter estimates for each regressor were estimated at each voxel by general linear model (GLM) using a least-squares fit to the data, for each condition and each individual participant. Statistical parametric maps of the *t*-statistic [SPM(T)] generated from linear contrasts between conditions in individual subjects were then included in a second-stage random-effects analysis, using one-sample *t*-tests on the contrast images obtained from each condition in each participant. The resulting random-effects maps SPM(T) was thresholded voxelwise at conventional statistical values ($p < 0.001$ uncorrected, with a cluster threshold of $p < 0.05$). Main comparisons were performed between each condition (distance and direction) and 0, between conditions, and for male vs. female participants. Activation results were visualized using the xjView toolbox for MATLAB.

## Task and Stimuli

Prior to the fMRI scanning, subjects were individually contacted in order to determine if each of them knew perfectly where the landmarks we preselected were located (they were chosen from among a set of common places in the city, such as the central train station, the main hospital, the university. . .). To do so, they were asked the question, "Do you know exactly where the [. . .] is?" for each landmark. If the participant hesitated, or if the answer was anything other than "yes," we considered that the participant did not really or clearly know where this landmark is.

The CMRT consists in a mental comparison between either distances or angles, which are both determined using those known landmarks. Subjects are first asked to imagine themselves at a *reference point*, which is here a known landmark in the city (e.g., "Imagine yourself in front of the train station").

Then, for the *distance comparison* condition, the subjects are given the names of two other distant, known landmarks (that could not be seen even if the participant was physically at the reference point and looking in the right direction; further referred to as *targets*). They must choose which of the two targets is farther from the reference point.

For the *direction comparison* condition, an orienting, or *reference*, direction must first be defined. Subjects are therefore given a second distant landmark, and they must imagine being oriented toward it (e.g., participants could be asked to imagine

[1] www.fil.ion.ucl.ac.uk/spm

themselves standing in front of the train station, additionally facing the Natural History Museum, which lies 1.7 km away from the station). Subjects are then given the names of two other distant targets, and they are asked for which of those they would have to rotate more in order to face it. For instance, for the reference direction we just gave them (i.e., from the train station facing the Natural History Museum), the instruction could be: "Would you have to rotate more to face the university building or the hospital?" (for further details on this task, see Descloux and Maurer, 2018).

Sets of three, respectively four, locations for the test were generated, by means of *ad hoc* software, with several constraints ensuring that items would be neither too easy nor too hard to solve. More specifically, for the distance condition, the larger distance was between 1.3 and 1.7 times bigger than the smaller one, and the two directions from the reference point to the targets were at least 45° apart, in order to avoid an alignment, which could be simpler to solve and may involve sequential processing rather than cognitive map readout For the direction condition, the difference between the smallest and the largest rotation was between 45° and 60°, and measured from the given reference direction, every required mental rotation was between 45° and 135°.

Based on the set of common landmarks and the aforementioned constraints, we were then able to build four equivalent versions of the task, matched to each participant's knowledge (i.e., each participant knew every landmark he/she was asked to process during the task).

While the original CMRT (Descloux and Maurer, 2018) was presented orally to the subjects, we adapted it for written presentation on a screen for use in the MRI scanner. We used E-prime/E-run 2.0 to present the questions on a back-projection screen just outside the scanner. The subjects could read them by means of a 45° tilted mirror set right in front of their eyes while they were lying in the scanner.

We further adapted the CMRT to be usable in an fMRI block design. The run had a total of five blocks of 10 items each; each block was split into two miniblocks of five items (one miniblock per condition, i.e., five were direction comparison items and five were distance comparison items; items from the two conditions were not mixed, and items within a miniblock were randomized). Miniblock order was neutralized (the first block contained distance item and then direction items; the second contained direction items and then distance items, etc.), and each item was presented only once to avoid a learning effect.

At the beginning of each miniblock, a slide would first ask the subject to imagine being in the required location (and, for directions, oriented toward a specific landmark) and would show the question, for example, "Imagine you are standing in front of the station, which is the farthest location? Press a key to continue." This slide was presented only once.

Upon key press by the subject, a fixation cross centered on the screen appeared during 500 ms. This was followed by the alternative, for example, "the church or the parking?" The subjects had to use button 1 for the first choice, and button 2 for the second choice. After their response, the next item was presented, beginning again with the fixation cross. If subjects took more than 15 s to respond, the current item was automatically discarded, and the next one was presented.

On the upper part of each slide, the reference landmark—for direction items, the *two* landmarks defining the reference direction—was always printed as a reminder. This precaution was taken to allow participants to keep in mind the reference(s) point(s) as the block proceeded, because five items followed one another without intervening instruction screen.

# RESULTS

## Behavioral Results

We wanted to check that the two conditions (*distance* and *direction*, henceforth referred to as DIST and DIR, respectively) were equivalent in difficulty. To assess this point, a repeated-measures analysis of variance was used (with condition as independent variable). The difference in the number of correct responses in conditions DIST (mean = 16.61, $SD$ = 2.71) and DIR (mean = 16.91, $SD$ = 3.41) was not statistically significant ($F_{(1, 22)}$ = 0.17, $P$ = 0.69). However, the response time was significantly different in conditions DIST (mean = 5, 444.86 ms, $SD$ = 1, 416.32) and DIR (mean = 6, 085.93 ms, $SD$ = 1, 492.50): ($F_{(1, 22)}$ = 14.62, $P < 0.001$). Additionally, correct response rates were statistically different from chance level for both conditions DIST (66.44%) and DIR (67.64%): ($P < 0.001$ for both conditions).

## fMRI Results

Standard realignment, coregistration, normalization, and smoothing (Ashburner et al., 2013) were applied on raw data. Additionally, in order to focus more specifically on brain activation subtending the operations on the cognitive map, we only kept the MRI signals associated with correct responses.

All fMRI results were obtained with an uncorrected $p$-value of 0.001 and a cluster size threshold of 8 (which means that any cluster containing fewer than eight voxels does not appear). Below are given their MNI $x$, $y$, and $z$ coordinates and $Z$ scores.

Results for DIST-only and DIR-only activations (compared to 0) can be viewed on **Table 1** and **Figure 1** and are described below. All other contrasts (DIST–DIR and female–male) showed no significant results.

The main contrast DIST >0 showed activity bilaterally in the temporal cortex, with clusters in the left temporal lobe ($xyz$ = −45/−40/1, $Z$ = 5.14) and in the right inferior temporal lobe ($xyz$ = 45/−58/−14; $Z$ = 4.41); in the left frontal cortex, with clusters in the frontal inferior opercule ($xyz$ = −33/8/28, $Z$ = 4.13), the inferior frontal gyrus ($xyz$ = −51/5/34, $Z$ = 4.00), and the superior frontal lobe ($xyz$ = −24/−4/46, $Z$ = 4.91); bilaterally in the parietal cortex, with clusters peaking in the left inferior parietal lobe ($xyz$ = −21/−64/25, $Z$ = 4.67, $xyz$ = −27/−55/40, $Z$ = 4.74, and $xyz$ = −39/−37/43, $Z$ = 4.25) and extending into the precuneus, the inferior parietal lobule, and the superior parietal lobule, a cluster in the left postcentral gyrus ($xyz$ = −42/−22/52, $Z$ = 4.10), a cluster peaking in the left superior parietal lobe and extending into the precuneus ($xyz$ = −15/−76/58, $Z$ = 4.07), and a cluster in the right precuneus ($xyz$ = 9/−64/49, $Z$ = 4.27 and $xyz$ = 18/−61/28,

**TABLE 1** | Peak MNI coordinates, split between each region, then between distance and direction (DIST and DIR).

| | | Region | | *xyz* Peak coordinates | BA location of peak voxel | Cluster size |
|---|---|---|---|---|---|---|
| Frontal | DIST | iFO | L | −33/8/28 | N/A | 9 |
| | | iFG | L | −51/5/34 | 9 | 14 |
| | | sFL | L | −24/−4/46 | N/A (6) | 27 |
| | DIR | PreCG | L | −33/−10/58 | 6 (4) | 133 |
| Temporal | DIST | iTL | R | 45/−58/−14 | N/A (37) | 44 |
| | | TL | L | −45/−40/1 | N/A (37) | 63 |
| | DIR | FG | R | 33/−37/−17 | N/A (20/36/37) | 73 |
| | | CC | R | 18/−55/16 | N/A | 13 |
| Parietal | DIST | PL | L | −21/−64/25 | N/A | 16 |
| | | PreC | R | 9/−64/49 | N/A (7) | 61 |
| | | PreC | R | 18/−61/28 | N/A (31) | 24 |
| | | iPL | L | −27/−55/40 | N/A (7) | 58 |
| | | iPL | L | −39/−37/43 | 40 | 13 |
| | | PCG | L | −42/−22/52 | 3 (40/2) | 18 |
| | | N/A | L | −15/−76/58 | N/A (7) | 13 |
| | DIR | PreC | L | −12/73/55 | N/A (7) | 19 |
| | | sPL | L | −18/−58/64 | 7 | 10 |
| Occipital | DIST | | | | | |
| | DIR | mOL | R | 42/−79/34 | N/A (39/19) | 20 |
| | | iPL | L | −36/−49/46 | 40 (7) | 47 |
| Cerebellum | DIST | CPL | R | 24/−64/−23 | N/A | 46 |
| | DIR | CPL | R | 21/−64/−47 | N/A | 40 |
| | | CAL | L | −15/−43/−14 | N/A (36/37/35/20) | 147 |
| | | CAL | R | 6/−58/−29 | N/A | 27 |

*Broadman Area (BA) of peak voxels are also given (adjacent BA on which some clusters spill over in parenthesis), when applicable, as well as cluster size.*

$Z$ = 4.26); and finally in the right cerebellum, with a cluster in the posterior lobe (*xyz* = 24/−64/−23, $Z$ = 4.49).

The main contrast DIR > 0 showed activation in the right temporal cortex, with a cluster peaking in the fusiform gyrus and extending into the posterior parahippocampal gyrus (*xyz* = 33/−37/−17, $Z$ = 5.18) and another in the calcarine sulcus (*xyz* = 18/−55/16, $Z$ = 4.28); in the left frontal cortex, with a cluster peaking in the precentral gyrus (PCG) and extending into the frontal eye field and the middle frontal gyrus (MFG; *xyz* = −33/−10/58, $Z$ = 6.15); in the left parietal cortex, with clusters in the precuneus (*xyz* = −12/−73/55, $Z$ = 4.43), the superior parietal lobe (*xyz* = −18/−58/64, $Z$ = 3.84), and a cluster peaking in the inferior parietal lobe and extending into the retrosplenial cortex (*xyz* = −36/−49/46, $Z$ = 5.12); in the right occipital cortex, with a cluster in the middle occipital lobe (*xyz* = 42/−79/34, $Z$ = 4.09); and finally bilaterally in the cerebellum, with a cluster peaking in the left anterior lobe and extending into the posterior parahippocampal gyrus (*xyz* = −15/−43/−14, $Z$ = 6.05), another in the right anterior lobe (*xyz* = 6/−58/−29, $Z$ = 4.24), and yet another in the right posterior lobe (*xyz* = 21/−64/−47, $Z$ = 4.86).

## DISCUSSION

With this study, our goal was to assess the neuroanatomic basis of mental comparisons of distances and directions read off the participants' cognitive map, by submitting them to the CMRT. As this task is supposed to tap into the same resources as real navigation, we expected hippocampal, parahippocampal, and parietal activations, with a bias in favor of the right side, reflecting the activation of structures usually involved in navigation.

The hippocampus showed no activity. Even though it may seem contradictory and unexpected for a spatial task, it is consistent with many recent studies. For instance, Schinazi et al. (2013) showed that hippocampal size only predicted subjects' performances in the learning phase, that is, not during navigation in an *already well-known* environment. This could mean that as soon as the environment is known, the hippocampus is not needed anymore to retrieve and process spatial knowledge. This hypothesis is also supported by the results of Spiers and Maguire (2007), who did not find any hippocampal activity in professional London taxi drivers performing a navigation task in a virtual reality (VR) setting of London.

This idea that the role of the hippocampus is mainly to contribute to the construction of a cognitive map (but less so, or even not at all for storage, recovery, and processing) is also shown in Rosenbaum et al. (2004), Shrager et al. (2007), and Shrager et al. (2008). This idea is consistent with recent cognitive models of memory (for a comprehensive view on current knowledge, see Axmacher and Rasch, 2017) and with neurobiological evidence (for a recent review, see Dudai et al., 2015). Because our task tapped into already existing knowledge (the subjects were asked about landmarks of a city where they had lived for at least 2 years), it might have needed little (in this case, infra-threshold) to no hippocampal processing at all.

In addition, the absence of visible significant activity does not mean that nothing happens at all in the hippocampus, but could instead result from a Type II error (failing to detect an actual effect). As reported by Lieberman and Cunningham (2009), wanting at all costs to avoid Type I errors (i.e., false positives) in fMRI research, and especially in tasks allowing multiple cognitive solutions—like ours—may lead to a disproportionate increase in the number of Type II errors.

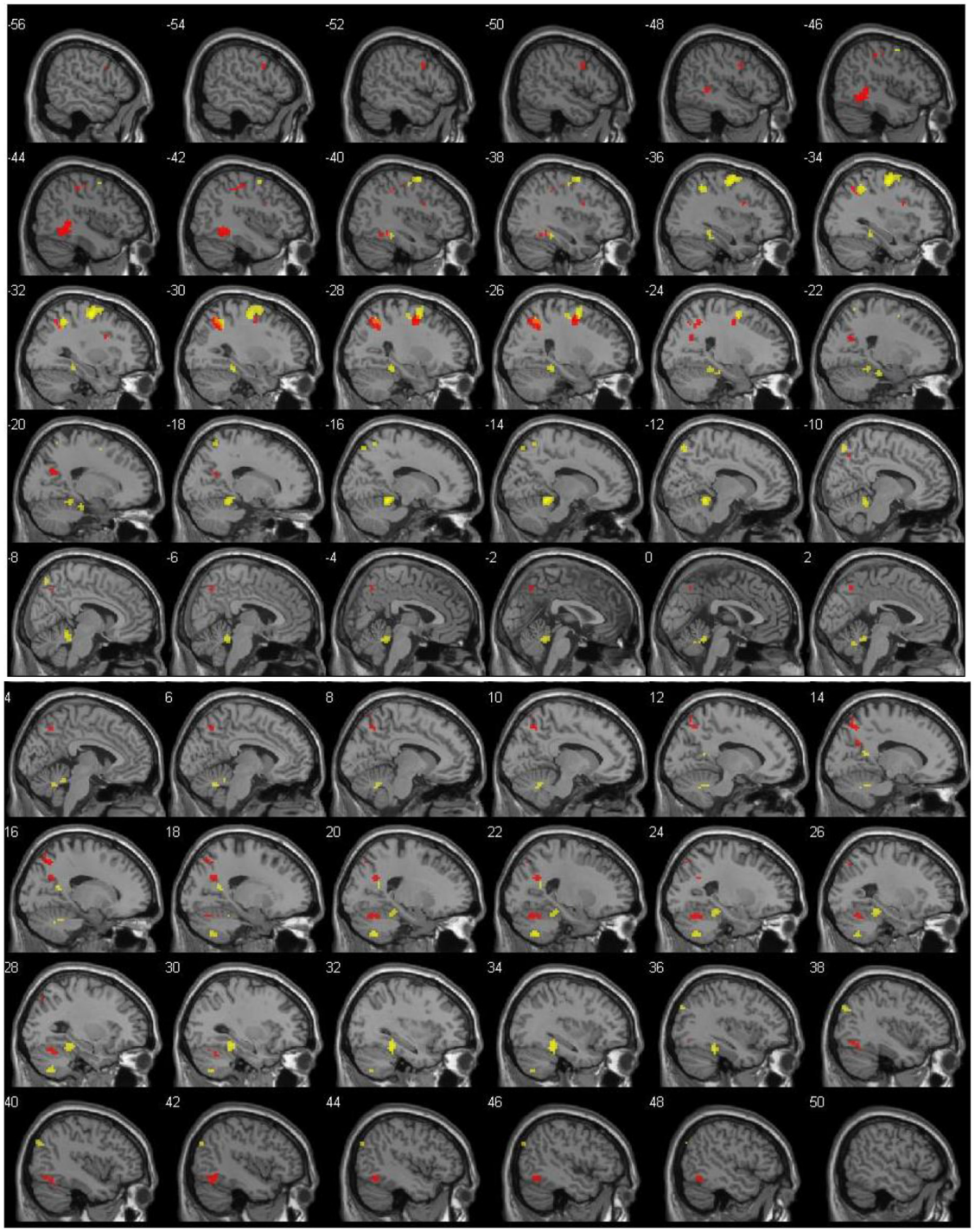


**FIGURE 1 |** Left (top) and right (bottom) hemisphere activation ($p$ = 0.001, uncorrected), shown with 2-mm spacing between each slice. Value on the top left of each slice shows $x$ coordinate. Red voxels show suprathreshold activation for distance (DIST) condition, whereas yellow voxels stand for direction (DIR) condition. Top left number of each slice indicate MNI $x$ coordinate.

Lieberman and Cunningham (2009) suggest different types of corrections, in order to avoid this; among them are $p$-value adjustment, cluster size thresholding, and family-wise error corrections. We settled for an intermediate solution, that is, an uncorrected $p$-value, but with cluster-size thresholding set at 8, which, according to Lieberman and Cunningham (2009), is a conservative solution that nonetheless already reduces Type II errors.

Interestingly, the posterior parahippocampal cortex showed significant activity in both hemispheres, but only for direction comparisons.

These results are in line with the double dissociation between the anterior and the posterior hippocampus (linked specifically to the learning and the reading phase, respectively) observed by Iaria et al. (2007) and Schinazi et al. (2013). As our task taps into already known and consolidated memories, it should only activate the most posterior regions of the hippocampal area.

However, our results show a parahippocampal cortex activation and not a posterior activation of the hippocampus. Interestingly, Libby et al. (2012), who analyzed functional connectivity on resting-state fMRI data, found that the connectivity pattern of the hippocampus with the surrounding subregions differs between its anterior and posterior part. More precisely, the anterior hippocampus shows preferential connectivity with the perirhinal cortex, whereas the posterior hippocampus connects preferentially to the parahippocampal cortex (which is more posterior than the perirhinal cortex). This pattern could in turn support the aforementioned cognitive double dissociation observed in the hippocampus by Iaria et al. (2007) and Schinazi et al. (2013), by extending this dissociation to regions downstream of the hippocampus (i.e., perirhinal and entorhinal cortex vs. parahippocampal cortex). In other words, the learning phase could be preferentially supported by anterior regions (anterior hippocampus, perirhinal, and entorhinal cortex), whereas the reading phase would be supported by more posterior regions (posterior hippocampus and parahippocampal cortex).

The reason why distance processing does not also elicit activity in the posterior parahippocampal area remains unaccounted for by the aforementioned hypothesis. Maybe distance processing does not rely enough on allocentric representations, and/or on episodic memory, to elicit suprathreshold parahippocampal activity.

Interestingly, the present body of data is echoed by Epstein (2008) in his review and by Cona and Scarpazza (2019) in their thorough fMRI meta-analysis: instead of being processed primarily in the hippocampus, navigation and spatial long-term memory tasks could preferentially and selectively be processed by the right parahippocampal gyrus and bilateral retrosplenial areas. Although our data show only very little activity in retrosplenial areas and rather bilateral activity in the parahippocampal gyrus, our study confirms an involvement of the parahippocampal gyrus in the cognitive processing required to perform items of the CMRT, which includes most probably spatial long-term memory retrieval and navigational skills (Descloux and Maurer, 2018).

Our data also indicate that parietal regions displayed activity in both hemispheres, most notably in the left superior parietal lobule and bilaterally in the precuneus. In addition, the left parietal cortex was twice as active compared to the right. We also found large displays of activity in the left frontal lobe, more specifically in the MFG and PCG, partially overlapping the frontal eye field. Taken together, these results are compatible with the nonaggregate network model suggested by Ekstrom et al. (2014), which suggested a distributed processing of navigational representations involving the very same brain regions as those shown active in our results.

Given the nature of our task, and of cognition in general (after all, all cognitive processes are embodied, and as such done from a certain point of view), isolating a purely egocentric or allocentric task, or cognitive process, is most probably impossible. Because our task requires subjects to adopt a certain perspective, especially for direction evaluation, and imagining a self-rotation in regard of *external* landmarks, it is both an egocentric and allocentric task. This dual nature, arguably inherent to navigation, is also described by Wilber et al. (2014). These authors describe a vector-based navigation model in which the direction of an unseen navigational goal is computed by combining the local egocentric landmark bearings (i.e., the location of landmarks from the subject perspective) with an allocentric head direction representation. It is relevant to our task, because the two aforementioned subcomponents are also found in the CMRT (respectively, when we asked our subjects to imagine themselves in a given surrounding, and when we asked them to represent themselves and compare three allocentric head directions). Their results, recorded *via* internal electroencephalogram (iEEG), show the posterior parietal cortex (PPC) of rats is highly involved in both these subcomponents, as is the PPC of our human participants while performing our task.

Alexander et al.'s (2020) results also highlight the importance of egocentric modulation in navigational processes. These authors recorded *via* iEEG the activity of cells in rats' retrosplenial cortex while the animal was freely exploring its 2D environment. They report a large percentage of these cells that have spatial receptive fields responsive to surrounding boundaries with specific orientation and distance, which is coded in an egocentric code. Furthermore, they found a subpopulation of these cells whose activity is synchronize with hippocampal theta waives. The role of theta in memory processes and navigation has been thoroughly studied (for interesting reviews, see Colgin, 2016; Korotkova et al., 2018; Buskila et al., 2019) and will be described within the scope of its various correlates with gamma waves and the CMRT in one of the author's upcoming study.

Recently, Bicanski and Burgess (2018) developed a simulation modeling how signals of specific neurons types (PC, HDC, and GC among others) can map onto navigation-related high-level cognitive functions. For instance, this model highlighted how GCs could account for the ability of mentally visualizing viewpoints during route planning and taking shortcuts by directly modulating PC activity.

Regarding now the frontal activity, we found a large cluster in the left PCG and in the left MFG. Cona and Scarpazza (2019) found in their meta-analysis that only the left PCG is involved in spatial tasks, whereas its right counterpart is not. More precisely, the left PCG was shown to be involved only in tasks requiring spatial attention and spatial working memory, whereas the MFG was active bilaterally and also involved in mental rotation tasks. Interestingly, we found here the same lateralization pattern for the PCG, but not for the MFG. This could mean that our task relies at least on spatial attention, spatial memory, and

spatial rotation. More generally, our results confirm that the left PCG and MFG are involved in mental navigation and spatial processing.

Interestingly, structures found active in the frontoparietal (FP) region in our study suggest that our task also heavily relies on brain structures involved in spatial attention and working memory (WM; Cona and Scarpazza, 2019). In line with their results, we also found a FP pattern of activation, looking very much like the one they observe in their study, that is, an activation pattern resembling the dorsal attention network (DAN; Majerus et al., 2018). This FP circuitry is composed of the frontal eye field, superior parietal lobule, and intraparietal sulcus, and it is usually recruited for perceptive visuospatial tasks, but also for spatial operations made on objects mentally visualized. More generally, the DAN is associated with the internal maintenance of task-related representations (for a review, see Majerus et al., 2018), which obviously means spatial representations for spatial tasks. Given their results, and as part of their conclusions, Cona and Scarpazza (2019) suggest that the DAN is likely to play a key role for working memory, episodic retrieval, and mental imagery.

This is, intuitively, not so striking, when considering how our distance condition requires subjects to recall three known locations (one serving as reference, the other two being targets), and their spatial relationship to each other, and then to keep them in WM to compute the two reference-to-target distances, and then to keep these two distance representations active in order to tell which one is the largest.

The cognitive processes needed to compare two directions, at least given how our task was built, require to keep even more representations active in WM before being able to answer: the subjects had to recall four known locations (two giving a reference direction, the other two being targets) and their spatial relationships to each other.

That the processing of directions is more WM-intensive than the processing of distances is supported by our findings. We indeed found that frontal regions were more than twice as active for condition direction compared to condition distance.

However, there are two important differences to be noted between, on the one hand, our results, and on the other hand, the results of Cona and Scarpazza (2019) and the most common hypothesis (see below) about the lateralization of spatial processing and WM.

The first difference is that we found a significant lateralization of the FP activity, whereas Cona and Scarpazza (2019) found *bilateral* involvement of this FP circuitry. The second difference is that the lateralization we found in the FP area is in favor of the left hemisphere. Consequently, our results do not support a right FP dominance for visuospatial working memory, but indicate a left dominance. Third, we also found in our results some cerebellum activity, which was unexpected. Yakusheva et al. (2007) and Angelaki et al. (2010) studied the vermis region of the cerebellum in macaques. They showed that the vermis is involved in the processing and transformation of self-motion information (stemming from vestibular afferents and vestibular nuclei neurons) and suggested that this region participates in spatial orientation.

Long-term depression (LTD) is a plasticity mechanism that has been hypothesized to be at work in the cerebellum as an error-based learning process (Albus, 1971). L7-PKCI transgenic mice are especially useful in the study of LTD mechanisms, because these animals display a selectively disrupted plasticity of their cerebellar Purkinje cells synapses, thus resulting in impaired LTD. Burguière et al. (2005) have shown that L7-PKCI transgenic mice did not perform as well as their wild-type peers in the Morris water maze and Starmaze tasks (which required them to find an escape platform while swimming in opaque water). The authors thus suggest that cerebellar LTD is involved is sensorimotor optimization and spatial navigation.

Rochefort et al. (2011) also worked with wild-type mice, and with strains of transgenic L7-PKCI animals. Their hippocampal CA1 cells (place cells) activity was recorded as they were exploring a circular arena, then their behavior was recorded during a path integration task (in total darkness) in a Morris water maze. Following cue manipulation in the first task, the authors showed that the firing fields of hippocampal place cells were not efficiently controlled by self-motion cues in the transgenic mice; in the water maze task, which required the use of self-motion cues, those mice were also impaired compared to the wild-type mice. Interestingly, Rochefort et al. (2011) also found that L7-PKCI mice had a significantly lower proportion of place cells than their wild-type peers. These findings suggest that plasticity-dependent mechanisms are involved in the processing of self-motion information in mice and, maybe more importantly, that these mechanisms have a direct impact on hippocampal cell recruitment and spatial representations.

Together, all these studies describing cerebellar involvement in spatial orientation in animals suggest an important and seemingly underestimated role of the cerebellum in human spatial cognition. This is probably related to its function: the cerebellum seems involved in the transformation of self-motion cues into rotational information that could be of use to build higher-level representations of space. In order to investigate the role of the cerebellum in the processing of such cues in humans, it would of course be necessary to allow subjects to move freely while their cerebellar activity is being recorded. To the authors' knowledge, such telemetry techniques are either nonexisting, not precise enough, or not applicable on the large environmental scales that are relevant to study human spatial navigation.

Regarding occipital activations, they were the smallest in terms of cluster size and number of active voxels. Interestingly, though, this lobe displayed activation only for distance processing. In general, a top-down process explains occipital activation in mental imagery tasks (O'Craven and Kanwisher, 2000). This this top-down activation theory does not explain why distance processing, and not direction processing, seemed to rely on the occipital lobe. This is even truer when considering how direction processing relies probably even more on mental imagery than distance comparisons.

Finally, the neat right-sided lateralization we expected was not observed. On the contrary, every brain region showed more left than right activation, with an exception for the occipital lobe and the cerebellum, which both showed more right- than left-sided

activation. This would tend to show that there is no clear right-sided specialization for navigation and that, depending on the nature of the task, the left hemisphere may even be more involved than the right (Lambrey et al., 2003).

## CONCLUSION

In this study, our aim was to assess which brain structures were involved in reading and processing the information stored in the cognitive map of a well-known environment. To that effect, we submitted our participants to a mental navigation task, the CMRT; we assumed that this mental map-processing task would tap into the same brain structures as real navigation. The main exploratory focus here was to identify if partly different brain structures process distances and directions. Generally, we have shown that our task indeed involves brain areas usually associated with navigation, that is, a circuitry involving the posterior parahippocampal cortex, the parietal lobule, the precuneus, and the PCG and MFG. We also found areas that are far less often associated with spatial navigation in humans, in particular the cerebellum and the occipital cortex. In contrast, hippocampal activity was low, and this is in line with the fact that the task required the recall of old, well-established spatial relations. As for the processing of distances vs. directions, only direction comparisons elicited significant bilateral activity in the posterior parahippocampal cortex. It is not clear why distance comparisons did not cause a similar pattern of activity; this will require further investigations, especially through methods with better temporal resolution, allowing the analysis of dynamic connectivity patterns involved in the processing of distance and direction. It remains true that, as pointed out by Epstein et al. (2017, p. 1509), "an important question for future research is how distance and direction are processed in highly familiar environments, where the hippocampus is not as needed for navigation."

## DATA AVAILABILITY STATEMENT

The raw data supporting the conclusions of this article will be made available by the authors, without undue reservation.

## ETHICS STATEMENT

The studies involving human participants were reviewed and approved by FPSE Faculty Ethical Committee (Commission Facultaire D'éthique De La FPSE). The patients/participants provided their written informed consent to participate in this study.

## AUTHOR CONTRIBUTIONS

IF: conceptualization, methodology, investigation, data curation, writing—original draft, visualization, and formal analysis. VD: methodology. AS: formal analysis. RM: supervision, writing—review and editing, project administration, and funding acquisition.

## REFERENCES


Aguirre, G. K., and D'Esposito, M. (1999). Topographical disorientation: a synthesis and taxonomy. *Brain.* 122, 1613–1628. doi: 10.1093/brain/122.9.1613

Albus, J. S. (1971). A theory of cerebellar function. *Math. Biosci.* 10, 25–61. doi: 10.1016/0025-5564(71)90051-4

Alexander, A. S., Carstensen, L. C., Hinman, J. R., Raudies, F., Chapman, G. W., and Hasselmo, M. E. (2020). Egocentric boundary vector tuning of the retrosplenial cortex. *Sci. Adv.* 6:eaaz2322. doi: 10.1126/sciadv.aaz2322

Angelaki, D. E., Yakusheva, T. A., Green, A. M., Dickman, J. D., and Blazquez, P. M. (2010). Computation of egomotion in the macaque cerebellar vermis. *Cerebellum* 9, 174–182. doi: 10.1007/s12311-009-0147-z

Ashburner, J., Barnes, G., Chen, C., Daunizeau, J., Flandin, G., Friston, K., et al (2013). *SPM8 Manual.* London: Functional Imaging Laboratory, Institute of Neurology, UCL.

Axmacher, N., and Rasch, B. (2017). *Cognitive Neuroscience of Memory Consolidation.* Cham, Switzerland: Springer International Publishing. doi: 10.1007/978-3-319-45066-7

Barry, C., and Burgess, N. (2014). Neural mechanisms of self-location. *Curr. Bio.* 24, R330–R339. doi: 10.1016/j.cub.2014.02.049

Bastin, J., Committeri, G., Kahane, P., Galati, G., Minotti, L., Lachaux, J. P., et al (2013). Timing of posterior parahippocampal gyrus activity reveals multiple scene processing stages. *Hum. Brain Mapp.* 34, 1357–1370. doi: 10.1002/hbm.21515

Bates, E., Wilson, S. M., Saygin, A. P., Dick, F., Sereno, M. I., Knight, R. T., et al (2003). Voxel-based lesion-symptom mapping. *Nat. Neurosci.* 6, 448–450. doi: 10.1038/nn1050

Bicanski, A., and Burgess, N. (2018). A neural-level model of spatial memory and imagery. *Elife* 7:e33752. doi: 10.7554/eLife.33752

Burgess, N. (2008). Spatial Cognition and the Brain. *Annals of the New York Academy of Sciences* 1124, 77–97.

Burguière, E., Arleo, A., Hojjati, M. R., Elgersma, Y., De Zeeuw, C. I., Berthoz, A., et al (2005). Spatial navigation impairment in mice lacking cerebellar LTD: a motor adaptation deficit? *Nat. Neurosci.* 8, 1292–1294. doi: 10.1038/nn1532

Buskila, Y., Bellot-Saez, A., and Morley, J. W. (2019). Generating brain waves, the power of astrocytes. *Front. Neurosci.* 13:1125. doi: 10.3389/fnins.2019.01125

Colgin, L. L. (2016). Rhythms of the hippocampal network. *Nat. Rev. Neurosci.* 17:239. doi: 10.1038/nrn.2016.21

Cona, G., and Scarpazza, C. (2019). Where is the "where" in the brain? A meta-analysis of neuroimaging studies on spatial cognition. *Hum. Brain Mapp.* 40, 1867–1886. doi: 10.1002/hbm.24496

Descloux, V. (2013). *Troubles De L'orientation Spatiale: Développement D'une Batterie D'évaluation et Corrélats Neuroanatomiques*. University of Geneva. Doctoral dissertation.

Descloux, V., and Maurer, R. (2018). Cognitive map recall test: a new specific test to assess topographical disorientation. *Appl. Neuropsychol. Adult.* 25, 91–109. doi: 10.1080/23279095.2016.1247094

Descloux, V., Bellmann, A., and Maurer, R. (2015). Assessment of topographical disorientation: first application of new tests and case report. *J. Appl. Neuropsychol.: Adult* 22, 373–380. doi: 10.1080/23279095.2014.940525

Doeller, C. F., Barry, C., and Burgess, N. (2010). Evidence for grid cells in a human memory network. *Nature* 463, 657–661. doi: 10.1038/nature08704

Dudai, Y., Karni, A., and Born, J. (2015). The consolidation and transformation of memory. *Neuron* 88, 20–32. doi: 10.1016/j.neuron.2015.09.004

Ekstrom, A. D., Arnold, A. E., and Iaria, G. (2014). A critical review of the allocentric spatial representation and its neural underpinnings: toward a network-based perspective. *Front. Hum. Neurosci.* 8:803. doi: 10.3389/fnhum.2014.00803

Ekstrom, A. D., Kahana, M. J., Caplan, J. B., Fields, T. A., Isham, E. A., Newman, E. L., et al (2003). Cellular networks underlying human spatial navigation. *Nature* 425, 184–188. doi: 10.1038/nature01964

Epstein, R. A. (2008). Parahippocampal and retrosplenial contributions to human spatial navigation. *Trends Cogn. Sci.* 12, 388–396. doi: 10.1016/j.tics.2008.07.004

Epstein, R. A., Patai, E. Z., Julian, J. B., and Spiers, H. J. (2017). The cognitive map in humans: spatial navigation and beyond. *Nat. Neurosci.* 20, 1504–1513. doi: 10.1038/nn.4656

Hafting, T., Fyhn, M., Molden, S., Moser, M.-B., and Moser, E. I. (2005). Microstructure of a spatial map in the entorhinal cortex. *Nature* 436, 801–806. doi: 10.1038/nature03721

Iaria, G., Chen, J. K., Guariglia, C., Ptito, A., and Petrides, M. (2007). Retrosplenial and hippocampal brain regions in human navigation: complementary functional contributions to the formation and use of cognitive maps. *Eur. J. Neurosci.* 25, 890–899. doi: 10.1111/j.1460-9568.2007.05371.x

Javadi, A., Emo, B., Howard, L. R., Zisch, F. E., Yu, Y., Knight, R., et al (2017). Hippocampal and prefrontal processing of network topology to simulate the future. *Nat. Commun.* 8:14852. doi: 10.1038/ncomms14652

Korotkova, T., Ponomarenko, A., Monaghan, C. K., Poulter, S. L., Cacucci, F., Wills, T., et al (2018). Reconciling the different faces of hippocampal theta: the role of theta oscillations in cognitive, emotional and innate behaviors. *Neurosci. Biobehav. Rev.* 85, 65–80. doi: 10.1016/j.neubiorev.2017.09.004

Lambrey, S., Samson, S., Dupont, S., Baulac, M., and Berthoz, A. (2003). Reference frames and cognitive strategies during navigation: is the left hippocampal formation involved in the sequential aspects of route memory? *Int. Cong. Ser.* 1250, 261–274. doi: 10.1016/s0531-5131(03)00997-x

Libby, L. A., Ekstrom, A. D., Ragland, J. D., and Ranganath, C. (2012). Differential connectivity of perirhinal and parahippocampal cortices within human hippocampal subregions revealed by high-resolution functional imaging. *J. Neurosci.* 32, 6550–6560. doi: 10.1523/jneurosci.3711-11.2012

Lieberman, M. D., and Cunningham, W. A. (2009). Type I and type II error concerns in fMRI research: re-balancing the scale. *Soc. Cogn. Affect. Neurosci.* 4, 423–428. doi: 10.1093/scan/nsp052

Majerus, S., Péters, F., Bouffier, M., Cowan, N., and Phillips, C. (2018). The dorsal attention network reflects both encoding load and top-down control during working memory. *J. Cogn. Neurosci.* 30, 144–159. doi: 10.1162/jocn_a_01195

Nedelska, Z., Andel, R., Laczo, J., Vlcek, K., Horinek, D., Lisy, J., et al (2012). Spatial navigation impairment is proportional to right hippocampal volume. *Proc. Natl. Acad. Sci. U S A.* 109, 2590–2594. doi: 10.1073/pnas.1121588109

O'Craven, K. M., and Kanwisher, N. (2000). Mental imagery of faces and places activates corresponding stimulus-specific brain regions. *J. Cogn. Neurosci.* 12, 1013–1023. doi: 10.1162/08989290051137549

O'Keefe, J., and Nadel, L. (1978). *The Hippocampus as a Cognitive Map*. Oxford: Oxford University Press.

Park, S., Intraub, H., Yi, D. J., Widders, D., and Chun, M. M. (2007). Beyond the edges of a view: boundary extension in human scene-selective visual cortex. *Neuron* 54, 335–342. doi: 10.1016/j.neuron.2007.04.006

Rauchs, G., Orban, P., Balteau, E., Schmidt, C., Degueldre, C., Luxen, A., et al (2008). Partially segregated neural networks for spatial and contextual memory in virtual navigation. *Hippocampus* 18, 503–518. doi: 10.1002/hipo.20411

Rochefort, C., Arabo, A., André, M., Poucet, B., Save, E., and Rondi-Reig, L. (2011). Cerebellum shapes hippocampal spatial code. *Science* 334, 385–389. doi: 10.1126/science.1207403

Rosenbaum, R. S., Ziegler, M., Winocur, G., Grady, C. L., and Moscovitch, M. (2004). "I have often walked down this street before": fMRI studies on the hippocampus and other structures during mental navigation of an old environment. *Hippocampus* 14, 826–835. doi: 10.1002/hipo.10218

Schinazi, V. R., Nardi, D., Newcombe, N. S., Shipley, T. F., and Epstein, R. A. (2013). Hippocampal size predicts rapid learning of a cognitive map in humans. *Hippocampus* 23, 515–528. doi: 10.1002/hipo.22111

Shrager, Y., Bayley, P. J., Bontempi, B., Hopkins, R. O., and Squire, L. R. (2007). Spatial memory and the human hippocampus. *Proc. Natl. Acad. Sci. U S A.* 104, 2961–2966. doi: 10.1073/pnas.0611233104

Shrager, Y., Kirwan, C. B., and Squire, L. R. (2008). Neural basis of the cognitive map: path integration does not require hippocampus or entorhinal cortex. *Proc. Natl. Acad. Sci. U S A.* 105, 12034–12038. doi: 10.1073/pnas.0805414105

Silk, T. J., Bellgrove, M. A., Wrafter, P., Mattingley, J. B., and Cunnington, R. (2010). Spatial working memory and spatial attention rely on common neural processes in the intraparietal sulcus. *Neuroimage* 53, 718–724. doi: 10.1016/j.neuroimage.2010.06.068

Spiers, H. J., and Maguire, E. A. (2007). A navigational guidance system in the human brain. *Hippocampus* 17, 618–626. doi: 10.1002/hipo.20298

Wilber, A. A., Clark, B. J., Forster, T. C., Tatsuno, M., and McNaughton, B. L. (2014). Interaction of egocentric and world-centered reference frames in the rat posterior parietal cortex. *J. Neurosci.* 34, 5431–5446. doi: 10.1523/JNEUROSCI.0511-14.2014

Wolbers, T., and Büchel, C. (2005). Dissociable retrosplenial and hippocampal contributions to successful formation of survey representations. *J. Neurosci.* 25, 3333–3340. doi: 10.1523/JNEUROSCI.4705-04.2005

Wolbers, T., and Wiener, J. M. (2014). Challenges for identifying the neural mechanisms that support spatial navigation: the impact of spatial scale. *Front. Hum. Neurosci.* 8:571. doi: 10.3389/fnhum.2014.00571

Yakusheva, T. A., Shaikh, A. G., Green, A. M., Blazquez, P. M., Dickman, J. D., and Angelaki, D. E. (2007). Purkinje cells in posterior cerebellar vermis encode motion in an inertial reference frame. *Neuron* 54, 973–985. doi: 10.1016/j.neuron.2007.06.003

**Conflict of Interest**: Since the 1st of February 2020, the co-author IF has been employed by Frontiers Media SA. IF declared his affiliation with Frontiers, and the handling Editor states that the process nevertheless met the standards of a fair and objective review.

The remaining authors declare that the research was conducted in the absence of any commercial or financial relationships that could be construed as a potential conflict of interest.

*Copyright © 2020 Faulmann, Descloux, Saj and Maurer. This is an open-access article distributed under the terms of the Creative Commons Attribution License (CC BY). The use, distribution or reproduction in other forums is permitted, provided the original author(s) and the copyright owner(s) are credited and that the original publication in this journal is cited, in accordance with accepted academic practice. No use, distribution or reproduction is permitted which does not comply with these terms.*

frontiers in Behavioral Neuroscience

BRIEF RESEARCH REPORT
published: 26 August 2020
doi: 10.3389/fnbeh.2020.00144

# False Opposing Fear Memories Are Produced as a Function of the Hippocampal Sector Where Glucocorticoid Receptors Are Activated

*Nadia Kaouane[1,2†], Eva-Gunnel Ducourneau[1,2], Aline Marighetto[1,2], Menahem Segal[3] and Aline Desmedt[1,2*]*

[1]INSERM, Neurocentre Magendie, Physiopathologie de la Plasticité Neuronale, Bordeaux, France, [2]University of Bordeaux, Bordeaux, France, [3]Department of Neurobiology, The Weizmann Institute, Rehovot, Israel

Injection of corticosterone (CORT) in the dorsal hippocampus (DH) can mimic post-traumatic stress disorder (PTSD)—related memory in mice: both maladaptive hypermnesia for a salient but irrelevant simple cue and amnesia for the traumatic context. However, accumulated evidence indicates a functional dissociation within the hippocampus such that contextual learning is primarily associated with the DH whereas emotional processes are more linked to the ventral hippocampus (VH). This suggests that CORT might have different effects on fear memories as a function of the hippocampal sector preferentially targeted and the type of fear learning (contextual vs. cued) considered. We tested this hypothesis in mice using CORT infusion into the DH or VH after fear conditioning, during which a tone was either paired (predicting-tone) or unpaired (predicting-context) with the shock. We first replicate our previous results showing that intra-DH CORT infusion impairs contextual fear conditioning while inducing fear responses to the not predictive tone. Second, we show that, in contrast, intra-VH CORT infusion has opposite effects on fear memories: in the predicting-tone situation, it blocks tone fear conditioning while enhancing the fear responses to the context. In both situations, a false fear memory is formed based on an erroneous selection of the predictor of the threat. Third, these opposite effects of CORT on fear memory are both mediated by glucocorticoid receptor (GR) activation, and reproduced by post-conditioning stress or systemic CORT injection. These findings demonstrate that false opposing fear memories can be produced depending on the hippocampal sector in which the GRs are activated.

**Keywords: dorsal hippocampus, ventral hippocampus, fear memory, fear conditioning, glucocorticoid receptors, mice**

OPEN ACCESS

***Edited by:***
*Michael Fanselow, University of California, Los Angeles, United States*

***Reviewed by:***
*Janine Lynn Kwapis, Pennsylvania State University (PSU), United States*
*Travis D. Goode, Harvard University, United States*

****Correspondence:***
*Aline Desmedt*
*aline.desmedt@inserm.fr*

***†Present address:***
*Nadia Kaouane, Research Institute of Molecular Pathology (IMP), Vienna Biocenter (VBC), Vienna, Austria*

***Specialty section:***
*This article was submitted to Learning and Memory, a section of the journal Frontiers in Behavioral Neuroscience*

***Received:*** *29 May 2020*
***Accepted:*** *27 July 2020*
***Published:*** *26 August 2020*

***Citation:***
*Kaouane N, Ducourneau E-G, Marighetto A, Segal M and Desmedt A (2020) False Opposing Fear Memories Are Produced as a Function of the Hippocampal Sector Where Glucocorticoid Receptors Are Activated. Front. Behav. Neurosci. 14:144. doi: 10.3389/fnbeh.2020.00144*

## INTRODUCTION

Exposure to an extreme stress can produce highly fearful memories, which contribute to the development of stress-related disorders (de Quervain et al., 1998). In such a situation, excess glucocorticoids, whose the hippocampus constitutes a key brain site of action, impair hippocampus-dependent memory consolidation of the event (McEwen, 2000; Roozendaal, 2003). Therefore, this may explain the emergence of pathological fear memories like those observed in post-traumatic stress disorder (PTSD; Layton and Krikorian, 2002; Desmedt et al., 2015a). In accordance with this, we previously demonstrated in mice that, under a high stressful situation, post-training infusion of glucocorticoids into the dorsal hippocampus (DH) impairs contextual fear memories while inducing fear memory for an irrelevant (i.e., not predicting the threat) simple tone, thereby mimicking both contextual amnesia and the maladaptive hypermnesia observed in PTSD (Kaouane et al., 2012).

However, accumulated evidence demonstrates a functional dissociation along the dorsal–ventral axis of the hippocampus (Fanselow and Dong, 2010). The DH receives polymodal sensory information from cortical areas (Witter and Amaral, 2004) and primarily contributes to contextual learning. In contrast, the ventral hippocampus (VH) is strongly connected to the subcortical structures, especially the amygdala, and may rather contribute to emotion-related processes (Moser and Moser, 1998; Bannerman et al., 2004), particularly fear conditioning (Maren, 1999; Bast et al., 2001; Maren and Holt, 2004) and anxiety-related behaviors (Bannerman et al., 2004; Calhoon and Tye, 2015). In addition, stress and glucocorticoids differentially regulate long-term potentiation (LTP) and long-term depression (LTD) in the DH and the VH (Maggio and Segal, 2007a,b, 2009a,b). In particular, they impair LTP in the DH while enhancing it in the VH (Maggio and Segal, 2007b), whereas stress increases LTD in the DH while converting LTD to LTP in the VH (Maggio and Segal, 2009a).

Moreover, the glucocorticoid receptors (GRs), on which depend the glucocorticoids' memory effects (Oitzl et al., 2001), show a higher density in the DH than in the VH (Robertson et al., 2005; Segal et al., 2010). Of particular interest in the context of normal vs. pathological fear memory, GR activation within the hippocampus is crucial for the consolidation of contextual fear memories and can even enhance them (Donley et al., 2005; Revest et al., 2005, 2010, 2014) whereas full GR activation results in impaired spatial memory (Conrad et al., 1999; Brinks et al., 2007). Furthermore, specific activation of GRs also abolishes *in vitro* synaptic excitability in both DH and VH (Segal et al., 2010) and facilitates LTD in both hippocampal sectors (Maggio and Segal, 2009a). Together, these data strongly suggest that GR activation in either DH or VH could differentially contribute to the deleterious effects of glucocorticoids on fear memories.

To address this issue: (1) we compared the effects of local infusions of corticosterone (CORT), the major glucocorticoid in rodents, into either the DH or the VH, on the consolidation of tone and contextual fear memories; (2) we assessed whether these effects are mediated by GR activation; and (3) we tested whether these effects could be physiologically mimicked by post-training stress or systemic CORT injection.

## MATERIALS AND METHODS

### Subjects

Three-month-old male mice (C57Bl/6 JI Company, Charles River Laboratories) were individually housed a week before experiments in standard Macrolon cages in a temperature- and humidity-controlled room under a 12-h light/dark cycle (lights on at 07:00) and had *ad libitum* access to food and water. As all the present experiments were restricted to male mice, future experiments will have to determine the extent to which the present findings can be extended to female mice. Mice were handled a few days before experiments and habituated to intracerebral or systemic injection procedures. All experiments took place during the light phase. All animal care and behavioral tests were conducted in compliance with the European Communities Council Directive (86/609/EEC).

### Surgical Procedure

Mice were anesthetized with ketamine (80 mg/kg body weight, i.p.) and xylazine (16 mg/kg body weight, i.p.; Bayer) and secured in a David Kopf Instruments stereotaxic apparatus. Stainless-steel guide cannulas (26 gauge, 8-mm length) were implanted bilaterally 1 mm above either the dorsal hippocampus (A/P, −2 mm; M/L, ±1.3 mm; D/V, 1 mm) or the ventral hippocampus (A/P, −3.6 mm; M/L, ±3 mm; D/V, 3.3 mm; relative to dura and bregma; Franklin and Paxinos, 1997), then fixed in place with dental cement and two jeweler screws attached to the skull. Mice were then allowed to recover in their home cage for at least 8 days before behavioral experiments.

### Fear Conditioning Procedures

The procedures have been fully described in previous studies (Calandreau et al., 2005, 2006, 2007; Kaouane et al., 2012). Briefly, mice were placed in the conditioning chamber and, after a baseline period of 100 s, received two tone cues (63 dB, 1 kHz, 15 s) either paired (intertrial interval of 60 s) or unpaired (pseudo-random distribution of the stimuli) with two electric footshocks (0.8 mA, 50 Hz, 3 s). With the tone presentation always followed by the shock delivery (cue–shock *pairing* procedure), the animals identified the tone as the main threat predictor of the shock (predicting-cue group). In contrast, when the tone presentation was never followed by shock delivery (cue–shock *unpairing* procedure), the animals identified the conditioning context as the right predictor of the shock (predicting-context group; **Figure 1**). Specifically, in the CS–US unpairing procedure, 100 s after being placed into the chamber, animals received a shock, then, after a 20-s delay, a tone; finally, after a 30-s delay, the same tone and the same shock spaced by a 30-s interval were presented. After 20 s, animals were returned to the home cage. The relatively high footshock intensity used (i.e., 0.8 mA) is known to produce a strong fear conditioning to the tone or to the context in the predicting-cue group and the predicting-context group, respectively, as demonstrated in our previous study (Kaouane et al., 2012). The quality of the

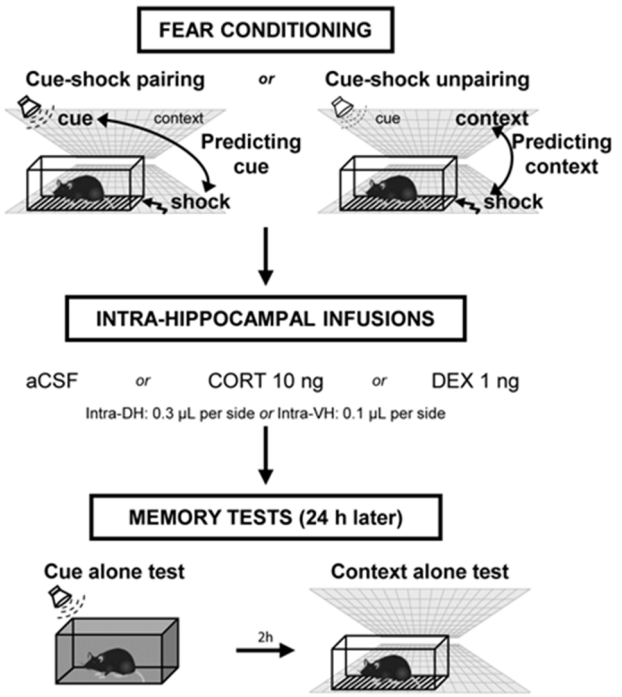


**FIGURE 1 |** Experimental design of the behavioral procedure. Mice were either submitted to a cue–shock *pairing* procedure (predicting-cue group) or to a cue–shock *unpairing* procedure (predicting-context group). Immediately after conditioning, animals received intra-hippocampal infusions of artificial cerebrospinal fluid (aCSF), corticosterone (CORT), or dexamethasone (DEX). The next day, mice were first re-exposed to the cue alone in a neutral chamber, then (2 h later) were re-exposed to the conditioning context without the cue. During these tests, the freezing responses were measured during 2-min periods.

memory formed was assessed the following day when mice were submitted to two memory tests. First, after a 2-min baseline period in a neutral chamber, mice were exposed for 2 min to the tone cue alone, followed by a 2-min post-tone period. Conditioned fear to the tone is expressed by the percentage of freezing during the tone presentation, and the strength and specificity of this conditioned fear is attested by a ratio that considers the percentage of freezing increase to the tone with respect to a baseline freezing level (i.e., pre- and post-tone periods mean) and that was calculated as follows: [% freezing during tone presentation − (% pre-tone period freezing + % post-tone period freezing)/2]/[% freezing during tone presentation + (% pre-tone period freezing + % post-tone period freezing)/2]. Two hours later, mice were re-exposed for 6 min to the conditioning context alone for the assessment of their contextual freezing, which attests of their contextual memory of the aversive event. As for the tone test, the percentage of freezing is assessed during three 2-min blocks. However, because all contextual fear responses decline on the second and third 2-min blocks of the context test because of a classical fear extinction and that the first 2-min block is the only one that allows the observation of key optimal differences between the different groups, we chose to restrict the data to the first block. Freezing behavior of animals, defined as a lack of all movement except for respiratory-related movements, was used as an index of conditioned fear response. Animals were continuously recorded on videotape for off-line second-by-second scoring of freezing by an observer blind of experimental groups.

## Intracerebral Infusions

Immediately after the acquisition of fear conditioning, animals were placed back in their home cage and received intra-DH or intra-VH bilateral infusions (0.3 or 0.1 µl per side, respectively) of artificial cerebrospinal fluid (aCSF), CORT (2-hydroxypropyl-β-cyclodextrin complex; Sigma–Aldrich; 10 ng per side), or the specific GR agonist dexamethasone (DEX: 2-hydroxypropyl-β-cyclodextrin complex; Sigma–Aldrich; 1 ng per side). The dose of CORT was selected based on our previous study reporting that post-training intra-DH infusions of 10 ng disturbed the selection of the right predictor of the shock under a 0.8-mA footshock intensity (Kaouane et al., 2012). The dose of DEX was selected on the basis of previous *in vivo* studies using similar concentration for intra-DH infusions in rats (Mizoguchi et al., 2007) and reporting that dose 10-fold lower than for CORT is efficient to mimic *in vitro* CORT effects (Maggio and Segal, 2007b; Chaouloff et al., 2008). For infusions, stainless-steel cannulas (32-gauge, 9 mm) attached to 1-µl Hamilton syringes with polyethylene catheter tubing were inserted through the guide cannula. The syringes were fixed in a constant rate infusion pump (0.1 µl/min). The cannulas were left in place for an additional 1 min before removal to guarantee diffusion of the drug.

## Restraint Stress

Immediately after the acquisition of fear conditioning using a footshock of 0.8 mA or a lower one (0.3 mA) known to be too weak for inducing significant fear responses but with which post-training stress can enhance contextual fear conditioning (Kaouane et al., 2012), mice were placed during 20 min in a transparent Plexiglas cylinder (diameter: 2.5 cm, 11 cm long) in a room adjacent to the fear conditioning room. After immobilization, mice were returned to their home cage.

## Systemic Injection of Corticosterone

CORT (2-hydroxypropyl-β-cyclodextrin complex) or vehicle (NaCl 0.9%) was administrated intraperitoneally (i.p.) immediately after the acquisition of fear conditioning. The complex of corticosterone with cyclodextrins allows dissolving this steroid in aqueous solutions. After the injection, animals were returned to their home cage. We selected a relatively low (1.5 mg/kg) and a high (10 mg/kg) dose of corticosterone (in a volume of 0.1 ml/10 g bodyweight) known to produce dose-dependent effects on fear memories as shown in our previous study (Kaouane et al., 2012).

## Histology

After behavioral testing, animals were given an overdose of pentobarbital and transcardially perfused with physiological saline, followed by 10% buffered formalin. Brains were postfixed in formalin–sucrose 30% solution for 1 week, frozen, cut coronally on a sliding microtome into 60-µm sections that were

mounted on gelatin-coated glass slides, and stained with thionine to evaluate the cannula placements (**Supplementary Figure S1**).

## Data Analysis

Data are presented as the mean ± SEM. Statistical analyses were performed using, on StatView software, analysis of variance (ANOVA) followed by Bonferroni–Dunn *post hoc* test when appropriate. Values of $p < 0.05$ were considered as significant. Several experiments using a similar behavioral protocol led to the conclusion that 6–8 mice per group were enough to reach statistical significance. To face the variability of surgery, we increased the sample size to 10 mice per group. For indication, the power of these experiments, with $n = 8$ mice per group and an alpha of 0.05, is 85%.

# RESULTS

## Activation of GR in the DH Produces a Simple Tone-Based Fear Memory at the Expense of Contextual Fear Memory

This experiment first replicates our previous findings showing that intra-DH injection of CORT mimicked a simple/salient tone fear conditioning at the expense of contextual conditioning, thereby reproducing the PTSD-like pathological hypermnesia and contextual amnesia (Kaouane et al., 2012). Second, the present results reveal that such abnormal fear memory can also be produced by intra-DH injection of DEX, indicating that GR activation is sufficient to induce such memory alteration. The effects of the intra-DH injections of CORT and DEX on the fear responses to the tone (**Figure 2A**) and the conditioning context (**Figure 2B**) were dependent on the conditioning procedure (i.e., predicting-cue vs. predicting-context) as they were both restricted to the predicting-context condition [Tone conditioning ratio: effect of treatment ($F_{(2,38)} = 8.19$, $p < 0.01$) and treatment × procedure ($F_{(2,38)} = 13.00$, $p < 0.001$); Context test: effect of treatment ($F_{(2,38)} = 6.20$, $p < 0.01$) and treatment × procedure ($F_{(2,38)} = 7.04$, $p < 0.01$)].

First, compared with their aCSF-injected controls, CORT- and DEX-injected mice submitted to the predicting-context procedure displayed increased fear responses to the tone, attested by a significant increased tone conditioning ratio (**Figure 2A**, left, both CORT and DEX: Bonferroni–Dunn *post hoc* test $p < 0.001$), and a significant increase in the percentage of freezing level to the tone *per se* (**Figure 2A**, right, CORT: $p < 0.01$, DEX: $p < 0.05$; see also **Supplementary Figure S2A**), so that they did not differ anymore from animals submitted to the predicting-tone procedure (in CORT and DEX groups: both $p > 0.05$). It must be noted that in our previous study (Kaouane et al., 2012), we also showed that CORT-injected mice displayed a fear response to a previously unexperienced cue (2-kHz tone) at some extent similar to the one experienced during the conditioning (1-kHz tone), but not to a completely different cue (white noise). Thus, as in PTSD, these mice showed a partial fear generalization to cues more or less similar to trauma-related cues, but not to very different cues.

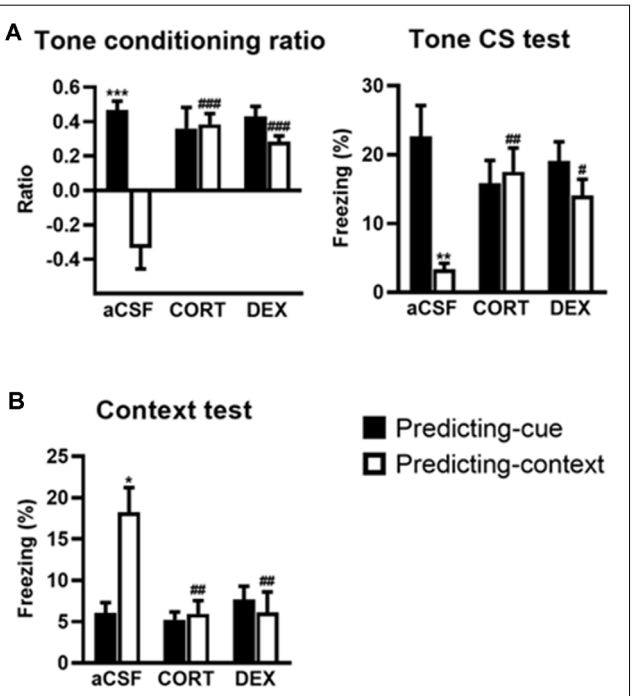


**FIGURE 2 |** Activation of glucocorticoid receptor (GR) in the dorsal hippocampus (DH) produces a simple tone-based fear memory at the expense of contextual fear memory. In controls (aCSF), mice of the predicting-cue group ($n = 7$) expressed a high tone conditioning ratio (**A**, *left*) and high percentage of freezing to the tone *per se* (**A**, *right*), as well as low freezing to the context **(B)**, in comparison with the predicting-context group ($n = 8$), which expressed low levels of freezing to the cue and high levels of freezing to the context. In mice submitted to the predicting-context condition, intra-DH CORT or DEX infusions increased the tone conditioning ratio (**A**, *left*), produced a fear response to the cue (**A**, *right*), while reducing the conditioned fear to the context (**B**; CORT: $n = 7$; DEX: $n = 6$). No change was observed in mice submitted to the predicting-cue condition (CORT: $n = 7$; DEX: $n = 9$). In all conditions, the ratio differed from zero (all $p < 0.05$). *Procedure effect (predicting cue vs. predicting context group; $^{*}p < 0.05$, $^{**}p < 0.01$, and $^{***}p < 0.001$); $^{\#}$treatment effect (aCSF vs. CORT or aCSF vs. DEX; $^{\#}p < 0.05$, $^{\#\#}p < 0.01$, and $^{\#\#\#}p < 0.001$).

In parallel, although the conditioning context is the objective predictive stimulus in this training condition, the same mice displayed significantly decreased contextual fear responses compared with aCSF controls (**Figure 2B**, both CORT and DEX: Bonferroni–Dunn *post hoc* test $p < 0.01$). As a result, their levels of contextual freezing were as low as those displayed by mice submitted to the predicting-tone condition (in CORT and DEX groups: $p > 0.05$).

## Activation of GR in the VH Promotes a Context-Based Fear Memory at the Expense of Tone-Based Fear Memory

The effects of intra-VH injections of CORT and DEX on the fear responses to the tone (**Figure 3A**) and the conditioning context (**Figure 3B**) were dependent on the conditioning procedure (i.e., predicting-cue vs. predicting-context), but in contrast to intra-DH injections, they were both restricted to the predicting-cue condition [Tone conditioning

ratio: effect of treatment ($F_{(2,40)}$ = 7.26, $p < 0.01$) and treatment × procedure ($F_{(2,40)}$ = 7.40, $p < 0.01$); Context test: effect of treatment × procedure ($F_{(2,40)}$ = 8.61, $p < 0.001$)].

First, compared with their aCSF-injected controls, CORT- and DEX-injected mice submitted to the predicting-cue procedure did not express any conditioned fear to the tone, which is the objective predictive stimulus in this training condition. This blockade is attested by a significant decreased tone conditioning ratio (**Figure 3A**, left, both CORT and DEX: Bonferroni–Dunn *post hoc* test $p < 0.001$) and a significant decrease in the percentage of freezing level to the tone *per se* (**Figure 3A**, right, both CORT and DEX: $p < 0.01$; see also **Supplementary Figure S2B**). As a result, these mice did not differ anymore from those submitted to the predicting-context procedure (in CORT and DEX groups: both $p > 0.05$).

In parallel, the same mice displayed significantly increased fear responses to the conditioning context (**Figure 3B**, CORT: $p < 0.01$, DEX: $p < 0.001$) to the extent that their levels of contextual freezing were as high as those of mice submitted to the predicting-context condition (in CORT and DEX groups: both $p > 0.05$).

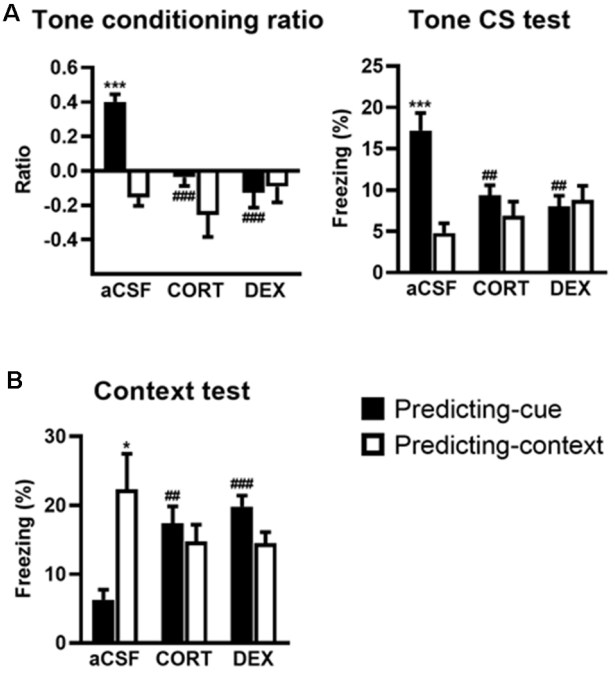


**FIGURE 3 |** Activation of GR in the ventral hippocampus (VH) promotes a context-based fear memory at the expense of tone-based fear memory. The controls (aCSF) expressed a high tone conditioning ratio (**A**, *left*) with high percentage of freezing to the tone *per se* (**A**, *right*; predicting-cue group: $n = 8$) and low conditioned fear to the context **(B)** when submitted to the predicting-cue condition ($n = 8$), whereas they expressed an inverse pattern of results when submitted to the predicting-context condition ($n = 8$). In the predicting-cue condition, intra-VH CORT or DEX infusions (CORT: $n = 8$; DEX: $n = 8$) abolished the tone conditioning ratio (**A**, *left*) and the conditioned fear to the tone *per se* (**A**, *right*), while increasing the fear responses to the context **(B)**. After CORT and DEX infusions, the ratios did not differ from zero (all $p > 0.05$). No change was observed in mice submitted to the predicting-context condition (CORT: $n = 7$; DEX: $n = 7$). *Procedure effect (predicting cue vs. predicting context group; $^{*}p < 0.05$ and $^{***}p < 0.001$); $^{\#\#}$treatment effect (aCSF vs. CORT or aCSF vs. DEX; $^{\#\#}p < 0.01$ and $^{\#\#\#}p < 0.001$).

## Stress or Systemic CORT Injection Mimics the Effects of Local CORT Infusion on Fear Memories

We previously showed that post-training (restraint) stress or systemic CORT injection performed after a *predicting-context* conditioning mimicked the effects of intra-DH CORT infusions on fear memories, i.e., promoting the selection of the tone cue instead of the context as predictor of the shock when a relatively high stress intensity was used (Kaouane et al., 2012, and see **Figure 4A** for a summary). Here, in the same perspective of more physiological stress-related manipulations, we tested whether similar manipulations performed after a *predicting-cue* conditioning could mimic the effects of intra-VH CORT infusions on fear memories, i.e., the selection of the context instead of the tone cue as predictor of the shock.

First, we analyzed whether post-training stress had differential effects on tone fear conditioning depending on the shock intensity, as demonstrated for contextual fear conditioning (Kaouane et al., 2012). The amplitude of the conditioned fear to the tone (**Figure 4B**, left and middle, **Supplementary Figure S2C**) was dependent on the footshock intensity (0.3 vs. 0.8 mA; effect of intensity on tone conditioning ratio: $F_{(1,30)}$ = 16.26, $p < 0.001$; on freezing to the tone *per se*: $F_{(1,30)}$ = 37.47, $p < 0.001$), and depending on this intensity the post-training stress had an opposite effect on the tone conditioning (intensity × stress for tone conditioning ratio: $F_{(1,30)}$ = 15.21, $p < 0.001$; for freezing to the tone *per se*: $F_{(1,30)}$ = 30.17, $p < 0.001$). As expected, the conditioned fear responses to the tone were higher after a footshock of 0.8 mA than 0.3 mA in the control condition (Bonferroni–Dunn *post hoc* test $p < 0.001$), but this difference disappeared in the post-training stress condition because both the tone conditioning ratio and the percentage of freezing to the tone increased after a 0.3-mA footshock ($p < 0.05$ and $p < 0.001$, respectively) whereas they decreased after a 0.8-mA footshock (both $p < 0.05$). In parallel, the amplitude of the fear responses to the conditioning context (**Figure 4B**, right) increased with the footshock intensity (effect of intensity: $F_{(1,30)}$ = 14.12, $p < 0.001$) and the post-training stress (effect of stress: $F_{(1,30)}$ = 7.7, $p < 0.01$), which produced a significant enhancement of contextual freezing when the highest footshock intensity was used during training ($p < 0.05$).

Second, we analyzed whether systemic (i.p.) injection of CORT could mimic the deleterious effects of intra-VH CORT injections on fear memory when performed after tone fear conditioning using a 0.8-mA footshock (**Figure 4C**). Systemic CORT injection decreased both the tone conditioning ratio (**Figure 4C**, left, treatment: $F_{(2,24)}$ = 8.13, $p < 0.01$) and the percentage of freezing to the tone *per se* (**Figure 4C**, middle, treatment: $F_{(2,24)}$ = 15.82, $p < 0.001$; see also **Supplementary Figure S2D**), whatever the dose used (1.5 mg/kg: $p < 0.01$ and $p < 0.001$, respectively; 10 mg/kg: $p < 0.05$ and $p < 0.01$, respectively), but increased the fear responses to the conditioning

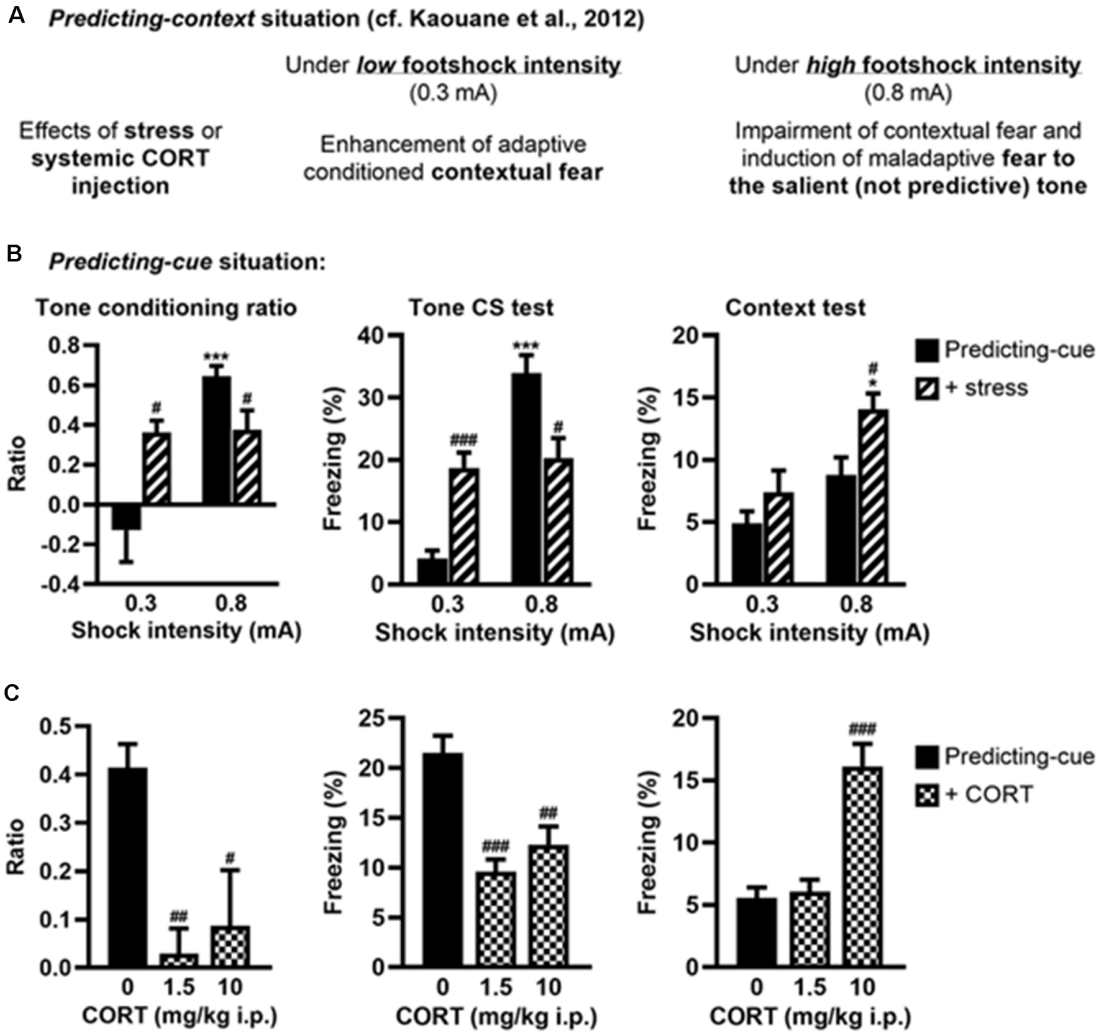


**FIGURE 4 |** Stress or systemic CORT injection mimics the effects of local CORT infusion on fear memories. **(A)** Summary of previously published data relative to the effects of post-training stress or systemic CORT injection on fear memory after a *predicting-context* procedure. **(B)** Post-training stress after a *predicting-cue* procedure using a low shock intensity (0.3 mA) increased the tone conditioning ratio (*left*) and the fear responses to the tone *per se* (*middle*), whereas the same stress applied after this conditioning procedure using a high shock intensity (0.8 mA) reduced them and significantly increased the fear responses to the context (*right*). 0.3 mA control: $n = 8$; 0.3 mA + stress: $n = 9$; 0.8 mA control: $n = 9$; 0.8 mA + stress: $n = 8$. **(C)** Intraperitoneal (i.p.) corticosterone injection after a 0.8-mA predicting-cue conditioning decreased the tone conditioning ratio (*left*), the fear responses to the tone *per se* (*middle*), and increased at 10 mg/kg the fear responses to the context (*right*). After CORT injection, the ratios decreased such that it did not differ from zero (both $p > 0.05$). Control (0): $n = 9$; CORT 1.5: $n = 10$; CORT 10: $n = 8$. *Effect of shock intensity (0.3 vs. 0.8 mA; $^{*}p < 0.05$ and $^{***}p < 0.001$); $^{\#}$effect of stress or injection compared with controls ($^{\#}p < 0.05$, $^{\#\#}p < 0.01$, and $^{\#\#\#}p < 0.001$).

context (**Figure 4C**, right, treatment: $F_{(2,24)} = 23.11$, $p < 0.001$) at 10 mg/kg ($p < 0.001$). Therefore, peripheral CORT administrations after tone fear conditioning dose-dependently reproduced the effects of local VH injections.

## DISCUSSION

The present results show that CORT differentially alters fear memories depending on the hippocampal sector where GRs are activated and the fear learning considered. Replicating our previous results (Kaouane et al., 2012), intra-DH CORT infusion impaired contextual fear conditioning and induced fear responses to a salient cue, non-predicting the threat. Strikingly, the present study shows that intra-VH infusion produced the exact opposite pattern: it blocked cue fear conditioning while inducing fear responses to the (background) conditioning context which was not yet the main predictor of the shock. The fact that these opposite effects could be reproduced by local infusions of DEX indicates that they are mediated by activation of GRs in the DH and VH, respectively. Finally, post-training stress or systemic CORT injections reproduced the alterations of fear memories induced by local infusions of glucocorticoids.

The replication of the deleterious effect of intra-DH infusion of CORT on contextual fear memory is fully congruent with a

vast literature indicating that the dorsal part of the hippocampus supports the establishment of a unified representation of the context (Rudy et al., 2002; Matus-Amat et al., 2004) and is crucial for contextual fear conditioning (Kim and Fanselow, 1992; Phillips and LeDoux, 1992; Anagnostaras et al., 2001). In accordance with previous studies, our past and present results also support the idea that CORT can have different effects on hippocampus-dependent memories, promoting contextual fear memories under low stress situations (Pugh et al., 1997; Cordero and Sandi, 1998; Revest et al., 2005, 2010, 2014; Kaouane et al., 2012), while disrupting spatial (de Quervain et al., 1998; Conrad et al., 1999) and contextual memory (Kaouane et al., 2012) when high doses or high stress situations are used. Interestingly, intra-DH infusion of CORT also resulted in the selection of the simple tone instead of contextual cues as predictor of the shock, leading to a prevalent, although maladaptive, tone-based fear memory. Similar switch from contextual to cue fear conditioning was already observed after pharmacological manipulations that reduced the dorsal hippocampal activity (Calandreau et al., 2006; Desmedt et al., 2015b). This indicates that, when the consolidation of predicting contextual information is disrupted by alteration of the DH, a cognitive switch promotes an association between the footshock and the most salient simple cue (i.e., the tone), despite the absence of any explicit cue–shock pairing during training.

In contrast, when CORT was infused into the VH, the present study shows that tone cue conditioning was blocked to the benefit of contextual fear. Conditioned fear to a discrete tone is classically viewed to involve a brain circuit restricted to the amygdala and the thalamus (LeDoux, 2000). However, numerous studies have reported that tone cue conditioning can be impaired by electrolytic (Maren and Holt, 2004), neurotoxic lesions (Maren, 1999; Bast et al., 2001; Zhang et al., 2001), or inactivation of the VH (Maren and Holt, 2004; Esclassan et al., 2009). Because the VH is strongly connected to the amygdala (Maren and Fanselow, 1995; Pitkänen et al., 2000), it could convey information about the tone to it (Sakurai, 2002). This transmission would be here disrupted by excess glucocorticoids in the VH.

In parallel, intra-VH CORT infusion also increased conditioned fear to the context in animals for which the tone is yet the objective predictor of the shock, and as such known to normally overshadow contextual cues. The role of the VH in contextual fear conditioning is unclear because it receives little visuo-spatial information from the sensory cortices (Pitkänen et al., 2000; Witter and Amaral, 2004), displays less numerous and less specific place cells than the DH (Jung et al., 1994), and its lesion or inactivation resulted in opposite results (Bast et al., 2001; Zhang et al., 2001; Kjelstrup et al., 2002; Hunsaker and Kesner, 2008). It could thus be hypothesized that CORT-induced alteration of the VH could promote cognitive processes based on the DH functioning. Particularly, previous data have shown that promoting the activity of the DH can abolish tone fear conditioning while promoting background contextual conditioning (Calandreau et al., 2006), mimicking the present effects of intra-VH CORT infusions. Therefore, our results suggest that when a simple cue–shock association is blocked by interfering with VH-dependent processes, a context–shock association, which could be mainly supported by the DH, is preferentially consolidated, leading to a prevalent contextual fear memory even if the context, which is consigned in the background in this learning situation, is not the best predictor of the threat.

The present study also shows that activation of the same receptor (GRs), by infusion of the specific agonist DEX either into the DH or the VH, mimicked the opposite CORT-induced alterations of fear memories. CORT can act on two subtypes of nuclear receptors: the high-affinity mineralocorticoid receptor (MR) and the low-affinity GR (de Kloet et al., 1998). Both receptors are found in the hippocampus and often co-localized on the same neurons (Joëls, 2007). At the basal level, only MRs are occupied. During mild stress, the increase in CORT levels results in full MR and moderate GR occupancy, resulting in enhanced synaptic plasticity in the hippocampus (Diamond et al., 1992). This effect is thought to mediate the facilitating effects of glucocorticoids on hippocampus-dependent memory function (Conrad et al., 1999; Brinks et al., 2007). In contrast, full GR occupancy, which occurs during high stressful situation, impairs synaptic excitability and hippocampus-dependent memory functions (Conrad et al., 1999; Brinks et al., 2007). Specifically, GR activation in the DH was shown to disrupt excitability and synaptic plasticity (Diamond et al., 1992; Kim and Yoon, 1998; Garcia, 2001; Maggio and Segal, 2007b), which is crucial for contextual fear conditioning (Sacchetti et al., 2001). In the VH, whereas stress or direct corticosterone bath application promotes LTP *via* the MRs, specific activation of GRs results in low excitability and synaptic plasticity (Maggio and Segal, 2009a,b), which could explain the disruption of the cue fear conditioning in the present study.

Using more physiological conditions, our last experiment shows that post-training (restraint) stress or systemic injection of CORT mimicked the effects of local CORT injections on fear memories. More specifically, we had previously shown that in a *predicting-context* situation, post-training stress or systemic CORT injection reproduced the effects of intra-DH CORT injections, i.e., enhancing adaptive contextual fear memory after a low stress condition, but producing a false tone fear memory after a high stress condition (Kaouane et al., 2012; see **Figure 4A**). In contrast, the present study shows that in a *predicting-cue* situation, the same manipulations reproduced the effects of intra-VH CORT injections, i.e., promoting an adaptive tone fear memory after a low stress condition while promoting a maladaptive contextual fear memory after a high stress condition. Under the low stress condition, the increase in tone fear memory is in accordance with previous studies showing that post-training glucocorticoid injections increase cued fear memory in low or mild stress situations (Hui et al., 2004; Marchand et al., 2007). Under the high stress condition, the observed CORT-induced maladaptive contextual fear memory and deficit in cue fear conditioning strongly suggest that activation of GR, in the VH specifically, constitutes a key molecular device for such fear memory disturbances. Now, how can we explain that the same biological manipulation (GR activation) can have drastically different, and even opposite, effects on fear memory as a function

of the learning procedure used? Even if GRs respond similarly to systemic CORT/DEX injection in the DH and VH, the deleterious impact of this systemic injection on fear behavior is supposed to differ as a function of the specific recruitment of the DH and VH in the training procedure considered. Because the DH and VH are known to be differentially involved in contextual and tone fear conditioning, the present findings suggest that the opposite effect of systemic CORT/DEX injection on fear behavior may result from an imbalance between the recruitment of the DH and that one of the VH as a function of the training procedure used.

In conclusion, our study shows that glucocorticoids alter fear memories in an opposite way as a function of the hippocampal sector where GR are activated, providing evidence for a functional dissociation between the DH and the VH. These findings indicate that glucocorticoids, under high stressful situation, can produce false fear memories on the basis of the erroneous selection of the most salient, but irrelevant, simple cue or the background context as predictor of an aversive event. Classically, "false memory" applies to memories formed without the actual experience of the items that constitute the object of these memories. Here, "false memories" refer to totally erroneous memory representation of the stressful situation as regards to the objective training situation. Indeed, animals wrongly attribute an aversive predictive value to the salient but not predictive tone instead of the (foreground) context in the unpairing situation, and to the (overshadowed) context instead of the predictive tone in the pairing situation. These erroneous representations, based on distorted meanings of both the salient tone and the context, are clearly akin to "false memories." These opposing false fear memories might be related to the development of different stress-related disorders. On the one hand, in human, specific alterations in the posterior hippocampus (DH in rodents) have been linked to PTSD-related cue-based hypermnesia and contextual amnesia (Brewin, 1996; Brewin and Holmes, 2003; American Psychiatric Association, 2013). We precisely reproduced this paradoxical memory alteration with intra-DH CORT (Kaouane et al., 2012) or DEX infusions in mice. On the other hand, the anterior hippocampus in human (Satpute et al., 2012) and the VH in rodents (Degroot and Treit, 2004) have been involved in anxiety-related behaviors including intense and irrational fear reactions to particular stressful situation (American Psychiatric Association, 2013). Such abnormally high fear behaviors to (background) contextual elements under stress were precisely those observed after intra-VH CORT or DEX infusions in the present study. Furthermore, highlighting different roles for the DH and the VH in *adaptive* and *maladaptive* (anxiety-like) contextual fear, respectively, our findings are congruent with an optogenetic study reporting similar functional dissociation (i.e., contextual fear vs. anxiety-like behaviors) along the dorso-ventral axis of the dentate gyrus (Kheirbek et al., 2013). Altogether, our findings strongly suggest the different effects of glucocorticoids induced by their action along the dorso-ventral axis of the hippocampus might explain the constellation of memory alterations observed after stressful situations, thereby contributing to a better understanding of the pathophysiology of stress-related disorders.

## DATA AVAILABILITY STATEMENT

The raw data supporting the conclusions of this article will be made available by the authors, without undue reservation.

## ETHICS STATEMENT

The animal study was reviewed and approved by Bordeaux ethic committee; European Communities Council Directive (86/609/EEC).

## AUTHOR CONTRIBUTIONS

NK, E-GD, and AD conceived, designed, performed the experiments, and analyzed the data. NK, AM, MS, and AD wrote the article.

## FUNDING

This work was supported by Centre National de la Recherche Scientifique, Institut National de la Santé et de la Recherche Médicale, Fondation pour la Recherche sur le Cerveau, Conseil Régional d'Aquitaine, Ministère de l'Enseignement supérieur et de la Recherche, and University of Bordeaux. This study was also performed in the framework of the Laboratoire Européen Associé "France–Israel Laboratory of Neuroscience" and the International Research Network "France–Israel Center for Neural Computation."

## ACKNOWLEDGMENTS

We thank C. Dupuy, A. Faugere, A. Grel, and F. Rougé-Pont for technical help. We also thank Alice Shaam Al Abed for her helpful comments on this article and suggestions for the English revision.

## SUPPLEMENTARY MATERIAL

The Supplementary Material for this article can be found online at: https://www.frontiersin.org/articles/10.3389/fnbeh.2020.00144/full#supplementary-material.

## REFERENCES

American Psychiatric Association. (2013). *Diagnostic and Statistical Manual of Mental Disorders.* 5th Edn. Washington, DC: American Psychiatric Association.

Anagnostaras, S. G., Gale, G. D., and Fanselow, M. S. (2001). Hippocampus and contextual fear cnditioning: recent controversies and advances. *Hippocampus* 11, 8–17. doi: 10.1002/1098-1063(2001)11:1<8::aid-hipo1015>3.0.co;2-7

Bannerman, D. M., Rawlins, J. N. P., McHugh, S. B., Deacon, R. M. J., Yee, B. K., Bast, T., et al. (2004). Regional dissociations within the hippocampus—memory

and anxiety. *Neurosci. Biobehav. Rev.* 28, 273–283. doi: 10.1016/j.neubiorev.2004.03.004

Bast, T., Zhang, W. N., and Feldon, J. (2001). The ventral hippocampus and fear conditioning in rats. Different anterograde amnesias of fear after tetrodotoxin inactivation and infusion of the $GABA_A$ agonist muscimol. *Exp. Brain Res.* 139, 39–52. doi: 10.1007/s002210100746

Brewin, C. R. (1996). Scientific status of recovered memories. *Br. J. Psychiatry* 169, 131–134. doi: 10.1192/bjp.169.2.131

Brewin, C. R., and Holmes, E. A. (2003). Psychological theories of posttraumatic stress disorder. *Clin. Psychol. Rev.* 23, 339–376. doi: 10.1016/s0272-7358(03)00033-3

Brinks, V., van der Mark, M. H., de Kloet, E. R., and Oitzl, M. S. (2007). Differential MR/GR activation in mice results in emotional states beneficial or impairing for cognition. *Neural Plast.* 2007:90163. doi: 10.1155/2007/90163

Calandreau, L., Desmedt, A., Decorte, L., and Jaffard, R. (2005). A different recruitment of the lateral and basolateral amygdala promotes contextual or elemental conditioned association in Pavlovian fear conditioning. *Learn. Mem.* 12, 383–388. doi: 10.1101/lm.92305

Calandreau, L., Jaffard, R., and Desmedt, A. (2007). Dissociated roles for the lateral and medial septum in elemental and contextual fear conditioning. *Learn. Mem.* 14, 422–429. doi: 10.1101/lm.531407

Calandreau, L., Trifilieff, P., Mons, N., Costes, L., Marien, M., Marighetto, A., et al. (2006). Extracellular hippocampal acetylcholine level controls amygdala function and promotes adaptive conditioned emotional response. *J. Neurosci.* 26, 13556–13566. doi: 10.1523/JNEUROSCI.3713-06.2006

Calhoon, G. G., and Tye, K. M. (2015). Resolving the neural circuits of anxiety. *Nat. Neurosci.* 18, 1394–1404. doi: 10.1038/nn.4101

Chaouloff, F., Hémar, A., and Manzoni, O. (2008). Local facilitation of hippocampal metabotropic glutamate receptor-dependent long-term depression by corticosterone and dexamethasone. *Psychoneuroendocrinology* 33, 686–691. doi: 10.1016/j.psyneuen.2007.12.013

Conrad, C. D., Lupien, S. J., and McEwen, B. S. (1999). Support for a bimodal role for type II adrenal steroid receptors in spatial memory. *Neurobiol. Learn. Mem.* 72, 39–46. doi: 10.1006/nlme.1998.3898

Cordero, M. I., and Sandi, C. (1998). A role for brain glucocorticoid receptors in contextual fear conditioning: dependence upon training intensity. *Brain Res.* 786, 11–17. doi: 10.1016/s0006-8993(97)01420-0

de Kloet, E. R., Vreugdenhil, E., Oitzl, M. S., and Joëls, M. (1998). Brain corticosteroid receptor balance in health and disease. *Endocr. Rev.* 19, 269–301. doi: 10.1210/edrv.19.3.0331

de Quervain, D. J. F., Roozendaal, B., and McGaugh, J. L. (1998). Stress and glucocorticoids impair retrieval of long-term spatial memory. *Nature* 394, 787–790. doi: 10.1038/29542

Degroot, A., and Treit, D. (2004). Anxiety is functionally segregated within the septo-hippocampal system. *Brain Res.* 1001, 60–71. doi: 10.1016/j.brainres.2003.10.065

Desmedt, A., Marighetto, A., and Piazza, P.-V. (2015a). Abnormal fear memory as a model for posttraumatic stress disorder. *Biol. Psychiatry* 78, 290–297. doi: 10.1016/j.biopsych.2015.06.017

Desmedt, A., Marighetto, A., Richter-Levin, G., and Calandreau, L. (2015b). Adaptive emotional memory: the key hippocampal-amygdalar interaction. *Stress* 18, 297–308. doi: 10.3109/10253890.2015.1067676

Diamond, D. M., Bennett, M. C., Fleshner, M., and Rose, G. M. (1992). Inverted-U relationship between the level of peripheral corticosterone and the magnitude of hippocampal primed burst potentiation. *Hippocampus* 2, 421–430. doi: 10.1002/hipo.450020409

Donley, M. P., Schulkin, J., and Rosen, J. B. (2005). Glucocorticoid receptor antagonism in the basolateral amygdala and ventral hippocampus interferes with long-term memory of contextual fear. *Behav. Brain Res.* 164, 197–205. doi: 10.1016/j.bbr.2005.06.020

Esclassan, F., Coutureau, E., Di Scala, G., and Marchand, A. R. (2009). Differential contribution of dorsal and ventral hippocampus to trace and delay fear conditioning. *Hippocampus* 19, 33–44. doi: 10.1002/hipo.20473

Fanselow, M. S., and Dong, H.-W. (2010). Are the dorsal and ventral hippocampus functionally distinct structures? *Neuron* 65, 7–19. doi: 10.1016/j.neuron.2009.11.031

Franklin, K. B. J., and Paxinos, G. (1997). *The Mouse Brain in Stereotaxic Coordinates.* San Diego, CA: Academic Press.

Garcia, R. (2001). Stress, hippocampal plasticity, and spatial learning. *Synapse* 40, 180–183. doi: 10.1002/syn.1040

Hui, G. K., Figueroa, I. R., Poytress, B. S., Roozendaal, B., McGaugh, J. L., and Weinberger, N. M. (2004). Memory enhancement of classical fear conditioning by post-training injections of corticosterone in rats. *Neurobiol. Learn. Mem.* 81, 67–74. doi: 10.1016/j.nlm.2003.09.002

Hunsaker, M. R., and Kesner, R. P. (2008). Dissociations across the dorsal-ventral axis of CA3 and CA1 for encoding and retrieval of contextual and auditory-cued fear. *Neurobiol. Learn. Mem.* 89, 61–69. doi: 10.1016/j.nlm.2007.08.016

Joëls, M. (2007). Role of corticosteroid hormones in the dentate gyrus. *Prog. Brain Res.* 163, 355–370. doi: 10.1016/s0079-6123(07)63021-0

Jung, M. W., Wiener, S. I., and McNaughton, B. L. (1994). Comparison of spatial firing characteristics of units in dorsal and ventral hippocampus of the rat. *J. Neurosci.* 14, 7347–7356. doi: 10.1523/JNEUROSCI.14-12-07347.1994

Kaouane, N., Porte, Y., Vallée, M., Brayda-Bruno, L., Mons, N., Calandreau, L., et al. (2012). Glucocorticoids can induce PTSD-like memory impairments in mice. *Science* 335, 1510–1513. doi: 10.1126/science.1207615

Kheirbek, M. A., Drew, L. J., Burghardt, N. S., Costantini, D. O., Tannenholz, L., Ahmari, S. E., et al. (2013). Differential control of learning and anxiety along the dorsoventral axis of the dentate gyrus. *Neuron* 77, 955–968. doi: 10.1016/j.neuron.2012.12.038

Kim, J. J., and Fanselow, M. S. (1992). Modality-specific retrograde amnesia of fear. *Science* 256, 675–677. doi: 10.1126/science.1585183

Kim, J. J., and Yoon, K. S. (1998). Stress: metaplastic effects in the hippocampus. *Trends Neurosci.* 21, 505–509. doi: 10.1016/s0166-2236(98)01322-8

Kjelstrup, K. G., Tuvnes, F. A., Steffenach, H.-A., Murison, R., Moser, E. I., and Moser, M.-B. (2002). Reduced fear expression after lesions of the ventral hippocampus. *Proc. Natl. Acad. Sci. U S A* 99, 10825–10830. doi: 10.1073/pnas.152112399

Layton, B., and Krikorian, R. (2002). Memory mechanisms in posttraumatic stress disorder. *J. Neuropsychiatry Clin. Neurosci.* 14, 254–261. doi: 10.1176/jnp.14.3.254

LeDoux, J. E. (2000). Emotion circuits in the brain. *Annu. Rev. Neurosci.* 23, 155–184. doi: 10.1146/annurev.neuro.23.1.155

Maggio, N., and Segal, M. (2007a). Unique regulation of long term potentiation in the rat ventral hippocampus. *Hippocampus* 17, 10–25. doi: 10.1002/hipo.20237

Maggio, N., and Segal, M. (2007b). Striking variations in corticosteroid modulation of long-term potentiation along the septotemporal axis of the hippocampus. *J. Neurosci.* 27, 5757–5765. doi: 10.1523/JNEUROSCI.0155-07.2007

Maggio, N., and Segal, M. (2009a). Differential modulation of long-term depression by acute stress in the rat dorsal and ventral hippocampus. *J. Neurosci.* 29, 8633–8638. doi: 10.1523/JNEUROSCI.1901-09.2009

Maggio, N., and Segal, M. (2009b). Differential corticosteroid modulation of inhibitory synaptic currents in the dorsal and ventral hippocampus. *J. Neurosci.* 29, 2857–2866. doi: 10.1523/JNEUROSCI.4399-08.2009

Marchand, A. R., Barbelivien, A., Seillier, A., Herbeaux, K., Sarrieau, A., and Majchrzak, M. (2007). Contribution of corticosterone to cued versus contextual fear in rats. *Behav. Brain Res.* 183, 101–110. doi: 10.1016/j.bbr.2007.05.034

Maren, S. (1999). Neurotoxic or electrolytic lesions of the ventral subiculum produce deficits in the acquisition and expression of Pavlovian fear conditioning in rats. *Behav. Neurosci.* 113, 283–290. doi: 10.1037//0735-7044.113.2.283

Maren, S., and Fanselow, M. S. (1995). Synaptic plasticity in the basolateral amygdala induced by hippocampal formation stimulation *in vivo*. *J. Neurosci.* 15, 7548–7564. doi: 10.1523/JNEUROSCI.15-11-07548.1995

Maren, S., and Holt, W. G. (2004). Hippocampus and Pavlovian fear conditioning in rats: muscimol infusions into the ventral, but not dorsal, hippocampus impair the acquisition of conditional freezing to an auditory conditional stimulus. *Behav. Neurosci.* 118, 97–110. doi: 10.1037/0735-7044.118.1.97

Matus-Amat, P., Higgins, E. A., Barrientos, R. M., and Rudy, J. W. (2004). The role of the dorsal hippocampus in the acquisition and retrieval of context memory representations. *J. Neurosci.* 24, 2431–2439. doi: 10.1523/JNEUROSCI.1598-03.2004

McEwen, B. S. (2000). Effects of adverse experiences for brain structure and function. *Biol. Psychiatry* 48, 721–731. doi: 10.1016/s0006-3223(00)00964-1

Mizoguchi, K., Sun, N., Jin, X.-L., Kase, Y., Takeda, S., Maruyama, W., et al. (2007). Saikokaryukotsuboreito, a herbal medicine, prevents chronic stress-induced dysfunction of glucocorticoid negative feedback system in rat brain. *Pharmacol. Biochem. Behav.* 86, 55–61. doi: 10.1016/j.pbb.2006.12.007

Moser, M. B., and Moser, E. I. (1998). Functional differentiation in the hippocampus. *Hippocampus* 8, 608–619. doi: 10.1002/(sici)1098-1063(1998)8:6<608::aid-hipo3>3.0.co;2-7

Oitzl, M. S., Reichardt, H. M., Joëls, M., and de Kloet, E. R. (2001). Point mutation in the mouse glucocorticoid receptor preventing DNA binding impairs spatial memory. *Proc. Natl. Acad. Sci. U S A* 98, 12790–12795. doi: 10.1073/pnas.231313998

Phillips, R. G., and LeDoux, J. E. (1992). Differential contribution of amygdala and hippocampus to cued and contextual fear conditioning. *Behav. Neurosci.* 106, 274–285. doi: 10.1037//0735-7044.106.2.274

Pitkänen, A., Pikkarainen, M., Nurminen, N., and Ylinen, A. A. (2000). Reciprocal connections between the amygdala and the hippocampal formation, perirhinal cortex, and postrhinal cortex in rat. A review. *Ann. N Y Acad. Sci.* 911, 369–391. doi: 10.1111/j.1749-6632.2000.tb06738.x

Pugh, C. R., Tremblay, D., Fleshner, M., and Rudy, J. W. (1997). A selective role for corticosterone in contextual-fear conditioning. *Behav. Neurosci.* 111, 503–511. doi: 10.1037/0735-7044.111.3.503

Revest, J.-M., Di Blasi, F., Kitchener, P., Rougé-Pont, F., Desmedt, A., Turiault, M., et al. (2005). The MAPK pathway and Egr-1 mediate stress-related behavioral effects of glucocorticoids. *Nat. Neurosci.* 8, 664–672. doi: 10.1038/nn1441

Revest, J.-M., Kaouane, N., Mondin, M., Le Roux, A., Rougé-Pont, F., Vallée, M., et al. (2010). The enhancement of stress-related memory by glucocorticoids depends on synapsin-Ia/Ib. *Mol. Psychiatry* 15, 1140–1151. doi: 10.1038/mp.2010.40

Revest, J.-M., Le Roux, A., Roullot-Lacarrière, V., Kaouane, N., Vallée, M., Kasanetz, F., et al. (2014). BDNF-TrkB signaling through Erk1/2 MAPK phosphorylation mediates the enhancement of fear memory induced by glucocorticoids. *Mol. Psychiatry* 19, 1001–1009. doi: 10.1038/mp.2013.134

Robertson, D. A. F., Beattie, J. E., Reid, I. C., and Balfour, D. J. K. (2005). Regulation of corticosteroid receptors in the rat brain: the role of serotonin and stress. *Eur. J. Neurosci.* 21, 1511–1520. doi: 10.1111/j.1460-9568.2005.03990.x

Roozendaal, B. (2003). Systems mediating acute glucocorticoid effects on memory consolidation and retrieval. *Prog. Neuropsychopharmacol. Biol. Psychiatry* 27, 1213–1223. doi: 10.1016/j.pnpbp.2003.09.015

Rudy, J. W., Barrientos, R. M., and O'Reilly, R. C. (2002). Hippocampal formation supports conditioning to memory of a context. *Behav. Neurosci.* 116, 530–538. doi: 10.1037//0735-7044.116.4.530

Sacchetti, B., Lorenzini, C. A., Baldi, E., Bucherelli, C., Roberto, M., Tassoni, G., et al. (2001). Long-lasting hippocampal potentiation and contextual memory consolidation. *Eur. J. Neurosci.* 13, 2291–2298. doi: 10.1046/j.0953-816x.2001.01609.x

Sakurai, Y. (2002). Coding of auditory temporal and pitch information by hippocampal individual cells and cell assemblies in the rat. *Neuroscience* 115, 1153–1163. doi: 10.1016/s0306-4522(02)00509-2

Satpute, A. B., Mumford, J. A., Naliboff, B. D., and Poldrack, R. A. (2012). Human anterior and posterior hippocampus respond distinctly to state and trait anxiety. *Emotion* 12, 58–68. doi: 10.1037/a0026517

Segal, M., Richter-Levin, G., and Maggio, N. (2010). Stress-induced dynamic routing of hippocampal connectivity: a hypothesis. *Hippocampus* 20, 1332–1338. doi: 10.1002/hipo.20751

Witter, M. P., and Amaral, D. G. (2004). "Hippocampal formation," in *The Rat Nervous System*, ed. G. Paxinos (San Diego, CA: Academic Press), 635–704.

Zhang, W. N., Bast, T., and Feldon, J. (2001). The ventral hippocampus and fear conditioning in rats: different anterograde amnesias of fear after infusion of N-methyl-D-aspartate or its noncompetitive antagonist MK-801 into the ventral hippocampus. *Behav. Brain Res.* 126, 159–174. doi: 10.3389/fnmol.2020.00055

**Conflict of Interest**: The authors declare that the research was conducted in the absence of any commercial or financial relationships that could be construed as a potential conflict of interest.

*Copyright © 2020 Kaouane, Ducourneau, Marighetto, Segal and Desmedt. This is an open-access article distributed under the terms of the Creative Commons Attribution License (CC BY). The use, distribution or reproduction in other forums is permitted, provided the original author(s) and the copyright owner(s) are credited and that the original publication in this journal is cited, in accordance with accepted academic practice. No use, distribution or reproduction is permitted which does not comply with these terms.*

frontiers in Cellular Neuroscience

ORIGINAL RESEARCH
published: 17 September 2020
doi: 10.3389/fncel.2020.00277

# Integration of Within-Cell Experimental Data With Multi-Compartmental Modeling Predicts H-Channel Densities and Distributions in Hippocampal OLM Cells

*Vladislav Sekulić*[1,2†], *Feng Yi*[3], *Tavita Garrett*[4], *Alexandre Guet-McCreight*[1,2], *J. Josh Lawrence*[5,6,7*‡] *and Frances K. Skinner*[1,8*‡]

[1] Krembil Research Institute, University Health Network, Toronto, ON, Canada, [2] Department of Physiology, University of Toronto, Toronto, ON, Canada, [3] Department of Biomedical and Pharmaceutical Sciences, Center for Biomolecular Structure and Dynamics, Center for Structural and Functional Neuroscience, University of Montana, Missoula, MT, United States, [4] Neuroscience Graduate Program and Vollum Institute, Oregon Health & Science University, Portland, OR, United States, [5] Department of Pharmacology and Neuroscience, Texas Tech University Health Sciences Center, Lubbock, TX, United States, [6] Center for Translational Neuroscience and Therapeutics, Texas Tech University Health Sciences Center, Lubbock, TX, United States, [7] Garrison Institute on Aging, Texas Tech University Health Sciences Center, Lubbock, TX, United States, [8] Departments of Medicine (Neurology) and Physiology, University of Toronto, Toronto, ON, Canada

Determining biophysical details of spatially extended neurons is a challenge that needs to be overcome if we are to understand the dynamics of brain function from cellular perspectives. Moreover, we now know that we should not average across recordings from many cells of a given cell type to obtain quantitative measures such as conductance since measures can vary multiple-fold for a given cell type. In this work we examine whether a tight combination of experimental and computational work can address this challenge. The oriens-lacunosum/moleculare (OLM) interneuron operates as a "gate" that controls incoming sensory and ongoing contextual information in the CA1 of the hippocampus, making it essential to understand how its biophysical properties contribute to memory function. OLM cells fire phase-locked to the prominent hippocampal theta rhythms, and we previously used computational models to show that OLM cells exhibit high or low theta spiking resonance frequencies that depend respectively on whether their dendrites have hyperpolarization-activated cation channels (h-channels) or not. However, whether OLM cells actually possess dendritic h-channels is unknown at present. We performed a set of whole-cell recordings of OLM cells from mouse hippocampus and constructed three multi-compartment models using morphological and electrophysiological parameters extracted from the same OLM cell, including per-cell pharmacologically isolated h-channel currents. We found that the models best matched experiments when h-channels were present in the dendrites of each of the three model cells created. This strongly suggests that h-channels must be present in OLM cell dendrites and are not localized to their somata. Importantly, this work shows that a tight integration of model and experiment can help tackle the challenge

OPEN ACCESS

**Edited by:**
*Akiva Cohen, University of Pennsylvania, United States*

**Reviewed by:**
*Richardson N. Leão, Federal University of Rio Grande Do Norte, Brazil*
*Ilya A. Fleidervish, Ben-Gurion University of the Negev, Israel*

***Correspondence:**
*J. Josh Lawrence*
*john.lawrence@ttuhsc.edu*
*Frances K. Skinner*
*frances.skinner@gmail.com*

**†Present address:**
*Vladislav Sekulić*
*RIKEN Center for Brain Science, Wako, Japan*

‡*These authors share senior authorship*

**Specialty section:**
*This article was submitted to Cellular Neurophysiology, a section of the journal Frontiers in Cellular Neuroscience*

**Received:** *13 May 2020*
**Accepted:** *05 August 2020*
**Published:** *17 September 2020*

**Citation:**
*Sekulić V, Yi F, Garrett T, Guet-McCreight A, Lawrence JJ and Skinner FK (2020) Integration of Within-Cell Experimental Data With Multi-Compartmental Modeling Predicts H-Channel Densities and Distributions in Hippocampal OLM Cells. Front. Cell. Neurosci. 14:277. doi: 10.3389/fncel.2020.00277*

of characterizing biophysical details and distributions in spatially extended neurons. Full spiking models were built for two of the OLM cells, matching their current clamp cell-specific electrophysiological recordings. Overall, our work presents a technical advancement in modeling OLM cells. Our models are available to the community to use to gain insight into cellular dynamics underlying hippocampal function.

**Keywords: hippocampus, interneuron, inhibitory cell, dendrite, h-channels, multi-compartment model, electrophysiology**

## INTRODUCTION

The challenge of understanding brain function given its many cell types and circuits is being greatly aided by the development of sophisticated experimental techniques, big data, and interdisciplinary collaborations (Ecker et al., 2017). Furthermore, the use of computational brain models is becoming established as an important tool that can bridge across scales and levels (Cutsuridis et al., 2010; O'Leary et al., 2015; Bassett et al., 2018). It is now clear that it is essential to consider the unique contributions of specific cell types and circuits in order to understand brain behavior (Luo et al., 2018). In particular, we know that different inhibitory cell types can control circuit output and brain function in specific ways (Kepecs and Fishell, 2014; Roux and Buzsáki, 2015; Abbas et al., 2018; Cardin, 2018) and, by extension, disease states (Marín, 2012; Giovannetti and Fuhrmann, 2019).

The contribution of a specific cell type to network and behavioral function is necessarily grounded in its biophysical properties. While immunohistochemical and single-cell transcriptomic studies provide insight into which ion channels might be present in a particular cell type, how different cell types contribute to function must necessarily include their activity within circuits (Kopell et al., 2014). An individual neuron's electrical activity largely arises from its ion channel kinetics, densities, and localization across its neuronal compartments. In this regard, mathematical multi-scale (channel and cellular), multi-compartment computational models are needed to help provide insights and hypotheses of how specific cell types contribute to brain function and disease processes. However, creating such models requires quantitative knowledge of the precise characteristics of the particular cell type, and it is highly challenging, if not impossible, to obtain comprehensive knowledge of all the relevant biophysical parameters of each compartment of each cell type experimentally. All experiments come with their own set of caveats and limitations, and mathematical models, no matter how detailed, are always a simplification relative to the biology. It is therefore important not to lose sight of the limitations of both model and experiment by having an ongoing dialogue between the two.

It is now well-known that the characteristics of a given cell type are not fixed (Marder and Goaillard, 2006), and thus a component of experimental variability reflects heterogeneity inherent in specific neuronal populations and thus in circuits. Moreover, such variability is likely to be functionally important (Wilson, 2010). Previous work has shown that conductance densities for a given ion channel in an identified cell type can have a two- to six-fold range of values (Goaillard et al., 2009; Ransdell et al., 2013). Despite this variability in channel conductances, robust neuronal as well as circuit output is maintained, as most clearly shown in the crustacean stomatogastric ganglion circuit (Bucher et al., 2005; Schulz et al., 2006; Tang et al., 2012). The conservation of individual neuronal electrical output despite variable underlying ion channel conductance densities has furthermore been demonstrated in mammalian CNS neurons (Swensen and Bean, 2005), most likely arising from complex homeostatic mechanisms for maintaining circuit stability that are not fully understood. How should one proceed in building cellular, computational models? Averaging of experimental variables such as conductance densities as a way of accounting for variability leads to erroneous conductance-based models (Golowasch et al., 2002). As a consequence, single, "canonical" biophysical models cannot capture inherent variability in the experimental ion channel data. A more desirable approach is to develop multiple models to capture the underlying biological variability (Marder and Taylor, 2011). Indeed, such populations of models representing a given cell type have been developed to examine, for example, co-regulations between different conductances that might exist in a given cell type (Hay et al., 2011; Soofi et al., 2012; Sekulić et al., 2014). In this way, populations of models could help suggest what balance of conductances are important for cellular dynamics and their function in circuits. Ideally, one should obtain biophysical properties of a given cell type using recordings from the *same* cell. It is of course unrealistic to consider an experimental characterization of all the various ion channel types using the same cell of a given cell type. This impracticality is further enhanced in consideration of channel types in the dendrites of neurons. Besides needing to patch from the same cell, there are also the practical limitations of invasively investigating the biophysical characteristics of fine dendritic compartments, performing multiple solution changes to pharmacologically isolate specific conductances, and acquiring high quality data within the time frame of optimal cell health. However, dendrites are where most synaptic contacts are made and where signal integration in neurons occurs (Stuart and Spruston, 2015). Thus, these aspects must be tackled along with considerations of cellular variability.

In this work we focus on the oriens-lacunosum/moleculare (OLM) cell, an identified inhibitory cell type in the hippocampal CA1 area (Maccaferri and Lacaille, 2003; Müller and Remy, 2014). OLM cells receive excitatory glutamatergic input predominantly from local CA1 pyramidal neurons and form

GABAergic synapses onto the distal dendrites of CA1 pyramidal neurons, as well as onto other CA1 inhibitory cells (Blasco-Ibáñez and Freund, 1995; Maccaferri et al., 2000; Klausberger, 2009; Leão et al., 2012). Functionally, proposed roles of OLM cells include gating sensory and contextual information in CA1 (Leão et al., 2012), and supporting the acquisition of fear memories (Lovett-Barron et al., 2014). Moreover, OLM cell firing is phase-locked to the prominent theta rhythms in the hippocampus of behaving animals (Klausberger et al., 2003; Klausberger and Somogyi, 2008; Varga et al., 2012; Katona et al., 2014). Although it has long been known that OLM cells express hyperpolarization-activated cation channels (h-channels) (Maccaferri and McBain, 1996), it is still unclear whether these channels are present in their dendrites. From a functional perspective, the consequences of dendritic h-channel expression in OLM cells was explored in our previous computational study where h-channels were found to modulate the spiking preference of OLM cell models—incoming inhibitory inputs recruited either a higher or lower theta frequency (akin to Type 1 or Type 2 theta, respectively—Kramis et al., 1975) depending on the presence or absence of dendritic h-channels (Sekulić and Skinner, 2017). In that computational study, our OLM cell models were derived from previously built populations of OLM cell multi-compartment models in which appropriate OLM cell models were found with h-channels present either in the soma only or uniformly distributed in the soma and dendrites (Sekulić et al., 2014). We had previously leveraged these models and showed that appropriate OLM cell model output could be maintained, even if h-channel conductance densities and distributions co-vary, so long as total membrane conductance due to h-channels is conserved (Sekulić et al., 2015)—a finding that was also demonstrated in cerebellar Purkinje neurons (Angelo et al., 2007). Moreover, these OLM cell models were developed using morphological and electrophysiological data obtained from different OLM cells as well as h-channel characteristics from the literature, resulting in non-uniqueness of the fitted model parameters (Rall et al., 1992; Holmes et al., 2006). However, we do not actually know whether h-channels are present in the dendrites of OLM cells. The existence of dendritic h-channels has not been directly assessed using patch-clamp recordings from OLM cell dendrites, and immunohistochemistry studies have so far demonstrated expression of the HCN2 subunit of h-channels only in the somata of OLM cells (Matt et al., 2011; Hilscher et al., 2019).

Considering all of the above, in this paper we aimed to build "next generation" multi-compartment models of OLM cells to achieve a two-pronged goal. First, to determine whether multi-compartment models built using morphological and electrophysiological data from the *same* cell would produce *consistent* results regarding h-channel localization to dendrites or not, and second, to determine the biophysical characteristics of h-channels in OLM cells. We consider the models developed here to be next generation relative to previous multi-compartment OLM cell modeling efforts (Lawrence et al., 2006; Sekulić et al., 2014) because each model was built using experimental data from the same cell, including its morphology, passive properties, and biophysical h-channel characteristics. Using transgenic mice in which yellow fluorescent protein (YFP) was expressed in somatostatin (SOM)-containing neurons, we visually targeted OLM cells from CA1 hippocampus, and fully reconstructed three OLM cells for multi-compartment model development with h-channel characteristics fit to each particular cell. We found that in order to be compatible with the experimental data, all three models needed to have h-channels present in their dendrites. Using two of these reconstructed models, we completed their development into full spiking models by including additional ion channel currents whose parameters were optimized based on voltage recordings from the same cell. These resulting models and associated experimental data are publicly available and can be subsequently used to develop further insight into the biophysical specifics of OLM cells and to help understand their contributions to circuit dynamics and behavior. This work demonstrates the feasibility of combining experimental and computational studies to address the challenging issue of determining the density and distribution of specific dendritic ion channel types.

# MATERIALS AND METHODS

## Ethics Statement

All procedures were performed in accordance with the University of Montana (Animal Use Protocols 026-11 and 017-14) and Texas Tech University Health Sciences Center (Animal Use Protocols 15025, 15031, and 16037) Institutional Animal Care and Use Committees.

## Animals and Brain Slice Preparation

Heterozygous crosses of homozygous somatostatin-CRE mice (SOM-CRE; stock no. 013044; Jackson Labs) and Rosa26YFP mice (Jackson Labs stock no. 007920) were obtained as previously described (Yi et al., 2014). Transverse hippocampal slices were prepared as described previously (Yi et al., 2014). Briefly, SOM-CRE$^{+/-}$:Rosa26YFP$^{+/-}$ (SOM-YFP) mice of both sexes (9–10 weeks, $n = 6$) were anesthetized with isoflurane and then transcardially perfused with ice-cold partial sucrose solution (PSS) containing (mM): 80 NaCl, 2.5 KCl, 24 $NaHCO_3$, 0.5 $CaCl_2$, 4 $MgCl_2$, 1.25 $NaH_2PO_4$, 25 glucose, 75 sucrose, 1 ascorbic acid, 3 sodium pyruvate, saturated with 95% O2/5% $CO_2$, pH 7.4 (Bischofberger et al., 2006). After carefully extracting, blocking, and mounting the brain, transverse hippocampal slices (300 $\mu$m) were cut in ice-cold oxygenated PSS with a 1200 S Vibratome (with Vibrocheck accessory; Leica Microsystems, Bannockburn, IL, USA), and then were incubated in warm (36°C) oxygenated PSS at least 30 min before use.

## Chemical Reagents

DL-APV was purchased from R&D Systems (Minneapolis, MN, USA). Tetrodotoxin (cat# 5651), TEA (cat# 2265), 4-AP (cat# A78403), DNQX (cat# D0540), SR-95531 (cat# S106), and ZD7288 hydrate (cat# Z3777) were purchased from Sigma-Aldrich, Inc. (Saint Louis, MO, USA). Salts and chemicals for saline solutions, including biocytin, were also purchased from Sigma-Aldrich, Inc.

**TABLE 1 |** Experimental protocols performed on OLM cells.

| Order | Bath solution | Recording mode | Description of protocol |
|---|---|---|---|
| #1 | ACSF | VC at −60 mV | Seal test |
| #2 | ACSF + DNQX/APV/Gabazine | CC at −60 mV | 2s-long steps from −120 to +90 pA in 30 pA steps |
| #3 | ACSF + DNQX/APV/Gabazine | VC at −40 mV | $I_h$ activation: 1.2 s-long step at progressively hyperpolarized potentials to −120 mV in −10 mV increments |
| #4 | ACSF + DNQX/APV/Gabazine + TTX/4-AP/TEA | CC at −60 mV | Same protocol as #2 |
| #5 | ACSF + DNQX/APV/Gabazine + TTX/4-AP/TEA | VC at −40 mV | Same protocol as #3 |
| #6 | ACSF + DNQX/APV/Gabazine + TTX/4-AP/TEA | VC at −40 mV | $I_h$ tail currents: a prepulse to −120 mV for 1.2 s to fully activate h-channels. Then, a depolarized relaxation step at −110 mV was performed for 1 s before returning to the holding potential. Repeated multiple times, with the relaxation steps becoming successively more depolarized at 10 mV intervals across each repeated sweep. |
| #7 | ACSF + DNQX/APV/Gabazine + TTX/4-AP/TEA + ZD | CC at −60 mV | Same protocol as #2 |
| #8 | ACSF + DNQX/APV/Gabazine + TTX/4-AP/TEA + ZD | VC at −40 mV | Same protocol as #3 |

*The order column displays the sequential order in which the protocols were performed.*
*Reagents concentration: DNQX (25 μM), APV (50 μM), Gabazine (5 μM), TEA (10 mM), 4-AP (5 mM), TTX (1 μM), ZD (10 μM). Further details in section Methods. VC, voltage clamp; CC, current clamp.*

## Electrophysiological Recordings and Analyses

Hippocampal slices were transferred to a recording chamber and submerged in artificial cerebrospinal fluid (ACSF) solution containing (mM): 125 NaCl, 2.5 KCl, 25 $NaHCO_3$, 2 $CaCl_2$, 1 $MgCl_2$, 1.25 $NaH_2PO_4$ and 20 glucose, saturated with 95% $O_2$/5% $CO_2$, pH7.4, at 34–35°C. SOM-YFP cells in the CA1 stratum oriens layer of hippocampus were visualized using IR-Dodt contrast and fluorescence video-microscopy (Zeiss Axiovision 4.7) on either a Patch Pro 2000 (Scientifica Ltd, Uckfield, East Sussex, UK) or Infrapatch (Luigs and Neumann, Ratingen, Germany) on an upright Zeiss microscope (Axio Examiner; Carl Zeiss Microscopy, LLC, Thornwood, NY, USA). On the Patch Pro 2000, live YFP-positive cells were visualized with a 505 nm LED (LED4C11-SP; Thorlabs) driven by a four-channel LED driver (DC4100; Thorlabs). On the Infrapatch rig, a 505 nm LED was controlled by the Colibri LED illumination system (Carl Zeiss Microscopy). Patch pipettes (2–4 MΩ) were fabricated using a two-step vertical electrode puller (PC-10; Narishige, East Meadow, NY, USA) and filled with internal solution containing (mM): 110 potassium gluconate, 40 KCl, 10 HEPES, 0.1 EGTA, 4 MgATP, 0.3 $Na_2GTP$, 10 $Na_2$ phosphocreatine and biocytin 0.2%, titrated to pH 7.2 with KOH, osmolarity 295–305 mOsm/L. Whole cell recordings were made using a Multiclamp 700B amplifier (Molecular Devices, Union City, CA, USA), filtered at 4 kHz, and digitized at 20 kHz (Digidata 1440A; Molecular Devices). Current and voltage traces were acquired on a PC running Axograph X (Axograph Scientific, Sydney, Australia). Solutions were heated to 34–35°C with an inline solution heater (HPT-2, Scientifica; SH-27B/TC-324B, Warner, Hamden, CT, USA). Access resistance ($R_s$) was monitored during recording. Cells with initial $R_s$ less than 20 MΩ were recorded. If $R_s$ changed more than 20% during the course of the whole cell recording, the data were excluded from further analyses. In all recordings, the AMPA receptor antagonist DNQX (25 μM), the NMDA receptor antagonist DL-APV (50 μM), and the $GABA_A$ receptor antagonist SR-95531 (gabazine; 5 μM) were included in the ACSF. For blocking intrinsic voltage-gated channels to isolate h-channel currents ($I_h$), TEA (10 mM), 4-AP (5 mM), and TTX (1 μM) were applied. The h-channel specific blocker ZD7288 (10 μM) was used to obtain and constrain $I_h$ parameters on a per-cell basis.

The order of protocols is important to consider during the subsequent procedures of obtaining OLM cell passive properties in light of varying stages of cell health and deterioration as the recordings progressed. The chronological order of current clamp and voltage clamp experimental protocols performed are shown in **Table 1**. The approximate length of experiment for a given cell patched was at most 30 min. At the end of the recording, pipettes were withdrawn to outside-out

patch configuration. Slices were kept on the rig for several minutes to facilitate diffusion of biocytin to distant subcellular compartments. Electrophysiological data were analyzed with Axograph X. The junction potential was calculated to be 11.88 mV and was subtracted from all experimentally recorded voltage values prior to use in subsequent data analysis and creation of multi-compartment computational models.

## Visualization of Biocytin-Filled Cells and Confocal Imaging

During electrophysiological experiments, recorded SOM-YFP cells were filled with biocytin for *post-hoc* morphological reconstruction. After recording, slices were fixed overnight at 4°C in 0.1 M phosphate-buffered saline (PBS) containing 4% paraformaldehyde. After several washes in PBS, and 2 h permeabilization with 0.3% Triton X-100 in PBS at room temperature, slices were incubated overnight at 16°C in PBS with Alexa 633-conjugated streptavidin (final concentration 1 $\mu$g/mL, catalogue no. S-21375; Invitrogen). Slices were cryopreserved in 30% sucrose containing PBS and then re-sectioned at 100–150 $\mu$m thickness using a sliding freezing microtome (HM430; Thermo Scientific, Waltham, MA, USA). After staining with Neurotrace 435/455 (1:100 in PBS) and mounting on gelatin-coated slides in Vectashield (catalogue no. H-1400; Vector Laboratories), sections were imaged with a Fluoview FV-1000 confocal imaging system (Olympus) with 4x, 25x, and 60x objectives. Tiled confocal stacks (800 × 800 pixels; 0.2 $\mu$m z-step) of SOM-YFP cells were flat projected, rotated and cropped in PhotoShop 13.0 or ImageJ for display.

## Morphological Reconstruction of OLM Cells

Confocal microscope images at 60X magnification were acquired for the cells used in this work. The field of view of each image was restricted to 200 × 200 $\mu$m, resulting in 2–11 image "stacks" per cell. Bitplane Imaris was used for viewing reconstructions in 3D and for validating the z-stack. The microscope step size was 0.2 $\mu$m in the Z-plane, resulting in 150–200 images per stack. Variation in contrast between stacks were likely due to photobleaching, as stacks acquired later in the image acquisition process for each cell were more apparently bleached than the ones acquired earlier. Bleach correction was performed using ImageJ (Schneider et al., 2012) by normalizing the contrast of all stacks for each cell according to the average intensity value across all stacks per cell. Stacks were then stitched together to recover the volume information for the entire cell. Stitching was performed using the XuvTools software package (Emmenlauer et al., 2009). We next performed volumetric reconstruction of the soma, dendrites, and axons. This was done using the freely-available Neuromantic software package that implements semi-automated tracing (Myatt et al., 2012).

## Criteria for Selection of OLM Cells

Patch clamp recordings were performed on a total of 45 cells from the stratum oriens of SOM-YFP cells from SOM-Cre/Rosa26YFP mice. After histological processing was complete, neurons were classified as OLM cells if they possessed a horizontally-oriented cell body and dendrites within the oriens layer and a major axon projecting perpendicularly with ramifications in the lacunosum/moleculare layer. Additional criteria were developed for stability of access and input resistance, completeness of electrophysiological protocols, and signal-to-noise level in both current and voltage clamp recordings. Only those cells that exhibited <20% change in input resistance over the course of the experiment were considered for further modeling. The full suite of electrophysiological protocols, including wash-in of ZD7288 blocker to be able to determine $I_h$ was required to fulfill selection criteria. Of the 45 cells recorded from in total, 11 OLM cells met electrophysiological criteria for stability, completeness, and noise level. Of these 11 OLM cells, three (*Cell 1*, *Cell 2*, *Cell 3*) were advanced for subsequent detailed experimental analyses and multi-compartment computational model development. Over the course of the recordings for these three cells, the input resistances as determined from seal test recordings changed from: 260.5 to 216.9 $M\Omega$ (−16.7%) for *Cell 1*; 147.3 to 175.1 $M\Omega$ (+18.9%) for *Cell 2*; and 458.7 to 390.6 $M\Omega$ (−14.8%) for *Cell 3*. The sources of these modest changes in input resistance are not clear, but mechanical drift, activity-dependence (execution of many protocols), and intracellular dialysis are suspected to be contributing factors.

## Multi-Compartment Model Creation and Passive Property Fitting Considerations

Reconstructed OLM cells yielded soma and somatodendritic surface areas ($\mu m^2$) of: 7,651 and 29,378 for *Cell 1*; 13,035 and 35,159 for *Cell 2*; 6,911 and 21,990 for *Cell 3*. The NEURON simulation environment (Hines and Carnevale, 2001) was used to create the multi-compartment models. Compartmentalization of the models was done using the $d_\lambda$ rule where compartment lengths are set to a fraction of the length constant $\lambda_f$, where $f$=100 Hz. We set the fraction of $d_\lambda$ to be 0.1 for all models. The finalized number of compartments (after staggered re-fitting) in each of the model cells is: 303, 632, and 837 for *Cell 1*, *Cell 2*, and *Cell 3*, respectively.

We selected long current clamp steps for the fitting of passive membrane properties rather than shorter voltage clamp "seal test" protocols due to the incomplete clamping of the membrane by short voltage clamp steps (Holmes, 2010). Recordings with synaptic blockers in addition to potassium and sodium blockers are referred to as *"TTX traces"* (i.e., step #4 in **Table 1**), due to TTX application. Recordings with synaptic blockers obtained in the presence of h-channel blocker ZD7288 in addition to TTX/4-AP/TEA are referred to as *"ZD traces"* and are given by step #7 in **Table 1**. Recordings performed with synaptic- and all voltage-gated channels blocked (i.e., ZD traces) were initially considered preferable for passive membrane property fitting in the models. However, due to the possibility of changes in membrane responses as a function of the length of the recording session, we compared the membrane time constants ($\tau_m$) during the charging portion of the current clamp step for the voltage traces obtained across recordings with synaptic- and voltage-gated blockers applied. We found that the −30 pA ZD traces, being the last traces recorded in the session, showed noisier membrane responses compared to the −120 pA ZD traces obtained earlier. This manifested as an "undershoot" of the −30 pA ZD traces (see **Supplementary Figure 1**). After normalization

of the traces was done, it was clear that the −30 pA ZD traces showed a marked slowing of $\tau_m$ compared to both the −120 pA ZD as well as −30 pA TTX traces, the latter two being largely overlapping. This demonstrated that in the case of the −30 pA TTX current injection, few or no h-channels were activated as the $V_m$ response was nearly identical to that of the ZD traces.

We fitted the passive membrane properties of multi-compartment models, as well as the h-channel parameters, using a virtual current clamp and the Multiple Run Fitter (MRF) of the NEURON simulation environment (Hines and Carnevale, 2001). The −120 pA ZD traces (or TTX traces for fitting h-channels) for each cell were used as the experimental recording for which the models' $V_m$ trajectories needed to match in response to −120 pA virtual current. During use of the MRF in NEURON for the passive property fitting procedure, certain regions of the traces were discounted from fitting, such as the first 500 ms portion so that initial model transients did not affect the fitting. Furthermore, because the charging portion of $V_m$ was very short—on the order of 100 ms—it was given a greater weight value (10X) compared to the rest of the trace, in the MRF. For fitting passive responses, typically only the initial portion of the steady-state response during the hyperpolarizing current clamp step was used for fitting, that is, about 50–60 ms after the charging portion was completed. This was because for some cells, a small depolarization was present even under ZD7288 block, which could have been due to noise or the presence of another, unidentified inward current that was not blocked. For cells where no such depolarization was present, the entire current membrane trace during the current clamp step was used for fitting. Additionally, approximately 1 second of the trace after the current clamp step was completed was used for fitting for each cell, to ensure the model's response to the release from the current clamp was captured. When fitting with h-channels, the entire steady-state response was used for fitting the model parameters, but with 10X higher weights assigned to the charging portion of $V_m$ portions of the trace, as when doing the passive fitting. Also, when fitting the h-channel parameters in the model using the TTX traces, the post-inhibitory rebound portion of the experimental traces were also considered during the fits. An exception was for *Cell 3* where the post-inhibitory rebound region was not included, since for this cell model, no appropriate fits of h-channel parameters that could also adequately capture the sag response could be found (see section Discussion).

In summary, the duration of the experimental recordings is from 0 to at least 5,000 ms, with the current clamp step starting after one second for two seconds, i.e., from 1,000 to 3,000 ms. Model traces from 500 to 5,000 ms were used in the MRF for fitting both passive and $I_h$ parameters.

## Passive Membrane Model and Experiment Comparisons

Input resistance ($R_{in}$) in the passive models computed using a current clamp protocol of −120 pA, i.e., the same protocol used to fit the passive properties, is given by values of $V_m$ taken at the start and end of the current clamp step: $R_{in}$=($V_{start} - V_{end}$)/(120$pA$). Using experimental −120 pA ZD traces, the input resistance is also computed. These computed values are: $R_{in}$ (MΩ) (passive model) = 411 (*Cell 1*), 332 (*Cell 2*), and 550 (*Cell 3*); $R_{in}$ (MΩ) (expt with ZD7288) = 363 (*Cell 1*), 326 (*Cell 2*), and 531 (*Cell 3*).

We note that for the comparison of membrane time constants ($\tau_m$) of the OLM cells used to the models, we fitted exponential curves to the charging portion of $V_m$ for each cell at various time points of the recording session using a nonlinear least squares regression (see above). The amplitude of the traces were normalized at the time point at which depolarizing responses in the TTX traces due to $I_h$ cause the membrane potential to deviate from the (putatively) passive response under the ZD traces. The fitted values are: $\tau_m$ (ms) (using −30 pA TTX trace) = 32.8 (*Cell 1*), 29.1 (*Cell 2*), and 40.5 (*Cell 3*). $\tau_m$ (ms) (using −120 pA ZD trace) = 32.3 (*Cell 1*), 33.8 (*Cell 2*), and 39.3 (*Cell 3*). *Cell 1* in particular exhibited a very good match between the −30 pA TTX and −120 pA ZD traces. We also fitted the membrane time constant for the models, using a −120 pA current clamp step in the models without $I_h$ included. Resulting $V_m$ traces were fit in the same way as the experimental traces, except that the $V_m$ data points were weighted by the relative time step of integration in the NEURON simulations such that data points in the $V_m$ vector closely spaced in time would be weighed less. This ensured that the fit was not disproportionately weighed by the early, rapidly changing charging portion with many more data points. The fitted values are: $\tau_m$ (ms) (passive model) = 30.4 (*Cell 1*), 27.4 (*Cell 2*), and 36.4 (*Cell 3*).

## Mathematical Equations for the Current Due to H-Channels

The specification of the current for h-channels, $I_h$, was taken from our previous work (Lawrence et al., 2006; Sekulić et al., 2014). However, the kinetics for activation and deactivation, the steady-state activation curves, and the conductance densities were defined on a per-cell basis in the present work. This required moving the relevant variables in the $I_h$ MOD-file into the PARAMETER block to allow per-cell configuration in the NEURON code.

The conductance-based mathematical formulation used to represent current flow through h-channels is given by:

$$I_h = G_h \cdot r\,(V - E_h) \tag{1}$$

$$\frac{dr}{dt} = \frac{r_\infty - r}{\tau_h} \tag{2}$$

$$r_\infty = \frac{1}{1 + \exp\left(\frac{V - V_{1/2}}{k}\right)} \tag{3}$$

where $G_h$ is the maximal channel conductance for the h-channels, $r$ is the activation variable, $E_h$ is the h-channel reversal potential, $r_\infty$ is the steady-state activation, $k$ is the slope of activation and $V_{1/2}$ is the potential of half-maximal activation of $I_h$, $\tau_h$ is the time constant of activation, $V$ is the membrane potential, and $t$ is time. The voltage dependence of $\tau_h$ is given by a double

exponential expression with parameters $t_1, t_2, t_3, t_4, t_5$ as follows:

$$\tau_h(V) = \frac{1}{\exp(-t_1 - t_2 V) + \exp(-t_3 + t_4 V)} + t_5 \qquad (4)$$

## Extraction of H-Channel Characteristics From Voltage and Current Clamp Traces

Given our experimental protocol (see **Table 1**), we were able to obtain h-channel current ($I_h$) reversal potentials, activation kinetics, and steady-state activation for each of the three chosen cells.

### Reversal Potential

To obtain the reversal potential for $I_h$, we first removed the leak components and capacitive transients from the voltage clamp recordings in order to isolate the $I_h$ components. This was done by taking the traces obtained by the reversal potential protocol (step #6 in **Table 1**) and subtracting from them the capacitive response generated by an equivalent magnitude voltage clamp deflection from the $I_h$ activation protocol with ZD7288 application (step #8 in **Table 1**), resulting in $I_h$ tail currents (see **Supplementary Figure 2**). The traces were then smoothed using the *rloess* smoothing function in MATLAB, which performs local linear regression over a window, using weighted linear least squares. The smoothing window was set to 25 ms so that only noise in the recordings was removed, and not time-dependent changes attributable to ion channel currents.

To create the current-voltage (I–V) plot, a fixed time point after the capacitive transient ended was determined by eye, which allowed us to obtain the time point of maximum deflection after the voltage clamp step (Magee, 1998; Molleman, 2003). We refer to this as the "fixed" time point for determining the I–V plot. The validity of this technique relies on the assumption that the maximal number of h-channels are still open by the time the capacitive transient is abolished, so that the resulting current does not depend on changes in the conductance, only on the driving force. The fact that $I_h$ deactivates slowly means that this assumption is likely to be a safe one. However, to account for the possibility of early channel closure, a second method for extracting the current values and constructing an I–V plot was used. This consisted of fitting single exponential functions to the time course of the decay of current upon the step relaxation of the voltage clamp, which is used primarily to determine the voltage-dependent time constants of deactivation. The fitted exponential functions were then evaluated at the time of the relaxation of the voltage clamp step. In this way, we could deduce the amount of current that is masked by the capacitive transient by extrapolating the value from the exponential functions that were fitted on the non-capacitive portions of the current trace. That is, the functions were fitted to a window corresponding to the fixed point as the start time, and the end of the voltage clamp step as the end time. We refer to the current values and resulting I–V plot as the "extrapolated" method. We note that the smoothed traces were only used for the fixed method so that noisy fluctuations in the current traces did not unduly influence the resulting I–V plot; however, for the extrapolated method the exponential functions were fitted using the original, non-smoothed subtracted traces. The current traces with fitted exponentials are shown in **Supplementary Figure 2**, and I–V plots for both fixed and extrapolated methods are shown in **Figure 2B**. The resulting reversal potential ($E_h$) values for each cell were determined by fitting a first-order polynomial to the linear portion of the I–V curve only. For *Cell 1* and *Cell 2*, the linear portion of the extrapolated I–V curve overlapped with the fixed I–V curve, and the resulting $E_h$ values were similar between the two methods. For these cells, we therefore took $E_h$ from the extrapolated I–V curves. For *Cell 3*, however, the capacitive transients disrupted the response and affected the fitting so that the extrapolated I–V values did not exhibit as strong of a linear relationship as the fixed I–V values. One possible explanation for the distorted (non-linear) measurements of I–V values with *Cell 3* is that the current traces for $I_h$ deactivation, from which the reversal potential I–V plots were determined, did not match fully between the control case (with only TTX/4-AP/TEA blockers) and the later protocol with the $I_h$ blocker ZD7288, due to the effects of noise. Thus, the subtraction of the two to remove the leak components introduced some distortion in the resulting current traces. As a result, although the resulting $E_h$ values between extrapolated and fixed points were similar, we took $E_h$ for *Cell 3* from the fixed I–V curve instead, to minimize possible error from using the line fitted with only 4 out of the 8 possible I–V datapoints (**Figure 2B**, *Cell 3*). The resulting $E_h$ values for all cells are given in **Table 3**. These values are in general agreement with literature values of $I_h$ reversal potentials in OLM cells (Maccaferri and McBain, 1996).

### Voltage-Dependent Time Constant of Activation and Deactivation and Steady-State Activation

To obtain the time constants of activation/deactivation for $I_h$ ($\tau_h$) we used the recordings where a voltage clamp protocol with an initial clamp at a holding potential was then stepped to various hyperpolarized potentials, measuring the resulting transmembrane current (#3 in **Table 1**). The identical protocol was then performed with the $I_h$-specific blocker ZD7288 (#8 in **Table 1**). Using this data, we subtracted the ZD7288 traces from the control traces to isolate $I_h$ for the activation time constants. Then, single exponential functions were fitted to the time-varying change in current upon each voltage step. $I_h$ showed no voltage-dependent inactivation. To obtain the deactivation time constants, single exponential functions were fitted to the tail currents as obtained above (in the Reversal potential section). To construct the curve of voltage-dependent activation and deactivation kinetics, the time constants of activation were combined with the deactivation time constants obtained from the tail currents (see **Supplementary Figure 2**).

The time course of activation and deactivation was then described using a double exponential function of the form given by Equation (4) in section Methods, with parameters $t_1, t_2, t_3, t_4, t_5$ to be fit. Fitting of the double exponential functions was done using a nonlinear least squares fit in MATLAB. However, due to the method of leak subtraction, some noisy differences in the capacitive transients between the two traces used in the subtraction may have overlapped with the initially observable $I_h$ deactivation kinetics in the short time window

upon current clamp release (see **Supplementary Figure 2A**). Accordingly, many of the deactivation time points were clear outliers and thus not reasonable measures of $I_h$ deactivation, and these were not included in the fitting. All of the data points (including those not included in the fitting are shown in **Supplementary Figure 3A**). The resulting fitted values for the voltage-dependent time constant of activation and deactivation are given in **Table 3** and plotted in **Figure 2C**. We note that the shape of the time constant of activation function is roughly similar across the three cells, with particular overlap between *Cell 1* and *Cell 2*. In all three cases, the slowest component of the time constant activation function is around 300 ms, whereas the fast component is less than 100 ms for all three cells.

### Steady-State Activation

The steady-state activation curves, $r_\infty$, for the OLM cells were constructed by measuring the current amplitude in the ZD7288-subtracted traces at the end of each step of the voltage clamp protocol for $I_h$ activation (see **Supplementary Figure 2**). The current at each voltage step was plotted and normalized to the greatest recorded current value which for h-channels is at the most hyperpolarized range. Then, a Boltzmann function for $r_\infty$ (Equation 3) with parameters $V_{1/2}$ for the voltage at half-activation and slope factor $k$ for the steepness of the sigmoidal curve, was fitted to each cell's voltage-dependent activation data. The fitted values are given in **Table 3**, and the resulting activation curves for the three cells are shown in **Figure 2D**.

### Maximal Conductances

To determine the maximal conductance for $I_h$, $G_h$, we used the tail currents from the reversal potential step protocol as this corresponded to the point in time when $I_h$ was fully activated (Magee, 1998; Dougherty et al., 2013). These currents were thus measured when all h-channels are opened, and thus describe the ratio of maximum current to voltage needed to obtain I-V plots for determining $G_h$ (Molleman, 2003). The slope of the linear portion of the I–V plot for the tail currents, with the reversal potential as origin (denoting zero current flow), was used as the measure of $G_h$. As described above, a line was fitted to the linear portion of the I–V plots for all three cells to determine the reversal potential. The slope of the line gives $G_h$ and the resulting values for the three cells are given in **Table 3**. When scaled by the surface area, we obtain an $G_h$ as a conductance density that is used in the model code.

## Full Spiking Multi-Compartment Model Optimizations

In creating full spiking models, we used the final passive model backbone with h-channels in the dendrites, and used the same complement of ion channel types that had been used in previous instantiations of the OLM cell model (Lawrence et al., 2006; Sekulić et al., 2014). The equations used are all given in the Appendix of Lawrence et al. (2006). They include transient sodium, fast and slow delayed rectifier potassium, A-type potassium, M-type, T- and L-type calcium, and calcium-dependent potassium channels. Their conductances in soma ($s$), axon ($a$), or dendrites ($d$) are represented respectively as $G_{NaT}, G_{Kdrf}, G_{Kdrs}, G_{KA}, G_M, G_{CaT}, G_{CaL}, G_{KCa}$ as given in **Supplementary Table 2**.

In our optimizations, we allowed $G_{NaT}, G_{Kdrf}, G_{Kdrs}$ to vary independently in the soma, dendrites, and axon, and we also allowed the sodium channel to have some flexibility by allowing alterations in its voltage dependency, i.e., introducing a free parameter, $V_{shift}$ that could change by $\pm$ 7 mV. Note that soma, dendrites, and axon each have an independent $V_{shift}$ parameter, but the $V_{shift}$ value remains the same across forward and backward rate activations and inactivations such that activation and inactivation curves shift by the same amount and the "activation/inactivation window" stays constant. Except for the inclusion of $V_{shift}$, the activation and inactivation equations underlying the sodium current are the same as used previously (Lawrence et al., 2006), and as based on experimental data of Martina et al. (2000). For completeness, the equations for the sodium current, $I_{NaT}$, are shown below:

$$I_{NaT} = G_{NaT} \cdot m^3 h \, (V - E_h) \tag{5}$$

$$\frac{dm}{dt} = \alpha_m(1 - m) - \beta_m m \tag{6}$$

$$\frac{dh}{dt} = \alpha_h(1 - h) - \beta_h h \tag{7}$$

where, for somatic compartments,

$$\alpha_m(V) = \frac{-0.1(V + 38 - V_{shift})}{\exp(-(V + 38 - V_{shift})/10) - 1} \tag{8}$$

$$\beta_m(V) = 4\exp(-(V + 63 - V_{shift})/18) \tag{9}$$

$$\alpha_h(V) = 0.07\exp(-(V + 63 - V_{shift})/20) \tag{10}$$

$$\beta_h(V) = \frac{1}{1 + \exp(-(V + 33 - V_{shift})/10)} \tag{11}$$

and for dendritic and axonal compartments,

$$\alpha_m(V) = \frac{-0.1(V + 45 - V_{shift})}{\exp(-(V + 45 - V_{shift})/10) - 1} \tag{12}$$

$$\beta_m(V) = 4\exp(-(V + 70 - V_{shift})/18) \tag{13}$$

$$\alpha_h(V) = 0.07\exp(-(V + 70 - V_{shift})/20) \tag{14}$$

$$\beta_h(V) = \frac{1}{1 + \exp(-(V + 40 - V_{shift})/10)} \tag{15}$$

### Optimization Approach and Parameter Details

For the optimizations, we did the following:

1. Performed multi-objective optimizations using the BluePyOpt module in Python (Van Geit et al., 2016) and high performance computing resources via the Neuroscience Gateway (Sivagnanam et al., 2013) to find ion channel conductances in order to minimize the error across multiple features in the electrophysiology (see **Supplementary Table 3**).
2. Fine-tuned the parameter ranges and objectives to avoid areas of the parameter space that generate undesirable results and keep re-doing the optimizations using this approach until the top models consistently generate appropriate

electrophysiologies. The parameter ranges used that produced the final models are shown in **Supplementary Table 2**.

During the optimizations, the fitness for each model is quantified as the sum of the number of standard deviations away from the experimental target efeature values and as such, is a unitless quantity. Standard deviation values (**Supplementary Table 3**) are chosen manually in order to weight each efeature (i.e., since we are fitting each model to a single voltage trace, there is no standard deviation that can be derived from the experimental data). Note that because the standard deviation values are chosen manually, choosing smaller standard deviation values to weight specific efeatures will increase the magnitude of the fitness values since this increases the number of standard deviations away from the target value. As such, since we used small standard deviation values, this caused the fitness values of the model to artifactually be quite large. The top five optimized models for *Cell 1* and *Cell 2* are presented in **Figure 6A** and **Supplementary Figure 4**. Their fitness values are: (*Cell 1:* 411.53, 425.38, 430.68, 430.93, 438.65; *Cell 2:* 660.96, 665.49, 669.06, 678.58, 684.60).

In order of model rankings (i.e., [1*st*,...,5*th*]), the values below are the $V_{shift}$ parameters (in mV) for the top five full spiking models (see **Figure 5C** to see the resulting voltage-dependencies).
*Cell 1:*
$V_{shift,s} = [-4.83, -6.55, -6.70, -6.46, -6.68]$,
$V_{shift,d} = [4.85, 6.37, 3.71, 2.86, 4.17]$,
$V_{shift,a} = [2.49, 2.82, 2.84, 5.70, 2.82]$.
*Cell 2:*
$V_{shift,s} = [-4.36, -4.69, -4.88, -4.36, -4.36]$,
$V_{shift,d} = [-1.26, -1.12, -0.54, -1.46, -1.41]$,
$V_{shift,a} = [6.57, 6.57, 6.30, 6.57, 6.57]$.
After performing several optimizations and adjusting the parameters to improve the optimization outputs, we used the following optimization parameters for both models: Number of Offspring = 100, Number of Generations = 200, Mutation Rate = 0.15, Crossover Rate = 0.85, Eta (i.e., learning rate) = 0.5, Optimizer = "IBEA," Random Seed = 61 (*Cell 1*) and 9 (*Cell 2*).

All of the objective features that were used in the optimization are listed in **Supplementary Table 3**, and the parameter ranges are given in **Supplementary Table 2**. Features 1–10 were used for the +30, +60, and +90 pA current injection protocols. Features 11–12 were only used for the +60 and +90 pA current injection protocols, since the +30 pA current injection did not always generate a sufficient number of spikes for those features to be calculated. Since we were fitting the models to single current injection traces, standard deviation values were chosen manually for each objective feature, in order to weight each objective feature by hand. Since standard deviation is used in computing the fitness for each model (i.e., fitness is quantified as the sum of the number of standard deviations away from the experimental target efeature values), manipulating these values offered a way to weight particular target measurements. More specifically, we initially chose standard deviations that were 1–2 order of magnitudes smaller than the largest significant digit for each measurement. For example, *AP_duration_half_width* in the somatic area of a neuron is usually a small value between 0.5 and 2 ms, and we used a standard deviation of 0.01 ms for this efeature. If the optimization ended up under-performing on any specific efeature measurements, we would sometimes attempt to improve it by using smaller standard deviation values for those measurements. Though this had some mild effects on improving the optimizations, constraining the free parameter ranges ended up showing much better improvements in the optimization results. We also added a heavy penalization on models that generated spikes during the baseline periods. Finally, in order to make BluePyOpt compatible with the OLM cell model compartmentalization, we adjusted BluePyOpt's method for compartmentalization such that it uses the $d_\lambda$ rule (Hines and Carnevale, 2001).

To check if axonal properties were appropriate for what is known experimentally (Martina et al., 2000), we performed simulations with our final optimized spiking models of *Cell 1* and *Cell 2* to investigate morphological sites of action potential (AP) initiation. Specifically, Martina et al. (2000) previously showed that depending on whether a short high-intensity current or a long low-intensity current was injected into the soma, an AP would occur initially in the soma or axon-*bearing* dendrite, respectively. For both models of *Cell 1* and *Cell 2*, short high-intensity current evoked action potential initiation in the soma, but long low-intensity current evoked action potential initiation in axon-*lacking* dendrites. This suggests that specialized distributions of spike-initiating channels are missing in the axon of the model and are necessary for correctly setting the action potential initiation site. Given that OLM cell axonal channel properties are unknown, we did not venture further into specializing axonal properties in our models.

# RESULTS

## YFP-Positive Stratum Oriens Interneurons From SOM-Cre/Rosa26YFP Mice Contain a Population of OLM Cells

Patch-clamp recordings from 45 SOM-YFP neurons in the stratum oriens of SOM-Cre/Rosa26YFP mice were obtained using a detailed protocol as given in **Table 1**. Of these recordings, 11 of them met criteria for stability (see section Methods) and were morphologically confirmed as OLM interneurons, having horizontal cell body and dendrites confined to the oriens layer, and perpendicularly projecting axons which ramify in the lacunosum/moleculare layer. An analysis of these 11 cells is given in **Table 2** in which the experimental data analysis was performed as in Yi et al. (2014). From these 11 OLM cells, three (*Cell 1*, *Cell 2*, *Cell 3*) were chosen for subsequent detailed analyses and computational model creation. Their specific properties are given in **Table 2**. Morphological and electrophysiological characteristics for these three OLM cells are shown in **Figures 1A–L**.

SOM-YFP stratum oriens interneurons mice had slow membrane time constants and relatively high input resistances, in accordance with our previous study (Yi et al., 2014). Action potential half-widths were larger and membrane time constants were slower than previously reported for YFP neurons from PV-CRE/Rosa26YFP mice, consistent with the exclusion of

**TABLE 2 |** Passive and active properties of OLM cells from SOM-Cre/Rosa26YFP mice.

| Property | SOM-YFP ($n = 11$) | Cell 1 | Cell 2 | Cell 3 |
|---|---|---|---|---|
| $R_{in}$ (MΩ) | 314.3 ± 33.8 | 360.1 | 259.0 | 490.2 |
| $C_m$ (pF) | 107.1 ± 13.0 | 62.8 | 123.7 | 79.6 |
| Sag ratio (SS/peak) | 0.89 ± 0.03 | 0.70 | 0.84 | 0.74 |
| $\tau_m$ (ms) | 31.1 ± 2.5 | 22.6 | 32.0 | 39.0 |
| $I_{hold}$ (pA) | 3.4 ± 4.8 | 2.7 | −2.8 | 2.5 |
| First AP half-width ($\mu$s) | 595.1 ± 26.4 | 617.2 | 551.2 | 691.6 |
| First AP height (mV) | 66.0 ± 2.7 | 69.3 | 61.4 | 67.7 |
| Adaptation coefficient | 0.5 ± 0.1 | 0.41 | 0.61 | 0.49 |
| Frequency at 90 pA (Hz) | 15.5 ± 2.1 | 20 | 19.5 | 8 |
| Frequency at 60 pA (Hz) | 8.3 ± 1.5 | 12.5 | 11.5 | 3 |
| Frequency at 30 pA (Hz) | 2.1 ± 0.8 | 4 | 1 | 1 |

*Values are presented as means ± SEM. $R_{in}$, input resistance; $\tau_m$, membrane time constant; AP, action potential; $C_m$, membrane capacitance; SS, steady state; $I_{hold}$, the current injected to hold the recorded cell at −60 mV (not junction potential corrected). Passive properties were extracted at a current injection of −60 pA. Active properties were extracted at a current injection of 90 pA, unless otherwise specified. APs were detected at a derivative threshold of 20 mV/ms. The adaptation coefficient was calculated by dividing the first inter-spike interval by the last inter-spike interval of the AP train during current injection of 90 pA.*

PV-positive basket and bistratified cells from this population. Moreover, this population had considerable hyperpolarization-induced sag, which, when combined with their higher input resistance, is considered a hallmark feature of OLM cells (Maccaferri and Lacaille, 2003).

## Multi-Compartment OLM Cell Models Capture Corresponding Passive Responses

We used the NEURON simulation environment (Hines and Carnevale, 2001) to develop our multi-compartment models. **Figures 1A–J** shows representative confocal images of the three cells, with the reconstructed cell morphologies shown in **Figures 1C–K**, paired with electrophysiological OLM cell profiles featuring hyperpolarization-induced sag. Details of the model reconstructions are given in section Methods.

To capture the passive response of the three cells we used the 2 s-long −120 pA current clamp traces in which all synaptic and voltage-gated channels were blocked. This choice was made because we found that the −30 pA traces were noisier in general (see **Figure 2A**, top panels), and the −120 pA traces best captured the passive response of the cells. This can be seen from a comparison of the membrane time constants ($\tau_m$) for different current clamp steps (see **Figure 2A**, bottom panels) and consideration of the protocol ordering of the recording session as in **Table 1**. Time constants were obtained by quantitatively fitting single exponential equations to the $V_m$ responses from the time point of the onset of the hyperpolarization current clamp step (1,000 ms) to the point at which the steady-state of the $V_m$ response was approximately achieved (**Figure 2A**, top panels). We refer to "TTX" and "ZD" traces as those with blockers given respectively by steps #4 and #7 in **Table 1**. For all cells, $\tau_m$ for the −30 pA TTX trace was most closely matched by the −120 pA ZD trace (dashed red line), with the subsequent ZD traces (−90, −60, and −30 pA) exhibiting an increased, and hence slower, membrane response (**Figure 2A**, bottom panels). The fact that the −120 pA ZD trace exhibited a similar response as a current injection of one quarter magnitude and without h-channels being blocked (i.e., −30 pA TTX) indicated that in both cases, the response of the membrane was mostly passive. Thus, given the lower signal-to-noise of the −30 pA ZD traces, we considered that the passive properties obtained using the −120 pA ZD traces would be better representations of the electrotonic features of the experimental cells. Further details are provided in section Methods.

To confirm that the −120 pA ZD traces led to better fits of the cells' passive properties, we compared the fits obtained using −120 and −30 pA ZD traces. The resulting fitted passive parameters of axial resistivity ($R_a$), specific capacitance ($C_m$), leak conductance ($G_{pas}$), and leak reversal potential ($E_{pas}$) are displayed in **Supplementary Table 1**. For each cell, the cumulative root-mean-square error (RMSE) across all traces used for each fit was lower when the −120 pA ZD trace was used for fitting the passive properties (**Supplementary Table 1**, left column for each cell). These parameters with the respective cell morphologies form the "backbone" of the OLM cell models, and there was a favorable comparison of input resistances and time constants between model and experiment (see section Methods for details). We noted that the $C_m$'s obtained from our model fits were lower than the $\approx 0.9$–$1\mu$F/cm$^2$ that have been previously reported as a "standard" value in mammalian neurons (Gentet et al., 2000). To consider potential errors in dendritic estimations due to tissue shrinkage, swelling and other limitations, we did a simple dendritic scaling check as described in Appendix 1 (**Supplementary Material**), that provided support for these low capacitance values.

## OLM Cell Multi-Compartment Models With Constrained Passive Properties and Added H-Channel Models Do Not Match Experimental Recordings

We use a standard conductance-based formalism to represent the ionic current due to h-channels ($I_h$), and we obtain $I_h$ parameter values as fits to the experimental data for each of the three cells (see section Methods). The parameters extracted from each of the OLM cells in this work included the $I_h$ reversal potential ($E_h$), the time constants of activation and deactivation of $I_h$ ($\tau_h$), the steady-state activation curve of $I_h$ ($r_\infty$), and the $I_h$ maximum conductance density ($G_h$). They are plotted in **Figures 2B–D** and parameter values are shown in **Table 3**. These h-channel models are added to our OLM cell multi-compartment models' "backbone" of morphological reconstructions and passive property fits.

We demonstrated in our previous work that OLM cell models exhibited a tradeoff between total membrane $G_h$ and the dendritic distribution of h-channels so that if the total $G_h$ was conserved, the resulting model output would be appropriate (Sekulić et al., 2015). Now, for the first time, we have a measure

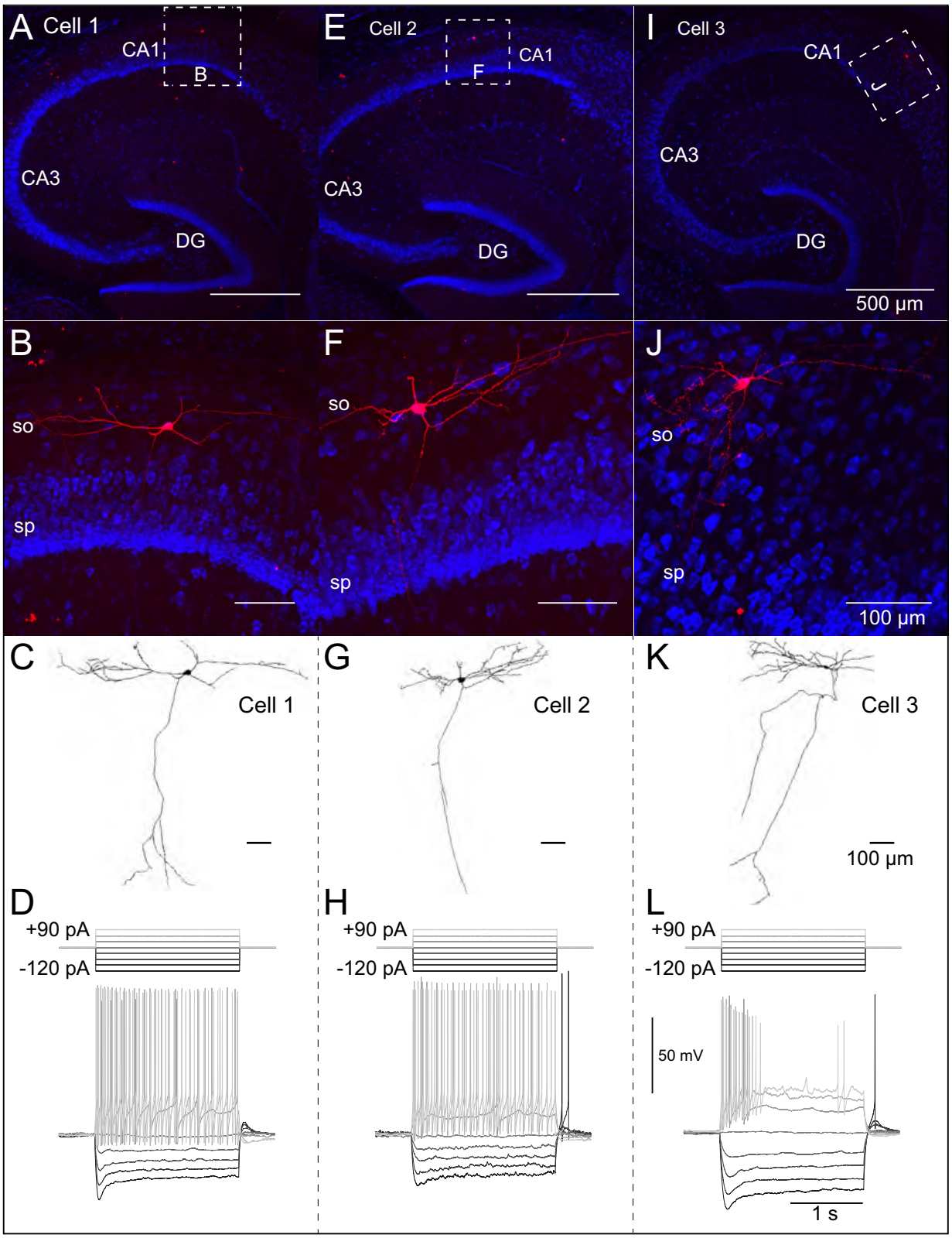


**FIGURE 1 |** Morphological and electrophysiological properties of OLM interneurons. Anatomical and electrophysiological properties of three OLM cells: **(A–D)** (*Cell 1*), **(E–H)** (*Cell 2*), and **(I–L)** (*Cell 3*) are shown. **(A)** Low magnification confocal image of the hippocampus showing *Cell 1* localized within CA1. Dashed square in **(A)**

*(Continued)*

**FIGURE 1 |** indicate boundaries of higher resolution images in **(B)**. **(B)** Expanded view of *Cell 1* localized to the stratum oriens layer of CA1. **(C)** Reconstructed morphology of *Cell 1*, **(D)** Voltage responses to a family of 2 s-long current hyperpolarizing (black; −90, −60, −30 pA) and depolarizing (light gray; +90, +60, +30 pA) current steps from −73 mV for *Cell 1*. Synaptic blockers were present (see section Methods). Hyperpolarization-induced sag is evident upon introduction of the −90 pA current step. *Cell 2* and *Cell 3* are shown in **(E–H,I–L)**, respectively.

of total $G_h$. Thus, a key prediction for the resulting multi-compartment models is that the total $G_h$ will constrain the distribution of h-channels to allow the models to appropriately capture the OLM cell electrophysiological characteristics. To consider this, we added an additional parameter to our models termed $H_{dist}$, which is defined as the centripetal extent for which h-channels are inserted in the dendrites. It is defined by a real-valued number in the range of [0, 1] and represents the fraction of maximum dendritic path length from the soma on a per-cell basis. Compartments with a path length from the soma that was smaller than any given $H_{dist}$ value were included when subsequently inserting h-channels, whereas those compartments whose distance from soma exceeded $H_{dist}$ were excluded. The boundary condition of $H_{dist} = 0$ is defined as the case where h-channels are only present in somatic compartments and not present in the dendrites. A non-zero value for $H_{dist}$ meant that the amount of dendrite specified by $H_{dist}$ itself had h-channels in addition to the somatic compartments. $H_{dist} = 1$ refers to full somatodendritic presence of h-channels, i.e., uniform distribution in the dendrites and soma. The per-cell $I_h$ parameters were inserted into each of the three models and two cases of $H_{dist}$ were initially considered to test the boundary cases: either no dendritic h-channels ($H_{dist} = 0$) or full, uniform distribution of h-channels in the dendrites ($H_{dist} = 1$). The resulting h-channel conductance density was calculated by dividing total $G_h$ by the resulting surface area of only somatic or somatodendritic compartments. These values and the other h-channel parameters are given in **Table 3**. The model outputs were fitted to experimental traces similarly as in the case with passive properties and ZD traces (see section Methods). The $V_m$ output of each of the three models being developed here, with boundary conditions of $H_{dist} = 0$ or 1 for the case of −120 pA current clamp injection, compared to the experimental TTX trace for each cell, is shown in **Figure 3A**. It is clear that these models do not fully match the experimental traces. Although we did explore $H_{dist}$ values that were between 0 and 1 (not shown), it is clear that given the fits shown in **Figure 3A**, it is unlikely that changing $H_{dist}$ to a value between 0 and 1 would improve the fits to the experimental data.

## A Staggered Re-fitting Procedure Yields Consistent and Generalized Model Fits for OLM Cells With Dendritic H-Channels

Given the sub-optimal match of our models with the experimental data, even with model parameters determined from experiment on a per-cell basis, we considered the possibility that one or more of the parameters were mismatched between the experimental cells and the parameter values derived from the recordings. We considered re-fitting the various parameters in the model to ensure that $I_h$ and passive parameters resulted in correct output for each cell. However, due to the sheer number of parameters present in the model, care needed to be taken in how the parameters were adjusted as there are many interdependencies between the fitted parameters. For instance, when $I_h$ is present, the trajectory of the $V_m$ response upon a step of hyperpolarizing current in a cell depends not just on $C_m$ and $R_a$, but also on the time constants of activation and deactivation of h-channels ($\tau_h$) and, to a degree, the h-channel steady-state activation curve ($r_\infty$). Therefore, if there is error in the model $V_m$ response compared to the experimental trace in this portion of the trace (**Figure 3A**), the mismatch between model and experiment may have been either due to the passive parameters, or due to $\tau_h$ or $G_h$, which gated by the activation, determines the amount of $I_h$. The problem, then, is how to attribute errors in any particular portion of a $V_m$ trace to any given parameter in the model.

We noted that the initial mismatch in the case of $H_{dist}$=1 and for *Cell 1* and *Cell 2* seem primarily to be located in the initial hyperpolarizing phase and the sag portion (see **Figure 3A**). Because the $\tau_h$ functions were constructed using a limited set of data, it was reasonable to suppose that a large source of mismatch in this portion of $V_m$ could be due to errors in the $\tau_h$ function itself. We thus re-fitted the parameters for $\tau_h$, namely $t_1, t_2, t_3, t_4, t_5$ for all three cells, against each respective −120 pA TTX trace and then compared the models' responses to the other current clamp steps to see how much of the error could be accounted for by re-fitting $\tau_h$ alone **Figure 3B** shows how the −120 pA $\tau_h$ re-fit parameters compares to the −90 pA TTX trace for each cell. This re-fitting of $\tau_h$ alone could not address the mismatch in $V_m$ between model and experiment although it may have played some role, as evidenced by improving the match in $V_m$ in some cases. Thus other parameter re-fitting needed to be considered.

We adopted the following approach and rationale. Since the passive properties were not as tightly constrained as the $I_h$ properties, and could account for some of the mismatch in both the transient and steady state portions of the traces, we re-fitted them first. That is, $R_a$, $C_m$, $G_{pas}$, $E_{pas}$. Turning to the $I_h$ properties, we first re-fitted the total $G_h$, which determines the per-compartment conductance density, as well as the steady-state activation curve $r_\infty$ since it determines the voltage dependency of how many channels are open. We could not fit $G_h$ and $r_\infty$ in the reverse order because any error in $G_h$—that is, how $I_h$ scales with voltage when all channels are opened—could be accounted for by refitting $r_\infty$ by "flattening" it, thus lowering the total number of channels that are open at any given voltage. This would not be physiologically correct since the model would then imply that $I_h$ is never fully activated, i.e., $r_\infty$ does not reach unity. Thus, by re-fitting $G_h$ first, followed by $r_\infty$, we increased the likelihood that $r_\infty$ did not diverge too much from the experimental data points obtained from the protocol for $I_h$ activation. Finally, we re-fitted $\tau_h$. If the passive properties and steady-state $I_h$ due to $G_h$ and $r_\infty$

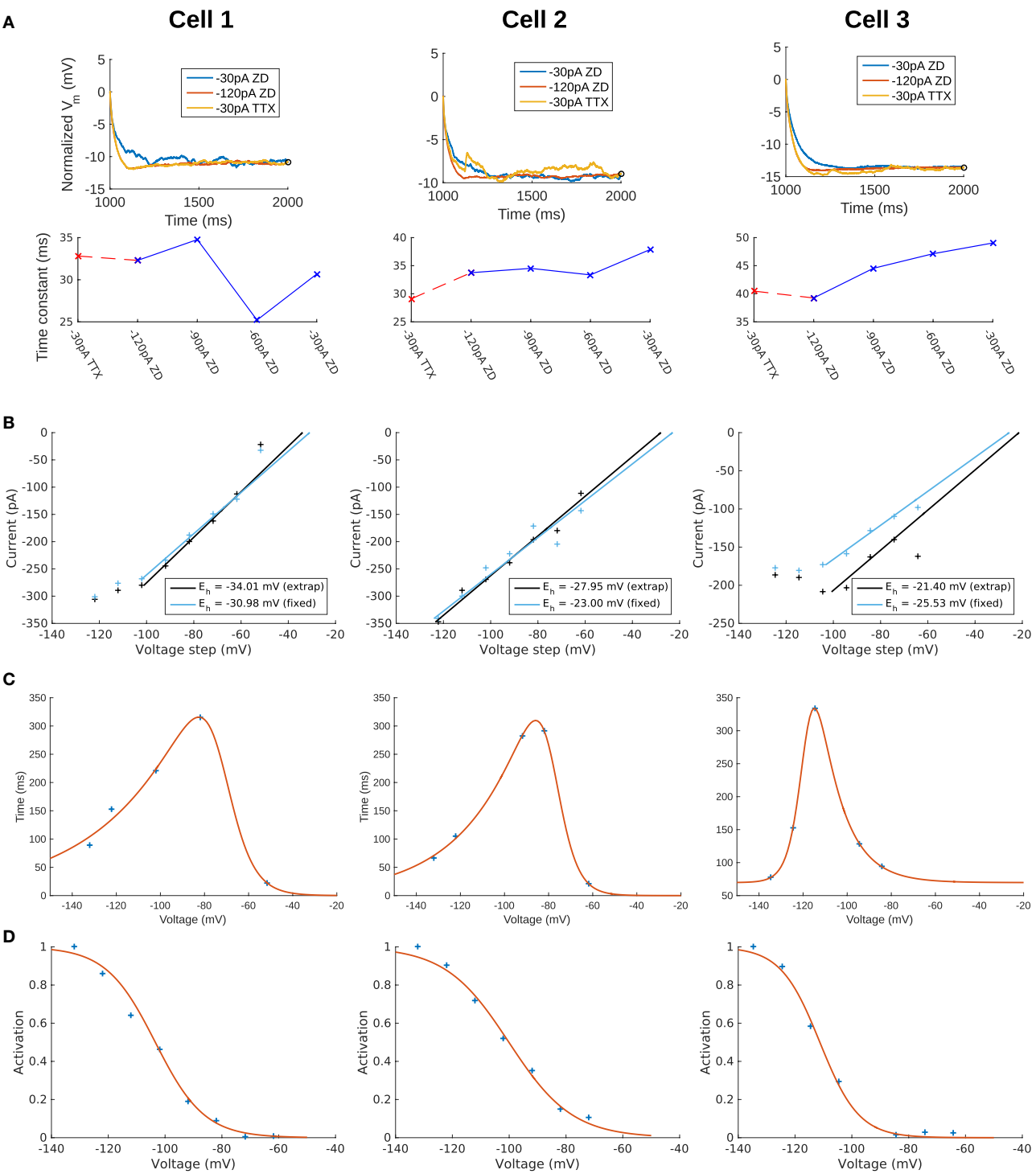


**FIGURE 2 |** Extracted passive and $I_h$ properties of OLM cells from experiment. **(A)** (Top) Membrane potential ($V_m$) normalized at steady-state, showing noisier responses of −30 pA ZD trace compared to the −120 pA ZD trace. (Bottom) Fitted membrane time constants ($\tau_m$) for all current clamp steps with ZD7288 application, as well as the −30 pA TTX trace. "ZD traces" are those in which synaptic and voltage-gated currents are blocked including h-currents with ZD7288 application, and "TTX traces" are the same except that h-currents are not blocked (protocols #7 and #4, respectively in **Table 1** of section Methods). **(B)** $I_h$ reversal potential as determined from current-voltage obtained from tail currents. See section Methods for difference between "extrap" and "fixed" values in plots and further details. **(C)** Time constants ($\tau_h$) or kinetics of activation and deactivation as determined from voltage clamp experiments. **(D)** Steady-state activation curves ($r_\infty$) as determined from voltage clamp experiments. See section Methods for details.

**TABLE 3 |** Computed $I_h$ parameter values obtained from fits to experimental data with computed conductance densities for somatic or somatodendritic distributions.

| Parameter | Cell 1 | Cell 2 | Cell 3 |
|---|---|---|---|
| $E_h$ (mV) | −34.0 | −27.9 | −25.2 |
| $V_{1/2}$ (mV) | −103.4 | −100.1 | −111.3 |
| $k$ (slope factor) | 8.63 | 11.16 | 6.88 |
| $t_1$ (ms) | 8.03 | 8.98 | 35.09 |
| $t_2$ (ms) | 0.025 | 0.035 | 0.24 |
| $t_3$ (ms) | −4.40 | −8.49 | −4.28 |
| $t_4$ (ms) | 0.15 | 0.19 | 0.088 |
| $t_5$ (ms) | $7.32 \times 10^{-6}$ | $3.57 \times 10^{-7}$ | 69.72 |
| Total $G_h$ (nS) | 4.17 | 3.64 | 2.20 |
| $G_h$ (pS/$\mu$m$^2$), $H_{dist} = 0$ | 0.546 | 0.279 | 0.380 |
| $G_h$ (pS/$\mu$m$^2$), $H_{dist} = 1$ | 0.142 | 0.104 | 0.120 |

accounted for much of the mismatch in $V_m$, then the last step of re-fitting $\tau_h$ should allow for any mismatch due to $\tau_h$ to be corrected for.

Using this approach, which we termed a "staggered" re-fitting, we show the model outputs in **Figure 3C** where only the −120 pA TTX traces were used for fitting the parameters, with the −90 pA TTX traces provided test data to validate the fits. The results with this approach were clearly more successful than the previous approaches, as shown by the errors in **Figure 3D**. By fitting the parameters in such a way that the ones most likely to be responsible for errors in particular portions of the mismatched model $V_m$ traces were fitted first, the resulting fits were now generalizable relative to the case of either re-fitting the passive properties alone, or re-fitting $\tau_h$ alone, since the staggered re-fitted values were able to match all of the other current clamp traces that were not used for fitting. Figures detailing this as well as considerations of overfitting, especially the pitfall of simultaneously adjusting all model parameters, are provided in Appendix 2 (**Supplementary Material**).

All the models in the staggered re-fit were done with $H_{dist} = 1$, because that value was the one that provided the closest fit to the experimental traces (**Figure 3A**) when only passive properties were fit to the $V_m$ traces and $I_h$ parameter values were obtained from the voltage clamp protocols. These staggered re-fitted values are shown in **Table 4**, $H_{dist} = 1$ column. Model parameters before staggered re-fitting can be found in **Supplementary Table 1** (passive properties) and **Table 4** ($I_h$ properties). We examined whether using $H_{dist} = 0$ and applying our staggered re-fitting approach could also produce good, generalizable fits to the experimental data. The models with $H_{dist} = 0$ fitted the experimental $V_m$ traces well in all four current clamp steps as it did for $H_{dist} = 1$, and we show the comparison to the −90 pA TTX trace for $H_{dist}$ values of both 0 and 1 in **Figure 4A**, noting that the −120 pA TTX trace was used for the fitting. The staggered re-fitted values for $H_{dist} = 0$ are also shown in **Table 4**. From a comparison across **Table 4** of parameter values for $H_{dist} = 0$, 1 and original $I_h$ parameter values fit to the experimental data (see **Table 3**, it is clear that the re-fitted parameter values using $H_{dist}$=0 are inappropriate, specifically due to total $G_h$ differences (experimental total $G_h$ values from **Table 3** shown in bold in **Table 4** for convenience). For the case of $H_{dist} = 1$, $G_h$ values are reasonably close to what was measured directly from the I–V plot of the reversal potential experimental protocol, unlike $H_{dist} = 0$, which exhibited $G_h$ values that were much less than half of the experimentally-derived values. Given that this parameter was taken from the slope of the I–V plot, the values from $H_{dist} = 0$, if correct, would imply that the recorded current values were double the "true" values in the cell. This is graphically depicted in **Figure 4B**. We deemed this unlikely, and concluded that the divergence in the re-fitted $G_h$ with $H_{dist} = 1$ compared to the experimental case indicated a much more reasonable error. Model $I_h$ time constants of activation ($\tau_h$) and steady-state activation curves ($r_\infty$) for $H_{dist} = 0$,1 are shown for comparison along with the experimental fits in **Supplementary Figure 3**, lending further support for $H_{dist} = 0$ being unlikely.

Hence, the fact that it was possible to match the experimental $V_m$ traces using both $H_{dist} = 0$ (**Figure 4A**) and $H_{dist} = 1$ (**Figure 3C**) did not mean that they were equally valid. The benefit of having directly measured experimental values representing $G_h$, $\tau_h$, $r_\infty$ from the *same* cell meant that we could confidently state that models with $H_{dist} = 0$, though they fitted the $V_m$ traces, were not appropriate models because they did not match the experimentally-derived values. Thus, only when h-channels were spread into the dendrites did we find models whose $V_m$ responses matched the experimental traces and whose total $G_h$ and other parameter values were in reasonable agreement with the experimentally measured values. We thus predict that the experimental cells in the dataset used here have h-channels expressed in their dendrites, with biophysical characteristics as given in **Table 4**, $H_{dist} = 1$.

## Optimized Full Spiking Models of OLM Cells Capture Responses to Current Step Stimuli

We have so far developed three multi-compartment models of OLM cells with fitted passive and $I_h$ parameter values. The presence of h-channels in the dendrites of these models was found to be the most appropriate distribution given the experimental data. We now focus on two of the OLM cell models—*Cell 1* and *Cell 2*—and move forward to include a full repertoire of ion channel types as used in previous OLM cell models (Lawrence et al., 2006), thus creating full spiking models available for use in further studies.

To do this, we optimized the parameter values (see **Supplementary Table 2** for parameters and ranges) to depolarizing steps of the particular cell, where most voltage-gated ion channels were expected to be activated. We used BluePyOpt (Van Geit et al., 2016) to perform multi-objective optimizations that provided sets of parameter values which generated appropriate OLM cell voltage output at +30, +60, and +90 pA depolarizing steps (#2 in **Table 1**), given specified features (see **Supplementary Table 3**). We note that our fits were done using the specific experimental data sets and not to a set of experimental data with variances associated with

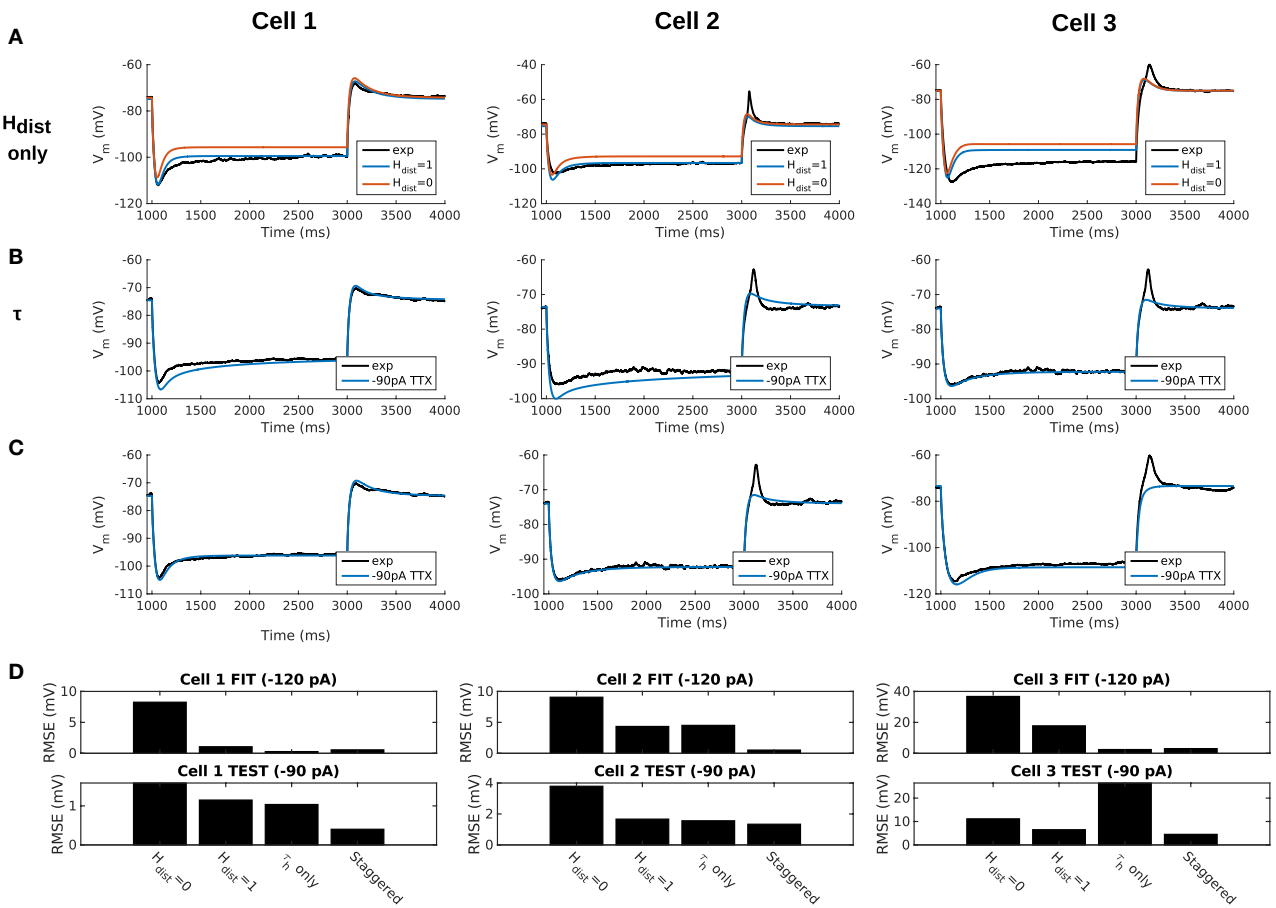


**FIGURE 3 |** Staggered re-fitting of $I_h$ and passive property parameters successfully captures experimental cell responses to current clamp steps. **(A)** Boundary conditions of $H_{dist}$ parameter [0, 1] showing inappropriate fits when putting all experimentally derived parameters together with fitted passive "backbone." **(B)** Re-fitting only $\tau_h$ does not provide good fits ($H_{dist} = 1$). **(C)** Staggered re-fitting of parameters results in good fits. Shown in **(B,C)** are −90 pA TTX traces which are "test" traces not used for fitting (−120 pA TTX trace was used for fitting, not shown). **(D)** Root-mean-square error (RMSE) of model responses to experimental traces in the case of traces used for fitting (top) and those for validation (bottom).

electrophysiological features. We further note that we did our fitting using holding currents in line with the experimental data (4 pA for *Cell 1* and −5 pA for *Cell 2*). Further details are provided in section Methods.

The optimized spiking model features for the top five models relative to the experimental data are shown in **Figure 5A**, and the optimized parameter values are given in **Figures 5B,C**. Further details of the objective features and fitness values are provided in the Methods. The models with the resulting best fits are shown in **Figure 6A**, and the next four top fits are given in **Supplementary Figure 4**. Similar outputs were obtained in the top five ranked optimized models and all performed well in terms of capturing electrophysiological feature measurements (**Figure 5A**). *Cell 2* in particular had more difficulty with the "AHP_depth" electrophysiological feature, which is likely because the model failed to attain a high enough spike threshold, and thus the resulting "AHP_depths" were too low. While we tried to encourage the models to reach higher spike thresholds by allowing the sodium voltage dependencies to vary as free parameters in the optimizations (**Figure 5C**), in the end, the models could not fully capture the adaptation in spike threshold that was seen experimentally (i.e., the spike threshold appeared to increase during spiking at higher frequencies). These top models also had similar optimized parameter values (**Figures 5B,C**), though this may be a result of over-constraining the optimizations (see approach and parameter ranges in section Methods).

To ensure that the full spiking models did not affect the $I_h$ fits, we applied hyperpolarizing steps to the full spiking models as done experimentally, and found that they were in full agreement with the experimental data, as shown in **Supplementary Figure 5**. It was expected that adding the full set of ion channel mechanisms would not affect the model's ability to match the hyperpolarizing steps since the additional currents are not active at these hyperpolarized values. This can be appreciated by looking at the contributions from the different currents at the different current steps using "currentscapes," a novel visualization technique (Alonso and Marder, 2019). As

**TABLE 4 |** Final fitted model parameters using either $H_{dist} = 0$ or $H_{dist} = 1$.

| Parameter | Cell 1 | | Cell 2 | | Cell 3 | |
|---|---|---|---|---|---|---|
| | $H_{dist} = 0$ | $H_{dist} = 1$ | $H_{dist} = 0$ | $H_{dist} = 1$ | $H_{dist} = 0$ | $H_{dist} = 1$ |
| $R_a$ (Ωcm) | 34.4 | 125.2 | 285.4 | 348.1 | 211.8 | 317.9 |
| $C_m$ ($\mu$F/cm$^2$) | 0.20 | 0.27 | 0.37 | 0.38 | 0.52 | 0.58 |
| $G_{pas}$ (S/cm$^2$) | $7.36 \times 10^{-6}$ | $7.58 \times 10^{-6}$ | $1.16 \times 10^{-5}$ | $1.19 \times 10^{-5}$ | $8.26 \times 10^{-6}$ | $8.68 \times 10^{-6}$ |
| $E_{pas}$ (mV) | −64.0 | −64.6 | −61.5 | −61.8 | −75.7 | −76.1 |
| $E_h$ (mV) | −34.0 | −34.0 | −27.9 | −27.9 | −25.2 | −25.2 |
| $V_{1/2}$ (mV) | −103.1 | −103.7 | −100.6 | −99.6 | −108.4 | −113.8 |
| $k$ (mV) | 9.99 | 9.99 | 9.93 | 9.99 | 9.39 | 9.99 |
| $t_1$ (ms) | 12.30 | 8.56 | 12.73 | 11.28 | 36.77 | 41.84 |
| $t_2$ (ms) | 0.063 | 0.029 | 0.071 | 0.056 | 0.25 | 0.29 |
| $t_3$ (ms) | −22.87 | −6.91 | −20.38 | −19.28 | −3.22 | −4.03 |
| $t_4$ (ms) | 0.39 | 0.18 | 0.36 | 0.34 | 0.084 | 0.089 |
| $t_5$ (ms) | 0.026 | $4.35 \times 10^{-5}$ | $3.54 \times 10^{-6}$ | 0.006 | 5.69 | 4.29 |
| Total $G_h$ (nS) | 1.91 | 3.12 | 0.75 | 2.14 | 0.77 | 1.82 |
| (Expt) Total $G_h$ Cell 1 = 4.17 nS | | | | | | |
| (Expt) Total $G_h$ Cell 2 = 3.64 nS | | | | | | |
| (Expt) Total $G_h$ Cell 3 = 2.20 nS | | | | | | |

shown in **Figure 6B** it is clear that only $I_h$ and the leak current are active during the hyperpolarization steps, and not other ionic currents. In fact, contributions from all other currents during these hyperpolarization steps were minimized beyond being able to see them on the plots and outward current can become non-existent since the reversal potential for potassium is passed.

Taking advantage of our generated currentscapes (**Figure 6B**), we were able to easily observe several features in our optimized models. A prominent feature was the large contributions from A-type potassium currents during both the baseline periods as well as during spiking regime activities. Since we minimized slow delayed rectifier potassium conductances on purpose in order to achieve better fits (see section Methods and **Figure 5**), it was not surprising that the major contribution of outward currents during spikes was from fast delayed rectifier potassium ones. However, it was perhaps surprising that M-type and calcium-activated potassium currents provided such large contributions to outward currents, despite having considerably smaller conductances relative to the other outward ion channel types (**Figure 5**). Particularly, M-type exhibited larger current contributions during the after-hyperpolarization periods (AHP) at higher spike rates. In terms of inward current contributions, we did not see any observable contributions from the L-type and T-type calcium channel types. Mostly, inward current contributions in the spiking regimes were from sodium channels. However, $I_h$ provided some observable contributions during the spike recovery periods, and also provided a larger contribution leading up to the first spike.

We note that our goal was to obtain spiking models that could adequately capture the data for the particular cell, that is, starting idealized "base" models of OLM cells. These base models should be further explored for degeneracy and can be leveraged for additional insights and hypothesis generation moving forward (see section Methods). However, they represent the most comprehensive multi-compartment models of OLM cells to date, having been produced using morphologies and electrophysiological recordings obtained from the same biological OLM cells.

# DISCUSSION

In this work, we obtained a set of recordings from OLM cells in hippocampal CA1 that allowed us to explicitly link morphological, passive, and h-channel biophysical parameters within the same cell. From this set, we constructed three "next generation" experimentally constrained multi-compartment models of CA1 OLM cells. The models developed here are considered "next generation" in that, unlike all previous computational models of OLM cells (Skinner and Ferguson, 2018), we have here for the first time matched morphology and electrophysiology to characterize h-channels on an individual per-cell basis and, further, to constrain two full spiking models of OLM cells. At present, it is unknown whether OLM cells express h-channels on their dendrites. Our models predict that h-channels are not confined to the soma, but rather are expressed along the dendrites of OLM cells. Our models can be used in future studies to explore the synaptic and network consequences of dendritic h-channels on OLM cells within the context of hippocampal microcircuit function. Importantly, our work shows that it is possible to robustly characterize *dendritic* ion channels by tight interactions between multi-compartment model building and somatic electrophysiological recordings.

## OLM Cells: H-Channels and Hippocampal Microcircuit Operations

The existence of h-channels, mixed cation channels that activate with hyperpolarization, has long been known since

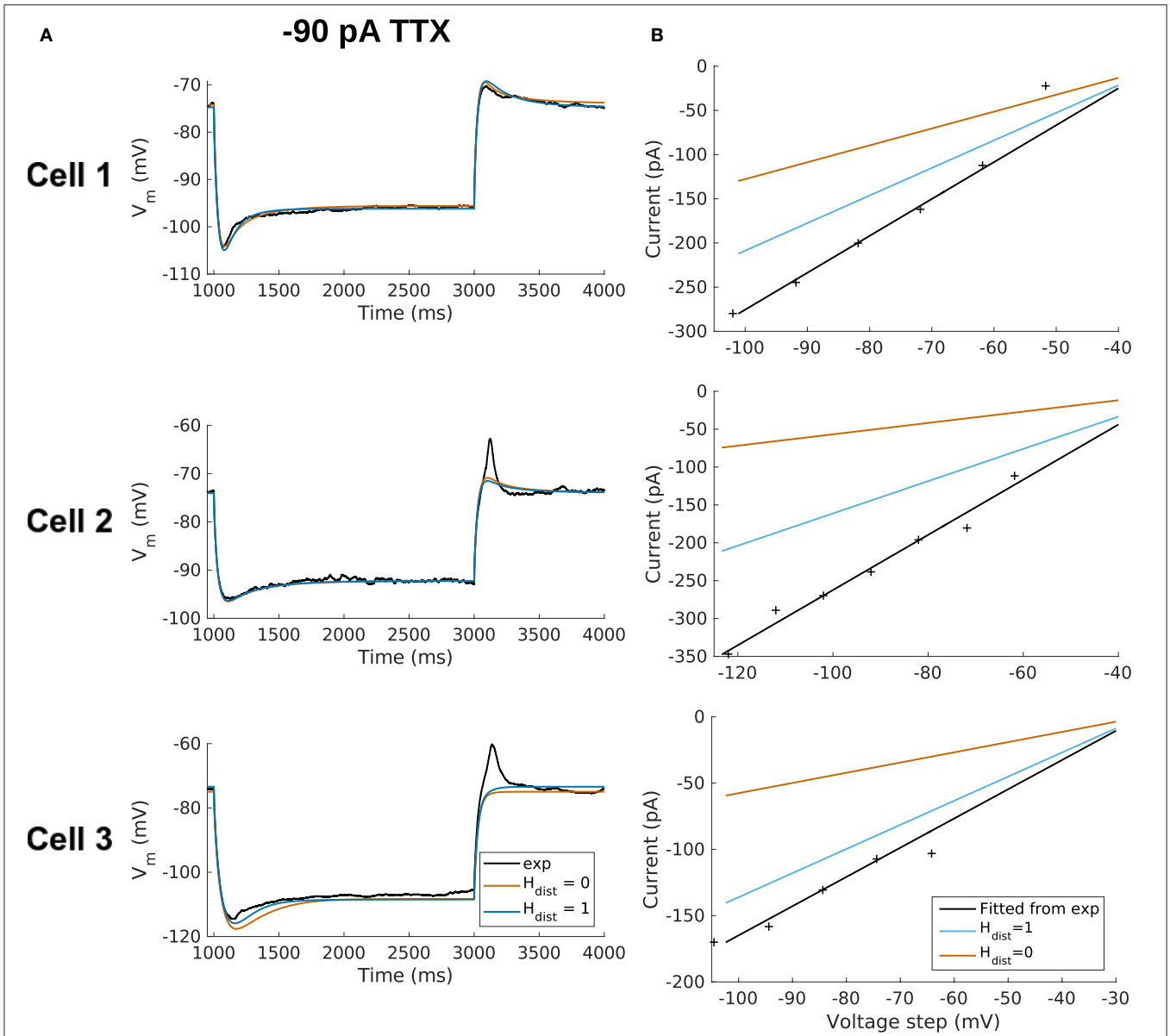


**FIGURE 4 |** OLM cell models with somatodendritic h-channels, but not somatic only, appropriately capture experimental data. **(A)** Using a staggered re-fitting, both $H_{dist} = 0$ or 1 are good fits to the experimental data. Note that the −90 pA TTX traces are "test" traces and were not used for fitting (−120 pA TTX used for fitting), $H_{dist} = 0$ or 1. **(B)** $H_{dist} = 1$ is clearly more appropriate than $H_{dist} = 0$ relative to the experimental data as shown in plotting I–V curves.

first discovered as "funny" currents in the heart (Brown et al., 1979), and in the CNS, they contribute to maintenance of the resting membrane potential, pacemaking ability, and synaptic integration (Magee, 1998; Lörincz et al., 2002; Biel et al., 2009). The contribution of h-channels in pyramidal cells to subthreshold resonance and spiking output features in hippocampus and cortex has been much studied (Santoro and Baram, 2003; Biel et al., 2009; Zemankovics et al., 2010; Narayanan and Johnston, 2012). In particular, it is known that the distribution of HCN1-containing channels increases from soma to distal dendrite and as such, have been shown to control the temporal summation of synaptic inputs from dendrites to soma (Magee, 1998; Vaidya and Johnston, 2013). However, h-channels in cerebellar Purkinje neurons are uniformly distributed in their dendrites and do not strongly affect temporal summation to the soma (Angelo et al., 2007). For interneurons, and OLM cells in particular, it is known that they express HCN channels, as seen by a large sag upon hyperpolarization (Maccaferri and McBain, 1996).

H-channels in OLM cells have been implicated in pacemaking and oscillatory activities of the hippocampus (Maccaferri and McBain, 1996; Gloveli et al., 2005), and theta (4–12 Hz) rhythms

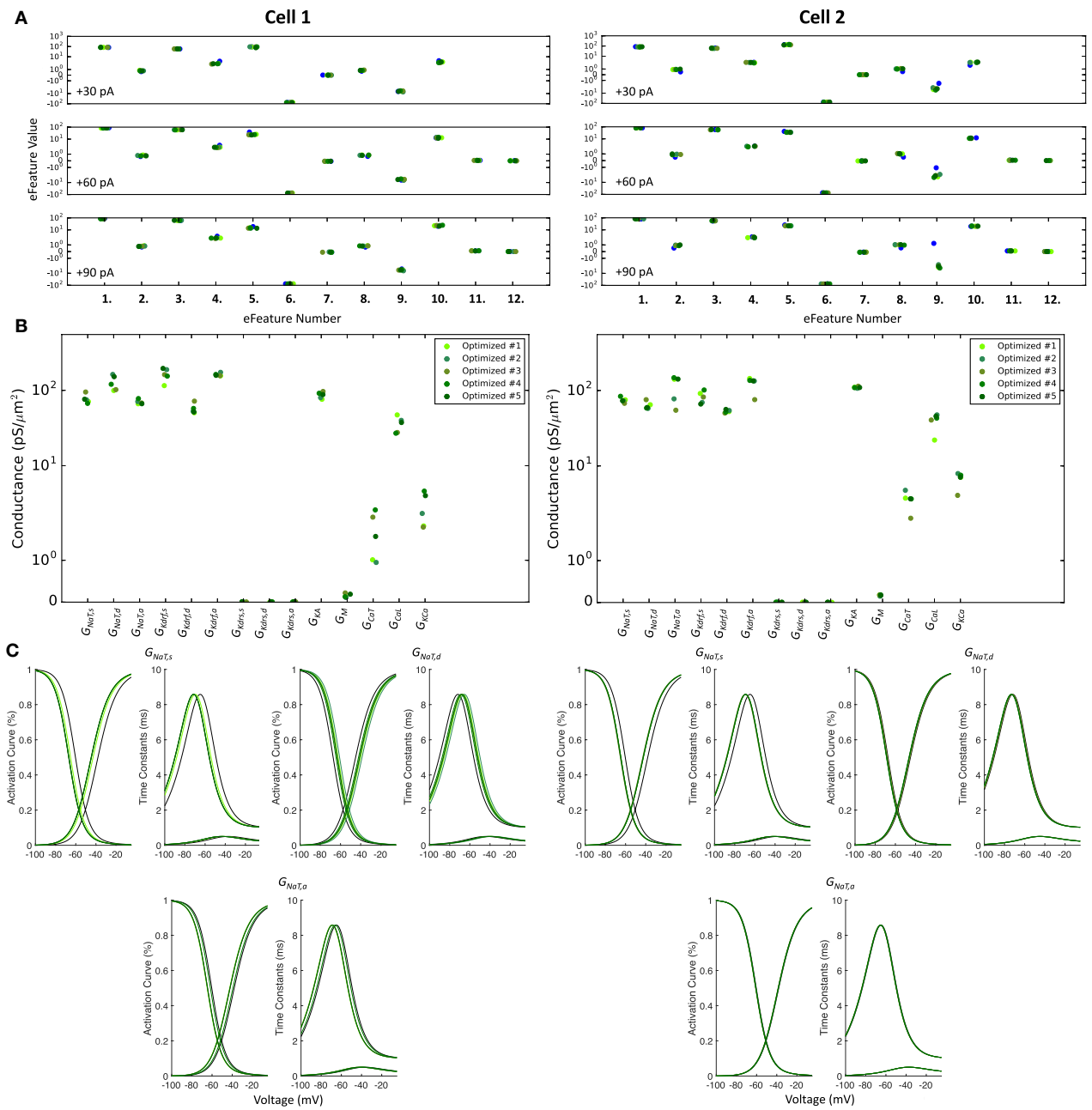


**FIGURE 5 |** Optimized spiking model features and parameters. **(A)** Measurements of objective e-features for each of the top five optimized models (shades of green) during the +30, +60, +90 pA current injection steps. Each number on the x-axis corresponds to an e-feature. For corresponding e-feature names and descriptions, see **Supplementary Table 3**. The corresponding target values obtained from the experimental data are shown as blue dots. **(B)** Optimized conductance values in the top five spiking models. **(C)** Voltage-dependency of somatic, dendritic, and axonal sodium channels were allowed to shift during the optimizations. Here we show the resulting voltage-dependent activation curves and time constants in the top five spiking models (shades of green) as compared to the activation curve used in previous instantiations of the OLM cell model (black curves). See section Methods for specific numbers.

in particular (Maccaferri and Lacaille, 2003; Rotstein et al., 2005). Subsequent experimental studies found that OLM cells did not have any preferred spiking frequency response to broadband artificial synaptic inputs (Kispersky et al., 2012). Kispersky et al. (2012) did find, however, that OLM cells exhibited a phase-locked spiking preference to theta frequency modulated inputs, but this spike resonance did not depend on h-channels. However, these frequency modulated synaptic inputs were delivered exclusively to the soma of OLM cells via dynamic clamp technology. Using computational model databases of OLM cells in the absence

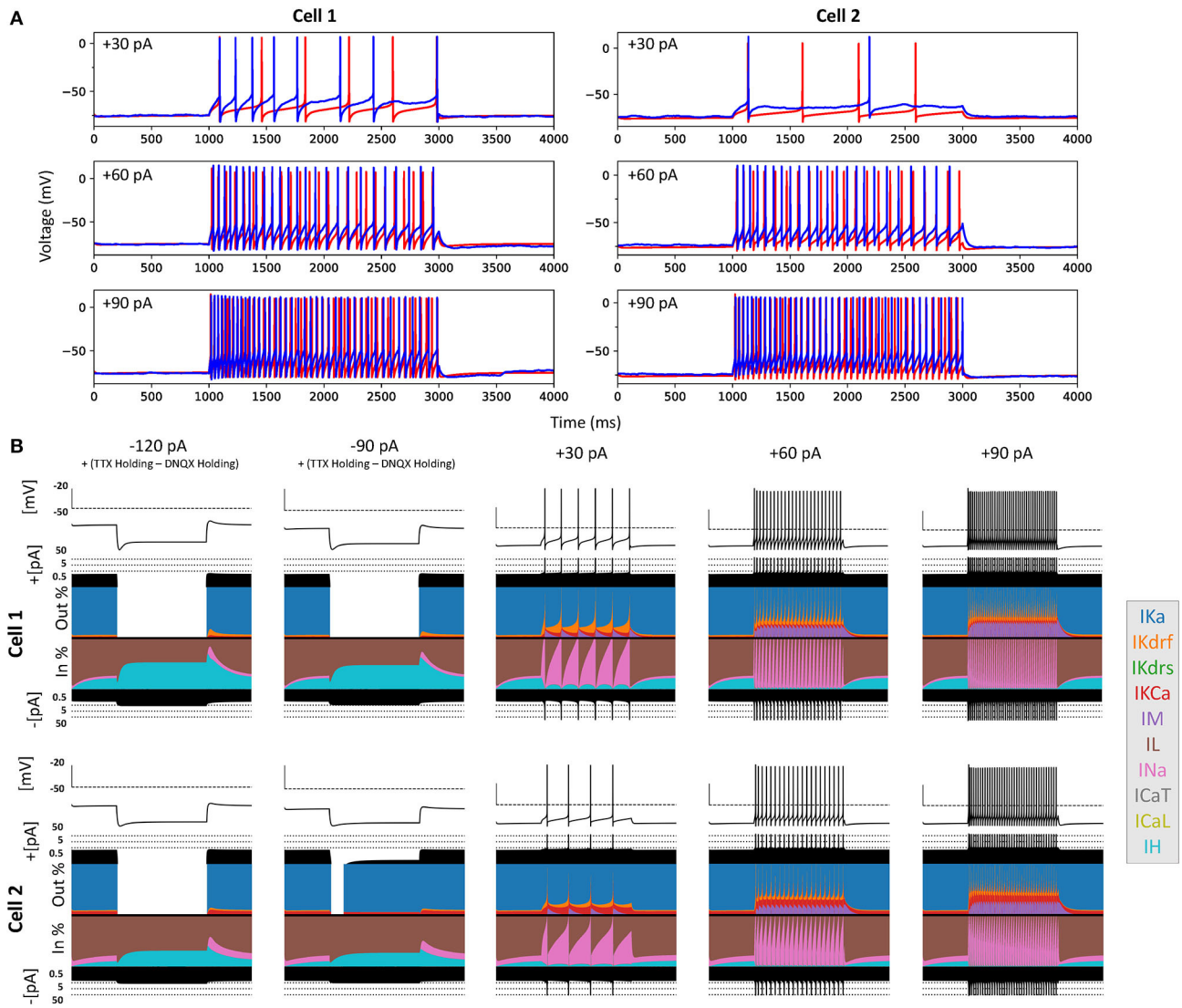


**FIGURE 6 |** Full spiking optimized OLM cell models and underlying currents. **(A)** The most highly ranked optimized models for *Cell 1* and *Cell 2* are plotted in red, and the experimental data is plotted in blue. Model parameters were optimized using depolarizing +30, +60, and +90 pA current step recordings from protocol #2 given in **Table 1**. **(B)** Currentscapes for top spiking models. Using −120, −90, +30, +60, and +90 pA current injection steps, the currentscape plots (Alonso and Marder, 2019) indicate the relative current contributions (i.e., the color areas in the plots) of the total inward or outward channel currents (i.e., black areas at the top and bottom of each currentscape plot). Note that the recordings shown here are from the first dendritic compartment adjacent to the soma since calcium channels are not present in the somatic compartment. During hyperpolarizing steps, it is evident from these plots that $I_h$ (IH) and the leak current (IL) are the primary contributors to the electrophysiological output. For depolarizing steps, we see the largest contributions are from A-type potassium current (IKa), fast delayed-rectifier current (IKdrf), sodium current (INa), and calcium-dependent potassium current (IKCa), with increasing contributions from M-type current (IM) as the current step magnitude gets larger. Slow delayed-rectifier current (IKdrs) contributes minimally.

or presence of h-channels in dendritic compartments revealed that OLM cells modeled to be in a simplified *in vivo*-like scenario could exhibit a theta frequency spiking resonance when inputs were delivered to their dendrites (Sekulić and Skinner, 2017). We further found that a high or low theta frequency spike resonance was possible and is respectively dependent on whether h-channels were present in the dendrites or not of the OLM cell models, reminiscent of Type 1 and 2 theta rhythms in the behaving animal (Kramis et al., 1975). Our modeling work examining dendritic distributions of h-channels in OLM cells found that the distributions could vary so long as total conductance was conserved (Sekulić et al., 2015), as was also found in Purkinje cells (Angelo et al., 2007). Thus a motivating factor in the present study was to constrain this extra "free parameter" by obtaining direct measurements of the total conductance in OLM cells. In doing this, we were able to show that our OLM cell models best matched the experimental data if h-channels are present in the dendrites. Interestingly, while

the total h-channel conductance ranged from 2.2–4.2 nS in the three cells that were fully analyzed (**Table 4**), the conductance density in each of the three cells is about 0.1 pS/$\mu$m$^2$, which is the value found in highly ranked OLM cell models from our previously developed model databases (Sekulić et al., 2014; Sekulić and Skinner, 2017). Zemankovics et al. (2010) obtained total conductance values averaging approximately 4 nS, which are near the upper limit of our measurements. However, total h-channel conductance values were obtained in OLM cells in rat, which had a two-fold larger measured capacitance (208 pF) than our mouse OLM cells (107 pF). Therefore, given the difference in measured surface area between rat and mouse, our data is in accordance with this previous study. Compared with Maccaferri and McBain (1996) and Zemankovics et al. (2010) who obtained, respectively, mean reversal potentials of −32.9 and −37 mV, activation curves with mean half-activation voltages ($V_{1/2}$) of −84.1 and −97.7 mV, and slope factors ($k$) of −10.2 and −8.9 mV, our reversal potentials ranged from −25.2 to −34 mV, with model $V_{1/2}$ fits of −99.6 to −113.8 mV, and $k$ of −9.99 mV (**Table 4**). The voltage-dependence of the time constant yielded fits that were different but with overlapping values for the three cells (**Figure 3C**). A direct comparison of steady-state activation and voltage-dependent time constants in previous and present models are provided in **Supplementary Figure 3C**.

It has been proposed that OLM cells play a gating role (Leão et al., 2012), akin to earlier work by Blasco-Ibáñez and Freund (1995) who showed that "horizontal interneurons" (i.e., putative OLM cells) could act as a switch controlling activation of local pyramidal cells via Schaeffer collaterals or perforant path input from entorhinal cortex. Further work has shown that OLM cells in intermediate regions of CA1 exert a bidirectional control on learning and memory (Siwani et al., 2018), and ventral OLM cells control Type 2 theta rhythms and are associated with increased risk-taking (Mikulovic et al., 2018). In a recent modeling study, OLM cells were shown to be critical in producing a robust intrinsic theta output (Chatzikalymniou and Skinner, 2018), which suggests that their neuromodulation may be key to the maintenance of theta rhythms.

In building our next generation OLM cell models using morphological and electrophysiological data from the same cell, we were able to robustly show, and thus predict, the presence of h-channels in the dendrites of OLM cells. In doing this, it was critically important that the experimental data came from the same cell. OLM cells have been discovered to be comprised of parvalbumin- and 5-HT$_{3A}$ receptor subtypes (Chittajallu et al., 2013). With the advent of sophisticated genetic sequencing techniques (Harris et al., 2018; Cembrowski and Spruston, 2019), additional OLM cell subtypes can be recognized. It has been found that CA1 pyramidal cells have a continuous, rather than discrete, variation on the longitudinal axis of the hippocampus, indicating this as an organizational principle (Cembrowski et al., 2016), and structural-functional correlations are apparent for ventral, intermediate and dorsal regions of the long axis (Fanselow and Dong, 2010). Given this observation, it is interesting to note that *Cell 1* and *Cell 2* from an intermediate CA1 region have more similar characteristics than *Cell 3* which is from a more ventral CA1 region (see **Figure 2**). This suggests that hippocampal CA1 interneurons may also exhibit gradients in channel, morphology, or physiological features along the hippocampal longitudinal axis, although further study is needed to verify this.

## Exposing and Exploiting Limitations in Experiments and Multi-Compartment Model Development, and a "Cycling" Strategy

It was initially unexpected that a model with fitted passive properties and morphologies obtained in conjunction with h-channel parameters extracted from the same cell did not capture corresponding experimental voltage traces (**Figure 3A**). To explain why this may be the case, some general issues in building multi-compartment models directly from limited experimental data need to be considered.

In an attempt to constrain as many distinct parameters within the same cell as possible, we deliberately sacrificed depth for breadth so that practical choices were inevitable in the distribution of efforts. Thus the quality of the passive and h-channel data obtained from experimentally recorded OLM cells was not optimal. For example, there are inherent limitations to cell stability that require rapid succession through a sequence of experimental protocols (**Table 1**). In our hands, the limit of stability was approximately 30 min. In this time, we were able to obtain recordings, bath changes, and biocytin fills that allowed us to do reconstructions, and obtain passive property and h-channel biophysical properties, but having several protocols prevented multiple sweeps of any given protocol. The I–V relation for determining maximum conductance and reversal potential was not always linear across all voltage steps, as required from theoretical perspectives in the mathematical model formulations. Furthermore, there was some error associated with fitting the Boltzmann function describing the steady-state activation curves to all data points obtained from the h-channel activation protocol. Indeed, due to inherent biological variability and experimental constraints, some measure of error is expected whenever experimental data is fitted to theoretical or mathematical models, such as a Boltzmann function for the activation curves, or a dual exponential function for the time constant of activation. Accordingly, although we obtained the requisite experimental data for fully characterizing h-channels and fitting to mathematical models of them, we should not expect that the resulting parameters will necessarily result in fully appropriate cellular output when initially used. That is, even when inserted into multi-compartment models built of the same cells from which the h-channel characteristics were obtained, there may be error in the resulting model's $V_m$'s output compared to that of the experimental recordings. In essence, this is due to the accumulation of errors in estimating the various parameters used, and is compounded with increasing number of experimentally-constrained parameters in the model.

To overcome this, we found that an approach of a staggered re-fitting of the parameters in the model was able to produce generalizable results so that the $V_m$ output could match all of the experimental traces including those for which it was not specifically optimized. This approach can be thought of as correcting for errors in the procedures for extracting the

parameter values from the experimental data. Having many recordings from the same cell allowed us to do a staggered re-fitting of model parameters that avoided overfitting and allowed validation (see Appendix 2 in **Supplementary Material**), as well as consideration of the voltage dependence of h-channel activation time constants. It may be possible to use more sophisticated optimization schemes to obtain generalized fits, but the challenge of fitting detailed multi-compartment models with many parameters to experimental data is recognized, and has led to use of two-stage fitting processes (Roth and Bahl, 2009; Hay et al., 2011). We note that our staggered re-fitting can be considered as a form of two-stage fitting where in our situation, we determined how to proceed with the re-fitting stages based on how robust the experimental recordings were considered to be.

Clearly, it is important to keep in mind what one's goal(s) are in the building of a multi-compartment model in the first place. Without making some simplifying assumptions, such as uniform passive properties, and having constraining experimental data, we are necessarily faced with the curse of dimensionality (Almog and Korngreen, 2016). In our original multi-compartment models of OLM cells (Saraga et al., 2003), we were motivated to include dendrites because of clear evidence of highly active dendrites (Martina et al., 2000) in OLM cells. Moving forward, we expanded the extent of ion channels present in the models when experimental data specific to M-channels in OLM cells was available (Lawrence et al., 2006). A key notion in experimentally-constrained computational modeling is that the models are never complete. A reciprocal transfer of knowledge between model and experiment where experimental data is used to constrain models which, in turn, both point out gaps in our understanding of the underlying cellular neurophysiology as well as generate hypotheses, refine protocols, and consider additional measurable parameters that can then be incorporated into future model revisions.

A particular conceptualization of the role of computational modeling in neuroscience is to help resolve, or at least reframe, these basic concerns of how "realistic" detailed models can be. Rather than the idea of obtaining a detailed model as a crystallized end point of any given study, we consider the role of the detailed modeling as an integral component of a cyclical process of knowledge generation in neuroscience. We have expressed this as an experiment-modeling cycling approach (Sekulić and Skinner, 2018) and we consider that an essential goal in multi-compartment modeling is the back-and-forth cycling between experiments and models that leads to continual refinement of the model relative to the biological cell, thus allowing for the generation of predictions for further experiments.

## Limitations and Future Work

Although doing more than three full reconstructions, analysis and multi-compartment model building may be desirable, we felt that consistently obtaining best matches with dendritic h-channels in all three of our models when fit with data from the same cell was enough to allow for predictions as to dendritic expression of h-channels in OLM cells. Also, we focused on uniform h-channel distribution in the dendrites since our starting models using either no h-channels or h-channels fully and uniformly distributed in the dendrites did not match the experimental data (**Figure 3A**). Considering distributions that were not uniformly distributed (e.g., distributed only in proximal dendrites) would be unlikely to capture the data given that the total h-channel conductance would remain the same. It is also possible that decreasing or increasing conductance density distributions may be present in the dendrites, but this was not specifically explored here as additional parameters to fit would be required (see previous computational explorations in Sekulić et al., 2015), which could confound the staggered re-fitting process. Indeed, a limitation of the electrophysiological data is that our recordings were somatic. Due to the relatively compact nature of OLM cell dendrites, this is not a major limitation unlike what it may be for pyramidal cells which have extended dendritic trees. Specifically, looking at attenuation in the OLM cell models as well as previous work (Lawrence et al., 2006), space clamp is expected to be good up to at least 100 $\mu$m. Placing h-channels only in the soma failed to capture the experimental results. In the end, we obtained a strong prediction of h-channels being present in the dendrites since all three individual model fits supported this interpretation, indicating the robustness of our staggered re-fitting procedure.

Our development of full spiking OLM cell models here, as based on *Cell 1* and *Cell 2*, are available for future use. In particular, it would be interesting to use currentscape visualization analyses (Alonso and Marder, 2019) to help disentangle the interacting dynamics, perhaps using it to direct how one might best reduce the model complexity to allow dynamical system analyses to be applied, as well as applying sensitivity analysis techniques such as `uncertainpy` (Tennøe et al., 2018). In turn, this could help decipher how OLM cells preferentially respond to different theta frequencies based on their biophysical profile as shown in our previous computational models (Sekulić and Skinner, 2017). Further, these models now provide a foundation or canonical start for the creation of new databases designed to address specific biophysical questions as done in our original database that was developed to ask whether h-channels were present in the dendrites (Sekulić et al., 2014). Interestingly, co-regulation of h-channels and A-type channels are apparent in the currentscapes (see **Figure 6B**) as was observed in our original OLM cell databases.

A discrepancy between model and experimental outputs has to do with the post-inhibitory rebound responses in *Cell 2* and *Cell 3*. These rebound responses are unlikely to be solely due to $I_h$ as the models with only $I_h$ do not capture this aspect in *Cell 2* or *Cell 3* for example (see **Figure 3C**). This indicates that other currents such as T-type calcium currents that were not blocked (see **Table 1**) are contributing to rebound responses in *Cell 2* and *Cell 3*, but less so for *Cell 1*. Given that calcium currents, calcium-activated potassium currents and calcium handling aspects in previous OLM cell models did not have any direct experimental data constraints (Lawrence et al., 2006), we elected not to focus on calcium specifics here, but rather on the spiking activities with the existing current models and adjusting only the maximal conductance values, as described in detail in the Methods. Preliminary simulations with *Cell 2* indicates that increases in T-type calcium conductances on its own can produce rebound spikes, but this necessarily makes

other spiking features inappropriate. For the models to more fully capture electrophysiological responses, one could consider using these models to build new model populations, but now with calcium currents rather than $I_h$ as the focused question (Sekulić and Skinner, 2018). It would also be helpful to acquire data on axonal properties of OLM cells beyond Martina et al. (2000) to figure out their properties, and new theoretical insights could perhaps be harnessed (Goethals and Brette, 2020).

We have previously shown that using virtual networks, or creating *in vivo*-like representations with multi-compartment cellular models, as done with our earlier OLM cell models (Sekulić and Skinner, 2017), can lead to insights of circuit function from cellular specifics. Further, we have now used the current OLM cell models to do detailed, dendritic explorations of ion channel dynamics that would not be possible to do experimentally (Guet-McCreight and Skinner, 2020). We have also created *in vivo*-like states with interneuron-specific interneuron models (Guet-McCreight and Skinner, 2019), and used them to make links between *in vitro* and *in vivo* studies (Luo et al., 2020). In essence, it seems possible that an understanding of the contribution of biophysical cellular details to circuits in the behaving animal can emerge by using virtual networks.

In a review, Almog and Korngreen (2016) demonstrate the limitations associated with the re-usability of layer 5 pyramidal cell models, and also state that there is a need for proving that multi-compartment models are valid within the context of network simulations. These are challenging issues to consider but an important step that they suggest is to ensure that models are linked with the experimental data. Along these lines, neuroinformatic tool developments (e.g., Nexus—https://bluebrainnexus.io) can help reduce the workload.

In conclusion, our work has shown that if the development of multi-compartment models are done for a specific cell type in which ion channel characterization and morphological and passive data can be obtained from the same cell, it is possible to determine their ion channel distribution and biophysical characterization from somatic recordings alone. In this way, one can envisage doing this in a cyclic fashion to characterize other ion channel types and distributions that are unknown.

## DATA AVAILABILITY STATEMENT

The datasets presented in this study can be found in online repositories. The names of the repository/repositories and accession number(s) can be found below: NEURON code for all the models are available at: https://github.com/FKSkinnerLab/OLMng and associated experimental data available at: https://osf.io/qvnu9/.

## ETHICS STATEMENT

The animal study was reviewed and approved by University of Montana, Texas Tech University.

## AUTHOR CONTRIBUTIONS

FS: conceptualization, resources, supervision, funding acquisition, validation, writing–original draft, project administration, writing–review, and editing. VS: conceptualization, resources, data curation, software, formal analysis, validation, investigation, visualization, methodology, writing–original draft, project administration, writing–review, and editing. JL: conceptualization, resources, supervision, funding acquisition, writing–original draft, project administration, writing–review, and editing. AG-M: conceptualization, software, formal analysis, investigation, visualization, methodology, writing–original draft, writing–review, and editing. FY and TG: conceptualization, data curation, formal analysis, investigation, writing–review, and editing. All authors contributed to the article and approved the submitted version.

## FUNDING

This work was supported by Natural Sciences and Engineering Research Council of Canada (NSERC) Discovery Grant: RGPIN-2016-06182 (FS); National Institutes of Health (NIH): R01 NS069689 (JL), NS069689-03S1 (TG); South Plains Foundation (JL). The funders had no role in study design, data collection and analysis, decision to publish, or preparation of the manuscript. P20RR015583, P20RR017670, and P20GM10356 grants supported confocal imaging core facilities and the Bitplane Imaris license.

## ACKNOWLEDGMENTS

Preliminary studies of this work have appeared in the form of several published Society for Neuroscience poster abstracts. FKS thanks Dr. Scott Rich for an overall reading of this work. This manuscript has been released as a pre-print at Sekulić et al. (2019).

## SUPPLEMENTARY MATERIAL

The Supplementary Material for this article can be found online at: https://www.frontiersin.org/articles/10.3389/fncel.2020.00277/full#supplementary-material

## REFERENCES

Abbas, A. I., Sundiang, M. J. M., Henoch, B., Morton, M. P., Bolkan, S. S., Park, A. J., et al. (2018). Somatostatin interneurons facilitate hippocampal-prefrontal synchrony and prefrontal spatial encoding. *Neuron* 100, 926–939.e3. doi: 10.1016/j.neuron.2018.09.029

Almog, M., and Korngreen, A. (2016). Is realistic neuronal modeling realistic? *J. Neurophysiol.* 116, 2180–2209. doi: 10.1152/jn.00360.2016

Alonso, L. M., and Marder, E. (2019). Visualization of currents in neural models with similar behavior and different conductance densities. *eLife* 8, 1–28. doi: 10.7554/eLife.42722

Angelo, K., London, M., Christensen, S. R., and Hausser, M. (2007). Local and global effects of IH distribution in dendrites of mammalian neurons. *J. Neurosci.* 27, 8643–8653. doi: 10.1523/JNEUROSCI.5284-06.2007

Bassett, D. S., Zurn, P., and Gold, J. I. (2018). On the nature and use of models in network neuroscience. *Nat. Rev. Neurosci.* 19, 566–578. doi: 10.1038/s41583-018-0038-8

Biel, M., Wahl-Schott, C., Michalakis, S., and Zong, X. (2009). Hyperpolarization-activated cation channels: from genes to function. *Physiol. Rev.* 89, 847–885. doi: 10.1152/physrev.00029.2008

Bischofberger, J., Engel, D., Li, L., Geiger, J. R., and Jonas, P. (2006). Patch-clamp recording from mossy fiber terminals in hippocampal slices. *Nat. Protoc.* 1, 2075–2081. doi: 10.1038/nprot.2006.312

Blasco-Ibáñez, J. M., and Freund, T. F. (1995). Synaptic input of horizontal interneurons in stratum Oriens of the hippocampal CA1 subfield: structural basis of feed-back activation. *Eur. J. Neurosci.* 7, 2170–2180. doi: 10.1111/j.1460-9568.1995.tb00638.x

Brown, H. F., Difrancesco, D., and Noble, S. J. (1979). How does adrenaline accelerate the heart? *Nature* 280:235. doi: 10.1038/280235a0

Bucher, D., Prinz, A. A., and Marder, E. (2005). Animal-to-animal variability in motor pattern production in adults and during growth. *J. Neurosci.* 25, 1611–1619. doi: 10.1523/JNEUROSCI.3679-04.2005

Cardin, J. A. (2018). Inhibitory interneurons regulate temporal precision and correlations in cortical circuits. *Trends Neurosci.* 41, 689–700. doi: 10.1016/j.tins.2018.07.015

Cembrowski, M., Bachman, J., Wang, L., Sugino, K., Shields, B., and Spruston, N. (2016). Spatial gene-expression gradients underlie prominent heterogeneity of CA1 pyramidal neurons. *Neuron* 89, 351–368. doi: 10.1016/j.neuron.2015.12.013

Cembrowski, M. S., and Spruston, N. (2019). Heterogeneity within classical cell types is the rule: lessons from hippocampal pyramidal neurons. *Nat. Rev. Neurosci.* 20, 193–204. doi: 10.1038/s41583-019-0125-5

Chatzikalymniou, A. P., and Skinner, F. K. (2018). Deciphering the contribution of oriens-lacunosum/moleculare (OLM) cells to intrinsic $\theta$ rhythms using biophysical local field potential (LFP) models. *eNeuro* 5, 1–24. doi: 10.1523/ENEURO.0146-18.2018

Chittajallu, R., Craig, M. T., Ashley, M., Yuan, X., Gerfen, S., Tricoire, L., et al. (2013). Dual origins of functionally distinct O-LM interneurons revealed by differential 5-HT3AR expression. *Nat. Neurosci.* 16, 1598–1607. doi: 10.1038/nn.3538

Cutsuridis, V., Graham, B., Cobb, S., and Vida, I. (2010). *Hippocampal Microcircuits: A Computational Modeler's Resource Book, 1st Edn*. New York, NY: Springer. doi: 10.1007/978-1-4419-0996-1

Dougherty, K. A., Nicholson, D. A., Diaz, L., Buss, E. W., Neuman, K. M., Chetkovich, D. M., et al. (2013). Differential expression of HCN subunits alters voltage-dependent gating of h-channels in CA1 pyramidal neurons from dorsal and ventral hippocampus. *J. Neurophysiol.* 109, 1940–1953. doi: 10.1152/jn.00010.2013

Ecker, J. R., Geschwind, D. H., Kriegstein, A. R., Ngai, J., Osten, P., Polioudakis, D., et al. (2017). The BRAIN initiative cell census consortium: lessons learned toward generating a comprehensive brain cell Atlas. *Neuron* 96, 542–557. doi: 10.1016/j.neuron.2017.10.007

Emmenlauer, M., Ronneberger, O., Ponti, A., Schwarb, P., Griffa, A., Filippi, A., et al. (2009). XuvTools: free, fast and reliable stitching of large 3d datasets. *J. Microsc.* 233, 42–60. doi: 10.1111/j.1365-2818.2008.03094.x

Fanselow, M. S., and Dong, H.-W. (2010). Are the dorsal and ventral hippocampus functionally distinct structures? *Neuron* 65, 7–19. doi: 10.1016/j.neuron.2009.11.031

Gentet, L. J., Stuart, G. J., and Clements, J. D. (2000). Direct measurement of specific membrane capacitance in neurons. *Biophys. J.* 79, 314–320. doi: 10.1016/S0006-3495(00)76293-X

Giovannetti, E. A., and Fuhrmann, M. (2019). Unsupervised excitation: GABAergic dysfunctions in Alzheimer's disease. *Brain Res.* 1707, 216–226. doi: 10.1016/j.brainres.2018.11.042

Gloveli, T., Dugladze, T., Rotstein, H. G., Traub, R. D., Monyer, H., Heinemann, U., et al. (2005). Orthogonal arrangement of rhythm-generating microcircuits in the hippocampus. *Proc. Natl. Acad. Sci. U.S.A.* 102, 13295–13300. doi: 10.1073/pnas.0506259102

Goaillard, J.-M., Taylor, A. L., Schulz, D. J., and Marder, E. (2009). Functional consequences of animal-to-animal variation in circuit parameters. *Nat. Neurosci.* 12, 1424–1430. doi: 10.1038/nn.2404

Goethals, S., and Brette, R. (2020). Theoretical relation between axon initial segment geometry and excitability. *eLife* 9:e53432. doi: 10.7554/eLife.53432

Golowasch, J., Goldman, M. S., Abbott, L. F., and Marder, E. (2002). Failure of averaging in the construction of a conductance-based neuron model. *J. Neurophysiol.* 87, 1129–1131. doi: 10.1152/jn.00412.2001

Guet-McCreight, A., and Skinner, F. K. (2019). Using computational models to predict *in vivo* synaptic inputs to interneuron specific 3 (IS3) cells of CA1 hippocampus that also allow their recruitment during rhythmic states. *PLoS ONE* 14:e0209429. doi: 10.1371/journal.pone.0209429

Guet-McCreight, A., and Skinner, F. K. (2020). Computationally going where experiments cannot: a dynamical assessment of dendritic ion channel currents during *in vivo*-like states. *F1000Research* 9:180. doi: 10.12688/f1000research.22584.2

Harris, K. D., Hochgerner, H., Skene, N. G., Magno, L., Katona, L., Gonzales, C. B., et al. (2018). Classes and continua of hippocampal CA1 inhibitory neurons revealed by single-cell transcriptomics. *PLoS Biol.* 16:e2006387. doi: 10.1371/journal.pbio.2006387

Hay, E., Hill, S., Schürmann, F., Markram, H., and Segev, I. (2011). Models of neocortical layer 5b pyramidal cells capturing a wide range of dendritic and perisomatic active properties. *PLoS Comput. Biol.* 7:e1002107. doi: 10.1371/journal.pcbi.1002107

Hilscher, M. M., Nogueira, I., Mikulovic, S., Kullander, K., Leão, R. N., and Leão, K. E. (2019). Chrna2-OLM interneurons display different membrane properties and h-current magnitude depending on dorsoventral location. *Hippocampus* 29, 1224–1237. doi: 10.1002/hipo.23134

Hines, M. L., and Carnevale, N. T. (2001). NEURON: a tool for neuroscientists. *Neuroscientist* 7, 123–135. doi: 10.1177/107385840100700207

Holmes, R. W. (2010). "Passive cable modeling," in *Computational Modeling Methods for Neuroscientists*, ed E. De Schutter (Cambridge, MA: MIT Press), 233–258. doi: 10.7551/mitpress/9780262013277.003.0011

Holmes, W. R., Ambros-Ingerson, J., and Grover, L. M. (2006). Fitting experimental data to models that use morphological data from public databases. *J. Comput. Neurosci.* 20, 349–365. doi: 10.1007/s10827-006-7189-8

Katona, L., Lapray, D., Viney, T. J., Oulhaj, A., Borhegyi, Z., Micklem, B. R., et al. (2014). Sleep and movement differentiates actions of two types of somatostatin-expressing GABAergic interneuron in rat hippocampus. *Neuron.* 82, 872–886. doi: 10.1016/j.neuron.2014.04.007

Kepecs, A., and Fishell, G. (2014). Interneuron cell types are fit to function. *Nature* 505, 318–326. doi: 10.1038/nature12983

Kispersky, T. J., Fernandez, F. R., Economo, M. N., and White, J. A. (2012). Spike resonance properties in hippocampal O-LM cells are dependent on refractory dynamics. *J. Neurosci.* 32, 3637–3651. doi: 10.1523/JNEUROSCI.1361-11.2012

Klausberger, T. (2009). GABAergic interneurons targeting dendrites of pyramidal cells in the CA1 area of the hippocampus. *Eur. J. Neurosci.* 30, 947–957. doi: 10.1111/j.1460-9568.2009.06913.x

Klausberger, T., Magill, P. J., Márton, L. F., Roberts, J. D. B., Cobden, P. M., Buzsáki, G., et al. (2003). Brain-state- and cell-type-specific firing of hippocampal interneurons *in vivo*. *Nature* 421, 844–848. doi: 10.1038/nature01374

Klausberger, T., and Somogyi, P. (2008). Neuronal diversity and temporal dynamics: the unity of hippocampal circuit operations. *Science* 321, 53–57. doi: 10.1126/science.1149381

Kopell, N. J., Gritton, H. J., Whittington, M. A., and Kramer, M. A. (2014). Beyond the connectome: the dynome. *Neuron* 83, 1319–1328. doi: 10.1016/j.neuron.2014.08.016

Kramis, R., Vanderwolf, C. H., and Bland, B. H. (1975). Two types of hippocampal rhythmical slow activity in both the rabbit and the rat: relations to behavior and effects of atropine, diethyl ether, urethane, and pentobarbital. *Exp. Neurol.* 49, 58–85. doi: 10.1016/0014-4886(75)90195-8

Lawrence, J. J., Saraga, F., Churchill, J. F., Statland, J. M., Travis, K. E., Skinner, F. K., et al. (2006). Somatodendritic Kv7/KCNQ/M channels control interspike interval in hippocampal interneurons. *J. Neurosci.* 26, 12325–12338. doi: 10.1523/JNEUROSCI.3521-06.2006

Leão, R. N., Mikulovic, S., Leão, K. E., Munguba, H., Gezelius, H., Enjin, A., et al. (2012). OLM interneurons differentially modulate CA3 and

entorhinal inputs to hippocampal CA1 neurons. *Nat. Neurosci.* 15, 1524–1530. doi: 10.1038/nn.3235

Lörincz, A., Notomi, T., Tamás, G., Shigemoto, R., and Nusser, Z. (2002). Polarized and compartment-dependent distribution of HCN1 in pyramidal cell dendrites. *Nat. Neurosci.* 5, 1185–1193. doi: 10.1038/nn962

Lovett-Barron, M., Kaifosh, P., Kheirbek, M. A., Danielson, N., Zaremba, J. D., Reardon, T. R., et al. (2014). Dendritic inhibition in the hippocampus supports fear learning. *Science* 343, 857–863. doi: 10.1126/science.1247485

Luo, L., Callaway, E. M., and Svoboda, K. (2018). Genetic dissection of neural circuits: a decade of progress. *Neuron* 98, 256–281. doi: 10.1016/j.neuron.2018.03.040

Luo, X., Guet-McCreight, A., Villette, V., Francavilla, R., Marino, B., Chamberland, S., et al. (2020). Synaptic mechanisms underlying the network state-dependent recruitment of VIP-expressing interneurons in the CA1 hippocampus. *Cereb. Cortex*. 30, 3667–3685. doi: 10.1093/cercor/bhz334

Maccaferri, G., David, J., Roberts, B., Szucs, P., Cottingham, C. A., and Somogyi, P. (2000). Cell surface domain specific postsynaptic currents evoked by identified GABAergic neurones in rat hippocampus *in vitro*. *J. Physiol.* 524, 91–116. doi: 10.1111/j.1469-7793.2000.t01-3-00091.x

Maccaferri, G., and Lacaille, J.-C. (2003). Interneuron diversity series: hippocampal interneuron classifications? making things as simple as possible, not simpler. *Trends Neurosci.* 26, 564–571. doi: 10.1016/j.tins.2003.08.002

Maccaferri, G., and McBain, C. J. (1996). The hyperpolarization-activated current (Ih) and its contribution to pacemaker activity in rat CA1 hippocampal stratum oriens-alveus interneurones. *J. Physiol.* 497(Pt 1), 119–130. doi: 10.1113/jphysiol.1996.sp021754

Magee, J. C. (1998). Dendritic hyperpolarization-activated currents modify the integrative properties of hippocampal CA1 pyramidal neurons. *J. Neurosci.* 18, 7613–7624. doi: 10.1523/JNEUROSCI.18-19-07613.1998

Marder, E., and Goaillard, J.-M. (2006). Variability, compensation and homeostasis in neuron and network function. *Nat. Rev. Neurosci.* 7, 563–574. doi: 10.1038/nrn1949

Marder, E., and Taylor, A. L. (2011). Multiple models to capture the variability in biological neurons and networks. *Nat. Neurosci.* 14, 133–138. doi: 10.1038/nn.2735

Marín, O. (2012). Interneuron dysfunction in psychiatric disorders. *Nat. Rev. Neurosci.* 13, 107–120. doi: 10.1038/nrn3155

Martina, M., Vida, I., and Jonas, P. (2000). Distal initiation and active propagation of action potentials in interneuron dendrites. *Science* 287, 295–300. doi: 10.1126/science.287.5451.295

Matt, L., Michalakis, S., Hofmann, F., Hammelmann, V., Ludwig, A., Biel, M., et al. (2011). HCN2 channels in local inhibitory interneurons constrain LTP in the hippocampal direct perforant path. *Cell. Mol. Life Sci.* 68, 125–137. doi: 10.1007/s00018-010-0446-z

Mikulovic, S., Restrepo, C. E., Siwani, S., Bauer, P., Pupe, S., Tort, A. B. L., et al. (2018). Ventral hippocampal OLM cells control type 2 theta oscillations and response to predator odor. *Nat. Commun.* 9:3638. doi: 10.1038/s41467-018-05907-w

Molleman, A. (2003). *Patch Clamping: An Introductory Guide to Patch Clamp Electrophysiology*. New York, NY: John Wiley & Sons. doi: 10.1002/0470856521

Müller, C., and Remy, S. (2014). Dendritic inhibition mediated by O-LM and bistratified interneurons in the hippocampus. *Front. Synapt. Neurosci.* 6:23. doi: 10.3389/fnsyn.2014.00023

Myatt, D., Hadlington, T., Ascoli, G., and Nasuto, S. (2012). Neuromantic from semi-manual to semi-automatic reconstruction of neuron morphology. *Front. Neuroinform.* 6:4. doi: 10.3389/fninf.2012.00004

Narayanan, R., and Johnston, D. (2012). Functional maps within a single neuron. *J. Neurophysiol.* 108, 2343–2351. doi: 10.1152/jn.00530.2012

O'Leary, T., Sutton, A. C., and Marder, E. (2015). Computational models in the age of large datasets. *Curr. Opin. Neurobiol.* 32, 87–94. doi: 10.1016/j.conb.2015.01.006

Rall, W., Burke, R. E., Holmes, W. R., Jack, J. J., Redman, S. J., and Segev, I. (1992). Matching dendritic neuron models to experimental data. *Physiol. Rev.* 72(Suppl. 4), S159–S186. doi: 10.1152/physrev.1992.72.suppl_4.S159

Ransdell, J. L., Nair, S. S., and Schulz, D. J. (2013). Neurons within the same network independently achieve conserved output by differentially balancing variable conductance magnitudes. *J. Neurosci.* 33, 9950–9956. doi: 10.1523/JNEUROSCI.1095-13.2013

Roth, A., and Bahl, A. (2009). Divide et impera: optimizing compartmental models of neurons step by step. *J. Physiol.* 587(Pt 7), 1369–1370. doi: 10.1113/jphysiol.2009.170944

Rotstein, H. G., Pervouchine, D. D., Acker, C. D., Gillies, M. J., White, J. A., Buhl, E. H., et al. (2005). Slow and fast inhibition and an H-current interact to create a theta rhythm in a model of CA1 interneuron network. *J. Neurophysiol.* 94, 1509–1518. doi: 10.1152/jn.00957.2004

Roux, L., and Buzsáki, G. (2015). Tasks for inhibitory interneurons in intact brain circuits. *Neuropharmacology* 88, 10–23. doi: 10.1016/j.neuropharm.2014.09.011

Santoro, B., and Baram, T. Z. (2003). The multiple personalities of h-channels. *Trends Neurosci.* 26, 550–554. doi: 10.1016/j.tins.2003.08.003

Saraga, F., Wu, C. P., Zhang, L., and Skinner, F. K. (2003). Active dendrites and spike propagation in multi-compartment models of oriens-lacunosum/moleculare hippocampal interneurons. *J. Physiol.* 552(Pt 3), 673–689. doi: 10.1113/jphysiol.2003.046177

Schneider, C. A., Rasband, W. S., and Eliceiri, K. W. (2012). NIH Image to ImageJ: 25 years of image analysis. *Nat. Methods* 9, 671–675. doi: 10.1038/nmeth.2089

Schulz, D. J., Goaillard, J.-M., and Marder, E. (2006). Variable channel expression in identified single and electrically coupled neurons in different animals. *Nat. Neurosci.* 9, 356–362. doi: 10.1038/nn1639

Sekulić, V., Chen, T.-C., Lawrence, J. J., and Skinner, F. K. (2015). Dendritic distributions of Ih channels in experimentally-derived multi-compartment models of oriens-lacunosum/moleculare (O-LM) hippocampal interneurons. *Front. Synapt. Neurosci.* 7:2. doi: 10.3389/fnsyn.2015.00002

Sekulić, V., Lawrence, J. J., and Skinner, F. K. (2014). Using multi-compartment ensemble modeling as an investigative tool of spatially distributed biophysical balances: application to hippocampal oriens-lacunosum/moleculare (O-LM) cells. *PLoS ONE* 9:e106567. doi: 10.1371/journal.pone.0106567

Sekulić, V., and Skinner, F. K. (2017). Computational models of O-LM cells are recruited by low or high theta frequency inputs depending on h-channel distributions. *eLife* 6:e22962. doi: 10.7554/eLife.22962

Sekulić, V., and Skinner, F. K. (2018). "Experiment-modelling cycling with populations of multi-compartment models: application to hippocampal interneurons," in *Hippocampal Microcircuits, Springer Series in Computational Neuroscience*, eds V. Cutsuridis, B. P. Graham, S. Cobb, and I. Vida (Cambridge, MA: Springer). doi: 10.1007/978-3-319-99103-0_25

Sekulić, V., Yi, F., Garrett, T., Guet-McCreight, A., Lopez, Y. Y., Solis-Wheeler, M., et al. (2019). Somatodendritic HCN channels in hippocampal OLM cells revealed by a convergence of computational models and experiments. *bioRxiv* 633941. doi: 10.1101/633941

Sivagnanam, S., Majumdar, A., Yoshimoto, K., Astakhov, V. B. A., Martone, M., and Carnevale, N. T. (2013). "Introducing the neuroscience gateway," in *Vol. 993 of CEUR Workshop Proceedings of CEUR Workshop Proceedings* (San Diego, CA). doi: 10.1145/2484762.2484816

Siwani, S., França, A. S. C., Mikulovic, S., Reis, A., Hilscher, M. M., Edwards, S. J., et al. (2018). OLM$\alpha$2 cells bidirectionally modulate learning. *Neuron* 99, 404–412.e3. doi: 10.1016/j.neuron.2018.06.022

Skinner, F. K., and Ferguson, K. A. (2018). "Hippocampus, model inhibitory cells," in *Encyclopedia of Computational Neuroscience*, eds D. Jaege, and R. Jung (New York, NY: Springer). doi: 10.1007/978-1-4614-7320-6_29-2

Soofi, W., Archila, S., and Prinz, A. (2012). Co-variation of ionic conductances supports phase maintenance in stomatogastric neurons. *J. Comput. Neurosci.* 33, 77–95. doi: 10.1007/s10827-011-0375-3

Stuart, G. J., and Spruston, N. (2015). Dendritic integration: 60 years of progress. *Nat. Neurosci.* 18, 1713–1721. doi: 10.1038/nn.4157

Swensen, A. M. A., and Bean, B. P. B. (2005). Robustness of burst firing in dissociated Purkinje neurons with acute or long-term reductions in sodium conductance. *J. Neurosci.* 25, 3509–3520. doi: 10.1523/JNEUROSCI.3929-04.2005

Tang, L. S., Taylor, A. L., Rinberg, A., and Marder, E. (2012). Robustness of a rhythmic circuit to short- and long-term temperature changes. *J. Neurosci.* 32, 10075–10085. doi: 10.1523/JNEUROSCI.1443-12.2012

Tennøe, S., Halnes, G., and Einevoll, G. T. (2018). Uncertainpy: a python toolbox for uncertainty quantification and sensitivity analysis in computational neuroscience. *Front. Neuroinformatics* 12:49. doi: 10.3389/fninf.2018.00049

Vaidya, S. P., and Johnston, D. (2013). Temporal synchrony and gamma-to-theta power conversion in the dendrites of CA1 pyramidal neurons. *Nat. Neurosci.* 16, 1812–1820. doi: 10.1038/nn.3562

Van Geit, W., Gevaert, M., Chindemi, G., Rössert, C., Courcol, J.-D., Muller, E. B., et al. (2016). BluePyOpt: leveraging open source software and cloud infrastructure to optimise model parameters in neuroscience. *Front. Neuroinformatics* 10:17. doi: 10.3389/fninf.2016.00017

Varga, C., Golshani, P., and Soltesz, I. (2012). Frequency-invariant temporal ordering of interneuronal discharges during hippocampal oscillations in awake mice. *Proc. Natl. Acad. Sci. U.S.A.* 109, E2726–E2734. doi: 10.1073/pnas.1210929109

Wilson, R. I. (2010). It takes all kinds to make a brain. *Nat. Neurosci.* 13, 1158–1160. doi: 10.1038/nn1010-1158

Yi, F., Ball, J., Stoll, K. E., Satpute, V. C., Mitchell, S. M., Pauli, J. L., et al. (2014). Direct excitation of parvalbumin positive interneurons by m1 muscarinic acetylcholine receptors: roles in cellular excitability, inhibitory transmission and cognition. *J. Physiol.* 592, 3463–3494. doi: 10.1113/jphysiol.2014.275453

Zemankovics, R., Kli, S., Paulsen, O., Freund, T. F., and Hjos, N. (2010). Differences in subthreshold resonance of hippocampal pyramidal cells and interneurons: the role of H-current and passive membrane characteristics: impedance characteristics and h-current of hippocampal neurons. *J. Physiol.* 588, 2109–2132. doi: 10.1113/jphysiol.2009.185975

**Conflict of Interest:** The authors declare that the research was conducted in the absence of any commercial or financial relationships that could be construed as a potential conflict of interest.

*Copyright © 2020 Sekulić, Yi, Garrett, Guet-McCreight, Lawrence and Skinner. This is an open-access article distributed under the terms of the Creative Commons Attribution License (CC BY). The use, distribution or reproduction in other forums is permitted, provided the original author(s) and the copyright owner(s) are credited and that the original publication in this journal is cited, in accordance with accepted academic practice. No use, distribution or reproduction is permitted which does not comply with these terms.*

frontiers in Cellular Neuroscience

ORIGINAL RESEARCH
published: 14 October 2020
doi: 10.3389/fncel.2020.554405

# Alterations in Intrinsic and Synaptic Properties of Hippocampal CA1 VIP Interneurons During Aging

*Ruggiero Francavilla[1,2*†], Alexandre Guet-McCreight[3], Sona Amalyan[1,2], Chin Wai Hui[2], Dimitry Topolnik[2], Félix Michaud[1,2], Beatrice Marino[1,2], Marie-Ève Tremblay[2,4,5], Frances K. Skinner[3,6,7] and Lisa Topolnik[1,2*]*

[1] Department of Biochemistry, Microbiology and Bioinformatics, Faculty of Science and Engineering, Université Laval, Québec, QC, Canada, [2] Neuroscience Axis, Centre Hospitalier Universitaire (CHU) de Québec Research Center – Université Laval, Québec, QC, Canada, [3] Krembil Research Institute, University Health Network, University of Toronto, Toronto, ON, Canada, [4] Department of Molecular Medicine, Faculty of Medicine, Université Laval, Québec, QC, Canada, [5] Division of Medical Sciences, University of Victoria, Victoria, BC, Canada, [6] Department of Physiology, University of Toronto, Toronto, ON, Canada, [7] Departments of Medicine (Neurology) and Physiology, University of Toronto, Toronto, ON, Canada

Learning and memory deficits are hallmarks of the aging brain, with cortical neuronal circuits representing the main target in cognitive deterioration. While GABAergic inhibitory and disinhibitory circuits are critical in supporting cognitive processes, their roles in age-related cognitive decline remain largely unknown. Here, we examined the morphological and physiological properties of the hippocampal CA1 vasoactive intestinal peptide/calretinin-expressing (VIP+/CR+) type 3 interneuron-specific (I-S3) cells across mouse lifespan. Our data showed that while the number and morphological features of I-S3 cells remained unchanged, their firing and synaptic properties were significantly altered in old animals. In particular, the action potential duration and the level of steady-state depolarization were significantly increased in old animals in parallel with a significant decrease in the maximal firing frequency. Reducing the fast-delayed rectifier potassium or transient sodium conductances in I-S3 cell computational models could reproduce the age-related changes in I-S3 cell firing properties. However, experimental data revealed no difference in the activation properties of the Kv3.1 and A-type potassium currents, indicating that transient sodium together with other ion conductances may be responsible for the observed phenomena. Furthermore, I-S3 cells in aged mice received a stronger inhibitory drive due to concomitant increase in the amplitude and frequency of spontaneous inhibitory currents. These age-associated changes in the I-S3 cell properties occurred in parallel with an increased inhibition of their target interneurons and were associated with spatial memory deficits and increased anxiety. Taken together, these data indicate that VIP+/CR+ interneurons responsible for local circuit disinhibition survive during aging but exhibit significantly altered physiological properties, which may result in the increased inhibition of hippocampal interneurons and distorted mnemonic functions.

**Keywords: circuit disinhibition, VIP, action potential, synapse, hippocampus, aging, calretinin**

OPEN ACCESS

***Edited by:***
*Enrico Sanna,*
*University of Cagliari, Italy*

***Reviewed by:***
*Enrico Cherubini,*
*European Brain Research Institute, Italy*
*Imre Vida,*
*Charité – Universitätsmedizin Berlin, Germany*

***Correspondence:**
*Ruggiero Francavilla*
*ruggiero.francavilla@umontreal.ca*
*Lisa Topolnik*
*lisa.topolnik@bcm.ulaval.ca*

**†Present address:**
*Ruggiero Francavilla, Department of Neuroscience, Brain and Child Development Axis, Centre de recherche du CHU Sainte-Justine, Université de Montréal, Montréal, Canada*

***Specialty section:***
*This article was submitted to Cellular Neurophysiology, a section of the journal Frontiers in Cellular Neuroscience*

***Received:*** *21 April 2020*
***Accepted:*** *10 September 2020*
***Published:*** *14 October 2020*

***Citation:***
*Francavilla R, Guet-McCreight A, Amalyan S, Hui CW, Topolnik D, Michaud F, Marino B, Tremblay M-È, Skinner FK and Topolnik L (2020) Alterations in Intrinsic and Synaptic Properties of Hippocampal CA1 VIP Interneurons During Aging. Front. Cell. Neurosci. 14:554405. doi: 10.3389/fncel.2020.554405*

## INTRODUCTION

Aging is an inevitable and extremely complex physiological process often associated with a progressive deterioration of brain functions (Peters, 2006). Cognitive decline and memory deficits are considered hallmarks of the aging brain, with cortical circuits being affected the most during age-dependent functional decline (Murman, 2015). In particular, significant age-related structural and functional changes have been consistently reported in the human and rodent hippocampus (Pyapali and Turner, 1996; Rosenzweig and Barnes, 2003; Markham et al., 2005; Bamidis et al., 2014; Rizzo et al., 2014). Specifically, it was reported that while hippocampal pyramidal cells (PCs) survive in aging, their intrinsic and synaptic excitability is altered (Barnes, 1994; Moyer and Disterhoft, 1994; Rapp and Gallagher, 1996; Moyer et al., 2000; Power et al., 2002). For example, different studies have shown an age-related increase in the action potential (AP) threshold and duration, enhanced after hyperpolarization and a greater spike frequency adaptation in rodent CA1 PCs, revealing altered intrinsic excitability (Potier et al., 1992, 1993; Moyer et al., 2000; Power et al., 2002; Randall et al., 2012). In addition, hippocampal CA1 PCs in aged rodents show significantly reduced synaptic inhibition (Potier et al., 2006; Stanley et al., 2012) and, likely, enhanced excitation (El-Hayek et al., 2013). Specifically, the main excitatory input arriving to the CA1 from the hippocampal CA3 region shows abnormal activation with seizure-like electrical patterns in aged rodents (Wilson et al., 2005, 2006; Koh et al., 2010; El-Hayek et al., 2013). Interestingly, CA3 hyperactivity has been also reported in patients with the amnestic mild cognitive impairment (aMCI) and was among the risk factors for the development of Alzheimer's disease (Bakker et al., 2012). Moreover, using a low dose of antiepileptic drug was beneficial in animal model and patients' studies (Koh et al., 2010; Bakker et al., 2012), revealing imbalanced network activity as a primary mechanism for aMCI during aging.

The hippocampal CA1 network is composed of a large diversity of GABAergic inhibitory interneurons, which generate specific patterns of oscillatory activity playing a crucial role in different mnemonic processes (Somogyi et al., 1998). Quantitative anatomical studies showed that, compared to PCs, the populations of GABAergic interneurons are more vulnerable during aging. In particular, a significant reduction in the number of hippocampal CA1 somatostatin (SST+) but not parvalbumin (PV+)-expressing interneurons has been reported in aged rats (Stanley et al., 2012). The age-related changes in other interneuron types, including the cholecystokinin (CCK+)-, the neuropeptide Y (NPY+)- and the vasoactive intestinal peptide (VIP+)- or calretinin (CR)-expressing cells remain largely unknown.

Over the last several years, the disinhibitory circuits formed by the VIP+/CR+ interneuron-specific (I-S) interneurons that innervate GABAergic cells selectively (Acsády et al., 1996a,b; Gulyas et al., 1996) and can set a balance between network excitation and inhibition, have captured the attention of neuroscientists (Guet-McCreight et al., 2020). Despite their important role in coordinating hippocampal inhibition during spatial learning and goal-oriented behavior (Magnin et al., 2019; Turi et al., 2019), very little is currently known about the survival and functioning of I-S interneurons during aging. Here, we addressed this question by focusing on the type 3 VIP+/CR+ interneuron-specific (I-S3) cells that target different types of CA1 stratum oriens/alveus (O/A) interneurons and control both the perisomatic and dendritic inhibition converging onto CA1 PCs (Acsády et al., 1996b; Chamberland et al., 2010; Tyan et al., 2014; Francavilla et al., 2015). We provide evidence that I-S3 cells survive and preserve their morphology during aging in mice. However, the physiological properties of these cells undergo specific modifications over the course of aging. Thus, this study provides new evidence to support the functional remodeling of disinhibitory circuits in the aged hippocampus, leading to a compensatory potential reorganization of inhibition of the hippocampal CA1 interneurons, which may have an important impact on CA1 network activity and related mnemonic processes.

## MATERIALS AND METHODS

### Mouse Line

Data presented in this study were obtained from VIP-eGFP mice [MMRRC strain#31009, STOCK Tg(Vip-EGFP)37Gsat, CD1 genetic background, University of California, Davis, CA, United States]. In this mouse line, virtually all interneurons that express VIP endogenously were confirmed to also express eGFP using a rabbit anti-VIP primary antibody (catalog #20077, 1:400; Immunostar; see **Figure 1A,B** in Tyan et al., 2014 and **Supplementary Figure 2G** in Francavilla et al., 2018). The animals were separated into two experimental groups: young (P90-150) and old (P410–680). The age range of old group was determined by a low life duration of VIP-eGFP mice, with most animals being lost by P520 (**Figure 1A**). For all experiments both males and females were used (young: $n$ = 46 vs. old: $n$ = 34). All experiments were conducted in accordance with the Animal Protection Committee of Université Laval and the Canadian Council on Animal Care.

### Behavior Assays

General exploratory activity in the open field was assessed using the automated VersaMax Animal Activity Monitoring System (AccuScan Instruments, Columbus, OH). The open field was a square arena (20 × 20 × 30.5 cm) made of plexiglass equipped with photocell beams for automatic detection of activity. On day 1, mice were placed in the open field (**Figure 1C**, left) and left to freely explore for a 10 min test session. The number of vertical beam breaks was taken as a measure of vertical activity. The stereotypic activity was detected automatically using the VersaMax software (Omnitech Electronics Inc, OH, United States). Test chambers were cleaned with 70% ethanol between subjects.

The object-place task was performed in the same arena used for open field. On day 2, during the Sample phase (**Figure 1C**, middle), a single mouse was placed in the arena containing two different sample objects (A + B; 4 × 4 cm each) for 10 min, after which it was returned to its home cage for 24 h retention interval. On day 3, during the Test phase (**Figure 1C**, right), mice

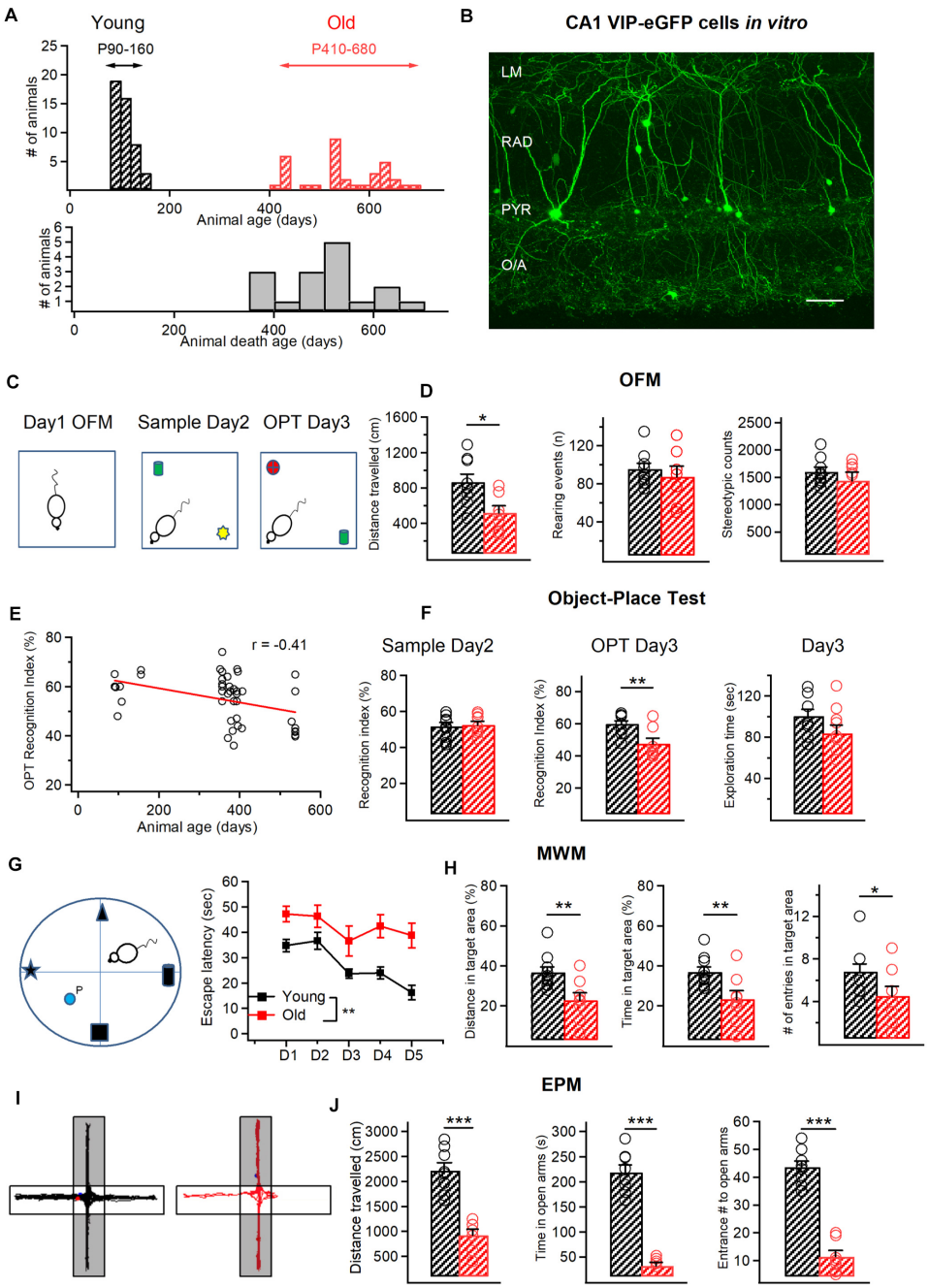


**FIGURE 1 |** Age-related behavioral changes in VIP-eGFP mice. **(A)** Top, distribution of the age of animals used in this study with two experimental groups: young (P90–150) and old (P420–680). Bottom, cumulative histogram indicating the age of death of VIP-eGFP mice (days). **(B)** Two-photon image of the CA1 area from an acute hippocampal slice (300 μm) of a VIP-eGFP mouse showing the location of VIP+ cells in different layers of CA1 area. Scale bar: 100 μm. **(C)** Schematics of the open field maze (OFM) and the object place test (OPT) with open field arena exploration on day 1 (left), sample phase (middle) with object A (green) and object B (yellow) on day 2, and test phase (right) with object C (red) and object A (green) on day 3. **(D)** Summary data for two groups of animals (young–black, old–red) showing a significant decrease in distance traveled with aging ($p < 0.05$, *t*-test, left), and no change in rearing events (middle) and stereotypic counts (right) during OFM test. **(E)** Negative correlation between the OPT recognition index (RI) and the mouse age ($R = -0.41$, $p < 0.05$, Spearman correlation). **(F)** Summary data showing no change in the RI during the sample phase (left) and the exploration time spent with the 2 objects on day 3 (right), but a significant decrease in the RI in the object-place test ($p < 0.01$, unpaired *t*-test, middle). **(G)** Schematics of the Morris Water Maze (MWM) test with four different spatial cues and a hidden platform (P) (left) and the escape latency from day 1 (D1) to Day 5 (D5) of training for young (black) and old (red) mice. **(H)** Summary data for two groups of animals (young–black, old–red) showing a significant reduction in the distance traveled ($p < 0.01$, *t*-test, left) and time ($p < 0.01$, *t*-test, middle) within the target area and the number of entries to the target area ($p < 0.05$, *t*-test, right) in old mice. **(I)** Representative activity tracks for young (left) and old mice (right) showing decreased activity for old mice in the open arms of the elevated plus maze (EPM). **(J)** Summary data showing that old animals explored less ($p < 0.001$, unpaired *t*-test, left), spent less time ($p < 0.001$, unpaired *t*-test, middle) and entered less frequently ($p < 0.001$, unpaired *t*-test, right) in the open arms of the EPM. *$p < 0.05$, **$p < 0.01$, ***$p < 0.01$.

re-entered the arena with two objects, one was identical to the Sample phase and the other was novel (C + A; 4 × 4 cm each). To reinforce the object novelty aspect of this test, we altered the spatial location of the old object explored by the mouse. The results are expressed as Recognition Index (RI, %), defined as the ratio of the time spent with new object divided by the total exploration time for novel and familiar objects [RI = $(T_C)/(T_C + T_A)$]. An exploration time was also calculated for the time spent with the two objects in the Test phase ($ET_T = T_C + T_A$).

For Morris water maze (MWM) test, a white, circular, polypropylene pool (158 cm in diameter, 60 cm height) that was filled with water (21°) made opaque by the addition of powdered milk was used. A clear Plexiglas, adjustable platform (35 cm height, 14 cm circumference), was submerged 2.0 cm below the water surface or elevated 0.5 cm above the water level. The proximal cues comprising a black cardboard in the shape of a star, a triangle, a cylinder, or a cube (10 × 7 × 2.5 cm) hung on the pool walls above the water level at one of four possible starting points (e.g., north, south, east, west) (**Figure 1G**). Mice ($n$ = 10, young; $n$ = 8 old) received five trials in the MWM during 4 subsequent days. In all trials, an individual mouse was placed into the water, facing the outer edge of the pool, at one of four possible starting points (e.g., north, south, east, west). The starting location for each trial was determined randomly. A trial was terminated, and the latency was recorded when the animal reached the platform and remained on it for 10 s. If the animal did not reach the platform within 60 s, the trial was terminated by placing the animal on the platform for 10 s. After the trial, animals were transferred to a dry holding cage where they remained for 60 s until the next trial. During testing, the submerged platform remained stationary in one quadrant of the maze, and the latency to find the platform as well as the distance traveled within the target quadrant, the time spent within the target area and the number of entries to this area were recorded using the Any-Maze software (Stoelting, IL, United States). The distance in target area was then expressed as a fraction of the total distance (in %), while the time in target area was expressed as a fraction of the total time of exploration.

For the anxiety test, the elevated plus maze (EPM) was used (**Figure 1I**). The maze was made of beige plexiglas and consisted of four arms (30 × 5 cm) elevated 40 cm above floor level. Two of the arms contained 15 cm high walls and ceiling (enclosed arms) and the other two none (open arms). Each mouse was placed in the middle section facing a close arm and left to explore the maze for 10 min. After each trial, the floor of the maze was wiped clean with 70% ethanol and dried. The total distance traveled, open arm entries and duration of stay within open arm zones were recorded using the Any-Maze software.

## Slice Preparation and Patch-Clamp Recordings

Coronal hippocampal slices (thickness, 300 μm) were prepared from VIP-eGFP mice of either sex. Briefly, animals were anesthetized deeply with ketamine-xylazine mixture (10/100 mg/mL), transcardially perfused with 25 mL of ice-cold cutting solution (containing the following in mM: 250 sucrose, 2 KCl, 1.25 $NaH_2PO_4$, 26 $NaHCO_3$, 7 $MgSO_4$, 0.5 $CaCl_2$, and 10 glucose, pH 7.4, 330–340 mOsm/L) and decapitated. Slices were cut in the cutting solution using a vibratome (VT1000S; Leica Microsystems or Microm; Fisher Scientific), and transferred to a heated (37.5°C) oxygenated recovery solution containing the following (in mM): 124 NaCl, 2.5 KCl, 1.25 $NaH_2PO_4$, 26 $NaHCO_3$, 3 $MgSO_4$, 1 $CaCl_2$, and 10 glucose; pH 7.4; 300 mOsm/L, and allowed to recover for 45 min. During experiments, slices were continuously perfused (2 mL/min) with standard artificial cerebrospinal fluid (ACSF) containing the following (in mM): 124 NaCl, 2.5 KCl, 1.25 $NaH_2PO_4$, 26 $NaHCO_3$, 2 $MgSO_4$, $2CaCl_2$, and 10 glucose, pH 7.4 saturated with 95% $O_2$ and 5% $CO_2$ at near physiological temperature (30–33°C). VIP-positive interneurons (VIP+) located in CA1 stratum radiatum (RAD) and pyramidale (PYR) were visually identified as eGFP-expressing cells under an epifluorescence microscope with blue light (filter set: 450–490 nm). All electrophysiological recordings were carried out using a 40x water-immersion objective. Two-photon images of eGFP-expressing interneurons were acquired in the same layers of acute slices obtained from VIP-eGFP mice, using a two-photon microscope (TCS SP5; Leica Microsystems) based on a Ti-Sapphire laser tuned to 900 nm (**Figure 1B**). Images were acquired with a 25x water-immersion objective (NA 0.95). A Flaming/Brown micropipette puller (Sutter Instrument Co.) was used to make borosilicate glass capillaries (3.5–6 MΩ). Whole-cell patch-clamp recordings from VIP+ interneurons were performed in voltage or current-clamp mode. Pipettes filled with $K^+$-based solution were used for current-clamp recordings from VIP+ interneurons located in RAD and PYR (in mM): 130 $KMeSO_4$, 2 $MgCl_2$, 10 di-Na-phosphocreatine, 10 HEPES, 4 ATP-Tris, 0.4 GTP-Tris, and 0.3% biocytin (Sigma), pH 7.2–7.3, 280–290 mOsm/L. Passive and active membrane properties were analyzed in current clamp mode: active membrane properties were recorded by subjecting cells to multiple current step injections of varying amplitudes (–200 to 200 pA). Passive membrane properties (resting membrane potential, input resistance, and membrane capacitance) were obtained immediately after membrane rupture. Series resistance (in voltage-clamp) or bridge balance (in current-clump) were monitored throughout the experiment. In current-clamp experiments, interneurons were held at –70 mV by injecting current (–10 to –30 pA), if necessary. Voltage-clamp recordings were performed to analyze the excitatory and inhibitory drives received by VIP+ cells. Cells that had a resting membrane potential more positive than –45 mV, or showed an increase in holding current (>–30 pA) or changes in series resistance or bridge balance (>15%) during recording were discarded. For recordings of spontaneous excitatory postsynaptic currents (sEPSCs), whole-cell patch-clamp recordings were performed in voltage-clamp at –70 mV. Spontaneous inhibitory postsynaptic currents (sIPSCs) and miniature inhibitory postsynaptic currents (mIPSCs) were recorded in voltage-clamp at 0 mV in the presence of tetrodotoxin (TTX; 1 μM; Alomone Labs). For all voltage-clamp recordings we used an intracellular $Cs^+$-based solution containing (in mM): 130 $CsMeSO_4$, 5 CsCl, 2 $MgCl_2$, 10 phosphocreatine, 10 HEPES, 0.5 EGTA, 4 ATP-TRIS, 0.4

GTP-TRIS, 0.3% biocytin, 2 QX-314 (pH 7.2–7.3; 280–290 mOsm/L). For the isolation of voltage-dependent delayed rectifier potassium 3.1 (Kv3.1) currents (Hernandez-Pineda et al., 1999), voltage-clamp recordings in whole-cell configuration with holding membrane potential at –40 mV were performed. In these recordings, extracellular solution was supplemented with 1 μM TTX and Cadmium Chloride ($CdCl_2$, 100 μM; Sigma) to block voltage-dependent sodium and calcium currents, respectively. Depolarizing pulses were applied from –40 to +30 mV with an increment of +10 mV and recordings were performed both in the presence and in the absence of tetraethylammonium (TEA, 1 mM; Sigma) applied to the extracellular solution. Data acquisition (filtered at 2–3 kHz and digitized at 10 kHz; Digidata 1440, Molecular Devices, CA, United States) was performed using the Multiclamp 700B amplifier and the Clampex 10.5 software (Molecular Devices).

## Electrophysiological Data Analysis

Analysis of electrophysiological recordings was performed using Clampfit 10.6 (Molecular Devices). For the analysis of the AP properties, the first AP appearing at the rheobase current pulse within a 50 ms time window was analyzed. The AP amplitude was measured from the AP threshold to the peak. The AP half-width was measured at the voltage level of the half of AP amplitude. The AP rise time was detected between the AP threshold and the maximal AP amplitude, while the AP fall time between the maximal AP amplitude and the AP end. The hyperpolarization-activated cation current (Ih)-associated voltage rectification was determined as the amplitude of the membrane potential sag from the peak hyperpolarized level to the level at the end of the hyperpolarizing step when the cell was hyperpolarized to –100 mV. The membrane time constant (τ) was measured offline using an exponential fit of voltage response to a hyperpolarizing current step of –40 to –50 pA. The firing pattern in I-S3 cells was assessed at 2x rheobase current. The maximum firing frequency was obtained from the inter-spike interval between the first two APs evoked by a current pulse of +140–150 pA. The number of APs was assessed at the current pulse of +140–150 pA.

For the analysis of spontaneous synaptic currents, a minimum of 100 events (for EPSCs) and 200 events (for IPSCs) were sampled per cell over a 10 min period using an automated template search algorithm in Clampfit. All events were counted for frequency analysis. The inhibitory (Gi) or excitatory (Ge) synaptic conductance (**Figure 6E**) was calculated as $G = I/(V_{hold} - V_{rev})$. Charge transfer (**Figure 7D**) was calculated by integrating the area under the PSC waveform. The mean PSC synaptic current (**Figures 6F**, **7E**) was calculated as the charge transfer of the averaged PSC multiplied by mean PSC frequency (Park et al., 2006; Potapenko et al., 2011).

For the isolation of Kv3.1 currents (TEA-sensitive component), the digital subtraction of the TEA-insensitive component from the total current obtained without TEA application was performed (Hernandez-Pineda et al., 1999). For computing the conductance, a $K^+$ reversal potential of –95 mV was assumed (Lien et al., 2002). For fitting activation curves, a non-linear least squares algorithm (Lien et al., 2002) was used to fit the following sigmoid: $G/Gmax(V) = 1/(1 + \exp(-(V - Vhalf)/k))$.

## Anatomical Reconstruction and Immunohistochemistry

For *post hoc* reconstruction, neurons were filled with biocytin (Sigma) during whole-cell recordings. Slices with recorded cells were fixed overnight with 4% paraformaldehyde (PFA) at 4°C. To reveal biocytin, the slices were permeabilized with 0.3% Triton X-100 and incubated at 4°C with streptavidin conjugated Alexa-488 (1:1,000) in Trizma-buffer (TB). Z-stacks of biocytin-filled cells were acquired with a 1 μm step using a 20x oil-immersion objective and Leica SP5 confocal microscope. Confocal stacks were merged for detailed reconstruction in Neurolucida 8.26.2 (MBF Bioscience). The I-S3 cell phenotype was confirmed by the presence of axon in the O/A (Acsády et al., 1996b; Tyan et al., 2014). The quantitative analysis of soma size and dendritic morphology was performed following 3D reconstructions of I-S3 cells in Neurolucida. Sholl analysis (**Figure 2G**) was performed in radial coordinates, using a 50 μm step size from $r = 0$, with the origin centered on the cell soma, and counting the number of compartments crossing a given radius.

All immunohistochemical tests were performed on free-floating sections (50–70 μm thick) obtained with Leica VT1000S or PELCO EasySlicer vibratomes. VIP-eGFP mice were deeply anaesthetized with ketamine–xylazine mixture (ketamine: 100mg/kg, xylazine: 10mg/kg) and perfused intracardially with 4% PFA, and the brains were sectioned. Coronal sections (AP; –2.0–2.8; $n = 20$ sections/age group, 6–7 sections/animal from 3 different mice) were permeabilized with 0.25% Triton X-100 in PBS and incubated overnight at 4°C with primary antibodies followed by the secondary antibodies. The following primary antibodies were used in this study: goat anti-CR (1:1,000; Santa Cruz, #sc-11644), chicken anti-GFP (1:1,000; Aves, #GFP-1020), mouse anti-NeuN (1:500; Millipore, #MAB377), and rat anti-SST (1:500; Millipore, #MAB354). In control immunohistochemical tests, the primary antibodies were omitted, and sections were incubated with the secondary antibodies only. Confocal images of the hippocampal CA1 area were acquired sequentially using a 20x oil-immersion objective (0.8 NA) and Leica TCS SP5 imaging system coupled with a 488 nm argon, a 543 nm HeNe and a 633 nm HeNe lasers. The imaging parameters were kept constant across all sections/animals. Cells were considered immunopositive when the corresponding fluorescence intensity was at least twice the background fluorescence. For representation only, the overall brightness and contrast of images were adjusted manually. Portions of images were not modified separately in any way.

Cell counting was performed blind to the experimental conditions within the CA1 area using stereological analysis. The cells were first counted in different sections ($n = 6–7$) originating from the same animal, and the data was then compared between different animals ($n = 3$ animals/age group) and pooled together

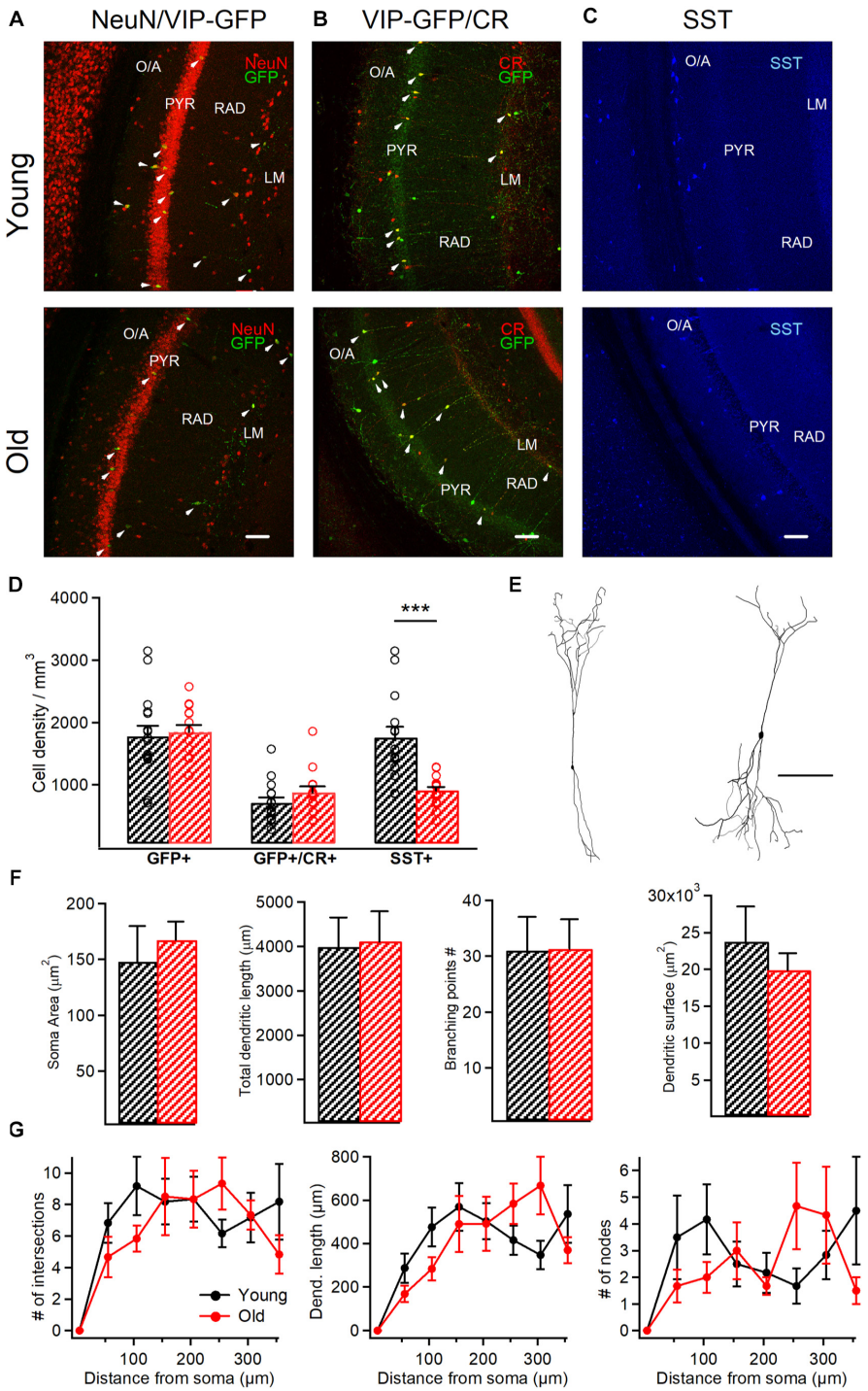


**FIGURE 2 |** VIP+/CR+ interneurons exhibit no changes in morphological properties in aged mice. **(A)** Representative confocal images of the hippocampal CA1 area of VIP-eGFP mice showing immunoreactivity for eGFP and NeuN **(A)**, eGFP and CR **(B)** and SST **(C)** in young and old mice. White arrowheads point to cells showing the colocalization of eGFP and NeuN **(A)** or eGFP and CR **(B)**. Scale bars: 100 μm. **(D)** Summary data showing no change in the cell density for VIP-eGFP and VIP-eGFP+/CR+ interneurons ($p > 0.05$, unpaired *t*-test) but a significant decrease in SST+ interneurons ($p < 0.001$, $^{***}p < 0.01$, unpaired *t*-test) between the two age groups. **(E)** Anatomical reconstructions of I-S3 cells filled with biocytin during whole-cell patch-clamp recordings. Scale bar: 100 μm. **(F)** Summary data showing no differences in somatic and dendritic parameters between the two age groups ($p > 0.05$ for all comparisons, unpaired *t*-test/ Mann-Whitney test). **(G)** Sholl analysis of I-S3 dendritic branch patterns revealed no differences in the number of dendritic intersections (left), nodes (right), or dendritic length (middle) ($p > 0.05$ for all comparisons, unpaired *t*-test/ Mann-Whitney test).

for young vs. old groups. Cell density was estimated within regions of interest (500 × 700 μm) selected randomly in the middle of the CA1.

## Multi-Compartment Models of I-S3 Cells

For multi-compartment modeling we used previously developed I-S3 cell models (Guet-McCreight et al., 2016), and simulations were done using the NEURON software environment (Carnevale and Hines, 2006). We included two model variants, which either had A-type $K^+$ current in the proximal dendrites (SDprox1) or had A-type $K^+$ current restricted to the soma (SDprox2). Because it remains unclear what the morphological distributions of A-type $K^+$ currents are in I-S3 cells, we used both model variants in this study. Both models possess only a minimal complement of ion channel mechanisms to capture the basic spiking activity of I-S3 cells (Guet-McCreight et al., 2016). These include transient $Na^+$ current, persistent $Na^+$ current, A-type $K^+$ current, fast delayed rectifier $K^+$ current, and random Gaussian noise current to capture subthreshold fluctuations and irregular firing observed in I-S3 cell recordings. To probe the possible channel currents that might be modulated given observed changes in I-S3 cell active properties during aging, we looked at a variety of changes in these ion channel conductances in the I-S3 cell models, and selected the conductance change that was able to best capture the changes that are seen experimentally. Note that these simulations were conducted in a systematic way, where conductances were either reduced from 100 to 0% of their initial values or increased from 100 to 200% of their initial values. As such, there were no attempts to fit the aging electrophysiology data or perform parameter searches; we were simply looking at the effects of upscaling or downscaling the ion channel conductances in a way that was illustrative. Simulated voltage traces were analyzed in Python 3 using the eFEL module. Specifically, we used this module to obtain measurements for the AP amplitude, half-width, rise rate, and fall rate. The AP rise and fall rates can both be described as the ratio of the voltage differences (rise/fall voltages) and the time differences (rise/fall times) as calculated using the AP begin, end, and peak indices.

## Statistics

For statistical analysis, distributions of data were first tested for normality with a Shapiro–Wilcoxon test. If data were normally distributed, standard parametric statistics were used: unpaired two-tailed *t*-tests for comparisons of two groups and one-way or repeated-measures ANOVA for comparisons of multiple groups followed by Tukey, Kruskal–Wallis or $Chi^2$ *post hoc* tests. If data were not normally distributed, non-parametric Mann–Whitney test was instead used for comparisons of two groups. The Kolmogorov-Smirnov (K-S) test was used for comparison of spontaneous synaptic events. All statistical analysis was conducted in Sigma Plot 11.0, Clampfit 10.6 and Igor Pro. The "*p*" values $< 0.05$ were considered significant. Error bars correspond to standard error of the mean (SEM). Error bars for potassium conductances and kinetics correspond to standard deviations, and shaded areas correspond to SEM.

# RESULTS

## VIP-eGFP Mice Display Age-Dependent Behavioral Deficits

To examine the impact of aging on the morphological and electrophysiological properties of VIP+/CR+ IS3 cells, VIP-eGFP mice were used. As demonstrated previously (Tyan et al., 2014), in this mouse model, all interneurons immunoreactive for VIP express eGFP, and VIP+ cells of different subtypes, including bipolar/bitufted IS3 cells with soma located within the CA1 PYR and RAD (**Figure 1B**), can be targeted for patch-clamp recordings. To define the age of experimental animals to be included in the study, we first examined the longevity of VIP-eGFP mice, which have a CD1 genetic background. We found that, differently from C57BL/6 mice (Goodrick, 1975), VIP-eGFP mice had shorter life duration (P365–660), with most animals dying by P500 (**Figure 1A**). Accordingly, for all experiments on old mice we choose the age range of P420–P680 (the oldest possible animals in our colony) ($n = 34$ mice). The young group included animals from P90 to P160 ($n = 46$ mice) (**Figure 1A**). In some experiments (**Figures 1E**, **3G**), an additional age group (P350–410; $n = 29$ mice) was included for age-dependent correlation analyses.

The age-dependent decline in spatial memory has been reported in different lines of mice previously (Fordyce and Wehner, 1993; Bach et al., 1999). To examine whether this is the case for VIP-eGFP mice, we compared the performance of young vs. old animals in the object-place test (OPT) and the Morris water maze (MWM) (**Figures 1C–H**). We first determined whether aging is associated with a decline in locomotor performance by analyzing the activity of VIP-eGFP mice in the open field maze (OFM) (**Figures 1C,D**). Old mice showed a smaller total distance traveled (young: $n = 9$ vs. old: $n = 8$, $p < 0.05$, *t*-test, **Figure 1D**, left), with no change in rearing events (young: $n = 9$ vs. old: $n = 8$, $p > 0.05$, *t*-test, **Figure 1D**, middle) and stereotypy counts (young: $n = 9$ vs. old: $n = 8$, $p > 0.05$, *t*-test, **Figure 1D**, right). Overall, these data indicate a decreased locomotor activity in old VIP-eGFP mice. On day 2, mice were tested in the OPT. The data showed that, during the Sample phase (**Figure 1C**, middle), mice of both age groups were spending similar amount of time exploring two different sample objects (A and B) as indicated by their RI (young: $n = 9$ vs. old: $n = 8$, $p > 0.05$, *t*-test, **Figure 1F**, left). However, 24 h later, once the mice were re-introduced in the same maze containing a new object (C) and the sample object (A) positioned in a different spatial location (**Figure 1C**, right), a significant difference was observed in the RI for the novel object recognition betwee young and old mice ($p < 0.05$, *t*-test, **Figure 1F**, middle), pointing to a decline in the novelty recognition with age. Indeed, when additional age group of animals (P350–410; $n = 29$) was included in this analysis, the decline in the novel object recognition RI correlated well with the mouse age ($R = 0.41$, $p < 0.001$, Spearman correlation, **Figure 1E**). Importantly, the total exploration time during the OPT was not significantly different between the two age groups ($p > 0.05$, *t*-test, **Figure 1F**, right), indicating that the lower

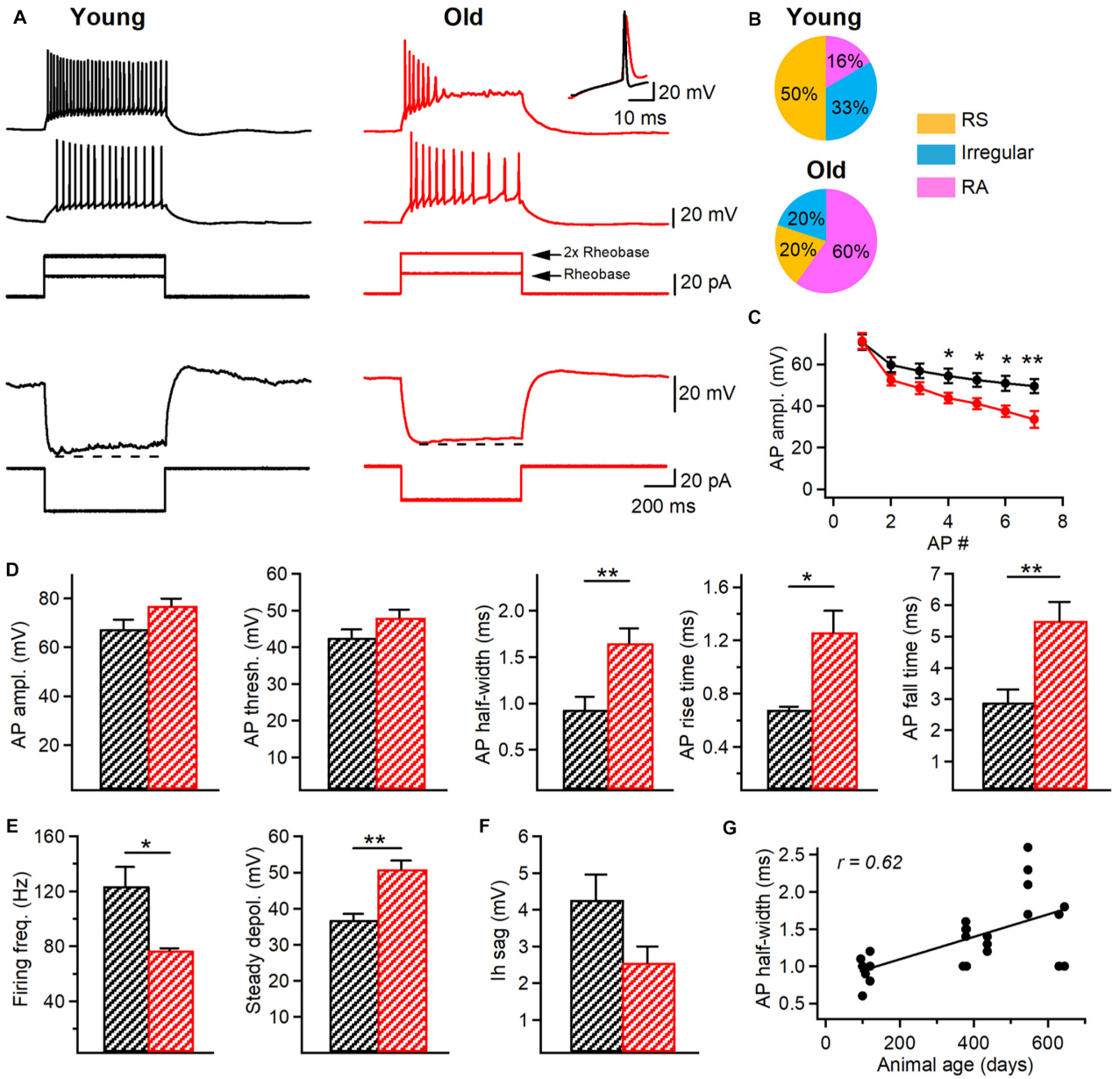


**FIGURE 3 |** Changes in the firing properties of I-S3 cells of aged mice. **(A)** Top, representative voltage responses (top) indicating the firing pattern of I-S3 cells in young (black) and old (red) mice in response to depolarizing (+20 pA and +40 pA) current injections corresponding to rheobase and 2x rheobase current, respectively. Inset on the top right corresponds to the superimposed traces showing the longer AP duration in old mice. Bottom, representative voltage responses of I-S3 cells in the two age groups to a hyperpolarizing current injection used to assess the Ih-associated voltage rectification (dashed line). **(B)** Pie charts illustrating the percentage of the regularly spiking (RS), irregular spiking (Irregular) and rapidly adapting (RA) firing patterns in I-S3 cells from the two age groups. **(C)** Summary plot (mean ± SEM) showing changes in the AP amplitude during the train of APs in I-S3 cells (*$p < 0.05$, **$p < 0.01$, unpaired *t*-test). **(D)** Summary data showing no changes in the AP amplitude and AP threshold between young and old mice ($p > 0.05$, unpaired *t*-test) but a significant increase in the AP half-width ($p < 0.01$, unpaired *t*-test), rise time ($p < 0.05$, unpaired *t*-test) and fall time ($p < 0.01$, unpaired *t*-test). **(E)** Summary data for two groups of animals showing a significant decrease in the maximal firing frequency ($p < 0.05$, unpaired *t*-test) in parallel with an increase in the steady state depolarization ($p < 0.01$, unpaired *t*-test). **(F)** Summary data for two groups of animals showing no changes in the Ih sag ($p < 0.05$, unpaired *t*-test). **(G)** Positive correlation between the AP half-width and the animal age ($R = 0.62$, $p < 0.01$, Spearman correlation).

RI in the aged group reflects poorer memory performance and not decreased exploratory behaviors. To investigate the potential spatial memory deficits in old mice, we next performed the MWM test (young: $n = 10$ mice, old: $n = 8$ mice; **Figures 1G,H**). The data showed that old VIP-eGFP mice showed a significantly longer escape latency to find a fixed hidden platform ($p < 0.01$, one-way ANOVA; **Figure 1G**, right). Also, on the final day of training, old mice demonstrated a lower distance traveled

($p < 0.01$, *t*-test) and time spent ($p < 0.01$, *t*-test) in the target quadrant with fewer entries into the target zone ($p < 0.05$, *t*-test) (**Figure 1H**). Taken together, these data indicate that old VIP-eGFP mice exhibit significant impairments in the hippocampus-dependent memory.

Together with memory performance deficits, aging has also been associated with an increase in the anxiety-like behavior (Gorina et al., 2017). To test whether this is the case in aged VIP-eGFP mice, we performed the EPM test (young: $n = 8$ mice, old: $n = 7$ mice; **Figures 1I,J**). Our data showed that old VIP-eGFP mice spent much less time in the open arms ($p < 0.001$, *t*-test; **Figures 1I,J**, center) with less entries into open arms ($p < 0.001$, *t*-test; **Figures 1I,J**, right), indicative of increased anxiety although decreased locomotion could also account for these changes. Thus, similar to other mouse strains, in VIP-eGFP mice, aging is associated with decreased locomotion, memory deficits, and anxiety-like behavior.

## I-S3 Cells Survive During Aging and Preserve Their Morphology

To investigate whether aging has an impact on the survival of CA1 VIP+ interneurons, we performed immunohistochemistry on hippocampal slices from young *vs.* old VIP-eGFP mice (young: $n = 8$ mice; old: $n = 5$ mice), using antibodies against NeuN to label all neurons and GFP to label all VIP-expressing interneurons (Tyan et al., 2014; Francavilla et al., 2018). We found that VIP+ interneurons survive during aging as no change in their cell density was measured in the CA1 area ($p > 0.05$, *t*-test; **Figures 2A,D**). Furthermore, our data showed no difference in the VIP+ population co-expressing CR and VIP and corresponding to I-S3 cells ($p > 0.05$, *t*-test; **Figures 2B,D**), indicating that I-S3 interneurons in the hippocampal CA1 area also survive during animal aging. These data contrasted with the density of SST+ GABAergic interneurons located within CA1 O/A (**Figures 2C,D**), which was significantly decreased in old VIP-eGFP mice ($p < 0.001$, *t*-test).

As aging is often associated with changes in morphological properties of neurons, such as reduced dendritic branching (Scheibel, 1979; Hanks and Flood, 1991), we next explored the age-dependent structural changes in the anatomically confirmed I-S3 interneurons that were filled with biocytin during patch-clamp recordings and reconstructed in Neurolucida (young: $n = 4$ cells vs. old: $n = 6$ cells; **Figure 2E**). Our data showed that aging had no impact on I-S3 cell morphology. In particular, no difference was found in such morphological parameters as soma area ($p > 0.05$, *t*-test), total dendritic length ($p > 0.05$, *t*-test), number of branching points ($p > 0.05$, Mann-Whitney test) and area occupied by dendrites ($p > 0.05$, *t*-test) (**Figure 2F**). Furthermore, dendritic Sholl analysis revealed no differences in the number of dendritic intersections ($p > 0.05$, one-way ANOVA; **Figure 2G**, left), dendritic length ($p > 0.05$, one-way ANOVA; **Figure 2G**, middle) or number of dendritic nodes ($p > 0.05$, one-way ANOVA; **Figure 2G**, right) at different distances from the soma. Together, these data indicate that I-S3 cells survive at later stages of the animal's life and preserve their morphology.

## Aging Modifies the Physiological Properties of I-S3 Cells

As cognitive deficits during aging can be associated with changes in electrophysiological properties of neurons (Rizzo et al., 2014), we performed targeted patch-clamp recordings from I-S3 cells in slices obtained from young ($n = 9$ cells) vs. old ($n = 11$ cells/) VIP-eGFP mice, and analyzed the active and passive membrane properties of these cells (**Figure 3**). We found no changes in the resting membrane potential ($V_m$ young: $-59.8 \pm 1.7$ mV; $V_m$ old: $-60.6 \pm 1.7$ mV; $p > 0.05$, *t*-test), input resistance ($R_{in}$ young: $619.7 \pm 78$ MΩ; $R_{in}$ old: $486 \pm 61$ MΩ; $p > 0.05$, *t*-test), membrane capacitance ($C_m$ young: $34.1 \pm 3.3$ pF; $C_m$ old: $27.3 \pm 2.3$ pF; $p > 0.05$, *t*-test) or membrane time constant ($\tau_m$ young: $31.1 \pm 2.0$ ms; $\tau_m$ old: $31.4 \pm 3.8$ ms; $p > 0.05$, *t*-test) in I-S3 cells of old mice. However, analysis of active membrane properties revealed significant changes in I-S3 firing and AP properties (**Figure 3A**). First, while in young mice I-S3 cells exhibited a regularly spiking (RS), an irregularly spiking or a rapidly adapting (RA) firing pattern (**Figure 3A**, left and **Figure 3B**, top), the RA firing pattern was seen more often in old animals (**Figure 3A**, right and **Figure 3B**, bottom), revealing a stronger firing adaptation in I-S3 cells in aged mice. Moreover, there was a significant decrease in the amplitude of spikes during the train in old animals ($p < 0.05$, *t*-test; **Figure 3C**). Furthermore, the level of the steady-state depolarization was significantly higher in old animals (young: $36.8 \pm 1.7$ mV; old: $50.9 \pm 2.4$ mV; $p < 0.01$, *t*-test; **Figure 3E**) in parallel with a significant decrease in the maximal firing frequency (young: $123.7 \pm 13.9$ Hz; old: $76.9 \pm 1.6$ Hz; $p < 0.05$, *t*-test; **Figure 3E**). The detailed analysis of the first AP in the train recorded at the rheobase current showed that while aging had no impact on the AP amplitude (young: $67.4 \pm 3.9$ mV; old: $76.7 \pm 2.9$ mV; $p > 0.05$, *t*-test) and threshold (young: $-42.6 \pm 2.2$ mV; old: $-48.1 \pm 2.1$ mV; $p > 0.05$, *t*-test), the AP half-width (young: $0.9 \pm 0.1$ ms; old: $1.6 \pm 0.2$ ms; $p < 0.01$, Mann-Whitney test), rise time (young: $0.68 \pm 0.02$ ms; old: $1.26 \pm 0.16$ ms; $p < 0.05$, Mann-Whitney test) and fall time (young: $2.9 \pm 0.4$ ms; old: $5.5 \pm 0.6$ ms; $p < 0.01$, *t*-test) were significantly increased (**Figure 3D**). Importantly, when an additional set of data from I-S3 cells of younger mice (P370–380, $n = 6$ cells) was included in this analysis, there was a positive correlation between the AP half-width and the animal's age ($R = 0.62$, $p < 0.05$, Spearman correlation, **Figure 3G**), in line with the age-dependent progress of changes in the AP kinetics. We found no changes in the hyperpolarization-activated membrane conductances, such as $I_h$ current ($V_m$ sag young: $4.3 \pm 0.7$ mV; $V_m$ sag old: $3.2 \pm 0.9$ mV; $p > 0.05$, *t*-test; **Figure 3F**), pointing to specific age-dependent changes in voltage-gated channels involved in the generation of APs in I-S3 cells.

## Modeling Provides Insights Into the Age-Related Changes Occurring in I-S3 Cells

To probe the possible changes in intrinsic properties associated with age-related modifications of active properties of I-S3 cells, we used two model variants of the previously developed

multi-compartment computational models of I-S3 cells (Guet-McCreight et al., 2016): a variant possessing dendritic A-type potassium channels (SDprox1) and one lacking dendritic A-type potassium channels (SDprox2).

In upscaling and downscaling several intrinsic ion channel conductances we observed that the age-related changes seen experimentally were best captured when fast delayed rectifier potassium conductances were reduced (**Figures 4A–C**), when transient sodium conductances were reduced (**Figures 4D–F**), and when both were reduced proportionally (**Figures 4G–I**). Generally, reducing these conductances allowed the models to enter the depolarization block states more easily, most likely due to a change in the balances between sodium to potassium currents (Bianchi et al., 2012; Tucker et al., 2012). More specifically, reducing these channel conductances in the models led to increases in the first spike half-width rates, as scaled by spike amplitude (**Figures 4C,F,I**, left panels). We scaled the spike half-widths by spike amplitude to disambiguate spike duration measurements from effects due to changes in spike amplitude. Correspondingly, we also measured the spike rise rate (V/s; **Figures 4C,F,I**, middle panels) and spike fall rates (V/s; **Figures 4C,F,I**, right panels). We found that reducing fast delayed rectifier potassium conductance leads to slower spike fall rates (**Figure 4C**, right panel), but does have a large impact on spike rise rates (**Figure 4C**, middle panel). On the other hand, reducing transient sodium conductance results in slower spike rise rates (**Figure 4F**, middle panel), with some impact at slowing spike fall rate as well (**Figure 4F**, right panel). Reducing both conductances had an effect of slowing both the spike rise and fall rates (**Figure 4I**). Kinetically, the fast delayed rectifier potassium channel model used in the I-S3 cell models most likely corresponds with currents generated by the Kv3.1 potassium channel subunits (Guet-McCreight et al., 2016) and the transient sodium channel could correspond with sodium channel subunits Nav1.2, Nav1.3, and beta-2.

Since these models possess a minimal complement of ion channel mechanisms (see Methods) and I-S3 cell ion channel conductances and kinetics remain largely uncharacterized, we did not attempt to fit the aging data more closely. Therefore, while these simulations suggest that changes in fast delayed rectifier potassium and transient sodium conductances contribute to the aging-related changes seen in electrophysiological recordings from I-S3 cells, they do not exclude other intrinsic mechanisms.

## The TEA-Sensitive and Insensitive $K^+$ Currents Remain Unaltered in I-S3 Cells of Old Mice

To test the model predictions that the down-regulation of Kv3.1 channels can be responsible for age-related increases in the steady-state depolarization and AP duration in I-S3 cells, we performed voltage-clamp recordings in whole-cell configuration with holding membrane potential at –40 mV to facilitate the isolation of Kv3.1 currents from I-S3 cells in young and old VIP-eGFP mice (young: $n$ = 9 cells; old: $n$ = 6 cells). To isolate the TEA-sensitive Kv3.1-mediated current (**Figure 5A**, left), we subtracted the TEA-insensitive component (**Figure 5C**, left) from the total current recorded before application of TEA. TEA-sensitive and TEA-insensitive currents were measured at 8 different membrane potentials from –40 to +30 mV in 10 mV steps (**Figures 5A,C**, left) to determine the steady-state conductance-voltage relationships (**Figures 5A,C**, right). As previously found in type A globus pallidus or CA1 neurons (Hernandez-Pineda et al., 1999; Alshuaib et al., 2001), the TEA-sensitive currents begin to activate at ∼–20 mV (**Figure 5A**, right, and **Figure 5B**, left). Our data showed no significant difference at each of the voltage levels for steady-state conductance of both TEA-sensitive ($p > 0.05$ for all comparisons, $t$-test, **Figure 5A**, right) and TEA-insensitive currents ($p > 0.05$ for all comparisons, $t$-test, **Figure 5C**, right) in old mice. In addition, the normalized conductance (G/Gmax) for TEA-sensitive (**Figure 5B**, left) and TEA-insensitive currents (**Figure 5D**, left) allowed us to fit the data to a Boltzmann equation to obtain the half-activation voltages ($V_{1/2}$) and activation slopes (k) of both currents. Here again, we found no difference for $V_{1/2}$ (young vs. old, $p > 0.05$, $t$-test) and k (young vs. old, $p > 0.05$, $t$-test) of the TEA-sensitive currents (**Figure 5B**, right) and $V_{1/2}$ (young vs. old, $p > 0.05$, $t$-test) and k (young vs. old, $p > 0.05$, $t$-test) of the TEA-insensitive currents (**Figure 5D**, right). Thus, these data indicate that there was no significant difference in the activation properties of TEA-sensitive A-type $K^+$ and TEA-insensitive Kv3.1 currents, and that the ionic mechanisms underlying the observed changes in the AP and firing properties of I-S3 cells in old mice remain to be determined.

## The Inhibitory Synaptic Drive to I-S3 Cells Increases During Aging

Next, to examine whether I-S3 cells could exhibit changes in their synaptic properties, we performed whole-cell voltage-clamp recordings of sIPSCs (young: $n$ = 7 cells; old: $n$ = 5 cells) and sEPSCs (young: $n$ = 6 cells; old: $n$ = 6 cells) (**Figure 6**). Our data revealed significant changes in both sEPSCs and sIPSCs in I-S3 cells of old mice. In particular, there was an increase in the amplitude (young: 15.6 ± 3.0 pA; old: 24.4 ± 3.3 pA, $p < 0.001$, K-S test; $p < 0.05$, $t$-test; **Figures 6A,B**, left) and an increase in the frequency (young: 5.5 ± 1.1 Hz; old: 8.7 ± 1.3 Hz, $p < 0.001$, K-S test; $p < 0.05$, $t$-test; **Figures 6A,B**, right) of sIPSCs. In parallel, the amplitude of sEPSCs was also increased (young: 9.1 ± 1.0 pA; old: 13.8 ± 1.4 pA, $p < 0.001$, K-S test; $p < 0.05$, $t$-test; **Figures 6C,D**, left), however, with no change frequency (young: 4.0 ± 0.7 Hz; old: 4.8 ± 0.8 Hz, $p > 0.05$, K-S test; $t$-test; **Figures 6C,D**, right). To determine the overall impact of these changes in sEPSCs and sIPSCs on the excitation/inhibition balance in I-S3 cells, we first calculated the inhibitory (Gi) and excitatory (Ge) conductances, and then compared these parameters and their ratio between the young and old animals. Our data showed that in both age groups, I-S3 cells receive a stronger inhibitory conductance (**Figure 6E**), and that the Ge/Gi ratio remains unaltered during aging due to a concomitant increase in both Gi and Ge (**Figure 6E**). As these parameters do not consider changes in event frequency, we next calculated a mean PSC as a product of mean PSC charge transfer and event frequency (**Figure 6F**). These data revealed

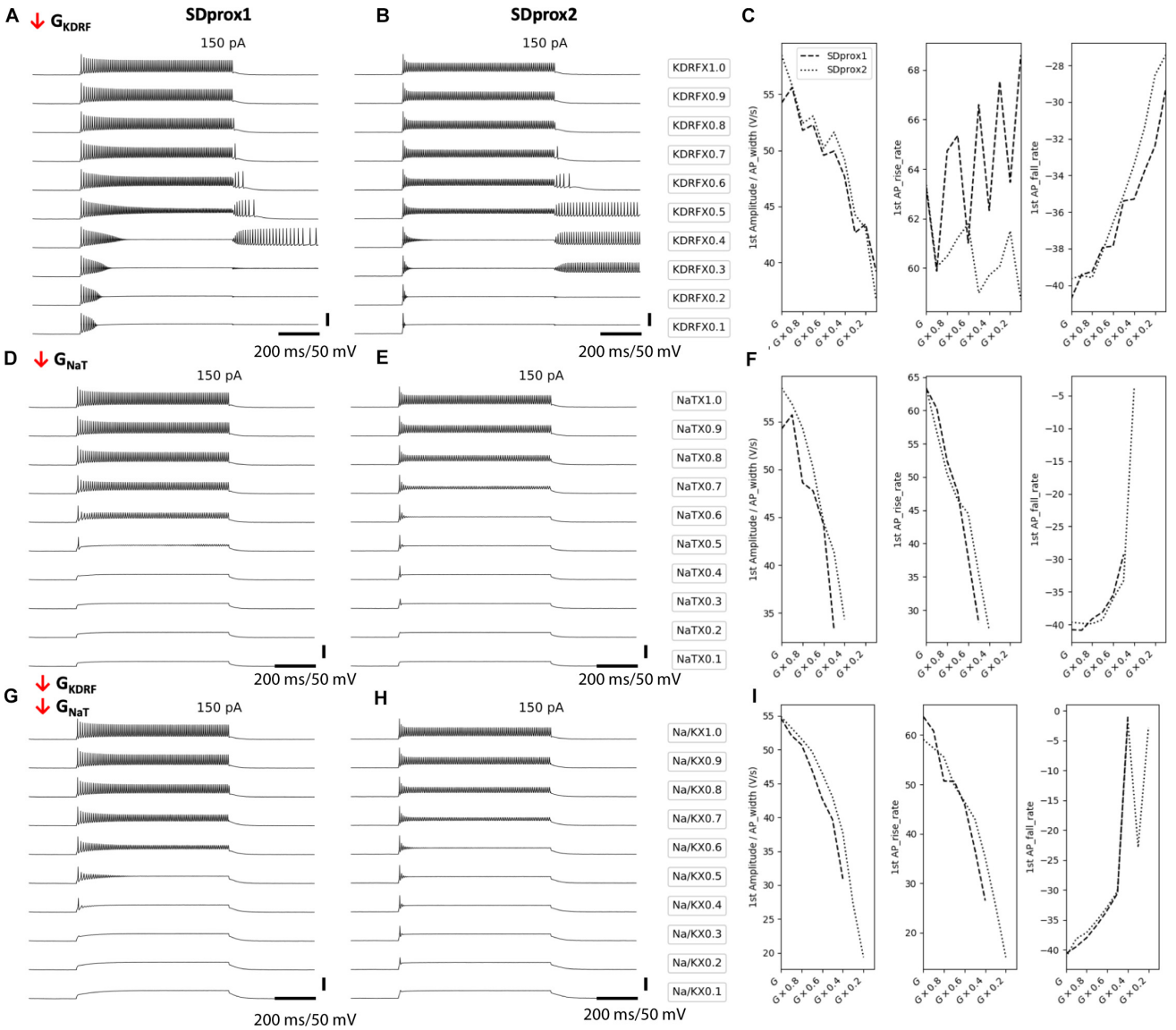


**FIGURE 4 |** Downscaling fast delayed rectifier potassium and transient sodium channels in I-S3 cell models mimics the cell firing properties in aged animals. **(A,B)** Simulated voltage recordings of I-S3 cell spiking using models SDprox1 **(A,D,G)** and SDprox2 **(B,E,H)**, respectively. From top to bottom, fast delayed rectifier potassium conductance **(A,B)**, transient sodium conductance **(D,E)**, and both **(G,H)** are downscaled from 100% of its initial value to 10%. **(C,F,I)** Changes in ratio of the first AP amplitude over half-width (V/s) (left panels), first AP rise rate (middle panel), and first AP fall rate (right panel) as conductances are downscaled. Note that the AP rise and fall rates are computed as the ratio of the voltage difference over time difference (V/s) of the rise and fall portions of the AP, respectively. For all three measurements, values closer to zero (i.e., slower rates) correspond with slower durations.

that, while the mean EPSC remained unaltered, the mean IPSC was significantly increased due to increase in both the amplitude and frequency of sIPSCs (**Figure 6B**), pointing to the enhanced inhibitory drive to I-S3 cells in aged animals (**Figure 6F**).

## The Inhibition of I-S3 Cells Postsynaptic Targets Increases With Aging

The age-dependent increase in the AP duration in IS3 cells observed in our study suggests that these cells may exert a stronger impact on their postsynaptic targets via enhanced GABA release. On the other hand, an increased inhibitory drive to I-S3 cells together with a lower frequency of AP firing indicate that these cells may be less active in old mice. IS3 cells inhibit different types of O/A interneurons (Tyan et al., 2014), which, in turn, provide inhibition to different subcellular domains of CA1 PCs. To investigate wheather specific alterations in AP and firing/synaptic properties of IS3 cells could translate into a modified inhibition of O/A interneurons, we performed whole-cell voltage-clamp recordings of mIPSCs from O/A interneurons of young vs. old mice (**Figure 7**). Our data showed that both the amplitude (young: 17.2 ± 1.2 pA, $n$ = 8; old: 27.5 ± 3.4 pA,

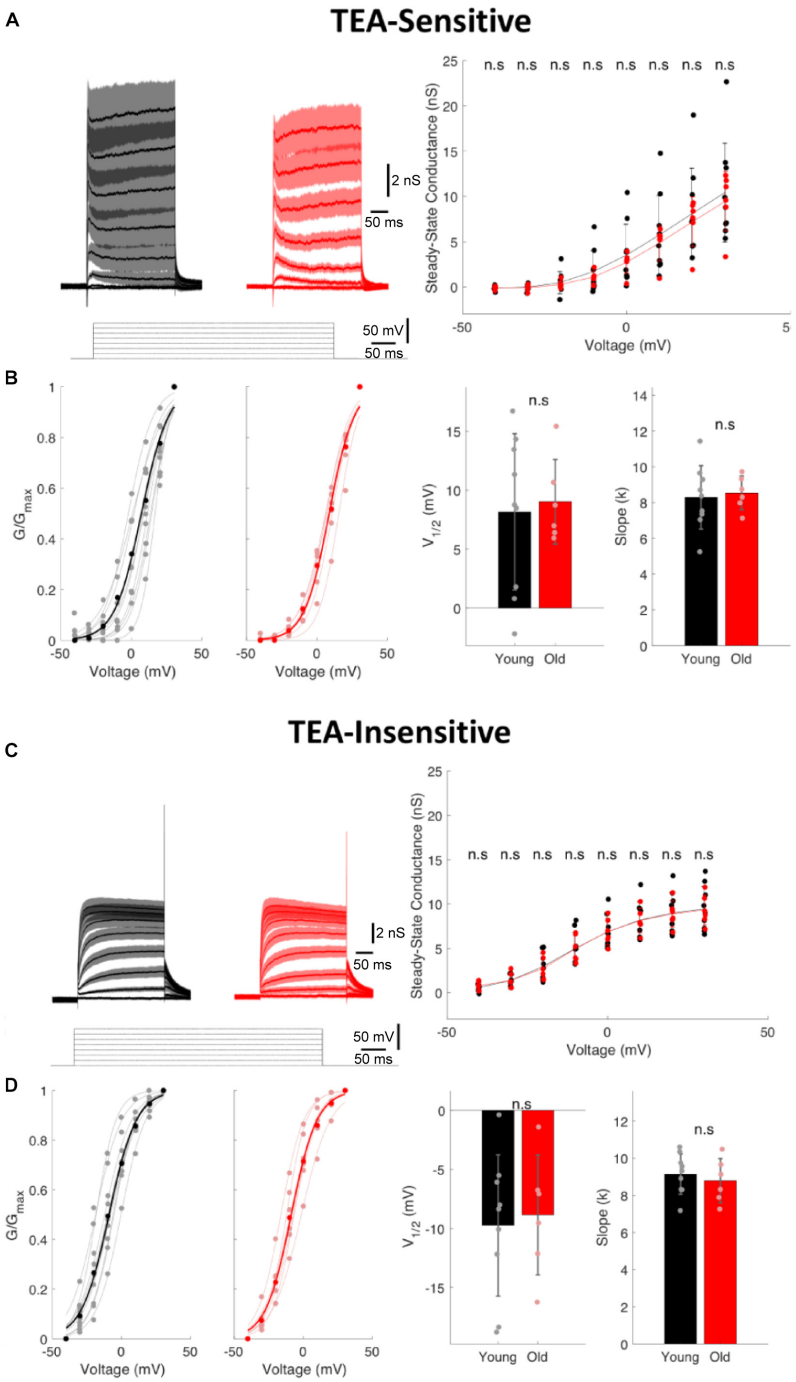


**FIGURE 5 |** The TEA-sensitive and TEA-insensitive potassium currents remain unaltered in I-S3 cells. **(A)** Left, currents obtained from an I-S3 cell held at –40 mV and subjected to depolarizing pulses from –40 to +30 mV in 10 mV increments after application of 1 mM TEA in young (black) and old (red) mice. Traces show the TEA-sensitive component obtained by digital subtraction of the traces recorded in the presence of TEA (**C**, left; TEA-insensitive currents) from those in control (total currents). Right, the steady-state conductance of the TEA-sensitive component as a function of voltage in young and old mice showing no changes in the TEA-sensitive currents ($p > 0.05$, unpaired *t*-test; error bars show standard deviation). **(B)** Left, plots of relative conductance (G/Gmax) of the TEA-sensitive current in I-S3 cells of young and old mice with a Boltzmann fit function. Right, summary data showing no significant change in $V_{1/2}$ and k of the TEA-sensitive currents ($p > 0.05$, unpaired *t*-test; error bars show standard deviation). **(C)** Left, current traces recorded in the presence of TEA during the depolarizing pulses from –40 to +30 mV in 10 mV increments and corresponding to the TEA-insensitive component in young (black) and old (red) mice. Right, the steady-state conductance of the TEA-insensitive component as a function of voltage in young and old mice showing no difference in this component between the two age groups ($p > 0.05$, unpaired *t*-test; error bars show standard deviation). **(D)** Left, plots of relative conductance (G/Gmax) of the TEA-insensitive current in young and old mice fit to a Boltzmann function. Right, summary data showing no significant change in $V_{1/2}$ and k of the TEA-insensitive currents ($p > 0.05$, unpaired *t*-test; error bars show standard deviation).

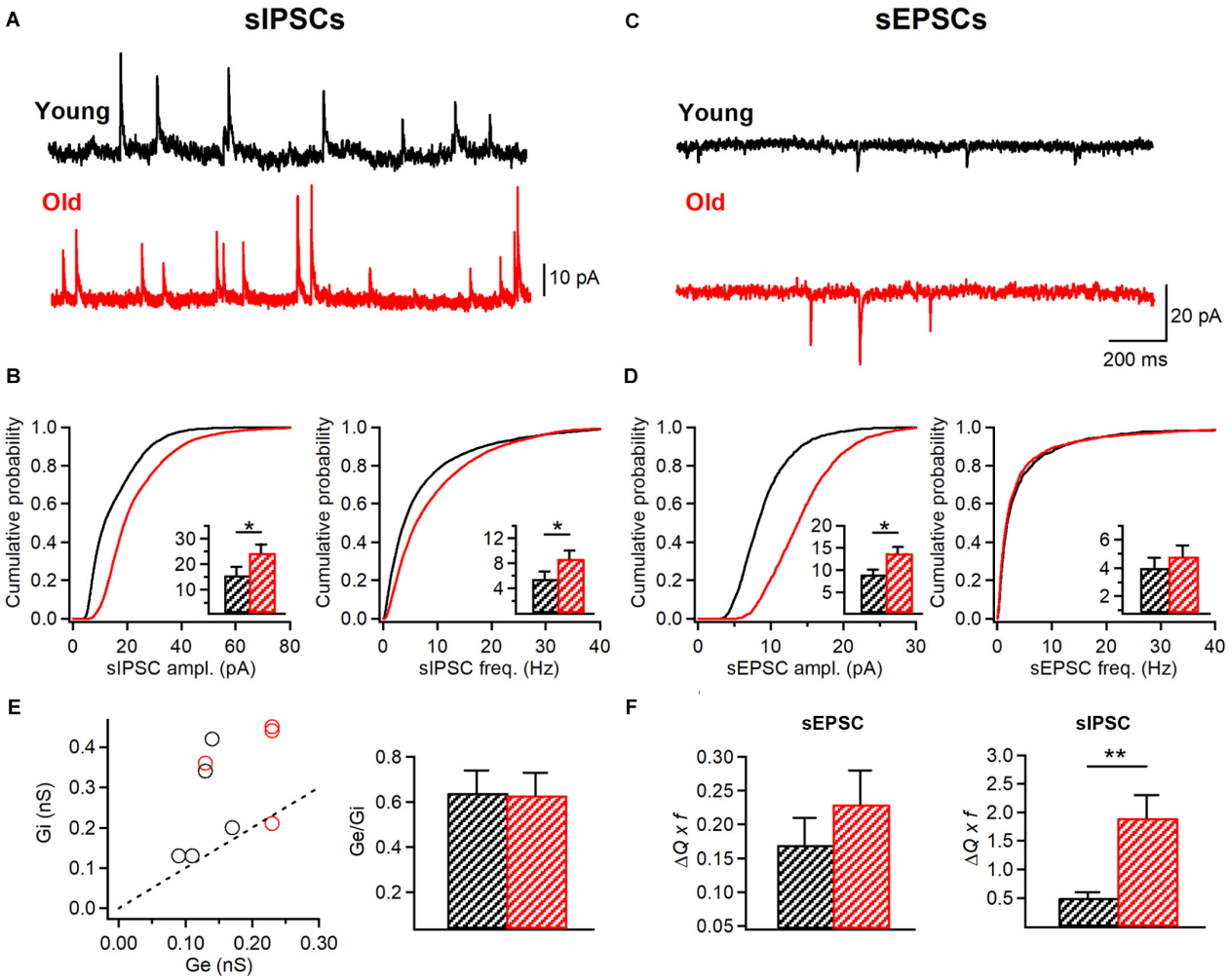


**FIGURE 6 |** I-S3 cells receive a stronger inhibitory drive in aged mice. **(A,C)** Representative traces of sIPSCs **(A)** and sEPSCs **(C)** recorded in I-S3 cells from young (black) and old mice (red). **(B)** Summary data showing a significant increase in the amplitude and frequency of sIPSCs in I-S3 cells of aged mice ($p < 0.001$, K-S test). Insets illustrate significant differences in the sIPSC amplitude and frequency for inter-cell mean comparison (*$p < 0.05$, unpaired *t*-test). **(D)** Summary data showing a significant increase in the amplitude of sEPSCs ($p < 0.001$, K-S test; inset, *$p < 0.05$, unpaired *t*-test) with no change in the frequency ($p > 0.05$, K-S test; inset, $p > 0.05$, unpaired *t*-test). **(E)** The inhibitory (Gi) to excitatory (Ge) conductance plot (left) illustrating a dominant inhibitory conductance in I-S3 cells across the animal lifespan. Summary data (right) for the Ge/Gi ratio in two age groups show no change in Ge/Gi in old mice due to a comparable increase in both Gi and Ge (**B,D**, left). **(F)** Summary data for the mean excitatory (left) and inhibitory (right) charge transfer when frequency of events is considered. Note a significant increase in the mean inhibitory current in I-S3 cells of old animals. *$p < 0.05$, **$p < 0.01$.

$n = 5$, $p < 0.001$, K-S test; $p < 0.01$, *t*-test; **Figures 7A,B**, left) and the frequency (young: 8.6 ± 0.5 Hz, $n = 8$; old: 11.2 ± 1.4 Hz, $n = 4$, $p < 0.001$, K-S test; $p < 0.05$, *t*-test; **Figures 7A,B**, right) of mIPSCs recorded in O/A interneurons were significantly higher in aged animals in line with age-dependent changes at both pre- and postsynaptic sites of inhibitory synapses converging onto O/A interneurons. Furthermore, the overal charge transfer (area under curve) during mIPSC was significantly increased in O/A interneurons of old mice (young: 137.7 ± 7.1 pA x ms, $n = 8$; old: 224.2 ± 32.4 pA x ms, $n = 5$, $p < 0.001$, K-S test; $p < 0.05$, *t*-test; **Figure 7C**, left; **Figure 7D**) without significant changes in the rise time (young: 0.71 ± 0.05 ms, $n = 8$; old: 0.7 ± 0.2 ms, $n = 5$, $p > 0.05$, *t*-test; **Figure 7C**, right) or the decay time constant (young: 9.9 ± 0.7 ms, $n = 8$; old: 9.9 ± 0.5 ms, $n = 5$, $p > 0.05$, *t*-test; **Figure 7C**, right) of mIPSCs, indicating no change in the $GABA_A$ receptor subunit composition. Finally, considering the increased frequency of mIPSCs we also found a significant increase in the mean IPSC charge transfer in O/A interneurons (**Figure 7E**). Taken together, these data reveal an age-dependent increase in inhibition of their postsynaptic targets.

## DISCUSSION

In this study, we provide novel data on the morphological and physiological properties of a specific GABAergic interneuron subtype in aged animals. We demonstrate that VIP+/CR+ I-S3 cells survive during aging and preserve their morphological

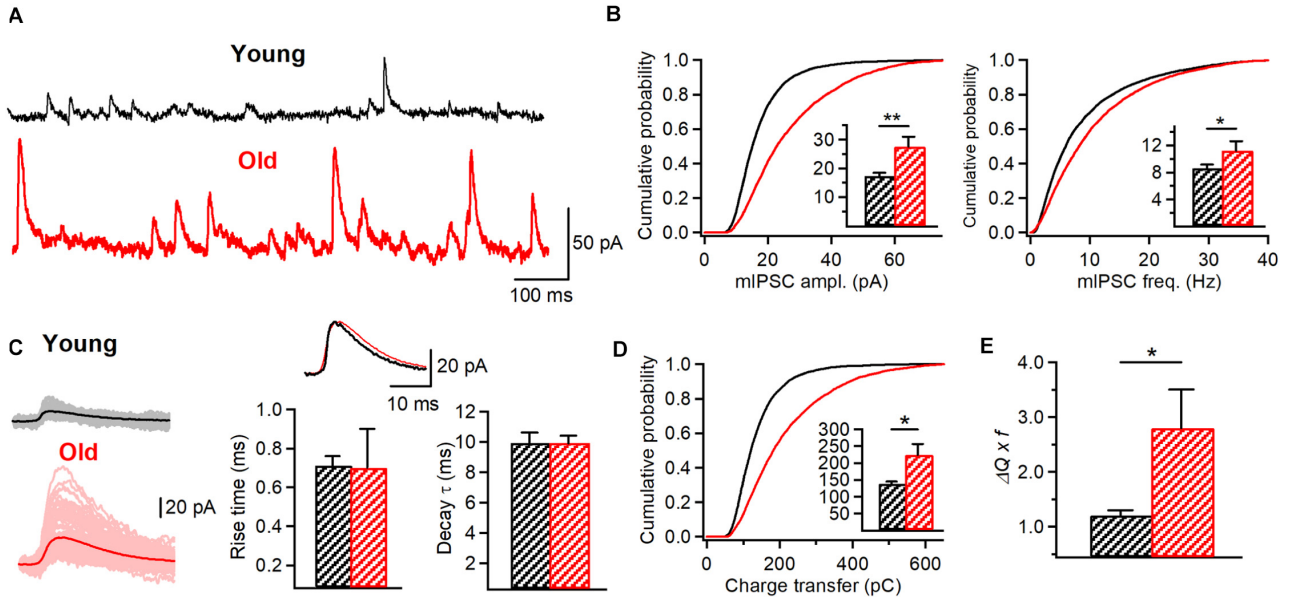


**FIGURE 7 |** Increased inhibitory drive to O/A interneurons in aged animals. **(A)** Representative traces of mIPSCs recorded in O/A interneurons in young (black) and old (red) mice. **(B)** Cumulative probability plots of the mIPSC amplitude (left) and frequency (right) in young and old animals (K-S test, $p < 0.001$ for both plots). Insets illustrate significant differences in the mIPSC amplitude (**$p < 0.01$, unpaired *t*-test) and frequency ($p < 0.05$, unpaired *t*-test) for inter-cell mean comparison. **(C)** Representative examples of individual mIPSC events (100 pale sweeps, left) and average traces (bold trace, left) detected in I-S3 cells of young (black) and old animals (red). Superimposed scaled traces (right top) and summary bar graphs for a group of cells (right bottom) show no significant differences in the IPSC kinetics. **(D)** Cumulative probability plot of the mIPSC charge transfer (area under curve) in young and old animals (K-S test, $p < 0.001$). Inset illustrates significant differences (*$p < 0.05$, unpaired *t*-test) for inter-cell mean comparison. **(E)** Summary data for the mean inhibitory charge transfer when frequency of events is considered (*$p < 0.05$, unpaired *t*-test), showing a significant increase in the inhibitory drive to O/A interneurons. *$p < 0.05$, **$p < 0.01$.

features but exhibit significant changes in the active membrane and synaptic properties, thus highlighting an age-induced functional rather than structural remodeling of this interneuron subtype. These age-dependent changes are associated with increased memory deficits as well as anxiety-like behavior reflecting pathological aging.

It is widely recognized that neuronal loss in the neocortex and hippocampus can be involved in cognitive deficits associated with aging (Morrison and Hof, 1997; Mattson and Magnus, 2006), with the dendrite-targeting SST+ interneurons such as hippocampal O-LM cells being affected the most (Stanley et al., 2012). In the current study conducted on VIP-eGFP mice, SST+ O/A interneurons were also vulnerable but VIP+/CR+ I-S3 cells remained structurally unaltered. While I-S3 cells represent less than 1% of all CA1 neurons (Bezaire and Soltesz, 2013), they are among the most excitable interneuron subtypes in the hippocampus due to a particularly high input resistance (Chamberland et al., 2010; Tyan et al., 2014). By providing behavioral state-dependent disinhibition, these cells play a critical role in spatial coding and goal-oriented reward learning (Magnin et al., 2019; Turi et al., 2019). Our data show that, in the aged hippocampus, both sEPSC and sIPSC amplitudes in I-S3 cells are significantly increased. As a result, the balance between excitatory and inhibitory conductances remains unaltered. However, inhibitory drive to I-S3 cells becomes more prominent due to a concomitant increase in sIPSC frequency and may dampen the recruitment of these cells to network activity. Interestingly, GABAergic septohippocampal innervation of CA1 CR+ interneurons is decreased during aging (Rubio et al., 2012). Thus, changes in the spontaneous inhibitory tone observed in our study may reflect increased activity of local inhibitory interneurons contacting I-S3 cells, such as other VIP+ and CR+ interneurons (Luo et al., 2020). Furthermore, while I-S3 cells receive excitatory input from the CA3 area (Luo et al., 2020), which can become hyperactive in old rodents (El-Hayek et al., 2013; Simkin et al., 2015), we have not observed any sign of hyperactivity or seizure-like excitatory patterns arriving to I-S3 cells from this region. Rather the opposite, the overall frequency of sEPSCs was very low and remained at this level during aging.

We also found an increased AP duration and steady-state depolarization in parallel with a decreased firing rate and rapid adaptation in I-S3 cells of old mice. What biophysical mechanisms could account for the observed modifications? Model simulations predicted that decreasing the fast-delayed rectifier and/or transient sodium conductances should increase the AP half-width and induce a steady-state depolarization-dependent block of firing. However, the experimental data showed no changes in the amplitude and kinetics of the fast-delayed rectifier Kv3.1 or the A-type $K^+$ currents. This suggests that other subtypes of voltage-gated $K^+$ channels or $Na^+$ channels could be responsible for age-dependent changes in the AP and firing properties and should be examined in further studies. Moreover, recording of $K^+$ currents in the soma

does not discount for any possible age-dependent changes in dendritic distributions of Kv3.1 or A-type $K^+$ channels. As well, age-dependent changes in currents could be occluded by variability in ion channel expression across individual cells. Importantly, increased steady-state depolarization with a prevalent rapidly adapting firing pattern of I-S3 cells in aged mice may indicate that these cells are likely to fire shorter trains of a fewer APs in response to a strong excitatory input. Although this suggests a decreased I-S3 cell output, it has been shown in CA1 PCs that full amplitude somatic APs, attenuated APs, and even small spikelets of 5–10 mV can co-occur in the axon (Apostolides et al., 2016). More specifically, somatic spikelets represent axonal APs that fail to initiate into full APs (Apostolides et al., 2016). Further, experimental and modeling data indicated that PCs APs recovered to full amplitude at more distal axonal locations as the AP-mediated $K^+$ channel activation effectively counteracted the depolarizing effect of the somatic plateau (Apostolides et al., 2016). These observations indicate that I-S3 cells entering the depolarization block and having a reduction in somatic firing could still maintain the same spike frequency and train duration in axons with wider spikes leading to a longer depolarization in I-S3 axonal terminals. The tonic activation of VIP+ cells may occur during arousal and attentional tasks (Steriade, 1991) due to activation of nicotinic acetylcholine or metabotropic serotonin 5HT2 receptors (Prönneke et al., 2020) but may be impaired in aging hippocampus, with direct consequences on mnemonic processes.

Furthermore, our data show that intrinsic and synaptic remodeling of I-S3 cells may be associated with a significant increase in inhibition of their postsynaptic targets. I-S3 cells contact several distinct subtypes of O/A interneurons, including O-LM, bistratified and basket cells (Tyan et al., 2014). An increase in the AP duration in I-S3 cells during aging could indicate significant changes at I-S3 synapses, with a larger presynaptic calcium influx due to changes in $Na^+/K^+$ conductances, increased vesicular and non-vesicular GABA release, extracellular GABA accumulation and enhanced tonic inhibition through activation of extrasynaptic $GABA_A$ receptors (Attwell et al., 1993; Zoli et al., 1999; Glykys and Mody, 2007), although the latter has not been detected in O-LM cells of young mice (Salesse et al., 2011). In addition, the increased inhibition of O/A interneurons reported here may be associated with a homeostatic strengthening of inhibitory synapses (Peng et al., 2010; Rannals and Kapur, 2011; Pribiag et al., 2014) following a decrease in the I-S3 input due to a higher inhibitory drive on I-S3 cells and their lower firing rate in aged hippocampus.

Importantly, aging is associated with deficits in the theta oscillation power resulting in the impaired encoding of novel spatial information in the dorsal hippocampus or emotional states in the ventral hippocampus (Jacobson et al., 2013). Modeling data combined with imaging *in vivo* of I-S3 cell activity in awake mice indicated that I-S3 cells are recruited during theta oscillations (Luo et al., 2020) and may play a role in modulating the activity of O-LM cells at theta frequency (Tyan et al., 2014). Indeed, in young animals, optogenetic activation of CR+ cells increased the post-inhibitory firing of O-LM cells specifically at theta frequency (Tyan et al., 2014). Here, we show that during aging, I-S3 cells may become less available but fire with a broader spike, resulting in the increased inhibition to O-LM cells. Whether this increased inhibition may lead to a complete suppression of O-LM cell firing remains unknown, but given a critical role of O-LM cells in theta oscillations (Gillies et al., 2002; Gloveli et al., 2005; Mikulovic et al., 2018), their silencing may have a direct impact on the frequency and power of theta rhythms as well as the encoding of novel spatial and emotion-related information. Supporting this idea, the AP broadening in I-S3 cells occurred in parallel with cognitive deficits in VIP-eGFP mice, and both variables showed a strong correlation with animal age, suggesting a causal connection.

In addition, O-LM cells play a major role in disinhibition of distal dendritic domains of CA1 PCs and facilitation of dendritic spike initiation and burst firing (Chamberland et al., 2010; Lovett-Barron et al., 2012; Müller et al., 2012; Royer et al., 2012; Tyan et al., 2014). In this regard, the increased inhibition of O-LM cells along with their decreased density in the aged hippocampus may contribute to the increased burst firing or even hyperactivity of CA1 PCs. It is to be noted that all these age-dependent modifications in the local circuit inhibition may occur in parallel with other intrinsic and synaptic changes of different cell types making up hippocampal networks. Our data reveal specific functional changes in one subtype of disinhibitory interneuron that may have an impact on the balance between hippocampal inhibition and disinhibition. However, further experiments involving cell type-specific interventions will be required to understand the mechanisms of the observed phenomena and the impact of modified disinhibitory circuits on hippocampal network activity and mnemonic processing.

## DATA AVAILABILITY STATEMENT

The raw data supporting the conclusions of this article will be made available by the authors, without undue reservation, to any qualified researcher.

## ETHICS STATEMENT

The animal study was reviewed and approved by the Animal Protection Committee of Université Laval and the Canadian Council on Animal Care.

## AUTHOR CONTRIBUTIONS

RF, SA, CH, and DT performed the experimental work. RF, AG-M, CH, FM, BM, DT, and LT analyzed the experimental data. AG-M conducted the computational modeling. RF, AG-M, and LT wrote the manuscript. RF, AG-M, M-ÈT, FS, and LT edited the manuscript. FS, M-ÈT, and LT provided resources and supervised

the research. All authors contributed to the article and approved the submitted version.

## FUNDING

This work was supported by the Canadian Institutes of Health Research (CIHR) (Grants #MOP-137072 and MOP-142447, 2014-2019) and the Natural Sciences and Engineering Research Council of Canada (NSERC) (Grant #342292-2012, 2014-2019) to LT, CIHR Grant (MOP-148420) to M-ÈT, as well as NSERC Grant (RGPIN-2016-06182) to FS. CWH was recipient of a postdoctoral fellowship from Fonds de Recherche du Québec – Santé. M-ÈT was a Tier 2 Canada Research Chair in *Neurobiology of Aging and Cognition.*

## ACKNOWLEDGMENTS

We thank the members of Topolnik's Lab for providing comments on different versions of the manuscript.

## REFERENCES

Acsády, L., Arabadzisz, D., and Freund, T. F. (1996a). Correlated morphological and neurochemical features identify different subsets of vasoactive intestinal polypeptide-immunoreactive interneurons in rat hippocampus. *Neuroscience* 73, 299–315. doi: 10.1016/0306-4522(95)00610-9

Acsády, L., Görcs, T. J., and Freund, T. F. (1996b). Different populations of vasoactive intestinal polypeptide immunoreactive interneurons are specialized to control pyramidal cells or interneurons in the hippocampus. *Neuroscience* 73, 317–334. doi: 10.1016/0306-4522(95)00609-5

Alshuaib, W. B., Hasan, S. M., Cherian, S. P., Mathew, M. V., Hasan, M. Y., and Fahim, M. A. (2001). Reduced potassium currents in old rat CA1 hippocampal neurons. *J. Neurosci.* 63, 176–184. doi: 10.1002/1097-4547(20010115)63:2<176::aid-jnr1009>3.0.co;2-h

Apostolides, P. F., Milstein, A. D., Grienberger, C., Bittner, K. C., and Magee, J. C. (2016). Axonal filtering allows reliable output during dendritic plateau-driven complex spiking in CA1 neurons. *Neuron* 89, 770–783. doi: 10.1016/j.neuron.2015.12.040

Attwell, D., Barbour, B., and Szatkowski, M. (1993). Nonvesicular release of neurotransmitter. *Neuron* 11, 401–407. doi: 10.1016/0896-6273(93)90145-h

Bach, M. E., Barad, M., Son, H., Zhuo, M., Lu, Y. F., Shih, R., et al. (1999). Age-related defects in spatial memory are correlated with defects in the late phase of hippocampal long-term potentiation in vitro and are attenuated by drugs that enhance the cAMP signaling pathway. *Proc. Natl. Acad. Sci. U.S.A.* 96, 5280–5285. doi: 10.1073/pnas.96.9.5280

Bakker, A., Krauss, G. L., Albert, M. S., Speck, C. L., Jones, L. R., Stark, C. E., et al. (2012). Reduction of hippocampal hyperactivity improves cognition in amnestic mild cognitive impairment. *Neuron* 74, 467–474. doi: 10.1016/j.neuron.2012.03.023

Bamidis, P. D., Vivas, A. B., Styliadis, C., Frantzidis, C., Klados, M., Schlee, W., et al. (2014). A review of physical and cognitive interventions in aging. *Neurosci. Biobehav. Rev.* 44, 206–220. doi: 10.1016/j.neubiorev.2014.03.019

Barnes, C. A. (1994). Normal aging: regionally specific changes in hippocampal synaptic transmission. *Trends Neurosci.* 17, 13–18. doi: 10.1016/0166-2236(94)90029-9

Bezaire, M. J., and Soltesz, I. (2013). Quantitative assessment of CA1 local circuits: knowledge base for interneuron-pyramidal cell connectivity. *Hippocampus* 23, 751–785. doi: 10.1002/hipo.22141

Bianchi, D., Marasco, A., Limongiello, A., Marchetti, C., Marie, H., Tirozzi, B., et al. (2012). On the mechanisms underlying the depolarization block in the spiking dynamics of CA1 pyramidal neurons. *J. Comput. Neurosci.* 33, 207–225. doi: 10.1007/s10827-012-0383-y

Carnevale, N. T., and Hines, M. L. (2006). *The Neuron Book*. Cambridge: Cambridge University Press. doi: 10.1017/CBO9780511541612

Chamberland, S., Salesse, C., Topolnik, D., and Topolnik, L. (2010). Synapse specific inhibitory control of hippocampal feedback inhibitory circuit. *Front. Cell. Neurosci.* 4:130. doi: 10.3389/fncel.2010.00130

El-Hayek, Y. H., Wu, C., Ye, H., Wang, J., Carlen, P. L., and Zhang, L. (2013). Hippocampal excitability is increased in aged mice. *Exp. Neurol.* 247, 710–719. doi: 10.1016/j.expneurol.2013.03.012

Fordyce, D. E., and Wehner, J. M. (1993). Effects of aging on spatial learning and hippocampal protein kinase C in mice. *Neurobiol. Aging* 14, 309–317. doi: 10.1016/0197-4580(93)90116-S

Francavilla, R., Luo, X., Magnin, E., Tyan, L., and Topolnik, L. (2015). Coordination of dendritic inhibition through local disinhibitory circuits. *Front. Synaptic Neurosci.* 7:5. doi: 10.3389/fnsyn.2015.00005

Francavilla, R., Villette, V., Luo, X., Chamberland, S., Munoz, E. P., Camire, O., et al. (2018). Connectivity and network state-dependent recruitment of long-range VIP-GABAergic neurons in the mouse hippocampus. *Nat. Commun.* 9:5043. doi: 10.1038/s41467-018-07162-5

Gillies, M. J., Traub, R. D., LeBeau, F. E. N., Davies, C. H., Gloveli, T., Buhl, E. H., et al. (2002). A model of atropine-resistant theta oscillations in rat hippocampal area CA1. *J. Physiol.* 543, 779–793. doi: 10.1113/jphysiol.2002.024588

Gloveli, T., Dugladze, T., Rotstein, H. G., Traub, R. D., Monyer, H., Heinemann, U., et al. (2005). Orthogonal arrangement of rhythm-generating microcircuits in the hippocampus. *Proc. Natl. Acad. Sci. U.S.A.* 102, 13295–13300. doi: 10.1073/pnas.0506259102

Glykys, J., and Mody, I. (2007). The main source of ambient GABA responsible for tonic inhibition in the mouse hippocampus. *J. Physiol.* 582, 1163–1178. doi: 10.1113/jphysiol.2007.134460

Goodrick, C. L. (1975). Life-span and the inheritance of longevity of inbred mice. *J. Gerontol.* 30, 257–263. doi: 10.1093/geronj/30.3.257

Gorina, Y. V., Komleva, Y. K., Lopatina, O. L., Volkova, V. V., Chernykh, A. I., Shabalova, A. A., et al. (2017). The battery of tests for experimental behavioral phenotyping of aging animals. *Adv. Gerontol.* 7, 137–142. doi: 10.1134/S2079057017020060

Guet-McCreight, A., Camiré, O., Topolnik, L., and Skinner, F. K. (2016). Using a semi-automated strategy to develop multi-compartment models that predict biophysical properties of interneuron-specific 3 (is3) cells in hippocampus. *eNeuro* 3:ENEURO.0087-16.2016. doi: 10.1523/ENEURO.0087-16.2016

Guet-McCreight, A., Skinner, F. K., and Topolnik, L. (2020). Common principles in functional organization of VIP/calretinin cell-driven disinhibitory circuits across cortical areas. *Front. Neural Circuits* 14:32. doi: 10.3389/fncir.2020.00032

Gulyas, A. I., Hajos, N., and Freund, T. F. (1996). Interneurons containing calretinin are specialized to control other interneurons in the rat hippocampus. *J. Neurosci.* 16, 3397–3411. doi: 10.1523/jneurosci.16-10-03397.1996

Hanks, S. D., and Flood, D. G. (1991). Region-specific stability of dendritic extent in normal human aging and regression in Alzheimer's disease. I. CA1 of hippocampus. *Brain Res.* 540, 63–82. doi: 10.1016/0006-8993(91)90493-f

Hernandez-Pineda, R., Chow, A., Amarillo, Y., Moreno, H., Saganich, M., Vega-Saenz de Miera, E., et al. (1999). Kv3.1-Kv3.2 channels underlie a high voltage-activating component of the delayed rectifier K+ current in projecting neurons from the globus pallidus. *J. Neurophysiol.* 82, 1512–1528. doi: 10.1152/jn.1999.82.3.1512

Jacobson, T. K., Howe, M. D., Schimdt, B., Hinman, J. R., Escabi, M. A., and Markus, E. J. (2013). Hippocampal theta, gamma, and theta-gamma coupling: effects of aging, environmental change, and cholinergic activation. *J. Neurophysiol.* 109, 1852–1865. doi: 10.1152/jn.00409.2012

Koh, M. T., Haberman, R. P., Foti, S., McCown, T. J., and Gallagher, M. (2010). Treatment strategies targeting excess hippocampal activity benefit aged rats with cognitive impairment. *Neuropsychopharmacology* 35, 1016–1025. doi: 10.1038/npp.2009.207

Lien, C. C., Martina, M., Schultz, J. H., Ehmke, H., and Jonas, P. (2002). Gating, modulation and subunit composition of voltage-gated K+ channels in dendritic inhibitory interneurones of rat hippocampus. *J. Physiol.* 538, 405–419. doi: 10.1113/jphysiol.2001.013066

Lovett-Barron, M., Turi, G. F., Kaifosh, P., Lee, P. H., Bolze, F., Sun, X. H., et al. (2012). Regulation of neuronal input transformations by tunable dendritic inhibition. *Nat. Neurosci.* 15, 423–430, S1–S3. doi: 10.1038/nn.3024

Luo, X., Guet-McCreight, A., Villette, V., Francavilla, R., Marino, B., Chamberland, S., et al. (2020). Synaptic mechanisms underlying the network state-dependent recruitment of VIP-expressing interneurons in the CA1 hippocampus. *Cereb. Cortex* 30, 3667–3685. doi: 10.1093/cercor/bhz334

Magnin, E., Francavilla, R., Amalyan, S., Gervais, E., David, L. S., Luo, X., et al. (2019). Input-specific synaptic location and function of the α5 GABAA receptor subunit in the mouse CA1 hippocampal neurons. *J. Neurosci.* 39, 788–801. doi: 10.1523/JNEUROSCI.0567-18.2018

Markham, J. A., McKian, K. P., Stroup, T. S., and Juraska, J. M. (2005). Sexually dimorphic aging of dendritic morphology in CA1 of hippocampus. *Hippocampus* 15, 97–103. doi: 10.1002/hipo.20034

Mattson, M. P., and Magnus, T. (2006). Ageing and neuronal vulnerability. *Nat. Rev. Neurosci.* 7, 278–294. doi: 10.1038/nrn1886

Mikulovic, S., Restrepo, C. E., Siwani, S., Bauer, P., Pupe, S., Tort, A. B. L., et al. (2018). Ventral hippocampal OLM cells control type 2 theta oscillations and response to predator odor. *Nat. Commun.* 9:3638. doi: 10.1038/s41467-018-05907-w

Morrison, J. H., and Hof, P. R. (1997). Life and death of neurons in the aging brain. *Science* 278, 412–419. doi:10.1126/science.278.5337.412

Moyer, J. R., and Disterhoft, J. F. (1994). Nimodipine decreases calcium action potentials in an age- and concentration-dependent manner. *Hippocampus* 4, 11–18. doi: 10.1002/hipo.450040104

Moyer, J. R., Power, J. M., Thompson, L. T., and Disterhoft, J. F. (2000). Increased excitability of aged rabbit CA1 neurons after trace eyeblink conditioning. *J. Neurosci.* 20, 5476–5482. doi:10.1523/JNEUROSCI.20-14-05476.2000

Müller, C., Beck, H., Coulter, D., and Remy, S. (2012). Inhibitory control of linear and supralinear dendritic excitation in CA1 pyramidal neurons. *Neuron* 75, 851–864. doi: 10.1016/j.neuron.2012.06.025

Murman, D. L. (2015). The impact of age on cognition. *Semin. Hear.* 36, 111–121. doi: 10.1055/s-0035-1555115

Park, J. B., Skalska, S., and Stern, J. E. (2006). Characterization of a novel tonic gamma-aminobutyric acidA receptor-mediated inhibition in magnocellular neurosecretory neurons and its modulation by glia. *Endocrinology* 147, 3746–3760. doi: 10.1210/en.2006-0218

Peng, Y. R., Zeng, S. Y., Song, H. L., Li, M. Y., Yamada, M. K., and Yu, X. (2010). Postsynaptic spiking homeostatically induces cell-autonomous regulation of inhibitory inputs via retrograde signaling. *J. Neurosci.* 30, 16220–16231. doi: 10.1523/JNEUROSCI.3085-10.2010

Peters, R. (2006). Ageing and the brain. *Postgrad. Med. J.* 82, 84–88. doi: 10.1136/pgmj.2005.036665

Potapenko, E. S., Biancardi, V. C., Florschutz, R. M., Ryu, P. D., and Stern, J. E. (2011). Inhibitory-excitatory synaptic balance is shifted toward increased excitation in magnocellular neurosecretory cells of heart failure rats. *J. Neurophysiol.* 106, 1545–1557. doi:10.1152/jn.00218.2011

Potier, B., Jouvenceau, A., Epelbaum, J., and Dutar, P. (2006). Age-related alterations of GABAergic input to CA1 pyramidal neurons and its control by nicotinic acetylcholine receptors in rat hippocampus. *Neuroscience* 142, 187–201. doi: 10.1016/j.neuroscience.2006.06.040

Potier, B., Lamour, Y., and Dutar, P. (1993). Age-related alterations in the properties of hippocampal pyramidal neurons among rat strains. *Neurobiol. Aging* 14, 17–25. doi: 10.1016/0197-4580(93)90016-5

Potier, B., Rascol, O., Jazat, F., Lamour, Y., and Dutar, P. (1992). Alterations in the properties of hippocampal pyramidal neurons in the aged rat. *Neuroscience* 48, 793–806. doi: 10.1016/0306-4522(92)90267-6

Power, J. M., Wu, W. W., Sametsky, E., Oh, M. M., and Disterhoft, J. F. (2002). Age-related enhancement of the slow outward calcium-activated potassium current in hippocampal CA1 pyramidal neurons in vitro. *J. Neurosci.* 22, 7234–7243. doi: 10.1523/JNEUROSCI.22-16-07234.2002

Pribiag, H., Peng, H., Shah, W. A., Stellwagen, D., and Carbonetto, S. (2014). Dystroglycan mediates homeostatic synaptic plasticity at GABAergic synapses. *Proc. Natl. Acad. Sci. U.S.A.* 111, 6810–6815. doi:10.1073/pnas.1321774111

Prönneke, A., Witte, M., Möck, M., and Staiger, J. F. (2020). Neuromodulation leads to a burst-tonic switch in a subset of VIP neurons in mouse primary somatosensory (barrel) cortex. *Cereb. Cortex* 30, 488–504. doi: 10.1093/cercor/bhz102

Pyapali, G. K., and Turner, D. A. (1996). Increased dendritic extent in hippocampal CA1 neurons from aged F344 rats. *Neurobiol. Aging* 17, 601–611. doi: 10.1016/0197-4580(96)00034-6

Randall, A. D., Booth, C., and Brown, J. T. (2012). Age-related changes to Na+ channel gating contribute to modified intrinsic neuronal excitability. *Neurobiol. Aging* 33, 2715–2720. doi:10.1016/j.neurobiolaging.2011.12.030

Rannals, M. D., and Kapur, J. (2011). Homeostatic strengthening of inhibitory synapses is mediated by the accumulation of GABA(A) receptors. *J. Neurosci.* 31, 17701–17712. doi: 10.1523/JNEUROSCI.4476-11.2011

Rapp, P. R., and Gallagher, M. (1996). Preserved neuron number in the hippocampus of aged rats with spatial learning deficits. *Proc. Natl. Acad. Sci. U.S.A.* 93, 9926–9930. doi: 10.1073/pnas.93.18.9926

Rizzo, V., Richman, J., and Puthanveettil, S. V. (2014). Dissecting mechanisms of brain aging by studying the intrinsic excitability of neurons. *Front. Aging Neurosci.* 6:337. doi: 10.3389/fnagi.2014.00337

Rosenzweig, E. S., and Barnes, C. A. (2003). Impact of aging on hippocampal function: plasticity, network dynamics, and cognition. *Prog. Neurobiol.* 69, 143–179. doi: 10.1016/s0301-0082(02)00126-0

Royer, S., Zemelman, B. V., Losonczy, A., Kim, J., Chance, F., Magee, J. C., et al. (2012). Control of timing, rate and bursts of hippocampal place cells by dendritic and somatic inhibition. *Nat. Neurosci.* 15, 769–775. doi: 10.1038/nn.3077

Rubio, S. E., Vega-Flores, G., Martinez, A., Bosch, C., Perez-Mediavilla, A., Del Rio, J., et al. (2012). Accelerated aging of the GABAergic septohippocampal pathway and decreased hippocampal rhythms in a mouse model of Alzheimer's disease. *FASEB J.* 26, 4458–4467. doi: 10.1096/fj.12-208413

Salesse, C., Mueller, C. L., Chamberland, S., and Topolnik, L. (2011). Age-dependent remodelling of inhibitory synapses onto hippocampal CA1 oriens-lacunosum moleculare interneurons. *J. Physiol.* 589, 4885–4901. doi: 10.1113/jphysiol.2011.215244

Scheibel, A. B. (1979). The hippocampus: organizational patterns in health and senescence. *Mech. Ageing Dev.* 9, 89–102. doi:10.1016/0047-6374(79)90123-4

Simkin, D., Hattori, S., Ybarra, N., Musial, T. F., Buss, E. W., Richter, H., et al. (2015). Aging-related hyperexcitability in CA3 pyramidal neurons is mediated by enhanced A-type K+ channel function and expression. *J. Neurosci.* 35, 13206–13218. doi: 10.1523/JNEUROSCI.0193-15.2015

Somogyi, P., Tamás, G., Lujan, R., and Buhl, E. H. (1998). Salient features of synaptic organisation in the cerebral cortex. *Brain Res. Rev.* 26, 113–135. doi: 10.1016/s0165-0173(97)00061-1

Stanley, E. M., Fadel, J. R., and Mott, D. D. (2012). Interneuron loss reduces dendritic inhibition and GABA release in hippocampus of aged rats. *Neurobiol. Aging* 33, 431.e1–431.e13. doi:10.1016/j.neurobiolaging.2010.12.014

Steriade, M. (1991). "Alertness, quiet sleep, dreaming," in *Cerebral Cortex*, Vol. 9, ed. A. Peters (New York, NY: Plenum Publishing Corporation), 279–357. doi: 10.1007/978-1-4615-6622-9_8

Tucker, K. R., Huertas, M. A., Horn, J. P., Canavier, C. C., and Levitan, E. S. (2012). Pacemaker rate and depolarization block in nigral dopamine neurons: a somatic sodium channel balancing act. *J. Neurosci.* 32, 14519–14531. doi: 10.1523/JNEUROSCI.1251-12.2012

Turi, G. F., Li, W. K., Chavlis, S., Pandi, I., O'Hare, J., Priestley, J. B., et al. (2019). Vasoactive intestinal polypeptide-expressing interneurons in the hippocampus support goal-oriented spatial learning. *Neuron* 101, 1150–1165.e8. doi: 10.1016/j.neuron.2019.01.009

Tyan, L., Chamberland, S., Magnin, E., Camiré, O., Francavilla, R., David, L. S., et al. (2014). Dendritic inhibition provided by interneuron-specific cells controls the firing rate and timing of the hippocampal feedback inhibitory circuitry. *J. Neurosci.* 34, 4534–4547. doi: 10.1523/JNEUROSCI.3813-13.2014

Wilson, I. A., Gallagher, M., Eichenbaum, H., and Tanila, H. (2006). Neurocognitive aging: prior memories hinder new hippocampal encoding. *Trends Neurosci.* 29, 662–670. doi: 10.1016/j.tins.2006.10.002

Wilson, I. A., Ikonen, S., Gallagher, M., Eichenbaum, H., and Tanila, H. (2005). Age-associated alterations of hippocampal place cells are subregion specific. *J. Neurosci.* 25, 6877–6886. doi: 10.1523/JNEUROSCI.1744-05.2005

Zoli, M., Jansson, A., Syková, E., Agnati, L. F., and Fuxe, K. (1999). Volume transmission in the CNS and its relevance for neuropsychopharmacology. *Trends Pharmacol. Sci.* 20, 142–150. doi: 10.1016/s0165-6147(99)01343-7

**Conflict of Interest:** The authors declare that the research was conducted in the absence of any commercial or financial relationships that could be construed as a potential conflict of interest.

*Copyright © 2020 Francavilla, Guet-McCreight, Amalyan, Hui, Topolnik, Michaud, Marino, Tremblay, Skinner and Topolnik. This is an open-access article distributed under the terms of the Creative Commons Attribution License (CC BY). The use, distribution or reproduction in other forums is permitted, provided the original author(s) and the copyright owner(s) are credited and that the original publication in this journal is cited, in accordance with accepted academic practice. No use, distribution or reproduction is permitted which does not comply with these terms.*

frontiers in Molecular Neuroscience

ORIGINAL RESEARCH
published: 22 October 2020
doi: 10.3389/fnmol.2020.527543

# Object Recognition Memory: Distinct Yet Complementary Roles of the Mouse CA1 and Perirhinal Cortex

*David A. Cinalli Jr.*[1,2†], *Sarah J. Cohen*[1,3†], *Kathleen Guthrie*[4,5] *and Robert W. Stackman Jr.*[1,2,3,5*]

[1]Jupiter Life Science Initiative, Charles E. Schmidt College of Science, Florida Atlantic University, Jupiter, FL, United States, [2]Department of Psychology, Charles E. Schmidt College of Science, Florida Atlantic University, Boca Raton, FL, United States, [3]Center for Complex Systems and Brain Sciences, Florida Atlantic University, Boca Raton, FL, United States, [4]Department of Biomedical Science, Charles E. Schmidt College of Medicine, Florida Atlantic University, Boca Raton, FL, United States, [5]FAU Brain Institute, Florida Atlantic University, Jupiter, FL, United States

While the essential contribution of the hippocampus to spatial memory is well established, object recognition memory has been traditionally attributed to the perirhinal cortex (PRh). However, the results of several studies indicate that under specific procedural conditions, temporary or permanent lesions of the hippocampus affect object memory processes as measured in the Spontaneous Object Recognition (SOR) task. The PRh and hippocampus are considered to contribute distinctly to object recognition memory based on memory strength. Allowing mice more, or less, exploration of novel objects during the encoding phase of the task (i.e., sample session), yields stronger, or weaker, object memory, respectively. The current studies employed temporary local inactivation and immunohistochemistry to determine the differential contributions of neuronal activity in PRh and the CA1 region of the hippocampus to strong and weak object memory. Temporary inactivation of the CA1 immediately after the SOR sample session impaired strong object memory but spared weak object memory; while temporary inactivation of PRh post-sample impaired weak object memory but spared strong object memory. Furthermore, mRNA transcription and *de novo* protein synthesis are required for the consolidation of episodic memory, and activation patterns of immediate early genes (IEGs), such as c-Fos and Arc, are linked to behaviorally triggered neuronal activation and synaptic plasticity. Analyses of c-Fos and Arc protein expression in PRh and CA1 neurons by immunohistochemistry, and of Arc mRNA by qPCR after distinct stages of SOR, provide additional support that strong object memory is dependent on CA1 neuronal activity, while weak object memory is dependent on PRh neuronal activity. Taken together, the results support the view that both PRh and CA1 are required for object memory under distinct conditions. Specifically, our results are consistent with a model that as the mouse begins to explore a novel object, information about it accumulates within PRh, and a weak memory of the object is encoded. If object exploration continues beyond some threshold, strong memory for the event of object exploration is encoded; the consolidation of which is CA1-dependent. These data serve to reconcile the dissension in the literature by demonstrating functional and complementary roles for CA1 and PRh neurons in rodent object memory.

**Keywords: muscimol, Arc, hippocampus, object recognition, qRT-PCR**

OPEN ACCESS

***Edited by:***
*Akiva Cohen, University of Pennsylvania, United States*

***Reviewed by:***
*Jean-Pascal Morin, National Autonomous University of Mexico, Mexico*
*Almira Vazdarjanova, Augusta University, United States*

***Correspondence:**
*Robert W. Stackman Jr.*
*rstackma@fau.edu*

*†These authors have contributed equally to this work*

***Received:*** *16 January 2020*
***Accepted:*** *18 September 2020*
***Published:*** *22 October 2020*

***Citation:***
*Cinalli DA Jr, Cohen SJ, Guthrie K and Stackman RW Jr (2020) Object Recognition Memory: Distinct Yet Complementary Roles of the Mouse CA1 and Perirhinal Cortex. Front. Mol. Neurosci. 13:527543. doi: 10.3389/fnmol.2020.527543*

## INTRODUCTION

Declarative, or explicit, memory is dependent on several brain structures within the mammalian medial temporal lobe (Eichenbaum, 2000; Squire et al., 2004). Unimodal sensory information is conveyed from the perirhinal cortex (PRh) to the hippocampus *via* the lateral entorhinal cortex (LEC), while contextual/spatial information is conveyed from the parahippocampal and postrhinal cortices to the hippocampus *via* the medial entorhinal cortex (MEC; Burwell and Amaral, 1998; Witter and Amaral, 2004). Lesions of the hippocampus impair rodent performance on spatial learning and memory tasks (Morris et al., 1982; Riedel et al., 1999); results that have established the functional significance of the hippocampal formation to spatial and temporal memory processes (O'Keefe, 1976; Eichenbaum et al., 1990; McNaughton et al., 2006; Eichenbaum, 2014). Lesions of the hippocampus also disrupt non-spatial memory as assessed by several tasks (Cave and Squire, 1991; Bunsey and Eichenbaum, 1996; Eichenbaum et al., 1999; Alvarez et al., 2001). However, non-spatial object memory has been attributed to the PRh based on studies of primates and rodents (Buffalo et al., 1999; Winters and Bussey, 2005). Indeed, compelling evidence demonstrates that lesions of the rodent PRh impair object recognition memory while sparing spatial memory (Winters et al., 2004). Such findings have promoted the view that while the PRh supports item (i.e., what) memory, the hippocampus supports spatial (i.e., where) memory. This dichotomous argument complicates our understanding of the neural mechanisms underlying event memory—that is, the memories for what has happened within the context of space and time. Interestingly, lesions of the PRh affect the location-specific firing properties of rat CA1 hippocampal neurons (Muir and Bilkey, 2001). Further, the functional inactivation of the PRh disrupts the performance of an object-place paired association task, likely by affecting object-place firing correlates of CA1 neurons in the hippocampus (Lee and Park, 2013). These results indicate that the PRh contributes significantly to hippocampal representations of spatial information and conjunctive representations of object-in-place. Finally, several reports indicate that under certain circumstances the rodent hippocampus is critical for object recognition memory (Cave and Squire, 1991; Wood et al., 1993; Clark et al., 2000; De Lima et al., 2006; Rossato et al., 2007; Broadbent et al., 2010; Clarke et al., 2010; Cohen et al., 2013; Stackman et al., 2016). Mixed results of the effects of PRh and hippocampal lesions on object memory indicate that there may be multiple, to be determined, principles by which these regions operate within memory circuits. Perhaps both structures are necessary for object memory but in different capacities, as we suggested in a recent review article (Cohen and Stackman, 2015). Additional systematic experiments are needed to reconcile the interaction of structures within the temporal lobe memory system.

The functional dichotomy between the hippocampus and the PRh has been heavily studied, resulting in different theories for the types of non-spatial memory processes supported by each region. One theory posits that recollection is attributed to the hippocampus while familiarity is attributed to the PRh. For example, results indicate that rats with hippocampal lesions exhibit impaired recollection but enhanced familiarity, arguing that these structures are either functionally independent with hippocampus mediating recollection only (Fortin et al., 2004; Sauvage et al., 2008), or that the two regions can interact competitively. Similarly, local silencing of rat PRh neuronal activity by microinfusion of lidocaine impairs object memory, a result interpreted as evidence that the PRh is necessary for familiarity (Winters and Bussey, 2005). An alternative view states that the functional difference between the hippocampus and PRh is concerning strong and weak forms of non-spatial object memory (Squire et al., 2007). According to this view, we assert that the functional difference between these structures is rooted in the gradient of object memory strength; strong object memory depends more on the hippocampus than PRh, and weak object memory depends more on PRh than the hippocampus. The apparent variability in the reported contributions of these structures to object memory may stem from differences in the experimental protocol used. To investigate this concept in mice, we manipulated the Spontaneous Object Recognition (SOR) sample session exploration criterion to produce either strong or weak memories. Preliminary studies demonstrated that limiting the duration of sample session object exploration to shorter or longer periods affected the strength of the resulting object memory as demonstrated by relative differences in object discrimination during the subsequent test session. Bilateral inactivation of CA1 of the dorsal hippocampus after weak object memory training did not affect test session discrimination performance; however, inactivation of CA1 after strong object memory training significantly impaired object discrimination. In contrast, bilateral inactivation of PRh after weak memory training significantly impaired object discrimination, but inactivation after strong object memory training did not affect object discrimination. These findings provide compelling evidence that the hippocampus supports strong object memory, while the PRh supports weak object memory.

Also, immunohistochemical techniques were employed to quantify the first proteins produced following neuronal activation, known as immediate early gene (IEG) proteins (Jones et al., 2001). Classically, neuronal expression of the IEGs, Fos, and the activity-regulated cytoskeletal protein (Arc), has been used to map rodent brain regions that are recruited at specific time points within a given task (Kubik et al., 2007; Kovács, 2008; Kawashima et al., 2014). We designed our IEG behavioral protocol similar to our inactivation studies to permit comparisons of c-Fos and Arc protein expression between CA1 and PRh neurons after strong and weak object memory training and testing conditions. Significant increases in IEG protein expression were only observed in CA1 neurons following a strong object memory sample session. However, a weak object memory sample session elicited increased IEG protein expression only in PRh neurons. To gain a better understanding of how Arc protein levels are modulated to support this double dissociation in the object memory circuitry, Arc mRNA expression was also quantified. These immunohistochemical results were largely supported by quantitative real-time PCR (qRT-PCR) analyses

of Arc mRNA expression in hippocampal and PRh samples after weak and strong object training. Based on both our pharmacological inactivation and IEG findings, we assert that strong object memory relies on the CA1 region of the dorsal hippocampus and weak object memory on PRh. Taken together, the results of the present studies support the view that the functionally distinct contributions of these two medial temporal lobe structures to object memory is dependent on memory strength.

# MATERIALS AND METHODS

## Mice

Male C57BL/6J mice (7–10 week old; Jackson Labs, Bar Harbor, ME) were housed 4 per cage with *ad libitum* access to food and water. The room temperature was maintained at 22 ± 4°C and humidity at 50 ± 5%. A 12-h light/dark cycle was maintained beginning at 7:00 AM. All experimental procedures were conducted during the light period following NIH guidelines; procedures were reviewed and approved by the Florida Atlantic University's Institutional Animal Care and Use Committee before the initiation of experiments. For mice used in the inactivation experiments ($n$ = 90), guide cannulae were implanted after 1-week acclimatization to the vivarium, and testing began 7 days post-operatively when the mice were 9 week old. For mice used in the immunostaining experiments ($n$ = 66), testing began after 1-week acclimatization to the vivarium, when the mice were 8 week old.

## Intrahippocampal Cannulation and Microinfusion

For the inactivation experiments, mice were implanted with chronic bilateral guide cannulae (Plastics One, Inc., Roanoke, VA, USA) above the CA1 region of the dorsal hippocampus (A/P − 2.0 mm, M/L ± 1.5 mm, D/V − 1.1 mm from Bregma; corresponding to intermediate CA1), as previously described (Cohen et al., 2013), or above the PRh (A/P − 2.25 mm, M/L ± 4.0 mm, D/V − 3.25 mm from Bregma; Franklin and Paxinos, 2008). Behavioral testing began 7 days later to permit postoperative recovery. Each mouse received a "mock infusion" each day for 2 days, immediately after the arena habituation, to acclimate the mice to the microinfusion procedure, as previously described (Cohen et al., 2013). For the actual microinfusions, mice were briefly restrained while caps and dummy cannula were replaced with infusion cannula and received bilateral (0.35 μl/side, 0.33 μl/min) intra-CA1/intra-PRh muscimol (Tocris, 1 μg/μl in 0.9% sterile saline) or 0.9% sterile saline immediately after the sample session. For both mock and actual microinfusions, the mice were awake for the entire 3-min procedure; after placement of the infusion cannulae, the mice were released into an empty holding cage and allowed to freely explore. The procedures for the actual bilateral microinfusion followed that described above for the mock infusion; however, this time the inserted infusion cannulae penetrated 1 mm beyond the tip of the guide cannulae to achieve bilateral intra-CA1/intra-PRh infusion.

## Spontaneous Object Recognition (SOR) Tasks and Protocols for Inactivation Studies

For all experiments, the apparatus consisted of two open-top, high-walled square arenas made of white ABS (each: 37.5 × 37.5 × 50 cm). For the inactivation experiments, during days 1 and 2, each mouse was habituated to one of the arenas for a 10-min empty arena session. On days 3 and 4, each mouse received one sample session and one test session, respectively, in the habituated (i.e., familiar) arena. During the sample session, each mouse was returned to the familiar arena that now contained two identical novel 3D objects (stainless steel cabinet leveling feet, each attached to a Plexiglas base, 4.2 cm dia and 6.0 cm tall, or plastic toy gorillas, each attached to a Plexiglas base) positioned in the northwest and southeast corners. To test strong object memory, each mouse was removed from the arena upon accumulating 30 s of exploration of each object or 38 s of either object; a time limit of 10 min was set for this event to occur. To test weak object memory, each mouse was removed from the arena upon accumulating 10 s of exploration of each object or 13 s of either object; again, this event was required to occur within 10 min. Preliminary studies were performed in which different object exploration time criteria were imposed to determine memory strength at a 24-h delay. Mice that achieved the strong object memory exploration criteria (i.e., 30/38 s) exhibited an average 70% preference for the novel object during the test session imposed 24 h later, while mice that achieved the weak object memory exploration criteria (i.e., 10/13 s) exhibited an average 60% preference for the novel object during the test session 24 h later. Imposing the respective sample object exploration criteria had the added advantage of ensuring that all mice were matched for sample session performance. The data from five mice that failed to reach the sample session exploration criteria were removed from the analyses. Microinfusions were administered immediately after the mouse was removed from the arena. During the test session, presented 24 h later, the familiar arena contained one of the familiar objects and one novel object (see **Figure 1A**). The mouse was removed from the arena after 5 min. The objects, arena floor, and walls were cleaned with 10% ethanol after each session to remove olfactory cues.

A modified SOR protocol was used for the immunostaining and qRT-PCR experiments, to ensure that comparisons could be made between memory trained groups of mice and respective yoked control groups of mice (see **Figure 1B**). Groups of mice were perfused 90 min after each respective behavioral session. All behavioral testing data was digitally acquired by the EthoVision XT (Noldus Inc., Leesburg, VA, USA) software package. Object exploration was scored off-line from the digital video files by experimenters that were blind to the treatment condition of the mice. Object memory was inferred from the discrimination ratio—calculated for each mouse by subtracting the time spent exploring the familiar object from the time spent exploring the novel object, and then dividing the result by the total time spent exploring both items. Discrimination ratio scores range from −1 to 1, with positive scores indicating novel object preference, negative scores indicating familiar object preference, and a

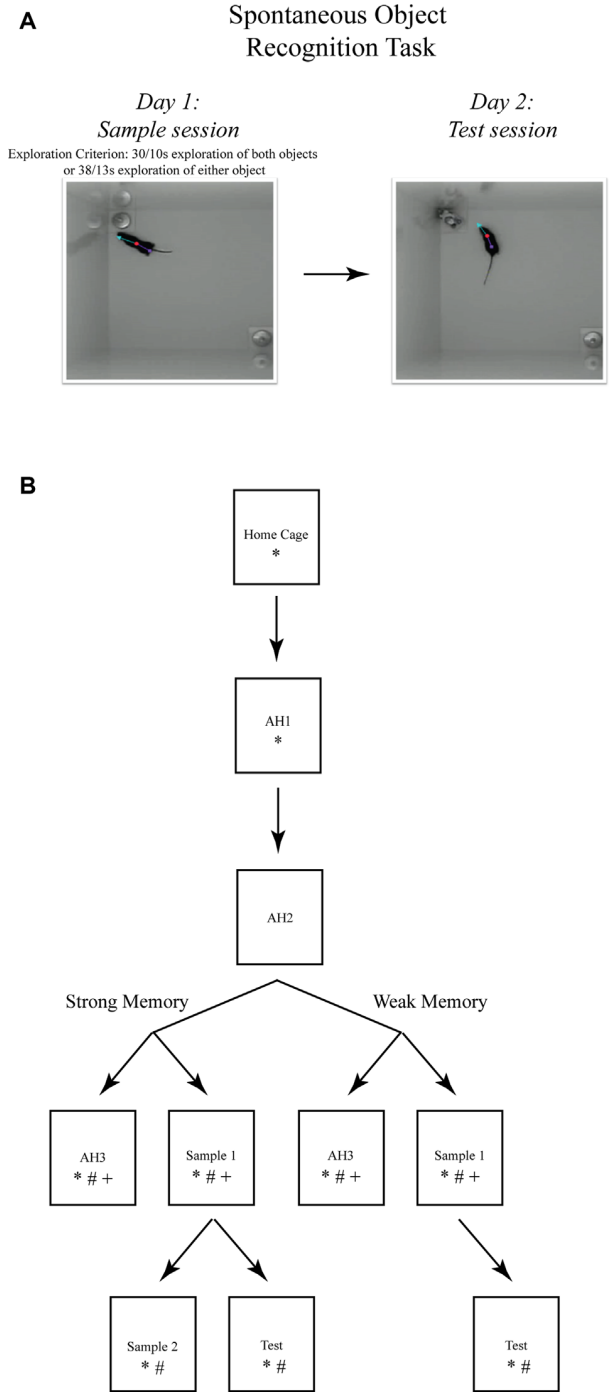


**FIGURE 1 |** The spontaneous object recognition (SOR) task. **(A)** The object recognition memory task protocol consisted of a sample session (left) and a test session (right) conducted within a familiar rectangular arena. During the sample session, the mouse was placed into the familiar arena to freely explore two presented objects until a prescribed sample session exploration criterion was reached. The criteria for strong object memory training was 38 s of exploration of one sample session object, or 30 s of exploration of both objects. The criteria for weak object memory training was 13 s of exploration on one object or 10 s of exploration of both objects. After a 24 h delay, the mouse was returned to the familiar arena for a 5 min test session in which (*Continued*)

**FIGURE 1 |** Continued
one of the sample objects was replaced with a novel object. Object memory was inferred from an analysis of the differences in time spent exploring both test session objects. These photographs depict an example of the arena configuration and the objects our lab has used to test object memory in mice using the SOR task (Cohen et al., 2013). **(B)** The SOR task protocols used for immunohistochemical staining of immediate early genes (IEGs) and quantification of mRNA after strong or weak object memory training. Each box represents a behavioral session and each arrow represents a 24 h delay between sessions. *, signifies a group of mice euthanized following that session for Fos protein quantification; #, signifies a group of mice euthanized following that session for Arc protein quantification; and +, signifies a group of mice euthanized following that session for *Arc* mRNA quantification. Boxes located next to one another, and connected by a common arrow, indicate that the groups were matched for the time in the testing arena.

ratio = 0 indicating chance performance or a lack of preference for one object over another. Mice were randomly assigned to the different experimental conditions (i.e., weak memory or strong memory) ahead of any behavior evaluations to ensure unbiased group selections. However, it is important to note that for the IEG experiments, each mouse of the sample session groups was yoked to a mouse in the respective arena habituation session group mouse. In this manner, the actual time in the arena would not be a factor influencing IEG expression levels.

## Behavioral Data Analysis

Measures of latency (in seconds) to achieve the sample object exploration criterion were compared using two-tailed Student's *t*-tests and discrimination ratio measures of saline- and muscimol-treated mice were compared using a three-factor ANOVA. For the immunostaining and qRT-PCR experiments, strong and weak object memory protocol groups were compared using two-tailed Student's *t*-tests.

## Histology

After the inactivation studies, each surgically implanted mouse was deeply anesthetized with 5% isoflurane and then the brain was dissected and preserved in 4% paraformaldehyde. Cannulae placements were confirmed by examination of cresyl violet-stained coronal 50 μm brain sections under a Nikon 55i light microscope. A subset of mice received a bilateral intra-PRh infusion of fluorophore-conjugated muscimol. Tissue was processed as above and then a Nikon 80i fluorescence microscope was used to image distribution within PRh. Data for any mice determined to have inappropriately placed cannulae were excluded from the analyses ($n$ = 6). See **Figures 2A,C** for representative photomicrographs of appropriate cannula placement.

## Immunohistochemistry

Ninety min following the conclusion of testing, mice were deeply anesthetized with sodium pentobarbital (i.p.). Each mouse was transcardially perfused with 0.1 M phosphate buffer, followed by 4% paraformaldehyde, and brains were dissected and preserved in 4% paraformaldehyde for 5 days. Fixed brains were serially sectioned at 30 μm using a cryostat (Leica CM1850). Free-floating coronal sections were immunostained to localize Fos or Arc protein. Endogenous peroxidase activity was

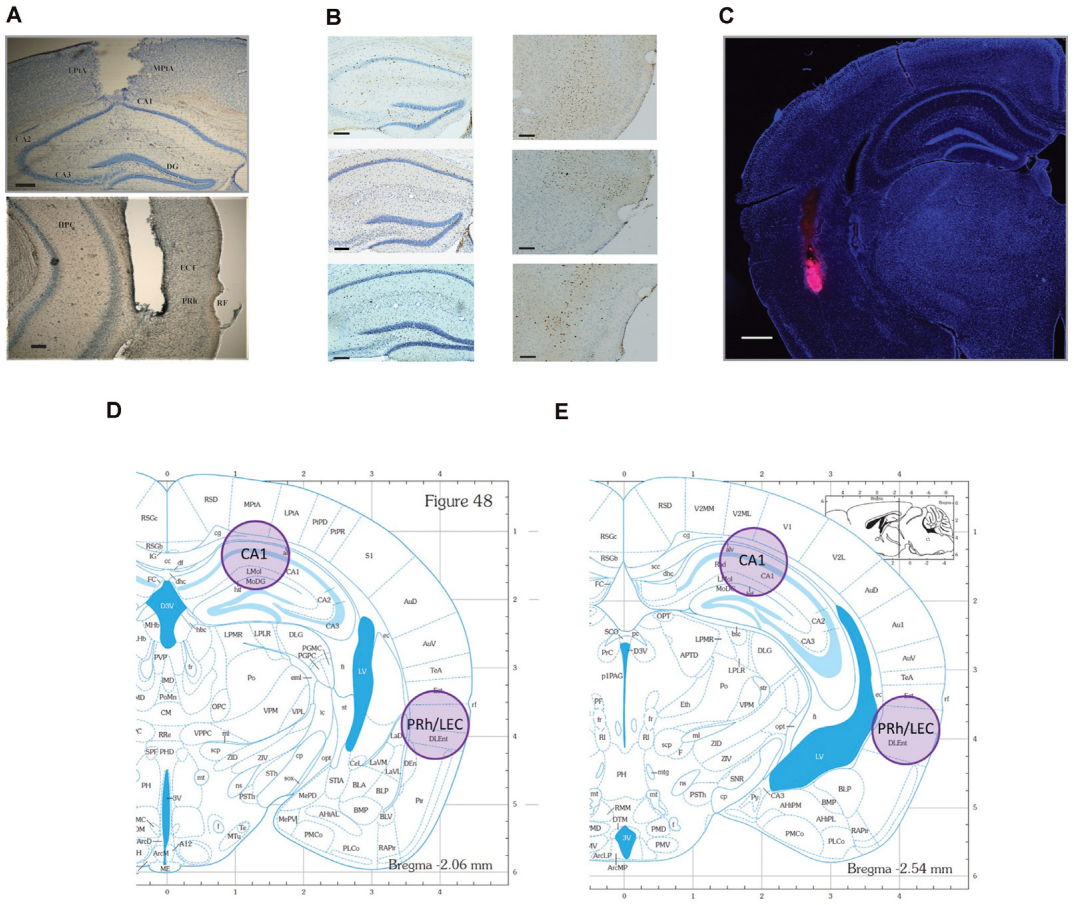


**FIGURE 2 |** Representative photomicrographs of tissue sections analyzed for Fos and Arc protein expression and the representative locations where tissue punches were taken for analysis of *Arc* mRNA. locations. **(A)** CA1 (top), and PRh (bottom) photomicrographs of guide cannulae placement (scale bars: 200 μm). Data for mice with improper placement were removed from further analyses. **(B)** Representative photomicrographs of the regions where IEG proteins were counted. Neurons are stained blue, while IEG-positive protein is stained dark brown (scale bars: 100 μm). **(C)** Representative distribution of muscimol in perirhinal cortex (PRh). This figure depicts a representative example of drug distribution in mice that received bilateral infusions of fluorophore-conjugated muscimol (red fluorescence, BODIPY TMR-X, Molecular Probes). DAPI Fluoromount (Thermo-Fisher) was used to improve visualization of the locally infused fluorophore-conjugated muscimol within the tissue (scale bar: 500 μm). Analysis of images revealed that the fluorophore-conjugated muscimol diffused within the rhinal cortex, but largely remained within the PRh. For representative CA1 spread, see Cohen et al. (2013) and Stackman et al. (2016). **(D,E)** Shaded circles indicate tissue punch isolation regions for qRT-PCR against respective coronal plates from the mouse stereotaxic atlas (numbers refer to millimeter from Bregma; Franklin and Paxinos, 2008).

quenched by incubation in 1% hydrogen peroxide for 5 min. Sections were then blocked in 5% normal goat serum (NGS) and 0.3% Triton X-100 in 0.1 M phosphate buffer (PB) for 1 h. Tissue sections were then transferred to PB containing rabbit polyclonal antibody to Fos (Santa Cruz Biotech, sc-52) or Arc (R&D Systems, AF636) at 1:500 dilution, for incubation overnight at 20° C with rotation. Following rinses in PB, sections were incubated in biotinylated goat anti-rabbit secondary antibody (Thermo Fisher Scientific, NC9256157) at 1:200 dilution in PB with 3% NGS. After 2 h, the tissue was washed and treated with avidin-biotin-peroxidase enzyme complex (ABC, Vector Labs, PK-4000) at 1:40 dilution in PB for 90 min. Chromagen was developed with diaminobenzidine, and sections were then rinsed in PB, mounted on gelatin-coated microscope slides, counter-stained with Cresyl violet, and cover-slipped. Every third section was examined for immunostaining for Fos or Arc. To quantify Fos- or Arc-, positive neurons in the hippocampus and PRh, six images per mouse were taken at the septal, intermediate, and temporal levels of CA1. The cytoarchitectonic subregions were identified from coronal sections and regional borders correspond to the levels depicted in **Figures 2D,E**. Bilateral images were matched across all mice for each respective level. Representative images are presented in **Figure 2B**.

## Cell Counting

The tissue sections were analyzed using a brightfield Nikon Eclipse 55i compound microscope with a 10× objective, photographed using a Nikon DS-Fi1 camera (100× total magnification), and acquired using Nikon Elements software. Estimates of Fos- or Arc-positive cells in CA1 and PRh were made by both of the primary experimenters (DC and SC),

who were blind to the experimental condition due to the randomization of the order the tissue sections were presented to confirm unbiased counting. Cytoarchitectonic subregions of CA1 of the dorsal hippocampus and rostral PRh were identified from coronal sections near AP −2.00 to −2.50 from Bregma, consistent with prior reports (Burwell, 2001; Bast et al., 2009). Preliminary staining was completed on tissue using a non-specific serum (secondary antibody only) to assess normal DAB background staining levels in the regions of interest. Clearly labeled cells in the target regions were counted if the color intensity of the respective stain was greater than that of the background. If the expression was ambiguous with the 10× objective, then localization was examined with a 40× objective for confirmation. Three bilateral sections were sampled from each mouse, such that analyzed sections were 90–150 μm apart (similar to the method described in Bernstein et al., 2019). The six total counts were averaged to generate the mean count for each mouse for each region. Group mean comparisons were made to test for significant differences in regional activation.

## Immunostaining Data Analysis

Averaged regional cell counts were normalized by dividing cell counts for each mouse by the average of the respective AH3 group (e.g., normalized count = total counts for a mouse that completed weak object training divided by the average number of counts for the weak AH3 group). This method of normalization was necessary to ensure that any activation differences between mice were not simply the result of time spent in the arena. Normalized counts were then analyzed using a three-factor (condition: AH3 vs. sample session; region: CA1 vs. PRh; memory strength: weak vs. strong) ANOVA, followed by Holm-Sidak multiple comparison tests where appropriate. Group comparisons between the home cage and AH1, AH1 and AH3, S1 and S2, and S and T, were analyzed by two-tailed Student's *t*-tests.

## RNA Isolation and qRT-PCR

Forty min following the conclusion of testing, mice were euthanized by rapid decapitation, and brains were quickly extracted and sliced into 1-mm thick coronal sections. Brain tissue from two adjacent 1-mm thick sections was pooled to increase the likelihood of successful RNA isolation. Samples were taken bilaterally from CA1 in the dorsal hippocampus and from PRh/LEC with a tissue biopsy punch 1 mm in diameter (see **Figures 2D,E**) and immediately frozen on dry ice. Punch samples from two adjacent sections were pooled for RNA isolation using TRIzol reagent (Ambion, 15596018) and purified using the RNeasy Mini Kit (Qiagen, kit # 74104). DNA removal was performed by on-column deoxyribonuclease digestion for 15 min using the RNase-Free DNase Set (Qiagen, 79254). cDNA was prepared using the High Capacity cDNA Reverse Transcription Kit (Applied Biosystems, kit # 4368814). Probes used to amplify *Arc* and *GAPDH* mRNAs were obtained from ThermoFisher (TaqMan, 4331182). qRT-PCR was performed with the Bio-Rad CFX96 Real-Time PCR detection system using the following amplification parameters: 95°C for 10 min; 50 cycles of 95°C for 15 s, 60°C for 15 s, 72°C for 15 s; 95°C for 15 s, 60°C for 15 s; to generate dissociation curves for PCR products. Reactions were performed in triplicate for each tissue sample.

## qRT-PCR Data Analysis

*Arc* mRNA levels were normalized to *GAPDH* levels measured in parallel. The data were analyzed by comparing C($t$) values obtained for each experimental condition (e.g., Weak AH3 vs. Weak Sample; Strong AH3 vs. Strong Sample) with the $\Delta\Delta C(t)$ method (Tsankova et al., 2006; Robison et al., 2014). Comparisons were made between cohorts of mice tested with strong and weak object memory experimental protocols groups using two-tailed Student's *t*-tests.

# RESULTS

## Inactivation Findings

Naïve mice received bilateral microinfusions of saline or muscimol into the CA1 or PRh immediately after completing a sample session in which the mice acquired weak or strong object memory training by exploring two identical novel objects for 10 s each, or 30 s each, respectively (see **Figure 2A** for representative placement of CA1 and PRh injection sites). Each mouse received a test session 24 h after the sample session. Results of these inactivation experiments were analyzed by a three-factor (region: CA1 vs. PRh; treatment: saline vs. muscimol; memory strength: weak vs. strong) ANOVA on the discrimination ratio measures. The three-factor ANOVA yielded a significant region × treatment × memory strength interaction ($F_{(1,89)} = 9.56$, $P < 0.01$), a significant treatment × memory strength interaction ($F_{(1,89)} = 3.88$, $P = 0.05$), but a non-significant region × memory strength interaction ($F_{(1,89)} = 0.99$, n.s.). As expected, the ANOVA yielded a significant main effect of treatment ($F_{(1,89)} = 7.69$, $P = 0.01$), indicating that the discrimination ratio scores were significantly greater for the saline-treated mice as compared to the muscimol-treated mice. The ANOVA also yielded a significant main effect of memory strength ($F_{(1,89)} = 4.35$, $P = 0.04$), with the follow-up *post hoc* test indicating that discrimination ratio scores were greater for mice given strong object memory training as opposed to weak object memory training. Last, the ANOVA yielded a non-significant main effect of region ($F_{(1,89)} = 0.44$, n.s.), and a non-significant region × treatment interaction ($F_{(1,89)} = 0.14$, n.s.). Given the significant three-way interaction, *post hoc* tests were conducted to focus on the specific main effects. The results of the *post hoc* tests are summarized below according to memory strength and region, and details are provided as to respective numbers of mice per treatment group, etc.

## Strong Object Memory

### Post-training CA1 Inactivation

Naïve mice received bilateral intra-CA1 muscimol ($n = 11$) or saline ($n = 12$) immediately following the sample session. The sample session concluded for each mouse when the strong sample session exploration criterion event was completed within 10 min (30 s of exploration of each object or 38 s of either object).

Both groups reached this sample session exploration criterion at similar times (saline 469 s, muscimol 459 s; $t_{(21)} = 1.93$, n.s.). During the test session, 24 h later, both groups spent equivalent amounts of time exploring the test session objects, but the mean discrimination ratio of the intra-CA1 muscimol group was significantly lower than that of the saline group [$t_{(21)} = 5.93$, $P < 0.001$, see **Figure 3A**, reprinted from Cohen et al. (2013)]. These findings suggest that inactivation of the CA1 region of the hippocampus after a sample session requiring considerable exploration of objects within a familiar context, prevented the consolidation of a strong object, or event memory (Cohen et al., 2013).

### Post-training Perirhinal Cortex Inactivation

Naïve mice received bilateral intra-PRh muscimol ($n = 15$) or saline ($n = 12$) immediately following the mice achieving the strong sample session exploration criterion event (see **Figure 2C** for representative distribution of fluorophore-conjugated muscimol within PRh). Both groups reached the sample session exploration criterion at similar times (saline 565 s, muscimol 523 s; $t_{(25)} = 1.30$, n.s.). During the test session, 24 h later, both groups spent equivalent amounts of time exploring the test session objects and demonstrated similar discrimination of the novel object from that of the familiar ($t_{(25)} = 0.62$, n.s., see **Figure 3A**). These results suggest that inactivation of the PRh after a sample session requiring considerable exploration of the objects did not impair the consolidation of a strong object or event memory.

## Weak Object Memory

### Post-training CA1 Inactivation

Naïve mice received bilateral intra-CA1 muscimol ($n = 10$) or saline ($n = 10$) immediately following the sample session. The sample session concluded for each mouse when the weak sample session exploration criterion was completed within 10 min (10 s of exploration of each object or 13 s of either object). Both groups reached sample session exploration criterion at similar times (saline 208 s, muscimol 153 s; $t_{(18)} = 0.05$, n.s.). During the test session, 24 h later, both groups spent equivalent amounts of time exploring the test session objects, and the mean discrimination ratios were also equivalent ($t_{(18)} = -1.11$, n.s., see **Figure 3B**). These findings suggest that inactivation of the hippocampus after a sample session requiring minimal exploration of the objects did not impair the consolidation of weak object memory.

### Post-training Perirhinal Cortex Inactivation

Naïve mice received bilateral intra-PRh muscimol ($n = 10$) or saline ($n = 10$) immediately following the mice achieving the weak sample session exploration criterion. Both groups reached sample session exploration criterion at similar times (saline 184 s, muscimol 182 s; $t_{(18)} = 0.07$, n.s.). During the test session, 24 h later, both groups spent equivalent amounts of time exploring the test session objects; however, the mean discrimination ratio of the saline-treated mice was significantly greater than that of the muscimol-treated mice ($t_{(18)} = 2.73$, $P = 0.01$, see **Figure 3B**). These findings suggest that inactivation of the PRh after a sample session requiring minimal exploration of the objects significantly impaired the consolidation of weak object memory.

## Immunohistochemical Findings

### Test Session Object Discrimination

Mean discrimination ratio scores were calculated for those mice that received a test session 24 h after the strong ($n = 6$) or weak object memory ($n = 4$) training session to confirm that the object memory inferred from the object discrimination was equivalent to that observed in the functional inactivation experiments. Mean discrimination ratios of both groups were significantly greater than chance (i.e., 0; strong memory: $t_{(5)} = 8.53$, $P < 0.01$; weak memory: $t_{(3)} = 6.71$, $P < 0.01$); however, the discrimination ratio of the strong object memory group was significantly greater than that of the weak object memory group ($t_{(8)} = 2.76$, $P = 0.03$, see **Figure 4A**).

### Fos Protein Expression After Strong Object Training

The expression of Fos protein was quantified within the CA1 region of the hippocampus as a preliminary test of object memory-triggered activation during distinct stages of the SOR task. Planned comparisons were made of the Fos expression patterns between specific groups of mice (and given the preliminary nature of this experiment, we restricted quantification of Fos to only CA1 following strong object memory training). Mice ($n = 8$) were euthanized immediately upon removal from the home cage to obtain a baseline level of Fos expression in CA1. Comparisons were made to mice ($n = 6$) euthanized 90 min after an Arena Habituation 1 session (AH1). As predicted, exploration of a novel environment activated the dorsal hippocampus, and Fos expression in CA1 neurons was significantly increased compared to that of home cage mice ($t_{(12)} = -7.15$, $P < 0.01$). Counts of Fos-positive CA1 neurons in mice after AH1 ($n = 6$), were compared to those of mice sacrificed 90 min after AH3 ($n = 7$), revealing that numbers of Fos-positive neurons in CA1 were significantly greater for the AH1 mice compared to the AH3 mice ($t_{(11)} = 3.47$, $P < 0.01$). Presumably, this result was due to the higher environmental novelty associated with exploration during AH1 than that during AH3. Finally, to investigate CA1 neuronal activation in the presence of only one novel object, normalized counts of Fos-positive neurons for mice that experienced a second sample session (that is, exploration of two now familiar objects, S2; $n = 8$) were compared those of mice that experienced a test session (one familiar and one novel object, $n = 8$). As expected, the mean numbers of Fos-positive cells in CA1 was significantly greater for test session mice compared to S2 mice ($t_{(14)} = -3.72$, $P < 0.01$); likely reflecting activity related to the process of detecting the novel object and encoding a memory of it during the test session. These Fos imaging studies provided initial confirmation of the engagement of CA1 neurons in strong object memory. Next, we conducted a comparative analysis of Arc protein expression in CA1 and PRh neurons after weak or strong memory training, as Arc protein is a direct indicator of synaptic plasticity, interacting with cytoskeletal proteins (Plath et al., 2006; Korb et al., 2013).

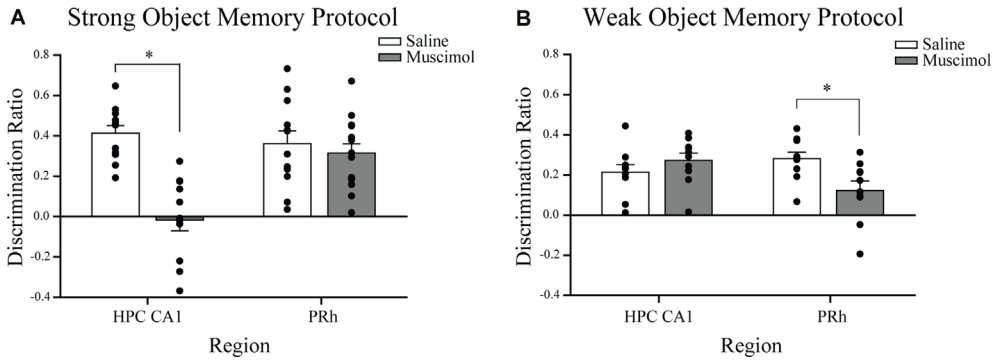


**FIGURE 3 |** Influence of post-sample session local muscimol-induced inactivation of the CA1 or PRh on test session object discrimination depends on strength of object memory training. **(A)** Mice that achieved the strong object memory training criterion and then received an intra-CA1 infusion of muscimol exhibited significant impairment of object discrimination relative to the intra-CA1 saline-treated mice during the test session. Mice that achieved the strong object memory training criterion and then received an intra-PRh infusion of muscimol exhibited test session object discrimination that was comparable to that of intra-PRh saline-treated mice. **(B)** Mice that achieved the weak object memory training criterion and then received intra-CA1 muscimol exhibited object discrimination that was comparable to that of intra-CA1 saline-treated mice. Mice that achieved the weak object memory training criterion and then received intra-PRh muscimol exhibited significant impairment of object discrimination relative to the intra-PRh saline-treated mice. Note that the overall object discrimination performance of mice that received weak object memory training was significantly lower than that of mice that received strong object memory training. $^*P < 0.05$ vs. vehicle group; mean ± SEM. Individual data points are represented by the small black filled circles superimposed over the respective group mean bar.

## Arc Protein Expression After Weak or Strong Object Training

As a more selective indicator of behaviorally triggered neuronal activity required for memory formation, we quantified numbers of neurons expressing Arc protein, known to play a crucial role in synaptic plasticity (Bramham et al., 2010; Gallo et al., 2018). Cell counts of CA1 and PRh Arc-positive neurons were made in cohorts of mice following the same behavioral protocol used to assess Fos expression described above, and in cohorts of mice following a weak object memory training session (see section "Behavioral Data Analysis"). To validate the accuracy of the staining technique used, groups of mice, with predictable activation patterns, were analyzed for Arc-positive neurons precisely as described for Fos (see section "Intrahippocampal Cannulation and Microinfusion"). Mice ($n = 7$) were sacrificed upon removal from the home cage to obtain an estimate of the baseline Arc expression in CA1 neurons. Comparisons were made to Arc-positive cell counts in CA1 from mice euthanized 90 min after an Arena Habituation 1 session (AH1; $n = 7$). Mean Arc-positive cell counts for AH1 mice were significantly greater than that of home cage mice ($t_{(12)} = -5.50$, $P < 0.01$); a predictable result. This finding confirmed that the staining protocol yielded appropriate patterns of activity-dependent Arc expression. As outlined in **Figure 1**, mice completed either a weak training or a strong training sample session. Respective groups of mice completed a third arena habituation session (yoked weak AH3 group or yoked strong AH3 group). Mice were euthanized and brains dissected 90 min after training. The mean distance traveled by the mice in the AH3 group (2,665.63 cm) was not significantly different than that of the respective sample session group (2,928.59 cm; $t_{(14)} = 0.60$, n.s.), suggesting that the presence of novel objects in the arena did not alter the perception of the context as being familiar. The novel, but otherwise non-threatening contexts tend to elicit greater amounts of exploratory locomotor responses in rodents. A subset of mice that received weak and strong object training was presented with a test session 24 h later. These mice were euthanized, and brains dissected 90 min after testing. Three tissue sections from the CA1 and PRh of each mouse were processed immunohistochemically to detect the neuronal expression of Arc protein.

First, to examine whether there were differences in Arc counts between the AH3 conditions, a two-factor (region: CA1 vs. PRh; "memory" strength: weak vs. strong) ANOVA was conducted on the raw Arc counts from mice that completed either the weak or strong AH3 control condition. The analysis revealed a significant strength × region interaction, $F_{(1,12)} = 10.28$; $P < 0.01$; a significant main effect of strength, $F_{(1,12)} = 23.33$, $P < 0.001$, and a significant main effect of region, $F_{(1,12)} = 39.48$; $P < 0.001$. The *post hoc* Holm Sidak tests following the significant interaction indicated a significant difference in raw Arc counts within the PRh between mice that completed a weak AH3 condition and those that completed a strong AH3 condition ($P < 0.001$). The raw PRh Arc counts following weak AH3 were higher than the PRh Arc counts following strong AH3. However, there was no significant difference in raw Arc counts within the CA1 between mice that completed a weak AH3 and those that completed a strong AH3 condition. *Post hoc* tests also yielded a significant difference in raw Arc counts between the PRh and CA1 for mice that completed the weak AH3 condition ($P < 0.001$), but no difference in raw Arc counts between the two regions for mice that completed the strong AH3 condition. These results suggest that exploration of the empty arena for the amount of time required of the weak AH3 condition and that for the strong AH3 condition did not differentially activate neurons of the CA1 region but did so for neurons of the PRh. The differences observed in raw Arc counts in the PRh after the two AH3 control conditions

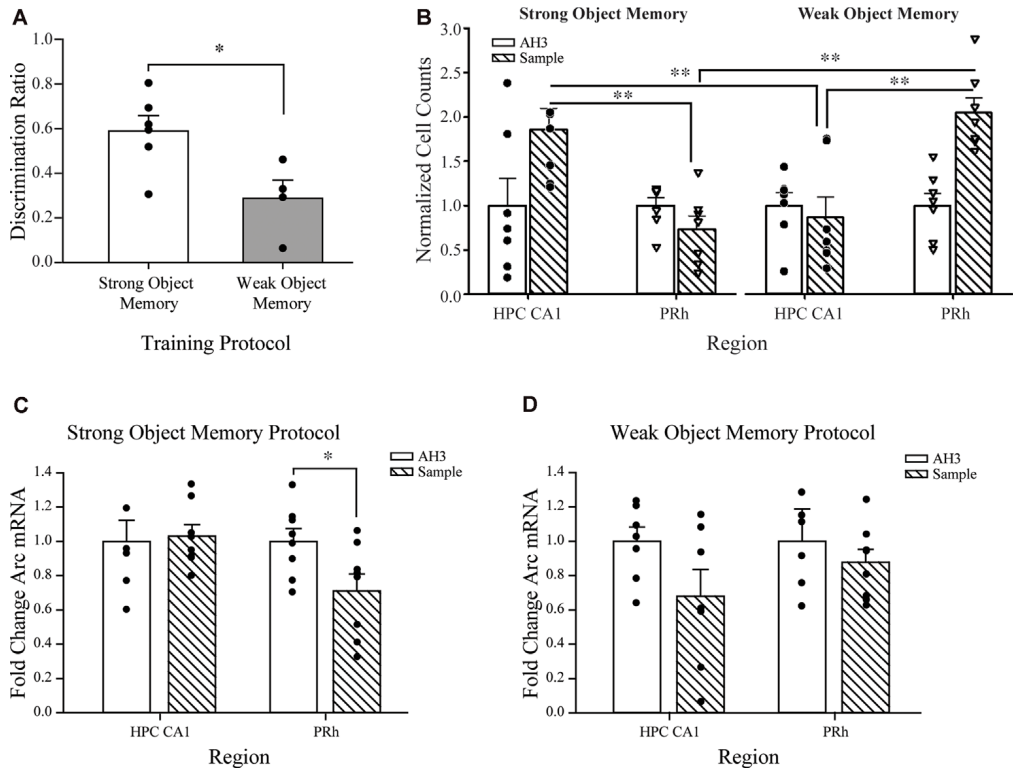


**FIGURE 4 |** Object discrimination, Arc protein expression, and *Arc* mRNA quantification in mice that received strong or weak object memory training during a sample session of the SOR task. **(A)** Test session discrimination ratios of mice 24 h after training in the strong memory protocol are significantly greater than those of mice trained in the weak memory protocol. Importantly, both groups perform significantly above a chance ratio of 0. $^{*}P < 0.05$. **(B)** Normalized counts of Arc-positive neurons in the CA1 region of the hippocampus and the PRh after completion of strong or weak object training or the respective arena habituation (AH3) session (see **Figure 1B** for a schematic diagram of the protocols). The graph illustrates the significant results from Holm-Sidak multiple comparison tests that followed the significant condition × region × memory strength interaction revealed by the three-factor ANOVA on normalized Arc counts (see "Materials and Methods" section "Spontaneous Object Recognition (SOR) Tasks and Protocols for Inactivation Studies" for complete details). Arc counts were significantly higher in the CA1 of mice that received strong object memory training compared to those in the PRh, as well as those of mice that received the strong AH3 session. Arc counts were significantly higher in the PRh of mice that received weak object memory training compared to those in the CA1, as well as those mice that received the weak AH3 session. $^{**}P < 0.001$ vs. the respective region or memory strength as indicated by the overlying brackets. **(C)** A separate cohort of mice was used to examine *Arc* mRNA expression in the CA1 and PRh after strong or weak object training during a sample session or the respective strong or weak AH3 session. *Arc* mRNA expression in the CA1 was comparable between groups of mice that received strong object memory training and those that received AH3. However, *Arc* mRNA expression in the PRh/LEC was significantly less in mice that received strong object memory training than for mice that received the strong AH3 control session. $^{*}P < 0.05$ vs. AH3 group. **(D)** For the weak object memory protocol, *Arc* mRNA expression in CA1 and in the PRh/LEC was not significantly different between mice that received weak object memory training compared to those that received the respective AH3 session. Data points and error bars on all graphs represent mean ± SEM. Individual data points are depicted in the respective panels by black filled circles and open triangles. Individual data points are represented by the small black filled circles, or open, inverted triangles, superimposed over the respective group mean bar.

perhaps provide some degree of justification for our choosing to normalize Arc counts by the respective AH3 condition before pursuing analyses of Arc protein expression after the two object training conditions.

Next, a three-factor (condition: AH3 vs. sample session; region: CA1 vs. PRh; memory strength: weak vs. strong) ANOVA was conducted on the normalized Arc counts (see **Figure 4**). The analysis yielded a significant condition × region × strength interaction ($F_{(1,48)} = 21.65$, $P < 0.001$), indicating that the level of condition determined the effect of the region × strength interaction. Analysis of the three-way interaction revealed that the region × strength interaction was significant at the sample session level of the condition variable ($P < 0.001$), but not significant at the AH3 level ($P = 0.568$). The three-factor ANOVA also yielded a significant region × strength interaction ($F_{(1,48)} = 14.75$, $P < 0.001$), and a significant main effect of condition ($F_{(1,48)} = 6.59$, $P < 0.015$). Holm-Sidak pairwise multiple comparison tests revealed that Arc counts in the CA1 region were significantly higher after strong object training compared to after weak training ($P < 0.001$). This result suggests that some threshold duration of object exploration must be reached to up-regulate Arc protein expression in the CA1 region; 10 s of exploration of each sample object is not sufficient, while 30 s of exploration of each object is sufficient.

Arc counts were significantly higher in the PRh after weak object training compared to after strong training ($P < 0.001$). Arc counts were significantly higher in the CA1 than in the PRh after strong training compared to after weak training

($P < 0.001$), while Arc counts were significantly higher in the PRh after weak training compared to after strong training ($P < 0.001$). These Holm-Sidak test results are indicated by the asterisks in **Figure 4B**. This pattern of results is consistent with the interpretation of our inactivation data; that is, the consolidation of a strong object or event memory is not dependent upon neuronal activity in the PRh nor does this behavioral experience appear to drive synaptic plasticity there. The finding that the limited amount of exploration of, or exposure to, novel objects or stimuli dictated by the weak training protocol, elicited greater numbers of Arc-positive cells in the PRh as compared to CA1 of the hippocampus, is consistent with results of prior analyses of Fos expression (Wan et al., 1999, 2001; Barbosa et al., 2013), and was expected since object recognition memory processes have been widely attributed to the PRh.

Finally, the analyses revealed that Arc counts in CA1 after strong, but not weak, training was significantly greater than that after the respective AH3 session ($P < 0.001$). This pattern of results supports the view that neuronal activity and synaptic plasticity in CA1 is necessary for the consolidation of a strong object, or event memory. The data are also consistent with the view that the consolidation of a weak memory for objects explored does not engage CA1 neuronal activity or drive synaptic plasticity there. Likewise, Arc counts in PRh after weak, but not strong, training was significantly greater than that after the respective AH3 session ($P < 0.001$). For clarity, these significant results were not labeled in **Figure 4B** but will be fairly obvious to the reader. The differential impact of object training compared to an equivalently timed arena habituation session on the number of Arc expressing neurons in the CA1 and PRh runs counter to the argument that differences in Arc protein expression between strong and weak sample sessions are attributable to the time spent within the arena.

We conducted linear regression analyses to further examine the relationship between object training-induced Arc protein expression in the PRh and CA1 after a weak or strong sample session. The number of PRh neurons expressing Arc protein correlated with the number of CA1 hippocampal neurons expressing Arc protein in mice that had received weak object training; Pearson's $r = 0.91$, $P = 0.004$. However, no correlation was found between the number of Arc protein-expressing neurons in the PRh and that in the CA1 in mice that had received strong object training, Pearson's $r = 0.25$, n.s. While the significant correlation between regions after weak training is interesting and consistent with the results from the three-factor ANOVA described above, it should be considered with the proviso that caution should be exercised when interpreting results of regression analyses based on fewer than 10 pairs of observations.

Similar to the analysis of Fos immunolabeling reported in sections "Intrahippocampal Cannulation and Microinfusion," a cohort of mice received strong object training during a sample session and then 24 h later, received either a test session or a second sample session (S2) as a control condition. Mice were euthanized and brains dissected 90 min after testing, and tissue sections from the CA1 were processed for Arc protein expression. Raw counts of Arc positive cells in CA1 were normalized against the average Arc cell counts from the S2 control group. Arc-protein expression in CA1 neurons was significantly higher in mice that had experienced the test session compared to the S2 group (Mean ± SEM, Test = 2.49 ± 0.58; S2 = 1.00 ± 0.19; $t_{(14)} = -2.44$, $P < 0.05$). The difference in CA1 Arc protein expression observed in the test session mice compared to that of the S2 mice likely reflects the process of discriminating the presented test session objects (one being novel) with the retrieved memory of the objects explored during the previous sample session. Except for the novel object, all other stimuli present during the test session are identical to that of the S2 condition. Presumably, both the test session and the S2 session experiences promote retrieval of the memory for the previous sample session, yet the respective groups of mice use that information distinctly. Thus, the significant difference in Arc protein expression in CA1 between the two groups of mice indicates the sensitivity of immunohistochemical analysis of activity-dependent Arc expression and provides further support for a critical role of CA1 in strong object memory.

## qRT-PCR Findings

### Strong Object Memory

Arc mRNA expression was quantified within CA1 of the dorsal hippocampus and in PRh/LEC after strong object training during a sample session or after equivalently timed arena habituation sessions to further elucidate the molecular mechanisms underlying the induction of synaptic plasticity during object memory consolidation. The behavioral protocol was consistent with the Arc immunohistochemistry experimental design and planned comparisons analyses were conducted on *Arc* mRNA transcript expression following the exploration of objects to achieve the strong object memory training criterion ($n = 8$) or after exploration during the yoked AH3 session ($n = 7$). There was no significant difference in *Arc* mRNA expression in CA1 between the strong sample session and the AH3 session groups ($t_{(13)} = -0.23$; n.s., see **Figure 4C**), a result that is inconsistent with the increase in CA1 Arc protein expression observed in similarly trained groups of mice compared to AH3 mice. Thus, the increased expression of Arc protein in CA1 neurons after strong object memory training occurs independently of a net change in the level of *Arc* mRNA transcripts.

*Arc* mRNA was similarly measured in PRh/LEC samples after mice had achieved the strong sample exploration criterion ($n = 8$) or had received an AH3 session ($n = 8$). There was a significant decrease in *Arc* mRNA levels in PRh/LEC for mice that completed the strong sample session compared to those of the strong AH3 exploration groups ($t_{(14)} = 2.34$, $P < 0.05$, see **Figure 4C**). This result suggests that exploration of objects that reaches or exceeds our strong sample session criterion of 30-s on each object, or 38 s on one object triggers a down-regulation of *Arc* mRNA in PRh/LEC, which may account for the observed lack of significant increase in Arc-positive neurons in PRh following a strong object memory sample session. This pattern of results

suggests a potential mechanism that down-regulates *Arc* mRNA transcripts in PRh/LEC; a mechanism that may be essential to the recruitment of CA1 during the consolidation of strong object memory. Such mechanisms for Arc mRNA degradation have been discussed (for reviews see Bramham et al., 2008, 2010).

### Weak Object Memory

Arc mRNA expression was quantified within CA1 of the dorsal hippocampus and in PRh/LEC after weak object training during a sample session or after an equivalently timed arena habituation session. The behavioral protocol was consistent with the Arc immunohistochemistry experimental design, and planned comparisons were conducted on *Arc* mRNA transcripts of mice following exploration of objects to achieve the weak object memory training criterion ($n$ = 7) or after exploration during the yoked AH3 session ($n$ = 7). Analyses revealed no significant difference in *Arc* mRNA expression within CA1 in mice that had completed the weak sample session or a weak AH3 session ($t_{(12)}$ = 1.82; n.s., see **Figure 4D**). This result is consistent with our immunohistochemistry results, described above, suggesting that *Arc* mRNA expression in CA1 was not affected by weak sample exploration, likely due to the lack of change in protein expression in CA1 following weak sample session training—given that CA1 neurons were not activated by this behavioral event. This result supports the view that CA1 activity is not critically involved in the consolidation of weak object memory.

A similar analysis of Arc mRNA expression in PRh/LEC in mice that had completed the weak sample session ($n$ = 8) or a weak AH3 session ($n$ = 7) revealed no significant difference between training groups ($t_{(13)}$ = 0.64; n.s., see **Figure 4D**). The equivalent *Arc* mRNA expression levels between weak sample sessions and AH3 trained mice is in contrast to the observed significant increase in Arc protein expression in PRh neurons between similarly trained groups of mice. The increased Arc protein expression in the PRh after weak sample session training is independent of a net change in the level of *Arc* mRNA transcript expression, suggesting that weak training drives an increase in translation of *Arc* mRNA transcripts.

## DISCUSSION

The present set of experiments was designed to investigate the differential contributions of the CA1 region of the hippocampus, and PRh to object memory in male C57BL/6J mice. Our experiments used local microinfusion of muscimol to temporarily block neuronal activity in the CA1 and PRh during object memory consolidation, and immunohistochemistry to stain for Fos and Arc proteins, and qRT-PCR to quantify Arc mRNA expression triggered by behaviors associated with the encoding, consolidation, and retrieval of object memory. It was predicted that if the amount of time the mice were permitted to explore objects during the sample session of the SOR task was increased or decreased, then the strength of the resulting memory of the objects would be altered accordingly. Based on test session measures of discrimination ratio, we characterized the resulting memory after a limited 10 s exploration of each sample session object (or 13 s of one object) as a weak object memory, while that after a more extensive 30 s exploration of each sample session object (or 38 s of one object) as a strong object memory. Indeed, the novel object preference exhibited by mice during the test session was significantly greater in mice that had completed 30/38 s exploration of the sample session objects (strong object memory training) compared to those mice that had only completed 10/13 s of exploration (strong object memory training). These two different sample session object exploration criteria were then used to test whether the formation of strong object memory or weak object memory differentially recruited CA1 or PRh neuronal activity.

Our experiments yielded several key results. First, the bilateral inactivation of CA1 after strong, but not weak, object memory training impaired object discrimination during the test session presented 24 h later. This result suggests that CA1 neuronal activity is essential for the consolidation of strong object memory or the memory of the event of exploring novel objects within a familiar context. The second key result was the complement: the bilateral inactivation of neuronal activity in the PRh after weak, but not strong, object memory training impaired object discrimination during the test session 24 h later. This result supports the view that PRh neuronal activity is required for the consolidation of object memory that guides discrimination based on object familiarity but is not necessary for the consolidation of stronger event memory. Although the local microinjections of muscimol were bilateral and restricted to the respective regions, both regions extend in the septo-temporal or rostral-caudal plane. Therefore, one might caution against concluding the role of a given hippocampal or extra-hippocampal structure based on the behavioral results after functional inactivation of a restricted subset of its neurons. For the present study, all aspects of the injection volume, rate, and respective cannula placements were consistent across the groups of mice. However, whether the bilateral injections of muscimol into the CA1 or PRh impaired test session behavior depended on the amount of time the mouse was permitted to explore objects during the sample session. Specifically, the same degree of post-training inactivation of neuronal activity in the PRh (e.g.,) only impaired novel object preference in those mice given weak memory training. Thus, the effect of inactivation appears to have been dependent on the degree of behavioral experience rather than any methodological difference. It is also important to note that by controlling the duration of the sample session by requiring the mice to accumulate 10 s or 30 s of sample object exploration, effectively matches all mice for sample session experience. This procedural control provides some assurance that the differences observed in subsequent test session behavior are most likely a consequence of the post-sample manipulation rather than due to sensorimotor, motivational, or attentional differences in the mice during the sample session.

In parallel with the regional inactivation experiments, we analyzed brain sections acquired from an additional cohort of mice to examine the behaviorally triggered expression of Arc protein, which is an IEG marker for neuronal plasticity.

The Arc protein analyses revealed that a significantly larger ensemble of CA1 neurons was recruited as a result of the exploration of objects during the sample session of the strong memory protocol, as compared to the ensemble recruited as a result of the exploration of an empty arena during AH3. The increase in Arc protein-labeled neurons triggered by object exploration likely reflects the encoding and/or consolidation of strong object memory within CA1 and is similar to an earlier comparative study of c-Fos expression in CA1 and PRh after object exploration (Albasser et al., 2010). This finding, that strong object memory is supported by the activity of CA1 neurons, but not PRh neurons is consistent with the finding that the firing of individual PRh neurons is modulated by object familiarity (Ahn and Lee, 2015; Brown and Banks, 2015). The contribution of CA1 to strong object memory reported here is also consistent with previous reports that when mice are allowed to explore each sample object for at least 30 s, the memory that is encoded for that object is dependent on an intact and fully functioning hippocampus (Cohen et al., 2013; Tuscher et al., 2018). In contrast, analyses of Arc protein revealed that an equivalent, but lower number of CA1 neurons were recruited during the sample session of the weak object memory protocol and AH3. Moreover, the Arc protein analyses revealed that the CA1 neuronal ensemble recruited by the AH3 group yoked to the strong object memory trained group was not significantly different from that of the AH3 group yoked to the weak object memory trained group. This means that exploration of the empty familiar arena, regardless of time spent within the arena, did not differentially activate CA1 neurons. Therefore, we can conclude that the significantly greater activation of CA1 neurons observed after the strong object memory training reflects the object exploration-induced encoding and consolidation of object memory rather than simply a consequence of exploring the familiar context.

Last, we utilized a naïve cohort of mice and qRT-PCR to quantify *Arc* mRNA expression in CA1 and PRh/LEC following strong and weak object memory training or in the respective yoked AH3 control groups, similar to that of our immunohistochemistry experiments. Analyses revealed no significant difference in *Arc* mRNA expression in the CA1 after strong object memory training compared to the strong AH3 control condition, and no significant difference in *Arc* mRNA expression in the PRh after weak object memory training compared to the weak AH3 control condition. Taken together with the results from the present inactivation and Arc protein expression studies, the Arc mRNA indicates a somewhat consistent pattern of results. We observed that strong object training, shown to require CA1 neuronal activity and perhaps CA1 synaptic plasticity, does not alter the net level of *Arc* mRNA in the CA1 relative to the strong AH3 condition. Likewise, weak object training, shown to require PRh neuronal activity and perhaps PRh synaptic plasticity, does not alter the net level of *Arc* mRNA in the PRh/LEC relative to the weak AH3 condition. In summary, the data suggest that object memory consolidation that promotes Arc protein expression does so without altering the level of *Arc* mRNA expression beyond that induced by the respective AH3 control condition. The pattern of results may also indicate that increases in Arc protein expression in the CA1 or PRh after strong or weak training, respectively deplete local stores of *Arc* mRNA, and homeostatic mechanisms are engaged to replenish basal levels of *Arc* mRNA.

A significant decrease in *Arc* mRNA in the PRh/LEC was observed after strong object memory training as compared to that after a strong AH3 control session (see **Figure 4C**). Note that Arc protein expression in PRh was significantly higher after weak object training compared to the weak AH3 condition. Collectively, the data suggest that if object exploration continues beyond the weak training, as it would during strong object training, then there is a significant increase in Arc protein expression in CA1, perhaps triggered by PRh dependent activation of hippocampal circuits consistent with the notion of transferal of object information from PRh to the hippocampus. The observed decrease in PRh/LEC *Arc* mRNA after strong training suggests two possibilities. One, the transfer of object information from PRh to the hippocampus requires significant translation (i.e., turnover) of available *Arc* mRNA in the PRh, which may account for the fact that Arc protein expression in PRh after strong object memory training is equivalent to that after a strong AH3 session. Thus, as strong object memory training disengages the PRh, *Arc* mRNA is down-regulated. Alternatively, the transfer from PRh to the hippocampus involves the active reduction of Arc protein built up during weak object training and the degradation of *Arc* mRNA in the PRh/LEC. This result alludes to the potential for a downregulating mechanism influencing baseline levels of *Arc* mRNA transcripts as a potential target underlying the recruitment of CA1 to support strong object memory (Bramham et al., 2008, 2010).

Analyses also revealed a decrease, albeit not significant, in *Arc* mRNA in the CA1 after weak object memory training compared to that after a weak AH3 control session (see **Figure 4D**). This result suggests that *Arc* mRNA expression is decreased in the brain region not engaged by the object memory training. Specifically, as weak object memory training did not engage the CA1 region beyond that of the weak AH3 session, *Arc* mRNA was degraded in the CA1. These results suggest that the increase in Arc protein observed in our immunohistochemical studies was not dependent on an increase in *Arc* mRNA expression. We acknowledge that the utilization of the biopsy punch for tissue sampling introduces variability, particularly in CA1 samples, which may include white matter and portions of the overlying cortex. A more precise tissue sampling technique (e.g., laser capture microscopy) may increase the likelihood of observing memory load-dependent differences in *Arc* mRNA expression in CA1. Together, the data suggest that weak object memory is dependent on the PRh/LEC and that there is a down-regulation of *Arc* mRNA in the PRh/LEC after strong memory training, which may promote the recruitment of CA1 activity to support the consolidation of strong object memory.

Collectively, these findings suggest that a sufficient degree of exploration of a novel or familiar object is necessary before synaptic plasticity is induced within the CA1 region, and thereafter CA1 neuronal activity is required to successfully consolidate the memory of the objects. Our previous work (Stackman et al., 2016) indicated that pre-test silencing of

CA1 neuronal activity abolished test session novel object preference of mice that had completed strong object exploration criteria 24 h earlier. Therefore, it seems that the strong object memory-training event triggers synaptic plasticity within CA1, necessary for the consolidation (and subsequent retrieval) of the memory for the object exploration event, both of which are dependent on CA1 neuronal activity. It remains to be determined whether the pre-test inactivation of PRh neuronal activity affects novel object preference in mice that completed strong object exploration criteria. However, the present data suggest a transfer of critical regional neuronal activity supporting object memory consolidation from PRh to CA1, depending on the amount of time the mice are permitted to explore the novel objects during the sample session. We recently reported that muscimol inactivation of CA1 neuronal activity impaired novel object preference of strong memory trained mice when the test session was presented 20 min, but not 5 min, after the sample session (Ásgeirsdóttir et al., 2020). We interpreted that result as evidence that a working memory mechanism, perhaps in the PRh, supported object recognition when a <20 min delay was imposed between sample and test. Taken together with the present results, we propose that the transfer of object information from the PRh to the CA1 requires time, but also depends on a critical degree of memory load. These findings may be viewed as largely consistent with the notion that PRh is critical for object recognition based on familiarity; however, the recollection of the memory for the event of exploring novel objects within the spatial and temporal context of the testing arena requires CA1.

Furthermore, the immunohistochemical analyses of the brain tissue of mice that explored the novel objects for only 10 s each (i.e., the weak memory sample session group) indicate that the ensemble of Arc protein-expressing CA1 neurons was not significantly different from the CA1 ensemble in mice that explored the empty familiar arena (i.e., the weak memory AH3 group). Limiting the amount of novel object exploration during the sample session results in a weak memory, as demonstrated by significantly lower object discrimination exhibited during the test session. Our results reveal that the consolidation of such a weak object memory does not recruit CA1 neurons. Both AH3 mice and mice that received weak object training mice engaged in similar patterns of exploratory behavior and equivalent movement during their respective sessions; however, the information acquired is likely different, yet this difference was not reflected in CA1 Arc protein or mRNA expression. The lack of difference in CA1 Arc protein and mRNA expression could be interpreted in at least two ways.

One possibility is that the CA1 region may not contribute to the encoding of object memory, whether weak or strong. Testing the specific contribution of CA1 to object memory encoding will require silencing selective populations of neurons with high temporal precision. Certainly, pharmacological tools such as local muscimol microinfusion would not permit such highly precise time locking, although chemogenetic and optogenetic tools may be effective (Madisen et al., 2012; Boyden, 2015). The second possibility is that CA1 is only recruited after the mouse achieves some threshold amount of object exploration. Before reaching that object exploration threshold, the processing of memory for the objects is supported by PRh. This argument then suggests that there is some information threshold or storage buffer-like mechanism within PRh that once surpassed triggers the recruitment of CA1. A similar interpretation of mnemonic transfer from PRh to the hippocampus was stated in earlier reports (Gaffan and Parker, 1996; Liu and Bilkey, 1998), and more recent reports suggest that interactions between hippocampal regions and extra-hippocampal regions including the PRh are critical for encoding object-based episodic memory (Vilberg and Davachi, 2013). Such a transfer mechanism would be consistent with the downregulation of *Arc* mRNA observed in the PRh following strong object memory training compared to that observed in mice that experienced the AH3 control condition. Moreover, the significant increase in the count of Arc protein-positive PRh neurons of mice trained in the weak object memory protocol compared to the yoked AH3 group is consistent with the contribution of the PRh to object recognition, perhaps based on object familiarity. The finding that muscimol inactivation of PRh neurons impaired object memory encoded after limited exploration of objects, is also consistent with reports from studies of humans, nonhuman primates, and rodents, that damage to the PRh increases the rate of forgetting of recently acquired information (Wiig et al., 1996; Buffalo et al., 1998; Eichenbaum et al., 2007; Squire et al., 2007). These results are in agreement with previous findings that have shown that when mice explored sample objects for a limited amount of time (in this case 10 s on each object), test session object recognition was not impaired by hippocampal lesion or inactivation (Winters and Bussey, 2005; Winters et al., 2008). Taken together, these data imply that minimal exploration of novel objects promotes PRh neuronal activity; without recruiting CA1.

There is a limit to the interpretations one can draw from the results of traditional lesion studies related to the function of a specific brain region since the lesion technique renders the region of interest destroyed and unavailable to process incoming information. Temporary inactivation is an alternative technique that avoids some of the pitfalls of the lesion approach. Previous reports indicate that with a strong object memory protocol, pre-sample, or pre-test, intra-CA1 muscimol impairs object discrimination during the test session (De Lima et al., 2006; Cohen et al., 2013; Stackman et al., 2016; Ásgeirsdóttir et al., 2020). The results of the present regional inactivation studies extend the evidence demonstrating a significant role for CA1 in strong object memory. Additionally, the current immunohistochemical findings demonstrate that a significantly greater number of CA1 neurons are active after a strong sample session as compared to after a weak sample session, as represented by an increase in Arc expression. Also, the significant decrease in *Arc* mRNA expression in the PRh/LEC following a strong sample session suggests a down-regulation in that region. Alternatively, in a weak object memory protocol, the only inactivation of PRh led to impairments in test session object memory. These results are supported by the immunostaining findings showing increased neuronal activation in PRh following a weak object memory sample session. While infusion techniques have proven to be an effective

treatment to temporarily inactivate a given region of the brain, the technique is limited (for review, see Cohen and Stackman, 2015). Future studies could employ optogenetics to selectively inactivate neurons in a given region for a discrete amount of time. This technique would allow for cellular inactivation only while the mice are exploring the objects to provide more precise control of the onset and offset of neuronal inactivation.

The present studies lend support to the notion that stronger event memories depend more upon the hippocampus than upon the PRh, as originally proposed by Squire et al. (2007). Their proposal was that the differences in memories supported by the hippocampus and PRh were determined by memory strength, suggesting that medial temporal lobe structures neighboring the hippocampus were responsible for encoding weak memory, as opposed to familiarity. Furthermore, the present studies provide molecular evidence for a phenomenon that has been well characterized on the behavioral level. Increased hippocampal activation, and down-regulation of *Arc* mRNA in PRh after the exploration of novel objects, and the observed impairments in object discrimination following CA1 inactivation in the strong object memory protocol, provides clear evidence for the contribution of the hippocampus to strong object recognition memory. On the other hand, in agreement with much of the literature on the effects of permanent lesions of PRh, the inactivation and immunohistochemical staining results after the weak object memory protocol add to the current knowledge about a functional role of PRh in the consolidation of a relatively weaker associative memory for objects.

This study provides evidence to suggest that both the PRh and the CA1 of the hippocampus in rodents support object memory processing, but that the recruitment of each structure depends on the strength of the memory, or the memory load, dictated by the amount of time the mouse engages in the exploration of the novel objects. Our present findings, which dissociate the contributions of the PRh and the CA1 region of the hippocampus to weak object memory and strong event memory, respectively, provide a unifying theory on object memory processing. Importantly, our results and the accompanying theory provide evidence for the necessity of both structures in object recognition memory.

## DATA AVAILABILITY STATEMENT

The datasets generated for this study are available on request to the corresponding author.

## ETHICS STATEMENT

The animal study was reviewed and approved by the Institutional Animal Care and Use Committee of Florida Atlantic University.

## AUTHOR CONTRIBUTIONS

DC designed and performed the experiments, analyzed data and wrote the article. SC designed and performed the experiments, analyzed data and wrote the article. KG designed the experiments. RS designed the experiments and wrote the article. All authors contributed to the article and approved the submitted version.

## FUNDING

This project was supported in part by a grant from the National Institute of Mental Health (MH086591) and a seed grant from the Charles E. Schmidt College of Science at Florida Atlantic University to RS.

## ACKNOWLEDGMENTS

We thank Alcira Munchow for expert assistance with behavioral testing and Dr. Huan Liu for technical guidance with the immunohistochemical analysis of Fos expression. We are also grateful for the advice and support provided by Drs. Paula Gajewski-Kurdziel and Randy Blakely (both of FAU) regarding measuring behaviorally triggered *Arc* mRNA expression in mouse brain samples.

## REFERENCES

Ahn, J.-R., and Lee, I. (2015). Neural correlates of object-associated choice behavior in the perirhinal cortex of rats. *J. Neurosci.* 35, 1692–1705. doi: 10.1523/JNEUROSCI.3160-14.2015

Albasser, M. M., Poirier, G. L., and Aggleton, J. P. (2010). Qualitatively different modes of perirhinal-hippocampal engagement when rats explore novel vs. familiar objects as revealed by c-Fos imaging. *Eur. J. Neurosci.* 31, 134–147. doi: 10.1111/j.1460-9568.2009.07042.x

Alvarez, P., Lipton, P. A., Melrose, R., and Eichenbaum, H. (2001). Differential effects of damage within the hippocampal region on memory for a natural, nonspatial Odor–Odor Association. *Learn. Mem.* 8, 79–86. doi: 10.1101/lm.38201

Ásgeirsdóttir, H. N., Cohen, S. J., and Stackman, R. W. Jr. (2020). Object and place information processing by CA1 hippocampal neurons of C57BL/6J mice. *J. Neurophysiol.* 123, 1247–1264. doi: 10.1152/jn.00278.2019

Barbosa, F. F., Santos, J. R., Meurer, Y. S., Macedo, P. T., Ferreira, L. M., Pontes, I. M., et al. (2013). Differential cortical c-Fos and Zif-268 expression after object and spatial memory processing in a standard or episodic-like object recognition task. *Front. Behav. Neurosci.* 7:112. doi: 10.3389/fnbeh.2013.00112

Bast, T., Wilson, I. A., Witter, M. P., and Morris, R. G. (2009). From rapid place learning to behavioral performance: a key role for the intermediate hippocampus. *PLoS Biol.* 7:e1000089. doi: 10.1371/journal.pbio.1000089

Bernstein, H. L., Lu, Y.-L., Botterill, J. J., and Scharfman, H. E. (2019). Novelty and novel objects increase c-Fos immunoreactivity in mossy cells in the mouse dentate gyrus. *Neural Plast.* 2019:1815371. doi: 10.1155/2019/1815371

Boyden, E. S. (2015). Optogenetics and the future of neuroscience. *Nat. Neurosci.* 18, 1200–1201. doi: 10.1038/nn.4094

Bramham, C. R., Alme, M. N., Bittins, M., Kuipers, S. D., Nair, R. R., Pai, B., et al. (2010). The Arc of synaptic memory. *Exp. Brain Res.* 200, 125–140. doi: 10.1007/s00221-009-1959-2

Bramham, C. R., Worley, P. F., Moore, M. J., and Guzowski, J. F. (2008). The immediate early gene Arc/Arg3.1: regulation, mechanisms, and function. *J. Neurosci.* 28, 11760–11767. doi: 10.1523/JNEUROSCI.3864-08.2008

Broadbent, N. J., Gaskin, S., Squire, L. R., and Clark, R. E. (2010). Object recognition memory and the rodent hippocampus. *Learn. Mem.* 17, 5–11. doi: 10.1101/lm.1650110

Brown, M. W., and Banks, P. J. (2015). In search of a recognition memory engram. *Neurosci. Biobehav. Rev.* 50, 12–28. doi: 10.1016/j.neubiorev.2014.09.016

Buffalo, E. A., Ramus, S. J., Clark, R. E., Teng, E., Squire, L. R., and Zola, S. M. (1999). Dissociation between the effects of damage to perirhinal cortex and area TE. *Learn. Mem.* 6, 572–599. doi: 10.1101/lm.6.6.572

Buffalo, E. A., Reber, P. J., and Squire, L. R. (1998). The human perirhinal cortex and recognition memory. *Hippocampus* 8, 330–339. doi: 10.1002/(SICI)1098-1063(1998)8:4<330::AID-HIPO3>3.0.CO;2-L

Bunsey, M., and Eichenbaum, H. (1996). Conservation of hippocampal memory function in rats and humans. *Nature* 379, 255–257. doi: 10.1038/379255a0

Burwell, R. D. (2001). Borders and cytoarchitecture of the perirhinal and postrhinal cortices in the rat. *J. Comp. Neurol.* 437, 17–41. doi: 10.1002/cne.1267

Burwell, R. D., and Amaral, D. G. (1998). Perirhinal and postrhinal cortices of the rat: interconnectivity and connections with the entorhinal cortex. *J. Comp. Neurol.* 391, 293–321. doi: 10.1002/(sici)1096-9861(19980216)391:3<293::aid-cne2>3.0.co;2-x

Cave, C. B., and Squire, L. R. (1991). Equivalent impairment of spatial and nonspatial memory following damage to the human hippocampus. *Hippocampus* 1, 329–340. doi: 10.1002/hipo.450010323

Clark, R. E., Zola, S. M., and Squire, L. R. (2000). Impaired recognition memory in rats after damage to the hippocampus. *J. Neurosci.* 20, 8853–8860. doi: 10.1523/JNEUROSCI.20-23-08853.2000

Clarke, J. R., Cammarota, M., Gruart, A., Izquierdo, I., and Delgado-Garcia, J. M. (2010). Plastic modifications induced by object recognition memory processing. *Proc. Natl. Acad. Sci. U S A* 107, 2652–2657. doi: 10.1073/pnas.0915059107

Cohen, S. J., Munchow, A. H., Rios, L. M., Zhang, G., Ásgeirsdóttir, H. N., and Stackman, R. W. Jr. (2013). The rodent hippocampus is essential for nonspatial object memory. *Curr. Biol.* 23, 1685–1690. doi: 10.1016/j.cub.2013.07.002

Cohen, S. J., and Stackman, R. W. Jr. (2015). Assessing rodent hippocampal involvement in the novel object recognition task. A review. *Behav. Brain Res.* 285, 105–117. doi: 10.1016/j.bbr.2014.08.002

De Lima, M. N., Luft, T., Roesler, R., and Schroder, N. (2006). Temporary inactivation reveals an essential role of the dorsal hippocampus in consolidation of object recognition memory. *Neurosci. Lett.* 405, 142–146. doi: 10.1016/j.neulet.2006.06.044

Eichenbaum, H. (2000). A cortical-hippocampal system for declarative memory. *Nat. Rev. Neurosci.* 1, 41–50. doi: 10.1038/35036213

Eichenbaum, H. (2014). Time cells in the hippocampus: a new dimension for mapping memories. *Nat. Rev. Neurosci.* 15, 732–744. doi: 10.1038/nrn3827

Eichenbaum, H., Dudchenko, P., Wood, E., Shapiro, M., and Tanila, H. (1999). The hippocampus, memory, and place cells: is it spatial memory or a memory space? *Neuron* 23, 209–226. doi: 10.1016/s0896-6273(00)80773-4

Eichenbaum, H., Stewart, C., and Morris, R. G. (1990). Hippocampal representation in place learning. *J. Neurosci.* 10, 3531–3542. doi: 10.1523/JNEUROSCI.10-11-03531.1990

Eichenbaum, H., Yonelinas, A. P., and Ranganath, C. (2007). The medial temporal lobe and recognition memory. *Annu. Rev. Neurosci.* 30, 123–152. doi: 10.1146/annurev.neuro.30.051606.094328

Fortin, N. J., Wright, S. P., and Eichenbaum, H. (2004). Recollection-like memory retrieval in rats is dependent on the hippocampus. *Nature* 431, 188–191. doi: 10.1038/nature02853

Franklin, K. B. J., and Paxinos, G. (2008). *The Mouse Brain in Stereotaxic Coordinates.* San Diego, CA: Academic Press.

Gaffan, D., and Parker, A. (1996). Interaction of perirhinal cortex with the fornix-fimbria: memory for objects and "object-in-place" memory. *J. Neurosci.* 16, 5864–5869. doi: 10.1523/JNEUROSCI.16-18-05864.1996

Gallo, F. T., Katche, C., Morici, J. F., Medina, J. H., and Weisstaub, N. V. (2018). Immediate early genes, memory and psychiatric disorders: focus on c-Fos, Egr1 and Arc. *Front. Behav. Neurosci.* 12:79. doi: 10.3389/fnbeh.2018.00079

Jones, M. W., Errington, M. L., French, P. J., Fine, A., Bliss, T. V., Garel, S., et al. (2001). A requirement for the immediate early gene Zif268 in the expression of late LTP and long-term memories. *Nat. Neurosci.* 4, 289–296. doi: 10.1038/85138

Kawashima, T., Okuno, H., and Bito, H. (2014). A new era for functional labeling of neurons: activity-dependent promoters have come of age. *Front. Neural Circuits* 8:37. doi: 10.3389/fncir.2014.00037

Korb, E., Wilkinson, C. L., Delgado, R. N., Lovero, K. L., and Finkbeiner, S. (2013). Arc in the nucleus regulates PML-dependent GluA1 transcription and homeostatic plasticity. *Nat. Neurosci.* 16, 874–883. doi: 10.1038/nn.3429

Kovács, K. J. (2008). Measurement of immediate-early gene activation- c-fos and beyond. *J. Neuroendocrinol.* 20, 665–672. doi: 10.1111/j.1365-2826.2008.01734.x

Kubik, S., Miyashita, T., and Guzowski, J. F. (2007). Using immediate-early genes to map hippocampal subregional functions. *Learn. Mem.* 14, 758–770. doi: 10.1101/lm.698107

Lee, I., and Park, S. B. (2013). Perirhinal cortical inactivation impairs object-in-place memory and disrupts task-dependent firing in hippocampal CA1, but not in CA3. *Front. Neural Circuits* 7:134. doi: 10.3389/fncir.2013.00134

Liu, P., and Bilkey, D. K. (1998). Perirhinal cortex contributions to performance in the Morris water maze. *Behav. Neurosci.* 112, 304–315. doi: 10.1037//0735-7044.112.2.304

Madisen, L., Mao, T., Koch, H., Zhuo, J. M., Berenyi, A., Fujisawa, S., et al. (2012). A toolbox of Cre-dependent optogenetic transgenic mice for light-induced activation and silencing. *Nat. Neurosci.* 15, 793–802. doi: 10.1038/nn.3078

McNaughton, B. L., Battaglia, F. P., Jensen, O., Moser, E. I., and Moser, M. B. (2006). Path integration and the neural basis of the 'cognitive map'. *Nat. Rev. Neurosci.* 7, 663–678. doi: 10.1038/nrn1932

Morris, R. G., Garrud, P., Rawlins, J. N., and O'Keefe, J. (1982). Place navigation impaired in rats with hippocampal lesions. *Nature* 297, 681–683. doi: 10.1038/297681a0

Muir, G. M., and Bilkey, D. K. (2001). Instability in the place field location of hippocampal place cells after lesions centered on the perirhinal cortex. *J. Neurosci.* 21, 4016–4025. doi: 10.1523/JNEUROSCI.21-11-04016.2001

O'Keefe, J. (1976). Place units in the hippocampus of the freely moving rat. *Exp. Neurol.* 51, 78–109. doi: 10.1016/0014-4886(76)90055-8

Plath, N., Ohana, O., Dammermann, B., Errington, M. L., Schmitz, D., Gross, C., et al. (2006). Arc/Arg3.1 is essential for the consolidation of synaptic plasticity and memories. *Neuron* 52, 437–444. doi: 10.1016/j.neuron.2006.08.024

Riedel, G., Micheau, J., Lam, A. G., Roloff, E. L., Martin, S. J., Bridge, H., et al. (1999). Reversible neural inactivation reveals hippocampal participation in several memory processes. *Nat. Neurosci.* 2, 898–905. doi: 10.1038/13202

Robison, A. J., Vialou, V., Sun, H. S., Labonte, B., Golden, S. A., Dias, C., et al. (2014). Fluoxetine epigenetically alters the CaMKIIα promoter in nucleus accumbens to regulate ΔFosB binding and antidepressant effects. *Neuropsychopharmacology* 39, 1178–1186. doi: 10.1038/npp.2013.319

Rossato, J. I., Bevilaqua, L. R., Myskiw, J. C., Medina, J. H., Izquierdo, I., and Cammarota, M. (2007). On the role of hippocampal protein synthesis in the consolidation and reconsolidation of object recognition memory. *Learn. Mem.* 14, 36–46. doi: 10.1101/lm.422607

Sauvage, M. M., Fortin, N. J., Owens, C. B., Yonelinas, A. P., and Eichenbaum, H. (2008). Recognition memory: opposite effects of hippocampal damage on recollection and familiarity. *Nat. Neurosci.* 11, 16–18. doi: 10.1038/nn2016

Squire, L. R., Stark, C. E., and Clark, R. E. (2004). The medial temporal lobe. *Annu. Rev. Neurosci.* 27, 279–306. doi: 10.1146/annurev.neuro.27.070203.144130

Squire, L. R., Wixted, J. T., and Clark, R. E. (2007). Recognition memory and the medial temporal lobe: a new perspective. *Nat. Rev. Neurosci.* 8, 872–883. doi: 10.1038/nrn2154

Stackman, R. W. Jr., Cohen, S. J., Lora, J. C., and Rios, L. M. (2016). Temporary inactivation reveals that the CA1 region of the mouse dorsal hippocampus plays an equivalent role in the retrieval of long-term object memory and spatial memory. *Neurobiol. Learn. Mem.* 133, 118–128. doi: 10.1016/j.nlm.2016.06.016

Tsankova, N. M., Berton, O., Renthal, W., Kumar, A., Neve, R. L., and Nestler, E. J. (2006). Sustained hippocampal chromatin regulation in a mouse model of depression and antidepressant action. *Nat. Neurosci.* 9, 519–525. doi: 10.1038/nn1659

Tuscher, J. J., Taxier, L. R., Fortress, A. M. and Frick, K. M. (2018). Chemogenetic inactivation of the dorsal hippocampus and medial prefrontal cortex, individually and concurrently, impairs object recognition and spatial memory consolidation in female mice. *Neurobiol. Learn. Mem.* 156, 103–116. doi: 10.1016/j.nlm.2018.11.002

Vilberg, K. L., and Davachi, L. (2013). Perirhinal-hippocampal connectivity during reactivation is a marker for object-based memory consolidation. *Neuron* 79, 1232–1242. doi: 10.1016/j.neuron.2013.07.013

Wan, H., Aggleton, J. P., and Brown, M. W. (1999). Different contributions of the hippocampus and perirhinal cortex to recognition memory. *J. Neurosci.* 19, 1142–1148. doi: 10.1523/JNEUROSCI.19-03-01142.1999

Wan, H., Warburton, E. C., Kuśmierek, P., Aggleton, J. P., Kowalska, D. M., and Brown, M. W. (2001). Fos imaging reveals differential neuronal activation of areas of rat temporal cortex by novel and familiar sounds. *Eur. J. Neurosci.* 14, 118–124. doi: 10.1046/j.0953-816x.2001.01625.x

Wiig, K. A., Cooper, L. N., and Bear, M. F. (1996). Temporally graded retrograde amnesia following separate and combined lesions of the perirhinal cortex and fornix in the rat. *Learn. Mem.* 3, 313–325. doi: 10.1101/lm.3.4.313

Winters, B. D., and Bussey, T. J. (2005). Transient inactivation of perirhinal cortex disrupts encoding, retrieval, and consolidation of object recognition memory. *J. Neurosci.* 25, 52–61. doi: 10.1523/JNEUROSCI.3827-04.2005

Winters, B. D., Forwood, S. E., Cowell, R. A., Saksida, L. M., and Bussey, T. J. (2004). Double dissociation between the effects of peri-postrhinal cortex and hippocampal lesions on tests of object recognition and spatial memory: heterogeneity of function within the temporal lobe. *J. Neurosci.* 24, 5901–5908. doi: 10.1523/JNEUROSCI.1346-04.2004

Winters, B. D., Saksida, L. M., and Bussey, T. J. (2008). Object recognition memory: neurobiological mechanisms of encoding, consolidation and retrieval. *Neurosci. Biobehav. Rev.* 32, 1055–1070. doi: 10.1016/j.neubiorev.2008.04.004

Witter, M. P., and Amaral, D. G. (2004). *Hippocampal Formation.* San Diego, CA: Elsevier Academic Press.

Wood, E. R., Mumby, D. G., Pinel, J. P., and Phillips, A. G. (1993). Impaired object recognition memory in rats following ischemia-induced damage to the hippocampus. *Behav. Neurosci.* 107, 51–62. doi: 10.1037//0735-7044.107.1.51

**Conflict of Interest**: The authors declare that the research was conducted in the absence of any commercial or financial relationships that could be construed as a potential conflict of interest.

*Copyright © 2020 Cinalli, Cohen, Guthrie and Stackman. This is an open-access article distributed under the terms of the Creative Commons Attribution License (CC BY). The use, distribution or reproduction in other forums is permitted, provided the original author(s) and the copyright owner(s) are credited and that the original publication in this journal is cited, in accordance with accepted academic practice. No use, distribution or reproduction is permitted which does not comply with these terms.*

frontiers in Neuroscience

BRIEF RESEARCH REPORT
published: 15 December 2020
doi: 10.3389/fnins.2020.568200

# Unraveling Early Signs of Navigational Impairment in APPswe/PS1dE9 Mice Using Morris Water Maze

*Smitha Karunakaran**

*Centre for Brain Research, Indian Institute of Science, Bangalore, India*

Mild behavioral deficits, which are part of normal aging, can be early indicators of an impending Alzheimer's disease. Using the APPswe/PS1dE9 (APP/PS1) mouse model of Alzheimer's disease, we utilized the Morris water maze spatial learning paradigm to systematically evaluate mild behavioral deficits that occur during the early stages of disease pathogenesis. Conventional behavioral analysis using this model indicates that spatial memory is intact at 2 months of age. In this study, we used an alternative method to analyze the behavior of mice, aiming to gain a better understanding of the nature of cognitive deficits by focusing on the unsuccessful trials during water maze learning rather than on the successful ones. APP/PS1 mice displayed a higher number of unsuccessful trials during the initial days of training, unlike their wild-type counterparts. However, with repeated trial and error, learning in APP/PS1 reached levels comparable to that of the wild-type mice during the later days of training. Individual APP/PS1 mice preferred a non-cognitive search strategy called circling, which led to abrupt learning transitions and an increased number of unsuccessful trials. These findings indicate the significance of subtle intermediate readouts as early indicators of conditions such as Alzheimer's disease.

**Keywords: Alzheimer's disease, search strategy, morris water maze, APPswe/PS1dE9, mild behavioral impairment, circling strategy**

OPEN ACCESS

***Edited by:***
*Akiva Cohen,*
*University of Pennsylvania,*
*United States*

***Reviewed by:***
*Marie-Christine Pardon,*
*University of Nottingham,*
*United Kingdom*
*Raquel Sanchez-Varo,*
*University of Malaga, Spain*

***Correspondence:**
*Smitha Karunakaran*
*smitha@iisc.ac.in*

***Specialty section:***
*This article was submitted to Neurodegeneration, a section of the journal Frontiers in Neuroscience*

***Received:*** *31 May 2020*
***Accepted:*** *16 November 2020*
***Published:*** *15 December 2020*

***Citation:***
*Karunakaran S (2020) Unraveling Early Signs of Navigational Impairment in APPswe/PS1dE9 Mice Using Morris Water Maze. Front. Neurosci. 14:568200. doi: 10.3389/fnins.2020.568200*

## INTRODUCTION

Behavioral impairments lacking prominent clinical symptoms can be indicative of normal aging or mild cognitive impairment. However, in some cases, these impairments develop into Alzheimer's disease (AD), a progressive neurodegenerative disorder that is neuropathologically characterized by extracellular senile plaques, formed by amyloid-β (Aβ) accumulation and intracellular neurofibrillary tangles, composed of a hyperphosphorylated microtubule-associated protein called tau (Ashe and Zahs, 2010; Tarawneh and Holtzman, 2012). Carriers of mutations associated with familial autosomal-dominant AD are known to develop subtle cognitive deficits <25 years before they develop dementia (Mondadori et al., 2006; Mosconi et al., 2006). Therefore, timely and accurate diagnosis is critical for the development of treatments for the initial stages of AD. Biomarkers directly or indirectly relevant to the histopathology of AD, such as blood and cerebrospinal fluid biomarkers, along with PET ligands are highly valuable in this scenario (Dubois et al., 2014). Recently, early behavioral markers that recognize and predict underlying pathology have gained importance in the diagnosis of AD (Webster et al., 2014; Hassenstab et al., 2016).

For example, significant episodic memory impairments are reported 10–12 years before symptom onset in familial AD patients (Bateman et al., 2012). Thus, subtle behavioral markers can make early diagnosis more feasible, opening up a new avenue in AD prevention and therapeutics. Therefore, the aim of this study was to identify early behavioral markers in a well-studied mouse model of AD amyloidosis, APPswe/PS1dE9 (APP/PS1: Jankowsky et al., 2001; Borchelt Line 85).

Transgenic mouse models designed based on the genes underlying AD have increased our knowledge of AD mechanisms tremendously (LaFerla and Green, 2012; Webster et al., 2014). Although no single mouse model fully exemplifies human AD pathology and cognitive deficits (Jankowsky and Zheng, 2017), transgenic mice with an established underlying neuropathology are excellent model systems to study specific questions, such as early behavioral impairments. Identifiable amyloid deposition in this APP/PS1 model has been observed at approximately 4–6 months of age, but no identifiable plaques have been observed at 2 months (Jankowsky et al., 2004; Garcia-Alloza et al., 2006). This provides us with a window to study the earliest signs of mild behavioral impairments that are independent of Aβ plaque deposition.

Cognitive deficits in this model were first described at 3 to 4 months of age in the Radial Arm Water Maze spatial working memory task (Jankowsky et al., 2001; Park et al., 2006). Other studies reported normal performance at 7 months of age and reduced performance at 13 months (Volianskis et al., 2010) or at 10–15 months (Sood et al., 2007) with the same task. However, Morris water maze (MWM) deficits are reported at just 6 months of age in APP/PS1 (Cao et al., 2007; Ding et al., 2008) and are associated with increased amyloid deposition (Cao et al., 2007; Reiserer et al., 2007; Ding et al., 2008). Deficits have also been well characterized across the lifespan of other related amyloid lines in water-based spatial working memory tasks (Gong et al., 2004; Trinchese et al., 2004; Lalonde et al., 2005; Puzzo et al., 2009; Cramer et al., 2012).

All MWM experiments performed with APP/PS1 mice thus far have used conventional behavioral readouts based on average performances, such as escape latencies and probe tests, to arrive at a conclusion (**Table 2**). These readouts do not effectively identify subtle behavioral deficits in APP/PS1 with high sensitivity and an acceptable degree of specificity due to their focus on endpoints. Therefore, this study introduces a modified method of analysis by focusing more on the individual learning sequences of mice. Our study revealed cognitive deficits in 2-month-old male APP/PS1 in comparison to their age-matched WT counterparts. Water maze learning forces mice to develop efficient navigational strategies that focus on local associations to find the hidden platform. However, the specific mechanisms of strategic searching toward the goal remain unclear (Sutton and Barto, 1998; Botvinick et al., 2009). Detailed search strategy recruitment-based studies have been conducted in many AD mouse models, such as TgCRND8 mice (Janus, 2004; Granger et al., 2016), PDAPP mice (Brody and Holtzman, 2006), TgF344 mice (Berkowitz et al., 2018), tetO-APPswe/ind 102 line (Chiang et al., 2018), and APP21 rats (Weishaupt et al., 2018). However, only two studies (Schrott et al., 2015; Zhang et al., 2016) have briefly attempted search strategy classification in APP/PS1 mice. This prompted a further analysis of our data based on the hierarchical recruitment of strategies during MWM learning. Our detailed longitudinal analysis revealed statistically significant differences in the pattern of search strategies employed by 2-month-old male APP/PS1 and age-matched WT mice. Taken together, our study investigates mild behavioral deficits in MWM learning during an early stage of disease pathogenesis in an amyloidogenic mouse model of AD.

# MATERIALS AND METHODS

## Experimental Animals

The generation, care, and use of mice, as well as all experimental procedures, were approved by the Institutional Animal Ethics Committee of the Indian Institute of Science, Bangalore. These animal experiments also complied with the Animal Research: Reporting of *In Vivo* Experiments (ARRIVE) guidelines. Transgenic mice B6C3-Tg (APPswe/PS1dE9) 85Dbo/J (https://www.jax.org/strain/005864) obtained from The Jackson Laboratory were kindly provided by Prof. Vijayalakshmi Ravindranath, Director, Center for Brain Research, Bangalore, India. Wild-type (WT) and APP/PS1 mice were bred at the Institutional Central Animal Facility, were housed in standard mouse cages under conventional laboratory conditions (12-h dark and 12-h light cycle, constant temperature and humidity), and were given food and water *ad libitum*. We performed behavioral experiments using male and female APP/PS1 and WT mice, with WT mice serving as the control.

No statistical methods were used to predetermine sample sizes; our sample sizes are instead similar to those generally employed in the field. The sample size per group is mentioned in the respective figure legends, and no samples were excluded from any of the experiments described herein, unless otherwise mentioned in the analysis. The WT and APP/PS1 mice were assigned randomly to respective groups based on their genotype. Different litters of the same age group were taken and were divided into control and experimental groups. The mice were housed individually for 3 days and were handled for 5 min every day prior to behavioral testing. All behavioral experiments were conducted at approximately the same time during the light cycle (9:00–15:00) by the same experimenter.

## Morris Water Maze

The MWM experiments were conducted, as described in previous studies (Vorhees and Williams, 2006; Ruediger et al., 2012; Karunakaran et al., 2016), on two separate days with two batches of male animals. Each batch had nine WT and nine APP/PS1 male mice. The results of two replicates (batches) of the same experiment have been combined and represented as $n = 18$. Results from individual data sets have been represented in the supplementary data. A separate set of MWM experiments was also performed with seven male WT and APP/PS1 mice each.

The experimental setup consisted of a large circular black pool (diameter: 180 cm) filled with water, maintained at 22–25°C and a depth of 60 cm, in a room with visual cues (triangle, square, cross, and circle) under soft and diffuse light conditions. The

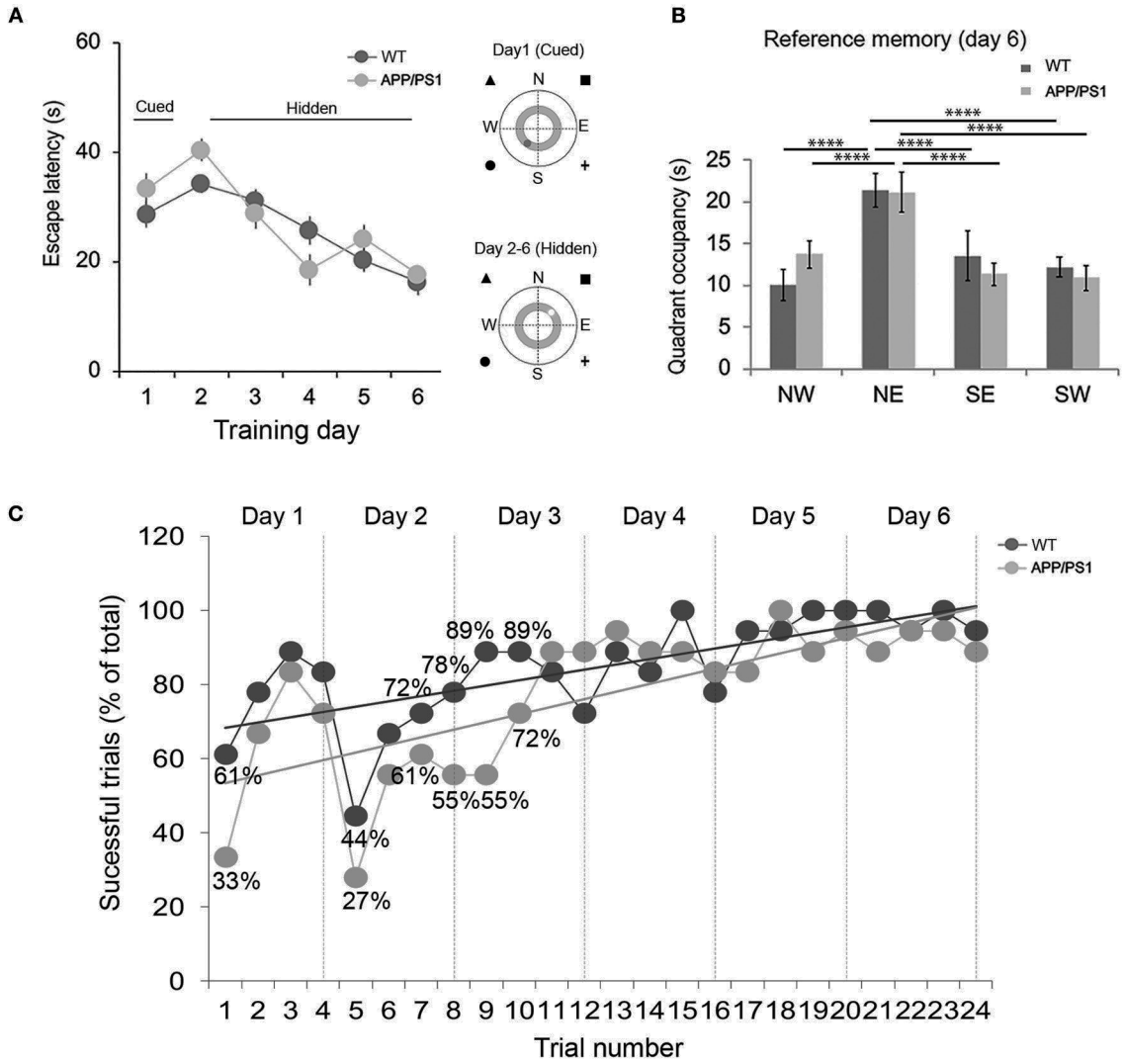


**FIGURE 1 |** Evaluation of spatial learning in APP/PS1 mice using the Morris water maze [**(A)**, to the right] Illustration depicting the water maze pool virtually divided into four equal quadrants (NE, NW, SE, and SW) with four starting positions (N, S, E, and W), along with the extra maze cues. The inner gray circle represents the annulus zone. [**(A)**, to the left] Performance was evaluated as average escape latency between 2-month-old wild-type (WT; dark circle) and APP/PS1 (light circle) mice. **(B)** Reference memory was evaluated 2 h after the final trial on day 6. **(C)** Performance was evaluated as the percentage of successful trials between 2-month old WT and APP/PS1 mice during learning acquisition from days 1 to 6. Greater than 10% differences in successful trials across days 1, 2, and 3 between WT and APP/PS1 are highlighted with corresponding numbers. The trendline depicts the percentage difference across successful trials across WT (dark gray) and APP/PS1 (light gray). Data are presented as mean ± SEM; $n = 18$. $^{****}P < 0.0001$.

water was made opaque by adding non-toxic white paint (Faber Castell Tempera Fun Paint). The pool was then virtually divided into four equal quadrants (NE, NW, SE, and SW; see **Figure 1A** for illustration) with four starting positions (N, S, E, and W). The platform (visible or hidden) was placed in the middle of one of the virtual quadrants, and this position was maintained across the training. An overhead video camera was used to record and monitor behavior.

## Visible Platform (Cued) Testing

The escape platform (diameter: 10 cm) was positioned at a fixed location in the SW quadrant, 0.5 cm above the water surface, and was marked with a red tape. The 1st day (day 1) of training involved four trials by placing the animal in the water facing the pool wall at one of the four starting positions (N, S, E, and W). The animals were given 60 s to locate the platform and were returned to their home cage under an infrared lamp for 5 min between the trials. The animals had to remain on the platform for at least 5 s for the trial to be considered a success.

## Hidden Platform (Place) Testing

From days 2 to 6, the escape platform was positioned at a fixed location in the NE quadrant, 2.54 cm below the water surface and without the red tape. The acquisition training involved four

trials, each lasting 60 s. Mice that failed to reach the platform were guided to the location by the experimenter, allowed to stay on the platform for 15 s before being removed from the water, and then returned to their home cage under an infrared lamp for 5 min between the trials. Learning acquisition with the hidden platform ended on day 6 with a single probe test for 60 s, either 2 or 24 h after the last training trial. The probe test was conducted in the absence of a platform to assess the reference memory of the animals for the learned position of the platform.

## Spatial Reversal Learning

Reversal trials were conducted from days 7 to 11 with the platform hidden and placed in the opposite quadrant (SW). Reversal learning trials ended on day 11 with a single probe test for 60 s, 2 h after the last learning trial. The probe test was conducted in the absence of a platform to assess the reference memory of the animals for the new platform location.

## Search Strategy Analysis

The path traveled by the mouse was video-tracked by an overhead camera. The video files of each trial were processed frame by frame using OpenCV. In the first frame, Hough Circle Transform was used to detect the outer edge of the maze. Canny edge and contour detection were used to identify the location of the mouse, and its coordinates were stored in a list. The path trace of the mouse was created by connecting the coordinates from the list, and the total distance traveled (in pixels) was calculated as the sum of their Euclidean distances, which was then converted to meters. Average speed was calculated from the total distance traveled divided by the total time taken.

For search strategy analysis, videos were randomized and initially scored for strategy by a single investigator, who assigned a predominant search strategy to each trial using a categorization scheme similar to those developed previously (Wolfer and Lipp, 2000; Graziano et al., 2003; Lang et al., 2003; Janus, 2004; Brody and Holtzman, 2006; Ruediger et al., 2012; Vouros et al., 2018). The strategies were further validated independently by two more investigators in the laboratory. When mice occasionally switched strategies during a trial, the strategy that best described the majority of the swim path was assigned. Conditions to delineate search strategies were defined as: thigmotaxis, >65% of the time 5–10 cm closer to the pool wall; random search, >70% coverage of the pool area; scanning, <70% random search inside the annulus; chaining, > 65% of the time along the annulus zone; directed search, >80% of the time the search was directed toward the target quadrant; focal search, >80% of the time in the target quadrant closer to the hidden platform; direct swim, 100% in the target quadrant closer to the hidden platform; and circling, when an animal performed tight repeated loops (Janus, 2004; Brody and Holtzman, 2006; Chiang et al., 2018), not wider concentric loops, anywhere in the pool. The results are expressed as percentage of incidence (% incidence) of each search strategy and search strategy habits by day of training over the total population of mice. A sequence of at least three trials with the same strategy was defined as a strategy block. Total block length is the sum of all blocks per strategy per mouse.

## Statistical Analysis

Data analysis was performed using Prism 7 (GraphPad Software Inc.). The statistical analyses were designed with the assumption of normal distribution and similar variance among groups. They were performed using two-tailed unpaired Student's *t*-test for paired comparisons and two-way repeated-measures analysis of variance (ANOVA) followed by *post hoc* tests for time × group comparisons, and two-way ANOVA followed by *post hoc* tests was performed when two factors were compared. The results are presented as mean ± SEM. The statistical design for each experiment can be found in the respective figure legend section. The results were considered significant at $p < 0.05$.

## Ethics Approval

This animal study was reviewed and approved by the Institutional Animal Ethics Committee of the Indian Institute of Science, Bangalore.

# RESULTS

## Individual Latency Curves of APP/PS1 Mice Oscillate Substantially Early During Learning Acquisition

The mice were trained on day 1 on the cued water maze. Escape latency decreased over the four trials, both in the WT and the APP/PS1 [**Figure 1A**; day 1: two-way repeated measures ANOVA: training effect: $F_{(3, 51)} = 13.78$, $P < 0.0001$; genotype effect: $F_{(1, 17)} = 1.806$, $P = 0.1966$; interaction: $F_{(3, 51)} = 3.105$, $P = 0.8177$]. This indicated that the APP/PS1 mice did not differ in visual function, swimming ability, and motivation to escape from the pool. From day 2 to 6, the mice were taken for hidden platform testing (**Figure 1A**). Monitoring of primary latency during acquisition trials revealed a progressive and statistically significant decrease in latencies across WT and APP/PS1 mice. At the end of 6 days of training, both APP/PS1 and WT mice performed similarly [days 2–6: two-way repeated-measures ANOVA: training effect: $F_{(4, 68)} = 26.12$, $P < 0.0001$; genotype effect: $F_{(1, 17)} = 0.0121$, $P = 0.9134$; interaction: $F_{(4, 68)} = 2.295$, $P = 0.0681$]. Spatial reference memory was assessed on day 6 (**Figure 1B**), 2 h after the last training trial. Both APP/PS1 and WT mice exhibited a significant preference for the target quadrant [two-way ANOVA: $F_{(3, 136)} = 44.4$, $P < 0.0001$; genotype effect: $F_{(1, 136)} = 0.0557$, $P = 0.8137$; interaction: $F_{(3, 136)} = 3.845$, $P = 0.0111$]. Tukey's multiple-comparisons test further indicated statistically significant differences between the time spent in the target quadrant (NE) *vs.* the SW, SE, and NW quadrants in both WT and APP/PS1 mice. We further tested long-term reference memory at 24 h (day 7) in a separate batch of WT and APP/PS1 mice to check whether APP/PS1 mice maintain the strategies acquired during learning [**Supplementary Figure 1A**: two-way repeated-measures ANOVA; day 1: training effect: $F_{(3, 18)} = 3.599$, $P = 0.0339$; genotype effect: $F_{(1,6)} = 4.219$, $P = 0.0858$; interaction: $F_{(3, 18)} = 2.311$, $P = 0.1106$; days 2–6: training effect: $F_{(4, 24)} = 4.56$, $P = 0.0070$; genotype effect: $F_{(1, 6)} = 0.8192$, $P = 0.4003$; interaction: $F_{(4, 24)} = 0.3855$, $P = 0.8168$]. During the probe trial,

**TABLE 1 |** Percentage of successful trial analysis.

| | Total number of successful trials | | | | % of successful trials | | | |
|---|---|---|---|---|---|---|---|---|
| | Trial 1 | Trial 2 | Trial 3 | Trial 4 | Trial 1 | Trial 2 | Trial 3 | Trial 4 |
| **Wild type** | | | | | | | | |
| Day 1 | 11 | 14 | 16 | 15 | 61.1 | 77.7 | 88.8 | 83.3 |
| Day 2 | 8 | 12 | 13 | 14 | 44.4 | 66.6 | 72.2 | 77.7 |
| Day 3 | 16 | 16 | 15 | 13 | 88.8 | 88.8 | 83.3 | 72.2 |
| Day 4 | 16 | 15 | 18 | 14 | 88.8 | 83.3 | 100 | 77.7 |
| Day 5 | 17 | 17 | 18 | 18 | 94.4 | 94.4 | 100 | 100 |
| Day 6 | 18 | 17 | 18 | 17 | 100 | 94.4 | 100 | 94.4 |
| **APP/PS1** | | | | | | | | |
| Day 1 | 6 | 12 | 15 | 13 | 33.3 | 66.6 | 83.3 | 72.2 |
| Day 2 | 5 | 10 | 11 | 10 | 27.7 | 55.5 | 61.1 | 55.5 |
| Day 3 | 10 | 13 | 16 | 16 | 55.5 | 72.2 | 88.8 | 88.8 |
| Day 4 | 17 | 16 | 16 | 15 | 94.4 | 88.8 | 88.8 | 83.3 |
| Day 5 | 15 | 18 | 16 | 17 | 83.3 | 100 | 88.8 | 94.4 |
| Day 6 | 16 | 17 | 17 | 16 | 88.8 | 94.4 | 94.4 | 88.8 |

both APP/PS and WT mice exhibited increased preference for the target quadrant [**Supplementary Figure 1B**: two-way ANOVA followed by Tukey's *post hoc* test: $F_{(3, 48)} = 31.02$, $P < 0.0001$; genotype effect: $F_{(1, 48)} = 0.9173$, $P = 0.3430$; interaction: $F_{(3, 48)} = 0.3173$, $P = 0.8128$]. Furthermore, there were no significant differences between WT and APP/PS1 mice with regard to average speed (**Supplementary Figure 2A**: two-tailed unpaired Student's *t*-test; WT *vs.* APP/PS1, $t = 1.924$, df $= 214$, $P = 0.0556$) and distance traveled (**Supplementary Figure 2B**: two-tailed unpaired Student's *t*-test; WT *vs.* APP/PS1, $t = 0.9387$, df $= 214$, $P = 0.3489$) during the entire course of MWM learning.

Tangible differences emerged when we evaluated the percentage of successful trials during individual days of training between WT and APP/PS1 mice (**Figure 1C**; **Table 1**). The percentage of successful trials was highly compromised in APP/PS1 compared to WT mice, particularly on days 1–3 of training, and improved later to reach values comparable to WT on days 4–6 with repeated training. For example, on day 3, the total number of successful trials during trial 1 was 16/18 (88.8%) in WT in comparison to 10/18 (55.5%) in APP/PS1; meanwhile, on day 5, the total number of successful trials during trial 1 was 17/18 (94.4%) in WT in comparison to 15/18 (83.3%) in APP/PS1. Ultimately, APP/PS1 made more errors in finding the hidden platform during the initial days of training, but with repeated trials, they performed at a level comparable to the WT mice.

## APP/PS1 Mice Deploy Qualitatively Different Rules and Search Strategies During Water Maze Navigation

In addition to conventional readouts such as escape latency, we further augmented the strength of the analysis by classifying the behavior of individual mice based on the search strategies that they utilized to find the platform during the successive days of training. The search strategy normally evolves over time from the more non-spatial solutions used during the initial trials to the more direct spatial approaches. We cataloged all MWM studies conducted so far in APP/PS1 mice (**Table 2**); however, a detailed classification of search strategies has not been reported in any of these studies. It is well-known that the hippocampal integrity is essential for spatial memory, although other brain structures may also affect spatial memory by influencing spatial navigation and motor performances (D'Hooge and De Deyn, 2001). Therefore, we broadly classified the search patterns into two categories: (1) hippocampus-independent strategies, frequently used by mice that did not find the platform within the allotted time, which is highly non-spatial in nature, or (2) hippocampus-dependent spatial strategies, used by mice that learned the trained location and swam directly to it (**Figure 2A**).

The WT mice exhibited a consistent evolution in their search strategies over successive days of training (**Figure 2B**; **Supplementary Figures 3A,B**). They had three learning phases that made them more proficient at MWM learning. A detailed analysis of 18 individual learning curves revealed that most WT mice began with thigmotaxis or random swim, followed by local search strategies such as scanning and chaining that were predominant during days 3 and 4 of learning. Finally, on days 5 and 6, they opted for spatial search strategies such as directed search, focal search, and direct swim (**Figure 2C**; to the left). These shifts in strategy selection were explicit and distinct in WT mice. In contrast, the APP/PS1 mice exhibited disrupted transitions of strategies. The APP/PS1 mice began with an increased preference for circling over thigmotaxis or random swim, followed by an increased preference for directed search over local strategies, such as scanning and chaining, during days 2–4. Finally, on days 5 and 6, their preference swayed between scanning, directed search, and directed swim (**Figure 2C**; to the right). The search pattern utilized by APP/PS1 also indicated that they successfully used shortcuts by applying highly spatial and less challenging strategies, leading to the reduced deployment of search habits. This resulted in statistically significant differences in strategy implementation compared to WT mice [**Figure 3A**; day 1: two-way repeated-measures ANOVA: strategy: $F_{(7, 21)} = 2.52$, $P = 0.0477$; genotype effect: $F_{(1, 3)} = 0.4357$, $P = 0.5563$; interaction: $F_{(7, 21)} = 10.94$, $P < 0.0001$]. Tukey's multiple-comparisons test further revealed significant differences between WT and APP/PS1 mice with regard to preference for circling strategy ($P = 0.0002$). No statistically significant differences were noted in the preference for thigmotaxis between WT and APP/PS1 ($P = 0.1562$), unlike the 8-month-old APP/PS1 mice who exhibit significantly higher thigmotaxic swims than their age-matched controls during visible platform testing (Janus et al., 2015). From days 2 to 6, the trend in percentage changes with regard to strategy preferences for WT and APP/PS1 mice was even clearer [**Figure 3B**; days 2–6: two-way repeated-measures ANOVA: strategy: $F_{(7, 28)} = 11.37$, $P < 0.0001$; genotype effect: $F_{(1, 4)} = 0.6759$, $P = 0.4572$; interaction: $F_{(7, 28)} = 6.563$, $P = 0.0001$]. Tukey's multiple-comparisons test further revealed significant differences in preference for circling ($P = 0.0035$) and scanning ($P = 0.0091$) between WT and APP/PS1 mice. This data also indicated that WT mice utilized directed search and direct swim strategies beginning from day 1, and their

**TABLE 2 |** Summary of analysis done on Morris water maze data across different labs with APP/PS1 mice.

| Lab/year | Gender | Age | Analysis |
|---|---|---|---|
| Gong et al. (2019) | Female | 7 months | Escape latency, probe test, average speed |
| Li et al. (2019) | Male | 8 months | Escape latency, probe test, speed, path length |
| Vartak et al. (2019) | Not mentioned | 18 months | Escape latency, probe test, speed, distance traveled, platform crosses |
| Zhang et al. (2016) | Male | 8 months | Escape latency, probe test, strategy |
| Wang et al. (2016) | Male | 6 months | Escape latency, probe test |
| Schrott et al. (2015) | Not mentioned | 8 months | Escape latency, probe test, speed, distance traveled, search strategy |
| Kim et al. (2015) | Male | 10.5 months | Escape latency, probe test, velocity |
| Kummer et al. (2014) | Male and Female | 4 months | Escape latency, distance traveled |
| Edwards et al. (2014) | Not mentioned | 3.6, 9.3, and 14.8 months | Escape latency, probe test, mean velocity, distance traveled |
| Gallagher et al. (2013) | Female | 9 months | Escape latency |
| Zhang et al. (2011, 2013) | Male | 12–13 months | Escape latency, probe test |
| Hanson et al. (2012) | Male | 11 months | Escape latency, path length |
| Su et al. (2012) | Male and female | 7 months | Escape latency, probe test, average speed, distance traveled |
| Ma et al. (2012) | Male and female | 10–12 months | Escape latency, probe test |
| Wen et al. (2011) | Male | 7–8 months | Escape latency |
| Huang et al. (2011) | Male | 7 months | Escape latency, probe test |
| Montgomery et al. (2011) | Female | 12 months | Path length, probe test |
| Park et al. (2010) | Female | 8 months | Escape latency, probe test |
| Ding et al. (2008) | Male | 6 months | Escape latency, probe test |
| Cao et al. (2007) | Male | 6 months | Escape latency, probe test |

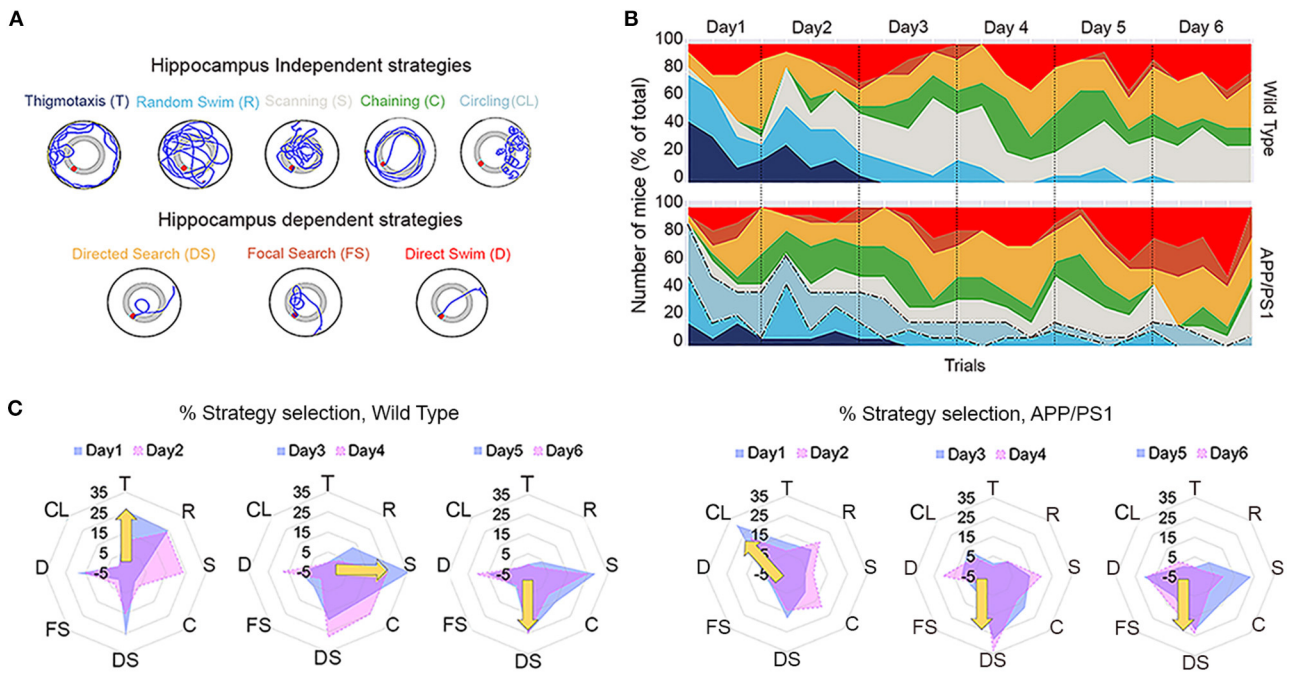


**FIGURE 2 |** Sequential strategies deployed by wild-type (WT) and APP/PS1 mice during Morris water maze learning. **(A)** Schematic representation, color code, and abbreviations for each search strategy. The strategies have been classified as hippocampus independent (T, R, S, C, and CL) and hippocampus dependent (DS, FS, and D). **(B)** The average prevalence of each strategy by trials across days of training is shown. Note the circling strategy preference (dotted lines) of APP/PS1 during water maze learning. **(C)** Radar plots describing the day-wise average percentage strategy preference during learning by APP/PS1 (right) mice in comparison to WT (left). Note the clear shifts in strategy preference from global to local to spatial in WT (yellow arrow) and the preference of APP/PS1 (yellow arrow) toward circling, followed by an abrupt shift to spatial strategies. Data are presented as mean ± SEM; $n = 18$.

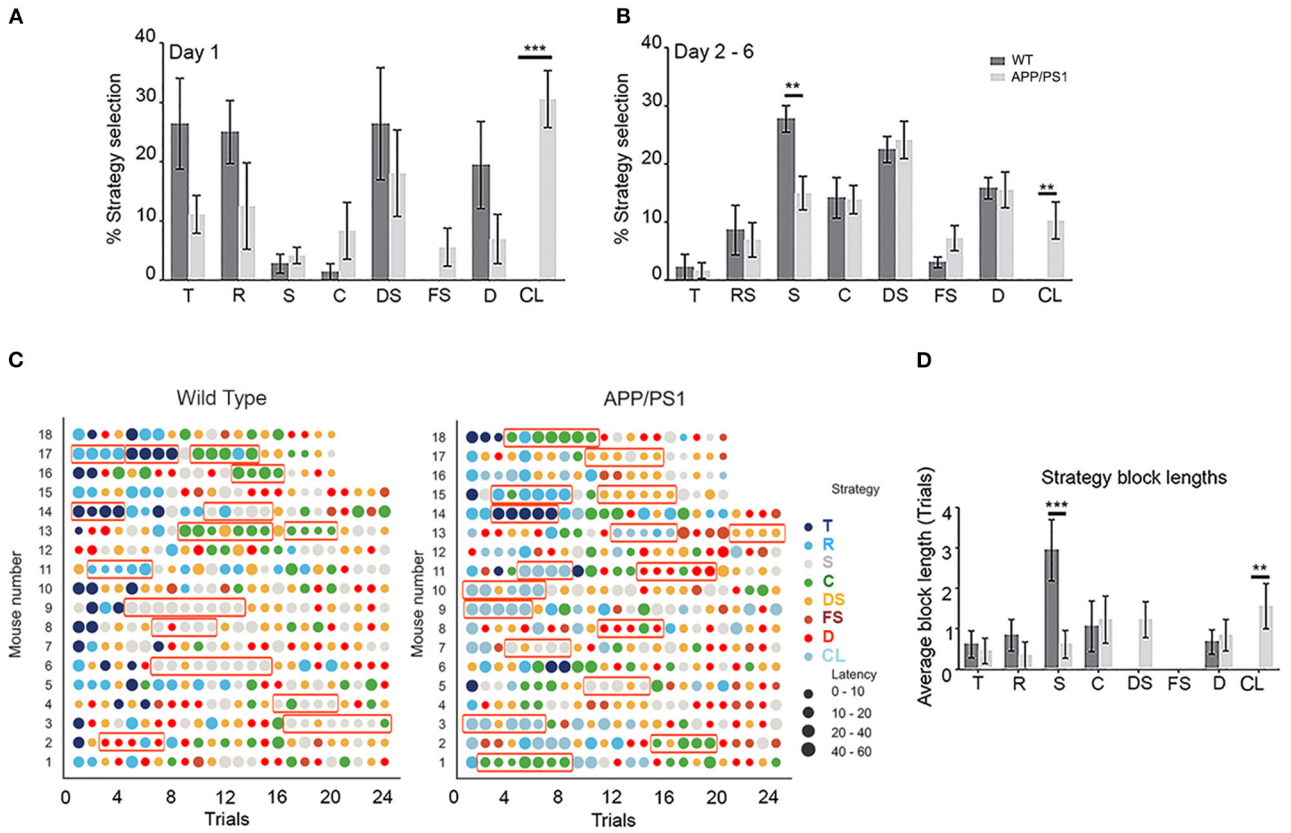


**FIGURE 3 |** Percentage changes in search strategies between wild-type (WT) *vs*. APP/PS1 mice. The percentage changes in search strategies between WT *vs*. APP/PS1 during day 1 **(A)**, followed by days 2–6 **(B)**, of training are depicted. **(C)** A scatter plot of varying latency (size) *vs*. strategy (color) across all trials in individual animals. The greater the size of the circle, the more the latency. Strategy block length is defined as a sequence of at least three trials with the same strategy. Total block length is the sum of all blocks per strategy per mouse and is highlighted with rectangular orange icons. The last four trial's representations are missing from WT animal nos. 16, 17, and 18 and APP/PS1 mice nos. 15, 16, 17, and 18 due to the bad quality of the recorded videos, which thus could not be used for strategy analysis. **(D)** Average total block lengths for each search strategy during water maze learning. Data are presented as mean ± SEM; $n = 18$. $^{**}P = 0.0021$, $^{***}P = 0.0002$.

percentage changes across days 2–6 of training were quite stable (**Figures 2B,C, 3A**). However, the APP/PS1 mice exhibited incremental percentage increases in directed search and direct swim strategies across days of training.

Circling was the more prominent non-spatial searching strategy in APP/PS1, along with thigmotaxis and random swim, which incrementally decreased over the days of training (**Figures 2B**, **3A,B**). During circling, APP/PS1 mice made tight 360° loops after being introduced into the pool, which was maintained across trials. Circling traversed most of the pool area, but not within the range of distances that would result in efficient arrival at the platform. The notably higher number of unsuccessful trials during learning in APP/PS1 could be a result of this unpredictable circling strategy, leading to variations in latencies. Deployment of these strategies was identical to habit learning where there was repeated use of the same search strategy in at least three consecutive trials interrupted by one or two trials involving an alternative called strategy blocks (**Figures 3C,D**). Circling was repeated as the preferred search strategy in at least three consecutive trials interrupted by one or two trials involving an alternative in APP/PS1 mice. The average strategy block length across trials from day 1 to 6 [two-way repeated-measures ANOVA followed by Tukey's multiple-comparisons test: strategy: $F_{(7, 119)} = 3.184$, $P = 0.0040$; genotype effect: $F_{(1, 17)} = 0.1175$, $P = 0.7360$; interaction: $F_{(7, 119)} = 3.984$, $P = 0.0006$] further indicated statistically significant differences in both scanning ($P = 0.0262$) and circling ($P = 0.0450$) strategies between APP/PS1 and WT (**Figures 3B,C**). This data clearly indicates that circling is the preferred non-spatial strategy utilized by APP/PS1 mice over the scanning strategy opted for by WT mice.

## Evaluation of Reversal Learning in APP/PS1 Mice Using the MWM

We further challenged the APP/PS1 mice with reversal learning to assess their ability to reuse strategies that have already been established. Therefore, on day 7, after 6 days of acquisition learning, the platform was hidden in the opposite quadrant (SW), and the mice were trained to learn this new hidden platform position with unchanged extra-maze context and cues. The escape latencies declined in both groups over days of training from day 7 to day 11 [**Figure 4A**, right; two-way repeated-measures ANOVA: training effect: $F_{(4,68)} = 10.86$,

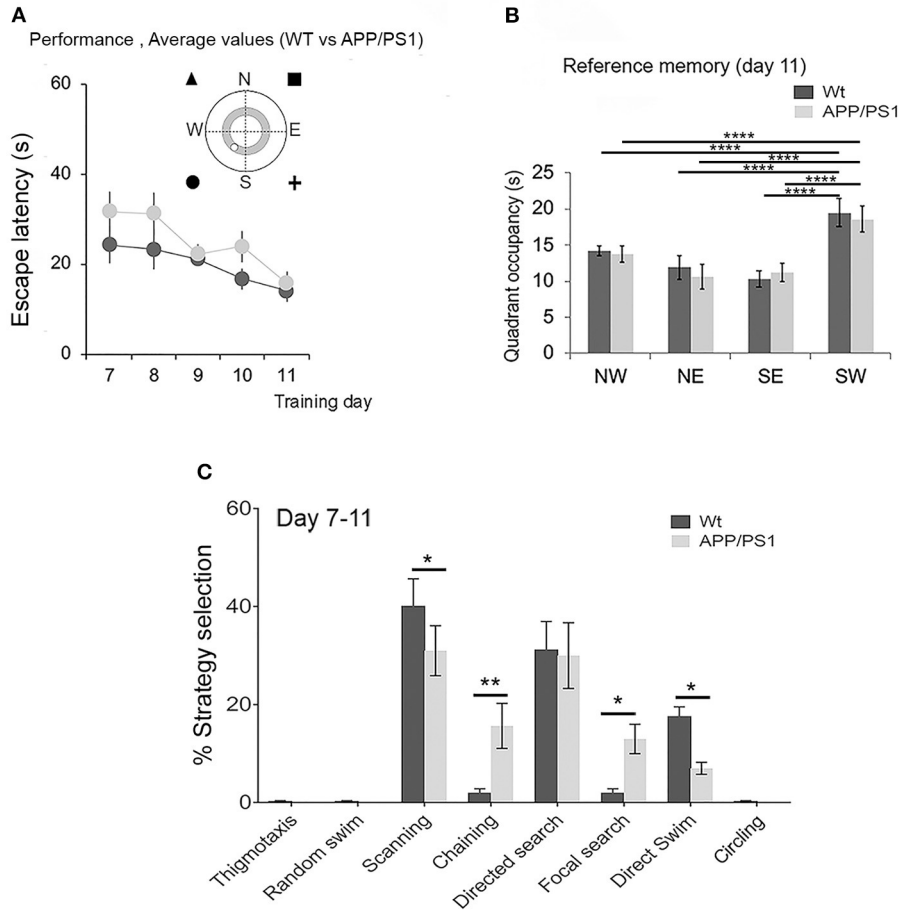


**FIGURE 4 |** Evaluation of reversal learning in APP/PS1 mice using the Morris water maze. **(A)** Acquisition of reversal learning where the platform was placed in the opposite SW quadrant. Performance was evaluated as average escape latency between 2-month-old wild-type (WT; dark circle) and APP/PS1 (light circle) mice. **(B)** Reference memory was evaluated 2 h after the last trial on day 11. **(C)** Percentage changes in search strategies between WT *vs*. APP/PS1 during days 7–11 of reversal learning. Data are presented as mean ± SEM; $n = 18$. *$P = 0.0332$, **$P = 0.0021$, ****$P < 0.0001$.

$P < 0.0001$; genotype effect: $F_{(1,17)} = 3.972$, $P = 0.0626$; interaction: $F_{(4,68)} = 1.228$, $P = 0.3074$]. Tukey's multiple-comparisons test did not indicate any significant differences between the groups. After 5 days of reversal, both the APP/PS1 and the WT mice exhibited a tendency to prefer the SW target quadrant over other quadrants during the probe trial [**Figure 4B**; two-way ANOVA: $F_{(3, 136)} = 29.2$, $P < 0.0001$; genotype effect: $F_{(1, 136)} = 0.0557$, $P = 0.1853$; interaction: $F_{(3, 136)} = 0.4437$, $P = 0.7222$]. Tukey's multiple-comparisons test further revealed significant differences between the time spent in the target quadrant (SW) *vs*. the NE, SE, and NW quadrants in both WT and APP/PS1 mice. Deficits in their behavior became more apparent when we analyzed the navigational strategies that they opted for during reversal learning. The WT mice displayed a very sharp and selective search strategy which involved scanning, directed search, and direct swim predominantly. However, in APP/PS1, the choice of strategies swayed between scanning, chaining, directed search, focal search, and direct swim, leading to statistically significant differences in strategy deployment [**Figure 4C**; two-way repeated-measures ANOVA: strategy: $F_{(7, 28)} = 20.59$, $P < 0.0001$; genotype effect: $F_{(1, 4)} = 0.0643$, $P = 0.8122$; interaction: $F_{(7, 28)} = 10.91$, $P < 0.0001$]. Tukey's multiple-comparisons test revealed a significant difference in preference for scanning ($P = 0.0326$), chaining ($P = 0.0027$), focal search ($P = 0.0123$), and direct swim ($P = 0.0180$) between WT and APP/PS1 mice. Taken together, the APP/PS1 mice, unlike the WT mice, exhibited notably unpredictable trajectories to reach the platform.

## DISCUSSION

In this study, we analyzed the average learning patterns of 2-month-old male APP/PS1 mice in the MWM task. This study is novel as it provides a detailed quantitative search strategy analysis which is crucial to understand the early stages of disease pathogenesis in APP/PS1 mice. Consistent with previous reports (Morris, 1984; Wolfer and Lipp, 2000; Garthe et al., 2009; Ruediger et al., 2012), detailed behavioral analysis revealed that WT mice utilized qualitatively different search strategies as they became more proficient at the MWM task. However, APP/PS1

mice exhibited an overt dependence on non-spatial strategies, especially circling, which led to distorted learning transitions. We did not observe any significant differences with regard to average learning patterns and strategy preferences between 2-month-old female WT and APP/PS1 mice (data not shown). Similar male-specific differences with regard to hippocampal metabolism (Agostini et al., 2020) and mGluR5 signaling (Abd-Elrahman et al., 2020) were recently demonstrated in this mouse model, further indicating that gender is an important modifier of AD progression.

Successful navigation to the hidden platform involves dynamic interactions between the hippocampal and striatal systems, enabling fluid transitions of navigational behavior. The increased dependence of APP/PS1 on less favorable strategies during learning might indicate deficits in feedback mechanisms in the striatal circuits mediating habit behavior (Graybiel and Grafton, 2015). The increased prevalence of circling may also be due to false recognition, impaired familiarity for the visual cues that guide the mice to the platform (Romberg et al., 2012), or an artifact of APP and PS1 overexpression influencing changes in gene expression, especially in the retina, at 2 months of age (Chintapaludi et al., 2020). The deficits were more apparent during the reversal learning trial (**Figure 4**) where previously adopted spatial search strategies or rules were successfully implemented faster by WT mice than APP/PS1 mice (**Figure 4C**). Therefore, the ability to efficiently adjust to reversal learning or behavioral flexibility also seemed compromised very early in APP/PS1 mice. However, with repeated trial and error, they eventually learned to find the hidden platform.

The repeated circling behavior in APP/PS1 mice was also reminiscent of topographical disorientation, which is common in human patients affected by mild cognitive impairment progressing to AD (Huang et al., 2002; Trivedi et al., 2006; Seo et al., 2007; Whitwell et al., 2007; Desikan et al., 2008). Furthermore, 41.9% of patients diagnosed with mild cognitive impairment have reported getting lost on a regular basis (Lim et al., 2010). This is associated with gray matter loss primarily in medial temporal regions such as the hippocampal complex, the amygdala, and the fusiform gyrus that affect orientation skills without causing severe and selective cognitive defects (Whitwell et al., 2007). In APP/PS1 mice, synaptic dysfunction and loss of synapses are documented in the cortex and hippocampus prior to pathophysiological changes (da Silva et al., 2016; Kommaddi et al., 2018). Since the APP/PS1 mice constitutively overexpress APP and PS1 genes, soluble oligomeric fractions of Aβ are present in their brain at 1–1.5 months of age (Ahmad et al., 2017). Elevated levels of toxic soluble oligomeric Aβ and synaptic deficits are also reported at 3.5 months of age in the cortex and hippocampus of APP/PS1 mice (Klein et al., 2001; Shemer et al., 2006; Hu et al., 2010; Ahmad et al., 2017). These deficits may underlie the mild behavioral impairments observed in this mouse model at a young age. Previous studies using APP/PS1 mice have not addressed these differences, owing to their focus on the endpoints of this complex learning paradigm (**Table 2**). Reference spatial memory deficits have been reported in 2- to 3-month-old APP/PS1 mice using cheeseboard maze (Pillay et al., 2008). However, the APP/PS1 mice in this study displayed a significantly decreased motivation to seek food compared to their WT counterparts, which could have been a confounding factor affecting exploratory behavior. Studying the exploratory strategies in such a scenario would provide insight into real cognitive deficits as well.

Amyloidogenic models are known to exhibit hyperactivity, which can potentially interfere with cognitive behavior readouts (Moechars et al., 1996; Dodart et al., 1999; Lalonde et al., 2003; Van Dam et al., 2003; Kobayashi and Chen, 2005). Therefore, we further evaluated the mice for hyperactivity by measuring the distance traveled and the average speed during MWM training (**Supplementary Figures 2A,B**) and did not find any significant differences between WT and APP/PS1 mice. Furthermore, open-field experiments report no hyperactivity in 6- to 18-month-old APP/PS1mice (Lalonde et al., 2004; Cao et al., 2007; Sood et al., 2007). Our results demonstrate that, even at 2 months of age, APP/PS1 display mild behavioral impairments in MWM. They further suggest that existing behavior assessment methodologies used to evaluate AD models must be systematically re-evaluated in light of our current understanding of AD progression and pathogenesis.

We recognize that our study has limitations. Firstly, it is limited to a single animal model of AD-like amyloidosis. Furthermore, we have not investigated a molecular mechanism that might explain the anomalous search strategies. Nevertheless, the findings in this study indicate the significance of early subtle readouts, which will be beneficial to tailor more informed treatment strategies in the future.

## DATA AVAILABILITY STATEMENT

The original contributions presented in the study are included in the article/**Supplementary Materials**, further inquiries can be directed to the corresponding author/s.

## ETHICS STATEMENT

The animal study was reviewed and approved by Institutional Animal Ethics Committee of the Indian Institute of Science, Bangalore.

## AUTHOR CONTRIBUTIONS

SK devised, carried out, analyzed all experiments, and wrote the manuscript.

## FUNDING

This work was supported by funds obtained from the Centre for Brain Research (CBR) and Pratiksha Trust.

## ACKNOWLEDGMENTS

The author is grateful to Prof. Vijayalakshmi Ravindranath, Director, CBR, for the support throughout the study. The author is specially thanking the Scientific Advisory Committee at CBR for their insightful inputs, Mr. Abhijith Shankaran for the detailed copyediting of the manuscript, and Mr. Byju

Abraham (Ferill Dynamics, Bangalore, India), who developed an application to trace mouse trajectories. The authors would also like to specially thank Mr. R. Radeesh, Mr. N. Muniraju, and the staff at Central Animal Facility, IISc.

## SUPPLEMENTARY MATERIAL

The Supplementary Material for this article can be found online at: https://www.frontiersin.org/articles/10.3389/fnins.2020.568200/full#supplementary-material

**Supplementary Figure 1 |** Reference spatial memory is intact in APP/PS1 at 24 h after the last Morris water maze learning trial: **(A)** mean acquisition latencies to reach the platform on six consecutive days (averaged of four trials per day) among wild-type (dark circle) and APP/PS1 (light circle) mice. **(B)** Reference memory evaluated at 24 h after the last trial on day 6. Data are presented as mean ± SEM; $n = 7$. $^{****}P < 0.0001$.

**Supplementary Figure 2 |** Average Morris water maze training performance. **(A)** The average of swimming speed (m/s) and **(B)** the average distance traveled (m) over 6 days of training between wild-type (dark gray) and APP/PS1 (light gray) mice. Data are presented as mean ± SEM; $n = 18$.

**Supplementary Figure 3 | (A,B)** Average prevalence of each strategy by trials across days of training: experiments with male wild-type (WT) and APP/PS1 mice were conducted on two separate days with two batches of animals. Each batch had nine WT and nine APP/PS1 male mice. The results of two replicate (batches) experiments are represented. Note the consistent circling strategy preference of APP/PS1 during water maze learning. Data are presented as mean ± SEM; $n = 9$.

## REFERENCES


Abd-Elrahman, K. S., Hamilton, A., de Souza, J. M., Albaker, A., Ribeiro, F. M., and Ferguson, S. S. G. (2020). Gender-specific pathophysiological mGluR5-dependent Aβ oligomer signaling in Alzheimer mice. *bioRxiv [Preprint]. bioRixv:803262.* doi: 10.2139/ssrn.3490653

Agostini, A., Yuchun, D., Li, B., Kendall, D. A., and Pardon, M. C. (2020). Sex-specific hippocampal metabolic signatures at the onset of systemic inflammation with lipopolysaccharide in the APPswe/PS1dE9 mouse model of Alzheimer's disease. *Brain Behav. Immun.* 83, 87–111. doi: 10.1016/j.bbi.2019.09.019

Ahmad, F., Singh, K., Das, D., Gowaikar, R., Shaw, E., Ramachandran, A., et al. (2017). Reactive oxygen species-mediated loss of synaptic Akt1 signaling leads to deficient activity-dependent protein translation early in Alzheimer's disease. *Antioxid. Redox Signal.* 27, 1269–1280. doi: 10.1089/ars.2016.6860

Ashe, K. H., and Zahs, K. R. (2010). Probing the biology of Alzheimer's disease in mice. *Neuron* 66, 631–645. doi: 10.1016/j.neuron.2010.04.031

Bateman, R. J., Xiong, C., Benzinger, T. L., Fagan, A. M., Goate, A., Fox, N. C., et al. (2012). Clinical and biomarker changes in dominantly inherited Alzheimer's disease. *N. Eng. J. Med.* 367, 795–804. doi: 10.1056/NEJMoa1202753

Berkowitz, L. E., Harvey, R. E., Drake, E., Thompson, S. M., and Clark, B. J. (2018). Progressive impairment of directional and spatially precise trajectories by TgF344-Alzheimer's disease rats in the morris water task. *Sci. Rep.* 8:16153. doi: 10.1038/s41598-018-34368-w

Botvinick, M. M., Niv, Y., and Barto, A. C. (2009). Hierarchically organized behavior and its neural foundations: a reinforcement-learning perspective. *Cognition* 113, 262–280. doi: 10.1016/j.cognition.2008.08.011

Brody, D. L., and Holtzman, D. M. (2006). Morris water maze search strategy analysis in PDAPP mice before and after experimental traumatic brain injury. *Exp. Neurol.* 197, 330–340. doi: 10.1016/j.expneurol.2005.10.020

Cao, D., Lu, H., Lewis, T. L., and Li, L. (2007). Intake of sucrose-sweetened water induces insulin resistance and exacerbates memory deficits and amyloidosis in a transgenic mouse model of Alzheimer disease. *J. Biol. Chem.* 282, 36275–36282. doi: 10.1074/jbc.M703561200

Chiang, A. C. A., Fowler, S. W., Reddy, R., Pletnikova, O., Troncoso, J. C., Sherman, M. A., et al. (2018). Discrete pools of oligomeric amyloid-β track with spatial learning deficits in a mouse model of alzheimer amyloidosis. *Am. J. Pathol.* 188, 739–756. doi: 10.1016/j.ajpath.2017.11.011

Chintapaludi, S. R., Uyar, A., Jackson, H. M., Acklin, C. J., Wang, X., Sasner, M., et al. (2020). Staging alzheimer's disease in the brain and retina of B6.APP/PS1 mice by transcriptional profiling. *J. Alzheimers. Dis.* 73, 1421–1434. doi: 10.3233/JAD-190793

Cramer, P. E., Cirrito, J. R., Wesson, D. W., Lee, C. Y., Karlo, J. C., Zinn, A. E., et al. (2012). ApoE-directed therapeutics rapidly clear β-amyloid and reverse deficits in AD mouse models. *Science* 335, 1503–1506. doi: 10.1126/science.1217697

da Silva, V. S., Haberl, M. G., Zhang, P., Bethge, P., Lemos, C., Gonçalves, N., et al. (2016). Early synaptic deficits in the APP/PS1 mouse model of Alzheimer's disease involve neuronal adenosine A2A receptors. *Nat. Commun.* 7:11915. doi: 10.1038/ncomms11915

Desikan, R. S., Fischl, B., Cabral, H. J., Kemper, T. L., Guttmann, C. R., Blacker, D., et al. (2008). MRI measures of temporoparietal regions show differential rates of atrophy during prodromal AD. *Neurology* 71, 819–825. doi: 10.1212/01.wnl.0000320055.57329.34

D'Hooge, R., and De Deyn, P. P. (2001). Applications of the morris water maze in the study of learning and memory. *Brain Res. Rev.* 36, 60–90. doi: 10.1016/S0165-017300067-4

Ding, Y., Qiao, A., Wang, Z., Goodwin, J. S., Lee, E. S., Block, M. L., et al. (2008). Retinoic acid attenuates beta-amyloid deposition and rescues memory deficits in an Alzheimer's disease transgenic mouse model. *J. Neurosci.* 28, 11622–11634. doi: 10.1523/JNEUROSCI.3153-08.2008

Dodart, J. C., Meziane, H., Mathis, C., Bales, K. R., Paul, S. M., and Ungerer, A. (1999). Behavioral disturbances in transgenic mice overexpressing the V717F beta-amyloid precursor protein. *Behav. Neurosci.* 113, 982–990. doi: 10.1037/0735-7044.113.5.982

Dubois, B., Feldman, H. H., Jacova, C., Hampel, H., Molinuevo, J. L., Blennow, K., et al. (2014). Advancing research diagnostic criteria for Alzheimer's disease: the IWG-2 criteria. *Lancet Neurol.* 13, 614–629. doi: 10.1016/S1474-442270090-0

Edwards, S. R., Hamlin, A. S., Marks, N., Coulson, E. J., and Smith, M. T. (2014). Comparative studies using the morris water maze to assess spatial memory deficits in two transgenic mouse models of Alzheimer's disease. *Clin. Exp. Pharmacol. Physiol.* 41, 798–806. doi: 10.1111/1440-1681.12277

Gallagher, J. J., Minogue, A. M., and Lynch, M. A. (2013). Impaired performance of female APP/PS1 mice in the Morris water maze is coupled with increased Aβ accumulation and microglial activation. *Neurodegener. Dis.* 11, 33–41. doi: 10.1159/000337458

Garcia-Alloza, M., Robbins, E. M., Zhang-Nunes, S. X., Purcell, S. M., Betensky, R. A., Raju, S., et al. (2006). Characterization of amyloid deposition in the APPswe/PS1dE9 mouse model of Alzheimer disease. *Neurobiol. Dis.* 24, 516–524. doi: 10.1016/j.nbd.2006.08.017

Garthe, A., Behr, J., and Kempermann, G. (2009). Adult-generated hippocampal neurons allow the flexible use of spatially precise learning strategies. *PLoS ONE* 4:e5464. doi: 10.1371/journal.pone.0005464

Gong, B., Vitolo, O. V., Trinchese, F., Liu, S., Shelanski, M., and Arancio, O. (2004). Persistent improvement in synaptic and cognitive functions in an Alzheimer mouse model after rolipram treatment. *J. Clin. Invest.* 114, 1624–1634. doi: 10.1172/JCI22831

Gong, Z., Huang, J., Xu, B., Ou, Z., Zhang, L., Lin, X., et al. (2019). Urolithin A attenuates memory impairment and neuroinflammation in APP/PS1 mice. *J. Neuroinflammation.* 16:62. doi: 10.1186/s12974-019-1450-3

Granger, M. W., Franko, B., Taylor, M. W., Messier, C., Hyslop, P. G., and Bennetta, S. A. L. (2016). A TgCRND8 mouse model of alzheimer's disease exhibits sexual dimorphisms in behavioral indices of cognitive reserve. *J. Alzheimers Dis.* 51, 757–773. doi: 10.3233/JAD-150587

Graybiel, A. M., and Grafton, S. T. (2015). The striatum: where skills and habits meet. *Cold Spring Harb. Perspect. Biol.* 7:a021691. doi: 10.1101/cshperspect.a021691

Graziano, A., Petrosini, L., and Bartoletti, A. (2003). Automatic recognition of explorative strategies in the morris water maze. *J. Neurosci. Methods* 130, 33–44. doi: 10.1016/S0165-027000187-0

Hanson, L. R., Fine, J. M., Renner, D. B., Svitak, A. L., Burns, R. B., Nguyen, T. M., et al. (2012). Intranasal delivery of deferoxamine reduces spatial memory loss in APP/PS1 mice. *Drug Deliv. Transl. Res.* 2, 160–168. doi: 10.1007/s13346-011-0050-2

Hassenstab, J., Chasse, R., Grabow, P., Benzinger, T. L. S., Fagan, A. M., Xiong, C., et al. (2016). Certified normal: Alzheimer's disease biomarkers and normative estimates of cognitive functioning. *Neurobiol. Aging* 43, 23–33. doi: 10.1016/j.neurobiolaging.2016.03.014

Hu, Y. S., Xu, P., Pigino, G., Brady, S. T., Larson, J., and Lazarov, O. (2010). Complex environment experience rescues impaired neurogenesis, enhances synaptic plasticity, and attenuates neuropathology in familial Alzheimer's disease-linked APPswe/PS1DeltaE9 mice. *FASEB J.* 24, 1667–1681. doi: 10.1096/fj.09-136945

Huang, C., Wahlund, L. O., Svensson, L., Winblad, B., and Julin, P. (2002). Cingulate cortex hypoperfusion predicts Alzheimer's disease in mild cognitive impairment. *BMC Neurol* 2:9. doi: 10.1186/1471-2377-2-9

Huang, H. J., Liang, K. C., Ke, H. C., Chang, Y. Y., and Hsieh-Li, H. M. (2011). Long-term social isolation exacerbates the impairment of spatial working memory in APP/PS1 transgenic mice. *Brain Res.* 1371, 150–160. doi: 10.1016/j.brainres.2010.11.043

Jankowsky, J. L., Fadale, D. J., Anderson, J., Xu, G. M., Gonzales, V., Jenkins, N. A., et al. (2004). Mutant presenilins specifically elevate the levels of the 42-residue beta-amyloid peptide in vivo: evidence for augmentation of a 42-specific gamma secretase. *Hum Mol Genet.* (2004) 13, 159–170. doi: 10.1093/hmg/ddh019

Jankowsky, J. L., Slunt, H. H., Ratovitski, T., Jenkins, N. A., Copeland, N. G., and Borchelt, D. R. (2001). Co-expression of multiple transgenes in mouse CNS: a comparison of strategies. *Biomol. Eng.* 17, 157–165. doi: 10.1016/S1389-034400067-3

Jankowsky, J. L., and Zheng, H. (2017). Practical considerations for choosing a mouse model of Alzheimer's disease. *Mol. Neurodegen.* 12:89. doi: 10.1186/s13024-017-0231-7

Janus, C. (2004). Search strategies used by APP transgenic mice during navigation in the Morris water maze. *Learn. Mem.* 11, 337–346. doi: 10.1101/lm.70104

Janus, C., Flores, A. Y., Xu, G., and Borchelt, D. R. (2015). Behavioral abnormalities in APPSwe/PS1dE9 mouse model of AD-like pathology: comparative analysis across multiple behavioral domains. *Neurobiol. Aging* 36, 2519–2532. doi: 10.1016/j.neurobiolaging.2015.05.010

Karunakaran, S., Chowdhury, A., Donato, F., Quairiaux, C., Michel, C. M., and Caroni, P. (2016). PV plasticity sustained through D1/5 dopamine signaling required for long- term memory consolidation. *Nat. Neurosci.* 19, 454–464. doi: 10.1038/nn.4231

Kim, H. Y., Kim, H. V., Jo, S., Lee, C. J., Choi, S. Y., Kim, D. J., et al. (2015). EPPS rescues hippocampus-dependent cognitive deficits in APP/PS1 mice by disaggregation of amyloid-β oligomers and plaques. *Nat. Commun.* 6:8997. doi: 10.1038/ncomms9997

Klein, W. L., Krafft, G. A., and Finch, C. E. (2001). Targeting small Abeta oligomers: the solution to an Alzheimer's disease conundrum? *Trends Neurosci.* 24, 219–224. doi: 10.1016/S0166-223601749-5

Kobayashi, D. T., and Chen, K. S. (2005). Behavioral phenotypes of amyloid-based genetically modified mouse models of Alzheimer's disease. *Genes Brain Behav.* 4, 173–196. doi: 10.1111/j.1601-183X.2005.00124.x

Kommaddi, R. P., Das, D., Karunakaran, S., Nanguneri, S., Bapat, D., Ray, A., et al. (2018). Aβ mediates F-actin disassembly in dendritic spines leading to cognitive deficits in Alzheimer's disease. *J. Neurosci.* 38, 1085–1099. doi: 10.1523/JNEUROSCI.2127-17.2017

Kummer, M. P., Hammerschmidt, T., Martinez, A., Terwel, D., Eichele, G., Witten, A., et al. (2014). Ear2 deletion causes early memory and learning deficits in APP/PS1 mice. *J. Neurosci.* 34, 8845–8854. doi: 10.1523/JNEUROSCI.4027-13.2014

LaFerla, F. M., and Green, K. N. (2012). Animal models of Alzheimer disease. *Cold Spring Harb. Perspect. Med.* 2:a006320. doi: 10.1101/cshperspect.a006320

Lalonde, R., Kim, H. D., and Fukuchi, K. (2004). Exploratory activity, anxiety, and motor coordination in bigenic APPswe + PS1/DeltaE9 mice. *Neurosci. Lett.* 369, 156–161. doi: 10.1016/j.neulet.2004.07.069

Lalonde, R., Kim, H. D., Maxwell, J. A., and Fukuchi, K. (2005). Exploratory activity and spatial learning in 12-month-old APP(695) SWE/co+PS1/DeltaE9 mice with amyloid plaques. *Neurosci. Lett.* 390, 87–92. doi: 10.1016/j.neulet.2005.08.028

Lalonde, R., Lewis, T. L., Strazielle, C., Kim, H., and Fukuchi, K. (2003). Transgenic mice expressing the betaAPP695SWE mutation: effects on exploratory activity, anxiety, and motor coordination. *Brain Res.* 977, 38–45. doi: 10.1016/S0006-899302694-5

Lang, U. E., Lang, F., Richter, K., Vallon, V., Lipp, H. P., Schnermann, J., et al. (2003). Emotional instability but intact spatial cognition in adenosine receptor 1 knock out mice. *Behav. Brain Res.* 145, 179–188. doi: 10.1016/S0166-432800108-6

Li, C., Shi, J., Wang, B., Li, J., and Jia, H. (2019). CB2 cannabinoid receptor agonist ameliorates novel object recognition but not spatial memory in transgenic APP/PS1 mice. *Neurosci. Lett.* 707:134286. doi: 10.1016/j.neulet.2019.134286

Lim, T., Iaria, G., and Moon, S. Y. (2010). Topographical disorientation in mild cognitive impairment: a voxel-based morphometry study. *J. Clin. Neurol.* 6, 204–211. doi: 10.3988/jcn.2010.6.4.204

Ma, T., Du, X., Pick, J. E., Sui, G., Brownlee, M., and Klann, E. (2012). Glucagon-like peptide-1 cleavage product GLP-1(9-36) amide rescues synaptic plasticity and memory deficits in Alzheimer's disease model mice. *J. Neurosci.* 32, 13701–13708. doi: 10.1523/JNEUROSCI.2107-12.2012

Moechars, D., Lorent, K., De Strooper, B., Dewachter, I., and Van Leuven, F. (1996). Expression in brain of amyloid precursor protein mutated in the alphα-secretase site causes disturbed behavior, neuronal degeneration and premature death in transgenic mice. *EMBO J.* 15, 1265–1274. doi: 10.1002/j.1460-2075.1996.tb00468.x

Mondadori, C. R., Buchmann, A., Mustovic, H., Schmidt, C. F., Boesiger, P., Nitsch, R. M., et al. (2006). Enhanced brain activity may precede the diagnosis of Alzheimer's disease by 30 years. *Brain* 129, 2908–2922. doi: 10.1093/brain/awl266

Montgomery, K. S., Simmons, R. K., Edwards, G. III, Nicolle, M. M., Gluck, M. A., Myers, C. E., et al. (2011). Novel age dependent learning deficits in a mouse model of Alzheimer's disease: Implications for translational research. *Neurobiol. Aging* 32, 1273–1285. doi: 10.1016/j.neurobiolaging.2009.08.003

Morris, R. (1984). Development of a water-maze procedure for studying spatial learning in the rat. *J. Neurosci. Methods* 11, 47–60. doi: 10.1016/0165-027090007-4

Mosconi, L., Sorbi, S., de Leon, M. J., Li, Y., Nacmias, B., Myoung, P. S., et al. (2006). Hypometabolism exceeds atrophy in presymptomatic early-onset familial Alzheimer's disease. *J. Nucl. Med.* 47, 1778–1786.

Park, J. H., Widi, G. A., Gimbel, D. A., Harel, N. Y., Lee, D. H., and Strittmatter, S. M. (2006). Subcutaneous nogo receptor removes brain amyloid-beta and improves spatial memory in Alzheimer's transgenic mice. *J. Neurosci.* 26, 13279–13286. doi: 10.1523/JNEUROSCI.4504-06.2006

Park, S., Ko, H., Lee, N., Lee, H., Rim, Y., Kim, H., et al. (2010). Aged wild-type littermates and APPswe+PS1/ΔE9 mice present similar deficits in associative learning and spatial memory independent of amyloid load. *Genes Genomics* 32, 63–70. doi: 10.1007/s13258-010-0833-8

Pillay, N. S., Kellaway, L. A., and Kotwal, G. J. (2008). Early detection of memory deficits and memory improvement with vaccinia virus complement control protein in an Alzheimer's disease model. *Behav. Brain Res.* 192, 173–177. doi: 10.1016/j.bbr.2008.03.038

Puzzo, D., Staniszewski, A., Deng, S. X., Privitera, L., Leznik, E., Liu, S., et al. (2009). Phosphodiesterase 5 inhibition improves synaptic function, memory, and amyloid-beta load in an Alzheimer's disease mouse model. *J. Neurosci.* 29, 8075–8086. doi: 10.1523/JNEUROSCI.0864-09.2009

Reiserer, R. S., Harrison, F. E., Syverud, D. C., and Mcdonald, M. P. (2007). Impaired spatial learning in the APPSwe + PSEN1DeltaE9 bigenic mouse model of Alzheimer's disease. *Genes Brain Behav.* 6, 54–65. doi: 10.1111/j.1601-183X.2006.00221.x

Romberg, C., McTighe, S. M., Heath, C. J., Whitcomb, D. J., Cho, K., Bussey, T. J., et al. (2012). False recognition in a mouse model of Alzheimer's disease: rescue with sensory restriction and memantine. *Brain* 135, 2103–2114. doi: 10.1093/brain/aws074

Ruediger, S.,Spirig, D., Donato, F., and Caroni, P. (2012). Goal-oriented searching mediated by ventral hippocampus early in trial-and-error learning. *Nat. Neurosci.* 15, 1563–1571. doi: 10.1038/nn.3224

Schrott, L. M., Jackson, K., Yi, P., Dietz, F., Johnson, G. S., Basting, T. F., et al. (2015). Acute oral bryostatin-1 administration improves learning deficits in the

APP/PS1 transgenic mouse model of Alzheimer's disease. *Curr. Alzheimer Res.* 12, 22–31. doi: 10.2174/1567205012666141218141904

Seo, S. W., Im, K., Lee, J. M., Kim, Y. H., Kim, S. T., Kim, S. Y., et al. (2007). Cortical thickness in single- versus multiple-domain amnestic mild cognitive impairment. *Neuroimage* 36, 289–297. doi: 10.1016/j.neuroimage.2007.02.042

Shemer, I., Holmgren, C., Min, R., Fülöp, L., Zilberter, M., Sousa, K. M., et al. (2006). Non-fibrillar beta-amyloid abates spike-timing-dependent synaptic potentiation at excitatory synapses in layer 2/3 of the neocortex by targeting postsynaptic AMPA receptors. *Eur. J. Neurosci.* 23, 2035–2047. doi: 10.1111/j.1460-9568.2006.04733.x

Sood, A., Warren, B. J., Webster, S. J., Terry, A. V., and Buccafusco, J. J. (2007). The effects of JWB1-84-1 on memory-related task performance by amyloid Abeta transgenic mice and by young and aged monkeys. *Neuropharmacology* 53, 588–600. doi: 10.1016/j.neuropharm.2007.06.028

Su, D., Zhao, Y., Xu, H., Wang, B., Chen, X., Chen, J., and Wang, X. (2012). Isoflurane exposure during mid-adulthood attenuates age-related spatial memory impairment in APP/PS1 transgenic mice. *PLoS ONE* 7:e50172. doi: 10.1371/journal.pone.0050172

Sutton, R. S., and Barto, A. G. (1998). *Reinforcement Learning: An Introduction* (Cambridge, MA: MIT Press). doi: 10.1109/TNN.1998.712192

Tarawneh, R., and Holtzman, D. M. (2012). The clinical problem of symptomatic Alzheimer disease and mild cognitive impairment. *Cold Spring Harb. Perspect. Med.* 2:a006148. doi: 10.1101/cshperspect.a006148

Trinchese, F., Liu, S., Battaglia, F., Walter, S., Mathews, P. M., and Arancio, O. (2004). Progressive age-related development of Alzheimer-like pathology in APP/PS1 mice. *Ann. Neurol.* 55, 801–814. doi: 10.1002/ana.20101

Trivedi, M. A., Wichmann, A. K., Torgerson, B. M., Ward, M. A., Schmitz, T. W., Ries, M. L., et al. (2006). Structural MRI discriminates individuals with Mild Cognitive Impairment from age-matched controls: a combined neuropsychological and voxel based morphometry study. *Alzheimers Dement* 2, 296–302. doi: 10.1016/j.jalz.2006.06.001

Van Dam, D., D'Hooge, R., Staufenbiel, M., Van Ginneken, C., Van Meir, F., and De Deyn, P. P. (2003). Age-dependent cognitive decline in the APP23 model precedes amyloid deposition. *Eur. J. Neurosci.* 17, 388–396. doi: 10.1046/j.1460-9568.2003.02444.x

Vartak, R. S., Rodin, A., and Oddo, S. (2019). Differential activation of the mTOR/autophagy pathway predicts cognitive performance in APP/PS1 mice. *Neurobiol. Aging* 83, 105–113. doi: 10.1016/j.neurobiolaging.2019.08.018

Volianskis, A., Kostner, R., Molgaard, M., Hass, S., and Jensen, M. S. (2010). Episodic memory deficits are not related to altered glutamatergic synaptic transmission and plasticity in the CA1 hippocampus of the APPswe/PS1deltaE9-deleted transgenic mice model of ss-amyloidosis. *Neurobiol. Aging.* 31, 1173–1187. doi: 10.1016/j.neurobiolaging.2008.08.005

Vorhees, C. V., and Williams, M. T. (2006). Morris water maze: procedures for assessing spatial and related forms of learning and memory. *Nat. Protoc.* 1, 848–858. doi: 10.1038/nprot.2006.116

Vouros, A., Gehring, T. V., Szydlowska, K., Janusz, A., Tu, Z., Croucher, M., et al. (2018). A generalised framework for detailed classification of swimming paths inside the Morris Water Maze. *Sci. Rep.* 8:15089. doi: 10.1038/s41598-018-33456-1

Wang, X., Miao, Y., Abulizi, J., Li, F., Mo, Y., Xue, W., et al. (2016). Improvement of electroacupuncture on APP/PS1 transgenic mice in spatial learning and memory probably due to expression of Aβ and LRP1 in hippocampus. *Evid. Based Complement Alternat. Med.* 2016:7603975. doi: 10.1155/2016/7603975

Webster, S. J., Bachstetter, A. D., Nelson, P. T., Schmitt, F. A., and Van Eldik, L. J. (2014). Using mice to model Alzheimer's dementia: an overview of the clinical disease and the preclinical behavioural changes in 10 mouse models. *Front. Genet.* 5:88. doi: 10.3389/fgene.2014.00088

Weishaupt, N., Liu, Q., Shin, S., Singh, R., Agca, Y., Agca, C., et al. (2018). APP21 transgenic rats develop age-dependent cognitive impairment and microglia accumulation within white matter tracts. *J. Neuroinflam.* 15:241. doi: 10.1186/s12974-018-1273-7

Wen, S. R., Qi, H. P., Ren, Y. J., Liu, G. J., Gong, F. C., Zhong, H., et al. (2011). Expression of δNp73 in hippocampus of APP/PS1 transgenic mice following GFP-BMSCs transplantation. *Neurol. Res.* 33, 1109–1114. doi: 10.1179/1743132811Y.0000000051

Whitwell, J. L., Przybelski, S. A., Weigand, S. D., Knopman, D. S., Boeve, B. F., Petersen, R. C., et al. (2007). 3D maps from multiple MRI illustrate changing atrophy patterns as subjects progress from mild cognitive impairment to alzheimer's disease alzheimer's disease. *Brain* 130, 1777–1786. doi: 10.1093/brain/awm112

Wolfer, D. P., and Lipp, H. P. (2000). Dissecting the behaviour of transgenic mice: is it the mutation, the genetic background, or the environment? *Exp. Physiol.* 85, 627–634. doi: 10.1111/j.1469-445X.2000.02095.x

Zhang, Q., Du, X., Xu, Y., Dang, L., Xiang, L., and Zhang, J. (2013). The effects of Gouqi extracts on morris maze learning in the APP/PS1 double transgenic mouse model of Alzheimer's disease. *Exp. Ther. Med.* 5, 1528–1530. doi: 10.3892/etm.2013.1006

Zhang, W., Hao, J., Liu, R., Zhang, Z., Lei, G., Su, C., et al. (2011). Soluble abeta levels correlate with cognitive deficits in the 12-month-old APPswe/PS1dE9 mouse model of Alzheimer's disease. *Behav. Brain Res.* 222, 342–350. doi: 10.1016/j.bbr.2011.03.072

Zhang, Z., Wu, H., and Huang, H. (2016). Epicatechin plus treadmill exercise are neuroprotective against moderate-stage amyloid precursor protein/presenilin 1 mice. *Pharmacogn. Mag.* 12, S139–S146. doi: 10.4103/0973-1296.182174

**Conflict of Interest:** The author declares that the research was conducted in the absence of any commercial or financial relationships that could be construed as a potential conflict of interest.

*Copyright © 2020 Karunakaran. This is an open-access article distributed under the terms of the Creative Commons Attribution License (CC BY). The use, distribution or reproduction in other forums is permitted, provided the original author(s) and the copyright owner(s) are credited and that the original publication in this journal is cited, in accordance with accepted academic practice. No use, distribution or reproduction is permitted which does not comply with these terms.*

frontiers in Molecular Neuroscience

ORIGINAL RESEARCH
published: 15 April 2021
doi: 10.3389/fnmol.2021.616178

# Depletion of TrkB Receptors From Adult Serotonergic Neurons Increases Brain Serotonin Levels, Enhances Energy Metabolism and Impairs Learning and Memory

*Madhusmita P. Sahu[1]*, Yago Pazos-Boubeta[1], Anna Steinzeig[1], Katja Kaurinkoski[1], Michela Palmisano[1], Olgierd Borowecki[1,2], Timo Petteri Piepponen[3] and Eero Castrén[1]**

*[1] Neuroscience Center, Helsinki Institute of Life Science HiLIFE, University of Helsinki, Helsinki, Finland, [2] Faculty of Philosophy and Social Sciences, Nicolaus Copernicus University in Toruń, Toruń, Poland, [3] Division of Pharmacology and Pharmacotherapy, University of Helsinki, Helsinki, Finland*

OPEN ACCESS

**Edited by:**
*Jochen C. Meier, Technische Universitat Braunschweig, Germany*

**Reviewed by:**
*Natalia Alenina, Max Delbrück Center for Molecular Medicine, Helmholtz Association of German Research Centers (HZ), Germany*
*Friederike Klempin, Charité – Universitätsmedizin Berlin, Germany*

***Correspondence:**
*Madhusmita P. Sahu*
*madhusmita.priyadarshini@gmail.com*
*Eero Castrén*
*eero.castren@helsinki.fi*

**Received:** *11 October 2020*
**Accepted:** *23 March 2021*
**Published:** *15 April 2021*

**Citation:**
*Sahu MP, Pazos-Boubeta Y, Steinzeig A, Kaurinkoski K, Palmisano M, Borowecki O, Piepponen TP and Castrén E (2021) Depletion of TrkB Receptors From Adult Serotonergic Neurons Increases Brain Serotonin Levels, Enhances Energy Metabolism and Impairs Learning and Memory. Front. Mol. Neurosci. 14:616178. doi: 10.3389/fnmol.2021.616178*

Neurotrophin brain-derived neurotrophic factor (BDNF) and neurotransmitter serotonin (5-HT) regulate each other and have been implicated in several neuronal mechanisms, including neuroplasticity. We have investigated the effects of BDNF on serotonergic neurons by deleting BDNF receptor TrkB from serotonergic neurons in the adult brain. The transgenic mice show increased 5-HT and Tph2 levels with abnormal behavioral phenotype. In spite of increased food intake, the transgenic mice are significantly leaner than their wildtype littermates, which may be due to increased metabolic activity. Consistent with increased 5-HT, the proliferation of hippocampal progenitors is significantly increased, however, long-term survival of newborn cells is unchanged. Our data indicates that BDNF-TrkB signaling regulates the functional phenotype of 5-HT neurons with long-term behavioral consequences.

**Keywords: serotonin, TrkB, BDNF, neuronal plasticity, neurotrophic factor**

## INTRODUCTION

Neurotrophin Brain-derived neurotrophic factor (BDNF) and neurotransmitter serotonin (5-HT) regulate neuronal survival, neurogenesis, and neuronal plasticity and they also co-regulate each other (Mattson et al., 2004; Martinowich and Lu, 2008). Changes or aberrations in these two systems, together or independently, are associated with neuropsychiatric disorders, which are a major health problem worldwide (Homberg et al., 2014).

Brain-derived neurotrophic factor is associated with the regulation of activity-dependent neuronal connectivity and plasticity. BDNF together with its high-affinity cognate receptor, neurotrophic tyrosine kinase receptor 2 (Ntrk2/TrkB) plays a significant role in neuronal survival, synaptic plasticity, and in mediating 5-HT metabolism (Mamounas et al., 2000). BDNF and TrkB induce serotonergic phenotype and increase the number of 5-HT expressing neurons (Galter and Unsicker, 2000a). BDNF and TrkB have been concomitantly related together with 5-HT in a myriad of neurochemical and behavioral responses (Martinowich and Lu, 2008).

5-HT is a major modulatory neurotransmitter produced by neurons that are located in the brainstem raphe nuclei and project massively throughout the brain serving different physiological

and behavioral functions (Dahlström and Fuxe, 1964; Steinbusch, 1981; Gaspar et al., 2003; Okaty et al., 2015). 5-HT is released both synaptically and through volume transmission (Halasy et al., 1992; Fuxe et al., 2007), and its effects are mediated by an ensemble of different receptors located on the target neurons as well as on 5-HT neurons themselves (Jacobs and Azmitia, 1992). Although a positive identification of BDNF and TrkB expression in serotonergic neurons is missing, TrkB are expressed in the region of raphe nuclei (Madhav et al., 2001; Lunden and Kirby, 2013; Adachi et al., 2017). However, the physiological role of the activation of TrkB in 5-HT neurons remains unclear.

Previous studies have demonstrated that BDNF controls the survival and maintenance of developing 5-HT neurons through an auto/paracrine loop mediated by its autoreceptors, mainly 5HT1a, followed by sequential activation of BDNF and TrkB (Galter and Unsicker, 2000b). The 5-HT neurons from the mid-brain (MB) project throughout the brain and exert trophic actions on the target cells by controlling their proliferation and differentiation (Lauder et al., 1982; Commons, 2016).

We recently found that TrkB plays a critical role in the maintenance of 5-HT and dopamine (DA) neurons in zebrafish brain (Sahu et al., 2019). Constitutive knockouts of both TrkB and BDNF are postnatally lethal in mammals (Erickson et al., 1996), so conditional and inducible transgenic mouse (TG) models have been utilized to delete TrkB in a regionally and temporally selective fashion. A recent study reported that deletion of TrkB from neurons in the midbrain raphe region resulted in a loss of antidepressant efficacy and heightened aggression (Adachi et al., 2017). In this study we have specifically deleted TrkB in Tph2 expressing 5-HT neurons in the adulthood, after the serotonergic system has fully matured, and demonstrate a key role for TrkB in serotonergic neurons in the regulation of 5-HT function. The effects of loss of TrkB in 5-HT neurons on behavior were also assessed by a battery of tests measuring anxiety, aggression, learning, and memory.

# MATERIALS AND METHODS

## Animals

The Tph2creERT2 animals were obtained from Prof. Pierre Chambon laboratory (Feil et al., 1996; Yadav et al., 2011). The animals were rederived and backcrossed to the C57BL/6J strain in our animal facility for several generations. The TrkBflox mice were obtained from the Jackson lab and have been maintained in our system with C57BL/6J background.

The Tph2creERT2 mice were crossed with homozygous TrkBflox mice to generate the Tph2creERT2:TrkBflox mice in the C57BL/6J strain background. The cre is hemizygous and TrkBflox is homozygous, therefore every internal mating produced Tph2creERT2:TrkBflox and TrkBflox mice. The animals that were cre positive have been grouped as transgenic and the flox alone as control throughout this manuscript. The cohorts were made by pooling several littermates born at the same time.

For cre activation, tamoxifen was dissolved in corn oil with continuous shaking at 37°C overnight. The tamoxifen stock was made into a final concentration of 20 mg/ml. For all the experiments we have used the same injection time. Six weeks old mice were administered tamoxifen at 0.1 mg/kg intra peritoneally (ip) dose daily for 5 days to activate the cre-mediated recombination. The control and transgenic mice that had received tamoxifen are called Ctrl and TG, respectively. The transgenic animals not injected with tamoxifen are represented as TG w/o TAM.

For reporter assay, tDtomato mice (JAX 007914, Jackson Lab) were crossed with Tph2creERT2 animals. The Tph2creERT2:tDtomato animals were divided into two groups, one receiving tamoxifen and others received only corn oil. All the animals were maintained according to the guidelines from the ethical committee of Southern Finland (License number-ESAVI/10300/04.10.07/2016).

## Behavioral Tests

Adult animals aged between 6 and 9 months were used for all the behavioral tests. Mice were single housed during the test period with unlimited access to food and water in the individually ventilated cage system. The single housing was done 1 week prior to the start of the behavior tests for a maximum of 1 month. Mice were kept at light/dark rhythm of 12 h each. The number of animals tested was 60 in total, with 30 experimental and 30 control group unless otherwise mentioned. The animals for most of the behavioral battery tests were males. The animals were always transferred to test rooms to adapt 30 min before starting the test. All behavioral tests were performed with the researcher blinded to the genotypes of the animals. We used three different cohorts of animals in this study. Therefore, in the first cohort we performed open field, light-dark, elevated plus maze and forced swim tests as well as Comprehensive lab animal monitoring system test, in the second cohort Barnes maze and resident intruder test, and in the third cohort the pattern separation test. The interval between the tests was usually 2 days for less stressful and 1 week for stressful experiments.

### Open Field Test (OF)

The open field test was done with a brightly illuminated (550 lux) polypropylene chamber (30 × 30 × 30 cm). One mouse was put into each of the chamber for 30 min and their movement was monitored by Activity monitor (Med Associates Inc., United States). In this test, the total time of locomotor activity was recorded. The total ambulatory distance traveled was compared between the groups. The number of animals used were $N = 30$/group.

### Light-Dark Test (LD)

The light–dark test was done in polypropylene chamber (30 × 30 × 30 cm), equipped with infrared light sensors detecting horizontal and vertical activity. A dark insert was used to divide the arena into two compartments. An opening on the wall of the dark insert ensured free movement of the animal between the two compartments. Illumination in the center of the light area was ∼550 lux. The mice were placed into the dark area at the start of the experiment. Their movements in and between the two areas were recorded and the data was collected with this activity monitoring setup for 30 min. Parameters for analysis were time

spent in different compartments, vertical counts on both of the sides, latency to dark and total distance moved. The number of animals used were $N = 30$/group.

### Elevated Plus Maze (EPM)

The elevated plus maze consisted of two open arms (30 × 5 cm) and two enclosed arms (30 × 5 cm) connected by a 5 × 5 cm central arena. The whole platform was 40 cm above the floor. The floor of the arms was light gray. The closed arms had transparent walls 15 cm high. The illumination during the test was ∼150 lux. The animal was placed in the center of the maze and tracked for a total of 5 min. The animals were tracked using Noldus EthoVision XT10 system (Noldus Information Technology, Netherlands). The parameters analyzed were latency to open arms, number of entries to the open and closed arms. The number of animals used were $N = 30$/group.

### Comprehensive Lab Animal Monitoring System (CLAMS)

For metabolic monitoring, animals were subjected to comprehensive lab animal monitoring system (CLAMS) (Columbus Instruments, United States) for 3 days. This included 1 day of acclimatization and 2 days for data collection. The number of animals used were $N = 12$/group.

### Resident-Intruder Test (RI)

The resident intruder test was performed in the animal's home cage and the trial was video recorded. The experimental animals were single-housed, and the intruder animals were group housed. This experiment was performed in the experimental animals (resident) home cage. The duration of the test was 10 min and the parameters analyzed were number of attacks by the resident animal, time of social interaction measured as duration spent on sniffing, chasing, climbing and non-social exploration such as digging, rearing, grooming, and scanning the intruder as it moves away. The total number of animals used were $N = 11$/group.

### Forced Swim Test (FST)

The mice were injected with fluoxetine 30 mg/kg intra peritoneally (ip) or saline ip 30 min prior to the test. A mouse was placed into a glass cylinder filled with tap water stabilized to room temperature. The water was filled to the height of 14 cm in the glass cylinder. The animals were tracked using the Noldus EthoVision XT10 system (Noldus Information Technology, Netherlands). The immobility time was measured during the 6-min testing period. The number of animals used were $N = 12$/group.

### Pattern Separation (PS) Test

The pattern separation test was based on a published protocol (Diaz et al., 2013) that uses a contextual fear discrimination learning paradigm. Both males and females were used in this paradigm. Males were tested first followed by females to avoid any discrepancies. The animals were subjected to two contexts A and B, which were highly similar to each other and subjected for the same duration of time. Context A was the training chamber and it referred to a fearful episode where the mice received a single 2 s foot shock of 0.8 mA at 180 s after being placed in the chamber. Context B was highly similar, except for a mild vanilla smell in the bedding and two different patterned paper inserts in the chamber wall. The test was carried out for 10 consecutive days. On test days 1, 4, 7, 8, and 10, mice were first exposed to context A before context B, and on test days 2, 3,5, 6, and 9 they were first exposed to context B followed by context A. The percentage of freezing in context A vs. B was evaluated on the last day. The number of animals used were $N = 20$/group.

### Barnes Maze Test (BM)

The Barnes Maze test was conducted based on the published protocol for a period of 6 days (Harrison et al., 2006). The acquisition training was done for 3 days with three trials per day and the inter-trial interval was for 1 h. On the 4th and 6th day the probe trial was performed. Reversal training was started on the 4th day, after the first probe trial. The latency to find the escape box was measured during training and time spent in the vicinity of the target hole was measured during probe trials. The number of animals used were $N = 12$/group.

## High Pressure Liquid Chromatography (HPLC)

The brains were dissected from adult animals after terminal anesthesia with $CO_2$. We used naïve animals, $N = 4$–5 per group. The different regions of the brain collected for analysis were the pre-frontal cortex (PFC), striatum, hippocampus (HC), hypothalamus, mid-brain (MB), and lower brain stem (LBS). The different brain structures were weighed, collected into tubes and frozen on dry ice. The samples were homogenized in 0.3 ml (pre-frontal cortex, striatum, hippocampus, hypothalamus) or 0.4 ml (mid-brain and lower brain stem) of homogenization solution consisting of six parts 0.2 M $HClO_4$ and one part antioxidant solution (1.0 mM oxalic acid, 0.1 M acetic acid, 3.0 mM L-cysteine) (Kankaanpaa et al., 2001) with Rinco ultrasonic homogenizer (Rinco Ultrasonics AG, Romanshorn, Switzerland). The homogenates centrifuged at 20,800 *g* for 35 min at 4°C. The supernatant was passed through 0.5 ml Vivaspin filter concentrators (10,000MWCO PES; Sartorius, Stonehouse, United Kingdom) and centrifuged at 8,600 *g* at 4°C for 35 min. The medium collected from the cell cultures were filtered and processed likewise.

Filtrates containing monoamines were analyzed using high-pressure liquid chromatography with electrochemical detection. Analyses of dopamine (DA), serotonin (5-HT) and its main metabolite 5-hydroxyindoleacetic acid (5-HIAA) were performed. The analytes were separated on a Phenomenex Kinetex 2.6 μm, 4.6 × 100 mm C-18 column (Phenomenex, Torrance, CA, United States). The column was maintained at 45°C with a column heater (Croco-Cil, Bordeaux, France). The mobile phase consisted of 0.1 M $NaH_2PO_4$ buffer, 120 mg/l of octane sulfonic acid, methanol (5%), and 450 mg/l EDTA, the pH of mobile phase was set to three using $H_3PO_4$. The pump (ESA Model 582 Solvent Delivery Module; ESA, Chelmsford, MA, United States) was equipped with two pulse dampers (SSI LP-21, Scientific Systems, State College, PA, United States) and provided a flow rate of 1 ml/min. One hundred microliters of the filtrate was injected into chromatographic system with a Shimadzu

SIL-20AC autoinjector (Shimadzu, Kyoto, Japan). Monoamines and their metabolites were detected using ESA CoulArray Electrode Array Detector with 12 channels (ESA, Chelmsford, MA, United States). The chromatograms were processed, and the concentrations of monoamines were calculated using CoulArray for Windows software (ESA, Chelmsford, MA, United States). The concentrations of analytes are expressed as ng/g of wet tissue.

## Western Blotting

The brains from both males and females were dissected out from adult animals ($N$ = 4/group). The different brain structures used for analysis were the hippocampus, hypothalamus, and mid-brain. The brain samples were homogenized using the standard RIPA lysis buffer, containing a cocktail of protease inhibitors and orthovanadate, followed by centrifugation at 13,000 rpm for 15 min at + 4°C. The Rn33b cells were lysed similarly and sonicated before centrifugation. The samples were then separated using gradient gels 4–15% (NuPAGE Protein gels, Invitrogen) and blotted on to a PVDF membrane. The primary antibodies were RD-TrkB (Cat# AF397, RD systems Inc., MN, United States) and GAPDH (Cat# ab75479, Abcam). The primary antibodies were used at 1:1,000 dilution. The respective HRP conjugated secondary antibodies was blocked for 1 h at room temperature. The chemiluminescent assay was performed using ECL (Pierce). All images obtained were analyzed using ImageJ software.

## Proliferation and Survival of Hippocampal Cells

Proliferation and survival of newborn cells in the dentate gyrus (DG) was quantified using a dot-blot method that was performed as previously described, with minor modifications (Wu and Castrén, 2009; Casarotto et al., 2021). The animals used for the assessment of cell proliferation and cell survival assay were 9–11 months old ($N$ = 4/group). Mice were injected with BrdU 75 mg/kg body weight four times at 2 h interval. For the proliferation study, the injection was done 24 h prior to sacrifice and for the survival study, the injection was done 4 weeks before the sacrifice. The animals were sacrificed 1 day or 4 weeks after BrdU administration, with terminal anesthesia using $CO_2$, and brains were quickly removed. Hippocampi were dissected on ice, instantly frozen on dry ice and stored at −80°C until further use. DNA was isolated from one the of the hippocampi using DNeasy® Blood and Tissue Kit (QIAGEN, Germany) according to the manufacturer's instruction. The DNA purity was assessed by the spectrophotometer NanoDrop 2000C (Thermo Fisher Scientific, United States). DNA was incubated with 1 volume of 4 N NaOH solution for 30 min at room temperature to render it as single stranded and immediately kept on ice to prevent reannealing. The DNA solution was neutralized by an equal volume of 1 M Tris–HCl (pH = 6.8). The single-stranded neutralized DNA (1 mg) was pipetted in triplicates onto a nylon transfer membrane (Schleicher and Schuell, Keene, NH, United States) with a dot-blot apparatus (Minifold, Schleicher and Schuell) under vacuum and the DNA was fixed by ultraviolet cross-linker (1,200 μJ × 100, Stratagene, La Jolla, CA, United States). The membranes were incubated with mouse anti BrdU monoclonal antibody (1:1,000, B2531, Sigma) as the primary antibody and anti-mouse horseradish peroxidase (HRP) conjugated (Bio-Rad, United States) as the secondary antibody. The Pierce ECL Plus kit (Thermo Fisher scientific, United States) was used as a chemiluminescent method to develop the membrane. The membranes were scanned by imaging using a Fuji LAS-3000 Camera (Tamro Medlabs, Finland) and the densitometry analysis was performed by ImageJ Software.

## Immunohistochemistry and *in situ* Hybridization

A mixed cohort of animals were used for immunohistochemistry. They were 9–11 months old at the time of processing. Except for the reporter mice we used for checking cre specificity were 3 months old. They were terminally anesthetized with pentobarbital (Mebunat vet 60 mg/ml) and Lidocaine followed by transcardial perfusion with 4% PFA. The brains were stored in 4% PFA overnight at + 4°C and later transferred to 30% sucrose in PBS. These brains were cryo-embedded in an embedding matrix and stored at −80°C until further use. The brains were sectioned into 40 μm thick slices and stored in cryoprotectant solution at −20°C. For BrdU labeling, DNA was denatured by incubating the sections for 30 min in 2 M HCl at + 37°C and then 15 min in 0.1 M boric acid at room temperature. All the samples were processed for immunostaining as described earlier (Karpova et al., 2011).

The primary antibodies used in this study were Calretinin (Rabbit 7697, Catalog number CR 7697, Swant Switzerland), Doublecortin (Catalog number 4604, Cell signaling technology), BrdU (Catalog number ab82421, Abcam, United Kingdom), NeuN (Catalog number MAB377X, Millipore), GFAP (Catalog number 12389, Cell Signaling Technology), and Tph2 (Catalog number PA1-778, Thermo Fisher Scientific). The respective secondary antibodies were Alexa conjugated antibodies (Invitrogen). All the sections were stained with Hoechst 33342 (Thermo Fisher Scientific) before mounting. Stacked images were obtained using a 25× objective on a Zeiss confocal microscope LSM 780 with 1 μm interval between the sections. To avoid cross talk between channels in double labeled samples, we used sequential scanning. The cell counting and quantitation was done with the experimenter blinded to the treatment groups. The cell counting was performed as mentioned in Karpova et al. (2011) using ImageJ software (ImageJ 1.51s version) (Karpova et al., 2011). The images were collected in stacks and cell counting was done in each stack ensuring no overlap in between the stacks, although a stereological counting was not performed. The number of cells were averaged for every stacked image. For sample processing, we used at least five sections per hemisphere per animal and $N$ = 4/group. The cell counting results are expressed as percentage to the control group.

For *in situ* hybridization, brains were collected on super-frost slides ($N$ = 3/group) and processed with the riboprobe synthesized for *Bdnf* (Hofer et al., 1990). The sections were probed with both sense and antisense probe labeled with digoxigenin. After washing the probes, they were labeled

with alkaline phosphatase conjugated anti-digoxigenin fab fragments (1:5,000, Roche Diagnostics, Germany) overnight. The probes were detected by a chromogenic substrate nitroblue tetrazolium/bromochloroindoyl phosphate (NBT/BCIP, Roche, Germany). The reaction was stopped, and brightfield images were obtained by a Nikon stereomicroscope.

## q-RT PCR

In this experiment we used $N = 7$ animals per group from a mixed cohort. The regions of interest including mPFC, hippocampus and midbrain were dissected and processed immediately for RNA isolation using the PureLink® RNA Mini Kit (Thermo Fisher Scientific, United States). Reverse transcription of RNA was carried out using the SuperScript IV reverse transcriptase enzyme (Invitrogen/Thermo Fisher Scientific, United States). The CFX96 Touch Real-Time PCR detection system (Bio-Rad, United States) with SYBR Green fluorescent DNA probe (Thermo Fisher Scientific, United States) was used to perform the real time PCR. The data were calculated by the normalization of the expression using Ct values of a housekeeping gene (Hprt) as the reference control. The primers used were as follows:

*Hprt* F: GGGCTTACCTCACTGCTTTCC
*Hprt R*: CTAATCACGACGCTGGGACTG
*5ht2b* F: CCATTTCCCTGGACCGCTAT
*5ht2b* R: GGCGATGCCTATTGAAATTAACCA
*Tph2* F: AGAGTTGGAGACGGAGTCGT
*Tph2* R: AAGGGCAGTGGCTTATGACC
*Bdnf* F:CGATGCCAGTTGCTTTGTCTTC
*Bdnf* R:AGTTCGGCTTTGCTCAGTGG

## Statistics

All the experiments were analyzed using GraphPad Prism software version 9.0 (GraphPad Software Inc., CA, United States). Student's *t* test (two-tailed) was used when two groups were compared. For more than two groups, the analyses performed were one-way or two-way analysis of variance (ANOVA) followed by Tukey's *post hoc* test. All the error bars represent mean ± standard error of the mean (SEM) unless specified otherwise. The exact *p* values are mentioned in the text. The significance value was accepted at $p \leq 0.05$.

# RESULTS

## Deletion of TrkB in the Tph2 Neurons Increases 5-HT Production

The timeline for all the experiments is summarized in **Figure 1A**. The specificity and effectiveness of creERT2-mediated recombination was verified by crossing the Tph2creERT2 mice with tDtomato reporter mice. One month after tamoxifen administration, tDtomato expression was observed to co-localize with the Tph2 antibody in the raphe nuclei of the mouse brain (**Figure 1B** and **Supplementary Figure 1**). In the control mice injected with corn oil, very few tDtomato expressing cells were visible and they were not colocalized with Tph2 antibody. This suggests that cre expression is activated with tamoxifen and is specific to the Tph2 specific serotonergic neurons.

For confirmation of TrkB deletion, brain tissues from the Tph2creERT2:TrkBflox (TG) and TrkBflox (Ctrl) mice were analyzed by western blotting. In the MB samples, where the 5-HT neurons are mostly located, the levels of TrkB were found to be reduced only in the cre- positive animals ($p = 0.0239$) (**Figure 1C**). A reduction, but not a total loss of TrkB signal was expected, since although 5-HT neurons are enriched in the MB regions, they nevertheless constitute a minority of all the TrkB positive cells in this region. No changes in TrkB levels were observed in the HC and hypothalamus (**Supplementary Figure 2A**).

Our previous study in zebrafish indicated that TrkB regulates 5-HT and DA neurons (Sahu et al., 2019). We therefore measured the levels of 5-HT, DA, and 5-HT metabolite 5-Hydroxyindoleacetic acid (5HIAA) in the MB containing the raphe nuclei, as well as in the projection regions of serotonergic neurons in the PFC and HC using HPLC. The levels of 5-HT were significantly increased in the MB and PFC and there was a trend toward increase in the HC (**Figure 1Da**). However, the levels of 5-HIAA were not significantly altered (**Figure 1Db**) and, consequently, the levels of 5-HIAA/5-HT ratio, a measure of 5-HT turnover was significantly reduced in the MB (**Figure 1Dc**). Furthermore, we found that the levels of DA were also increased in the MB as well as in the PFC in the TG animals (**Figure 1Dd**). The other brain regions without any significant changes are represented in **Supplementary Figure 2B**.

Consistent with increased 5-HT levels, q-RT-PCR experiments indicated that mRNA levels of the 5-HT synthetizing enzyme *Tph2* were significantly up-regulated ($p = 0.0070$) in the MB, which suggests that the capacity for 5-HT synthesis is increased in the transgenic animals (**Figure 1E**). We also investigated the mRNA levels for 5-HT receptors and found a significant decrease in the expression of *5ht2b* receptor in the PFC ($p = 0.0022$). No significant changes were found in the expression of other 5-HT receptors assayed, including *5ht1 (a,b,d), 5ht2 (a,c), 5ht3a, 5ht6*, and *5ht7* receptors (data not shown). Furthermore, the q-RT PCR (**Figure 1E**) indicated that *Bdnf* mRNA levels were upregulated in the PFC of the TG animals ($p = 0.0355$). A representative image of the *in situ* hybridization suggests increased reaction with the *Bdnf* probe in the TG animals (**Figure 1F**). Interestingly, we did not see any significant changes in the mRNA levels of *Bdnf* and *5ht2b* in the HC. Taken together, these results indicate that TrkB signaling significantly modulates the neurotransmitter phenotype of 5-HT neurons.

## Mice With Reduced TrkB in 5-HT Neurons Are Lean in Spite of Increased Food Intake

The TG littermates were found to be lean compared to the controls and transgenic mice not exposed to tamoxifen ($p = 0.0067$, **Figure 2A**). We therefore assessed the metabolic activity of the TG mice by subjecting the mice to the Comprehensive Laboratory Animal Monitoring System

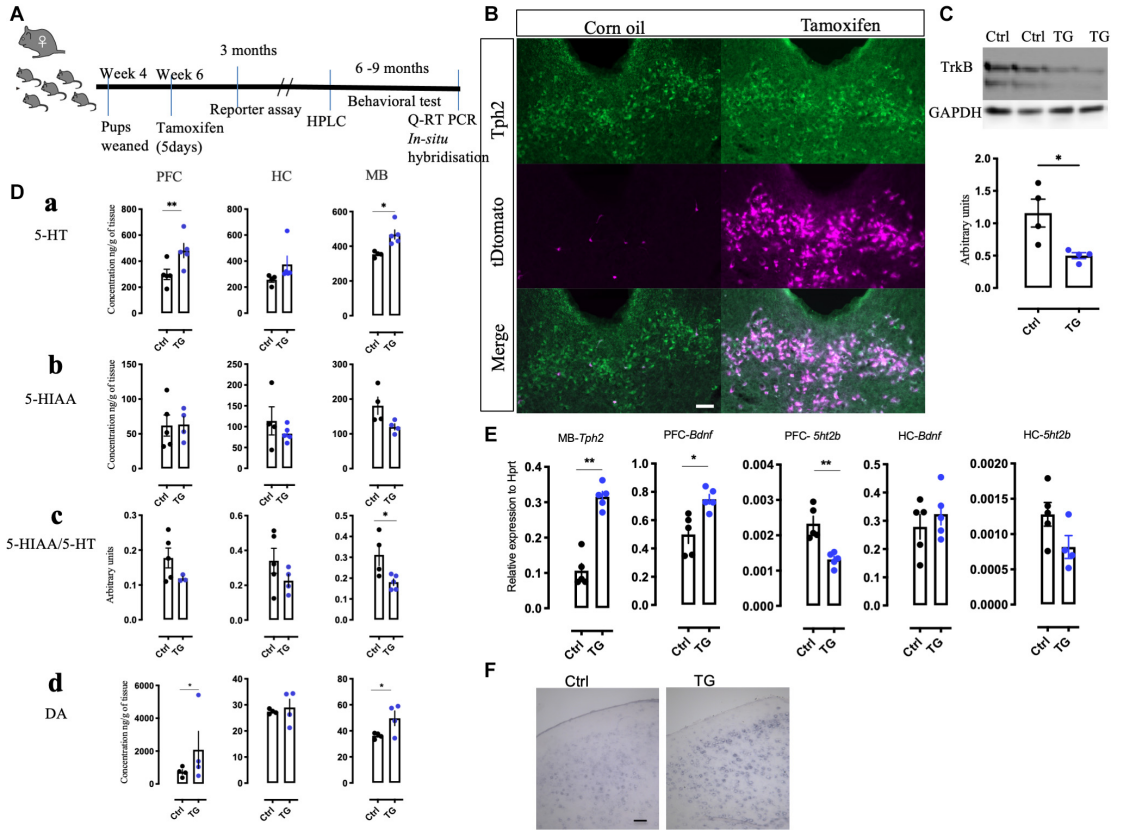


**FIGURE 1 |** Generation of conditional knockout mice, reporter expression and alteration of 5-HT and its metabolite in the transgenic mice. **(A)** An experimental scheme representing the time of injection, reporter assay, HPLC measurements and the duration when different behavioral battery tests were performed followed by molecular analysis. **(B)** Confirmation of Cre-recombination in the tDtomato reporter mice using immunohistochemistry with Tph2 antibody in tamoxifen injected and corn oil injected animals ($N = 4$). **(C)** Western blotting with TrkB monoclonal antibody on the mid-brain samples from the control and TG mice ($N = 4$). **(D) (a)** The total levels of 5-HT was measured by HPLC in naïve animal's different brain regions such as the PFC, HC, and MB. The levels in TG mice were significantly upregulated in the PFC and MB. **(b)** The levels of 5HIAA did not change in these brain regions. **(c)** The 5HIAA/5-HT ratio was also measured in these regions. The ratio was significantly down regulated in the MB of the TG mice. **(d)** The levels of DA were significantly upregulated in the PFC and MB of the TG mice ($N = 4$). **(E)** q-RT PCR results of the transcripts *Tph2* in the MB and *Bdnf* in the PFC was increased. The transcript for *5ht2b* was reduced in the PFC of the TG mice. No change in *Bdnf* and *5ht2b* transcripts in the HC was observed ($N = 4$). **(F)** *In situ* hybridization with *Bdnf* probe in the PFC of Ctrl and TG mice shows a robust expression ($N = 3$). Scale bar represents 100 μm, Student's *t*-test, **p*-value $< 0.01$, ***p*-value $< 0.01$. HPLC-High pressure liquid chromatography, 5-HT- Serotonin, 5HIAA- 5-Hydroxyindoleacetic acid, DA-Dopamine, PFC-pre-frontal cortex, HC-Hippocampus and MB-Mid-brain.

(CLAMS) for 3 days. Unexpectedly, we observed a significant increase in the feeding behavior ($p = 0.0351$) during daytime and a trend toward increase during nighttime. At the same time, locomotor activity was also increased ($p = 0.0221$) during daytime for the TG animal, again with a trend toward increase in nighttime activity (**Figures 2B,C**). Furthermore, the respiratory exchange rate (the ratio of the amount of $CO_2$ expelled and $O_2$ consumed) was elevated both during the day and night (**Figure 2D**) in the TG animals, indicating increased metabolic activity. These data suggest that, in spite of increased food intake, enhanced physical and metabolic activity led to a significant reduction in body weight of the TG mice.

## Behavioral Effects of TrkB Deletion in Adult Serotonergic Neurons

To assess the behavioral effect of TrkB loss in serotonergic neurons, we subjected both TG and Ctrl animals to a battery of behavioral tests, including tests for anxiety such as elevated plus maze (EPM), light dark test (LD) and open field (OF). For measuring aggression, we used the resident intruder (RI) test. The effect of Fluoxetine was studied using forced swim test (FST). The learning and memory were assessed using Pattern separation (PS) and Barnes maze (BM) test. These tests were performed in different cohorts of animals. The first cohort was exposed to OF, LD, EPM, CLAMS, and FST, in this order. There were 30 animals per group for OF, EPM, and LD. In the CLAMS and FST test we used $N = 12$/group. The second cohort was exposed to RI and BM and the $N = 12$/group. The third cohort was used for PS test and $N = 20$/group. The most stressful tests such as RI, FST, CLAMS, and PS test were performed in different cohorts of animals to reduce stress and variability arising from repeated exposures (Voikar et al., 2004).

In the EPM, no significant difference in the time spent in the open or close arm was observed between the groups (**Figure 3A**

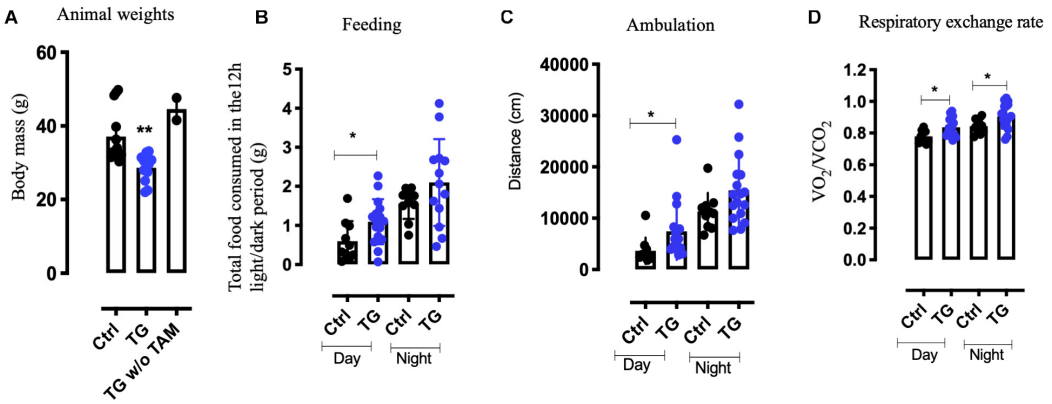


**FIGURE 2 |** Increased metabolism and a lean phenotype is observed in the transgenic animals. **(A)** Weights of tamoxifen injected (TG) $N = 10$, tamoxifen uninjected (TG w/o TAm) $N = 4$ and control animals (Ctrl) $N = 10$, at 11 months of age. **(B)** D Metabolic readings using CLAMS suggest increase in food intake **(B)** and increased activity **(C)** in the TG mice. **(D)** The respiratory exchange rate was higher both during day and night in the TG mice ($N = 12$). One-way ANOVA, Student's *t*-test, $^{*}p$-value $< 0.01$, $^{**}p$-value $< 0.001$, error bars represent Means ± SEM. CLAMS- comprehensive lab animal monitoring systems.

and **Supplementary Figure 3A**). In the LD test, the time spent in light compartment was increased in the TG mice (**Figure 3B**). In the open field test, in spite of the increased activity seen in the metabolic cages, we observed equal amount of ambulation for both the groups in total distance moved and time spent in the center (**Figure 3C** and **Supplementary Figure 3B**). To measure if these animals showed signs of aggression, they were subjected to RI paradigm. The experiment animals were residents in their home cage. No significant change was observed between the groups in the number of attacks on the intruder mice (**Figure 3D**). Interestingly, the non-social exploration behavior characterized by digging, rearing and scanning the intruder was increased in the TG animals (**Figure 3D**). The social exploration which included contacts with the intruder such as sniffing, chasing and climbing was unchanged (**Supplementary Figure 3C**). The acute effect of antidepressant fluoxetine was then assessed by the forced swim test. The drug fluoxetine was administered intraperitoneally 30 min before the test. Both groups responded similarly with decreased immobility (**Figure 3E**) suggesting that both the controls and TG animals responded to acute fluoxetine ($p < 0.0001$).

In a separate cohort of animals, we subjected the animals to a PS paradigm of fear conditioning (**Figure 3F**). The baseline activity of all the animals was analyzed before proceeding with the behavior protocol. We used both males and females in this experiment and found similar effects in both sexes. After 10 days of the training protocol, the control animals exhibited a significant pattern separation, while the TG animals showed no pattern separation by two-way ANOVA [$F(24,64) = 2.167$, $p = 0.007$] (**Figure 3F**). A detailed analysis of everyday freezing of both groups is shown in **Supplementary Figure 4**. This phenomenon of incomplete pattern separation is attributable to impairment in memory consolidation.

In order to characterize the effect of the TrkB deletion on spatial learning and memory, we performed a BM test. During training, the animals learned to find the escape box equally, irrespective of the genotype (**Figure 3G**). When after the initial training the goal was moved to the diagonally opposite quadrant, the TG animals needed significantly longer time to reach the new goal (**Figure 3H**), indicating impaired cognitive flexibility in the TG mice.

## Increased Newborn Cells and Altered Mature Neuron Markers in TG Mice

The 5-HT innervation is known to regulate neurogenesis in adult hippocampus (Gould, 1999). We therefore investigated proliferation and survival of cells in the DG of TG mice using the method of BrdU incorporation into the DNA (Wu and Castrén, 2009; Casarotto et al., 2021). A schematic representation of the experimental timeline for BrdU administration and immunostaining is represented in **Figure 4A**. One day after BrdU administration, we observed increased precursor cell proliferation in the TG mice when compared to controls (**Figure 4B**). However, 4 weeks after BrdU injection, the levels of BrdU were greatly reduced and no significant difference between the genotypes was observed (**Figure 4C**), indicating that the excessively produced newborn cells failed to survive (Malberg et al., 2000; Santarelli et al., 2003). Consistently, the number of doublecortin (DCX, a marker of early post-mitotic neurons) and calretinin (marker of late post-mitotic neurons) positive neurons were significantly increased in the DG of the TG mice (**Figures 4D,E**). Thus, absence of TrkB receptors in the 5-HT neurons projecting to the HC increased the rate of cell proliferation but did not influence the long-term survival of hippocampal progenitors.

# DISCUSSION

In this study, we have investigated the role of TrkB expression in Tph2 expressing 5-HT neurons. Our results suggest that loss of the TrkB receptor in the 5-HT neurons increases 5-HT levels, thereby regulating neuronal plasticity and behavior. Reduction of TrkB in 5-HT neurons increase proliferation, but not long-term

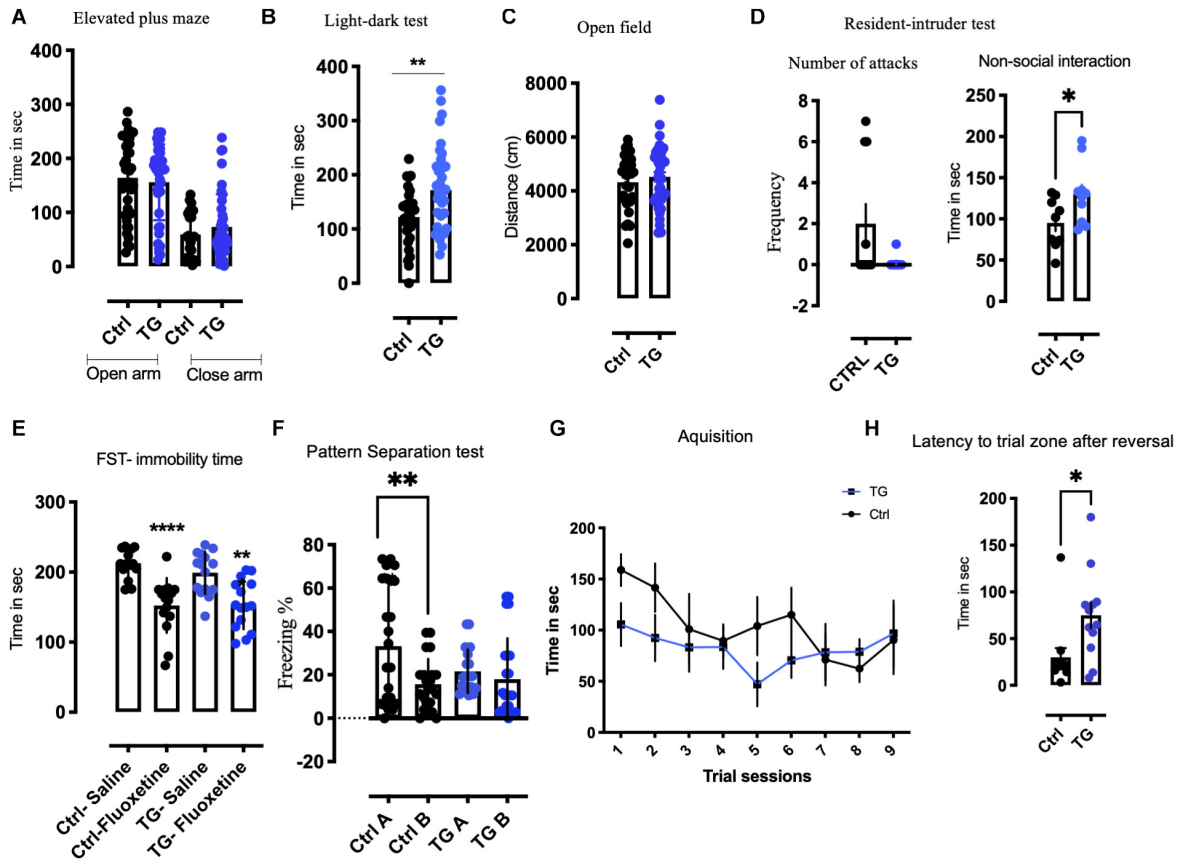


**FIGURE 3 |** Transgenic animals displayed anxiolytic like, non-aggressive interaction, altered pattern separation, and reversal learning in a battery of behavioral tests. **(A)** In the Elevated plus maze (EPM), no significant change was observed in the time spent in open or closed arm in both the groups (*N* = 30/group). **(B)** In the light-dark test (LD), time spent in the light by the TG animals was significantly higher than controls (*N* = 30/group). **(C)** In the open field (OF), the total distance traveled remained unchanged between the groups (*N* = 30/group). **(D)** In resident intruder test (RI), number of attacks was unaffected between the genotypes, whereas significant non-social behavior was observed. The TG animals showed non-social defensive behavior compared with the controls (*N* = 12/group). **(E)** The Immobility time was reduced after acute fluoxetine in both genotypes subjected to forced swim test (FST). **(F)** In Pattern separation experiment paradigm (PS), the control animals exhibit pattern completion distinguishing context A from context B after 10 days of continuous exposure to both the context. The TG animals contextual pattern separation is inhibited (*N* = 20/group). **(G)** In Barnes maze test (BM), both the animals learned during acquisition. **(H)** The latency to target zone during reversal training was significantly increased in the TG animals. Student's *t*-test, Two-way ANOVA, **p*-value < 0.01, ***p*-value < 0.001, and *****p*-value < 0.0001. Error bars represent Means ± SEM.

survival, of hippocampal cells that is consistent with increase in immature neuronal markers such as doublecortin and calretinin in the transgenic animals.

Previous studies have revealed a significant role for BDNF signaling in the early differentiation of 5-HT neurons (Galter and Unsicker, 2000a,b). Furthermore, excess 5-HT during development impairs cortical differentiation (Gaspar et al., 2003; Deneris and Gaspar, 2018). Deletion of monoamine oxidase A (MAOA) in transgenic mice increases 5-HT levels and interferes with the formation of visual and somatosensory maps (Cases et al., 1996; Salichon et al., 2001), and this phenotype was further accentuated when TrkB levels were reduced (Vitalis et al., 2013). To avoid potentially deleterious effects of TrkB loss on developing 5-HT neurons, we have used a conditional deletion of TrkB from these neurons in the adulthood and the early development of the 5-HT neurons is therefore intact. We did not observe any obvious loss of 5-HT neurons and the expression of *Tph2* was in fact increased, suggesting that BDNF does not appear to be a critical survival factor for adult serotonin neurons. Our data indicate that BDNF through TrkB plays an important role in the regulation of 5-HT neurons and is likely a key element in the control of its function.

Our data suggest that BDNF signaling through TrkB plays a major role in the proper functioning of the 5-HT neurons. Tph2, the 5-HT synthesizing enzyme in the brain (Walther et al., 2003) was increased in the TG mice which is consistent with increased 5-HT levels both in the MB as well as in the projection areas of these neurons in the PFC. Although the expression of most of the 5-HT receptors remained unchanged, the *5ht2b* transcripts were significantly lower in the PFC of TG mice. 5HT2b agonists show antidepressant like effect and works in modulating serotonergic tone like selective serotonin reuptake inhibitors (SSRIs) (Diaz et al., 2016). In mice, 5HT2b

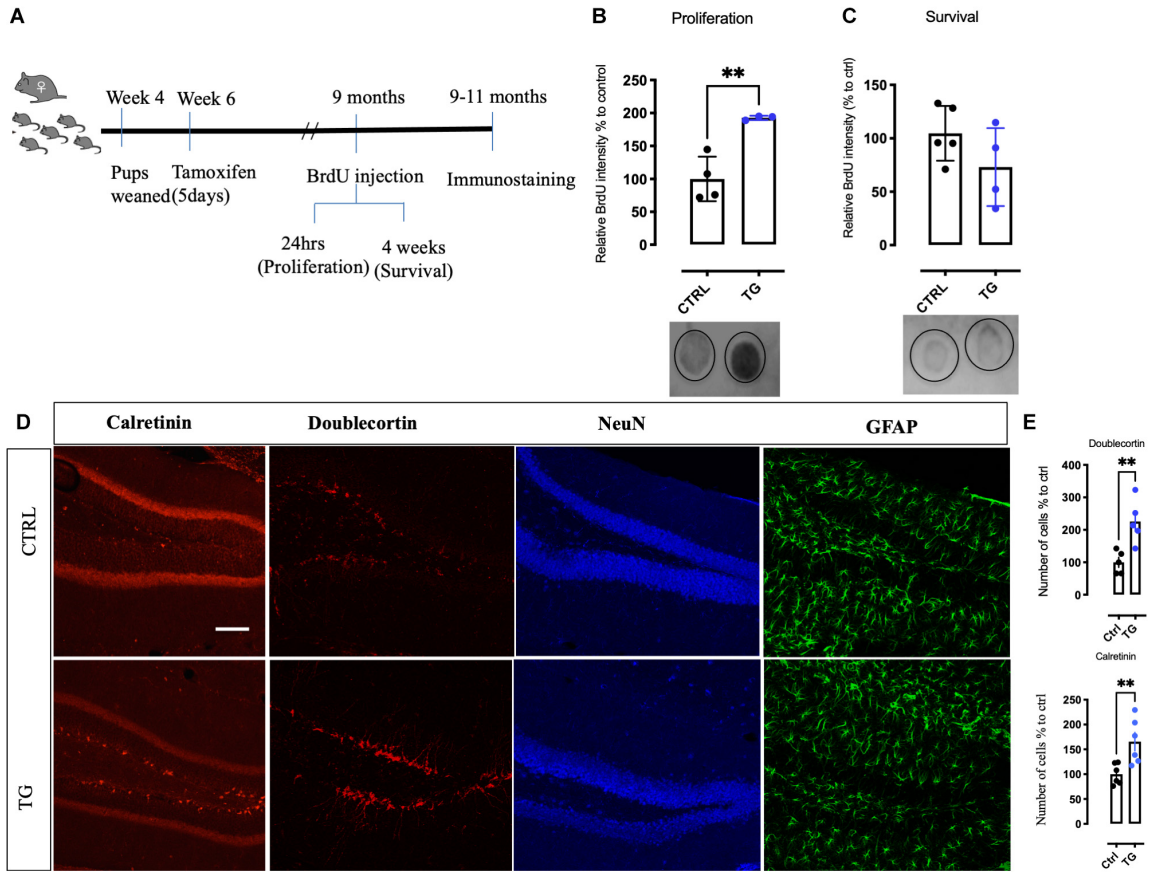


**FIGURE 4 |** Increased new born precursor cells and altered neuronal markers in the hippocampus of the transgenic mice. **(A)** A schematic representation of time points for BrdU injection to study proliferation and survival of hippocampal neurons. **(B)** Quantitation of new-born neurons with BrdU incorporation in the transgenic animals by dot-blot. In samples collected for proliferation, TG animals showed a robust increase. **(C)** In the survival samples, no difference in BrdU incorporation was observed in both the groups. **(D)** Markers for different stages of neurogenesis was studied in both the groups. In the DG of the HC, DCX, and Calretinin was increased in the transgenic animals, however, NeuN and GFAP immunoreactivity was found to be unaltered. **(E)** Quantitative analysis of the neurons for DCX and Calretinin shows significant increase in the TG animals. Scale bar represents 100 μm, *N* = 4/group, Unpaired *t*-test $^{**}p$-value $< 0.01$. Error bars represent Means ± SEM. HC-Hippocampus, DCX-Doublecortin, DG-Dentate gyrus.

receptors have been reported to regulate extracellular 5-HT levels (Callebert et al., 2006). However, the exact role of 5HT2b receptors in the increased serotonin levels observed in the TG mice requires further investigation.

Excess 5-HT, especially during development, produces structural and functional abnormalities that are long-lasting (reviewed in Gaspar et al., 2003; Deneris and Gaspar, 2018). Even if 5-HT levels were increased, the main 5-HT metabolite 5-HIAA was not significantly enhanced and the ratio of 5-HIAA/5-HT, a measure of 5-HT turnover (Valzelli and Bernasconi, 1979) was decreased. Several other factors, in addition to increased synthesis, including lowered degradation rate or increased storage capacity, may have contributed to increased serotonin levels. Our data suggest increased serotonergic tone in the TG mice, although additional studies with microdialysis and *in vivo* voltammetry will be needed to investigate the role of TrkB deletion in 5-HT release in more detail.

The serotonergic system is known to regulate appetite, and drugs that promote 5-HT release have been used for appetite reduction (Halford et al., 2005). We found that mice with loss of TrkB signaling in Tph2 expressing 5-HT neurons show significantly reduced body weight. Tph2 knockout mice lacking brain 5-HT have reduced weight at birth but their body weight normalizes during adulthood (Mosienko et al., 2015). Furthermore, we found that BDNF was increased in the TG mice. BDNF has been suggested to be one of the central factors regulating satiety in brain (Rios, 2013). Intraventricular BDNF administration reduces feeding and brain-wide reduction in the levels of BDNF or TrkB increases appetite and food intake, presumably acting at hypothalamic level, increasing body weight (Rios et al., 2001; Yeo et al., 2004; Gray et al., 2006; Rios, 2013). However, this reduced body weight is not produced by decreased appetite, as food consumption in the TG mice was actually increased, which suggest that the loss of weight was not a consequence of increased BDNF expression. Apparently, observed hyperactivity and increase in metabolic rate in mice with loss of TrkB in 5-HT neurons are sufficient to compensate the increased food intake. These data indicate that the effects of

TrkB signaling and 5-HT on food intake and metabolic activity are complex and dependent on the brain regions being affected.

Adachi et al. (2017) recently reported that a virally induced loss of TrkB in the dorsal raphe region also increased aggression. In spite of high 5-HT levels and hyperactivity mice deficient of TrkB specifically in 5-HT neurons showed normal phenotype in tests assessing anxiety and aggression. Furthermore, we observed a normal response to fluoxetine in the forced swim test in the TG mice, which is in contrast to the finding of Adachi et al. (2017) who reported a loss of responsiveness to fluoxetine in their mice. Our recent data show that mice where TrkB was deleted using an En1-cre promoter that is active in the midbrain region covering, but not confined to, the raphe nuclei, show increased aggression (Sahu and Castrén, unpublished). Since Adachi et al. (2017) used a local midbrain injection of cre-expressing viruses to delete TrkB, it is possible that deletion of TrkB in cells next to 5-HT neurons, such as GABAergic interneurons, might mediate the aggressive phenotype observed by Adachi et al. and the antidepressant mechanism.

The 5-HT innervation is known to regulate the proliferation of hippocampal precursor cells (Deneris and Gaspar, 2018). Chronic antidepressant treatment increases neurogenesis (Malberg et al., 2000; Santarelli et al., 2003) and long-term survival of these newborn neurons is regulated by BDNF signaling (Sairanen et al., 2005). We found a significant increase in hippocampal cell proliferation and early differentiation of newborn DG neurons, as indicated by increased BrdU incorporation and doublecortin as well as calretinin positive neurons, although the latter finding awaits confirmation with stereological methods. However, their long-term survival was at a wildtype level, which is consistent with the notion that long-term survival requires activity-dependent incorporation into hippocampal networks (Castren and Hen, 2013). The failure of long-term survival is also consistent with the impairment in cognitive flexibility and alterations in pattern separation, processes that are thought to be dependent on the hippocampal function,

We have previously observed that complete loss of TrkB in zebrafish has a major impact on the development of 5-HT and DA neurons (Sahu et al., 2019). Current findings indicate that the effects of TrkB signaling in the mammalian 5-HT neurons are predominantly at a functional level. Our data demonstrate that deleting a receptor in a circumscribed group of neurons can have widespread cell non-autonomous *trans* effects in many parts of the adult central nervous system. Through increased synthesis of 5-HT, lack of TrkB in these neurons significantly impacts on the maturation of hippocampal neurons and consequently the animal behavior. These findings underline the previously implicated close connectivity between neurotrophins and the 5-HT system (Mattson et al., 2004; Martinowich and Lu, 2008).

## DATA AVAILABILITY STATEMENT

The original contributions presented in the study are included in the article/**Supplementary Material**, further inquiries can be directed to the corresponding authors.

## ETHICS STATEMENT

The animal study was reviewed and approved by the Animal Ethical Committee of Southern Finland (Finland: ESAVI/10300/04.10.07/2016 and ESAVI/38503/2019).

## AUTHOR CONTRIBUTIONS

MS and EC planned the experiments and wrote the manuscript. MS, YP-B, MP, AS, OB, and KK performed the behavioral and biochemical experiments. TP performed the HPLC analysis on the animals. All authors contributed to the article and approved the submitted version.

## FUNDING

EC was received the ERC grant #322742 – iPLASTICITY; Sigrid Jusélius Foundation, Jane and Aatos Erkko Foundation, and the Academy of Finland grants #294710, #327192, and #307416. The Helsinki University Library has funded the processing fees for publication.

## ACKNOWLEDGMENTS

We thank Outi Nikkila, Sulo Kolehmainen, Seija Lågas, and Erja Huttu for their expert technical help. We are grateful for Dr. Pierre Chambon and Dr. Daniel Metzger for the Tph2-creERT2 mice. We also thank Dr. Vootele Voikar, in charge of the Mouse Behavioral Phenotyping Facility, which is supported by Biocenter Finland and HiLIFE.

## SUPPLEMENTARY MATERIAL

The Supplementary Material for this article can be found online at: https://www.frontiersin.org/articles/10.3389/fnmol.2021.616178/full#supplementary-material

**Supplementary Figure 1 |** Confirmation of cre activation and Tph2 expression by tamoxifen injection in comparison with the corn oil group. The arrow heads represent the expression location in the cre positive animals. In the corn oil injected animals only Tph2 immunoreactivity is observed. The scale bar = 5 mm.

**Supplementary Figure 2 | (A)** Western blotting with TrkB antibody in the hippocampus **(a)** and hypothalamus **(b)** of the Ctrl and TG mice, GAPDH antibody staining of the same gel was used for normalization ($N$ = 3/group). Histograms show quantitated TrkB bands normalized by GAPDH for hippocampus **(c)** and hypothalamus **(d)**. **(B)** HPLC of other brain regions for Dopamine, serotonin, and 5HIAA/5-HT ratio remains unchanged between the groups.

**Supplementary Figure 3 | (A)** Parameters for number of open arm entries and time spent in open arm remains unchanged between the groups. **(B)** No change with the time spent in the center of the open field. **(C)** Social interaction time in the resident intruder paradigm is unaffected between the groups.

**Supplementary Figure 4 |** Freezing percentage of every day tracking in the PS test for both the genotypes. **(A)** Controls and **(B)** TG animals.

## REFERENCES


Adachi, M., Autry, A. E., Mahgoub, M., Suzuki, K., and Monteggia, L. M. (2017). TrkB signaling in dorsal raphe nucleus is essential for antidepressant efficacy and normal aggression behavior. *Neuropsychopharmacology* 42, 886–894. doi: 10.1038/npp.2016.201

Callebert, J., Esteve, J. M., Herve, P., Peoc'h, K., Tournois, C., Drouet, L., et al. (2006). Evidence for a control of plasma serotonin levels by 5-hydroxytryptamine(2B) receptors in mice. *J. Pharmacol. Exp. Ther.* 317, 724–731. doi: 10.1124/jpet.105.098269

Casarotto, P. C., Girych, M., Fred, S. M., Kovaleva, V., Moliner, R., Moliner, R., et al. (2021). Antidepressant drugs act by directly binding to TRKB neurotrophin receptors. *Cell* 184, 1299–1313.e19. doi: 10.1016/j.cell.2021.01.034

Cases, O., Vitalis, T., Seif, I., DeMaeyer, E., Sotelo, C., and Gaspar, P. (1996). Lack of barrels in the somatosensory cortex of monoamine oxidase A-deficient mice: role of a serotonin excess during the critical period. *Neuron* 16, 297–307. doi: 10.1016/s0896-6273(00)80048-3

Castren, E., and Hen, R. (2013). Neuronal plasticity and antidepressant actions. *Trends Neurosci.* 36, 259–267. doi: 10.1016/j.tins.2012.12.010

Commons, K. G. (2016). Ascending serotonin neuron diversity under two umbrellas. *Brain Struct. Funct.* 221, 3347–3360. doi: 10.1007/s00429-015-1176-7

Dahlström, A., and Fuxe, K. (1964). Evidence for the existence of monoamine-containing neurons in the central nervous system. I. Demonstration of monoamines in the cell bodies of brain stem Neurons. *Acta Physiol. Scand. Suppl.* SUPPL 232, 1–55.

Deneris, E., and Gaspar, P. (2018). Serotonin neuron development: shaping molecular and structural identities. *Wiley Interdiscip. Rev. Dev. Biol.* 7:e301. doi: 10.1002/wdev.301

Diaz, S. L., Narboux-Neme, N., Boutourlinsky, K., Doly, S., and Maroteaux, L. (2016). Mice lacking the serotonin 5-HT2B receptor as an animal model of resistance to selective serotonin reuptake inhibitors antidepressants. *Eur. Neuropsychopharmacol.* 26, 265–279. doi: 10.1016/j.euroneuro.2015.12.012

Diaz, S. L., Narboux-Neme, N., Trowbridge, S., Scotto-Lomassese, S., Kleine Borgmann, F. B., Jessberger, S., et al. (2013). Paradoxical increase in survival of newborn neurons in the dentate gyrus of mice with constitutive depletion of serotonin. *Eur. J. Neurosci.* 38, 2650–2658. doi: 10.1111/ejn.12297

Erickson, J. T., Conover, J. C., Borday, V., Champagnat, J., Barbacid, M., Yancopoulos, G., et al. (1996). Mice lacking brain-derived neurotrophic factor exhibit visceral sensory neuron losses distinct from mice lacking NT4 and display a severe developmental deficit in control of breathing. *J. Neurosci.* 16, 5361–5371. doi: 10.1523/jneurosci.16-17-05361.1996

Feil, R., Brocard, J., Mascrez, B., LeMeur, M., Metzger, D., and Chambon, P. (1996). Ligand-activated site-specific recombination in mice. *Proc. Natl. Acad. Sci. U.S.A.* 93, 10887–10890. doi: 10.1073/pnas.93.20.10887

Fuxe, K., Dahlstrom, A., Hoistad, M., Marcellino, D., Jansson, A., Rivera, A., et al. (2007). From the Golgi-Cajal mapping to the transmitter-based characterization of the neuronal networks leading to two modes of brain communication: wiring and volume transmission. *Brain Res. Rev.* 55, 17–54. doi: 10.1016/j.brainresrev.2007.02.009

Galter, D., and Unsicker, K. (2000a). Brain-derived neurotrophic factor and trkB are essential for cAMP-mediated induction of the serotonergic neuronal phenotype. *J. Neurosci. Res.* 61, 295–301. doi: 10.1002/1097-4547(20000801)61:3<295::aid-jnr7>3.0.co;2-4

Galter, D., and Unsicker, K. (2000b). Sequential activation of the 5-HT1(A) serotonin receptor and TrkB induces the serotonergic neuronal phenotype. *Mol. Cell. Neurosci.* 15, 446–455. doi: 10.1006/mcne.2000.0841

Gaspar, P., Cases, O., and Maroteaux, L. (2003). The developmental role of serotonin: news from mouse molecular genetics. *Nat. Rev. Neurosci.* 4, 1002–1012. doi: 10.1038/nrn1256

Gould, E. (1999). Serotonin and hippocampal neurogenesis. *Neuropsychopharmacology* 21, 46S–51S.

Gray, J., Yeo, G. S. H., Cox, J. J., Morton, J., Adlam, A. L. R., Keogh, J. M., et al. (2006). Hyperphagia, severe obesity, impaired cognitive function, and hyperactivity associated with functional loss of one copy of the brain-derived neurotrophic factor (BDNF) gene. *Diabetes* 55, 3366–3371. doi: 10.2337/db06-0550

Halasy, K., Miettinen, R., Szabat, E., and Freund, T. F. (1992). GABAergic interneurons are the major postsynaptic targets of median raphe afferents in the rat dentate Gyrus. *Eur. J. Neurosci.* 4, 144–153. doi: 10.1111/j.1460-9568.1992.tb00861.x

Halford, J. C. G., Harrold, J. A., Lawton, C. L., and Blundell, J. E. (2005). Serotonin (5-HT) drugs: effects on appetite expression and use for the treatment of obesity. *Curr. Drug Targets* 6, 201–213. doi: 10.2174/1389450053174550

Harrison, F. E., Reiserer, R. S., Tomarken, A. J., and McDonald, M. P. (2006). Spatial and nonspatial escape strategies in the Barnes maze. *Learn. Mem.* 13, 809–819. doi: 10.1101/lm.334306

Hofer, M., Pagliusi, S. R., Hohn, A., Leibrock, J., and Barde, Y. A. (1990). Regional distribution of brain-derived neurotrophic factor messenger-rna in the adult-mouse brain. *EMBO J.* 9, 2459–2464. doi: 10.1002/j.1460-2075.1990.tb07423.x

Homberg, J. R., Molteni, R., Calabrese, F., and Riva, M. A. (2014). The serotonin-BDNF duo: developmental implications for the vulnerability to psychopathology. *Neurosci. Biobehav. Rev.* 43, 35–47. doi: 10.1016/j.neubiorev.2014.03.012

Jacobs, B. L., and Azmitia, E. C. (1992). Structure and function of the brain serotonin system. *Physiol. Rev.* 72, 165–229. doi: 10.1152/physrev.1992.72.1.165

Kankaanpaa, A., Meririnne, E., Ariniemi, K., and Seppala, T. (2001). Oxalic acid stabilizes dopamine, serotonin, and their metabolites in automated liquid chromatography with electrochemical detection. *J. Chromatogr. B* 753, 413–419. doi: 10.1016/s0378-4347(00)00553-3

Karpova, N. N., Pickenhagen, A., Lindholm, J., Tiraboschi, E., Kulesskaya, N., Ágústsdóttir, A., et al. (2011). Fear erasure in mice requires synergy between antidepressant drugs and extinction training. *Science (New York, N.Y.)* 334, 1731–1734. doi: 10.1126/science.1214592

Lauder, J. M., Wallace, J. A., Krebs, H., Petrusz, P., and McCarthy, K. (1982). In vivo and in vitro development of serotonergic neurons. *Brain Res. Bull.* 9, 605–625. doi: 10.1016/0361-9230(82)90165-4

Lunden, J. W., and Kirby, L. G. (2013). Opiate exposure and withdrawal dynamically regulate mRNA expression in the serotonergic dorsal raphe nucleus. *Neuroscience* 254, 160–172. doi: 10.1016/j.neuroscience.2013.08.071

Madhav, T. R., Pei, Q., and Zetterstrom, T. S. (2001). Serotonergic cells of the rat raphe nuclei express mRNA of tyrosine kinase B (trkB), the high-affinity receptor for brain derived neurotrophic factor (BDNF). *Brain Res. Mol. Brain Res.* 93, 56–63. doi: 10.1016/s0169-328x(01)00183-8

Malberg, J. E., Eisch, A. J., Nestler, E. J., and Duman, R. S. (2000). Chronic antidepressant treatment increases neurogenesis in adult rat hippocampus. *J. Neurosci.* 20, 9104–9110. doi: 10.1523/jneurosci.20-24-09104.2000

Mamounas, L. A., Altar, C. A., Blue, M. E., Kaplan, D. R., Tessarollo, L., and Lyons, W. E. (2000). BDNF promotes the regenerative sprouting, but not survival, of injured serotonergic axons in the adult rat brain. *J. Neurosc.* 20, 771–782. doi: 10.1523/JNEUROSCI.20-02-00771.2000

Martinowich, K., and Lu, B. (2008). Interaction between BDNF and serotonin: role in mood disorders. *Neuropsychopharmacology* 33, 73–83. doi: 10.1038/sj.npp.1301571

Mattson, M. P., Maudsley, S., and Martin, B. (2004). BDNF and 5-HT: a dynamic duo in age-related neuronal plasticity and neurodegenerative disorders. *Trends Neurosci.* 27, 589–594. doi: 10.1016/j.tins.2004.08.001

Mosienko, V., Beis, D., Pasqualetti, M., Waider, J., Matthes, S., Qadri, F., et al. (2015). Life without brain serotonin: reevaluation of serotonin function with mice deficient in brain serotonin synthesis. *Behav. Brain Res.* 277, 78–88. doi: 10.1016/j.bbr.2014.06.005

Okaty, B. W., Freret, M. E., Rood, B. D., Brust, R. D., Hennessy, M. L., deBairos, D., et al. (2015). Multi-scale molecular deconstruction of the serotonin neuron system. *Neuron* 88, 774–791. doi: 10.1016/j.neuron.2015.10.007

Rios, M., Fan, G. P., Fekete, C., Kelly, J., Bates, B., Kuehn, R., et al. (2001). Conditional deletion of brain-derived neurotrophic factor in the postnatal brain leads to obesity and hyperactivity. *Mol. Endocrinol.* 15, 1748–1757. doi: 10.1210/mend.15.10.0706

Rios, M. (2013). BDNF and the central control of feeding: accidental bystander or essential player? *Trends Neurosci.* 36, 83–90. doi: 10.1016/j.tins.2012.12.009

Sahu, M. P., Pazos-Boubeta, Y., Pajanoja, C., Rozov, S., Panula, P., and Castren, E. (2019). Neurotrophin receptor Ntrk2b function in the maintenance of dopamine and serotonin neurons in zebrafish. *Sci. Rep. UK* 9:2036.

Sairanen, M., Lucas, G., Ernfors, P., Castren, M., and Castren, E. (2005). Brain-derived neurotrophic factor and antidepressant drugs have different but coordinated effects on neuronal turnover, proliferation, and survival in the adult dentate gyrus. *J. Neurosci.* 25, 1089–1094. doi: 10.1523/jneurosci.3741-04.2005

Salichon, N., Gaspar, P., Upton, A. L., Picaud, S., Hanoun, N., De Maeyer, E., et al. (2001). Excessive activation of serotonin (5-HT) 1B receptors disrupts the formation of sensory maps in monoamine oxidase a and 5-HT transporter knock-out mice. *J. Neurosci.* 21, 884–896. doi: 10.1523/jneurosci.21-03-00884.2001

Santarelli, L., Saxe, M., Gross, C., Surget, A., Battaglia, F., Dulawa, S., et al. (2003). Requirement of hippocampal neurogenesis for the behavioral effects of antidepressants. *Science* 301, 805–809. doi: 10.1126/science.1083328

Steinbusch, H. W. (1981). Distribution of serotonin-immunoreactivity in the central nervous system of the rat-cell bodies and terminals. *Neuroscience* 6, 557–618. doi: 10.1016/0306-4522(81)90146-9

Valzelli, L., and Bernasconi, S. (1979). Aggressiveness by isolation and brain serotonin turnover changes in different strains of mice. *Neuropsychobiology* 5, 129–135. doi: 10.1159/000117674

Vitalis, T., Ansorge, M. S., and Dayer, A. G. (2013). Serotonin homeostasis and serotonin receptors as actors of cortical construction: special attention to the 5-HT3A and 5-HT6 receptor subtypes. *Front. Cell. Neurosci.* 7:93. doi: 10.3389/fncel.2013.00093

Voikar, V., Vasar, E., and Rauvala, H. (2004). Behavioral alterations induced by repeated testing in C57BL/6J and 129S2/Sv mice: implications for phenotyping screens. *Genes Brain Behav.* 3, 27–38. doi: 10.1046/j.1601-183x.2003.0044.x

Walther, D. J., Peter, J. U., Bashammakh, S., Hortnagl, H., Voits, M., Fink, H., et al. (2003). Synthesis of serotonin by a second tryptophan hydroxylase isoform. *Science (New York, N.Y.)* 299, 76. doi: 10.1126/science.1078197

Wu, X., and Castrén, E. (2009). Co-treatment with diazepam prevents the effects of fluoxetine on the proliferation and survival of hippocampal dentate granule cells. *Biol. Psychiatry* 66, 5–8. doi: 10.1016/j.biopsych.2009.01.023

Yadav, V. K., Oury, F., Tanaka, K. F., Thomas, T., Wang, Y., Cremers, S., et al. (2011). Leptin-dependent serotonin control of appetite: temporal specificity, transcriptional regulation, and therapeutic implications. *J. Exp. Med.* 208, 41–52. doi: 10.1084/jem.20101940

Yeo, G. S. H., Hung, C. C. C., Rochford, J., Keogh, J., Gray, J., Sivaramakrishnan, S., et al. (2004). A de novo mutation affecting human TrkB associated with severe obesity and developmental delay. *Nat. Neurosci.* 7, 1187–1189. doi: 10.1038/nn1336

**Conflict of Interest:** The authors declare that the research was conducted in the absence of any commercial or financial relationships that could be construed as a potential conflict of interest.

*Copyright © 2021 Sahu, Pazos-Boubeta, Steinzeig, Kaurinkoski, Palmisano, Borowecki, Piepponen and Castrén. This is an open-access article distributed under the terms of the Creative Commons Attribution License (CC BY). The use, distribution or reproduction in other forums is permitted, provided the original author(s) and the copyright owner(s) are credited and that the original publication in this journal is cited, in accordance with accepted academic practice. No use, distribution or reproduction is permitted which does not comply with these terms.*

frontiers in Systems Neuroscience

REVIEW
published: 28 April 2021
doi: 10.3389/fnsys.2021.665052

# A Neural Model of Intrinsic and Extrinsic Hippocampal Theta Rhythms: Anatomy, Neurophysiology, and Function

*Stephen Grossberg**

*Center for Adaptive Systems, Department of Mathematics and Statistics, Department of Psychological and Brain Sciences, and Department of Biomedical Engineering, Boston University, Boston, MA, United States*

This article describes a neural model of the anatomy, neurophysiology, and functions of intrinsic and extrinsic theta rhythms in the brains of multiple species. Topics include how theta rhythms were discovered; how theta rhythms organize brain information processing into temporal series of spatial patterns; how distinct theta rhythms occur within area CA1 of the hippocampus and between the septum and area CA3 of the hippocampus; what functions theta rhythms carry out in different brain regions, notably CA1-supported functions like learning, recognition, and memory that involve visual, cognitive, and emotional processes; how spatial navigation, adaptively timed learning, and category learning interact with hippocampal theta rhythms; how parallel cortical streams through the lateral entorhinal cortex (LEC) and the medial entorhinal cortex (MEC) represent the end-points of the What cortical stream for perception and cognition and the Where cortical stream for spatial representation and action; how the neuromodulator acetylcholine interacts with the septo-hippocampal theta rhythm and modulates category learning; what functions are carried out by other brain rhythms, such as gamma and beta oscillations; and how gamma and beta oscillations interact with theta rhythms. Multiple experimental facts about theta rhythms are unified and functionally explained by this theoretical synthesis.

**Keywords: hippocampus, entorhinal cortex, learning, grid cell, place cell, spatial navigation, adaptively timed learning, Adaptive Resonance Theory**

OPEN ACCESS

***Edited by:***
*James Ainge, University of St Andrews, United Kingdom*

***Reviewed by:***
*Tomoaki Nakazono, Fukushima Medical University, Japan*
*Marcelo Mattar, University of California, San Diego, United States*
*Homero Esmeraldo, University of California, San Diego, United States, in collaboration with reviewer MM*

***Correspondence:**
*Stephen Grossberg*
*steve@bu.edu;*
*sites.bu.edu/steveg*

***Received:*** *08 February 2021*
***Accepted:*** *29 March 2021*
***Published:*** *28 April 2021*

***Citation:***
*Grossberg S (2021) A Neural Model of Intrinsic and Extrinsic Hippocampal Theta Rhythms: Anatomy, Neurophysiology, and Function. Front. Syst. Neurosci. 15:665052. doi: 10.3389/fnsys.2021.665052*

## 1. INTRODUCTION: HIPPOCAMPAL LEARNING, THETA RHYTHM, AND CHOLINERGIC MODULATION

The topic of hippocampal theta rhythms combines several basic themes about how our brains work. These themes include, in varying degrees of generality:

- How theta rhythms were discovered;
- How theta rhythms organize brain information processing into temporal series of spatial patterns;

- How distinct theta rhythms occur within area CA1 of the hippocampus and between the septum and area CA3 of the hippocampus;
- What functions theta rhythms carry out in different brain regions, notably CA1-supported functions like learning, recognition, and memory that involve visual, cognitive, and emotional processes;
- How spatial navigation, adaptively timed learning, and category learning interact with hippocampal theta rhythms;
- How parallel cortical streams through the lateral entorhinal cortex (LEC) and the medial entorhinal cortex (MEC) represent the end-points of the What cortical stream for perception and cognition, and the Where cortical stream for spatial representation and action;
- How the neuromodulator acetylcholine interacts with the septo-hippocampal theta rhythm and modulates category learning;
- What functions are carried out by other brain rhythms, such as gamma and beta oscillations; and
- How gamma and beta oscillations interact with theta rhythms.

Before discussing theta rhythms *per se*, I will set the stage by discussing some of the main anatomical, neurophysiological, and functional properties of the hippocampus with which it interacts.

## 1.1. Hippocampal Place Cells

Brain circuits within the hippocampus (HC) interact with the MEC to regulate spatial learning and memory (Morris et al., 1982; Davis et al., 1992; Parron and Save, 2004). Particular cell types within these brain regions arise through this learning process to support spatial navigation. Perhaps the most important of these cell types are the place cells which fire whenever rats, or multiple other animals, are at particular localized regions, or "places," within an environment (**Figure 1C**; O'Keefe and Dostrovsky, 1971). Place cells can also exhibit multiple firing fields when animals navigate in large spaces (Fenton et al., 2008; Henriksen et al., 2010; Park et al., 2011). Different place cells fire at different locations in an environment, so that the ensemble of all place cells enables an animal to localize itself in an environment, and to navigate through it.

The classical article of O'Keefe and Dostrovsky (1971) reported that place cells receive two kinds of inputs: one conveying information about the sensory context experienced from a given place, and the other from a navigational, or path integration, system that tracks relative positions in the world by integrating self-movement angular and linear velocity estimates for instantaneous rotation and translation, respectively. An important open problem is to explain how sensory context and path integration information are combined in the control of navigation (Etienne et al., 1996; Gothard et al., 1996; Chen et al., 2013). Path integration information is generated by an animal's movements, including its distance and direction relative to a start location (Loomis et al., 1999). Path integration is the basis of "dead reckoning" which was used by sailors for hundreds of years to estimate the location of their ship using information about its speed, travel time, and direction when visible landmarks were not available.

## 1.2. Entorhinal Grid Cells

Entorhinal grid cells provide inputs to place cells in hippocampal area CA3. They occur in the superficial layers of MEC and exhibit one of the most remarkable receptive fields of any cell type in the brain. Indeed, each grid cell can fire in multiple locations that may form a regular hexagonal grid (**Figure 1B**; Hafting et al., 2005). It is known that path integration inputs are a primary cause of these grid cell properties (McNaughton et al., 2006).

Cells in a population of grid cells at a given dorsoventral location in rat MEC exhibit receptive fields that are offset from each other (Hafting et al., 2005). As the dorsolateral MEC is traversed from its dorsal to its ventral end, grid cell receptive field sizes increase, as does the spacing between these fields, on average (Sargolini et al., 2006; Brun et al., 2008; Stensola et al., 2012).

## 1.3. Place Cells Can Represent Spaces Which Are the Least Common Multiple of Their Grid Cell Scales

These grid cell properties have led to the suggestion that the receptive field of a place cell that fires at a given position may be derived by combining grid cells with multiple spatial phases and scales that are coactive at that position, thereby allowing a place cell to represent a spatial scale that is much larger than the spatial scales of the individual grid cells that input to it (O'Keefe and Burgess, 2005; McNaughton et al., 2006; Gorchetchnikov and Grossberg, 2007). Indeed, the GridPlaceMap model (**Figure 2**) and its earlier variants explains why the spatial scale of a place cell can be as large as the *least common multiple* of the grid cell scales that drive it (Gorchetchnikov and Grossberg, 2007; Grossberg and Pilly, 2012, 2014; Mhatre et al., 2012; Pilly and Grossberg, 2012).

For example, grid cell spatial scales of 40, 50, and 60 centimeters that input to place cells can endow the place cells with a spatial scale of 6 m. If the converging grid cell spatial scales are 50, 60, and 70 centimeters, then the place cell spatial scale is 21 m. Remarkably, grid cell spatial scales that are chosen to be 41, 53, and 59 centimeters can generate a place cell spatial scale of 1.282 km (Gorchetchnikov and Grossberg, 2007)! Whereas, the spatial scales of individual grid cells are too small to control navigation in real-world spaces, the spatial scales of place cells can do so.

## 1.4. Stripe Cells

Grid cells are learned within the GridPlaceMap model in response to inputs from multiple *stripe cells* (Sargolini et al., 2006; Krupic et al., 2012) each of which fires selectively in response to movements in a given direction with its own spatial scale and spatial phase. Each stripe cell codes the distance from a starting position by integrating the linear velocity of the navigator. In the GridPlaceMap model, stripe cells are organized into ring attractors (**Figure 3A**). All the stripe cells in a given ring attractor are tuned to movement along the same direction. Because they

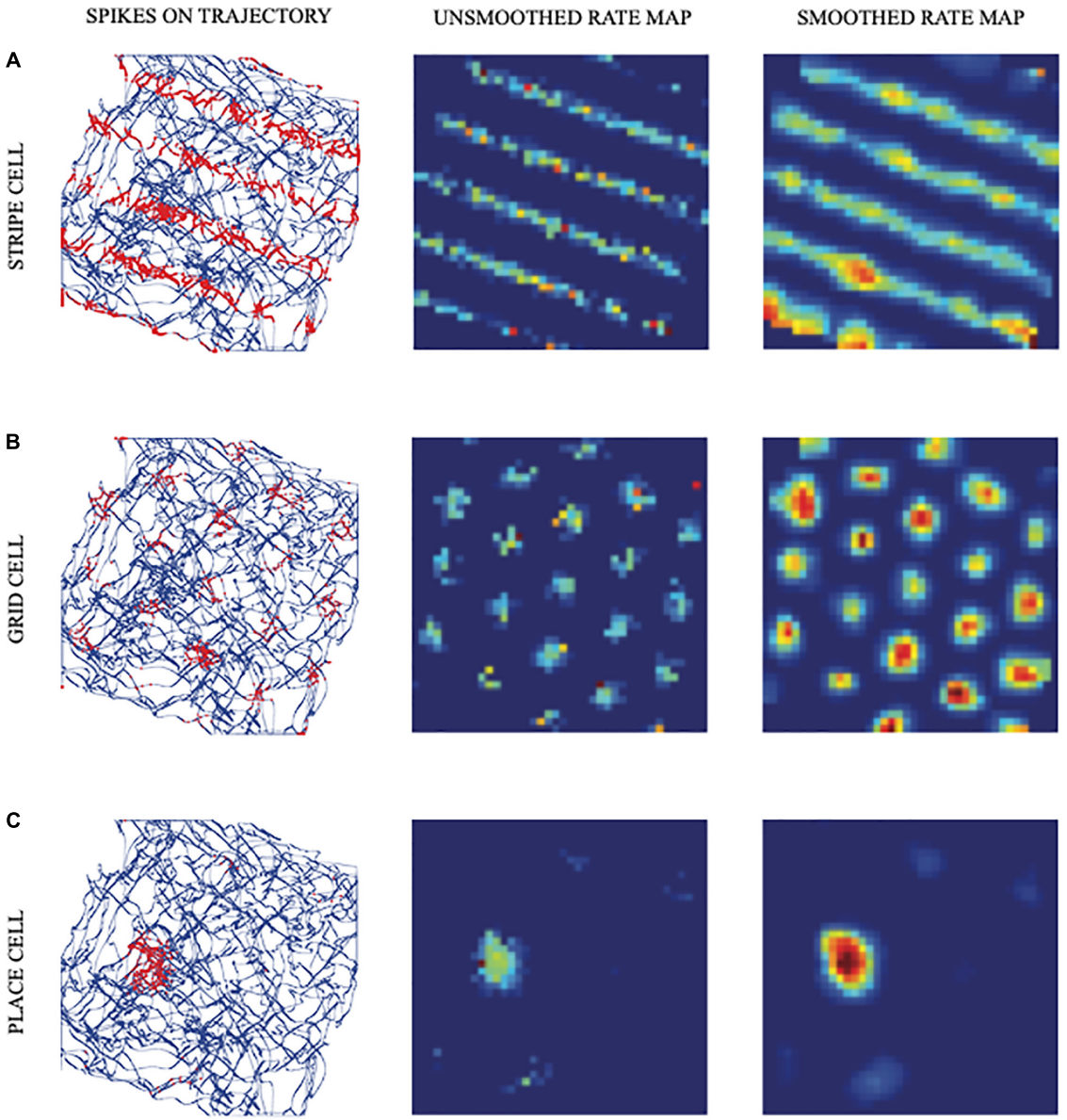


**FIGURE 1 |** Simulated responses of illustrative model **(A)** stripe cells, **(B)** grid cells, and **(C)** place cells in the spiking self-organizing map (SOM) model. The first column shows the realistic trajectory of the animat (blue lines and curves) on which are superimposed spikes (red dots) of firing cells. The second and third columns show unsmoothed and smoothed spatial rate maps of the cells, respectively. Color coding from blue (minimum) to red (maximum) firing generates each rate map (reprinted with permission from Pilly and Grossberg, 2013).

occur at different positions in the ring attractor, different stripe cells fire at different spatial phases (**Figure 3C**). An activity bump which integrates the distance traveled moves from one stripe cell to the next on the ring attractor as the animal moves in its prescribed direction (**Figure 3A**).

The name *stripe cell* describes the periodic directionally selective activations of these cells as the environment is navigated. Because the activity bump moves around the ring attractor as the model animal, or animat, moves in a given direction, a sufficiently long excursion executes a complete cycle, which activates the same stripe cell again (**Figure 3B**). This distance determines the spatial scale of that ring attractor. Parallel activations of multiple stripe cell ring attractors, each responding selectively to a different spatial scale and directional preference, implicitly represent the animal's position in the environment. Multiple stripe cells input to a given grid cell, just as multiple grid cells input to a given place cell (**Figure 2**). The GridPlaceMap model explains how learning prunes which stripe cells can activate particular grid cells to form their hexagonal spatial

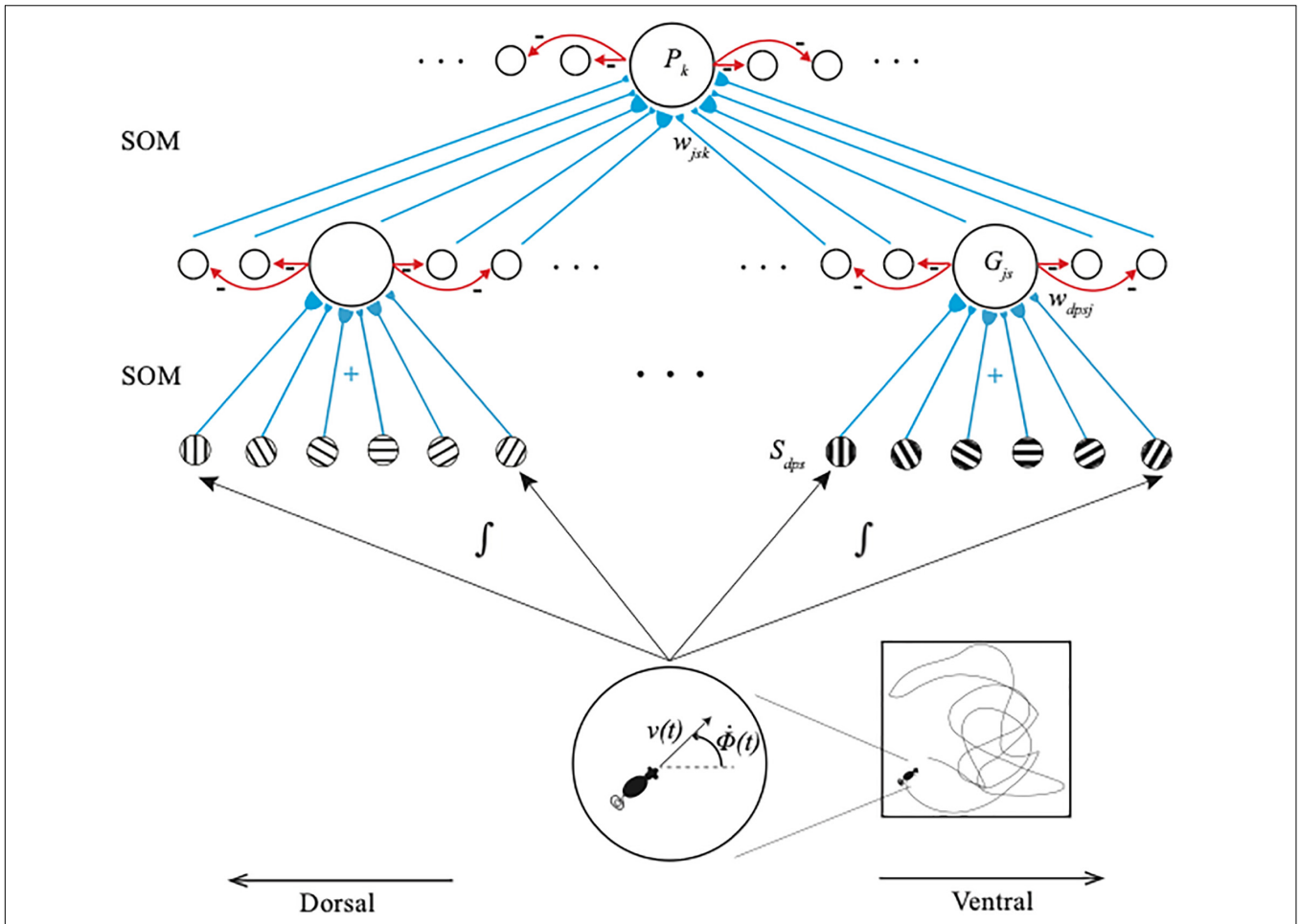


**FIGURE 2 |** The GridPlaceMap is defined by a hierarchy of self-organizing maps (SOM) whereby grid cells and place cells are learned and activated. Stripe cells $S_{dps}$ occur in the deeper layer of medial entorhinal cortex (MEC), grid cells $G_{js}$ occur in layer II of MEC, and place cells $P_k$ occur in hippocampal area CA3. Multiple stripe cells drive learning of individual grid cells, and multiple grid cells drive learning of individual place cells. Place cells can thereupon represent movements in large spaces in response to internally generated linear velocity [v(t)] and angular velocity [Φ(t)] movements through the environment. Bigger stripe fields and spacings occur from dorsal to ventral positions in the model (reprinted with permission from Grossberg and Pilly, 2014).

receptive fields, as it also prunes which grid cells can activate particular place cells.

## 1.5. A Parsimoniously Designed Hierarchy of Self-Organizing Maps Defines Grid and Place Cells

The GridPlaceMap model has a remarkably parsimonious and elegant design. Both grid cell and place cell receptive fields, despite their radically different properties, develop by detecting, learning, and remembering the most frequent and energetic co-occurrences of their inputs. The same self-organizing map (SOM) circuits automatically compute these co-occurrences to learn grid cell and place cell receptive fields, albeit at different levels of the learning hierarchy (**Figure 2**). SOMs occur in multiple parts of the brain, where they learn perceptual, cognitive, motor, or spatial recognition categories (Grossberg, 2021). In the GridPlaceMap model, place cells are spatial categories. More about how SOM models work will be described in the discussion in Section 3.3 of how SOMs learn perceptual and cognitive recognition categories.

All the inputs that drive grid cell learning arise from ring attractor circuits, as noted in Section 1.4. One type of ring attractor circuit processes linear velocity inputs that input to stripe cells. The other ring attractor circuit processes angular velocity inputs that input to head direction cells, which modulate the directional selectivity of different stripe cells.

## 1.6. Temporal-to-Spatial: Learning a Dorsoventral Gradient of Increasing Grid Cells and Time Cells

Populations of stripe cells with a given spatial period that exhibit multiple directional preferences and spatial phases initially project with random adaptive weights to cells in the category learning layer of a SOM (**Figure 2**). Learning tunes these weights until the SOM cells become grid cells of fixed spatial scales, just as such learned tuning responds to the emerging grid cells by

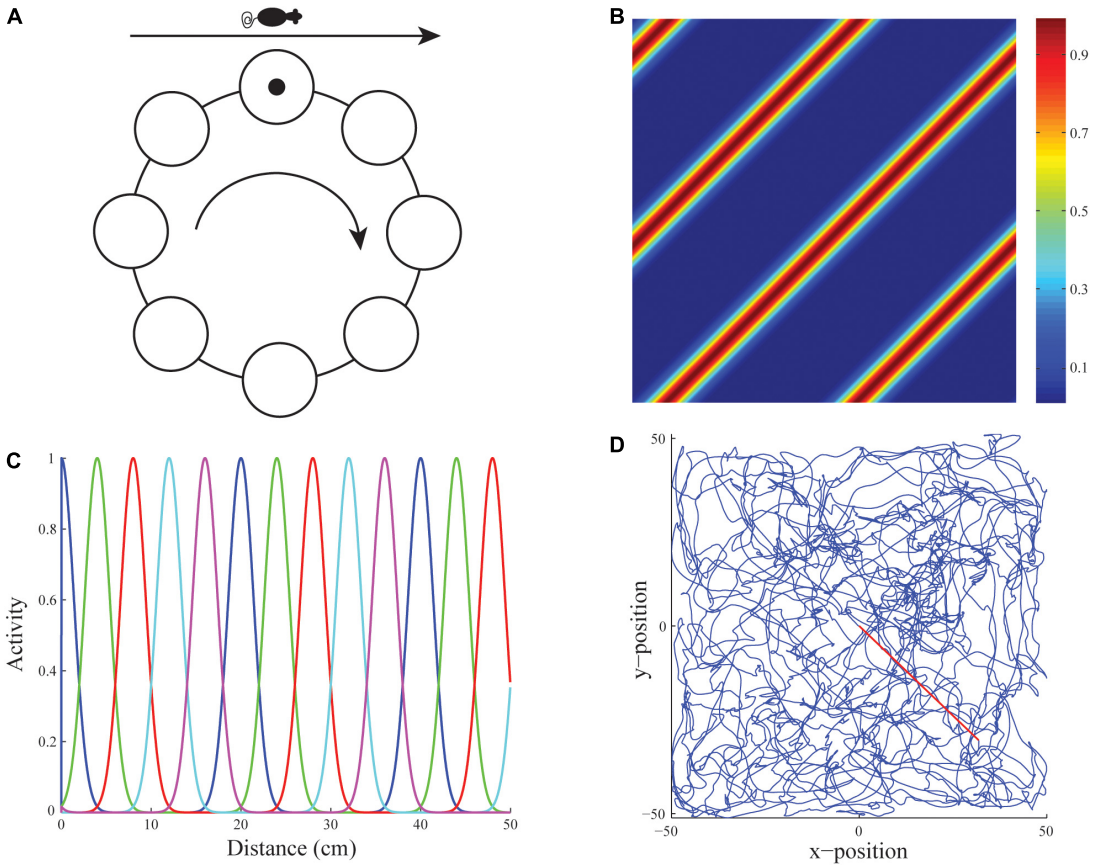


**FIGURE 3 |** Linear velocity path integration. **(A)** Linear velocity path integration signals input to a ring attractor neural circuit that translates them into an activity bump that moves from cell to cell along the ring. **(B)** Firing rate map of an illustrative stripe cell with a spacing of 35 cm whose firing fields respond to translational movement with a component along either 135° or −45°. **(C)** Activities of stripe cells of five different spatial phases (see colors) as a function of displacement from the origin along their preferred direction. **(D)** Real rat trajectory from Sargolini et al. (2006) of ∼10 min in a 100 cm × 100 cm environment that was used to train the model. The red segment depicts the straight path prefixed to the original trajectory to ensure the animat starts from the midpoint of the environment (reprinted with permission from Pilly and Grossberg, 2012).

creating SOM cells at the next processing stage with place cell receptive fields.

*In vivo*, grid cells and place cells of increasing spatial scale are found along a dorsoventral gradient. The GridPlaceMap model explains how stripe cells of different spatial scales learn to activate different locations along the dorsoventral axis in layer II of MEC, thereby triggering learning of grid cells with increasing spatial scales. The selection of different grid cell spatial scales on the dorsoventral gradient is driven by a gradient in the *rates* at which cells respond along the dorsoventral gradient, from fast to slow. Cells that respond more quickly are active for shorter time intervals than cells that respond more slowly.

A longer duration of sampling enables each grid cell to sample stripe cells over a larger spatial scale. The duration of sampling thus covaries with the spatial scale of the learned grid cells. Likewise, multiple entorhinal grid cell scales combine through learning to give rise to a dorsoventral gradient of hippocampal place cells, each of which can represent larger spaces than can an individual grid cell. Due to these temporal-to-spatial conversions, the SOM model shows how the dorsoventral gradient in response rates develops a spectrum of grid cell scales and place cell scales. It is thus called the Spectral Spacing model.

Remarkably, the response rate gradient for spatial learning is computationally homologous to a rate gradient that had, 20 years earlier, been used to explain hippocampal data about adaptively timed learning (Grossberg and Schmajuk, 1989; Grossberg and Merrill, 1992, 1996). The model for adaptively timed learning was called a Spectral Timing model because its different cell populations respond with a "spectrum" of different rates whose activities peak at different times, and whose total *population* activity can learn to peak hundreds of milliseconds after their onset. That is why the GridPlaceMap model of grid cell learning is called a Spectral Spacing model. The rate gradient for spatial learning occurs in the MEC and its hippocampal projections. The rate gradient for temporal learning occurs in the LEC and its hippocampal projections.

One of the most striking properties of the Spectral Timing model is its Weber Law property whereby cells in the spectrum that respond at larger times also respond with longer durations. This prediction was strongly confirmed by the discovery, 20

years after it was made, of *time cells* in the hippocampus by MacDonald et al. (2011). Indeed, MacDonald et al. (2011) write: "...the mean peak firing rate for each time cell occurred at sequential moments, and the overlap among firing periods from even these small ensembles of time cells bridges the entire delay. Notably, the spread of the firing period for each neuron increased with the peak firing time..." (p. 3). Their "small ensembles of time cells" are the cells in the spectrum, and the "spread of the firing period...increased with the peak firing time" is the Weber Law property. For a recent synthesis of hippocampal timing processes, see Banquet et al. (2020).

In summary, parallel dorsoventral gradients in the rates that cells respond within the entorhinal–hippocampal system may create multiple smaller spatial and temporal scales in the entorhinal cortex that can be fused into larger spatial and temporal scales in the hippocampal cortex, notably scales that are large enough to control adaptive behaviors during spatial navigation in large enclosures. The mechanistic homology between these spatial and temporal mechanisms suggests why they may occur side-by-side in MEC and LEC dorsoventral gradients through entorhinal cortex into the hippocampus.

Spatial representations in the dorsal, or Where, cortical stream for spatial representation and action go through postrhinal cortex and MEC on their way to hippocampal cortex, whereas object representations in the ventral, or What, cortical stream for perception and object recognition go through perirhinal cortex and LEC on their way to hippocampal cortex (Hargreaves et al., 2005; Norman and Eacott, 2005; Aminoff et al., 2007; Kerr et al., 2007; Eichenbaum and Lipton, 2008; van Strien et al., 2009; LaChance et al., 2019; Nilssen et al., 2019; Sethumadhavan et al., 2020), where they are merged.

## 1.7. Episodic Learning and Memory

These parallel and homologous spatial and temporal representations may clarify the role of hippocampus in supporting episodic learning and memory (Tulving, 1972; Tulving and Thomson, 1973), since each episode in memory consists of specific spatio-temporal combinations of cues, imagery, and behaviors.

Episodic learning combines information about particular *sequences* of object and spatial information. The importance of sequential processing during both episodic learning and spatial navigation have led Buzsáki (2005, p. 831) to suggest that "Learning of sequentially presented or inspected random items in an episodic task is formally identical to the coding of sequential places in a linear (1-dimensional) route" and, moreover, that "formation of episodes and neuronal representations of 1-dimensional routes require a temporal metric that we identify with the theta period." Buzsáki and Moser (2013, p. 130) have similarly suggested the hypothesis that "mechanisms of memory and planning have evolved from mechanisms of navigation in the physical world and hypothesize that the neuronal algorithms underlying navigation in real and mental space are fundamentally the same. We review experimental data in support of this hypothesis and discuss how specific firing patterns and oscillatory dynamics in the entorhinal cortex and hippocampus can support both navigation and memory."

The brain processes that underly the proposed homology between navigation and memory have been modeled in a series of studies over the years. One extensive set of psychophysical experiments about the storage and learning of sequential information has studied how context-sensitive searches are carried out for desired objects in scenes, under the rubric of *contextual cueing*. For example, when we are in our kitchen and see a refrigerator and a stove at particular positions, we then expect to see our sink at a prescribed different position. The psychophysical literature about contextual cueing describes how sequentially experienced objects and positions contribute to such expectations, and guide efficient searches to discover and act upon desired goal objects (e.g., Chun and Jiang, 1998; Olson and Chun, 2002; Brockmole et al., 2006; Jiang et al., 2006). The contextual cueing literature hereby provides a well-organized database for studying the learning of episodic memories, using brain regions that are also implicated in the learning of navigational trajectories.

The ARTSCENE Search model (Huang and Grossberg, 2010) simulates how sequences of experienced spatial locations and objects are temporarily stored in spatial and object working memories, before they trigger learning of spatial and object sequence categories, or list chunks, which in turn learn spatial and object priming signals whereby to predict and control what events to expect and act upon in that sequential context. These processes are modeled using interactions between the perirhinal and parahippocampal cortices, prefrontal cortex, temporal cortex, and parietal cortex to simulate key psychophysical data from contextual cueing experiments that are reviewed and simulated in Huang and Grossberg (2010). The ARTSCENE Search, Spectral Spacing, and START models (see Section 5.1) may in the future be fused to provide a foundation on which to build a more complete theory of episodic learning and memory.

## 1.8. Shared mGluR Dynamics of Spectral Timing in Hippocampus, Cerebellum, and Basal Ganglia?

To the present, spectral timing processes, with similar biophysics and circuitry, have been modeled in the hippocampus, cerebellum, and basal ganglia (Fiala et al., 1996; Brown et al., 1999, 2004). The proposed mechanism of spectral timing in the cerebellum has been supported by biophysical data concerning the calcium dynamics of the metabotropic glutamate receptor (mGluR) system that enables spectral timing to bridge temporal delays of hundreds of milliseconds (Fiala et al., 1996). The most parsimonious prediction is that a similar mechanism holds in all cases of spectral timing throughout the brain.

## 1.9. Linking Theta Rhythm to Grid Cells and Place Cells

The above brief review of grid cell and place cell properties has been given because brain rhythms, including the theta rhythm, are not disembodied abstract oscillators. Rather they modulate particular brain processes. It is known, for example, that a theta rhythm plays a key role in modulating the normal processing of entorhinal grid cells and hippocampal place cells. In this

regard, Stensola et al. (2012, p. 72) have shown that grid cells along the dorsoventral axis "cluster into a small number of layer-spanning anatomically overlapping modules with distinct scale, orientation, asymmetry and theta-frequency modulation." These grid cell modules are distributed across wide regions along the dorsoventral axis with substantial overlaps among the different clusters.

There is also an intrinsic theta rhythm generated endogenously within the hippocampus (Vanderwolf, 1988; Smythe et al., 1992; Bland and Colom, 1993), in addition to an extrinsic theta rhythm that is transmitted to hippocampal projections from the medial septal (MS) area in the basal forebrain, and that generates and maintains a theta rhythm in the hippocampal and parahippocampal areas (Vertes and Kocsis, 1997) via reciprocal interactions among GABAergic interneurons (Tóth et al., 1993; Wang, 2002). This theta rhythm can be reduced by inactivating the MS, which also disorganizes the hexagonal spatial firing patterns of grid cells (Brandon et al., 2011; Koenig et al., 2011). During MS inactivation, affected grid cells tend to code the rat's head direction, in keeping with how inputs from head direction cells form stripe cell, and thus grid cell, receptive fields (**Figure 1**). These and other properties of the intrinsic and extrinsic theta rhythm will be explained below.

## 2. DISCOVERY OF THETA RHYTHM AND BASIC PROPERTIES

### 2.1. Behaviors During Which Theta Rhythm Occurs

Winson (1974) provides an excellent account of when theta rhythms were first reported. Walter and Walter (1949) reported a theta rhythm in the frequency range of 3–7 cycles per second in their EEG scalp recordings of human subjects. Green and Arduini (1954) reported an "arousal reaction" in this frequency range within the hippocampus of the rabbit in response to natural sensory stimulation or electrical stimulation. Behavioral correlates of the theta rhythm were later recorded in several species (Bennett, 1971; Winson, 1972) including the rat, where a theta rhythm is found only if the animal carries out voluntary movements like exploration, as well as during paradoxical sleep (Vanderwolf, 1969).

Whishaw and Vanderwolf (1973) extended the list of behaviors that occur during a theta rhythm, and the species in which they occur. As they noted on p. 461, "slow electrical activity was recorded from the dorsal hippocampus in rats during running in a motor-driven wheel, swimming, conditioned avoidance (running, jumping), lever pressing for food and sleep, and in cats during walking in a treadmill, eating and lapping milk. Large-amplitude clear rhythmical slow activity (RSA) was recorded from the hippocampus proper and smaller amplitude RSA and fast activity was recorded from the dentate gyrus-CA 4 area. . .Increases in RSA frequency and amplitude during paradoxical sleep were associated with muscular twitches, suggesting that forebrain motor mechanisms were activated. The results are interpreted in support of the idea that RSA is related to higher level control of voluntary movement."

The authors noted additionally on p. 477 that "previous reports on the relation between hippocampal RSA and behavior were also confirmed. In the experiments with rats it was found that RSA was present in the pyramidal cell layer in all situations at all times when the animals walked, ran, jumped, etc. (voluntary movement), but that RSA was absent if the animals chewed food, washed their faces, etc. (automatic movement). The results also indicated that the mere repetition of the same motor act does not lead to a disappearance of hippocampal RSA, when such activity was initially present."

The article by Winson (1978) reported, for example, on p. 160 that "rats learned, using distal room cues, to run to a goal on an elevated circular track starting from any position on the track. The goal was one of eight equidistant, recessed cups set around the track, the goal cup being distinguished from the others solely by its position in the room. After learning, electrolytic lesions were made in the medial septal nucleus eliminating hippocampal theta rhythm. . .Rats without theta rhythm were no longer able to perform the spatial task. . ." These results showed how contextual visual cues could interact with a learned hippocampal spatial map to efficiently guide reinforced navigational behavior. They also showed that an important source of the extrinsic theta rhythm that supports such learned spatial behavior is the medial septum.

### 2.2. Intrinsic Theta Rhythm and Cholinergically Modulated Extrinsic Theta Rhythm

Several articles also reported that the septal projection that drives the extrinsic theta rhythm is modulated by acetylcholine (e.g., Stewart and Fox, 1990; Huerta and Lisman, 1993). Huerta and Lisman (1993) also noted on p. 723 that "theta rhythm occurs during periods of learning. . .during these oscillations, synapses are in a state of heightened plasticity [that] is sensitive to the timing of incoming stimuli with respect to the oscillatory activity. . ." In contrast to septally driven theta rhythms, intrinsic theta rhythms may be generated entirely within the CA1 region of the hippocampus where their atropine-resistance shows that their theta generators are not dependent upon acetylcholine (Kramis et al., 1975; Goutagny et al., 2009).

The subsequent discussion will situate the above facts within a larger modeling context that mechanistically and functionally explains them and many others.

## 3. SEPTO-HIPPOCAMPAL THETA RHYTHM, VIGILANCE CONTROL, AND GRID AND PLACE CELL CATEGORY LEARNING

The following facts and theoretical results clarify how cholinergic signals from the medial septum to the hippocampus influence the extrinsic theta rhythm. One measure of this effect is how disruption of the theta rhythm, or cholinergic modulation, or both influence the learned hexagonal spatial firing patterns of entorhinal grid cells.

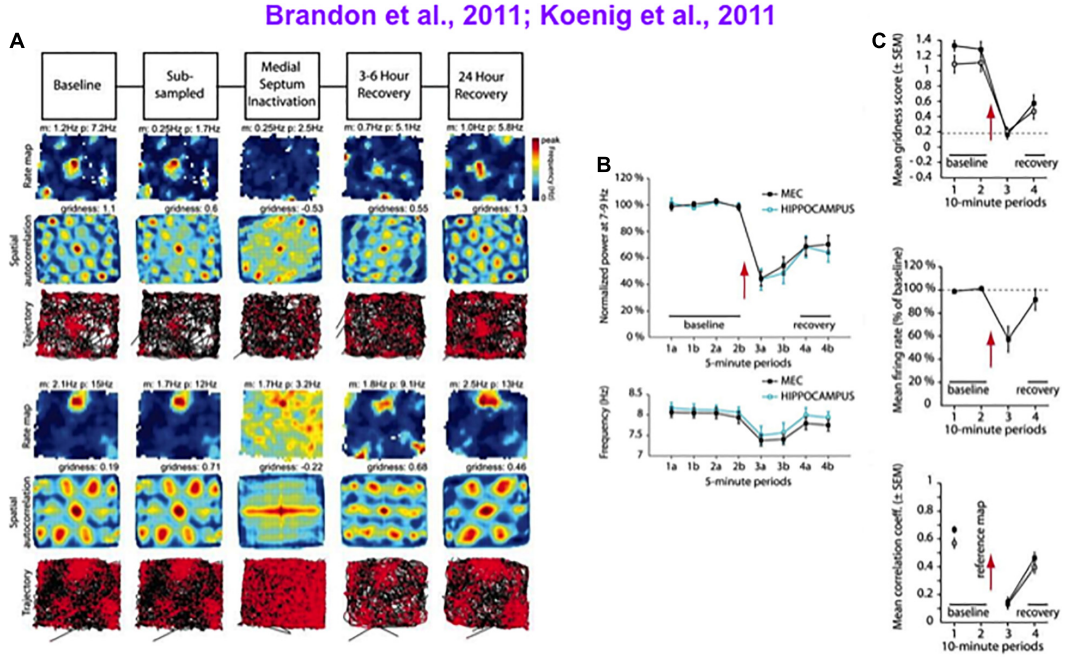


**FIGURE 4 |** Data showing effects of medial septum (MS) inactivation on grid cells and network theta oscillations in medial entorhinal cortex (MEC). **(A)** Examples of disruption of the hexagonal grid structure of two grid cells (Brandon et al., 2011). **(B)** Temporal reduction in the power and frequency of network theta oscillations (Koenig et al., 2011). **(C)** Temporary reduction in the gridness score, mean firing rate, and spatial stability of grid cells (Koenig et al., 2011) (data reprinted with permission from Brandon et al., 2011 and Koenig et al., 2011).

Experiments that reduce the theta rhythm by inactivating the septum cause a correlated reduction in the hexagonal spatial firing patterns of grid cells (Brandon et al., 2011; Koenig et al., 2011). **Figure 4** shows how septal inactivation causes the collapse of grid cell receptive fields, followed by their recovery after septal inactivation wears off. While the septum is inactivated, grid cells tend to code the rat's head direction (**Figure 4A**, sixth row, middle curve).

Does inactivation of the septum lead to grid cell disorganization because the theta rhythm collapses, or because cholinergic modulation of grid cells collapses, or both? Some authors, particularly those who have espoused that oscillatory interference causes grid cell receptive fields, have concluded from these data that "spatial coding by grid cells requires theta oscillations" and "support a role of neuronal oscillations in the coding of spatial information" (Brandon et al., 2011). In other words, these authors proposed that their data support a mechanism of oscillatory interference in the creation of hexagonal grid fields.

## 3.1. Acetylcholine Modulates Vigilance Control of Cognitive, Motor, and Spatial Category Learning

Pilly and Grossberg (2013) proposed an alternative mechanistic explanation and presented data and other theoretical concepts that undermine an explanation based upon oscillatory interference. Their explanation emphasizes that signals from the septum to entorhinal grid cells typically release acetylcholine, and that acetylcholine modulates the learning of recognition categories via a process of *vigilance control* (Carpenter and Grossberg, 1987a; Grossberg and Versace, 2008). The data about collapse of grid cells due to septal inactivation are explained as a collapse of vigilance control that is needed to learn hippocampal *spatial* categories, with or without a theta rhythm. Vigilance control also modulates the learning of cognitive and motor categories, as discussed below. ART is also contrasted with continuous attractor and SOM grid cell models in Grossberg and Pilly (2014).

## 3.2. How Reduction of Cholinergic Input to Grid Cells Causes Their Collapse

In the case of the entorhinal-hippocampal system, the inactivation of the medial septum eliminates, or greatly reduces, the cholinergic input to grid cells (Mitchell et al., 1982). This reduction increases the conductances of leak potassium and slow and medium after-hyperpolarization channels (Madison et al., 1987; Müller et al., 1988; Klink and Alonso, 1997; Lape and Nistri, 2000). The rate of membrane depolarization is hereby slowed, leading to greater spike frequency adaptation and longer refractory periods. Grid cell firing and spatial periodicity are

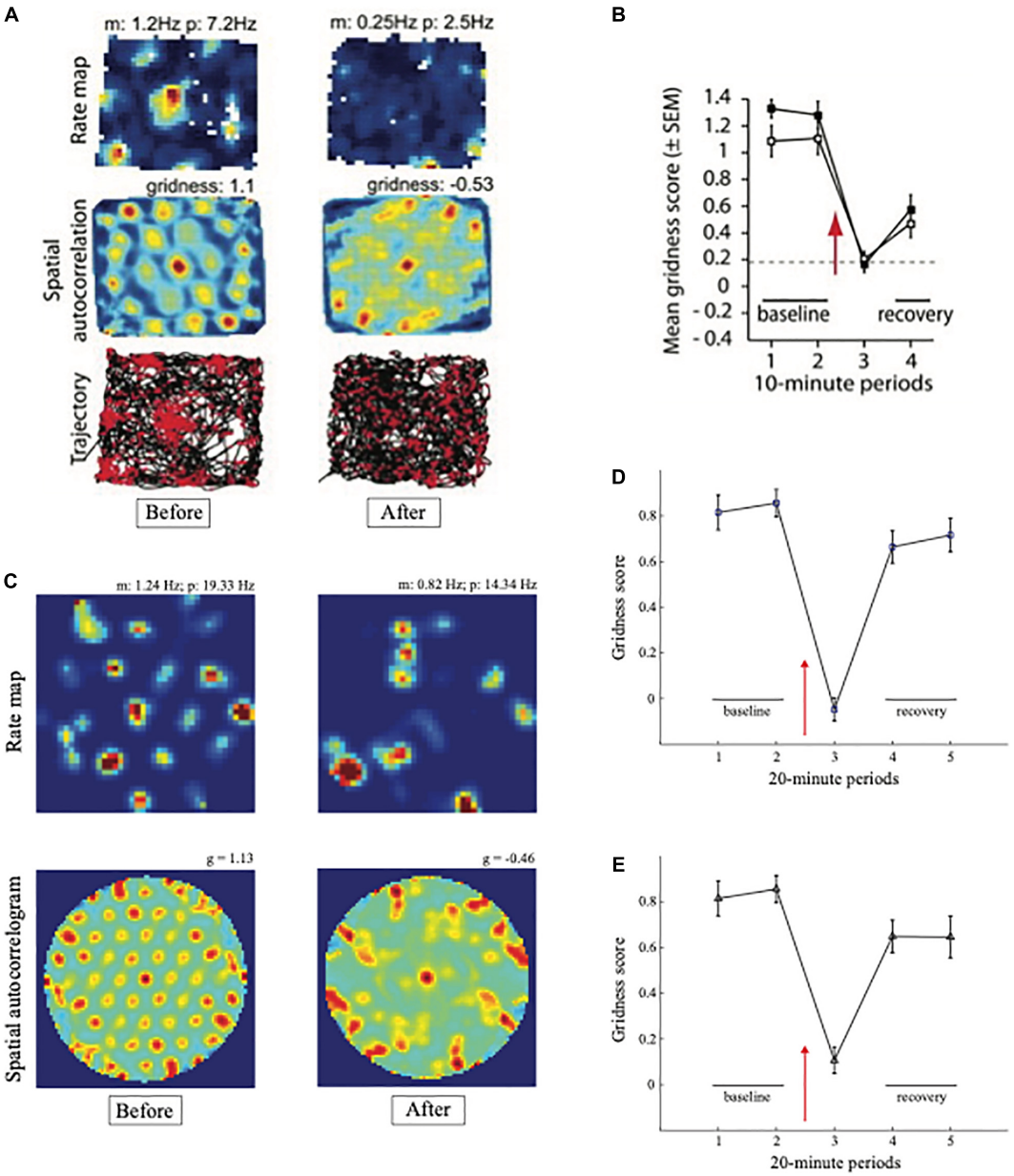


**FIGURE 5 |** Data and computer simulation of effects of septal inactivation on grid cells. **(A)** Each row shows data and different data-derived measures of grid cell responsiveness, starting from the left with the baseline response to the middle column with maximal inhibition (Data reprinted with permission from Brandon et al., 2011). **(B)** Data showing the temporary reduction in the gridness scores during septal inactivation, followed by recovery (Data reprinted with permission from Koenig et al., 2011). **(C)** Simulation of gridness collapse due to reduction in cell response rates that mimic reduced cholinergic transmission. **(D)** Simulations of gridness score reduction by reducing cell response rates. **(E)** Simulations of gridness score reduction by changing leak conductance [simulations in **(C–E)** reprinted with permission from Grossberg and Pilly, 2014].

hereby greatly impaired because a controlled duration of grid cell sampling of stripe cell inputs is needed to learn, and maintain, grid cells with any given spatial scale.

Model simulations in **Figure 5** support these conclusions by showing spatial disorganization of grid fields as well as reductions in firing rate and spatial stability (**Figure 5C**) when septal inactivation is caused either by a temporary reduction in cell response rates (**Figure 5D**) or a temporary increase in leak conductances (**Figure 5E**). A head direction bias remains after the duration of path integration sampling is disorganized due to the remaining head direction inputs from stripe cells to grid cells in the GridPlace Map model of **Figure 6**.

Newman et al. (2014) summarized experimental evidence that are consistent with this explanation by demonstrating that "administration of the muscarinic antagonist scopolamine flattens the typically positive correlation between running speed

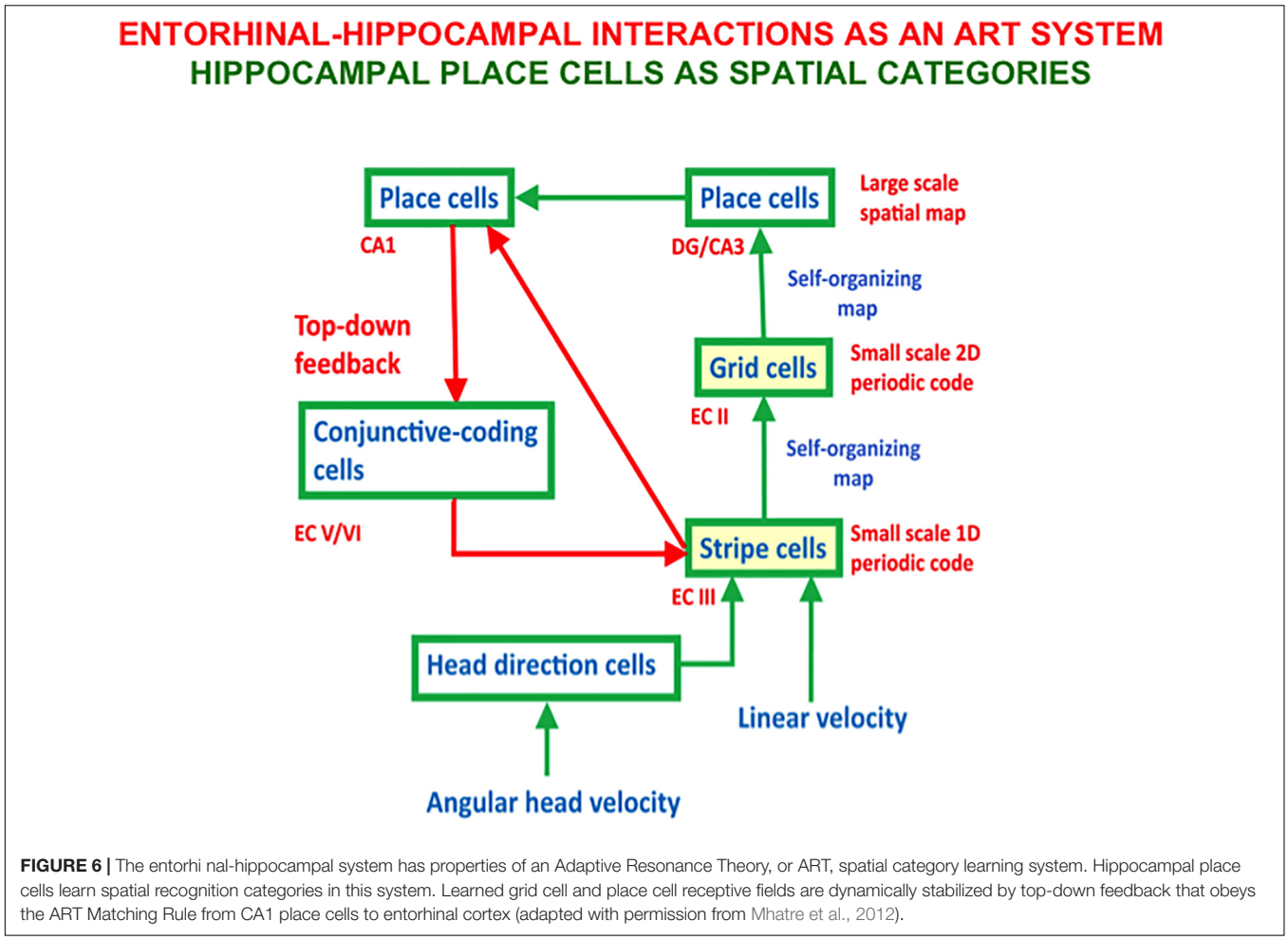


**FIGURE 6 |** The entorhi nal-hippocampal system has properties of an Adaptive Resonance Theory, or ART, spatial category learning system. Hippocampal place cells learn spatial recognition categories in this system. Learned grid cell and place cell receptive fields are dynamically stabilized by top-down feedback that obeys the ART Matching Rule from CA1 place cells to entorhinal cortex (adapted with permission from Mhatre et al., 2012).

and entorhinal theta frequency in rats. . .spatial tuning of grid cells was reduced following scopolamine administration. The tuning of head direction cells, in contrast, was not reduced by scopolamine" (p. 643). The authors go on to write "This is the first report to demonstrate a link between cholinergic function and grid cell tuning." It also supports the prediction by Pilly and Grossberg (2013) of the existence of this link, and how it works.

**Figure 6** also includes a top-down feedback pathway that dynamically stabilizes the learning of grid cells and place cells using an attentive matching process that obeys the ART Matching Rule, which will be described in the next section. The need for this feedback loop is clarified by the fact that place cells can develop in minutes, and some of them can retain their stability for months (Thompson and Best, 1990; Wilson and McNaughton, 1993; Muller, 1996; Ziv et al., 2013). However, a SOM does not have this property because learned SOM categories can undergo catastrophic forgetting. In the case of grid cells and place cells, this means, for example, that the grid cell receptive fields could drift through time. As noted below, Adaptive Resonance Theory, or ART, was introduced to explain how learned categories across the brain can dynamically stabilize their memories for many years.

## 3.3. Dynamically Stabilizing Learned Cognitive and Spatial Categories Using the ART Matching Rule

Vigilance control is an important process in regulating the concreteness or abstractness of the categories that can be learned by an ART model (**Figure 7**), whether these categories are cognitive, spatial, or motor. ART regulates how spatial patterns of activity, or short-term memory (STM) traces, across a network of cells respond on a fast time scale to external and internal inputs, as they interact with adaptive weights, or long-term memory (LTM) traces, to learn recognition categories without experiencing catastrophic forgetting.

The learning of recognition categories in ART builds upon the laws of a Self-Organizing Map, or SOM (Grossberg, 1976a, 1978, 1980; Kohonen, 1984), in which LTM traces multiply, or gate, bottom-up signals from a feature level $F_1$ to a category level $F_2$ before the gated signals compete to choose and store in STM the cell activity, or small number of cell activities, that received the largest inputs (**Figure 7A**). These active $F_2$ cells drive learning in the LTM traces that abut them, thereby tuning the LTM traces and causing the winning $F_2$ cells to become recognition categories that respond selectively to sets of similar feature patterns across $F_1$.

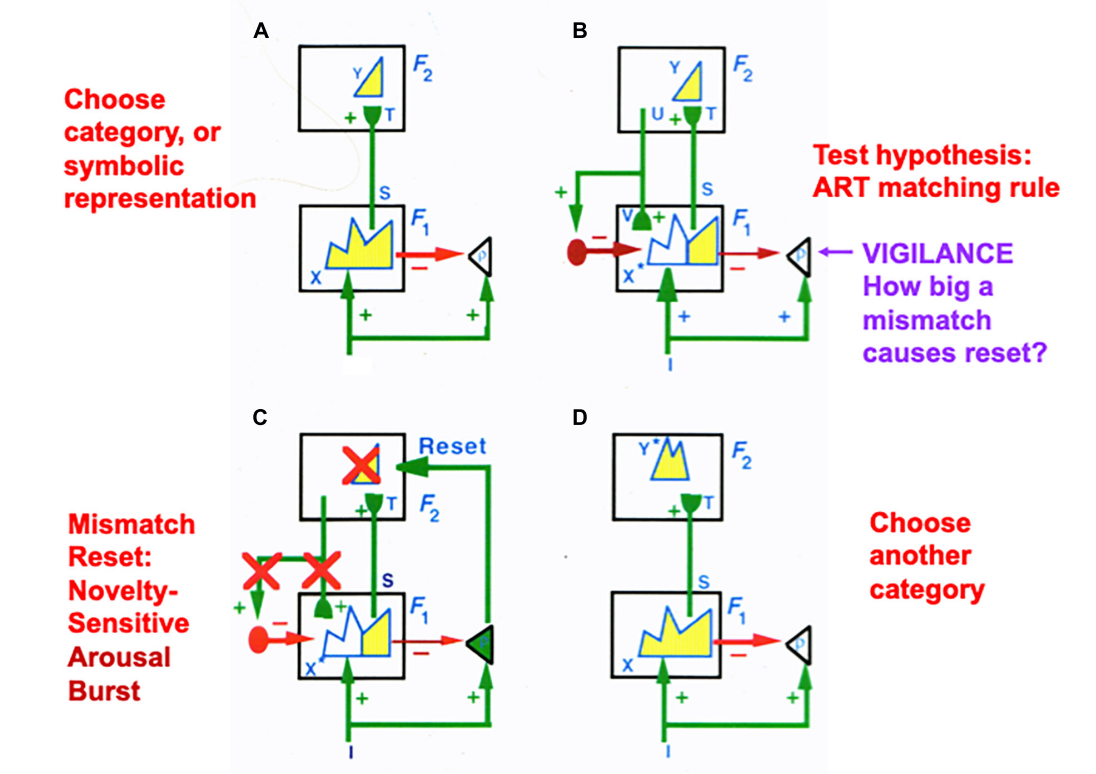


**FIGURE 7 | (A)** The ART hypothesis testing and category learning cycle begins when an input pattern $I$ is stored across feature detectors at level $F_1$ as an activity pattern $X$, which is shown in yellow. For simplicity, arrays of connections between processing stages are represented by a single connection. While $X$ is getting instated in $F_1$, $I$ also send excitatory signals via parallel pathways to the orienting system (the triangle with gain parameter $\rho$ inside it). The gain parameter $\rho$ is the *vigilance* parameter. As activity pattern $X$ is instated in $F_1$, it activates two output signal pathways: A bottom-up excitatory input pattern $S$ to category level $F_2$, and inhibitory inputs $\rho I$ to the orienting system. There are as many excitatory inputs as inhibitory inputs to the orienting system, because inputs $I$ activate pattern $X$. The net input to the orienting system is $\rho/\!/I/\!/ - /\!/X/\!/$, where $/\!/$ denotes the size of each total input. This net input is not positive because $\rho \leq 1$, so the orienting system remains quiet. Before activating a category in $F_2$, bottom-up signals $S$ are multiplied by learned adaptive weights (in the hemispherical synapses) to generate the input pattern $T$ to category level $F_2$. Inputs $T$ are contrast-enhanced and normalized within $F_2$ by a recurrent shunting on-center off-surround network that activates and stores a small number of cells within $F_2$ that receive the largest inputs. The chosen cells represent category $Y$ that codes feature pattern at $F_1$. **(B)** Category $Y$ generates top-down signals $U$ that are multiplied by adaptive weights to form a prototype, critical feature pattern, or expectation $V$ of what learned feature pattern to attend at $F_1$. Expectation $V$ delivers an excitatory modulatory signal to $F_1$ cells in its on-center, while inhibiting $F_1$ cells in its off-surround. Together, these signals embody the ART Matching Rule for object attention. The ART Matching Rule circuit ensures that category learning does not suffer from catastrophic forgetting. **(C)** If $V$ mismatches $I$ at $F_1$, then the ART Matching Rule chooses a new STM activity pattern $X^*$ (the yellow pattern) at cells where the bottom-up and top-down patterns match. Mismatched features (white area) are inhibited. If the pattern $X^*$ of attended features across $F_1$ represents a big enough mismatch to activate the orienting system (that is, if $\rho/\!/I/\!/ - /\!/X/\!/ > 0$), then a novelty-sensitive nonspecific arousal burst is activated there (cf. the N200 in **Figure 10**), which resets, or inhibits, the currently active category $Y$ and drives hypothesis testing and memory search until another category is chosen **(D)** that supports a good enough match to keep the orienting system quiet while category learning occurs. If, however, in **(B)** a good enough match occurs between $I$ and $V$ to keep the orienting system quiet, then it reactivates the pattern $Y$ at $F_2$ which, in turn, reactivates $X^*$ at $F_1$. Positive feedback loop hereby dynamically links, or binds, $X^*$ with $Y$. In both of these latter cases, a feature-category resonance focuses attention on the active critical feature pattern while learning it in both the bottom-up adaptive filter and top-down learned expectation (adapted with permission from Carpenter and Grossberg, 1987a).

ART models how top-down attentive matching (**Figure 7B**) dynamically stabilizes the learning by LTM traces both within bottom-up adaptive filters from level $F_1$ to $F_2$ *and* within top-down learned expectations from level $F_2$ to $F_1$, as described more fully below and in the caption of **Figure 7**.

The modulatory on-center of a top-down expectation learns a prototype that focuses attention upon the spatial pattern of *critical features* that controls predictive success. When such an expectation is read out in the absence of a bottom-up input pattern, the modulatory on-center of the ART Matching Rule can prime, or sensitize, feature-selective cells in the on-center, without firing them to suprathreshold activity levels. Bottom-up input patterns that match the on-center well enough are needed to fire on-center cells to suprathreshold activation levels, and to thereby begin the process of focusing attention upon the matched subset of critical features that are in the learned prototype of the expectation. While this matching process takes hold, the off-surround can fully suppress the cells that it inhibits, thereby preventing irrelevant cues from being learned and, along with it, catastrophic forgetting. Carpenter and Grossberg (1987a)

proved mathematically that the ART Matching Rule is necessary to dynamically stabilize the memories of learned categories.

The bottom-up adaptive filters and recurrent competition that control learning of grid cells and place cells in **Figure 2** are also SOMs, albeit SOMs that drive spatial category learning. As I noted above, within the GridPlaceMap model, the laws and parameters of each SOM in its network hierarchy are the same. The fact that grid cells and place cells learn such different receptive field properties is due to their different inputs: Arrays of stripe cells drive the learning of grid cells, while place cell learning is driven by inputs from arrays of emerging grid cells, even before their receptive fields are fully formed, leading to the beautiful receptive fields in **Figures 1B,C**. As in cognitive ART models, the top-down expectations in **Figure 6** also obey the ART Matching Rule of **Figure 7B** in order to dynamically stabilize learned grid cell and place cell receptive field properties.

## 3.4. Cholinergically Modulated Vigilance Control in Cognitive Category Learning and Maintenance

In the cognitive domain, vigilance control is realized by identified neurons in laminar cortical circuits that have been modeled by the Synchronous Matching ART, or SMART, model refinement of ART (Grossberg and Versace, 2008; Palma et al., 2012a,b; Grossberg et al., 2016). The SMART model is realized by spiking neurons that obey neurophysiologically measured parameters which interact within the detailed laminar cortical and subcortical circuits in **Figure 8** in response to bottom-up (BU) inputs. SMART explains how vigilance may be altered by acetylcholine release when the nucleus basalis of Meynert is activated via the nonspecific thalamus (**Figure 9**; van der Werf et al., 2002). The nonspecific thalamus is itself activated by corticothalamic mismatches that occur within a specific thalamic nucleus during an ART hypothesis testing and learning cycle (**Figures 7**, **8**).

**Figure 9** also summarizes how activation of the nucleus basalis of Meynert broadcasts cholinergic signals to layer 5 cells. The released acetylcholine inhibits afterhyperpolarization (AHP) currents, thereby increasing cell excitability and increasing vigilance.

The SMART model further develops a series of ART category learning and recognition models that have been developed over the years to include and explain increasingly detailed and system-wide thalamocortical and corticocortical interactions (e.g., Grossberg, 1976a,b, 2003, 2013a, 2017a,b, 2020, 2021; Carpenter and Grossberg, 1987a,b; Carpenter et al., 1989, 1991a,b, 1992; Grossberg et al., 1997a; Ames and Grossberg, 2008; Grossberg and Versace, 2008; Grossberg and Huang, 2009; Cao et al., 2011; Chang et al., 2014).

As illustrated in **Figure 10** (left panel), in all ART models, including SMART, a good enough top-down match with a bottom-up feature pattern triggers a *feature-category resonance* that drives learning of a new recognition category, or refinement of an already established one, as well as conscious recognition of the object that the category codes (Grossberg, 2017b). Both ART and SMART explain and simulate how sensory and cognitive information processing may be broken into cycles of match and mismatch (**Figures 7**, **10**), or resonance and reset, which will be seen below to correspond to cycles of faster gamma oscillations (40–60 Hz) and slower beta oscillations (16–20 Hz); see Buffalo et al. (2011) and Terporten et al. (2019). When theta rhythms (4–12 Hz) organize these cycles through time, then theta-modulated gamma oscillations and beta oscillations are the natural result.

## 3.5. Breakdowns in Vigilance Control of ART Dynamics Clarifies Mental Disorders

Within SMART, increased layer 5 excitability to predictive mismatches due to acetylcholine release may cause reset of a currently active category via the layer 5-to-$6^{I}$-to-4 circuit that realizes part of the model's ART Matching Rule (**Figure 8**). Such a reset can occur even if top-down feedback sufficiently matched a bottom-up input to avoid reset just moments before. An acetylcholine increment hereby drives a search for finer recognition categories, even when bottom-up and top-down signals have a pretty good match based on similarity alone.

How perceptual and cognitive vigilance control is modulated by the nucleus basalis of Meynert and acetylcholine has wide-ranging implications. For example, breakdowns of vigilance control that undermine the ART Matching Rule circuit via layer 5 can, depending on whether phasic or tonic vigilance control, or both, are affected, cause symptoms of Alzheimer's disease, autism, amnesia, and disrupted slow wave sleep (Grossberg, 2017a).

## 3.6. Gamma and Beta Oscillations Covary With PN and N200 Event-Related Potentials

ART and its variants such as SMART are supported by neurophysiological data on multiple organizational levels. For example, when a match is good enough to generate a feature-category resonance in SMART, it is supported by fast gamma oscillations, whereas a big enough mismatch triggers slower beta oscillations (Grossberg and Versace, 2008; Grossberg, 2009). Grossberg (2013a) reviews neurophysiological experiments that support this prediction, whether during different effects of attention on different layers in the primary visual cortex (Buffalo et al., 2011), spatial attention shifts in frontal eye fields (Buschman and Miller, 2007), or learning of new place cells in the hippocampus (Berke et al., 2008). Synchrony is a characteristic feature of the cells that participate in gamma frequency oscillations (Freeman, 1975; Eckhorn et al., 1988; Gray and Singer, 1989; Pollen, 1999; Engel et al., 2001; Buschman and Miller, 2007; Gregoriou et al., 2009), whether during preattentive perceptual grouping or attentive category learning and recognition (Grossberg, 1980; Grossberg and Somers, 1991; Maldonado et al., 2000; Yazdanbakhsh and Grossberg, 2004).

On a coarser level of neurophysiological measurement, a Processing Negativity, or PN, event-related potential or ERP (Näätänen et al., 1978) can be recorded by scalp electrodes during the match of a bottom-up feature pattern with a top-down learned expectation that triggers a gamma oscillation (Hermann and Knight, 2001). In contrast, a big enough mismatch can activate the ART orienting system to drive hypothesis testing

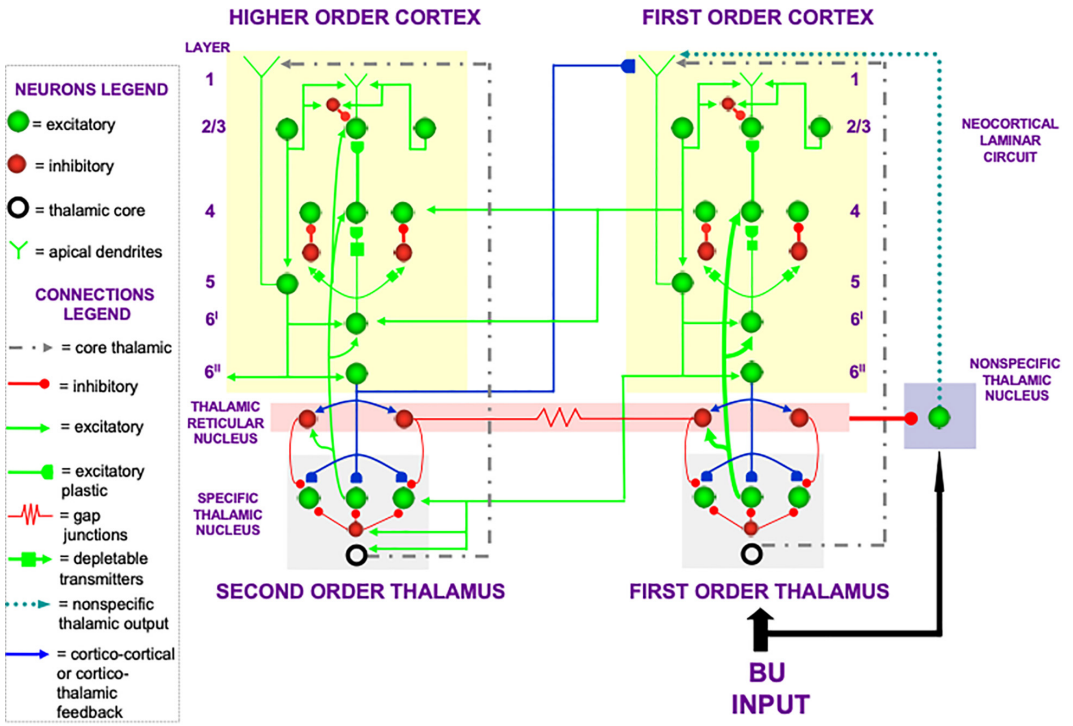


**FIGURE 8 |** The Synchronous Matching ART, or SMART, model describes how spiking neurons in a laminar cortical hierarchy interact with specific and nonspecific thalamic nuclei to learn perceptual or cognitive categories (reprinted with permission from Grossberg and Versace, 2008).

and memory search for a new, or better matching, category (**Figure 7C**), leading to a good enough match to again drive category learning. Such an activation of the orienting system is accompanied by a beta oscillation (Haenschel et al., 2000) and an N200 ERP (Näätänen et al., 1982). As summarized in **Figure 10**, the PN and N200 ERPs exhibit computationally complementary properties (Grossberg, 2000, 2017b).

## 3.7. What Happens to Place Cells When Grid Cells Collapse?

Many additional facts and explanations of how the extrinsic theta rhythm and vigilance control work in cognitive, motor, and spatial processing regions are found in Grossberg (2021). As just one example, if a septal lesion eliminates the extrinsic theta rhythm and causes grid cells to become disorganized, some place cells may remain intact. Since place cells are the hippocampal spatial categories that can represent spaces large enough to control spatial navigation, then why are grid cells needed at all? When grid cells collapse, place cells cannot represent the large spaces that are the least common multiple of the grid cell scales that previously input to them. These are, however, the place cells that enable us to navigate in many of the spaces that are ecologically important for our survival.

In addition, if grid cells collapse, then the feedback loop in **Figure 6** that dynamically stabilizes both grid cell and place cell receptive fields is broken, leading to unstable representations of space at even the level of place cells. Indeed, Kentros et al. (2004) noted that "conditions that maximize place field stability greatly increase orientation to novel cues. This suggests that storage and retrieval of place cells is modulated by a top-down cognitive process resembling attention and that place cells are neural correlates of spatial memory." The role of top-down attentive feedback in stabilizing place cell receptive fields is also supported by results of Morris and Frey (1997), who reported that hippocampal plasticity reflects an "automatic recording of attended experience." The importance of learning in these changes is shown by the fact that NMDA receptors mediate long-lasting hippocampal place field memory in novel environments (Kentros et al., 1998).

Some place cells develop before grid cells do. They could be learned directly from stripe cells, say via the direct pathway from entorhinal cortex to CA1 (**Figure 6**). This fact may clarify how rat pups behave before they are around two-and-one-half weeks old. Until then, rat pups tend to stay in or near their nests. Exploration of larger spaces occurs around the same time when grid cells rapidly develop (Langston et al., 2010; Wills et al., 2010, 2012; Muessig et al., 2015), and drive learning of place cells capable of controlling navigation in these larger spaces.

## 3.8. Disinhibition of the Septal Theta Rhythm via the Basal Ganglia

The basal ganglia play a key role in gating on or off perceptual, cognitive, emotional, and motor processes, thereby helping to coordinate them to achieve desired behavioral goals. Significant

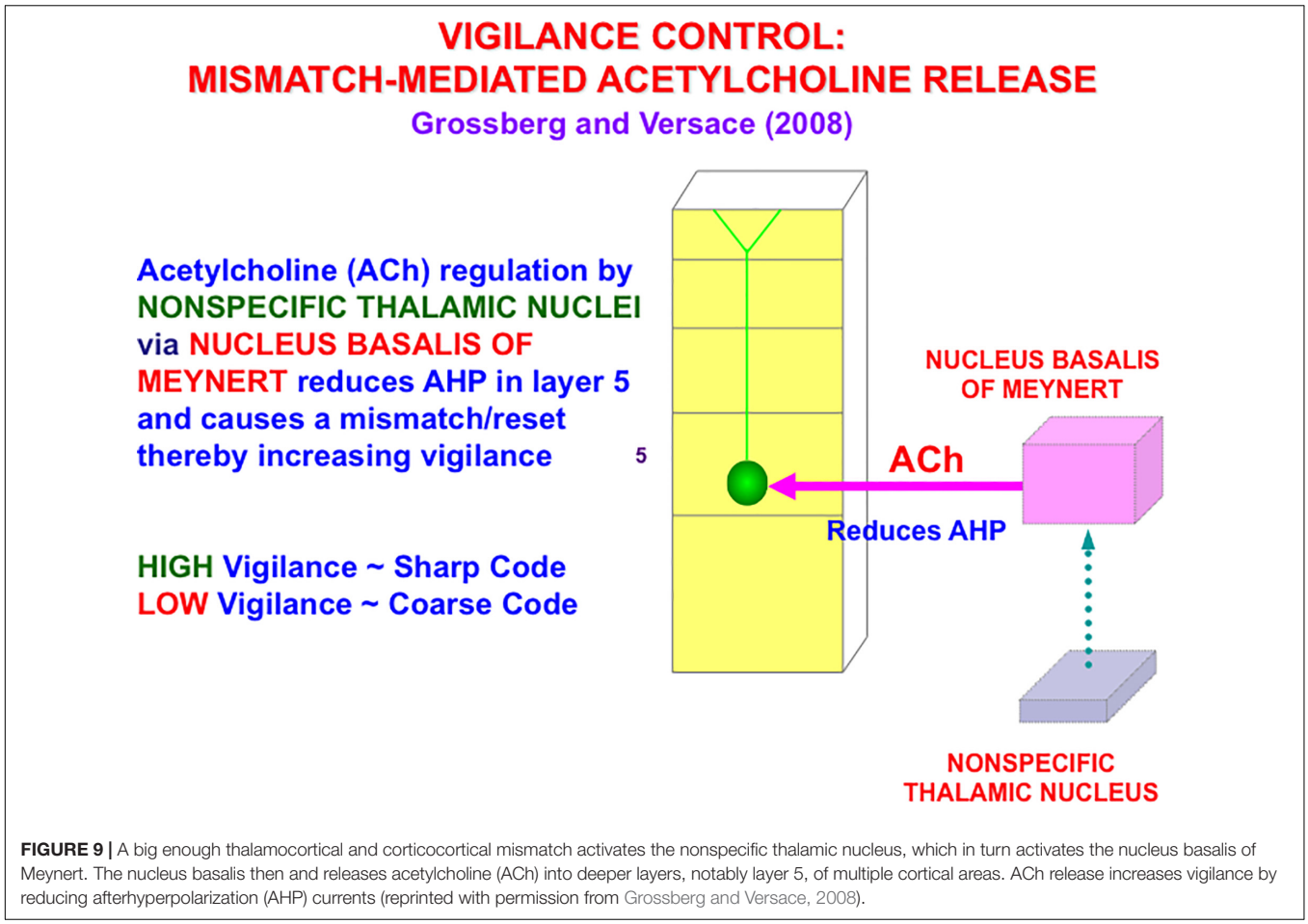


**FIGURE 9 |** A big enough thalamocortical and corticocortical mismatch activates the nonspecific thalamic nucleus, which in turn activates the nucleus basalis of Meynert. The nucleus basalis then and releases acetylcholine (ACh) into deeper layers, notably layer 5, of multiple cortical areas. ACh release increases vigilance by reducing afterhyperpolarization (AHP) currents (reprinted with permission from Grossberg and Versace, 2008).

progress has been made in developing neural models of how the basal ganglia work and realize these properties (e.g., Brown et al., 1999, 2004; Grossberg, 2016; Grossberg and Kishnan, 2018). Typically, turning on the basal ganglia substantia nigra pars reticulata, or SNr, inhibits a tonically active inhibitory pathway, thereby disinhibiting the cellular targets of that inhibition and enabling the disinhibited neural pathways to fire. A classical example is how disinhibition of the deeper layers of the superior colliculus by the basal ganglia, or direct electrical simulation, enables a saccadic eye movement of prescribed direction and length to be released to a desired target location (Schiller and Stryker, 1972; Hikosaka and Wurtz, 1985; McIlwain, 1986; Munoz and Wurtz, 1995a,b; Munoz et al., 2000; Watanabe and Munoz, 2010), a process that has also been extensively modeled (Grossberg et al., 1997b; Gancarz and Grossberg, 1998; Brown et al., 2004).

In the case of the septo-hippocampal theta rhythm, a volitional signal from the basal ganglia disinhibits an endogenous oscillator that drives this theta rhythm from cells outside the hippocampus (Silkis, 2008). Available data do not seem sufficient to derive an anatomically detailed model of the microcircuit of this oscillator. Instead, to clarify how this may happen in principle, I will summarize a type of minimal oscillator that is built from classical neurobiological components, such as cells whose potentials obey the membrane equations of neurophysiology—also called shunting interactions—as they interact within a recurrent on-center off-surround anatomy.

This kind of network has been used throughout the brain to carry out multiple functions, including functions where oscillatory dynamics may not occur some of the time, but do oscillate at other times. In particular, networks that do not oscillate with some parameter settings do oscillate when these parameters are changed, notably the rate with which inhibitory interneurons respond. For example, when recurrent on-center off-surround networks include inhibitory off-surround interneurons that react more slowly than their on-center cells, then they tend to oscillate when they also receive a sufficiently large volitional signal, also called a GO signal. This kind of result was first mathematically proved and simulated in Ellias and Grossberg (1975). It has been modeled in scores of articles since by many authors.

Specializations of this oscillator have been used to model a number of basal-ganglia disinhibited oscillatory dynamics, including the control of mammalian movement gaits (Pribe et al., 1997). **Figure 11A** describes a model central pattern generator, or CPG, that is capable of generating multiple gaits using a pair of recurrent on-center off-surround networks, one to control the forelimbs and the other to control the hindlimbs of a quadruped animal. The cells in the CPG obey shunting interactions. The

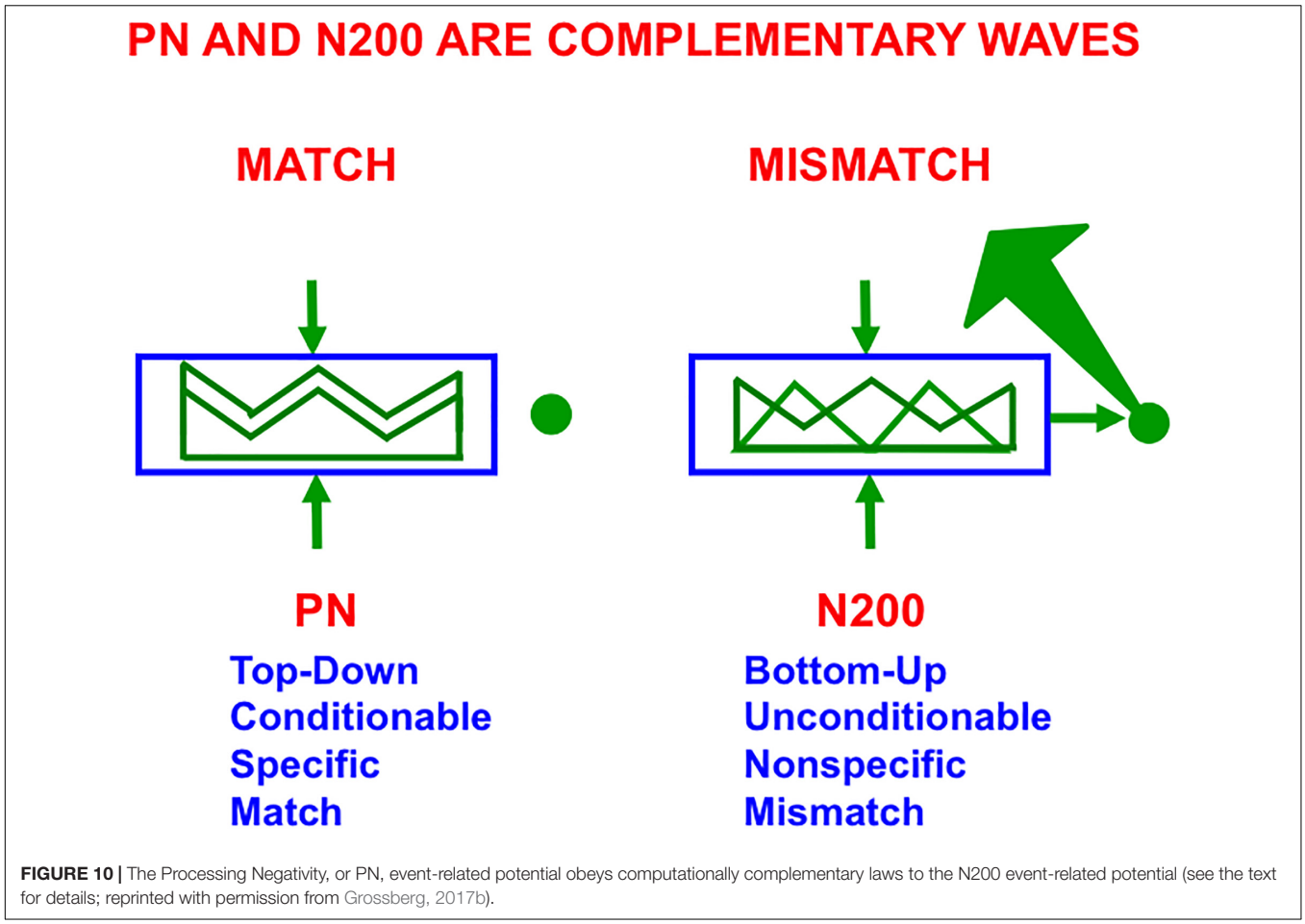


**FIGURE 10 |** The Processing Negativity, or PN, event-related potential obeys computationally complementary laws to the N200 event-related potential (see the text for details; reprinted with permission from Grossberg, 2017b).

gaits are activated by a volitional GO signal that sends signals to both the forelimb and the hindlimb circuits. This excitatory GO signal represents a simple way to model basal ganglia disinhibition. The need for a signal with this functionality was clear in modeling studies decades before detailed models of the basal ganglia were developed.

In the CPG of **Figure 11A**, increasing the GO signal increases the frequency of the gait, and also leads to bifurcations into different gaits that are stable at higher speeds. Excitatory neurons are denoted by open disks. Inhibitory interneurons are denoted by black disks. Self-inhibitory inhibition is labeled by parameter D0, inhibition between forelimbs and between hindlimbs is labeled by D1, inhibition between matched forelimbs and hindlimbs is labeled by D2, and inhibition between crossed forelimbs and hindlimbs is labeled by D3. **Figure 11B** summarizes computer simulations of four gaits (walk, trot, pace, and gallop) that arise due to different GO signal levels as an emergent property of network interactions. Variations of the model also generate the primary human gaits (walk, run) and elephant gaits (amble, walk).

The above type of circuit clarifies how increasing basal ganglia disinhibition of the septum can increase the theta rhythm frequency. It also clarifies how basal ganglia disinhibition of gait-controlling circuits in other parts of the brain (Takakusaki, 2017) can increase running speed. Many experiments have been done over the years to clarify how theta rhythms, in concert with closely related respiratory rhythms (Cao et al., 2012), can regulate the energizing, coordination, and learning of multiple actions, beyond the classically reported correlations between theta-modulated sniffing and whisking (Komisaruk, 1970; Macrides and Chorover, 1972; Semba and Komisaruk, 1984; Ranade et al., 2013) to a wide range of other brain regions and learned behaviors (Landfield et al., 1972; Macrides et al., 1982; DeCoteau et al., 2007; Kaplan et al., 2012; Kleinfeld et al., 2014, 2016; Grion et al., 2016; Rojas-Líbano et al., 2018).

## 3.9. The Olfactory Code as a Temporal Series of Spatial Patterns at a Theta Oscillatory Rate

Early experiments on theta-modulated sniffing were carried out by Walter Freeman. In these early classical experiments, Freeman (1975) discovered a resonance phenomenon by performing parallel electrode experiments on the cat prepyriform cortex. When a cat, or rabbit, smells an expected scent, its cortical potentials are amplified until a synchronized oscillation of activity is elicited across the cortical tissue. The oscillation organizes the cortical activity into a *temporal sequence of spatial*

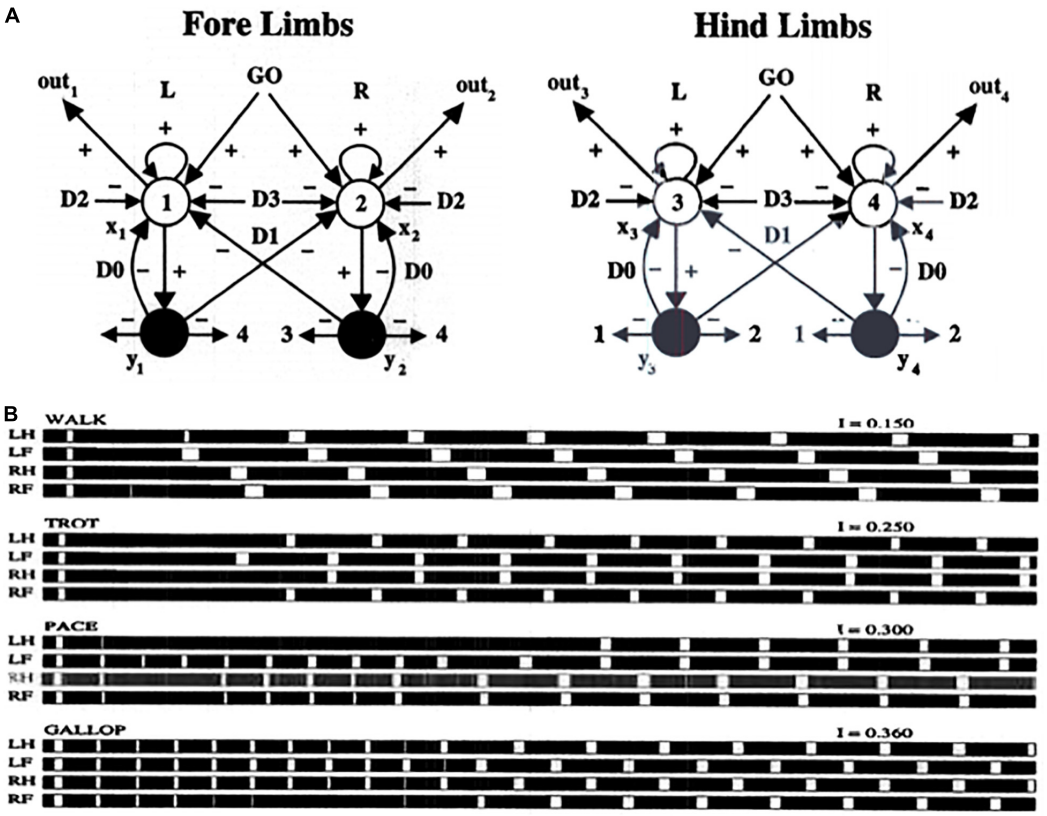


**FIGURE 11 | (A)** Multiple movement gaits are generated by suitably connected recurrent shunting on-center off-surround networks when they are activated by a volitional GO signal of variable size. Abbreviations in **(B)**: LH, left hind; LF, left front; RH, right hind; RF, right front (see the text for details; reprinted with permission from Pribe et al., 1997).

*patterns*. The spatial patterns of activity across cortical cells carry the olfactory code. The temporal series of spatial patterns drives the spatial patterns from the sensory periphery into higher sensory and cortical areas while continuing to bind the signals together in a spatial pattern code.

The concept that a distributed spatial pattern of activation across a network of cells constitutes a sensory neural code, whether or not it was energized by oscillatory dynamics, was supported even then by experiments from several labs (Pfaffman, 1955; Erickson, 1963; Freeman, 1972; Somjen, 1972). By contrast, when the cat or rabbit smells an unexpected scent, then cortical activity is markedly suppressed. Freeman traced differences in cortical activity after expected vs. unexpected scents to gain changes within the cortical tissue. Grossberg (1973, 1976a,b) showed how such gain changes, due to shunting dynamics, could also explain the tendency for the most active populations to phase-lead less active populations.

Freeman (1975) also reported the experiments of Dumenko (1968, 1970) on dogs who were trained to perform a conditioned response to both visual and auditory stimuli, leading to a high correlation between the EEGs of their visual and auditory cortices in the theta range 5–7 Hz.

These neurophysiological studies supported theorems about biological neural networks showing that the functional unit of fast neural information processing is a distributed *spatial pattern* of activity, or STM traces, across a network, and that the functional unit of learning is a distributed *spatial pattern* of adaptive weights, or LTM traces, across the network (Grossberg, 1968a,b, 1969, 1970, 1971, 1980), whether the energetic carrier of these patterns converges to an equilibrium point or rhythmically oscillates through time.

## 3.10. Toward Comprehensive Neural Architectures

It remains to develop a comprehensive neural model of how the entorhinal-hippocampal circuits that are described above work together with other brain regions to release, learn, gain-control, and coordinate sequences of goal-oriented naturalistic behaviors. Some neural architectures, such as the SOVEREIGN family of architectures (Gnadt and Grossberg, 2008; Grossberg, 2019), model how a brain can incrementally learn planned action sequences to navigate toward a rewarded goal, and can do so while being modulated by basal ganglia gating. The SOVEREIGN model's ability to do so was tested in a 3D virtual reality maze that the animat learned to navigate in order to acquire a reward.

The SOVEREIGN2 architecture embodies interactions between more of the brain processes whose interactions are needed to realize biological intelligence. These processes have

previously been modeled in multiple articles over the past 40 years. The Abstract of Grossberg (2019) summarizes these processes:

"Key new perceptual, cognitive, cognitive-emotional, and navigational processes require feedback networks which regulate resonant brain states that support conscious experiences of seeing, feeling, and knowing. Also included are computationally complementary processes of the mammalian neocortical What and Where processing streams, and homologous mechanisms for spatial navigation and arm movement control. These include: Unpredictably moving targets are tracked using coordinated smooth pursuit and saccadic movements. Estimates of target and present position are computed in the Where stream, and can activate approach movements. Motion cues can elicit orienting movements to bring new targets into view. Cumulative movement estimates are derived from visual and vestibular cues. Arbitrary navigational routes are incrementally learned as a labeled graph of angles turned and distances traveled between turns. Noisy and incomplete visual sensor data are transformed into representations of visual form and motion. Invariant recognition categories are learned in the What stream. Sequences of invariant object categories are stored in a cognitive working memory, whereas sequences of movement positions and directions are stored in a spatial working memory. Stored sequences trigger learning of cognitive and spatial/motor sequence categories or plans, also called *list chunks*, which control planned decisions and movements toward valued goal objects. Predictively successful list chunk combinations are selectively enhanced or suppressed via reinforcement learning and incentive motivational learning. Expected vs. unexpected event disconfirmations regulate these enhancement and suppressive processes. Adaptively timed learning enables attention and action to match task constraints. Social cognitive joint attention enables imitation learning of skills by learners who observe teachers from different spatial vantage points."

However, neither SOVEREIGN nor SOVEREIGN2 describes how all of these processes are coordinated by theta and respiratory rhythms. This should be a major goal of future research that builds upon this foundation.

# 4. INTRINSIC THETA RHYTHM DISSOCIATES LEARNED READ-OUT AND READ-IN

Part of this research would need to include the existence, neural mechanism, and functional roles of an intrinsic source of a theta rhythm which, unlike the septally mediated theta rhythm, is atropine-resistant and arises entirely within the hippocampal CA1 region (Kramis et al., 1975; Goutagny et al., 2009). Intrinsic and extrinsic theta oscillations can interact in complex ways (e.g., Montgomery et al., 2009) as part of the tri-synaptic hippocampal organization of CA1, CA3, and the dentate gyrus (**Figure 6**; Amaral and Witter, 1989; Amaral, 1993; Knierim, 2015).

Hippocampal area CA1 helps to support functions other than spatial navigation, including learning, recognition, and memory that involve visual, cognitive, and emotional functions (e.g., Zola-Morgan et al., 1986; Rempel-Clower et al., 1996; Leutgeb et al., 2004; Manns et al., 2007; Dong et al., 2009). As noted in Section 1.6, LEC seems to process cue-related information, including its adaptive timing in behavior, whereas MEC processes the kind of spatial information that is computed by grid cells and place cells. Both kinds of information may be processed through CA1, albeit in different cortical layers (Soltesz and Losonczy, 2018).

Such a sharing of processing resources is understandable from the perspective that "these areas, which receive multimodal inputs from various sensory and motor regions, represent the end-points of the what and where streams of visual processing, which are then integrated at the hippocampus" (Saleem, 2019, p. 73). For example, visual cues are used for visual object recognition, as well as to define landmarks with which to guide spatial navigation. Likewise, the commands for navigating in a fixed direction and distance to reach a desired goal object using *object vector cells* (Deshmukh and Knierim, 2011; Saleem, 2019), and for reaching a nearby object without navigational movement using *motor difference vectors*, both involve similar computations, albeit in different parts of the brain (e.g., Georgopoulos et al., 1981, 1982; Bullock and Grossberg, 1988; Gnadt and Grossberg, 2008). This extension of the classical What and Where cortical "two stream hypothesis" (Mishkin, 1982; Mishkin et al., 1983; Goodale et al., 1991; Goodale and Milner, 1992) has been further developed and refined by several authors (e.g., Hoang et al., 2018; Nilssen et al., 2019).

Below the discussion of CA1 will begin with an analysis of how an intrinsic theta rhythm enables large numbers of converging signals to be processed and tuned by learning on the dendrites of their target cells.

## 4.1. Preventing Saturation of Learned Synapses by Dissociating Read-Out and Read-In

I suggest that the intrinsic theta rhythm is an emergent property within the hippocampus of how our brains solve a general learning problem: If many learning trials continue throughout life, then what prevents the learned adaptive weights at synapses from saturating; that is, from hitting their maximal values and becoming unable to learn new associative contingencies in the future? A basic neural circuit called a REcurrent Associative Dipole, or READ, circuit (**Figure 12**) is able to regulate cognitive-emotional learning in response to rewards and punishments throughout the lifespan without saturating the adaptive weights that input to its *opponent* affective representations (Grossberg, 1972, 1975, 1982a, 1984; Grossberg and Schmajuk, 1987; Dranias et al., 2008; Gnadt and Grossberg, 2008; Grossberg et al., 2008), such as fear vs. relief.

The READ circuit does this by carrying out a process that I call *dissociation of associative read-out from read-in*, which leads in a natural way to a theta rhythm, as explained below. Many other brain systems realize this dissociation, including within the CA1 region of the hippocampus, to solve a general learning problem that I will describe after noting some important features of the READ circuit. Hasselmo (2005) has described

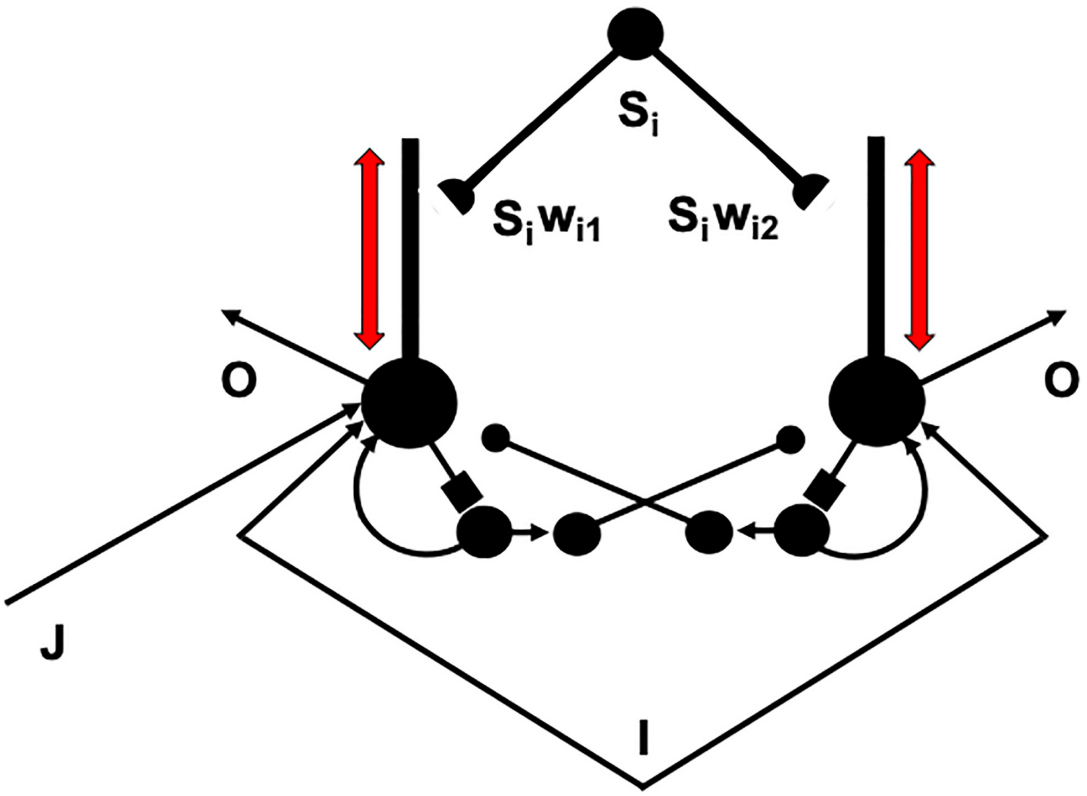


**FIGURE 12 |** A recurrent associative dipole, or READ, circuit is a recurrent shunting opponent processing network with habituative transmitter gates. The large closed disks represent opponent ON and OFF cells. The vertical rectangular bars that abut from them represent dendritic trees. Excitatory network pathways end in arrows. Inhibitory pathways end in closed disks. Habituative pathways end in squares. A nonspecific arousal input I equally excites the ON and OFF cells. A phasic input J activates only the ON cell in this circuit, but different phasic inputs can in general activate ON and OFF cells. Sensory cues $S_i$ sample the dendrites with LTM traces $w_{i1}$ and $w_{i2}$ and thereby become conditioned reinforcers when their abutting dendrite is activated by a back-propagating action potential (upward red arrow). Read-out from a conditioned reinforcer travels down the dendrite to the corresponding cell body (downward red arrow) (see the text for details; adapted with permission from Grossberg and Schmajuk, 1987).

neurobiological data that are consistent with such a dissociation and his model of it.

## 4.2. Uniform Activity Patterns Are Suppressed by a Recurrent On-Center Off-Surround Network

The problem is that read-*out* of a previously learned adaptive weight, such as $w_{i1}$ or $w_{i2}$ in **Figure 12**, to a target cell should *not* always trigger new learning—that is, read-*in*—by that adaptive weight, even if it succeeds in activating its target cell. Correlation learning *per se* is not sufficient. To understand why automatic read-in would cause a serious problem, consider the *total activity pattern* across all the cells of a network, not just the activity of a single cell. Multiple inputs can converge on each cell across such a network from multiple cue-activated stimuli, such as the signals $S_i$ in **Figure 12**. Each input can be active at different times and with different magnitudes to each cell in the network.

Consider what happens when all the inputs that converge upon the network's cells sum up to create approximately equal *total* inputs to *all* the cells; that is, a *uniform* input pattern perturbs the network. If this state of affairs persists for a while, then all activities the network's cells will also become approximately equal. Such a uniform pattern of activities carries no information because it does not prefer any particular feature combination that is represented by a subset of these cells to any other. A uniform activity pattern thus represents functional "noise." It should *not* drive new learning, because if it did, then previous learning could quickly be washed away by new learning of "noise." In order to avoid this disaster, associative read-out cannot always force new associative read-in. Somehow the "noise" must be suppressed, so that only the information in non-uniform feature patterns can be learned.

## 4.3. Competition Chooses Cells That Trigger Back-Propagating Teaching Signals

A READ circuit accomplishes noise suppression by letting contrast-enhancing competition—embodied by a recurrent on-center off-surround network—occur across the network in response to each input pattern (**Figure 12**), before the population that wins the competitive choice generates a teaching signal that drives new learning. If all the inputs are approximately equal,

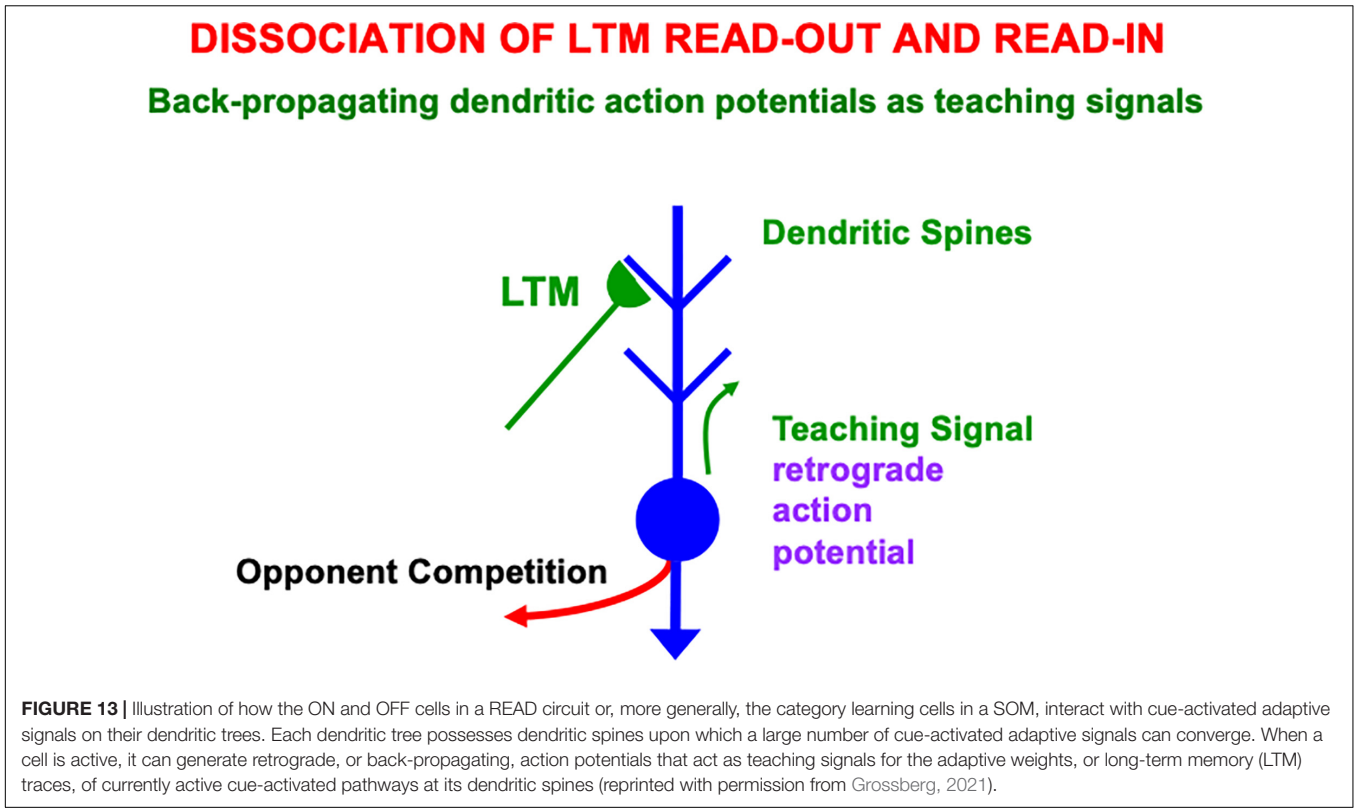


**FIGURE 13 |** Illustration of how the ON and OFF cells in a READ circuit or, more generally, the category learning cells in a SOM, interact with cue-activated adaptive signals on their dendritic trees. Each dendritic tree possesses dendritic spines upon which a large number of cue-activated adaptive signals can converge. When a cell is active, it can generate retrograde, or back-propagating, action potentials that act as teaching signals for the adaptive weights, or long-term memory (LTM) traces, of currently active cue-activated pathways at its dendritic spines (reprinted with permission from Grossberg, 2021).

then the uniform activity pattern that they cause is suppressed by the competition, no teaching signal will be emitted, and no new learning occurs. If some inputs are sufficiently bigger than others, then their activities will be contrast-enhanced, normalized, and stored by the recurrent on-center off-surround network, while the smaller activities are suppressed by the competition. A teaching signal will be emitted only by cells whose activities win the competition. Only the winning cells will therefore be able to drive learning of the incoming input pattern.

How does a winning activity trigger a teaching signal? In the READ circuit, the winning cells remain active long enough to trigger back-propagating action potentials in their dendrites (**Figures 12**, **13**), while they maintain their activities via the recurrent on-center off-surround interactions. These back-propagating action potentials serve as teaching signals that are associated with simultaneously active input signals to the chosen dendrites (Grossberg, 1975, 1982a; Markram et al., 1995, 1997; Magee and Johnston, 1997). If, for example, signal $S_3$ in **Figure 12** is active when the dendrite of cell $C_1$ is active (upward pointing red arrow), then the LTM trace $w_{31}$ will learn that association, while the LTM trace $w_{32}$ decreases because its abutting dendrite is then inactive.

Because the READ circuit is a recurrent on-center off-surround network whose cells obey shunting dynamics (Grossberg, 2013b), the competition computes teaching signals that are *normalized net activities* in which the smaller activity is inhibited to zero and the larger activity is sensitive to the ratio of the inputs. The LTM traces can continue to learn these normalized net values throughout life, without ever saturating.

## 4.4. A Rhythm Enables Associative Read-In and Read-Out Without a Noise-Learning Catastrophe

An electrical signal cannot go both down a dendrite and up it at the same time. Read-*out* from a previously learned LTM weight occurs when a signal goes down a dendrite to its basal cell. Read-*in* of a new LTM weight value occurs when a teaching signal goes up the dendrite from its basal cell. A single cue-activated signal $S_i$ that persists for hundreds of milliseconds or seconds needs to be able to read-out its previously learned LTM weight *and* to read-in any new information with which it is associated. A cyclic rhythm of signaling down and up the sampled dendrites enables a sustained input signal to experience both associative read-in and read-out on its abutting dendrites, without incurring a noise-learning catastrophe. Such a dendritic rhythm is the price of avoiding noise-driven catastrophic forgetting of previously learned featural differences.

In summary, the following cyclic processes are needed to dissociate associative read-out from read-in:

1. Read-*out* of cue-activated LTM-gated signals, as from the conditionable signals $S_i w_{ij}$ with adaptive weights $w_{ij}$, $j = 1,2$, in the READ circuit in **Figure 12**;
2. contrast-enhancing competition via the recurrent on-center off-surround feedback loop in **Figure 12**;
3. read-*in* of the contrast-enhanced and normalized activities into the adaptive weights $w_{ij}$ in **Figure 12**; and
4. repeat.

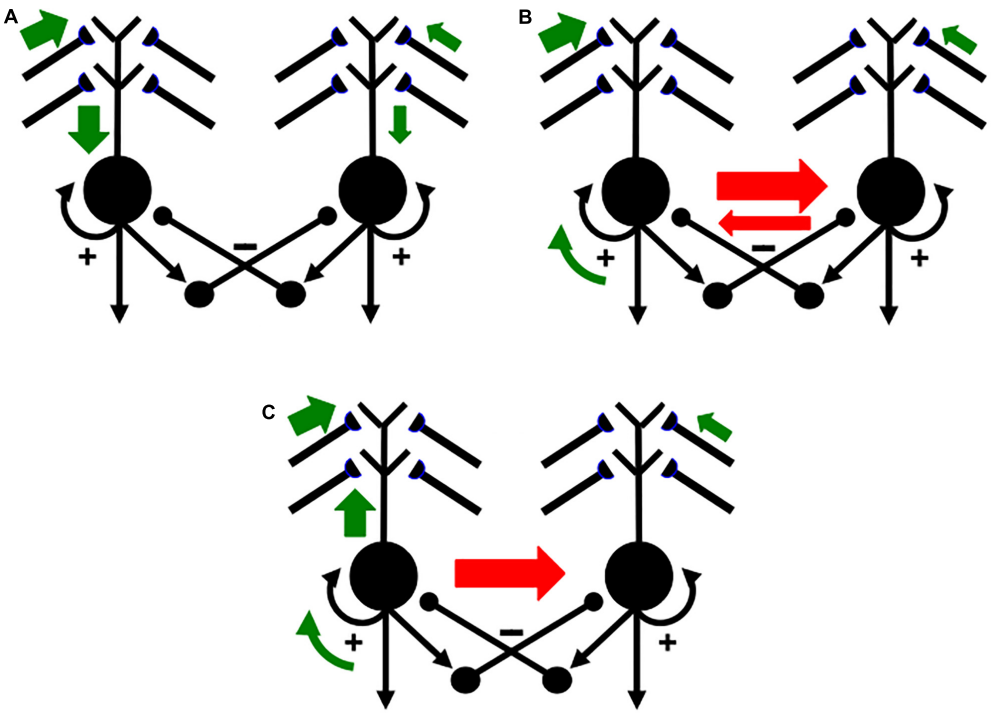


**FIGURE 14 |** Activation and learning dynamics on the dendritic spines of cells in a READ circuit or SOM. Green arrows depict currently active excitatory signals. Red arrows depict currently active inhibitory signals. The sizes of the arrows depict the relative strength of their signals (see the text for details; reprinted with permission from Grossberg, 2021).

## 4.5. SOM Theta Rhythm Dissociates Read-Out From Read-In With Back-Propagating Teaching Signals

Such a recurring read-out/choice/read-in cycle is assumed to also occur in self-organizing maps, or SOMs, during perceptual, cognitive, and spatial category learning (e.g., **Figure 7A**), not just in opponent READ circuits during reinforcement learning. A theta rhythm results in all these cases.

**Figure 14** summarizes how this cycle is proposed to occur in greater detail. **Figure 14A** shows two competing SOM category cells that each receive multiple inputs via their dendritic trees, which are drawn above the cell bodies. Dendritic trees greatly expand the total surface area where large numbers of inputs from multiple sources can send signals that converge upon a single cell (Rall, 1959, 1962, 1995). Both entorhinal grid cells (Schmidt-Hieber et al., 2017) and hippocampal place cells (Sheffield and Dombeck, 2015) have dendritic trees. In the hippocampus, these inputs arrive from the feature detectors of the SOM spatial category learning cells, whether from stripe cells to developing grid cells, or from developing grid cells to developing place cells (**Figure 2**).

In **Figure 14A**, the left cell receives a bigger total input than the right cell (thick vs. thin green arrows). The left cell can therefore inhibit the right cell more than conversely (thick vs. thin red arrows in **Figure 14B**) while its activity is contrast-enhanced by its recurrent on-center (curved green arrow). The left cell can hereby win the competition with the right cell and shut it off. As this is happening, the winning left cell also generates a back-propagating action potential through its dendritic tree (upward green arrow in **Figure 14C**; see also **Figure 12**). This back-propagating action potential is a teaching signal that drives associative learning in the LTM traces of pathways that are currently inputting to that dendritic tree. These dynamics repeat themselves through time as different input patterns choose different winning category cells.

Buzsáki (2002) summarizes many facts about the theta rhythm that are consistent with the above explanation. Buzsáki notes, in particular, that "theta oscillation may provide a mechanism for bringing together in time afferent-induced depolarization of pyramidal cell dendrites and dendritic invasion of fast spikes, the key elements for the induction of synaptic plasticity" (p. 325). His discussion describes many useful biophysical facts about this kind of learning, but not in terms of the basic design problem of how it prevents the catastrophic forgetting due to massive learning of noise that would have occurred without dissociation of associative read-out from read-in.

## 4.6. Gated Dipole Fields

The cyclic nature of this process can now be better understood mechanistically. As noted above, the first reason for cyclic learning is that an electrical signal cannot go both down a dendrite (**Figure 14A**) and up it (**Figure 14C**) at the same time. This property requires a rhythmic alternation between the down-state of read-out of previously learned memories, and the up-state

of read-in of new, or memory-refining, inputs. But how is this functional property achieved mechanistically?

The proposed answer, briefly stated, is by designing the competition that interpolates intervals of read-out and read-in as a *gated dipole field* (Grossberg, 1972, 1982a,b, 1984). A gated dipole field is simply a recurrent shunting on-center off-surround network whose recurrent feedback signals, notably its positive on-center feedback signals, *habituate* in an activity-dependent way, as illustrated by the habituative positive feedback signals (square synapses) in **Figure 12**. This activity-dependent habituation gradually weakens the signal that it gates through time. This simple refinement endows a gated dipole field with remarkable properties that are proved mathematically in the above articles, and which clarify why this network design occurs in multiple parts of the brain. Grossberg (2013b) more fully describes concepts and equations for recurrent shunting on-center off-surround networks and activity-dependent habituation.

In ART category learning circuits (**Figure 7**), a gated dipole field controls the recurrent competition between recognition categories at level $F_2$ of the network. This recurrent competition chooses the category that receives the largest total input from the currently active bottom-up feature pattern (**Figure 7A**). When the chosen category is activated, it reads-out a top-down learned expectation. A sufficiently big mismatch between the currently active bottom-up feature pattern and top-down learned expectation pattern (**Figure 7B**) can activate the orienting system (**Figure 7C**). Such activation causes a burst of nonspecific arousal that is delivered equally to all the category learning and recognition cells at level $F_2$, in keeping with the heuristic idea that "novel events are arousing."

Such a nonspecific novelty burst selectively resets the currently active category at $F_2$, leading to a memory search, or hypothesis testing, that ends by choosing a better matching category. But how does a *nonspecific* input *selectively* do *anything*? The answer is that the positive feedback signal in the on-center of the gated dipole weakens through time due to activity-dependent habituation. As a result, a nonspecific arousal burst can reset the currently active, but habituating cell, and thereby allow a better-matching category to get activated from among unhabituated category cells.

## 4.7. Gated Dipole Fields Control Perseveration, Normalization, Choice, Search, and Theta Rhythm

The same property of activity-dependent habituation that resets a currently active category in response to a nonspecific arousal burst is also responsible for preventing preservation of category activation when there is no reset. Said in another way, without activity-dependent habituation or competitive reset, the STM storage of activity by a recurrent on-center off-surround network could last indefinitely.

Activity-dependent habituation limits perseveration of the on-center activity in every gated dipole field. As one quantitatively simulated example, psychophysical data about visual persistence have been quantitatively simulated by a gated dipole network (Francis et al., 1994; Francis and Grossberg, 1996a,b). As the on-center habituates, the recurrent off-surround is disinhibited, and inhibits the previously active on-center cell. As the inhibited on-center recovers from habituation, its driving input can fire it again, after which the cycle repeats itself for as long as the input remains on.

Remarkable parsimony of design is realized by a gated dipole field because this single type of network normalizes total network activity, chooses winning category cells, limits perseveration, drives memory search, and supports a theta rhythm.

## 4.8. Why Phase Precession of the Theta Rhythm?

Using back-propagating action potentials as teaching signals also helps to explain intriguing parametric properties of the theta rhythm, such as the famous *phase precession* whereby action potentials occur on progressively earlier phases of the theta cycle as a rat traverses the place field of the recorded unit (O'Keefe and Recce, 1993; Skaggs et al., 1996). Phase precession in the GridPlaceMap model follows from two interacting properties:

First, each SOM category cell is activated through time via a receptive field whose input connections increase in strength as an animal navigates closer to the center of the receptive field. A Gaussian receptive field is a classical example.

Second, the category cells interact via shunting dynamics. As a result, larger inputs are integrated more quickly through time. Cells are thus activated earlier in each theta cycle as the center of the cell's receptive field is approached.

In summary, key properties of phase precession occur in the GridPlaceMap model because its category cells interact via shunting recurrent on-center off-surround networks whose cells receive inputs from receptive fields whose connections increase in strength as the animal approaches each cell's preferred position.

In addition to grid cells and place cells, several other types of cells have been reported that help to create a representation of space that animals use while they navigate. One such cell type is called a *border cell* because it fires when an animal is at or near the border of an enclosure. Solstad et al. (2008, p. 1865) reported that border cells are found throughout the MEC, as well as the parasubiculum, and "may be instrumental in planning trajectories and anchoring grid fields and place fields to a geometric reference frame." I will defer a discussion and analysis of how border cells may form and work to another place and time.

## 4.9. Theta-Modulated Gamma Rhythms

Another interesting and functionally important emergent property of the model presented here is the existence of theta-modulated gamma rhythms, whose existence follows immediately from the occurrence in SMART (Grossberg and Versace, 2008) of gamma oscillations in a match state that are modulated by an underlying theta rhythm. Compatible data are reported by Sirota et al. (2008, p. 683) who noted: "A significant fraction of putative pyramidal cells and interneurons as well as localized gamma oscillations in all recorded neocortical areas were phase biased by the hippocampal theta rhythm. We hypothesize that temporal coordination of neocortical gamma oscillators by hippocampal

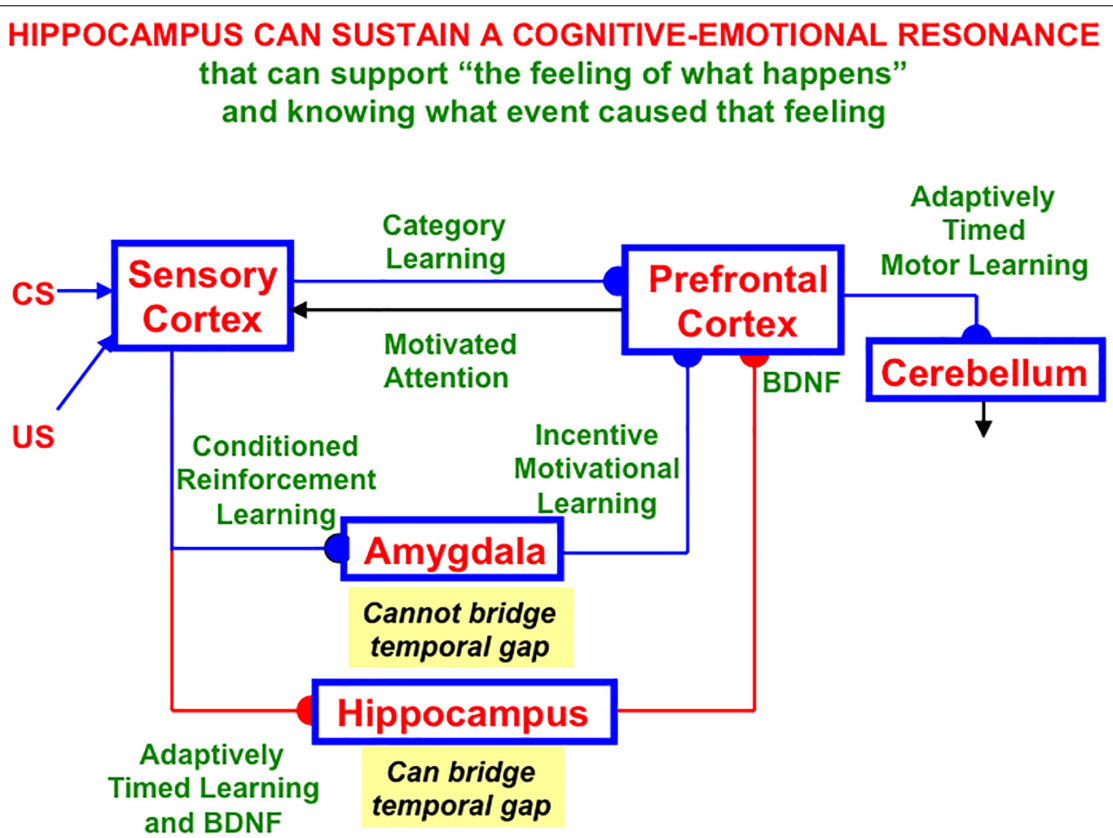


**FIGURE 15 |** The neurotrophic START, or nSTART, model. Multiple types of learning and neurotrophic mechanisms of memory consolidation cooperate in these circuits to generate adaptively timed responses. Connections from sensory cortex to orbitofrontal cortex support category learning. Reciprocal connections from orbitofrontal cortex to sensory cortex support attention. Habituative transmitter gates modulate excitatory conductances at all processing stages. Connections from sensory cortex to amygdala connections support conditioned reinforcer learning. Connections from amygdala to orbitofrontal cortex support incentive motivation learning. Hippocampal adaptive timing and brain-derived neurotrophic factor (BDNF) bridge temporal delays between CS offset and US onset during trace conditioning acquisition. BDNF also supports long-term memory (LTM) consolidation within sensory cortex to hippocampal pathways and from hippocampal to orbitofrontal pathways. The pontine nuclei serve as a final common pathway for reading-out conditioned responses. Cerebellar dynamics are not simulated in nSTART. arrowhead = excitatory synapse; hemidisk = adaptive weight; square = habituative transmitter gate (reprinted with permission from Grossberg, 2021).

theta is a mechanism by which information contained in spatially widespread neocortical assemblies can be synchronously transferred to the associative networks of the hippocampus." These cortical areas include the primary somatosensory area and the prefrontal cortex. "These data suggest that theta oscillation entrainment provides a mechanism by which activity in spatially widespread neocortical and hippocampal networks can be temporally coordinated. . .during either exploration or REM sleep" (p. 693) (see also Montgomery et al., 2009; Fujisawa and Buzsáki, 2011; Ito et al., 2018).

This conclusion carries the classical proposal of Freeman (1975) about the role of theta in organizing sensory information processing into temporal series of spatial patterns into the more modern context of theta-modulated gamma and beta oscillations occurring during periods of match and mismatch, or resonance and reset. Colgin (2015) has additionally described how such a theta-gamma coupling arises during a wide range of other behavioral paradigms, including word recognition, delayed non-match-to-place, and visual processing by cortical areas V1 and V2.

## 5. ADAPTIVELY TIMED REGULATION OF CATEGORY LEARNING: THETA, GAMMA, AND BETA OSCILLATIONS

The current article reviews, unifies, and extends neural modeling concepts that clarify how and why both extrinsic and intrinsic theta rhythms occur. Earlier modeling articles proposed how the hippocampus interacts with multiple brain regions to carry out various cognitive, emotional, and adaptive timing processes, and how these processes interact together during learning experiences. Some of these models have been discussed above, including the Adaptive Resonance Theory, or ART, models for cognitive, motor, and spatial category learning and the SOVEREIGN models for incrementally learning planned action sequences to navigate toward rewarded goals. SOVEREIGN2 summarizes a much larger number of brain processes that have been modeled over the years. These processes have yet to be synthesized within a mathematically rigorous comprehensive neural architecture.

### 5.1. Two Distinct, but Interacting, Hippocampal Mechanisms of Memory Consolidation

The START, or Spectrally Timed ART, model and its neurotrophically modulated refinement, nSTART (**Figure 15**; Grossberg and Merrill, 1992, 1996; Franklin and Grossberg, 2017), deserve special mention because they clarify how the hippocampus can coordinate ART category learning and memory consolidation with the adaptively timed learning, performance, and memory consolidation that are regulated by the LEC and the hippocampus to which it projects, all the while modulated by a theta rhythm.

The first mechanism of memory consolidation uses the ART hypothesis testing and category learning cycle (**Figure 7**) in the form of a cycle of resonance and reset. As explained above, the orienting system is activated by a sufficiently bad mismatch between the bottom-up sensory input pattern that activates the feature level $F_1$ and the top-down learned expectation that is read-out from category level $F_2$. This mismatch reduces inhibition of the orienting system, as in **Figure 7B**, which begins a memory search for a better matching category by triggering a nonspecific arousal burst to $F_2$, as in **Figure 7C**. The hippocampus is part of this novelty-sensitive orienting system. As objects and events become familiar due to the learning cycle, they can directly access and resonate with their best matching category without any memory search. The familiar object or event has hereby learned a self-stabilizing memory, which illustrates a form of dynamically maintained memory consolidation.

As simulated by the SMART model (Grossberg and Versace, 2008), the cycle of resonance and reset is embodied by a cycle of gamma oscillations and beta oscillations. As noted in Section 3.4, although theta oscillations have not yet been quantitatively simulated during this gamma-beta cycle, the manner in which a theta rhythm organizes sequences of brain states leads naturally to the existence of theta-modulated gamma rhythms that are interrupted by intervals of beta rhythm during hypothesis testing and memory search.

Carpenter and Grossberg (1993) and Grossberg (2013a) have proposed how these memory consolidation properties can qualitatively explain data about medial temporal amnesia when the model hippocampus is ablated, thereby eliminating memory search before consolidation can occur. Such an ablation leads to properties of unlimited anterograde amnesia, limited retrograde amnesia, perseveration, difficulties in orienting to novel cues, a failure of recombinant context-sensitive processing, and different degrees of learning by amnesic and normal individuals on easy vs. demanding categorization tasks. Lesions in CA1 during transient global amnesia are correlated with a corresponding deterioration of the theta rhythm (Park et al., 2016).

In nSTART, neuromodulation by Brain Derived Neurotrophic Factor, or BDNF, sustains cortico-cortical resonances that strengthen partial learning based on previous sensory inputs. Here both the hippocampus and the cerebellum participate in adaptively timed learning (Grossberg and Merrill, 1996). The hippocampus maintains adaptively timed incentive motivational signals between active cells in the sensory cortex and the prefrontal cortex, notably orbitofrontal cortex, when visual categories are being learned. The adaptively timed hippocampal support enables thalamocortical and corticocortial category learning (see horizontal pathway from sensory cortex to prefrontal cortex in **Figure 15**) to occur between events that are separated in time.

Such temporal separation occurs during trace conditioning when a conditioned stimulus (CS), such as a light or tone, shuts off hundreds of milliseconds before a rewarding or punishing unconditioned stimulus (US), such as a shock or food, turns on. This requires that a CS-activated memory trace be sustained during the inter-stimulus interval in order to learn an adaptively timed association between CS and US that enables the CS to elicit a CR. As these categories are learned, the hippocampus maintains inhibition of the orienting system (not shown), so that motivated attention can be maintained throughout the adaptively timed category learning interval. The prefrontal cortex can also, at the same time, learn to activate adaptively timed actions via the cerebellum. When category learning and performance is complete, the hippocampus is disengaged, memory consolidation has occurred, and the CS alone can elicit an adaptively timed conditioned response (CR). Franklin and Grossberg (2017) review data properties that nSTART simulates when consolidation is prevented. Different properties of early vs. late hippocampal lesions are challenging to explain because no training occurs after conditioning and before hippocampal ablation.

Data about theta modulation have been reported in autistic individuals (Lushchekina et al., 2014). The imbalanced START, or iSTART model (Grossberg, 2017a) shows how, if START becomes imbalanced in particular ways, then autistic symptoms arise (Grossberg and Seidman, 2006). iSTART proposes that various individuals with autism have their vigilance stuck at an abnormally high value due to abnormal cholinergic activity, leading to abnormal orienting and memory search, learning of hyperspecific recognition categories, and a narrow focus of attention. Abnormal iSTART orienting causes abnormal beta oscillations, which have been reported (Buard et al., 2018; de Vega et al., 2019). The breakdown of a fluent response to changing environmental challenges by autistic individuals would be expected to alter their theta rhythms. Indeed, lower levels of theta spectral power and mean coherence then occur (Lushchekina et al., 2014).

## 6. CONCLUDING REMARKS

This article summarizes neural models of cortico-hippocampo-cerebellar dynamics and of the gamma, beta, and theta rhythms that underlie these dynamics during both normal and abnormal conditions.

## AUTHOR CONTRIBUTIONS

The author confirms being the sole contributor of this work and has approved it for publication.

## REFERENCES


Amaral, D. G. (1993). Emerging principles of intrinsic hippocampal organization. *Curr. Opin. Neurobiol.* 3, 225–229. doi: 10.1016/0959-4388(93)90214-j

Amaral, D. G., and Witter, M. P. (1989). The three-dimensional organization of the hippocampal formation: a review of anatomical data. *Neuroscience* 31, 571–591. doi: 10.1016/0306-4522(89)90424-7

Ames, H., and Grossberg, S. (2008). Speaker normalization using cortical strip maps: a neural model for steady state vowel categorization. *J. Acoust. Soc. Am.* 124, 3918–3936. doi: 10.1121/1.2997478

Aminoff, E., Gronau, N., and Bar, M. (2007). The parahippocampal cortex mediates spatial and nonspatial associations. *Cereb. Cortex* 17, 1493–1503. doi: 10.1093/cercor/bhl078

Banquet, J.-P., Gaussier, P., Cuperlier, N., Hok, V., Save, T., Pucet, B., et al. (2020). Time as the fourth dimension in the hippocampus. *Prog. Neurobiol.* 199:101920. doi: 10.1016/j.pneurobio.2020.101920

Bennett, T. L. (1971). Hippocampal theta activity—a review. *Commun. Behav. Biol.* 6, 37–68.

Berke, J. D., Hetrick, V., Breck, J., and Green, R. W. (2008). Transient 23-30 Hz oscillations in mouse hippocampus during exploration of novel environments. *Hippocampus* 18, 519–529. doi: 10.1002/hipo.20435

Bland, B. H., and Colom, L. V. (1993). Extrinsic and intrinsic properties underlying oscillation and synchrony in limbic cortex. *Prog. Neurobiol.* 41, 157–208. doi: 10.1016/0301-0082(93)90007-f

Brandon, M. P., Bogaard, A. R., Libby, C. P., Connerney, M. A., Gupta, K., and Hasselmo, M. E. (2011). Reduction of theta rhythm dissociates grid cell spatial periodicity from directional tuning. *Science* 332, 595–599. doi: 10.1126/science.1201652

Brockmole, J. R., Castelhano, M. S., and Henderson, J. M. (2006). Contextual cueing in naturalistic scenes: global and local contexts. *J. Exp. Psychol. Learn. Mem. Cogn.* 32, 699–706. doi: 10.1037/0278-7393.32.4.699

Brown, J., Bullock, D., and Grossberg, S. (1999). How the basal ganglia use parallel excitatory and inhibitory learning pathways to selectively respond to unexpected rewarding cues. *J. Neurosci.* 19, 10502–10511. doi: 10.1523/jneurosci.19-23-10502.1999

Brown, J. W., Bullock, D., and Grossberg, S. (2004). How laminar frontal cortex and basal ganglia circuits interact to control planned and reactive saccades. *Neural Netw.* 17, 471–510. doi: 10.1016/j.neunet.2003.08.006

Brun, V. H., Solstad, T., Kjelstrup, K. B., Fyhn, M., Witter, M. P., Moser, E. I., et al. (2008). Progressive increase in grid scale from dorsal to ventral medial entorhinal cortex. *Hippocampus* 18, 1200–1212. doi: 10.1002/hipo.20504

Buard, I., Kronberg, E., Steinmetz, S., Hepburn, S., and Rojas, D. C. (2018). Neuromagnetic beta-band oscillations during motor imitation in youth with autism. *Autism Res. Treat.* 2018:9035793. doi: 10.1155/2018/9035793

Buffalo, E. A., Fries, P., Landman, R., Buschman, T. J., and Desimone, R. (2011). Laminar differences in gamma and alpha coherence in the ventral stream. *Proc. Natl. Acad. Sci. U.S.A.* 108, 11262–11267. doi: 10.1073/pnas.1011284108

Bullock, D., and Grossberg, S. (1988). Neural dynamics of planned arm movements: emergent invariants and speed-accuracy properties during trajectory formation. *Psychol. Rev.* 95, 49–90. doi: 10.1037/0033-295x.95.1.49

Buschman, T. J., and Miller, E. K. (2007). Top–down versus bottom–up control of attention in the prefrontal and posterior parietal cortices. *Science* 315, 1860–1862. doi: 10.1126/science.1138071

Buzsáki, G. (2002). Theta oscillations in the hippocampus. *Neuron* 33, 325–340. doi: 10.1016/s0896-6273(02)00586-x

Buzsáki, G. (2005). Theta rhythm of navigation: link between path integration and landmark navigation, episodic, and semantic memory. *Hippocampus* 15, 827–840. doi: 10.1002/hipo.20113

Buzsáki, G., and Moser, E. I. (2013). Memory, navigation, and theta rhythm in the hippocampal-entorhinal system. *Nat. Neurosci.* 16, 130–138. doi: 10.1038/nn.3304

Cao, Y., Grossberg, S., and Markowitz, J. (2011). How does the brain rapidly learn and reorganize view- and positionally-invariant object representations in inferior temporal cortex? *Neural Netw.* 24, 1050–1061. doi: 10.1016/j.neunet.2011.04.004

Cao, Y., Roy, S., Sachdev, R. N. S., and Heck, D. H. (2012). Dynamic correlation between whisking and breathing rhythms in mice. *J. Neurosci.* 32, 1653–1659. doi: 10.1523/jneurosci.4395-11.2012

Carpenter, G. A., and Grossberg, S. (1987a). A massively parallel architecture for a self-organizing neural pattern recognition machine. *Comput. Vis. Graph. Image Process.* 37, 54–115. doi: 10.1016/s0734-189x(87)80014-2

Carpenter, G. A., and Grossberg, S. (1987b). ART 2: stable self-organization of pattern recognition codes for analog input patterns. *Appl. Opt.* 26, 4919–4930. doi: 10.1364/ao.26.004919

Carpenter, G. A., and Grossberg, S. (1993). Normal and amnesic learning, recognition, and memory by a neural model of cortico-hippocampal interactions. *Trends Neurosci.* 16, 131–137. doi: 10.1016/0166-2236(93)90118-6

Carpenter, G. A., Grossberg, S., Markuzon, N., Reynolds, J. H., and Rosen, D. B. (1992). Fuzzy ARTMAP: a neural network architecture for incremental supervised learning of analog multidimensional maps. *IEEE Trans. Neural Netw.* 3, 698–713. doi: 10.1109/72.159059

Carpenter, G. A., Grossberg, S., and Mehanian, C. (1989). Invariant recognition of cluttered scenes by a self- organizing ART architecture: CORT-X boundary segmentation. *Neural Netw.* 2, 169–181. doi: 10.1016/0893-6080(89)90002-6

Carpenter, G. A., Grossberg, S., and Reynolds, J. H. (1991a). ARTMAP: supervised realtime learning and classification of nonstationary data by a self-organizing neural network. *Neural Netw.* 4, 565–588. doi: 10.1016/0893-6080(91)90012-t

Carpenter, G. A., Grossberg, S., and Rosen, D. B. (1991b). Fuzzy ART: fast stable learning and categorization of analog patterns by an adaptive resonance system. *Neural Netw.* 4, 759–771. doi: 10.1016/0893-6080(91)90056-b

Chang, H.-C., Grossberg, S., and Cao, Y. (2014). Where's Waldo? How perceptual cognitive, and emotional brain processes cooperate during learning to categorize and find desired objects in a cluttered scene. *Front. Integr. Neurosci.* 8:43. doi: 10.3389/fnint.2014.00043

Chen, C., King, J. A., Burgess, N., and O'Keefe, J. (2013). How vision and movement combine in the hippocampal place code. *Proc. Natl. Acad. Sci. U.S.A.* 110, 378–383. doi: 10.1073/pnas.1215834110

Chun, M. M., and Jiang, Y. (1998). Contextual cueing: implicit learning and memory of visual context guides spatial attention. *Cogn. Psychol.* 36, 28–71. doi: 10.1006/cogp.1998.0681

Colgin, L. L. (2015). Theta-gamma coupling in the entorhinal-hippocampal system. *Curr. Opin. Neurobiol.* 31, 45–50. doi: 10.1016/j.conb.2014.08.001

Davis, S., Butcher, S. P., and Morris, R. G. (1992). The NMDA receptor antagonist D-2-amino-5-phosphonopentanoate (D-AP5) impairs spatial learning and LTP in vivo at intracerebral concentrations comparable to those that block LTP in vivo. *J. Neurosci.* 12, 21–34. doi: 10.1523/jneurosci.12-01-00021.1992

de Vega, M., Padrón, I., Moreno, I. Z., García-Marco, E., Domínguez, A., Marrero, H., et al. (2019). Both the mirror and the affordance systems might be impaired in adults with high autistic traits. Evidence from EEG mu and beta rhythms. *Autism Res.* 12, 1032–1042. doi: 10.1002/aur.2121

DeCoteau, W. E., Thorn, C., Gibson, D. J., Courtemanche, R., Mitra, P., Kubota, Y., et al. (2007). Learning-related coordination of striatal and hippocampal theta rhythms during acquisition of a procedural maze task. *Proc. Natl. Acad. Sci. U.S.A.* 104, 5644–5649. doi: 10.1073/pnas.0700818104

Deshmukh, S. S., and Knierim, J. J. (2011). Representation of non-spatial and spatial information in the lateral entorhinal cortex. *Front. Behav. Neurosci.* 5:69. doi: 10.3389/fnbeh.2011.00069

Dong, H.-W., Swanson, L. W., Chen, L., Fanselow, S., and Toga, A. W. (2009). Genomic-anatomic evidence for distinct functional domains in hippocampal field CA1. *Proc. Natl. Acad. Sci. U.S.A.* 106, 11794–11799. doi: 10.1073/pnas.0812608106

Dranias, M., Grossberg, S., and Bullock, D. (2008). Dopaminergic and non-dopaminergic value systems in conditioning and outcome-specific revaluation. *Brain Res.* 1238, 239–287. doi: 10.1016/j.brainres.2008.07.013

Dumenko, V. N. (1968). Electrophysiological characteristics of the dynamic stereotype (in Russian, English summary). *Zh. Vyssh. Nerv. Deyat. Nosti* 18, 187–195.

Dumenko, V. N. (1970). "Electroencephalographic investigation of cortical relationships in dogs during formation of a conditioned reflex stereotype," in *Electrophysiology of the Central Nervous System*, ed. V. S. Rusinov (New York, NY: Plenum Press), 107–118. trans. B. Haigh, and R. W. Doty. doi: 10.1007/978-1-4684-1755-5_9

Eckhorn, R., Bauer, R., Jordan, W., Brosch, M., Kruse, W., Munk, M., et al. (1988). Coherent oscillations: a mechanism of feature linking in the visual cortex? *Biol. Cybern.* 60, 121–130. doi: 10.1007/bf00202899

Eichenbaum, H., and Lipton, P. A. (2008). Towards a functional organization of themedial temporal lobe memory system: role of the parahippocampal and medial entorhinal cortical areas. *Hippocampus* 18, 1314–1324. doi: 10.1002/hipo.20500

Ellias, S. A., and Grossberg, S. (1975). Pattern formation, contrast control, and oscillations in the short-term memory of shunting on-center off-surround networks. *Biol. Cybern.* 20, 69–98. doi: 10.1007/bf00327046

Engel, A. K., Fries, P., and Singer, W. (2001). Dynamic predictions: oscillations and synchrony in top-down processing. *Nat. Rev. Neurosci.* 2, 704–716. doi: 10.1038/35094565

Erickson, R. P. (1963). "Sensory neural patterns and gustation," in *Olfaction and Taste*, ed. Y. Zotterman (New York, NY: Pergamon Press), 205–213. doi: 10.1016/b978-1-4831-9834-7.50021-4

Etienne, A. S., Maurer, R., and Séguinot, V. (1996). Path integration in mammals and its integration with visual landmarks. *J. Exp. Biol.* 199, 201–209.

Fenton, A. A., Kao, H.-Y., Neymotin, S. A., Olypher, A., Vayntrub, Y., Lytton, W. W., et al. (2008). Unmasking the CA1 ensemble place code by exposures to small and large environments: more place cells and multiple, irregularly arranged, and expanded place fields in the larger space. *J. Neurosci.* 28, 11250–11262. doi: 10.1523/jneurosci.2862-08.2008

Fiala, J. C., Grossberg, S., and Bullock, D. (1996). Metabotropic glutamate receptor activation in cerebellar Purkinje cells as substrate for adaptive timing of the classically conditioned eye blink response. *J. Neurosci.* 16, 3760–3774. doi: 10.1523/jneurosci.16-11-03760.1996

Francis, G., and Grossberg, S. (1996a). Cortical dynamics of boundary segmentation and reset: persistence, afterimages, and residual traces. *Perception* 25, 543–567. doi: 10.1068/p250543

Francis, G., and Grossberg, S. (1996b). Cortical dynamics of form and motion integration: persistence, apparent motion, and illusory contours. *Vis. Res.* 36, 149–173. doi: 10.1016/0042-6989(95)00052-2

Francis, G., Grossberg, S., and Mingolla, E. (1994). Cortical dynamics of feature binding and reset: control of visual persistence. *Vis. Res.* 34, 1089–1104. doi: 10.1016/0042-6989(94)90012-4

Franklin, D. J., and Grossberg, S. (2017). A neural model of normal and abnormal learning and memory consolidation: adaptively timed conditioning, hippocampus, amnesia, neurotrophins, and consciousness. *Cogn. Affect. Behav. Neurosci.* 17, 24–76. doi: 10.3758/s13415-016-0463-y

Freeman, W. J. (1972). "Waves, pulses, and the theory of neural masses," in *Progress in Theoretical Biology*, eds R. Rosen, and F. Snell (New York, NY: Academic Press), 87–165. doi: 10.1016/b978-0-12-543102-6.50010-8

Freeman, W. J. (1975). *Mass Action in the Nervous System*. New York, NY: Academic Press.

Fujisawa, S., and Buzsáki, G. (2011). A 4 Hz oscillation adaptively synchronizes prefrontal, VTA, and hippocampal activities. *Neuron* 72, 153–165. doi: 10.1016/j.neuron.2011.08.018

Gancarz, G., and Grossberg, G. (1998). A neural model of the saccade generator in the reticular formation. *Neural Netw.* 11, 1159–1174. doi: 10.1016/s0893-6080(98)00096-3

Georgopoulos, A. P., Kalaska, J. F., Caminiti, R., and Massey, J. T. (1982). On the relations between the direction of two-dimensional arm movements and cell discharge in primate motor cortex. *J. Neurosci.* 2, 1527–1537. doi: 10.1523/jneurosci.02-11-01527.1982

Georgopoulos, A. P., Kalaska, J. F., and Massey, J. T. (1981). Spatial trajectories and reaction times of aimed movements: effects of practice, uncertainty, and change in target location. *J. Neurophysiol.* 46, 725–743. doi: 10.1152/jn.1981.46.4.725

Gnadt, W., and Grossberg, S. (2008). SOVEREIGN: an autonomous neural system for incrementally learning planned action sequences to navigate towards a rewarded goal. *Neural Netw.* 21, 699–758. doi: 10.1016/j.neunet.2007.09.016

Goodale, M. A., and Milner, A. D. (1992). Separate visual pathways for perception and action. *Trends Neurosci.* 15, 20–25. doi: 10.1016/0166-2236(92)90344-8

Goodale, M. A., Milner, A. D., Jakobson, L. S., and Carey, D. P. (1991). A neurological dissociation between perceiving objects and grasping them. *Nature* 349, 154–156. doi: 10.1038/349154a0

Gorchetchnikov, A., and Grossberg, S. (2007). Space, time, and learning in the hippocampus: how fine spatial and temporal scales are expanded into population codes for behavioral control. *Neural Netw.* 20, 182–193. doi: 10.1016/j.neunet.2006.11.007

Gothard, K. M., Skaggs, W. E., and McNaughton, B. L. (1996). Dynamics of mismatch correction in the hippocampal ensemble code for space: interaction between path integration and environmental cues. *J. Neurosci.* 16, 8027–8040. doi: 10.1523/jneurosci.16-24-08027.1996

Goutagny, R., Jackson, J., and Williams, S. (2009). Self-generated theta oscillations in the hippocampus. *Nat. Neurosci.* 12, 1491–1493. doi: 10.1038/nn.2440

Gray, C. M., and Singer, W. (1989). Stimulus-specific neuronal oscillations in orientation columns of cat visual cortex. *Proc. Natl. Acad. Sci. U.S.A.* 86, 1698–1702. doi: 10.1073/pnas.86.5.1698

Green, J. D., and Arduini, A. A. (1954). Hippocampal electrical activity in arousal. *J. Neurophysiol.* 17, 533–557. doi: 10.1152/jn.1954.17.6.533

Gregoriou, G. G., Gotts, S. J., Zhou, H., and Desimone, R. (2009). High-frequency, long-range coupling between prefrontal and visual cortex during attention. *Science* 324, 1207–1210. doi: 10.1126/science.1171402

Grion, N., Akrami, A., Zuo, Y., Stella, F., and Diamond, M. E. (2016). Coherence between rat sensorimotor system and hippocampus is enhanced during tactile discrimination. *PLoS Biol.* 14:e1002384. doi: 10.1371/journal.pbio.1002384

Grossberg, S. (1968a). A prediction theory for some nonlinear functional-differential equations, II: learning of patterns. *J. Math. Anal. Appl.* 22, 490–522. doi: 10.1016/0022-247x(68)90190-x

Grossberg, S. (1968b). Some nonlinear networks capable of learning a spatial pattern of arbitrary complexity. *Proc. Natl. Acad. Sci. U.S.A.* 59, 368–372. doi: 10.1073/pnas.59.2.368

Grossberg, S. (1969). On learning and energy-entropy dependence in recurrent and nonrecurrent signed networks. *J. Stat. Phys.* 1, 319–350. doi: 10.1007/bf01007484

Grossberg, S. (1970). Some networks that can learn, remember, and reproduce any number of complicated space-time patterns, II. *Stud. Appl. Math.* 49, 135–166. doi: 10.1002/sapm1970492135

Grossberg, S. (1971). Pavlovian pattern learning by nonlinear neural networks. *Proc. Natl. Acad. Sci. U.S.A.* 68, 828–831. doi: 10.1073/pnas.68.4.828

Grossberg, S. (1972). A neural theory of punishment and avoidance, II: quantitative theory. *Math. Biosci.* 15, 253–285. doi: 10.1016/0025-5564(72)90038-7

Grossberg, S. (1973). Contour enhancement, short-term memory, and constancies in reverberating neural networks. *Stud. Appl. Math.* 52, 213–257. doi: 10.1002/sapm1973523213

Grossberg, S. (1975). A neural model of attention, reinforcement, and discrimination learning. *Int. Rev. Neurobiol.* 18, 263–327. doi: 10.1016/s0074-7742(08)60037-9

Grossberg, S. (1976a). Adaptive pattern classification and universal recoding, I: parallel development and coding of neural feature detectors. *Biol. Cybern.* 23, 121–134. doi: 10.1007/bf00344744

Grossberg, S. (1976b). Adaptive pattern classification and universal recoding, II: feedback, expectation, olfaction, and illusions. *Biol. Cybern.* 23, 187–202.

Grossberg, S. (1978). "A theory of human memory: self-organization and performance of sensory-motor codes, maps, and plans," in *Progress in Theoretical Biology*, Vol. 5, eds R. Rosen, and F. Snell (New York, NY: Academic Press), 233–374. doi: 10.1016/b978-0-12-543105-7.50013-0

Grossberg, S. (1980). How does a brain build a cognitive code? *Psychol. Rev.* 87, 1–51. doi: 10.1037/0033-295x.87.1.1

Grossberg, S. (1982a). A psychophysiological theory of reinforcement, drive, motivation, and attention. *J. Theor. Neurobiol.* 1, 286–369.

Grossberg, S. (1982b). Processing of expected and unexpected events during conditioning and attention: a psychophysiological theory. *Psychol. Rev.* 89, 529–572. doi: 10.1037/0033-295x.89.5.529

Grossberg, S. (1984). "Some psychophysiological and pharmacological correlates of a developmental, cognitive, and motivational theory," in *Brain and Information: Event Related Potentials*, eds R. Karrer, J. Cohen, and P. Tueting (New York, NY: New York Academy of Sciences), 58–151. doi: 10.1111/j.1749-6632.1984.tb23523.x

Grossberg, S. (2000). The complementary brain: unifying brain dynamics and modularity. *Trends Cogn. Sci.* 4, 233–246. doi: 10.1016/s1364-6613(00)01464-9

Grossberg, S. (2003). Resonant neural dynamics of speech perception. *J. Phon.* 31, 423–445. doi: 10.1016/s0095-4470(03)00051-2

Grossberg, S. (2009). Beta oscillations and hippocampal place cell learning during exploration of novel environments. *Hippocampus* 19, 881–885. doi: 10.1002/hipo.20602

Grossberg, S. (2013a). Adaptive resonance theory: how a brain learns to consciously attend, learn, and recognize a changing world. *Neural Netw.* 37, 1–47. doi: 10.1016/j.neunet.2012.09.017

Grossberg, S. (2013b). Recurrent neural networks. *Scholarpedia* 8:1888.

Grossberg, S. (2016). "Neural dynamics of the basal ganglia during perceptual, cognitive, and motor learning and gating," in *The Basal Ganglia: Novel Perspectives on Motor and Cognitive Functions*, ed. J.-J. Soghomonian (Berlin: Springer), 457–512. doi: 10.1007/978-3-319-42743-0_19

Grossberg, S. (2017a). Acetylcholine neuromodulation in normal and abnormal learning and memory: vigilance control in waking, sleep, autism, amnesia, and Alzheimer's disease. *Front. Neural Circuits* 11:82. doi: 10.3389/fncir.2017.00082

Grossberg, S. (2017b). Towards solving the hard problem of consciousness: the varieties of brain resonances and the conscious experiences that they support. *Neural Netw.* 87, 38–95. doi: 10.1016/j.neunet.2016.11.003

Grossberg, S. (2019). The embodied brain of SOVEREIGN2: from space-variant conscious percepts during visual search and navigation to learning invariant object categories and cognitive-emotional plans for acquiring valued goals. *Front. Comput. Neurosci.* 13:36. doi: 10.3389/fncom.2019.00036

Grossberg, S. (2020). A path towards explainable AI and autonomous adaptive intelligence: deep learning, adaptive resonance, and models of perception, emotion, and action. *Front. Neurobot.* 14:36. doi: 10.3389/fnbot.2020.00036

Grossberg, S. (2021). *Conscious Mind/Resonant Brain: How Each Brain Makes a Mind*. New York, NY: Oxford University Press.

Grossberg, S., Boardman, I., and Cohen, C. (1997a). Neural dynamics of variable-rate speech categorization. *J. Exp. Psychol. Hum. Percept. Perform.* 23, 481–503. doi: 10.1037/0096-1523.23.2.481

Grossberg, S., Bullock, D., and Dranias, M. (2008). Neural dynamics underlying impaired autonomic and conditioned responses following amygdala and orbitofrontal lesions. *Behav. Neurosci.* 122, 1100–1125. doi: 10.1037/a0012808

Grossberg, S., and Huang, T.-R. (2009). ARTSCENE: a neural system for natural scene classification. *J. Vis.* 9, 1–19.

Grossberg, S., and Kishnan, D. (2018). Neural dynamics of autistic repetitive behaviors and Fragile X syndrome: basal ganglia movement gating and mGluR-modulated adaptively timed learning. *Front. Psychol. Psychopathol.* 9:269. doi: 10.3389/fpsyg.2018.00269

Grossberg, S., and Merrill, J. W. L. (1992). A neural network model of adaptively timed reinforcement learning and hippocampal dynamics. *Cogn. Brain Res.* 1, 3–38. doi: 10.1016/0926-6410(92)90003-a

Grossberg, S., and Merrill, J. W. L. (1996). The hippocampus and cerebellum in adaptively timed learning, recognition, and movement. *J. Cogn. Neurosci.* 8, 257–277. doi: 10.1162/jocn.1996.8.3.257

Grossberg, S., Palma, J., and Versace, M. (2016). Resonant cholinergic dynamics in cognitive and motor decision-making: attention, category learning, and choice in neocortex, superior colliculus, and optic tectum. *Front. Neurosci.* 9:501. doi: 10.3389/fnins.2015.00501

Grossberg, S., and Pilly, P. K. (2012). How entorhinal grid cells may learn multiple spatial scales from a dorsoventral gradient of cell response rates in a self-organizing map. *PLoS Comput. Biol.* 8:e1002648. doi: 10.1371/journal.pcbi.1002648

Grossberg, S., and Pilly, P. K. (2014). Coordinated learning of grid cell and place cell spatial and temporal properties: multiple scales, attention, and oscillations. *Philos. Trans. R. Soc. B* 369:20120524. doi: 10.1098/rstb.2012.0524

Grossberg, S., Roberts, K., Aguilar, M., and Bullock, D. (1997b). A neural model of multimodal adaptive saccadic eye movement control by superior colliculus. *J. Neurosci.* 17, 9706–9725. doi: 10.1523/jneurosci.17-24-09706.1997

Grossberg, S., and Schmajuk, N. A. (1987). Neural dynamics of attentionally-modulated Pavlovian conditioning: conditioned reinforcement, inhibition, and opponent processing. *Psychobiology* 15, 195–240.

Grossberg, S., and Schmajuk, N. A. (1989). Neural dynamics of adaptive timing and temporal discrimination during associative learning. *Neural Netw.* 2, 79–102. doi: 10.1016/0893-6080(89)90026-9

Grossberg, S., and Seidman, D. (2006). Neural dynamics of autistic behaviors: cognitive, emotional, and timing substrates. *Psychol. Rev.* 113, 483–525. doi: 10.1037/0033-295x.113.3.483

Grossberg, S., and Somers, D. (1991). Synchronized oscillations during cooperative feature linking in a cortical model of visual perception. *Neural Netw.* 4, 453–466. doi: 10.1016/0893-6080(91)90041-3

Grossberg, S., and Versace, M. (2008). Spikes, synchrony, and attentive learning by laminar thalamocortical circuits. *Brain Res.* 1218, 278–312. doi: 10.1016/j.brainres.2008.04.024

Haenschel, C., Baldeweg, T., Croft, R. J., Whittington, M., and Gruzelier, J. (2000). Gamma and beta frequency oscillations in response to novel auditory stimuli: a comparison of human electroencephalogram (EEG) data with in vitro models. *Proc. Natl. Acad. Sci. U.S.A.* 97, 7645–7650. doi: 10.1073/pnas.120162397

Hafting, T., Fyhn, M., Molden, S., Moser, M. B., and Moser, E. I. (2005). Microstructure of a spatial map in the entorhinal cortex. *Nature* 436, 801–806. doi: 10.1038/nature03721

Hargreaves, E. L., Rao, G., Lee, I., and Knierim, J. J. (2005). Major dissociation between medial and lateral entorhinal input to dorsal hippocampus. *Science* 308, 1792–1794. doi: 10.1126/science.1110449

Hasselmo, M. E. (2005). What is the function of the hippocampal theta rhythm? — linking behavioral data to phasic properties of field potential and unit recording data. *Hippocampus* 15, 936–949. doi: 10.1002/hipo.20116

Henriksen, E. J., Colgin, L. L., Barnes, C. A., Witter, M. P., Moser, M. B., and Moser, E. I. (2010). Spatial representation along the proximodistal axis of CA1. *Neuron* 68, 127–137. doi: 10.1016/j.neuron.2010.08.042

Hermann, C. S., and Knight, R. T. (2001). Mechanisms of human attention: event-related potentials and oscillations. *Neurosci. Biobehav. Rev.* 25, 465–476. doi: 10.1016/s0149-7634(01)00027-6

Hikosaka, O., and Wurtz, R. H. (1985). Modification of saccadic eye movements by GABA-related substances. II. Effects of muscimol in monkey substantia nigra pars reticulate. *J. Neurophysiol.* 53, 292–308. doi: 10.1152/jn.1985.53.1.292

Hoang, T.-H., Aliane, V., and Manahan-Vaughan, D. (2018). Novel encoding and updating of positional, or directional, spatial cues are processed by distinct hippocampal subfields: evidence for parallel information processing and the "what" stream. *Hippocampus* 28, 315–326. doi: 10.1002/hipo.22833

Huang, T.-R., and Grossberg, S. (2010). Cortical dynamics of contextually cued attentive visual learning and search: spatial and object evidence accumulation. *Psychol. Rev.* 117, 1080–1112. doi: 10.1037/a0020664

Huerta, P. T., and Lisman, J. E. (1993). Heightened synaptic plasticity of hippocampal CA1 neurons during a cholinergically induced rhythmic state. *Nature* 364, 723–725. doi: 10.1038/364723a0

Ito, H. T., Moser, E. I., and Moser, M. B. (2018). Supramammillary nucleus modulates spike-time coordination in the prefrontal-thalamo-hippocampal circuit during navigation. *Neuron* 99, 576–587.e5. doi: 10.1016/j.neuron.2018.07.021

Jiang, Y., King, L. W., Shim, W. M., and Vickery, T. J. (2006). "Visual implicit learning overcomes limits in human attention," in *Proceedings of the 25th Army Science Conference (ASC 2006)*, Orlando, FL.

Kaplan, R., Doeller, C. F., Barnes, G. R., Litvak, V., Düzel, E., Bendettini, P. A., et al. (2012). Movement-related theta rhythm in humans: coordinating self-directed hippocampal learning. *PLoS Biol.* 10:e1001267. doi: 10.1371/journal.pbio.1001267

Kentros, C., Hargreaves, E., Hawkins, R. D., Kandel, E. R., Shapiro, M., and Muller, R. V. (1998). Abolition of long-term stability of new hippocampal place cell maps by NMDA receptor blockade. *Science* 280, 2121–2126. doi: 10.1126/science.280.5372.2121

Kentros, C. G., Agnihotri, N. T., Streater, S., Hawkins, R. D., and Kandel, E. R. (2004). Increased attention to spatial context increases both place field stability and spatial memory. *Neuron* 42, 283–295. doi: 10.1016/s0896-6273(04)00192-8

Kerr, K. M., Agster, K. L., Furtak, S. C., and Burwell, R. D. (2007). Functional neuroanatomy of the parahippocampal region: the lateral and medial entorhinal areas. *Hippocampus* 17, 697–708. doi: 10.1002/hipo.20315

Kleinfeld, D., Deschênes, M., and Ulanovsky, N. (2016). Whisking, sniffing, and the hippocampal θ-rhythm: a tale of two oscillators. *PLoS Biol.* 14:e1002385. doi: 10.1371/journal.pbio.1002385

Kleinfeld, D., Deschênes, M., Wang, F., and Moore, J. D. (2014). More than a rhythm of life: breathing is a bind of orofacial sensation. *Nat. Neurosci.* 17, 647–651. doi: 10.1038/nn.3693

Klink, R., and Alonso, A. (1997). Muscarinic modulation of the oscillatory and repetitive firing properties of entorhinal cortex layer II neurons. *J. Neurophysiol.* 77, 1813–1828. doi: 10.1152/jn.1997.77.4.1813

Knierim, J. J. (2015). The hippocampus. *Curr. Biol.* 25, R1116–R1121.

Koenig, J., Linder, A. N., Leutgeb, J. K., and Leutgeb, S. (2011). The spatial periodicity of grid cells is not sustained during reduced theta oscillations. *Science* 332, 592–595. doi: 10.1126/science.1201685

Kohonen, T. (1984). *Self-Organization and Associative Memory*. New York, NY: Springer Verlag.

Komisaruk, B. R. (1970). Synchrony between limbic system theta activity and rhythmical behavior in rats. *J. Comp. Physiol. Psychol.* 10, 482–492. doi: 10.1037/h0028709

Kramis, R., Vanderwolf, C. H., and Bland, B. H. (1975). Two types of hippocampal slow activity in both the rabbit and the rat: relations to behavior and effects of atropine, diethyl ether, urethane, and pentobarbital. *Exp. Neurol.* 49, 58–85. doi: 10.1016/0014-4886(75)90195-8

Krupic, J., Burgess, N., and O'Keefe, J. (2012). Neural representations of location composed of spatially periodic bands. *Science* 337, 853–857. doi: 10.1126/science.1222403

LaChance, P. A., Todd, T. P., and Taube, J. S. (2019). A sense of space in postrhinal cortex. *Science* 365:eaax4192. doi: 10.1126/science.aax4192

Landfield, P. W., McGaugh, J. L., and Tusa, R. J. (1972). Theta rhythm: a temporal correlate of memory storage processes in the rat. *Science* 175, 87–89. doi: 10.1126/science.175.4017.87

Langston, R. F., Ainge, J. A., Couey, J. J., Canto, C. B., Bjerknes, T. L., and Witter, M. P. (2010). Development of the spatial representation system in the rat. *Science* 328, 1576–1580.

Lape, R., and Nistri, A. (2000). Current and voltage clamp studies of the spike medium afterhyperpolarization of hypoglossal motoneurons in a rat brain stem slice preparation. *J. Neurophysiol.* 83, 2987–2995. doi: 10.1152/jn.2000.83.5.2987

Leutgeb, S., Leutgeb, J. K., Treves, A., Moser, M.-B., and Moser, E. I. (2004). Distinct ensemble codes in hippocampal areas CA3 and CA1. *Science* 305, 1295–1298. doi: 10.1126/science.1100265

Loomis, J. M., Klatzky, R. L., Golledge, R. G., and Philbeck, J. W. (1999). "Chapter 5: Human navigation by path integration," in *Wayfinding Behavior: Cognitive Mapping and Other Spatial Processes*, ed. R. G. Golledge (Baltimore, MD: The Johns Hopkins University Press), 125–151.

Lushchekina, E. A., Podreznaya, E. D., Lushchekin, V. S., Novototskii-Vlasov, V. Y., and Strelets, V. B. (2014). Comparative studies of EEG theta and gamma rhythms in normal children and children with early childhood autism. *Neurosci. Behav. Phsyiol.* 44, 902–908. doi: 10.1007/s11055-014-9999-x

MacDonald, C. J., Lepage, K. Q., Eden, U. T., and Eichenbaum, H. (2011). Hippocampal "time cells" bridge the gap in memory for discontiguous events. *Neuron* 71, 737–749. doi: 10.1016/j.neuron.2011.07.012

Macrides, F., and Chorover, S. L. (1972). Olfactory bulb units: activity correlated with inhalation cycles and odor quality. *Science* 175, 84–87. doi: 10.1126/science.175.4017.84

Macrides, F., Eichenbaum, H. B., and Forbes, W. B. (1982). Temporal relationship between sniffing and the limbic θ rhythm during odor discrimination reversal learning. *J. Neurosci.* 2, 1705–1717. doi: 10.1523/jneurosci.02-12-01705.1982

Madison, D. V., Lancaster, B., and Nicoll, R. A. (1987). Voltage clamp analysis of cholinergic action in the hippocampus. *J. Neurosci.* 7, 733–741. doi: 10.1523/jneurosci.07-03-00733.1987

Magee, J. C., and Johnston, D. (1997). A synaptically controlled, associative signal for Hebbian plasticity in hippocampal neurons. *Science* 275, 209–213. doi: 10.1126/science.275.5297.209

Maldonado, P. E., Friedman-Hill, S., and Gray, C. M. (2000). Dynamics of striate cortical activity in the alert macaque: II. Fast time scale synchronization. *Cereb. Cortex* 10, 1117–1131. doi: 10.1093/cercor/10.11.1117

Manns, J. R., Zilli, E. A., Ong, K. C., Hasselmo, M. E., and Eichenbaum, H. (2007). Hippocampal CA1 spiking during encoding and retrieval: relation to theta phase. *Neurobiol. Learn. Mem.* 87, 9–20. doi: 10.1016/j.nlm.2006.05.007

Markram, H., Helm, P. J., and Sakmann, B. (1995). Dendritic calcium transients evoked by single back-propagating action potentials in rat neocortical pyramidal neurons. *J. Physiol.* 485, 1–20. doi: 10.1113/jphysiol.1995.sp020708

Markram, H., Lübke, J., Frotscher, M., and Sakmann, B. (1997). Regulation of synaptic efficacy by coincidence of postsynaptic APs and EPSPs. *Science* 275, 213–215. doi: 10.1126/science.275.5297.213

McIlwain, J. T. (1986). Effects of eye position on saccades evoked electrically from superior colliculus of alert cats. *J. Neurophysiol.* 55, 97–112.

McNaughton, B. L., Battaglia, F. P., Jensen, O., Moser, E. I., and Moser, M. B. (2006). Path integration and the neural basis of the 'cognitive map'. *Nat. Rev. Neurosci.* 7, 663–678. doi: 10.1038/nrn1932

Mhatre, H., Gorchetchnikov, A., and Grossberg, S. (2012). Grid cell hexagonal patterns formed by fast self-organized learning within entorhinal cortex. *Hippocampus* 22, 320–334. doi: 10.1002/hipo.20901

Mishkin, M. (1982). A memory system in the monkey. *Philos. Trans. R. Soc. Lond. B Biol. Sci.* 298, 83–95.

Mishkin, M., Ungerleider, L. G., and Macko, K. A. (1983). Object vision and spatial vision: two cortical pathways. *Trends Neurosci.* 6, 414–417. doi: 10.1016/0166-2236(83)90190-x

Mitchell, S. J., Rawlins, J. N., Steward, O., and Olton, D. S. (1982). Medial septal area lesions disrupt theta rhythm and cholinergic staining in medial entorhinal cortex and produce impaired radial arm maze behavior in rats. *J. Neurosci.* 2, 292–302. doi: 10.1523/jneurosci.02-03-00292.1982

Montgomery, S. M., Betancur, M. I., and Buzsáki, G. (2009). Behavior-dependent coordination of multiple theta dipoles in the hippocampus. *J. Neurosci.* 29, 1381–1394. doi: 10.1523/jneurosci.4339-08.2009

Morris, R. G. M., and Frey, U. (1997). Hippocampal synaptic plasticity: role in spatial learning or the automatic recording of attended experience? *Proc. R. Soc. Lond. Ser. B Biol. Sci.* 352, 1489–1503. doi: 10.1098/rstb.1997.0136

Morris, R. G. M., Garrud, P., Rawlins, J. N. P., and O'Keefe, J. (1982). Place navigation impaired in rats with hippocampal lesions. *Nature* 297, 681–683. doi: 10.1038/297681a0

Muessig, L., Hauser, J., Wills, T. J., and Cacucci, F. (2015). A developmental switch in place cell accuracy coincides with grid cell maturation. *Neuron* 86, 1167–1173. doi: 10.1016/j.neuron.2015.05.011

Muller, R. A. (1996). A quarter of a century of place cells. *Neuron* 17, 813–822. doi: 10.1016/s0896-6273(00)80214-7

Müller, W., Misgeld, U., and Heinemann, U. (1988). Carbachol effects on hippocampal neurons in vitro: dependence on the rate of rise of carbachol tissue concentration. *Exp. Brain Res.* 72, 287–298.

Munoz, D. P., Dorris, M. C., Paré, M., and Everling, S. (2000). On your mark, get set: brainstem circuitry underlying saccadic initiation. *Can. J. Physiol. Pharmacol.* 78, 934–944. doi: 10.1139/y00-062

Munoz, D. P., and Wurtz, R. H. (1995a). Saccade-related activity in monkey superior colliculus. I, characteristics of burst and buildup cells. *J. Neurophysiol.* 73, 2313–2333. doi: 10.1152/jn.1995.73.6.2313

Munoz, D. P., and Wurtz, R. H. (1995b). Saccade-related activity in monkey superior colliculus. II, spread of activity during saccades. *J. Neurophysiol.* 73, 2334–2348. doi: 10.1152/jn.1995.73.6.2334

Näätänen, R., Gaillard, A. W. K., and Mäntysalo, S. (1978). Early selective attention effect on evoked potential reinterpreted. *Acta Psychol.* 42, 313–329. doi: 10.1016/0001-6918(78)90006-9

Näätänen, R., Simpson, M., and Loveless, N. E. (1982). Stimulus deviance and evoked potentials. *Biol. Psychiatry* 14, 53–98. doi: 10.1016/0301-0511(82)90017-5

Newman, E. L., Climer, J. R., and Hasselmo, M. E. (2014). Grid cell spatial tuning reduced following systemic muscarinic receptor blockade. *Hippocampus* 24, 643–655. doi: 10.1002/hipo.22253

Nilssen, E. S., Doan, T. P., Nigro, M. J., Ohara, S., and Witter, M. P. (2019). Neurons and networks in the entorhinal cortex: a reappraisal of the lateral and medial entorhinal subdivisions mediating parallel cortical pathways. *Hippocampus* 29, 1238–1254. doi: 10.1002/hipo.23145

Norman, G., and Eacott, M. J. (2005). Dissociable effects of lesions to the perirhinal cortex and the postrhinal cortex on memory for context and objects in rats. *Behav. Neurosci.* 119, 557–566. doi: 10.1037/0735-7044.119.2.557

O'Keefe, J., and Burgess, N. (2005). Dual phase and rate coding in hippocampal place cells: theoretical significance and relationship to entorhinal grid cells. *Hippocampus* 15, 853–866. doi: 10.1002/hipo.20115

O'Keefe, J., and Dostrovsky, J. (1971). The hippocampus as a spatial map. Preliminary evidence from unit activity in the freely-moving rat. *Brain Res.* 34, 171–175. doi: 10.1016/0006-8993(71)90358-1

O'Keefe, J., and Recce, M. L. (1993). Phase relationship between hippocampal place units and the EEG theta rhythm. *Hippocampus* 3, 317–330. doi: 10.1002/hipo.450030307

Olson, I. R., and Chun, M. M. (2002). Perceptual constraints on implicit learning of spatial context. *Vis. Cogn.* 9, 273–302. doi: 10.1080/13506280042000162

Palma, J., Grossberg, S., and Versace, M. (2012a). Persistence and storage of activity patterns in spiking recurrent cortical networks: modulation of sigmoid signals by after-hyperpolarization currents and acetylcholine. *Front. Comput. Neurosci.* 6:42. doi: 10.3389.fncom.2012.00042

Palma, J., Versace, M., and Grossberg, S. (2012b). After-hyperpolarization currents and acetylcholine control sigmoid transfer functions in a spiking cortical model. *J. Comput. Neurosci.* 32, 253–280. doi: 10.1007/s10827-011-0354-8

Park, E. H., Park, E. H., Dvorak, D., and Fenton, A. A. (2011). Ensemble place codes in hippocampus: CA1, CA3, and dentate gyrus place cells have multiple place fields in large environments. *PLoS One* 6:e22349. doi: 10.1371/journal.pone.0022349

Park, Y. H., Kim, J.-Y., Yi, S., Lim, J.-S., Jang, J.-W., Im, C.-H., et al. (2016). Transient global amnesia deteriorates the network efficiency of the theta band. *PLoS One* 11:e0164884. doi: 10.1371/journal.pone.0164884

Parron, C., and Save, E. (2004). Evidence for entorhinal and parietal cortices involvement in path integration in the rat. *Exp. Brain Res.* 159, 349–359. doi: 10.1007/s00221-004-1960-8

Pfaffman, C. (1955). Gustatory nerve impulses in rat, cat, and rabbit. *J. Neurophysiol.* 18, 429–440. doi: 10.1152/jn.1955.18.5.429

Pilly, P. K., and Grossberg, S. (2012). How do spatial learning and memory occur in the brain? Coordinated learning of entorhinal grid cells and hippocampal place cells. *J. Cogn. Neurosci.* 24, 1031–1054. doi: 10.1162/jocn_a_00200

Pilly, P. K., and Grossberg, S. (2013). Spiking neurons in a hierarchical self-organizing map model can learn to develop spatial and temporal properties of entorhinal grid cells and hippocampal place cells. *PLoS One* 8:e60599. doi: 10.1371/journal.pone.0060599

Pollen, D. A. (1999). On the neural correlates of visual perception. *Cereb. Cortex* 9, 4–19. doi: 10.1093/cercor/9.1.4

Pribe, C., Grossberg, S., and Cohen, M. A. (1997). Neural control of interlimb oscillations, II: biped and quadruped gaits and bifurcations. *Biol. Cybern.* 77, 141–152. doi: 10.1007/s004220050375

Rall, W. (1959). Branching dendritic trees and motoneuron membrane resistivity. *Exp. Neurol.* 1, 491–527. doi: 10.1016/0014-4886(59)90046-9

Rall, W. (1962). Electrophysiology of a dendritic neuron model. *Biophys. J.* 2, 145–167. doi: 10.1016/s0006-3495(62)86953-7

Rall, W. (1995). *The Theoretical Foundation of Dendritic Function: Selected Papers of Wilfrid Rall with Commentaries*, eds E. Segev, J. Rinzel, and G. M. Shepherd Cambridge, MA: MIT Press.

Ranade, S., Hangya, B., and Kepecs, A. (2013). Multiple modes of phase locking between sniffing and whisking during active exploration. *J. Neurosci.* 33, 8250–8256. doi: 10.1523/jneurosci.3874-12.2013

Rempel-Clower, N. L., Zola, S. M., Squire, L. R., and Amaral, D. G. (1996). Three cases of enduring memory impairment after bilateral damage limited to the hippocampal formation. *J. Neurosci.* 16, 5233–5255. doi: 10.1523/jneurosci.16-16-05233.1996

Rojas-Líbano, D., Wimmer del Solar, J., Aguilar-Rivera, M., Montefusco-Siegmund, R., and Maldonado, P. E. (2018). Local cortical activity of distant brain areas can phase-lock to the olfactory bulb's respiratory rhythm in the freely behaving rat. *J. Neurophysiol.* 120, 960–972. doi: 10.1152/jn.00088.2018

Saleem, A. B. (2019). Two stream hypothesis of visual processing for navigation in mouse. *Curr. Opin. Neurobiol.* 64, 70–78. doi: 10.1016/j.conb.2020.03.009

Sargolini, F., Fyhn, M., Hafting, T., McNaughton, B. L., Witter, M. P., Moser, M.-B., et al. (2006). Conjunctive representation of position, direction, and velocity in entorhinal cortex. *Science* 312, 758–762. doi: 10.1126/science.1125572

Schiller, P., and Stryker, M. (1972). Single-unit recording and stimulation in superior colliculus of the alert rhesus monkey. *J. Neurophysiol.* 35, 915–924. doi: 10.1152/jn.1972.35.6.915

Schmidt-Hieber, C., Toleikyte, G., Aitchison, L., Roth, A., Clark, B. A., Branco, T., et al. (2017). Active dendritic integration as a mechanism for robust and precise grid cell firing. *Nat. Neurosci.* 20, 1114–1121. doi: 10.1038/nn.4582

Semba, K., and Komisaruk, B. R. (1984). Neural substrates of two different rhythmical vibrissal movements in the rat. *Neuroscience* 12, 761–774. doi: 10.1016/0306-4522(84)90168-4

Sethumadhavan, N., Hoang, T.-H., Strauch, C., and Manahan-Vaughan, D. (2020). Involvement of the postrhinal and perirhinal cortices in microscale and macroscale visuospatial information encoding. *Front. Behav. Neurosci.* 14:556645. doi: 10.3389/fnbeh.2020.556645

Sheffield, M. E. J., and Dombeck, D. A. (2015). Calcium transient prevalence across the dendritic arbour predicts place field properties. *Nature* 517, 200–204. doi: 10.1038/nature13871

Silkis, I. G. (2008). A mechanism for influencing the septo-hippocampal theta rhythm by dopamine through the basal ganglia. *Neurochem. J.* 2, 157–163. doi: 10.1134/s1819712408030045

Sirota, A., Montgomery, S., Fujisawa, S., Isomura, Y., Zugaro, M., and Buzsáki, G. (2008). Entrainment of neocortical neurons and gamma oscillations by the hippocampal theta rhythm. *Neuron* 60, 683–697. doi: 10.1016/j.neuron.2008.09.014

Skaggs, W. E., McNaughton, B. L., Wilson, M. A., and Barnes, C. A. (1996). Theta phase precession in hippocampal neuronal populations and the compression of temporal sequences. *Hippocampus* 6, 149–172. doi: 10.1002/(sici)1098-1063(1996)6:2<149::aid-hipo6>3.0.co;2-k

Smythe, J. W., Colom, L. V., and Bland, B. H. (1992). The extrinsic modulation of hippocampal theta depends on the coactivation of cholinergic and GABA-ergic medial septal inputs. *Neurosci. Biobehav. Rev.* 16, 289–308. doi: 10.1016/s0149-7634(05)80203-9

Solstad, T., Boccara, C. N., Kropff, E., Moser, M.-B., and Moser, E. I. (2008). Representation of geometric borders in the entorhinal cortex. *Science* 322, 1865–1868. doi: 10.1126/science.1166466

Soltesz, I., and Losonczy, A. (2018). CA1 pyramidal cell diversity enabling parallel information processing in the hippocampus. *Nat. Neurosci.* 21, 484–493. doi: 10.1038/s41593-018-0118-0

Somjen, G. (1972). *Sensory Coding in the Mammalian Nervous System*. New York, NY: Meredith Corp.

Stensola, H., Stensola, T., Solstad, T., Frøland, K., Moser, M.-B., and Moser, E. I. (2012). The entorhinal grid map is discretized. *Nature* 492, 72–78. doi: 10.1038/nature11649

Stewart, M., and Fox, S. E. (1990). Do septal neurons pace the hippocampal theta rhythm? *Trends Neurosci.* 13, 163–168. doi: 10.1016/0166-2236(90)90040-h

Takakusaki, K. (2017). Functional neuroanatomy for posture and gait control. *J. Mov. Disord.* 10, 1–17. doi: 10.14802/jmd.16062

Terporten, R., Schoffelen, J.-M., Dai, B., Hagoort, P., and Kösem, A. (2019). The relation between alpha/beta oscillations and the encoding of sentence induced contextual information. *Sci. Rep.* 9:20255.

Thompson, L. T., and Best, P. J. (1990). Long-term stability of the place-field activity of single units recorded from the dorsal hippocampus of freely behaving rats. *Brain Res.* 509, 299–308. doi: 10.1016/0006-8993(90)90555-p

Tóth, K., Borhegyi, Z., and Freund, T. F. (1993). Postsynaptic targets of GABAergic hippocampal neurons in the medial septum-diagonal band of broca complex. *J. Neurosci.* 13, 3712–3724. doi: 10.1523/jneurosci.13-09-03712.1993

Tulving, E. (1972). "Episodic and semantic memory," in *Organization of Memory*, eds E. Tulving, and W. Donaldson (New York, NY: Academic press).

Tulving, E., and Thomson, D. M. (1973). Encoding specificity and retrieval processes in episodic memory. *Psychol. Rev.* 80, 352–373. doi: 10.1037/h0020071

van der Werf, Y. D., Witter, M. P., and Groenewegen, H. J. (2002). The intralaminar and midline nuclei of the thalamus. Anatomical and functional evidence for participation in processes of arousal and awareness. *Brain Res. Rev.* 39, 107–140. doi: 10.1016/s0165-0173(02)00181-9

van Strien, N. M., Cappaert, N. L. M., and Witter, M. P. (2009). The anatomy of memory: an interactive overview of the parahippocampal-hippocampal network. *Nat. Rev. Neurosci.* 10, 272–282. doi: 10.1038/nrn2614

Vanderwolf, C. H. (1969). Hippocampal electrical activity and voluntary movement in the rat. *Electroencephalogr. Clin. Neurophysiol.* 26, 407–418. doi: 10.1016/0013-4694(69)90092-3

Vanderwolf, C. H. (1988). Cerebral activity and behavior: control by central cholinergic and serotonergic systems. *Int. Rev. Neurobiol.* 30, 225–340. doi: 10.1016/s0074-7742(08)60050-1

Vertes, R. P., and Kocsis, B. (1997). Brainstem-diencephalo-septohippocampal systems controlling the theta rhythm of the hippocampus. *Neuroscience* 81, 893–926.

Walter, V. J., and Walter, W. G. (1949). The central effects of rhythmic sensory stimulation. *Electroencephalogr. Clin. Neurophysiol.* l, 57–86. doi: 10.1016/0013-4694(49)90164-9

Wang, W.-J. (2002). Pacemaker neurons for the theta rhythm and their synchronization in the septohippocampal reciprocal loop. *J. Neurophysiol.* 87, 889–900. doi: 10.1152/jn.00135.2001

Watanabe, M., and Munoz, D. P. (2010). Presetting basal ganglia for volitional actions. *J. Neurosci.* 30, 10144–10157. doi: 10.1523/jneurosci.1738-10.2010

Whishaw, I. Q., and Vanderwolf, C. H. (1973). Hippocampal EEG and behavior: changes in amplitude and frequency of RSA (theta rhythm) associated with spontaneous and learned movement patterns in rats and cats. *Behav. Biol.* 8, 461–484. doi: 10.1016/s0091-6773(73)80041-0

Wills, T. J., Barry, C., and Cacucci, F. (2012). The abrupt development of adult-like grid cell firing in the medial entorhinal cortex. *Front. Neural Circuits* 6:21. doi: 10.3389/fncir.2012.00021

Wills, T. J., Cacucci, F., Burgess, N., and O'Keefe, J. (2010). Development of the hippocampal cognitive map in preweanling rats. *Science* 328, 1573–1576. doi: 10.1126/science.1188224

Wilson, M. A., and McNaughton, B. L. (1993). Dynamics of the hippocampal ensemble code for space. *Science* 261, 1055–1058. doi: 10.1126/science.8351520

Winson, J. (1972). Interspecies differences in the occurrence of theta. *Behav. Biol.* 7, 479–487. doi: 10.1016/s0091-6773(72)80210-4

Winson, J. (1974). Patterns of hippocampal theta rhythm in the freely moving rat. *Electroencephalogr. Clin. Neurophysiol.* 36, 291–301. doi: 10.1016/0013-4694(74)90171-0

Winson, J. (1978). Loss of hippocampal theta rhythm results in spatial memory deficit in the rat. *Science* 201, 160–163. doi: 10.1126/science.663646

Yazdanbakhsh, A., and Grossberg, S. (2004). Fast synchronization of perceptual grouping in laminar visual cortical circuits. *Neural Netw.* 17, 707–718. doi: 10.1016/j.neunet.2004.06.005

Ziv, Y., Burns, L. D., Cocker, E. D., Hamel, E. O., Ghosh, K. K., Kitch, L. J., et al. (2013). Long-term dynamics of CA1 hippocampal place codes. *Nat. Neurosci.* 16, 264–266. doi: 10.1038/nn.3329

Zola-Morgan, S., Squire, L. R., and Amaral, D. G. (1986). Human amnesia and the medial temporal lobe region: enduring memory impairment following a bilateral lesion limited to field CA1 of the hippocampus. *J. Neurosci.* 6, 2950–2967. doi: 10.1523/jneurosci.06-10-02950.1986

**Conflict of Interest:** The author declares that the research was conducted in the absence of any commercial or financial relationships that could be construed as a potential conflict of interest.

*Copyright © 2021 Grossberg. This is an open-access article distributed under the terms of the Creative Commons Attribution License (CC BY). The use, distribution or reproduction in other forums is permitted, provided the original author(s) and the copyright owner(s) are credited and that the original publication in this journal is cited, in accordance with accepted academic practice. No use, distribution or reproduction is permitted which does not comply with these terms.*

frontiers in Neuroscience

BRIEF RESEARCH REPORT
published: 13 August 2021
doi: 10.3389/fnins.2021.655901

# Basal Synaptic Transmission and Long-Term Plasticity at CA3-CA1 Synapses Are Unaffected in Young Adult PINK1-Deficient Rats

*Adeel A. Memon[1,2,3,4], Micah E. Bagley[4], Rose B. Creed[1,3,4], Amy W. Amara[1,3,5], Matthew S. Goldberg[1,3,5] and Lori L. McMahon[1,3,4,5]**

[1] Department of Neurology, The University of Alabama at Birmingham, Birmingham, AL, United States, [2] Department of Neuroengineering, School of Engineering, The University of Alabama at Birmingham, Birmingham, AL, United States, [3] Center for Neurodegeneration and Experimental Therapeutics, The University of Alabama at Birmingham, Birmingham, AL, United States, [4] Department of Cell, Developmental, and Integrative Biology, The University of Alabama at Birmingham, Birmingham, AL, United States, [5] Department of Neurobiology, The University of Alabama at Birmingham, Birmingham, AL, United States

OPEN ACCESS

**Edited by:**
Mariangela Chisari,
University of Catania, Italy

**Reviewed by:**
Deanna L. Benson,
Icahn School of Medicine at Mount Sinai, United States
Cristian Ripoli,
Catholic University of the Sacred Heart, Italy

***Correspondence:**
Lori L. McMahon
mcmahon@uab.edu

**Specialty section:**
This article was submitted to Neurodegeneration, a section of the journal Frontiers in Neuroscience

**Received:** 19 January 2021
**Accepted:** 07 June 2021
**Published:** 13 August 2021

**Citation:**
Memon AA, Bagley ME, Creed RB, Amara AW, Goldberg MS and McMahon LL (2021) Basal Synaptic Transmission and Long-Term Plasticity at CA3-CA1 Synapses Are Unaffected in Young Adult PINK1-Deficient Rats. Front. Neurosci. 15:655901. doi: 10.3389/fnins.2021.655901

Loss of function mutations in PARK6, the gene that encodes the protein PTEN-induced kinase 1 (PINK1), cause autosomal recessive familial Parkinson's disease (PD). While PD is clinically diagnosed by its motor symptoms, recent studies point to the impact of non-motor symptoms, including cognitive dysfunction in the early pre-motor stages of the disease (Aarsland et al., 2004; Chaudhuri and Schapira, 2009). As the hippocampus is a key structure for learning and memory, this study aimed to determine whether synaptic transmission is affected at CA3-CA1 excitatory synapses in PINK1 knockout rats at an age when we recently reported a gain of function at excitatory synapses onto spiny projection neurons in the dorsal striatum (Creed et al., 2020) and when motor symptoms are beginning to appear (Dave et al., 2014). Using extracellular dendritic field excitatory postsynaptic potential recordings at CA3-CA1 synapses in dorsal hippocampus 4-to 5-month old PINK1 KO rats and wild-type littermate controls, we observed no detectable differences in the strength of basal synaptic transmission, paired-pulse facilitation, or long-term potentiation. Our results suggest that loss of PINK1 protein does not cause a general dysfunction of excitatory transmission throughout the brain at this young adult age when excitatory transmission is abnormal in the striatum.

**Keywords: Parkinson's disease, PINK1, hippocampus, CA3-CA1 synapses, long term plasticity, basal synaptic transmission**

## INTRODUCTION

Human Parkinson's disease (PD) affects a variety of brain regions, leading to multiple motor and non-motor symptoms. Cognitive impairment is a disabling non-motor symptom, and affects approximately 25% of newly diagnosed PD patients (Ibarretxe-Bilbao et al., 2012). As the disease advances, up to 80% of PD patients without prior cognitive dysfunction develop mild cognitive impairment (PD-MCI) and dementia (Hely et al., 2008). Consequentially cognitive deficits have important implications in the disease management. Unfortunately, there are no effective

therapeutic options available due to the incomplete understanding of underlying synaptic mechanisms leading to cognitive dysfunction.

In recent years, the field of movement disorders has evolved from the conventional idea that hippocampal dysfunction plays a minor role in PD, to one that now regards deficits in hippocampal synaptic plasticity to contribute significantly to memory loss in PD. This concept is supported by studies showing hippocampal atrophy in PD patients with impaired cognition (Camicioli et al., 2003; Bruck et al., 2004; Calabresi et al., 2013; Kandiah et al., 2014), and studies showing lower baseline volume in the CA1 hippocampal region accompanied by deficits in baseline attention in PD patients with MCI. Longitudinally, the decline in episodic memory appears to be associated with increasing atrophy of CA2-CA3 regions over 18 months (Foo et al., 2017). Thickness of hippocampal CA1 stratum pyramidale is also associated with episodic memory impairment in PD patients (Boentert, 2019). Importantly, in neurodegenerative diseases such as PD, synaptic transmission is negatively impacted prior to overt structural and behavioral abnormalities (Wishart et al., 2006; Raymond et al., 2011). Thus, exploration of changes in synaptic networks using preclinical models with a well-established timeline of motor deficits can provide insight into how relevant synaptic circuits are altered prior to and after motor symptoms appear.

In this study we leveraged the recently developed PD rat model with loss of function mutation in *PARK6*, the gene that encodes the protein PTEN-induced kinase 1 (PINK1) (Valente et al., 2004), to study hippocampal excitatory transmission. In humans, loss of function PINK1 mutations cause an autosomal recessive early-onset form of PD with clinical symptoms similar to idiopathic PD (Kasten et al., 2010). However, the mechanism by which PINK1 deficiency causes PD is unknown. Under physiological conditions, PINK1 is involved in many functions such as mitochondrial autophagy (Kane et al., 2014; Lazarou et al., 2015; Truban et al., 2017) and bioenergetics (Rango et al., 2020), maintenance of mitochondrial calcium homeostasis (Heeman et al., 2011), and misfolded protein clearance (Du et al., 2017), plus neuronal branching (Dagda et al., 2014), regulation of adaptive immunity (Matheoud et al., 2019) and neuroinflammation (Sliter et al., 2018). In a mouse model of Alzheimer's disease, PINK1 overexpression rescued impairments in hippocampal LTP (Du et al., 2017). However, in PINK1 KO mice, no changes were detected in hippocampal LTP (Feligioni et al., 2016). The occurrence of both motor and non-motor phenotypes in PINK1 KO rats, specifically at ages prior to reported nigral cell loss, prompted our investigation of possible impairments in hippocampal synaptic transmission. Using PINK1 KO rats, we explored how loss of PINK1 impacts synaptic function at hippocampal CA3-CA1 synapses as this region represents the primary experimental model for the synaptic changes underlying learning and memory. We chose to perform these experiments in rats at 4 to 5 months of age because our laboratory previously found striatal circuit dysfunction at this age when motor symptoms begin to appear but prior to the age when dopaminergic neuronal loss becomes apparent (Creed et al., 2020).

# MATERIALS AND METHODS

## Animals

PINK1 KO rats on a Long-Evans background were obtained from Horizon Discovery with a breeding license and bred in-house at the University of Alabama at Birmingham (UAB) to obtain homozygous PINK1 KO and wild-type (WT) littermate controls (Dave et al., 2014). All breeding and experimental procedures were performed per the National Institutes of Health Guide for the Care and Use of Laboratory Animals with prior review and approval by the UAB Institutional Animal Care and Use Committee. Rats were provided food and water *ad libitum,* maintained on a 12-h light/dark cycle with lights on at 6 AM, 22°C, 50% humidity, and all standard laboratory conditions. Male rats were housed in same-sex groups and aged to 4 to 5 months for all experiments.

## Slice Preparation

Between 7 and 9 am, rats were anesthetized using isoflurane, rapidly decapitated and brains removed. 400 μm thick coronal slices encompassing the dorsal hippocampus were prepared using a vibratome (Leica VT 1000P). For input-output (I/O) curves and paired-pulse ratio (PPR) experiments, slices were sectioned in ice-cold, high sucrose, artificial cerebrospinal fluid (aCSF) containing (in mM: 85.0 NaCl, 2.5 KCl, 4.0 $MgSO_4 \times 7\ H_20$, 0.5 $CaCl_2 \times 2\ H_20$, 1.25 $NaH_2PO_4$, 25.0 $NaHCO_3$, 25.0 glucose, 75.0 sucrose) to preserve neuronal health and limit excitotoxicity. For long-term potentiation experiments, slices were prepared in aCSF containing, in mM: [119.0 NaCl, 2.5 KCl, 1.3 $MgSO_4$, 2.5 $CaCl_2$, 1.0 $NaH_2PO_4$, 26.0 $NaHCO_3$, 11.0 Glucose (saturated with 95% O2, 5% CO2, pH 7.4)]. Before transferring to the recording chamber for electrophysiology experiments, slices were recovered in a submersion chamber for at least 60 min in regular aCSF.

## Electrophysiology

Extracellular field excitatory postsynaptic potentials (fEPSPs) were measured from the dendritic region of CA1 pyramidal cells following stimulation of CA3 Schaffer collateral axons in dorsal hippocampus. All data were acquired with an Axopatch 200B amplifier, Digidata 1440A, and data acquisition software pClamp 10 (Molecular Devices, San Jose, CA, United States). Correct electrode placement for baseline fEPSPs was confirmed by the generation of paired-pulse facilitation (PPF) characteristic of CA3-CA1 synapses (Wu and Saggau, 1994). Schaffer collaterals were stimulated using insulated twisted nichrome wire (A-M Systems, Inc., Seqium, WA, United States) or tungsten electrodes (FHC, Frederick Haer and Co, ME, United States) placed in CA1 stratum radiatum within 200–300 μm of an aCSF filled glass recording electrode. Baseline fEPSPs (∼50% of maximal response) were recorded by delivering 0.1 Hz stimulation for 100 μs to generate fEPSPs of ∼0.5 mV in amplitude.

Input/Output Curves (I/O) were obtained after a stable 10-min baseline recording. The curves were produced by gradually increasing the stimulus intensity in 10 μA increments until it reached 200 μA intensity, which generated the maximal fEPSP slope. Ten fEPSP events collected at a single stimulus

strength were averaged and plotted as a single fEPSP slope for each stimulus intensity. Data collected from multiple slices from an individual animal were averaged together to generate I/O curves representing the data from that single animal.

Paired-Pulse Ratio (PPR) was generated using pairs of stimuli delivered at inter-stimulus interval (ISIs) of 10, 20, 50, 150, 200, and 400 milliseconds (ms). The ratio was calculated by dividing the slope of the second event by the slope of the first event. Like I/O, data collected from multiple slices from an individual animal were averaged to represent data from that animal.

Long-term potentiation was induced following a 20-min stable baseline, using either eight bouts of theta-burst stimulation (strong TBS) or four bouts of theta-burst stimulation (weak TBS) with each round consisting of 5 pulses at 100 Hz repeated 10× at 200 ms intervals, and each bout separated by 20 ms (Barnes et al., 1996; Watabe and O'Dell, 2003; Kumar et al., 2007).

## Statistical Analysis

GraphPad Prism 8 software was used for all statistical analyses and graphing. The researcher performing the slice electrophysiology experiments was blind to genotype, which was disclosed only at the final analysis. All data were analyzed using Repeated measures two-way ANOVA or paired *t*-test as appropriate. All results are reported as mean ± SEM with significance set at a *p*-value of less than 0.05 (*).

# RESULTS

## Basal Synaptic Transmission Is Not Altered at CA3-CA1 Synapses in PINK1 KO Rats

We generated fEPSP I/O curves at CA3-CA1 synapses to determine whether maximal synaptic strength is decreased in PINK1 KO rats compared to WT littermate controls at 4 to 5 months of age. I/O curves were obtained by incrementally increasing stimulus intensity from 0 to 200 μA in 10 μA intervals (**Figure 1A**). We found no significant difference in basal synaptic transmission between the two genotypes ($p > 0.05$; Repeated measures two- way ANOVA, **Figure 1B**). This finding shows that synaptic connectivity in area CA1 is not altered by loss of PINK1 protein at 4 to 5 months of age, the same age at which we have reported heightened excitatory transmission in dorsal striatum (Creed et al., 2020).

## Paired-Pulse Ratio Is Normal in PINK1 KO Rats

Next, we measured the PPR, which is an indirect measure of presynaptic neurotransmitter release probability (Dobrunz and Stevens, 1997). Paired-pulse stimulation generates PPF at CA3-CA1 synapses, as these synapses have low initial release probability (Dobrunz and Stevens, 1997). We analyzed PPR at 10, 20, 50, 100, 150, 200, and 400 ms inter-stimulus interval (**Figure 2A**) and found no significant difference between genotypes at any inter-stimulus interval ($p > 0.05$, Repeated measures two- way ANOVA, **Figure 2B**).

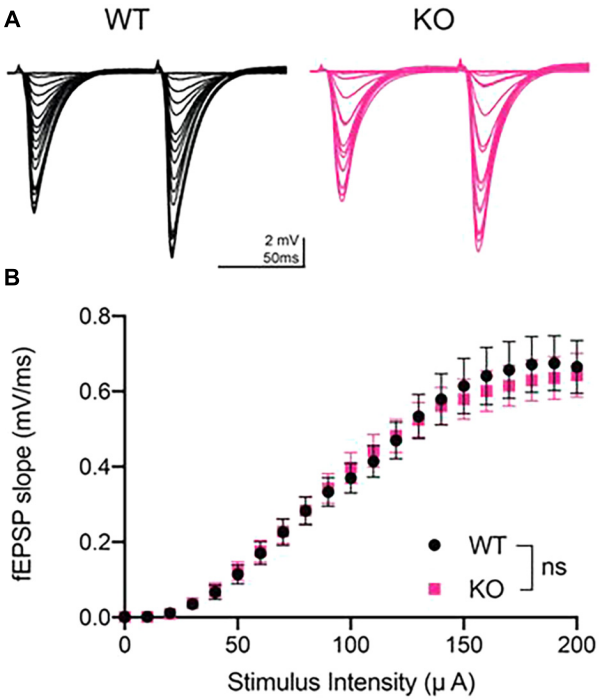


**FIGURE 1 |** Input/output curves showed no difference in basal synaptic strength at CA3-CA1 in PINK1 KO rats compared to WT littermate controls. **(A)** Representative fEPSP traces from 4 months WT (black) and PINK1 KO (Pink) rats. **(B)** After a stable 10 min baseline, input-output (I/O) curves were obtained by increasing the stimulus intensity (10 μA increments) until a maximal fEPSP slope was obtained, usually at 200 μA stimulus intensity. Initial slope of the ten fEPSPs generated at each stimulus intensity were averaged and plotted as a single value. No statistical difference ($p > 0.05$) was found after using repeated measures two-way ANOVA [$F_{(1,50)} = 0.01699$] at the maximal stimulus intensity between WT ($n = 26$ slices/11 animals) and PINK1 KO rats ($n = 26$ slices/11 animals).

## Long-Term Potentiation Is Not Different Between WT and PINK1 KO Rats

To determine the ability of CA3-CA1 synapses to undergo long-term plasticity at 4 to 5 months of age in PINK1 KO rats, we investigated LTP at CA3-CA1 synapses. Initially, we used a strong TBS stimulation to induce LTP. Comparison of averaged baseline fEPSP slope measured from last 6 sweeps of a stable 20 min recording to the averaged fEPSP slope from the last 6 sweeps at 60 min post-tetanus showed significant LTP in WT ($p = 0.0007$, paired *t*-test, $t = 5.301$, $df = 8$) and PINK1 KO ($p \leq 0.0001$, paired *t*-test, $t = 6.542$, $df = 12$) (**Figure 3** panel B3), with no significant differences in LTP magnitude between groups [$p > 0.05$, Repeated measures two-way ANOVA, $F(1,18) = 0.7216$, **Figure 3** panel B2]. To rule out the possibility that strong TBS might have masked a difference in LTP magnitude between the two groups, we next asked whether a difference could be observed using a weaker TBS stimulation. Comparison of baseline fEPSP slope measured at 20 min to the averaged fEPSP slope measured at 60 min post-weak TBS showed significant LTP in WT ($p \leq 0.0001$, paired *t*-test, $t = 6.366$, $df = 12$)

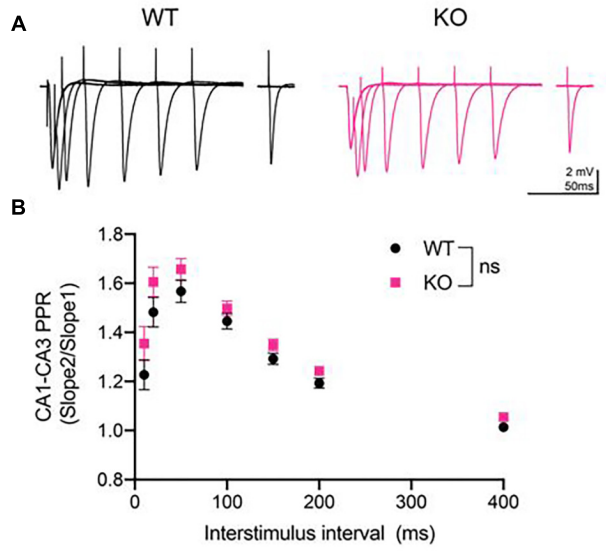


**FIGURE 2 |** Paired-pulse ratio (PPR) was unaltered at CA3-CA1 synapses in PINK1 KO rats compared to WT littermate controls. **(A)** Representative fEPSP traces from 4 months WT (black) and PINK1 KO (Pink) rats. **(B)** After a 10 min stable baseline, pairs of stimulation were delivered at 10, 20, 50, 150, 200, and 400 milliseconds (ms) inter-stimulus intervals (ISIs). PPR was calculated by dividing the initial slope of the first event. Repeated measures two-way ANOVA showed no statistical differences [$p > 0.05$, $F_{(1,54)} = 2.418$] between WT ($n = 26$ slices/11 animals) and PINK1 KO rats ($n = 26$ slices/11 animals).

and PINK1 KO ($p = 0.0002$, paired $t$-test, $t = 5.549$, $df = 10$) (**Figure 3** panel C3), with no significant differences in LTP magnitude between groups ($p > 0.05$; Repeated measures two-way ANOVA, $F$ (1,22) = 1.301, **Figure 3** panel C2). This suggests that there was no ceiling effect from strong TBS, confirming that long-term plasticity is not altered in PINK1 KO rats compared to WT littermates.

## DISCUSSION

The goal of this study was to determine whether hippocampal excitatory transmission in PINK1 KO rats is altered compared to WT rats at an age when motor and non-motor phenotypes are just appearing prior to reported nigral cell loss and when we have observed an increase in excitatory transmission in the dorsal striatum (Creed et al., 2020). We found no detectable changes in the strength of basal synaptic transmission, short-term presynaptic plasticity or LTP at CA3-CA1 synapses in PINK1 rats compared to WT rats. These results indicate that synaptic function is not significantly impacted by loss of PINK1 protein at this young adult age.

First, we investigated the strength of synaptic transmission at CA3-CA1 synapses by measuring maximum transmission using I/O curves and found no genotype differences. Similar results were observed in PINK1 KO mice where no change was observed in I/O curves at CA3-CA1 synapses in two and six-month-old animals. However, the frequency, but not amplitude, of spontaneous excitatory postsynaptic currents (sEPSCs) was increased at CA3-CA1 synapses at 6 months of age in PINK1 KO mice (Feligioni et al., 2016). This finding is similar to our finding of increased frequency and amplitude of spontaneous EPSCs recorded from striatal spiny projection neurons in PINK1 KO rats at 4 months of age, in the absence of a change in the corticostriatal I/O curve (Creed et al., 2020). In contrast to PINK1 KO rats, no difference was observed in PINK1 KO mice in the frequency or amplitude of spontaneous EPSCs or miniature EPSCs recorded from spiny projection neurons in dorsal striatum (Madeo et al., 2014). Further investigations of CA1 pyramidal neurons in PINK1 KO rats using whole-cell patch clamp is needed in future experiments to investigate whether there is a similar increase in frequency of spontaneous EPSCs, or other alterations in synaptic transmission not observed in the current study.

To determine if there was an alteration in presynaptic release probability, we measured the PPR and did not find any statistical difference between genotypes at any inter-stimulus interval. A similar result was reported in an analysis of PINK1 KO mice (Feligioni et al., 2016). Specifically, no changes in PPR between PINK1 KO and WT mice at 2 and 6 months of age was observed, although an increase in the frequency of the spontaneous EPSCs was found. The authors speculated that this effect on spontaneous EPSCs might be linked to increased presynaptic accumulation of alpha-synuclein. Previous studies from our lab and others reported the spontaneous appearance of proteinase K-resistant α-synuclein-immunoreactive aggregates in various brain regions of PINK1 KO rats, including cortex, thalamus, striatum, and ventral midbrain (Grant et al., 2015; Creed and Goldberg, 2018). Recently, using slice electrophysiology, we reported increased glutamate transmission onto dorsal striatum spiny projection neurons in PINK1 KO rats at 4 months of age (Creed et al., 2020). α-synuclein plays a vital role in the presynaptic mobilization of the reserve pool of neurotransmitter vesicles, not only for dopamine but also for glutamate (Gureviciene et al., 2007). Our inability to detect changes in short-term synaptic plasticity in acute hippocampal slices of PINK1 KO rats may be related to the apparent lack of α-synuclein pathology in this area at this age.

We found no impact of the loss of PINK1 on LTP induced either by strong or weak TBS at CA3-CA1 synapses. This suggests that these synapses do not differ in their ability to undergo long-term plasticity between the two genotypes, and there was no saturation effect from strong TBS. In transgenic mice expressing a 120 amino acid truncated form of α-synuclein, there is a reduction in striatal dopamine levels and impaired ability to generate hippocampal CA1 LTP (Tofaris et al., 2006; Costa et al., 2012). In both homozygous and heterozygous PINK1 KO mice, evoked dopamine release was decreased, leading to impaired corticostriatal LTP (Kitada et al., 2007; Madeo et al., 2014). Consistent with this, we have previously reported decreased dopamine tone in PINK1 KO rats at corticostriatal synapses at 4 months of age and decreased striatal dopamine levels at age 12 months compared to 4 months, measured using *in vivo* microdialysis (Creed et al., 2019; Creed et al., 2020). Because bidirectional plasticity

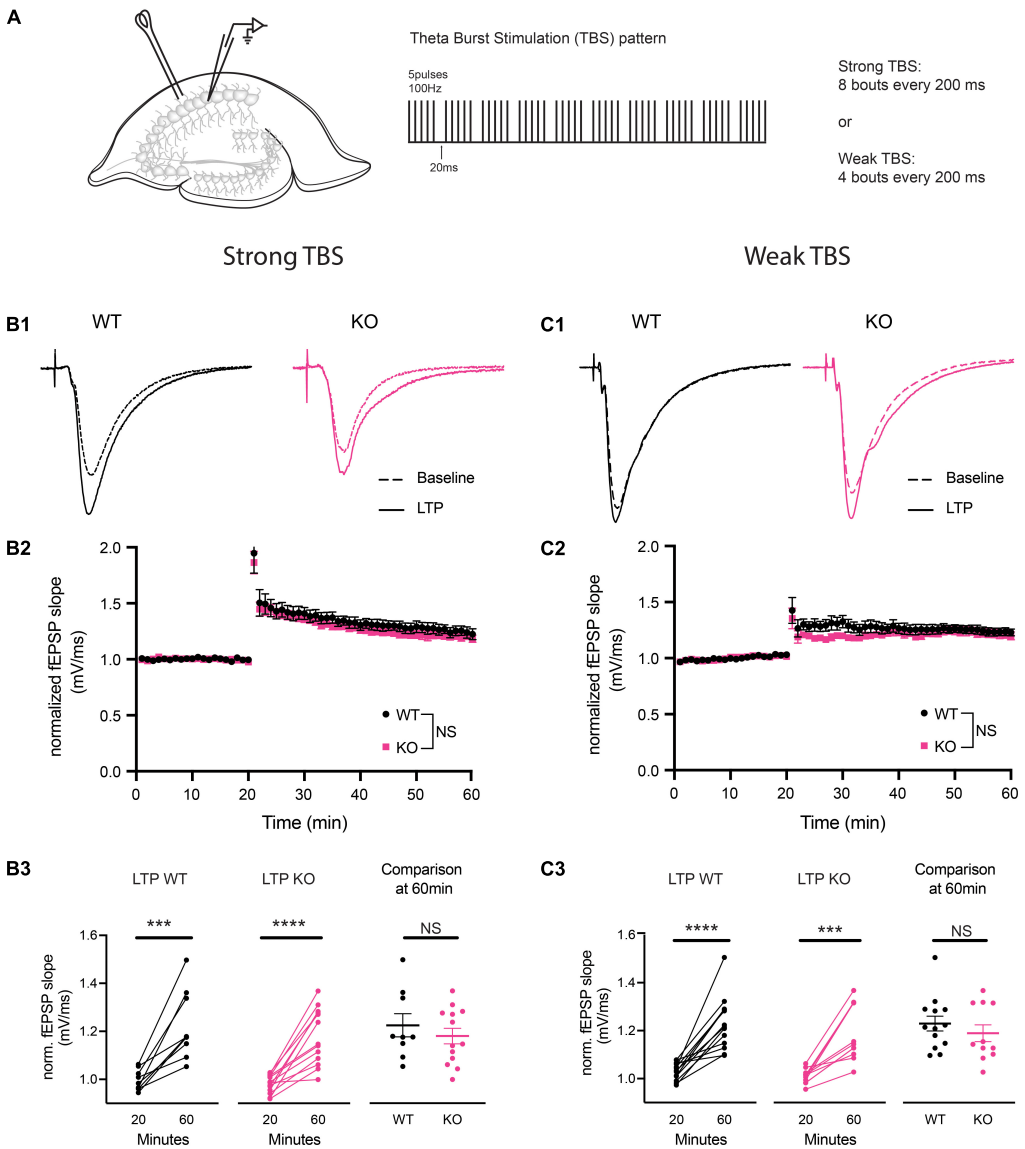


**FIGURE 3 |** Theta burst stimulation (TBS) induced long-term potentiation (LTP) was not different at CA3-CA1 synapses in PINK1 KO compared with WT littermate controls. **(A)** Schematic of stimulating and recording electrode in area CA1 of the hippocampus and the TBS pattern used to produce LTP (5 pulses of 100 Hz, each bout separated by 20 ms, repeated 10 times with 200 ms interstimulus interval). Initially, we performed LTP induction using a strong (8 bouts) TBS. To evaluate whether a strong TBS produced a ceiling effect at these synapses, we then induced LTP using a weak (4 bouts) TBS. Panels **(B1,C1)** show representative fEPSP traces from baseline and LTP induced by both strong and weak TBS from 4 months WT (black) and PINK1 KO (Pink) rats. Panels **(B2,C2)** show NMDA receptor (NMDAR) dependent LTP induction at CA3-CA1 synapses, following a 20 min stable baseline, using a strong TBS or a weak TBS. No statistical difference ($p > 0.05$) was found after using Repeated measures two-way ANOVA [strong TBS: $F(1,18) = 0.7216$; weak TBS: $F(1,22) = 1.301$] between WT littermate controls (strong TBS: $n = 9$ slices/6 animals; weak TBS: $n = 13$ slice/4 animals) and PINK1 KO rats (strong TBS: $n = 11$ slices/7 animals; weak TBS: $n = 11$ slices/3 animals). Panels **(B3,C3)** show comparison of fEPSP slope at 20 min baseline and 60 min post TBS successfully induced LTP in both WT (strong TBS: $p = 0.0007$, paired $t$-test, $t = 5.301$, $df$=8; weak TBS: $p = <0.0001$, paired $t$-test, $t = 6.366$, $df = 12$) and PINK1 KO (strong TBS: $p = <0.0001$, paired $t$-test, $t = 6.542$, $df = 12$; weak TBS: $p = 0.0002$ paired $t$-test, $t = 5.549$, $df = 10$) rats. However, no change was detected between WT and PINK1 KO rats when compared at 60 min post LTP induction (strong TBS: $p = 0.4299$; Unpaired Student's $t$-test, $t = 0.8056$, $df = 20$; weak TBS: $p = 0.3980$; unpaired Student's $t$-test, $t = 0.8619$, $df = 22$).

is critical for normal hippocampus dependent learning and memory (Wang et al., 2003), it will be important to determine in future studies whether LTD is intact at hippocampal excitatory synapses in PINK1 KO rats, and how loss of PINK1 during the aging process alters long-term plasticity that contributes to learning and memory.

In conclusion, this short report is the first hippocampal synaptic physiology study to investigate the impact of PINK1 deficiency in acute brain slices from PINK1 KO rats. By recording extracellular dendritic fEPSPs, we showed no early functional changes in mechanisms of short- and long-term plasticity as well as the strength of basal synaptic

transmission at CA3-CA1 hippocampal synapses. These results demonstrate that loss of PINK1 does not alter hippocampal synaptic plasticity at onset of both motor and non-motor phenotypes.

## DATA AVAILABILITY STATEMENT

The original contributions presented in the study are included in the article/supplementary material, further inquiries can be directed to the corresponding author/s.

## ETHICS STATEMENT

The animal study was reviewed and approved by the UAB Institutional Animal Care and Use Committee.

## AUTHOR CONTRIBUTIONS

AM conceptualized the study, performed the majority of the experiments and analyses, made the figures, and wrote the first draft of the manuscript. MB and RC performed some experiments, updated the figures, performed the statistics, and edited the manuscript. LM, AA, and MG conceptualized the study, reviewed, and edited the manuscript. All authors approved the submitted version.

## FUNDING

This study was supported by grants from the NIH/NINDS R25 NS079188 training award to AM, NIH/NINDS R01 NS082565 to MG, the Michael J. Fox Foundation for Parkinson's Research award 11380 to MG, and UAB Research Acceleration award to LM.

## REFERENCES

Aarsland, D., Andersen, K., Larsen, J. P., Wentzel-Larsen, T., Lolk, A., Kragh-Sørensen, P., et al. (2004). The rate of cognitive decline in Parkinson disease. *Arch. Neurol.* 61, 1906–1911.

Barnes, C. A., Rao, G., and McNaughton, B. L. (1996). Functional integrity of NMDA-dependent LTP induction mechanisms across the lifespan of F-344 rats. *Learn Mem.* 3, 124–137. doi: 10.1101/lm.3.2-3.124

Boentert, M. (2019). Sleep disturbances in patients with amyotrophic lateral sclerosis: current perspectives. *Nat. Sci. Sleep* 11, 97–111. doi: 10.2147/nss.s183504

Bruck, A., Kurki, T., Kaasinen, V., Vahlberg, T., and Rinne, J. O. (2004). Hippocampal and prefrontal atrophy in patients with early non-demented Parkinson's disease is related to cognitive impairment. *J. Neurol. Neurosurg. Psychiatry* 75, 1467–1469. doi: 10.1136/jnnp.2003.031237

Calabresi, P., Castrioto, A., Di Filippo, M., and Picconi, B. (2013). New experimental and clinical links between the hippocampus and the dopaminergic system in Parkinson's disease. *Lancet Neurol.* 12, 811–821. doi: 10.1016/s1474-4422(13)70118-2

Camicioli, R., Moore, M. M., Kinney, A., Corbridge, E., Glassberg, K., and Kaye, J. A. (2003). Parkinson's disease is associated with hippocampal atrophy. *Mov. Disord.* 18, 784–790. doi: 10.1002/mds.10444

Chaudhuri, K. R., and Schapira, A. H. (2009). Non-motor symptoms of Parkinson's disease: dopaminergic pathophysiology and treatment. *Lancet Neurol.* 8, 464–474. doi: 10.1016/s1474-4422(09)70068-7

Costa, C., Sgobio, C., Siliquini, S., Tozzi, A., Tantucci, M., Ghiglieri, V., et al. (2012). Mechanisms underlying the impairment of hippocampal long-term potentiation and memory in experimental Parkinson's disease. *Brain* 135(Pt. 6), 1884–1899.

Creed, R. B., and Goldberg, M. S. (2018). Analysis of alpha-synuclein pathology in PINK1 knockout rat Brains. *Front. Neurosci.* 12:1034. doi: 10.3389/fnins.2018.01034

Creed, R. B., Menalled, L., Casey, B., Dave, K. D., Janssens, H. B., Veinbergs, I., et al. (2019). Basal and evoked neurotransmitter levels in parkin, DJ-1, PINK1 and LRRK2 Knockout Rat Striatum. *Neuroscience* 409, 169–179. doi: 10.1016/j.neuroscience.2019.04.033

Creed, R. B., Roberts, R., Farmer, C., McMahon, L., and Goldberg, M. S. (2020). Increased glutamate transmission onto dorsal striatum spiny projection neurons in PINK1 knockout rats. *Neurobiol. Dis.* 150:105246. doi: 10.1016/j.nbd.2020.105246

Dagda, R. K., Pien, I., Wang, R., Zhu, J., Wang, K. Z., Callio, J., et al. (2014). Beyond the mitochondrion: cytosolic PINK1 remodels dendrites through protein kinase A. *J. Neurochem.* 128, 864–877. doi: 10.1111/jnc.12494

Dave, K. D., De Silva, S., Sheth, N. P., Ramboz, S., Beck, M. J., Quang, C., et al. (2014). Phenotypic characterization of recessive gene knockout rat models of Parkinson's disease. *Neurobiol. Dis.* 70, 190–203. doi: 10.1016/j.nbd.2014.06.009

Dobrunz, L. E., and Stevens, C. F. (1997). Heterogeneity of release probability, facilitation, and depletion at central synapses. *Neuron.* 18, 995–1008. doi: 10.1016/s0896-6273(00)80338-4

Du, F., Yu, Q., Yan, S., Hu, G., Lue, L. F., Walker, D. G., et al. (2017). PINK1 signalling rescues amyloid pathology and mitochondrial dysfunction in Alzheimer's disease. *Brain* 140, 3233–3251. doi: 10.1093/brain/awx258

Feligioni, M., Mango, D., Piccinin, S., Imbriani, P., Iannuzzi, F., Caruso, A., et al. (2016). Subtle alterations of excitatory transmission are linked to presynaptic changes in the hippocampus of PINK1-deficient mice. *Synapse* 70, 223–230. doi: 10.1002/syn.21894

Foo, H., Mak, E., Chander, R. J., Ng, A., Au, W. L., Sitoh, Y. Y., et al. (2017). Associations of hippocampal subfields in the progression of cognitive decline related to Parkinsons disease. *Neuroimage Clin.* 14, 37–42. doi: 10.1016/j.nicl.2016.12.008

Grant, L. M., Kelm-Nelson, C. A., Hilby, B. L., Blue, K. V., Paul Rajamanickam, E. S., Pultorak, J. D., et al. (2015). Evidence for early and progressive ultrasonic vocalization and oromotor deficits in a PINK1 gene knockout rat model of Parkinson's disease. *J. Neurosci. Res.* 93, 1713–1727. doi: 10.1002/jnr.23625

Gureviciene, I., Gurevicius, K., and Tanila, H. (2007). Role of alpha-synuclein in synaptic glutamate release. *Neurobiol. Dis.* 28, 83–89. doi: 10.1016/j.nbd.2007.06.016

Heeman, B., Van den Haute, C., Aelvoet, S. A., Valsecchi, F., Rodenburg, R. J., Reumers, V., et al. (2011). Depletion of PINK1 affects mitochondrial metabolism, calcium homeostasis and energy maintenance. *J. Cell Sci.* 124(Pt. 7), 1115–1125. doi: 10.1242/jcs.078303

Hely, M. A., Reid, W. G., Adena, M. A., Halliday, G. M., and Morris, J. G. (2008). The Sydney multicenter study of Parkinson's disease: the inevitability of dementia at 20 years. *Mov. Disord.* 23, 837–844. doi: 10.1002/mds.21956

Ibarretxe-Bilbao, N., Junque, C., Segura, B., Baggio, H. C., Marti, M. J., Valldeoriola, F., et al. (2012). Progression of cortical thinning in early Parkinson's disease. *Mov. Disord.* 27, 1746–1753. doi: 10.1002/mds.25240

Kandiah, N., Zainal, N. H., Narasimhalu, K., Chander, R. J., Ng, A., Mak, E., et al. (2014). Hippocampal volume and white matter disease in the prediction of dementia in Parkinson's disease. *Parkinson. Relat. Disord.* 20, 1203–1208. doi: 10.1016/j.parkreldis.2014.08.024

Kane, L. A., Lazarou, M., Fogel, A. I., Li, Y., Yamano, K., Sarraf, S. A., et al. (2014). PINK1 phosphorylates ubiquitin to activate Parkin E3 ubiquitin ligase activity. *J. Cell Biol.* 205, 143–153. doi: 10.1083/jcb.201402104

Kasten, M., Weichert, C., Lohmann, K., and Klein, C. (2010). Clinical and demographic characteristics of PINK1 mutation carriers–a meta-analysis. *Mov. Disord.* 25, 952–954. doi: 10.1002/mds.23031

Kitada, T., Pisani, A., Porter, D. R., Yamaguchi, H., Tscherter, A., Martella, G., et al. (2007). Impaired dopamine release and synaptic plasticity in the striatum

of PINK1-deficient mice. *Proc. Natl. Acad. Sci. U.S.A.* 104, 11441–11446. doi: 10.1073/pnas.0702717104

Kumar, A., Thinschmidt, J. S., Foster, T. C., and King, M. A. (2007). Aging effects on the limits and stability of long-term synaptic potentiation and depression in rat hippocampal area CA1. *J. Neurophysiol.* 98, 594–601. doi: 10.1152/jn.00249.2007

Lazarou, M., Sliter, D. A., Kane, L. A., Sarraf, S. A., Wang, C., Burman, J. L., et al. (2015). The ubiquitin kinase PINK1 recruits autophagy receptors to induce mitophagy. *Nature* 524, 309–314. doi: 10.1038/nature14893

Madeo, G., Schirinzi, T., Martella, G., Latagliata, E. C., Puglisi, F., Shen, J., et al. (2014). PINK1 heterozygous mutations induce subtle alterations in dopamine-dependent synaptic plasticity. *Mov. Disord.* 29, 41–53. doi: 10.1002/mds.25724

Matheoud, D., Cannon, T., Voisin, A., Penttinen, A. M., Ramet, L., Fahmy, A. M., et al. (2019). Intestinal infection triggers Parkinson's disease-like symptoms in Pink1(-/-) mice. *Nature* 571, 565–569. doi: 10.1038/s41586-019-1405-y

Rango, M., Dossi, G., Squarcina, L., and Bonifati, C. (2020). Brain mitochondrial impairment in early-onset Parkinson's disease with or without PINK1 mutation. *Mov. Disord.* 35, 504–507. doi: 10.1002/mds.27946

Raymond, L. A., Andre, V. M., Cepeda, C., Gladding, C. M., Milnerwood, A. J., and Levine, M. S. (2011). Pathophysiology of Huntington's disease: time-dependent alterations in synaptic and receptor function. *Neuroscience* 198, 252–273. doi: 10.1016/j.neuroscience.2011.08.052

Sliter, D. A., Martinez, J., Hao, L., Chen, X., Sun, N., Fischer, T. D., et al. (2018). Parkin and PINK1 mitigate STING-induced inflammation. *Nature* 561, 258–262. doi: 10.1038/s41586-018-0448-9

Tofaris, G. K., Garcia Reitbock, P., Humby, T., Lambourne, S. L., O'Connell, M., Ghetti, B., et al. (2006). Pathological changes in dopaminergic nerve cells of the substantia nigra and olfactory bulb in mice transgenic for truncated human alpha-synuclein(1-120): implications for Lewy body disorders. *J. Neurosci.* 26, 3942–3950. doi: 10.1523/jneurosci.4965-05.2006

Truban, D., Hou, X., Caulfield, T. R., Fiesel, F. C., and Springer, W. (2017). PINK1, parkin, and mitochondrial quality control: what can we learn about parkinson's disease pathobiology? *J. Parkinsons Dis.* 7, 13–29. doi: 10.3233/jpd-160989

Valente, E. M., Abou-Sleiman, P. M., Caputo, V., Muqit, M. M., Harvey, K., Gispert, S., et al. (2004). Hereditary early-onset Parkinson's disease caused by mutations in PINK1. *Science* 304, 1158–1160. doi: 10.1126/science.1096284

Wang, Z., Xu, N. L., Wu, C. P., Duan, S., and Poo, M. M. (2003). Bidirectional changes in spatial dendritic integration accompanying long-term synaptic modifications. *Neuron* 37, 463–472. doi: 10.1016/s0896-6273(02)01189-3

Watabe, A. M., and O'Dell, T. J. (2003). Age-related changes in theta frequency stimulation-induced long-term potentiation. *Neurobiol. Aging* 24, 267–272. doi: 10.1016/s0197-4580(02)00082-9

Wishart, T. M., Parson, S. H., and Gillingwater, T. H. (2006). Synaptic vulnerability in neurodegenerative disease. *J. Neuropathol. Exp. Neurol.* 65, 733–739. doi: 10.1097/01.jnen.0000228202.35163.c4

Wu, L. G., and Saggau, P. (1994). Presynaptic calcium is increased during normal synaptic transmission and paired-pulse facilitation, but not in long-term potentiation in area CA1 of hippocampus. *J. Neurosci.* 14, 645–654. doi: 10.1523/jneurosci.14-02-00645.1994

**Conflict of Interest:** The authors declare that the research was conducted in the absence of any commercial or financial relationships that could be construed as a potential conflict of interest.

**Publisher's Note:** All claims expressed in this article are solely those of the authors and do not necessarily represent those of their affiliated organizations, or those of the publisher, the editors and the reviewers. Any product that may be evaluated in this article, or claim that may be made by its manufacturer, is not guaranteed or endorsed by the publisher.

*Copyright © 2021 Memon, Bagley, Creed, Amara, Goldberg and McMahon. This is an open-access article distributed under the terms of the Creative Commons Attribution License (CC BY). The use, distribution or reproduction in other forums is permitted, provided the original author(s) and the copyright owner(s) are credited and that the original publication in this journal is cited, in accordance with accepted academic practice. No use, distribution or reproduction is permitted which does not comply with these terms.*

# Advantages of publishing in Frontiers

**OPEN ACCESS**
Articles are free to read for greatest visibility and readership

**FAST PUBLICATION**
Around 90 days from submission to decision

**HIGH QUALITY PEER-REVIEW**
Rigorous, collaborative, and constructive peer-review

**TRANSPARENT PEER-REVIEW**
Editors and reviewers acknowledged by name on published articles

**Frontiers**
Avenue du Tribunal-Fédéral 34
1005 Lausanne | Switzerland

**Visit us:** www.frontiersin.org
**Contact us:** frontiersin.org/about/contact

**REPRODUCIBILITY OF RESEARCH**
Support open data and methods to enhance research reproducibility

**DIGITAL PUBLISHING**
Articles designed for optimal readership across devices

**FOLLOW US**
@frontiersin

**IMPACT METRICS**
Advanced article metrics track visibility across digital media

**EXTENSIVE PROMOTION**
Marketing and promotion of impactful research

**LOOP RESEARCH NETWORK**
Our network increases your article's readership